NASA TECHNICAL MEMORANDUM

NASA TM X-53620

1967

NASA TM X-53620

RESEARCH ACHIEVEMENTS REVIEWS

VOLUME I

Series 1 through 22

RESEARCH AND DEVELOPMENT OPERATIONS
GEORGE C. MARSHALL SPACE FLIGHT CENTER
HUNTSVILLE, ALABAMA

GEORGE C. MARSHALL SPACE FLIGHT CENTER

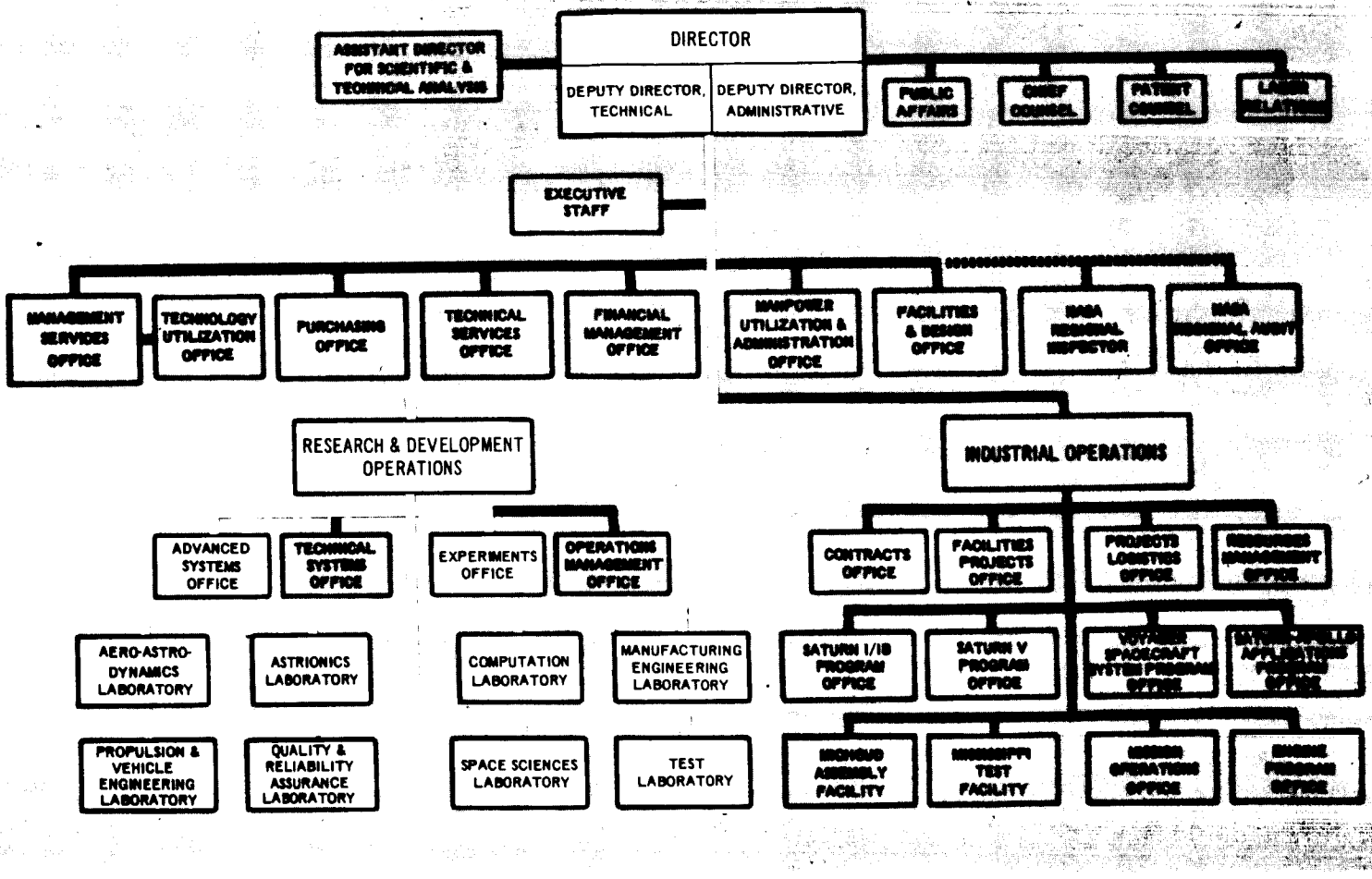

RESEARCH ACHIEVEMENTS REVIEWS COVER THE FOLLOWING FIELDS OF RESEARCH

- Radiation Physics
- Thermophysics
- Chemical Propulsion
- Cryogenic Technology
- Electronics
- Control Systems
- Materials
- Manufacturing
- Ground Testing
- Quality Assurance and Checkout
- Terrestrial and Space Environment
- Aerodynamics
- Instrumentation
- Power Systems
- Guidance Concepts
- Astrodynamics
- Advanced Tracking Systems
- Communication Systems
- Structures
- Mathematics and Computation
- Advanced Propulsion
- Lunar and Meteoroid Physics

967

NASA TM X-53620

RESEARCH ACHIEVEMENTS REVIEWS

VOLUME I

Research Program Office
Experiments Office
Research and Development Operations
George C. Marshall Space Flight Center
Huntsville, Alabama

For information concerning the Research Achievements Reviews, contact: Chief, Research Program Office, R-EO-R, Marshall Space Flight Center, Huntsville, Alabama.

PREFACE

In 1955, the team which has become the Marshall Space Flight Center (MSFC) began to organize a research program within its various laboratories and offices. The purpose of the program was two-fold: first, to support existing development projects by research studies, and second, to prepare future development projects by advancing the state-of-the-art of rockets and space flight. The effort during the first year was modest and involved relatively few tasks. The communication of results was, therefore, comparatively easy.

Today, more than ten years later, the two-fold purpose of MSFC's research program remains unchanged, but the present yearly effort represents major amounts of money and hundreds of tasks. The greater portion of the money goes to industry and universities for research contracts. However, a substantial research effort is conducted at the Marshall Center by all of the laboratories. The communication of the results from this impressive research program has become a serious problem by virtue of its very voluminous technical and scientific content.

A plan was initiated to give better visibility to the achievements of research at Marshall in a form readily usable by specialists, systems engineers, and program managers. This plan has taken the form of frequent Research Achievements Reviews, with each review covering selected fields of research. These verbal reviews are documented in the Research Achievements Review Series.

This volume is a compilation of the first series of Research Achievements Reviews which were held from February 25, 1965, through February 24, 1966. To make this volume complete, a summary has been prepared of the unclassified portions of Research Achievements Review No. 4. This review, which dealt with Chemical Propulsion, was not previously documented because of its classified content.

The Research Achievements Reviews are now in a second series. Seven reviews have already been held in this second series which, for reporting purposes, will extend from March 1966 through February 1968. Each of the reviews is being documented separately. When completed, the second series will also be reprinted in a single volume.

William G. Johnson
Director, Experiments Office

TABLE OF CONTENTS

RADIATION PHYSICS RESEARCH

by Russell D. Shelton

LIST OF ILLUSTRATIONS

LIST OF ILLUSTRATIONS (Concluded)

LIST OF TABLES

TABLE OF CONTENTS

RADIATION PHYSICS RESEARCH AT MSFC

February 25, 1965

by

Russell D. Shelton

CHEMICAL PROPULSION TECHNOLOGY RESEARCH AT MSFC

March 25, 1965

by

Keith B. Chandler
Richard N. Eilermann

Research Achievements Review No. 4 was comprised of two classified papers titled "Solid Propulsion Technology" (U) and "Liquid Propulsion Technology" (U). The following are reports that condense only the unclassified portions of the presentations.

RADIATION PHYSICS RESEARCH

By

Russell D. Shelton

Presented at Research Achievements Review
February 25, 1965

SUMMARY

The progress and scope of the radiation research program at MSFC is described in this report. The acquisition of radiation sources and radiation facilities by the several laboratories is reviewed. The several engineering efforts concerned with the effect of radiation on materials and components are discussed. In the Propulsion and Vehicle Engineering Laboratory, the emphasis is on the testing of materials under nuclear and space radiation environments. In the Astrionics Laboratory the interest is in the design and calibration of nuclear instruments for nuclear measurements and in the effects of radiation on electronic components. In the Research Projects Laboratory interest centers about the transport of nuclear radiation through shields; the penetration of charged particles such as electrons, protons, and alphas in various materials; the interaction of charged particles and electromagnetic fields; and electromagnetic shielding. Several engineering applications of radiation sources are discussed. These include devices for leak detection, liquid level, stage separation, and measurements.

References include the major MSFC research contracts and publications in the field of radiation physics. An appendix is also included listing current MSFC contracts in the field with a brief statement of the objectives of each contract.

GLOSSARY

Argus experiment	Explosion of nuclear device above the earth's atmosphere to test the feasibility of trapping electrons by the geomagnetic field.
Boltzmann transport equation	The fundamental equation describing the conservation of particles which are diffusing in a scattering, absorbing, and multiplying medium.
Bremsstrahlung	The process of producing electromagnetic radiation by the deceleration that a fast charged particle, such as an electron, undergoes when it is deflected by another charged particle, such as a nucleus.
Compton scattering	The elastic scattering of photons by electrons.
Coulomb field	The electric field produced by charged subatomic particles.
Cross section	A measure of the probability for collision reaction expressed in units of area.
Curie	A unit of radioactivity defined as the quantity of any radioactive nuclide in which the number of disintegrations per second is 3.700×10^{10}.
E	Denotes energy of a subatomic particle or electromagnetic radiation.
Elastic collision	A collision of particles in which the total kinetic energy of the particles remains unchanged.

Electrostatic shield	A shield based upon the principle of electrostatic repulsion of charged particles.
Faraday cup	A device for collecting electrons and integrating the charge thus produced.
Fast neutron	A neutron of relatively high energy.
FM	Abbreviation for frequency modulation.
Fluor	A device for producing light from electron bombardment.
Flux	The number of particles which traverse a unit area in a given unit of time.
G	Acceleration of the force of gravity.
Hard proton	A proton of relatively high energy.
Inelastic collision	A collision of particles in which the total kinetic energy of the system is reduced as a result of the collision.
Ion optics	The study of the behavior of ion beams under the influence of electric and magnetic fields.
Ionization	The process by which atoms in gases gain or lose electrons, usually through the agency of an electric discharge or the passage of radiation through the gas.
Linac	Abbreviation for linear accelerator.
Magnetic shield	A shield based upon the principle of charged particle deflections by a strong magnetic field.
MeV	The energy of a particle measured in millions of electron volts (1 Mev = 1.602×10^{-13} joule).
MHD	Abbreviation of magnetohydrodynamics, the study of electromagnetic fields with plasmas.
Monodirectional beam	A beam of particles all traveling in the same direction.
Monoenergetic beam	A beam of particles all having the same energy.
Monte Carlo	A numerical method used to obtain the solution of a group of physical problems by means of a series of statistical experiments. The statistical experiments are performed by applying mathematical operations to random numbers.
Mossbauer effect	The capability of a crystal lattice to absorb the momentum of a gamma emitted by one of the crystal atoms so that the gamma energy equals the energy between participating nuclear energy levels.
n, α reaction	A nuclear reaction, in which a neutron colliding with a nucleus produces a new nucleus and an alpha particle.
NERVA	Abbreviation for Nuclear Engine for Rocket Vehicle Application. A research and development program.
Orion	A nuclear propulsion system which uses the "shock" from small nuclear explosions to propel a spacecraft.
Outgas	The removal of impurities from the surface of a metal under the action of a high vacuum.
PAM	Abbreviation for Pulse Amplitude Modulation.
Pair production	The conversion of a photon into an electron and a positron (anticlectron) when the photon traverses a strong electric field.

Pegasus panels	Thin capacitor panels on the Pegasus satellite which are discharged when penetrated by micrometeoroids.
Plasma	A macroscopically neutral assembly of ions, electrons, neutral atoms, and molecules in which the motion of the particles is dominated by electromagnetic interaction
Potting compound	Encapsulating material used for environmental protection of electronic components and subsystems.
Quadrupole (axial, magnetic)	A magnetic field source composed of two coaxial, superimposed dipoles having opposed magnetic moments. A dipole field is generated by a closed current loop.
R	Roentgen - the quantity of gamma or X-radiation that produces an energy absorption of 83 ergs per gram of dry air.
Rad	Unit of radiation of absorption. One Rad is required to deposit 100 ergs per gram in any material by any kind of radiation.
Rest Mass	The mass of a particle measured in a frame of reference in which the particle is at rest.
RIFT	Abbreviation of Reactor in Flight Test.
Secondary particle	A particle produced by the interaction of a primary particle with matter.
Soft proton	A proton of relatively low energy.
Superconducting magnet	An electromagnet whose electric elements or wires are made from superconducting material. Superconductivity is the property of zero resistance possessed by some materials when cooled below a critical temperature, when the magnetic field and electric current are below critical values.
T-peel strength	Term used to denote resistance to separation of laminates of composite structures.
Thermionic diode	A vacuum tube consisting of two electrodes in which one of the electrodes is heated for the purpose of causing electron or ion emission.
Ω	Ohm, unit of electrical resistance.

I. INTRODUCTION

This report is concerned with electrons, protons, alphas, neutrons, and photons, the mass and charge characteristics of which are shown in Table I. Electrons are found in the radiation belts surrounding the earth and several other planets. In the case of the earth, electrons arise naturally from electromagnetic interactions and are injected heavily by high-altitude weapons testing. Electrons are also present in space as a relatively unimportant component of the cosmic rays and are emitted from many radioisotopes as beta rays.

TABLE I
PARTICLE RADIATIONS

Particle	Rest Mass*	Charge**
Electron	5.4860×10^{-4}	± 1
Proton	1.007277	+ 1
Alpha	4.00602	+ 2
Neutron	1.008665	0
Photon	0	0

* Unified atomic mass unit = 1.6604×10^{-27} kilograms

** Electronic charge unit = 1.6×10^{-19} coulombs.

Protons are present in large numbers in the radiation belts surrounding the earth and are the principal constituents of the cosmic rays and the energetic radiation resulting from solar flares. Alphas, much like protons, are important constituents of the radiation belts and the cosmic rays and were observed early in the emissions from radioisotopes. An alpha particle is a helium nucleus. Neutrons, which arise principally from fission reactions, decay with a lifetime of approximately 13 minutes into a proton, an electron, and a neutrino. Because of this short lifetime, neutrons are not an important constituent in space radiation. Energetic photons are sometimes called gammas, X rays, or bremsstrahlung, depending on their origin. As a rule, energetic charged particles are naturally present in space, whereas uncharged particles of interest in space shielding studies arise from the application of nuclear fission or radioisotope power.

With respect to radiation effects, all these particles can produce ionization, and the heavier particles -- protons, neutrons, and alphas -- are effective in displacing atoms from their proper locations in crystals and compounds. It is also possible for both the electron and the photon to produce atomic displacements. This ionization and atomic displacement can result in severe biological damage to living organisms -- from the simplest microscopic plant to man himself -- and can result in substantial changes in the properties of materials and components. Radiation shielding is concerned with stopping radiation by the interposition of matter and magnetic fields. Radiation effects are concerned with the changes which radiation causes in materials and components.

In several of our advanced propulsion concepts (e.g., RIFT, Orion, and nuclear electric space ships) propulsive power will be obtained from nuclear fission. Because of the anticipated use on Saturn-boosted experiments of some auxiliary power supplies built around reactors and radioisotopes, there is much interest in neutrons and gammas from the shielding and radiation effects point of view. The interest of NASA in booster systems and spacecraft which have prolonged lifetimes in the radiation belts and which travel through cislunar and interplanetary space has, in turn, stimulated interest in the electrons and protons captured in the radiation belts and associated with the solar flares and cosmic radiation. This interest is logically followed by an attention to methods of shielding against these particles, and the effects such particles have on materials and components. This interest in radiation is not restricted to speculative projects of the distant future. Current space projects such as Pegasus, Apollo, Gemini, and scientific payloads for R&D Saturns are making considerable demands on our knowledge of space radiation.

II. FACILITIES, PRESENT AND PLANNED

The disposition of radiation sources at MSFC is shown in Table II. This table is based on data from the MSFC Safety Office.

TABLE II
RADIATION ACTIVITY AT MSFC

AEC licenses	8*
Radioactive sources	31
Kinds of radioisotopes	12
Electron beam welders	5
X-ray units	20
Electron microscopes	2
Electron probe	1
Van de Graaff accelerators	1
X-ray spectrograph	1

* 10 AEC civil defense licenses not included.

Table III identifies most of the radioisotope users and their particular interests and is based on information furnished the AEC in their radioisotope licenses. Table IV lists some of the present, proposed, and possible uses of radioisotopes at MSFC. The development of instrumentation for radiation field housekeeping measurements on flight items such as RIFT and Pegasus requires a wide range of radiation sources for test and calibration. The use of radioisotopes for leak detection has already seen wide application at MSFC. The Mossbauer effect is observed with gamma-emitting isotopes in crystal form, and is very sensitive to relative motion between the radiation source and the radiation detector as well as to changes in gravitational potential. The inverse square law can also be used to advantage in indicating the position vector, the time derivative of which is velocity. Since radioisotope atoms decay randomly, the time intervals between successive decays are random in nature and can be used to generate random numbers.

The technique of radioisotope tracer chemistry has resulted in tremendous advances in biology and agriculture. The use of radioisotopes for wear studies on machinery and ablation studies on nose cones is already well known at MSFC.

TABLE III
RADIOISOTOPE USERS AT MSFC

User	No. of Sources	Purpose
A. M. Payne, R-TEST-IDT	16	Gas density measurements
H. D. Burke, R-ASTR-IMT	5	Instrument calibration and research
B. Corder, R-QUAL-AVR	3	Leak testing
A. Hafner, R-ASTR-IMP	2	Density measurements
J. Dabbs, R-ASTR-NGD	1	Teaching
R. Potter, R-RP-N	8	Electron density measurements
H. Hilker, R-QUAL	1	Leak testing
T. Knowling, R-P&VE-MEE	4	Instrument calibration

TABLE IV
USES OF RADIATION SOURCES

Design and calibration of radiation detectors	Random number generators
Leak detection	Tracer techniques
Velocity indication	Wear, Ablation, Flow rates, Chemical
Damage studies	and Biological processes
Materials	Solid state
Components	X-ray techniques
Radiation effects	Proton shield evaluation
Materials	Gas density measurements
Electronic components	Saturn V test stand checkout
Radiation research	Inspection of components
Shielding	Liquid level indicators
Activation	Disconnect signals

Radiation is generally damaging, but occasionally beneficial. These aspects will be discussed in more detail later. The fact that radiation is attenuated by matter makes it greatly convenient for measuring the presence or absence of matter, and it is widely used for this purpose in medical X-ray service, shield evaluation, gas density measurement, weld inspection, level indication, component inspection, etc. Radiation can also be used for shielding, activation, and solid-state research.

Almost every radioisotope source requires some facility for safety and ease of application. However, because of its versatility in producing all kinds of radiation, the Van de Graaff accelerator at the Propulsion and Vehicle Engineering Laboratory is of unusual interest. This instrument can be used to produce electrons, photons, protons, alphas, neutrons, and ions. When targets are bombarded and nuclear reactions induced, the energy spectrum of available particles extends much beyond the 2-MeV limitation imposed by the operating voltage. For example, the deuterium-tritium reaction, easily accessible to moderate-size accelerators, produces neutrons with energies above 14 MeV.

Another important facility will be the cobalt 60 gamma source planned by Astrionics Laboratory. One noteworthy feature of this facility is that the source operates constantly, and one should be able to perform an experiment without placing a large manpower demand on the facility custodian. Electrons and gammas are equivalent in many respects; this fact increases the value of the proposed gamma facility.

Figure 1 shows a layout of the Astrionics Laboratory radiation facility which is expected to be available in August 1965. This facility will eventually contain a 20,000-curie cobalt 60 gamma source which may be arranged to produce a uniform gamma exposure dose rate of 4×10^6 R/hr for instrument tests and calibration. Also available will be a one-kilocurie cesium 137 gamma source for instrument calibration in the intermediate energy range.

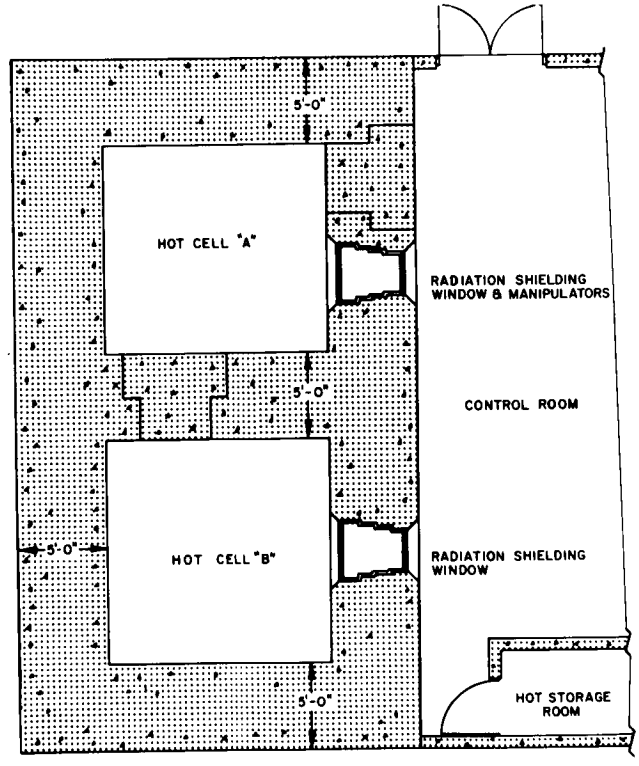

FIGURE 1. ASTRIONICS LABORATORY HOT CELL FACILITY

There is presently on hand the following equipment for the instrument calibration facility:

(1) A Neutron Generator - capable of producing 4×10^{10} fast neutrons/sec, a flux sufficient for the calibration and checkout of many of the RIFT neutron measuring instruments.

(2) An X-ray Generator - capable of producing up to 100 kv X rays for calibration of gamma-ray measuring instrumentation in the low-energy region.

(3) Other Equipment - including a variety of small calibration sources and manipulators by which an operator on the outside can arrange sources on the inside while he views the operation through glass shielding windows.

III. RADIATION EFFECTS ON MATERIALS

Radiation, because it produces ionization and displaces atoms, can change the basic properties of materials. In addition, neutron radiation can make materials radioactive [1], for the capture of a neutron by a nucleus creates a new isotope, which may be unstable. Radiation testing of materials is much like any other kind of environmental testing: good guesses can be based on experience, but confidence comes with testing.

In addition, one must consider interference effects such that changes resulting from environment are not simply additive. For example, the temperature may determine the rate at which a piece of optical glass discolors under irradiation, or the pressure and temperature may determine the rate at which a particular plastic outgases under irradiation. In other words, radiation is another environmental factor which must be considered, and it cannot be considered alone. Every imaginable engineering property of a material is subject to a possible synergistic and nonreversible environmental influence, and it takes a considerable test program systematically run to cover the material problems from the radiation viewpoint, where the radiation testing is only one aspect of a closely integrated materials testing program.

The Materials Division of the Propulsion and Vehicle Engineering Laboratory has promoted considerable testing of engineering materials at General Dynamics/Ft. Worth under various environmental combinations of nuclear radiation, vacuum, and cryotemperatures. These materials and tests included the types listed in Tables V and VI. The General Dynamics/Ft. Worth program [2] and the supporting work done in the Materials Division of the P&VE Laboratory at MSFC have produced an impressive amount of interesting and useful data.

TABLE V
ENGINEERING MATERIALS TESTED UNDER NUCLEAR RADIATION, VACUUM, AND CRYOGENIC ENVIRONMENTS

Adhesives
Seals
Thermal insulators
Electrical insulators
Structural laminates
Potting compounds
Sealants
Dielectrics
Lubricants
Thermal control coatings

TABLE VI
TYPICAL TESTS ON PREPARED SPECIMENS

Tensile-shear strength
Leakage
Ultimate tensile strength
Ultimate elongation
Stress-strain characteristics
Thermal conductivity
Pull-out strength of potted wire
T-peel strength

The Van de Graaff facility now being installed by the Materials Division will permit many of the same kind of engineering materials tests to be made at MSFC for electron, proton, ion, neutron, and gamma (bremsstrahlung) radiation. The ultraviolet environment can be included also in the present Van de Graaff facilities. The number of permutations of materials, tests, and environments is practically infinite, and all of them cannot be worked within any reasonable period of time. Therefore, the problem will be one of judicious selection of tests within the limitations of manpower and equipment.

Early work with the Van de Graaff will be directed toward establishing the realm of validity of the "equal energy-equal damage" theory which, if verified, would permit much broader application of data (such as that obtained at General Dynamics/Ft. Worth) to prediction of material behavior in the environment of space.

IV. ELECTRONIC COMPONENTS TESTING

The testing of electronic components in radiation fields received heavy emphasis from 1948-1958 as the Air Force pushed the development of the nuclear-powered airplane, and has continued since that time at a greatly reduced pace in the Air Force, AEC, NASA, and the Army. Many rules-of-thumb have been developed. Typical examples from the Astrionics Laboratory, which has been conducting a series of tests at the Lockheed-Georgia Nuclear Laboratory, will be shown.

As mentioned earlier in connection with materials testing, it is not practical to test everything under all possible conditions. From experience, one can design components to be more radiation resistant, but, as in any other environment, reliability is established only by testing. Since one cannot afford a test program which embodies the synergistic argument that whole systems must be tested, one must learn to look for the "weak links," or the components whose performance is likely to be marginal. Finally, a systems test under irradiation is done only after a thorough design (based on radiation resistant components). One may argue for going one step back and studying the materials from which components are made, and then using this materials knowledge to predict the performance of components, in the same way that one studies components to predict the performance of systems. This position is partially correct in that it is obvious that some materials must be avoided, and that it makes no sense to test components made of materials which are known to perform poorly in radiation fields. On the other hand, the materials engineer does not always understand electronic components well enough to know what the components require of the material.

The Astrionics Laboratory has taken the realistic approach that the radiation environment should be considered by each engineering specialist as another environmental factor affecting his particular kind of component [3]. This avoids the creation of a special group studying radiation effects in general without the motivation to solve specific problems. It also permits the specialist to be concerned with phenomena of interest to him. For example, solid-state devices show more sensitivity to total nuclear irradiation dose rate, whereas insulators for high-impedance circuits show important photoconductive and photovoltaic effects which depend on the dose rate.

In testing the effects of nuclear radiation on electronic components, commonly it is found that components which performed uniformly in other environments do not act uniformly under irradiation. This lack of

uniformity may be due to ordinarily insignificant variations in manufacturing processes or materials. This may mean that production processes must be more precisely defined and controlled if reliable components are to be obtained. This problem is illustrated in Figure 2.

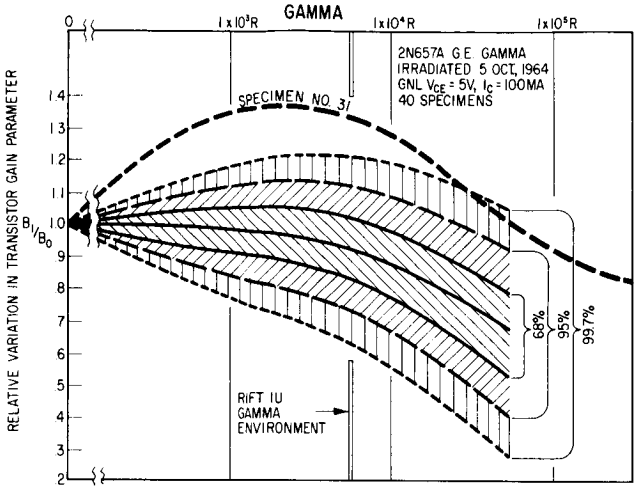

FIGURE 2. PERFORMANCE OF A GROUP OF TRANSISTORS UNDER GAMMA IRRADIATION

The design implications are evident when one asks what happens if the incompletely known component is used in a flight package on a vehicle subject to nuclear radiation. There are good empirical means for predicting the neutron damage to semiconductors, but the means for predicting gamma damage is less certain. The basis for this statement is that the principal effect of neutrons is the predictable production of lattice defects in semiconductor materials, whereas the effect of gamma action is not readily predictable because gamma rays interact with potting, mounting, and sealing materials, the composition and disposition of which are not always known or carefully controlled.

V. NUCLEAR INSTRUMENTATION

In the search for ways to determine vapor quality, gas density, liquid level, bubble inclusions in liquids and solids, etc., every promising physical phenomenon is usually explored [4-11]. Nuclear radiation techniques are often valuable, and the capability to use them and understand their limitations is associated closely with the attempt to develop nuclear instrumentation for nuclear vehicle housekeeping and radiation effects studies.

Radioisotope applications, radiation housekeeping on nuclear vehicles, and radiation testing of materials and components all require the understanding, development, and use of nuclear instrumentation to measure the radiation environment. The kind of radiation, the energy range, the directional distribution, and the application must be considered in selecting the detector or in designing the associated electronics and logic systems. If the radiation level is high, the radiation level can be measured by using the facts that radiation produces heat and that it considerably increases the conductivity of insulators such as air, methane, or polyethylene. If the radiation level is low or if the energy spectrum is of interest, one may look at the small electrical impulses available from individual particle tracks in crystals or gases or from nuclear reactions such as the (n, α) reaction in boron. When one deals with high-impedance input circuits and the statistics of random events, which is generally the case, the design of electronic and logic systems to feed into the telemetry is a challenge. Table VII shows some proposed requirements for instrument development for nuclear stage housekeeping [12]. The contents of the table represent a transition from a ground state of the art, which still contains many mysteries and uncertainties, to the constraints of flight.

TABLE VII
NEUTRON AND GAMMA SPECTROMETER SPECIFICATIONS FOR NUCLEAR STAGE HOUSEKEEPING

Time Response - Sufficient to follow propellant loss
Resolution - 8%, 0.1 < E < 14 MeV
Accuracy - Better than present state of the art
Output Impedance - 5000Ω
Restrictions - PAM/FM/FM, power, weight, volume allotments
Shock - 50 G

The statement on accuracy is reasonable, for there is considerable uncertainty in the absolute accuracy of many particle measurements, especially those concerning neutrons and gammas.

Moreover, even after the detector responses of a spectrometer are calibrated with monoenergetic, monodirectional streams of radiation, and test data are obtained, the energy spectrum is extracted only after considerable analysis and expenditure of computer time [13]. This aspect of nuclear instrumentation is often ignored.

VI. SHIELDING RESEARCH AT MSFC

Responsibility for the NASA space shielding effort rests mostly with the Office of Advanced Research Technology (OART), and MSFC participates heavily in this program from both the management and research points of view. Mr. Henry Stern and Mr. Martin Burrell of the Research Projects Laboratory are Center coordinators for the Radiation Shielding Information Center of the Oak Ridge National Laboratory (ORNL). Mr. Stern is also a member of the NASA Radiation Shielding Steering Committee, which has done much to bring professional responsibility to the NASA shielding interests, and which directs the million-dollar-a-year space shielding effort at ORNL.

Additionally some of the radiation shielding research supervised or performed at MSFC will be described in the following paragraphs.

A. PROTON SHIELDING

Solving the problem of shielding against charged particle radiation has many difficulties for several reasons: the high proton fluxes associated with solar flares have been unpredictable; the significance of biological effects of radiation is disputable; the secondary particle production by high-energy primary protons is poorly understood; and the methods available for making shielding calculations are not straightforward. With OART support, the Research Projects Laboratory has carried the major burden for NASA in its work on proton shielding.

Figure 3 shows how a typical solar flare proton energy spectrum is modified by successive layers of shielding [14]. Initially, the spectrum is highly peaked toward the low energy end, but the shielding quickly removes the softer protons. A little shielding is very effective, but better shielding comes at a much higher price after the spectrum has become hardened. Also, the dose from secondary particles becomes important for thick shields.

At one time, there was considerable fear that secondary gammas, caused by inelastic collisions of protons with nuclei, might contribute a significant fraction to the total dose. Experimental and theoretical results obtained recently [15] are compared in Figure 4.

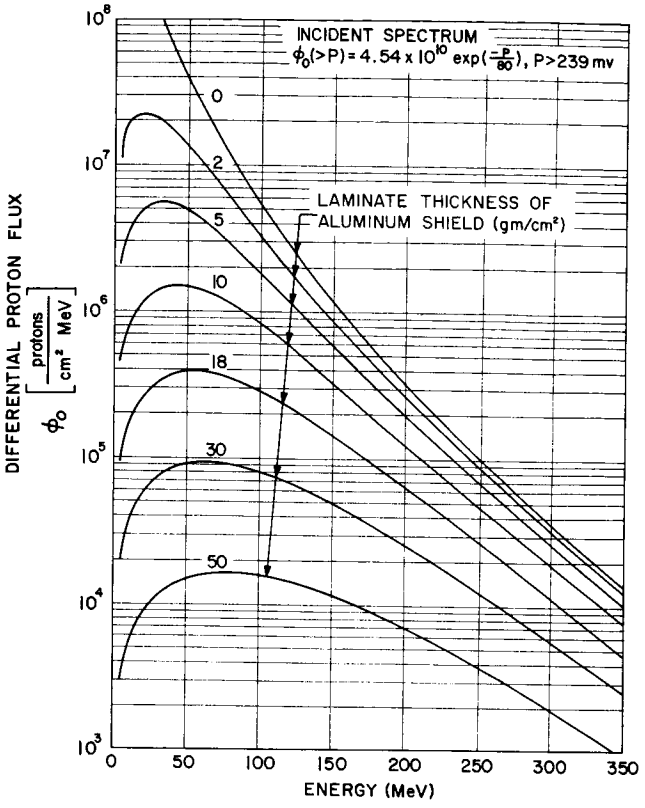

FIGURE 3. MODIFICATION OF SOLAR FLARE SPECTRUM BY SHIELDING

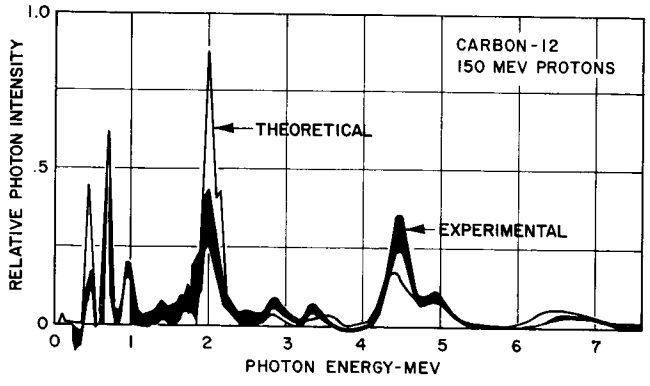

FIGURE 4. SPECTROMETER MEASUREMENTS VERSUS THEORETICAL CALCULATIONS FOR PROTON-INDUCED GAMMA RAYS

Exhibits like Figure 5 have done much to increase confidence and versatility in the analytical approach to the design of Apollo shields.

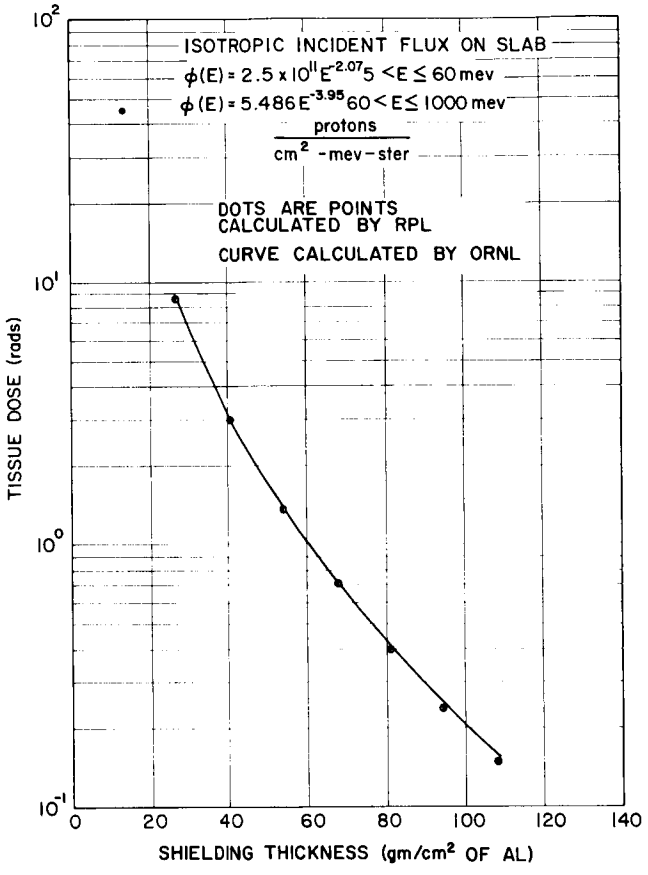

FIGURE 5. COMPARISON OF PROTON DOSE CALCULATIONS

These two curves compare a detailed numerical calculation of proton dose rates by Dr. Alsmiller [16] of ORNL with calculations made by Mr. M. O. Burrell [14] of Research Projects Laboratory, which use an analytical model developed for the dirty geometries of practical crew shields. Both primary and secondary radiations are considered.

Shielding studies for the Mobile Lunar Laboratory (MOLAB), conducted in-house, have shown the usefulness of efficient computer machine procedures for design studies [17]. Figure 6 shows a sample calculation.

These numbers are alarmingly high, because of the very thin MOLAB walls and the assumption of a solar flare with about a 0.01 probability of occurring in a two-week period.

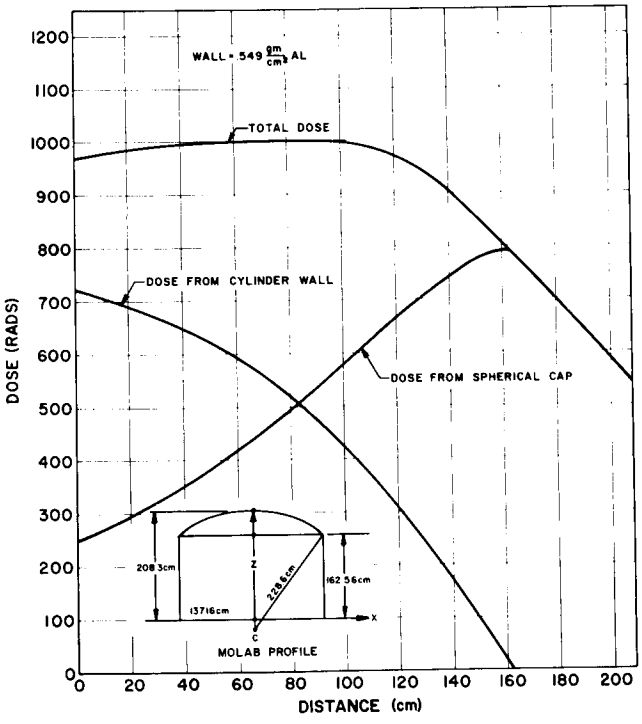

FIGURE 6. LUNAR SHELTER DOSES

Figure 7 shows the accumulated dose for a Mars mission [18].

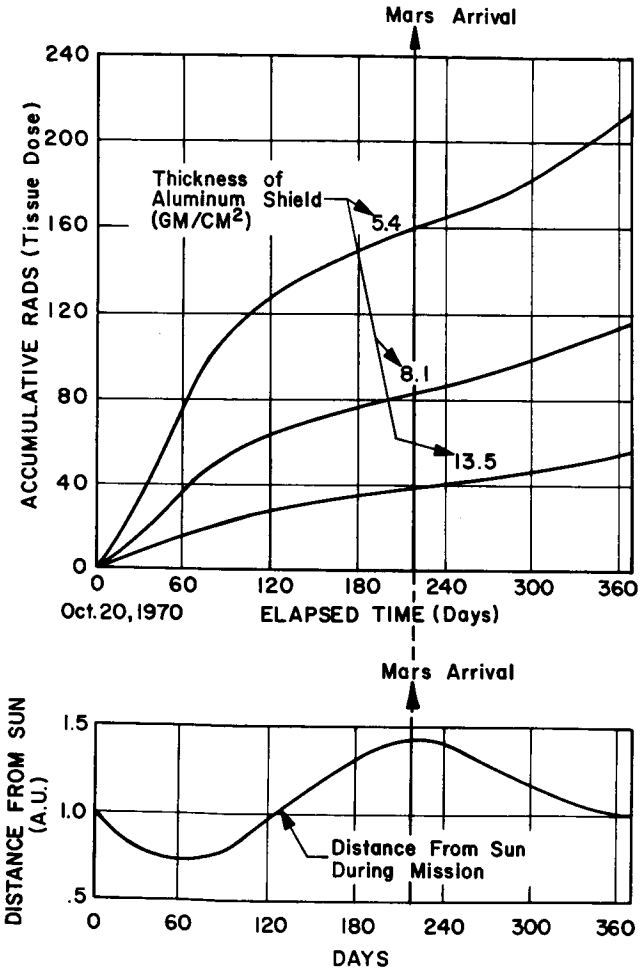

FIGURE 7. ACCUMULATIVE DOSE AT THE CENTER OF AN ALUMINUM SPHERE FROM SOLAR PROTONS AND COSMIC RAYS ON A MARS MISSION

The bottom chart shows the distance from the sun in astronomical units. These mission doses are time dependent. In Figure 8, the solid line represents an average of three possible dosages for the coming solar cycle.

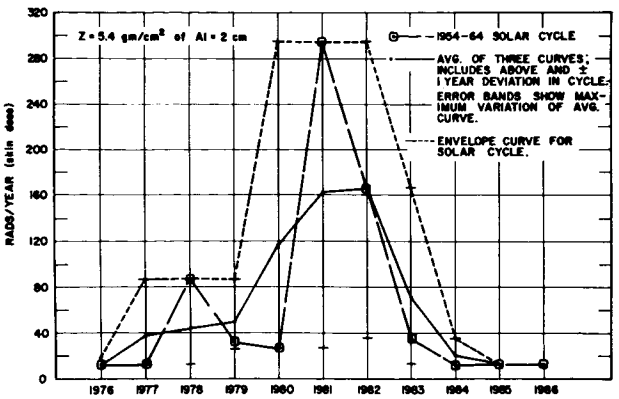

FIGURE 8. ANNUAL RADIATION DOSE AT CENTER OF 2-cm SPHERICAL SHELL FOR ONE-YEAR DEVIATIONS IN THE SOLAR CYCLE PERIOD OF 1954-1964

When the shield is heavily constrained by aerodynamic and structural considerations, the materials to be used and the methods of their distribution for a minimum weight shield are not immediately evident. Figure 9 shows an optimized shield for one configuration [19].

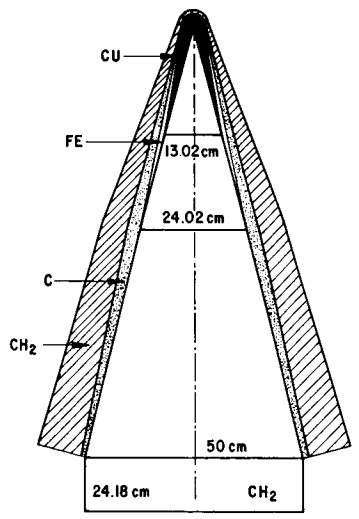

FIGURE 9. AN OPTIMIZED SHIELD IN THE SHAPE OF A REENTRY VEHICLE*

* Copper, Iron, Carbon and Polyethylene applied as shown in figure have been investigated in an optimized shield. Further details of this composite structure are given in United Nuclear Corp Report 5049 Page 37.

B. ELECTRON PENETRATION

Despite the fact that electron radiation in space is stopped well by a shield with a few kilograms of mass per square meter, there still are areas (listed in Table VIII) where electron problems arise.

TABLE VIII
ELECTRON INTERACTIONS OF IMPORTANCE

Damage to:
Solar cells
Surface coatings
Optics
People
Charge storage in :
Dielectrics
Spacecraft
Lunar dust
Astronaut suits
Transmission and scattering in :
Instrument design
Instrument calibration
Analysis of thin layers
Bremsstrahlung and X-ray production

In the protection of solar cells [20] against radiation trapped in the magnetic field of the earth, in the storage of charge in unshielded or partially shielded dielectrics [21], and in the damage to heat control and optical surfaces, electron radiation is an important consideration.

Presently, much ground testing of Pegasus panels is taking place with normally incident, monodirectional, monoenergetic electron streams. The electron spectrometer on Pegasus will yield crude measurements which will tell something about a radiation environment in which electrons are distributed widely in energy, direction, position, and time. For a derivation of meaningful results from the analysis of Pegasus data, there must be an analytical structure available for combining the satellite measurements with the ground data, and for determining with considerable confidence whether or not "hit" signals are to be interpreted as meteoroid penetrations.

For an interpretation of the results of instrument measurements, where calibrations are often extremely crude, considerable theoretical analysis of electron behavior is important. In some cases, after the satellite has flown, further studies on prototypes and spares have shown a remarkable state of uncertainty in the calibration of electron measuring instruments. For this and other reasons, we are trying to develop some capability of understanding how electrons interact with matter.

When an electron interacts with matter, it produces ionization by knocking electrons from their parent atoms and bremsstrahlung when the electron undergoes sudden changes in velocity. Because the electron has a relatively small mass, its path through matter is very erratic, and considerable straggling results. Table IX exhibits the fundamental processes of interest.

TABLE IX
ELECTRON COLLISION PROCESSES

Elastic collisions with free electrons
Inelastic collisions with attached electrons
Ionization
Interactions with nuclei
Bremsstrahlung
Atomic displacements
Bremsstrahlung reactions
Compton scattering
Photoelectric reaction
Pair production

The elastic interactions involve collisions between the impinging electrons and relatively unattached electrons in the target. The inelastic collisions are primarily collisions with electrons deep within the atom. These electrons have large binding energies, which must be supplied if the electron is to be removed. After collision, there is question as to which is the primary and which the secondary electron. When an electron feels the strong Coulomb field of the nucleus, it may undergo large angle scattering and bremsstrahlung emission. This bremsstrahlung interacts with matter to produce more energetic electrons by Compton collision, pair production, and photoelectric effects, and bremsstrahlung of lower energy.

Figure 10 shows the lack of careful experimental work in the energy ranges associated with electrons in space [22-25].

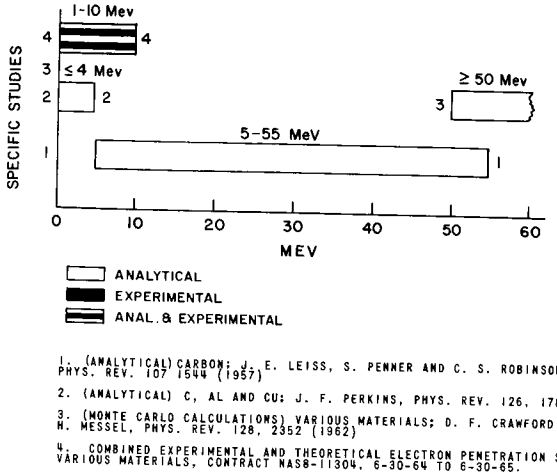

FIGURE 10. STUDIES OF ELECTRON PENETRATION OF MATERIALS IN ENERGY RANGES SHOWN

Figure 11 shows the experimental arrangement being used at General Dynamics/General Atomic (GD/GA) [26] under MSFC contract.

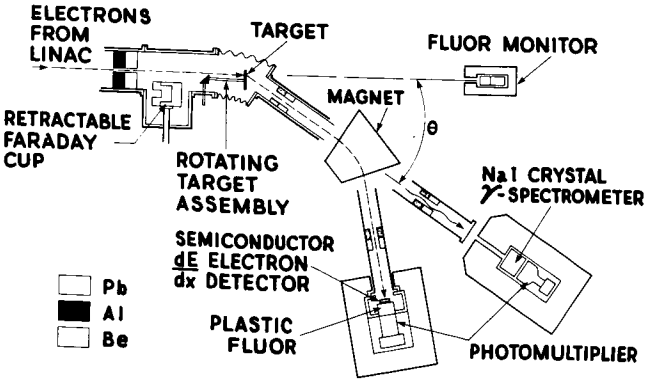

FIGURE 11. DIAGRAM OF FACILITIES FOR STUDYING ELECTRON INTERACTIONS

Electrons from the LINAC, a traveling wave accelerator, impinge on a thin target. The beam intensity is monitored by a retractable Faraday cup. Electrons and bremsstrahlung through an angle θ, which can be varied, are separated electromagnetically and resolved into directional and energy distributions. Later, thick targets will be used to test the transport methods with the basic data obtained from thin target studies.

Because of the broad application of the electron data and the fact that not enough careful experimental data exist, there is wide interest in the work at GD/GA, especially in the electron cross-section data which can be applied in analytical studies*. Table X lists a group of interested experts who are closely but informally associated in a cooperative program for computing electron cross sections. Naturally, they are intensely interested in finding out how accurate their application of the theory has been. There are many approximations and few exact calculations in nuclear physics, and for this reason those scientists involved in analytical and theoretical endeavors need something to check themselves with occasionally.

*In connection with "Electron Shielding Studies" [26], there exists a serious lack of cross-section data in the energy range of 1 to 10 MeV regarding the interaction of electrons with materials suitable for space shielding. On January 8, 1965, a meeting was held at the National Bureau of Standards by recognized leaders in the field (Table X) to discuss this problem. In general, this meeting concerned theoretical and experimental aspects of the electron problem. Dr. Edmonson suggested that an informal organization be formed. This group is being coordinated by Mr. Reetz (OART). Informal meetings will be held periodically to discuss progress.

TABLE X
INFORMAL GROUP STUDYING ELECTRON CROSS SECTIONS

Dr. Martin Berger	National Bureau of Standards
Dr. Nat Edmonson	MSFC/NASA
Dr. H. W. Koch	National Bureau of Standards
Dr. G. C. Pomraning	General Dynamics/General Atomic Corporation
Mr. Arthur Reetz	OART/NASA
Dr. Richard Scalletar	General Dynamics/General Atomic Corporation
Mr. Wayne Scott	Langley/NASA
Dr. Clayton Zerby	Union Carbide Research Institute

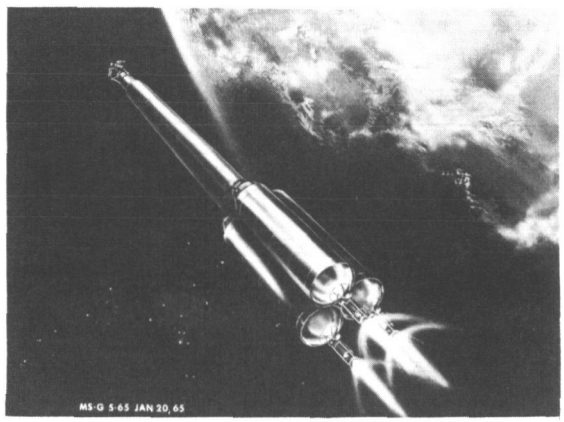

FIGURE 12. NUCLEAR STAGING OF MULTIPLE ENGINE CONCEPT FOR A MANNED MARS MISSION

C. NUCLEAR REACTOR RADIATION

The RIFT project found MSFC unprepared in several areas: there were not acceptable means for computing the neutron and gamma radiation fields in the vehicle; there were not enough data on the effects of nuclear radiation on materials and components; there was no capability for radiation environment housekeeping measurements; and there were many problems associated with launch facilities and operations. A lack of dependable knowledge generally results in enough overdesign to provide the necessary safety factors. Ideally, given a specific reactor and shield configuration, one would like to be able to specify accurately the neutron and gamma-ray dose rates at any location within or around the configuration, as well as the energy deposition or heating anywhere in the system, particularly in the liquid hydrogen storage tank and engine mounting structure.

To this end, a contract was awarded to General Dynamics/Fort Worth [27] to develop a fairly general computer program package capable of handling the complex geometries of a nuclear rocket system realistically and to calculate the above-mentioned data for stages such as the conception in Figure 12.

In addition, studies were performed in-house at MSFC to obtain efficient solutions to particular problems. For example, Martin Burrell, a member of the Nuclear and Plasma Physics Branch of RPL [28], developed some highly efficient machine calculation procedures to calculate the distribution of energy deposition in plane geometry or in a cylindrical tank of liquid hydrogen from a point source of neutrons or gamma rays located on the axis of the cylinder. By placing the point source at large distances from the tank bottom, a good approximation can be made to plane parallel beams of impinging radiation. The results obtained with these codes have become the standards against which more general programs can be checked, and the codes themselves have been used widely at other installations both within and outside NASA.

With the curtailment of the RIFT program, requirements for dose rate mapping around specific design configurations were eliminated. A reasonable course of action seemed to be to continue the development of a machine procedure designed specifically for nuclear stages, and to begin a comparison of some of the calculation methods currently available. This course of action appears advisable because, in spite of the fact that a large number of people have been seriously concerned with the problems of radiation transport and shielding for twenty years or so, there

are still many areas of inaccuracy and uncertainty. At the national meeting of the American Nuclear Society in November 1963 [29], the community of shielding analysts was rudely shaken by a report on a study performed to test the consistency of various shield calculation approaches. In this study, shielding people were invited to submit solutions to various standardized deep penetration problems, using any method of analysis they wished, and using the same basic input cross-section data. While it was known ahead of time that certain methods could not be expected to furnish good answers for large depths in thick shields, nonetheless it was not expected that some of the "old reliable" approaches would show considerable variances among themselves, and that overall discrepancies among all methods had existed in some cases for several decades. Thus, the problems of shielding analysis are today anything but trivial.

In an effort to shed further light on shielding analysis methods as applied to nuclear rocket systems, a contract for such study was awarded to the Lockheed-Georgia Company [30]. The approach taken in its work was to adopt simplified but fairly typical reactor and shield models and to try to calculate the pertinent radiation quantities employing several different methods. Figure 13 shows two such typical configurations. The sketches are sections of volumes of revolution.

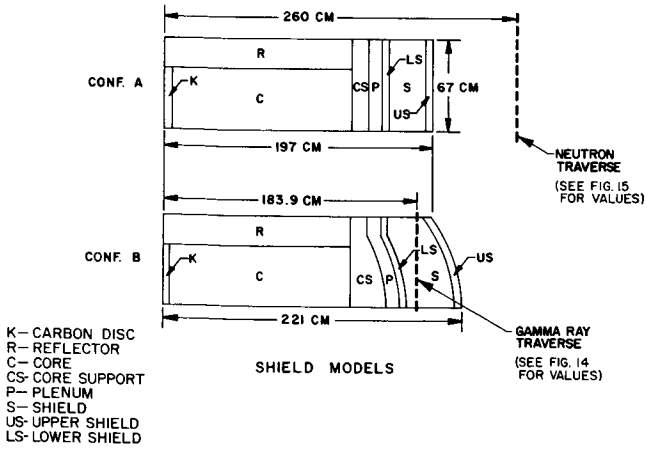

FIGURE 13. TYPICAL SHIELD CONFIGURATION MODELS A AND B

Following is a typical problem in radiation transport. For the reactor configuration shown in Figure 13, one wishes to obtain the neutron and gamma dose rates at arbitrarily selected points of interest. In this configuration the reactor materials may be divided into regions (in this case trapezoidal or quadric surfaces of revolution) and the determination of the transport of radiation through these sections can be managed analytically by a computer. In general, this is a tedious task of compilation from design drawings and machine programming. A machine procedure is chosen to compute the neutron and gamma fields, approximating the source of radiation as a set of discrete point sources within the reactor region. The two dotted vertical lines indicate the planes at which the data shown in Figures 14 and 15 were computed. Figure 14 shows a gamma-ray dose in configuration B as a function of radial distance in a plane within the shield assembly about 184 cm from the reference line. The curves are the result of two machine programs, both using "point kernel" or line-of-sight attenuation functions obtained from data computed in other programs.

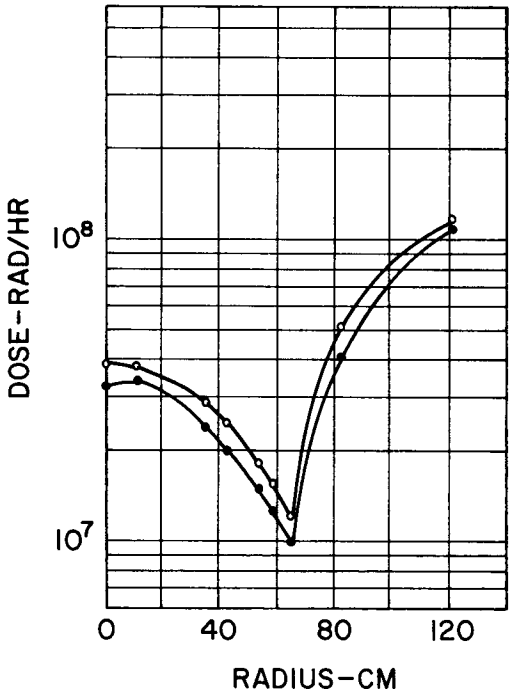

FIGURE 14. GAMMA DOSE TRAVERSES FOR CONFIGURATION B

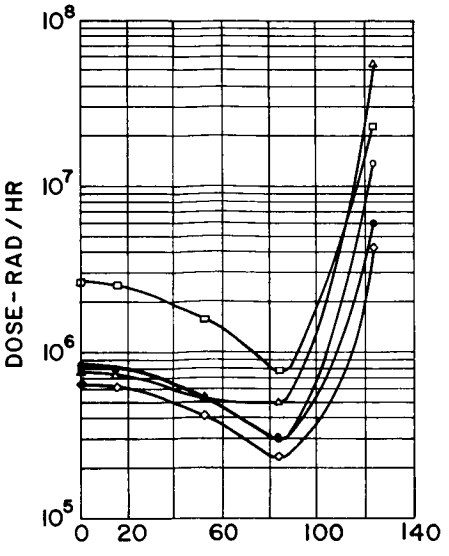

(SEE TRAVERSE AT 260cm IN FIG. 13)

KEY TO CALCULATION METHODS

∘ 14-O GENERAL ELECTRIC (Albert-Welton or Non-Hydrogenous)

LOS ALAMOS

- • QAD (Albert-Welton
- ◇ QAD (H_2O Moments)
- □ QAD (C Moments)
- △ DDK (Angular Segmentation

FIGURE 15. NEUTRON DOSE TRAVERSES FOR CONFIGURATION A

In addition, Lockheed has proposed a further study which would lead to the development of a special-purpose machine program utilizing the best features of the various programs now in existence and tailored specifically to nuclear rocket shielding systems. Consideration is being given to this proposal.

Although this work was done specifically for the case of neutrons and gammas arising from fissions in nuclear rocket reactors, the results should be useful for the treatment of neutrons and gammas resulting from the production of secondary radiation by high-energy protons impinging on thick shields.

D. PROTON SHIELD EVALUATION BY GAMMA TECHNIQUES

The first manned spacecraft to venture through the radiation belts into the solar proton storms and cosmic rays will not have much shielding versatility because of weight limitations. Nevertheless, the minimum hardware necessary for flight and reentry will have some shielding value, and some means of evaluating the shielding effectiveness of a complicated and inhomogeneous geometry is needed. There are those in NASA who feel that the analytical techniques are good enough to determine the material configurations from blueprints and make confident calculations of mission dose. Others in NASA feel that some experimental test of shielding effectiveness is needed.

It is unlikely that the time, money, and influence will be available to tie up the various proton accelerators in the country while spacecraft are rotated in a dispersed proton beam, and the energies are run up and down. Fortunately, the protons interact mostly with electrons, so if the electron density (expressed in electrons/cm^2 along the proton path) is known, dependable proton shielding calculations can be made. Fortunately also, the Compton collision probability when a gamma photon traverses a sheet of material is mostly a function of the electrons/cm^2 along the material path. Therefore, gamma rays can be used for proton shield evaluation. Ideally, the intensity of the gamma beam would be measured before and after traversing the shield, and the results fed directly into a computer along with a probable energy spectrum of protons, so that the expected mission dose through the crew shield under test would be read out immediately following the test.

In the simple configuration of Figure 16, one can imagine a stream of photons emanating from the source, traversing the shield, and resulting in pulse outputs through the detector and associated electronics. The unscattered photons produce bigger pulses because they suffer no energy loss by collisions. By counting these unscattered photons through techniques which discriminate against scattered photons, one can determine the number of electrons/cm^2 in the shield.

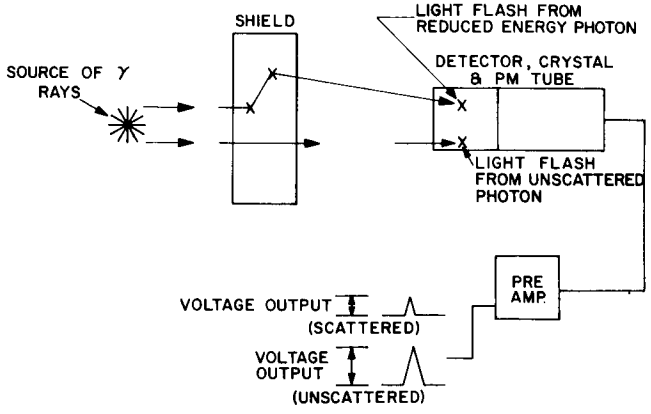

FIGURE 16. GAMMA EVALUATION OF PROTON SHIELDS

Table XI shows some of the possible parameters associated with this simple experiment. Research Projects Laboratory personnel are presently working experimentally to accumulate knowledge that will permit a best choice of parameters for a shield evaluation.

TABLE XI
IMPORTANT PARAMETERS OF THE GAMMA PROBE

Photon energy
Detector crystal size, shape, and composition
Source-detector-shield configuration
Kind of material
Pulse-height discrimination level
Scan rate
Usefulness of collimation
Detectable inhomogeneities

Mr. John Harris of MSC recently stated that the gamma probe, the study of which was initiated by MSFC with United Nuclear Corporation [31], will be used to evaluate Apollo shields. Command Module boiler plate 008 will be checked out at MSC in the first of such tests.

E. PLASMA PHYSICS

The starting point for neutron and gamma shielding calculations is the Boltzmann transport equation. Closely allied to it mathematically and physically are the Boltzmann-Vlasov, or collisionless Boltzmann equations, which govern the behavior of tenuous plasmas. In particular, the interaction of space plasmas and radiation, including charged particle motion in solar flares and in the Van Allen belts, is described by the Boltzmann-Vlasov equation. Table XII lists some of the problems which have design implications and which, it is hoped, will be treated by some of the techniques now under study.

Plasma physics activities in the Research Projects Laboratory (RPL) began with the Argus experiment [32, 33] and continued with studies of ion optics and charge neutralization in electric thrust devices [34-37]. Later, it was learned that the cesium plasma diode, a promising device for converting heat energy to electrical energy, was susceptible to similar theoretical treatment. During a visit to MSFC, Dr. Ralph Lovberg of Los Alamos Scientific Laboratory stated that he was very interested in some of the Research Projects Laboratory work because controlled

TABLE XII
PLASMA PHYSICS PROBLEMS

Ion optics
Charge neutralization
Thermionic diode
Plasma probes
Controlled thermonuclear reactions
Space experiments
Evaluation of propulsion schemes
Potentials on satellites and astronauts
Charged particle shielding

thermonuclear reaction diagnostics depended heavily on plasma probe measurements. Dr. Lovberg is co-author with Dr. Glasstone of a well-known text on controlled thermonuclear reaction [38]. Dr. Willard H. Bennett of North Carolina State College pointed out that a lot of papers based on satellite measurements with plasma probes had not been published because the experimental results could not be interpreted. The need to continue research in this field is apparent.

The basic problem is illustrated in Figure 17.

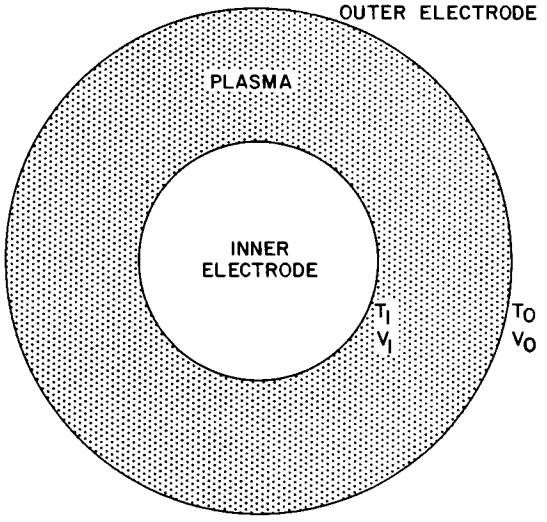

FIGURE 17. THE PLASMA PROBE PROBLEM

When a couple of electrodes are immersed in a plasma, it is desirable to relate currents through the plasma to temperatures and potentials on the boundaries and to intrinsic properties of the plasma. The inner electrode may be part of a plasma probe, the inside of a thermionic converter in a reactor, a satellite, or an astronaut. The outer electrode may be at infinity. The geometry for many practical problems may be more irregular than is pictured.

In trying to solve this classical and ubiquitous problem, Dr. Seitz [39] of RPL is attempting to remove the computer bottleneck by developing a new self-programming computer procedure designed for scientists and engineers. This will enable them to juggle the machine program to suit the boundaries or iterations of the kind of problem that requires an experimental approach with the scientists in the loop. The programming is done in normal mathematical format with buttons labeled in the notation of classical analysis. Visual displays of solutions and stylus inputs will be available.

This work provides exciting possibilities for our theoreticians, and has been most generously supported by the Computation Laboratory of MSFC, which, of course, has a much broader interest than that of merely solving plasma physics and shielding problems. One of the National Academy of Sciences (NAS) postdoctorate fellows at MSFC, Dr. Juris Reinfelds, is intensely interested in the on-line self-programming procedure for some of his quantum field theory problems.

F. ELECTROMAGNETIC SHIELDING STUDIES

The purpose of electromagnetic shielding studies is to obtain lighter shields for charged particles through the use of the principle that particles are susceptible to electromagnetic forces. For the design of effective electromagnetic shields, there is a need for more knowledge about particle behavior in electromagnetic fields for spacecraft use.

Considerable study has indicated that electrostatic shields alone are not feasible. Magnetostatic shields, operating on the principle that charged particles behave diamagnetically, may be useful. Electromagnetic shields, using both electric and magnetic fields, show promise in weight reduction, provided instabilities similar to those discovered earlier in the controlled thermonuclear reaction works do not occur. In all cases, the advantages of electromagnetic shields become more evident for large shielded volumes and for protection against high-energy radiation.

1. Charged Particle Motion. The behavior of charged particles in electromagnetic fields has been the subject of classical studies by Störmer, Alfvén, and many other physicists interested in cosmic rays, particle accelerators, and electronic devices. In order to estimate cosmic ray dose in low-earth orbits and to evaluate magnetic shielding configurations, RPL personnel have done considerable in-house study of particle distributions in axially symmetric magnetic fields. Figure 18 [40] shows the regions where particles with various impact parameters, γ, can be found in the neighborhood of a magnetic quadrupole located at the origin. The concept of allowed and forbidden regions of velocity space has been extended so that, at a given point in coordinate space, permissible energies and directions for charged particle radiations can be determined.

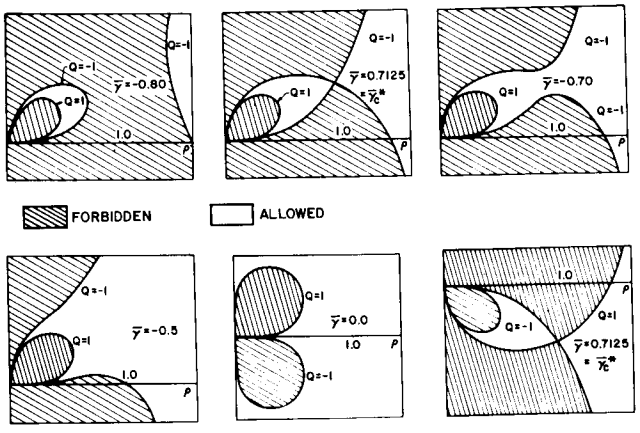

FIGURE 18. REGIONS ALLOWED AND FORBIDDEN TO CHARGED PARTICLES MOVING IN THE FIELD OF AN AXIAL MAGNETIC QUADRUPOLE

2. Development of Superconducting Magnets. Electromagnetic shields require large volumes filled with magnetic fields, and superconducting magnets [30] appear to be the only way to achieve these fields. Large magnetic fields are also of major importance to the containment of fusing materials in controlled thermonuclear reactions, MHD thrust and power generation devices, and many scientific experiments in a variety of areas.

Figure 19 shows the state of the art for superconducting magnets in the summer of 1964. The shaded area to the right shows the region of interest to electromagnetic shielding. The Lockheed points on the figure are associated with a large current loop prototype shield for an Air Force radiation experiment to be flown on the Agena.

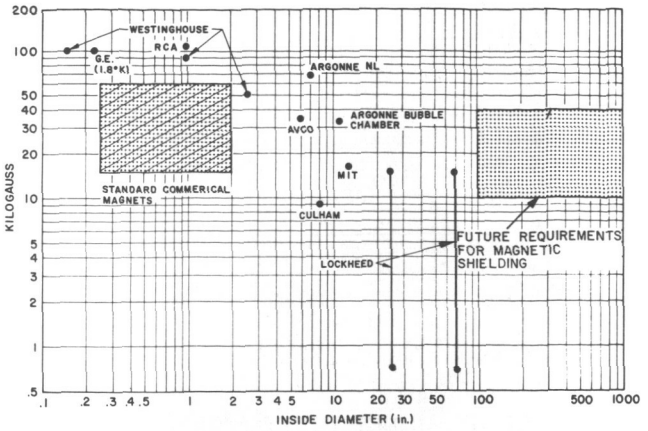

FIGURE 19. STATE OF THE ART FOR SUPERCONDUCTING MAGNETS IN THE SUMMER OF 1964

The basic limitations of superconducting magnets are shown in Figure 20. The maximum current in a superconductor depends on the externally applied magnetic field, which may be very large in magnet applications. The permissible current also is a function of operating temperatures.

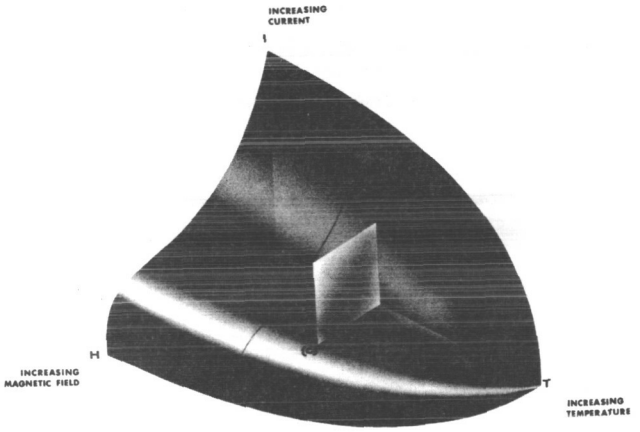

FIGURE 20. TYPICAL OPERATING REGION FOR A SUPERCONDUCTING MAGNET - A MATERIAL IS SUPERCONDUCTING, AS ILLUSTRATED IN EXAMPLE IN FIGURE, IF AT TEMPERATURE (a) CURRENT (b) AND MAGNETIC FIELD (c) THE POINT (s) LIES WITHIN THE ENVELOPE OF THE FIGURE

The principal problem has been to determine whether superconducting magnets with large volume and intense fields can be designed to operate satisfactorily within the basic limitations of superconducting materials. For example, a number of research groups have failed to achieve the current in magnet configuration to the maximum value predicted by the curve of Figure 20, the data for which was obtained from short straight samples not wound into a magnet. Work by contractors [42-47] indicates that the difficulties can be circumvented by the techniques of special metallurgical heat treatments of the superconducting wire or strip before winding the superconductor and by providing adequate thermal and electric shunting within the windings by embedding the superconductor intimately with a matrix of copper or other metal. Another important area of study involves the design of magnets which would prevent large catastrophic energy release should part of the superconductor revert to normal conductance.

Naturally, it would be desirable to ease the problem of refrigeration by finding materials which will be superconducting at higher temperatures, and to realize more versatility by finding materials that can tolerate large fields. However, the present concern is the profitable use of existing materials and the understanding of superconductors from the solid-state physics viewpoint in order to design shields more effectively. More work is needed.

3. Shield Design Studies. A comparison of magnetostatic and polyethylene shields is shown in Figure 21, which illustrates the ranges of parameters for which magnetostatic shields are superior to material shields.

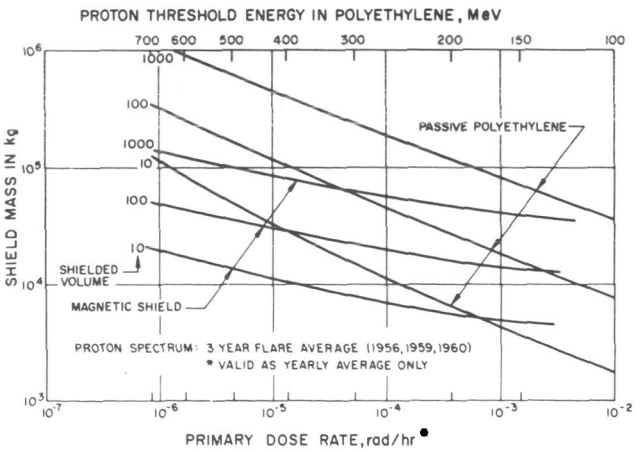

FIGURE 21. SHIELD MASS VERSUS PRIMARY PROTON DOSE RATE FOR THREE SHIELDED VOLUMES

A magnetostatic shield design [48] for an early Mars mission is shown in Figure 22. In this case, the field is confined entirely between two spherical shells to avoid interference with men and equipment.

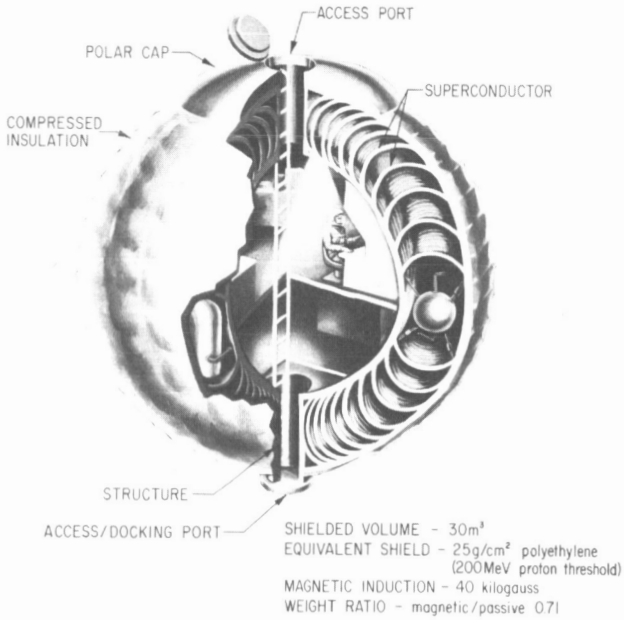

FIGURE 22. ARTIST'S CONCEPT OF MAGNETOSTATIC SHIELD

The plasma shield shown in Figure 23 is under contract for study by Drs. Levy and Janes of AVCO [49].

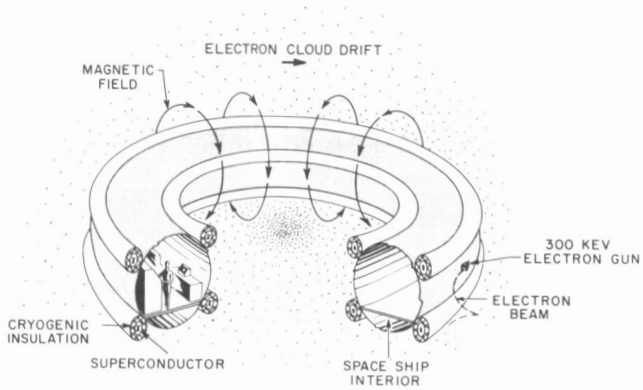

FIGURE 23. SCHEMATIC DIAGRAM OF A SPACE VEHICLE USING A PLASMA RADIATION SHIELD

Large currents circulate around the toroidal spacecraft in superconductors, and a magnetic field following the arrowed path is produced. Figure 24 explains the operation of the device.

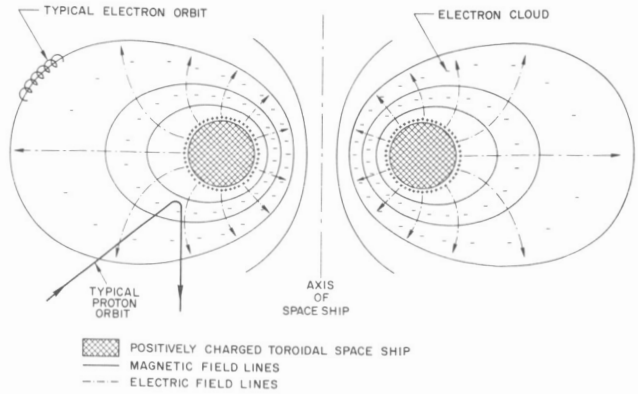

FIGURE 24. PRINCIPLE OF THE PLASMA RADIATION SHIELD

Electrons are pumped out, leaving the spacecraft positively charged. The electrons cannot get back because of the magnetic field, and the separation of charge produces an intense electric field which is in such a direction as to prohibit the entry of protons or other positively charged particles. This device can use a weaker magnetic field than magnetic shields which depend on magnetic fields alone for charge deflection, but may suffer from interference by dust and space plasma, and perhaps some of the instabilities common to the controlled thermonuclear reaction effort. Figure 25 shows a comparison by mass of the material, magnetostatic, and plasma shields.

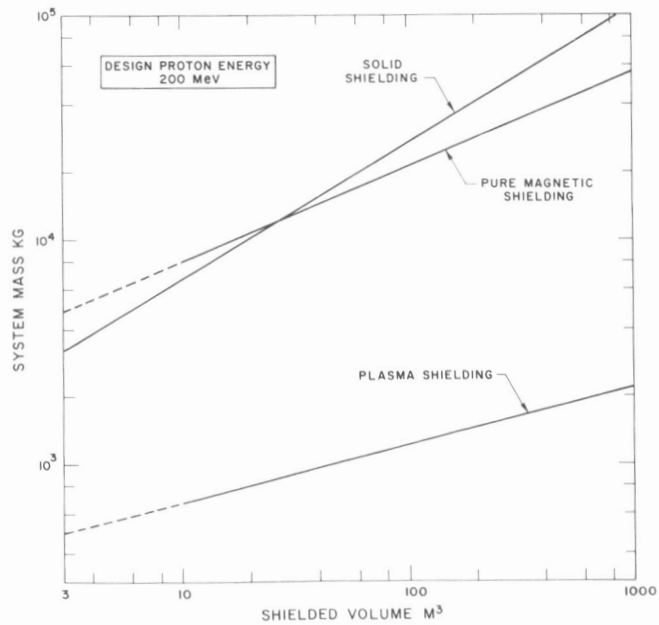

FIGURE 25. COMPARATIVE WEIGHTS FOR DIFFERENT SHIELDING SYSTEMS

VII. PROJECT SUPPORT

In addition to the regular assignment of shielding research, the Nuclear and Plasma Physics Branch of Research Projects Laboratory attempts to maintain the working capability necessary for support of current projects. A study of the Pegasus radiation problem begun in early 1963 [50] produced curves such as shown in Figure 26 [51].

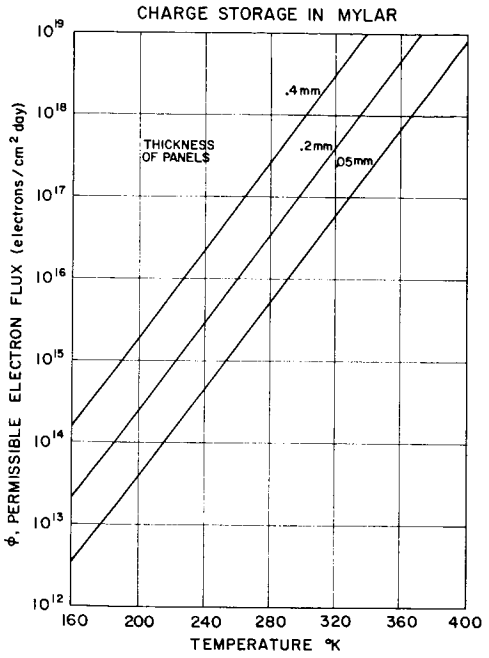

FIGURE 26. CHARGE STORAGE IN MYLAR

Charge is being injected in the Mylar dielectric of the Pegasus capacitor panel, and is leaking away because of the small conductivity of the Mylar, which is a sensitive function of temperature. Computed in this particular curve is the maximum permissible electron flux in electrons/cm^2 day to which the Pegasus can be exposed without producing radiation pulses. These calculations take into account the energy spectrum expected for the Pegasus orbit and contain a correction for the radiation arriving from all directions. These predictions are uncertain because of insufficient knowledge concerning the radiation environment, and because it is difficult to predict the net charge deposition in the dielectrics and to arrive at the basic parameters [52] (i.e., electrical conductivity and dielectric strength) of Pegasus panels. Now that the satellite is in orbit, various factors such as temperature [53], orientation [54], electron spectrometer readings [55], and experimental data from ground tests may be studied so that one can arrive at an evaluation of the radiation problem (which is hoped and believed not to be serious, but which must be examined critically if faith in the Pegasus meteoroid hit measurements is to be maintained).

Because of the similarity in physics and in computational techniques between the treatment of swarms of meteoroids interacting with gravitational fields and swarms of charged particles interacting with the magnetic fields of the earth, several members of the Nuclear and Plasma Physics Branch of the Research Projects Laboratory have become interested in the concentration of meteoroids in the vicinity of the earth [56-59]. This kind of study is necessary for an extrapolation of the experimental measurements made in the near-earth environment to the prediction of meteoroid impacts on the trip to the moon. Figure 27 [60] is a sample of some of these calculations. These techniques have been extended to the problem of captured particles and particles injected by exploding an orbiting vehicle.

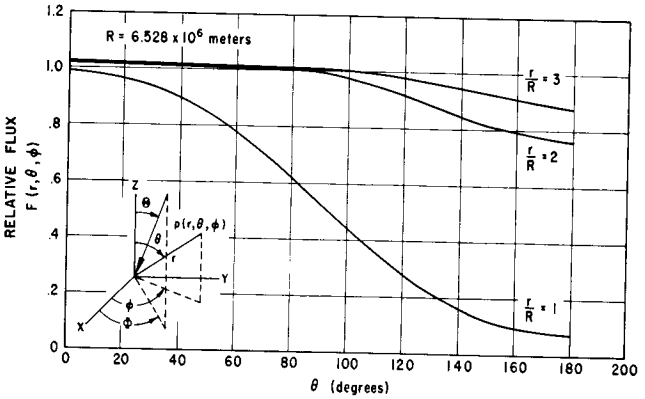

METEOROID FLUX FOR TRANSFORMED ISOTROPIC CASE WITH V_∞ = 40 km/sec, $0° \le \Theta \le \pi$, $0° \le \Phi \le 2\pi$ AND $\phi = 0°$ ASSUMING UNIT APPARENT FLUX AT INFINITY FOR A DETECTOR MOVING AT 30 km/sec IN POSITIVE Z DIRECTION

FIGURE 27. METEOROID FLUX FOR TRANSFORMED ISOTROPIC CASE

MOLAB dose rates have already been exhibited [17] (Fig. 6). In addition to these kinds of calculations, the Nuclear and Plasma Physics Branch will contribute to the planning of scientific payloads for future Saturn launchings.

The work connected with radiation in space, shielding, meteoroid distributions, materials and components testing, and plasma physics all have important bearings on planning and supporting future projects.

In addition to the work discussed in this report, there has been a large amount of significant work which the Test Laboratory has contributed to the development of nuclear rocket test facilities at Jackass Flats, studies of many radiation problems by the RIFT Project Office with support from MSFC laboratories. Also, there have been many performance studies on nuclear vehicles conducted by Mr. W. Y. Jordan, et. al., of Propulsion & Vehicle Engineering Laboratory [61-120], and many studies of nuclear systems conducted by Dr. Hilchey and Mr. Woodcock of Future Projects Office [121-139]. These important studies are mostly of a systems and operations research nature and are not concerned with radiation per se, although they may be motivated by the radiation problem or be forced to be considered along with other things such as the Saturn booster characteristics, NERVA development, and launch pad availability. Appendix I contains a description of current MSFC radiation effects and shielding studies.

VIII. CONCLUSIONS

The technology of radiation has become common enough to find application over a broad base of space engineering. As illustrated by our studies of the effects of radiation on materials and components and the use of radiation sources for determining liquid level, vehicle separations, and leakage rates, radiation sources have broad application in several engineering disciplines. The potential application of nuclear power for vehicle propulsion in space experiments almost guarantees that our interest in nuclear and space radiation will increase with time. The use of reactors and radioisotopes as sources of power for nuclear electric systems in space will necessitate our continuing competence in nuclear technology. The fact that men will need to work for long periods of time in the high-energy charged particle environment of space, perhaps with the additional radiation from nuclear systems, will require our best efforts in shielding. Finally, it must be recognized that competence in radiation physics is based on a thorough background in basic physics plus a considerable period of training in analytical and laboratory techniques.

REFERENCES

1. Contract NAS8-11160: Development and Validation of a Method for Predicting Neutron-Induced Activation in Materials. May 14, 1964 to May 14, 1965; Contractor: Illinois Institute of Technology; Technical Supervisor: Lowell Zoller, Propulsion and Vehicle Engineering Laboratory, MSFC.

2. Contract NAS8-2450: Investigation of the Combined Effects of Nuclear Radiation, Cryogenic Temperatures, and Vacuum on Engineering Materials. November 9, 1961 to September 9, 1965; Contractor: General Dynamics Corporation; Technical Supervisor: R. Gause, Propulsion and Vehicle Engineering Laboratory, MSFC.

3. Contract NAS8-5332: Irradiation of Electronic Components. June 1, 1962 to July 1, 1965; Contractor: Lockheed-Georgia Company; Technical Supervisor: W. T. White, Astrionics Laboratory, MSFC.

4. Contract NAS8-2582: The Study and Investigation of Principles, Methods and Equipment for Measuring the Density of Cryogenic Liquids. January 18, 1962 to July 31, 1963; Contractor: Oak Ridge Technical Enterprises Corporation; Technical Supervisor: A. E. Schuler, Test Laboratory, MSFC.

5. Contract NAS8-013: Development of a LH_2 Densitometer. August 1, 1960 to December 31, 1963; Contractor: Franklin Systems, Inc.; Technical Supervisor: A. E. Schuler, Test Laboratory, MSFC.

6. Contract H-71500: Measurement of Gas Density by Radiation Scattering. April 30, 1964 to September 30, 1964; Contractor: Arnold Engineering Development Center; Technical Supervisor: J. W. Clark, Aero. Laboratory, MSFC.

7. Contracts NAS8-5226 and NAS8-11220: Research on Ultra-High Altitude Measurement Systems for Pressure, Density, Temperature, and Winds. February 16, 1963 to January 11, 1965; Contractor: Electro-Optical Systems, Inc.; Technical Supervisor: J. P. Baur, Aero. Laboratory, MSFC.

8. MSFC In-House Task: Air Density Measuring Device for the Saturn Vehicle. Technical Supervisor: J. C. Derrington, Astrionics Laboratory, MSFC.

9. Contract NAS8-5394: Hermetic Seal Evaluation. May 15, 1963 to February 15, 1965; Contractor: Mississippi State; Technical Supervisor: M. Berkebile, Quality and Reliability Assurance Laboratory, MSFC.

10. Contract NAS8-11051: Program for Incorporating Additives in Adhesive for Radiographic Inspection of Adhesive-Bonded Honeycomb Structure. June 1, 1964 to February 1, 1965; Contractor: North American Aviation; Technical Supervisor: J. B. Beal, Quality and Reliability Assurance Laboratory, MSFC.

11. Contract NAS8-2579: The Improvement of Leak Detection Techniques. January 23, 1962 to July 31, 1964; Contractor: University of Michigan; Technical Supervisor: Vines, Quality and Reliability Assurance Laboratory, MSFC.

12. Contract pending: Development of Fast Neutron Spectrum System-Flyable Type Equipment. Contractor: to be selected; Technical Supervisor: H. D. Burke, Astrionics Laboratory, MSFC.

13. Annual Progress Report for Period Ending August 1, 1964, Neutron Physics Division, Oak Ridge National Laboratory, ORNL-3712, Vol. II, pp. 122-128.

14. Burrell, M. O.: The Calculation of Proton Penetration and Dose Rates. NASA TM X-53063, 1964, p. 52.

15. Zobel, W.; Maienschein, F. C.; and Scroggs, R. J.: The Spectra of Gamma Rays Produced by the Interaction of ~ 160-MeV Protons with Be, C, O, Al, Co, Bi. Oct. 12, 1964, ORNL (Second Symposium on the Protection Against Radiations Hazards in Space, Gatlinburg, Tenn., sponsored by AEC, NASA, and USAF, Oct. 12, 1964).

16. Alsmiller, R. G., Jr. et al.: From Neutron Physics Div. Space Radiation Shielding Research Annual Progress Report. August 31, 1962, pp. 148-155, (paper 1-10) ORNL 62-10-29.

17. Burrell, M. O.; and Watts, J. W.: Flare Proton Dose Inside Lunar Structures. MSFC R-RP-INN-64-16, May 22, 1964.

18. Burrell, M. O.: Space Radiation Doses During Planetary Missions. NASA TM X-53190, 1965.

19. Contracts NAS8-2658 and NAS8-5277: Minimum Weight Shield Synthesis for Space Vehicles. April 10, 1962 to April 10, 1964; Contractor: United Nuclear; Technical Supervisor: M. O. Burrell, Research Projects Laboratory, MSFC.

20. Keller, J. W.; Shelton, R. D.; Potter, R. A.; and Lacy, L.: A Study of the Effect of Geomagnetically Trapped Radiation on Bare Solar Cells. Proceedings of the IRE, November 1962.

21. Shelton, R. D.; and Urban, E. W.: Effects of Space Radiation on a Micrometeoroid Detector. MSFC M-RP-IN-63-9, June 18, 1963.

22. Leiss, J. E.; Penner, S.; and Robinson, C. S.: Range Straggling of High-Energy Electrons in Carbon. Phys. Rev., vol. 107, no. 6, Sept. 15, 1957, p. 1544.

23. Perkins, J. F.: Monte Carlo Calculation of Transport of Fast Electrons. Phys. Rev., vol. 126, no. 5, June 1, 1962, p. 1781.

24. Crawford, D. F.; and Messel, H.: Energy Distribution in Low-Energy Electron-Proton Showers in Lead Absorbers. Phys. Rev., vol. 128, no. 5, Dec. 1, 1962, p. 2352.

25. Contract NAS8-11304: Electron Shielding Studies, January 30, 1964 to January 30, 1965; Contractor: General Atomic Div., General Dynamics; Technical Supervisor: Nat Edmonson, Jr. Research Projects Laboratory, MSFC.

26. Contract NAS8-20010: A Generalized Approximation Scheme for Solution of the Transport Equation. January 26, 1965 to July 26, 1965; Contractor: General Atomic Div., General Dynamics; Technical Supervisor: Nat Edmonson, Jr. Research Projects Laboratory, MSFC.

27. Contracts NAS8-1573 and NAS8-5182: Monte Carlo Calculations of Energy Depositions and Radiation Transport in Nuclear Rocket Systems. December 31, 1961 to December 31, 1963; Contractor: General Dynamics/Ft. Worth; Technical Supervisor: H. E. Stern, Research Projects Laboratory, MSFC.

28. Burrell, M. O.: Nuclear Deposition Rates in Liquid Hydrogen. NASA TN D-1115, 1962.

29. Ashley, R. L.; and Kreger, W. E.: Neutron Attenuation in Optically Thick Shields. (A report of the special panel discussion sponsored by the shielding division of the American Nuclear Society at the 1963 winter meeting in New York City, N. Y., on November 20, 1963.) ANS-SD-1, April 23, 1964.

30. Contract NAS8-9500: Special Task: Evaluation of Theoretical Calculations in Methods for Determining Radiation Fields in Nuclear Rocket Systems. June 18, 1964 to December 18, 1965; Contractor: Lockheed-Georgia Company; Technical Supervisor: H. E. Stern, Research Projects Laboratory, MSFC.

31. Contract NAS8-5252: Evaluation of the Proton Shielding Effectiveness of Space Vehicles by Gamma Ray Probe Techniques. February 28, 1963 to December 25, 1963; Contractor: United Nuclear Co.; Technical Supervisor: H. E. Stern, Research Projects Laboratory, MSFC.

32. Shelton, R. D.; and Thompson, A. W.: Army Role in Project ARGUS. IRE, Transactions on Military Electronics, Vol. MIL 4, April to July 1960, (Nos. 2-3).

33. Shelton, R. D.; and Thompson, A. W.: Objectives and Experimental Results with the Army Explorers. Instrument Society of America, Sixth National Flight Test Instrumentation Symposium, May 2-5, 1960, San Diego, California.

34. Seitz, R. N.: A Method of Obtaining Exact Solutions of the Boltzmann-Vlasov Equations. (A thesis submitted to Case Institute of Technology in partial fulfillment of the requirements for the degree of Doctor of Philosophy), 1964.

35. Seitz, R. N.: A Method of Obtaining Some Exact (Nonlinear) Solutions of the Boltzmann-Vlasov Equations. August 1962; Nuclear and Ion Physics Branch, Research Projects Laboratory, MSFC.

36. Contract NAS8-5214: Computer Solutions of the Vlasov Equations. June 1, 1963 to November 30, 1964; Contractor: General Electric; Technical Supervisor: R. N. Seitz, Research Projects Laboratory, MSFC.

37. Seitz, R. N.; Shelton, R. D.; and Stuhlinger, E.: Electrostatic Propulsion. Present Status of the Beam Neutralization Problem. January 5, 1961; Research Projects Laboratory, MSFC.

38. Lovberg, R. C.; and Glasstone, S.: Controlled Thermonuclear Reaction: An Introduction to Theory and Experiment. 1960, Van Nostrand.

39. Seitz, R. N.: Electrostatic Potential Distributions in Low-Density Plasma Diodes. Bull. Am. Phys. Soc., Vol. 9, Ser. II, June 1964, p. 541.

40. Prescott, A. D.; Urban, E. W.; and Shelton, R. D.: The Application of the Liouville Theorem to Magnetic Shielding Problems. Paper presented at the Symposium on the Protection Against Radiation Hazards in Space, Gatlinburg, Tenn., 1964.

41. Contract NAS2-1101: Contract for Study of Plasma Radiation Shielding. December 17, 1964 to January 7, 1966; Contractor: AVCO; Technical Supervisor: R. N. Seitz, Research Projects Laboratory, MSFC.

42. Contract NAS8-5278: Analytic Study of Magnetic Radiation Shielding Systems. May 1963 to May 1964; Contractor: AVCO-Everett Res. Lab.; Technical Supervisor: E. W. Urban, Research Projects Laboratory, MSFC.

43. Contract NAS8-5279: Experimental Investigation of Advanced Superconducting Magnets. May 1963 to February 1966; Contractor: AVCO-Everett Res. Lab.; Technical Supervisor: E. W. Urban, Research Projects Laboratory, MSFC.

44. Contract NAS8-5356: Investigation of Current Degradation Phenomenon in Superconducting Solenoids. May 1963 to January 1966; Contractor: Atomics-International; Technical Supervisor: James C. Ashley, Research Projects Laboratory, MSFC.

45. Contract NAS8-11098: Investigation of the Mechanism of Superconductivity by Nuclear Irradiation. September 1963 to August 1965; Contractor: Westinghouse Res. Lab.; Technical Supervisor: James C. Ashley, Research Projects Laboratory, MSFC.

46. Contract NAS8-11727: Study of Properties of High Field Superconductors at Elevated Temperatures. June 1964 to June 1966; Contractor: Radio Corporation of America; Technical Supervisor: E. W. Urban, Research Projects Laboratory, MSFC.

47. Contract GOH-71484: Experimental Simulation of Large, High Field, Superconducting Magnet Operation. Apr. 1964 to Feb. 1966; Contractor: Oak Ridge National Laboratory; Technical Supervisor: E. W. Urban, Research Projects Laboratory, MSFC.

48. Gauster, W. F.: High Field Superconductors and the Development of Superconducting Magnets. Oak Ridge National Laboratory, October 2, 1964, p. 23.

49. Bernert, R. E.: Design of a Mars Class Radiation Shield Using a Superconducting Magnet. September 1964, pp. 1-4, (Contract NAS8-5278), AVCO-Everett; Technical Supervision: Research Projects Laboratory, MSFC.

50. Shelton, R. D.; and Urban, E. W.: Effects of Space Radiation on a Micrometeroid Detector. MSFC M-RP-IN-63-9, June 18, 1963.

51. Shelton, R. D.: Further Comments on the Pegasus Radiation Problem. (Informal Research Projects Laboratory paper), January 1, 1965, p. 7.

52. Contract NAS8-5388: Radiation on Mylar. May 27, 1963 to November 11, 1963; Contractor: Admiral; Technical Supervisor: Mary J. Smith, Pegasus Project Office, MSFC.

53. Bannister, T. C.: Thermal Considerations of the Micrometeoroid Measurement Capsule, SA-9. R-RP-P-WP-3-64, February 1964, (working paper, Research Projects Laboratory), MSFC.

54. Holland, R. L.: On the Motion of a Satellite about Its Center of Mass. March 15, 1964. (Paper written for the Conference on Mathematical Methods of Celestial Mechanics and Astronautics and Related Questions of Numerical Mathematics, March 15-21, 1964), Research Projects Laboratory, MSFC.

55. Watts, J.: Computation Laboratory Support for the Acquisition and Analysis of Data from the Electron Spectrometer Flying with Pegasus. November 23, 1964, Appendix A-D (Calibrations data, calibrations and coefficients for electron spectrometer).

56. Hale, D. P.; and Wright, J. J.: Meteoric Flux and Density Fields About an Infinitesimal Attractive Center Generated by a Stream Monoenergetic and Monodirectional at Infinity. NASA, TN D-2573, 1965.

57. Hale, D. P. and Wright, J. J.: On the Flux Density Patterns of Gravitationally Bound Particles About a Finite Attractive Center. (Submitted to J. Geophys. Res. for publication.) February 1965.

58. Shelton, R. D.; Stern, H. E.; and Hale, D. P.: Some Aspects of the Distribution of Meteoric Flux About an Attractive Center. NASA, TN D-2575, 1965.

59. Hale, D. P.; and Wright, J. J.: Meteoric Flux and Density Fields about a Finite Attractive Center Generated by a Stream Monoenergetic and Monodirectional at Infinity. NASA, TN D-2574, 1965.

60. Shelton, R. D.; Stern, H. E.; Hale, D. P.; and Wright J. J.: The Synthesis of Meteoroid Distributions from Monoenergetic Monodirectional Kernels. NASA, TN D-2630, 1965.

61. Final Report: Saturn D (Nuclear Rocket Upper Stage) Mission Studies, NAS8-1601, Report No. LMSC-B007036, CONFIDENTIAL Restricted Data, August 31, 1962.

62. Saturn D Mission Study Final Report, NAS8-1600, Report No. AE62-0667, SECRET Restricted Data, August 31, 1962.

63. Reusable Nuclear Ferry Vehicle Preliminary Design Study. NAS8-5020, Report No. LMSC-B007429. (Unclassified except Volume III), February 28, 1964.

64. Nuclear Pulse Space Vehicle Study. NAS8-11053, Report No. GA-5009, SECRET, January 1964.

65. Performance Evaluation of Uprated Saturn V Launch Vehicles Using Nuclear Third Stages. NAS8-9500 (Task 5.2), Report No. LMSC-A664-282, CONFIDENTIAL, June 10, 1964.

66. Module Designs for Assembly into Nuclear Orbital Vehicle. NAS8-9500 (Task 5.2), Report No. LMSC-A650541, June 11, 1964.

67. Nuclear Safety Study-Mission Model Analyses Final Report. NAS8-9500 (Task 5.4), Report No. LMSC-B108421, CONFIDENTIAL, July 31, 1964.

68. Nuclear Flight Executive Program, Phase IV Report, Nuclear Vehicle Flight Safety Study. NAS8-5203, Report No. LMSC-A66-4268, August 31, 1964.

69. Parametric Study of Rankine-Cycle Space Nuclear Power Systems. NAS8-5289, BECO Technical Note R-113, August 1964.

70. Parametric Performance Study of Nuclear Propelled Space Vehicles. NAS8-5289, BECO Technical Note R-114, September 1964.

71. Nuclear Heating Effects in Propellant in Clustered Pairs of Nuclear Stages. NAS8-9500 (Task 5.2), Report No. LMSC-A703725, November 1964.

72. Operational Safety Analysis for Advanced Nuclear Missions. NAS8-11131, Report No. GD/FW, FZK-220, CONFIDENTIAL Restricted Data, December 31, 1964.

73. Nuclear Vehicle Flight Safety Systems Performance Studies. NAS8-9500 (Task 5.4), Report No. LMSC-A651156, CONFIDENTIAL, January 11, 1965.

74. Final Report. Mission Oriented Advanced Nuclear System Parameters Study. NAS8-5371, STL reports 8423-6005-RU000 thru 8423-6013-RU000, (some volumes CONFIDENTIAL Restricted Data), February 1965.

75. Harris, R. J.; and Saxton, D. R.: Lunar Mission Velocity Requirements for Nuclear Vehicles. NASA TM X-51409, April 2, 1962 (also M-P&VE-FN-62-DRS-7).

76. Harris, R. J.: Trajectory Simulation Applicable to Stability and Control Studies of Large Multi-engine Vehicles. NASA TN D-1838, January 2, 1963 (also MTP-P&VE-F-63-1).

77. Fellenz, D. W.; and Harris, R. J.: Influence of Weight Parameters on the Propulsion Requirements of Orbit-Launched Vehicles. NASA TN D-1525, May 1963 (also MTP-P&VE-F-62-2).

78. Harris, R. J.; and Saxton, D. R.: Departure Weight and Propulsion Requirements for Manned Mars Landing Missions Employing Nuclear Propulsion. NASA TM X-50123, May 23, 1963 (also M-P&VE-FN-63-DRS-7).

79. Harris, F. J.; and Austin, R. E.: Orbit-Launched Nuclear Vehicle Design and Performance Evaluation Procedure for Escape and Planetary Missions. NASA TN D-1570, June 1963 (also MTP-P&VE-F62-11).

80. Austin, R. E.; and Kearns, G. B.: Lunar Mission Performance Evaluation Procedure for Orbit-Launched Nuclear Vehicles. NASA TN D-2157, April 1964 (also MTP-P&VE-A-63-20).

81. Jordan, W.Y.: Theoretical Performance and Thermodynamic Working Charts for the Nuclear Hydrogen Rocket. ABMA DSP-TN-6-58, July 22, 1958, SECRET Restricted Data.

82. Jordan, W. Y.: Some Considerations of Nuclear Rocket Propulsion for the Second Stage of Saturn. ABMA DSP-TN-3-59, February 10, 1959, SECRET.

83. Callaway, R. C.; Galzerano, A. W.; Thomas, P. G.; Whitehurst, D. C.; Jordan, W. Y.; and Saxton, D. R.: Preliminary Performance Data of Saturn Space Vehicles. ABMA DSP-TN-8-59, May 1, 1959, SECRET.

84. Jordan, W. Y.: Weight and Cost Data Comparison of Chemical and Nuclear Powered Vehicles for the Lunar Soft Landing Mission. ABMA DSP - Internal Note 8, May 13, 1959, SECRET.

85. Jordan, W. Y.: Saturn-Nuclear Rocket Flight Test Vehicle. ABMA DSP-TN-17-59, October 19, 1959, SECRET Restricted Data.

86. Saxton, D. R.: A Summary of Plasma Propulsion Systems. ABMA DSP-TN-1-60, February 2, 1960.

87. Haarmann, W. E.; and Saxton, D. R.: Comparison of Nuclear Rocket, Ion and Plasmajet Propulsion for a Mars Mission. ABMA DSP-TN-3-60, May 19, 1960, CONFIDENTIAL.

88. Whitehurst, D. C.: Optimization of Saturn D-2. ABMA DSP - Internal Note 4, June 3, 1960, CONFIDENTIAL.

89. Jordan, W. Y.; and Saxton, D. R.: Project Rover, A Summary of Thrust Vector Control Systems for Nuclear Rocket Upper Stages. ABMA DSP - Internal Note 4, June 30, 1960, SECRET.

90. Jordan, W. Y.; and Saxton, D. R.; (editors): Some Considerations of Nuclear Rocket Flight Testing. MTP-M-S&M-F-61-3, March 9, 1961, CONFIDENTIAL Restricted Data.

91. Heyer, J. W.: Nuclear Rocket Aftercooling Requirements. MTP-M-S&M-F-61-10, March 18, 1961, CONFIDENTIAL.

92. Nuclear/Saturn (C-4) Lunar Vehicle Study. MTP-M-S&M-F-61-17, Edited by Nuclear Systems and Applications Section, September 8, 1961, CONFIDENTIAL Restricted Data.

93. Sanford, E. M.: Summary of the ORION Nuclear Pulse Propelled Vehicle Studies. IN-M-P&VE-F-61-3, November 9, 1961, SECRET Restricted Data.

94. Prescott, A. D.: After-Shutdown Radiation Field of a 1000 MW Reactor in Space. MTP-P&VE-F-61-14, December 1, 1961, CONFIDENTIAL Restricted Data.

95. Fellenz, D. W.; and Harris, R. J.: Influence of Weight Parameters on the Propulsion Requirements of Orbit-Launched Vehicles. MTP-P&VE-F-62-2, May 29, 1962 (also NASA TN D-1525).

96. System Study of the Nuclear/Saturn (C-5) Lunar Vehicle. MTP-P&VE-F-62-5, Coordinated by Nuclear Systems and Applications Section, September 11, 1962, CONFIDENTIAL Restricted Data.

97. Harris, R. J.; and Austin, R. E.: Orbit-Launched Nuclear Vehicle Design and Performance Evaluation Procedure for Escape and Planetary Missions. MTP-P&VE-F-62-11, November 8, 1962 (also NASA TN D-1570).

98. Harris, R. J.: Trajectory Simulation Applicable to Stability and Control Studies of Large Multi-engine Vehicles. MTP-P&VE-F-63-1, January 2, 1963 (also NASA TN D-1838).

99. Nixon, R. F.: Nuclear Rocket Engine Performance, Isentropic Expansion of Frozen Hydrogen in the Nozzle. MTP-P&VE-F-63-4, January 9, 1963.

100. Cramer, S. N.: Two-group, Two-region Reactor Calculations. IN-P&VE-F-63-7, August 22, 1963, CONFIDENTIAL Restricted Data.

101. Harris, R. J.; and Jones, R. M.: An Investigation of an Earth Orbit Launch Window for a Manned Mars Mission with Constant Mars Arrival Date. IN-P&VE-F-63-8, August 29, 1963.

102. Dyess, O. M.: Meteoroid Protection for Space Vehicles, A Literature Survey. IN-P&VE-A-63-9, October 8, 1963.

103. Austin, R. E.; and Kearns, G. B.: Lunar Mission Performance Evaluation Procedure for Orbit-Launched Nuclear Vehicles. MTP-P&VE-A-63-20, October 8, 1963 (also NASA TN D-2157).

104. Mead, C. W.: Nuclear Engine Afterheat Removal. IN-P&VE-A-64-1, January 7, 1964.

105. Saxton, D. R.; Whiton, J. C.; Spier, R. C.; Dicus, D. L.; and Crosswell, A. R.: Indirect Crew Dose from Reactor Operation at Sea Level. IN-P&VE-A-64-6, April 30, 1964.

106. Priest, C. C.: Thermal Analysis of Nuclear Engine Core. IN-P&VE-A-64-14, July 20, 1964, CONFIDENTIAL Restricted Data.

107. Mercier, D. R.: Compressible Flow Parameters for Dissociating Hydrogen. IN-P&VE-A-64-15, August 5, 1964.

108. Jordan, W. Y.: Project Rover, Nuclear Rockets for the National Space Program. June 8, 1960, SECRET. Presented to the Ninth Meeting of the Rover Coordinating Group.

109. Jordan, W. Y.; Saxton, D. R.; and Thomas, P. S.: Nuclear Rocket Stages Increase Saturn's Payload Capability. IAS Paper No. 61-64, published in Aerospace Engineering vol. 20, no. 5, May 1961.

110. Nuclear Rocket Propulsion for Space Flight. M-P&VE-FN-62-WYJ-4, by Nuclear Systems and Applications Section, January 27, 1962. Presented by Dr. Rees at Atoms Forum, Germany.

111. Jordan, W. Y.; Heyer, J. W.; Saxton, D. R.; Whiton, J. C.; and Wilke, R. C.: Mating Nuclear Propulsion with Saturn for the Lunar Mission. M-P&VE-FN-62-WYJ-6, March 22, 1962, CONFIDENTIAL Restricted Data. Presented at IAS meeting, Cleveland, Ohio, March 8, 1962.

112. Jordan, W. Y.: The Use of Nuclear Rockets: Lunar Landing and Beyond. M-P&VE-FN-62-WYJ-26, October 12, 1962, AGARD Lecture, Brussels, Belgium.

113. Harris, R. J.; and Saxton, D. R.: Departure Weight and Propulsion Requirements for Manned Mars Landing Missions Employing Nuclear Propulsion. NASA TM X-50123, May 23, 1963. Presented at Mars Mission Technology Conference, Lewis Research Center (also M-P&VE-FN-63-DRS-7).

114. Manning, H. S.: Active Impact Control. M-P&VE-FN-63-HSM-5, April 30, 1963. Presented to the Rover Flight Safety Panel Meeting, Cape Canaveral, Florida, May 1, 1963.

115. Manning, H. S.: Safety Systems Design Integration: An Introductory Survey. M-P&VE-FN-63-HSM-13, August 23, 1963, CONFIDENTIAL Restricted Data. Presented at the 2nd RIFT WMDIWG Meeting.

116. Jordan, W. Y.; and Nixon, R. F.: Nuclear Rocket Propulsion. R-P&VE-AN-64-65, April 1, 1964 (Contribution to Marks' Handbook).

117. Summary of MSFC Nuclear Activities and Long-Range Forecast. R-P&VE-AN-64-110. Prepared by Nuclear Systems Group, June 15, 1964, CONFIDENTIAL Restricted Data.

118. Jordan, W. Y.: Nuclear Propulsion Systems Program Briefing. October 1, 1964. Presented to Center Future Plans and Missions Panel.

119. Jordan, W. Y.: Nuclear Vehicle Systems Briefing. R-P&VE-AN-64-193, November 13, 1964. Presented to Rover Committee.

120. Jordan, W. Y.: Nuclear Vehicle Systems Data. R-P&VE-AN-64-20, February 16, 1965. Presented at Los Alamos Scientific Lab. Rover Meeting.

121. Final Report: Study of Interplanetary Transportation Systems, Phase III. Lockheed Missiles and Space Company, NAS8-2469, Report No. 3-17-64-1, April 30, 1964.

122. A Consideration of the Problems Relating to Feasibility, Utility and Development of Electrical Propulsion Systems. RAND Corporation, NAS8-2677, Report No. RM3469, September 1963, CONFIDENTIAL Restricted Data.

123. Reusable Nuclear Ferry Vehicle Preliminary Design Study. Lockheed Missiles and Space Company, NAS8-5020, Report No. LMSC-B00 7429 (4 volumes), February 28, 1964, CONFIDENTIAL Restricted Data.

124. Post-Saturn Class III and IV Launch Vehicle Study (Phase III). Douglas Aircraft Company, NAS8-5021, Report No. SM-45804 (7 volumes), March 1964, CONFIDENTIAL.

125. Post-Saturn Launch Vehicles Study (Phase III) Class IV Vehicles, General Dynamics/Astronautics, NAS8-5022, Report No. GD/A-AOK 64-009 (5 volumes), March 11, 1964.

126. Manned Interplanetary Missions, Follow-on Study. Lockheed Missiles and Space Company, NAS8-5024, Report No. 8-32-64 (3 volumes), February 28, 1964, CONFIDENTIAL Restricted Data.

127. A Study of Manned Interplanetary Missions. General Dynamics/Astronautics, NAS8-5026, Report No. GD/A-AOK 64-006 (6 volumes), July 1, 1964.

128. Advanced Orbital Launch Operations. Ling-Temco-Vought, NAS8-5344, Report No. 00.368 (9 volumes), May 4, 1964, CONFIDENTIAL.

129. Manned Mars Exploration in the Unfavorable (1975-1985) Time Period. General Dynamics/Fort Worth, NAS8-11004, Report No. FZM-4039, February 15, 1964, CONFIDENTIAL Restricted Data.

130. Manned Mars Exploration in the Unfavorable (1975-1985) Time Period. Douglas Aircraft Company, NAS8-11005, Report No. SM-45575 through 45586 (12 volumes), February 1964.

131. Nuclear Pulse Space Vehicle Study. General Dynamics/General Atomic NAS8-11053, Report No. GA-5009 (4 volumes), September 19, 1964, SECRET.

132. Electrical Propulsion in Space: Mission Comparisons, Development Costs, Reliability, and Their Implications for Planning. RAND Corporation, NAS8-11081, Report No. RM-4056-NASA (1 volume), August 1964.

133. Design Criteria: Manned Nuclear Systems. Martin Co., NAS8-11425.

134. Operational Safety Analysis: Advanced Nuclear Missions. General Dynamics/Fort Worth. NAS8-11131.

135. Human Engineering Requirements: Ground Support of Nuclear System. Douglas Aircraft Company. NAS8-11188.

136. Advanced Nuclear System Parameters. Space Technology Labs. NAS8-5371.

137. Manned Mars and Venus Explorations. General Dynamics/Astronautics. NAS8-11327.

138. Low Acceleration Space Transportation Systems. United Aircraft Corp. NAS8-11309.

139. Low Acceleration Space Transportation Systems. General Electric. NAS8-11423.

APPENDIX I

LISTING OF CURRENT MSFC HIGH-ENERGY RADIATION EFFECTS AND SHIELDING STUDIES

A. Investigation of the Combined Effects of Nuclear Radiation, Cryogenic Temperatures, and Vacuum on Engineering Materials

Technical Supervisor: R. L. Gause, R-P&VE-ME, 876-4589

Contract Number: NAS8-2450, Nov. 9, 1961 - Sept 9, 1965

Contractor: General Dynamics Corporation, Fort Worth, Texas

This program is directed toward the development of experimental data on the combined effect of nuclear radiation, vacuum, and cryogenic temperatures on engineering materials. Materials of major interest to this project are primarily organic, such as lubricants, plastics, elastomers, and surface coatings. Tests are to be made during exposure to (1) radiation from a nuclear reactor, (2) reduced pressures of 10^{-6} millimeters of mercury, and (3) cryogenic temperatures to determine progressive changes in the physical and mechanical properties of selected materials of potential use in nuclear-propelled vehicles. Tests are to determine weight loss, gas evolution, and physical properties, as appropriate to the material and its proposed use.

B. Experimental Investigation of Advanced Superconducting Magnets

Technical Supervisors: Eugene W. Urban and James C. Ashley, R-RP-N, 876-4126

Contract Number: NAS8-5279, May 13, 1963 - June 12, 1965

Contractor: Avco-Everett Research Laboratory, Everett, Massachusetts

The purpose of this study is to advance the state of the art of advanced high-field superconducting solenoids with large field volumes by design, construction, and evaluation of a magnet using strip superconducting material rather than conventional superconducting wire. Ultimate application of superconducting magnets to the shielding of space vehicles against charged particle radiation requires early information as to the field strength, field volume, and mass characteristics of these devices. A considerable amount of supporting research is also to be accomplished.

C. Investigation of the Current Degradation Phenomenon in Superconducting Solenoids

Technical Supervisors: Eugene W. Urban and James C. Ashley, R-RP-N, 876-4126

Contract Number: NAS8-5356, May 14, 1963 - January 14, 1965

Contractor: Atomics International Division of North American Aviation Co., Canoga Park, California

The purpose of this study is to investigate theoretically and experimentally the phenomenon whereby the maximum current of a wound superconducting solenoid is less than the maximum current of a short sample of the same conductor in a similar magnetic field. Reduced current carrying capacity of a superconducting solenoid means that larger and heavier solenoids must be built to achieve the same magnetic field strength that would be realized if short sample currents were attainable. Thus with the goal of applications of high-field superconducting solenoids to the shielding of space vehicles against charged particle radiation, it is important to seek ways to remove or reduce the degraded current limitation.

D. Experimental Investigation of Advanced Superconducting Magnets

Technical Supervisors: Eugene W. Urban and James C. Ashley
R-RP-N, 876-4126

Contract Number: NAS8-5278, May 13, 1963 - May 12, 1964

Contractor: AVCO-Everett Research Laboratory, Everett, Mass.

The purpose of this study is to provide, by means of analytical studies based on current information on high-field superconductivity and related subjects, new information regarding the feasibility of protecting space vehicles against charged particle radiation by means of electromagnetic fields.

E. Transport of Neutrons Induced by Space Radiation

Technical Supervisor: M. O. Burrell, R-RP-N, 876-1629

Contract Number: NAS8-5278, May 13, 1963 - May 12, 1964

Contractor: Radiation Research Associates, Inc., Fort Worth, Texas

The purpose of this contract is to perform an extensive set of Monte Carlo calculations for the transport of energetic neutrons released by the nonelastic collisions of protons.

F. Minimum Weight Shields for Space Vehicles

Technical Supervisor: M. O. Burrell, R-RP-N, 876-1891

Contract Number: NAS8-5277, April 22, 1963 - March 22, 1964

Contractor: United Nuclear Corporation, White Plains, New York

The purpose of this study is to develop methods for obtaining minimum weight radiation shields for space vehicles. The major objective of the program is the extension and generalization of the proton shield synthesis technique originally developed for Marshall Space Flight Center. This technique allows the shield designer to determine which materials and/or mixtures should go into a minimum weight proton shield for a space vehicle. It also enables him to specify the thickness of each material or mixture and the order of these regions in the complete shield.

G. Data Compilation and Evaluation

Technical Supervisor: M. O. Burrell, R-RP-N, 876-1891

Contract Number: NAS8-11164, April 8, 1964 - April 17, 1965

Contractor: Lockheed-Georgia Company, Marietta, Georgia

The purpose of this project is to update and extend the radiation shielding data and methods developed by the contractor under previous contract; specifically NAS8-5252.

H. Evaluation of Simulated Radiation Shielding

Technical Supervisor: Richard A. Potter, R-RP-N, 876-8036

Contract Number: N/A

Contractor: N/A MSFC In-House

The purpose of this study is to conduct an in-house effort to evaluate the gamma probe technique as a possible tool for space radiation shield evaluation and space radiation shield design, to develop in-house competence for handling MSFC nuclear radiation problems.

I. Investigation of Mechanisms of Superconductivity by Nuclear Irradiation

Technical Supervisors: James C. Ashley and Eugene W. Urban
R-RP-N, 876-4126

Contract Number: NAS8-11098, Sept. 13, 1963 - March 1, 1965

Contractor: Westinghouse Research Laboratories, Pittsburgh, Pennsylvania

The main purpose of this project is to investigate the changes in the properties of high-field superconductor materials due to irradiation. These studies are particularly important for the operation of superconducting magnets in space. In the use of these magnets for active shielding of space vehicles, where the magnet system is exposed to cosmic ray protons, solar flare protons, and neutrons and gammas from nuclear reactors, the results of these studies will materially assist in determining the feasibility of various active shielding systems.

J. Compilation and Summary of Space Radiation and Shielding Data

Technical Supervisor: Henry E. Stern, R-RP-N, 876-3542

Contract Number: NAS8-11083, with two modifications, June 29, 1963 - January 29, 1965

Contractor: Advanced Research Corporation, Atlanta, Georgia

The purpose of this study is to compile, evaluate and summarize pertinent information concerning space radiation and shielding.

K. Electron Shielding Studies

Technical Supervisor: N. Edmonson, Jr., R-RP-N, 876-4126

Contract Number: NAS8-11304, January 30, 1964 - January 30, 1965

Contractor: General Atomic Div. of General Dynamics Corp., San Diego, Cal.

The purpose of this study is to investigate theoretically and experimentally the transport of electrons through materials covering a range of Z numbers and in the forms of slab targets of various thickness in the electron energy range 1-10 MeV. The theoretical results will be compared with the experimental results to develop reliable analytical procedures for shield design for space vehicles. Accurate shielding computation procedures are necessary for the construction of the lightest possible shields against the electron radiations in space.

L. Experimental Simulation of Large, High-Field Superconducting Magnet Operation

Technical Supervisors: James C. Ashley and Eugene W. Urban, R-RP-N, 876-4126

Contract Number: Government Order H-71484, April 3, 1964 - February 28, 1965

Contractor: United States Atomic Energy Commission, Oak Ridge, Tenn

The purpose of this study is to investigate the scaling laws which might apply to the design and construction of large, high-field superconducting magnets based on the behavior of lower field and/or smaller sized magnets. The high cost of superconducting magnets makes it highly important to be able, as much as possible, to predict the behavior of the types of magnets to be used for space radiation shields from experiments on laboratory sized magnets.

M. Study of Properties of High Field Superconductors at Elevated Temperatures

Technical Supervisors: James C. Ashley and Eugene W. Urban, R-RP-N, 876-4126

Contract Number: NAS8-11272, July 26, 1965 - April 26, 1966

Contractor: RCA Defense Electronics Products, Camden, New Jersey

The object of this study is to evaluate indirectly the possibilities of enhancing current density and magnetic field capabilities of superconducting solenoids by operating them at temperatures greater than 4.2°K.

THERMOPHYSICS RESEARCH AT MSFC

February 25, 1965

by

Gerhard B. Heller

TABLE OF CONTENTS

THERMOPHYSICS RESEARCH AT MARSHALL SPACE FLIGHT CENTER

by Gerhard B. Heller

LIST OF ILLUSTRATIONS

LIST OF ILLUSTRATIONS (Continued)

CONTENTS (Continued). . .

LIST OF ILLUSTRATIONS (Concluded)

THERMOPHYSICS RESEARCH AT MARSHALL SPACE FLIGHT CENTER

By

Gerhard B. Heller

SUMMARY

The scope and status of thermophysics research at MSFC (in-house and contract) is given in this report. It includes work in the thermal space environment, the physics of radiation and radiative properties of solids, computer programs for thermal control, thermal similitude of time-dependent problems, effects of space environment on thermal control coatings, infrared physics, and thermal flight experiments. The report covers theoretical research, early experimental studies, and some early results of thermal experiments on Pegasus I.

I. INTRODUCTION

The main incentive for the considerable expansion in thermophysics research in recent years has been our national space effort. Active and passive control of space vehicles and spacecraft has become an essential activity of design, test, and evaluation in all space programs. Consequently, thermophysics has developed into a specialty in national space and guided missile work. The technical community in this field now comprises about 500 engineers and scientists, employed in industry, university laboratories, and government agencies such as NASA, Army, Air Force, Navy, and National Bureau of Standards.

A number of major activities at Marshall Space Flight Center (MSFC) are concerned with thermal problems, with the work being carried out by MSFC and by industry and research institutions under contract with MSFC. The in-house and contract investigations constitute a well rounded research program. Some of its achievements are described in this report, which deals particularly with thermophysics research as it applies to the exchange of thermal energy between a space vehicle or craft and its surroundings, especially space, and to the action of this energy on satellite instrumentation.

Through the early Explorer program, beginning with Explorer I, MSFC contributed to the establishment of many concepts which are generally accepted today, for example, those concerning passive thermal control, thermal vacuum testing, emissivity, and effects of space environment.

Later, the need for more in-house research arose, especially in connection with Pegasus problems. Laboratories were established as a result of this need at the Research Projects Laboratory of MSFC. They proved to be extremely valuable in the Pegasus project, and later in Saturn projects as well. Research results, for example, have been applied to thermal control of the nine space vehicles illustrated in Figure 1.

Experience gained in such in-house work is enabling MSFC to supervise its contract work better. The development of in-house research facilities, moreover, is enabling MSFC to handle projects which cannot practicably be delegated to contractors. Much work, of course, has been done and is being done under contract. As an incidental but beneficial consequence of all contract work, an effective relationship has been established between contractors and the MSFC thermophysics laboratories. Such past and present research connections are shown in Figure 2.

II. RESEARCH ACHIEVEMENTS

A. SPACE ENVIRONMENT

The thermal space environment is important in the thermal radiative exchange between a space vehicle and its surroundings. The major influx of thermal energy to the space vehicle is due to insolation, earth or planetary albedo, and earth or planetary infrared radiation. The general status of knowledge of thermal space environment is discussed here briefly.

The thermal space environment is not too well known. No direct measurement of the solar constant

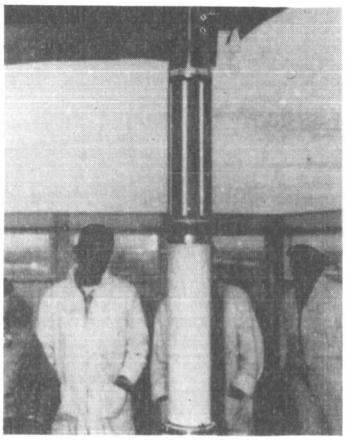

EXPLORER I

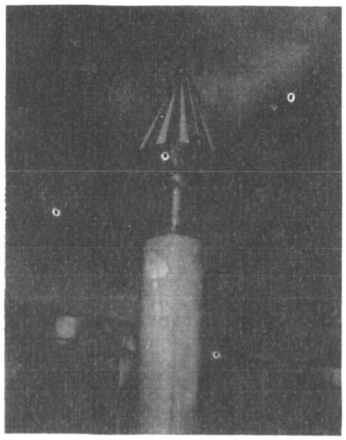

PIONEER III

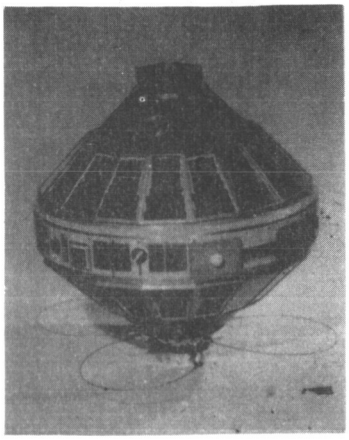

EXPLORER VII

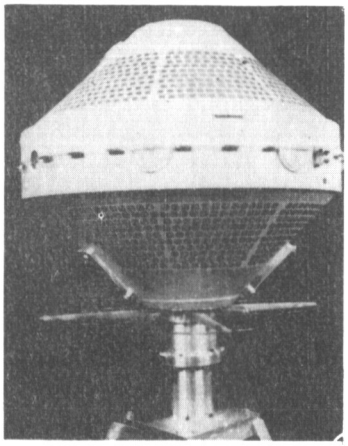

EXPLORER VIII

EXPLORER XI

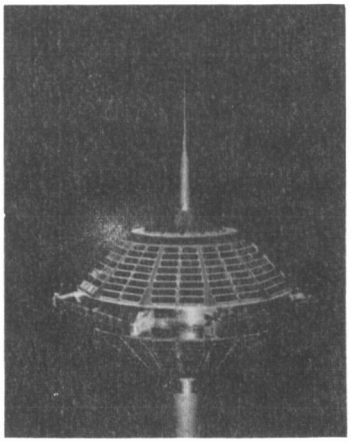

S-45 IONOSPHERE
SATELLITE

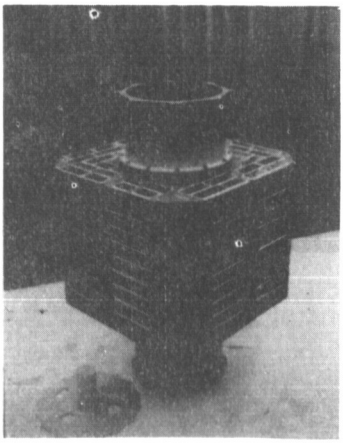

S-46 RADIATION
DETECTION SATELLITE

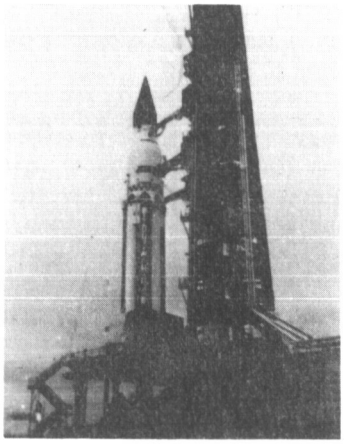

SATURN I
Flight SA-5

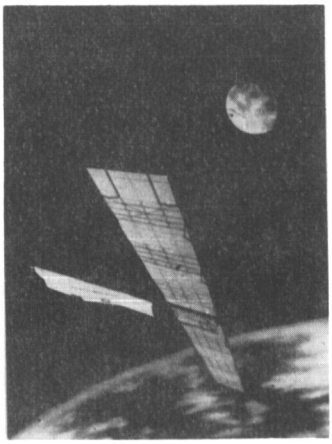

PEGASUS

FIGURE 1. SPACECRAFT THERMALLY DESIGNED BY RESEARCH PROJECTS LABORATORY

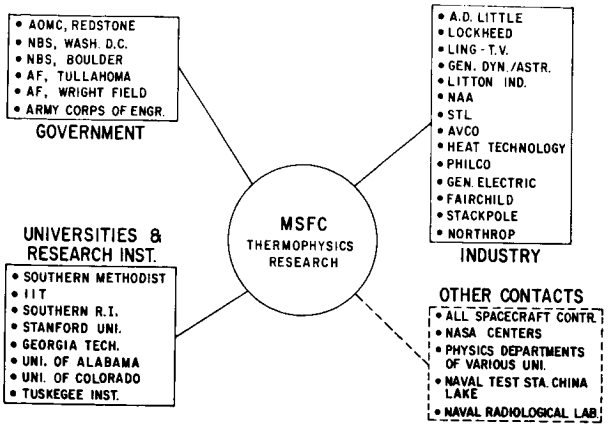

FIGURE 2. CONTRACTUAL AND PROJECT RELATIONSHIPS

in space has been made. Estimates from ground measurements are assumed to be accurate within 3 percent [1]. The spectral resolution is much less well known, and inaccuracies in the intensity of spectral lines can be expected to be 10 to 50 percent, or even higher [2]. More accurate information on solar ultraviolet is especially important because solar ultraviolet has a strong effect on the space stability of thermal control coatings.

The spectral distribution and intensity distribution of the earth albedo flux incident on the surface of a spacecraft constitutes another little-explored field of knowledge. The general equation for radiative transfer was written by Stokes [3] in 1852, and a solution was published nearly a hundred years later by Chandrasekhar [4], who solved the problem of an infinitely extended plane parallel atmosphere for the conservative case of scattering known as Rayleigh scattering. Chandrasekhar's equations were programed for computers by Coulson and others, and the results were published in table form [5]. This information was used by Snoddy [6] at MSFC in a study, discussed in this report, of the earth albedo due to Rayleigh scattering, and of the effect of the albedo on an area element of a satellite in space.

Figure 3 shows the Rayleigh diagram for scattering of nonpolarized electromagnetic radiation by molecules. The scattered radiation has two components of the distribution function, as shown by the equation:

$$I_{\theta,r} = \frac{f^4 p^2}{64\pi^2 \epsilon_0^2 c^4 r^2} (1 + \cos^2\theta)$$

in which

$I_{\theta,r}$ = intensity as a function of θ and r

θ = phase angle of radiation

r = radius of scattering molecule

f = frequency

p = induced dipole moment

ϵ_0 = dielectric constant

c = velocity of light

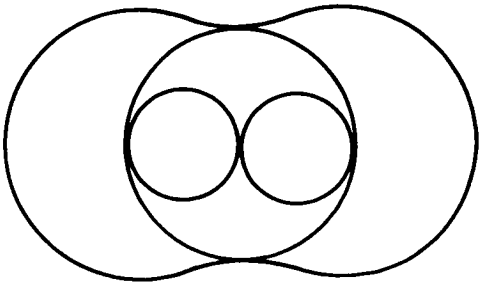

$$I_{\theta,r} = \frac{f^4 p^2}{64\pi^2 \epsilon_0^2 c^4 r^2} (1 + \cos^2\theta)$$

FIGURE 3. POLAR DIAGRAM OF RAYLEIGH SCATTERING OF UNPOLARIZED LIGHT

The outer envelope is the vector sum of these two functions. The radiative transfer equation has to account for multiple scattering. In this case, the scattering of fully elliptically polarized radiation must be considered. The Rayleigh scattering matrix, R, has to be used. For the "conservative case," only four elements of the matrix are required, as follows:

$$R = \frac{3}{2}\begin{pmatrix} \cos^2\theta & 0 & 0 & 0 \\ 0 & 1 & 0 & 0 \\ 0 & 0 & \cos\theta & 0 \\ 0 & 0 & 0 & \cos\theta \end{pmatrix} \quad (1)$$

From the four S-functions which are obtained through the solution of the matrix for multiple scattering, the four required Stokes parameters can be derived. These are necessary and sufficient to describe the state of fully elliptically polarized radiation emanating at the bottom or top of the atmosphere.

Figure 4 shows the geometry for the albedo radiation falling on a satellite element in space. The sun's direction is given by the direction cosine μ_0 measured at a surface area unit (called a "section") in the direction of the sun. The spacecraft surface area unit (called "element") is seen from the "section" under the direction cosine μ. The azimuthal angle between the two dotted planes is ϕ. Other variables shown in Figure 4 are the altitude H, the angle at the center of the earth δ_n, the angle between element→section vector and the normal to the element β, and the angle α_m between the meridian plane of the element and the plane containing the element→section vector.

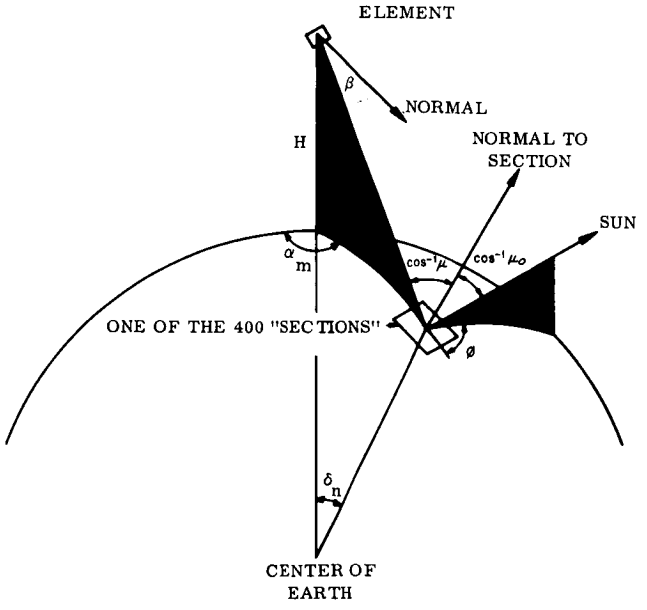

FIGURE 4. SECTION ON PLANET SURFACE

The four Stokes parameters, angular distribution, and spectral resolution of the radiation emanating at the top of the atmosphere depend upon five variables: (1) the direction cosine μ_0 of the solar radiation falling on the section , (2) the direction cosine μ of the section toward the satellite element, (3) the optical thickness of the atmosphere τ, (4) the earth surface albedo A, and (5) the azimuthal angle ϕ at the earth surface section between the vertical planes containing μ_0 and μ.

Snoddy determined the radiation intensity coming from each of the differential "sections." The total or effective albedo was obtained by numerically solving the following integral:

$$H_{R\lambda} = \int_{A_E} \frac{I_R(\mu, \mu_0, \phi, A, \tau) \cos\mu \cos\beta d A_E}{r^2} . \quad (2)$$

The results of the study are to be published separately; therefore, only a few examples are given here. Figure 5 is a map of isophotes for the area of the earth sensed by the spacecraft element as a function of given values of H, τ, A, and the solar incident angle at subelement point Θ_0. The illustration

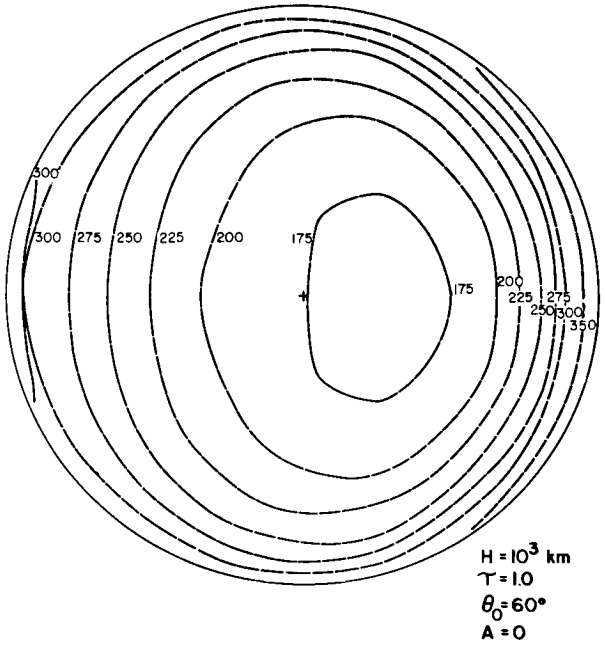

FIGURE 5. MAP OF ISOPHOTES FOR H = 10^3 km

shows the angular distribution as it affects the spacecraft thermal control computations. The sun vector is 30 degrees from the vertical to the right. The brightest area under the specific conditions of this case is not the subsolar point but the outside area. There is definitely a case of brightening toward the terminator. Figure 6 shows the isophotes for another set of parameters. Here, the conical intersection of the new field with the earth includes a shaded part of the earth.

Figure 7 shows the spectral resolution of the earth albedo incident on a spacecraft element. The surface albedo, A, of the earth is the variable parameter, and all other parameters are kept constant at the values indicated. These parameters are

the altitude H, the elevation angle of the normal to the satellite element Θ_p, and the azimuth angle of the normal to the satellite element ϕ_p. It can be seen that the spectral distribution varies considerably for the three albedos shown.

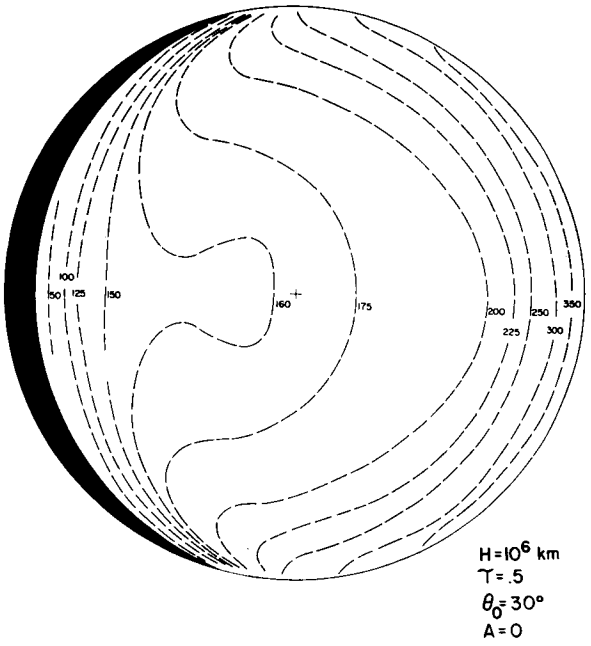

FIGURE 6. MAP OF ISOPHOTES FOR H = 10^6 km

Because of its great importance for spacecraft in the neighborhood of planetary bodies, further research in this field is needed.

B. EMISSIVITY

Emissivity was the first research study in thermophysics at MSFC. It began ten years ago in the Army Ballistic Missile Agency, and was supplemented by a research contract for early satellite studies. The research results were helpful in solving the thermal problems of Explorer I and other Explorer satellites [7]. Emissivity research is continuing; current problems are concerned with wider temperature ranges and the fundamentals of the interaction of electromagnetic waves with matter.

Figure 8 shows a rotating-specimen furnace developed under contract [8] by Richmond and Moore of the National Bureau of Standards in support of MSFC high-temperature emittance research. The furnace heats samples to 1673° to 2073° K (1400° to 1800° C) while rotating them, so that they are evenly heated and an equally hot area of the sample is always

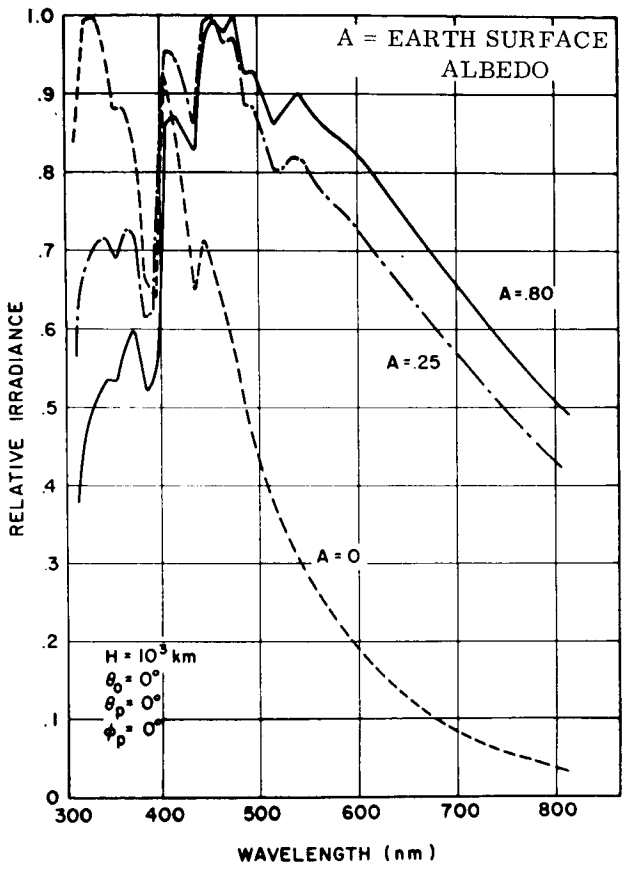

FIGURE 7. RELATIVE IRRADIANCE FOR THREE VALUES OF EARTH-SURFACE ALBEDO AS A FUNCTION OF THE WAVELENGTH

exposed to the viewing port. The emitted flux is taken out in near-normal direction and analyzed by an infrared (IR) spectroradiometer. A shallow hole, drilled into the sample, serves as a "blackbody." Earlier work on the emittance of shallow holes by Guffé has been extended, and the applicability of this emittance research has been proven by further theoretical and experimental research.

Figure 9 shows some results of emittance research in the far IR at room temperature and at cryogenic temperatures [9]. It has generally been assumed that it is sufficient to measure the emittance of surfaces in the IR from 1 to 15 microns. However, for a typical surface like the S-IV stage with a white control coating, the peak of the Planck black-body radiation curve is at approximately 15 microns. This means that 75 percent of the total energy is emitted above this value. Figure 9 shows a reflectance curve measured by Blau and Aronson of A. D. Little Co. under MSFC contract [9]. The reflectance is plotted against the

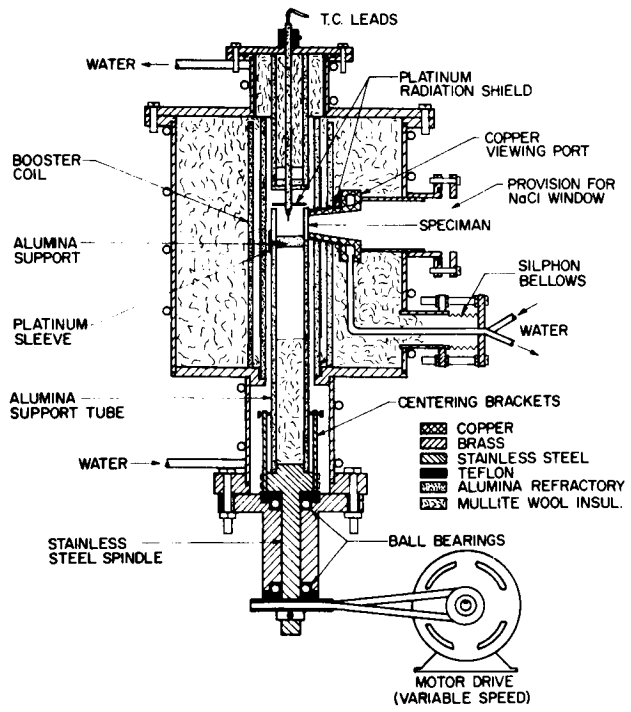

FIGURE 8. SCHEMATIC OF ROTATING-SPECIMEN FURNACE

wave number. The curve shows strong reflection bands. Any extrapolation of emittances beyond 15 microns, using the value measured at the wavelength, will mean a great error in the effective infrared absorptance. The far IR region of Figure 9 corresponds to wave numbers 667 cm^{-1} to 50 cm^{-1}. Very little study has been made of this region of the electromagnetic spectrum between IR and millimeter waves of the radio spectrum, partly because of the inherent experimental and theoretical difficulties. More research in this area is needed.

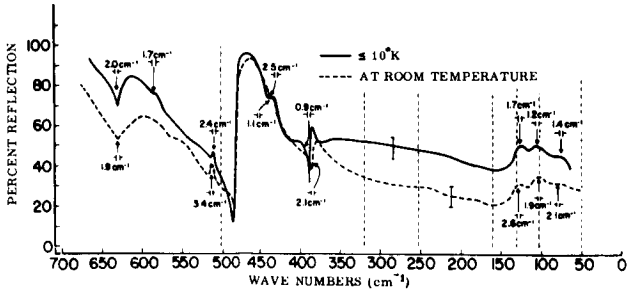

FIGURE 9. FAR INFRARED REFLECTION SPECTRUM OF Al_2O_3

Another outstanding research achievement in the field of emissivity is the quantum mechanical studies by Schocken (MSFC) and a group of physicists at Colorado State University (Burkhard and Ashby, with the assistance of Condon and Holstein) under a contract with P. E. C. Corp. at Boulder, Colorado [10, 11, 12]. The purpose of the studies was to derive emissivities ϵ and absorptivities α from basic principles. According to Kirchoff's law, the ratio of α/ϵ is always 1.0 for opaque substances, provided the same wavelength or the same spectrum distribution of the radiation is considered. Kirchoff's law can easily be derived for thermodynamic equilibrium from the laws of thermodynamics. The next step is to prove this on the basis of the electromagnetic wave fronts, using Huygen's principle. In the early part of this research, theoretical results previously obtained by other investigators were confirmed (i. e., Kirchoff's law is proven to be valid under the assumption of the wave theory). The final phase of this research was the analysis of the probability of photons leaving the lattice of a metal on the basis of principles of quantum mechanics. The main difficulty of this work was the generation of an attenuating function which provides an exponential decay of electric field strength. The total Hamiltonian takes into account interactions of photons with several different types of electrons and with lattice impurities. The overall result is a difference between emittance and absorptance. The main difference between these two nondimensional coefficients is due to the effect of the incoming electric vector field on the electronic states and on the probability of a quantum jump resulting in a photon leaving the lattice. Figure 10 shows the integrated gray-body radiation intensity as a function of the ratio of two temperatures: the temperature of the solid T_s and the temperature of the radiation environment T_r. The ratio of emissivity to absorptivity, ϵ/α, versus the temperature ratio, T_s/T_r, is shown. The deviations due to the quantum mechanical effects are especially great at low values of the nondimensional temperature ratio T_s/T_r. One interesting conclusion of this research is that the emissivity can no longer be defined and standardized as a materials property. It should also be pointed out that Figure 10 cannot be generalized for all applications, because in many cases the spectral distribution differs from the one used in the computation given. A corollary conclusion of this research is that geometry factors and radiative transfer coefficients can be in error if this effect is neglected.

Another research aspect of emissivity is the determination of effective emittance or IR absorptance values. Figure 11 shows the spectral distribution of the IR earth radiation [13]. It has two main components: (1) the radiation from the atmosphere,

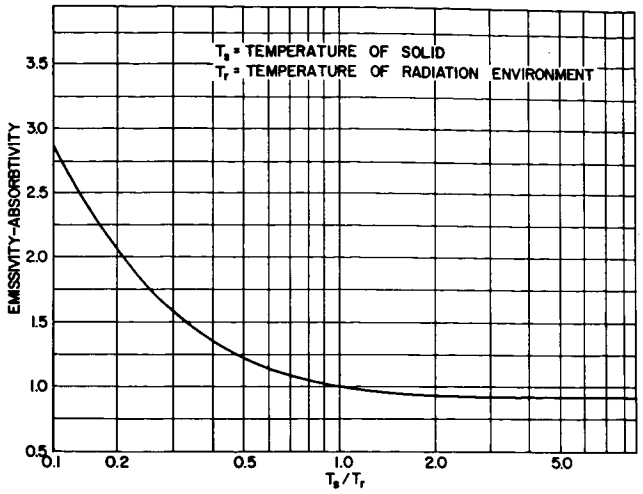

FIGURE 10. INTEGRATED GRAY-BODY RADIATION INTENSITY AS A FUNCTION OF THE RATIO T_s/T_r

which has nearly a black-body distribution corresponding to a temperature of 250°K and (2) radiation coming from the surface of the earth at about 288°K, with a peak about twice as high as the other component. However, only the bands for which the atmosphere is transparent (between 8 and 13 microns) contribute to the total radiative flux leaving the top of the atmosphere. The graph also shows a curve of the measured emittance of sand-blasted aluminum. The effective absorptance of the surface for IR radiation is shown as a third curve (data from Snoddy and Miller [14]). The value for ϵ (earth) = α (earth) is obtained by integrating the last curve from 0 to ∞. This is one of the inputs to the general computer program for thermal control which will be discussed in more detail.

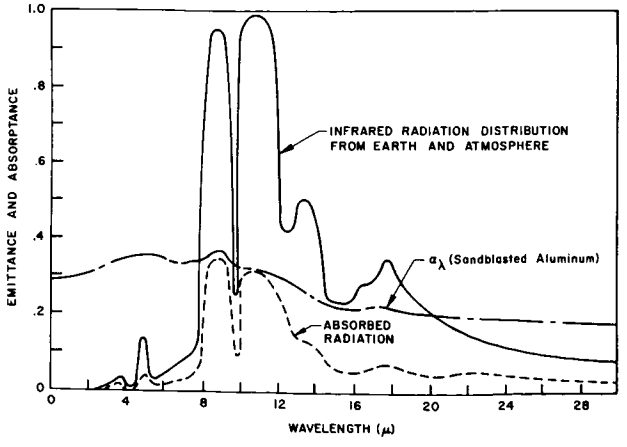

FIGURE 11. ABSORPTANCE OF SPACECRAFT SURFACE-TO-EARTH INFRARED RADIATION

C. COMPUTER PROGRAMS

The temperature of spacecraft depends mainly on: (1) the exchange of electromagnetic radiation with space and nearby celestial bodies, (2) spacecraft internal heat generation, and (3) energy fluxes between parts of the spacecraft. Computer programs have been developed at MSFC to analyze properly the complicated heat-exchange mechanisms. From the early phases of Explorer I thermal design, the computer program was developed to a high degree of sophistication. Papers on thermal design of Explorers and other space vehicles have been published by several investigators [15-26] at MSFC.

Research at MSFC has concentrated on computer-program use for satellite temperature prediction. Experimental research in the laboratory gives essential inputs and checks on specific points, but it does not replace the computed results. Our computer code is used as a powerful tool during the following phases of thermophysics activities:

1. Preliminary analysis during the study and early design of a satellite project. Requirements for thermal design are given during this phase.

2. Determination of thermal test requirements.

3. Verification of thermal design as expected throughout the lifetime of spacecraft. Design parameters, launch days and hours, results of thermal tests, and injection conditions are used in this thorough analysis.

4. Analysis of telemetered temperature measurements after successful launching of the satellite is accomplished. Special computer codes are used for analysis of data obtained from space environmental effects sensors which will be described in this report.

The establishment of thermal vacuum test requirements, a very important part of theoretical studies, is very often overlooked or ignored. It allows for the consideration of questions such as usefulness of solar simulation and accuracy requirements for simulation parameters. Often simulation knowledge is far behind spacecraft design, and therefore only comparatively low accuracies can be achieved in such testing. The use of a computer program shows whether the actual behavior of spacecraft in space can be determined better by a complete test, by improved determination of specific heat transfer coefficients, or by measurements of optical properties of thermal control surfaces immediately before launch. Thermal vacuum testing is a very active research field. In many

cases, a test can give only a few check points such as the "cold case" (lowest temperature conditions) or the "hot case" (highest temperature conditions). Since more than 20 parameters affect thermal control, only a few can be tested. Our computer code verifies the soundness of the test results obtained and the computation of transient conditions and simultaneous variations of other parameters which can never be included in a test program because of limitations in cost and time. Following is a discussion of the heat flux equation in its basic form.

The computation of satellite temperature is based on the heat flux equation written for an isothermal element A_j of the satellite:

$$A_j \alpha_1 SD_1 + A_j \alpha_2 g\, h\, BS \cos\theta\, D_2 + A_j \alpha_3 g\, h\, E\, S$$

$$-A_j \epsilon_{T_j} \sigma T_j^4 + \sum_{\substack{j,\, k = 1 \\ k \neq j}}^{n} \left[c_{kj} (T_k - T_j) + r_{kj} (T_k^4 - T_j^4) \right]$$

$$-A_j d_j c_p \rho \dot{T}_j + q_j = 0 \qquad (3)$$

$j = 1, 2, \ldots\ldots n.$

This equation has a number of flux terms which are explained here in more detail:

1. Flux terms for incoming energy are:

   Insolation = $A_j \alpha_1 S\, D_1$

   Albedo radiation = $A_j \alpha_2 g\, h\, B\, S \cos\theta\, D_2$

   IR earth radiation = $A_j \alpha_3 g\, h\, E\, S$

wherein

A_j = isothermal surface element

α_1 = α_s absorptance for solar radiation

S = solar constant

D_1 = step function ($D_1 = 1$ in sunlight, $= 0$ in earth shadow)

α_2 = absorptance for albedo radiation

g = radiative transfer function (depends upon spacecraft attitude angles)

h = radiative transfer function (depends upon spacecraft altitude)

B = earth albedo

$\cos\theta$ = direction cosine of albedo

D_2 = step function ($D_2 = 1$ in hemisphere toward sun, $= 0$ in opposite hemisphere)

α_3 = α_E absorptance for earth IR spectrum

E = ratio of earth IR flux to solar constant

2. Flux term for radiative energy leaving the surface element A_j to space

$$A_j \epsilon_{T_j} \sigma T_j$$

wherein

ϵ_{T_j} = emittance of surface element A_j for its Planck temperature T_j. In many cases ϵ_{T_j} is set equal to α_E.

σ = Stephan-Boltzmann constant

T_j = temperature of element A_j

3. Internal flux terms

   a. Heat exchange by conduction and radiation between isothermal surfaces

$$\sum_{j,\, k = 1}^{n} \left[c_{kj} (T_k - T_j) + r_{kj} (T_k^4 - T_j^4) \right]$$

$k \neq j$

wherein

c_{kj} = conductive transfer coefficient from element k to element j

r_{kj} = radiative transfer coefficient from element k to element j

T_k, T_j = temperature of elements k, j

   b. Heat flux absorbed due to heat capacity of the element A_j

$$-A_j d_j C_j \rho_j \dot{T}_j$$

wherein

d_j = thickness of area element A_j

C_j = specific heat of area element

ρ_j = density of area element

$\dot{T}_j$ = time derivative of T_j

c. Internal heat production of the element A_j

q_j

Equation (3) is a simplified version of the actual equation used for the computer program. It is a system of n (which may be up to 100) nonlinear fourth-order differential equations which are solved simultaneously on the 7094 computer. Many of the terms are functions of several variables, such as the step functions D_1 and D_2, which depend upon the six velocity and space coordinates of injection, the hour and day of injection, and the time after launch. Many parameters are also complicated functions of time. All surface properties are affected by the space environment, and the orbital parameters change by precession and rotation of the line of apsides.

Thermal control inputs to the computer program are shown in Figure 12. On the top line are the external parameters: insolation, albedo, earth IR, step functions, direction cosines, and station coordinates.

The terms are:

S(D) = solar constant dependent on day D

$B(\vec{R},\beta,\theta)$ = albedo, as function of radius $\vec{R}$ and angles β and θ

		S(D)	$B(\vec{R},\beta,\theta,)$	$E(\vec{R},\beta)$	STEP FUNCTION $D_1(t,D,H,l_0,\delta_0)$ $D_2(t,D,H,l_0,\delta_0)$	$\vec{R}\cdot\vec{\Gamma}$	$\vec{X},(t)\cdot\vec{\Gamma}(D,H,t)$ $\vec{Z},(t)\cdot\vec{\Gamma}(D,H,t)$	$\vec{X}\cdot\vec{R}$ $\vec{Z}\cdot\vec{R}$	STATION COORDINATES β_S, γ_S
PROPERTIES OF i OUTSIDE SURFACE ELEMENTS	$\alpha_{T,1}(t)$ $\alpha_{T,2}(t)$ ⋮ $\alpha_{T,n}(t)$ $\alpha_{S,1}(t)$ $\alpha_{S,2}(t)$ ⋮ $\alpha_{S,n}(t)$ c_1 c_2 ⋮ c_n	TEMPERATURE PREDICTION FOR TYPICAL CASES							
INTERNAL HEAT OF ELEMENT j	ΣQ_j								
GROSS LINKING TERMS BETWEEN ELEMENTS j,k	$\sum_{\substack{m=1 \\ j\neq k}}^{j,k} c(T_j^4 - T_k^4)$ $\sum_{\substack{m=1 \\ j\neq k}}^{j,k} c_r(T_j - T_k)$								
INJECTION h,β,γ PARAMETERS - V,ζ,τ					TIME IN SUNLIGHT PREDICTIONS FOR A YEAR				VISIBILITY FROM STATION

FIGURE 12. GENERAL COMPUTER PROGRAM INPUTS FOR THERMAL CONTROL

β = latitude of satellite position

θ = angle between sun vector and radius vector $\vec{R}$.

$E(\vec{R}, \beta)$ = earth IR radiation as function of radius $\vec{R}$ and latitude angle β.

D_1, D_2 = step functions dependent on day D and hour H of launching, the sun longitude l_0, and sun declination δ_0.

$\vec{R}$ = radius vector

$\vec{\Gamma}$ = sun vector

$\vec{X}$, $\vec{Z}$ = spacecraft fixed vectors

β_s, γ_s = latitude and longitude of observation station.

The input parameters in the vertical column are the properties of the surface elements, such as IR absorptance α_T at temperature T, solar absorptance α_s, and the heat capacities of these surface elements. There are the internal heat production and cross-linking terms for conductive and radiative exchange between all elements k and j. In addition there are the six injection parameters of the spacecraft. Figure 13 shows a table of the coefficients r_{kj} up to n isothermal areas A_j. These coefficients have to be determined by ground tests or by special analytical procedures based on view factors and emittances of inside or outside surfaces of the n area elements A_j. There are n (n-1) coefficients.

The computer program can be used to determine special aspects which have a bearing on the thermal control but which do not require step-by-step integration of the differential equations.

The time-in-sunlight of a spacecraft in earth orbit can be computed by combining the step function D_1 and the angular distance of the sun vector $\vec{\Gamma}$ from from the radius vector of the spacecraft $\vec{R}$ with the with the injection parameters of the satellite. The step function D_1 is, in turn, dependent on the day of

K \ J	1	2	3	4	5	6	7	8	9	10	11	12	13	14	15	16	17	•	•	n
1		$r_{2,1}$	$r_{3,1}$	$r_{4,1}$	$r_{5,1}$	$r_{6,1}$	$r_{7,1}$	$r_{8,1}$	$r_{9,1}$	$r_{10,1}$	$r_{11,1}$	$r_{12,1}$	$r_{13,1}$	$r_{14,1}$	$r_{15,1}$	$r_{16,1}$	$r_{17,1}$	•	•	$r_{n,1}$
2	$r_{1,2}$		$r_{3,2}$	$r_{4,2}$	$r_{5,2}$	$r_{6,2}$	•	•	•	•	•	•	•	•	•	•	$r_{17,2}$	•	•	•
3	$r_{1,3}$	$r_{2,3}$		$r_{4,3}$	$r_{5,3}$	$r_{6,3}$	•	•	•	•	•	•	•	•	•	•	•	•	•	•
4	$r_{1,4}$	$r_{2,4}$	$r_{3,4}$		$r_{5,4}$	•	•	•	•	•	•	•	•	•	•	•	•	•	•	•
5	$r_{1,5}$	$r_{2,5}$	$r_{3,5}$	$r_{4,5}$		•	•	•	•	•	•	•	•	•	•	•	•	•	•	•
6	$r_{1,6}$	$r_{2,6}$	$r_{3,6}$	•	•		•	•	•	•	•	•	•	•	•	•	•	•	•	•
7	$r_{1,7}$	$r_{2,7}$	•	•	•	•		•	•	•	•	•	•	•	•	•	•	•	•	•
8	$r_{1,8}$	$r_{2,8}$	•	•	•	•	•		•	•	•	•	•	•	•	•	•	•	•	•
9	$r_{1,9}$	•	•	•	•	•	•	•		•	•	•	•	•	•	•	•	•	•	•
10	$r_{1,10}$	•	•	•	•	•	•	•	•		•	•	•	•	•	•	•	•	•	•
11	$r_{1,11}$	•	•	•	•	•	•	•	•	•		•	•	•	•	•	•	•	•	•
12	$r_{1,12}$	•	•	•	•	•	•	•	•	•	•		•	•	•	•	•	•	•	•
13	$r_{1,13}$	•	•	•	•	•	•	•	•	•	•	•		•	•	•	•	•	•	•
14	$r_{1,14}$	•	•	•	•	•	•	•	•	•	•	•	•		•	•	•	•	•	•
15	$r_{1,15}$	•	•	•	•	•	•	•	•	•	•	•	•	•		•	•	•	•	•
16	$r_{1,16}$	•	•	•	•	•	•	•	•	•	•	•	•	•	•		•	•	•	•
17	$r_{1,17}$	$r_{2,17}$	$r_{3,17}$	•	•	•	•	•	•	•	•	•	•	•	•	•		•	•	•
•	•	•	•	•	•	•	•	•	•	•	•	•	•	•	•	•	•		•	•
•	•	•	•	•	•	•	•	•	•	•	•	•	•	•	•	•	•	•		$r_{n,n-1}$
n	$r_{1,n}$	•	•	•	•	•	•	•	•	•	•	•	•	•	•	•	•	•	$r_{n-1,n}$	

FIGURE 13. COEFFICIENT OF RADIATIVE TRANSFER OF TERMS

launching after the vernal equinox and the hour of launching (Fig. 12). The geometry involved is shown in Figure 14. A typical result for the Pegasus I spacecraft is shown in Figure 15; this shows a plot of the percentage time in sunlight versus the days after launch. Three hours of the solar day, $T_0 = 0$, 2, and 4, are used as parameters.

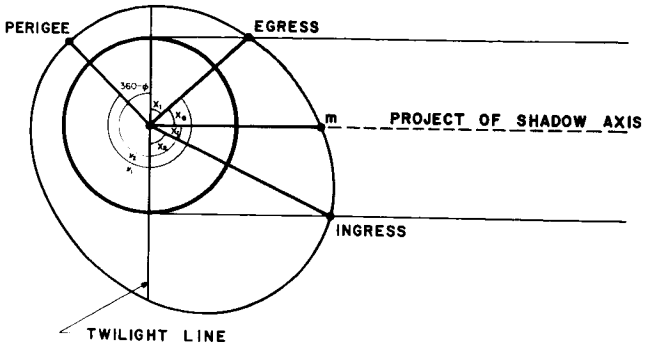

FIGURE 14. PARAMETERS IN CALCULATION OF SPACECRAFT TIME IN SUNLIGHT

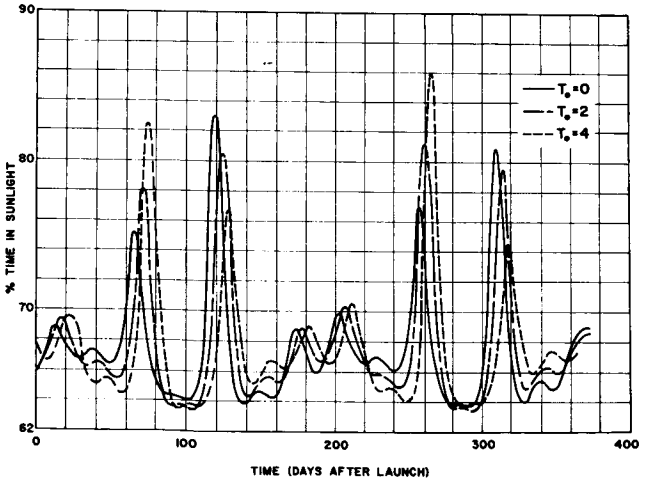

FIGURE 15. PERCENT TIME IN SUNLIGHT FOR PEGASUS I VS. DAYS AFTER LAUNCH

D. THEORETICAL THERMOPHYSICS

Although thermophysics research has been expanding rapidly under the stimulus of space programs, a great deal of fundamental knowledge has yet to be acquired. One field of thermophysics research which promises to yield basic information is that of thermal similitude. This deals with nondimensional numbers or π ratios; therefore, conclusions drawn from work on models may be usefully extrapolated. The theory of similitude has been well established in other areas of physics, such as mechanics (especially fluid mechanics). Wind-tunnel testing is a widely accepted tool of research and development for which π ratios like Mach and Reynolds numbers are common knowledge.

Such numbers are not well established in thermophysics, and even the problems or goals of the research activity are not well understood. Some investigators are trying to prove or disprove the usefulness of thermal modeling by running extensive series of tests in vacuum chambers. Claims have been made that these tests have proved that a space vehicle can be fully checked out by a thermal vacuum test of a model. This conclusion seems highly improbable, and may even be the wrong objective for this type of research. Model testing for aerodynamic shapes and problems has proved extremely valuable for airplane and space vehicle design. It is conceivable that its usefulness for solving thermal problems will develop ultimately in the same direction. It is not the checkout phase, however, but the research and development phase for which such techniques can become a powerful tool. Hence, the problems must be defined and solutions found by employing the proper set of experimental parameters. MSFC research is inclined in this direction. The greatest potential for thermal similitude research is in cost savings, because it may prove that expensive full-scale tests with solar simulation are not required. Thermal similitude investigations are more difficult in that six π ratios are required for the solution of the general case. These π's are the nondimensional numbers which must be considered in the similitude analyses. Such a set of π ratios can be obtained by trial and error methods, and a few of such sets have been proposed. The research done by Jones, in cooperation with the University of Alabama [27], started out with the theory of similitude rather than with a ready-made but limited solution. Some excellent research in thermal similitude is being done by Vickers of Jet Propulsion Laboratory [28]. Jet Propulsion Laboratory is interested in the equilibrium case for long periods of coasting in interplanetary space. Interest at MSFC is on the study of transient conditions as they occur in the eclipsing of satellites by the earth's shadow, and in thermal vacuum testing when heat is applied in terms of a step function. Research on thermal similitude at MSFC, therefore, includes the more general case in which the time derivatives of all functions have to be considered. A discussion of the early and very promising results of this research follows.

One example of many theoretically possible nondimensional groups is illustrated in Figure 16. The

π groups were derived on the basis of Brand's formulation of the π theorem in matrix form. This matrix has been programed for the 7094 computer

$$\pi_1 = \frac{C_j \, T_k}{R_{A_j} \, I_j \, t}$$

$$\pi_2 = \frac{C_{kj} \, t}{C_j}$$

$$\pi_3 = \frac{R_{A_j}^3 \, I_j^3 \, R_{kj} \, t^4}{C_j^4}$$

$$\pi_4 = \frac{I_{A_j}}{R_{A_j}}$$

$$\pi_5 = \frac{C_j \, T_j}{R_{A_j} \, I_j \, t}$$

$$\pi_6 = \epsilon_j$$

FIGURE 16. NONDIMENSIONAL π GROUPS

and solved. A total of 53 independent sets of six π ratios for thermal similitude has been obtained [29]. Theoretical and experimental work on the problem is being done at the University of Alabama. The experimental research by Matheny is directed toward time-scaling laws [30]. Figure 17 is a photograph of a prototype and model. The experimental setup provides for heating of the upper disk and for thermocouple measurements at various locations in the upper disk, stem, and lower disk. Some test results obtained by Matheny are shown in Figure 18. The temperature of upper disk T_1 and lower disk T_2 are plotted against time t. The time scale is not the same, but is compressed for the prototype by a factor of d^2, if d is the linear scaling factor. Theoretical evaluation of these results is made in connection with MSFC's in-house computer program [31].

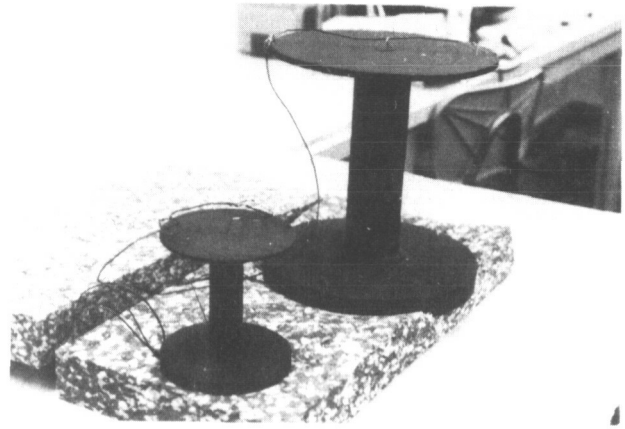

FIGURE 17. THERMAL SIMILITUDE PROTOTYPE AND MODEL

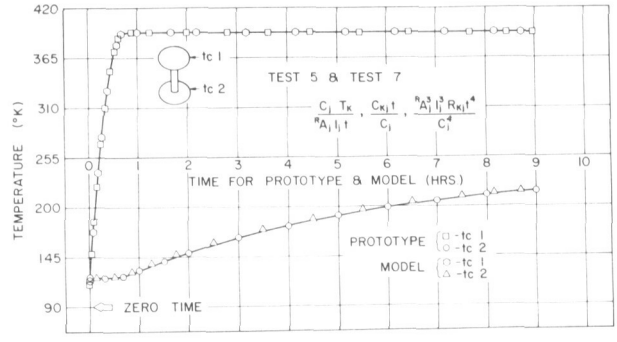

FIGURE 18. TRANSIENT TESTS ON PROTOTYPE AND MODEL

Other MSFC theoretical thermophysics research is concerned with the interface conductance of surfaces in the vacuum of space. The so-called "metallic contact" between two metal surfaces which are fastened together, such as in a flange, have very little thermal resistance under normal atmospheric conditions. It is known that the heat is mainly conducted across the interface by the absorbed or enclosed air in the gap. Research for space application is required to determine the parameters affecting the heat transfer in vacuum and the physical processes involved. Results of this research have been utilized by Astrionics Laboratory of MSFC in the design of the instrument unit (IU) of the Saturn vehicles S-IV, S-IVB, and S-V. The problem here is

to maintain and assure a high heat conductance between the IU instruments and "cold plates" on which they are mounted. Research in this field has been carried out by Atkins through in-house studies supported by contracted research [32]. A complete bibliography is given in Reference 33. The experimental apparatus of Astrionics Laboratory, which was used in connection with the IU thermal work, will be discussed in the Measuring Techniques section of this report.

Further experiments were performed by Fried under an MSFC contract with General Electric Co. [34, 35]. Figure 19 presents results compared with earlier investigations by Clausing of the University of Wisconsin. The slope of the first portion of the curve is close to the theoretical slope of 2/3, which is the exponent for elastic deformation of the contact points.

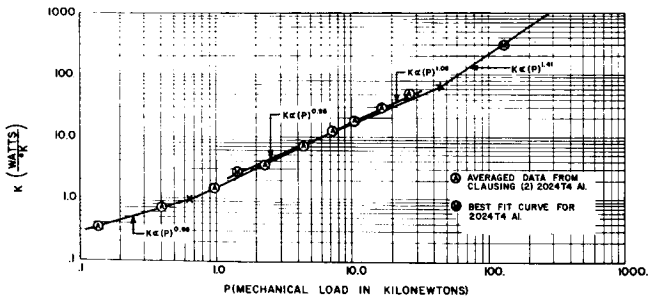

FIGURE 19. THERMAL INTERFACE CONDUCTANCE IN SPACE VS. LOAD APPLIED

Interface conductance between powder particles in "hard" vacuum (13×10^{-8} N/m^2 or 10^{-9} torr, and below) is of another type. Research Projects Laboratory at MSFC has measured thermal conductance of pumice powder with a special calorimeter, illustrated diagrammatically in Figure 20. This apparatus measures thermal conductivity of powders in the temperature range of 79°K (temperature of liquid nitrogen) to 450°K. Data on thermal conductivity of pumice powder as a function of vacuum and particle size are given in Figure 21. The vacuum causes a change of conductivity by two orders of magnitude. The effect of particle size is complex in that it varies with gas pressure. As shown in the illustration, at the lowest pressures tested, particles in the range of 44 to 104 microns had the lowest conductance. At intermediate pressure, however, particles less than 44 microns had the lowest conductance.

The research discussed was done mainly for information on insulating powders. Conclusions

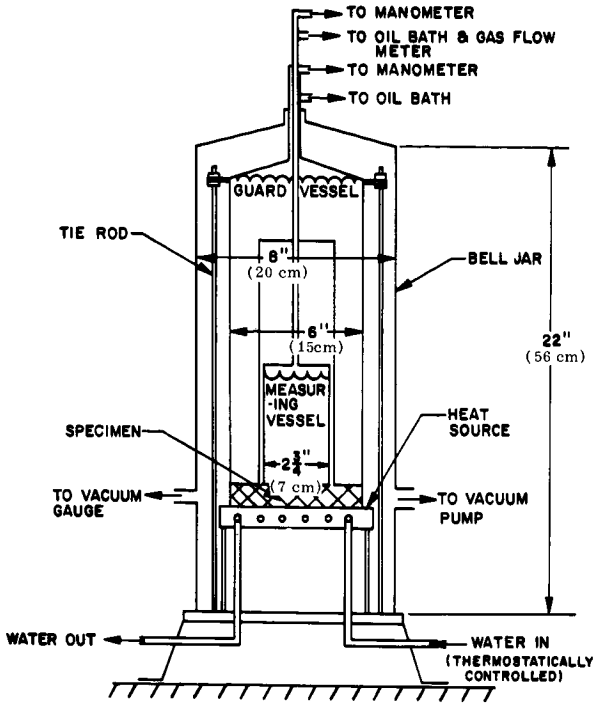

FIGURE 20. THERMAL CONDUCTIVITY CALORIMETER

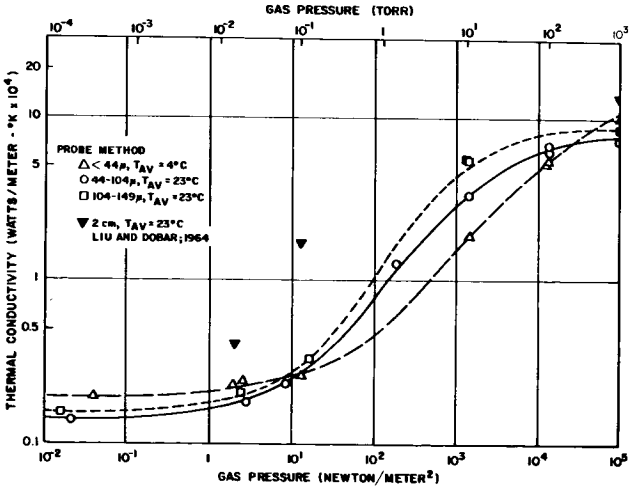

FIGURE 21. THERMAL CONDUCTIVITY OF PUMICE POWDER

can be drawn from this behavior and applied to the very underdense powders on the surface of the moon. Expansion of theoretical knowledge and the various techniques associated with the exploration of the lunar environment, and enlightenment on the composition of the "dust" layer of the moon seem to be

logical steps in the extension of this research [36-39]. Results of current studies indicate that the use of the concept of diffusivity, as in the Fourier differential equation for conduction in solids, is not necessarily applicable to thermal conductivity of powders. One reason is that the conduction through interfaces in "hard" vacuum is not well understood. Also, radiative conduction plays a major role since lunar "dust" is underdense by a factor of 10 to 30.

E. THERMAL CONTROL

Thermal control is one of the applied fields of thermophysics research. Most of the people mentioned as contributors in other sections of this report have contributed to space-vehicle thermal control at MSFC [40-48]. Research on the computer programs mentioned earlier contributes to this area. A study made by Snoddy and Miller on requirements for thermal control surfaces, which was given as a paper at the 1964 Thermophysics Specialist Conference [14], will be discussed here.

The outside surfaces of a space vehicle are among the essential parameters for effective thermal control. Figure 22 shows the result of a study of all available thermal control surfaces, such as metals with various surface characteristics, interference-type coatings, ceramic coatings, paints, etc. It reflects the status of knowledge early in 1964. The solar absorptance α_s is plotted against the IR absorptance at temperature α_T or ϵ_T, in which T is usually assumed to be 300°K. Solid lines have a constant ratio of α_s/ϵ_T. The white area indicates that they are available.

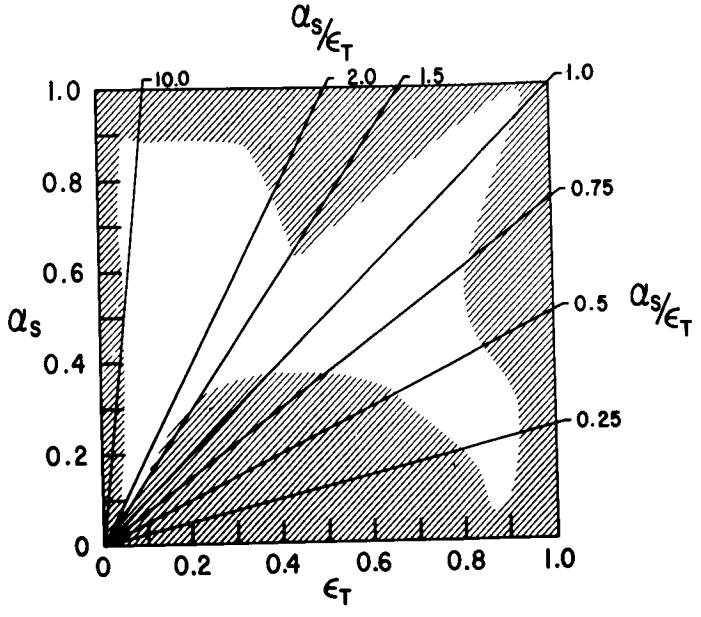

FIGURE 22. AVAILABLE THERMAL CONTROL SURFACES, OVERALL STATUS

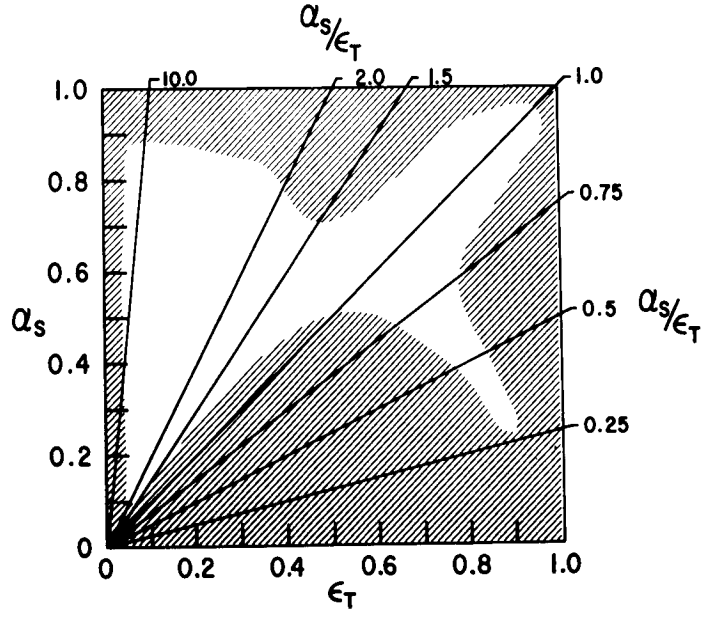

FIGURE 23. AVAILABLE THERMAL CONTROL SURFACES, ULTRAVIOLET-STABLE SURFACES

In Figure 23 data are given for coatings with the requirement of those in Figure 22 and the special requirement of ultraviolet stability. The white area in this figure is considerably smaller, especially for surfaces below the line $\alpha_s/\epsilon_T = 1.0$, which includes most of the nonmetallic surfaces. An important requirement for MSFC is the applicability of thermal control coatings to large surfaces of space vehicles. The availability of these surfaces is shown in Figure 24. Here, the white area is narrowed down considerably, mainly because, for many cases where surfaces are known, processes for the coating of large vehicles are unavailable or are too costly for consideration at the present time. Electrically conductive surfaces are required for some scientifically instrumented spacecraft. This is important if the outer satellite skin has to be an equal-potential surface. This requirement was imposed for Explorer X. Figure 25 shows the thermal control surfaces available for this purpose. The selection is narrowed considerably compared to the previous illustrations. If several of these restrictive requirements are applied, as is necessary for most vehicle considerations, only a narrow band of availability remains. Research to fill some of these critical gaps has been successful at MSFC, notably the studies of Gates in collaboration with Zerlaut of IIT Research Institute.

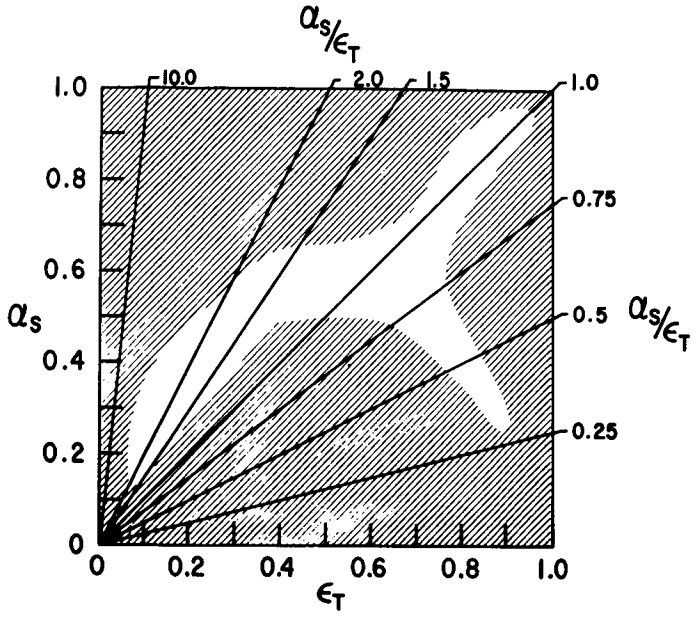

FIGURE 24. AVAILABLE THERMAL CONTROL SURFACES, LARGE-AREA SURFACES

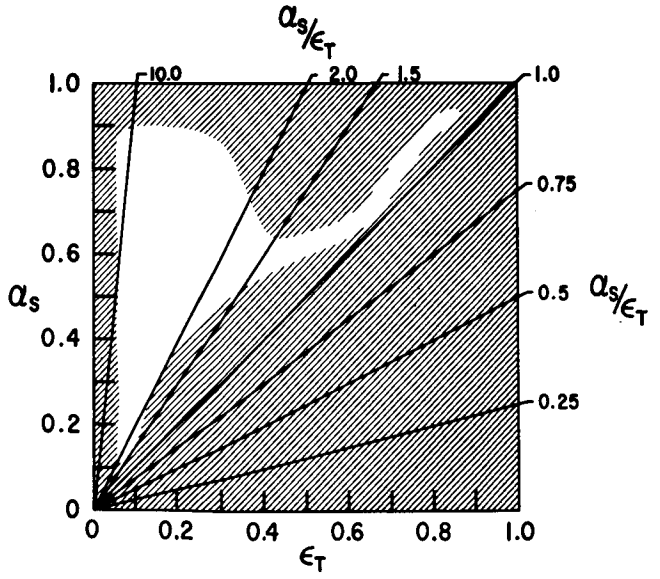

FIGURE 25. AVAILABLE THERMAL CONTROL SURFACES, ELECTRICALLY CONDUCTIVE SURFACES

The S-13 paint which found application as a coating for the S-IV stage and the Service Module Adapter of Saturn flights 8, 9, and 10, was a result of the research effort of Gates and Zerlaut over the past four years. A nation-wide survey, conducted two years ago by Fairchild-Hiller (the Pegasus prime contractor) and Miller of MSFC, revealed that no thermal control coating which would meet the Pegasus requirements was available. At that time, the decision was made to use the S-13 paint (90 gallons were required for a Saturn vehicle). Although the production of thermal control coating is not considered a research effort, it is mentioned here because the earlier research started in 1960 by Gates has found direct application to the Saturn coating problem. Several laboratories of MSFC have been involved in the procurement contract of the S-13 paint and its application to the Saturn vehicle. Materials research for improved thermal control paints is being done by Lucas and his coworkers in the Propulsion and Vehicle Engineering Laboratory of MSFC. This work in materials research is especially important for filling the large gaps which exist in the availability of thermal coatings shown in Figures 22 through 25.

F. EFFECTS OF SPACE ENVIRONMENT ON THERMAL CONTROL COATINGS

The effects of three environmental factors (ultraviolet, solar wind, and micrometeoroids) on thermal control coatings are discussed here.

1. Ultraviolet Effects. It was assumed in early Explorer experiments that inorganic white oxides such as TiO_2 or Al_2O_3 were stable in the space environment. Since then it has been learned that this is not necessarily correct, and a great number of substances now have been checked empirically in the laboratory for ultraviolet effects. It has been found that the semiconductor ZnO is less affected than many other oxides. The mechanisms of the interactions are not fully understood; consequently, a considerable amount of research is being conducted in this area. Research personnel who have made notable contributions are: Snoddy, Miller, and Arnett of MSFC [14], and Zerlaut of IIT Research Institute [49], under contract to MSFC. The S-13 coating already mentioned in connection with the S-IV application uses ZnO as a pigment, with a semiorganic silicone resin as binder. It is used to keep a component cool, especially under solar irradiation. Research is continuing toward a better understanding of the degradation mechanisms and to obtain better thermal control surfaces [50].

Research on UV effects is presently the most active research area of thermophysics. Each government and industrial thermophysics laboratory is engaged in research on UV effects because of the immediate need for space vehicle thermal control coatings. Unfortunately, most of this activity emphasizes testing rather than research. The status of laboratory UV degradation studies was the subject of a nation-wide "round-robin" at Ames Research

Center. Identical paint samples previously had been prepared from one batch and shipped at the same time to the sixteen participating laboratories. For the degradation experiments, all laboratories used the same high-pressure mercury UV lamps (A-H6 made by General Electric). Results of the experiments and information about special test conditions were sent to the Ames Research Center for evaluation. Figure 26 shows some of the results of this evaluation [51]. The increase of the absorptance for solar radiation $\Delta\alpha_s$ is plotted against the equivalent sun hours. The temperatures of the samples under the simulated illumination are indicated on the graph. The length of the dashes of each curve indicates the intensity used (in some cases, an intensity of 10 to 15 suns). This was also connected with the highest sample temperatures. The darkening of the surfaces could increase the temperature of the spacecraft by 30° to 50° C. It was impossible to arrive at a conclusive analysis of the effects. However, it became clear that the simulation techniques were completely inadequate at the times the measurements were made (end of 1963). Each of the round-robin participants knew that his measurements would be evaluated and correlated with others. Therefore, each experiment was carefully done. However, results differed by a factor of 5.

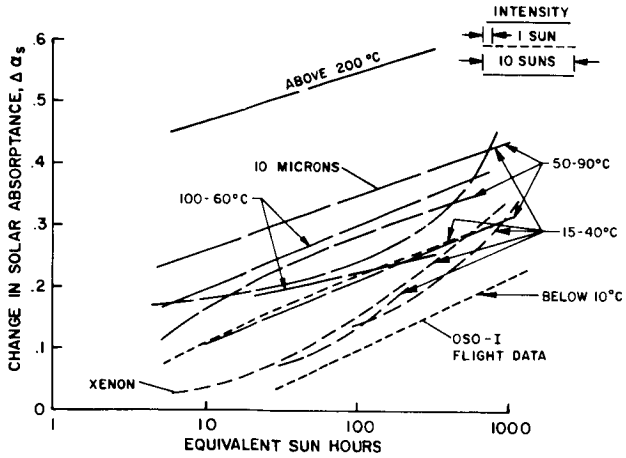

FIGURE 26. RESULTS OF ULTRAVIOLET DEGRADATION, "ROUND-ROBIN" TEST

Most determinations of UV stability of thermal control coatings of space hardware were made by the same laboratories. It is understandable that the thermal control of some spacecraft did not turn out as expected. The participants learned that more careful research is necessary. The experimental equipment recently acquired by MSFC under OART sponsorship has taken into account the lessons learned and additional experience gained since the time of the UV degradation experiments. Most of the UV experimental work still is done by contractors of MSFC. However, in-house effort has already proved to be very valuable in scientific research and in application to the Pegasus project.

A few illustrations will highlight some of the contract research results. Figure 27, taken from Reference 50, shows the spectral absorptance as a function of wavelength for the composite coating TiO_2 and epoxy resin. The solid line curve shows the unexposed sample with the sharp UV absorption edge which is typical for the TiO_2. After exposure to the UV rays of an A-H6 lamp, the absorption edge is shifted to lower energy and becomes less steep (dashed curve). Another fact shown is the increase of the absorptance at wavelengths in the visible and IR. The third curve between the other two gives the results of measurements after exposure of the yellowed sample to the light of a fluorescent lamp. A bleaching takes place. Apparently, some of the color centers can be activated by the less energetic light, and displaced electrons can fall back to their original positions. Similar bleaching also takes place by exposure of a UV-darkened sample to atmospheric oxygen or to a combination of oxygen and daylight. Some of the differences in past measurements could at least qualitatively be traced to such bleaching mechanisms. For all cases investigated, bleaching neither eliminated all color centers nor brought back the spectral absorptance to its original value. The mechanisms of degradation and the means to prevent or control it are not yet fully understood.

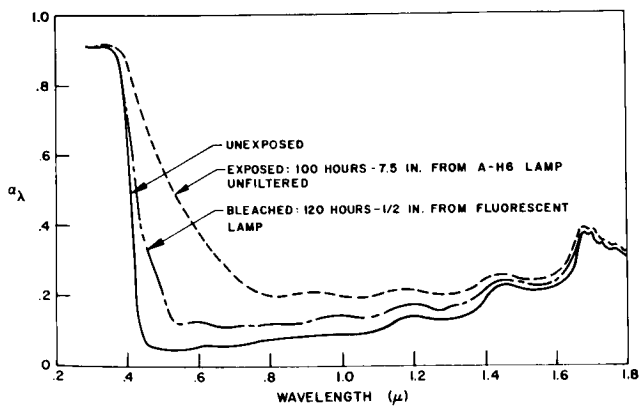

FIGURE 27. SPECTRAL ABSORPTANCE, TiO_2/EPOXY

Figure 28 shows an approach to the analysis taken by IIT Research Institute under a NASA Headquarters contract (OART), for which Gates of MSFC

is technical monitor [52, 53]. The upper portion of Figure 28 shows the scattering of light by a matrix of a UV-transparent substance, and embedded UV-absorbing particles are shown as black balls. Many paints follow this principle. If the matrix is completely nonabsorbent, and the particles absorb UV and are not affected, the combination is stable. Since about 5 percent of the solar spectrum energy is in the UV and is absorbed by such a combination, the solar absorptance α_s is limited to a minimum value of 0.12 to 0.18. A lower value may be obtained if the UV is scattered. The lower half of Figure 28 shows a combination of a matrix with a UV-transparent pigment which could be particles or voids (microbubbles). A smaller α_s could be

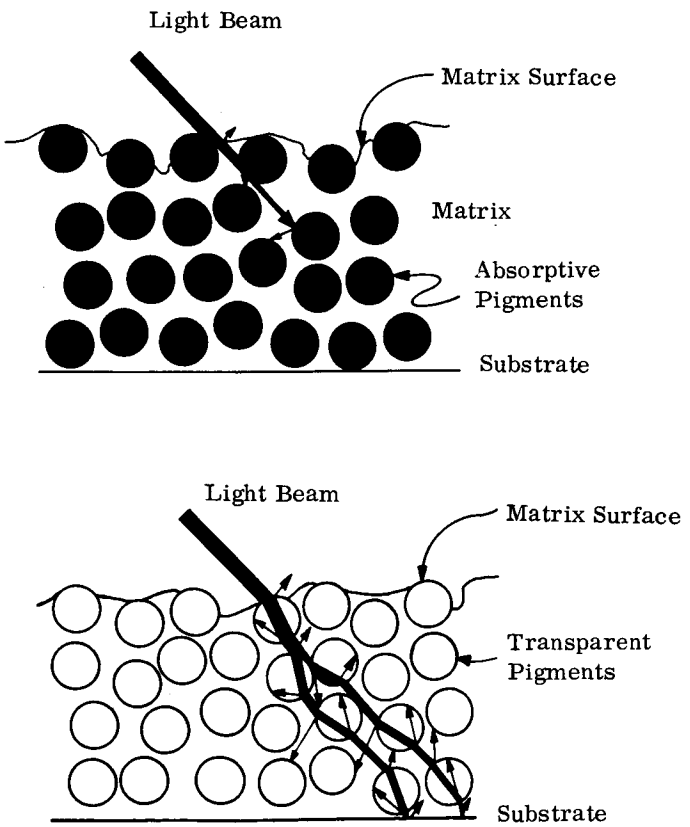

FIGURE 28. SCHEMATIC OF LIGHT WITH TWO TYPES OF PAINT MATRICES

achieved by such a combination, and this is the goal of present IIT research. The difficult problems are: (1) requirements for UV transparency of the matrix better than present by an order of magnitude and (2) a perfect reflectance at the matrix-substrate interface. Theoretical studies have been made by Miller and other scientists of MSFC and of Ling-Temco-Vought, in which Rayleigh-Gans and Mie scattering [54] is applied. Figure 29 shows a schematic of the system investigated. The purposes of the research are to obtain an understanding of the theory of the scattering process and to apply it to the development of thermal

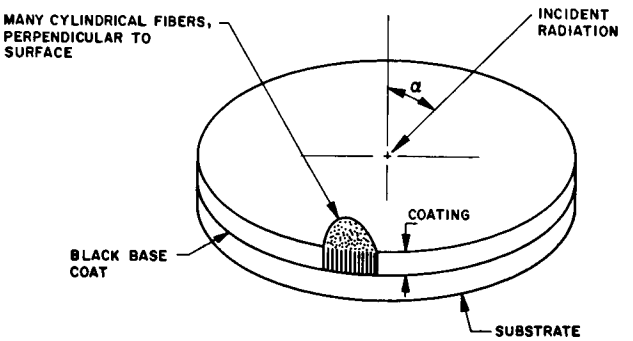

FIGURE 29. SCHEMATIC OF DIELECTRIC CYLINDER SCATTERING MODEL

control surfaces with directional characteristics. Figure 30 shows results of the study. The back-scattering coefficient is shown versus the angle of incidence for different length-to-diameter ratios of the cylinders. Strong directionality is obtained with high length-to-diameter ratios.

2. Solar Wind. For the low-eccentricity orbit of Pegasus, the problem of solar wind is negligible because of the shielding by the earth's magnetic field. For deep-space probes and vehicles traveling to the moon, however, solar-wind effects are important. A research program on solar-wind effects is being conducted through in-house studies by Miller and Arnett, and contract support by Wehner, of Litton Industries. Figure 31 is a schematic of Wehner's sputtering apparatus for simulating solar-wind effects [55]. The gas (hydrogen or helium) contained in the bell jar is ionized by a 40.68-MHz rf excitation coil. The ensuing plasma is accelerated by a second rf field of lower frequency (about 2.5 MHz) applied to the sample. Accelerating voltages of 100 to 3000 V can be achieved, and the sample is kept electrically neutral. Figure 32 shows some of Wehner's early results with samples furnished by Miller and Arnett. The ratio of solar reflectance to the initial solar reflectance is plotted against time of solar-wind bombardment simulated for one Astronomical Unit. The interesting result is that some inorganic composite samples (e. g., ZnO with potassium silicate) are strongly affected by the solar-wind bombardment. In general, the heavy (α particle) component of the solar wind seems to

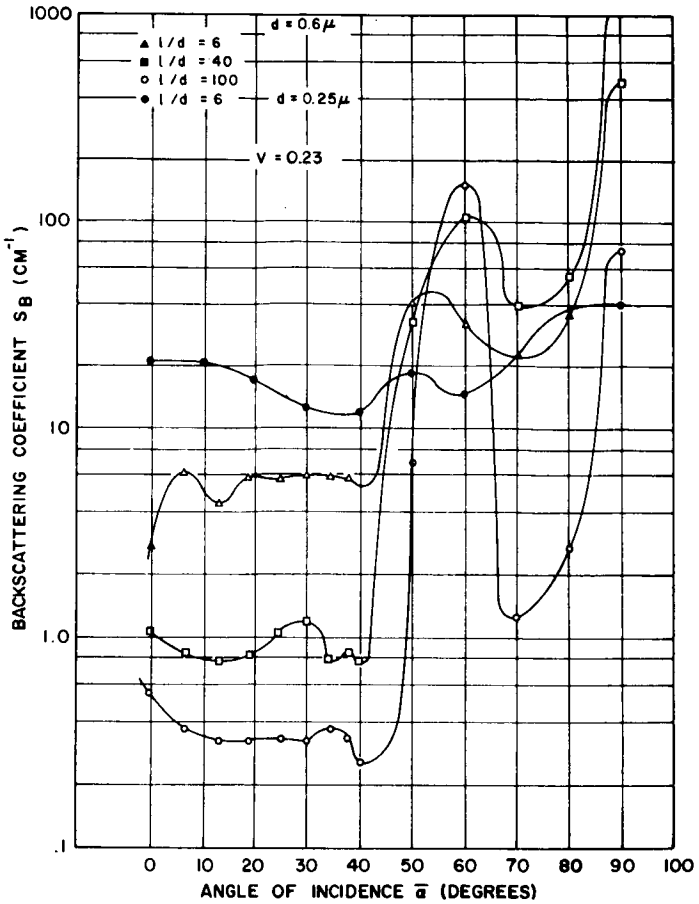

FIGURE 30. BACKSCATTERING COEFFICIENT VS. ANGLE OF INCIDENCE AS A FUNCTION OF LENGTH-TO-DIAMETER RATIOS OF THE CYLINDERS

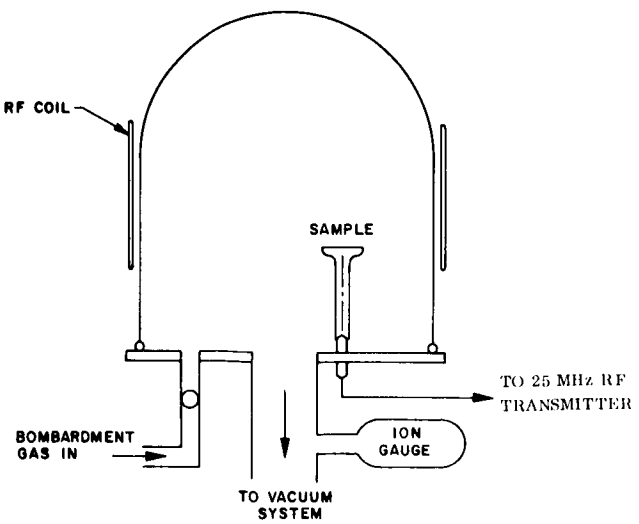

FIGURE 31. APPARATUS FOR SIMULATING SOLAR-WIND BOMBARDMENT

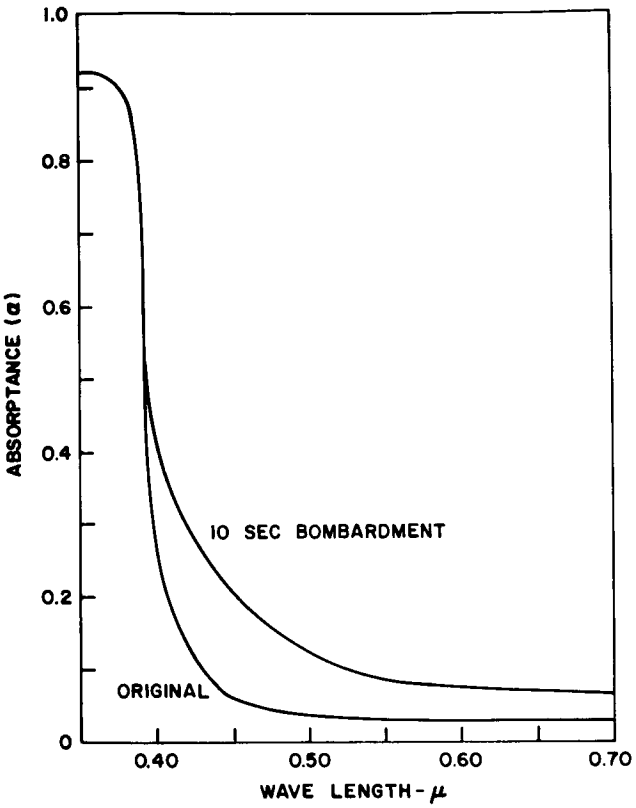

FIGURE 32. ABSORPTANCE VS. WAVELENGTH AS A FUNCTION OF PROTON BOMBARDMENT

have stronger effects than protons, although there is a greater abundance of protons. However, these results are tentative and require further analysis. In several cases, the reducing property of hydrogen on some metal oxides contributes to the generation of color centers. Research on the solar-wind effects and an understanding of the basic physical phenomena involved are particularly important to cislunar and deep-space operation.

3. Micrometeoroids. Deleterious effects of micrometeoroids on the optical properties were minimized in Explorer I and later spacecraft by using sandblasted metallic surfaces, which were assumed to be little affected by the erosion of micrometeoroids. The effect has never been successfully determined by a space experiment. Theoretical studies at MSFC (by Schocken, Merrill, and Fountain) are being supplemented by experimental investigations under contract. Figure 33 shows the Van deGraaf accelerator [56] used by Friichtenicht (Space Technology Laboratories) for the simulation of micrometeoroid bombardment of thermal control surfaces [57]. The particle injector and charging electrode generates a distinct spectrum of particles. The charge is the maximum possible, based on the

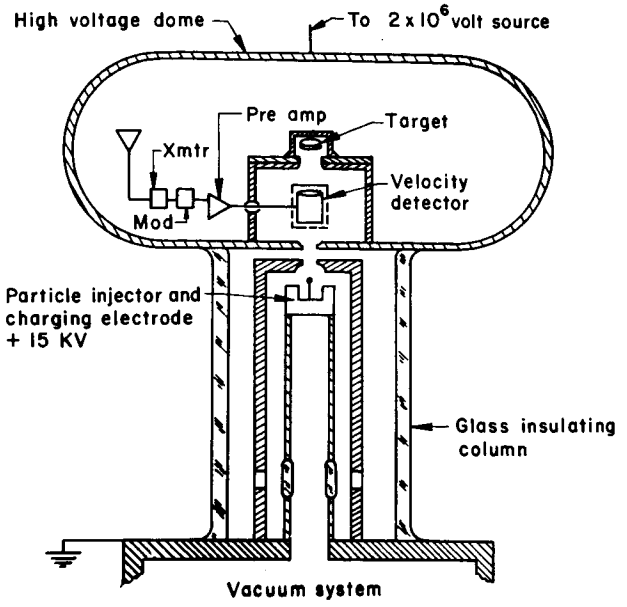

FIGURE 33. ELECTROSTATIC ACCELERATOR FOR MICROMETEOROID SIMULATION

radius of the spherical capacitors and the given charging voltage of 15 kV. Figure 34 (taken from Reference 57) shows some of the results obtained by bombarding a gold sample. The spectral reflectance is plotted against the wavelength. The solid-line curve is for the unbombarded sample and the two dashed-line curves are for the sample after bombardment by 200 000 and 400 000 particles. The sample dimensions were 3 by 12 millimeters. The sandblasting effect changes the reflectance at all wavelengths. It is strongest in the yellow and red of the visible spectrum and up to 5 microns in the near IR, while the effect becomes definitely smaller about 5 microns. It should be pointed out that plotting in this fashion gives only one number, namely the total energy of the reflected radiation. It is possible that after some micrometeoroid bombardment, the total reflectance changes very little, but that the percentages of diffuse light increases considerably. Further research is required for an understanding of these effects and of the correlation of laboratory results with flight experiments.

Research in environmental effects is of immediate importance for NASA's projects. Additional work at MSFC is being done on the effects of nuclear radiation or simulated Van Allen or cosmic radiation on materials, especially by Lucas and his co-workers in the Propulsion and Vehicle Engineering Laboratory. This work will be discussed in more detail in the nuclear physics and engineering materials reports of this research achievements review series.

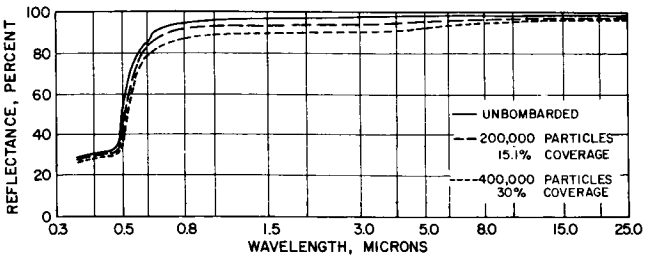

FIGURE 34. SPECTRAL REFLECTANCE OF A GOLD SAMPLE

G. THERMAL ENVIRONMENT FLIGHT EXPERIMENTS

Many spacecraft have been launched into space, and temperature measurements obtained from critical components onboard have confirmed or disproved the contention that the thermal radiation equilibrium in space has been correctly predicted. In many cases, it was sufficient to find out that the component stayed in the allowed temperature range (e. g., 0° to 50° C).

The most powerful tool for a detailed analysis of telemetered temperature data is the computer program which was used during the design phase. However, because of the more than 20 parameters (often there are more than 10 different thermal control surfaces on the outside), it is not possible to resolve the effects to better than ±10° to ±20° C. This means that the next spacecraft must be designed with the same amount of uncertainty.

This problem arose in the analysis of telemetry data of Explorer satellites. At that time, some people at MSFC began thinking of methods for obtaining meaningful results which would allow analysis of the space environment and effects of the space environment on thermal control surfaces. Work was initiated by Snoddy of Research Projects Laboratory, who started a thermal environment measuring device [58, 59]. The instrument was fabricated by Burke of Astrionics Laboratory, and the design will be described in another report of this series. For a scientific instrument, the measuring device is comparatively simple in principle; however, it took five years to develop it to its present state.

Figure 35 shows the type of instrument flown on the Explorers. It is a disk, mounted flush with the vehicle surface and connected by an insulating stem to the housing which is bolted to the spacecraft. This flight instrument can serve as a tool for engineering tests to qualify thermal control surfaces, but it also allows for the determination of space environmental effects. Because of its small time constant, effects

of insolation, albedo, and infrared can be resolved. The analysis of the results is not as simple as might be expected. A knowledge of the space-fixed attitude is required. From the dot products of the vehicle-fixed vector with the sun vector and radius vector, the direction cosines of the sun and earth can be derived. Two independent measurements are needed to determine these vectors. The attitude information is needed to explain fluctuations of temperatures due to variable insolation, variable albedo, and infrared effects. Further variation of the orbital characteristics have to be taken into account. The proper tool for evaluation is the general thermal computer program.

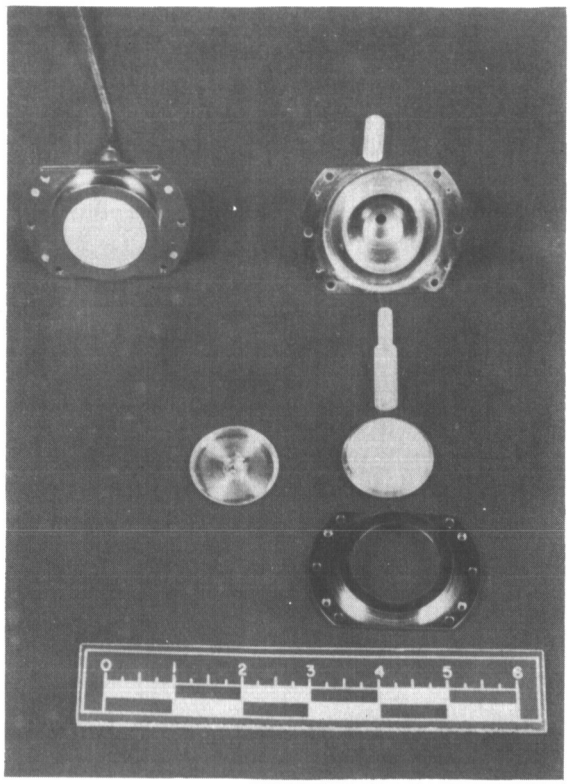

FIGURE 35. EARLY ENVIRONMENTAL EFFECT SENSOR

Figure 36 shows telemetered results of the sensor flown on Explorer XI [14, 58]. The coating of the sensor, applied by Haas of the Army Corps of Engineers, was a multiple layer, optically thin, with the following composition: one-half wavelength thickness of SiO over 20 nanometers of germanium over one and one-half wavelengths of SiO on an aluminum substrate.

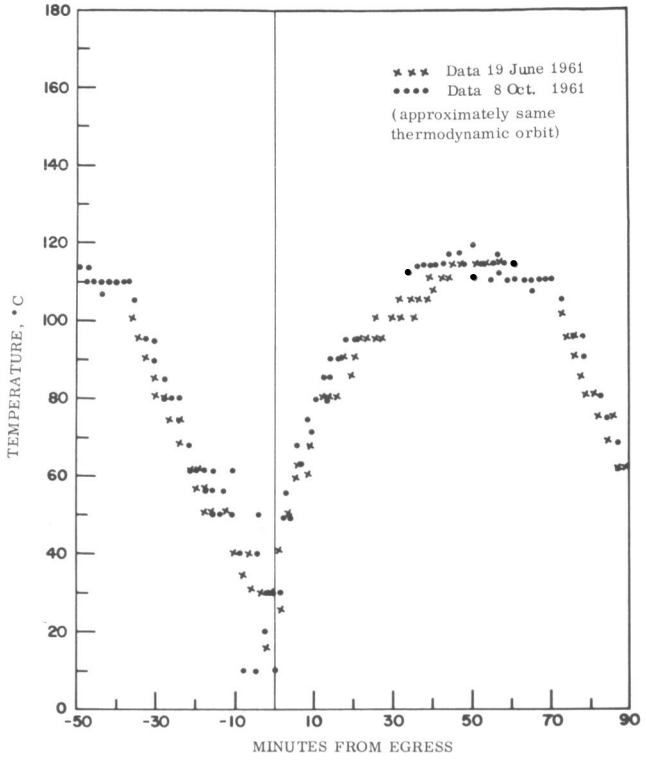

FIGURE 36. COMPARISON OF TEMPERATURES FOR TWO DAYS, EXPLORER XI SENSOR

The data points were assembled from several orbits of similar characteristics on June 19, 1961, and October 8, 1961. The spread of points is not due to lack of measuring accuracy, but to some of the effects described above. It shows clearly the difficulties involved. Through the use of the sensor, the number of variables has been reduced. However, a considerable variation of parameters has to be taken into account. A detailed analysis of the data presented in Figure 36 showed that the coating had not undergone a major change of its total absorption or emission characteristics in the three and one-half month period considered.

The environmental effects sensors flown on the Saturn I SA-4 suborbital flight are very similar to the one shown in Figure 35 [59]. Four of these sensors were arranged linearly in a common housing and mounted flush with the Saturn skin. The sensor coatings were: anodized aluminum, sandblasted aluminum, black paint, and vapor-deposited gold. The coatings were applied by Manufacturing Engineering Laboratory and Propulsion and Vehicle Engineering Laboratory, MSFC.

Figure 37 shows the telemetered temperatures of the four sensors and the internal housing temperature plotted against flight time of the Saturn space vehicle. The sharp increase at 125 seconds is due to the retrorocket firing of the solid-propellant rockets attached to the first stage.

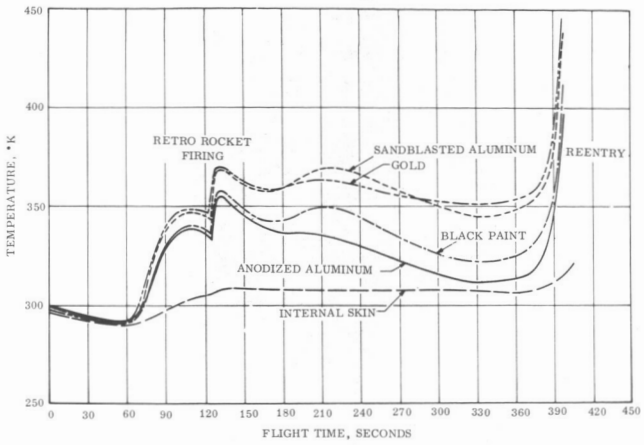

FIGURE 37. SA-4 FLIGHT OF ISOLATED TEMPERATURE SENSOR

Figure 38 is a photograph of the thermal environment sensors used on the SA-9, the first Pegasus satellite. The thermal control coatings [60] used were:

1. an Alodine inversion coating (same as used on meteoroid penetration detectors)

2. S-13 UV-stable white paint (same as used on Service Module Adapter and on Zener diodes)

3. black paint (same as used on frame of Pegasus; also used as a standard)

4. TiO_2-silicone paint (same as used on S-16 flight and by 16 laboratories participating in the round-robin tests).

The bottom portion of Figure 39 shows a theoretical curve of the temperature of the black standard. On the upper half of this figure are shown the measured results from the core memory for the Alodine coating. In both graphs, the temperature is plotted against the time of an orbit. The telemetered curve shows some interesting results due to variation of the thermal environment. A more thorough analysis will have to be made before conclusions can be drawn.

The thermal environment sensors have proved to be a very valuable experimental tool. They have

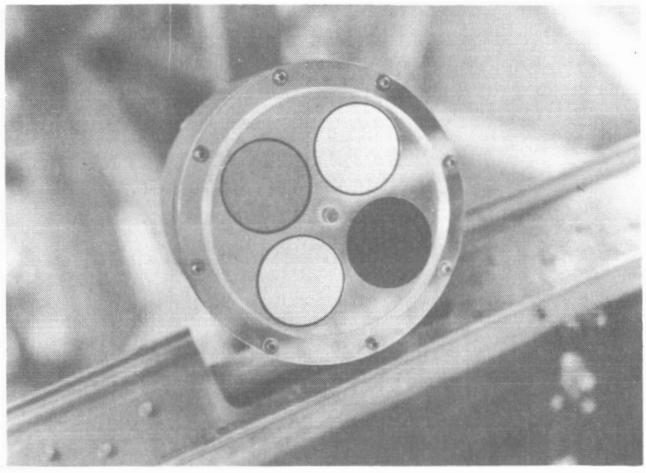

FIGURE 38. PEGASUS ENVIRONMENTAL EFFECT SENSOR

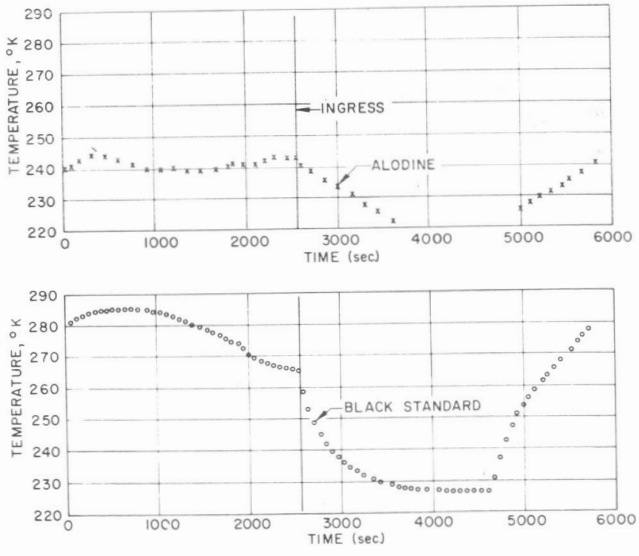

FIGURE 39. TELEMETERED TEMPERATURE OF ALODINE-COATED SENSOR, AND COMPUTED TEMPERATURE OF BLACK STANDARD

provided useful information on the space environment and its effects on thermal control surfaces. Conclusions drawn from the data acquired will be the basis for better thermal control in the future.

H. MEASURING TECHNIQUES

The greater part of the experimental research in thermophysics at MSFC is conducted under contracts to research institutes and research groups in industry, government, and universities. However, because of the urgent need for direct experimental support of MSFC projects, especially scientific payloads, in-house work has been started at the Research Projects Laboratory of MSFC.

Additional experimental facilities directly connected with Saturn vehicles have been built in other MSFC laboratories. Figures 40 and 41 illustrate research apparatus built in Astrionics Laboratory with the cooperation of Atkins of Research Projects Laboratory and its support contractor, General Electric. The apparatus was made for measuring interface conductance under the "hard" vacuum conditions of space. This research is of importance in connection with the problems of heat conduction between electronic packages of the IU and the mounting plates. Figure 19 shown previously in this report is an interface conductance curve measured by Fried of General Electric. Coating facilities have been built by Manufacturing Engineering Laboratory, and engineering materials investigations are being conducted in the Propulsion and Vehicle Engineering Laboratory. As mentioned earlier, some of the coatings were prepared by these laboratories.

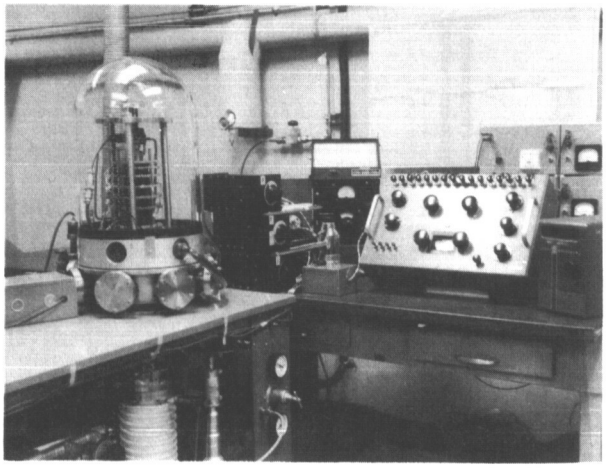

FIGURE 40. APPARATUS FOR MEASURING THERMAL INTERFACE CONDUCTANCE IN SIMULATED SPACE VACUUM

A small in-house research capability in experimental thermophysics is being established in

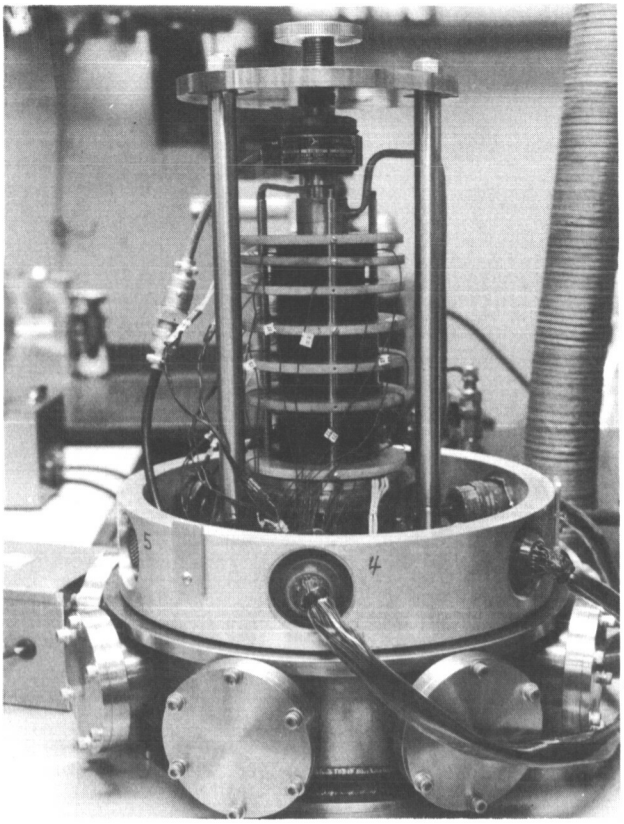

FIGURE 41. DETAILED VIEW OF THERMAL CONDUCTANCE MEASURING EQUIPMENT

Research Projects Laboratory. Research will deal mainly with problems in space thermal environment, ultraviolet, electromagnetic radiation, and emissivity. Approval and funding of the experimental research tasks was obtained by OART and OMSF.

A space thermal-environment chamber, shown in Figure 42, is an example of the research equipment in use. It has a chamber bakable at 450° C and an LN_2-cooled shroud with a special radiation absorptive coating. The chamber working space is 0.9 m in diameter and 1.5 m high. A carbon-arc lamp provides solar simulation through a quartz window. There is a viewing port and an infrared window for radiometric measurement, and provision for feed-through of thermocouples, high voltage, and high current. The maximum vacuum capability is 13×10^{-8} N/m^2 (10^{-9} torr).

I. PEGASUS THERMAL RESULTS

Pegasus A was launched on February 16, 1965. The primary purpose of the satellite experiment is the determination of the frequency of meteoroid

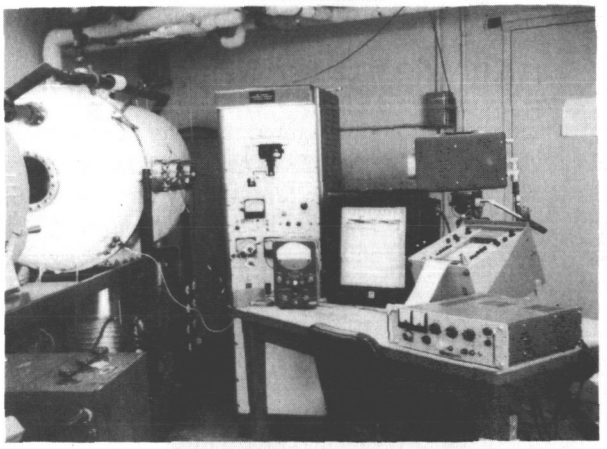

FIGURE 42. SPACE THERMAL-ENVIRONMENT-CHAMBER FACILITY

penetration of three thicknesses of aluminum. Two additional experiments being conducted with the satellite are considered vital for the scientific data evaluation and correlation of results. These deal with a radiation experiment and the four thermal environmental effects sensors described previously.

Besides other data, nineteen temperature measurements are telemetered over the Pulse Amplitude Modulation (PAM) channel. These measurements serve to check on the functioning of onboard equipment and to determine the correctness of the thermal control. The evaluation of the thermal effects sensors and temperature measurement is part of the scientific evaluation task of the Research Projects Laboratory. Thermal aspects of the Pegasus experiments were studied by Heller, Snoddy, Miller, Bannister, and Arnett. Other members of Research Projects Laboratory contributed in their specific areas of research to the Pegasus thermal measurements and thermal control of the electronic canister.

Some early results are reported to indicate the excellent type of information received over the various channels. Figure 43 shows a 14-day record of typical electronic canister temperatures. Only day-to-day changes are recorded because of the large time constant (15 hours) of the canister. The critical battery temperatures are in the middle of the band required by the design specifications. The forward solar panel temperatures are shown in Figure 44. Orbital variations occur; therefore, the maximum and minimum temperatures received during any day are shown. Figure 45 and 46 are examples of the stored Pulse Code Modulation (PCM) temperature data. Figure 45 shows the micrometeoroid detector panel temperature probes. Note

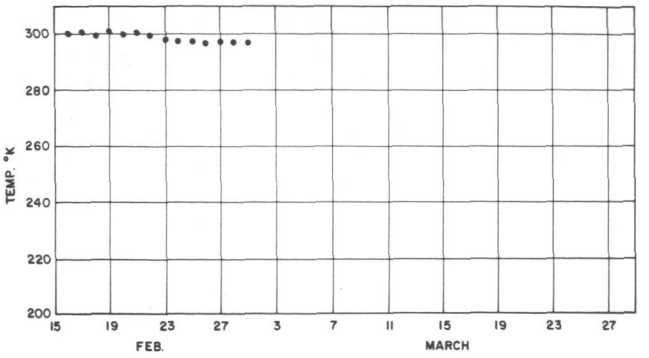

FIGURE 43. PEGASUS I ELECTRONIC CANISTER TEMPERATURES

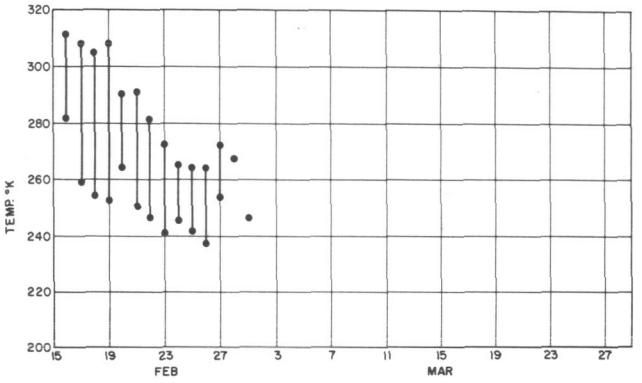

FIGURE 44. PEGASUS I FORWARD SOLAR PANEL TEMPERATURES

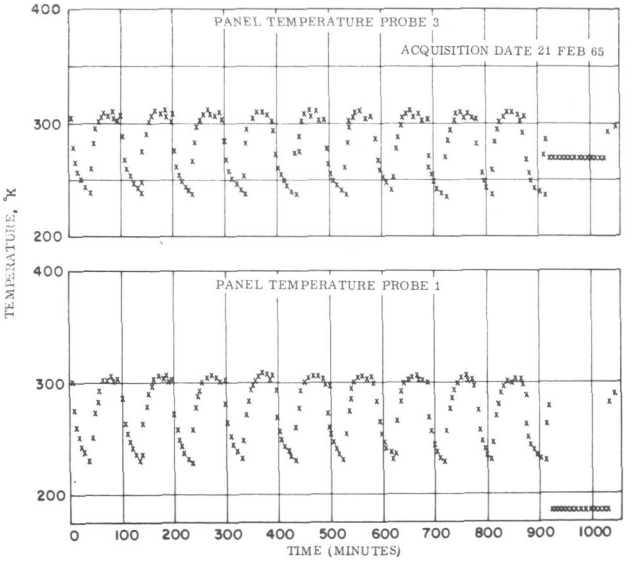

FIGURE 45. PEGASUS I MICROMETEOROID DETECTOR PANEL TEMPERATURES

the calibrations at 920 minutes. Figure 46 shows data obtained from the Alodine reference temperature sensor. Major fluctuations are caused by passages

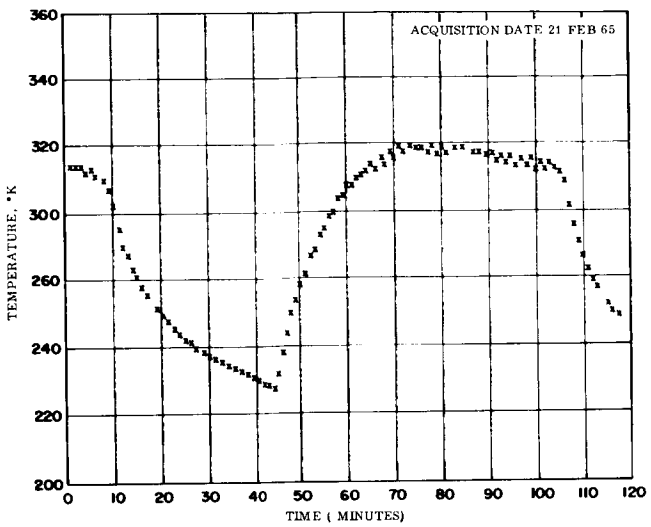

FIGURE 46. TYPICAL TEMPERATURES FROM ALODINE REFERENCE TEMPERATURE SENSOR

into and out of the earth's shadow, while the "ripple" is caused by vehicle roll. Detailed analysis of the data promises to be very interesting. Details of the Pegasus satellite experiments and data transmission channels may be found in Pegasus Bulletins No. 1 and No. 2 [61, 62].

In Figure 47 results of the Pegasus thermal control surface S-13 are shown in terms of its spectral absorptance. Measurements were made using a spectroreflectometer with an integrating sphere.

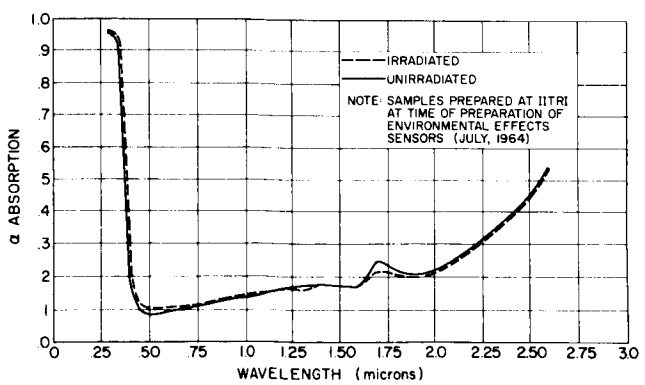

FIGURE 47. PEGASUS THERMAL CONTROL STUDIES OF S-13

III. PROJECT SUPPORT

In addition to the assignment of thermophysics research, the Space Thermodynamics Branch (RP-T) of Research Projects Laboratory is actively engaged in project support of MSFC. Contributions made to various SATURN I vehicles, as previously mentioned are:

SATURN flight IV	thermal environment sensor
SATURN flight V	thermal control sensor of orbiting upper stage
SATURN flight VIII SATURN flight IX	thermal control of canister of satellite and thermal environment sensors
SATURN flight X	coupons with 352 thermal control surfaces

Portable infrared equipment and reflectometers of RP-T have been used at Cape Kennedy to determine the IR and optical properties of thermal control surfaces prior to launch. These are compared to laboratory measurements and in-flight telemetered values.

IV. RESEARCH CONTRACTS OF THE SPACE THERMODYNAMICS BRANCH

A. TITLE: SOLAR WIND DAMAGE TO SPACECRAFT THERMAL CONTROL SURFACES

Technical Supervisor: Edgar R. Miller
Contract No: NAS8-11269
Contractor: Litton Systems, Inc.

Description of Research: To establish experimentally the effect of simulated solar wind bombardment on surfaces for thermal control, to perform theoretical and experimental investigation of the damage mechanisms involved, and to distinguish the separate factors that operate synergistically.

B. TITLE: RESEARCH ON THERMAL CONTROL SURFACES FOR THE EXTRATERRESTRIAL ENVIRONMENT

Technical Supervisor: Edgar R. Miller
Contract No.: GO #H71465

Interagency Purchase Order: Wright Air Development Center

Description of Research: To perform research and development on thrust control surfaces for the extraterrestrial environment, especially areas of large vehicles.

a. High solar absorptance to thermal emittance ratio surfaces (ratios of 1 - 3)

b. Universal reflector surfaces ($\alpha_s \simeq \alpha_{IR} < 0.1$)

C. TITLE: THERMAL CONTROL UTILIZING FUSIBLE MATERIALS

Technical Supervisor: Tommy C. Bannister
Contract No.: NAS8-11163
Contractor: Northrop Space Laboratories

Description of Research: Development of analytical and engineering techniques for utilizing (in a sealed passive system) the heat associated with changes in state, phase, and temperature of specially selected materials for the thermal control of temperature-sensitive vehicle and satellite components. Studies include operation in zero-g environment.

To advance the use of phase-change materials for thermal control to the point where space thermal design engineers will not have reservations about using the technique.

D. TITLE: RADIOMETRIC MODELS OF LUNAR SURFACE

Technical Supervisor: William C. Snoddy
Contract No.: NAS8-20512
Contractor: General/Dynamics Convair

Description of Research: The measurement and evaluation of the thermal (mainly radiometric) properties of simulated lunar material. This information will be related to known lunar characteristics with the end result being a thermal model of the moon.

E. TITLE: SOLAR-RADIATION-INDUCED DAMAGE TO OPTICAL PROPERTIES OF ZnO-TYPE PIGMENTS

Technical Supervisor: William C. Snoddy
Contract No.: NAS8-11266
Contractor: Lockheed Missiles and Space Co.

Description of Research: This study is directed toward identification of the primary mechanisms involved in solar-radiation-induced damage to the optical properties of ZnO-type semiconductor pigments, as exemplified by ZnO itself.

F. TITLE: INVESTIGATION OF SPACE STABLE COATINGS WITH LOW α_s / ϵ_{IR} RATIOS

Technical Supervisor: Daniel W. Gates
Contract No.: NAS8-5379
Contractor: IIT Research Institute

Description of Research: The purpose of this research is the study of thermal control surfaces suitable for space vehicle surfaces to be maintained at low temperatures. Emphasis is on the long-time space stability.

G. TITLE: STUDY OF MICROMETEOROID DAMAGE TO THERMAL CONTROL MATERIALS

Technical Supervisors: James A. Fountain and Klaus Schocken
Contract No.: NAS8-20120
Contractor: TRW Systems

Description of Research: The main purpose of this research is to simulate the micrometeoroid impacts (especially particles of micrometer size) in the laboratory, using a Van deGraaf accelerator. The effects of these impacts on the optical properties of thermal control surfaces are investigated with spectroradiometers.

H. TITLE: STUDY OF DIRECTIONALLY REFLECTIVE SURFACES

Technical Supervisor: Edgar R. Miller
Contract No.: NAS8-11273
Contractor: Ling-Temco-Vought

Description of Research: The purpose of this research is to conduct analytical and experimental studies on surfaces whose reflectance by scattering is directional with the angle of incidence. Fiber optics plates are being investigated whose backscattering characteristics are in the Rayleigh-Gans domain.

I. TITLE: EMITTANCE OF MATERIALS AT LOW TEMPERATURES

Technical Supervisor: Klaus Schocken
Contract No.: GO #H2153A
Interagency Purchase Order: National Bureau of Standards

Description of Research: Emissivity of surfaces at cryogenic temperatures is an important research area. It has been found that strong variations in reflectance occur at wave numbers below 500 cm^{-1}. The purpose of this research is to apply new equipment and new techniques to the determination of reflection bands in the far IR to wave numbers of 20 cm^{-1} and below.

J. TITLE: MATHEMATICAL ASPECTS OF DIMENSIONAL ANALYSIS AND THERMAL SIMILITUDE

Technical Supervisors: Jimmy R. Watkins and Billy P. Jones
Contract No.: NAS8-20065
Contractor: University of Michigan

Description of Research: To extend through a generalized approach the mathematical theory of dimensional analysis and the application of such mathematical models to physical systems of thermal problems. This is an extension of the work on π theorems by L. Brand and A. G. Hansen.

K. TITLE: THERMAL SIMILITUDE STUDIES APPLICABLE TO SPACECRAFT

Technical Supervisor: Jimmy R. Watkins
Contract No.: NAS8-11152
Contractor: Lockheed Missiles and Space Co.

Description of Research: The purpose of this research is an experimental determination of modeling laws for correlation with mathematical analyses based on the theory of thermal similitude. Emphasis is on the time-dependent problems.

L. TITLE: THERMAL DESIGN STUDIES TO DETERMINE LAWS OF THERMAL SIMILITUDE

Technical Supervisors: Jimmy R. Watkins and Billy P. Jones
Contract No.: NAS8-5270
Contractor: University of Alabama

Description of Research: The purpose of this research is to determine new mathematical approaches and the physical processes involved in the thermal similitude. Emphasis is on time-dependent relationships such as occur in transient conditions. The program is primarily experimental.

M. TITLE: EFFECTS OF REDUCED GRAVITY ON THERMAL PROPERTIES OF INSULATION MATERIALS

Technical Supervisor: Klaus Schocken
Contract No.: NAS8-5413
Contractor: Arthur D. Little, Inc.

Description of Research: It is the purpose of this research to study the effects of reduced gravity on heat transfer in particulate systems. Consideration of the mechanisms of heat transfer in particulate materials indicates that reduced gravity may affect solid thermal conduction across contact points and thereby influence heat transfer.

N. TITLE: RADIATIVE EMISSIVITY OF MATERIAL

Technical Supervisor: Klaus Schocken
Contract No.: NAS8-5210
Contractor: P. E. C. Research Associates

Description of Research: It is the purpose of this contract to develop a new theory of emissivity, to apply the new theory to a large number of specific substances, and to design and carry out experimental tests to verify deviations from Kirchhoff's Law under other than equilibrium conditions.

O. TITLE: INTERFACE THERMAL CONTACT CONDUCTANCE

Technical Supervisor: Harry L. Atkins
Contract No.: NAS8-5207
Contractor: General Electric

Description of Research: Two metals in contact touch only at small irregular points. The principal parameter which affects metallic interface conduction is the applied mechanical pressure. It is the purpose of the contract to measure thermal interface conductance of certain metals which are representative of those used in spacecraft components and structures

P. TITLE: THERMAL CONDUCTIVITY OF NON-METALLIC MATERIALS

Technical Supervisors: Klaus Schocken and Charles D. Cochran
Contract No.: NAS8-1567
Contractor: Arthur D. Little, Inc.

Description of Research: The purpose of the contract is an analytical and experimental investigation of the thermal and dielectric properties of nonmetallic materials. Special emphasis is on the contributions of solid conduction and thermal radiation to the effective thermal conductance of heterogeneous materials. The results of experimental measurements and theoretical analyses will be applied to the thermal behavior of lunar surface materials.

Q. TITLE: USE OF THERMAL MODELS FOR ENVIRONMENTAL TESTING

Technical Supervisors: James K. Harrison and Billy P. Jones
Contract No.: GO #H-71483
Interagency Purchase Order: Arnold Engineering Development Center
Description of Research: The purpose is to confirm by experiment the theoretical validity of dimensional analysis and similitude. Three shapes have been selected for study (flat plate, sphere, and cylinder). Scaling of gross dimensions from prototype to model is 2 to 1.

REFERENCES

1. Anon.: Solar Electromagnetic Radiation. NASA Space Vehicle Design Criteria, vol. I, part B, ch. I, sec. I (NASA Accession No. X65-18719; distribution limited to government agencies and contractors), June 1965.

2. Thekoekara, M. P.: Survey of the Literature on the Solar Constant and the Spectral Distribution of Solar Radiant Flux. NASA SP-74, 1965.

3. Stokes, G. G.: Trans. Camb. Philos. Soc. vol. 9, 1852, p. 399.

4. Chandrasekhar, S.: Radiative Transfer. Dover Publications, Inc., New York, 1960.

5. Coulson, K. L.; Dove, J. V.; and Sekera, Z.: Tables Related to Radiation Emerging from a Planetary Atmosphere with Rayleigh Scattering. University Press, Berkeley and Los Angles, Calif., 1960.

6. Snoddy, W. C.: Irradiation Above the Atmosphere Due to Rayleigh Scattering and Diffuse Terrestrial Reflections. AIAA Paper No. 65-666, presented at the AIAA Thermophysics Specialist Conference (Monterey, Calif.), Sept. 13-15, 1965 (see also Thesis for Masters Degree, Univ. of Ala., 1964).

7. Merrill, R. B.; Snoddy, W. C.; and Schocken, K.: The Results of Emittance Measurements Made in Relation to the Thermal Design of Explorer Spacecraft. NASA TN D-1116, May 1962.

8. Anon.: Equipment for Thermal Emittance Measurements Above 1400° K. National Bureau of Standards, Annual Summary Report, Contract No. H-41986, Jan. 1964.

9. Aronson, J. R.; and McLinden, H. G.: An Investigation of the Optical Properties of Materials at Room and Liquid Helium Temperatures. A. D. Little, Inc., Final Report, Contract No. NAS8-2537, Nov. 1963.

10. Schocken, K.; and Ashby, N.: The Theory of Emissivity of Metals. Paper presented at Symposium on Thermal Radiation of Solids (San Francisco, Calif.), Mar. 4-6, 1964.

11. Ashby, N.: Theoretical Study of the Radiative Emissivity of Materials. P. E. C. Corp., Interim Summary Report (period of Apr. 1, 1963 - Apr. 30, 1964), Contract No. NAS8-5210.

12. Ashby, N.: Theoretical Study of the Radiative Emissivity of Materials. P. E. C. Corp., Technical Summary Report (period Apr. 1, 1964 - Apr. 30, 1965), Contract No. NAS8-5210.

13. Johnson, F. S., ed.: Satellite Environment Handbook. Stanford Univ. Press, Stanford, Calif., 1961.

REFERENCES (Continued)

14. Snoddy, W. C.; and Miller, E. R.: Areas of Research on Surfaces for Thermal Control. Paper presented at Symposium on Thermal Radiation of Solids (San Francisco, Calif.), Mar. 4-6, 1964 (also NASA SP-55, 1965).

15. Snoddy, W. C.: Calculations Concerning the Passage of a Satellite Through the Earth's Shadow. MSFC, MTP-RP-61-1, Feb. 1961.

16. Zwiener, J. M.: General Space Thermal Program. MSFC, M-RP-T-WP-1-63, May 1963.

17. Meiners, H. F., Jr.: A Study of Efficient Computational Methods Related to Space Thermal Equations Research Projects Laboratory (MSFC), R-RP-T-WP-63-5, Aug. 1963.

18. Preston, R. A.: Heat of Fusion Program for 'Freeze and Fry' Testing. Research Projects Laboratory (MSFC), R-RP-T-WP-14-65, Sept. 1965.

19. Bannister, T. C.: A Computer Program Describing the MMC Electronic Canister Thermal Design. Research Projects Laboratory (MSFC), R-RP-WP-63-6, Nov. 1963.

20. Snoddy, W. C.: MSFC Computer Programs Utilized in the Thermal Design and Analysis of Satellites. Proceedings of Conference on Heat Transfer Computer Programs, NASA Headquarters, May 7, 1964.

21. Bannister, T. C.: Radiation Geometry Factor Between the Earth and a Satellite. NASA TN D-2750, July 1965.

22. Watkins, J. R.; and Hilliard, J. W.: A Computer Program for Derivation of Similarity Ratios for Use in Thermal Similitude Analyses and Experiments. Research Projects Laboratory (MSFC), R-RP-INT-64-14, Apr. 15, 1964.

23. Jones, B. P. : A Computer Program for Solving by Several Numerical Methods a System of First Order, Non-linear Differential Equations that Represent Transient Temperatures in Objects Used in the Study of Thermal Similitude. NASA TM X-53121, Aug. 5, 1964.

24. Harrison, J. K.: Computer Program—Cryogenic Storage on the Moon (Subroutines A and C). NASA TM X-53270, June 1965.

25. Harrison, J. K.: Modification of a Pegasus Spacecraft to Perform a Cislunar Mission. NASA TM X-53279, June 1965.

26. Harrison, J. K.: A Means of Determining the Infrared Emission of the Moon from Temperature Measurements of a Lunar Orbiting Object. Master's Thesis, Univ. of Ala., Aug. 1964.

27. Jones, B. P.: Thermal Similitude Studies. J. Spacecraft & Rockets, vol. 1, no. 4, Aug. 1964, pp. 364-369.

28. Vickers, J. M. F.: Space Programs Summary 37-30. Jet Propulsion Laboratory, vol. 4, Dec. 1964, pp. 75-77, and Feb. 1965, pp. 111-112.

29. Watkins, J. R.: A Computer Program for Derivation of Similarity Ratios. Research Projects Laboratory (MSFC), R-RP-INT-64-14, Apr. 15, 1964.

30. Matheny, J. D.: Thermal Design Studies. Bureau of Engineering Research, Univ. of Ala., Final Report, Contract NAS8-5270, Sept. 1965.

REFERENCES (Continued)

31. Jones, B. P.; and Harrison, J. K.: A Set of Experiments in Thermal Similitude. NASA-MSFC TM X-53346, Oct. 1965.

32. Atkins, H. L.; and Fried, E.: Thermal Interface Conductance in a Vacuum. Paper presented at 1st AIAA Annual Meeting and Technical Display (Washington, D. C.), June 29-July 2, 1964 (also published in AIAA J.).

33. Atkins, H. L.: Bibliography on Thermal Metallic Contact Conductance. NASA TM X-53227, Apr. 15, 1965.

34. Anon.: Study of Interface Thermal Contact Conductance. General Electric, Summary Report (period of 27 Mar. 1964-27 Mar. 1965), Contract No. NAS8-11247, Doc. No. 65SD4395.

35. Anon.: Study of Interface Thermal Contact Conductance. General Electric, Summary Report, Contract No. NAS8-5207, May 1, 1964.

36. Schocken, K.: Heat Transfer by Infrared Radiation in Powders. MSFC, R-RP-INT-64-7, Feb. 1964.

37. Schocken, K.: The Lunar Surface. MSFC, R-RP-INT-63-17, Nov. 1963.

38. Schocken, K.: Electromagnetic and Thermal Parameters of Powders. MSFC, R-RP-INT-62-6, May 1962.

39. Schocken, K.: The Thermal Properties of Powders. MSFC, R-RP-INT-65-4, Mar. 18, 1965.

40. Heller, G. B.: Temperatures of Explorer I. ABMA, TN-61-58, 1958.

41. Heller, G. B.; and Jones, B. P.: A Comparison of Experimental and Theoretical Temperatures of Explorer III. ABMA, TN-76-58, Sept. 26, 1958.

42. Heller, G. B.: Thermal Control of the Explorer Satellites. ABMA, TN-17-59, June 1, 1959.

43. Heller, G. B.: Problems Concerning the Thermal Design of the Explorer Satellites. ABMA, DV-TM-11-60, May 17, 1960.

44. Jones, B. P.: Solar Aspect of Explorer VII Compared with Certain Measured Temperatures (Satellite 1959 Iota). Research Projects Laboratory (MSFC), MTP-M-RP-60-2, Oct. 1960.

45. Lumpkin, W. L.: Heat Transfer Measurements on the Explorer XI Temperature Sensor. Research Projects Laboratory (MSFC), M-RP-INT-61-21, Sept. 1961.

46. Snoddy, W. C.: Theoretical and Measured Temperatures of Explorer IV. ABMA, TN-6-59, Mar. 14, 1959.

47. Lumpkin, W. L.: Temperature Data of Explorer XI (S-15 Payload). Research Projects Laboratory (MSFC), MTP-RP-62-6, Aug. 1962.

48. Lal, R. B.; and Arnett, G. M.: Electron Paramagnetic Resonance Spectroscopy. MSFC, R-RP-INT-11, 1965.

49. Zerlaut, G. A.: Utilization of Pigmented Coatings for the Control of Equilibrium Skin Temperatures of Space Vehicles. Proceedings, Aerospace Finishing Symposium, Ft. Worth, Tex., Dec. 1959.

REFERENCES (Concluded)

50. McKellar, L. A. (Project Leader): Solar-Radiation-Induced Damage to Optical Properties of ZnO-Type Pigments. Lockheed Missiles & Space Co., Tech. Summary Report (period June 27, 1964 to June 27, 1965), Contract No. NAS8-11266; this work is also found in Olson, R. L.; McKellar, L. A.; and Stewart, J. V.: The Effects of Ultraviolet Radiation on Low α_s/ϵ Surfaces. NASA SP-55, 1965, pp. 421-428.

51. Arvesen, J. C.; Neel, C. B.; and Shaw, C. C.: Preliminary Results from a Round-Robin Study of Ultraviolet Degradation of Spacecraft Thermal Control Coatings. NASA SP-55; Air Force ML-TDR-64-159, 1965, pp. 443-452.

52. Zerlaut, G. A.; Katz, S.; and Stockham, J.: Investigations of Light Scattering in Highly Reflecting Pigmented Coatings. IITRI-C6018-6, Contract No. NASr-65(07), Jan. 1964, STAR Access, N64-16757.

53. Raziunas, V.; Zerlaut, G. A.; and Stockham, J.: Experimental Studies of Light Scattering by Monodisperse and Bimodal Dispersions of AgBr. Results of IITRI Project C6018-14, Contract No. NASr-65(07), May 13, 1965.

54. Cox, R. L.: Directionally Reflective Coatings Study. Ling-Temco-Vought Astronautics, Tech. Summary Rpt. No. 00.603, Contract No. NAS8-11273, Mar. 12, 1965.

55. Wehner, G. K.: Solar Wind Damage to Spacecraft Thermal Control Coatings. Applied Sciences Division, Litton Systems, Inc., Summary Rpt. No. 2842 (period June 20, 1964 to June 20, 1965), Project No. 57006, Contract No. NAS8-11269, July 20, 1965.

56. Shelton, H.; Hendricks, C. D., Jr.; and Wuerker, R. F.: Electrostatic Acceleration of Microparticles to Hypervelocities. J. Appl. Phys., vol. 31, no. 7, July 1960, pp. 1243-1246.

57. Friichtenicht, J. F.: Study of Micrometeoroid Damage to Thermal Control Materials. Thompson-Ramo-Wooldridge (Space Technology Laboratories), Final Report, Contract No. NAS8-11149, Feb. 1965.

58. Snoddy, W. C.: Thermal Design of S-46. Juno II Summary Project Report, vol. II, ch. 6, NASA TND-608, 1962.

59. Merrill, R. B.: The Thermally Isolated Temperature Sensors for Saturn. Research Projects Laboratory (MSFC), M-RP-INT-63-1, Jan. 1963.

60. Bannister, T. C.: Special Temperature Sensors for MMC. Research Projects Laboratory (MSFC), R-RP-T-WP-6-64, June 1964.

61. Pegasus A Satellite Bulletin No. 1. Pegasus Data Evaluation Group, Research Projects Laboratory, MSFC, Feb. 23, 1965.

62. Pegasus A Satellite Bulletin No. 2. Pegasus Data Evaluation Group, Research Projects Laboratory, MSFC, Mar. 1, 1965.

CRYOGENIC TECHNOLOGY RESEARCH AT MSFC

March 25, 1965

by

C. C. Wood

TABLE OF CONTENTS

A REVIEW OF CRYOGENIC TECHNOLOGY RESEARCH AT MARSHALL SPACE FLIGHT CENTER

by C. C. Wood

LIST OF ILLUSTRATIONS

LIST OF ILLUSTRATIONS (Continued)

CONTENTS (Continued)...

LIST OF ILLUSTRATIONS (Concluded)

LIST OF TABLES

A REVIEW OF CRYOGENIC TECHNOLOGY RESEARCH AT MARSHALL SPACE FLIGHT CENTER

By

C. C. Wood

SUMMARY

Cryogenic research conducted in support of current space vehicle programs and in anticipation of future vehicle requirements is summarized in this review. Results are reported for investigations in fluid mechanics, propellant storage, and instrumentation. Advances in cryogenic technology are needed for missions lasting many days. Special support is needed for studies in transient fluid mechanics at reduced gravity, superinsulation for flight tankage, efficient cryogenic reliquefaction of evaporated cryopropellants, and system integration.

Mechanical design considerations are illustrated in part C, in which yield strength of aluminum and titanium is shown to increase with decreasing metal temperature. As the temperature decreases from 160° to 40° R (89° to 22°K), there is a significant increase in yield strength for titanium and a more modest increase for aluminum.

I. INTRODUCTION

Cryogenic technology research in support of space-vehicle programs encompasses a diverse field of investigation. A part of this research effort is discussed in this review under the divisions of fluid mechanics, cryogenic propellant storage, and instrumentation.

Hydrogen as a rocket-engine fuel has not been used as extensively as oxygen, and specific parameters are not commonly known. As an introduction to the work discussed in the next sections, comparative data on key characteristics are given in Figure 1. In part A of the illustration, a comparison is made of heat transfer coefficients as a function of temperature ratio, $T/T_{saturation}$ For temperature ratios expected in high-pressure thrust chambers, the liquid heat transfer ratio of hydrogen to oxygen is 12. This indicates that hydrogen systems would require simpler, lighter equipment, but the opposite would be required for propellant storage. Part B shows the liquid hydrogen temperature increase as twice that of oxygen for equal storage volumes and heat leaks. The pressure rise ratio of hydrogen and oxygen per unit propellant temperature increase varies between 8 and approximately 15. Obviously, hydrogen is far more difficult to store than oxygen.

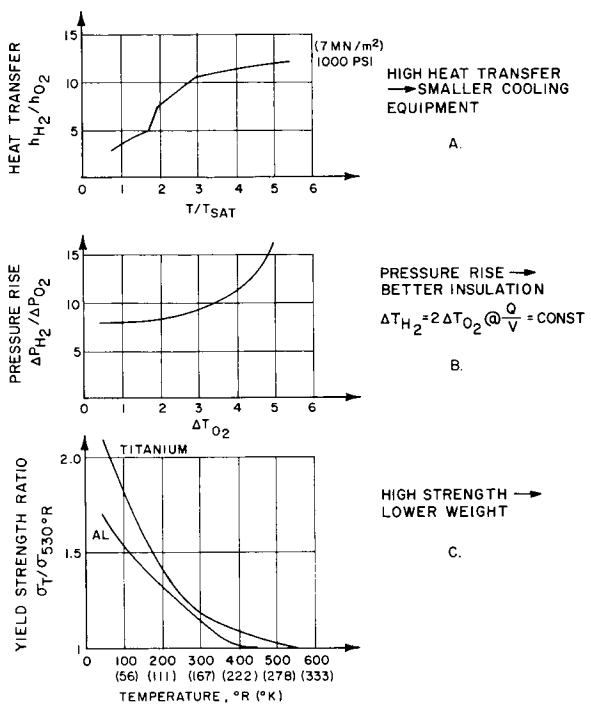

FIGURE 1. COMPARISON OF SOME H_2/O_2 PROPERTY EFFECTS

II. FLUID MECHANICS

A. PRESSURIZATION SYSTEMS

Several aspects of pressurization systems design have so far defied adequate analytical representation and require extensive testing for design verification. Two primary examples are the thermodynamic behavior of pressurization gases inside the propellant tank and flow instabilities in the pressurization gases of cryogenic liquid/gas systems. An understanding of the thermodynamics of gases within a tank is important for minimizing pressurant and weight and also for designing systems that do not possess transient flow instabilities. Flow instabilities originating within the heat generator of a pressurization system usually cannot be tolerated, and elimination of instabilities afterward imposes significant weight penalties and loss of system flexibility. Marshall Space Flight Center (MSFC) is currently studying both propellant tank thermodynamics and flow instabilities. Some results of these studies are explained in Figures 2 through 5.

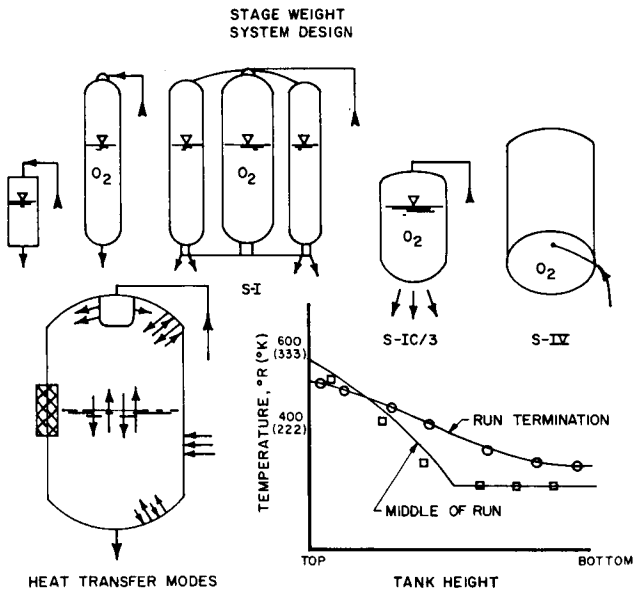

FIGURE 2. PROPELLANT PRESSURIZATION

Figure 2 illustrates tanks used in the MSFC experimental program to verify analytical procedures for predicting thermodynamic behavior. Existing modes of heat transfer and a comparison of analytical predictions with experimental data are shown. The test tanks vary significantly in size, shape, and number, and should provide ample variables for validating developed analytical procedures. The effects of propellant sloshing can be assessed on the large single oxygen container (6 ft by 40 ft; 1.8 m by 12.2 m) and on the one-third-scale S-IC container (13 ft by 26 ft; 4 m by 8 m). Liquid oxygen and nitrogen were pressurized by vaporized oxygen, nitrogen, and helium. Data in Figure 2 obtained midway and near the end of propellant drainage agree well with analytical procedures. Measured pressurant weights and pressurant weights established by analytical methods in most cases agree within 10 percent. Data accumulated from tests with these various tanks were published in NASA Technical Memorandum S-53165. Currently, liquid hydrogen data are being analyzed; the completion of these analyses will be the culmination of several years' work in this field by MSFC.

Figure 3 is an interesting plot of oxygen tank pressurant mass per unit pressure versus vehicle

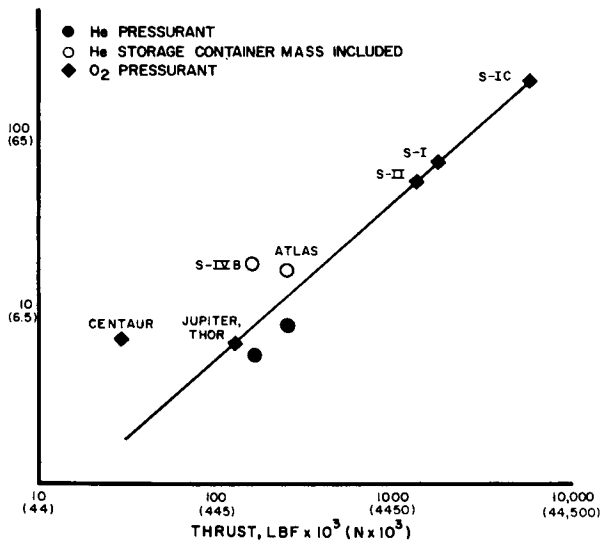

FIGURE 3. RELATIONSHIP BETWEEN OXYGEN TANK PRESSURANT MASS AND VEHICLE THRUST

thrust. Data are presented for several vehicles. The Saturn S-IVB stage and the Atlas vehicle use helium as pressurant. Helium is stored in these vehicles at liquid-hydrogen and liquid-oxygen temperatures, respectively. The pressurant masses for the S-IVB and Atlas include the mass of the storage bottles. All remaining vehicles, except Centaur, use liquid

oxygen, vaporized and superheated in heat exchangers, as pressurant. The Centaur stage is pressurized by flash boiling of the propellant; the resulting pressurant approaches the propellant saturation temperature and is heavy. Contrary to general opinion, the S-IVB and Atlas helium pressurization systems are heavier than those in vehicles of comparable thrust that use vaporized and superheated oxygen. Helium systems which weigh less than oxygen systems can be designed, but such systems are complex and costly.

Fluids undergoing phase change from liquid to gas usually undergo violent oscillations. Typical pressure instabilities of the J-2 rocket engine heat exchanger, which is designed to vaporize liquid oxygen, are shown in Figure 4. Also shown are

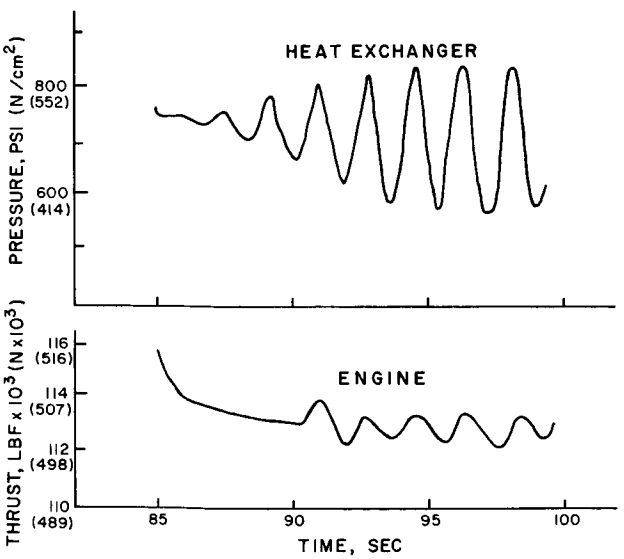

FIGURE 4. HEAT EXCHANGER INSTABILITY AND EFFECTS ON ENGINE INSTABILITY

variations in the J-2 rocket engine thrust caused by pressurant flow oscillations. Preliminary results of a study to determine factors that contribute to fluid instability are shown in Figure 5. Fluid studies for the subcritical state have been completed and regions of instability are mapped in this preliminary figure. Flow instabilities depend on fluid density ρ, fluid entrance velocity U, heat flux to the fluid Q/A, flow rate $\dot{W}$, heat exchanger geometry (tube diameter D and tube length L), and pressurant temperature rise ΔT. Flow instability for supercritical conditions is also being investigated.

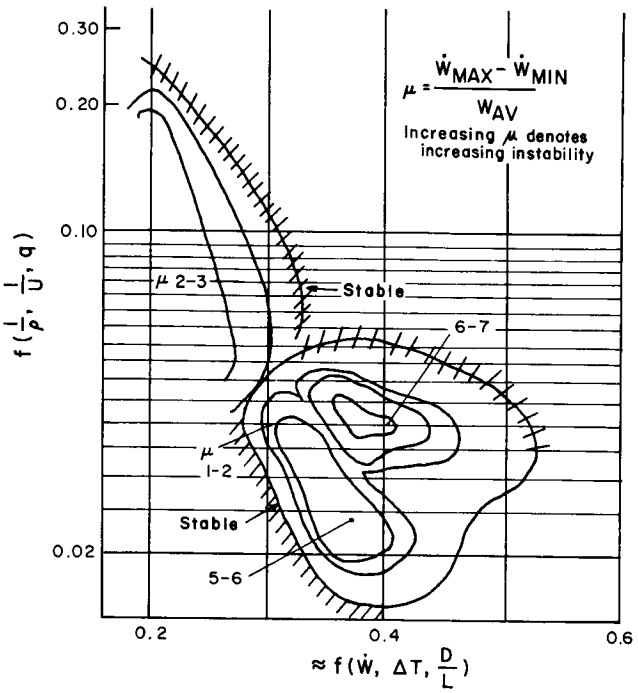

FIGURE 5. HEAT TRANSFER INSTABILITY MAP

B. ROCKET-ENGINE COOLING

Rocket engines developed for high-pressure operation appear to offer many advantages. One advantage is reduced size. Figure 6 illustrates anticipated rocket-engine thrust-chamber cooling requirements versus engine chamber pressure for two engine propellant combinations: liquid oxygen and RP-1, and liquid oxygen and hydrogen. The heat flux expected for a 5000-psi (34 MN/m^2) thrust chamber is approximately 100 Btu/in^2 sec (1.6×10^8 W/m^2), which is sufficient to evaporate a cup of water in approximately 2 seconds. This is approximately twice the heat flux on the nose cone of an intermediate range ballistic missile, during maximum reentry heating. Cooling criteria limit operating pressures of regeneratively cooled thrust chambers to approximately 2000 psi (14 MN/m^2) for hydrogen and 1500 psi (10 MN/m^2) for RP-1. Limitations are wall coking for the RP-1 system and excessive tube pressure drop for the hydrogen system. Stated limits of 2000 and 1500 psi represent significant increases relative to current engine designs.

Current studies to improve thrust-chamber cooling at higher pressure include other aspects of

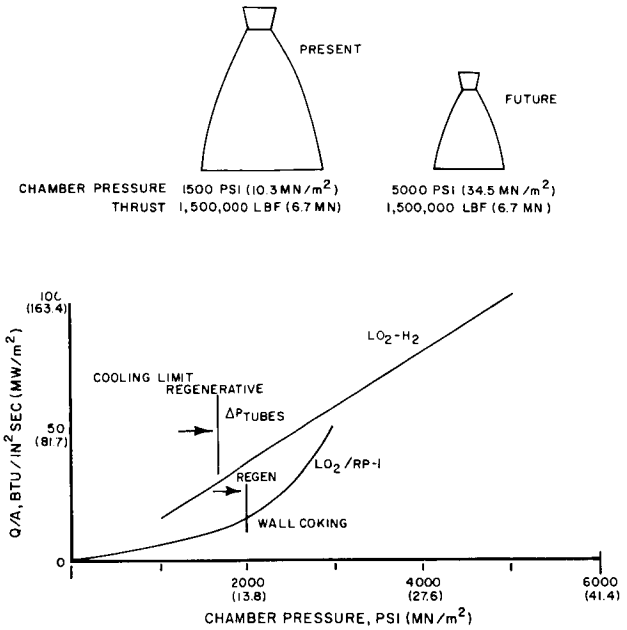

FIGURE 6. ENGINE COOLING

heat transfer and of heat dissipation principles such as film cooling, dump cooling, ablative cooling, etc. Figure 7 shows the results of one of these studies, the influence of surface roughness on heat transfer. The advantage of surface roughness, although significant, is not sufficient to extend existing design limits on chamber pressure.

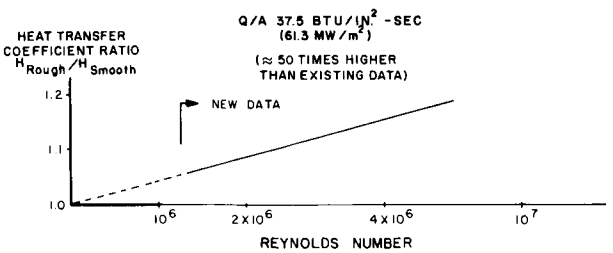

FIGURE 7. INFLUENCE OF SURFACE ROUGHNESS ON HEAT TRANSFER COEFFICIENT

C. GRAVITATIONAL EFFECTS ON HEAT TRANSFER

Gravitational influence on heat transfer for gravity levels both greater and less than 1 g_o are shown in Figure 8. Gravitational levels less than 1 g_o were obtained with a counterweighted package and a 32-foot (9.8-meter) drop tower. A centrifuge

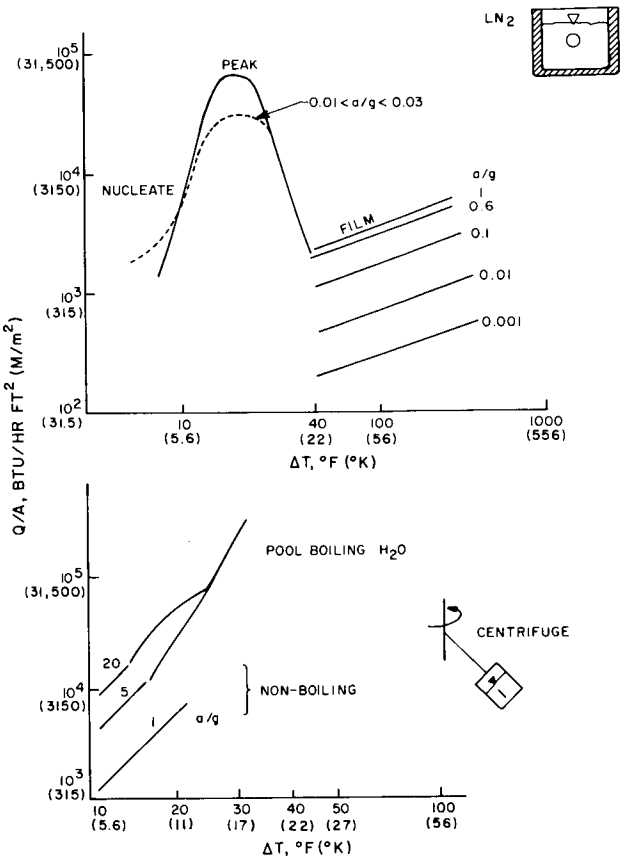

FIGURE 8. GRAVITATIONAL INFLUENCE ON HEAT TRANSFER

was used to produce gravity levels greater than 1 g_o. Saturated nitrogen and water were studied. Variation in the gravitational field from 1 to 0.001 g_o results in a heat-flux reduction of one order in magnitude in the film boiling region. Differences in peak heat flux and heat flux in the nucleate boiling region are smaller. Data are now being obtained with subcooled nitrogen and with a flat plate rather than a sphere as the test specimen. Similar data are to be obtained with liquid hydrogen. Of special interest is the critical heat flux for incipient boiling in liquid hydrogen.

The influence on heat transfer rate of gravitational fields greater than 1 g_o is important in the nonboiling region. These data, shown in Figure 8, were obtained with the heated surface perpendicular to the gravity vector. Data with the heated surface parallel to the gravity vector are also being obtained.

D. FLUID GEYSERING

Geysering is the sudden eruption of cryogenic propellants from lines and is caused by a

Taylor bubble formation within vertical lines attached to containers of large diameter or horizontal line sections. Geysering propellants create potentially dangerous forces when reimpacting with the remaining propellants within the tank. Pressures in excess of 900 psi (6 MN/m^2) were measured at the suction line/rocket engine interface immediately after a large liquid-oxygen tank had geysered. Pressures resulting from line geysering frequently exceed design pressures of feed system components. Considerable effort has been spent on controlling propellant geysering in vehicle suction and facility fill lines.

Figure 9 shows a correlation for predicting the initiation of geysering and the design used on the first stage (S-IC) of the Saturn V rocket to prevent geysering. The correlation is a function of suction-line geometry and heat flux Q/A entering the fluid, the Prandtl number N_{pr} and thermal diffusivity α

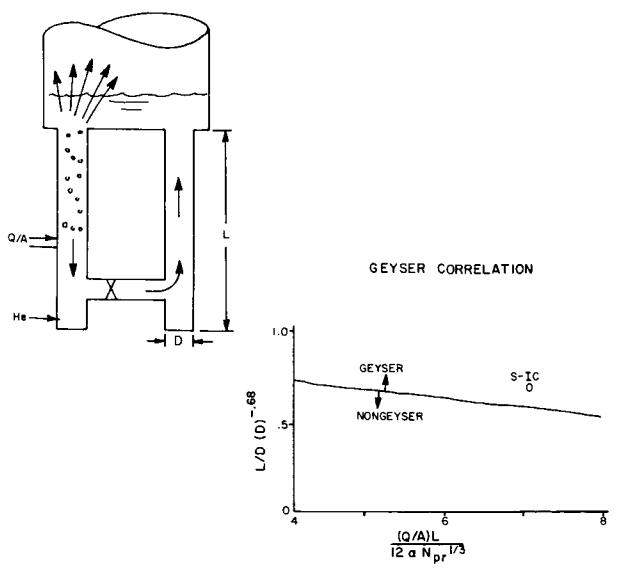

FIGURE 9. PROPELLANT GEYSERING

of the fluid. The correlation is valid for most fluids and has been applied and proven adequate for liquid hydrogen, oxygen, and nitrogen. Line diameters up to 8 inches (20 cm) were used to establish the correlation. Propellant feed lines for two MSFC stages fall within the geysering region as established by the correlation: the hydrogen lines for the S-II stage (which appear to offer no problem because of low propellant density), and the oxygen lines for S-IC. Fluid circulation between interconnecting suction lines prevents geysering in the S-IC; bubble accumulation within the lines, the suspected driving force for a geyser, is eliminated. Helium gas is injected to augment the flow as required. S-IC system performance has been successfully demonstrated, although complexities result because of the many possible operational situations. The correlation for predicting the initiation of geysering has also been validated for large vehicle lines.

E. PROPELLANT STRATIFICATION

Thermal energy entering the propellant tank through the side wall and tank bottom warms the adjacent subcooled propellant and initiates propellant flow within the tank. The propellant temperature increases, warm propellant collects at the liquid surface (stratification), or the two events combine. Figure 10 shows the expected flow patterns and temperature profiles of propellant within a tank at different times during propellant explusion. Stratification

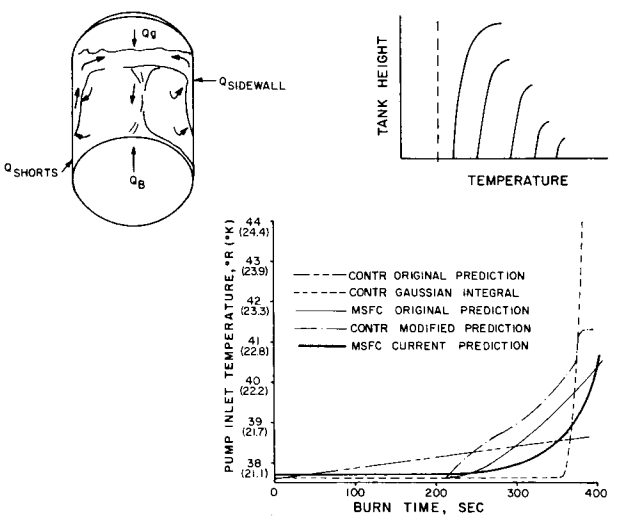

FIGURE 10. PROPELLANT STRATIFICATION

harmfully reduces available net positive suction head (NPSH) to propellant pumps. For compensation, tank pressure must be increased, the relatively warm propellants must be wasted as unusable residuals and left on board, or a combination of the two must be used. The usual solution is an increase in tank pressure. For hydrogen, however, each degree of temperature rise requires a tank pressure increase of 3 psi (21 kN/m^2) for NPSH compensation. This can result in a significant weight penalty. Also shown in Figure 10 are various propellant stratification predictions evolved during stage development. The curve marked "MSFC Current Prediction" is supported by test data from several test configurations including a test of a 22-foot (6.7 m)-diameter tank

with special instruments to provide stratification data. Identical prediction techniques have accurately represented propellant stratification during static tests. Between the initial and final stratification prediction, the efficiency of the thermal tank insulation was improved; this explains part of the differences in stratification temperatures shown.

Stratification can also occur under reduced gravity during orbital flight. Since the boundary layer for such conditions is usually laminar, the Navier-Stokes equation, the first law of thermodynamics, and the equation for mass conservation were solved and used for stratification prediction. Typical results are presented in Figure 11. These

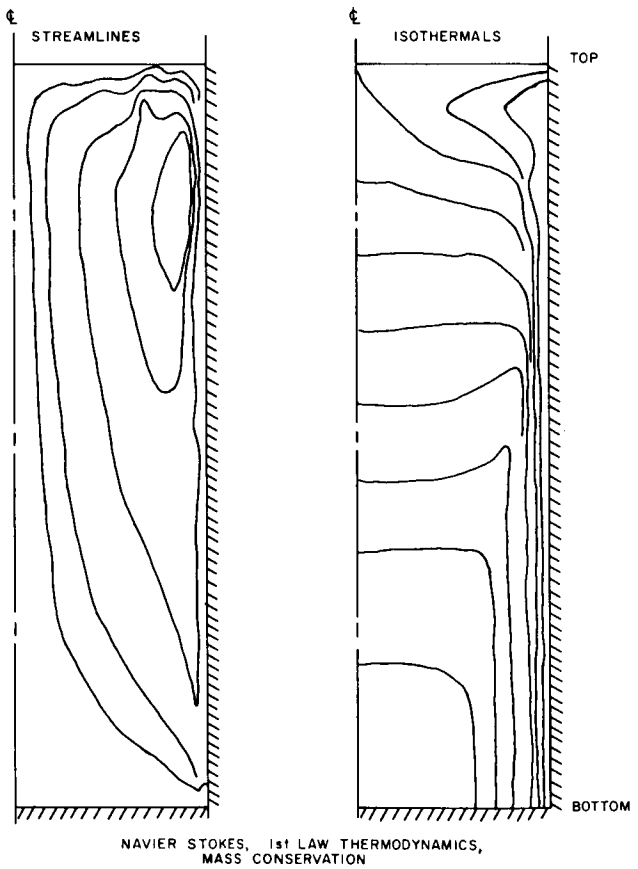

FIGURE 11. STRATIFICATION PREDICTION

results are preliminary and have no experimental verification. One interesting aspect of the data on streamlines is the apparent vortex located close to the tank wall and liquid surface.

F. FLUID DYNAMICS

Fluid dynamics problems of propellant feed systems are continually studied. Potential remedies for one such problem being explored, the so-called "Pogo" effect (the vibrational coupling of structure, propellant delivery system, and engine of a rocket vehicle), is discussed. Oscillatory forces may cause structural and propulsion problems as well as discomfort to astronauts. One potential solution to the Pogo effect is to change the acoustic velocity of the feed system by injecting a noncondensable gas; thus, frequencies of the feed system and structure are separated. Figure 12 shows how gaseous helium

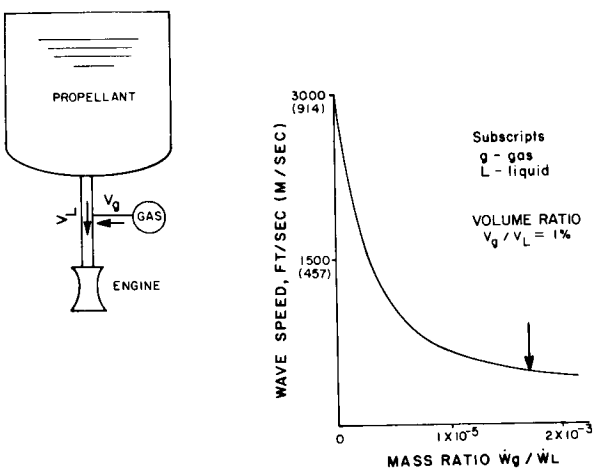

FIGURE 12. POTENTIAL SOLUTION TO FEED SYSTEM INSTABILITIES

injected into a column of liquid oxygen changes the acoustic velocity. In Figure 13, which shows the effect on frequency, the curve designated "system f" is based on actual data from a feed system including line, pump, etc. The large difference in frequency between the line and the complete feed system (Fig. 13) for low gas injection quantities results from a gas pocket or bubble near the pump inlet that accomplishes, to some extent, the same effect as helium injection into the line. This gas pocket is created by the pump and is not unusual. Gas injection significantly affects system frequency and offers a practical solution to the problem of undesirable oscillations. During developmental testing of the F-1 engine at MSFC, other oscillations were detected. Injected helium has shifted the frequency of these oscillations and reduced the amplitude. Gas injection below 2 percent by volume, the maximum tested, had no significant effect on engine thrust.

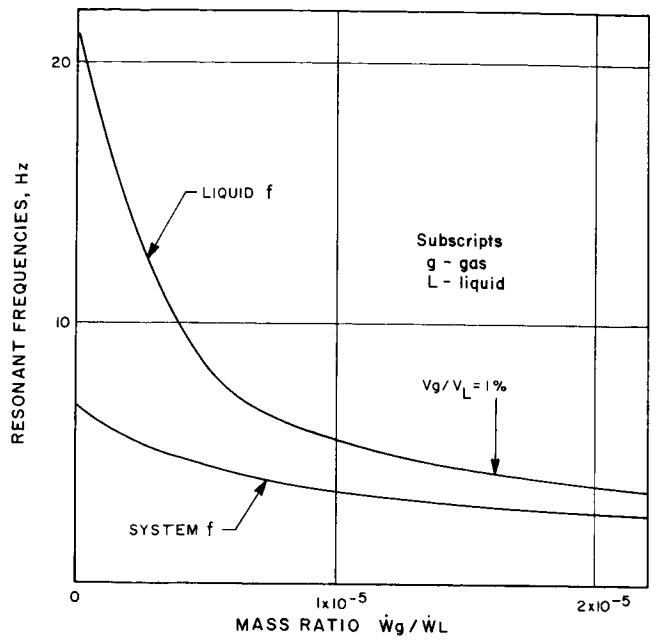

FIGURE 13. RESONANT FREQUENCIES VERSUS MASS RATIO

G. REDUCED GRAVITY FLUID MECHANICS

Figure 14 illustrates the equilibrium fluid configuration for a wetting fluid in gravitational fields of one and zero. Data are shown for two tank shapes and for varying amounts of propellants. Most research has dealt with equilibrium fluid mechanics for zero gravity and has ignored transient fluid mechanics, the situation most likely to be encountered on a practical mission. Marshall Space Flight Center is conducting analytical and experimental studies of transient fluid mechanics and has the assistance of several universities and industrial groups.

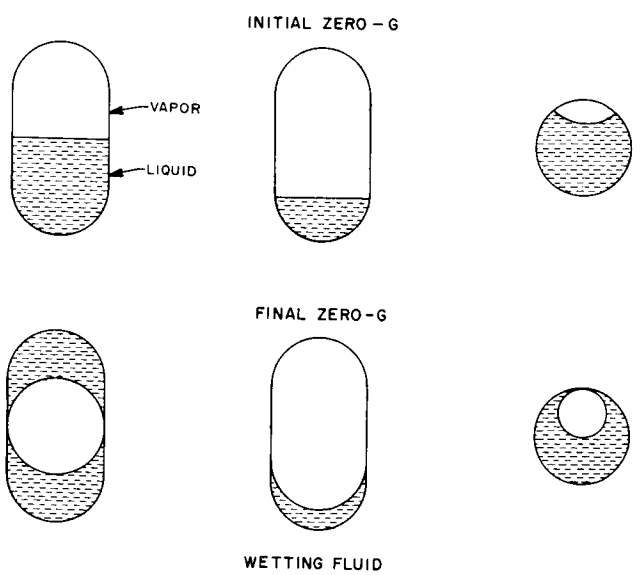

FIGURE 14. REDUCED GRAVITY FLUID MECHANICS

The Saturn S-IVB stage, developed by Douglas Aircraft Company and MSFC, burns cryogenic propellants and must restart in earth orbit after exposure to the orbital environment for not less than 1.5 hours and not more than 4.5 hours. Because of the reduction in gravitational force from the boost flight to the orbital phase, pre-insertion disturbances of propellants are magnified significantly after insertion. Figure 15 lists some sources of fluid disturbance at insertion of the S-IVB into orbit, expected

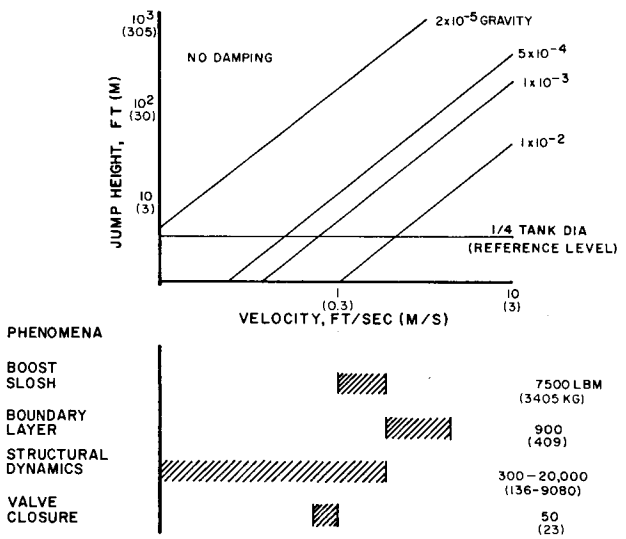

FIGURE 15. EXPECTED TRANSIENT PHENOMENA IN S-IVB

mass of hydrogen propellant involved, and velocity imparted to the propellant for each type of disturbance. The ordinate in Figure 15 shows propellant jump heights for the various disturbances; zero propellant damping and full conversion of all kinetic energy to potential energy are assumed. Gravitational forces provided on the S-IVB are 5×10^{-4} g_o for approximately 100 seconds immediately after orbital insertion. Gravitational forces are then reduced to 2×10^{-5} g_o and remain constant thereafter for earth orbit. These fluid motions are a potentially serious problem because hydrogen has low damping characteristics, and the hydrogen tank must be vented. As an example, a fluid motion possessing a vertical velocity of 1 ft/sec

(0.3 m/sec) during booster flight would jump 100 feet (30.5 m) at the sudden reduction of the gravitational field to 2×10^{-5} g_o. Although not listed in Figure 15, the attitude control system that limits vehicle attitude drift while in orbit is considered a major source of fluid disturbances. Firing in a random fashion, this system may create fluid disturbances during the entire orbital period.

Marshall Space Flight Center constructed a drop tower to study these problems, and experimentation began in mid-1965. Various features of the tower are shown in Figures 16 and 17. Free-fall distance for the test package is 294 feet (89.6 m), and the test duration is 4.3 seconds. Figure 18 illustrates

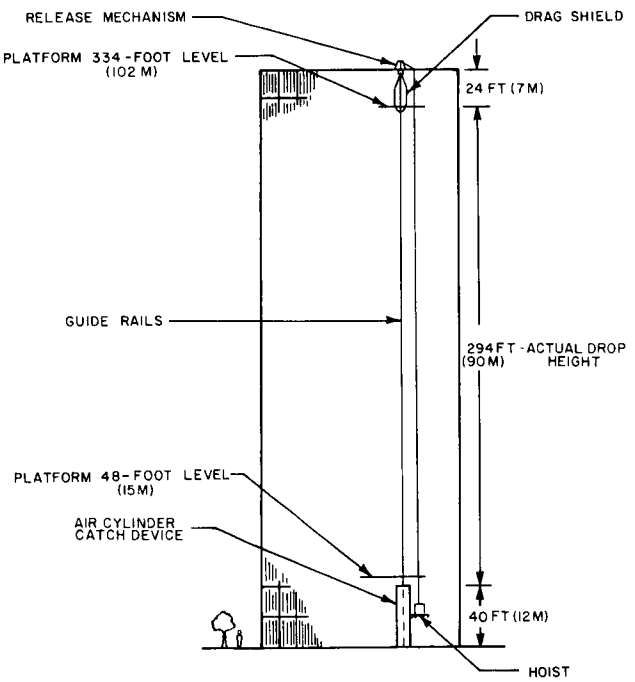

FIGURE 16. MSFC 300-FOOT DROP TOWER

typical subjects being explored through analyses and experimentation. An appropriate system design for the Apollo program requires adequate information about the following: time for propellant to travel along the propellant tank, type of propellant interface failure, time required to dampen fluid motion, optimum thrust for settling propellants, tendency for bubbles to collect on walls and in crevices, extent of propellant foaming and frothing caused by sudden tank pressure drop during venting, etc.

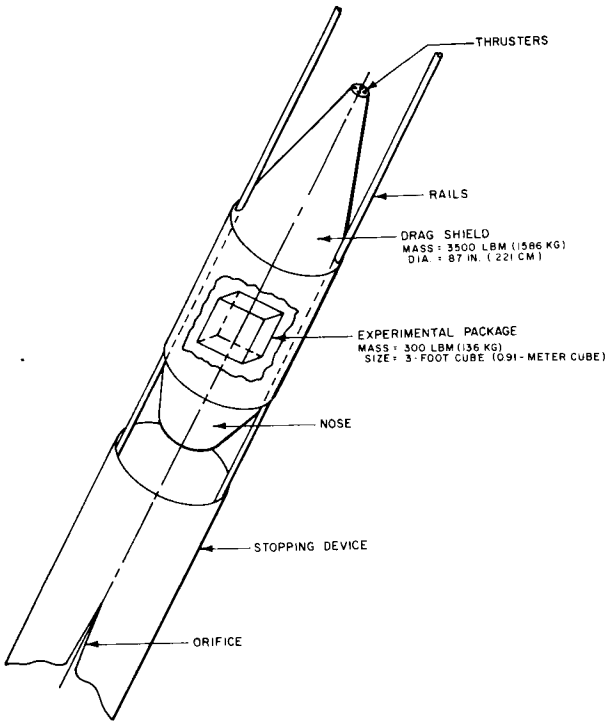

FIGURE 17. MSFC DROP TOWER DECELERATION DEVICE AND EXPERIMENTAL PACKAGE

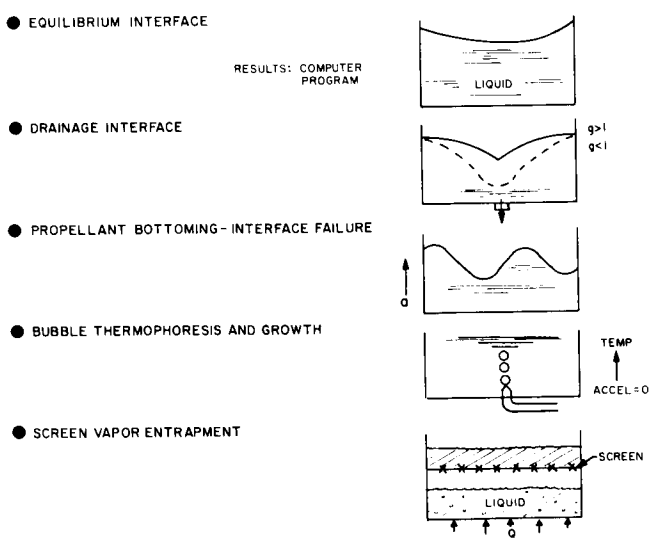

FIGURE 18. REDUCED GRAVITY FLUID MECHANICS STUDIES

H. DETONATION AND EXPLOSIVE HAZARD

Contributing to combustion hazards are propellants exhausted in the gaseous, liquid, or solid state from tank vents on engine chill systems. Vehicle systems designed to eliminate hazards on current vehicles are shown in Figure 19. The systems are heavy and complex, they degrade reliability, and they

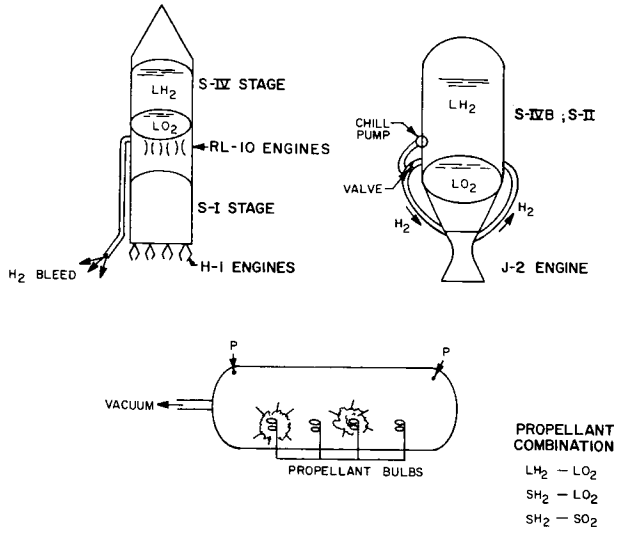

FIGURE 19. SYSTEMS TO ELIMINATE DETONATION AND EXPLOSIVE HAZARD

are costly. Available criteria for assessing hazards caused by oxygen and hydrogen mixtures in liquid, gaseous, and solid states are inadequate. Such criteria are being established under various degrees of vacuum and for various ignition sources. The investigation has only recently been initiated and results are not available.

III. PROPELLANT STORAGE

The storage of cryogenic propellants involves many technical concepts, such as insulation for reducing heat flow into the tank, surface coating for reflecting incident energy, shadow shields for reducing energy available to the storage container, devices for reliquefying propellant boiloff, the optimum state for stored propellant (slush, jell, etc.), and a combination of these (Table I). Current research dealing with some of these concepts is discussed in this section.

TABLE I. CRYOGEN PROPELLANT STORAGE

INSULATION SYSTEMS
Booster Vehicles, 6 hrs. Spacecraft, 96 hrs. Space Operations, 6 - 12 months
PASSIVE SYSTEMS
Coatings, Shadow Shields
ACTIVE SYSTEMS
Refrigeration
CRYOGEN STATE
Slush, Subcritical, Supercritical
SYSTEM INTEGRATION

A. INSULATION

Insulation is arbitrarily classified according to three types: Booster insulation (6 hours maximum storage), spacecraft insulation (96 hours maximum storage), and space operation insulation (6 to 12 months storage). Booster insulation used on the hydrogen tank of several stages and the index to insulation performance for each (product of insulation density and thermal conductivity) are shown in Figure 20.

The Centaur insulation is outside the hydrogen tank and has a passage for helium purge between the insulation and the tank wall. The Centaur insulation can be jettisoned; thus, the effective insulation performance index, K, is dependent upon flight time for insulation jettisoning. Insulation that is not jettisoned must have a K-value between 0.05 and 0.12 to be as efficient as the Centaur insulation.

The S-IV and S-IVB stage insulations are inside the hydrogen tank. They consist of polyurethane foam reinforced with small fiberglass threads (analogous to reinforced concrete) and have a vapor or hydrogen barrier of fiberglass cloth coated with epoxy resin. Performance degradation occurs with use because of hydrogen permeation of the barrier. The insulation performance index is approximately half that of the Centaur insulation, a significant improvement.

The S-II stage insulation is external to the hydrogen tank and consists of fiberglass honeycomb filled with polyurethane foam. A composite of epoxy-impregnated nylon and Teflon constitute the outer

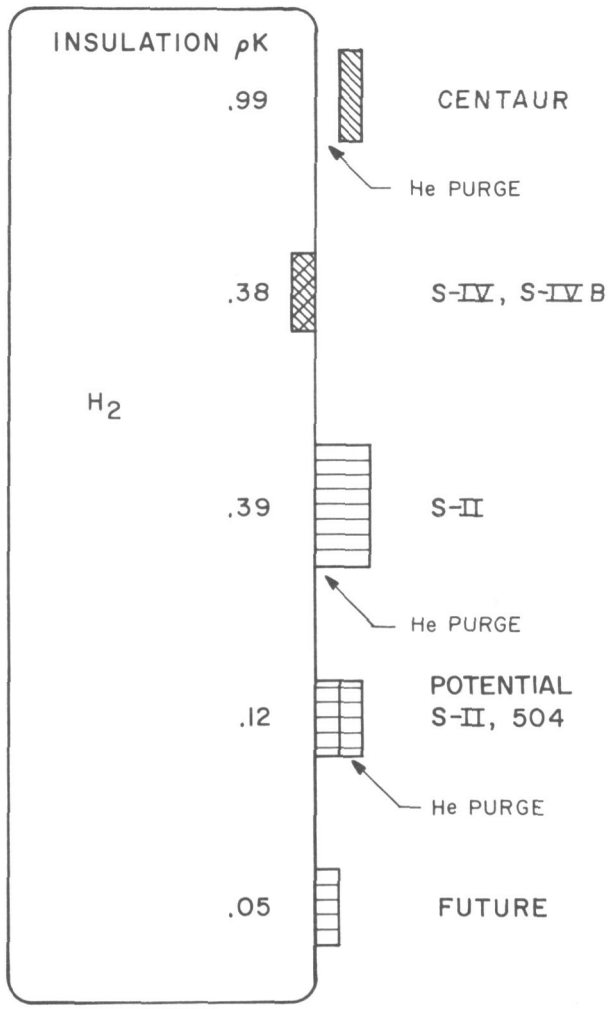

FIGURE 20. BOOSTER STAGE INSULATION

layer and vapor seal. The insulation is helium purged to eliminate hazards. Insulation performance for the S-II and S-IVB vehicles is equal. The S-II insulation considered for use on later vehicles, 504 and subsequent, will consist of a mylar honeycomb sealed inner layer and a fiberglass honeycomb outer layer. The outer layer is merely a channel for the required helium purge gas. The intermediate layer and outer layer are aluminum foil. No foam is utilized. The performance index of this insulation, 0.18, is significantly less than that for any known insulation exclusive of the superinsulations. Figure 21 shows this insulation applied to a 24-inch (61-cm) diameter calorimeter tank.

The availability of higher temperature materials permits development of an insulation that omits the outer channel portion of the S-II insulation. A performance index of 0.05 is believed to be possible for

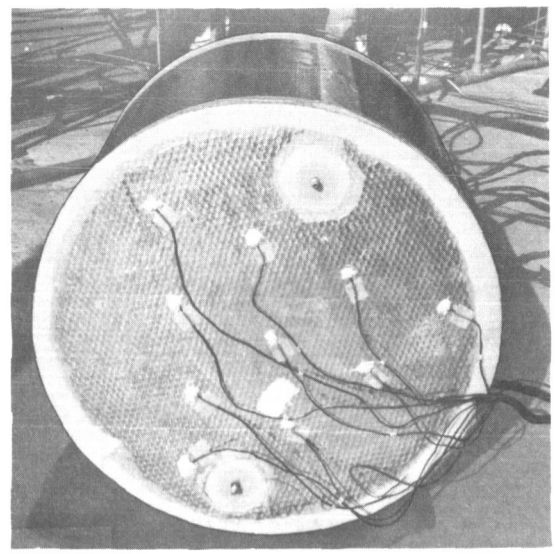

FIGURE 21. CALORIMETER WITH S-II STAGE, BACKUP 504-TYPE INSULATION

this insulation, a reduction factor of 8 from the current S-IVB insulation. Although significant progress in insulation for hydrogen containers has been made in the past few years, further improvements are imperative.

Spacecraft insulation of cryogenic vehicles for a 96-hour mission requires heat-leak reduction ratios of 150 to 500 relative to the S-IVB insulation. Marshall Space Flight Center is engaged, as are other organizations, in an insulation development program for realizing this goal (Fig. 22). This program includes significant contractor participation. Goodyear Aircraft Corporation, for example, is conducting basic research aimed toward new insulation systems that will be simple to apply and that will provide for meteoroid protection.

Lockheed Aircraft Corporation is attempting to improve existing computer programs and to devise new programs for predicting thermal system performance. The tank shown in Figure 23 is used as a model for the Lockheed work on helium-purged superinsulation. A typical propellant boiloff curve for hydrogen, for tank volumes comparable to that of the cryogenic service-module-type tank, is shown in Figure 24. Also given are ambient and internal pressures of the insulation versus time for a typical mission. Tests to verify insulation evacuation rates and thermal performance for various mission profiles, insulation concepts, and designs will be conducted in the test chamber illustrated in Figure 25. This chamber uses radiation barriers and controlled

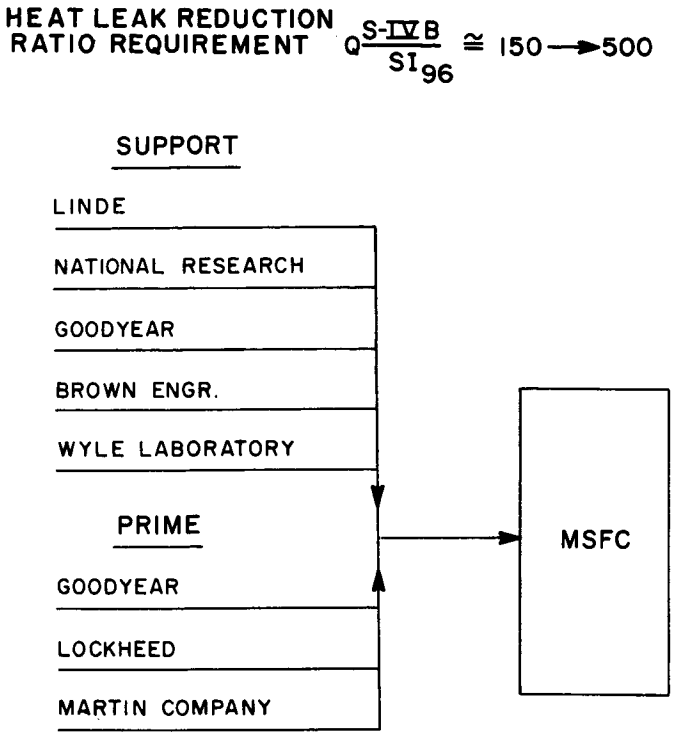

FIGURE 22. CONTRACTOR PARTICIPATION IN SPACECRAFT INSULATION PROGRAM FOR 96-HOUR MISSION

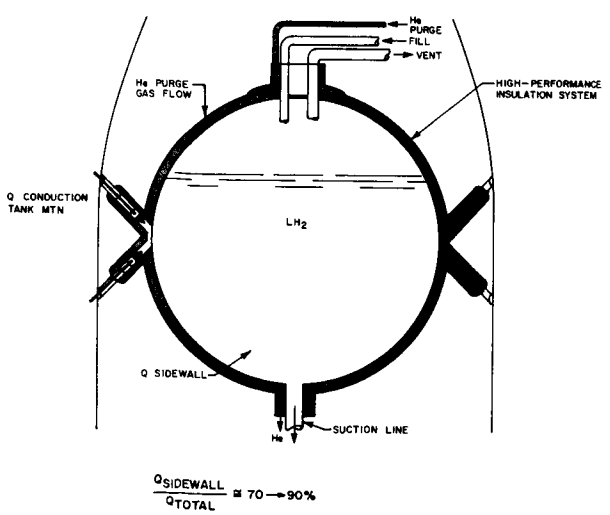

FIGURE 23. TANK MODEL FOR SUPERINSULATION RESEARCH

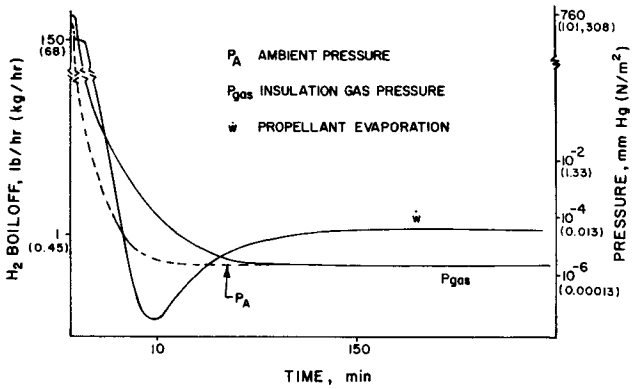

FIGURE 24. PREDICTED PROPELLANT EVAPORATION RATES AND INSULATION PRESSURES FOR SUPERINSULATED TANK

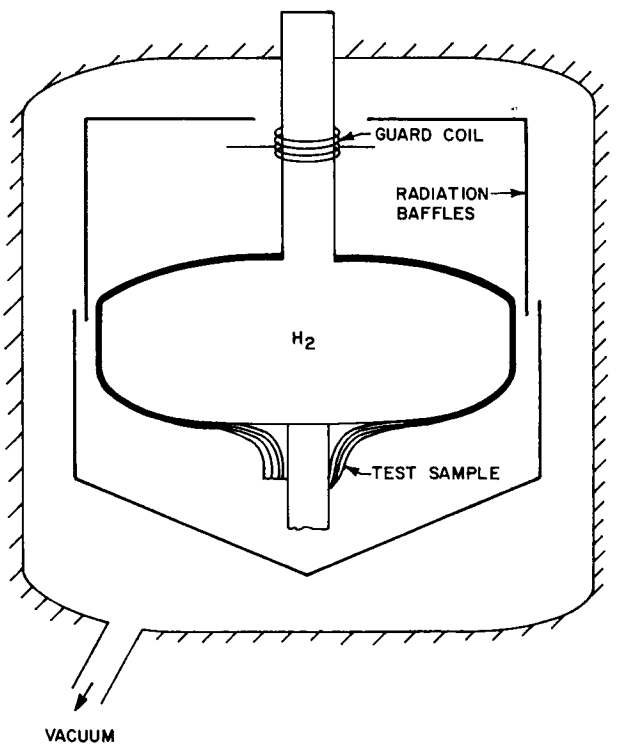

FIGURE 25. THERMAL PERFORMANCE TEST CHAMBER

conduction heat leaks for accurate thermal assessments of individual components.

Martin-Marietta Corporation is studying structural and thermal integration of insulation systems and will demonstrate performance for the selected concept at Marshall Space Flight Center, using a 105-inch (267-cm) diameter tank.

The MSFC in-house program uses two commonly known superinsulation concepts (Fig. 26), the National Research Corporation's (NRC) aluminized mylar radiation shield enclosed within a flexible jacket and

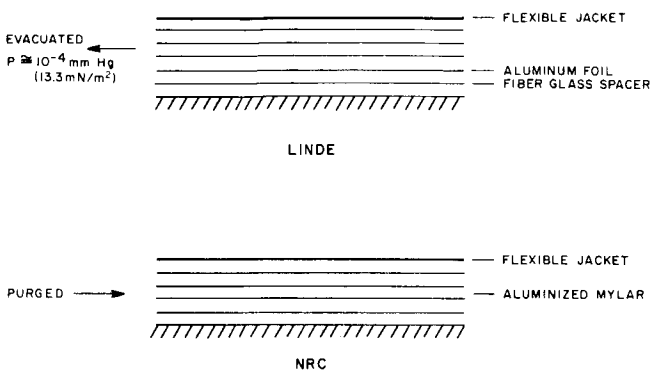

FIGURE 26. SUPERINSULATION CONCEPTS

purged, and the Linde Corporation's alternating layers of fiberglass and aluminum foil enclosed within a flexible jacket and evacuated. The milestone of the program is the demonstration of adequate thermal and structural performance for an insulated 105-inch diameter flight configuration tank as required for a 96-hour mission (Fig. 27).

There are many supporting programs in progress, and many have been completed. Typical component programs are flexible jacket material development, jacket fabrication, insulation evacuation rates, and penetration wrapping techniques. The program status for the 105-inch diameter tank is shown in Figure 28. The performance of the tank insulated with Linde SI-62 and tested in 1964 was unsatisfactory. Component tests have been initiated and are virtually complete, thus permitting this concept to be reapplied to the 105-inch diameter flight-configured tank. The NRC insulation purged with helium gas (concept 2 of Figure 28) has relatively high propellant boiloff during ground hold (Fig. 24). This system has been successfully tested. Insulation concept 3 (Fig. 28) uses a sublayer of insulation for reducing ground boiloff and is expected to perform the same as concept 2 at the low pressure in orbit. Application of insulation concept 3 to the 105-inch tank depends upon successful development of the mylar honeycomb sublayer for the tank bulkhead regions. Concept 4 will be established for the work of Martin-Marietta Corporation, and cannot be defined at this time.

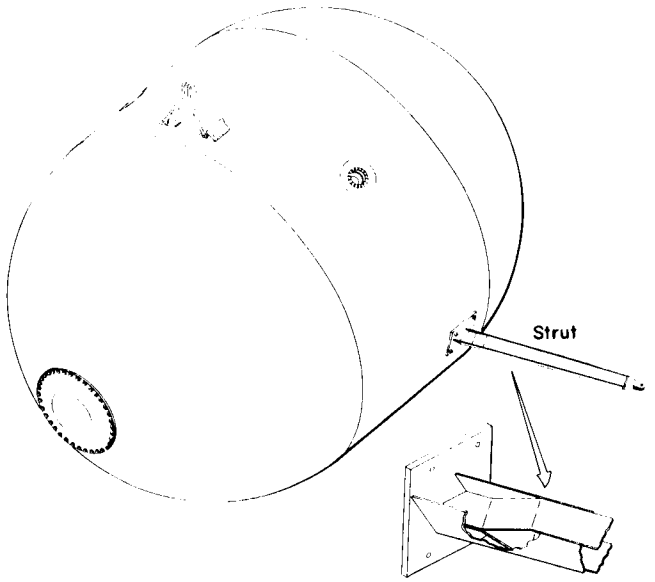

FIGURE 27. MSFC 105-I[illegible]H TANK ASSEMBLY

Tests are being conducted for both ground standby and orbital conditions. Figure 29 shows the vacuum chamber test facility used to simulate the orbital environment. Acceptable insulations will be tested under expected flight accelerations (Fig. 30), and retested for thermal performance at the expected orbital environment. Figures 31 through 33 show various insulated components, and Figure 34 shows the insulated tank.

Cryogenic propellant storage durations of 6 to 12 months or longer require heat transfer reductions between 2500 and 8500 relative to the S-IVB-type insulation. The present state of the art for long-duration storage of small quantities of propellant (liquid hydrogen and liquid oxygen), thermal requirements for the Gemini and Apollo spacecraft, and a possible Molab design (established during feasibility studies) are shown in Figure 35. Significant advances in technology are required to obtain the established Molab heat-leak requirement of approximately 2 Btu/hr (0.586 W) for each of the liquid-hydrogen and liquid-oxygen containers. Both MSFC and Manned Spacecraft Center (MSC) have initiated development programs for long-term storage of cryogenic propellants. In studies at MSFC, superinsulation is used for reducing the heat leak, while at MSC discrete radiation shields are used. Results of

MSFC	MSFC	MSFC	MARTIN
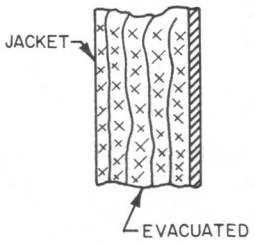 (1) LINDE	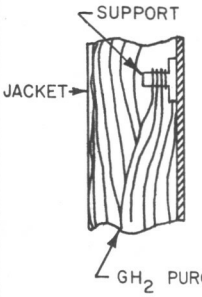 (2) NRC, SHINGLES	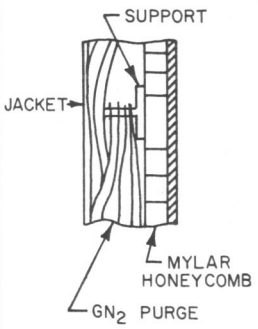 (3) NRC, SHINGLES	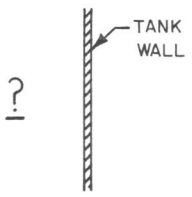 (4) DECISION PENDING

SUMMARY				
INSULATED	1964	CURRENT	1966	1966
TESTED	1964	JAN 1966	1966	1966
CURRENT EFFORT	TANK RETEST-1966	TANK AND COMPONENT	TANK AND COMPONENT	COMPONENT
MAJOR PROBLEMS	● JACKET LEAKS ● WRAPPING PENETRATIONS ● INS. RECOVERY	● GROUND HEAT LEAK ● SLOW EVACUATION	● BONDING MHC TO CURVED SURFACES	?

FIGURE 28. IN-HOUSE PROGRAM STATUS

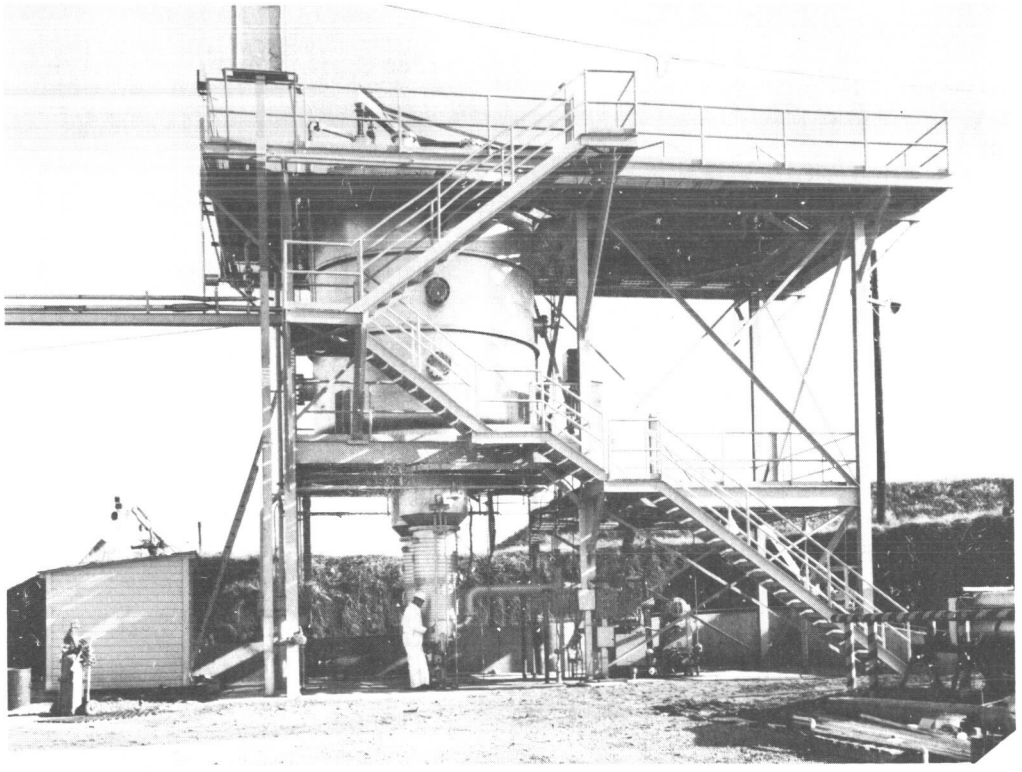

FIGURE 29. VACUUM FACILITY AT MSFC

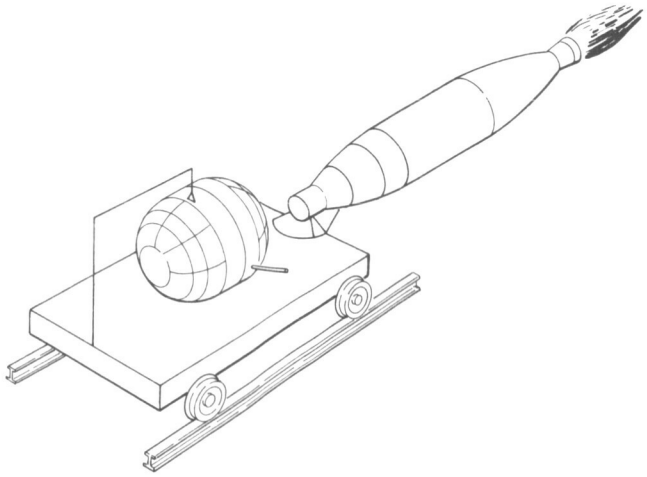

FIGURE 30. ACCELERATION TEST

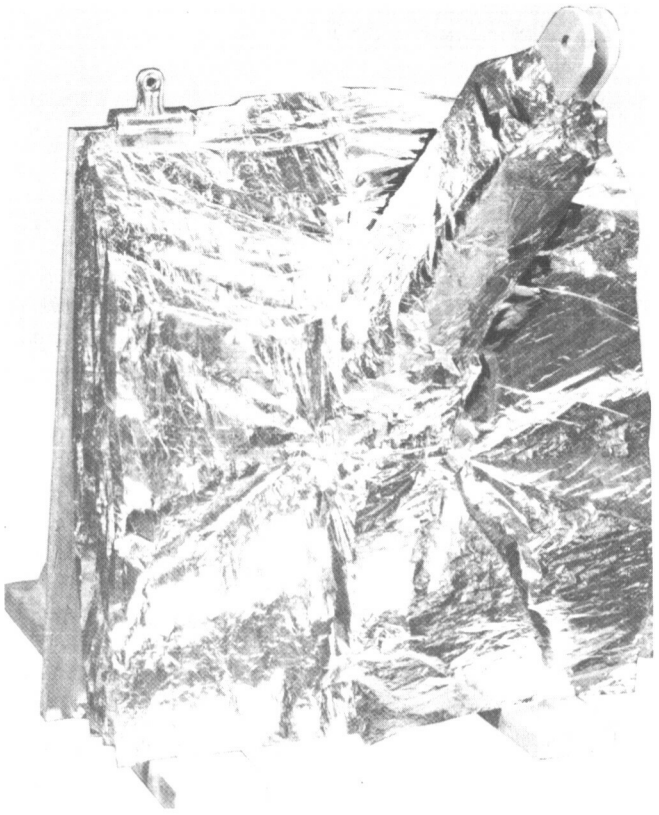

FIGURE 32. INSULATED SUPPORT-STRUT MOCK UP

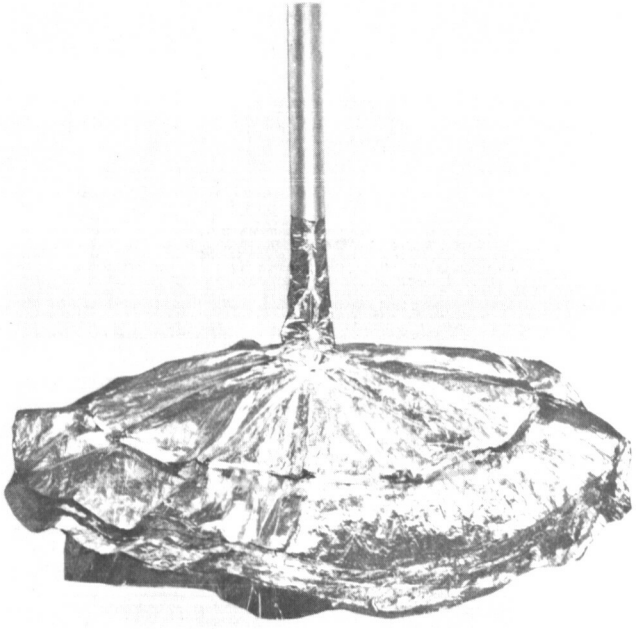

FIGURE 31. INSULATED MANHOLE COVER

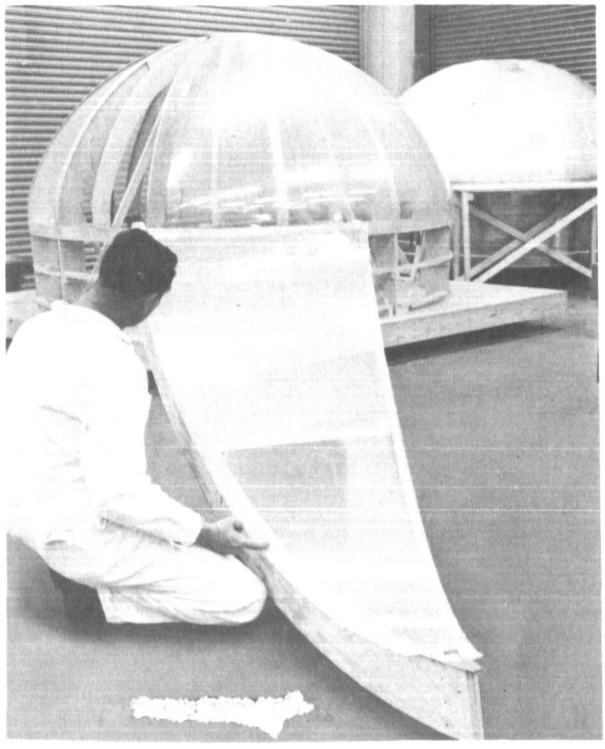

FIGURE 33. FLEXIBLE BAG MANUFACTURING

SOLID PROPULSION TECHNOLOGY

By

Richard N. Eilermann

SUMMARY

Project Vector, a joint effort between Marshall Space Flight Center and Langley Research Center, has resulted in the development of a concept to permit the use of rotating auxiliary solid motors for attitude, velocity, and thrust vector control. The control package consists of four solid propellant motors with an 80-degree nozzle, a frame, and associated actuators and position sensors. The first stage of the launch vehicle was powered by an XM33-E8 rocket motor plus two strapped-on Recruit rockets. Stability was provided by four 1.115-m^2 (12-ft^2) fins. The second stage was powered by an Antares rocket motor (ABLX-254). One vehicle was flight-tested at Wallops Island, Virginia. In spite of two serious malfunctions which affected the guidance, the control system recaptured the vehicle and maintained its trajectory until thrust reduction of the control motors occurred as programmed. All major objectives of the test were accomplished.

START-STOP-RESTART CAPABILITIES

A large scale start-stop-restart system for solid propellant rockets has been successfully demonstrated. Full scale quench and re-ignition system tests were conducted on two 0.736-m (29-in.) diameter solid rocket motors containing 680 kg (1500 lb) of composite-modified double-base propellant having flame temperatures in excess of 3590° K (6000° F). The final test used 4.54 $liter^3$ (1.2 gal) of water to quench the 1.32 m^2 (2200 in^2) of burning surface, or 3.16 kg/m^2 (0.0045 lb/in^2), and this quantity of water is small enough for practical flight application. The total quantity of water required to achieve quench is inversely proportional to the rate at which it is injected into the motor. It is believed that the amount of water required for quench is also a function of such factors as propellant type, motor operating conditions, size of unit, and water distribution effects such as overlapping coverage and water jet diameter.

MALFUNCTION PREDICTION AND ABORT IMPLEMENTATION

The objective of this program is to determine the requirements for a complete malfunction prediction and control system for large diameter solid propellant rocket motors. This includes the establishment of the abort implementation requirement, the possible malfunctions that should be sensed, and the corrective action or abort sequencing possibilities.

Two combustion termination methods investigated were a head-end liquid injection quench system and a head-end dry salt quench system. The capability of the liquid injection system was demonstrated with the firing of a 1.016-m (40-in.) diameter 10.5-m (413-in.) long rocket motor and the dry salt method was tested through salt-canister and small motor tests. The dry salt quench concept tested in this program is not feasible at the present time. The shock wave created by the exploding salt canister and the resulting cooling effect from the decomposing salt in the chamber did not disturb the combustion process sufficiently to terminate burning.

LIQUID PROPULSION TECHNOLOGY

By

Keith B. Chandler

SUMMARY

The Liquid Propulsion Technology Program has two primary objectives: the improvement and uprating of present systems and the preparation for future systems. The major effort related to the improvement of present systems is an experimental engine program known as the "J-2X." The specific improvements include minimization of engine prefire conditioning, test and evaluation of a tapoff turbine drive system, simplification of engine control system, test and evaluation of a catalytic ignition system, and test and evaluation of operation on mixed-phase propellants.

Nineteen tests have been conducted, and the feasibility of eliminating the gas generator by the use of thrust chamber tapoff has been demonstrated. The J-2 Engine requires a cold chamber (172° K or -150° F) in order to start without stalling the fuel pump. The J-2X has been operated at a chamber temperature of 255° K (0° F) without incident. The goal is to eliminate the chilldown requirement entirely.

COMBUSTION INSTABILITY

Almost every engine development program has been plagued with the problem of "combustion instability," which consists of high-frequency pressure oscillations in the combustion chamber. Theoretically, combustion instability can be eliminated by the use of a liner in the chamber which is perforated, much as ordinary acoustic tile used on ceilings. Uncooled liners made of stainless steel and coated with zirconia, and cooled liners consisting of a bundle of copper tubes with a manifold at each end have been successfully tested in a 17800 N-thrust (4000 lb-thrust) engine at Marshall.

A program has been started at Bell Aerosystems Company to obtain data on propellant droplet size and distribution under actual combustion conditions, which can be correlated with stability and performance characteristics. Bell will do this by obtaining high speed, high resolution photographs of ignition sprays under combustion conditions in a small scale rocket engine with transparent walls.

One of the more difficult tasks required in the testing in rocket engines is the accurate measurement of pressure oscillations that occur during periods of combustion instability. The instrument must be capable of measuring high-amplitude pressure oscillations at frequencies up to several thousand hertz, and it must be capable of withstanding the high heating rates which result when placed near the oscillating combustion process. These two requirements are incompatible. Princeton University is in the process of evaluating commercially available transducers and providing consultation in the means for improving transducers. To date, no transducer has met the program goal of measuring frequencies to ten thousand hertz at mean pressures of 6.89×10^6 N/m^2 (1000 psia) and heating rates up to $\frac{4100 \text{ joules}}{\text{cm}^2 - \text{sec}}$ (25 BTU/in^2 - sec). A unique measuring system developed by Princeton University, known as the "small passage technique," consists of a transducer connected to the combustion chamber through a small drilled passage. The passage is continuously purged with helium or hydrogen and is tuned to a resonant frequency higher than the frequency being measured.

STORABLE PROPELLANT FACILITY

Marshall has established a test facility for engines using storable propellants (N_2O_4/Hydrazine mixtures). The facility will provide for verification of manufacturer performance data and investigations of off-design operating regimes of the S-IVB auxiliary propulsion system (APS) engines. The facility is now ready for qualification of the GEMINI 445 N-thrust (100 lb-thrust) Orbital Attitude Maneuvering System (OAMS) engine for S-IVB ullage application and is ready to support the C-1 Engine program which is just getting under way.

INDUCER TESTING

One of the shortcomings of the presently used "helical" inducers is the loss in performance caused by the back-flow of propellants between the tip of the inducer blade and the wall of the pump. An improved design known as the "hubless" inducer designed by the Worthington Corp. is being tested in an H-1 LOX pump at Marshall. Compared to the standard H-1 inducer and using water as the pumped medium, the hubless design showed an improvement in suction performance of from 2.44 to 3.048 m (8 to 10 ft) over the entire flow range.

SECONDARY INJECTION USING HYDROGEN

Hot firing tests on an RL-10 Engine have been conducted at Pratt & Whitney's Florida Research and Development Center to correlate cold-flow tests of secondary injection systems conducted at the research laboratories of the United Aircraft Corporation in Hartford, Connecticut. The conclusions are that the lateral force characteristics are improved by increasing the up-stream angle, using a large number of small holes and locating the injection slot near the nozzle exit.

INSTRUMENTATION FOR MEASURING PERFORMANCE

A measuring technique has been demonstrated at the Bell Aerosystem Company for measuring the performance of rocket engines with thrust from 222 to 890 N (50 to 200 lb), and pulse widths from 10 to 100 msec.

ADVANCED LAUNCH VEHICLE ENGINES

In the preparation for future systems, work is being done on advanced chambers and nozzles, new power cycles, and higher chamber pressure. Two concepts which utilize already developed engines in a cluster arrangement are the "Multi-Chamber Expansion Deflection" and the "Plug Multi-Chamber." A third concept called the "Toroidal Aerospike" is one offering considerable promise but requires substantial technology investigation. Studies related to these concepts consist of analytical and experimental investigations.

An Advanced Engine Design Study consisting of analysis and design is underway to investigate high performance propulsion systems in the thrust level of 1.33 to 1.78 million N (300 to 400 thousand lb). The purpose is to define systematically the propulsion systems over a range of design constraints such as envelope, thrust, mixture ratio and specific impulse. This program will point out deficiencies, if any should exist in available technology data, which require immediate remedial action before continued definition and evaluation of advanced systems and components can proceed.

Although the specific design of an advanced engine has not been determined, some general requirements are known, particularly the advantages of higher pressure levels. Therefore, a program is under way to design, fabricate and test a breadboard high pressure liquid hydrogen pump to verify the performance characteristics that are desirable for advanced rocket engines.

ELECTRONICS RESEARCH AT MSFC

April 29, 1965

by

Joseph L. Randall
James C. Taylor
Charles L. Wyman

TABLE OF CONTENTS

LIST OF ILLUSTRATIONS

CONTENTS (Continued)...

LIST OF ILLUSTRATIONS

CONTENTS (Continued)...

LIST OF ILLUSTRATIONS

OPTICAL TECHNOLOGY PROGRAM

By

Joseph L. Randall

SUMMARY

A research and development program in optical and infrared technology is described in this review. The purpose of the program is to develop advanced optical systems for guidance, tracking, and communication in aerospace missions. The program is divided into four categories: (1) component and device development, (2) technique development, (3) in-house supporting research and development, and (4) optical system study and development.

Component and device development deals with laser sources, detectors, modulators, beam scanners, and ring lasers; all for use in optical systems. Superheterodyne receiver development and laser frequency stabilization compose the technique work, the aim of which is the development of communication and tracking techniques for particular systems.

In-house research and development, which provide essential support for the entire program, include the theoretical and experimental study of the effects of the atmosphere in optical tracking and communication and the design, fabrication, and evaluation of optical lenses, mirrors, and telescopes. The part of the optical system study and development discussed in this review refers to an optical technology satellite program, which has two important purposes. One is the development of an optical system for deep-space communication. The other is the determination of the effects of space environment on large diffraction-limited optics in order to obtain engineering data which can be used for designing 250 to 500 cm telescopes.

I. INTRODUCTION

With the development of the coherent light source (laser) in 1960, its potential for optical tracking and communication became apparent. Optical systems, compared to conventional RF techniques, should require smaller antennas, use less power, weigh less, give greater tracking accuracy, and increase deep-space communication capability. However, considerable research will be required to develop optical systems that will be practical and reliable. Marshall Space Flight Center has been engaged in an optical technology research and development program for several years with the aim of developing advanced optical systems for aerospace use.

This review will discuss the optical technology program, which is conducted in house and through out-of-house contracts. At present, most of the program is being carried on out of house under approximately 20 contracts.

The program is divided into (1) components and devices, (2) techniques, (3) supporting research and development (in-house), and (4) optical systems. The purpose of the component and device work is to develop better laser sources, detectors, optical modulators, beam-scanning devices, ring lasers, etc., for use in optical systems. The technique work is aimed at the development of communication and tracking techniques for use in a particular system. The in-house research and development work supports the overall program and allows the laboratory to maintain its technical competence. Examples of such work include the design, fabrication, and evaluation of optical lenses, mirrors, and telescopes used on other in-house projects; and the theoretical and experimental study of the effects of atmosphere on optical tracking and communication. The optical systems now being studied or developed are: (1) a precision optical tracking system for advanced launch vehicles, (2) an optical guidance system for rendezvous of spacecraft, and (3) an optical technology satellite system. Each of these systems will be discussed in detail, the latter in this report and the first two in the report on laser research (Wyman).

Figures 1 through 10 illustrate the extent to which Astrionics Laboratory is equipped for its research and development programs.

II. COMPONENTS AND DEVICES

The development of components and devices includes laser sources, detectors, modulators, beam scanners, and ring lasers.

A. SOURCES

For communication and tracking, it is desirable to have continuous wave (cw) operation or a pulsed laser that has a high repetition rate; therefore, research and development have been aimed toward these ends. Research in these sources can be divided into three areas: solid-state optically pumped lasers, semiconductor injection lasers, and gas lasers.

1. Solid-State Optically Pumped Lasers. In this area the goal has been to develop a cw, room-temperature laser that is efficient and practical. In 1963, Marshall Space Flight Center awarded a contract to the Linde Company to grow crystals that could be evaluated spectroscopically for potential laser materials. In this way, many materials were studied. This contract led to the development of yttrium aluminum garnet doped with neodymium ($YAG:Nd^{+3}$). This material is now used in the most practical cw solid-state optically pumped laser. It operates cw at 1.06 microns, is water cooled at room temperature, and is pumped with a tungsten lamp. It operates for extended periods with little degradation, and outputs of over one watt have been achieved. Figure 11 shows the cavity and laboratory setup. Its limitations are that the overall efficiency is less than one percent and that the output is not diffraction limited as is that of a gas laser. A contract is now in effect with the Linde Company to improve the optical homogeneity of the laser material. It is hoped that this will improve the diffraction-limited narrow beam. In-house work will be done to evaluate the performance of the Linde-grown rods for better efficiency and beam divergence and to design and build laser cavities to increase the power output to several watts. A continued effort will be made to improve $YAG:Nd^{+3}$ as a laser material.

2. Semiconductor Injection Lasers. Semiconductor injection lasers, because of their small size and high efficiency, offer great promise as spaceborne laser sources. They have a disadvantage, however, in that their emitting aperture is very small and is rectangular. This means that the emitted beam is very broad (several degrees). In general, the output is not diffraction limited to the aperture size. Thus, the power output per solid angle is not nearly as good or usable as that of gas lasers for applications in which tight beam divergence is a necessity. However, for some applications, such as the optical guidance system for rendezvous, it is very good because a very tight beam is not desired.

Marshall Space Flight Center is now sponsoring research in two areas: basic research in operation of semiconductor lasers and development of a gallium arsenide diode laser array. The basic research contract, with Carnegie Institute of Technology, is for the study of the basic physics of operation. It is expected that the study will yield information leading to the design of better lasers. The laser array contract, with Radio Corporation of America, calls for the development of an array that will give outputs of 50 watts peak on a pulsed basis at several kHz. At the start, it was expected to operate at 77°K; now it appears that the goal can be achieved at room temperature. This development is in support of the optical guidance system, and it is hoped that this source will increase the acquisition range.

3. Gas Lasers. Gas lasers have the property of being diffraction limited and, consequently, can be beamed through a large telescope to project extremely narrow beams (of the order of 1 arc second or less, depending upon the telescope primary size). The gas laser is the only laser that has this advantageous property. The disadvantageous feature of gas lasers is a low overall efficiency (a few hundredths of a percent). For ground-based beacons in tracking and communication, however, this is not a serious drawback.

The only gas laser work sponsored out of house has been the development of a special gas laser for the precision optical tracking system being developed by MSFC. This laser (50 by 20 by 20 cm) will produce 50 mW cw at 6828Å, and a beam width no greater than 25 arc seconds.

Recent work with argon and the rare-gas ionized laser has been very impressive. For instance, it was recently reported that 8 watts total cw in effectively two lines (at 5145Å and 4880Å) has been achieved. The limitation in this laser is that of developing dielectric reflectors to act as the cavity end plates that do not burn up at such power levels. It is anticipated that this problem will be solved in the near future and power outputs of up to 100 watts are expected early in 1966. These argon lasers are inefficient; however, the output is diffraction limited and should be the answer to the ground beacon for deep-space optical communication systems. At present, the argon laser is the best choice for the ground beacon for the optical technology satellite system. No work on the argon laser has been sponsored by MSFC, but future plans call for its development.

B. DETECTORS

In the visible and near infrared spectrum, two types of detectors are useful for tracking and communication: photoemissive surfaces, as used in photomultipliers, and semiconductor junction detectors, in which photons create electron hole pairs that are detected.

1. Photomultiplier Tubes. Photomultiplier tubes are sensitive in the visible wavelengths; the sensitivity is low from about 0.8 to 0.9 micron on to longer wavelengths. The quantum efficiency (photo electrons to incident number of photons) is low, but efficient detection is possible because of the low-noise amplification process of 10 dynodes with gains of 10^6. The frequency response is limited to a few hundred MHz. For coherent or superheterodyne detection, where relative velocity between the spacecraft and earth may cause optical Doppler shifts as high as 10 to 20 GHz, higher frequency response is desired.

2. Semiconductor Diode Detectors. Semiconductor diode detectors have high quantum efficiencies from the visible wavelengths to as high as 6 to 7 microns. The frequency response is limited partly by the capacitance of the p-n junction and, since these diodes are of the order of 25 microns on a side, the frequency response can be high and therefore advantageous for coherent detection. For some applications, the small size is a disadvantage. Also, even though the quantum efficiency is almost one, careful design is necessary to amplify the signal so that the signal-to-noise ratio is equivalent to that obtainable in the photomultipliers.

In 1963, MSFC sponsored work by Philco Corp. on the development of high-frequency-response diodes for the visible and near infrared spectrum for use in coherent detection. A result of this work has been the development of GaAs, Si, and Ge diode detectors which have frequency responses in the order of 8 to 10 GHz. These detectors are the fastest known today and have been made commercially available to the laser research community. They are widely used now in many laboratories. Philco still is under contract with MSFC, and the present and future research plans call for further development in which some gain may be incorporated in the diode without increase in noise. It is hoped that larger detector areas will be developed to enhance their use, while there will be little decrease in frequency response.

MSFC has not sponsored out-of-house contract work on photomultiplier detectors. The main emphasis has been on procuring commercially available photomultipliers and evaluating their sensitivity and frequency response. In addition, work is being done in house to improve the shielding against background pickup. Figure 10 shows a specially designed photomultiplier housing and the setup for evaluation.

C. MODULATORS

For the transmission of information by optical beam, the beam must be modulated in some manner. For high rates of data transmission, the modulators must have a wide bandwidth. The most efficient way to modulate a gas laser or an optically pumped solid-state laser is to modulate the cw laser beam outside the laser cavity. Semiconductor injector lasers, however, may be amplitude modulated by directly modulating the current into the laser. MSFC has worked with commercially procured electro-optic and interference modulators, evaluating their performance for the laser system being developed. In addition MSFC has worked on circuit design for the modulation of semiconductor injector lasers to be used with a pulse position modulation communication system.

D. BEAM SCANNERS

In many cases it is desirable to scan an optical beam for an acquisition operation. Where high-frequency scanning is desired, mechanical modulators are not serviceable. A device with an electrical input to control the beam with very little mass motion would be ideal. In 1963, MSFC awarded a contract to General Telephone and Electronics Co. to develop a beam scanner. This device, which uses piezoelectric shear plates to scan an optical beam, will scan up to 2 kHz and will deviate the beam to about 1 degree. The deviation in this case corresponds to about 100 spot diameters. Each scanner deflects the beam in one direction; therefore, two scanners are used to achieve a two-directional scan. Figure 12 shows the laboratory setup of a two-dimensional beam scanner and a rectangular scan pattern of the beam on a wall. This system will be used as a part of the acquisition system for precision optical tracking.

E. RING LASERS

A very interesting device developed since the conventional laser was invented is the ring laser, an angular motion sensor. In the ring laser the cavity is formed by three or more mirrors rather than by two. The cavity will oscillate as it does in the conventional laser when the resonance condition of the length equals an integral number of half wavelengths. This resonance condition can be satisfied for a wave moving clockwise and a wave moving counterclockwise. If the ring is allowed to rotate, the path length is longer for one wave and shorter for the other wave; hence, the

resonant frequency is increased for one wave and decreased for the other wave. If the two waves are then optically mixed on a photodetector, the difference frequency is obtained. This frequency is proportional to the angular velocity.

MSFC is now sponsoring work with Sperry Gyroscope Co. and Perkin-Elmer Corp. to study the basic properties and to determine the ultimate sensitivity of the ring laser as a rotation sensor. The most obvious application would be to use it in a guidance system on a space vehicle. In addition, it might be used for accurate angular motion sensing on a tracking pedestal. Such devices are planned for use on the pedestal of the precision optical tracking system under development if the angular rotation sensitivity is sufficient. The contracts with Sperry and Perkin-Elmer call for a sensitivity of 1 degree per hour (or 1 arc second/second). This device is contained in a triangular case 38 cm high, 68.6 cm on the base, and 12.7 cm thick. Indications at this time are that the sensitivity of 1 degree/hour will be obtained by early 1966. The plans for future research aim at increasing the sensitivity to 10^{-3} degrees/hour (or 10^{-3} arc second/second).

III. TECHNIQUES

Techniques development is divided into superheterodyne receiver development and laser frequency stabilization development.

A. SUPERHETERODYNE RECEIVER DEVELOPMENT

Coherent or superheterodyne detection is more sensitive than incoherent detection in receiving in the presence of a high-level background. For no background light, the coherent receiver gains nothing as compared to a receiver using predetection narrowband filtering or incoherent detection. However, since there will be background light for almost all applications envisioned, development of the coherent receiver is warranted.

Coherent detection is more complicated than straight AM detection. Coherent detection is the optical mixing of two light waves of different frequency; the phase of the two waves must always remain spatially constant for optimum heterodyning. This means that the optics in the receiver must not distort the received wavefront, and the local oscillator must be frequency stable so that the beat frequency will be constant. The atmosphere tends to destroy the spatial coherence so that the received signal is not coherent across the receiver aperture. This has the same effect as poor quality optics, namely, that of degrading the output signal. Since the atmosphere distortion changes with time, the output signal from the receiver will be randomly modulated in amplitude and difference frequency. In spite of the problems, the coherent receiver offers great potential, especially outside the atmosphere.

MSFC now has a contract with Sylvania Corp. to design and fabricate an optical superheterodyne receiver capable of receiving modulated laser signals such as might be used in space communication. This receiver must be capable of accounting for the large optical Doppler shifts which change the carrier frequency when large velocities exist between the transmitter and receiver. This receiver is being designed to track a transmitter to 0.1 mrad and account for Doppler shifts up to 0.5 to 1 GHz.

Future plans call for development of the transmitter and for establishment of a communication link to evaluate and improve the technique.

B. FREQUENCY STABILIZATION OF LASERS

As previously mentioned, frequency stable lasers are needed for superheterodyne receivers. However, stabilizing the frequency of a laser is no small task. For this reason, frequency stabilization work is being conducted on contract separate from the superheterodyne receiver work. The Technical Research Group is now under contract with MSFC to develop a HeNe laser operating at 6328Å and stable in frequency to 1 part in 10^{11}. The current program is to develop a prototype model demonstrating the stable laser. Future plans are to design a more practical field model which may be incorporated into the superheterodyne receiver.

IV. IN-HOUSE SUPPORTING RESEARCH AND DEVELOPMENT

As part of its support of the overall program in optical technology, MSFC has an in-house research and development program in selected areas. This serves to maintain technical competence in house, which in turn is necessary for effective direction of out-of-house work. The in-house work program consists of (1) optical design, fabrication, and evaluation, (2) atmospheric measurements, and (3) spectroscopic measurements.

A. OPTICAL DESIGN, FABRICATION, AND EVALUATION

Optical design for many components and telescopes used in in-house research is being done with the aid of a computer. Limited fabrication and evaluation are now being performed. The Pilot Manufacturing Branch at MSFC is setting up an optical shop in which lenses, mirrors, and flats up to 20 cm can be made. The Applied Research Branch is engaged in a program to set up facilities and establish techniques for evaluating nearly all optical components purchased outside or fabricated in house. Multilayer dielectric filters, reflectors, and coatings can now be made at MSFC.

B. ATMOSPHERIC MEASUREMENTS

In support of the precision optical tracking system and optical superheterodyne receiver work, atmospheric effects on laser beams are being studied. Measurements are being made on atmospheric effects on coherent mixing and on angular deviation of a laser beam by the atmosphere. The measurements have been made in the dome situated east of Astrionics Laboratory. Many measurements have been made with optical path lengths up to 3 kilometers. Figures 7 and 8 show experimental facilities for these measurements.

C. SPECTROSCOPIC MEASUREMENTS

As previously mentioned, lasers of all types have been measured and study in which spectroscopic and electronic analysis of the output is made is continuing.

V. OPTICAL TECHNOLOGY SATELLITE SYSTEM

The optical technology satellite program has two purposes. The first is to develop a two-way optical system for use in deep-space communication. The second is to determine the effects of space environment on large diffraction-limited optics to obtain engineering data useful in the design of 250 to 500 cm telescopes of future space observatories.

One of the more serious problems facing NASA in its deep-space missions is how to transmit large quantities of data from spacecraft to earth. Theoretical studies have shown that, because of its narrow beam divergence, the optical communication system may prove superior in some respects to microwave communication systems, provided that certain problems peculiar to optical communication can be solved. One of the most serious problems is how to point such narrow beams (0.2 to 1 arc sec) accurately enough to hit a receiver.

It has been said that, in the future, astronomy will require large diffraction-limited telescopes in space laboratories. However, there have been no orbital flights of large diffraction-limited optics nor are any planned. Orbiting such a system has two equally important purposes. The first is to develop the techniques for establishing two-way optical communications for use in deep space. The second is to determine the effects of the space environment on large diffraction-limited optics. It would be planned to monitor the figure of the primary mirror and to make corrections, if possible, to bring it back to the diffraction limit.

A study has been performed for NASA by the Perkin-Elmer Corp. to examine the problems and to make a preliminary conceptual design of the satellite and ground station necessary to perform selected experiments.

Experiments have been chosen to simulate deep-space communication for ranges up to 160 million kilometers. The following experiments have been chosen tentatively:

1. Atmospheric scintillation effects on coherent beams.
2. Atmospheric effects on plane and circularly polarized light.
3. Remote manual optical alignment on earth by an eye/hand servoloop.
4. Optical heterodyne detection on earth.
5. Optical heterodyne detection on the satellite.
6. One-tenth arc second tracking in the satellite.
7. Point ahead.
8. Space-to-ground-to-space loop closure.
9. Tracking in the presence of spacecraft motion.
10. Telescope suspension system.
11. Transfer of tracking from one ground station to another.
12. Earthshine effects on acquisition and tracking.

13. Optical communication system with a bandwidth of 10 MHz.

14. Onboard determination of the effects of space environment on large diffraction-limited optics.

A conceptual design (Fig. 13) of how these experiments might be performed has been made.

A synchronous circular orbit with the orbit plane tilted 50 to 60 degrees to the equatorial plane has been tentatively chosen to simulate the angular tracking rates encountered for the deep-space conditions and to allow continuous observation and communication.

Preliminary weight estimates for the satellite are shown in Figure 14. A Saturn-IB Centaur would be capable of placing this load in synchronous orbit. Preliminary estimates of power consumption are shown in Figure 15.

Future plans call for preliminary design study under the AES program that would include design of the integrated experiments, spacecraft, and ground station based on the conceptual design.

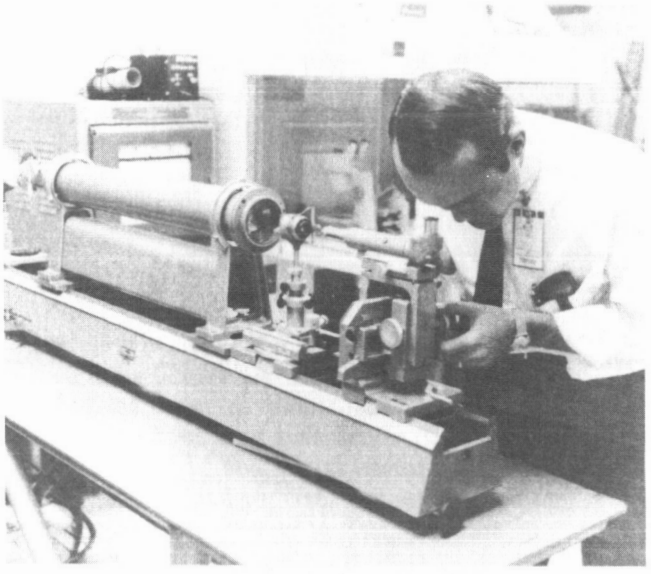

FIGURE 1. LENS PARAMETER MEASUREMENTS

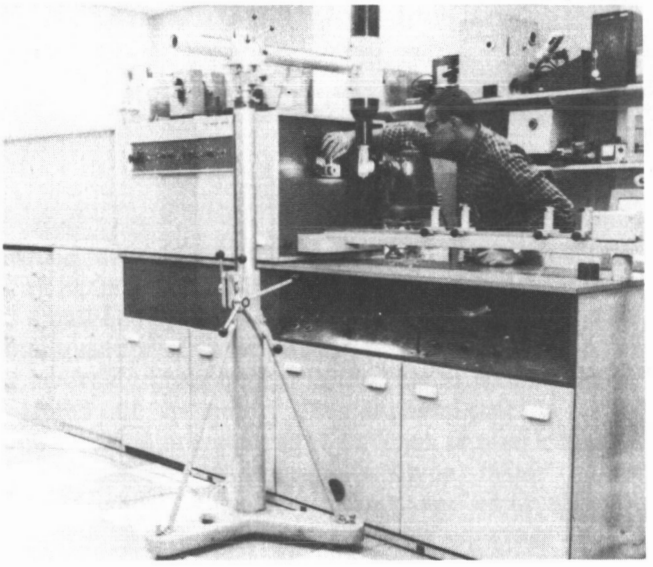

FIGURE 3. JARRELL-ASH SPECTROGRAPH

FIGURE 2. THIN-FILM DEPOSITION AND VACUUM CHAMBER

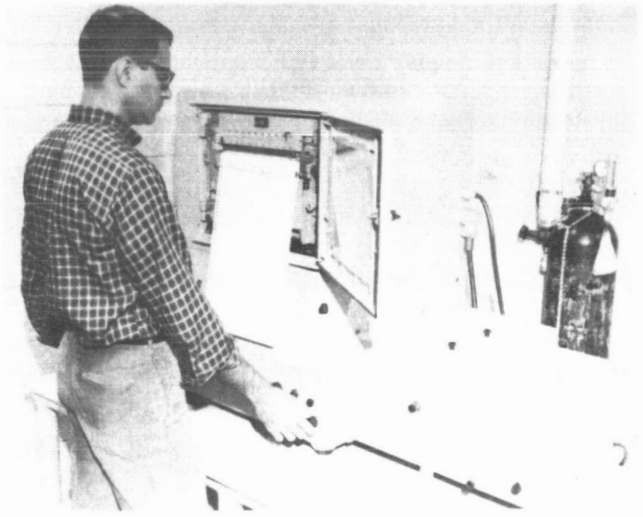

FIGURE 4. CARY SPECTROPHOTOMETER

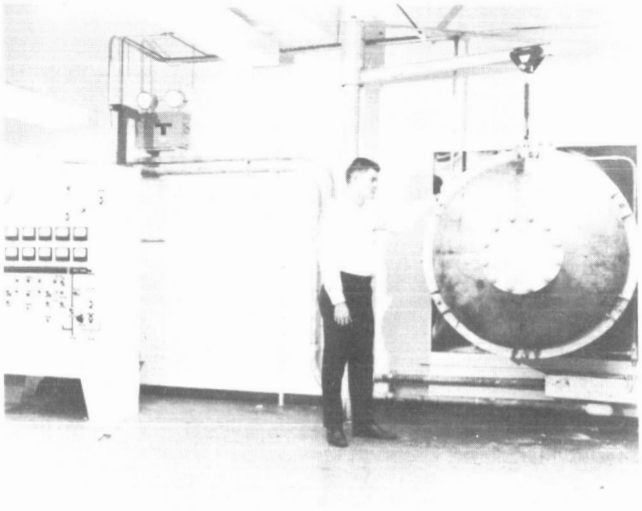

FIGURE 5. CONTROL ROOM FOR EVACUATION OF OPTICAL TUNNEL

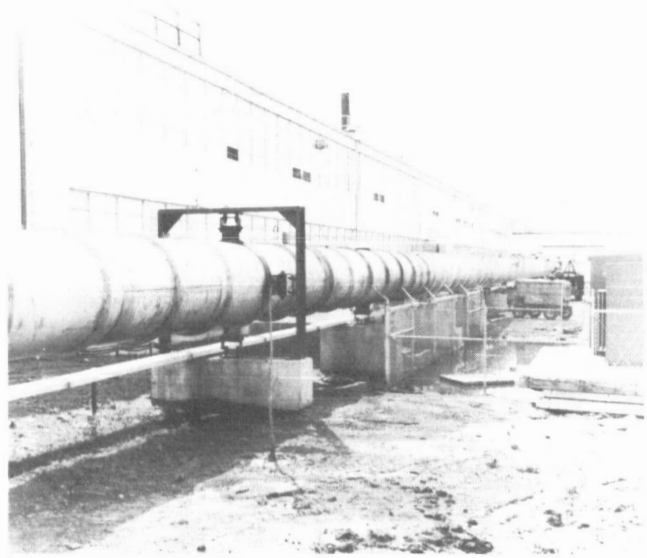

FIGURE 6. VACUUM TUNNEL FOR OPTICAL EXPERIMENTS

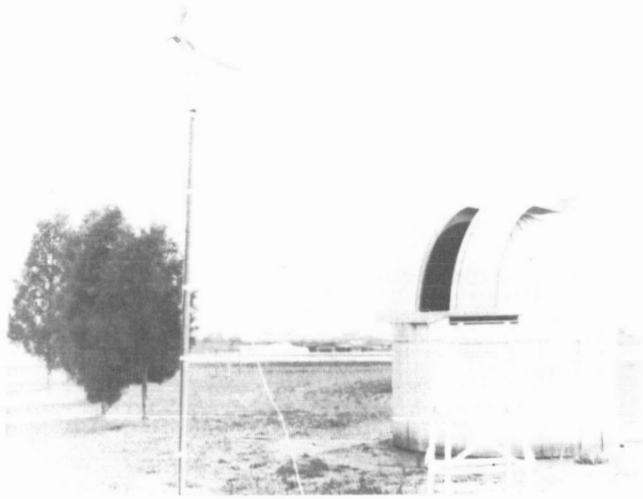

FIGURE 7. OBSERVATORY DOME FOR LASER ATMOSPHERIC EXPERIMENTATION

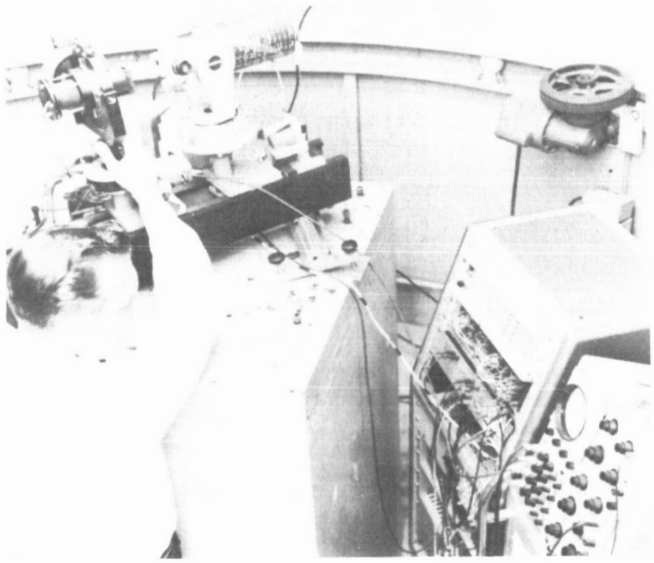

FIGURE 8. ATMOSPHERIC ANGULAR FLUCTUATIONS MEASURING SYSTEM

FIGURE 9. OPTICAL DOPPLER SHIFT USING CONSTANT-VELOCITY RECIPROCATOR

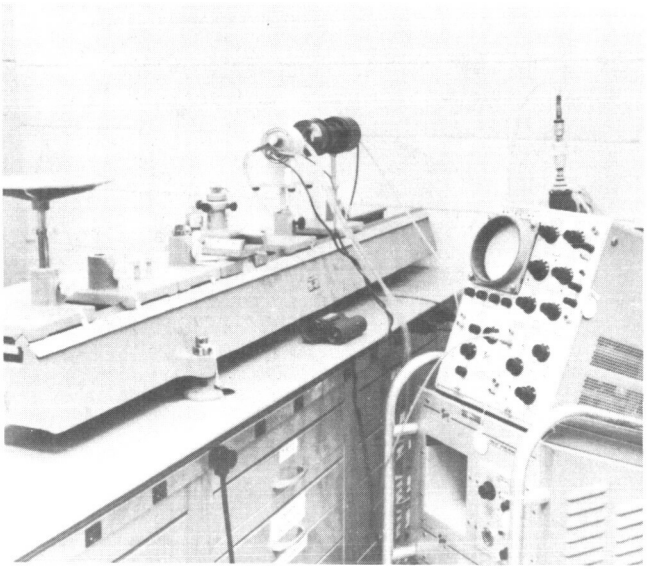

FIGURE 11. NEODYMIUM YAG CW LASER SYSTEM

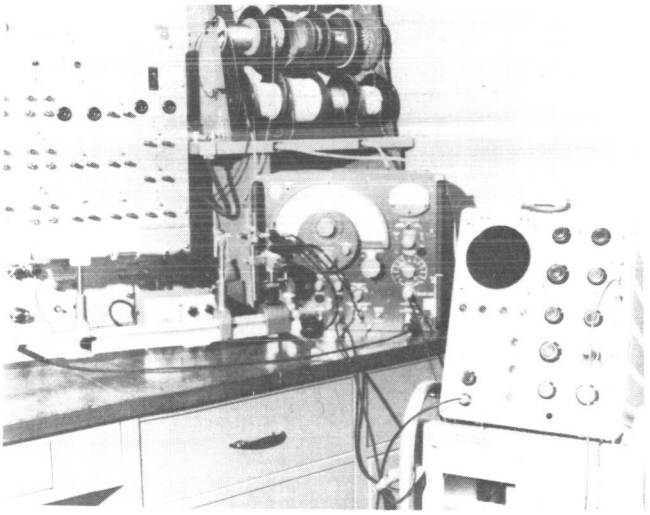

FIGURE 10. PHOTOMULTIPLIER TUBE CALIBRATION SYSTEM

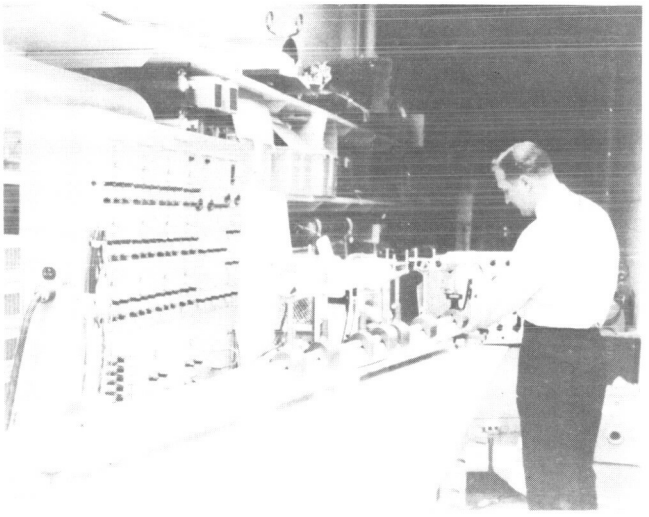

FIGURE 12. LASER BEAM STEERER AND EQUIPMENT

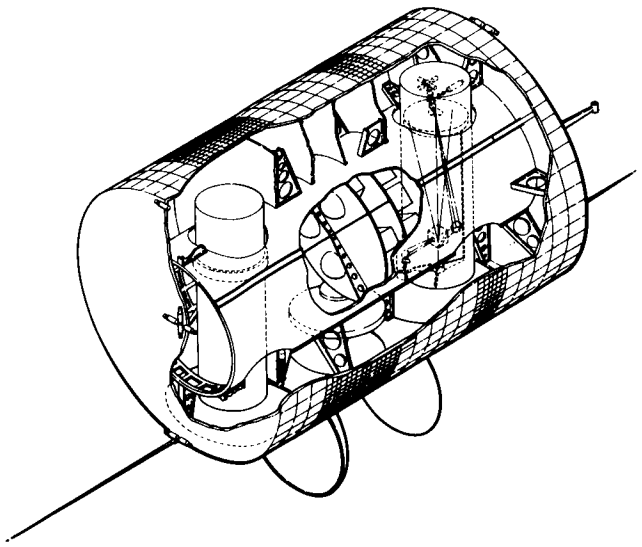

FIGURE 13. OPTICAL TECHNOLOGY SATELLITE

	kg
STRUCTURE AND SKIN	839.16
SOLAR CELLS AND BATTERIES	272.16
AUTOPILOT AND GUIDANCE	45.36
INERTIA WHEELS AND CONTROL	226.80
PULSED JET FUEL TANKS	226.80
MICROWAVE PACKAGE WITH ANTENNA	45.36
PULSED JET MOTORS, PLUMBING, AND CONTROLS	45.36
CABLING	45.36
THERMAL CONTROL	79.38
CONTROL COMPUTER	6.80
SOLAR SENSOR SUBSYSTEM AND COARSE ACQUISITION MECHANISM	6.49
TELESCOPE 1	295.20
TELESCOPE 2	360.97
DC TO AC INVERTERS	9.07
TELESCOPE 1 SUN SHIELD DRIVE ASSEMBLY	6.80
TELESCOPE 2 SUN SHIELD DRIVE ASSEMBLY	6.80
TOTAL	2,517.87
ADD APPROXIMATELY 10% FOR UNIDENTIFIED MISCELLANEOUS ITEMS	226.80
SATELLITE WEIGHT	2,744.67

FIGURE 14. PRELIMINARY WEIGHT ESTIMATE FOR THE OPTICAL TECHNOLOGY EXPERIMENTS SATELLITE AND MAJOR SUBSYSTEMS

MODE OF OPERATION	AVERAGE POWER CONSUMPTION (WATTS) SATELLITE WITH TELESCOPE NO. 1	SATELLITE WITH TELESCOPE NO. 2
QUIESCENT	15	15
ACQUISITION	300	370
TRACKING	260	330
COMMUNICATIONS	370	460

FIGURE 15. PRELIMINARY POWER CONSUMPTION ESTIMATE FOR THE OPTICAL TECHNOLOGY SATELLITE IN MAJOR OPERATIONAL MODES

LASER SYSTEMS RESEARCH AT MARSHALL SPACE FLIGHT CENTER

By

Charles L. Wyman

SUMMARY

Laser systems research and development at MSFC have been concerned with communication, guidance, and tracking applications. This report describes two laser radar systems which are at an advanced stage of development. One is an airborne optical guidance system for rendezvous maneuvers and the other is a ground-based precision optical tracking system for advanced launch vehicles.

In advances beyond this breadboard development, work is being done on room-temperature continuous injection lasers, image dissectors and beam steerers, an optical superheterodyne receiver, a precision gas-bearing tracking mount, and other instruments and techniques.

Advantages that are expected to result from the research and development program are a reduction in system size and power requirements, elimination of problems associated with microwave techniques (e.g., ground clutter and backscatter), greatly increased operation range, and very high accuracy in tracking and ranging.

I. INTRODUCTION

The Marshall Space Flight Center is pursuing a laser systems research and development program directed primarily toward applications for guidance, tracking, and communications. Such systems are important to the national space program for a variety of reasons. Most of these reasons are based on two fundamental characteristics of laser beams: first, lasers are highly directional and, second, optical beams can carry tremendous information bandwidths.

By judicious application of these characteristics and by appropriate use of systems, the following potentials for laser systems can be seen:

1. Communicating at interplanetary distances with television bandwidths using systems of reasonable size and power.

2. Tracking objects, expecially cooperative ones, with unprecedented accuracy.

3. Developing guidance, tracking, and communications systems for use in space that are smaller, more accurate, and use less power than comparable systems using conventional techniques.

Several systems concepts are being investigated. Two systems in the advanced development stage are discussed in detail. These are the optical guidance system for rendezvous and the precision optical tracking system for advanced launch vehicles. Communications and tracking systems for deep space are being investigated under the optical technology satellite program. This work is in a preliminary study phase and is not discussed in this report.

The optical guidance system and the optical tracking system are both laser radars. The former is for spaceborne application and the latter is ground based. Certain techniques are common to both; consequently, similarities will be noted. However, the requirements and the overall systems are very different.

As an aid to the discussion of the two systems, the directional characteristics of lasers are briefly discussed and basic range equations are presented.

II. LASER BEAM DIRECTIVITY AND BASIC RANGE EQUATIONS

The diffraction of coherent electromagnetic radiation by a circular aperture causes an angular distribution of the energy for which, from the maximum intensity of the beam to the first minima, the beamwidth θ can be expressed as:

$$\theta = \frac{1.22\ \lambda}{D}$$

θ = beamwidth
λ = wavelength
D = aperture diameter.

To a close approximation, the half power beamwidth θ_{hp} is expressed as:

$$\theta_{hp} = \frac{\lambda}{D} \quad .$$

For optical wavelengths the beamwidths are thousands of times smaller than the beamwidths for radio frequencies.

If the aperture is regarded as an antenna of area A_t, the gain or directivity D_t is expressed as:

$$D_t = \frac{4 \pi A_t}{\lambda^2} \quad .$$

When equation 2 is substituted in equation 3, the expression for D_t is simplified to:

$$D_t = \frac{\pi^2}{\theta^2_{hp}} \quad .$$

A transmitter with directivity D_t illuminates a target at range R with a power density P_{dt} expressed by the equation:

$$P_{dt} = \frac{P_t D_t}{4\pi R^2} = \frac{P_t \pi}{4 \theta^2_{hp} R^2} \quad .$$

A straightforward calculation will indicate that a laser transmitter will illuminate a target with an intensity millions of times greater than a radio frequency source of equal power and antenna size.

A complete development of range equations for the precision optical tracker is given in Reference 1. Range equations and signal-to-noise analyses for the optical guidance system are given in Reference 2.

III. OPTICAL GUIDANCE SYSTEM FOR RENDEZVOUS

This system is the result of a research and development program for the Office of Advanced Research and Technology (OART) to investigate the feasibility of using optical and laser techniques to generate guidance information during rendezvous maneuvers. The study has resulted in the development of a breadboard optical guidance system which is being evaluated at MSFC. The breadboard development has clearly established the feasibility and practicality of the project and is being followed up by development of a complete miniaturized prototype system for performance testing in aircraft or on a rendezvous simulator. Table I lists characteristics of the breadboard model and the miniaturized prototype.

TABLE I. OPTICAL GUIDANCE SYSTEM

Breadboard			
Parameters	Long Range above 3 km	Intermediate Range 3 km to 100 m	Short Range 100 m to 0
Acquisition range	14 km		
Acquisition angle	10°		
Range accuracy	± 0.5% of measured range	+0.5%	+0.1 m
Range rate	120 m/s	50 to 0.3 m/s	50 to 0.3 m/s
Range rate accuracy	+0.2%	+0.3 m/s	+0.03 m/s
Angular accuracy	+0.1°	+0.1°	+0.1°
Angular rate accuracy	+0.5 m rad/s	+0.05 m rad/s	+0.05 m rad/s
Test Prototype			
Acquisition range	50 km minimum		
Other parameters identical to breadboard system			
Prototype weight	less than 22.7 kg		
Power consumption	less than 50 watts		
Receiver telescope	16 cm aperture, 35 cm long, coaxial with acquisition telescope		
Mounting	tracking pedestal for simulation of automatic angular tracking		

The basic system configuration is depicted by the block diagram of Figure 1. An image dissector tube and a telescope are used for angular acquisition and tracking. The image dissector is a photomultiplier in which an internal aperture is used to limit the active area of the photocathode. By means of electrostatic focusing and magnetic deflection of the electrons emitted from the photocathode, the active area can be made to scan across the face of the tube. Thus, because there is a quadrature magnetic field, the small instantaneous field of view of the system can be scanned over a larger total field of view to generate angular information for acquisition and tracking purposes. Acquisition is performed as indicated in Figures 2 and 3. The target beacon and the long-range source on the chaser are thermoelectrically cooled pulsed gallium arsenide lasers. The laser on the chaser also supplies coarse-range information by measuring the time delay of the pulse reflected by corner reflectors on the target vehicle. The long-range system is indicated by the block diagram of Figure 4. Fine-range resolution is determined from three kilometers to docking, with a second ranging system consisting of an incoherent-light-emitting diode modulated continuously at 4.88 MHz. Both range systems use phase lock techniques to enhance signal-to-noise ratio. The short-range system is shown in Figure 5.

Figures 6 and 7 show the breadboard system. The chaser vehicle transceiver for the prototype system has been miniaturized to the configuration shown in Figure 8. The prototype electronics use microcircuitry and will occupy less than 1/30 cubic meter.

The concept depicted in Figure 9, a logical extension of this prototype system, utilizes room-temperature continuous injection lasers for a simplified and

more accurate ranging system.* It also uses laser beam steerers; these eliminate the necessity of controlling the attitude of the spacecraft or of gimbaling the telescopes. The beam steerers are under development and are being designed into an acquisition system for the precision optical tracker. Room-temperature continuous injection lasers are also under development and are expected to be operational in a year or two. As the lasers become more powerful and efficient, the size of the optical guidance system shrinks because smaller telescopes are required. In the concept of Figure 9, only one telescope and one detector are used on each vehicle. Less than one watt of continuous power from the laser is required to extend the range of this system to over 100 km with an acquisition angle of 30 degrees. Furthermore, with one watt available, the telescope collector would be only 7 cm in diameter and the telescope and detector package would be less than 15 cm long.

IV. PRECISION OPTICAL TRACKING SYSTEM FOR ADVANCED LAUNCH VEHICLES

Laser radar systems have the potential of tracking objects to an unprecedented degree of accuracy. Areas in which precision tracking information is of interest to NASA are as follows:

1. Tracking advanced launch vehicles.
2. Tracking reentry vehicles.
3. Tracking satellites.
4. Tracking deep-space probes for communications purposes and position information.

With these applications in mind, an experimental and developmental program was undertaken for OART to develop and evaluate various acquisition, tracking, and ranging techniques with lasers. The results of the program ultimately will apply to specification of optimum techniques and systems configurations for various tracking problems.

Early in the project, it was determined that the best results could be obtained by choosing one particular tracking problem and developing an experimental prototype that could be used for testing under realistic conditions. Tracking advanced launch vehicles was chosen because it has many characteristics similar to other possible systems and is an area in which the parameters are well known. Furthermore, some requirements for tracking the vehicle during the early launch phase have never been fulfilled. For example, when microwave radar systems operate near the horizon during the early launch phase, they are useless because of ground clutter and backscatter problems. In addition, photographic and television techniques do not have range measuring capability and lack in angular resolution.

Consequently, development of a precision optical tracking system for advanced launch vehicles is well under way. Reference 1 has a discussion of the general system philosophy and several preliminary analyses and studies including error analysis, trajectory analysis, range analysis, refractive and turbulence effects of the earth's atmosphere, and servo analysis.

Table 2 lists characteristics and parameters of the system, which is being designed and assembled in-house. There is work under contract for developing a precision gas-bearing tracking mount and for fabricating a tracking and acquisition subsystem that utilizes image dissectors and beam steerers. Figure 10 is a simplified block diagram of the system.

TABLE II. PRECISION OPTICAL TRACKING SYSTEM*

Early Launch Phase Tracking Requirements				
Flight Interval (Seconds)	Data Required	Reduced Data Accuracy		
		Class I	Class II	Class III
0 to 5	position	0.5 m	0.1 m	0.1 m
	velocity	1.0 m/s	0.1 m/s	0.1 m/s
	acceleration	0.2 m/s^2	0.5 m/s^2	0.01 m/s^2
5 to 25	position	5.0 m	1.0 m	1.0 m
	velocity	1.0 m/s	0.1 m/s	0.1 m/s
	acceleration	0.5 m/s^2	0.1 m/s^2	0.02 m/s^2
25 to 50	position	30 m	10 m	5 m
	velocity	1.0 m/s	0.2 m/s	0.1 m/s
	acceleration	0.5 m/s^2	0.1 m/s^2	0.02 m/s^2

System Parameters	
Angular resolution	1.25 arc sec
Angular accuracy	5.0 arc sec
Range resolution	1 cm
Maximum range accuracy	5 to 10 cm
Acquisition field of view	0.25°
Tracking field of view	30 to 90 arc sec
Maximum range	10 km
Maximum range rate	200 m/s
Maximum angular rate	5°/s
Maximum angular acceleration	1°/s^2
Telescope collector aperture	15 cm
Transmitted laser power	50 mW
Beam divergence	30 to 90 arc sec

* This is an experimental system to be used to evaluate laser tracking and ranging techniques.

Techniques that will be evaluated but which are not indicated in the diagram include:

1. Measurement of the radial component of velocity by optical superheterodyne techniques.

2. Measurement of angular velocity information of the tracking mount, using ring lasers.

* Pulsed room-temperature injection lasers are available from several sources. One order of magnitude decrease in threshold of these lasers will allow continuous wave operation. Several materials show promise of continuous wave operation. Research contracts with IBM, RCA, and Tyco Laboratories are directed toward eventual continuous wave room-temperature operation.

Much work has been done at MSFC on optical superheterodyne techniques [3]. In addition, there is work under contract for the development of an optical superheterodyne receiver.

V. CONCLUSIONS

The two developmental models of the optical guidance system will demonstrate the practicality of using laser and optical techniques for space guidance problems. Future models will use essentially the same ranging and tracking techniques but will become smaller and operate over longer ranges as better laser sources become available. Furthermore, use of other optical techniques such as laser beam steerers will result in very advantageous systems configurations for which there are no microwave counterparts.

The optical tracking system being developed will be a versatile research tool in experimentation and investigations leading to design data for optimum optical tracking and ranging systems. Moreover, the system will perform with accuracies unobtainable in the past.

The useful application of lasers has required much work in the development of associated technologies including devices, components, and techniques. Much more work is required in these areas and in the development of the systems themselves. However, the usefulness of lasers for application in the space program is established, and practical systems are beginning to appear.

REFERENCES

1. Wyman, C. L.; Juergensen, K.; Kurtz, R. L.; Hayes, L.; and Gould, J. M.: Precision Optical Tracking System for Advanced Launch Vehicles. NASA TM X-53076, June 25, 1964.

2. Optical Guidance Feasibility Study - Quarterly Reports and Summary Report. Contract NAS8-2661, Request No. TP-2-83-1469-S1; Data Corporation, Dayton, Ohio, March 1965.

3. Lee, C.: An Investigation of Photoelectrically Heterodyning Coherent Light. Astrionics Research and Development Report No. 2, NASA TM X-53044, May 1, 1964.

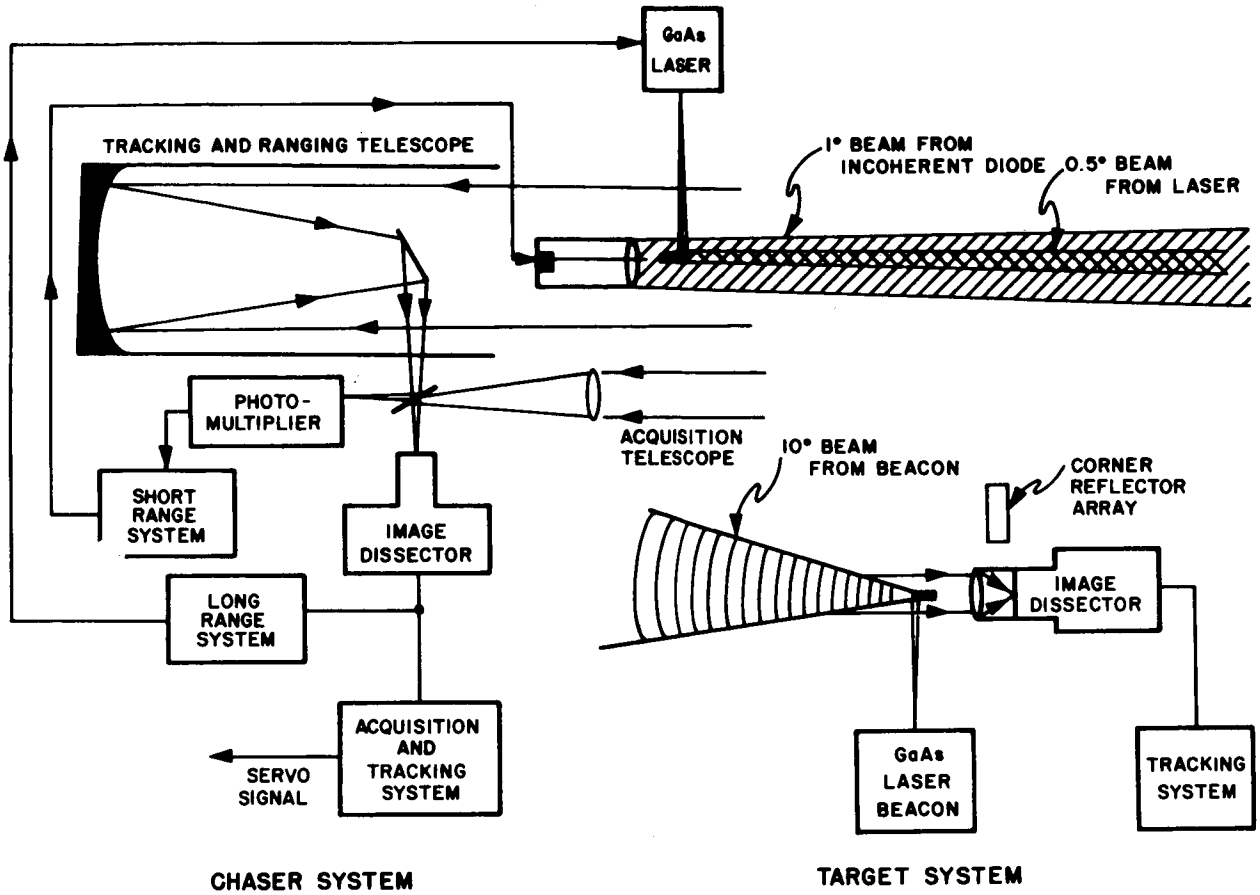

FIGURE 1. OPTICAL GUIDANCE SYSTEM

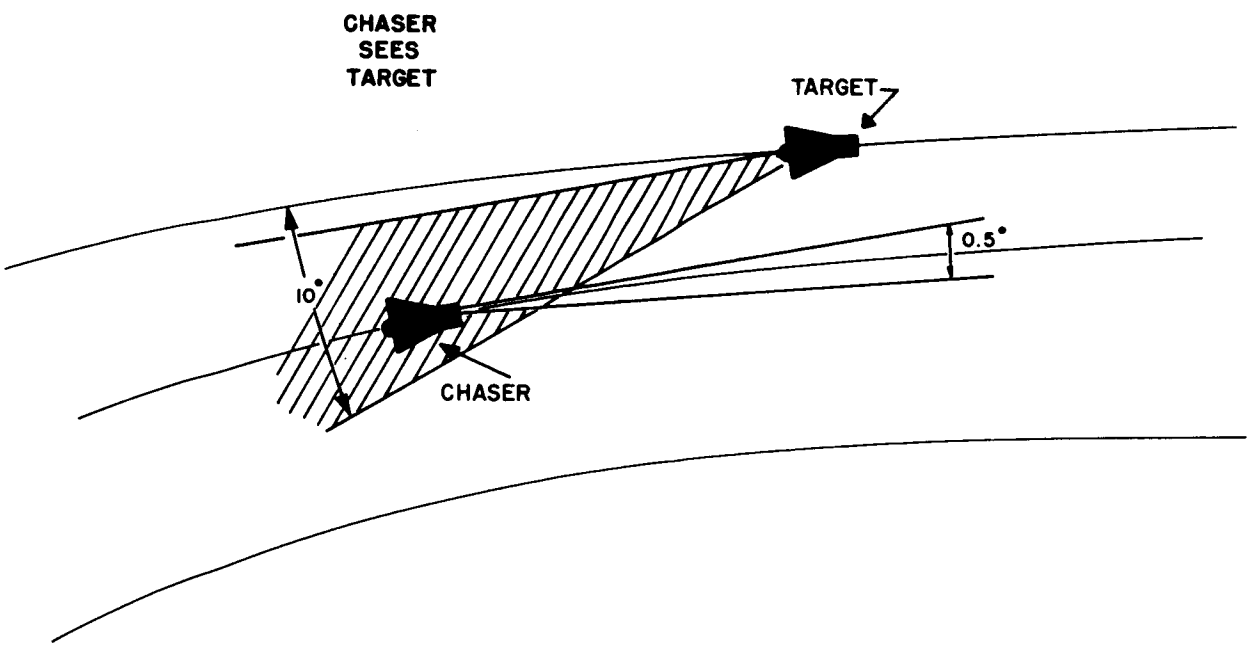

FIGURE 2. PHASE I OF ACQUISITION

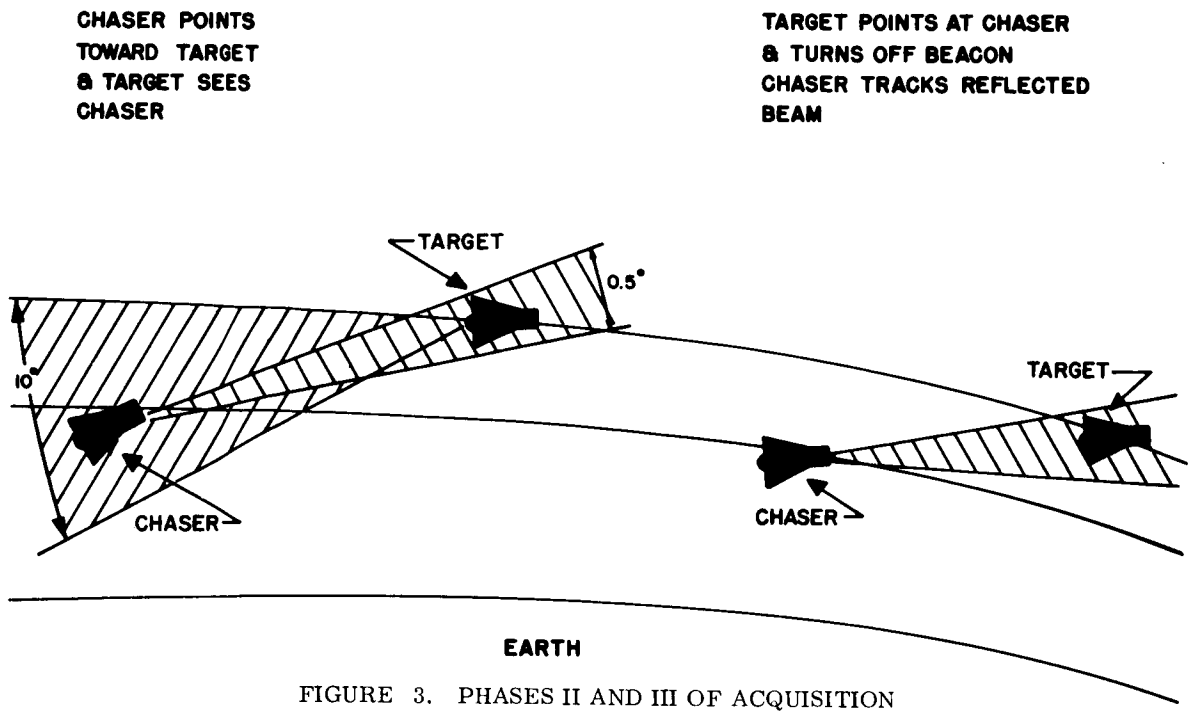

FIGURE 3. PHASES II AND III OF ACQUISITION

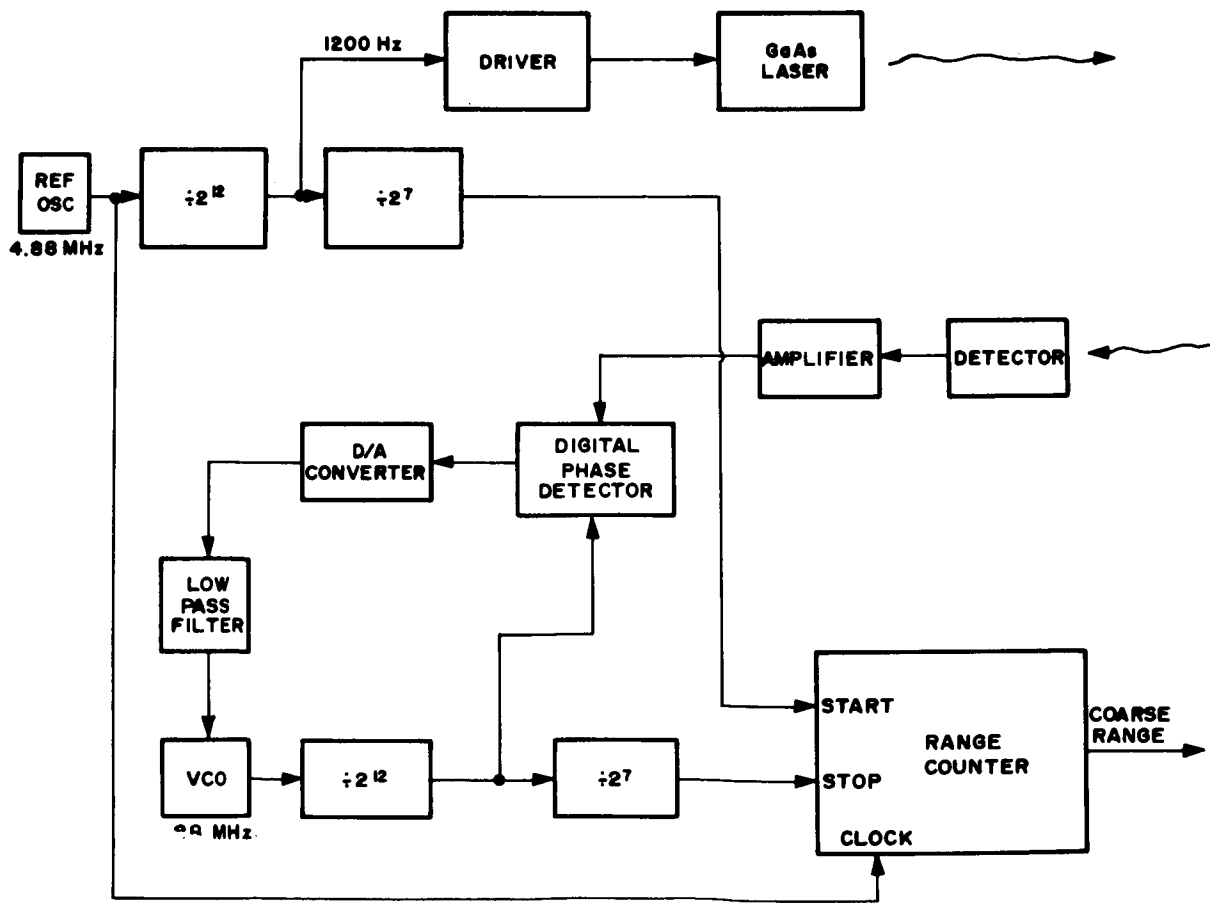

FIGURE 4. LONG-RANGE SYSTEM

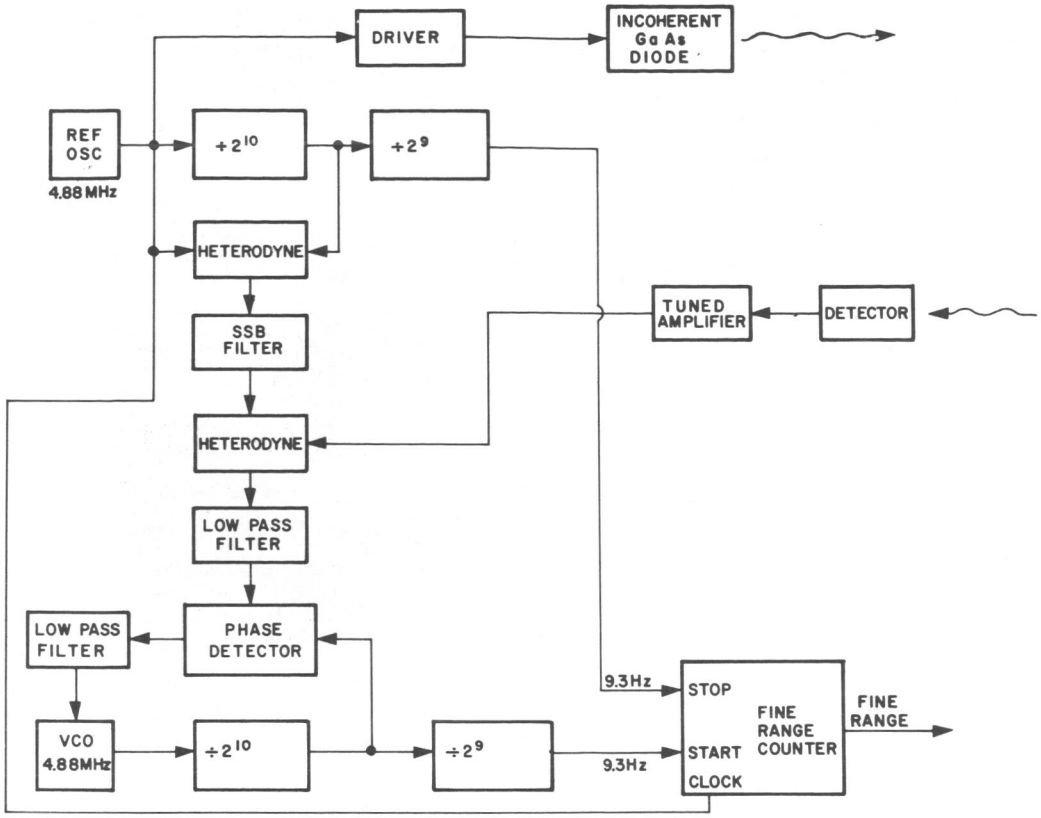

FIGURE 5. SHORT-RANGE SYSTEM

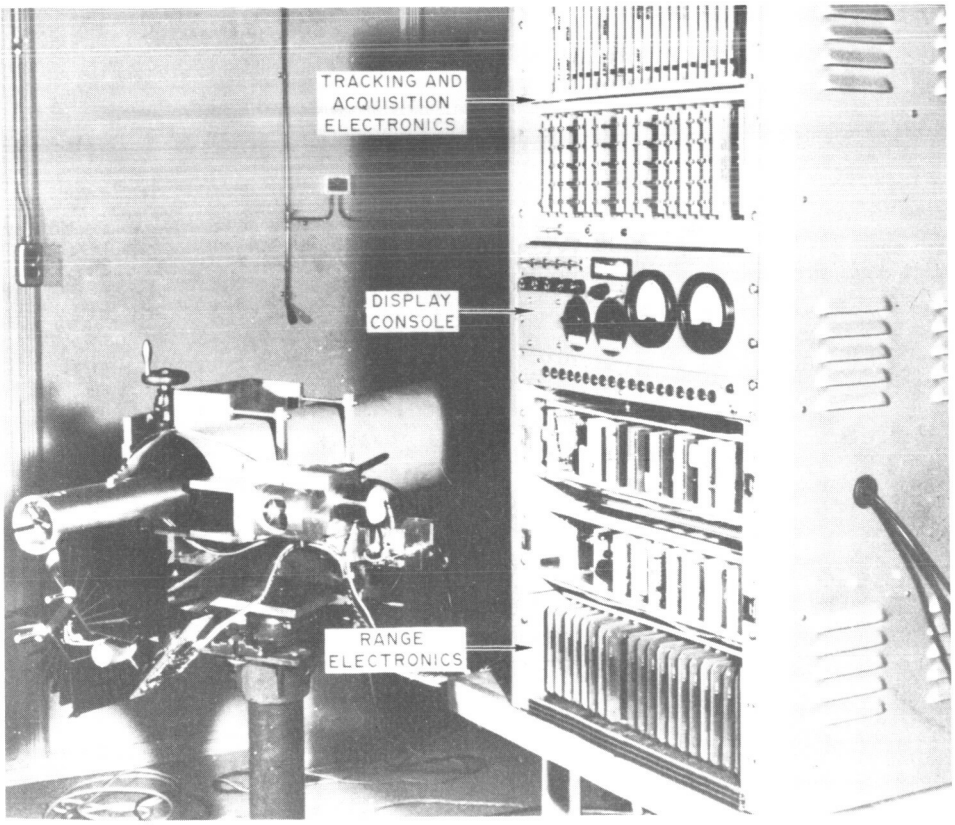

FIGURE 6. BREADBOARD SYSTEM, OVERALL VIEW

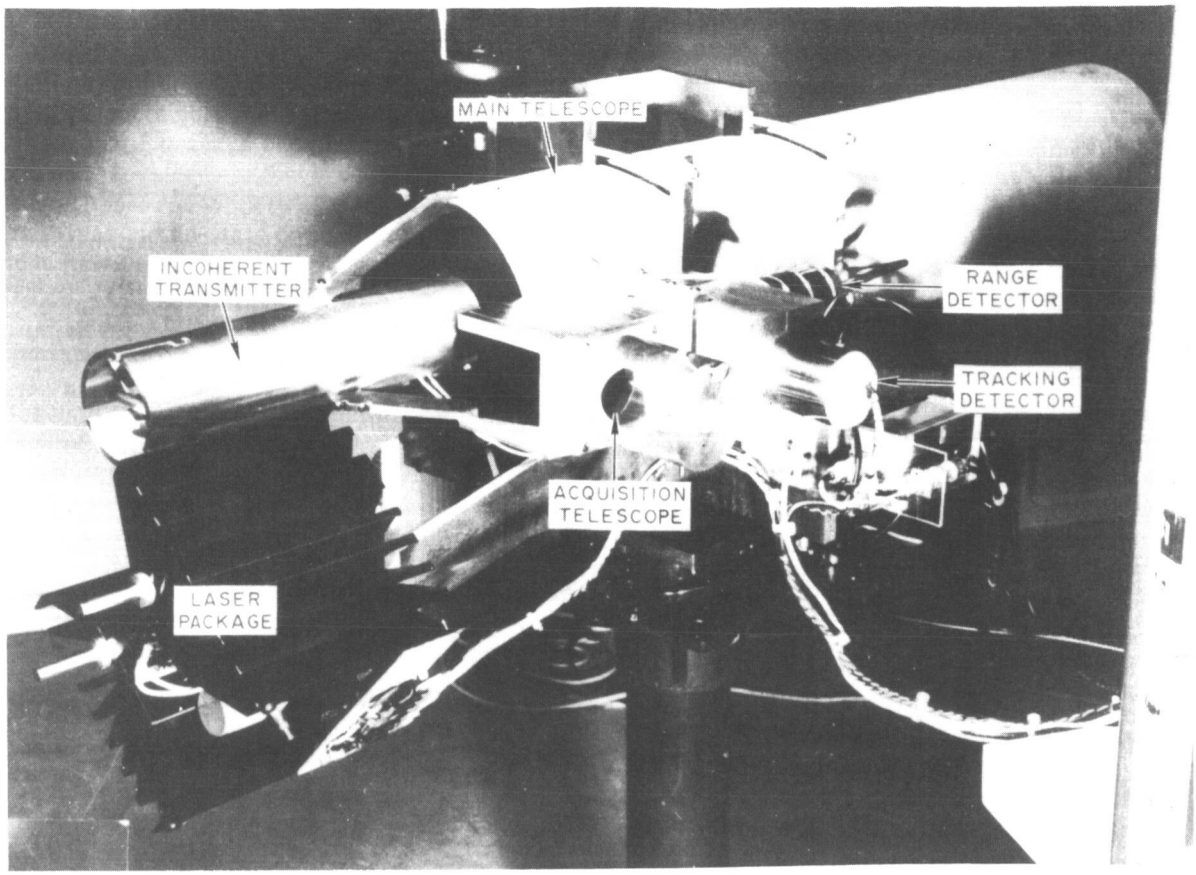

FIGURE 7. BREADBOARD SYSTEM, ACQUISITION AND DETECTION COMPONENTS

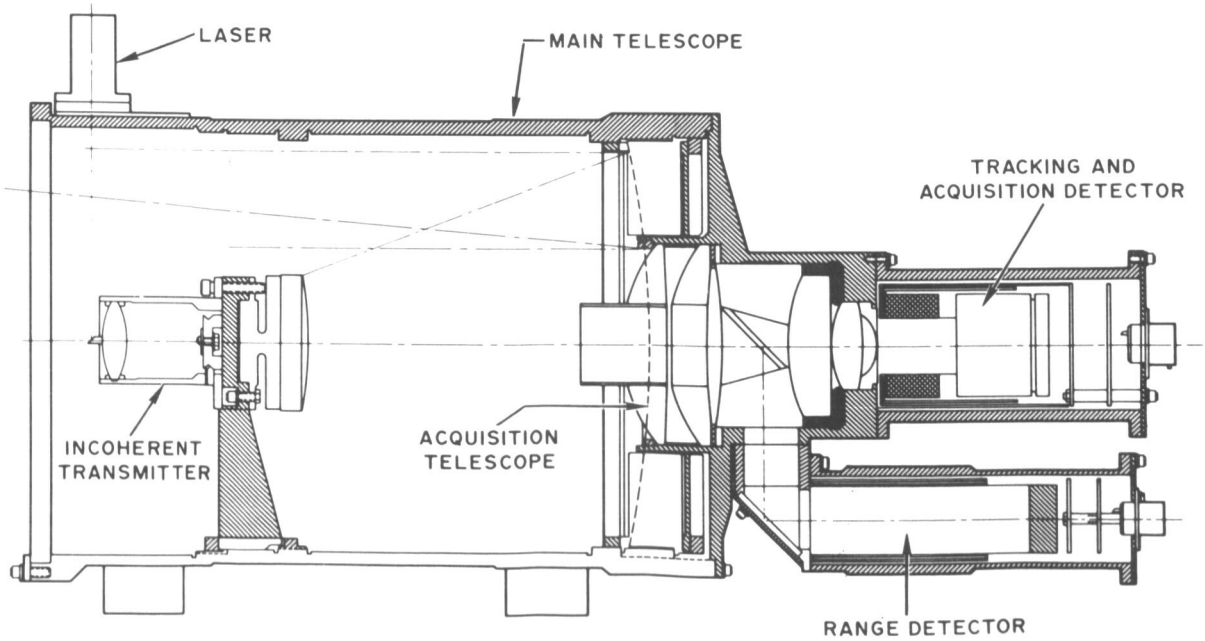

FIGURE 8. PROTOTYPE OPTICAL GUIDANCE SYSTEM TELESCOPE

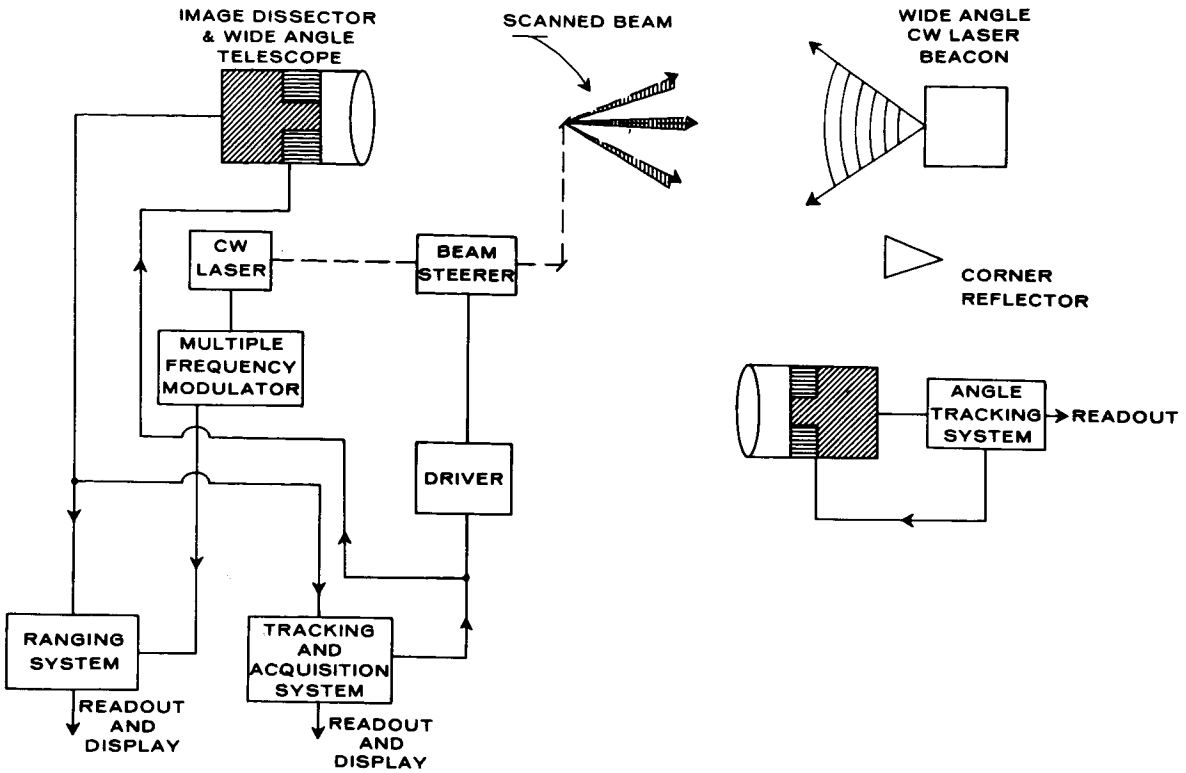

FIGURE 9. OPTICAL GUIDANCE SYSTEM OF THE FUTURE

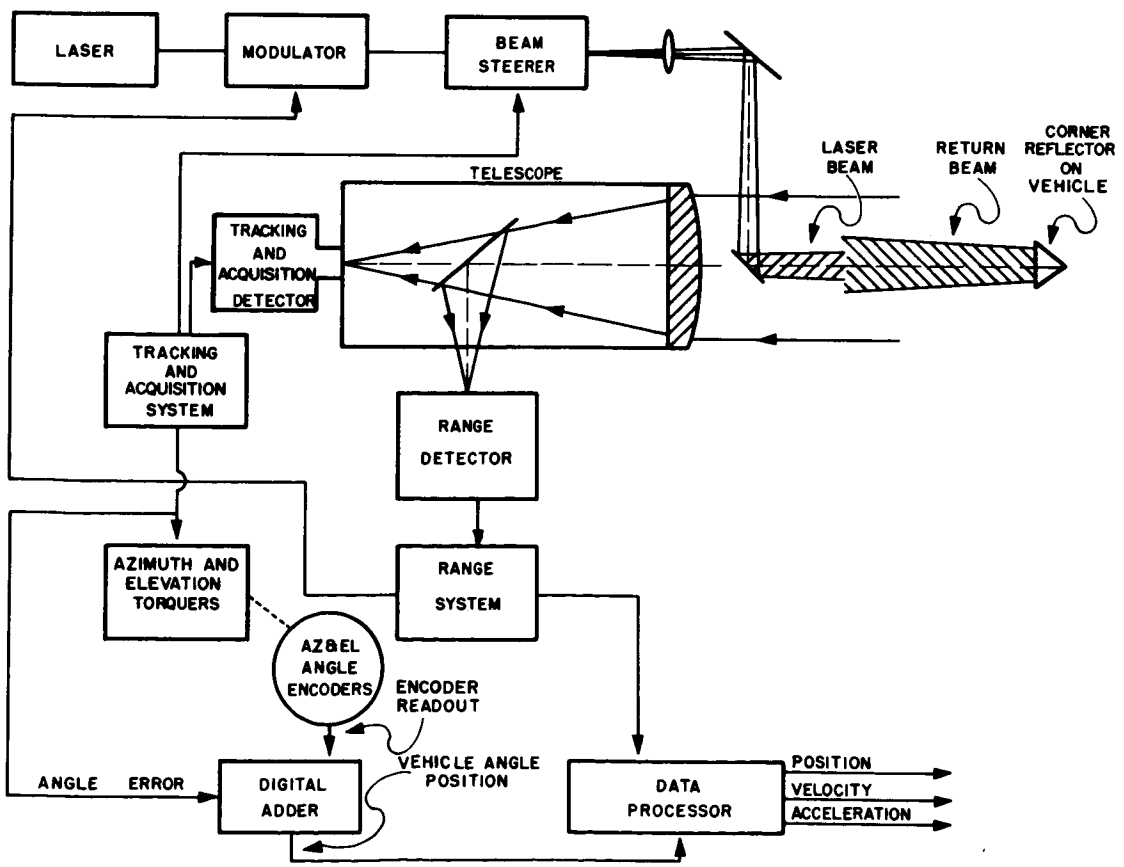

FIGURE 10. SIMPLIFIED DIAGRAM OF PRECISION OPTICAL TRACKER

CONTROL SYSTEMS RESEARCH AT MSFC

April 29, 1965

by

J. A. Lovingood
David N. Schultz

TABLE OF CONTENTS

LAUNCH VEHICLE CONTROL SYSTEMS RESEARCH

by J. A. Lovingood

LIST OF ILLUSTRATIONS

RESEARCH IN PULSED MASS EXPULSION CONTROL SYSTEMS

by David N. Schultz

LIST OF ILLUSTRATIONS

CONTENTS (Continued)...

LIST OF ILLUSTRATIONS (Concluded)

LAUNCH VEHICLE CONTROL SYSTEMS RESEARCH

By

J. A. Lovingood

SUMMARY

Launch vehicle control research at MSFC has been concerned with problems in adaptive bending stabilization, adaptive load relief, and minimax control. One result of this research has been the development of a spectral identification adaptive control system for dealing with problems in bending stabilization. The feasibility of the system's general concept has been established; additional analysis is necessary before the system can be recommended for in-flight testing.

A second research achievement has been the development of a system capable of adapting to changes in disturbance forces. Called a switched integral control system, it has been applied to problems in load relief. Its use has indicated that an appreciable reduction in maximum bending moment over all wind speeds can be achieved. However, it is not considered to be the ultimate in a load relief system.

Other research has attempted to formulate a mathematical statement of the launch vehicle control program to provide an analytical procedure for designing nonlinear load relief systems. Some solutions have been found for restricted cases of the load relief problem, called the minimax problem of vehicle control. However, much more work must be done for the successful treatment of more realistic cases.

I. INTRODUCTION

The control systems research program in the Aero-Astrodynamics Laboratory deals primarily with control of launch vehicles during powered flight in the atmosphere and, in particular, with the control problems encountered in the maximum dynamic pressure region. In this max q region, the aerodynamic forces acting normal to the vehicle attain their largest values. Also, the effect of these forces on vehicle pitching moments is increased because of the large aerodynamic moment arm, which is due to extreme forward location of the center of pressure. This undesirable situation is usually compounded by the fact that the max q region occurs in the jet stream, which is the altitude range from 10 to 14 km. In this altitude range, not only do maximum wind speeds occur but also the largest wind shear and wind turbulence or gusts are encountered. Because of these severe environmental conditions, control problems arising at max q are receiving the greatest attention in Aero studies.

Before the specific factors which motivate the research are outlined, the problem of launch vehicle control will be discussed and objectives the control system must accomplish will be indicated. The primary purpose of the control system is to execute commands generated by the guidance system. In the present Saturn vehicles, there is no feedback to generate guidance commands during first stage flight; instead, the guidance command is time-programed as a reference pitch attitude. The control system for Saturn vehicles, therefore, executes guidance commands by causing the vehicle to rotate to achieve the desired attitude.

In the execution of commands from the guidance computer, there are certain constraints which must not be violated. Some typical ones are: structural load limits or tolerable bending moments must not be exceeded; for vehicles employing engine gimbaling to generate control torques, allowable swivel angles must not be exceeded; flight path or control system following errors must be kept below certain values; in manned vehicles, crew safety and comfort requirements impose limits on accelerations experienced by the spacecraft; and, of course, there are stability considerations, which to a certain extent are implied in the other constraints.

Before a control system which will meet these requirements can be designed, information describing the dynamics of the vehicle in its operating environment must be available. That is, one must know how the vehicle will respond to external disturbances and to the control forces and torques generated by the control system. The lack of such knowledge, or rather the anticipated lack of such knowledge for future launch vehicles, has been the reason for establishing a substantial part of the Aero-Astrodynamics Laboratory research program.

Presently, control systems are designed by describing the dynamics of the vehicle using linearized differential equations of motion, with the various

forces, torques, and damping terms which enter into these equations being determined experimentally by elaborate testing facilities. For example, frequencies and mode shapes of structural vibration modes are determined by conducting dynamic tests on a full-scale vehicle. Full-scale testing will probably be impractical for vehicles larger than Saturn V. Scale model testing and analytical calculations will probably yield information concerning structural characteristics, but such procedures may not yield the degree of accuracy required to synthesize satisfactory conventional control systems.

The importance of having the capability of synthesizing control systems when knowledge of vehicle dynamic characteristics is limited also becomes apparent when consideration is given to developing a launch vehicle system with alternate mission capability. That is, after some major system failure has eliminated the possibility of achieving the primary mission objective, it would be desirable to make necessary changes in the guidance system so that some secondary objective could be realized. In some cases, it might be possible to continue the primary mission after certain changes are made. An example of this occurs in Saturn V/ Apollo when loss of thrust on a single engine at certain flight times precludes continuing a lunar mission unless alterations are made to the tilt program. Such tilt program changes alter the trajectory of the vehicle and consequently change the aerodynamic environment in which the vehicle operates. Present control schemes consisting of time-programed gains will not necessarily cope with such environmental changes, since Mach numbers and dynamic pressure values will not coincide with the times which were used in determining the gain program.

Control systems designed to operate with only fragmentary information concerning vehicle response characteristics are called adaptive control systems, this terminology being derived from the ability of such systems to adapt to whatever vehicle dynamic characteristics might arise.

II. ADAPTIVE SYSTEMS

A conceptual block diagram of a typical adaptive system is shown in Figure 1. Inclosed in the broken rectangle are launch vehicle dynamics, the control device, and the usual feedback path necessary for generating control action. For an adaptive system, there is an additional path or combination of paths and additional processes which are performed. These processes are identification, decision, and adjustment.

The identification process determines the dynamic characteristics of the launch vehicle, that is, how the vehicle responds to control inputs. This could involve determining or estimating aerodynamic parameters and bending mode frequencies and mode shapes; or it might be an observation of the nature of the output, considering only such characteristics as predominant frequencies, damping ratios, magnitude of certain output variables, etc.

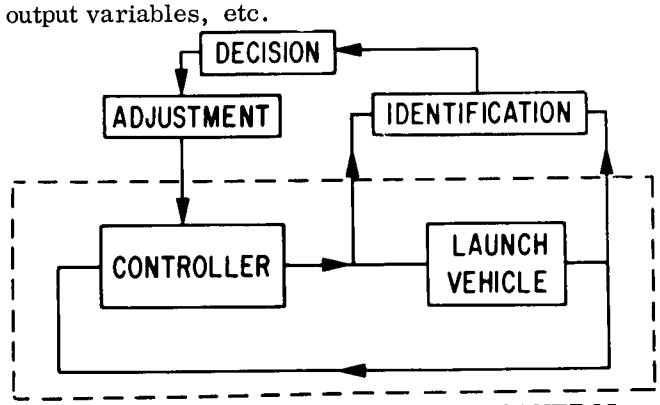

FIGURE 1. A TYPICAL ADAPTIVE CONTROL SYSTEM

The second process in the adaptation channel is the decision block. Here a computer examines the information obtained from the identification process and selects one action out of perhaps several actions which might be taken. Typically, the decision might be to increase the amount of rate feedback based on the identification process' indication of insufficient damping of the output.

The last process involves making the necessary adjustments on the controller in order to implement the decision which is made. In the case of increasing the amount of rate feedback, the adjustment mechanism might be a servo potentiometer or any type of gain adjusting device.

A. ADAPTIVE BENDING STABILIZATION

One area of application of adaptive control is the bending stabilization problem. A considerable portion of the control system design effort for a flexible vehicle is directed toward ensuring that the elastic modes do not couple back through the control force to produce a dynamic instability. Present bending stabilization schemes consist of filtering sensor outputs so that the elastic components of the control signal are either eliminated or are phased so as to counteract the elastic vibrations instead of regenerating them. Such a design requires precise knowledge of bending mode frequencies and their variation with flight time. Furthermore, it is necessary to select specific sensor locations before the design can be accomplished; there-

fore, any change in sensor location requires a redesign of the filter. If precise information is not obtainable or if flexibility with respect to sensor location is required, an adaptive system will be needed for bending mode stabilization.

One such system developed in the Aero research program is the "spectral identification adaptive control system" of the Autonetics Division of North American Aviation (NAA) [1]. A simplified functional block diagram of the system is shown in Figure 2. The basic idea is that the total rigid-elastic signal from an accelerometer is processed to identify the flexible mode frequencies. This frequency information is then used to adjust notch filters which either eliminate the elastic components from the total signal or provide proper phasing for stabilization. The flexible body compensation is thus accomplished in flight without the requirement of prior knowledge of the mode frequencies other than their general broad range of occurrence.

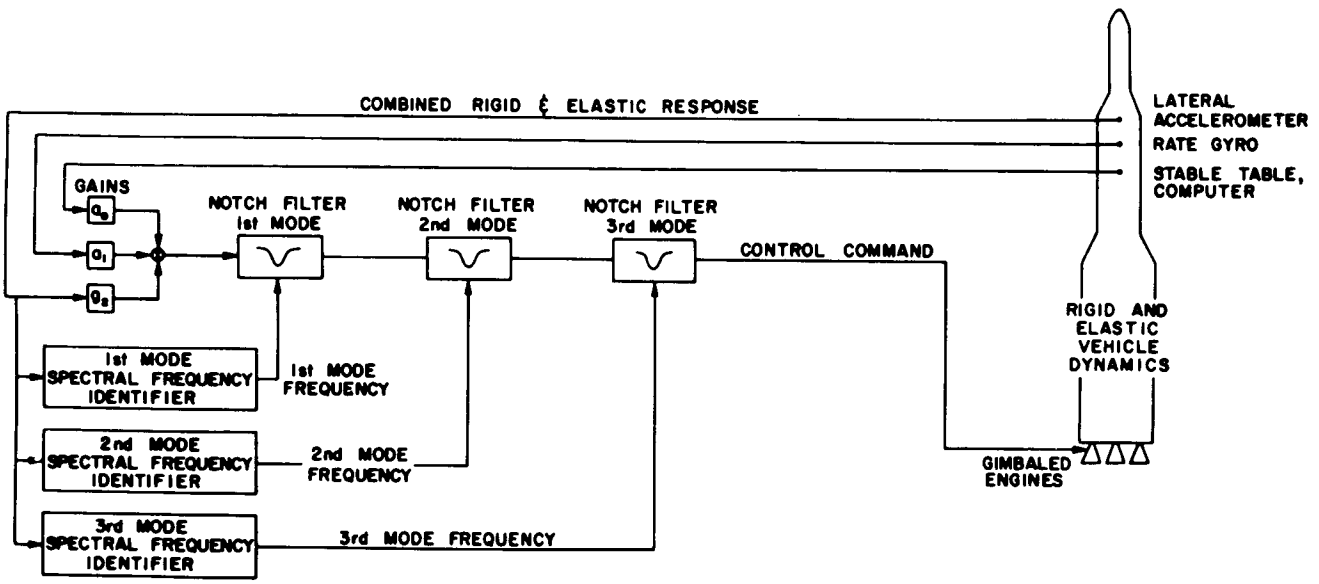

FIGURE 2. SPECTRAL IDENTIFICATION ADAPTIVE CONTROL SYSTEM

The heart of the system is the spectral frequency identifier. The identification technique makes use of integral filters which provide a sharply defined peak output whenever the input signal contains components at or near the tuned filter frequency. The mathematical form of the filter function is given by the integral expression shown in Figure 3, in which $p(\omega_0 t)$ is some periodic function (e.g., sine wave, square wave) with frequency ω_0 and period T. Since this integral product of the input and "kernel" function p is an approximation of the cross-correlation of the two functions, the filter output will peak significantly when the frequency of the input is similar to that of the kernel function. This is illustrated in Figure 4, which shows the frequency response of an integral filter with a square wave kernel function. Here it can be seen that the output has a sharply defined maximum whenever the input frequency equals the tuned frequency.

A spectral frequency identifier for a given elastic mode is composed of several (for example, 4 or 5) of these integral filters tuned to different frequencies, ω_1, ω_2, etc., which cover the expected range of elastic

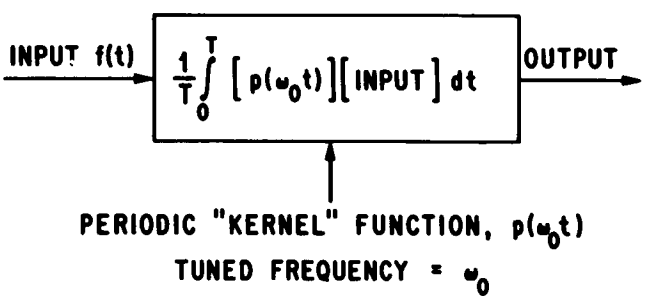

FIGURE 3. INTEGRAL FILTER

mode frequency variation (Fig. 5). The outputs of the filters are compared on an amplitude basis. If an accelerometer or gyro signal containing flexible mode components is applied to the filter array, the filter having a tuned frequency closest to the mode frequency being identified will have the largest output and thus will provide mode frequency identification. The identified mode frequency is then used to adjust the corresponding notch filter in the gimbal command loop.

Interpolation schemes may be used to define the frequency with more accuracy.

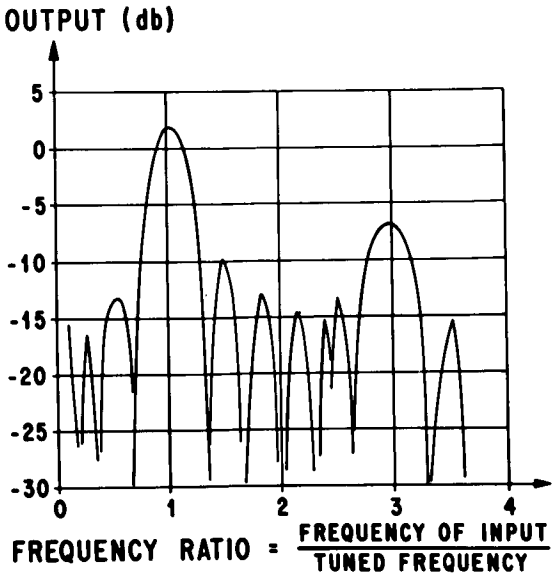

FIGURE 4. COMBINED INTEGRAL FILTER FREQUENCY RESPONSE

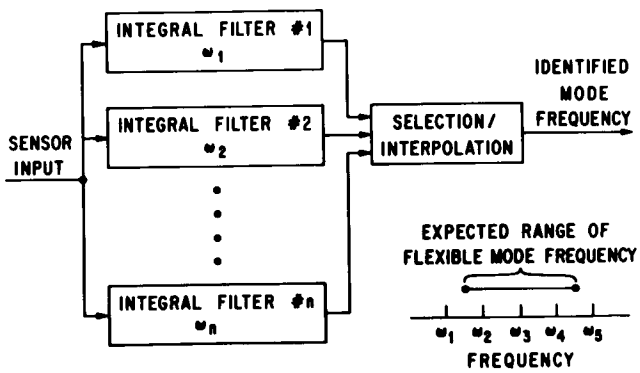

FIGURE 5. SPECTRAL FREQUENCY IDENTIFIER

Figure 6 is an illustration of the adaptive operation of the system. The third bending mode frequency was arbitrarily increased from 24 to 30 radians a second. The lower figure shows the operation of the system in tracking the frequency variation. The upper figure is a plot of vehicle lateral acceleration. As seen from the graph, an oscillation occurs at the third mode frequency when the frequency variation is begun. As the filter tracks and the system adapts to the new frequency, however, the oscillation is damped out.

Although feasibility of the general concept has been proven in preliminary studies, there is a need for additional analysis before the system can be recommended for in-flight testing. Currently, efforts are

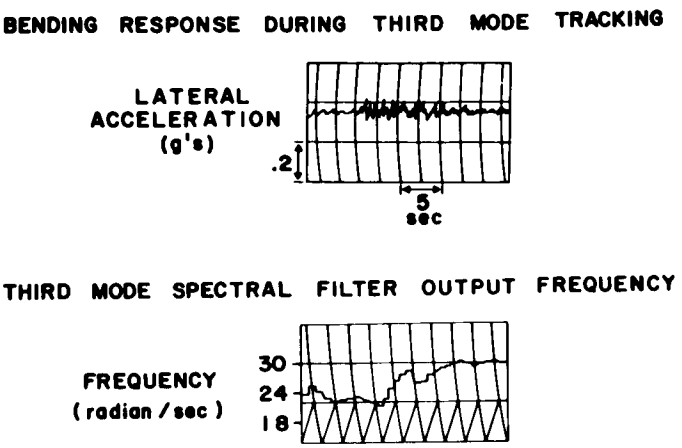

FIGURE 6. CLOSED LOOP ADAPTIVE FILTER TRACKING

being directed toward determining performance limitations under an extreme range of parameter and system variations and toward improving the particular method used by NAA to implement the concept.

Implementation improvement is being accomplished in two ways. In the first, speed and accuracy of identification by the spectral frequency identifier are being improved by developing "kernels" and interpolation methods which are more sophisticated than the ones presently used. Implementation of the techniques will still be relatively simple for a small onboard digital computer to achieve even with time-sharing operation of the computer. In the second, the technique requires notch filters, as mentioned above, to eliminate the elastic components of the control signal. However, sometimes there are advantages to feeding back a bending signal with proper phase angle for increasing stability margin rather than eliminating the signal completely. For these cases, NAA is developing methods of using the output of the frequency identifier to adjust phase stabilizing devices rather than notch filters.

B. ADAPTIVE LOAD RELIEF SYSTEMS

Another class of adaptive control systems consists of systems with the capability of adapting to changes in disturbance forces. An important application of the adaptive concept arises in the development of so-called load relief systems. Before a launch vehicle reaches the max q region, aerodynamic loads are not critical because Mach number is relatively low and the disturbing forces of wind shears and gusts are not excessively large. Since loading is not critical, the control system can concentrate on its primary ob-

jective of following guidance commands with little concern for loads. However, when the max q region is entered and large disturbing forces are encountered, load considerations begin to override the guidance requirements. Then it is necessary that the load constraint on control performance be given more weight than the flight path requirements of the controller. Thus, it is desirable to have a control capability based on different performance criteria, with the particular criterion being utilized depending on both the aerodynamic environment and the magnitude of wind shears and gusts.

Such a control system was studied by Space Technology Laboratories under Aero sponsorship [2]. A summary report on the system was presented at the 1964 annual AIAA meeting [3]. This system, known as a switched integral controller, attempts to make use of the best features of the familiar "drift minimum" control law to maintain small flight path errors and of the "load minimum" control law to reduce the bending load.

The switched integral control system, diagramed in Figure 7, makes use of these principles by adapting

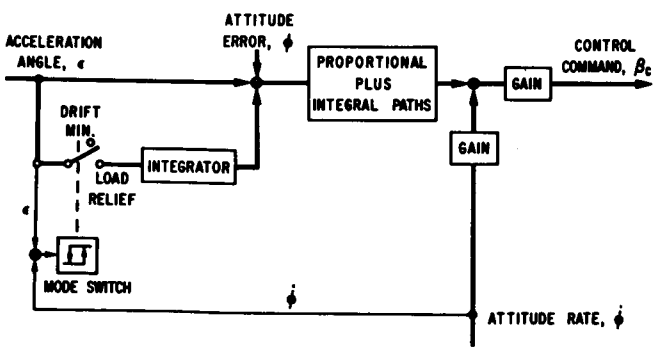

FIGURE 7. SWITCHED - INTEGRAL CONTROLLER

the control law to the magnitude of the wind. Thus, identification for this adaptive system is provided by the determination of the wind level. For low-level winds, the system causes the vehicle to fly a near drift-minimum path; but high-level winds, as sensed by an accelerometer, cause the system to switch to near load-minimum control in order to reduce the aerodynamic loading below the critical level. Adjustment of the control law is provided by a simple switching device.

The system utilizes inputs from the attitude reference and rate gyros and a pendulous accelerometer, which senses the angle between the acceleration vector and the longitudinal axis of the vehicle. This angle is denoted by ϵ on the block diagram of Figure 7. The pendulous accelerometer is used instead of a conventional lateral accelerometer to avoid gain scheduling. To achieve drift-minimum control, the measured vehicle acceleration vector is forced along the nominal trajectory. This is accomplished with the switch in the up position by commanding the vehicle attitude ϕ to be equal to the pendulous accelerometer output ϵ. In high winds, the system switches and achieves load-minimum control by commanding ϵ toward zero through addition of its integral to the control command. The switching is accomplished by using the measured acceleration angle, which is an indirect measure of wind level, to determine when load relief is required. The rate signal and hysteresis in the switching circuit are introduced to provide switching stability and to reduce the magnitude of the limit cycle.

The performance of the switched integral system in response to a high wind is indicated in the time history shown in Figure 8. For comparison, a time

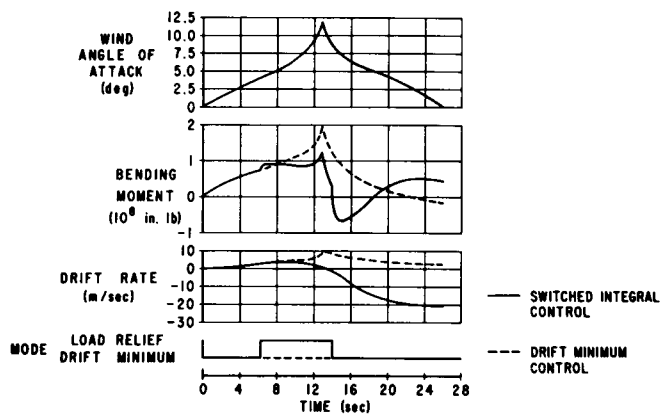

FIGURE 8. TIME HISTORY SWITCHED INTEGRAL RESPONSE VERSUS DRIFT MINIMUM RESPONSE

history of drift-minimum response to the same wind disturbance is shown by dashed lines. The change-over to load minimum is indicated on the switching trace as the wind builds up (occurring at about 6 seconds). The increase in drift rate associated with the load relief control is apparent. As the disturbance decreases, the system switches back to drift minimum (at about 14 seconds), and the drifting condition is eventually arrested.

For the maximum design wind, a 20-percent to 30-percent reduction in bending moment over the pure drift-minimum control is achieved. However, the system exhibits an undesirable wind sensitivity characteristic. This can be seen from the curves of Figure 9, which are plots of peak bending moment versus wind magnitude for the switched integral controller

and, for comparison, the standard drift-minimum controller. It can be seen here that, although the adaptive system provides significant load reduction at the maximum wind conditions, a load increase is produced at the lower wind values. Even so, an appreciable reduction in the maximum bending moment over all wind speeds is achieved by the adaptive system.

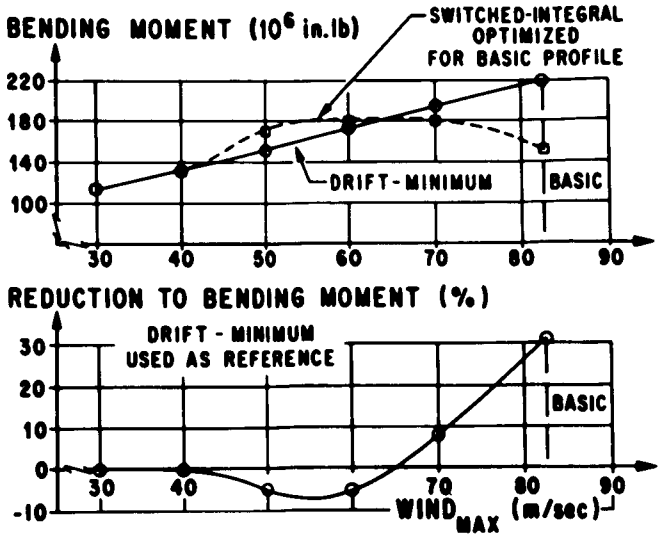

FIGURE 9. WIND EFFECT ON SWITCHED INTEGRAL CONTROL PERFORMANCE

In conclusion, it can be said that the switched integral adaptive system indicates some of the advantages available from input adaptation and provides a first step toward realizable load relief systems. However, it is clear that this is not the ultimate in load relief systems, and the fact that it is adaptive does not remove the requirement for examining in detail the system performance under the complete range of deterministic wind inputs.

III. MINIMAX CONTROL RESEARCH

The approach to the synthesis of load relief systems just described is an engineering approach to the problem in which some particular scheme evolves from a trial-and-error procedure. After a basic control concept is determined from such an approach, one must test the system's performance with various levels of disturbing forces acting on the vehicle in order to determine whether the system operates satisfactorily for the range of disturbances the vehicle is expected to encounter.

Present design philosophy at MSFC is to use the worst wind out of a class of winds in determining loads for which the structure is to be designed.

The class of winds used is determined from actual wind measurements made at Cape Kennedy over a span of several years. In design philosophy the wind is worst in the sense that it causes the vehicle to experience maximum structural loading. With linear, well-damped feedback control systems, design experience leads one to select statistical values representing extreme wind conditions for use in design load studies. Thus, the Saturn V design loads are based on wind profiles constructed from 95-percent probability wind-speed values and 99-percent probability wind-shear and gust values.

When nonlinear feedback systems are employed, as in the load relief system previously discussed, winds still must satisfy the statistically stated constraints, but there is no assurance nor any reason to suspect that a wind profile constructed using extreme values is necessarily the worst-case wind. Consequently, if MSFC's present plan of designing for the worst case is to be continued, techniques will be required for determining what the worst disturbance is for a particular control law.

Consideration of this requirement has led to the formulation of a mathematical statement of the launch vehicle control problem which, it is hoped, will result in an analytical procedure that will provide guidelines for designing nonlinear load relief systems. In this context, the load relief problem is called the minimax problem of vehicle control.

The statement of the minimax problem is very simple, but its solution continues to be very difficult. To give the reader an idea of what this concept entails, Figure 10 shows a mathematical statement of the problem and gives an example of what is being attempted.

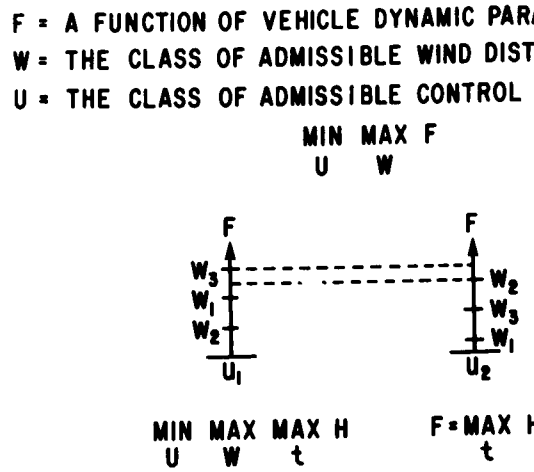

FIGURE 10. MINIMAX PERFORMANCE CRITERIA

First, there is some mathematical function, F, of the vehicle parameters which provides a measure of

the vehicle's performance. Typically, F might be the maximum value of the bending moment at a particular vehicle station over some interval of time. Next, there is a mathematical model of the disturbances or winds represented by the class W. Here W might be chosen to be all winds bounded in magnitude by 95-percent wind-speed values and in slope by 99-percent shear values. Finally, there is a class of admissible control functions, U, which could represent allowable engine gimbal responses. For example, swivel angle might be limited to 5 degrees, with a swivel rate limit of 5 degrees/ second.

Therefore, there is a mathematical description of the winds, the control forces, and the vehicle's performance. The objective is to choose the control law, out of the class U, which minimizes the maximum value of the function F where the maximization of F occurs as a result of a particular wind in the class W. This last statement is more easily understood by use of the example shown on the lower part of Figure 10.

Suppose that class U consists of only two control laws u_1 and u_2, and that the class W consists of three disturbance functions w_1, w_2, and w_3. In the figure are shown two scale representations of the values of the function F, one scale for each control law. Suppose u_1 with the three winds--w_1, w_2, and w_3-- yields values for F as shown on the scale on the left. For example, u_1 with w_2 yields the lower value of F, and u_1 with w_3 the upper value. Then for u_1, w_3 is the worst disturbance in the sense that it yields the maximum value of F.

Similarly for u_2, the three winds yield different values of F as plotted on the scale on the right. Thus for u_2, w_2 is the worst wind disturbance.

By comparing the values of F which result for the three winds, considering each scale separately, the maximization over the class W is performed. Minimization over the class U is performed by comparing the largest value on each scale to determine which control law yields the smallest of the maximums. Projecting the maximum on the u_2 scale to the u_1 scale shows that u_2 yields the lesser maximum value; therefore, the control law u_2 is the solution to the problem.

Of course, this is an oversimplification of the actual problem, and it is not feasible to conduct the type of comparison just made for complex launch vehicle problems. In fact, the comparison has been made on the basis of each class containing a finite number of functions, which is not a very realistic situation. The example serves to illustrate the nature of the minimax problem and indicates some of the difficulties which might be encountered in attempting to develop mathematical techniques for solving it.

In addition, it was decided to concentrate on the particular case in which the function F corresponds to the maximum value of another function of the vehicle parameters as shown at the bottom of Figure 10, this choice of F being motivated primarily by the objective of reducing the maximum bending moment experienced by the vehicle. Thus, there is an additional maximization over an interval of time of some function H, F being the maximum value of this function, and this maximization must be performed concurrently with the others.

Because the generalized minimax problem is not amenable to complete solution by currently known techniques, the approach taken in the minimax research has been to study restricted cases of the problem which offer promise of solution, and to extend the results to greater generality upon successful solution of the simplified cases.

Several contractors have been working on various aspects of the problem. As an example, the work done by Honeywell will be summarized here [4]. Honeywell has restricted the problem to consideration of linear, constant-gain feedback controllers. The wind considered is bounded in amplitude only, and the performance index chosen is the maximum over time of drift rate.

The Honeywell method involves an arbitrary choice of control system configuration as shown in Figure 11.

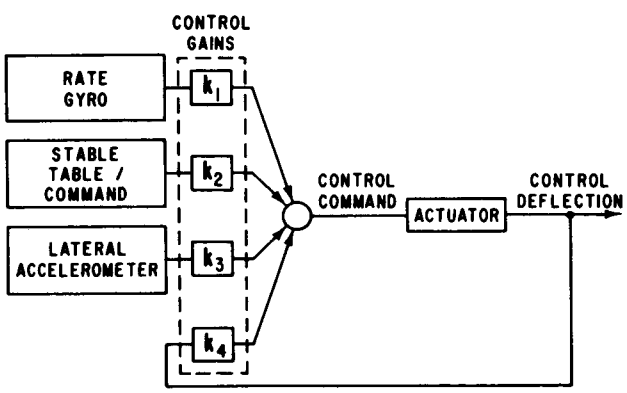

FIGURE 11. LINEAR CONTROL SYSTEM TO BE OPTIMIZED

In this example, the configuration chosen consists of lateral acceleration, attitude error, attitude rate, and engine gimbal angle feedback paths. For this configuration, the control gains k_1, k_2, k_3, and k_4 are optimized according to the minimax criterion.

Ordinary optimization theory is used to determine the maximizing wind for a given set of the feedback gains. This wind is then used as a disturbance function to numerically compute the vehicle's response.

Thus, for a given set of control gains or for a given control law, a corresponding wind is determined which maximizes the performance measure for that particular gain set. After the performance measure for each set of control gains has been computed, a comparison can be made of the resulting performance measures to determine the particular set of control gains which is minimizing.

To accomplish the minimization over the allowable class of control functions, a four-dimensional grid of control gains is chosen to represent the control law class. For illustrative purposes, this grid is shown as being two-dimensional in Figure 12. For each controller, as represented by a gain set in the grid, the worst wind is computed and the performance index for that worst disturbance is calculated. The best controller of the set, therefore, is the one which provides the minimum of the performance index under this worst disturbance.

A second grid then is chosen as a "fine tuning" on the controller selected. An area around the first grid "optimum" is searched to find further performance improvement. This refinement process may be repeated if additional accuracy is desired.

A complication arises from the fact that the optimum system chosen is dependent on the initial conditions of the vehicle parameters as well as on the wind. This results in another dimension being added to the search grid, that of initial conditions. However, for this problem the sensitivity to initial conditions is apparently not extreme, since consideration of seventeen initial condition sets of sizeable variation produced only four different optimum gain sets.

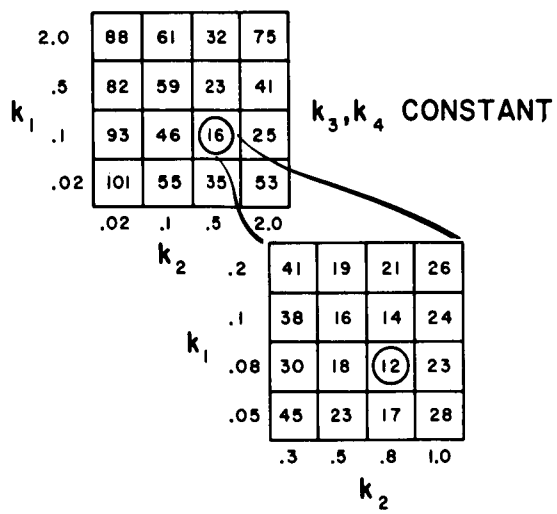

FIGURE 12. GAIN GRID SELECTION

As might be expected, the worst wind in the class of bounded amplitude winds turns out to be "bang-bang"; that is, one which changes instantaneously from its extreme positive value to its extreme negative value. A more realistic case of bounded wind shear is currently under investigation. Vehicle response to the "bang-bang" worst wind with the minimum control is shown in Figure 13. The oscillations appearing in

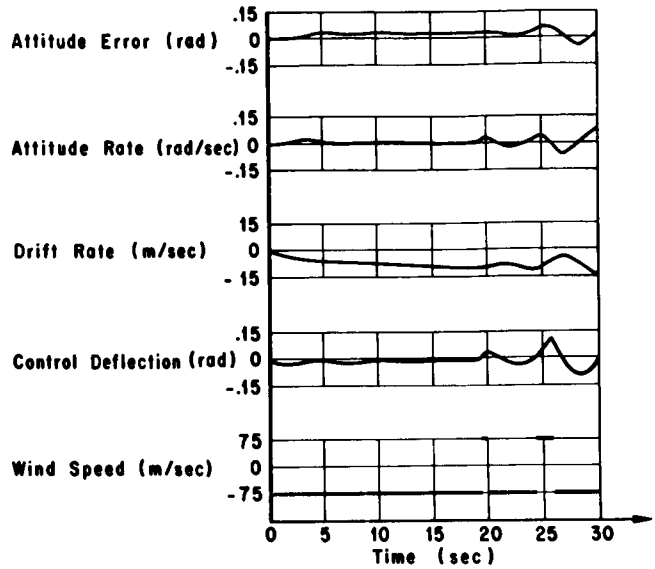

FIGURE 13. RESPONSE TO EXTREMAL DISTURBANCE WHICH MAXIMIZES DRIFT RATE

the responses are due to the oscillatory character of the wind.

Other approaches to the minimax problem have been directed toward developing new mathematical techniques for solving the problem rather than toward using the classical approach which is restricted to special cases. However, Honeywell's efforts have produced a tractable method of minimax solution for the restricted cases considered. Work is being directed toward the removal of some of the restrictions and toward the treatment of more realistic cases, such as bounded wind rate and nonlinear control.

IV. FUTURE DIRECTION

As is apparent from this discussion, the Aero-Astrodynamics program is strongly based on two requirements. One is the acquisition of a capability for stabilizing large flexible launch vehicles, vehicles even larger than Saturn V. The other is the determination of control techniques which will permit significant reduction in bending moment loads in the maximum dynamic pressure region.

At the time of initiation of the program in 1960, it was thought that the problems of bending stabilization

and structural loads would be critical for the Saturn V vehicle. In late 1962 or early 1963, after Saturn V stability studies had been conducted, it was determined that the current conventional methods of stabilization would probably be adequate for suppressing structural vibrations. However, in anticipation of the post-Saturn launch vehicle, research was continued toward developing advanced techniques for treating the bending problem for large launch vehicles. Out of this research have come two satisfactory schemes, one presented here and another, sponsored by Astrionics Laboratory, which is identical in concept to the Autonetics system but differs in mechanization. (Mechanization of the Astrionics system is analog, whereas mechanization of the Autonetics system is digital [5].)

Research directed toward reducing loads in the max q region was initiated with the assumption that large structural weight savings with consequent payload gains would be realized through the use of adaptive load relief systems on Saturn V. Studies have shown that control techniques applied to Saturn V provide only limited total load reduction, since the major portion of the design loads is established by burnout and lift-off conditions. Consequently, bending moment reductions at max q do not significiantly affect the weight of the vehicle structure. However, this does not mean that significant weight reductions and payload gains will not be achieved for other launch vehicle systems. Thus, the plans are to continue activities on the application of load relief systems in order to achieve greater payload capability. However, since post-Saturn launch vehicle systems studies have been decreased, some of the effort will be directed to applications of load relief systems to vehicles whose structural design is "frozen."

For vehicles whose structural design has been finalized, it is often the case that the system will not meet the loading conditions encountered for certain types of missions. Then, load reductions of only a few percent may be necessary in order to achieve the required design safety factor. Such cases have already occurred in the Saturn-Apollo program and are likely to arise in Apollo Applications Program (AAP) missions. AAP launch vehicles will be composed of stages from various launch vehicle systems and, consequently, the structural design of these stages will be "frozen." In considering combinations of stages to comprise an AAP, some missions may impose excessive loading conditions on the spacecraft or launch vehicle structure. In order to alleviate such load problems, either more restrictive launch wind conditions must be imposed or some structural redesign must be considered, unless an effective load relief control system can be determined.

In addition to loading problems which might be encountered, AAP vehicles may exhibit elastic mode characteristics which cannot be handled by conventional stabilization techniques. Thus, adaptive bending mode stabilization systems may also be necessary for obtaining satisfactory performance of these systems. Of course, in considering the use of adaptive systems for both load relief and bending stabilization, the increased complexity of mechanization which will be required must be weighed against the gain in system performance which will result from the use of such systems.

Another area of interest is the application of stochastic optimization theory to the control synthesis problem. Such an approach to controller design has not been acceptable in the past because of the limited knowledge of the statistical properties of the wind. However, as better statistical models of the wind are determined and confidence is established in these models, the design of control systems on a statistical basis will become an acceptable design philosophy.

Finally, effort will be directed toward developing improved techniques for the design, analysis, and synthesis of control systems. Present procedures are costly in terms of both man-hours and machine time primarily because the techniques being utilized were developed prior to the advent of large digital computers. Root locus, frequency response, and other conventional tools for stability analysis were developed during and in the years immediately after World War II. Also, methods for studying time-response characteristics of vehicle performance are largely patterned so that they are amenable to analog-computer solution. Little advantage has been taken of the control technology developed in the past decade and its potential for system design utilizing digital computers.

V. CONCLUSIONS

Problems have been considered in adaptive bending stabilization, adaptive load relief, and minimax control with the motivation provided primarily by post-Saturn launch vehicle requirements. Various schemes have been developed for bending stabilization and load relief, but much additional research will be required before the minimax problem can be solved.

Future research activities will be directed toward solving problems relating to achieving an alternate mission capability for Saturn V, Apollo Applications Program missions, and control system requirements of future launch vehicles.

REFERENCES

1. Box, J. L., et al.: Spectral Identification Adaptive Control System Study, Final Report. Autonetics C4-126/33, February 1964.

2. Blackburn, E. P., et al.: A Study of the Design of an Adaptive Control System for Saturn Type Vehicles, Final Report. STL 8681-6004-RL-000, April 1963.

3. Klenk, W. J.: An Adaptive System for Load Relief and Accurate Control of Launch Vehicles. AIAA Paper No. 64-239, June 1964.

4. Research Study of a Large Flexible Launch Booster Control, Progress Report No. 6. Honeywell MPG Report 12003-PR6, November 1964.

5. Hart, W. G., and McGowan, G. F.: Advanced Control System for Saturn V Phase III, Final Report (U). Martin CR-64-72, November 1964, Confidential.

MATERIALS RESEARCH AT MSFC

May 27, 1965

by

W. R. Lucas

TABLE OF CONTENTS

MATERIALS RESEARCH AT MARSHALL SPACE FLIGHT CENTER

by W. R. Lucas

LIST OF ILLUSTRATIONS

LIST OF ILLUSTRATIONS (Concluded)

LIST OF TABLES

RESEARCH IN PULSED MASS EXPULSION CONTROL SYSTEMS

by

David N. Schultz

SUMMARY

The problem of space vehicle attitude control has received much attention over the past few years. The evolution of attitude control systems thus far has followed a course that has led to serviceable but nonoptimum designs of mass expulsion control systems. The purpose of the work described in this report is to improve and optimize the design of these systems in terms of system weight, energy utilization, and actuator duty cycle. This optimization has become necessary because the problem of obtaining efficient, versatile, and economical attitude control systems becomes one of paramount importance as mission durations increase and mission requirements become more demanding.

Because the dynamic range of an attitude control system usually must be large, the conventional attitude control system design approach usually has used some type of pulse modulation scheme to fulfill the requirement that the control engines produce thrust pulses of either short or long on-times. This corresponds to minimum impulse generation and compensation of large disturbances, respectively. Over a certain range of the input signal applied to a pseudo rate modulator, which represents a typical conventional control system design approach, the output is caused to be both pulse-width and pulse-rate modulated as a function of the input signal level. It is shown that pseudo rate modulation has desirable characteristics of both of these modulation schemes.

A concept that has been called the "advanced limit-cycle control technique" is also described. This concept was developed to minimize the fuel consumption of an on-off jet system used for space vehicle attitude control when extended mission durations must be considered. The control system, which uses on-off jet engine thrust for vehicle-restoring torque control, is caused to operate with a special type of control logic. This logic causes the vehicle to be placed close to a specific reference attitude with the attitude error drift rate for each axis as small as possible. If undisturbed steady-state limit-cycle operation is assumed, the vehicle will maintain these low drift rates for a very long time, i.e., until the specified attitude deadband is reached. After the deadband for any axis is exceeded, the remaining portions of the limit cycle must have a finite value of attitude error rate that brings the vehicle back to reference attitude rapidly and allows the use of large-thrust jet engines with correspondingly large minimum impulse.

Before the advanced limit-cycle technique can be extended to a three-axis space vehicle control system, however, the thrust-vector error effects that are cross-coupled from one axis to another must be considered. To evaluate these effects, an optimization study was performed utilizing a three-axis digital computer program for control system analysis and comparison. Three basic engine and vehicle configurations were analyzed by this computer program and five control techniques were investigated for each of three different acceleration values. Two simple (conventional) limit-cycle techniques and three advanced limit-cycle techniques were studied. The nonlinearities of these control systems were also considered in the analysis.

Even though a complete study has not been accomplished, parametric trends were established for the important parameters of the program. This optimization study program has provided sufficient information to show that the advanced limit-cycle control techniques are extremely valuable and should be the subject of further detailed study.

An attitude motion simulator facility that has been fabricated at MSFC also is described. This facility is a research and development tool that permits dynamic testing of various attitude-control systems connected with space-flight investigations under a variety of realistic conditions.

I. INTRODUCTION

The purpose of a research program in the field of pulsed mass expulsion attitude-control systems is to improve and optimize the design of these systems for use on Saturn and future space-vehicle

missions. The problem of space-vehicle attitude control has received much attention over the past few years. The evolution of attitude-control systems, to date, has followed a course leading to serviceable but nonoptimum designs of mass expulsion control systems. Current systems leave much to be desired in terms of system weight, energy utilization, and actuator duty cycle. This has not caused much concern in present systems; but as mission durations are increased and mission requirements become more demanding, the problem of obtaining efficient, versatile, and economical attitude-control systems becomes one of paramount importance.

Two requirements usually are imposed on three-axis attitude-control systems. An efficient quiescent or limit-cycle period during required vehicle coasting phases must be obtained to conserve the total energy consumed because any mass or energy expended directly affects the payload and mission duration. However, the usual attitude-control problem requires a system with more flexibility than one that simply has the ability to follow attitude-reference changes. In particular, the torque-producing elements of the control system must also provide the high torque needed to control stage-separation transients, internal movements, maneuvering sequences, and thrust-vector errors of prime propulsion units. When extended mission durations must be considered, these varied and conflicting requirements sometimes lead to the design of control systems with two or more modes of operation. For example, both high- and low-thrust reaction jets might be utilized, thereby increasing the complexity of the resulting control-system design. In using engines of only one thrust level, however, the conventional system design approach is to size the attitude-control engines to meet the high-torque requirements, and then to provide relatively short engine on-times of minimum impulse operation to maintain the propellant consumption or mass expenditure within acceptable limits during specified vehicle coasting phases. Use of this conventional approach would allow the vehicle to limit cycle within a prescribed attitude deadband with vehicle drift rates as dictated by the minimum impulse capability of the particular engines used. For maximum efficiency during undisturbed steady-state operation, an attempt is made to reduce the minimum impulse of the control engines to the lowest possible value. Because the dynamic range from minimum impulse limit cycle to full-on operation usually must be large, some sort of pulse modulation scheme is used to fulfill the requirement that the control engines produce thrust pulses of either short or long on-times. As an illustration of this conventional control-system design approach, the results of an analysis of "pseudo rate modulation" are presented.

A new and different approach, however, may be taken for the attitude-control-system design to minimize propellant consumption. Called the "advanced limit-cycle technique," it differs from the conventional approach in that no attempt is made to reduce the minimum impulse of the control engines to its smallest possible value. Instead, a control logic (as a function of certain sensed inputs) causes the vehicle to be placed close to a specified reference attitude, with the vehicle attitude drift rate for each axis as small as possible. If an undisturbed steady-state limit-cycle operation is assumed, the vehicle will maintain these low drift rates for a very long time, i.e., until the specified deadband is reached. After the deadband for any axis is exceeded, the remaining portions of the limit cycle must have a finite value of attitude error rate which brings the vehicle back to reference attitude relatively fast and allows the use of large-thrust jet engines with correspondingly large minimum impulse. It will be shown that extremely long limit-cycle periods, which depend on performance repeatability of the sensed inputs and the engine system, can be obtained for undisturbed steady-state operation. This represents optimum performance with respect to both propellant consumption and number of pulses or on-off engine actuations.

Before the design of control logic or the adoption of one control technique can be achieved, however, an important effect must be considered: thrust-vector errors in one axis can give rise to accelerations in other axes. These errors could produce vehicle error rates that are of the same magnitude as the conventional limit-cycle drift rates. Should this be the case, there would be no justification for pursuing the advanced limit-cycle control techniques. These advanced control techniques have been examined, however, and first-order answers as to their value have been obtained. The results of these studies will give direction to more sophisticated methods of analysis in the future.

To investigate, test, and check out various potential control systems connected with space-flight studies, an attitude-motion simulator facility has been fabricated at MSFC. In this facility, actual torques are exerted on the inertia of a platform supported on a virtually friction-free spherical air bearing. Thus, this facility is a research and development tool permitting dynamic testing of attitude-control systems and providing a high level of confidence in the analytical results.

II. SPACE-VEHICLE ATTITUDE CONTROL USING PSEUDO RATE MODULATION

A. GENERAL DESCRIPTION

Use of on-off pulse modulation techniques in space-vehicle attitude-control applications has been extensively studied and many workable schemes have been advocated [1, 2, 3]. To illustrate a conventional space-vehicle control-system design approach, the results are given for an analysis of one particular modulation scheme called "derived rate increment stabilization" [1] or, as it is commonly called in Saturn V/S-IVB studies, "pseudo rate modulation."

Because the dynamic range of an attitude-control system usually must be large, pulse modulation is used to fulfill the requirement that the control engines produce thrust pulses of either short or long on-times. This corresponds to minimum impulse generation and compensation of large disturbances, respectively. Over a certain range of the input signal applied to the pseudo rate modulator, the output is caused to be both pulse-width and pulse-rate modulated as a function of the input signal level. As will be shown, pseudo rate modulation has desirable characteristics of both of these modulation schemes.

To provide this type of operation, each actuator or on-off contactor has a preset amount of deadspace, a specified amount of positive-switching hysteresis, and a negative feedback consisting of a first-order lag network. The deadspace is adjusted to satisfy a required amount of control-system attitude deadband or attitude rate deadband (if rate control modes are used). Both the amount of switching hysteresis and the feedback network characteristics are usually sized to ensure control-system minimum-impulse operation of the particular engines used.

An additional characteristic of the feedback lag network is the provision of a small amount of control-system damping. Although this capability is sometimes not the dominant consideration for selecting the network and gain factors, it is nevertheless desirable and an important consideration for analysis because the amount of damping is normally sufficient to maintain control-system limit-cycle operation in the event of a rate-sensor failure. All modulator gain factors and network characteristics are mathematically analyzed to obtain all possible control-system operating ranges, and the results are presented graphically.

Figure 1 shows a simplified single-axis control-system block diagram which includes a pseudo rate modulator. As illustrated, there are three cases for sensed rate input into the ϵ summing junction. For Case I, ϵ is equivalent to sensed attitude information only. This case will be analyzed first and is given not only to demonstrate the basic characteristics of pseudo rate modulation but also to illustrate the provision of control-system damping by the lag network of the pseudo rate modulator. For Case II, sensed rate information is provided using an active rate sensor. For Case III, electronic differentiation is assumed to provide the sensed rate signal. If the attitude reference is held constant with time, Cases II and III give similar single-axis closed-loop response. For simplicity, the analysis for these cases will be considered similar, especially if the time lags and gain factors through the respective rate-sensing loops can be assumed to be the same.

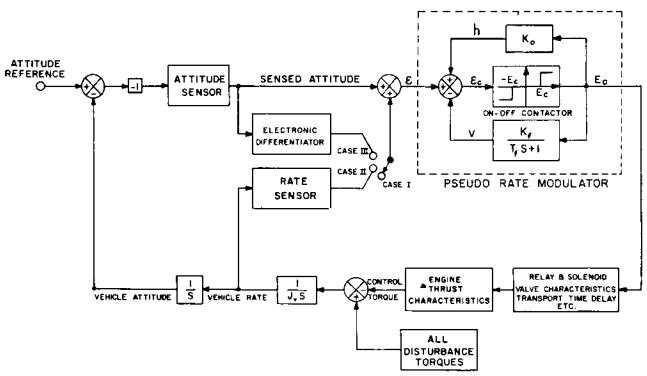

FIGURE 1. SIMPLIFIED SINGLE-AXIS CONTROL SYSTEM

Note that Figure 1 also includes the effects of engine-thrust characteristics as well as relay (if used) and solenoid-valve characteristics, transport time delay, etc. These effects as well as sensor lags and contactor switching hysteresis usually dictate minimum-impulse operation of an on-off control system. If some sort of pulse-modulation scheme were not used, large values for minimum impulse could result.

B. STATIC CHARACTERISTICS OF PSEUDO RATE MODULATION (INPUT HELD CONSTANT)

Regardless of the state of the system, and in terms of the parameters defined by Figure 1, the input voltage $\epsilon_c(t)$ to the on-off contactor may be expressed as:

$$\epsilon_c(t) = \epsilon(t) + h(t) - V(t) \qquad (1)$$

in which $\epsilon(t)$ is the combined error-signal voltage (sensed attitude only for Case I), $h(t)$ is the positive switching hysteresis, and $V(t)$ is the voltage of the negative-feedback lag network. For $|\epsilon_c| < |E_c|$, the contactor is off; for $|\epsilon_c| \geq |E_c|$, the contactor is on, with the polarity depending upon that of ϵ_c.

To derive the static characteristics of the pseudo rate modulator, assume the modulator input error signal ϵ is adjusted to some constant value equal to ϵ_o. Since no steady-state pulsing action will take place for $|\epsilon_o| < |E_c|$, consider that $|\epsilon_o| \geq |E_c|$. At the instant $t = 0^-$ (just prior to contactor actuation), $h = 0$ and $\epsilon_c = E_c$ so that equation (1) reduces to:

$$\epsilon_c = \epsilon_o - V_o = E_c$$

or

$$V_o = \epsilon_o - E_c \tag{2}$$

in which V_o is the initial condition of V at $t = 0$. At the instant $t = 0^+$ (just after contactor actuation), in terms of the parameters given by Figure 1, $V(t)$ and h may be expressed as:

$$V(t) = K_f E_o - (K_f E_o - V_o) e^{-t/\tau_f}$$

$$h = K_o E_o \ . \tag{3}$$

The contactor will remain energized until $t = t_1$, at which time $\epsilon_c(t_1) = E_c$. For the instant just prior to cutoff, when equation (3) is used, equation (1) may be written as:

$$\epsilon_c(t_1) = \epsilon_o + K_o E_o - [K_f E_o - (K_f E_o - V_o) e^{-t_1/\tau_f}]$$

$$= E_c. \tag{4}$$

Using V_o as given by equation (2), equation (4) may be solved for t_1:

$$t_1 = \tau_f \ln \left[\frac{K_f - \dfrac{\epsilon_o - E_c}{E_o}}{K_f - K_o - \dfrac{\epsilon_o - E_c}{E_o}} \right] , \tag{5}$$

in which

$$|\epsilon_o| \geq |E_c|$$

$$\epsilon_o = \text{constant}.$$

In general, for steady-state operation, this expresses the contactor on-time increment t_1 as a function of constant values of ϵ_o and the circuit parameters K_o, K_f, τ_f, E_c, and E_o. It is interesting to solve equation 5 for $\epsilon_o = E_c$ to obtain the expression for the minimum on-time $t_1 = \Delta t$.

$$\Delta t = \tau_f \ln \left[\frac{K_f}{K_f - K_o} \right] = \tau_f \ln \left[\frac{1}{1 - \dfrac{K_o}{K_f}} \right] \begin{array}{l} \text{expression} \\ \text{for} \\ \text{minimum} \\ \text{on-time} \\ (\epsilon_o = E_c) \end{array} \tag{6}$$

$$\Delta t \simeq \tau_f \left(\frac{K_o}{K_f} \right) \text{ for } \frac{K_o}{K_f} << 1 \ .$$

The simplified expression for Δt is an approximation obtained by expanding the natural logarithm in a Maclaurin's series and considering K_o/K_f small with respect to unity. The error is less than five percent for values of $K_o/K_f \leq 0.1$.

Two observations may be made from the expression for minimum on-time given by equation (6). First, because for most attitude-control systems it is reasonable to assume that ϵ is very nearly constant during minimum impulse limit-cycle operation (Case I of Fig. 1), this equation establishes the minimum impulse of the control system. In addition, if there is a sufficient amount of transport time delay through the engine and valve characteristics along with time lags through the sensors, equation (6) also enforces minimum impulse for Cases II and III. Second, equation (6) is independent of output voltage E_o as long as E_o is not zero. This means that, even if the output voltage falls off because of power supply trouble or relay or solenoid loading, the minimum impulse of the control system will not change, provided E_c remains constant (this threshold is usually carefully controlled) and the passive-network parameters K_o, K_f, and τ_f do not change.

The following relationship applies in the general expression for on-time, equation (5):

$$t_1 \to \infty \text{ as } \frac{\epsilon_o - E_c}{E_o} \to (K_f - K_o) \ . \tag{7}$$

Since this relationship shows the contactor to be continuously on for this condition of input, the modulation range may be defined as:

$$0 \le \frac{\epsilon_o - E_c}{E_o} \le (K_f - K_o) , \qquad (8)$$

which may be normalized and expressed as:

$$0 \le \Psi \le 1, \qquad (9)$$

in which

$$\Psi \equiv \frac{\epsilon_0 - E_c}{E_o(K_f - K_o)} = \text{normalized input.}$$

In terms of normalized input, equation (5) may be rewritten as:

$$t_1 = \tau_f \ln \frac{K_f - \Psi(K_f - K_o)}{(K_f - K_o)(1 - \Psi)} \quad 0 \le \Psi \le 1 \qquad (10)$$

for the general expression for on-time increment as a function of the normalized input Ψ.

Similar reasoning may be used to derive the expression for the off-time increment as a function of constant values of modulator input error signal ϵ_o. Because only time increments are of interest, the origin of the time axis may be redefined so that $t = 0^-$ at the instant just before contactor cutoff. Equation (1) then may be expressed as:

$$\epsilon_c = \epsilon_o + h - V_1 = E_c \qquad (11)$$

or

$$V_1 = \epsilon_o - E_c + K_o E_o ,$$

in which V_1 is the initial condition of $V(t)$ at this instant of time. Just after cutoff, $t = 0^+$; therefore when equation (11) is used, $V(t)$ may be expressed as:

$$V(t) = V_1 e^{-t/\tau_f} = (\epsilon_o - E_c + K_o E_o) e^{-t/\tau_f} \qquad (12)$$

When $t = t_2$ is considered to be the instant just prior to the time the contactor is again actuated, and when equations (1) and (12) are used, equation (13) is obtained:

$$\epsilon_c(t_2) = \epsilon_o - V(t_2) = E_c$$

$$\epsilon_o - (\epsilon_o - E_c + K_o E_o) e^{-t_2/\tau_f} = E_c . \qquad (13)$$

The off-time increment t_2 in equation (13) is defined as follows:

$$t_2 = \tau_f \ln \left[\frac{\frac{\epsilon_o - E_c}{E_o} + K_o}{\frac{\epsilon_o - E_c}{E_o}} \right] . \qquad (14)$$

When the normalized input as given by expression (9) is used, equation (14) is rewritten as:

$$t_2 = \tau_f \ln \frac{\Psi(K_f - K_o) + K_o}{\Psi(K_f - K_o)} , \quad 0 \le \Psi \le 1 , \qquad (15)$$

which is the general expression for the off-time increment. Observation of equation (15) reveals the following relationship:

$$t_2 \to \infty \text{ as } \Psi \to 0 . \qquad (16)$$

This illustrates the important characteristic of pseudo rate modulation: for minimum-impulse operation, the off-time increment approaches a high value (theoretically infinity) as the minimum on-time Δt is accurately timed to a fixed specified amount. This long off-duration usually gives the control system time to recover from all lags around the various loops.

To graphically portray the on- and off-time increments versus the normalized input Ψ, equation (6) is used to eliminate τ_f from equations (10) and (15), giving the following equations:

$$\frac{t_1}{\Delta_t} = \frac{\ln\left[\dfrac{1-\Psi\left(1-\dfrac{K_o}{K_f}\right)}{\left(1-\dfrac{K_o}{K_f}\right)(1-\Psi)}\right]}{\ln\left[\dfrac{1}{1-\dfrac{K_o}{K_f}}\right]} \quad \text{normalized on-time increment} \qquad (17a)$$

$$\frac{t_2}{\Delta t} = \frac{\ln\left[\dfrac{\Psi\left(1-\dfrac{K_o}{K_f}\right)+\dfrac{K_o}{K_f}}{\Psi\left(1-\dfrac{K_o}{K_f}\right)}\right]}{\ln\left[\dfrac{1}{1-\dfrac{K_o}{K_f}}\right]} \quad \text{normalized off-time increment} \qquad (17b)$$

$$0 \le \left[\Psi = \frac{\epsilon_o - E_c}{K_f E_o - K_o E_o}\right] \le 1 \quad \text{normalized input.} \qquad (17c)$$

Figure 2 graphs expressions (17) which (more fundamentally) normalize the on- and off-time increments against Δt, which is usually specified. The normalized increments $t_1/\Delta t$ and $t_2/\Delta t$ are graphed as a function of Ψ with K_o/K_f as a varied parameter. The value of K_o/K_f must be different from zero but is usually as small as possible (for reasons given later), so that the maximum value for this ratio considered in Figure 2 is 0.2. With reference to Figure 2, as Ψ increases from 0 to 0.5, $t_1/\Delta t$ (on-time) slowly increases while $t_2/\Delta t$ (off-time) rapidly decreases. Just the reverse occurs for Ψ increasing from 0.5 to 1.0, because $t_1/\Delta t$ rapidly increases toward the full-on condition while $t_2/\Delta t$ decreases slowly toward the fixed level of 1.0. This is characteristic of a combination of pulse-width and pulse-rate modulation, and is the means by which desirable characteristics of both modulation schemes are obtained. These are the previously mentioned long off-time intervals (pulse-rate modulation) during minimum-impulse limit-cycle operation and the pulse widening effect (pulse-width modulation) to give maximum restoring torque capability when needed. Figure 2 also shows that, for a given value of K_o/K_f, $\Psi = 0.5$ when $t_1 = t_2$. This is easily verified by solving expressions (17) for Ψ when $t_1 = t_2$.

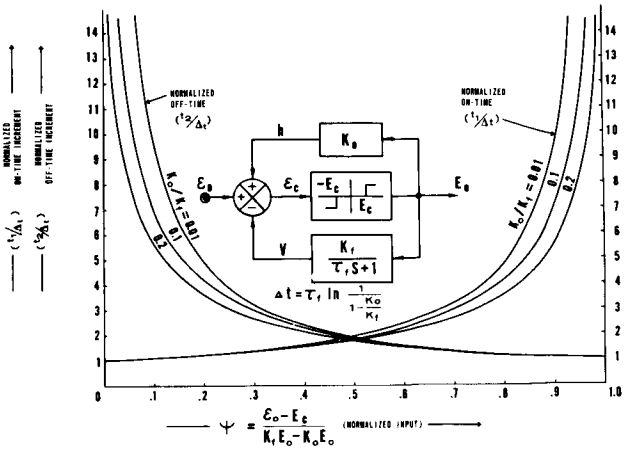

FIGURE 2. NORMALIZED ON-TIME AND OFF-TIME INCREMENTS VERSUS NORMALIZED INPUT

A deeper insight into the nature of pseudo rate modulation may be obtained by using expressions (17) to plot $t_1/\Delta t$ versus $t_2/\Delta t$, holding K_o/K_f constant as the normalized input Ψ is varied. This same graph also provides a convenient comparison of pseudo rate modulation with both pulse-rate and pulse-width modulation techniques. In reference to the insert of Figure 3, pulse-rate modulation is represented as a straight horizontal line passing through $(t_1/\Delta t)_{min}$ as the normalized input Ψ is varied, because the on-time must remain fixed as the off-time is varied [2]. Pulse-width modulation, however, retains a constant period or carrier frequency [2] as both the on- and off-times are varied. The period may be expressed as:

$$\frac{P}{\Delta t} = \frac{t_1}{\Delta t} + \frac{t_2}{\Delta t} \; . \qquad (18)$$

For $P/\Delta t$ equal to a positive constant, equation (18) represents a straight line with negative slope on the graph for $t_1/\Delta t$ versus $t_2/\Delta t$. As Ψ is varied, pulse-width modulation is also easily depicted on this graph (insert, Fig. 3). For pulse-width modulation, the on-time goes to zero as Ψ becomes zero ($\epsilon_o \rightarrow E_c$); also the off-time goes to zero as Ψ increases (ϵ_o increases). In certain instances, especially for very short on-times, this is disadvantageous since control-system power can be consumed with no generation of thrust, i.e., the pulses are too short for the solenoid valves to respond. Pseudo rate modulation may be seen to be a combination of pulse-rate and pulse-width

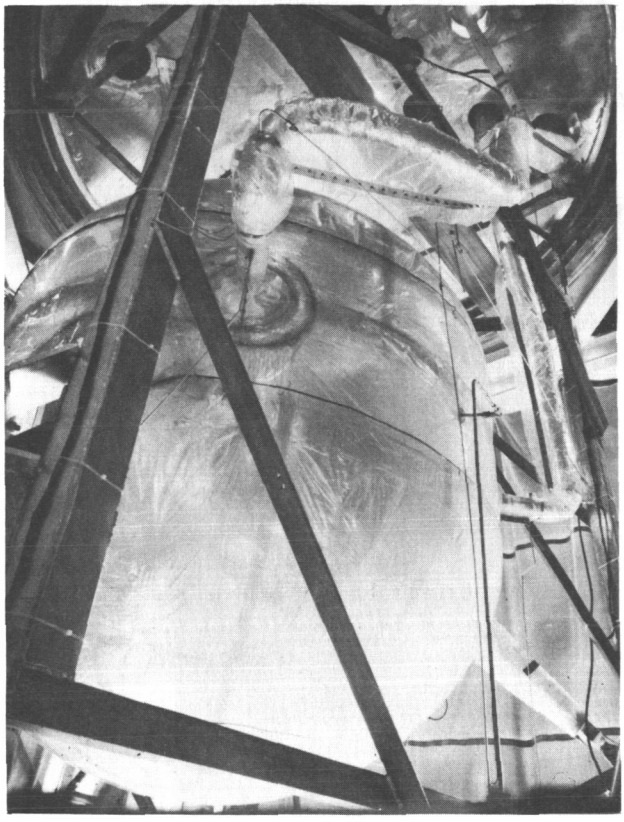

FIGURE 34. INSULATED TANK IN TEST CHAMBER

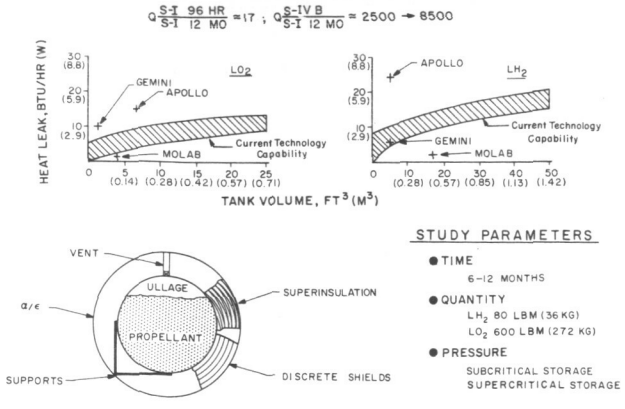

FIGURE 35. CRYOGENIC STORAGE (6-12 MONTHS)

preliminary analyses that consider nonvented liquid-hydrogen storage (Fig. 36) indicate that approximately 600 lbm (272 kg) of system mass is required per 100 lbm (45 kg) of usable liquid hydrogen for

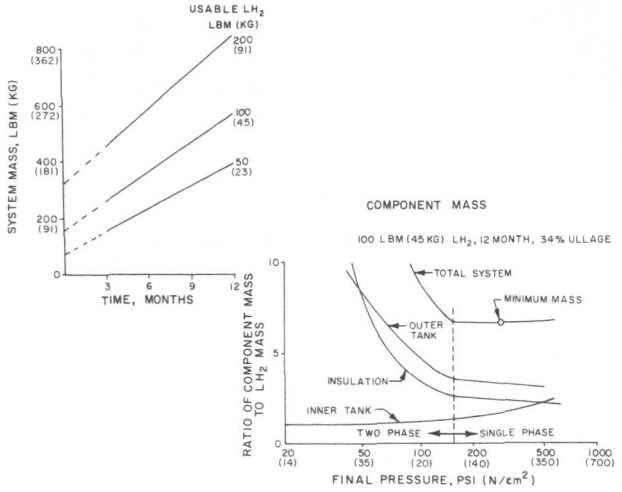

FIGURE 36. LH_2 NONVENTED LUNAR STORAGE SYSTEM

storage durations of 12 months. The required insulation thickness is approximately 12 inches (30 cm), and the primary mass-contributing component is the outer shell. Numerous other analytical studies are in progress, including storage without the nonvent requirement, system optimization, liquid-oxygen storage, and others.

B. SHADOW SHIELDS

Another approach to cryogen storage in space uses shadow shields for reducing the energy incident on the storage vessel. Results of a recently completed feasibility study of an inflatable shadow shield are shown in Figure 37. Inflatable shadow shields were optimized and analyzed for a typical Lunar Orbit Rendezvous (LOR) mission with a cryogenic service module and for a manned Mars landing mission. The shadow shield configurations depend on mission phase; and such factors as basic shape, optical coating, development and storage mechanism were optimized.

Distinct weight advantages are not obvious for the lunar mission; however, shadow shields showed payload savings in excess of 5000 lbm (2268 kg) for the Mars mission. Effective shield design protects against direct solar radiation but does not completely exclude planetary albedo and planetary thermal emission. Therefore, the thermal effectiveness of a shadow shield is reduced during the LOR mission and during the Mars orbit phase of the manned Mars landing mission. However, system mass penalties with and without a shield are comparable during planetary orbit phases, and a detailed design analysis,

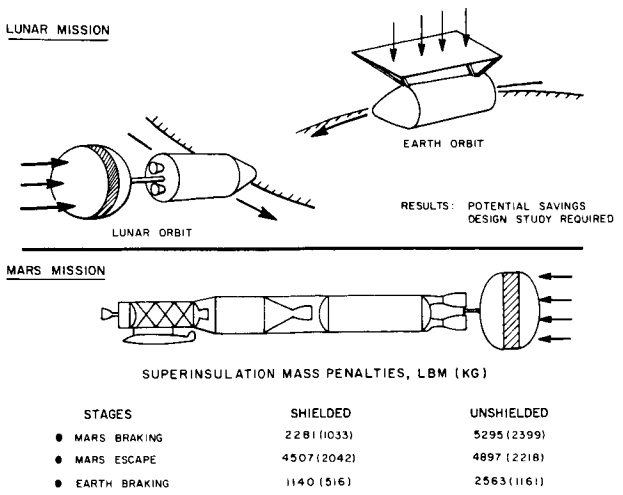

FIGURE 37. SHADOW SHIELDS (INFLATABLE)

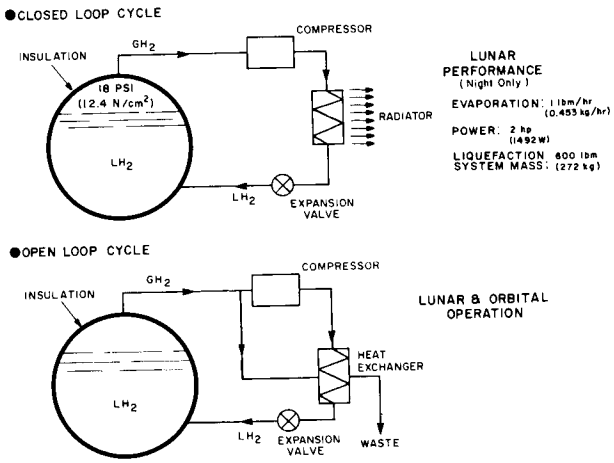

FIGURE 38. H_2 RELIQUEFACTION

including thermal integration of all vehicle systems, is required before final vehicle design.

Conventional and high-performance insulation systems were considered in conjunction with shadow shields. Shield configurations were optimized and preliminary design studies were used to establish system mass comparisons. Structural design criteria and properties of particular thermal coatings were determined in a test program. The importance of inflatable shadow shields was established for future cryogenic vehicles.

C. CRYOGENIC RELIQUEFACTION/REFRIGERATION

Cryogenic refrigeration studies have been in progress for two years. Initial studies were limited to reliquefaction of stored hydrogen boiloff on the lunar surface. Recent studies have considered both hydrogen and oxygen reliquefaction on the lunar surface and in earth orbit. Figure 38 shows, in simplified form, the basic elements of the systems considered. The prime energy source for lunar systems operation is electricity from the nuclear auxiliary power systems (SNAP). Design investigation was based on hydrogen boiloff of 1 lb/hr (0.5 kg/hr) from a 20-foot (6 m) spherical superinsulated storage tank containing 19,600 pounds (8800 kg) of liquid hydrogen. The reliquefier would operate only during the lunar night to take advantage of the lower effective sink temperature (thus, there would be higher cycle efficiency). During the lunar day, the pressure in the storage tank would be allowed to rise approximately 5 psi (34 kN/m^2). Propellant boiloff during 12-month storage without reliquefaction would be approximately 2200 pounds (1000 kg). The estimated mass of the reliquefaction system is 600 pounds (272 kg); thus, the break-even point is approximately 4 months storage time. For smaller tanks, the boiloff rate would be less, although the ratio of boiloff to stored propellant would be more.

Preliminary studies of the closed-loop reliquefaction system for earth orbital operation showed excessive weight penalties due to greater radiator area and power requirements. As a consequence, open-loop systems are currently under investigation for these missions. Studies considering the energy of the stored hydrogen in open-loop systems show that theoretical limits of about 60 percent reliquefaction can be reached. Realistic reliquefaction percentages and systems weights are being determined.

D. THERMAL INTEGRATION

A study to determine vehicle thermal integration criteria for interplanetary travel is under way. This study (Fig. 39) considers effects of surface coatings, shadow shields, insulation, refrigeration, and required acceleration for propellant control. Thermal integration criteria for each of the following flight missions are being established: (1) unmanned Mars orbital reconnaissance, (2) unmanned Venus orbital reconnaissance, (3) manned Mars flyby, and (4) manned Mars landing. The importance of this study cannot be overemphasized, and it should establish a guide for future research efforts and vehicle configurations.

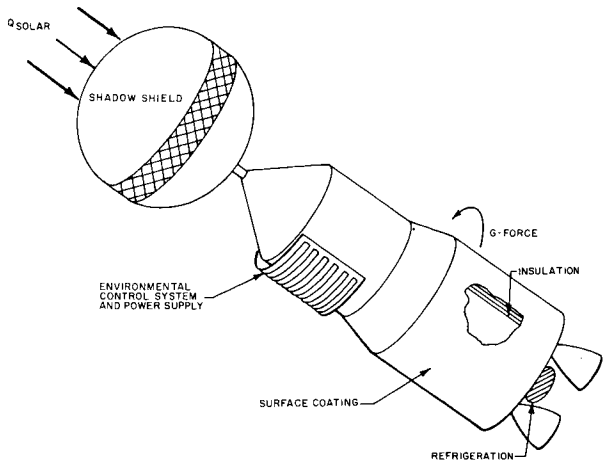

FIGURE 39. VEHICLE THERMAL INTEGRATION CRITERIA

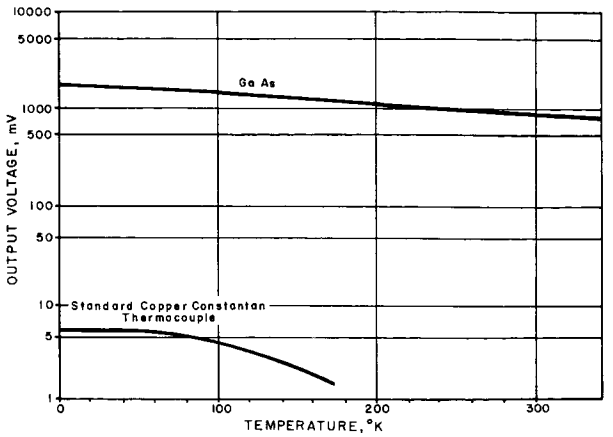

FIGURE 40. GALLIUM ARSENIDE DIODE SENSOR

IV. INSTRUMENTATION

Many commercially available temperature, pressure, and point-density sensors, and liquid-level systems, are being tested at MSFC to obtain background information that will facilitate proper equipment selection for each application. The programs are far too numerous for detailed reporting in this paper. Instrumentation research and development programs to provide improved instrumentation for special requirements are in progress. Some typical programs are discussed in this section.

A. TEMPERATURE SENSOR

The performance of a gallium arsenide diode sensor is compared with that of a standard thermocouple in Figure 40. Response time of the gallium arsenide diode sensor in the liquid hydrogen temperature region, where standard thermocouples have poor response, is 0.5 second to produce 63 percent of the total temperature change when the probe is extracted from the liquid and exposed to circulating gas.

B. FIRE DETECTION AND WARNING

A fire detection and warning system under development is illustrated in Figure 41. The system compares rocket plume radiation, solar radiation, and radiation from within the compartment that contains the system. The detection system discriminates between OH^- radicals, ultraviolet bands, and the flicker frequencies to differentiate a fire, the rocket

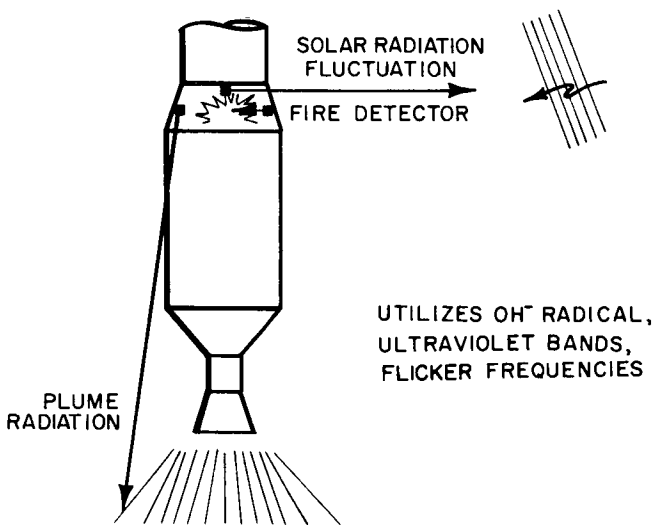

FIGURE 41. FIRE DETECTOR AND WARNING SYSTEM

plume, and solar radiation. The system either warns of a hazard or initiates the operation of protection devices to combat the hazard.

Two other hydrogen detectors under development are shown in Figure 42. The polarographic detector, restricted to the prelaunch pressure environment, is useful for hydrogen concentration ranges of 0.01 to 98 percent and has a response of 60 milliseconds. The ultrasonic detector is applicable for concentrations ranging between 0.01 and 0.1 percent hydrogen for any pressure environment. Preliminary results suggest that this detector may be thermally unstable. The polarographic detector is a disk approximately

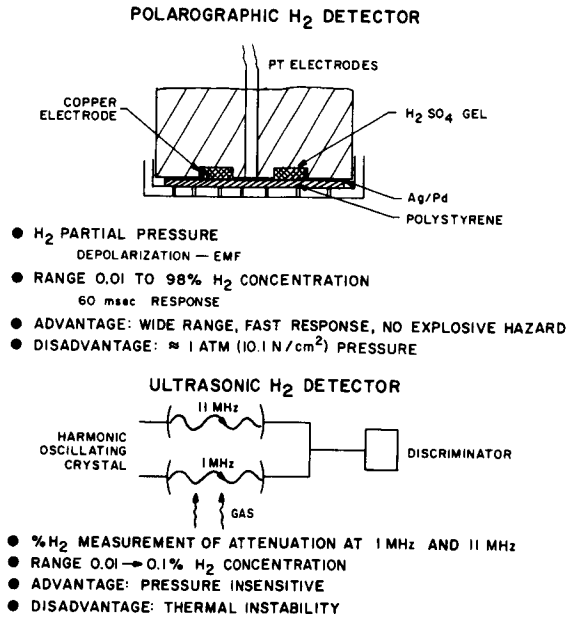

FIGURE 42. POLAROGRAPHIC AND ULTRASONIC H_2 DETECTORS

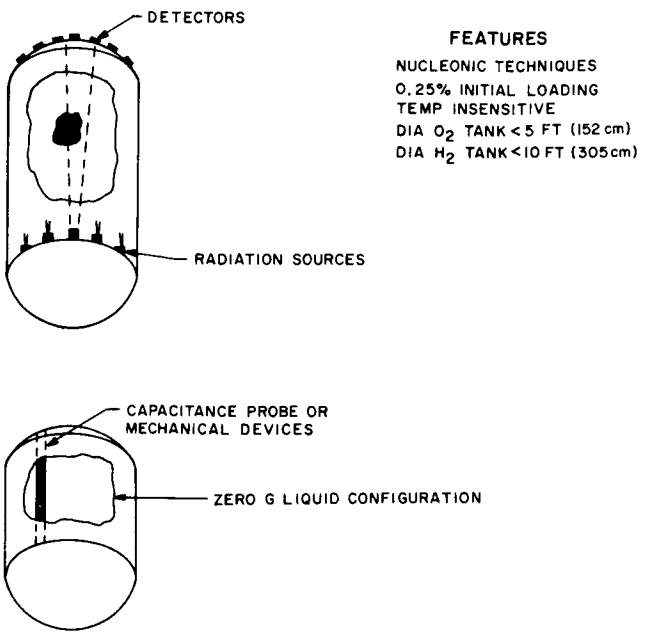

FIGURE 43. PROPELLANT MASS MEASUREMENT

$1\frac{1}{2}$ inches (3.8 cm) in diameter and $\frac{1}{4}$-inch (0.64 cm) thick. In this detector, the hydrogen gas permeates a polystyrene or similar membrane and depolarizes the two electrodes to establish an electric potential. The hydrogen concentration can be established from the measured electromotive force and appropriate device calibrations.

The ultrasonic detector uses two harmonic oscillating crystals and discriminators. The influence of hydrogen on attenuation at 1 MHz and 11 MHz can be used to establish the hydrogen concentration. This principle of operation can also be used for detection of other gases.

C. PROPELLANT MASS DEVICE

Propellant mass determination has always caused problems in launch vehicle design and is expected to cause even more difficulties for vehicles operating in a reduced-gravity environment. The existence of small surface-tension forces of the fluid (in reality large forces relative to gravitational forces) will result in liquid collection in the often-used capacitance probe or similar device. Studies indicate that such difficulties can be overcome through the use of nuclear techniques; therefore, research and development efforts with nuclear systems are in progress. In Figure 43 one or more gamma radiation sources, about one-half curie (1.85×10^{10} disintegrations/sec) each, are on the common bulkhead of the propellant tank, and the detectors are on the opposite tank bulkhead. For defined propellant location, propellant mass is estimated to be predictable within 0.25 percent accuracy. For random propellant orientation, propellant mass determination within 1 percent is considered possible. The nuclear-principle technique appears to offer the additional advantage of reduced weight. An earth orbital experiment is being designed for exploration of the system at near zero gravity. The feasibility for early verification of a complete system on the S-IVB vehicle is also being established.

D. FLUID QUALITY METER

The same nuclear principle (as applied to the propellant mass device) was studied for the quantitative assessment of the proportion of gas within a liquid (Fig. 44). A device for installation within a vent pipe of a liquid-hydrogen container has been designed and tested. The device is accurate to ± 5 percent for vent mixtures of gas-to-liquid ranging between 0 and 100 percent. The device constitutes a vital portion of the instrumentation for a large hydrogen tank to be launched into earth orbit for studying fluid behavior under reduced gravitational forces. Similar devices are currently being calibrated to measure propellant quality in vehicle suction lines.

modulation. For small values of Ψ, all lines of constant K_o/K_f are asymptotic to the straight line passing through $(t_1/\Delta t)_{min}$ which represents pulse-rate modulation; for midrange values of $\Psi(0.4 < \Psi < 0.6)$, the system very nearly displays the characteristics of pulse-width modulation. As Ψ changes over all possible values (considering steady-state operation for each), neither the on-time nor the off-time can become zero (each approaches a fixed specified level) Therefore, during steady-state operation, pseudo rate modulation does not have the disadvantage of the continuously vanishing on-time that is characteristic of pulse-width modulation.

An important characteristic immediately obvious from Figure 3 is that for $\Psi = 0.5$ the period of the modulator-pulse waveform is always minimum for a given ratio of K_o/K_f, thereby giving the maximum steady-state pulse frequency. When expressions (17) are substituted into equation (18) for $\Psi = 0.5$, the following equations are obtained:

$$\left(\frac{P_{min}}{\Delta t}\right)_{\Psi = 0.5} = 2\left[1 - \frac{\ln\left(1 + \frac{K_o}{K_f}\right)}{\ln\left(1 - \frac{K_o}{K_f}\right)}\right] \qquad (19)$$

$$\left(\frac{P_{min}}{\Delta t}\right)_{\Psi = 0.5} \approx 2\left[2 - \frac{K_o}{K_f}\right] \text{for } \frac{K_o}{K_f} << 1.$$

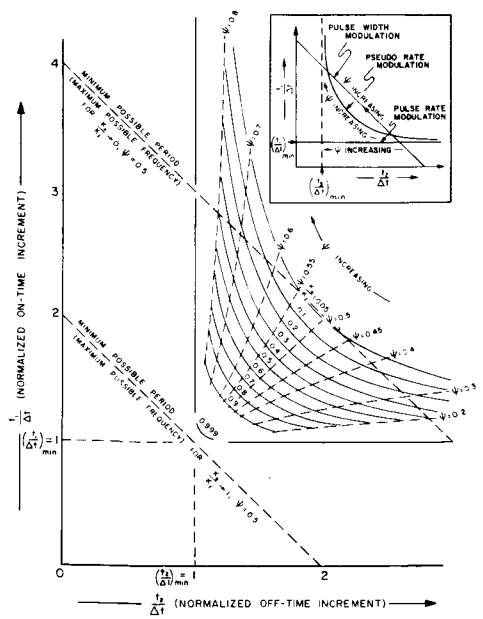

FIGURE 3. NORMALIZED ON-TIME VERSUS NORMALIZED OFF-TIME

This simplified expression for $(P_{min}/\Delta t)_{\psi = 0.5}$, which was obtained using the first two terms of a Maclaurin's series expansion for the natural logarithm with all second order terms neglected, gives less than one-percent error when $K_o/K_f \leq 0.1$.

With reference to equation (6), the range with K_o/K_f varied from 0 to 1 corresponds to variation of $\Delta t/\tau_f$ from 0 to ∞, thereby covering all possible variations of these parameters with respect to the minimum period (maximum frequency) of the pseudo rate modulator output waveform. When K_o/K_f approaches 1 and 0, respectively, in equation (19), the following relations are obtained:

$$\lim_{K_o/K_f \to 1} \left(\frac{P_{min}}{\Delta t}\right)_{\Psi = 0.5} = 2 ,$$

$$\lim_{K_o/K_f \to 0} \left(\frac{P_{min}}{\Delta t}\right)_{\Psi = 0.5} = 4 ;$$

therefore,

$$2 \leq \left(\frac{P_{min}}{\Delta t}\right)_{\Psi = 0.5} \leq 4 \text{ as } 1 \geq \frac{K_o}{K_f} \geq 0 . \qquad (20)$$

This range of $(P_{min}/\Delta t)_{\psi = 0.5}$ applies for all possible values for K_o, K_f, and τ_f. Figure 4 graphs equation (19), and the range of $(P_{min}/\Delta t)_{\psi = 0.5}$ given by relations (20) is clearly shown. To minimize the design value for maximum steady-state frequency of the particular modulator used, Figure 4 and relations

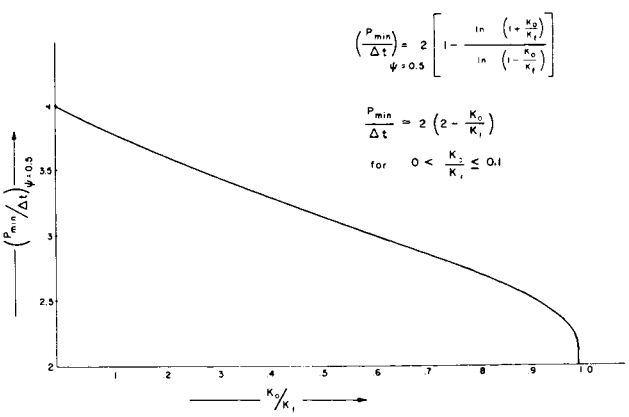

FIGURE 4. GRAPH OF $(P_{min}/\Delta t)_{\psi = 0.5}$ VERSUS K_o/K_f

20 show that K_o/K_f must be small. For example, if $\Delta t = 0.05$ second and K_o/K_f is made as small as possible, then $P_{min} = 4\Delta t = 0.2$ second and the maximum steady-state pulse frequency of the modulator output would be five pulses per second. The pulse frequency would be less than five pulses per second for any other value of Ψ (Fig. 3).

A plot of $t_1/(t_1 + t_2)$ versus Ψ is of interest since this is the variation of average modulator output which is proportional to control torque (control system considered to be open looped). Expressions (17) were used to show this relationship, as given by Figure 5. Even though the curves are nonlinear, as K_o/K_f becomes smaller, the average output waveform becomes more linear as a function of the normalized input Ψ.

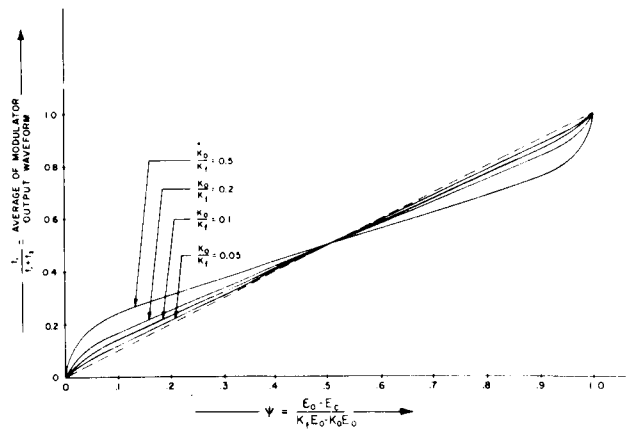

FIGURE 5. AVERAGE OF MODULATOR OUTPUT WAVEFORM VERSUS NORMALIZED INPUT

Up to this point, no restrictions have been placed on the variables defining the modulation range Ψ. However, for $|\epsilon| > |E_c|$, when ϵ is suddenly reduced to zero (because of loss of signal or an intentional command), the contactor may be inadvertently energized if $|V(t)| \geq |E_c|$ at this instant. This condition will be called a "reverse firing" since the polarity of the contactor output will be opposite to that of ϵ prior to loss of signal; the time duration can be considerable if the lag network has charged to its maximum voltage. The maximum value for $|V(t)|$ is $|K_f E_o|$ and the requirement for the contactor to remain off is that $|\epsilon_c| < |E_c|$. When the contactor turns off, h(t) must go to zero; therefore, the following relationship is obtained [1] when $\epsilon(t) = 0$:

$$|K_f E_o| \leq |E_c|$$

or

$$K_f \leq \frac{E_c}{E_o} \quad . \tag{21}$$

If noise is present at the contactor input, even though inequality (21) is satisfied, the contractor can be momentarily triggered into a reverse firing and can then be held on when $h = K_o E_o$ for an interval as long as Δt. Therefore, the absolute requirement for no reverse firings is specified by the expression:

$$|K_f E_o| + |K_o E_o| \leq |E_c|$$

or

$$K_f\left(1 + \frac{K_o}{K_f}\right) \leq \frac{E_c}{E_o} \quad . \tag{22}$$

Thus,

$$(K_f)_{max} = \frac{E_c}{E_o\left(1 + \frac{K_o}{K_f}\right)} \quad .$$

As Ψ varies from 0 to 1, the modulation range that satisfies the requirement of no reverse firings can be obtained by substituting inequality (22) into expression (8), thus:

$$0 \leq \frac{\epsilon_o - E_c}{E_o} \leq \left(\frac{E_c}{E_o} - 2K_o\right) \quad . \tag{23}$$

This latter expression indicates that for values of $|\epsilon| \geq |2E_c| - |2K_o E_o|$ the contactor must be continuously on if reverse firings are to be avoided.

As previously mentioned, it is usually desirable to keep the K_o/K_f ratio small, which requires that K_o should be made small and/or K_f should be made large. Usually, some lower limit for the value of K_o is dictated by the hardware used; however, the bottom equation of expressions (22) specifies an upper limit for the value of $K_f = (K_f)_{max}$. Use of $(K_f)_{max}$ then gives the smallest possible value for K_o/K_f if it is required to avoid reverse firings.

C. DYNAMIC CHARACTERISTICS OF PSEUDO RATE MODULATION (INPUT TIME VARYING)

Even through equation (1) describes the input voltage to the on-off contactor in general, up to this point it has been used with constant values ($\epsilon = \epsilon_o$) for modulator input error voltage to derive the steady-state or static characteristics of pseudo rate modulation. These static characteristics describe closed-loop on and off times over any time interval such that $\epsilon(t)$ can be assumed to be very nearly constant (during Case I minimum-impulse operation, for example).

The dynamic characteristics will now be analyzed by allowing $\epsilon(t)$ to vary as a function of the control-system sensed inputs. When all disturbance torques are neglected and idealized sensor characteristics are assumed, Figure 1 is redrawn as Figure 6. For Cases II and III and in terms of the variables defined in this figure, $\epsilon(t)$ may be expressed as:

$$\epsilon(t) = a_0\phi(t) + a_1\dot{\phi}(t) \tag{24}$$

in which $\phi(t)$ is the vehicle attitude for $\phi_{REF} = 0$, $\dot{\phi}(t)$ is the vehicle angular rate, and a_0 and a_1 are the respective control gain factors. When $a_1 = 0$, equation (24) then applies for Case I. If it is now assumed that the vehicle angular acceleration $\ddot{\phi}$ is constant whenever control torque is generated, the vehicle attitude and rate may be written as:

$$\dot{\phi}(t) = \dot{\phi}_0 + \ddot{\phi}t$$

$$\phi(t) = \phi_o + \dot{\phi}_o t + \frac{1}{2}\ddot{\phi}t^2 \quad , \tag{25}$$

in which ϕ_o and $\dot{\phi}_o$ are any specified set of initial conditions of attitude and rate at $t = 0$. Substitution of equation (25) into equation (24) gives the following equation:

$$\epsilon(t) = \epsilon_o + \dot{\epsilon}_o t + \frac{1}{2}\ddot{\epsilon}_o t^2 \qquad \begin{array}{l}\text{Cases II and III}\\ \ddot{\phi} = \text{constant}\\ \text{(for Case I, } a_1 = 0)\end{array} \tag{26}$$

in which

$$\epsilon_o = a_0\phi_o + a_1\dot{\phi}_o$$

$$\dot{\epsilon}_o = a_0\dot{\phi}_o + a_1\ddot{\phi}$$

$$\ddot{\epsilon}_o = a_0\ddot{\phi}.$$

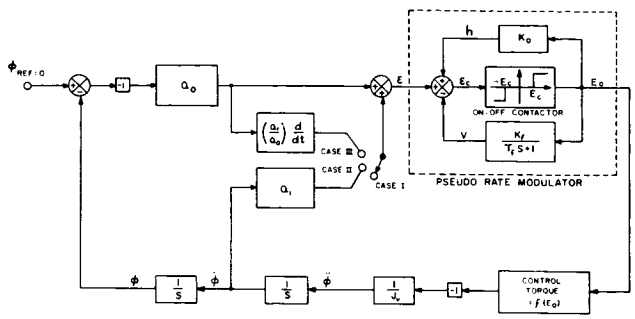

FIGURE 6. CONTROL SYSTEM WITH IDEALIZED SENSOR CHARACTERISTICS

This equation describes the input voltage to the pseudo rate modulator as a function of time and the initial state (ϕ_o and $\dot{\phi}_o$) of the vehicle with time measured from the instant that constant control acceleration is applied. Whenever $\ddot{\phi} = 0$, $\ddot{\epsilon}_o$ is also zero and equation (26) reduces to:

$$\epsilon(t) = \epsilon_o + \dot{\epsilon}_o t \qquad \begin{array}{l}\text{Cases II and III}\\ \ddot{\phi} = 0\\ \text{(for Case I, } a_1 = 0)\end{array} \tag{27}$$

in which

$$\epsilon_o = a_0\phi_o + a_1\dot{\phi}_o$$

$$\dot{\epsilon}_o = a_0\dot{\phi}_o \quad .$$

Equation (27) again describes the input voltage to the pseudo rate modulator with the instant of contactor cutoff now defining both the time reference origin and the initial conditions ϕ_o and $\dot{\phi}_o$.

Several interpretations may be given to equations (26) and (27). For example, the overall control system could be idealized by assuming that whenever the contactor is on, $\ddot{\phi}$ is constant and equation (26) applies, and whenever the contactor is off, $\ddot{\phi}$ is zero and equation (27) applies. Because of the previously mentioned transport time delays through the engine

and solenoid-valve characteristics, it could also be assumed that there are time intervals during which the contactor is on, but during which no control torque is produced. Equation (27) applies during these on-time intervals. Even though other combinations are possible, to show the damping capability of pseudo rate modulation, the idealized control system will be assumed.

Damping of an on-off control system is normally depicted on the system phase plane ($\dot{\phi}$ versus ϕ) by a specified amount of slope of the on-off switching lines. This slope is usually a function of the rate-to-attitude gain ratio a_1/a_0 of the system. As previously mentioned, even though active rate sensing is not used (i.e., $a_1 = 0$), a system using pseudo rate modulation still possesses a certain amount of closed-loop control-system damping. This may be shown by deriving the equation for the cutoff boundary as illustrated by Figure 7, which is a plot of $\dot{\epsilon}$ versus ϵ instead of $\dot{\phi}$ versus ϕ, since equations (26) and (27) show these to be equivalent. Since control-system operation is similar for both polarities of ϵ, the cutoff boundary for positive ϵ only will be considered. The cutoff boundary is defined as the locus of points $(\dot{\epsilon}_o, \epsilon_o)$ within the modulation range $0 \le \Psi \le 1$ such that $\dot{\epsilon}(t) = \dot{V}(t)$ when the contactor switching condition $\epsilon_c(t) = E_c$ is met. On one side of this boundary (shaded portion of Fig. 7), $|\dot{\epsilon}(t)|$ decreases faster than $|\dot{V}(t)|$ after cutoff. Since $V(t)$ always tends to turn the contactor off because it is fed back negatively (with the exception of reverse firings), the contactor will remain off as the control system returns to the specified deadband. On the other side of the boundary, however, $|\dot{V}(t)|$ decreases faster than $|\dot{\epsilon}(t)|$, thereby causing the contactor to be reactivated before the deadband is reached.

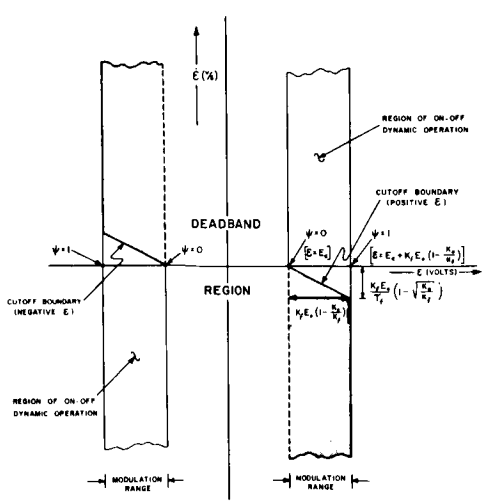

FIGURE 7. PHASE PLANE REPRESENTATION FOR PSEUDO RATE MODULATION CUTOFF BOUNDARIES (CASE I)

If it is assumed that $\ddot{\phi}$ and t are zero at the instant of contactor cutoff, $\epsilon(t)$ and $V(t)$ for any time after cutoff are given by equations (27) and (12), respectively. The voltage rates $\dot{\epsilon}(t)$ and $\dot{V}(t)$ are given by the following equations:

$$\dot{\epsilon}(t) = \dot{\epsilon}_o$$

$$\dot{V}(t) = -\frac{V_1 e^{-t/\tau_f}}{\tau_f} = -\frac{(\epsilon_o - E_c + K_o E_o)}{\tau_f} e^{-t/\tau_f} . \qquad (28)$$

If t_2 is defined as the time just prior to a possible contactor reactivation and $h = 0$, the contactor switching condition $\epsilon_c(t_2) = E_c$ may be expressed as:

$$\epsilon(t_2) - E_c = V(t_2)$$

or

$$(\epsilon_o + \dot{\epsilon}_o t_2) - E_c = (\epsilon_o - E_c + K_o E_o) e^{-t_2/\tau_f} . \qquad (29)$$

When $\dot{\epsilon}(t_2) = \dot{V}(t_2)$ in equation (28) and t_2 is eliminated from equations (28) and (29), the cutoff boundary may be expressed as:

$$\tau_f \dot{\epsilon}_o = -[(\epsilon_o - E_c) + K_o E_o] e^{\left(1 + \frac{\epsilon_o - E_c}{\tau_f \dot{\epsilon}_o}\right)} , \qquad (30)$$

which represents the required $(\dot{\epsilon}_o, \epsilon_o)$ locus as a function of the parameters τ_f, K_o, E_c, and E_o. Whenever the control torque goes to zero for the assumed idealized control system, and if the initial conditions at cutoff are within the modulation range Ψ and are as specified by equation (30), there will be no more contactor actuations as the input error signal $\epsilon(t)$ drifts into the specified deadband. Equation (30) may be normalized by dividing by $K_f E_o$, to give the equation:

$$Y = -\left[X + \frac{K_o}{K_f}\right] e^{\left(1 + \frac{X}{Y}\right)} \qquad (31)$$

in which

$$X = \frac{\epsilon_o - E_c}{K_f E_o} \quad \text{and} \quad Y = \frac{\tau_f \dot{\epsilon}_o}{K_f E_o} .$$

Even though equation (31) cannot be explicitly solved for Y as a function of X, a digital computer solution was obtained, with Figure 8 representing the graph of the resulting data for the normalized cutoff boundary.

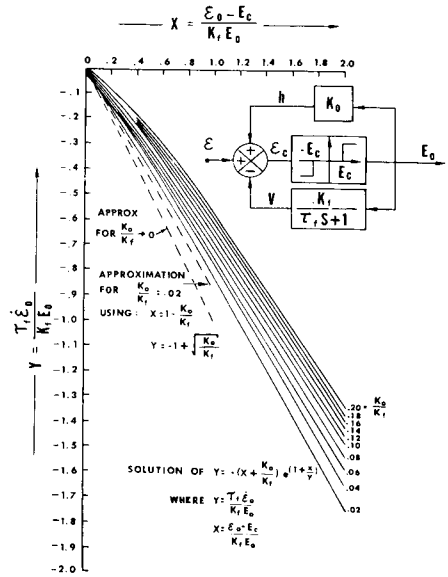

FIGURE 8. NORMALIZED CUTOFF BOUNDARY

If the definition of X in equation (31) is used, equation (9) for $\Psi = 1$ may be expressed as:

$$X = 1 - \frac{K_o}{K_f} \quad . \tag{32}$$

When equation (32) is substituted in equation (31), the following expressions are obtained:

$$Y = -e^{\left(1 + \frac{1 - K_o/K_f}{Y}\right)}$$

$$\lim_{K_o/K_f \to 0} Y = -e^{\left(1 + \frac{1}{Y}\right)} \tag{33}$$

The last of these expressions has the solution $Y = -1$, and from equations (32), $X = -1$ for $(K_o/K_f) \to 0$. It would therefore seem reasonable to approximate the cutoff boundary for $(K_o/K_f) \to 0$ in the X - Y plane by a straight line passing from the origin to the point $X = -1$, $Y = -1$ as indicated by the lower dashed line of Figure 8. When the ratio K_o/K_f is small, the exponent of equation (33) is also small, allowing the exponential to be expanded in a Maclaurin's series to give the following equations:

$$Y = -\left[2 + \frac{1 - \frac{K_o}{K_f}}{Y}\right] \tag{34}$$

or

$$Y^2 + 2Y + 1 - \frac{K_o}{K_f} = 0 \quad .$$

Thus,

$$Y = -1 + \sqrt{\frac{K_o}{K_f}} \quad .$$

When the ratio K_o/K_f is small, the cutoff boundary can then be approximated by a straight line in the X - Y plane passing from the origin to the point

$X = 1 - (K_o/K_f)$ [equation (32)].

$Y = -1 + \sqrt{\frac{K_o}{K_f}}$ [equation (34)].

In Figure 8, the approximation for $K_o/K_f = 0.02$ is shown by the second dashed line, which is reasonably close to the actual curve for this value of K_o/K_f. The estimate is conservative since the approximate cutoff line everywhere falls below the actual curve. When the definitions of X and Y in equations (31) are used, equations (32) and (34) may be written as:

$$\dot{\epsilon}_o = E_c + K_f E_o \left(1 - \frac{K_o}{K_f}\right)$$

$$-\dot{\epsilon}_o = \frac{K_f E_o}{\tau_f} \left(1 - \sqrt{\frac{K_o}{K_f}}\right) ; \tag{35}$$

these are the coordinates that specify the cutoff boundary at $\Psi = 1$ (Fig. 7). From both the approximate and exact expressions for $\dot{\epsilon}_o$ (equations (35) and (30), respectively), maximum damping is obtained for τ_f as high as possible (i.e., minimum slope of the

cutoff boundary). With reference to equation (6) and with the assumption that Δt is a fixed specification, another reason to make the ratio K_0/K_f as small as possible would be to obtain a high value for τ_f, which corresponds to maximum damping. Figure 7 indicates, however, that the damping because of pseudo rate modulation alone (Case I) is only obtainable within the modulation range which is bounded by equation (23) if reverse firings are to be avoided.

Since the damping derived from pseudo rate modulation can be approximated as a straight cutoff line on the phase plane ($\dot{\epsilon}$ versus ϵ), the cutoff slopes will be additive over the modulation range when active rate damping is used (Cases II and III). Figure 9 illustrates this effect.

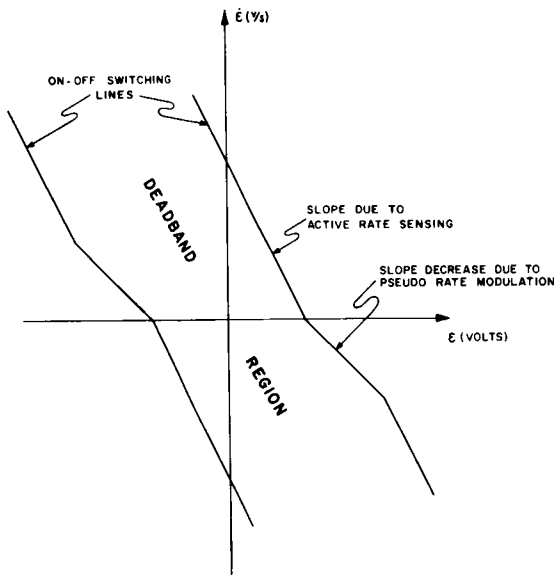

FIGURE 9. PHASE PLANE OF SYSTEM (BOTH ACTIVE RATE SENSING AND PSEUDO RATE MODULATION)

The dynamic on and off times within the modulation ranges illustrated by Figures 7 and 9 could also be derived using equations (26) and (27) along with reasoning similar to that used in the static characteristic analysis. However, since the dynamic on-off time derivations for an idealized control system are adequately covered [4], these derivations are not included.

D. NORMAL ON-OFF DEADBAND OPERATION

When a typical pulse modulator such as pseudo rate is used to enforce minimum-impulse operation of the control engines, the vehicle will drift with constant attitude error rate within the specified attitude deadband for undisturbed steady-state operation. For a stable control system, the phase-plane trajectory will eventually be located somewhere within the limit-cycle boundary as shown by part A of Figure 10,

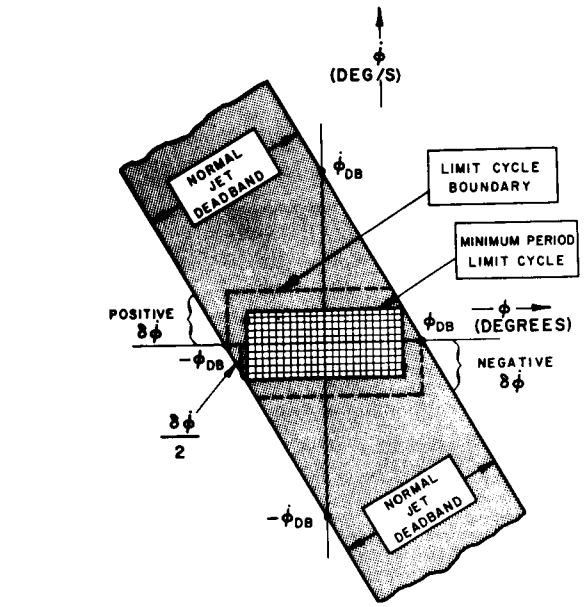

δφ̇ = VELOCITY CHANGE DUE TO MINIMUM RELIABLE JET IMPULSE

A. PHASE PLANE DIAGRAM FOR NORMAL JET DEADBAND OPERATION

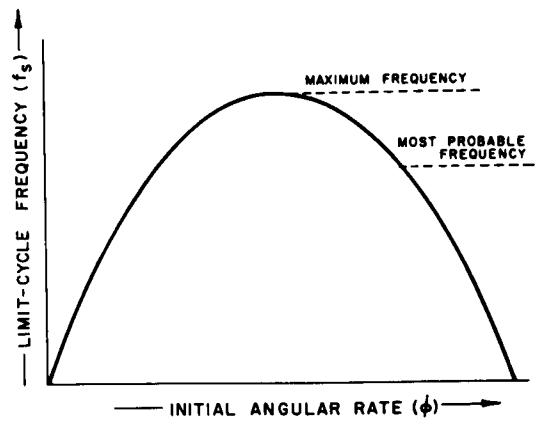

B. VARIATION OF LIMIT-CYCLE FREQUENCY WITH INITIAL ANGULAR RATE

FIGURE 10. NORMAL ON-OFF JET DEADBAND OPERATION

which illustrates normal on-off jet deadband operation. For simplicity, the slope decrease caused by the pseudo rate modulator is neglected. The variation of limit-cycle frequency as a function of initial angular rate within the limit-cycle boundary is shown in part B of Figure 10. The limit-cycle boundary is defined

by the specified jet deadband and both the positive and negative $\delta\dot{\phi}$ (in which $\delta\dot{\phi}$ is the change in attitude error rate caused by the minimum jet-engine impulse). If the jet torques of opposite polarity are not exactly balanced (and this is usually the case), the phase-plane trajectory will drift throughout the entire area enclosed by this limit-cycle boundary.

To minimize the undisturbed steady-state fuel consumption for a control system using this normal jet deadband operation, the conventional approach is to consider the minimum period (maximum frequency) limit cycle as illustrated by part A of Figure 10 with the trajectory enclosing the squared region symmetrically located in the center of the deadband. An attempt is made to make this minimum period as large as possible (maximum frequency as small as possible), therefore requiring $\delta\dot{\phi}$ to be minimized if the attitude deadband is fixed. Usually, however, the thrust of the attitude-control engines is sized to compensate the large disturbance torques acting upon the vehicle. Thus, optimum propellant consumption during undisturbed steady-state operation is obtained by reducing the engine minimum on-time (and therefore the minimum impulse) to the smallest possible value.

III. ADVANCED LIMIT-CYCLE CONTROL TECHNIQUE (SINGLE AXIS)

A. GENERAL DESCRIPTION

A new concept called the "advanced limit-cycle control" has been developed to minimize the fuel consumption of an on-off jet system used for space-vehicle attitude control. For a wide variety of attitude-control requirements, emphasis has also been placed on hardware simplicity of the system. It is therefore assumed that a system of jet engines rigidly attached to the vehicle is available to provide on-off thrust of fixed magnitude for vehicle-restoring-torque control.

As previously described, in the usual approach to minimize the fuel consumed by an on-off attitude-control system, an attempt is made to reduce the minimum impulse of the jet engines to the smallest possible value during undisturbed steady-state limit-cycle operation. The system developed by this study [5], however, differs from that of the usual approach. Instead, a control logic (as a function of certain sensed inputs) causes the vehicle to be placed close to the desired reference attitude with the attitude error rate for each axis as small as possible. The control logic always forces the system to have a special type of limit-cycle operation. At zero attitude error, the attitude error rate is reduced to a very small value. After this, the vehicle will slowly drift with respect to the attitude reference frame for a considerable time (for undisturbed steady-state operation). After the deadband is exceeded, the remaining portion of the limit cycle must have a finite value of attitude error rate which brings the vehicle back to reference attitude relatively fast and also allows the use of large-thrust jet engines with correspondingly large minimum impulse. For a given axis, the attitude-control system, therefore, can utilize the same engines for both optimum limit-cycle operation and compensation of large disturbance torques (which are normally used to size the thrust of the control engines). The extent to which the attitude error drift rate can be nulled at vehicle reference position depends upon the accuracy of the sensed inputs and the performance repeatability of the jet engine system. For undisturbed steady-state limit-cycle operation, however, optimum performance with respect to jet fuel consumption is obtained when the attitude error drift rate is reduced to its theoretical value of zero, because a limit cycle of infinite period will result.

During a previous study [5] the required inputs for the control logic were attitude error, attitude error rate, and a combined error signal defined as the sum of these first two quantities multiplied by their respective gain factors. Usually, these signals are available in any space-vehicle attitude-control system, or they can be generated easily.

B. DISTURBANCE TORQUES

Any attitude-control system must be able to cope with various types of disturbance torque. This was an important factor considered for the control logic developed by this study. Three basic types of vehicle disturbance torque that usually must be considered are: (1) impulse disturbance, (2) disturbance as a function of vehicle attitude, and (3) constant disturbance.

An impulse disturbance torque is characterized by a rapid change in vehicle attitude rate with very little change in attitude. This can result from main or vernier engine cutoff and ignition disturbance (during initial injection or rendezvous operation), from rendezvous-docking maneuvers, and possibly from meteorite impacts or internal moving parts. If on-off deadband operation (with or without the jet control logic) is used, the vehicle control system would recover from this transitory disturbance to reestablish limit-cycle operation. An important characteristic for minimum fuel consumption is that, starting from the initial condition of attitude error

rate, the system phase-plane trajectory should converge to steady-state limit-cycle operation with as few attitude error overshoots beyond the specified deadband as possible. The jet control logic developed by this study can greatly improve the system's ability to meet this requirement.

Disturbances as a function of vehicle attitude can result from gravity gradient torques, aerodynamic torques (for sufficiently low orbits), and, to a lesser extent, from the earth's magnetic field or solar pressure. It can often be shown that the dominant steady-state disturbance torque during vehicle orbital coasting phases is caused by gravity gradient effects. This is especially true for a vehicle with a moment-of-inertia ellipsoid of high eccentricity.

To keep attitude orientation when the vehicle is disturbed by a constant torque, the jet-control system must generate enough average restoring torque to compensate for the disturbance. Constant disturbance torques can occur during periods of main engine burning, for example, because of thrust misalignments and exhaust swirl. In some cases, when the local vertical is part of the attitude reference frame, gravity gradient torque can be approximated as constant if, over a given time interval, the vehicle axis of minimum moment of inertia maintains a relatively large angle with respect to the local vertical (maximum disturbing torque at 45 degrees). For a sufficiently high constant disturbance torque, the phase-plane trajectory will be symmetrical about the attitude error axis at one side of the deadband. The trajectory within the deadband will be parabolic because of the constant disturbance. Outside the deadband, the available restoring torque will be reduced because the disturbance subtracts from the control torque of the jets. The vehicle-restoring torque will still be constant, however, so that the trajectory outside the deadband will also be parabolic. Periods of constant disturbance, with the exception of that approximated by gravity gradient, usually will be relatively short.

If the attitude reference frame for the vehicle is inertially fixed, gravity gradient torque will, in general, vary as a function of orbital position. However, when the local vertical is part of the attitude reference frame, there are two optimum reference positions for the vehicle. The first is a stable position for which vehicle reference would be defined so that the vehicle axis of minimum moment of inertia is aligned along the local vertical. If the attitude error rate is reduced to a very small value when the vehicle is aligned close to this reference (nose or tail down), gravity gradient torque will tend to keep the vehicle near reference position. The second is an unstable position for which vehicle reference would be the position at which the axis of minimum moment of inertia would be aligned perpendicular to the local vertical. Both of these optimum reference positions show that the attitude error rate should be nulled when the attitude error is near zero, as is done by the advanced limit-cycle control logic, so that the disturbance torque effectively will be removed while the vehicle has a low drift rate. If only gravity gradient disturbance is considered, the phase-plane trajectories within the deadband will be elliptical for the vehicle using the stable reference, and hyperbolic when the unstable reference is used.

C. CONTROL LOGIC

Even though the benefit of reducing $\delta\dot{\phi}$ for a normal jet deadband control system is clearly demonstrated by Figure 10, an analysis has shown that this is sometimes difficult to do because, as previously mentioned, the jet-control thrust usually must be sized to compensate for the large disturbance torques acting upon the vehicle. This often leads to the requirement of having large "back-up" jets for the disturbances, as well as small jets, for optimum limit-cycle operation. The deadband for the small jets will usually lie within the deadband for the larger "back-up" jets. However, the thrust ratio of the large to the small jets is limited, if it is assumed that the thrust of each is fixed (no throttling). This limitation is based on the fact that after cutoff of the large jets the vehicle attitude error rate conceivable can be high enough to prevent the phase-plane trajectory from getting captured within the deadband of the small jets.

The approach taken for the advanced limit-cycle control technique, therefore, is to ensure that a limit-cycle period of very long duration is obtained without the restriction of an extremely small $\delta\dot{\phi}$. This is done by always forcing the limit-cycle operation away from the condition of symmetry as illustrated by the minimum-period limit cycle of Figure 10. In reference to Figure 10, and for fixed values of ϕ_{DB}, $\dot{\phi}_{DB}$, and $\delta\dot{\phi}$, the limit-cycle period can be made to approach infinity when the phase-plane trajectory for the limit cycle approaches either one of two locations on the graph. Both lie at the limit-cycle boundary, one along the upper edge of and the other along the lower edge of the boundary. A control logic to force the limit-cycle trajectories for undisturbed steady-state operation to either of these positions would lengthen the limit-cycle period appreciably while basically placing no restrictions on

$\delta\dot{\phi}$. Thus, regions of very long drift time between jet firings are obtained, thereby reducing the jet fuel consumed per limit-cycle period to a very small value for undisturbed steady-state operation.

Using the available signals, $a_o\phi$, $a_1\dot{\phi}$, and ϵ, a single-axis block diagram with control logic that was used in a previous study [5] is illustrated by Figure 11. The phase-plane diagrams explaining the concept for the control logic are illustrated by Figures 12 and 13.

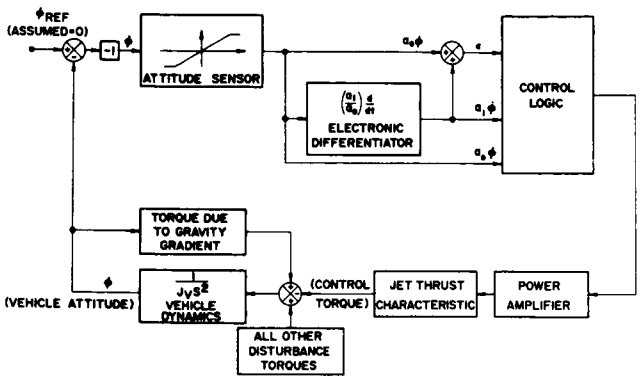

FIGURE 11. SINGLE-AXIS BLOCK DIAGRAM WITH CONTROL LOGIC

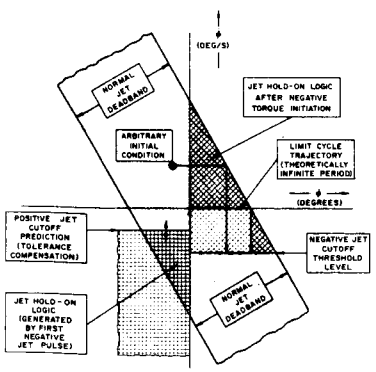

FIGURE 12. ADVANCED LIMIT-CYCLE CONTROL LOGIC CONCEPT (POSITIVE SEQUENCE)

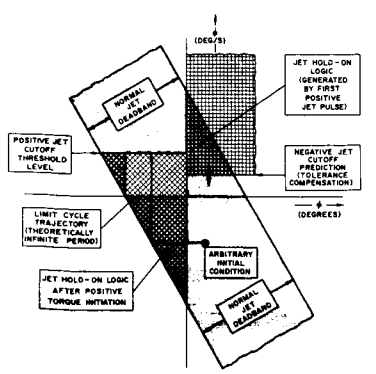

FIGURE 13. ADVANCED LIMIT-CYCLE CONTROL LOGIC CONCEPT (NEGATIVE SEQUENCE)

These figures indicate that the vehicle, starting from an arbitrary initial condition, will drift as in a normal deadband until the threshold to fire the jets is reached. Here, a sequence of events is initiated, the polarity of which depends upon the polarity of the threshold exceeded. As shown by Figure 12, after initiation of negative torque (giving negative change of attitude error rate), a jet hold-on logic is enforced until the negative jet-cutoff threshold is reached. If there are no disturbances, the vehicle then drifts with decreasing attitude error. When the polarity of the attitude error changes sign, positive jet torque (giving positive change of attitude error rate) is applied to the vehicle until the positive jet-cutoff prediction level is reached. The region for this last jet hold-on logic (shown by a squared area in Figure 12) was generated by the first negative jet pulse at the deadband boundary. Even though the jet-restoring torque is commanded off by the control system, the attitude error rate continues to change because of the inherent time lags and engine shut-down transients associated with on-off operation of any jet-control system. For this reason, the jet-engine control signal is shown by Figure 12 to be deactivated at a cutoff prediction level before zero-attitude error rate is sensed. After this sequence is completed, the control logic is automatically reset and the system is left with a low value of attitude error rate within the deadband, causing the vehicle to drift for a very long time, until the jet threshold is again reached. Figure 13 shows the control-logic concept for the opposite polarity. The logic is symmetrically designed so that the sequence of events for only one polarity can occur at any one time.

If the factors causing the continuous change in attitude error rate (after jet-engine cutoff command) can be predicted within reasonable limits, the jet-cutoff prediction can be adjusted to a fixed-bias setting before vehicle launch. Automatic adjustment of the bias during flight is also possible. If undisturbed steady-state operation and repeatability of the jet-control system are assumed, the vehicle will always return to near zero reference attitude with practically zero-attitude-error drift rate at the completion of the logic maneuver.

It should be noted that the limit-cycle trajectories marked by the X's in Figures 12 and 13 differ from the infinite period limit-cycle (zero frequency) positions of Figure 10. This difference stems from consideration of disturbance torques caused by gravity gradient. The control logic was primarily developed for use with either of the optimum vehicle-reference positions as previously described for orbital missions. This was the basic reason for nulling the attitude error rate when zero attitude error was sensed.

Another reason, however, would be the use of this type of control logic during interplanetary missions. For these missions, the nulling of attitude error rate near some commanded attitude reference position could be very useful when star or planet sightings are made for vehicle-alignment maneuvers or when accurate antenna-pointing periods are required for long-distance communication.

When this type of control logic is used for an orbital mission with the reference attitude for which the gravity gradient torque is stabilizing, the phase-plane trajectory for one vehicle axis will oscillate about the reference position over a closed elliptical path with very small attitude and attitude-rate amplitudes. If no other disturbances are present, it is entirely conceivable that the vehicle would coast within the jet deadband without any jet firings for extended periods of time. In this respect it may be observed that a normal on-off jet-control system does not have this capability and therefore basically differs from the system using the control logic. Even if the jet minimum impulse is made infinitesimally small, the normal on-off jet-control system will always null the attitude error at the edge of the attitude deadband where, for limit-cycle operation, the gravity gradient disturbance is maximum rather than minimum. If the vehicle is assumed to be torqued by gravity gradient only, the phase-plane trajectory will extend across the specified attitude deadband to cause jets of opposite polarity to fire alternately as time progresses. Between jet firings, the trajectory will be elliptical with the maximum attitude rate depending upon the magnitude of the gravity gradient disturbance.

IV. OPTIMIZATION STUDY

A. PURPOSE AND SCOPE

The purpose of this optimization study was to evaluate a three-axis space-vehicle attitude-control system utilizing advanced limit-cycle control techniques when thrust-vector errors which are cross-coupled from one axis to another must be considered. The method of evaluating the advanced limit-cycle control techniques is based on a three-axis digital computer program.

The vehicle and control systems were assumed to have the following characteristics:

1. The configurations of interest are as given in Figure 14.
2. All engines of a given configuration are of the same thrust level. The mass expulsion system that was investigated utilized fixed-thrust engines with provision for engine on-time control.
3. The vehicle polar moments of inertia of the pitch and yaw axes are equal.
4. The vehicle polar moments of inertia are constant.
5. Angular accelerations about the pitch and yaw axes that are caused by the nominal thrust level are defined as unity in any convenient dimension. Angular acceleration about the roll axis due to the same nominal thrust level is greater than unity by a factor between one and one hundred.
6. The vehicle angular velocity is sufficiently small that Eulerian rigid-body mechanics can be neglected.
7. External disturbance torques are neglected.
8. For the parametric study, angular errors are taken to be no greater than 2 degrees, thrust variations no greater than 5 percent of nominal, and a steady-state impulse error of not more than 10 percent of the command impulse.

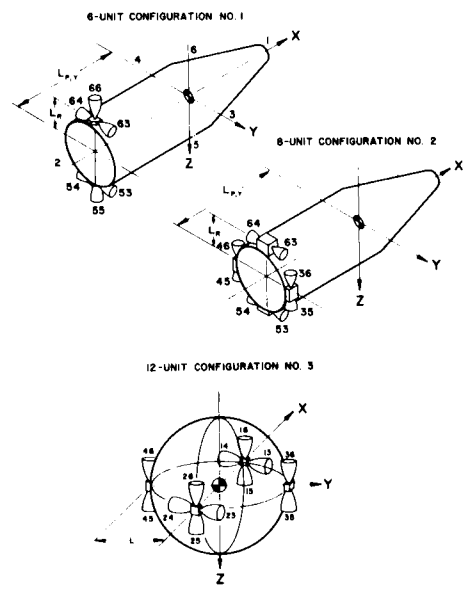

FIGURE 14. VEHICLE AND ENGINE CONFIGURATIONS

A program was evolved that encompassed the following control techniques:

1. Simple box limit cycle (fixed impulse delivered when position attitude deadband for each axis is exceeded).

2. Advanced limit cycle with velocity information (accurate attitude sensing).

3. Advanced limit cycle with velocity calculations (moderate attitude sensing).

4. Advanced limit cycle with rate cutoff (extremely accurate rate sensing).

5. Simple diamond-error limit cycle with rate-switching option (fixed impulse delivered when dictated by coupled-axis error signal).

For comparison of the control techniques, a selected engine and vehicle configuration was used. This configuration and the selected control technique are examined in terms of propellant expended and number of engine firings over an extended period of simulated space operation neglecting external-disturbance torques. A second control technique with either the same or another vehicle configuration was then substituted and the procedure was repeated. To analyze effectively the control philosophies, the same initial conditions, vehicle-design parameters, design thrust levels, attitude deadband, etc., were used in each corresponding control technical comparison.

A detailed discussion of the results of this study was given by The Marquardt Company [6]. The discussion is summarized here.

B. DESCRIPTIONS OF CONTROL TECHNIQUES

1. Simple Box Limit Cycle. The most straightforward attitude-control technique for space-vehicle stabilization is to apply full control torque once the desired attitude deadband has been reached. This is the conventional control-system design approach as previously described. Figure 10 illustrates the control-system operation that, for this optimization study, has been called the simple box limit cycle.

2. Advanced Limit Cycle with Velocity Information. The approach employed in this technique involves the application of a sequence of two jet-engine pulses when the specified vehicle attitude deadband is exceeded as previously described. However, it is assumed that the last pulse of the sequence can be activated only by a predetermined on-time command that has been sized to generate a minimum impulse bit that the engines can accurately and repeatedly produce. Information to size this predetermined on-time command is based on prior engine-test data. Angular-velocity information is assumed to be available to enforce jet-engine cutoff for the first pulse of the sequence. The cutoff vehicle rate of this first pulse is made equal to the angular-velocity change of the vehicle resulting from the predetermined impulse bit.

3. Advanced Limit Cycle with Velocity Calculations. This method presents an alternate technique that assumes velocity information as obtained from active rate sensors is not available during limit-cycle operation. A vehicle angular-position sensing device with appropriate circuitry is combined into a system which produces a cycle of three pulses firing in alternating directions, the last of which is intended to reduce the angular velocity to zero at vehicle reference position without the use of angular rate sensors. The average drift velocity during the time between the first and second pulses of the series is obtained by a measure of the elapsed time between these pulses and from a knowledge of the magnitude of the nominal attitude deadband. This information is processed by the system intelligence to establish the magnitude of the second pulse. The difference between the magnitude of the second pulse and the third pulse corresponds to an angular-velocity increment equal to the average vehicle drift velocity mentioned above. The effect of the second and third pulses combined is to cancel the vehicle angular velocity that exists prior to the second pulse. The third pulse is timed to arrest the vehicle angular velocity at vehicle attitude reference position.

4. Advanced Limit Cycle with Rate Cutoff. This technique is similar to the advanced limit cycle with velocity information technique and differs only in the assumption of an accurate continuous rate sensor. This sensor is used to provide rate information near zero rate to cut off the final pulse of the sequence. The impulse delivered after the electrical signal-off will drive the vehicle to near zero rate. This method fires the last pulse not as a function of time but when the attitude sensor switches sign (vehicle attitude reference position). Since active rate sensing provides the engine cutoff command, this system is free from the integrated effects of system errors that plague the other methods if accurate sensed rate information for extremely small vehicle drift rates can be obtained. The only gross errors with this method are those associated with the impulse bit after electrical-off signal and the angular rate sensor.

5. Simple Diamond Error Limit Cycle (Rate Switching Option). Depending upon the engine configuration used, the commanded control torques in addition to the thrust-vector error effects can be cross-coupled between axes for a three-axis control system. For example, when using configuration no. 1 of Figure 14, four of the six engines (if operated singly rather then in pairs) can be commanded to simultaneously control about the X and Z vehicle axes (roll and yaw). All four approaches described above avoid this cross-coupling of commanded control torques by requiring that the proper engines be operated in pairs rather than singly. Sufficient logic is incorporated into the control system to ensure that opposing engines at the same vehicle location can never be actuated at the same time.

The diamond error limit-cycle technique utilizes control-signal mixing of the axes that are cross-coupled not only to ensure that an engine pair at the same vehicle location can never be actuated in opposition but also to allow only one engine at a time to be operated (although two can be energized if so commanded). In all other respects, this technique is similar to the simple box limit-cycle technique.

C. THRUST VECTOR AND IMPULSE ERRORS

In the absence of outside torques, the vehicle angular velocity for each axis will be reduced to zero after the first cycling of an ideal advanced limit-cycle system. However, in the case of real systems that inherently contain errors, the mean time between cycling is finite. In the discussion which follows, the errors are determined that were used in a computer program [6] to establish quantitative relationships between the system errors and the pulsing frequency or mean propellant consumption.

Errors are known to exist in thrust magnitude, pointing direction, and pulse widths. Some of these errors can be associated with a particular system or unit, such as mounting or installation errors. These errors are fixed throughout the history of the unit in question, but can vary from one system to another. Other system errors are assumed to be time dependent. In the general case, the total error is due to errors of both kinds. Since the important factor to be considered in thrusting errors of a space-vehicle attitude-control system is the error of total impulse delivered about the control axis, the pulse-width errors are included at the same time as the thrust-magnitude and orientation errors. The errors are a function of thrust level and pulse width. The parameters of interest include:

1. Total-impulse-per-pulse errors
2. Steady-state thrust-level variations
3. Time from electrical signal on to:
   a. Start of valve travel
   b. 90-percent full thrust
   c. Centroid of pulse
   d. Electrical signal off
   e. 90-percent full thrust on tail off
   f. End of pulse
4. Total impulse contributions due to:
   a. Rise transient
   b. Steady state
   c. Decay transient
   d. Shutdown transient (after electrical signal off)
5. Specific-impulse variations with pulse width.

Recorded pulse errors include instrumentation errors that are difficult to compensate. Instrumentation errors could be a major constituent of the recorded error, especially for small pulse widths. For this reason any rigorous treatment of pulse errors should consider the instrumentation errors. Thus, one of the tasks of the optimization study described previously [6] was to provide data which would allow more valid assumptions concerning the associated pulse errors. A more refined treatment of the pulse errors was not necessary because state of the art errors continue to change as technology is advanced, and a generalized treatment of the control techniques and errors was desired so that any range of errors and error distribution could be used.

The pulse characteristics of prime importance used in the optimization study were:

1. Total impulse-per-pulse errors
2. Impulse error associated with shutdown transient (after electrical signal off)
3. Specific-impulse variations.

A survey of existing data was made as part of this optimization study. Pulse errors arising from typical hypergolic bipropellant pulse rocket engines

were investigated to establish better the statistical range and distribution of pulse errors. In this investigation, the mean value of an individual parameter was not of particular concern, but the associated error and the nature of the error distribution were, because these items have a great influence on the performance of the more sophisticated attitude-control systems.

Only a limited amount of data was examined because there were few data available in a form applicable to this optimization study. Figure 15 is a typical distribution curve of data from a series of tests of 67 N (15 lbf) bipropellant thruster. Superimposed on the distribution bar chart is a Gaussian distribution curve having the same variance as the data population. From this curve the normality of the distribution can be clearly seen.

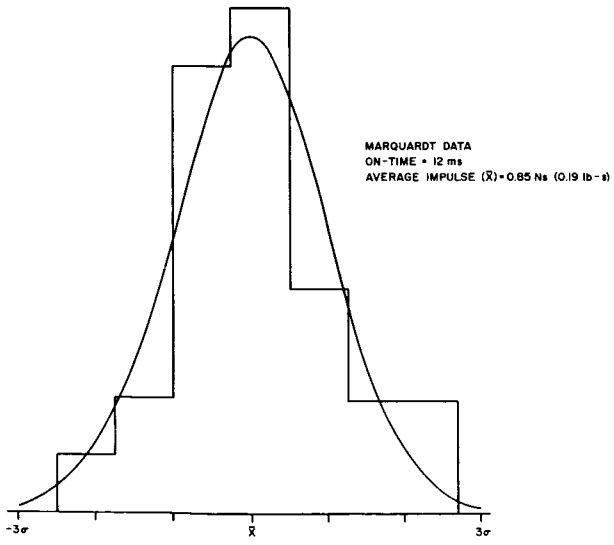

FIGURE 15. IMPULSE DISTRIBUTION FOR A 67 N (15 lbf) BIPROPELLANT THRUSTER

Immediately available rocket-impulse data were also surveyed to determine a mean value of specific impulse as a function of pulse width. Figure 16 is based on approximately 1000 pulses of various thrust levels. This characteristic (specific impulse versus pulse width) was used in the digital computer program and it is accurate within eight percent of the data used.

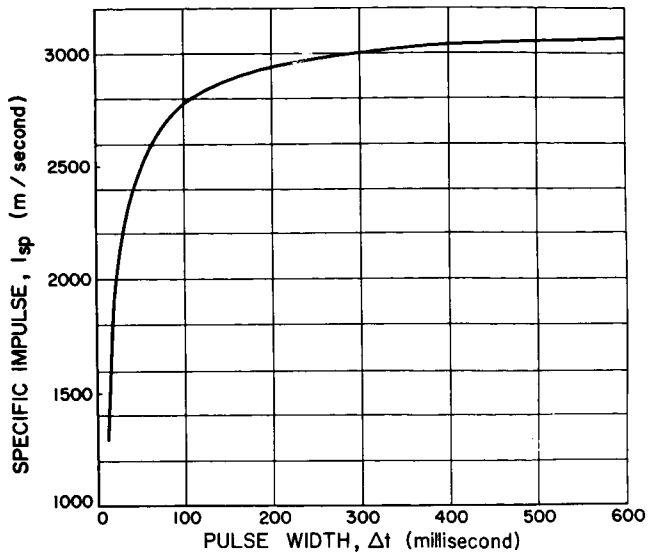

FIGURE 16. MEAN VALUE OF SPECIFIC IMPULSE AS A FUNCTION OF PULSE WIDTH

D. COMPUTER RESULTS

A series of 18 computer runs was made with 100 pulses to check out the computer logic. To determine whether these runs would produce a mean propellant consumption rate, propellant consumption rate was compared with pulse time. Although some mission times were not long enough to produce a mean propellant consumption rate, the values of propellant consumption rate after 100 pulses were used to obtain preliminary system comparative trends. Typical normalized results are shown by Figure 17.

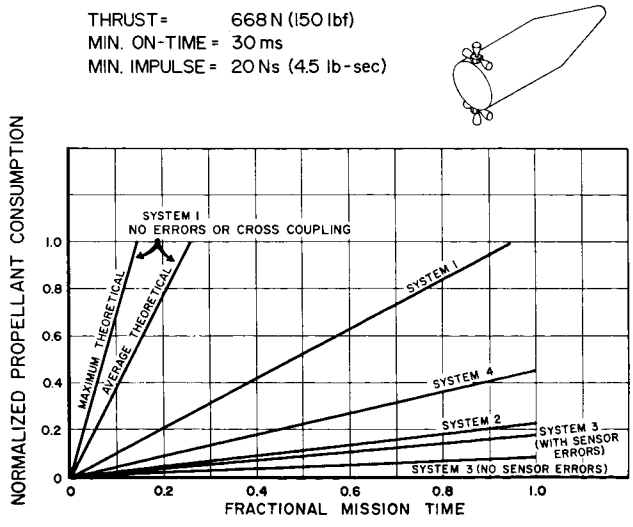

FIGURE 17. CONTROL SYSTEM COMPARATIVE TREND

The three system 1 plots present the propellant consumption for the maximum theoretical, average theoretical, and computer calculations. Systems 2, 3, and 4 utilize advanced limit-cycle control techniques with different implementations for the control logic. System 3 was run both with and without rate sensor errors. Systems 2 and 3 are two-pulse systems; system 2 fires the last pulse as a predicted function of time whereas system 3 uses active rate sensing to cut off the final pulse of the sequence. System 4 is a three-pulse implementation of the advanced limit-cycle control technique. This assumes no active rate sensing because the extra pulse allows velocity calculations to be made using elapsed time and the knowledge of the magnitude of the nominal attitude deadband.

To determine the mission time required before a mean propellant consumption value becomes valid, a system was run for the equivalent of 82.5 days. Random points in time were used. The total propellant consumed at given times was used to compute the mean propellant consumption rate. For the system considered, the propellant consumption rate was valid after approximately 3×10^6 seconds. The results of this test of mission time for the system considered showed that the random values deviated no more than ± 1.2 percent after 3×10^6 seconds.

V. ATTITUDE-MOTION SIMULATOR FACILITY

An attitude-motion simulator (AMS) facility has been fabricated at MSFC. This facility is a research and development tool that permits dynamic testing of attitude-control systems connected with space-flight investigations under a variety of realistic conditions. In the facility, actual torques are exerted on the inertia of a real body with three degrees of angular freedom. Thus the level of confidence in study results obtained from the simulator is considerably greater than that obtained from a pure computer study.

The facility consists primarily of three parts: a gas-bearing platform or vehicle AMS, a pair of movable arm trusses and carts, and a control console.

The AMS shown in the concept drawing of Figure 18 consists primarily of a platform that can rotate freely because it is supported on a virtually friction-free spherical gas bearing. The angular freedom of the platform is ± 95 degrees about two horizontal axes (pitch and yaw) and is unlimited about the vertical axis (roll). Because of extremely accurate balancing of the platform so that it will remain at any fixed attitude when positioned (or will retain any initial angular velocity given it), the platform behaves dynamically as if it were in a gravity-free state. The physical geometry of the platform is that of a disk approximately 1.5 m (5 ft) in diameter and 20 cm (8 in.) thick with a weight of approximately 5300 N (1200 lbf). This allows an adequate mounting area for the various attitude control systems to be studied, developed, or checked out.

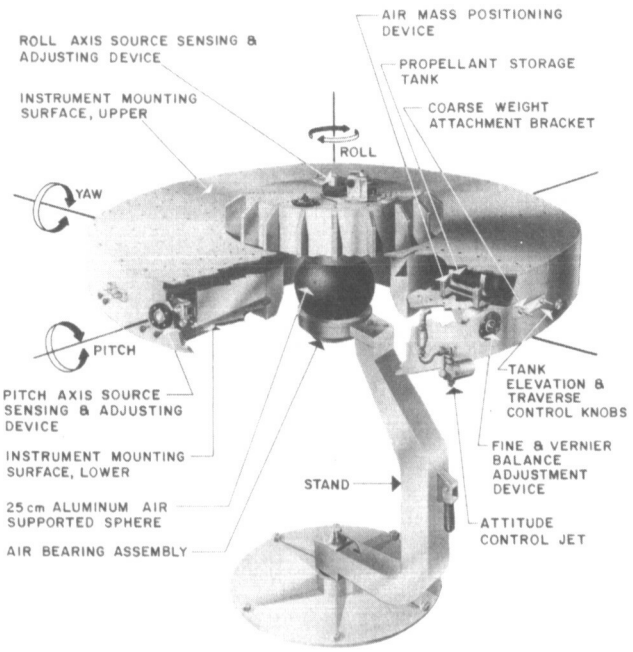

FIGURE 18. ATTITUDE MOTION SIMULATOR (AMS)

The platform is equipped with a 120-amplifier analog computer that permits a great deal of flexibility in programing for various control systems under study. To provide restoring torque control, the platform also contains three orthogonal sets of reaction jets along with associated air bottles and regulators which supply pressure up to 3.4 MN/m^2 (500 psi). To avoid extraneous external disturbance torques, direct connections to the platform are not permitted. Therefore a 14-channel rf transmitter is provided to obtain output information on the performance of the onboard control system. In addition, a 5-channel switching-command transmitter is available in the control console to provide switching commands into the onboard equipment for various functions such as on-off control of power, system gain changes, etc. Nickel-cadmium battery packs that have sufficient capacity to operate for approximately 4 hours before recharging provide ± 30 Vdc electric power for the equipment mounted on the platform.

Surrounding the AMS is a support structure and a circular floor track to support a pair of movable arm trusses and carts. Figure 19 is a sketch illustrating the AMS facility and Figure 20 is a photograph of the facility at its present state of operation. Each cart can be servo-driven up and down along its arm truss (for elevation) as the arm is servo-driven around the track (for azimuth). Each arm truss forms a circular segment of approximately 103 degrees of arc with a radius of 3.7 m (12 ft). As the cart and arm trusses move, a portion of a spherical surface is generated by a given reference point on each cart. This sphere-shaped surface covers 360 degrees in azimuth (arm truss motion) and from -18 to +85 degrees in elevation (cart motion). The radial center of the spherical surface is the rotation point of the AMS.

One of the cart-arm truss combinations is designated as a reference system that provides optical attitude reference command signals to the control system mounted on the gas-bearing platform. With a reference light source fixed to the cart, azimuth inputs are generated by rotating the arm truss around the track. Elevation reference inputs are obtained by moving the cart up and down on the arm truss. Rotation inputs about the optical reference line of sight are obtained by polarizing the reference light source.

Although the other cart-arm truss combination could also function as another reference system, its primary function is to follow or track the gas-bearing platform, thereby providing platform attitude readout information. Again utilizing a light source and an optical system, this follower system provides azimuth, elevation, and rotation (roll, yaw, and pitch, respectively) signals that are determined by the angular position of the platform as a function of time.

A control console provides the power and control functions to operate the servos for the reference and follower systems. It also contains all interface connections with the telemetry system. To provide a capability for programed inputs and input data processing, the console is also connected by a set of 40 trunk lines to a general-purpose analog computer that is available external to the AMS facility. Thus, depending on the problem to be solved, signals generated by this computer can be connected through the control console to drive the reference system. Similarly, readout information from the follower system can be transmitted to the computer, thereby allowing either data processing or closed-loop simulations such as those required for orbital-rendezvous studies.

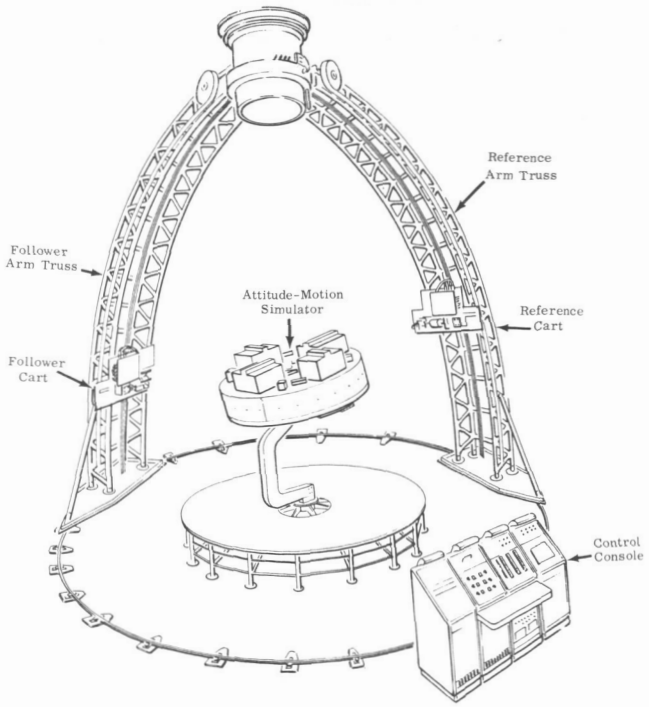

FIGURE 19. SKETCH OF AMS FACILITY

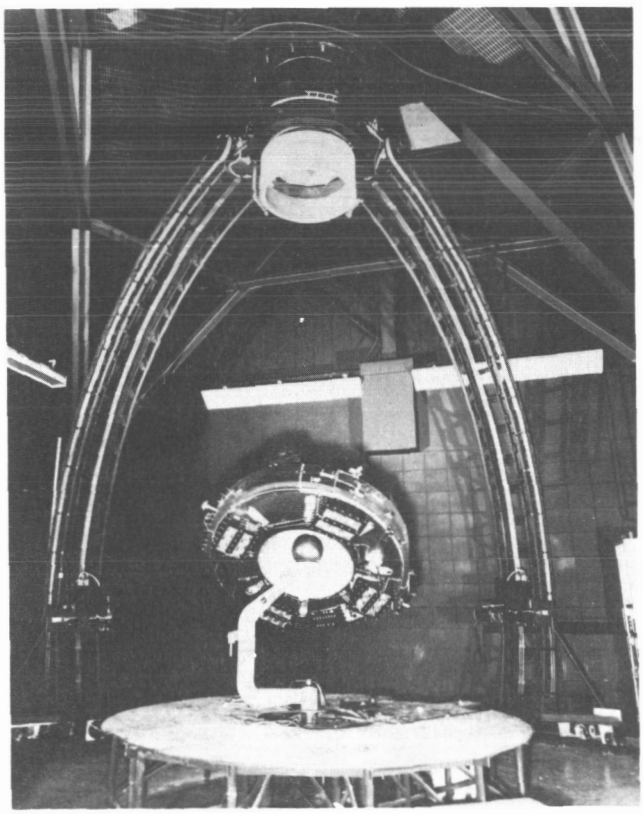

FIGURE 20. PHOTOGRAPH OF AMS FACILITY

VI. CONCLUSIONS

An analysis to describe mathematically the concept of pseudo rate modulation for use with space-vehicle attitude control has been described. Both static and dynamic characteristics were investigated, as required by the assumptions for the modulator input.

The static characteristics can be used to describe closed-loop control system on- and off-times over any time intervals for which the modulator input is approximately constant. These characteristics show that the dominant function of pseudo rate modulation is to enforce minimum-impulse operation for a control system which includes appreciable effects of engine and solenoid-valve characteristics, transport time delays, sensor lags, etc. As shown by the static-characteristic equations and associated graphs, the off-time increment (t_2) approaches a high value (theoretically infinity) as the minimum on-time (Δt) is accurately timed to a fixed specified value. This is characteristic of pulse rate modulation, and the long off-times usually enable the system to recover from all lags around the control loops during steady-state limit-cycle operation. Pseudo rate modulation has an additional benefit in that the minimum on-time is independent of modulator output voltage and, therefore, of output loading (as long as E_o remains different from zero). With increase of signal into the modulator, the pulse-widening effect (which is characteristic of pulse-width modulation) also gives maximum restoring torque capability when needed.

As the ratio K_o/K_f is varied from 0 to 1 (which corresponds to the variation of $\Delta t/\tau_f$ from 0 to ∞), it has been shown (expression 20 and Fig. 4) that the minimum period for the steady-state modulator output waveform varies from four to two times the specified minimum on-time Δt. Therefore, to minimize the design value for maximum steady-state frequency of the particular modulator used, the K_o/K_f ratio should be kept as small as possible. An important restriction that must be placed on the modulator gain factors and modulation range is obtained from the requirement of avoiding reverse firings. In essence, this restriction places an upper limit on the value for K_f. Use of $(K_f)_{max}$ always yields the smallest possible K_o/K_f ratio where the lower limit for the value of K_o is usually dictated by the hardware used.

The dynamic characteristics were then introduced in a general way to allow complete determination of modulator on and off times as a function of the state of the control system and the assumptions made. For example, the damping capability of pseudo rate modulation was shown by deriving the cutoff boundary in terms of $\dot{\epsilon}$ versus ϵ. This capability can be obtained only within the modulation range (Fig. 7), and maximum damping is obtained with the value of τ_f as high as possible (equations 30 and 35). To satisfy the requirement for minimum on-time Δt, equation 6 shows that the K_o/K_f ratio should again be minimized to obtain a high value for τ_f and, therefore, for maximum damping.

If an idealized control system with negligible transport-time delay is assumed, it is possible for on-time intervals less than the specified Δt to be produced when active rate sensing is used (Cases II and III of Fig. 6). Since the effect of the sensed rate signal is to provide control system stability, this signal will help the lag network of the pseudo rate modulator turn off the contactor. To obtain on-time intervals appreciably less than Δt, either the value for angular acceleration $\ddot{\phi}$ must be high or the rate gain factor a_1 must be large. Since active rate sensing is responsible for an early cutoff, it may be observed that it is not possible for on-times less than the specified Δt to be generated unless actual thrust of the engines is produced. Usually there is a sufficient amount of transport-time delay through the engine and valve characteristics along with time lags through the sensors so that on-time intervals considerably less than Δt will not be generated.

Use of a typical pulse modulator (such as pseudo rate), to enforce minimum-impulse operation of the particular control engines used, represents a typical conventional design approach for a space-vehicle attitude-control system. To minimize both propellant consumption and number of on-off engine actuations, an attempt is usually made to reduce the minimum impulse of the control engines to the smallest possible value.

However, a new concept called the advanced limit-cycle control technique has been developed that utilizes a control logic as a function of certain sensed inputs to cause the vehicle to be placed close to the attitude reference position with the drift rate for each axis as small as possible. Depending upon the performance repeatability of the sensed inputs and the jet engine system, exceedingly long limit-cycle periods can be obtained for undisturbed steady-state operation. This represents optimum performance with regard to jet-fuel consumption.

Since gravity gradient is usually the dominant steady-state disturbance torque for orbital missions of long duration, the local vertical must be part of

the attitude reference frame for proper utilization of the control logic to minimize jet-fuel consumption. Two optimum reference positions exist for the vehicle. If the attitude error rate is reduced to a very small value when the vehicle is aligned near the stable reference (nose or tail down), gravity gradient torque will tend to keep the vehicle at reference position. For the unstable reference position (vehicle axis of minimum moment of inertia aligned perpendicular to the local vertical), the attitude error rate should also be nulled when the sensed attitude error is zero to reduce the disturbing torque to as low a value as possible.

It may be observed that a normal conventional on-off control system does not possess this capability. Even if $\delta\dot{\phi}$ can be made to be very small, the attitude error rate is reduced to its minimum value at the edge of the attitude deadband where the torque caused by gravity gradient is usually appreciable.

Before the advanced limit-cycle technique can be extended to a three-axis space-vehicle control system, however, the thrust vector error effects that are cross-coupled from one axis to another must be considered.

Although the results of the optimization study of these effects are preliminary and general, they show trends and demonstrate quantitative support for previous qualitative thinking on the advantages of using advanced limit-cycle techniques. For example, this study showed that the advanced limit-cycle techniques are capable of satisfactory attitude-control operation with only 15 percent of the propellant previously used in less sophisticated systems. The techniques examined in the study also indicated that a proportional reduction of engine duty cycle is realized essentially with present equipment and without undue complications of the control system.

The attitude-motion facility that has been built at MSFC should prove to be a useful research and development tool for realistic testing of various attitude-control systems associated with space flight. Since actual motion of a physical body is displayed and in certain instances actual control-system equipment can be included in the simulation, there will be a high level of confidence in study results obtained from this simulation facility.

Because the studies conducted have been preliminary and have included only incomplete error and error-distribution data, additional work is required before the full value of various control schemes (such as advanced limit-cycle techniques) can be quantitatively stated. It is anticipated that future studies of pulsed mass expulsion attitude-control systems for use on Saturn and future space-vehicle missions will be broadened to include additional vehicle and engine configurations as well as other important parameters, thereby allowing both requirements and performance of future systems to be established.

REFERENCES

1. Nicklas, J. C.; and Vivian, H. C.: Derived-Rate Increment Stabilization: Its Application to the Attitude Control Problem. Joint Automatic Control Conference, Boulder, Colorado, June 28-30, 1961, Paper No. 61-JAC-9.

2. Schultz, David N.: Space Vehicle Attitude Stabilization Using Pulse Modulated Jet Control. MTP-M-G&C-61-32, July 13, 1961.

3. Schultz, David N.: Saturn S-IVB Attitude Control Using Minimum Hardware Pulse Width Modulation. M-ASTR-NAV 461/62, September 27, 1962.

4. Thrust Vector Control Study Group: Study of S-IVB Attitude Control System With Pseudo Rate Modulation. Auburn University, Seventh Technical Report, October 29, 1963.

5. Kennel, Hans F.; and Schultz, David N.: A New Concept to Minimize ON-OFF Jet Fuel Consumption Used for Space Vehicle Attitude Control. MTP-ASTR-N-62-14, December 19, 1962.

6. Adlhoch, R. W.; and Englehart, W. C.: Optimization Study of Mass Expulsion Attitude Control Systems by Means of Advanced Limit Cycle Techniques. Report No. 6077, The Marquardt Corporation, Van Nuys, California, October 16, 1964.

MATERIALS RESEARCH AT MARSHALL SPACE FLIGHT CENTER

By

W. R. Lucas

SUMMARY

The materials research program at Marshall Space Flight Center (MSFC), which combines in-house and contract work, has resulted in the development and improvement of many materials and techniques, and in the acquisition of new information on the behavior of materials in rocketry and space-flight environments.

The types of materials developed or in a developmental stage encompass a wide range. Some examples are: magnesium-lithium alloys, which are the lightest structural alloys available; wrought- and cast-aluminum alloys with superior strength and toughness at cryogenic temperatures; wire-reinforced, high-strength wrought aluminum; brazed aluminum honeycomb; low-density inorganic insulation for use on large, complexly shaped structures; insulation for cryogens; dry-film lubricants; electrical brush materials for use in vacuum; polymers usable in a new high-temperature range; cryogenic seals and adhesives; and adhesive compatible with liquid oxygen.

The materials research program has been attempting to solve specific problems through these developments. As an additional consequence of this work, it has contributed effectively both to metal and polymer technology and to an understanding of the behavior of materials in entirely new environments.

I. INTRODUCTION

Materials research at MSFC may be called directed research in that it is oriented primarily toward solving current or anticipated problems and toward providing knowledge needed in current or anticipated MSFC programs. Although the investigations which make up the research effort have been divided into in-house and contract tasks, MSFC direction has attempted to coordinate them into a single program. In this way the contracts supplement in-house capability and provide continuity of effort through periods of heavy involvement of MSFC workers in materials engineering. An essential feature responsible for program coordination is the direction of contract tasks by MSFC personnel who are involved directly with similar or related work in MSFC laboratories. Although the discussion of research achievements in this report covers an integral program, any substantial contribution by a contractor is identified by the contract number.

Practically every known type of material is utilized in the broad areas of rocketry and space flight, and many so-called conventional problems become very unconventional in the peculiar environments in which rockets and space vehicles must function. As a consequence, the materials research program has not been limited to structural materials but has been concerned with a very diverse array of applications as shown in Table I. Table II gives a breakdown of materials by quantity used in the Saturn V vehicle. Aluminum is the major structural material. Carbon steel is used primarily for fasteners. Titanium is used for fasteners in the S-IC stage and for pressure bottles in the S-II and S-IVB stages. The stainless steel is used largely for ducts and tubes. The mixed metal category includes components such as valves, black boxes, and instruments containing several materials. The list covers metals, nonmetallic inorganics, and organics. Although metals constitute the largest quantity of materials used, the demands on technology are as great, or greater, for other materials.

TABLE I. CATEGORIES OF MATERIALS

Structural materials
Fasteners and Fittings
Ducts and Tubes
Thermal control materials
Electrical/Magnetic materials
Lubricants
Seals and Gaskets
Adhesives
Encapsulating materials
Working fluids

TABLE II. SATURN V MATERIALS

MATERIAL	MASS PER STAGE, kg (lbm)			
	S-IC	S-II	S-IVB	I. U.
Aluminum	77,587	20,019	5670	567
	(171,047)	(44,133)	(12,501)	(1250)
Carbon steel	2663	55	237	
	(5871)	(121)	(523)	
Stainless steel	1599	2565		9
	(3525)	(5654)		(20)
Titanium	3255	117	61	
	(7176)	(259)	(135)	
Mixed Metals	135	2258	2483	1017
	(298)	(4977)	(5475)	(2243)
Wire/Cables	1699	1472	392	313
	(3745)	(3245)	(864)	(689)
Metal honeycomb	1011			
	(2229)			
Nonmetallic insulation, Fabrics, Fiberglass	742	3937	1045	11
	(1635)	(8679)	(2304)	(25)
Engines	41,922	7736	1554	
	(92,420)	(17,055)	(3427)	
Miscellaneous	510	595	66	
	(1124)	(1312)	(146)	
Paint	191	107	54	5
	(420)	(235)	(120)	(10)
Total	131,314	38,861	11,562	1922
	(289,490)	(85,670)	(25,495)	(4237)

The first selection of materials is usually based on the physical and mechanical properties, but the compatibility of the material with its anticipated environment and the capacity to maintain design properties finally dictate the selection of the material. Thus, later in the discussion research into the environmental effects will be covered, but because of the strong influence of these effects on the development of materials, they are identified here (Table III). These factors distinguish materials science and engineering as applied to rocketry from more conventional applications.

Another factor affecting materials technology is producibility or processibility. Most important developments begin as laboratory curiosities, but these items must be transformed into engineering materials through processing techniques and through a knowledge of the use and application of the material. Some direct routes from the laboratory to the finished product will be demonstrated later in this report.

TABLE III. ENVIRONMENTAL EFFECTS

Temperature Extremes:
Elevated
Sub-Zero (to 20°K, -423° F)
Corrosion
Atmospheric
Galvanic
Stress
Vacuum
Radiation
Meteoroids

II. MATERIALS

The materials investigated in the MSFC research programs are discussed under the categories of metals, composites, lubricants, electrical contact materials, and polymers. Metals, constituting the greatest weight of all materials used, are discussed first. A short review of former applications will help to explain the direction of future work.

A. METALS

The metals discussed here are aluminum alloys, magnesium-lithium alloys, beryllium, and a beryllium-aluminum composite.

1. Aluminum Alloys. Eight aluminum alloys have been used widely in MSFC applications. Some of their properties are shown in Table IV. The utilization of these alloys has paralleled their development in this country, as illustrated in the following review of alloy use. Weldability probably was the most important criterion in the selection of these alloys.

TABLE IV. ALUMINUM ALLOYS

ALLOY	ULTIMATE TENSILE STRENGTH MN/m^2 (ksi)	YIELD STRENGTH MN/m^2 (ksi)	YIELD STRENGTH TO DENSITY RATIO 2540 m (10^5 in.)
5052-H32	214 (31)	145 (21)	2.16
5086-H34	303 (44)	234 (34)	3.54
5456-H343	365 (53)	283 (41)	4.27
2219-T87	427 (62)	345 (50)	4.90
2014-T6	441 (64)	393 (57)	5.64
7075-T6	558 (81)	496 (72)	7.12
7075-T73	483 (70)	421 (61)	6.04
7079-T6	545 (79)	483 (70)	7.07

Alloy 5052 was used in the Redstone missile in section thicknesses up to 3.18 mm (0.125 in.). The newer and better alloy, 5086, which had become available, was used in the Jupiter missile in section thicknesses up to 9.51 mm (0.375 in.). It was planned to use alloy 5456 for a later model of Jupiter (which was not built), but the alloy was used in the first stage of Saturn I in section thicknesses up to 9.51 mm. In the second stage of Saturn I and the second and third stages of Saturn V, alloy 2014-T6 is used. Because the first stage of Saturn V required the welding of section thicknesses of 12.7 mm (0.5 in.) or more, and because fewer welding problems are encountered with alloy 2219 than with alloy 2014 (especially in these thick sections), alloy 2219 was used instead of alloy 2014, although 2219 has a slightly lower strength. The 7000-series alloys have been used primarily in unpressurized areas where fastening can be done mechanically, for example, in the interstage between tanks, and for forgings and fittings. If higher strength alloys become available, they likely will come from the aluminum-magnesium-zinc system. Thus, the need is to develop weldable alloys in this system with acceptable behavior at cryogenic temperatures and with resistance to stress corrosion. Because of the corrosion susceptibility of 7079-T6, its use in heavy forgings has caused difficulty. Alloy 7075-T73, although lower in strength than the other 7000-series alloys listed, is the best from the standpoint of stress corrosion.

Toughness at cryogenic temperature is one of the most important criteria in the selection of the greatest quantity of Saturn structural materials. A satisfactory index as to the fracture toughness of alloys can be achieved by comparing the strength of a notched specimen to that of a smooth specimen. Figure 1 indicates the notched/unnotched ratio of some Saturn alloys. One would desire this ratio to remain as near to 1.0 as possible. Note that the notched/unnotched tensile ratio of 5456-H343 is somewhat inferior to that of the other alloys in this comparison. This is probably due to the comparatively high magnesium content of this alloy. One would not expect to use, at cryogenic temperature, 5000-series aluminum alloys with greater magnesium content than about five percent. This figure shows very clearly that alloy 7079-T6 (as a forging) is not satisfactory for use at the temperature of liquid hydrogen if toughness is required. The notched/unnotched ratios of some 7000-series aluminum alloys are shown in Figure 2. Only alloy 7002 would be suitable for use at liquid-hydrogen temperature if toughness is required.

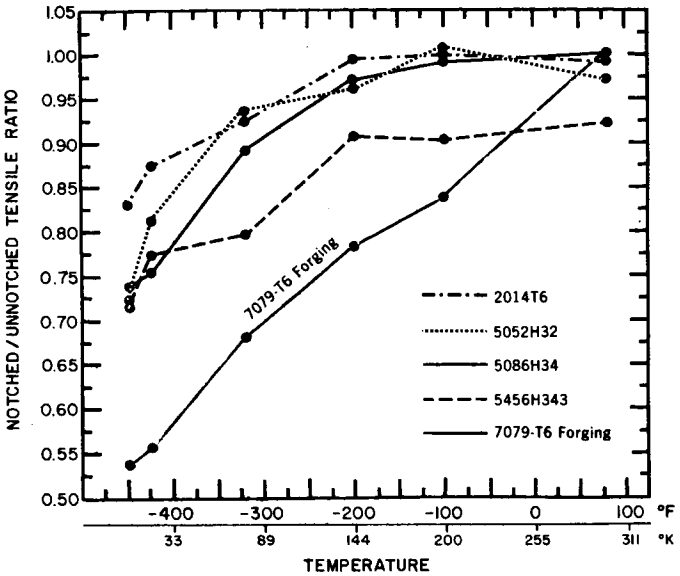

FIGURE 1. NOTCHED/UNNOTCHED TENSILE RATIOS OF FOUR WROUGHT-ALUMINUM ALLOYS AND ONE FORGING

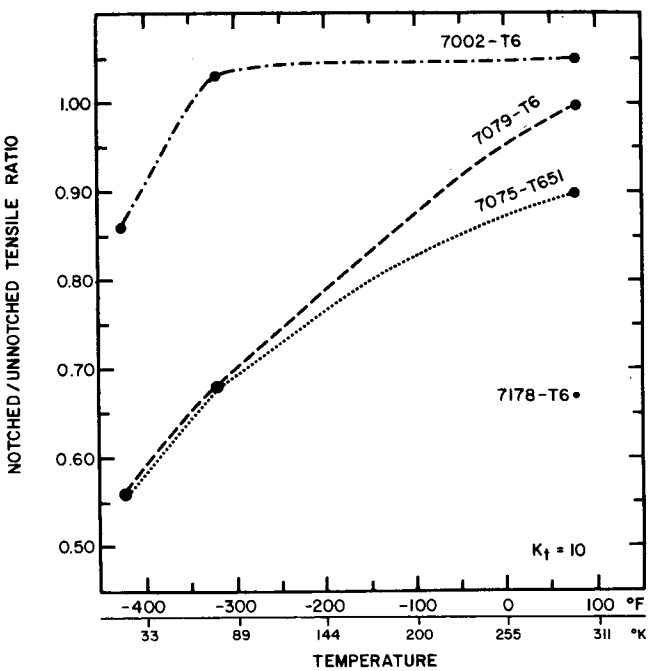

FIGURE 2. NOTCHED/UNNOTCHED TENSILE RATIOS OF FOUR WROUGHT-ALUMINUM ALLOYS

In the belief that useful aluminum alloys of higher strength than is now attainable in weldable alloys can be developed, MSFC is sponsoring a program at Alcoa (NAS8-5452) with the goals of 517 MN/m^2 (75 ksi) ultimate tensile strength, 448 MN/m^2 (65 ksi) tensile

yield strength, 15 percent elongation, and notched/unnotched ratios of 1.0 at room temperature and 0.9 at 20.4°K (-423°F). So far, the aluminum-copper alloy M825 (recently designated X2021) and the aluminum-zinc-magnesium alloy M826 (recently designated X7007) are most promising. In Table V, it is shown that M825 differs from 2219 primarily by the addition of cadmium and tin, and that M826 is a modification of X7106 with respect to content of copper, magnesium, and zinc. In Table VI, the mechanical properties of M825 and M826 are compared with those of commercial alloys and the established goals. It appears that these alloys will meet the strength and toughness criteria. Weldability tests and stress corrosion tests, although encouraging, are inconclusive at this time.

TABLE V. CHEMICAL COMPOSITION OF EXPERIMENTAL ALLOYS M825 AND M826 AND COMMERCIAL ALLOYS

ALLOYING ELEMENT	M825	2219	M826	X7106
Cu	6.3	6.3	0.10	---
Mn	0.30	0.30	0.20	0.20
Mg	---	---	1.8	2.25
Cr	---	---	0.12	0.10
Zn	---	---	6.5	4.25
Ti	0.06	0.06	---	0.03
V	0.10	0.10	---	---
Zr	0.18	0.18	0.12	0.11
Cd	0.15	---	---	---
Sn	0.05	---	---	---
Al	balance	balance	balance	balance

Many aluminum castings are used on the Saturn vehicle, and other castings could be used if better alloys were available. Under contract NAS8-1689 with Battelle Memorial Institute, a heat-treatable aluminum casting alloy (M-45) of high strength and toughness at cryogenic temperatures has been developed. The chemical composition of this alloy is compared with other high-strength aluminum casting alloys in Table VII. Note the difference from alloy 195 with respect to cadmium, silicon, and iron. The mechanical properties of M-45-T6 are compared in Table VIII with those of other aluminum casting alloys in corresponding tempers. This alloy is comparable to alloy 195 in castability. It can be welded to itself and to wrought-aluminum alloys. Recent Saturn castings from this alloy have been found to have ultimate tensile strength of 407 MN/m^2 (59 ksi), yield strength of 359 MN/m^2 (52 ksi), and an elongation of three percent. The material is available from ingot suppliers on special order. Two types of castings, one weighing 42.2 kg (93 lb) and one weighing 0.91 kg (2 lb), are being considered for the S-IVB stage. Several hundred of the latter casting have been made. Rocketdyne is also making experimental castings for possible use on engines.

TABLE VI. COMPARISON OF MECHANICAL PROPERTIES OF EXPERIMENTAL ALLOYS WITH COMMERCIAL ALLOYS AND GOALS

PROPERTY	TESTING TEMP.	M825	M826[1]	2219-T87	X7106-T6351	5456-H343	GOALS
Tensile Strength, MN/m^2 (ksi)	R.T.	519.9 (75.4)	548.1 (79.5)	466.1 (67.6)	452.3 (65.6)	386.8 (56.1)	517.1 (75.0)
	78°K (-320°F)	619.1 (89.8)	636.4 (92.3)	586.1 (85.0)	598.5 (86.8)	497.1 (72.1)	---
	20°K (-423°F)	683.3 (99.1)	---	685.3 (99.4)	706.7 (102.5)	515.7 (74.8)	---
Yield Strength, MN/m^2 (ksi)	R.T.	455.1 (66.0)	497.8 (72.2)	386.1 (56.0)	400.6 (58.1)	306.1 (44.4)	448.2 (65.0)
	78°K (-320°F)	508.8 (73.8)	598.5 (86.8)	466.1 (67.6)	486.1 (70.5)	360.6 (52.3)	---
	20°K (-423°F)	570.9 (82.8)	---	497.8 (72.2)	517.1 (75.0)	377.8 (54.8)	---
Elongation, % in 50.8 mm (2 in.)	R.T.	9.0	12.2	10.5	12.8	10.2	15.0[2]
	78°K (-320°F)	12.7	2.2	11.0	14.0	13.9	---
	20°K (-423°F)	10.0	---	13.5	15.2	7.0	---
Notched/Unnotched[3] Tensile Ratio	R.T.	0.98	1.31	1.13	1.36	0.95	1.0
	78°K (-320°F)	1.06	0.95	1.03	1.06	0.85	---
	20°K (-423°F)	1.03	0.95	0.94	0.94	0.88	0.9

1. 20°K Test Data on M826 Not Complete
2. Recently Changed to 10%
3. $K_t = 10.0$

TABLE VII. CHEMICAL COMPOSITION OF M-45 AND OTHER HIGH-STRENGTH ALUMINUM CASTING ALLOYS

ALLOYING ELEMENT	NOMINAL COMPOSITION[1], MASS PERCENT				
	M-45	A 356	TENS-50	ALMAG 35[2]	195
Cu	3.90-4.50	0.20	0.20	0.01	4.00-5.00
Cd	0.08-0.12	---	---	---	---
Mg	0.06-0.10	0.25-0.40	0.40-0.60	7.00	0.03
Ti	0.02-0.05	0.20	0.10-0.20	0.10	0.20
Si	0.017	6.50-7.50	7.60-8.60	0.10	0.50-1.2
Fe	0.010	0.35	0.40	0.10	0.80
Cr	0.001	---	0.20	---	---
Mn	---	0.10	0.20	0.10	0.20
Zn	---	0.10	0.20	---	0.20
Be	---	---	0.10-0.30	---	---
Al	balance	balance	balance	balance	balance

1. Composition given is maximum permissible unless given as a range
2. Typical

TABLE VIII. MECHANICAL PROPERTIES OF ALUMINUM CASTING ALLOYS

ALLOY	ULTIMATE TENSILE STRENGTH MN/m^2 (ksi)	TENSILE YIELD STRENGTH MN/m^2 (ksi)	ELONGATION PERCENT IN 51 mm (2 in.)	CHARPY IMPACT J (ft-lb)
M-45	331(48)	310(45)	5	17.6(13)
A 356	234(34)	200(29)	2	2.7(2)
Tens-50	255(37)	221(32)	2	1.4(1)
Almag 35	207(30)	110(16)	7	4.1(3)
195	207(30)	165(24)	2	4.1(3)

2. Magnesium-Lithium Alloys. The magnesium-lithium alloys are the lightest structural metals commercially available (1.349 g/cm^3, 0.049 $lbm/in.^3$), and applications for these alloys are increasing. Battelle has developed for MSFC two alloys, LA-141 and LAZ-933, which are compared in Table IX. The initial interest in these alloys was their use in the space environment, where corrosion would not be a problem. However, these alloys are now being used for several applications in the earth environment. For example, about 31.8 kg (70 lb) of LA-141 are used in the Saturn V Instrument Unit, and about 2.3 kg (5 lb) are used in an angle-of-attack meter. It is expected that greater use will be made of these lightweight alloys.

TABLE IX. MAGNESIUM AND MAGNESIUM-LITHIUM ALLOYS

	PURE MAGNESIUM	LA 141	LAZ 933
DENSITY, kg/m^3 ($lb/in.^3$)	1743.834 (.063)	1356.315 (.049)	1550.075 (.056)
ULTIMATE TENSILE STRENGTH, MN/m^2 (ksi)	165 (24)	145 (21)	228 (33)
TENSILE YIELD STRENGTH, 0.2% Offset, MN/m^2 (ksi)	97 (14)	117 (17)	179 (26)
YIELD STRENGTH/DENSITY RATIO, 2540 m (10^5 in.)	2.2	3.5	4.6
MODULUS OF ELASTICITY, 6898 MN/m^2 (10^6 psi)	6.5	6.5	6.4
MODULUS/DENSITY RATIO, 2540 km (10^8 in.)	1.0	1.3	1.1

3. Beryllium and Beryllium-Aluminum. Beryllium is used in the inertial guidance system of the Saturn V, approximately 75 kg (165 lb) per vehicle. The mass stability required of the gyroscope structures is very high, and only the slightest imbalance is tolerable. The parts must be amenable to polishing to a high surface finish, 0.1 μm (4 μin.) or better and be free from corrosion. Beryllium was chosen for this application because of its dimensional stability, high elastic modulus, high specific heat, high thermal conductivity, low coefficient of thermal expansion, low density, and a high degree of isotropy in the conventional hot-pressed and sintered form. MSFC work has been related to processing of the beryllium powder and to the development of a system for protection against corrosion. Other applications have been considered but none has been implemented yet, primarily because of the brittleness of the material.

A much more potentially useful material for structural applications is the beryllium-aluminum (Be-Al) composite, which is compared with beryllium in Table X. Although the initial development of the Be-Al composite was sponsored by Lockheed, MSFC has contributed to the development (contract NAS8-11448) by the determination of properties of sheet material from production lots. The final report has just been received, and the reproducibility of properties between lots is surprisingly good although only one sheet thickness (1.5 mm or 0.060 in.) was studied. The sheet is now available in dimensions of 0.305 m by 0.61 m (1 ft by 2 ft), but larger sheet sizes will be available.

TABLE X. BERYLLIUM AND BERYLLIUM-ALUMINUM COMPOSITE

	Be SHEET (FROM POWDER)	Be-38%Al SHEET
DENSITY, kg/m^3 ($lb/in.^3$)	1826.874 (.066)	2092.601 (.0756)
ULTIMATE TENSILE STRENGTH, MN/m^2 (ksi)	483 (70)	347 (50.4)
TENSILE YIELD STRENGTH, 0.2% OFFSET MN/m^2 (ksi)	338 (49)	252 (36.6)
MODULUS OF ELASTICITY, 6898 MN/m^2 (10^6 psi)	44	29
MODULUS/DENSITY RATIO, 2540 km (10^8 in.)	6.6	3.9

B. COMPOSITE MATERIALS

A class of materials with perhaps more potential than any other is composite materials. Composite materials can be defined so broadly as to encompass practically every engineering material; however, here reference is to the macrostructural level. Sandwich composites will be discussed first. The increasing application of sandwich composites arises from the high strength-to-density ratio and high section modulus or stiffness of most sandwich materials and low thermal conductivity of special sandwich materials. Furthermore, this type of

material allows the maximum flexibility in the utilization of the most favorable properties of each element of the composite.

1. Double-Seal Insulation. The flexibility of sandwich composites can be illustrated by the double-seal insulation concept developed at MSFC to insulate the liquid-hydrogen tank of the S-II stage. This composite consists of a layer of Mylar honeycomb with a Mylar film bonded to one side and aluminum foil bonded to the other, so that each cell of the honeycomb is sealed as shown in Figure 3. To this layer is bonded a perforated phenolic-fiberglass honeycomb core and, finally, aluminum film is bonded to the exterior. The complete composite can be preformed to the appropriate curvature and bonded to the tank wall. The liquid hydrogen evacuates the sealed cells of Mylar honeycomb by cryopumping (condensing and solidifying) and, thus, provides the insulation. The external layer is designed to withstand temperatures up to 492° K (425° F), which are encountered in aerodynamic heating. By being perforated, it can be purged with helium to protect the Mylar core from condensed oxygen, with which it would be incompatible. The thermal gradient across this material may be more than 700° K (800° F). This scheme has been reduced to practice and will be used on flight vehicles.

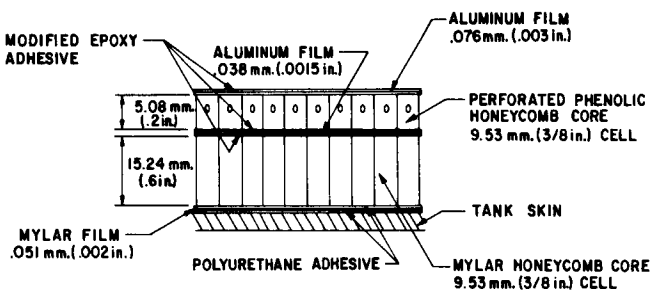

FIGURE 3. DOUBLE-SEAL INSULATION

The requirements for nondestructive inspection of the dual-seal insulation involved another facet of MSFC work. Based upon this need, MSFC developed an acoustic technique involving both audible and ultrasonic frequency ranges to detect defects of less than one 9.5 mm (0.38 in.) cell diameter. When the acoustical energy echo in two planes is recorded on an x-y type tape, the defect shape can be depicted. The Space and Information Systems Division of North American Aviation is adapting this technique for both the dual-seal cryogenic insulation and the S-II stage common bulkhead in production facilities.

Under contract NAS8-11761, Goodyear Aircraft Company is extending in-house work by modifying the version of the dual seal just described, and is studying related concepts. On another contract, NAS8-11747, Goodyear Aircraft Company is developing materials concepts to be useful as cryogenic insulation and as micrometeoroid bumpers.

2. Nonmetallic Composites. In regard to nonmetallic composites, significant achievements have resulted from contract NAS8-11070. The achievements have been in the development of meaningful physical and mechanical test methods and in the generation of data which are indicative of the true structural potential of fiber-reinforced plastics at cryogenic temperatures.

3. Brazed Aluminum Honeycomb. To avoid the temperature limitations and other deficiencies of adhesive bonding, a task was initiated with Aeronca Manufacturing Corporation (NAS8-5445) to develop a brazed aluminum honeycomb. Considerable success has been achieved. First, it has been demonstrated that aluminum face sheets can be brazed to aluminum core. Second, it has been shown that the composite can be strengthened by quenching directly from the brazing furnace into liquid nitrogen with a minimum of distortion. Typical room-temperature mechanical properties of brazed and adhesively bonded aluminum face sheet (X7106) and core (6951) are shown in Table XI. The increase in core shear strength is due to the fact that this aluminum core normally is not heat treated. The strength differentials would be more favorable at elevated temperatures and at cryogenic temperatures. Work is continuing with other high-strength aluminum alloys and in improving processes.

TABLE XI. TYPICAL MECHANICAL PROPERTIES OF ALUMINUM HONEYCOMB*

	FLATWISE TENSILE kN/m² (psi)	FLATWISE COMPRESSION kN/m² (psi)	EDGEWISE COMPRESSION kN/m² (psi)	CORE SHEAR kN/m² (psi)
BRAZED	13,100	8270	468,840	8960
	(1900)	(1200)	(68,000)	(1300)
ADHESIVE BONDED (FM 1000)	5515	8270	379,210	4830
	(800)	(1200)	(55,000)	(700)

* Face Sheets: X7106: 1.57 mm (0.062 in.) thick
Core: 6951: 15.24 mm (0.6 in.) thick

4. Wire-Reinforced Aluminum. Another type of composite material being investigated is metal-fiber- or wire-reinforced wrought aluminum and aluminum castings. Significant progress in the

work has been made recently through contract NAS8-11508 with Harvey Aluminum Company. The purpose of this investigation is to produce wire-reinforced aluminum in thicknesses of 6.35 mm (0.25 in.) and 19 mm (0.75 in.) having a minimum tensile strength of 1.2 GN/m^2 (175 ksi) and a maximum density of 3.986 g/cm^3 (0.144 lbm/$in.^3$). This density results from a volume percentage of 75 percent aluminum and 25 percent steel. Small samples up to 19 mm thick have been produced with fairly uniform distribution of the reinforcement wire in the aluminum matrix, as shown in Figure 4. These plates were made by pressing the reinforcing wire into thin sheets and then laminating the sheets. Although the wires in these samples are unidirectional, it is not necessary that they be this way using the current

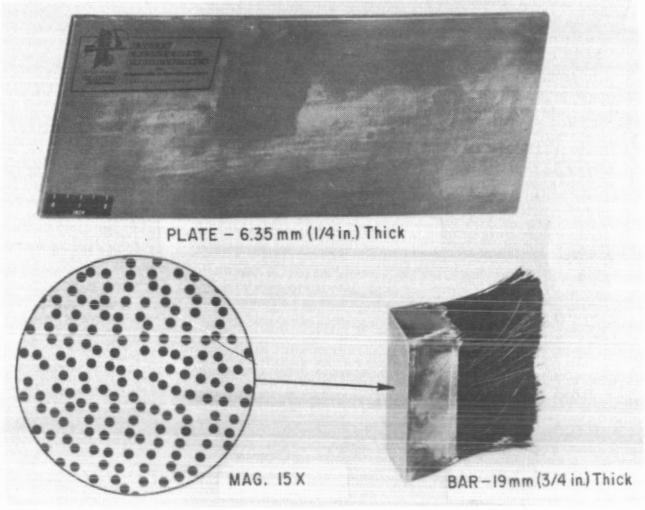

FIGURE 4. ULTRA HIGH-STRENGTH COMPOSITE MATERIALS

technique. The aluminum alloys which have been used and corresponding tensile strengths obtained from the composite are shown in Table XII. In each case, the reinforcing wire is AM-355 with an approximate diameter of 0.254 mm (0.010 in.) and an approximate tensile strength of 3.45 GN/m^2 (500 ksi). The contractor is prepared now to produce plates 0.3 m (12 in.) wide by 2.4 m (96 in.) long, and is expected to deliver some of these plates in July 1965. Study is continuing on development of the material and on joining techniques. Plates have been joined by diffusion bonding with an efficiency of 92 percent.

5. M-31. Another type of composite material was developed specifically for the heat shield of the S-IC stage of Saturn V. This material, known as M-31, was developed to be low in density, to have

TABLE XII. WIRE-REINFORCED ALUMINUM ALLOY PLATES

ALUMINUM MATRIX	COMPOSITE CONDITION	ULTIMATE TENSILE STRENGTH, MN/m^2 (ksi)
5456	as fabricated	945 (137)
2024	sol. ht. treated, cw 3% aged, cw 3%	1193 (173)
2219	sol. ht. treated, cw 3%, aged	1093 (158.5)
7075	sol. ht. treated, cw 3%, aged	1200 (174)
7178	sol. ht. treated, cw 2% aged, cw 2%	1210 (175.5)

low thermal conductivity, to be nonburning, and to be applied easily by trowel and cured at relatively low temperatures. The composition of the material as developed is shown in Table XIII. Tipersul is a trade name of E. I. du Pont de Nemours and Company and consists of fibrous potassium titanate. Ludox is colloidal silica. Figure 5 is a diagram of a section of honeycomb heat shield to which M-31 is applied.

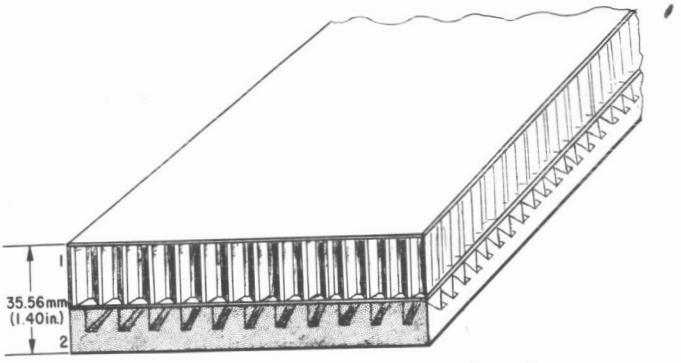

FIGURE 5. S-IC HEAT SHIELD

The metallic part of the heat shield consists of a stainless-steel honeycomb which serves as the load-carrying member, and a crimped, open-face honeycomb brazed to the load-carrying member. M-31 is applied to the open face as plaster is applied to a wall (Fig. 6). The completed assembly is dried at approximately 344° K (160° F). As applied to the S-IC stage of Saturn, the mass of the composite is about 10.3 kg/m^2 (2.1 lbm/ft^2). The density of M-31 can be varied between 753 kg/m^3 (47 lbm/ft^3) and 881 kg/m^3 (55 lbm/ft^3).

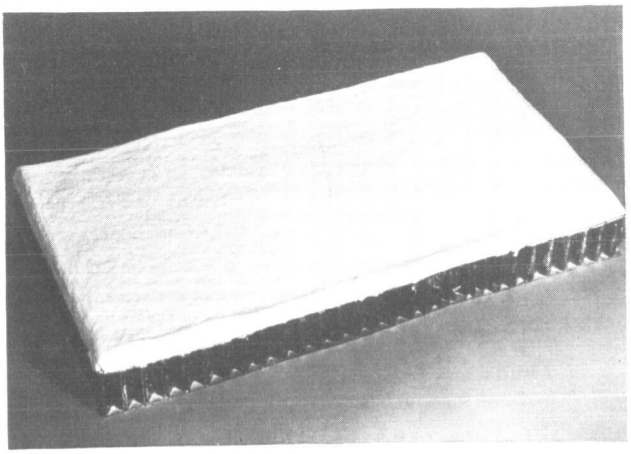

FIGURE 6. HONEYCOMB SANDWICH CONSTRUCTION WITH M-31 INSULATION

TABLE XIII. BATCH COMPOSITION OF M-31 THERMAL INSULATION

MATERIAL	PARTS BY WEIGHT
"Tipersul" block	90
Asbestos fibers	10
"Ludox" HS	420

The effectiveness of M-31 in a radiant environment is shown in Figure 7, in which the temperature rise at the back surface of a sheet-steel blank 1 mm (0.040 in.) thick is compared to that at the back surface of a coating of M-31 8.1 mm (0.320 in.) thick when both were exposed to a heat flux of 272 kW/m^2 (24 Btu/ft^2 sec). M-31 has been shown to be an effective insulator in radiant heating environments up to 794 kW/m^2 (70 Btu/ft^2 sec). The material is also an effective insulator in a convective environment. Optical properties of interest are essentially constant; absolute spectral reflectance is illustrated in Figure 8, and total normal emittance in Figure 9.

Illinois Institute of Technology Research Institute has a contract (NAS8-11333) to develop improved lightweight insulation materials for tail heating protection, and significant progress has been reported on ceramic foams which are being thermally and structurally optimized now.

C. LUBRICANTS

The problem of lubrication in the vacuum of space has been one of the most pressing ones, particularly for intermittently moving parts. Mating metal parts tend to weld together in the space environment. This appears to be particularly true when

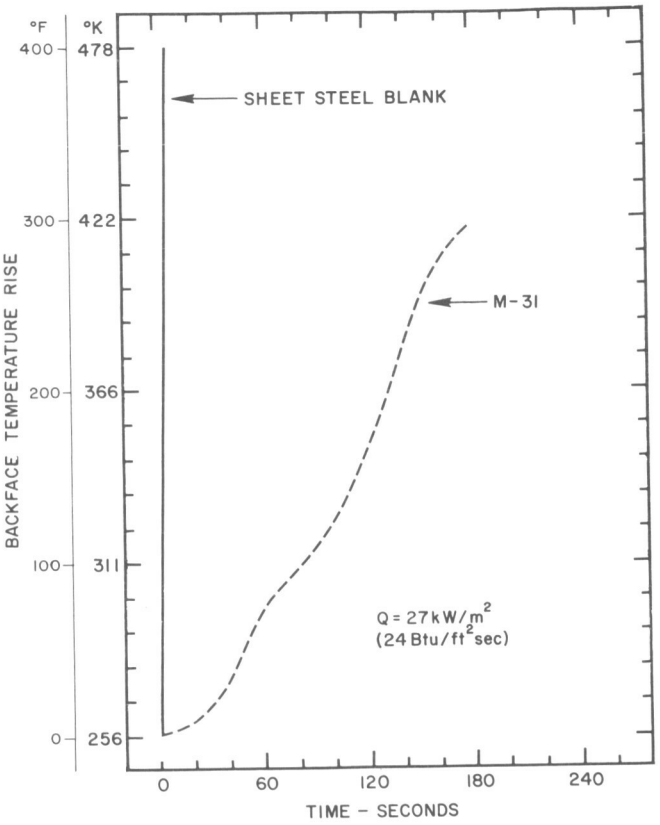

FIGURE 7. RESISTANCE OF M-31 TO RADIANT HEATING

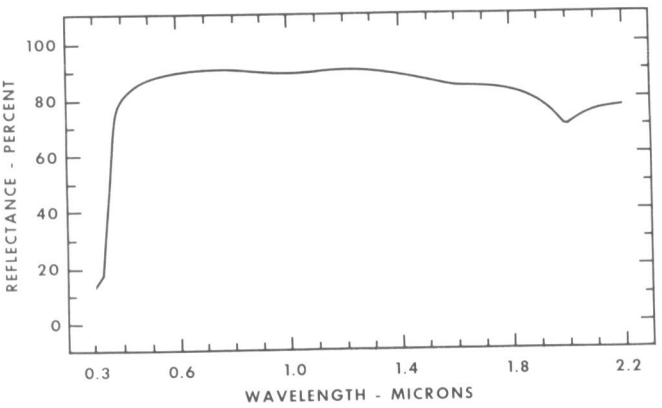

FIGURE 8. ABSOLUTE SPECTRAL REFLECTANCE OF M-31

mating parts are of the same material or when of different materials and one of the materials tends to form a stable, solid solution in the other. Exposure of clean surfaces either by plastic deformation or by some other means such as ion bombardment can result in extreme friction and seizing of mating surfaces even at modest vacuum. Moreover, the better known organic lubricants will be subject to evaporation in space, or they may be degraded by irradiation.

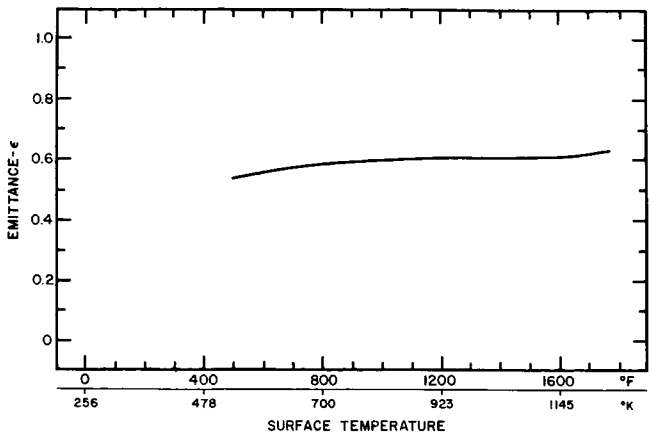

FIGURE 9. TOTAL NORMAL EMITTANCE OF M-31

1. Dry-Film Lubricants. The first significant contribution by MSFC to the dry-film lubricant field was the lubricant, MLF-5. MLF-5 was developed to MSFC requirements by Midwest Research Institute under contract NAS8-1540 and was evaluated by MSFC (described in MSFC-SPEC-253). Some of its features are listed in Table XIV. This lubricant now is being used on the RL-10A3 engine gimbal bearing on the S-IV stage of Saturn I and the Centaur because the lubricants used initially were shown to be unsatisfactory for vacuum operations. A comparison of MLF-5 with some better dry-film lubricants is given in Table XV. All except graphite were tested under uniform conditions. Although the graphite was tested under a higher load (75.8 kN/m^2 or 11 psi compared to 15.2 kN/m^2 or 2.2 psi for the others) and a higher speed (8.1 m/sec or 1600 fpm compared to 3.9 m/sec or 765 fpm for the others), the results substantiate the generally accepted conclusion that graphite is an ineffective lubricant in vacuum because of the absence of oxygen and moisture on the surfaces of the graphite flake.

TABLE XIV. MLF-5 DRY-FILM LUBRICANT, MSFC-SPEC-253

PREPARATION:

	INGREDIENT	PARTS
1.	Molybdenum disulfide	10
2.	Graphite	1
3.	Gold	5
4.	Sodium silicate	7
5.	Water	60

APPLICATION:

Spray and bake

ADVANTAGES:

1. Extreme pressure
2. Constant, low friction
3. Not sensitive to environment
4. LOX compatible
5. Moisture resistant

TABLE XV. DRY-FILM LUBRICANTS

LUBRICANT	BINDER	COEFFICIENT OF FRICTION (AVERAGE) 101 kN/m^2 (760 torr)	133 μN/m^2 (1×10^{-6} torr)
Gold	Electroplated	0.21	0.24
MoS_2	Teflon	0.25	0.25
MoS_2	Na_2OSiO_2	0.21	0.35
MoS_2/Graphite (10:1)	Na_2OSiO_2	0.21	0.26
MLF-5	Na_2OSiO_2	0.17	0.10
Graphite[1]	---	0.15	0.70[2]

1. From Ramadanoff & Glass
2. 1333 N/m^2 (10 torr)

In Figure 10, the coefficient of friction of MLF-5 as a function of bearing pressure in vacuum is compared with that of Ease-Off 990, the commercial lubricant originally specified for the RL-10A3 gimbal bearing. In Figure 11, the coefficient of friction of MLF-5 as a function of temperature in vacuum is compared with that of Fabroid, the commercial lubricant currently specified for the J-2 engine gimbal bearing. Inasmuch as Fabroid is a glass-reinforced Teflon, higher bearing pressure would be expected to show Fabroid less favorably.

The utility of dry-film lubricants is not restricted to space-related applications. The Saturn V hold-down arms will be lubricated with a new related compound, MLF-9, described in Table XVI. The choice of this lubricant for the hold-down arms was based on data such as shown in Figure 12. Experi-

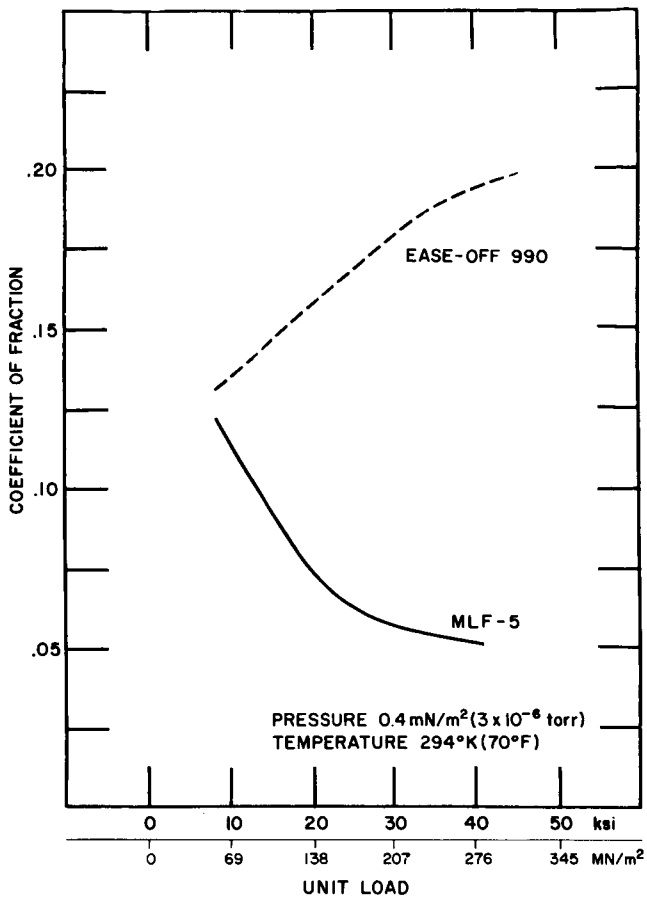

FIGURE 10. COEFFICIENT OF FRICTION VERSUS UNIT LOAD FOR MLF-5 AND EASE-OFF 990

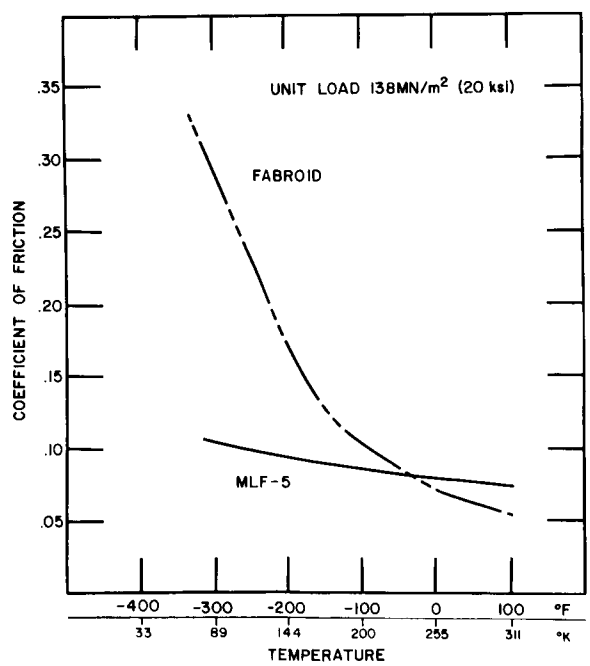

FIGURE 11. COEFFICIENT OF FRICTION VERSUS TEMPERATURE FOR MLF-5 AND FABROID

TABLE XVI. MLF-9 DRY-FILM LUBRICANT

PREPARATION:

INGREDIENT	PARTS
1. Molybdenum disulfide	10
2. Graphite	1
3. Bismuth	14
4. Aluminum phosphate	9
5. Water	60

APPLICATION:

Spray and bake

ADVANTAGES:

1. Extreme pressure
2. Constant, low friction
3. Not sensitive to environment
4. LOX compatible
5. Moisture resistant

mental data on commercial greases and the special lubricants, MLF-5 and MLF-9, some of which are plotted here as coefficient of friction versus bearing pressure, demonstrated clearly the superiority of dry films over greases at the bearing pressures of concern (more than 689 MN/m^2 or 100 ksi) in the

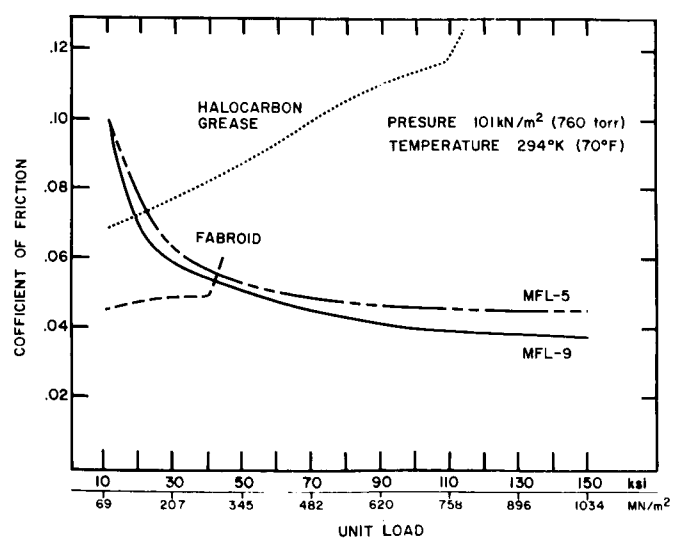

FIGURE 12. COEFFICIENT OF FRICTION VERSUS UNIT LOAD, FOUR LUBRICANTS

Saturn V hold-down arm application. In addition to having a somewhat more favorable coefficient of friction than MLF-5, MLF-9 is not hygroscopic as is MLF-5. The substitution of bismuth for gold also reduces the price of MLF-9.

2. Cold-Welding Problem. An interesting adjunct to the lubrication studies has been the work on the "cold welding" of metals in vacuum. Much concern has been expressed over the possible welding of metals, cleaned by long exposure to space, when they come into contact, such as in a docking operation. Under contract NAS8-11066, Hughes Aircraft Company developed the data shown in Figure 13. This chart depicts loads which can be tolerated without causing "welding" of representative materials when exposed to a pressure of 667 nN/m^2 (5×10^{-9} torr) for 19 hours. The samples were cleaned chemically before they were loaded in vacuum. Results of this program demonstrate that in essentially all cases no "cold welding" occurred at static loads of up to 75 percent of the compressive yield strength of the materials. However, under dynamic loads, the mechanical cleaning caused by vibration may enhance the "cold welding" prospects, but the existence of any non-metallic inorganic film (e.g., a surface oxide) on either faying surface will preclude the possibility of "welding." These data indicate that the problems of "cold welding" during docking maneuvers may not be severe.

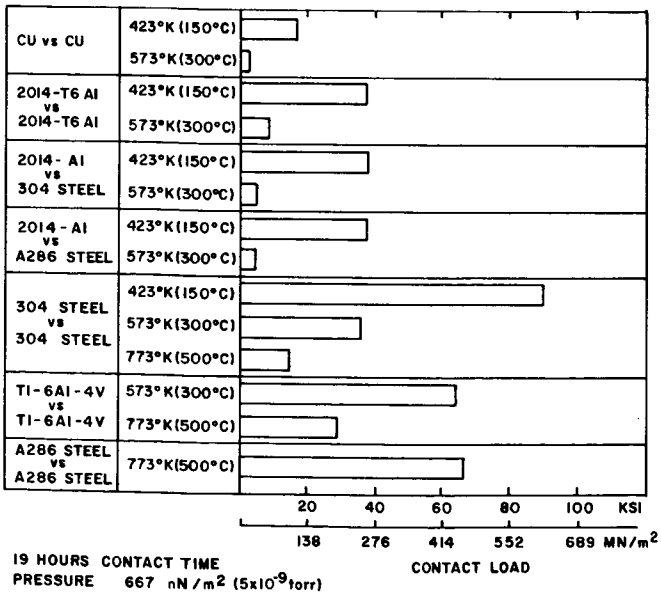

FIGURE 13. MAXIMUM ALLOWABLE LOADS FOR NO WELDING

D. ELECTRICAL CONTACT MATERIALS

The deficiencies of commercial sliding contact material (slip rings and brushes) in the space environment have been thoroughly established. The complexities involved in circumventing these problems by using ac power, and the sacrifices realized by neglecting the attributes of dc equipment, prompted MSFC to embark on a program to develop sliding contact materials applicable to the space environment.

In a vacuum environment, the problem with standard graphite brushes is excessive wear rate, as illustrated in Table XVII. The additives developed for airplane flight altitudes are not adequate for space flight. It was shown in the vacuum lubrication program that molybdenum disulfide is a good lubricant in vacuum; however, it is not an electrical conductor. To utilize the lubricity in vacuum of molybdenum disulfide, a composite of MoS_2 and metallic powder was prepared.

TABLE XVII. WEAR RATES OF GRAPHITE AND GRAPHITE/ADDITIVE MIXTURES

MATERIAL	PRESSURE N/m^2 (torr)	DURATION hours	WEAR RATE mm/hr (in./hr)
Graphite	101 k (sea level) (760)	---	0.0025 (1×10^{-4})
Graphite	30 k (9 km) (225) (30,000 ft)	6	2.54 (1×10^{-1})
Graphite plus Halide additive	30 k (9 km) (225) (30,000 ft)	112	101.6 (4×10^{-3})
Graphite plus MoS_2 pockets	30 k (9 km) (225) (30,000 ft)	---	7.6 (3×10^{-4})
Graphite	133 μ (152 km) (1×10^{-6}) (500,000 ft)	0.5	30.48 (1.2)
Graphite plus Halide additives	133 μ (152 km) (1×10^{-6}) (500,000 ft)	1.5	8.89 (3.5×10^{-1})
Graphite plus MoS_2 pockets	133 μ (152 km) (1×10^{-6}) (500,000 ft)	16	0.51 (2×10^{-2})

Both silver and copper were evaluated as the metal powder. The processing technique involved hot-pressing the mixed powder to a dense, composite material capable of being ground to any desired geometric shape. To date, the most successful compositions have been prepared at a temperature of 1200°K (1700° F) and a pressure of 27.6 MN/m^2 (4000 psi). Compositions containing volume percentages shown in Table XVIII have been evaluated, and results indicate that a composition of 14 percent Ag-86 percent MoS_2 represents the most desirable lubrication and conductivity compromise. The conduction of these

TABLE XVIII. BRUSH MATERIAL COMPOSITIONS

COMPOSITION NUMBER	VOLUME PERCENT				
	MOLYBDENUM DISULFIDE	SILVER	COPPER	TUNGSTEN DISULFIDE	SILVER SULFIDE
1	95		5		
2	90		10		
3	80		20		
4	90	10			
5	86	14			
6	80	20			
7	73.5	26.5			
8	61.8	38.2			
9	82.5	14.5	3		
10	74.2	20			5.8
11	60	30			10
12		18		82	
13		23.7		76.3	
14				67	33

composites has been studied, and indications are that the composite does not contain sufficient metal atoms to permit metallic conduction. Although this is not conclusive evidence, the photomicrograph of the composite (Fig. 14) indicates that the silver particles are not connected. Furthermore, the electrical conductivity is less than that of silver. A semiconducting

FIGURE 14. PHOTOMICROGRAPH OF MoS_2-Ag COMPOSITE

process may be involved in the composite brush to provide electrical conductivity between the silver particles. Work is being done now to verify this possibility. There is experimental evidence that the 14 percent Ag-86 percent MoS_2 composite brush will function satisfactorily in pressures as low as 133 nN/m^2 (10^{-9} torr). Brushes have been run in excess of 7000 hours continuously without failure in simulated commutator tests and have been run in 75-watt (1/10 hp) motors successfully for a total of 5580 hours. Preliminary testing has been completed successfully on 186-watt (1/4 hp) motors. A comparison of the wear rate of these brushes with other experimental brush materials and with commercial brushes is shown in Table XIX. The composite-brush wear rates at 304,800 meters (1 million feet) are less than the wear rates (2.54 μm) of commercial brushes at 0.1 MN/m^2 (1 atm), as shown in Table XVII. There is no reason to believe that these composite brushes would not be applicable to motors of much higher power than have been tested. As indicated by MSFC's experimental program, the dc motor can be used efficiently in space or on the surface of our moon or other planets.

TABLE XIX. WEAR RATE OF BRUSH MATERIALS

MATERIAL	PRESSURE $\mu N/m^2$ (torr)	DURATION hours	WEAR RATE mm/hr (in./hr)
Graphite	133 at 152 km	0.5	30.48
	(1×10^{-6} at 500,000 ft)		(1.2)
Graphite plus Halides	133 at 152 km	1.5	8.89
	(1×10^{-6} at 500,000 ft)		(.35)
Graphite plus MoS_2 pockets	133 at 152 km	16	0.508
	(1×10^{-6} at 500,000 ft)		(.02)
MoS_2 - Ag Hot pressed material	13.3 at 305 km	6,914	0.03556 μ
	(1×10^{-7} at 1 million ft)		(1.4×10^{-6})

E. POLYMERS

Many materials of critical interest to MSFC fall in the category of polymers; structural adhesives, plastics, and synthetic rubber are common examples. Some applications of polymers to MSFC work are listed in Table XX.

A polymer may be described as an assemblage of long, chain-like molecules. These molecules are built up of repetitive identical linkages or chemical building blocks which are induced to couple together during a chemical reaction. Actually, one obtains a statistical distribution of chain lengths or molecular weights which depends upon the nature of the materials and the process used to prepare the polymer. It is possible in most cases to ascertain experimentally an average molecular weight.

TABLE XX. POLYMER APPLICATIONS

ADHESIVES
1. Bonding clips, Brackets
2. Bonding composite materials
SEALING AND ENCAPSULATING
1. Seals, Gaskets, Valve seats
2. Conformal coatings, Potting
COMPOSITES (STRUCTURAL AND INSULATION)
1. Reinforced plastics (laminates, filament wound)
2. Foams
3. Films
4. Honeycomb cores
COATINGS
1. Temperature control
2. Corrosion protection
LINERS AND BLADDERS
1. Propellant expulsion
2. Fluid containment

At the molecular level, a linear polymer may be compared with a bucket of worms. The long, worm-like molecules would be coiling and tangling around one another in continuous motion; the extent and frequency of this motion would be dictated by the temperature and other factors. It is this capacity for relatively free molecular motion, as compared with metals and ceramics, which confers unique physical properties on the polymer solid state. These properties can be regulated in many instances by what we call the degree of crosslinking or the number of times an average worm-like molecule is attached to one of its neighboring molecules. If there are no attachment points along any of these continuous molecular chains, the material may be a linear polymer like Teflon, which readily undergoes permanent plastic deformation. With only a moderate degree of crosslinking, the molecular lattice develops an elastic memory and tends to return to its original form when a stress is removed. This material may be an elastomer or rubber and, in this case, the crosslink density is usually slightly over unity. If this crosslinking can be continued further, a highly complex three-dimensional molecular array can be developed that will be characterized by extreme strength and rigidity. An attempt is made to achieve this highly crosslinked state in structural adhesives during the curing step. In fact, curing can be defined as a chemically controllable process for increasing the crosslink density.

1. Polymers for High-Temperature Application. A combined program of internal and contractual work was started several years ago for the study of polymers containing silicon-nitrogen bonds. This type of polymer is compared with silicones in Figure 15. As shown, starting with silicon dihalides, a silicone results through reaction with water, or a silazane (silicon-nitrogen polymer) through reaction with ammonia. The high-temperature properties of silicones are well known, and it was expected, and now appears, that silazanes will have substantially better high-temperature properties. Furthermore, silazanes serve as intermediates, as will be demonstrated later, to make polymers of still higher-temperature utility.

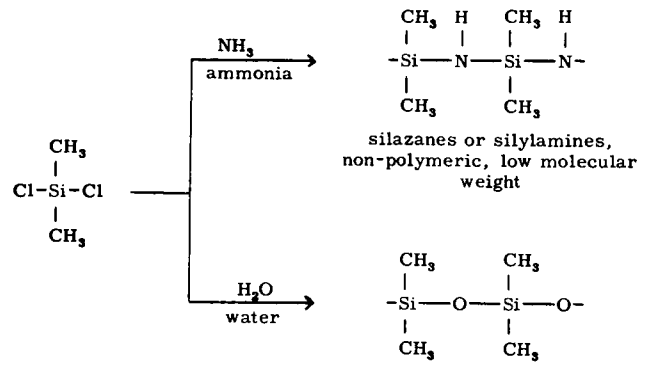

FIGURE 15. FORMATION OF SILAZANES AND SILICONES

The current joint effort in this area with Southern Research Institute has elicited a great deal of interest. Both linear polymers and cyclic compounds have been prepared by direct reactions such as those shown in Figure 16. A direct halosilane-amine reaction can be used to produce cyclic compounds or low molecular-weight silazane polymers. In addition, these materials can be modified by reactions involving an exchange process between a Si-N compound or polymer and an organic diamine.

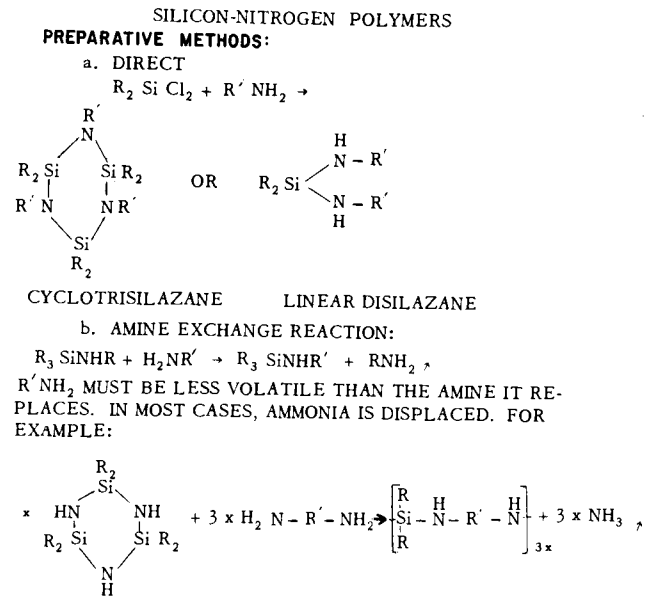

FIGURE 16. FORMATION OF CYCLIC AND LINEAR SILICON-NITROGEN POLYMERS

Some of the cyclic silazanes have the property of undergoing complex condensation reactions at elevated temperatures (Fig. 17). The brown, benzene-soluble resin is tractable up to 793° K (520° C), but, at this temperature, it suddenly undergoes a condensation reaction, producing a porous, intractable polymer which is stable to about 973° K (700° C). Although the ultimate products of these reactions are extremely stable materials, there are drawbacks to their immediate use that will necessitate further development. One potential application for this type

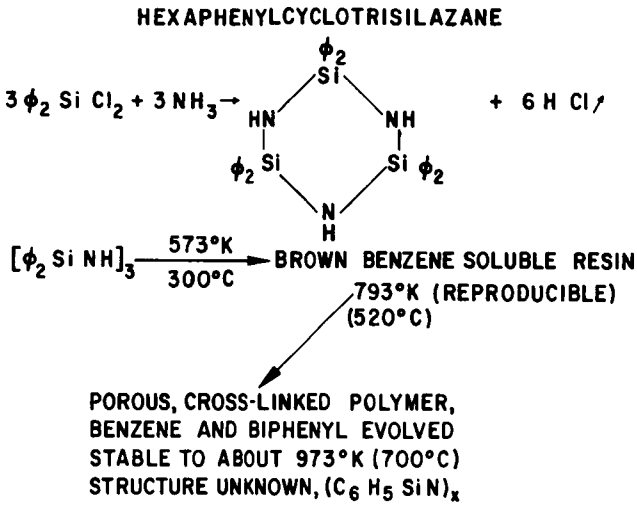

FIGURE 17. CONDENSATION REACTION OF A CYCLIC SILAZANE

of polymer is in protective coatings. Some work has been done to test this potentiality. Aluminum panels were coated with pigmented (Al and TiO_2) silazane coatings and held at 673° K (400° C) for four hours. Only the middle portions of the panels were coated, and the edges were exposed. At the temperature of exposure, the aluminum is so soft that it must be supported. Following the temperature exposure, the panels were exposed 14 days to a standard salt-spray test for protective coatings. As shown in Figure 18, the coated areas were not affected appreciably by this treatment.

A development that originated at MSFC was the evaluation of simple silazane compounds as intermediates for the formation of other polymers. Figure 19 indicates how silazanes can be used to prepare an extremely interesting family of hybrid polymers. These are half ether and half silicone, and the ordered spacing of these units down the chain length offers interesting possibilities for the development of crystalline order. The structural formula of a specific polymer of this family is given in Figure 20, and an outstanding property of this material is shown in

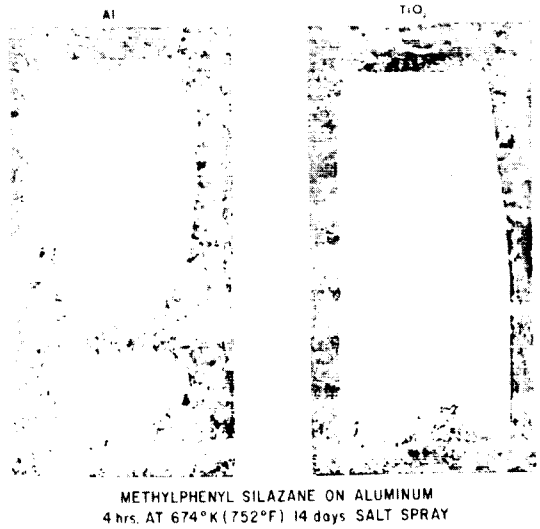

FIGURE 18. PIGMENTED SILAZANE AS PROTECTIVE COATING

INTERNAL RESEARCH

ORDERED SILICONE-PHENYL ETHER COPOLYMERS

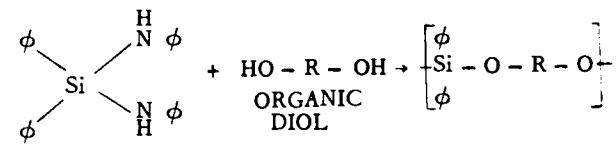

DISILAZANE

PROPERTIES:

GOOD THERMAL STABILITY
GOOD FILM FORMING PROPERTIES
SOLUBILITY
RESISTANT TO ULTRAVIOLET RADIATION (?)

FIGURE 19. ORDERED SILICONE-PHENYL ETHER COPOLYMERS

Figure 21. This shows the weight loss of the hybrid polymer under a uniformly programed rate of temperature rise in comparison with a commercial polybenzimidazole adhesive which may represent the ultimate thermal stability obtainable in a practical adhesive system. The polymer prepared locally is relatively stable and, on the basis of this behavior, it is being studied intensively to further define its high-temperature potential. The polymer has been made into fiber and film, and is being studied now as an "organic solder" in the hope that it can be converted into a crosslinkable adhesive. Full details of this work were reported by Curry and Byrd of the Materials Division (Propulsion and Vehicle Engineering Laboratory, MSFC) in Journal of Applied Polymer

Science (vol. 9, 1965), and this publication has aroused considerable interest in the future of these materials.

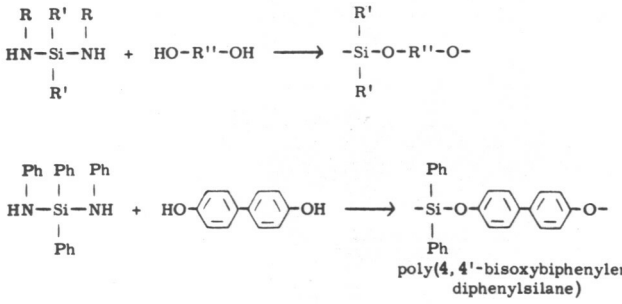

FIGURE 20. DIOL-DIAMINOSILANE REACTION

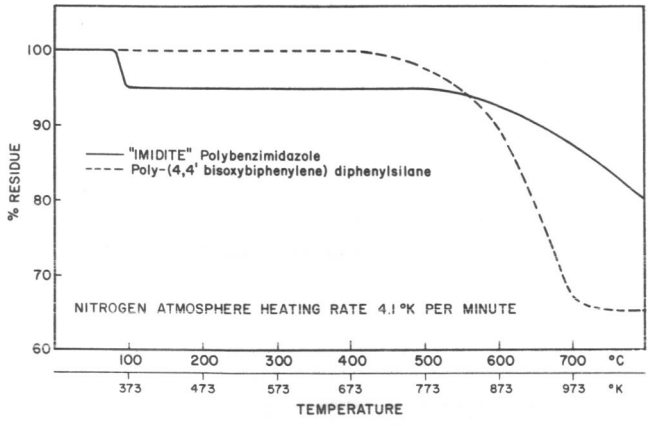

FIGURE 21. WEIGHT LOSS AT HIGH-TEMPERATURE EXPOSURE, HYBRID POLYMER VERSUS COMMERCIAL ADHESIVE

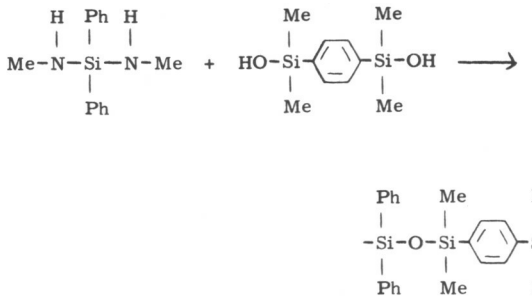

FIGURE 22. HYBRID POLYMER CONVERSION TO HIGH-TEMPERATURE ELASTOMER

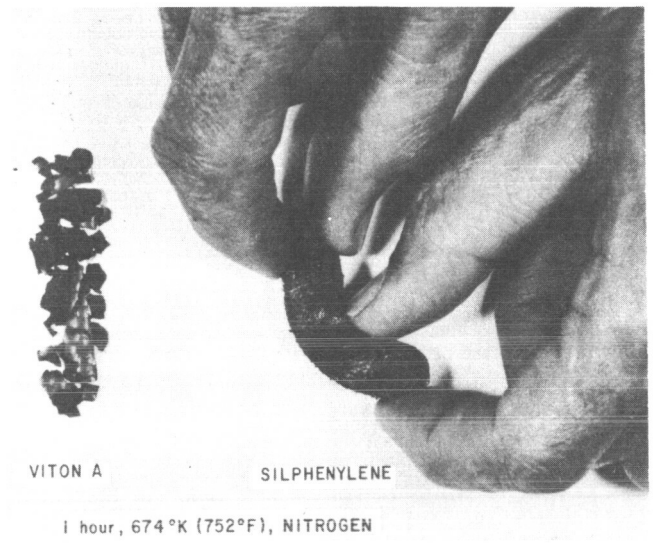

FIGURE 23. HIGH-TEMPERATURE EXPOSURE, SILPHENYLENE VERSUS VITON A

Southern Research Institute has prepared interesting variations of these polymers from silicon diols bridged by phenylene groups (Fig. 22). These materials appear to merit study as high-temperature elastomers because they respond to the same curing agents that are employed for conventional silicone rubber. In a comparison of one of the elastomers (silphenylene) with a high-temperature rubber (Viton A) under identical high-temperature exposure, the silphenylene was found to retain its elasticity while the Viton A dried and crumbled (Fig. 23).

Another idea which originated at MSFC is explained graphically in Figure 24. This appears to be a greatly improved process for the preparation of complex polymers known as polybenzoxazoles.

These polymers are not new and have been made before by a number of methods. The new feature of this process, which is the basis of another patent disclosure being submitted from the Materials Division, is the use of an aromatic diamide to form a linear polymer which is converted thermally to the highly stable polyaromatic configuration. This idea has been offered to one of our polymer research contractors who has had very good success in preparing stable polymers by this route. Although the ramifications of this explosively growing field of polymer chemistry may be discussed at much greater length, it cannot be done here. It may be noted here, however, that workers at MSFC are highly optimistic that this process will yield materials useful in many aspects of their work.

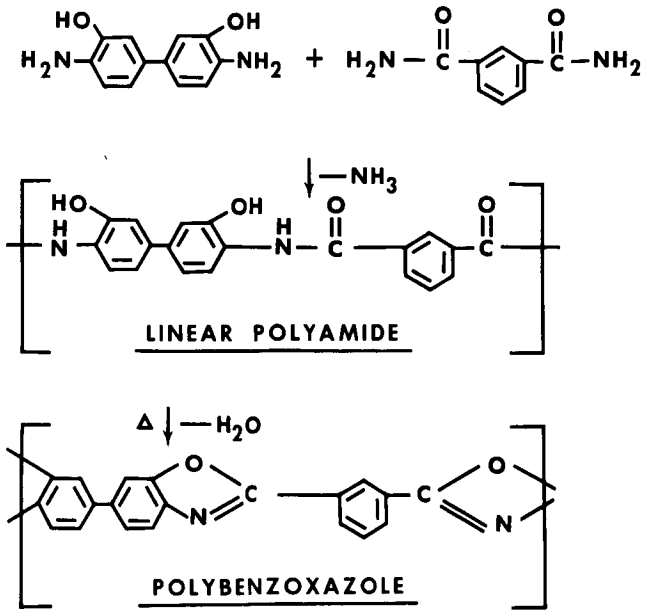

FIGURE 24. POLYBENZOXAZOLE FORMATION

2. Polymers for Low-Temperature Application. Two adhesive development programs will be discussed first. Narmco Research and Development Division of Telecomputing Corporation is continuing its original contract effort which resulted in the development of Narmco 7343, the only adhesive now available commercially that was developed specifically for cryogenic applications. The goal of this new program (NAS8-11068) is a structural adhesive that is compatible with liquid oxygen; it might be a sticky Teflon-like material which can be cured under reasonable temperature and pressure conditions. This promises to be a problem because Teflon-like materials are renowned for their lack of adhesiveness. However, the contractor has made very significant progress in the preparation of new starting intermediates which may prove capable of forming curable LOX-compatible polymers that will function as adhesives. One sample of Narmco LOX-compatible adhesive (hot melt) had a peel strength of 222 N (50 lbf) at room temperature for specimens 51 mm (2 in.) wide. This compares with 111 N (25 lbf) for a 76 mm (3 in.) specimen of HT-424.

Monsanto Research Corporation, under contract NAS8-11371, is investigating semiorganic or metal-containing polymers of potential value as adhesives. There are theoretical reasons to hope that these materials may provide usable strengths over a very broad temperature range, which may extend into the cryogenic realm.

Narmco Research and Development Division has developed an interesting new cryogenic seal material under contract NAS8-5053. Alternating plies of glass fabric and Teflon film are pressed under conditions which cause a partial flow and wetting of the fabric by the resin (Fig. 25). The resulting laminate has unique spring-like characteristics, which suggest its potential as a gasket and seal material.

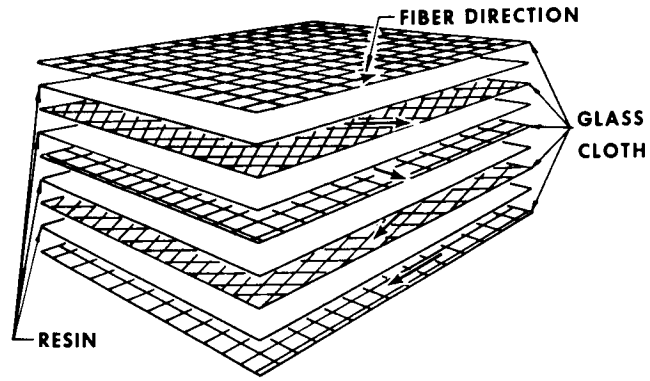

FIGURE 25. LAMINATED CRYOGENIC SEAL DEVELOPMENT

One of MSFC's oldest contract programs, and incidentally the least expensive one, has yielded some valuable information on the allowable installed lifetimes of rubber and plastic components in a semi-tropical environment. The University of Florida has a contract (NAS8-1523) to expose representative hardware containing rubber and plastic components to weather conditions in the area of Gainesville, Florida. Periodically, these valves and other items are pressure tested and cycled for evidence of seal failure due to age degradation. A parallel exposure and testing program is being conduoted in the Huntsville environment by Materials Division personnel. The findings of this program have indicated that aging under the environmental conditions of concern is not as important a problem as once was thought. Consequently, the age control documentation has been relaxed, resulting in considerable saving of cost and effort.

III. ENVIRONMENTAL EFFECTS AND PROCESSES

As was indicated earlier, considerable effort is devoted to effects of processes and environments on the properties of materials. Being studied are such things as thermal and mechanical treatment of metals, corrosion protection, and compatibility of materials with working fluids. In addition to their compatibility with materials, propellants are being studied from the standpoints of mixing phenomena, reaction

kinetics, and resultant blast effects. The Materials Division of MSFC has made and continues to make a significant contribution to the knowledge of the behavior of materials, especially metals, at cryogenic temperatures. Part of its work in this area was summarized recently in a report, "Effects of Low Temperatures on Structural Metals," NASA SP-5102, prepared by the Technology Utilization Office.

At the beginning of the RIFT Program, the Materials Division initiated a study of nuclear radiation effects on nonmetallic materials under anticipated combined environments of extreme temperatures and hard vacuum. The work was concentrated on organic materials because of their greater susceptibility to degradation and because of their critical applications in a nuclear stage.

The radiation effects studies have been done primarily at General Dynamics/Fort Worth (NAS8-2450), with less extensive but equally important support from in-house studies and cooperative programs with AEC/ORNL.

The program required the development of experimental apparatus and testing techniques that can be used under combined environmental conditions for in-situ measurements and this, alone, was a significant achievement. The devices, which are designed around standard laboratory testing methods and procedures, ensure consistency with existing data and permit direct utilization for other combined environment or hazardous testing as well as for in-flight experiments.

The evaluation of synergistic effects was necessitated because the mechanisms of material property degradation are different and competitive for the several different environments. Data on the effects of irradiating certain materials in air and in vacuum are given in Table XXI. Note the almost complete degradation of the tensile strength of neoprene and Buna N as a result of irradiation in vacuum. The Buna N became weak, tacky, and ductile as a result of the vacuum irradiation, and hard and brittle as a result of air irradiation. On the other hand, Viton A appears to be satisfactory for this environment on the basis of increased tensile strength; however, the decreased elongation would be an important consideration in the application of this material as a seal, particularly as a dynamic seal. Furthermore, Viton A is unsatisfactory for very low temperature application.

The effect of irradiating Teflon in air, vacuum, and in vacuum at a cryogenic temperature is illustrated in Figure 26. The improved stability of Teflon

TABLE XXI. COMBINED ENVIRONMENTAL TESTING OF ELASTOMERS

MATERIAL	TEST	PRESSURE N/m^2(torr)	TEMP. °K(°C)	RADIATION J(ergs/gm) (C)	TENSILE STRENGTH MN/m^2(psi)	ELONGATION PERCENT	WHERE TESTED
Neoprene (RA 24160)	Air	101 k	300	0	21.6	426	GD/FW
		(760)	(27)		(3135)		
	Vac	1.3 m	300	0	23.1	405	MSFC
		(1×10^{-5})	(27)		(3350)		
	Air/Rad	101 k	300	190	19.1	265	GD/FW
		(760)	(27)	(1.9×10^{9})	(2769)		
	Vac/Rad	667 μ	300	190	1.3	218	GD/FW
		(5×10^{-6})	(27)	(1.9×10^{9})	(191)		
Buna N (RA 30760)	Air	101 k	300	0	18.1	685	GD/FW
		(760)	(27)		(2630)		
	Vac	1.3 m	300	0	18.2	700	MSFC
		(1×10^{-5})	(27)		(2640)		
	Air/Rad	101 k	300	190	14.9	390	GD/FW
		(760)	(27)	(1.9×10^{9})	(2175)		
	Vac/Rad	667 μ	300	170	1.4	450	GD/FW
		(5×10^{-6})	(27)	(1.7×10^{9})	(203)		
Viton A (RA 26360)	Air	101 k	300	0	9.3	172	GD/FW
		(760)	(27)		(1343)		
	Vac	1.3 m	300	0	8.1	238	MSFC
		(1×10^{-5})	(27)		(1168)		
	Air/Rad	101 k	300	2000	18.1	31	GD/FW
		(760)	(27)	(2×10^{10})	(2629)		
	Vac/Rad	67 μ	316	1600	12.6	36	GD/FW
		(5×10^{-7})	(43)	(1.6×10^{10})	(1830)		

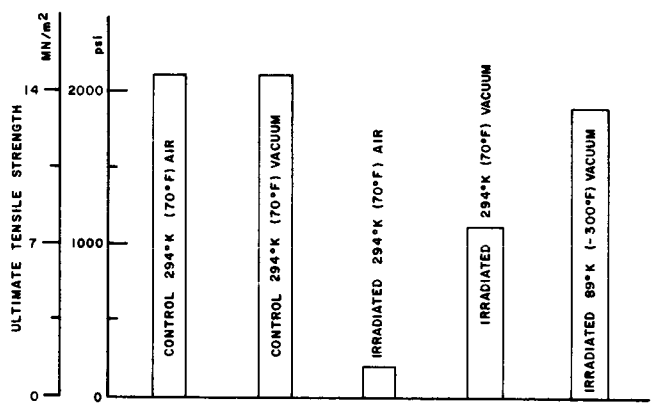

FIGURE 26. ULTIMATE TENSILE STRENGTH OF TEFLON

under the vacuum irradiation condition is well established; the combined radiation, vacuum, and cryogenic temperature environmental results, while not unexpected, were demonstrated as part of this program. The effects of irradiation of fiberglass-polyester laminate (Paraplex P-43) under several conditions are illustrated in Figure 27. As will be noticed, the effects of radiation in combination with one or more other environments cannot be determined from data for another particular combination of environments.

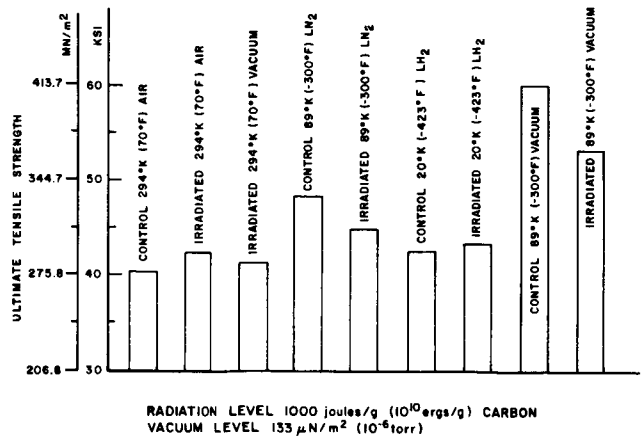

FIGURE 27. ULTIMATE TENSILE STRENGTH OF PARAPLEX P-43

Since the radiation effects testing has been done parametrically, it is believed that applicable data are now available for the design of nuclear-powered space vehicles. So that the great store of radiation effects data may be used for the design of spacecraft as well, recent work has included correlation studies between nuclear reactor radiation effects and space indigenous radiation effects.

IV. CONCLUSIONS

Some recent achievements in materials research have been discussed in this report. Some of these already have been applied in the Saturn program and others will be applied.

Although the research program has made substantial gains, all recognized problems have not been solved, and all worthy ideas for improvement have not been exploited. It is believed that the demands of advancing technology for more performance from materials will be met not by dramatic breakthroughs but by the continuous application of significant resources in a program flexible enough to allow the specialists to modify lines of investigation to take advantage of changing trends.

MANUFACTURING RESEARCH AT MSFC

May 27, 1965

by

Gordon Parks
R. J. Schwinghamer
James R. Williams
H. F. Wuenscher

TABLE OF CONTENTS

LIST OF ILLUSTRATIONS

CONTENTS (Continued). . .

ESTABLISHING A COMMON DENOMINATOR IN WELDING

by Gordon Parks

LIST OF ILLUSTRATIONS

CONTENTS (Continued). . .

RESEARCH IN SUPERPOWER LASERS AND INTENSE MAGNETIC FIELDS

by R. J. Schwinghamer

CONTENTS (Continued). . .

LIST OF ILLUSTRATIONS

INTRODUCTION TO MANUFACTURING RESEARCH AT MARSHALL SPACE FLIGHT CENTER

By

H. F. Wuenscher

Research and development in manufacturing has gained importance with the advance of the space programs. In the Apollo program, the state of the art in manufacturing technology seemed to be extended to practical limits; consequently, in many instances new approaches had to be made available by more intensified manufacturing research activity. This manufacturing research activity has the following broad purposes:

1. To provide the scientific basis for manufacturing and to establish the principles for control of all variables and boundary conditions.

2. To develop new manufacturing concepts by application of existing and new scientific principles.

3. To verify the feasibility of advanced concepts in experimental manufacturing applications.

The major areas in which MSFC is doing in-house or contract-supporting manufacturing research and development in fulfillment of these general purposes are listed in Table I.

TABLE I. MANUFACTURING RESEARCH AND DEVELOPMENT AT MSFC

MANUFACTURING RESEARCH	
Techniques	
Welding	Bonding
Brazing	Chemical processing
Soldering	Electrical processing
Mechanical joining	Thermal treatment
Forming	
Material removal	
Material deposition	
Sterilization	
Concepts	
Tooling	Metrology
Handling and Cleaning	
EXPERIMENTAL MANUFACTURING	
Element development for structures and systems	
Configuration development for structures and systems	
Space manufacturing for orbital and lunar operations	

The three reports which follow cover research achievements such as welding, bonding, forming, and the use of intense magnetic fields and lasers for novel processing and tooling concepts. The status and results of MSFC research work in all the other areas are given in the supporting research and technology reports published in the semiannual progress reports issued by Research Projects Laboratory. Although this achievement review cannot give details of all Manufacturing Engineering research and development, some of the interesting projects which are not covered in detail in the reports which follow will be mentioned here.

Research and development contracts in the field of high-frequency welding and in diffusion bonding were started late in fiscal year 1965. This work will pioneer the "perfect" joining of metals to form large, one-piece ("unitized") structures. Beyond structural improvement for the present programs, such joining processes are important for possible manufacturing application in space vehicle programs.

In regard to tooling research, the modular tooling concepts in weld joining of large structures, new approaches in automation and measuring technology, and local environmental control concepts have gained basic importance for the present program.

Experimental manufacturing, which provides the only realistic test bed for large-scale verification of manufacturing research results, is subdivided under the categories of development of structural elements, configuration development, and manufacturing development for space programs.

One example of the development of structural elements is the 2.4-meter (8-foot) long ultralightweight box beam series, in which similar beams are optimized in high-strength aluminum, titanium, beryllium, Lockalloy, magnesium-lithium alloy, and fiberglass. This work is being done to establish state of the art limitations and to provide the necessary support in manufacturing process research to the point at which space vehicle application becomes feasible.

Another example is the insulation systems development in the short-duration double seal and the

long-duration multilayer radiation barrier superinsulation. Here the manufacturing feasibility for system elements such as penetrations by the supporting structure and fuel lines, and manhole cover closeouts and vacuum-sealed jackets, determine to a large extent the systems configuration. The research work in energy-absorbing elements should be mentioned, because the extruding tube mode, used for absorbing the Saturn V launch release shock loads, basically uses a manufacturing process. There is a very promising new mode under development in which wire rings are rolled over and over between telescoping tubes. This is a unique reusable energy absorber and is now under consideration for use on the Lunar Excursion Module and the Lunar Hopper.

The configuration development program consists of a number of common-dome conceptions such as the bonded strip seal and the all-welded face-sheet versions. Furthermore, a series of configuration developments for tanks 5 meters (200 inches) in diameter provide the basis for development and verification of many manufacturing research projects. As an example, the magnetomotive hammer principle was first used for the experimental multicell tank. Also, tack welding and subsequent automatic skate welding were first used at MSFC as a new modular concept for large space vehicle manufacture.

The second experimental tank, being assembled now, is a torus tank, made of a new type high-strength aluminum alloy, 7039, for which new forming processes, magnetomotive flaring processes, and advanced welding concepts are used. A third experimental tank of semitoroidal shape is in preparation.

Application of manufacturing processes in orbit and on the moon for maintenance, repair, modification, and even orbital assembly and lunar manufacturing, is entering the study phase within the Apollo Applications Program. MSFC is selecting manufacturing processes which could utilize the space environment to their advantage, and is looking for tooling concepts suitable for the given payload and power conditions. All this is in preparation for the planned activities in the fiscal year 1966 and beyond.

MANUFACTURING RESEARCH IN SUPPORT OF SATURN V

By

James R. Williams

SUMMARY

Research achievements applicable to the production of Saturn V components are described in this report.

Leakage at the mechanical connections in high-pressure lines has been minimized or eliminated through the use of precisely flared tubes. Flaring to close tolerance is done with an orbital flaring adapter, and the forming operation is precisely controlled with an electronic control console.

A technique of "aging" or heat-treatment hardening of aluminum materials has been used to form cylindrical-tank segments and double-contoured gore segments precisely, and to remove weld distortions.

The control of weld porosity has been improved as a result of research which demonstrated the close correlation between electrical energy input per inch of weld and weld porosity and metallurgical quality. Based on this information, the gas metallic arc method has been used successfully for two-pass welding, and thinner gage aluminum has been welded (LOX tunnel to fuel bulkhead) with an MSFC designed gas metallic arc unit.

Much research has been done in processing and assembly techniques as they apply to composite structures and materials. Using brackets and fasteners on Saturn wall structures as well as strengthening and repairing substandard tank structures have been made possible by the studies in adhesive formulation and application. Other investigations are concerned with the fabrication of double-curvature common bulkheads and with improvements in fabrication technology of other bulkhead structures.

Tooling costs have been reduced as a result of the development of skate-type tooling for S-IC gore-edge trimming. Research is continuing on self-regulating skate systems.

Control techniques for milling by chemical etching have been developed. As a consequence, chemical milling has been used extensively for Saturn V gore segments.

I. INTRODUCTION

This report reviews manufacturing research achievements which are being used today to assist in the production of Saturn V components. Manufacturing technology required for the Saturn V vehicle covers a broad range of requirements. The following, which are typical areas of research application, are discussed in detail:

1. High-pressure liquid and pneumatic ducting systems
2. Age forming and sizing
3. Welding research applications
4. Composite structures research applications
5. Tooling research and applications
6. Chemical milling.

These research applications reflect the cooperative effort of MSFC and the stage contractors in defining common problem areas, outlining research projects, and applying the gain of knowledge to the original problem.

II. HIGH-PRESSURE LIQUID AND PNEUMATIC DUCTING SYSTEMS

A problem which has been general for all organizations building Saturn hardware is manufacturing leak-tight liquid and pneumatic ducting systems for the vehicle. The defect is leakage at the mechanical connector of the higher pressure ducting systems, which operate at pressures up to 27.6 MN/m^2 (4000 psi). The connectors join the many subsystems throughout the Saturn vehicle. For example, the first stage alone of the Saturn V space launch vehicle required over 1000 flared-tube connectors of the design shown in Figure 1.

Component designers and fabrication research personnel are working to eliminate mechanical connections through welding and brazing. However,

many mechanical connections are still required to permit effective use of subassembly and modular fabrication principles.

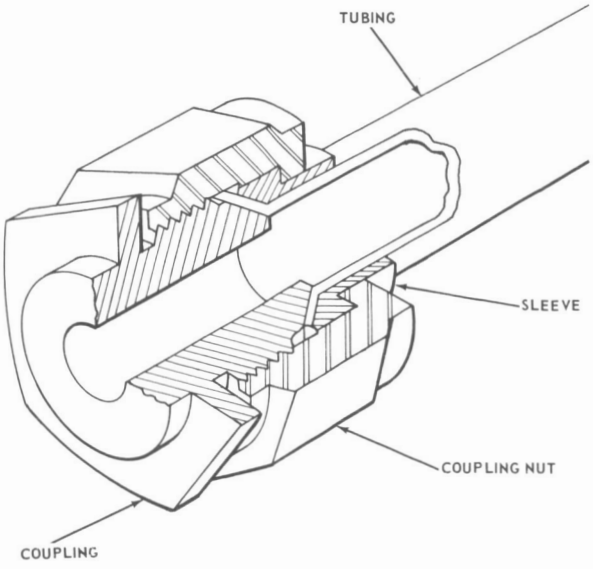

FIGURE 1. FLARED TUBE CONNECTOR USED ON THE S-IC STAGE, SATURN V

A typical installation using hundreds of these flared-tubing connections is the S-II stage (built by North American Aviation) shown in Figure 2. The majority of the flares are on tubes with a diameter of 25.4 mm (1 inch) or less.

The major deficiency of this type of connector has been the inconsistent configuration of the tube flare. Experience and testing indicated that if the flare could be formed to very close dimensions, the major leakage problem would be eliminated.

Research funding during the past three years has made it possible for Manufacturing Engineering Laboratory of MSFC to develop a unique technique of precision tube flaring which produces the characteristics required by tube flare design standard MC-146. These basic requirements are shown in Figure 3. The flared end of the tube must be round within 0.02 mm (0.0008 inch) TIR, the ID angle and OD angle each must be within ±0.0087 radian ($\pm\frac{1}{2}$ degree) of the basic 0.65 radian (37 degree) and 0.58 radian (33 degree) designation, respectively, and it is necessary to control the major diameter of the flare within 0.254 mm (0.010 inch). The roughness allowance of the sealing surfaces is 0.0004 mm (16 microinches) for stainless steel and 0.0008 mm (32 microinches) for aluminum tubing.

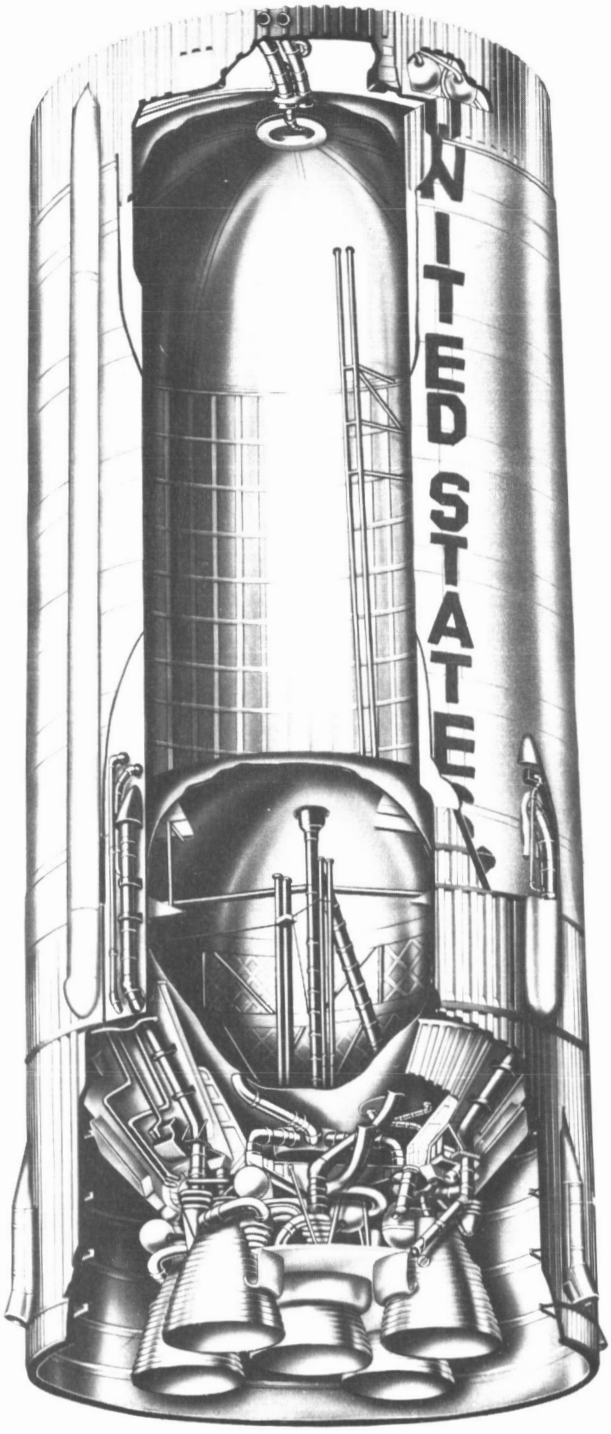

FIGURE 2. INSTALLATION WITH FLARED TUBING CONNECTIONS ON THE S-II STAGE, SATURN V

This dimensional quality is constantly reproducible by use of the orbital flaring adapter developed by MSFC (Fig. 4). The tool, which attaches to a standard Leonard 3CP flaring machine, exploits the principle of rolling the material on the

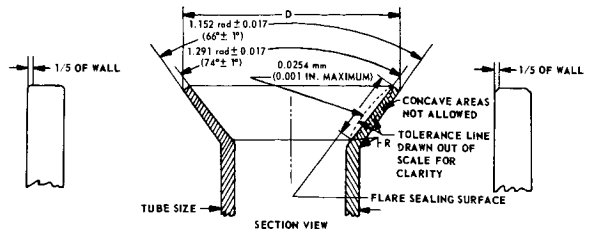

NOTE 6 DEBURR EDGES BEFORE FLARING.

NOTE 3 FLARE SEALING SURFACE TO BE CONCENTRIC WITH O.D. OF TUBE WITHIN 0.7620 mm (0.0030 IN.) TIR

NOTE 4 FLARE SEALING SURFACE TO BE ROUND WITHIN 0.0203 mm (0.0008 IN.) TIR.

NOTE 5 SEALING SURFACE NOT TO EXCEED 16 FOR STEEL AND 32 FOR ALUMINUM

NOTE 7 NO RADIAL SCRATCHES ON FLARE

TUBING OD mm	TUBING OD (IN.)	D, DIA mm	D, DIA (IN.)	D, TOL mm	D, TOL (IN.)
3.2	(1/8)	5.1	(.200)		
6.4	(1/4)	9.1	(.359)	+0.000	
9.5	(3/8)	12.3	(.484)	-0.254	(-0.010)
12.6	(1/2)	16.7	(.656)		
19.1	(3/4)	23.8	(.937)		
25.4	(1)	30.1	(1.187)	+0.000 -0.381	.0.015

FIGURE 3. BASIC REQUIREMENTS OUTLINED BY TUBE FLARE DESIGN STANDARD MC-146

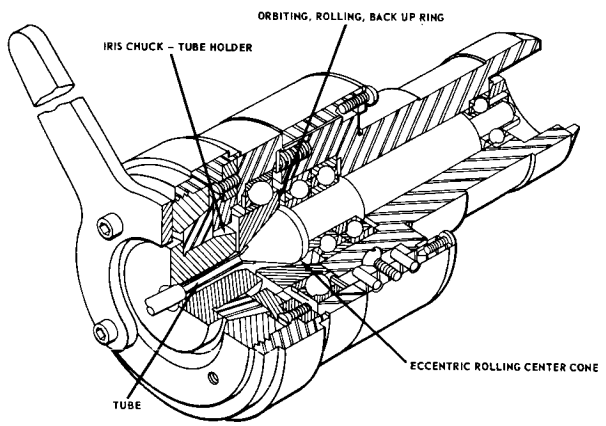

FIGURE 4. ORBITAL FLARING ADAPTER DEVELOPED BY MSFC

flared end of the tube from both sides simultaneously with an ID cone and an OD rolling die.

Precision control of the forming operation is obtained by use of an MSFC-developed electronic control console, shown in Figure 5. The electronic console provides the operator with precision control over important phases of the forming operation such as flaring pressure, machine speed, and the number of revolutions.

The results of this improved flaring capability are shown in Figure 6. Here a comparison is made of the spread of angular tolerance for seven different sizes of tubing produced by the new dual-rolling technique and by the split-die method.

Although efforts are currently underway to automate completely the flaring operation to improve the quality of the flare further, all of the required characteristics of the design specification MC-146 can now be produced with a high degree of consistency.

This development of the flaring tool and electronic control console is currently being introduced into manufacturing engineering shops. Many of the Saturn stage contractors are already using or are evaluating this new development for use in their programs.

III. AGE FORMING AND SIZING

An interesting research project using the "aging" or heat treatment hardening of aluminum resulted in precise forming of contours of the very large Saturn V first-stage cylindrical tank segments and the double contoured gore segments. The aging process consists very simply of restricting the oven-warm aluminum alloy material to a shape for a period of time until it conforms to the desired contour.

Aging, as related to type 2219 aluminum alloy, is the metallurgical process which is used to obtain the maximum strength from the material. Relatively soft 2219 aluminum alloy is heated to 436°K (325° F) for 24 hours. During this time there is rearrangement of the crystalline structure of the alloy, with the result that the material increases its strength approximately 40 percent.

Exploiting this phenomenon, Boeing Company and MSFC embarked on several research programs to determine whether the 2219 aluminum components of Saturn V could be formed or their contours corrected during this aging cycle. An MSFC-funded research program at Boeing proved that 2219 aluminum alloy would respond desirably to the age-forming techniques.

Figure 7 illustrates the practice now employed by Boeing to form the large cylindrical skin panels for the S-IC LOX (liquid oxygen) and fuel tanks. The flat machined parts are wrapped onto a ruggedly built contoured fixture and then placed in a furnace for the prescribed time and temperature. During this period, stresses are relieved and hardening takes place. A 25-percent springback allowance is compensated for in the design of the holding fixture. After release from the fixture, the part is perfectly contoured to the desired radius. The completed part in a contour inspection gage is shown in Figure 8.

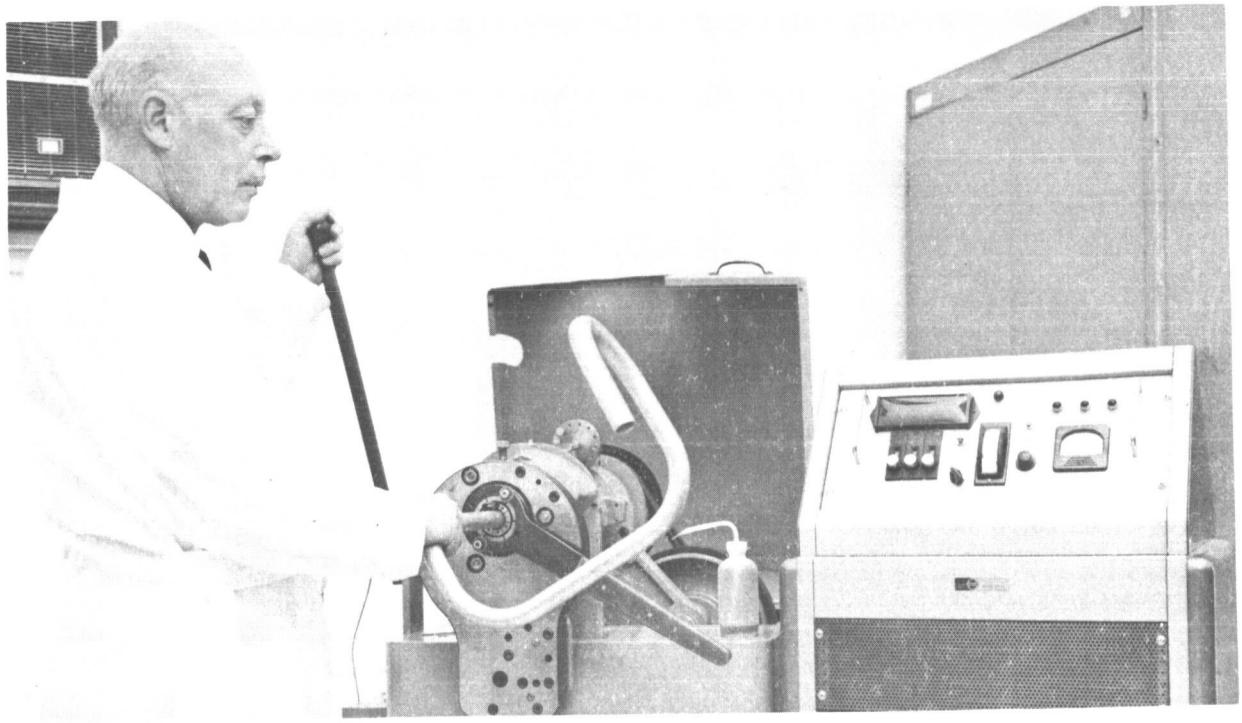

FIGURE 5. ELECTRONIC CONTROL DEVELOPED BY MSFC FOR TUBE FLARING

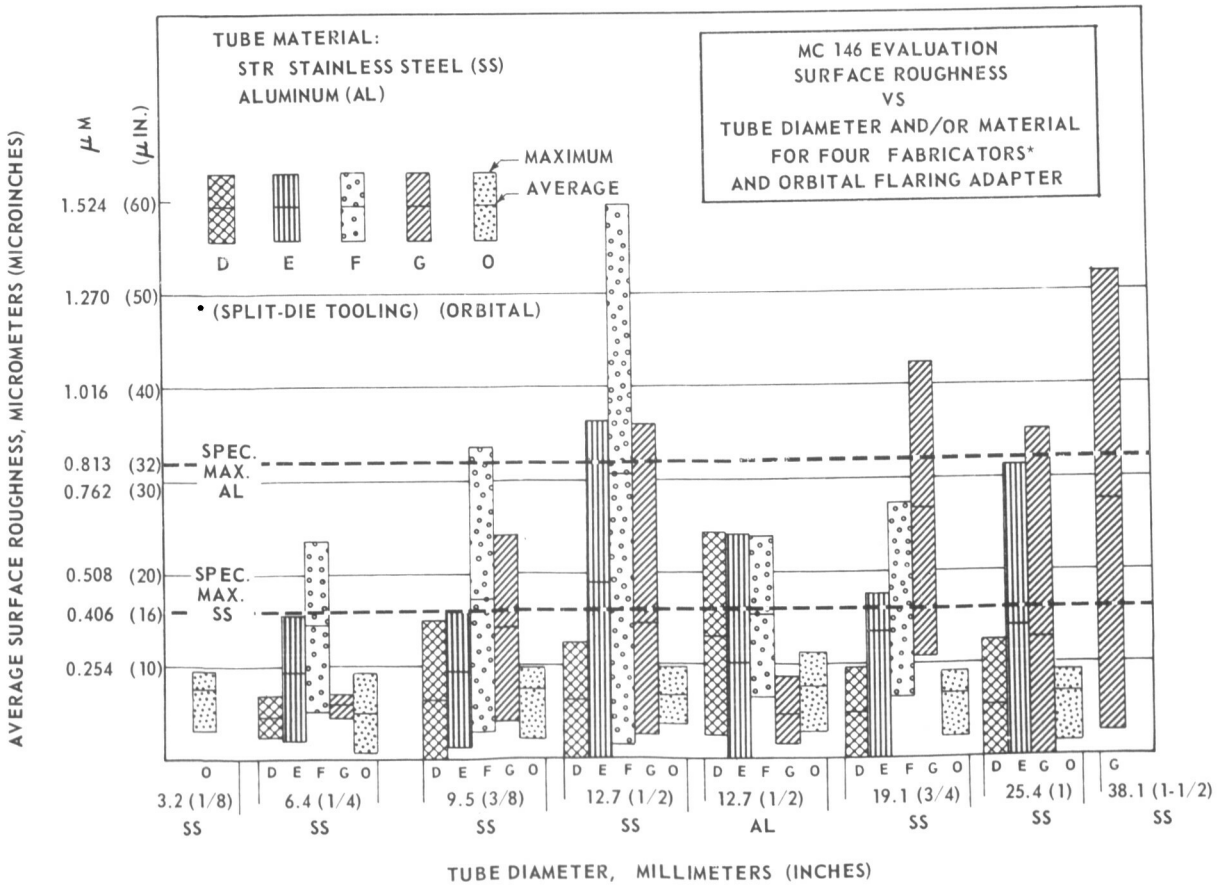

FIGURE 6. COMPARISON OF TUBE SURFACE ROUGHNESS, ORBITAL FLARING VERSUS SPLIT-DIE METHOD

MSFC engineers also exploited this age-hardening principle to remove weld distortion from the gore segment and fitting subassemblies. The gore segments for the LOX and fuel bulkheads are welded in the T-4 or semihard condition. Figure 9 shows a correct-contour fixture of the type provided for holding the distorted part to the desired contour during the aging cycle.

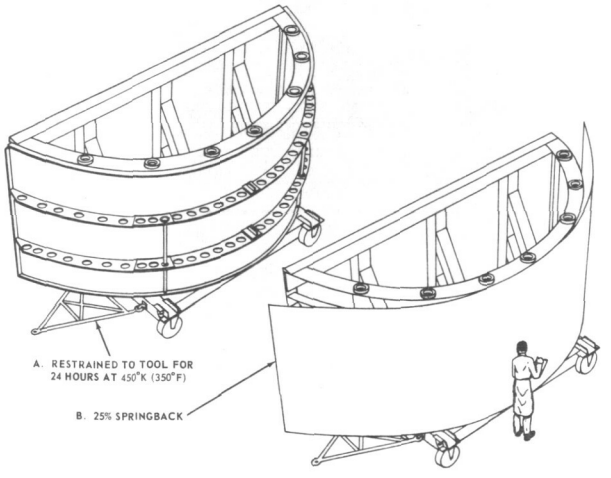

FIGURE 7. AGE FORMING THE LARGE SKIN PANELS FOR CYLINDRICAL S-IC LOX AND FUEL TANKS

After the part has been clamped to the fixture, it is subjected to furnace heat treatment for 24 hours at 436°K (Fig. 10). During this time, most of the weld stresses are relieved and the material becomes metallurgically stronger and more rigid, and after removal from the fixture it resists returning to its distorted contour.

North American Aviation has also adapted this age-sizing technique to improve the contour of the welded 2014 aluminum alloy gore segment subassemblies on the S-II stage.

The applications of the research project findings to full-scale hardware at MSFC, Boeing, and North American Aviation have resulted in reduced processing costs and improved quality of parts.

IV. WELDING RESEARCH APPLICATIONS

A major problem in welding type 2219 aluminum alloy is porosity control as related to the mechanical and metallurgical properties of the weld. During the past two years, several welding research projects were directed toward relating weld porosity and metallurgical quality to the electrical energy input per inch of weld. The research projects revealed a very distinct correlation for these factors in reference to aluminum alloys used on the Saturn

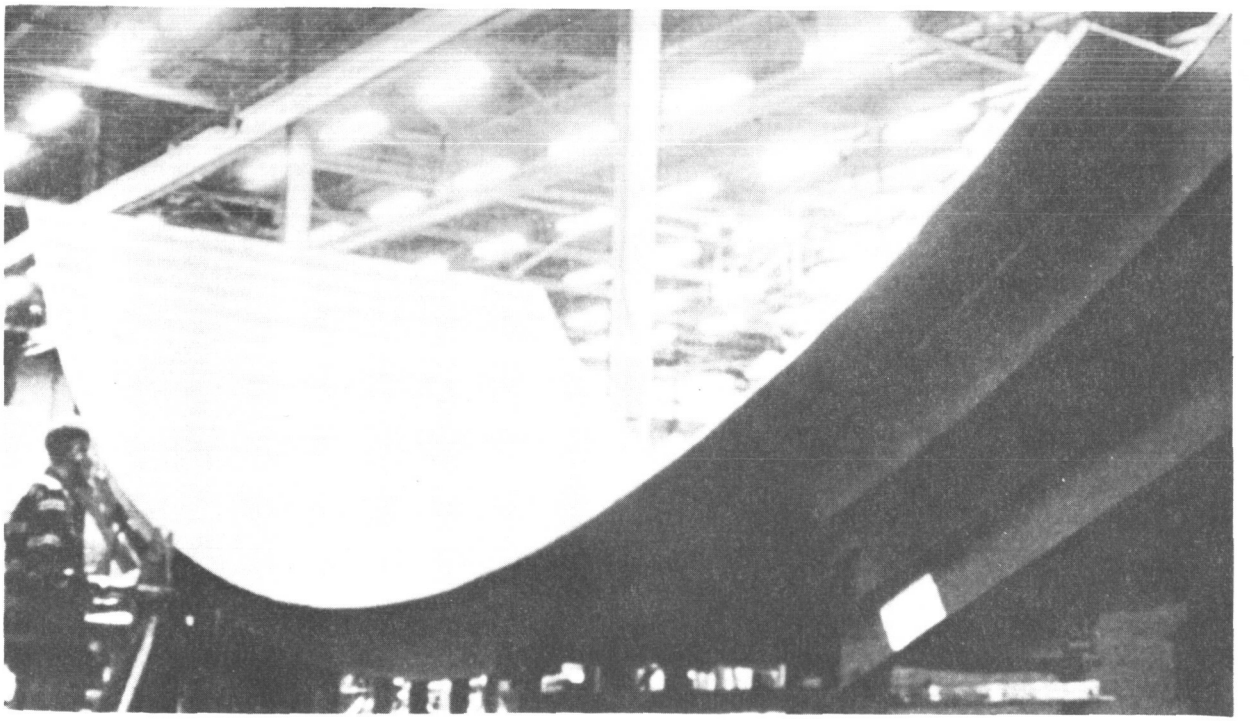

FIGURE 8. FORMED PART IN A CONTOUR INSPECTION GAGE

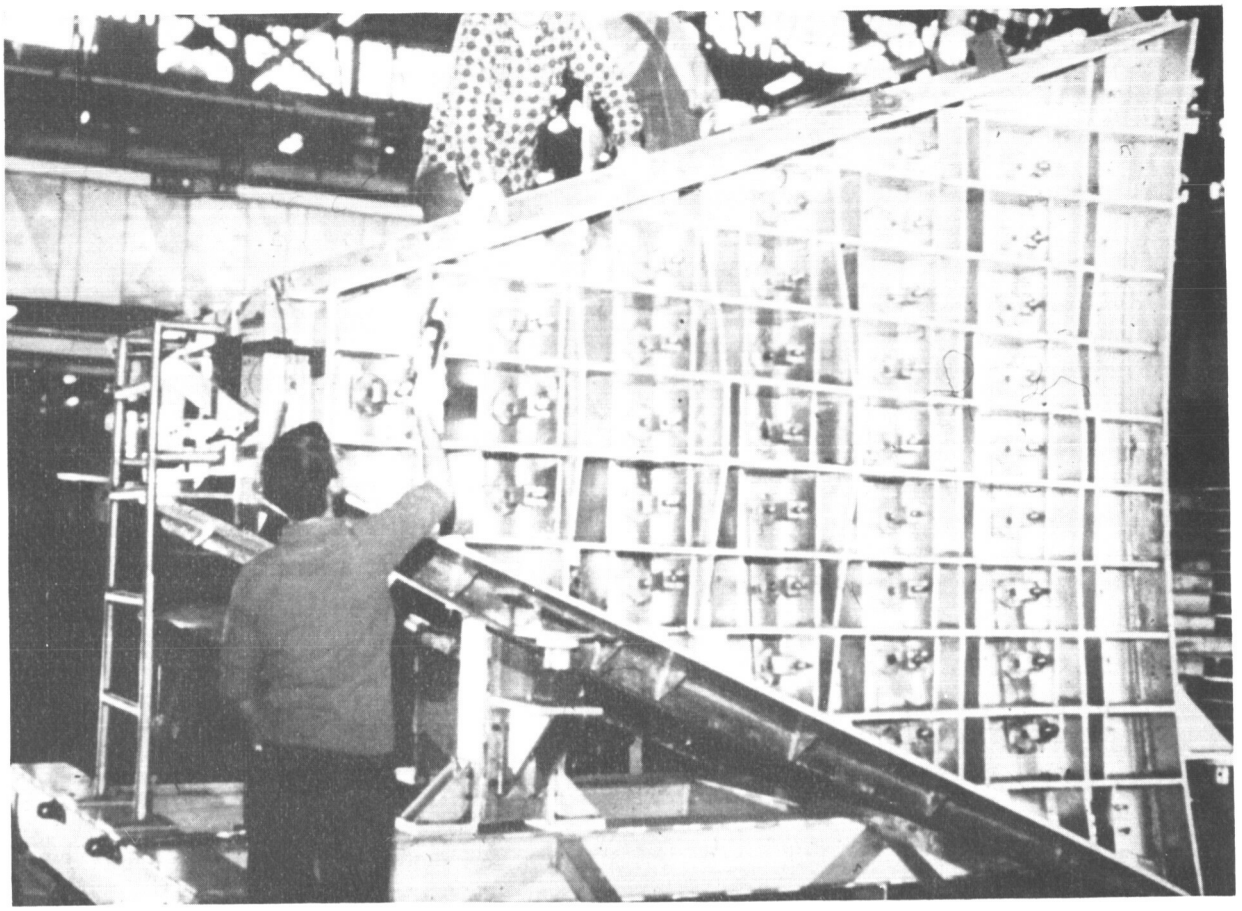

FIGURE 9. CONTOUR FIXTURE

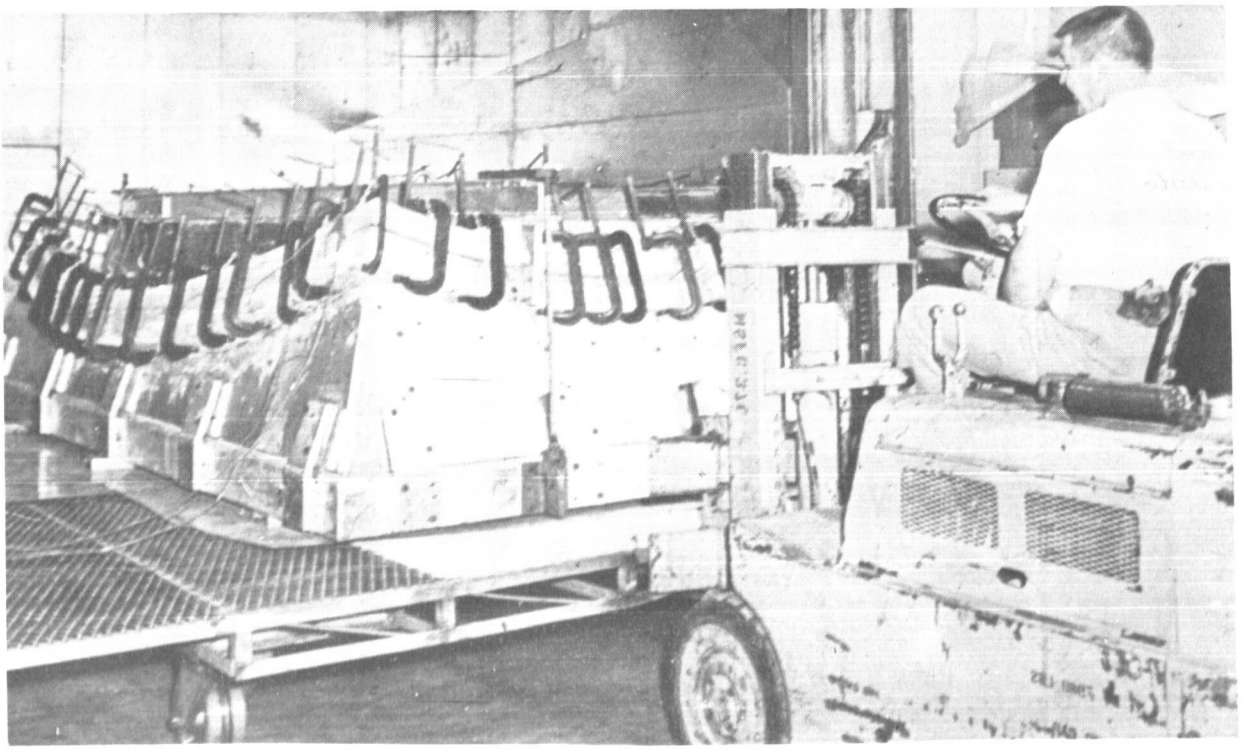

FIGURE 10. AGING FIXTURE

vehicle. Basically, as the energy input rate was lowered, porosity decreased and the mechanical and metallurgical properties improved.

The knowledge gained in this series of research projects is now used throughout the Saturn program and it also applies to material other than aluminum, such as the hardenable stainless steels.

The findings of the weld research program are particularly applicable in welding the thinner gages [6.35 to 25.4 mm ($\frac{1}{4}$ to 1 inch)] of 2219 aluminum alloy used on the Saturn S-IC tank structure.

Figure 11 illustrates the horizontal welding of the Y-shaped transition ring to the dome-shaped tank closure. Initially, MSFC used the gas tungsten arc (GTA) process on this 5.7 mm (0.224 inch) thick joint, but the quantity of weld porosity was unacceptable.

Data obtained in MSFC research dictated the use of a lower-energy level type of weld. The final selection was a two-pass weld with the gas metallic arc (GTA) process, which produced excellent results on the first effort.

Another recent application of this energy control technology was the welding of aluminum LOX tunnels into the fuel tank (Fig. 12). Previously MSFC had attempted to produce this horizontal circular weld by means of the GTA process, but the slow rate of deposition of the weld metal caused objectionable weld porosity and excessive distortion of the relatively thin walls of the 2219 aluminum alloy tube.

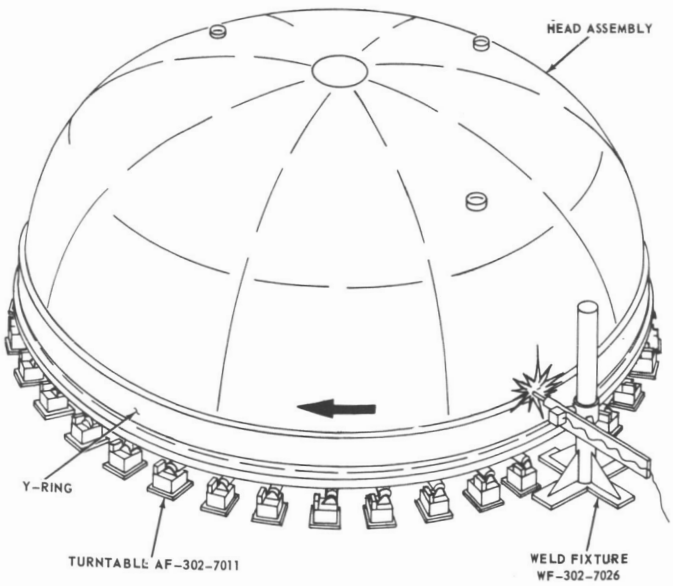

FIGURE 11. HORIZONTAL WELDING OF Y-SHAPED TRANSITION RING TO THE DOME-SHAPED TANK CLOSURE

Using research data and the knowledge gained by MSFC and Boeing in welding the thinner gage aluminum bulkheads by the high-speed GMA process, MSFC engineers designed and built a GMA mechanized unit for welding the LOX tunnel end to the lower bulkhead. Figure 13 is a diagrammatic illustration of the machine attached to the vehicle in position for welding.

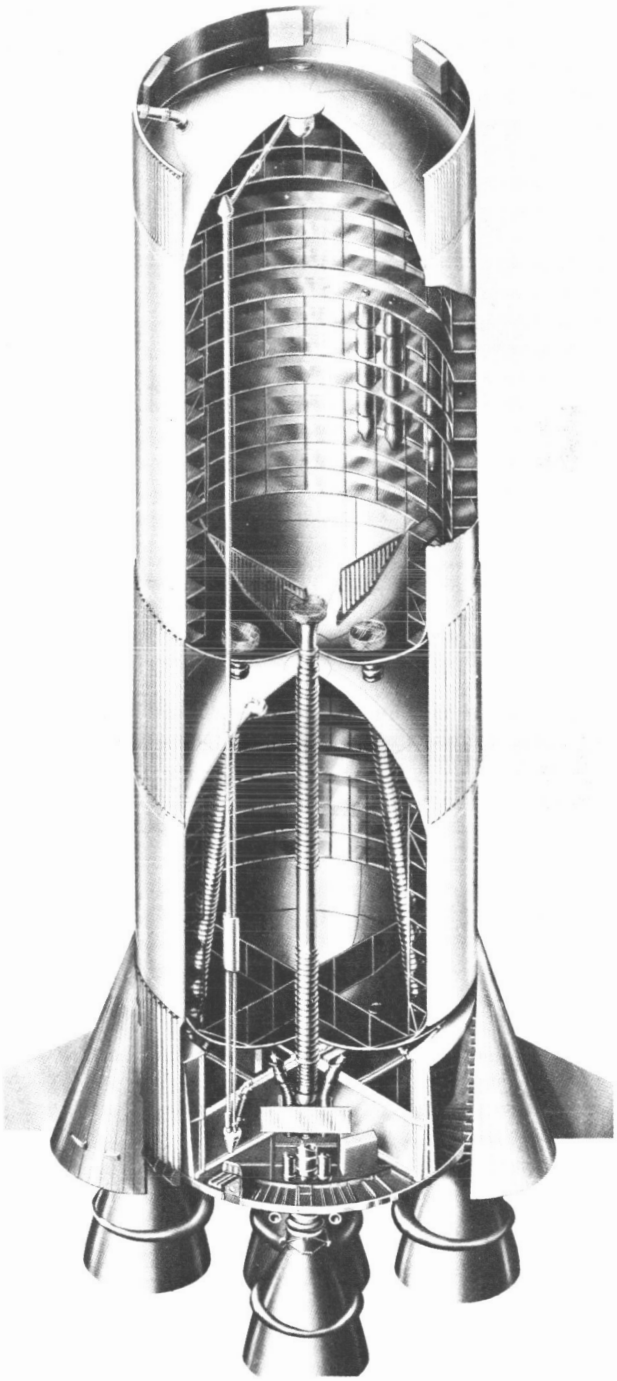

FIGURE 12. CUTAWAY VIEW OF LOX-TUNNEL WELD

The above-mentioned examples do not mean that GTA welding does not have its place within Saturn V welding requirements. On the contrary, it is particularly applicable to 2219 aluminum alloy in gages above 9.5 mm (3/8 inch) thickness. Shown in Figure 14 is a typical GTA welding setup. Electrical energy input rate, which must be considered, is determined by the ability of the thicker materials being welded to carry away excessive and damaging heat generated during welding.

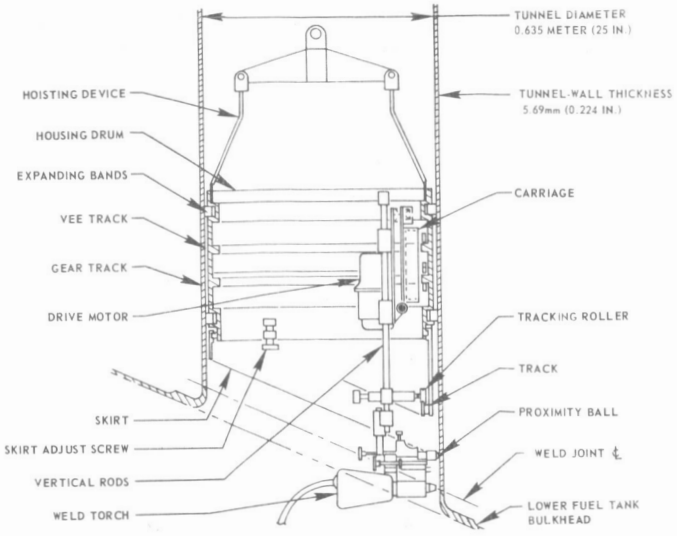

FIGURE 13. LOX-TUNNEL WELDING MACHINE

Energy control research has not provided answers to all MSFC welding problems, but it has provided experience and information which have become useful for determining the causes of many other Saturn V welding problems and for solving them.

V. COMPOSITE STRUCTURES RESEARCH APPLICATIONS

One of the newer areas of fabrication development applicable to Saturn hardware is the composite type of structure. A composite structure is defined as one composed of a variety of materials (e.g., aluminum, plastics, etc.) joined by adhesives, mechanical fasteners, welding, etc. This type of structure offers major advantages in weight savings and insulation characteristics, which are important

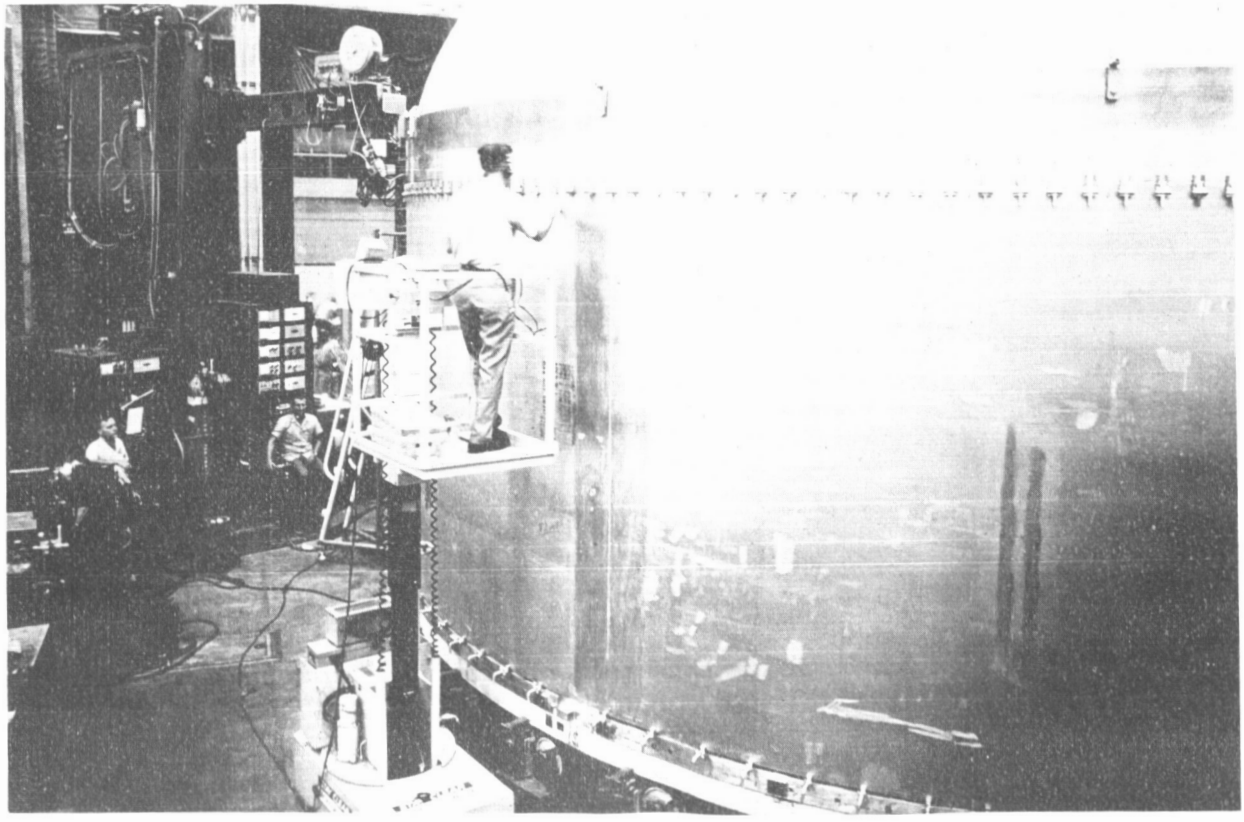

FIGURE 14. TYPICAL GTA WELDING SETUP

in producing a more efficient space vehicle. A typical composite structure is shown in Figure 15, and actual and potential applications are illustrated in Figure 16.

Manufacturing Engineering Laboratory has sponsored many research programs on composite structures. Because the advantage of the best of any material selection can easily be nullified by improper fabrication processes, the objective usually has been related to developing assembly and processing techniques for materials previously selected by the Propulsion and Vehicle Engineering Laboratory.

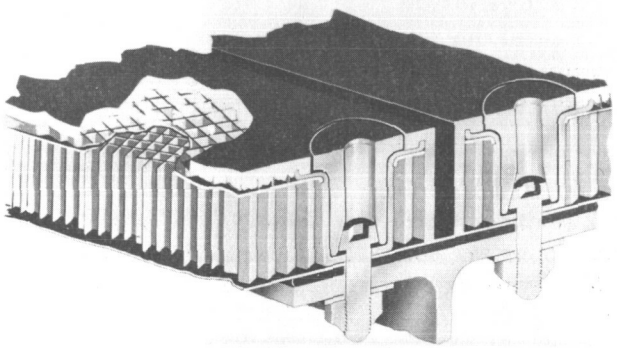

FIGURE 15. TYPICAL COMPOSITE STRUCTURE

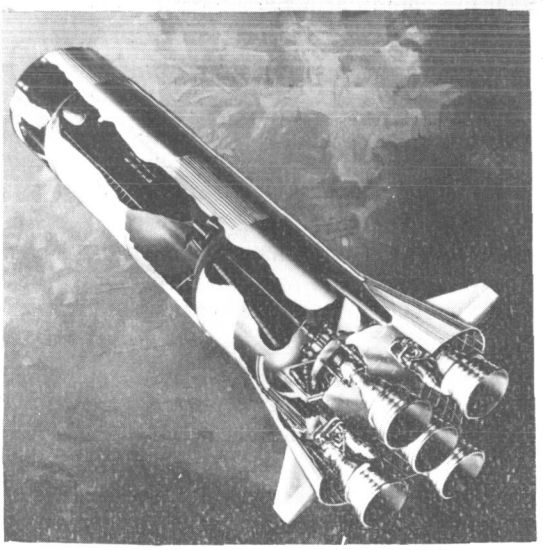

FIGURE 16. CURRENT AND POSSIBLE APPLICATIONS OF COMPOSITE STRUCTURE ON S-IC STAGE, SATURN V

Figure 17 shows the S-II test panels fabricated by Manufacturing Engineering Laboratory being fitted to an evaluation tank. The Laboratory's research in this project helped to define characteristics such as material preparation and cleaning, application techniques for the various adhesives, vacuum-bagging methods, development of time and temperatures to obtain desired properties from the adhesives, and the handling methods for the large insulation panels during all phases of fabrication.

Problems often reveal themselves during a phase of fabrication; an example is the cracking at the seal or doubler strips between the large subassembled panels. Numerous closeout configurations were considered, fabricated, and tested. Figure 18 illustrates a type of joint which can offer adequate flexibility and expansion characteristics to prevent cracking and thus maintain the gas-tight seal required for optimum insulation properties.

Adhesives developed through research in adhesive fabrication currently are being used to bond special bracketry and fasteners on the tank walls of

FIGURE 17. S-II TEST PANELS BEING FITTED TO AN EVALUATION TANK

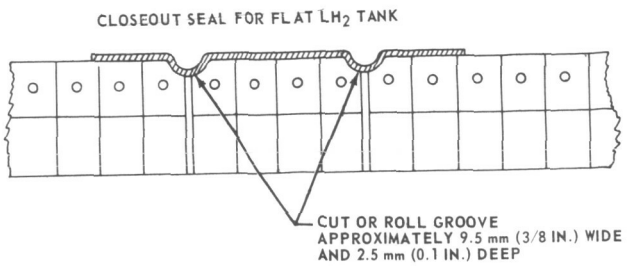

FIGURE 18. FLEXIBLE GAS-TIGHT SEAL

the Saturn structure. This bracketry is used for a variety of purposes, for example, holding special instruments in place and providing support points for flight electrical control cables. Adhesively bonded patches also have been successfully used to strengthen a damaged or substandard tank structure.

Another important composite fabrication problem under intensive investigation deals with the techniques for building common bulkheads or a structure of double curvature. A typical common bulkhead structure on the third stage of the Saturn vehicle is shown in Figure 19. Current research projects also are intended to improve fabrication technology and subsequent reliability of similar bulkhead structure for the Saturn V second stage.

VI. TOOLING RESEARCH AND APPLICATIONS

Tooling research as related to welding and routing skates is being done at MSFC in an attempt to lower tooling costs.

Figure 20 illustrates the principle of skate-type tooling. A track is attached to, or aligned along, a weld seam or edge trim zone. A carriage carrying a weld head, or a router, skates along the track at a preset rate.

Figure 21 shows an application of skate research which involves the S-IC gore-edge trimming operation. The part is held in position against the polka-dot vacuum chuck and the skate travels along the arc-shaped track.

Figure 22 shows a similar application of surface trimming the honeycomb core during the manufacture of the S-II common bulkhead.

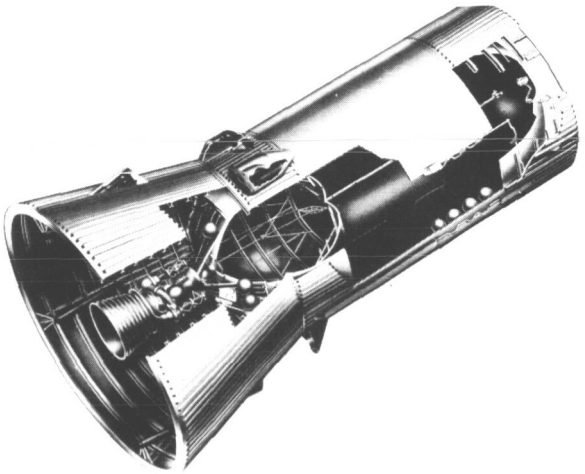

FIGURE 19. TYPICAL COMMON BULKHEAD STRUCTURE ON THIRD STAGE OF SATURN VEHICLE

Currently research work is underway on skate systems which are self-regulated through the use of various systems of arc guidance or analog computers, or both.

VII. CHEMICAL MILLING

The purpose of an important series of research projects on the chemical processing of types 2219 and 2014 aluminum alloy has been to determine the control techniques for chemically milling and surface treating these Saturn V materials. Chemical milling is the process of removing metal by chemical etching. Results of this process on the base and apex gore segments are shown in Figure 23.

Undesirable results of chemical milling included a wavy milled surface or one with a rough texture caused by an uneven rate of etching in recessed areas.

A series of research contracts was established with several commerical chemical companies to develop etchants and processes to avoid these defects. As a result of these contracts, hundreds of large gore segments used on all stages of the Saturn V vehicle have been chemically milled, with thickness and surface roughness successfully controlled.

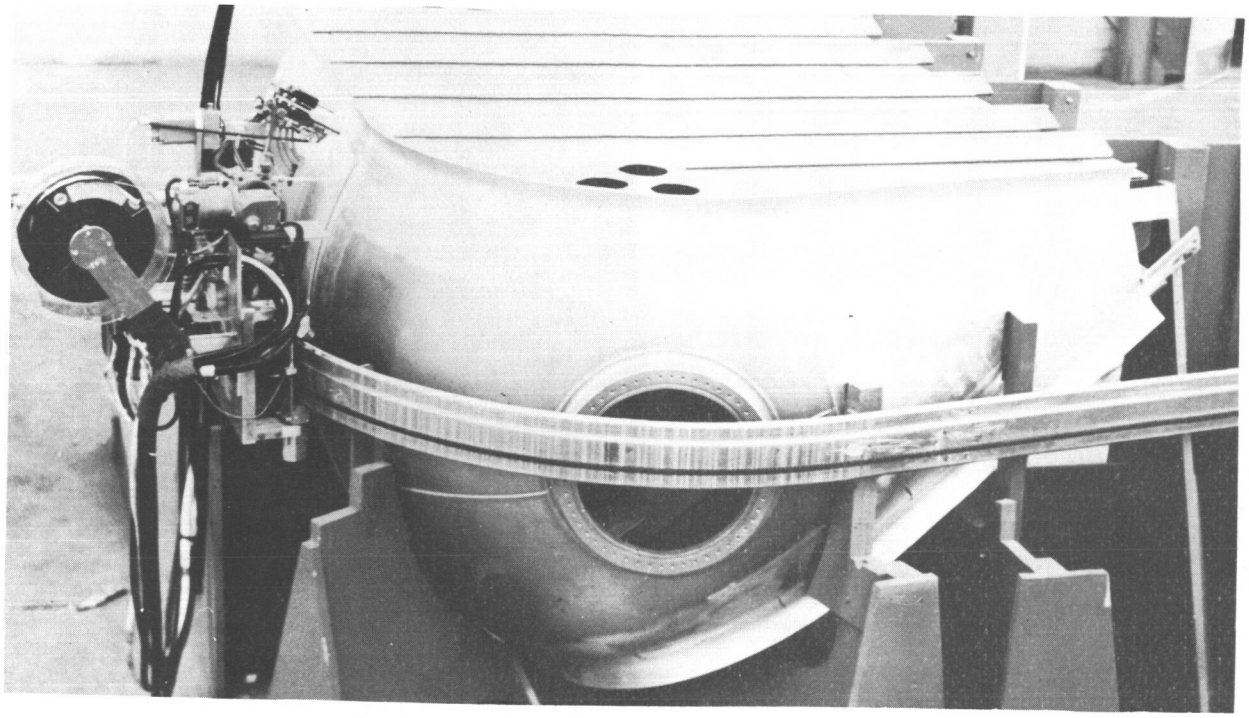

FIGURE 20. EXAMPLE OF SKATE-TYPE TOOLING

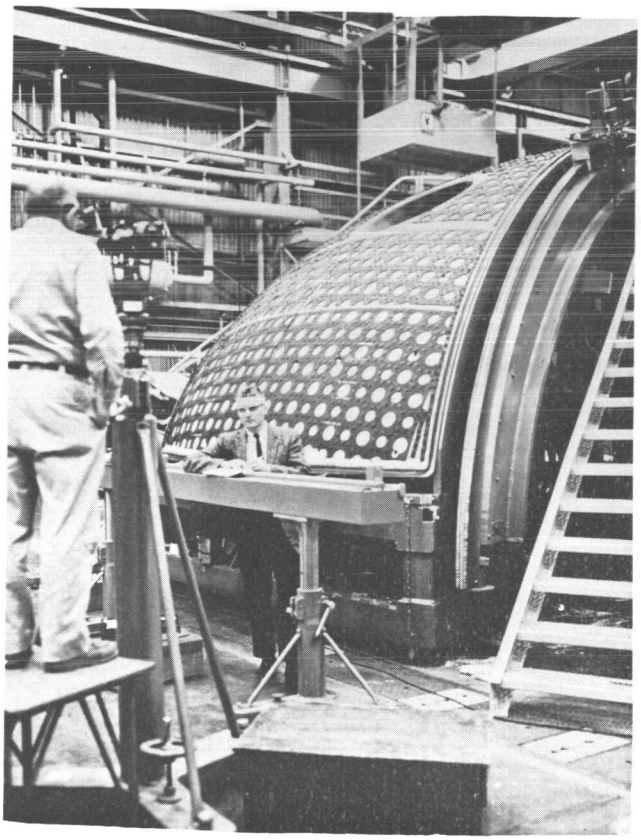

FIGURE 21. S-IC GORE-EDGE-TRIM OPERATION

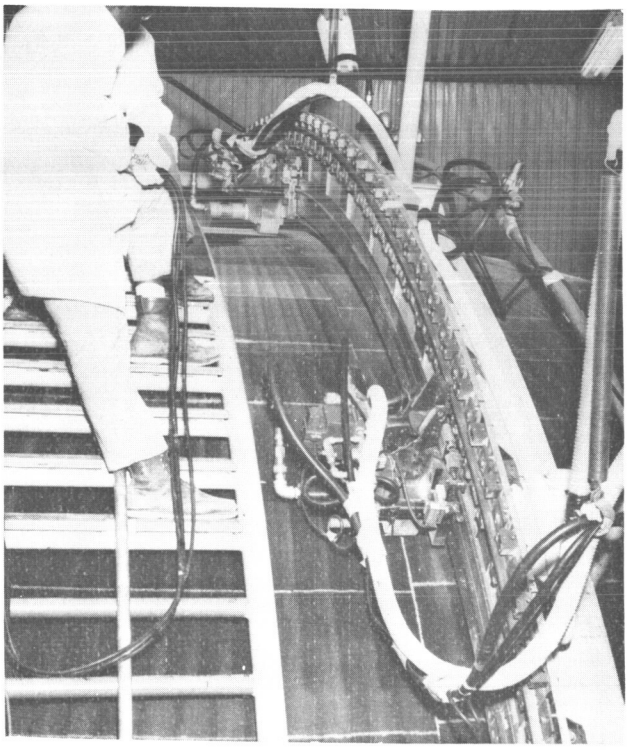

FIGURE 22. S-II COMMON BULKHEAD HONEYCOMB-CORE-TRIM OPERATION

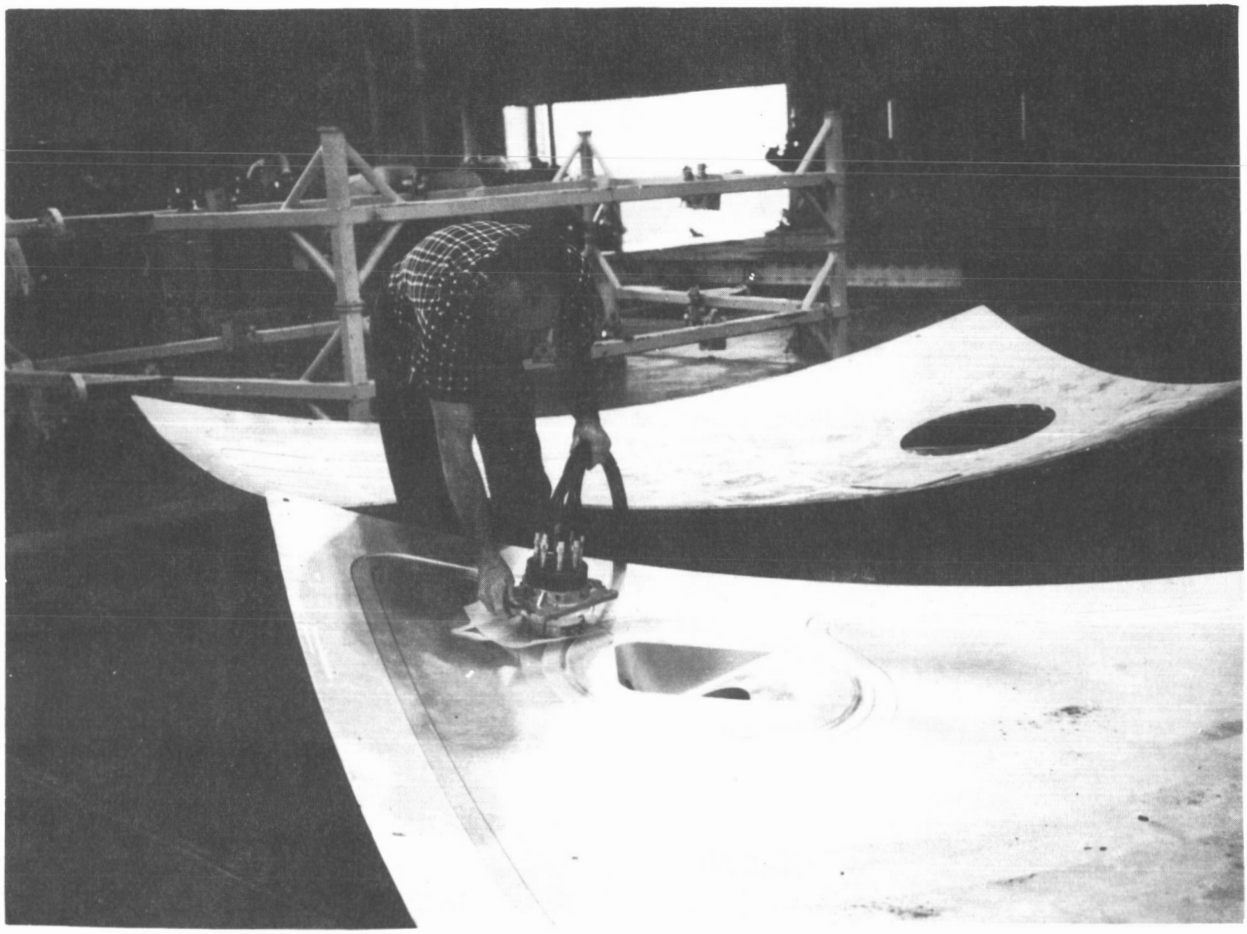

FIGURE 23. BASE AND APEX GORE SEGMENTS AND THE CHEMICALLY MILLED SURFACES

ESTABLISHING A COMMON DENOMINATOR IN WELDING

By

Gordon Parks

SUMMARY

The solutions to various welding problems ultimately depend upon the establishment of a more systematic and scientific basis for welding practices than has existed. One of the approaches to welding fundamentals undertaken at MSFC has been to relate all welding processes and materials to a common denominator of time-temperature relationship.

With this basic relationship applied to the various welding parameters, relationships can be drawn for better systemized information. For example, there may be optimum time-temperature curves for yield strength, ultimate tensile strength, elongation, porosity, distortion, material thickness, etc.

The efficiency of gas metallic arc and gas tungsten arc, the chief welding methods used in Saturn V manufacture, differs with the electric current used (AC or DC). A statistical study is being made to obtain quantitative measurements of the various responses in AC and DC welding.

Investigations on the very efficient and practical electron-beam technique are aimed at minimizing or removing the need for a vacuum welding environment. Three conceptions have been considered to achieve this aim. One is a split, or local, chamber method in which only the joint to be welded is in vacuum. The second is a plasma electron-beam system in which a hollow electron gun operates in a low vacuum provided by a mechanical pump. The third is a nonvacuum system in which the material to be welded is in a normal atmosphere and the vacuum is maintained within the electron gun.

I. INTRODUCTION

A weld may be defined as a continuous defect surrounded by sound metal. This is not meant to be facetious nor disparaging; rather it expresses an acceptance of a problem, and thus places the investigator in the favorable position of emotionally unhindered investigation. Two weld-development objectives may be postulated: (1) to minimize this total defect to the maximum extent possible and (2) to establish a high level of confidence in the reproduction of known weld quality.

Much of what must be considered in attaining these objectives is well delineated in the welding handbook chapter, "The Physics of Welding," published by the American Welding Society:

"Welding involves more sciences and variables than any other industrial process, which may explain why most of those concerned are satisfied with a very crude understanding of its problems.

"The principal sciences involved in welding are physics, chemistry and metallurgy. Of these, the physics problems are the ones most neglected and least understood, specifically from the quantitative point of view. These involve heat, mechanics, elasticity, plasticity, electricity and magnetism, as well as those very complicated and as yet little understood phenomena of the welding arc. Testing and research work in this field require a knowledge of optics, including polarized light, X-rays, X-ray diffraction, crystal theory, and the constitution of matter."

In reference to the present stage of welding theory and techniques, no common abstraction is found to which all processes and materials can be related. The absence of such an abstraction has made welding appear to be an art, consisting of isolated, unrelated modes and materials. Therefore, welding research at MSFC has involved: (1) the formulation of a common, unifying denominator or general index based on theory and experiments, (2) a program which will arrange the various elements of the welding complex into their proper, quantitative relationships, and (3) the methods and means of applying such knowledge to manufacturing of space vehicles.

II. THE COMMON DENOMINATOR

Realizing that energy, or heat, in some span of time results in degradation of material, one may go directly to the core of the problem and select time-

temperature relationships as the common denominator to which welding processes and their effects on metals can be related. The time-temperature relationships are more clearly defined in Figure 1, in

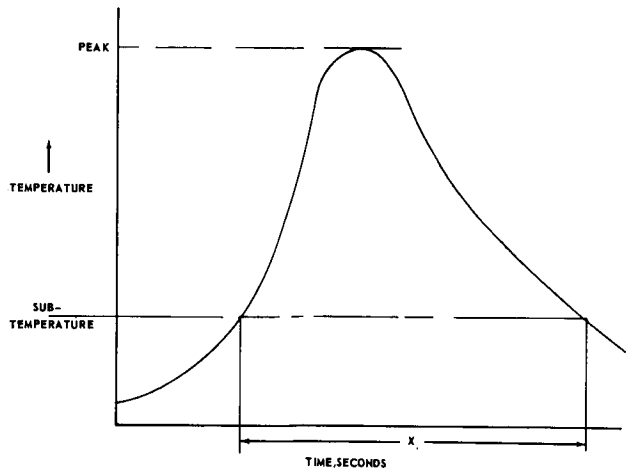

FIGURE 1. TIME-TEMPERATURE CHARACTERISTICS CURVE

which the welding temperature gradient reflects the peak temperature, and the time above a subtemperature adversely affects the material. Such curves can be related to the responses, strength, and porosity, as shown in the chart below and in Figure 2. There will be an optimum curve for each response sought, for example, ultimate tensile strength, yield strength, elongation, distortion, and porosity. Thickness and material changes may require other time-temperature curves.

$$Y_1 = f(X_1, X_2)$$
$$Y_2 = f(X_1, X_2)$$
$$Y_3 = f(X_1, X_2)$$

IN WHICH:

Y_1 = YIELD STRENGTH
Y_2 = ULTIMATE STRENGTH
Y_3 = ELONGATION
X_1 = MAXIMUM TEMPERATURE
X_2 = TIME ABOVE TEMPERATURE

Each welding process has its limits in the manipulation of variables that produce time-temperature curves; thus, processes can be located on a curve of time-temperature versus strength or other response (Fig. 3). Lowest in efficiency is the tungsten inert gas DCSP (straight polarity), and highest in efficiency is electron beam welding. In a similar manner, we can consider different materials, material thickness, mass, and joint geometry. With this general index of time-temperature relationships, a coherent, logical framework of the metals-joining complex may be formulated.

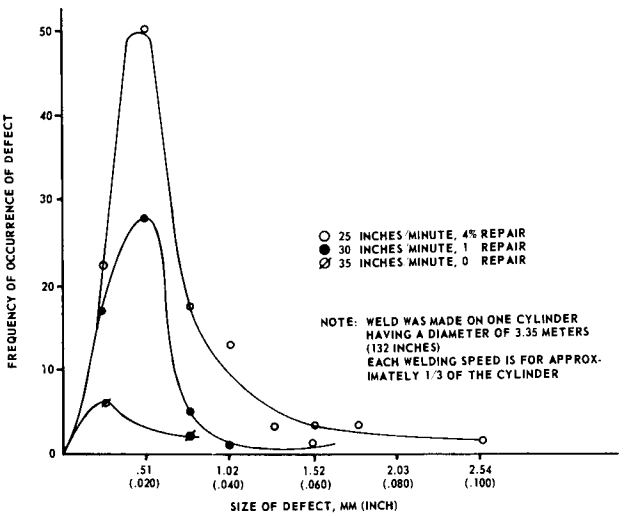

FIGURE 2. WELD DEFECTS, FREQUENCY OF OCCURRENCE VERSUS SIZE

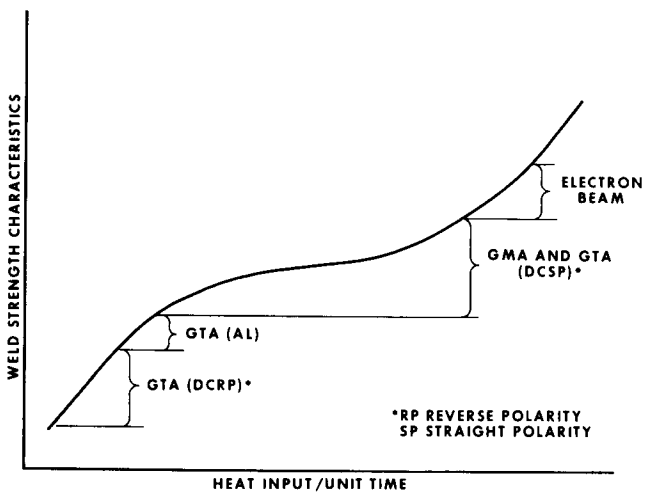

FIGURE 3. RELATIVE EFFECT OF PROCESS HEAT INPUT VERSUS WELD STRENGTH CHARACTERISTICS

III. PROCESS DEFINITION

A. INERT GAS ARC WELDING

Two welding processes are predominant in Saturn V manufacturing: consumable electrode, gas metallic arc (GMA), and nonconsumable electrode,

gas tungsten arc (GTA). Efficiency differences in the processes using alternating current (AC) and direct current (DC) can readily be seen by a comparison of the melt areas shown in Figure 4. A

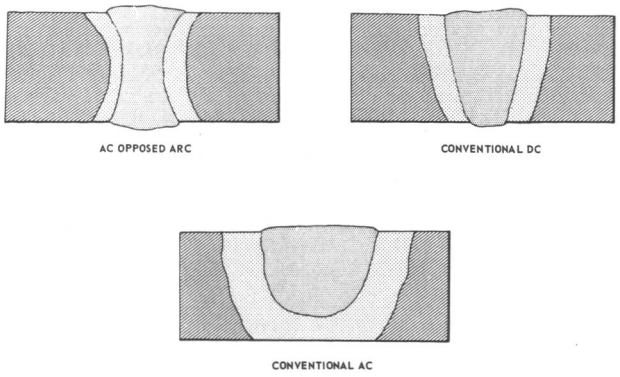

FIGURE 4. MELT AREA COMPARISON

narrower bead and deeper penetration are produced with DC than with AC. The GTA DCSP offers more potential of increasing the conventionial AC arc efficiency, while retaining the assumed advantages of cathodic cleaning and nugget structure refinement caused by the AC stirring of the molten puddle. On the other hand, when the AC cleaning and refinement potentials are not considered, two opposed DC arcs may have a still greater efficiency. A statistical study is being conducted to place quantitative measurements on these responses of AC and DC welding. The study will ultimately include all the processes, as shown in Figure 5.

B. ELECTRON-BEAM WELDING

The most efficient and practical process related to the common denominator of time-temperature is electron-beam welding (EB). A GTA weld on 6.4 mm ($\frac{1}{4}$ inch)-thick plate through which an EB weld has been made is shown in Figure 5, and aptly illustrates the gain in efficiency. The EB process can be used to weld material 76 to 102 mm (3 to 4 inches) thick, whereas the GTA process is limited to materials approximately 19 mm (3/4 inch) thick. The lower time-temperature of EB welding results in higher strength and quality.

Electron beam welding has been limited in application because of its higher vacuum requirement (0.013 N/m^2 or 10^{-4} mm Hg). Three approaches have been made toward removing this limitation, and thus they make this most efficient process as versatile as the GTA and GMA modes. These approaches, in progression, are as follows:

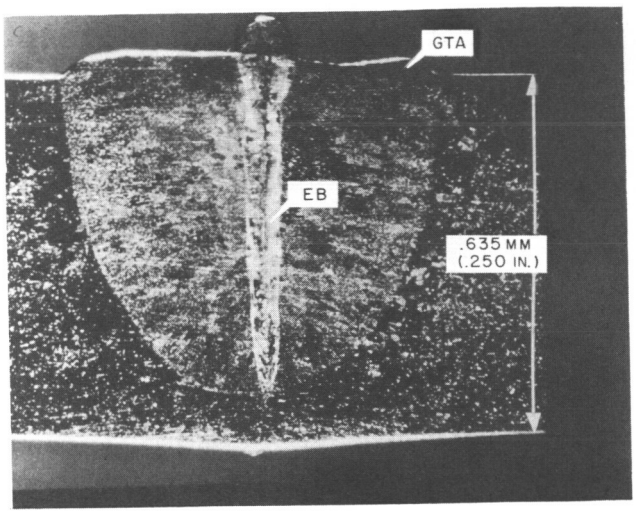

FIGURE 5. COMPARISON OF WELD ZONES, ELECTRON BEAM VERSUS GTA

1. Split, or Local, Chamber Concept. A conventional high-vacuum chamber is often impractical if large components must be completely enclosed. The split chamber, with adequate local sealing, reduces the vacuum chamber size to that necessary to encompass the joint to be welded. An example of this technique is shown in Figure 6. The welding of fittings into bulkhead gore segments by the low time-temperature EB process will eliminate the severe distortion and buckling which result from the high-energy TIG process, and the consequent shrinkage stresses.

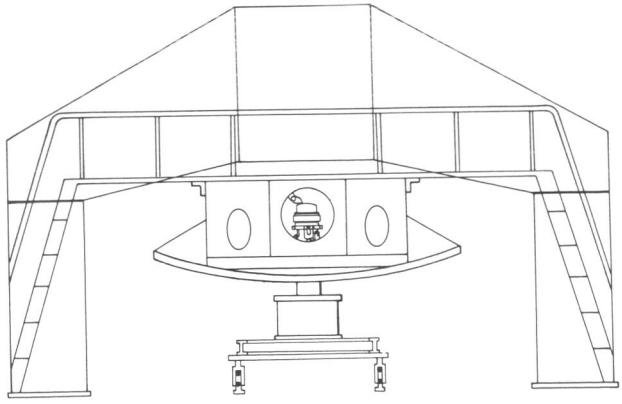

FIGURE 6. SPLIT-CHAMBER VACUUM SYSTEM

2. Plasma Electron-Beam Welding. As stated before, the conventional EB system requires a high vacuum and uses a complex and bulky gun. The plasma electron beam system (PEB), on the other hand, uses a simple, hollow electrode gun which will

function in a vacuum of 13.3 N/m^2 (0.1 mm Hg) provided by a mechanical pump (Fig. 7). The higher positive pressure of the system may permit the use of a simple, inexpensive ducting system rather than the complex, directly coupled, diffusion-pumped, high-vacuum system now being used. Developmental tests indicate that weld joint efficiencies will be equal to those produced by the high vacuum. In addition, the PEB system can be combined with the split-chamber method to increase the system's potential versatility.

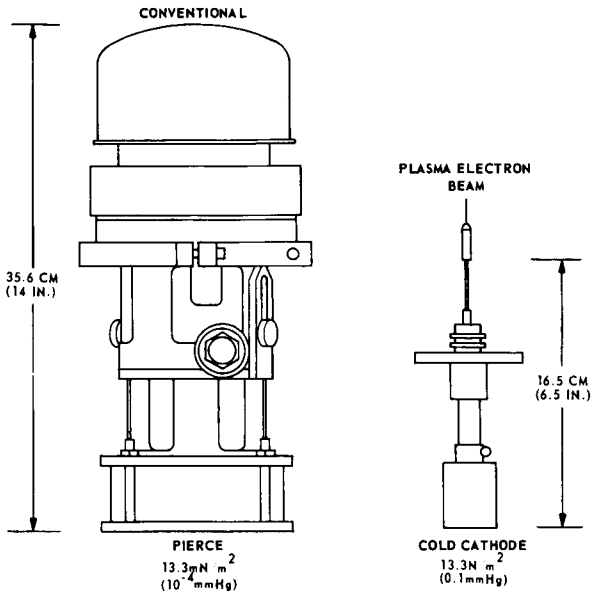

FIGURE 7. ELECTRON-BEAM WELDING DEVICES

3. Nonvacuum Electron-Beam System. The most direct approach toward versatility is to remove the vacuum requirement, i.e., to remove the material being welded from a vacuum. Such a system exists, and currently is being improved and refined for selected application studies. It eliminates the need for chambers and ducting systems. Figure 8 shows schematically a method of bringing the electron beam out of the chamber. The vacuum is maintained within the gun as the beam passes through a series of orifices which separate the differentially evacuated compartments. Helium gas is introduced outside the last orifice to minimize beam scatter. In welding 12.7 mm ($\frac{1}{2}$ inch) type 2219 aluminum alloy, the gun-to-work distance is approximately 9.5 mm (3/8 inch).

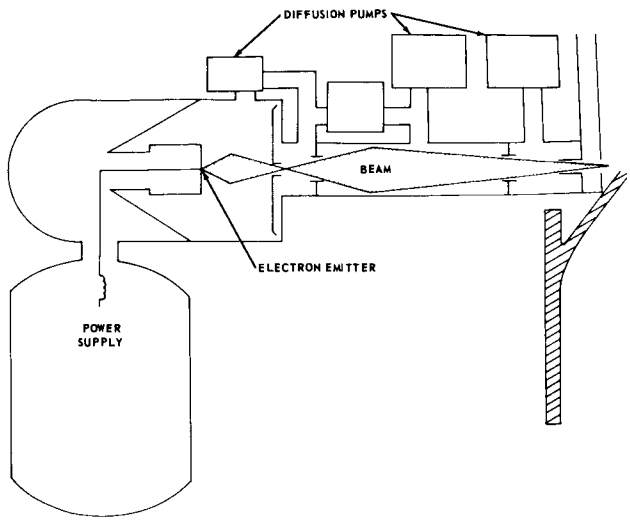

FIGURE 8. NONVACUUM ELECTRON-BEAM WELDER

Comparison of a two-pass tungsten arc weld with a nonvacuum EB weld is shown in Figure 9. The tungsten arc weld was made at 15 cm (6 inches) per minute, and the EB weld at 318 cm (125 inches) per minute, with an energy input about 90 percent less than the tungsten arc weld.

The present nonvacuum EB package has a mass of 102 kg (225 lbm). The equipment, shown in Figure 10, will be used at MSFC for application development.

4. Lightweight, Hand-Held EB Gun. The EB system is not necessarily earthbound. It has the intriguing potential of being usable in a space environment (in which a very high vacuum exists). Figure 11 shows conception of hand-held EB guns which would have a mass less than 20 kg (45 lbm). The gun on the right would be powered by self-contained, rechargeable batteries. The gun on the left would obtain power from an independent source.

IV. DEVELOPMENT AND APPLICATION STUDIES

Our development effort, which can be represented as a welding development complex, is shown

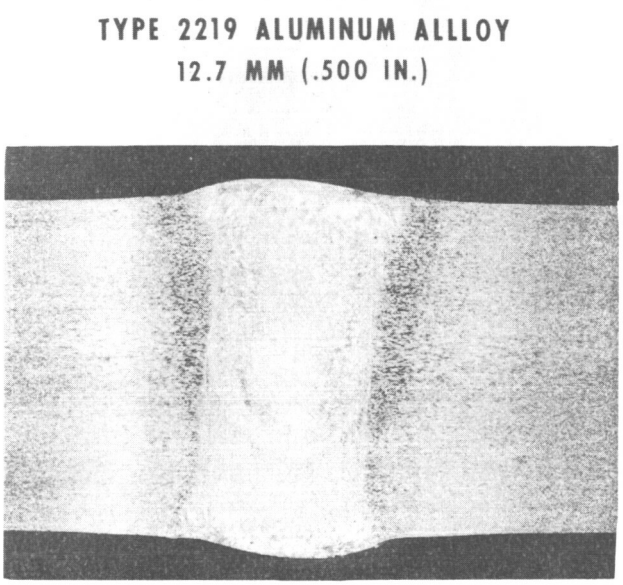

FIGURE 9. COMPARISON OF A TWO-PASS TUNGSTEN ARC WELD WITH A NONVACUUM ELECTRON-BEAM WELD

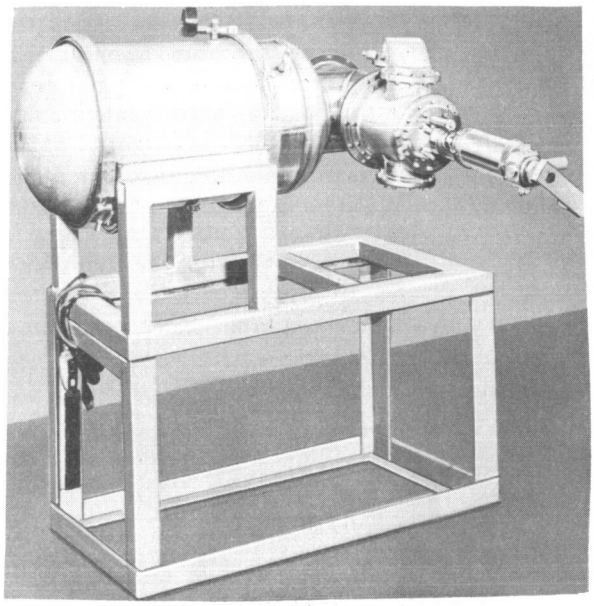

FIGURE 10. NONVACUUM ELECTRON-BEAM SYSTEM

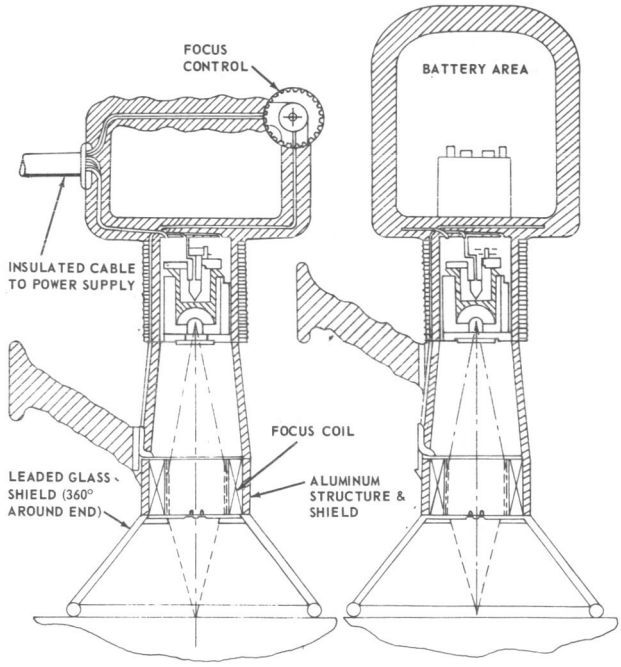

FIGURE 11. PORTABLE ELECTRON-BEAM WELDER

in Figure 12. The complex of projects constitutes an ordered and coherent program, each project being a logical step toward the goal of high joint performance and reliability. Thus, basic studies now being made are: base metal analysis at Battelle Memorial Institute to determine the weld defect potential in materials; mechanism of porosity at Douglas Aircraft; time-temperature effects at MSFC; means of controlling time-temperature at Harvey Aluminum; arc shaper, to increase process efficiency; electron beam studies; and so on to the industry/NASA verifications and application, specifically to the Apollo program, and to space vehicles in general.

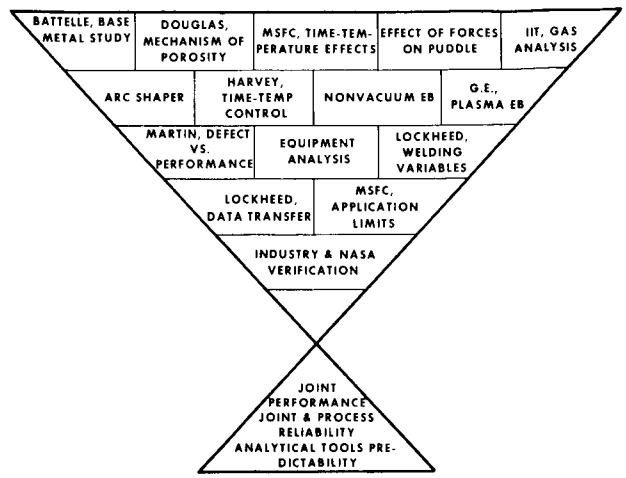

FIGURE 12. WELDING DEVELOPMENT COMPLEX

RESEARCH IN SUPER POWER LASERS AND INTENSE MAGNETIC FIELDS

By

R. J. Schwinghamer

SUMMARY

New tools and tooling concepts based upon MSFC research developments in superpower lasers and intense magnetic fields are discussed in this review.

Superpower lasers are being investigated for drilling and welding applications. One of the most promising lasers, a pink-ruby type in a coaxial gun, with a Cassegrainian focusing system, has an input power of 240 000 joules and an output of 2000 joules, sufficient for vaporizing any material. Since this welding system operates in a normal ambient pressure while its beam can be projected into vacuum to do work, it has potential for use in space as well as the laboratory and shop.

Research developments in intense transient magnetic fields are being successfully applied to many manufacturing problems. An electromagnetic constriction technique, employing high-intensity pulsed fields, is used to correct oversized metal tunnels (Saturn V LOX and others). Pneumatically clamped and hand-held magnetomotive hammers, based upon the same principle of pulsed magnetic fields, have been developed for removing weld distortions from Saturn V heavy skin sections, gore segments, and bulkheads. Other magnetic-field tools for manufacturing processes such as fastening, swaging, blanking, sizing, and coining are being developed and tested.

I. INTRODUCTION

New research developments in superpower lasers and magnetic fields are reported in this review, and some of their current and potential applications are discussed.

The very considerable potential of lasers is well recognized, as evidenced by the many research and development programs being conducted by numerous laboratories and agencies. The broad objective of such work by Manufacturing Engineering Laboratory is a laser tool which will be used in the shop, in the laboratory, and in space.

The Laboratory's work in intense magnetic fields also has a very practical objective. It has been based upon magnetic-field phenomena discovered at Harvard Cyclotron Laboratory in 1955, and these have led, at MSFC, to significant new tooling concepts.

II. SUPERPOWER LASERS

Manufacturing Engineering Laboratory has concentrated on doped-crystal lasers available. There are about five other basic types of lasers: gas discharge, semiconductor junction, liquid, plastic, and glass. The number of laser materials has increased very rapidly, so that it has become difficult to keep up with all the details of new developments.

For drilling and welding studies, Manufacturing Engineering Laboratory has considered both red and pink ruby (there are two kinds, depending on the amount of chromium dopant) and the glass lasers. While general agreement on their relative merit by no means exists even now, the pink ruby seems best suited for high-power drilling and welding studies because: (1) it has a very high thermal conductivity, (2) its emission wavelength is more suitable for welding because this laser is characterized by less reflection and more absorption (3) life of the crystal still is better than that of any other laser material because the crystal does not craze or solarize easily, and (4) the unfocused beam spread is very small, being approximately 0.15 mrad (30 seconds) of arc.

Subsequent events have verified the superiority of the choice made two years ago. Features of the superpower laser work are discussed briefly in the following paragraphs.

A. PINK RUBY LASER SYSTEM

Figure 1 shows a typical transition diagram for the so-called three-level ruby laser. The conventional excited chromium atom population inversion is shown by the solid lines; a less likely and rather unusual transition is shown by the dotted lines.

Transitions can be considered roughly as a shifting of electron orbits.

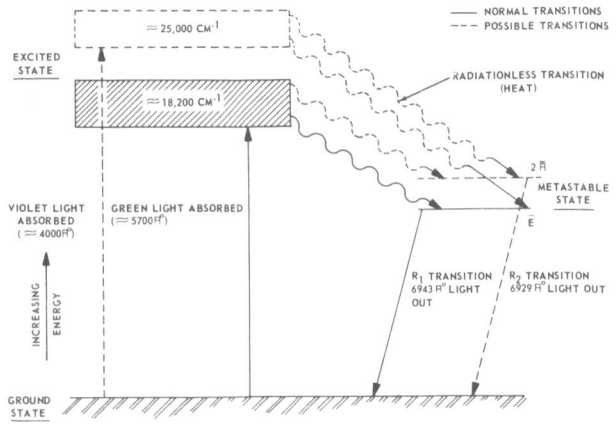

FIGURE 1. TRANSITION DIAGRAM FOR THREE-LEVEL RUBY LASERS

B. TYPICAL HIGH-POWERED LASER GUN DESIGNS

The laser gun is the next important system element. There are three basic high-powered gun designs which are shown in Figure 2. The coaxial design was selected primarily bacause this was, and still is, the only configuration able to handle the full 240 000-joule input that was available from the Medusa capacitor bank.

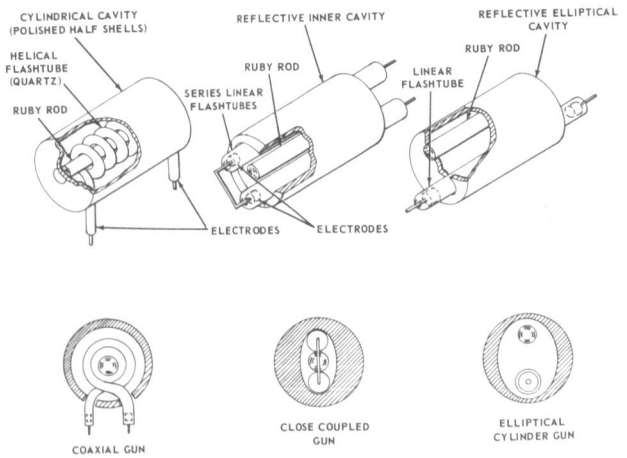

FIGURE 2. THREE BASIC HIGH-POWER GUN DESIGNS

Building such a gun required a flashtube of unprecedented size. The Kemlite Company of Chicago provided a special tube which is said to be the largest in the world.

C. LASER GUN WITH FLASHTUBE AND RUBY

Figure 3 shows the flashtube in the first version of a 240 000-joule gun. The top half of the reflector

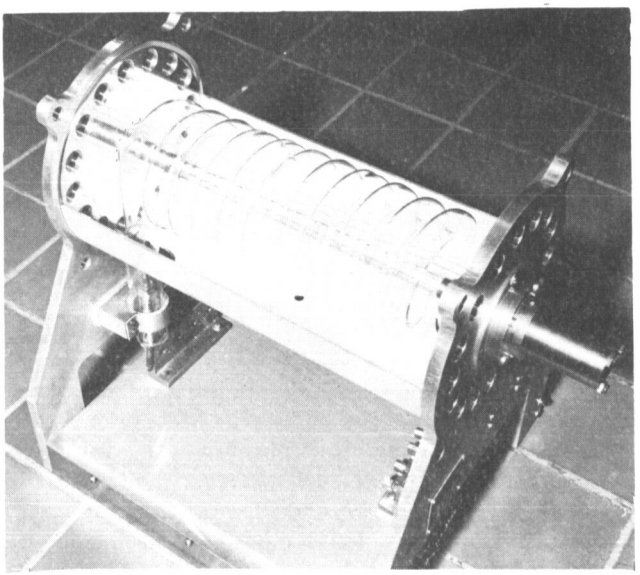

FIGURE 3. FLASHTUBE IN THE FIRST VERSION OF A 240 000-JOULE GUN

cavity has been removed. The flashtube helix is approximately 13 cm (5 inches) in diameter and 33 cm (13 inches) long, while the ruby is 1.6 cm (0.625 inch) in diameter and 30.5 cm (12 inches) long. The flashtube has very high light output, as can be seen by the graph in Figure 4.

D. XENON FLASHTUBE LIGHT OUTPUT VS. ENERGY INPUT

With full energy input of 240 000 joules to the system, the light output of the Xenon flashtube is a little over 7.8-billion candelas (8-billion horizontal candle power). Earlier in this research the question was raised as to what kind of energy

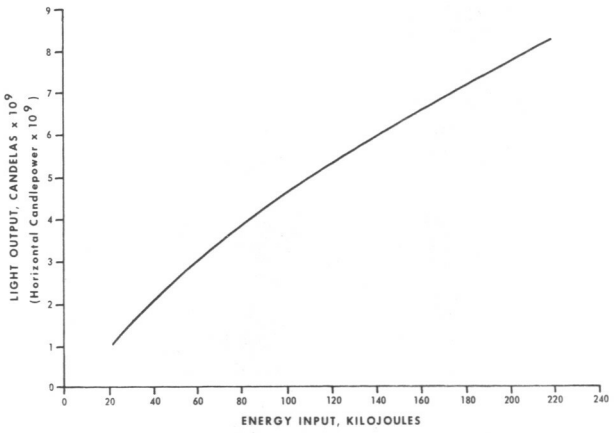

FIGURE 4. XENON FLASHTUBE LIGHT OUTPUT

density could be produced from this output so that it could be used for drilling and welding. A focusing system was considered as a basic requirement for obtaining an adequate energy density. The early efforts at focusing were frustrating because ordinary crown glass and composite lenses disintegrated. Finally some success with single quartz lenses was achieved, and later the Cassegrainian focusing system shown in Figure 5 was developed.

E. CASSEGRAINIAN FOCUSING SYSTEM

This system is basically of the astronomical telescope type except that it functions in reverse order. In the astronomical telescope the terminus is behind the large reflector, but in the laser system it is somewhat beyond the small reflector, and has a

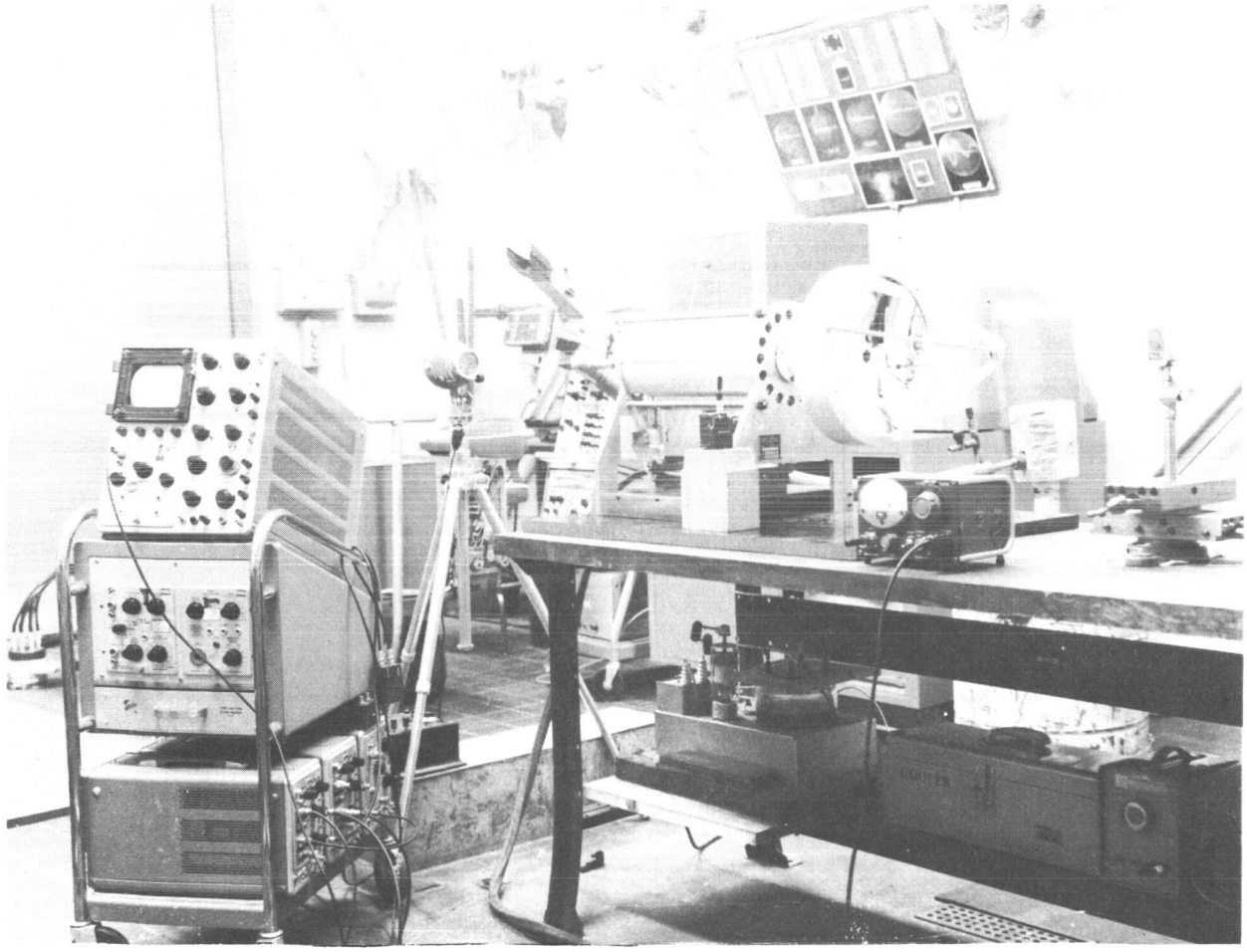

FIGURE 5. CASSEGRAINIAN FOCUSING SYSTEM

focal length of about 0.6 meter. The maximum power density attained to date has been on the order of 218-million watts per square centimeter, with an input energy of 240 000 joules and an output of about 2000 joules. This is sufficient to vaporize any material, even diamond. About 300 000 watts per square centimeter produces vaporization of the metals that the laser is being developed to drill and weld. The efficiency is almost 1 percent, which is commendable for the ruby laser.

F. WELDING WITH THE LASER

In 1962 a small, 4000-joule system was used to weld type 304 stainless steel 0.2 mm (0.008 inch) thick, and types 5086 and 2219 aluminum 0.127 mm (0.005 inch) thick. Stainless steel was easy to weld even in air, but the same technique was not suitable for aluminum. The short pulses were not as effective in preventing oxidation as had been expected. At that point, Manufacturing Engineering Laboratory demonstrated that a laser could be operated in a "shirt-sleeve environment," (i.e., a normal ambient pressure) and that the beam could be projected into vacuum to do work. The laser is the only welding device which can be operated in this manner, and this is one of its very advantageous features for space use. The aluminum welds made in vacuum were of good quality because of the absence of an oxidizing atmosphere. Figure 6 shows stainless steel welds being made by a repetitive pulsing technique, and Figure 7 shows one of these welds.

FIGURE 6. STAINLESS STEEL WELDS MADE BY A REPETITIVE PULSING TECHNIQUE

Although these studies conclusively proved the suitability of small lasers for microwelding applications, much more power was needed to handle the kind of materials in which Manufacturing Engineering Laboratory was interested. Inasmuch as the Medusa capacitor bank was already available, this led to the development of the 240 000-joule system.

Subsequent studies indicate that the quality of the large rubies varies over a wide range, and in some cases threshold (the point where lasing begins) varies between supposedly identical rubies by as much as 70 000 joules. This means that, at present, the individual characteristics of the rubies must be taken into account and, therefore, the rubies cannot be interchanged routinely in equipment.

G. MEASUREMENTS OF 240 000-JOULE LASER OUTPUTS

Figure 8 shows the diagnostics apparatus employed in making laser output measurements. It goes by the title of a rat's nest calorimeter because of the mass of fine wire used in its construction.

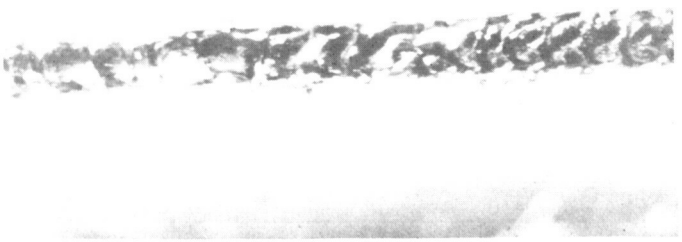

FIGURE 7. STAINLESS STEEL WELD

H. RUBY FILAMENTARY LASING MODE

Another phenomenon which caused concern, but which has not yet created much trouble, is the filamentary lasing mode of the ruby.

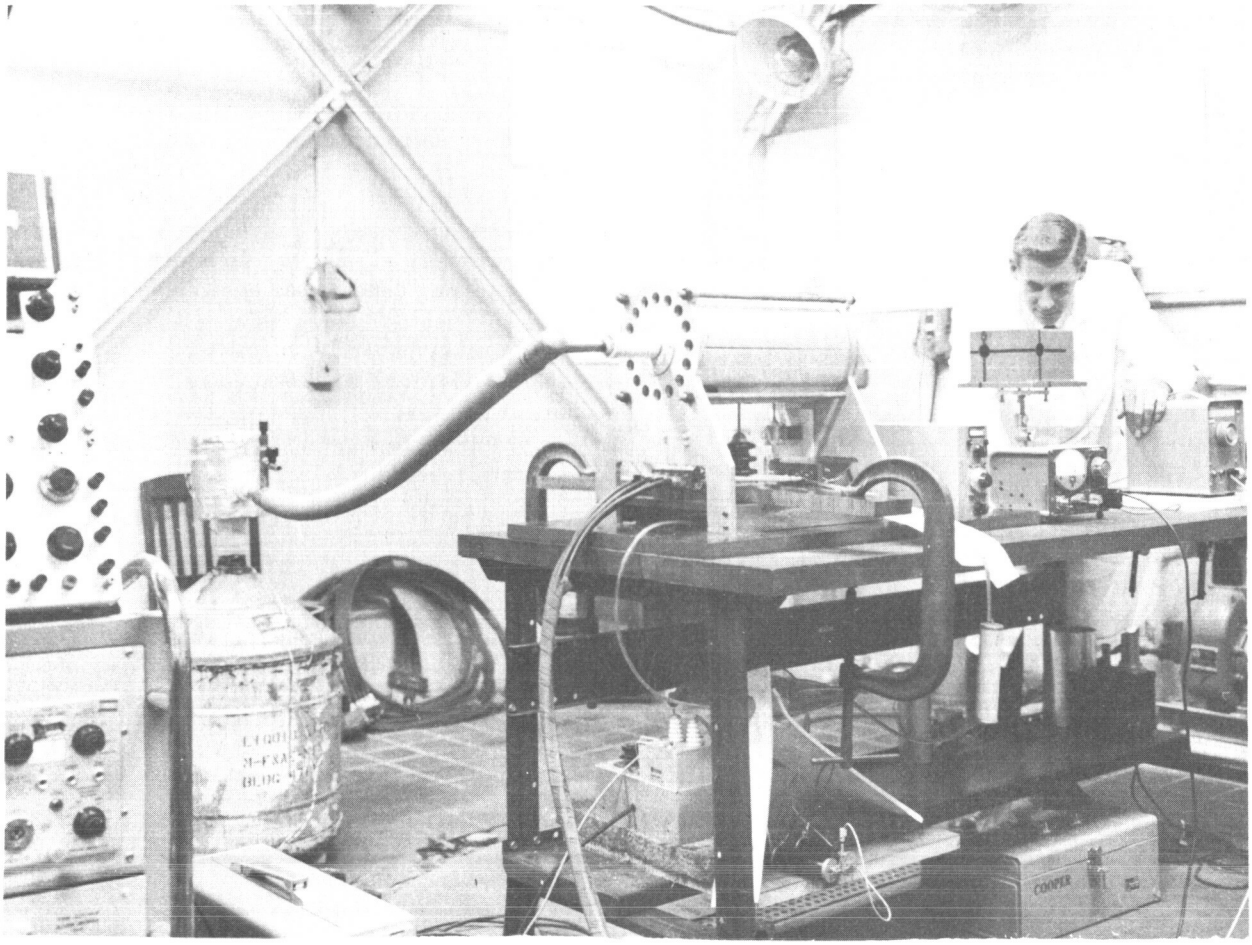

FIGURE 8. RAT'S NEST CALORIMETER

Figure 9 represents three separate laser shots. The three exposures of one shot at the left exhibit this filamentary lasing mode. The beam is random and pulsating across the cross-sectional area, but evidently does not cause much trouble after the beam is focused. It is doubtful whether anyone as yet completely understands this phenomenon. This photograph was made with a Space Technology Laboratory image converter camera focused into the eye of the laser gun at a low power level. Welding data recorded so far, in which the large system was used, indicate that the best welding results can be obtained by reducing spot density and increasing the pulse repetition rate. Studies by Newman at Ames Research Center, in which laser beams were used to simulate micrometeoroid impacts, tend to verify what has been observed experimentally on metals. Giant pulsing or Q-spoiling techniques have not been found good for welding, and now emphasis is being placed on focusing, flash-lamp waveform, and pulse repetition rate optimization. Mathematical analysis indicates that aluminum 3.2 to 6.4 mm (1/8 to 1/4 inch) thick can be welded at an equivalent rate of 127 mm (5 inches) per minute. So far, type

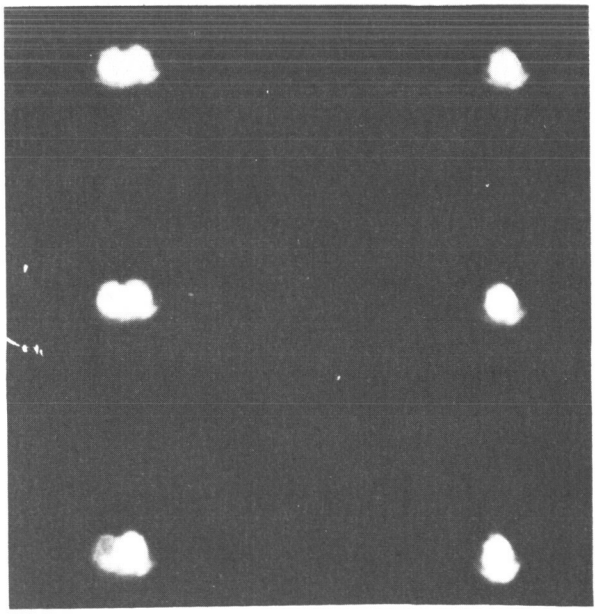

FIGURE 9. FILAMENTARY LASING MODE

2219 aluminum 3.2 mm thick has been drilled through easily, but the pulsed laser still cannot match the electron beam welders with respect to average power for continuous welding.

I. CONTINUOUS-WAVE ARGON LASER

Figure 10 shows a continuously emitting, or continuous-wave, laser being developed by Raytheon under an MSFC-supporting contract. Raytheon has operated this type of laser sporadically at 18 watts continuous wave. This could be the beginning of a new generation of laser welders that do not have to be pulsed and that can weld in a continuous manner.

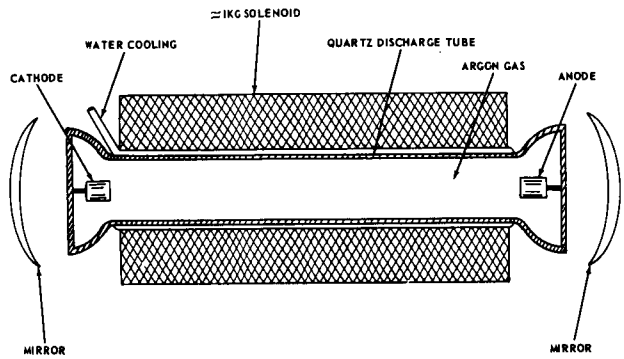

FIGURE 10. CONTINUOUS-WAVE ARGON LASER

III. INTENSE MAGNETIC FIELDS

The following commonplace magnetic fields are given as a frame of reference for this discussion of research in intense magnetic fields: the field of an ordinary toy bar magnet amounts to 0.2 or 0.3 tesla (2000 or 3000 gauss), and for an electromagnet it may be 6 teslas (60 000 gauss). Superconducting coils recently have been made to attain field strengths in excess of 10 teslas (100 000 gauss), and Montgomery at the National Magnet Laboratory (Massachusetts Institute of Technology) has reported fields slightly above 20 teslas (200 000 gauss). For much higher field strengths, the coil core must be eliminated, so that the magnetic field is produced in air or vacuum.

The use of magnetic fields is obvious in such mundane devices as electric motors, relays, and other electrical equipment. A newer, less obvious use was introduced through the discovery of unusual magnetic field phenomena by Furth and Waniek (1955, Harvard Cyclotron Laboratory). They found that with high enough transient magnetic fields they could work tough metal as though it were soft plastic, and could cause even the hardest steel to flow like water and sometimes to explode.

This discovery was incidental to their research on the determination of the charge and momentum of particles by their deflection in a high magnetic field region. This incidental, practical result and the results of work by Colgage at Livermore, a group at General Atomics, and MSFC, have proved utilitarian, and a new tooling concept has evolved as a consequence.

The manner in which intense transient fields are created is illustrated diagrammatically in Figure 11. Features of the pulsed magnetomotive power system and its practical applications are discussed in the subsequent paragraphs.

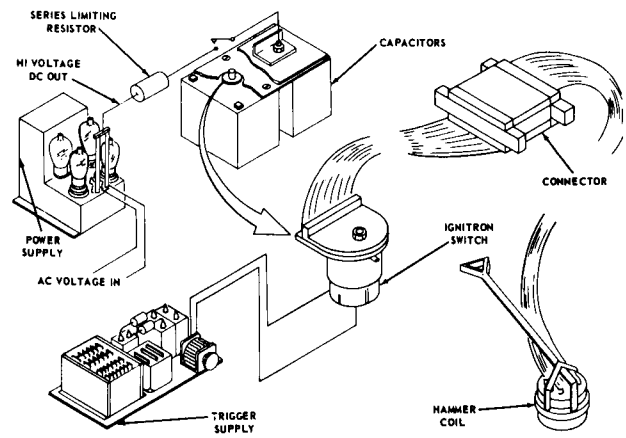

FIGURE 11. THE MANNER IN WHICH INTENSE TRANSIENT FIELDS ARE CREATED

A. MAGNETOMOTIVE PULSE POWER SYSTEM

This is the type of system needed to generate high-intensity pulsed fields. Static magnetic fields are not effective in forming metals, but pulsed or transient fields are.

Figure 12 is a pictorial representation of what takes place when a powerful transient current pulse is discharged through a coil with an electrically conductive workpiece in proximity. The coil current creates a magnetic field, and this field causes induced or eddy current to flow in the workpiece. The induced field associated with eddy current interacts with the initiating coil's magnetic field to create high magnetic field pressure between the coil and workpiece (the JXB force equation for a physicist, or the BLI relationship for the engineering force equation). If the coil is either physically or inertially stronger than the workpiece, the workpiece yields and is formed.

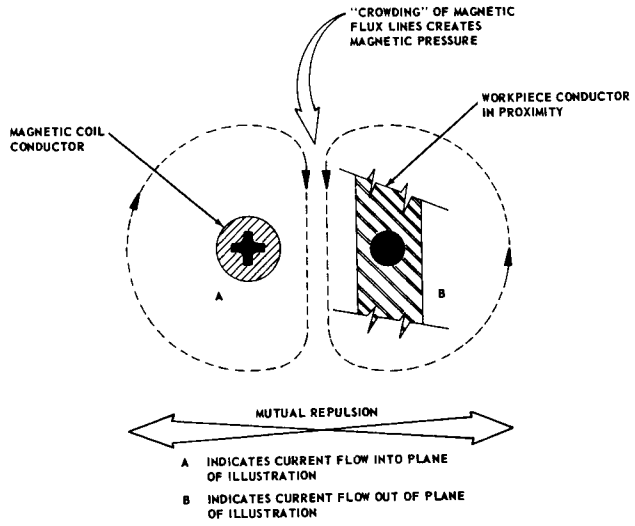

FIGURE 12. POWERFUL TRANSIENT CURRENT PULSE DISCHARGE THROUGH A COIL WITH AN ELECTRICALLY CONDUCTIVE WORKPIECE IN PROXIMITY

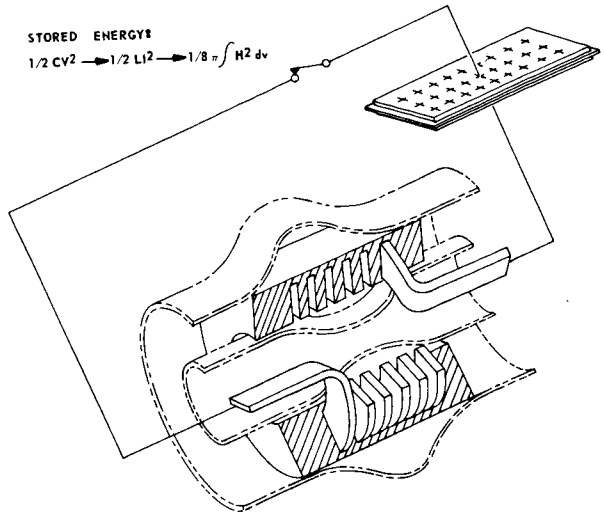

FIGURE 13. ELECTROMAGNETIC PRECISION FORMING

B. MAGNETOMOTIVE ENERGY RELATIONSHIPS

The pertinent energy relationships in the system are as follows: the electrical charge stored in the capacitors ($1/2\ CV^2$) is converted into magnetic field energy in the coil ($1/2\ LI^2$) which, in turn, creates magnetic field pressure proportional to the field strength squared over the volume V. The electrical discharge which accomplishes this is usually a damped oscillatory wave in the middle audiofrequency range.

C. ELECTROMAGNETIC PRECISION FORMING

Manufacturing Engineering Laboratory developed an electromagnetic technique for the precise forming of annular bulges in a metal cylinder. (The method is illustrated diagrammatically in Fig. 13.) In the spring of 1962 the Laboratory suggested this technique for use in stiffening Saturn V LOX tunnels. The idea could not be applied by the interested design group because its schedule commitments did not allow time for obtaining required test and design data. Three years later, however, this research development provided a successful solution to a serious manufacturing problem, described in the next paragraph.

D. SATURN V LOX TUNNEL CONSTRICTION

In February 1965 MSFC received Saturn V LOX tunnels that were oversize because of inherent difficulties in their manufacture. To deal with the important considerations of cost, reliability, and scheduling, an emergency program was begun to correct the tunnel defects. Manufacturing Engineering Laboratory, through its technique developed for precision bulging, was able to design, manufacture, and test a large magnetomotive coil to size precisely (constrict) the oversize tunnels. In this work, done in a 2 1/2- week crash program, the technique was converted to produce metal-tube constriction by fitting the magnetomotive coil over the outside of the tunnel. Since this application, the constriction method has been used to correct size defects in tunnels for Saturn facilities checkout and for "502" vehicles (Fig. 14).

E. PNEUMATICALLY CLAMPED MAGNETOMOTIVE HAMMER

Until 1964, welding of heavy S-IC skin sections produced undesirable distortions. Manufacturing Engineering Laboratory developed a magnetomotive device which employed pneumatic clamping and delivered a powerful impulse. This device was then used to remove distortions. As shown in Figure 15, the device is not hand held. Its special advantages are: it has no surface marring results; the pressure is unique in that it is isodynamic (three-dimensional); and the strain rates are thousands of inches per inch per second.

F. HAND-HELD MAGNETOMOTIVE HAMMER

An outgrowth of the pneumatically clamped magnetomotive hammer is a hand-held magnetomotive hammer, developed by Manufacturing Engineering Laboratory (Fig. 16). It has been used to remove distortions from S-IC gore segments of

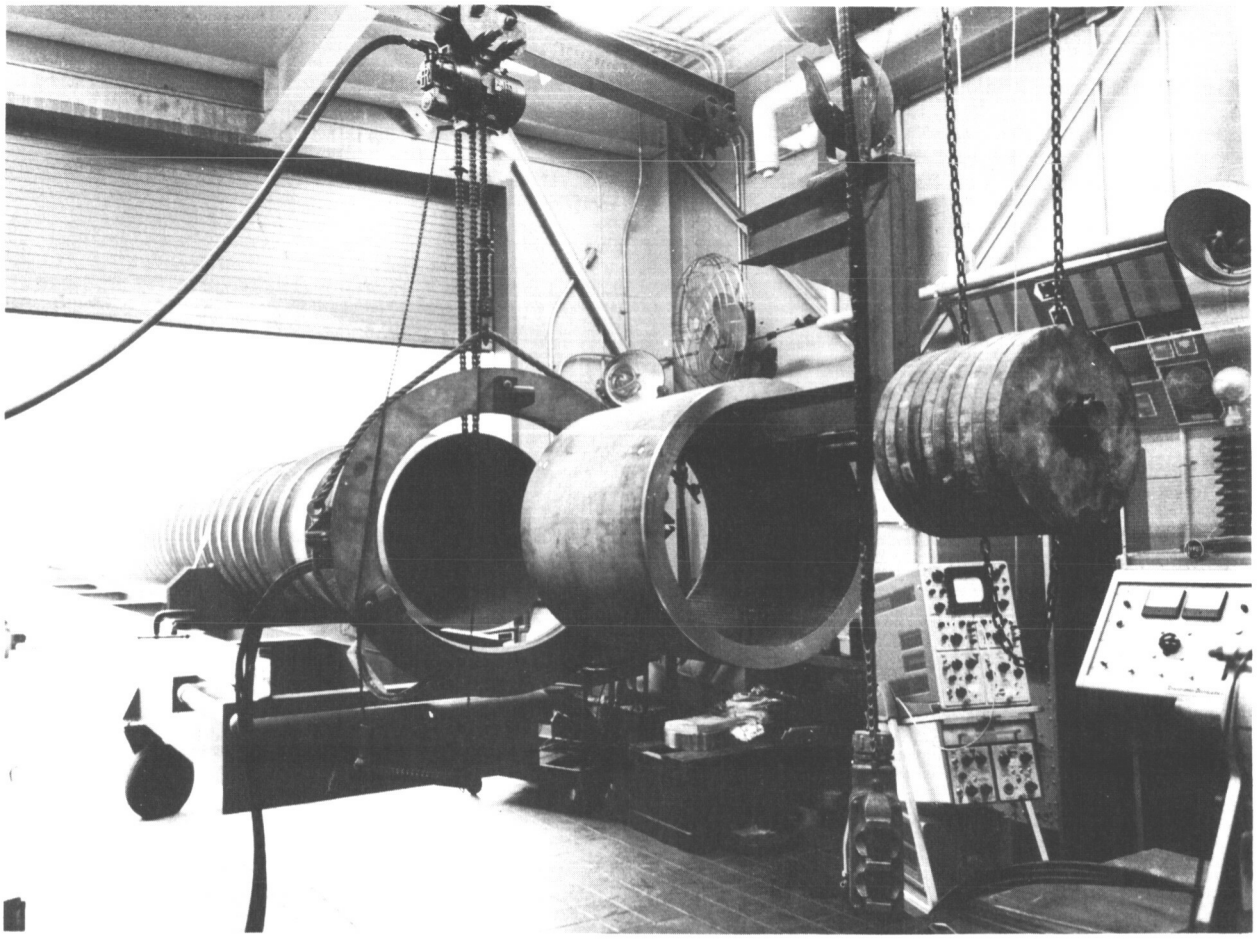

FIGURE 14. MAGNETOMOTIVE COIL FOR PRECISION SIZING LOX TUNNELS

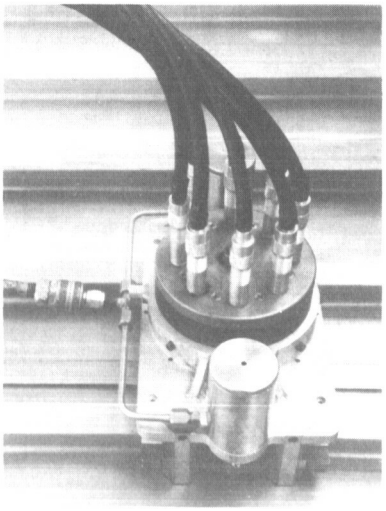

FIGURE 15. PNEUMATICALLY CLAMPED MAGNETOMOTIVE HAMMER

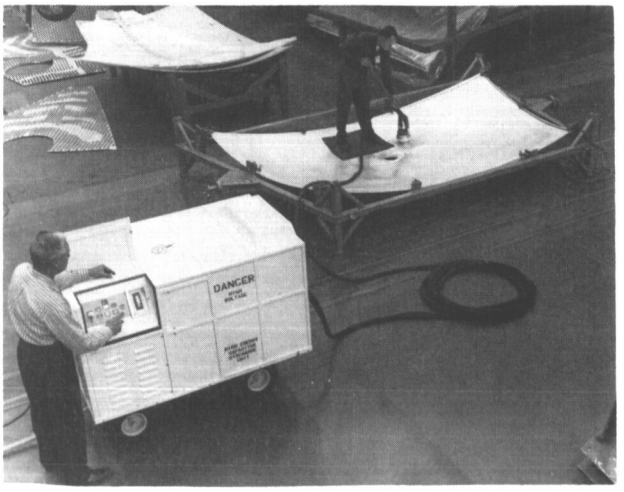

FIGURE 16. HAND-HELD MAGNETOMOTIVE HAMMER

the Saturn V (approximately 44 gore segments have been saved, up to May 1965). Similar prototype systems have been provided to MSFC prime contractors. They are being used for various purposes at Boeing's Michoud plant, North American's Seal Beach plant, and Douglas' Santa Monica plant. Boeing's Seattle plant will receive the next unit when it is completed. The new development data and results obtained at the various locations will be coordinated by MSFC.

G. DISTORTION REMOVAL FROM FINISHED SATURN BULKHEAD

Distortions of unprecedented magnitude have resulted from welding work on the very heavy sections in Saturn V. This is a serious problem because it gives rise to unknown stress conditions in the final configuration. Use of the magnetomotive hammer to correct these distortions has been very successful. Figure 17 shows precision-controlled sizing in operation on a Saturn V bulkhead. In one case, MSFC sent a crew to Michoud to demonstrate the technique on an early S-IC bulkhead so that now the Michoud plant itself can handle these problems.

H. TOOLS UNDER DEVELOPMENT AT MSFC

Manufacturing Engineering Laboratory also is developing and testing a wide variety of magnetic-field tools for potential applications to fastening, swaging, flaring, blanking, sizing, coining, compacting of metallurgical powders, etc. Some of the diagnostic apparatus and measuring techniques are second to none, so that MSFC in many respects is doing pioneer work in pulse power systems and magnetic field tools, and in their applications. Some of the tools and systems under development in the

FIGURE 17. PRECISION CONTROLLED SIZING IN OPERATION ON A SATURN V BULKHEAD

Manufacturing Engineering Laboratory are illustrated in Figure 18. In addition, Manufacturing Engineering Laboratory soon will have the largest known portable pulse power system. This is a 240 000-joule, completely portable system which will power lasers and large magnetic-field tools such as the tunnel-constricting coil.

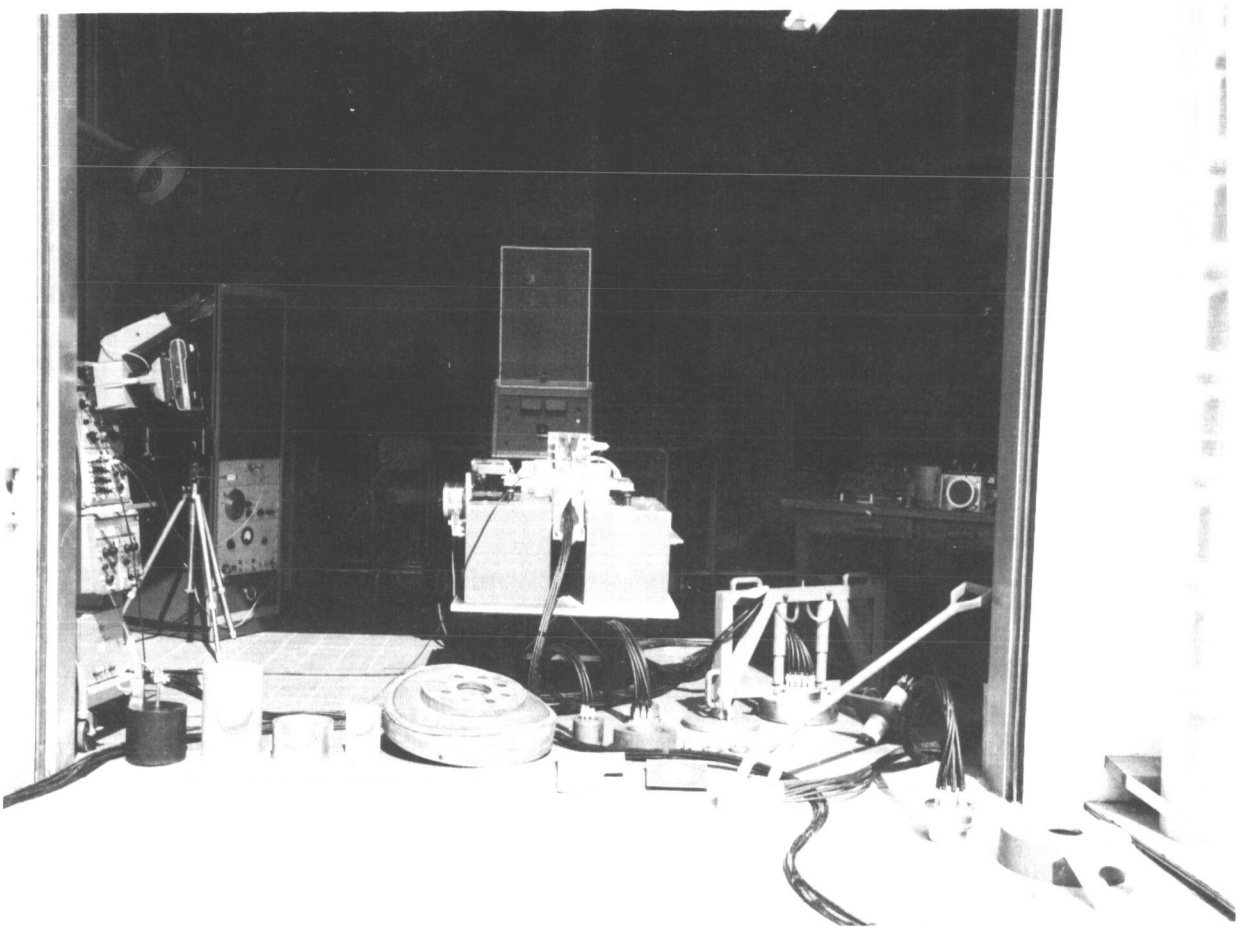

FIGURE 18. TOOLS AND SYSTEMS UNDER DEVELOPMENT IN MANUFACTURING ENGINEERING LABORATORY

GROUND TESTING RESEARCH AT MSFC

June 24, 1965

by

Fritz Kramer
Gerhard H. R. Reisig
Albert E. Schuler

TABLE OF CONTENTS

LIST OF ILLUSTRATIONS

CONTENTS (Continued). . .

RESEARCH AND DEVELOPMENT IN INSTRUMENTATION FOR STATIC TESTING

by Albert E. Schuler

CONTENTS (Continued)

LIST OF ILLUSTRATIONS

LIST OF TABLES

SOUND SUPPRESSION TECHNOLOGY RESEARCH AT MARSHALL SPACE FLIGHT CENTER

by Fritz Kramer

LIST OF ILLUSTRATIONS

LIST OF TABLES

ANALYSIS OF EMPIRICAL SOUND FIELDS

By

Gerhard H. R. Reisig

SUMMARY

The large-scale field collection of acoustic data and their analysis are described in this review. The entire sound-field program has the purpose of solving complex problems of excessive noise propagation associated with the static test firing of large space-booster powerplants.

The site of data collection has been Mississippi Test Facility (MTF), where far-field sound-propagation and correlated meteorological measurements were initiated in 1962.

The statistical evaluation of sound-measurement data shows that the polar distribution of sound in the springtime (at MTF) is determined mainly by the temperature field of the atmosphere. Greater deformation of sound-intensity polar distribution occurs in the autumn as a result of the influence of the wind field.

The data on sound attenuation as a function of distance from its source revealed attenuation in excess of the expected magnitude. The excess was mainly between 1 and 10 kilometers from the source, with maximum attenuation (17 to 18 decibels) near 6 kilometers. Excess sound attenuation was compared with calculated sound dispersion. For all sound frequencies in all seasons the deviation between reference and empirical attenuation values formed a bell-shaped distribution on a semilogarithmic plot. The physical causes for the sound-attenuation behavior are considered to be atmospheric diffraction and scattering effects.

Statistical analysis of sound-intensity extremes indicated amplification of the sound signals by focusing which could be expected along selected azimuths. Empirical amplification values showed the maximum occurring in winter (50 decibels at 22 kilometers).

For the analysis of correlation between empirical sound data and local atmospheric sound-propagation conditions, the concept of analytical classification of sound-velocity profiles has been developed. Examination of over a quarter-million individual sound-velocity profiles indicates that 33 profile types for heights up to 3 kilometers constitute the empirical possibilities of sound-propagation conditions in southeastern United States.

Since the focusing qualities of each sound-velocity profile can be determined as a class characteristic, the overall probabilities of focusing occurrence can be obtained. The severity of focusing, as based upon lateral spread of focusing areas, has been determined. The data for MTF indicate focusing is most severe in winter, with the direction toward east being most affected.

Sound propagation is a fluctuating phenomenon because atmospheric conditions vary continuously. A measuring system for analyzing the nonstationary sound-propagation phenomena has been established. The analysis of the acoustic fluctuation data is supposed to provide "dynamic" perturbation functions of sound, which are to be superimposed on the related characteristic sound-velocity-profile type.

The ultimate result of the program will be the establishment of reliable contingency tables showing the relationship between atmospheric parameters and far-field sound intensities. These data will be the basis for more accurate sound-propagation forecasting for static firing tests.

I. INTRODUCTION

Associated with static test firing of large space-booster powerplants are complex problems in noise generation and propagation. Current knowledge of the acoustical behavior of the atmosphere is insufficient for an analytical treatment of the problems of excessive noise propagation. Therefore, these problems require evaluation and analysis of information which must be obtained empirically, and on the largest practicable scale.

It was necessary to have an operational guide for test-noise monitoring available at the time the Mississippi Test Facility (MTF) was activated. The Mississippi Test Site (MTS), therefore, was selected for the collection of statistical data on far-field sound propagation. Routine sound-propagation and meteorological measurements were begun at MTS in late 1962. Work since that time has included

a statistical evaluation of MTF sound-field data of the year 1963 in terms of an analysis of the excessive sound attenuation; an appraisal of the sound amplification; the classification of sound-velocity profile types; an analysis of the probability of sound focusing with regard to season, azimuth, and directionality; and the development of a measuring system to detect and analyze the nonstationary properties of atmospheric sound propagation.

The goal of the extensive acoustic measuring program at MTF is the provision of comprehensive and reliable contingency tables for the relationships between atmospheric parameters and far-field sound intensities. These tables are a basic prerequisite for high-confidence sound-propagation forecasting for static rocket-firing tests.

II. ROUTINE SOUND-FIELD AND METEOROLOGICAL MEASUREMENTS AT MISSISSIPPI TEST FACILITY

In late 1962, both an acoustical and a meteorological sound station were activated at the Mississippi Test Site near Gainesville, Mississippi (Fig. 1).

Eight azimuths around the wind rose were selected for routine sound-propagation measurements. (The azimuths were 30, 76, 103, 140, 175, 232, 280, and 342 degrees.) One series of measurements was made at least each morning and afternoon, 7 days a week. The sound to be monitored was generated by a pneumatic horn of about 5000 acoustic

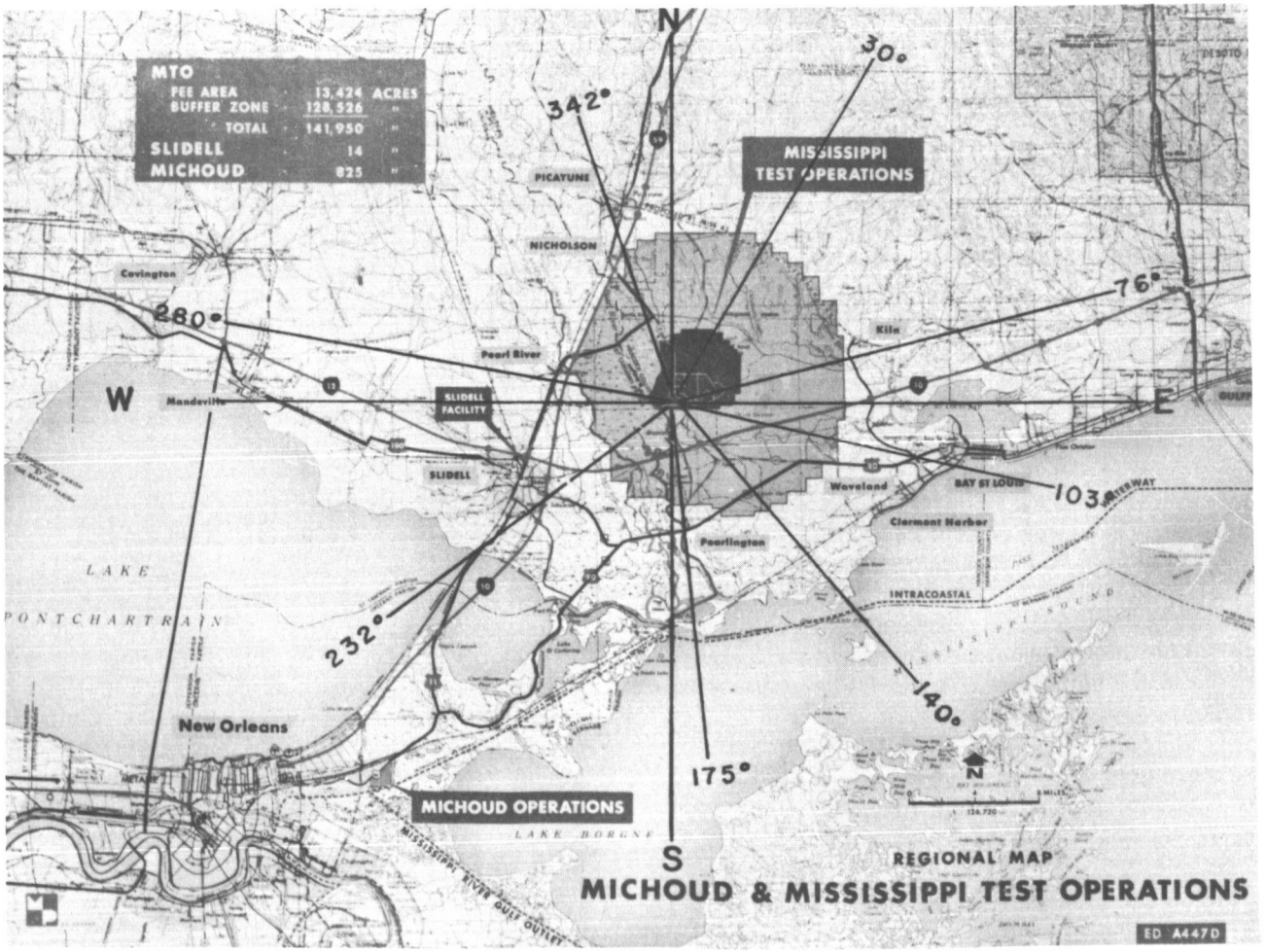

FIGURE 1. ORIENTATION OF MISSISSIPPI TEST FACILITY (MTF), WITH ACOUSTIC SOUNDING AZIMUTHS

watts power, which transmitted four discrete low frequencies (40, 80, 120, and 160 Hz) and a spectrum of random noise (Fig. 2). Personnel with hand-carried sound-pressure-level meters for visual data gathering were dispatched along the established azimuth lines. Sound emission from the horn and acquisition of sound data were coordinated by radio communication. The horn soundings were about 10 seconds per measurement.

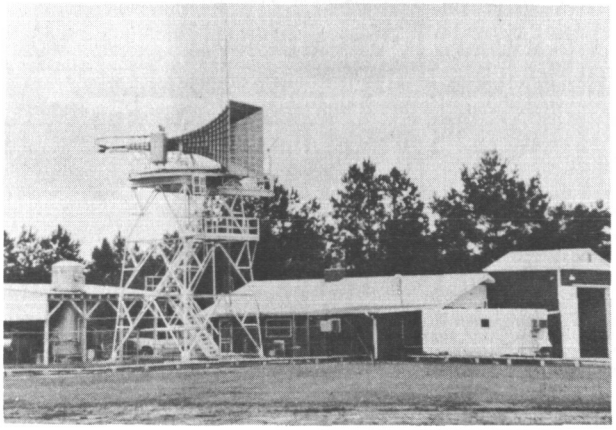

FIGURE 2. ACOUSTIC SOUNDING STATION AT MTF

To obtain the closest possible correlation between acoustic and atmospheric data, the acoustic measuring series and radiosonde ascents from the meteorological sound station (Fig. 3) were run simultaneously.

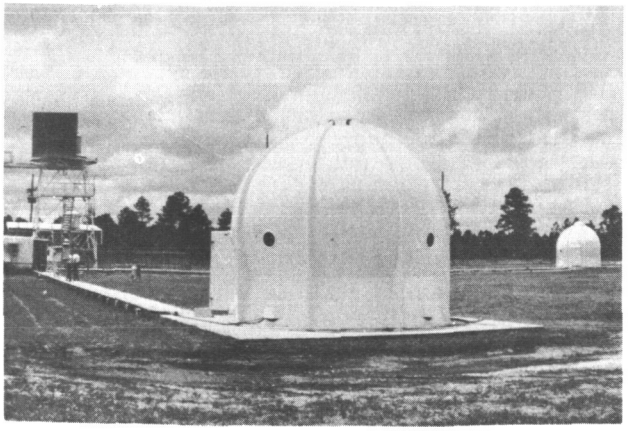

FIGURE 3. METEOROLOGICAL SOUNDING STATION AT MTF

III. STATISTICAL EVALUATION OF MTF SOUND-FIELD DATA FOR THE YEAR 1963

The first phase of the statistical analysis of atmospheric sound propagation was concerned with the evaluation of the MTF acoustic data population for 1963. Twenty-five measuring locations were selected along each of the specified azimuth directions. If each of the 25 stations had contributed a complete set of useful data for each measuring series, each azimuth would have provided 5921 sound pressure level (SPL) measurements for the year. The series was incomplete, however, because of a number of adverse conditions. The chief ones were temporary inaccessibility of the measuring locations because of poor ground conditions, and the weakness of the horn signal because of adverse sound-propagation conditions in the atmosphere, which resulted in the predominance of background noise over the acoustical signal. The graphic presentation of the number of available observations as a function of distance (Fig. 4), for example, indicates that, at 6 kilometers, the number of actual observations dropped to about 70 percent of all possible ones, and beyond 7 kilometers it dropped to 34 percent. Because these data favored cases of atmospheric conditions leading to sound amplification, the sound data at greater distances from the source are considered biased. To improve homogeneity of the data population, measuring sequence gaps not wider than two consecutive stations were closed by linear interpolation of sound-level values.

The statistical evaluation of the 1963 sound-measuring data, based on the conditions described, revealed the following main features of the sound field at MTF.

During springtime, the polar coordinate plot of average sound attenuation shows an almost circular pattern for a 40-Hz sound frequency (Fig. 5). The numerals on the polygons of Figures 5 and 6 indicate the seasonal root-mean-square values of sound attenuation, in decibels. The polygons are drawn only for identification of locations of equal sound-intensity values. The lines between the corners of these polygons do not have any numerical meaning. A slight shift of the distances of equal sound intensity toward the east indicates the influence of western winds on the polar sound-intensity distribution. Because the wind factor is slight, this polar distribution is essentially determined by the temperature field of the atmosphere. This means that a sound-velocity profile without wind influence, and depending

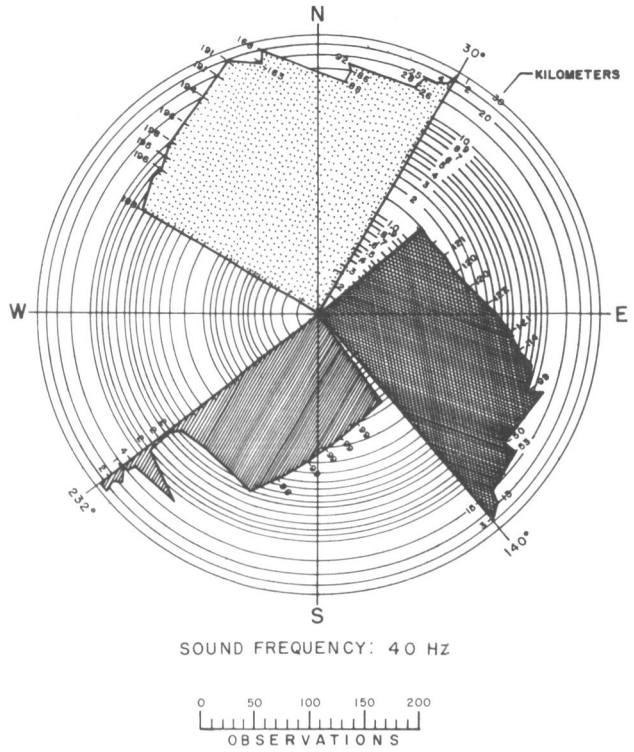

FIGURE 4. NUMBER OF SOUND OBSERVATIONS ALONG SELECTED AZIMUTHS; MTF, 1963

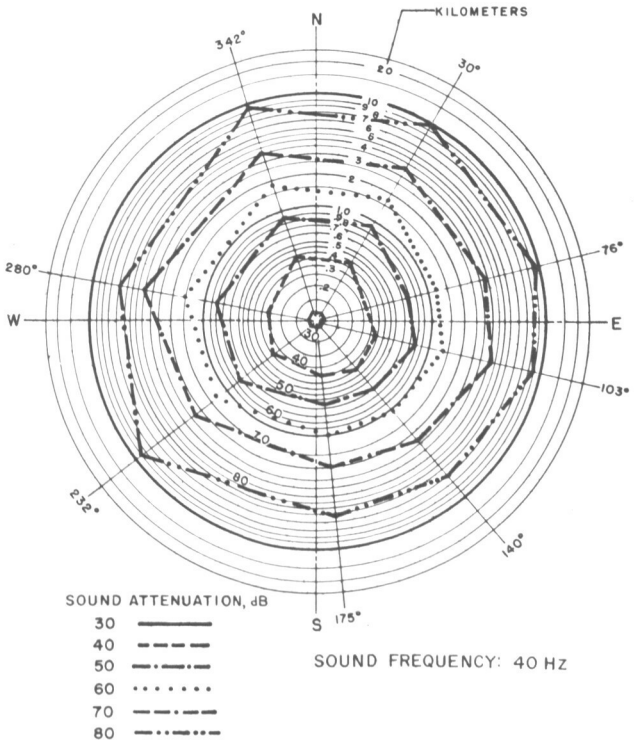

FIGURE 5. POLAR DISTRIBUTION OF AVERAGE SOUND ATTENUATION; MTF, SPRING 1963

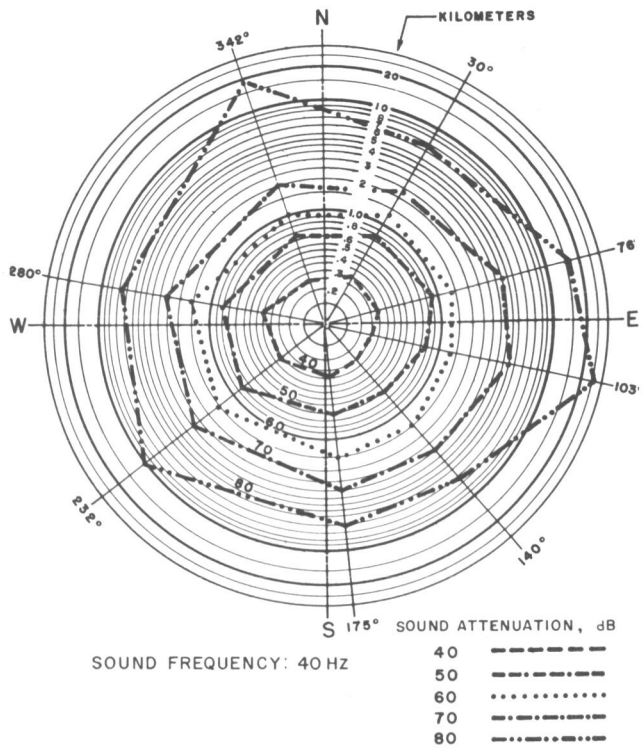

FIGURE 6. POLAR DISTRIBUTION OF AVERAGE SOUND ATTENUATION; MTF, AUTUMN 1963

only upon atmospheric temperature, generates identical sound-propagation conditions in any azimuth around the wind rose. A circular polar diagram of sound attenuation is produced in this case.

For the same sound frequency (40 Hz) in the autumn, there is a more pronounced deformation of the polar distribution of sound intensity. As indicated in Figure 6, deviations from the circular shape are obvious in the western, northeast, and southeast quadrants. This configuration indicates the dominance of stronger wind components from the west, northwest, and southwest over the temperature field.

The springtime average sound attenuation is presented in Figure 7 as a function of the distance from the sound source, for four selected azimuths. (The selected azimuths, 103, 175, 280, and 342 degrees, were the closest to the desired 90-degree intervals that could be obtained practicably.) For comparison, a long-short dashed straight line represents pure geometric dispersion of sound energy of spherical wave fronts (inverse square law for sound intensity); the attenuation rate is 6 decibels per octave of radial distance. The remarkable feature of this distance function of sound attenuation is the excessive attenuation between 1 and 10 kilometers from the sound source. The excessive attenuation reached a maximum at 6 kilometers (approximately), with a value about 18 decibels from the line of geometric sound dispersion.

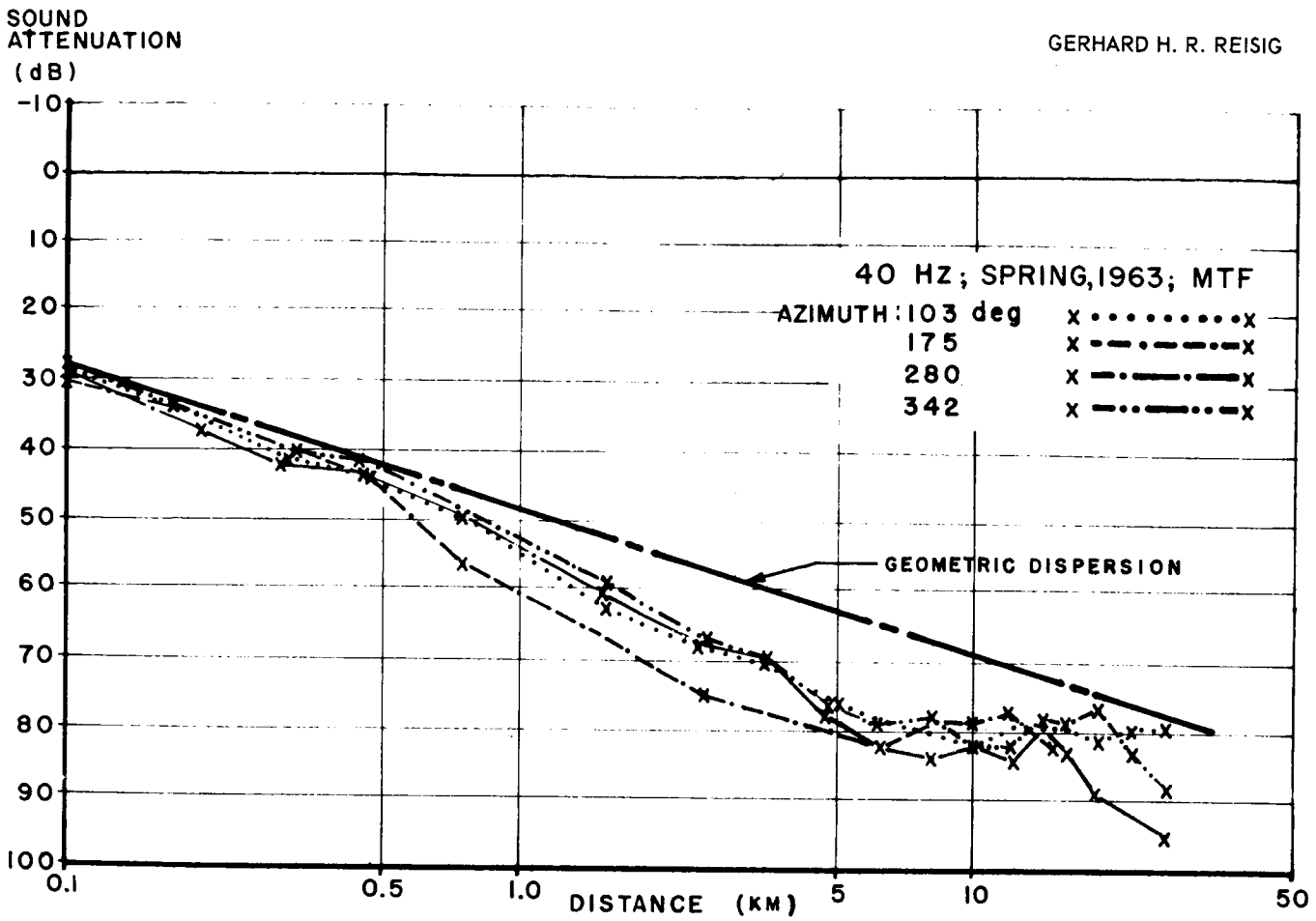

FIGURE 7. DISTANCE FUNCTION OF AVERAGE SOUND ATTENUATION (ROOT MEAN SQUARE); MTF, SPRING 1963

The distance function of sound attenuation in the autumn exhibits the same features as for spring, but is less uniform (Fig. 8). The maximum excessive attenuation also is at 6 kilometers, and its value is 17 decibels. This feature of excess attenuation proved to be typical with various excess amplitudes, for all azimuths, seasons, and sound frequencies.

A. EMPIRICAL EXCESS SOUND ATTENUATION AT MTF

The distance function of sound attenuation was compared with the expected local attenuation, so that the physical reasons for the distance-dependent excessive sound attenuation could be analyzed. The following known physical contributors to sound attenuation were taken into account (Fig. 9): (1) the classical attenuation, including air viscosity, air heat conduction, heat radiation of the atmosphere, and diffusion of the air molecules; (2) atmospheric attenuation due to molecular absorption in the air, which is a second order function of the sound frequency; and (3) a not too precisely defined amount of sound attenuation due to atmospheric scattering of sound waves.

For a sound frequency of 40 Hz, the distance function of expected sound attenuation is practically identical with the geometric sound dispersion function (Fig. 10). For a sound frequency of 160 Hz, the distance function of the expected sound attenuation gradually deviates from the geometric function; this deviation results from the quadratic dependency on frequency of the classical, molecular, and scattering attenuation (expressed as the terms B_k, B_m, and B_s, respectively, in the attenuation equation of Figure 9). Thus, at a 50-kilometer distance, the total expected attenuation increases by about 6.5 decibels above the geometric sound dispersion (the zero line).

During all seasons, in all azimuth directions, and for all sound frequencies, the deviation of average empirical sound attenuation from the expected value exhibits a typical trend in the form of a bell-shaped curve on a semilogarithmic plot (Figs. 11 and 12). The peak value of the average deviation is 21 decibels for 40 Hz (azimuth 280 degrees, summer, Fig. 11), and 24 decibels for 160 Hz (azimuth 175 degrees, spring and summer, Fig. 12). The peak signal strength for both frequencies occurs in summer.

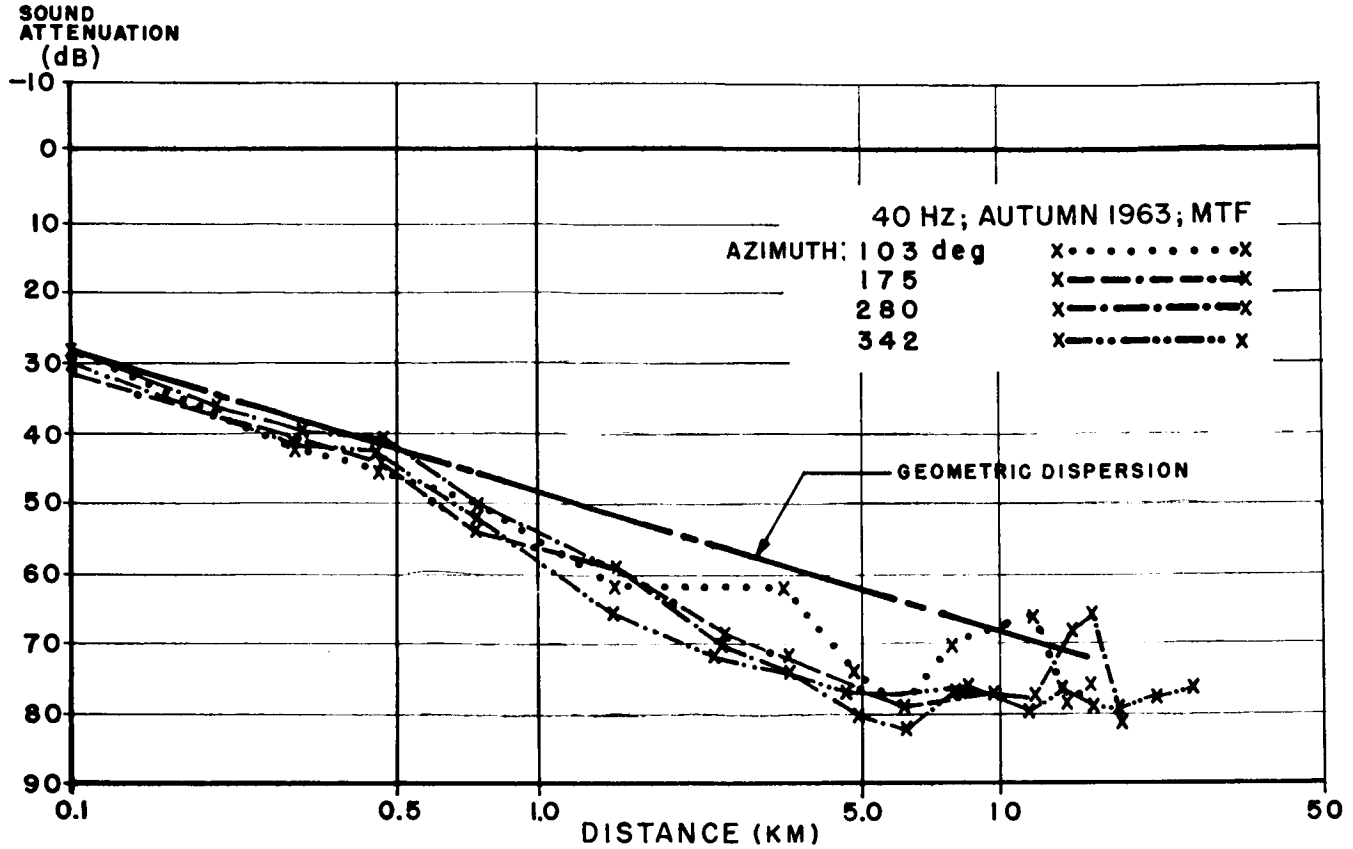

FIGURE 8. DISTANCE FUNCTION OF AVERAGE SOUND ATTENUATION (ROOT MEAN SQUARE); MTF, AUTUMN 1963

A physical explanation of this sound-attenuation phenomenon may be found in atmospheric diffraction and scattering effects (Fig. 13). The diffraction component of sound attenuation results from the negative gradients of the sound-velocity profile in the atmosphere. The negative gradients can be caused by either a negative atmospheric temperature-gradient profile or a negative wind-gradient profile, or a combination of both [1,2].

With regard to a given azimuth direction, a head wind will bend the sound rays upward, thus causing the diffractive attenuation of the sound waves, or a silent zone. However, no absolute silence has been observed in the actual sound field; the theoretically infinite attenuation is limited to a value of 24 decibels. The physical reason for the finite limit of attenuation in the silent zones is the scattering or "spilling" of sound energy into these zones. This scattering of sound is an effect of the condition of the atmosphere, which is inhomogeneous and constantly changing because of heat convection in the form of buoyant air bubbles and because of turbulence eddies generated by wind shear. Available empirical sound-field data so far are not comprehensive enough to permit a detailed analysis of the very significant sound-scattering effect. A sound-measuring project has been initiated at MTF for collecting sound-scattering data over large distances and on a statistical scale over all seasons of the year.

An essential instrumentation problem in the sound measurement was the monitoring of the background noise, which garbled a substantial amount of the sound-measuring data at MTF for the year 1963. Hence, the question which has to be answered is whether the limit of 24-decibel sound attenuation above the expected sound attenuation is caused by the sound-propagation conditions of the atmosphere, or whether this limit possibly represents a cutoff value caused by a masking background noise.

B. EXTREMES OF SOUND AMPLIFICATION

The statistical analysis of the empirical sound-propagation data at MTF also permits an appraisal of the magnitude of the local sound amplification, particularly that caused by focusing of sound energy. The criterion selected for the analysis of extreme amplification of sound intensity during propagation through the atmosphere was the limit formed by the negative three standard deviations from the average

$$A = \log \frac{d}{d_o} + (B_k + B_m + B_s) \cdot d \quad (dB)$$

d = DISTANCE (km)

d_o = 0.1 (km)

B_k = "CLASSICAL" ATTENUATION

B_m = MOLECULAR ATTENUATION

B_s = SCATTERING ATTENUATION

B_k:

f = 40 HZ : $B_{k40} = 2 \times 10^{-4}$ (dB / km)

80 HZ : $B_{k80} = 8 \times 10^{-4}$ (dB / km)

120 HZ : $B_{k120} = 2.0 \times 10^{-3}$ (dB / km)

160 HZ : $B_{k160} = 3.5 \times 10^{-3}$ (dB / km)

B_m:

f = 40 HZ : $B_{m40} = 3 \times 10^{-3}$ (dB / km)

80 HZ : $B_{m80} = 1.3 \times 10^{-2}$ (dB / km)

120 HZ : $B_{m120} = 3 \times 10^{-2}$ (dB / km)

160 HZ : $B_{m160} = 5 \times 10^{-2}$ (dB / km)

B_s:

f = 40 HZ : $B_{s40} = 5.5 \times 10^{-3}$ (dB / km)

80 HZ : $B_{s80} = 2 \times 10^{-2}$ (dB / km)

120 HZ : $B_{s120} = 4.0 \times 10^{-2}$ (dB / km)

160 HZ : $B_{s160} = 7.5 \times 10^{-2}$ (dB / km)

FIGURE 9. COMPONENTS OF EXPECTED ATMOSPHERIC SOUND ATTENUATION

attenuation deviation. This limit of three standard deviations, or "three-sigma" values, comprises 99.73 percent of all empirical sound-attenuation data obtained during the year 1963 at MTF. This three-sigma limit indicates the strength of actual sound amplification by focusing that can be expected in the large majority of cases along the selected azimuth directions.

The 40-Hz sounding frequency, as an example, shows the three-sigma sound-amplification probabilities in four azimuth directions during spring (Fig. 14). The highest sound-amplification values during this season occur at 1.5 kilometers distance, and beyond 7 kilometers. In the distance functions presented, the maximum amplitude of sound amplification amounts to about 20 decibels. However, the extreme amplification occurs during winter on the 140-degree azimuth. At 1.5 kilometers distance, it rises to 35 decibels above the expected value. At 22 kilometers distance, a peak value of almost 50 decibels amplification is reached, probably because of focusing.

The 160-Hz sounding frequency during autumn shows a maximum amplitude of 16 decibels (Fig. 15). The absolute extreme sound amplification occurs during winter and on the 140-degree azimuth (as for 40-Hz sound), with peak values of about 32 decibels above the expected attenuation at both 1.5 and 22 kilometers distance from the sound source.

C. CLASSIFICATION OF SOUND-VELOCITY PROFILE TYPES

The first physical and statistical results of the analyses of empirical sound-field data serve as a guide to the sound-propagation phenomena to be encountered at MTF. The next step in the analysis of the distance functions of observed local sound intensities calls for the closest possible correlation between empirical sound data and the local atmospheric sound-propagation conditions at the time of the acoustic observation. For this novel and intricate analysis, the vertical profile of sound velocity versus altitude was selected as the atmospheric parameter function responsible for the sound-intensity distribution in the sound field at the surface. The vertical sound-velocity profile is determined from the meteorological data of each radiosonde ascent in support of acoustic measurements.

The basic idea for the newly conceived correlation analysis consists of the classification of the vertical sound-velocity profiles into characteristic types (Fig. 16). The statistical populations of these profile types preserve the physical features which characterize each significant class of atmospheric sound-propagation conditions. Thus, the individual statistical populations of sound profiles are determined only by the structure of the atmosphere at a particular instant. Theoretically, each profile type could occur at any time, independent of a particular day, month, or season. This concept does not suppress the physical features of the profiles, as conventional statistical treatments usually do, for instance, by averaging physical quantities over arbitrary time intervals without specific physical meaning.

The method of classification of the vertical sound-velocity profiles has been developed by Essenwanger, US Army Missile Command [3]. With this method, the profiles are represented in terms of polynomials up to the sixth order. The profile representation is accomplished either by "pure" polynomials of the

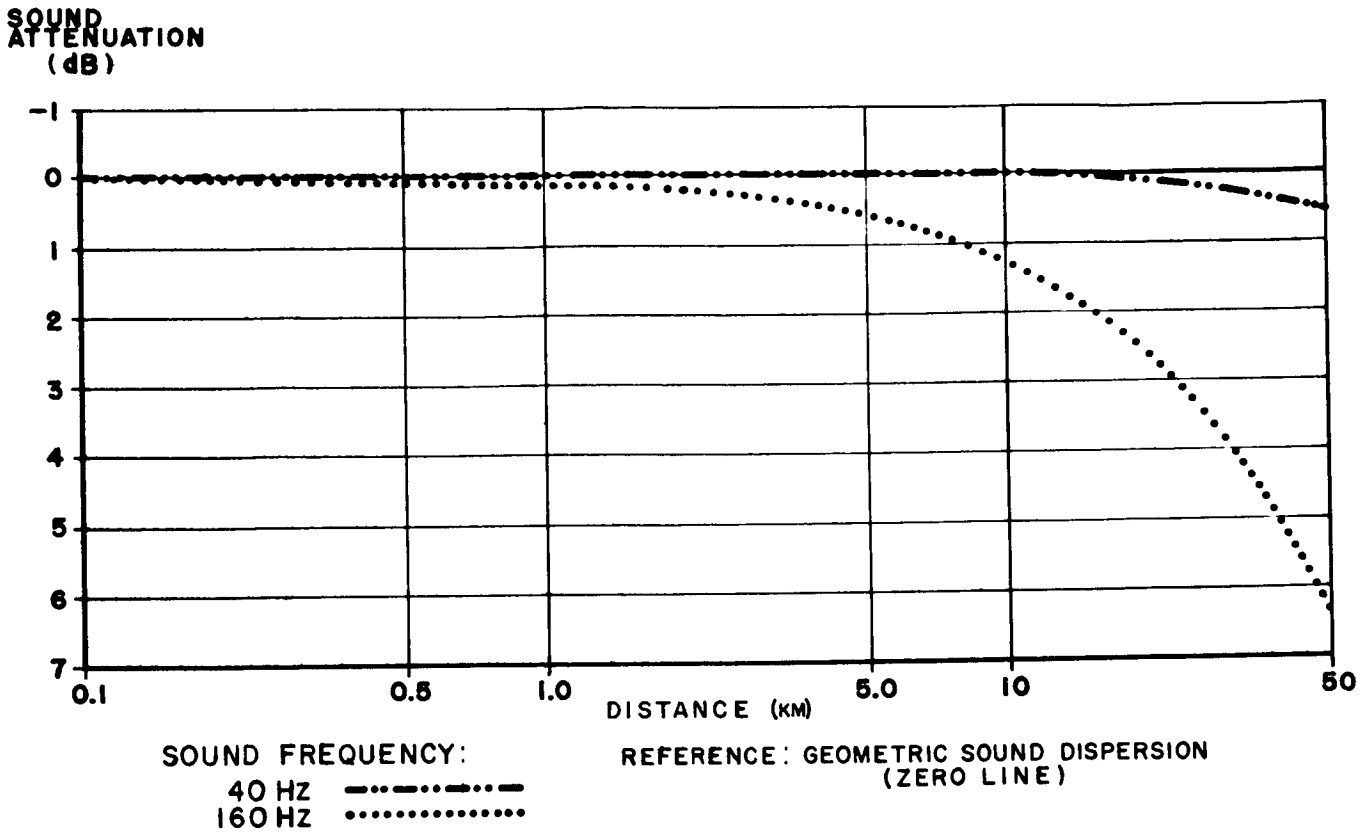

FIGURE 10. DISTANCE FUNCTION OF EXPECTED PHYSICAL SOUND ATTENUATION

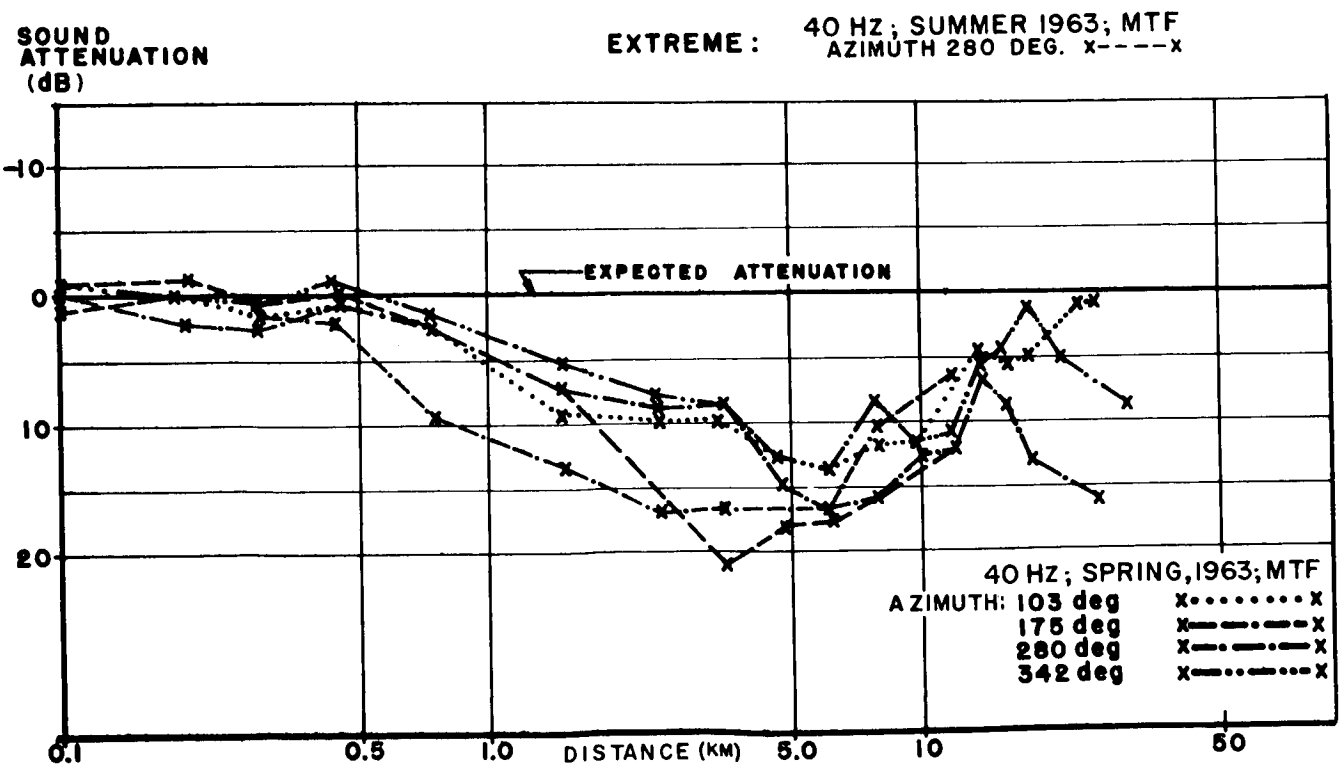

FIGURE 11. AVERAGE DEVIATION OF EMPIRICAL SOUND ATTENUATION FROM EXPECTED VALUES, 40 Hz; MTF, SPRING 1963

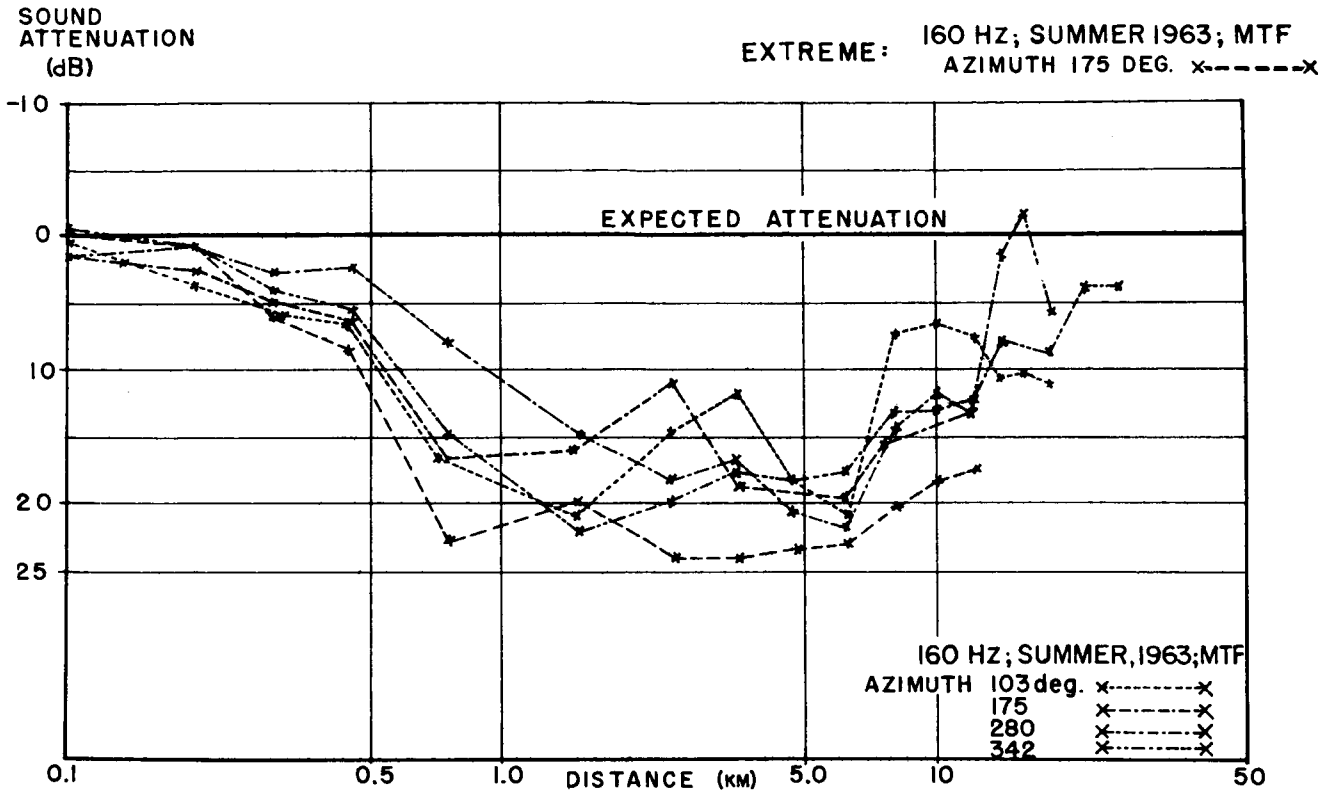

FIGURE 12. AVERAGE DEVIATION OF EMPIRICAL SOUND ATTENUATION FROM EXPECTED VALUES, 160 Hz; MTF, SPRING 1963

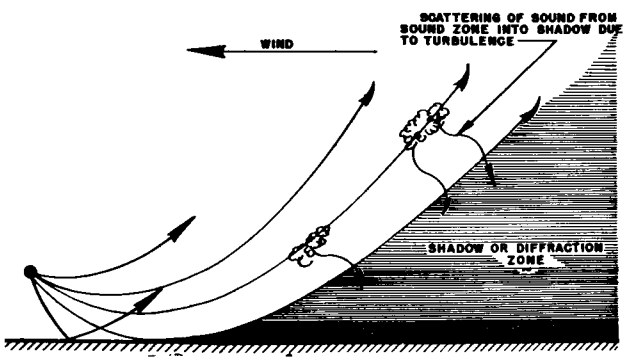

FIGURE 13. SOUND DIFFRACTION AND SCATTERING IN ATMOSPHERE

order one through six, like types 1 and 11 in Figure 16, or by a superposition of a basic polynomial of predominant weight with higher order components of lesser weight, like types 22 and 27. The analytical investigation of about 252,000 individual sound-velocity profiles of the stations at MTF, at Huntsville, Alabama (Marshall Space Flight Center), and at Nashville, Tennessee, has established that, up to a height of 3 kilometers, 33 sound-velocity profile types essentially constitute the empirical possibilities of the sound-propagation conditions in the southeastern United States.

The quality of matching between the empirical sound-velocity profile and its analytical prototype has to result in a correlation coefficient of at least 0.7, which is a strict requirement. However, in most cases of matching of the investigated sound-velocity profiles, a correlation coefficient of 0.9 has been achieved, which is an excellent result.

Certain profile types rarely occur in their ideal form. They are sensitive to "static" perturbations of the atmospheric parameters which express themselves in higher order polynomial components of small weights. These perturbations lead to focusing properties of profile types which, according to acoustic ray theory, could not affect focal concentration of sound energy. This phenomenon explains the focusing probabilities for the profile types such as 1 and 22 in Figure 16.

D. PROBABILITY AND DIRECTIONALITY OF SOUND FOCUSING

The focusing or nonfocusing qualities of each established type of sound-velocity profile can now be

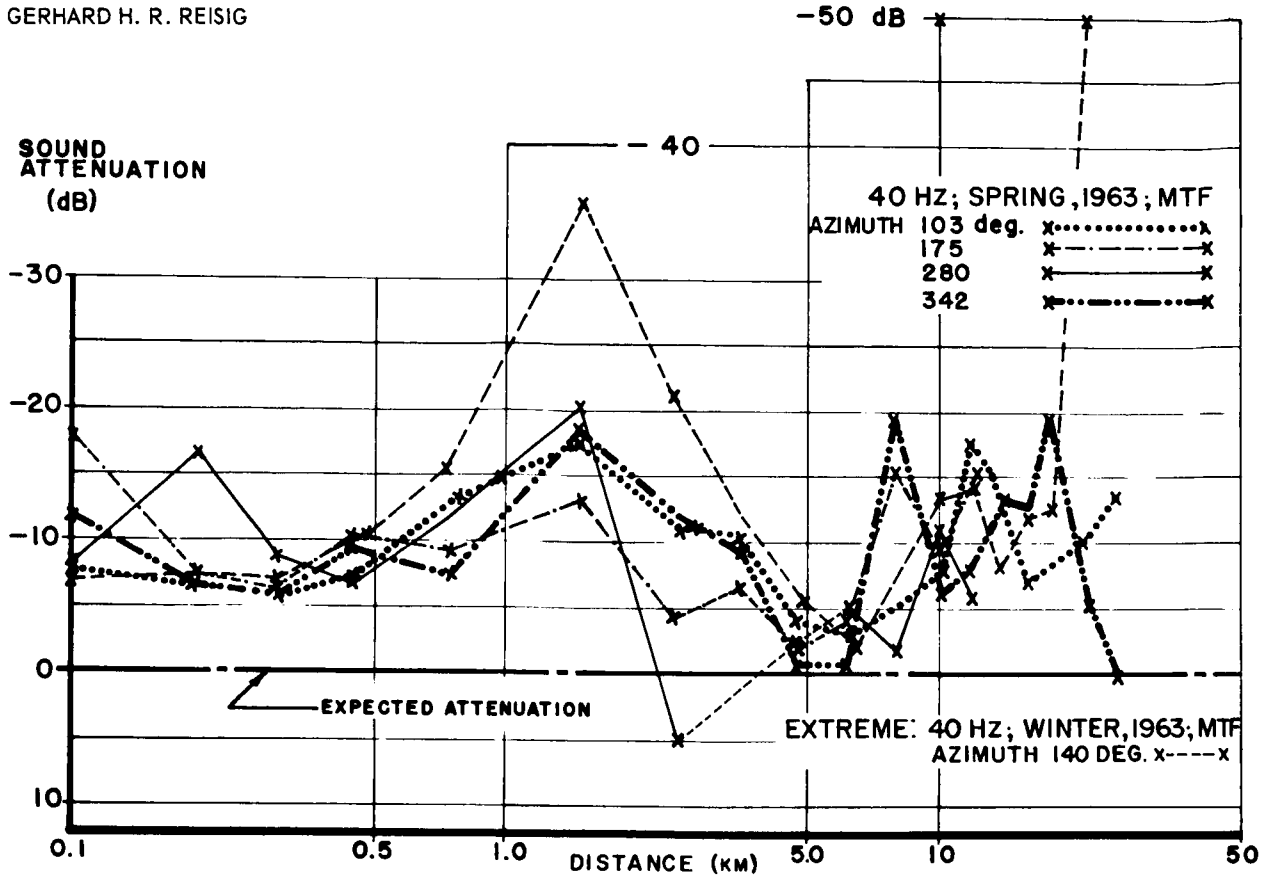

FIGURE 14. THREE-SIGMA NEGATIVE ATTENUATION DEVIATION, 40 Hz; MTF, SPRING 1963

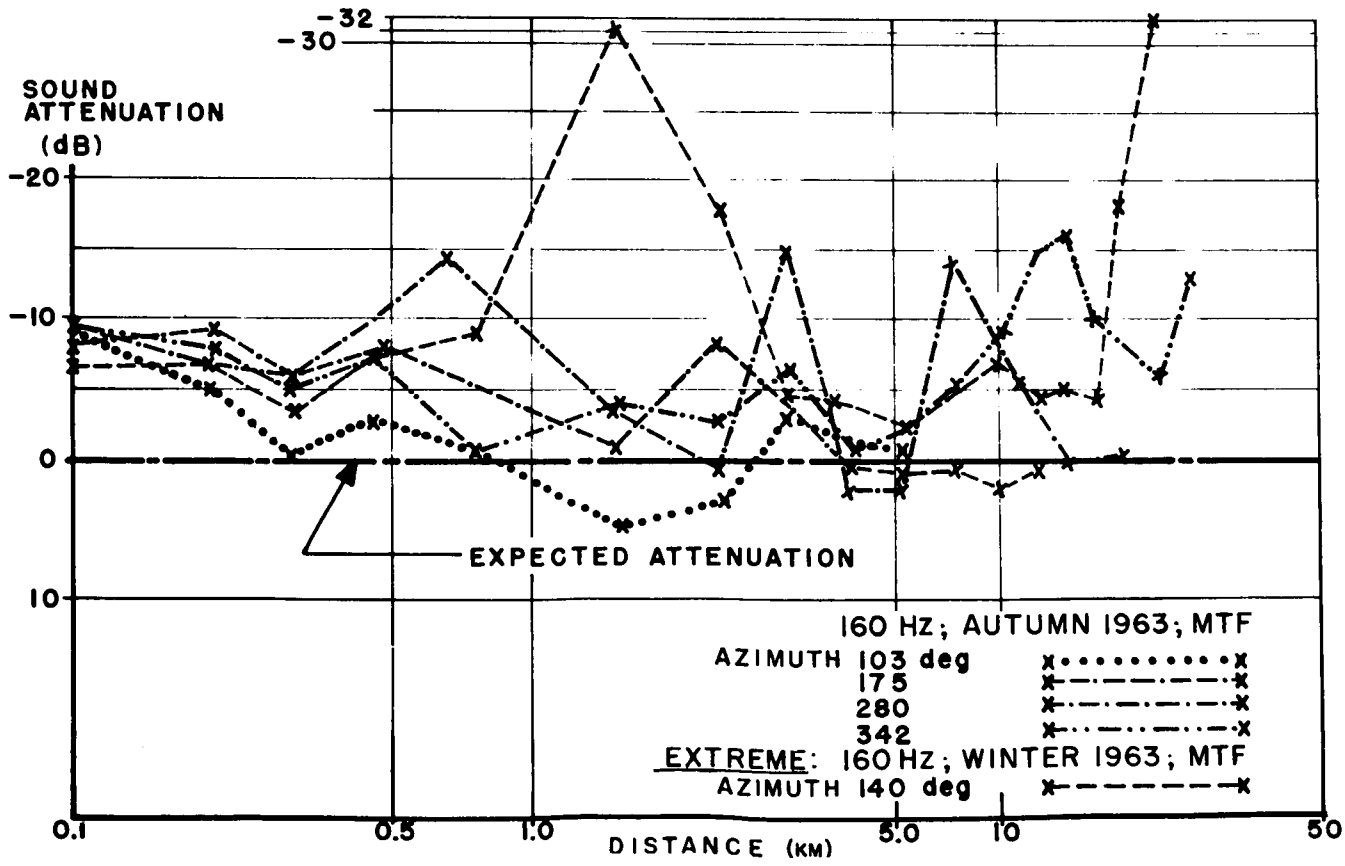

FIGURE 15. THREE-SIGMA NEGATIVE ATTENUATION DEVIATION, 160 Hz; MTF, AUTUMN 1963

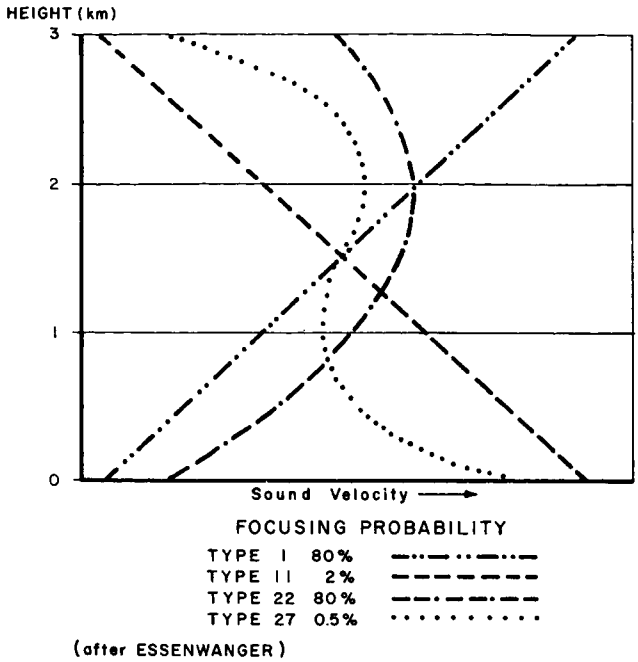

FIGURE 16. SELECTED TYPES OF CHARACTERISTIC SOUND-VELOCITY PROFILES

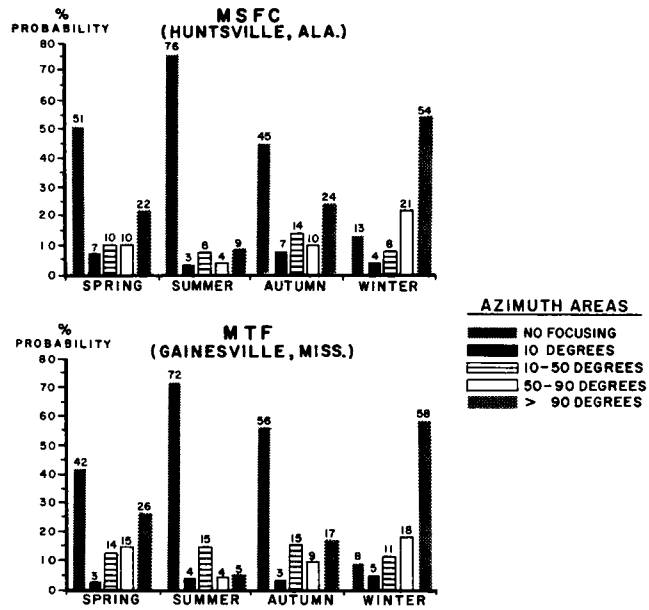

FIGURE 17. PROBABILITY OF AZIMUTH COVERAGE OF SOUND FOCUSING, MSFC AND MTF

determined as a class characteristic. The sound-focusing properties of each empirical sound-velocity profile of the MTF and Huntsville, Alabama (MSFC), stations have been analyzed [4] with this established classification. A summary of these investigations (Fig. 17) gives the overall probabilities of focusing occurrence in the two stations, for the four seasons of the year in the afternoon (1200 to 1700 hours, local time). The favorable conditions of nonfocusing during summer are readily evident, with 72 percent nonfocusing at MTF and 76 percent at MSFC. Figure 17 also indicates the severity of focusing by expressing the lateral spread of focusing areas (directionality) covered by high-intensity sound amplification. For instance, during winter the total focusing probability at MTF is 92 percent, and for MSFC, 87 percent. In these cases, the focusing area extends over an azimuth sector of more than 90 degrees, with a probability of 58 percent at MTF and 54 percent at MSFC. During the forenoon hours, the focusing probabilities have been found even more severe because of the peculiar structure of the atmosphere. During summer, however, the focusing probability is only 28 percent at MTF and 24 percent at MSFC. The lateral spread of the focusing area in severe cases (azimuth sector over 90 degrees) occurs with a probability of only 5 percent at MTF and 9 percent at MSFC.

For rocket-firing tests, it is essential to know which areas around the test facility will be most affected by strong noise amplification. Figure 18 shows the distribution of focusing probabilities as a function of the azimuth around the whole wind rose for the four seasons at MTF. Again, the severity of focusing during winter is obvious, and the direction toward east is affected most. In contrast, the focusing during summer is spread almost evenly over the whole wind rose, with a low probability of less than 6 percent. Figure 19 shows the same presentation of azimuthal focusing distribution for MSFC. The overall features of areal focusing coverage are very similar to those at MTF. Figure 20 presents a comparison of winter focusing distribution for MTF and MSFC. It can be seen that the focusing around east is somewhat more severe at MSFC than at MTF.

E. MEASUREMENTS OF NONSTATIONARY SOUND PROPAGATION

The matching of a specific empirical sound-velocity profile with its simultaneously measured sound-intensity distance function proved to be greatly disappointing. A fair match of calculated sound-intensity amplification and relative sound-intensity maxima, measured in the field, could be obtained only in isolated cases. The reason for this failure of method was recognized early: the atmosphere as the medium of sound-wave propagation is not in a stationary condition, but is continuously changing [5]. The oversimplified mathematical model of the sound-ray-tracing method cannot do justice to these nonstationary conditions of the atmosphere, particularly because it uses only a two-dimensional concept. The

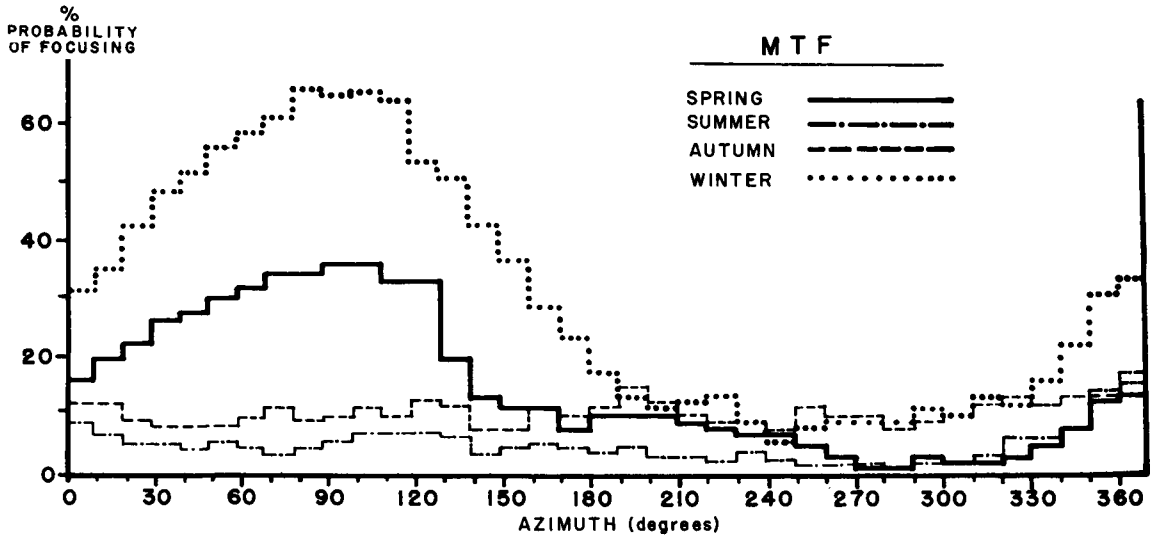

FIGURE 18. PROBABILITY OF SOUND FOCUSING, BY AZIMUTH; MTF

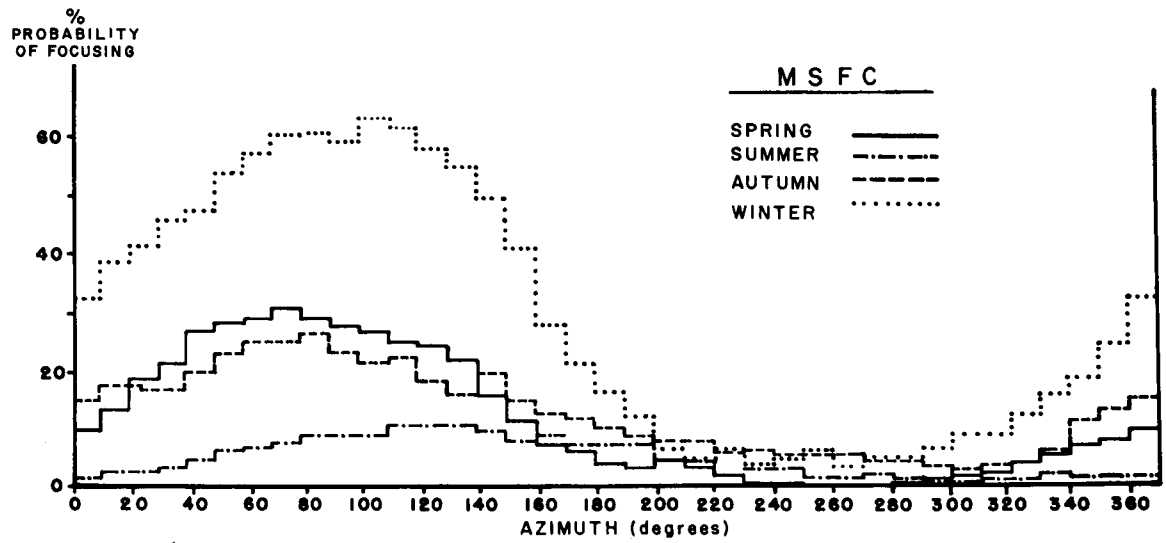

FIGURE 19. PROBABILITY OF SOUND FOCUSING, BY AZIMUTH; MSFC

extensive experience gained with the sound-intensity measurements at MTF strongly indicated the three-dimensional nature of the sound-propagation phenomena.

A novel approach for analyzing the nonstationary sound-propagation phenomena was conceived. The basic idea of this new method consists of the superposition of empirically determined "dynamic" perturbation functions on the pertinent characteristic sound-velocity profile types. Logically, these perturbation functions have to account for the nonstationary components of the individual sound-propagation conditions.

For the experimental task of establishing the "dynamic" perturbation functions, two measuring areas, each of about 600 by 600 meters side length, have been selected at MTF. One measuring area is situated on the 45-degree azimuth at a distance of 3.6 kilometers from the sounding horn, and the other measuring field is located on the 110-degree azimuth at a distance of 14 kilometers. In each of the two areas, a measuring network of five microphones has been laid out to cover the area in a cross-shaped pattern (Figs. 21 and 22). Background noise was reduced sufficiently by means of filtering networks and microphone screening (Fig. 23). The measuring series of the sound-propagation fluctuations were

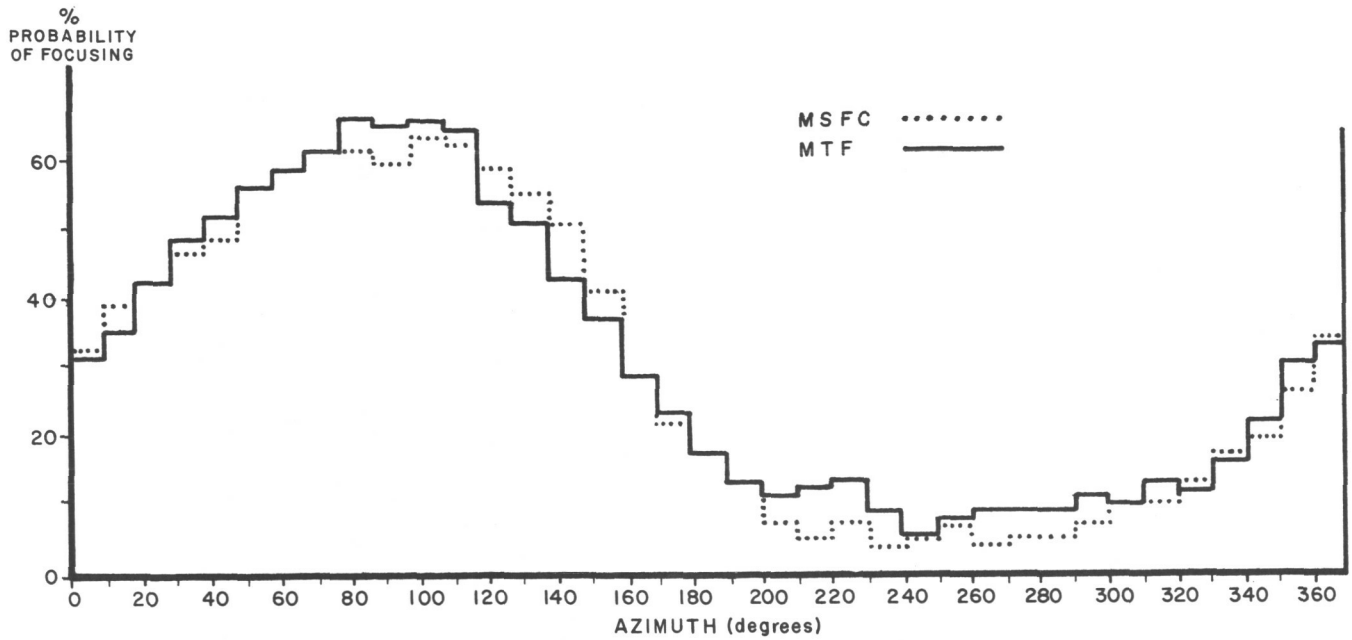

FIGURE 20. COMPARISON OF WINTER SOUND-FOCUSING PROBABILITIES, BY AZIMUTH; MTF AND MSFC

started in summer, 1965. The initial mode of operation of the whole measuring system is scheduled as a 10-second-sounding horn blast, with a 10-minute-repetition rate for 2 hours. Instrumentation design and data analysis of the multicross-correlation problem of the microphone array, supplemented by micrometeorological measurements in the microphone area, are handled by Tulane University Engineering School.

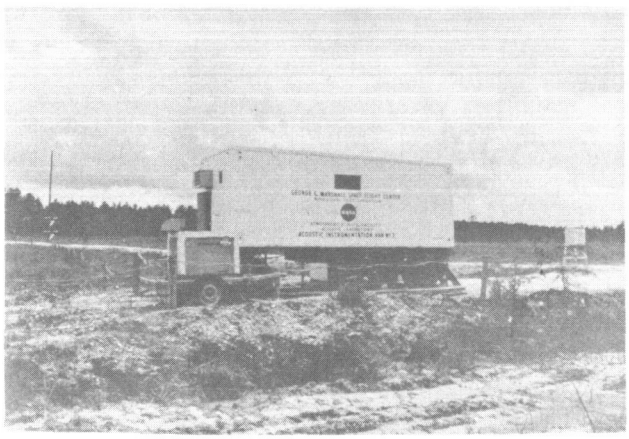

FIGURE 21. A SOUND-FLUCTUATION MEASURING STATION, MTF

A first sample of the sound fluctuation measurements in the microphone area at 3.6-kilometer distance from the sound source is presented in Figure 24. In Graph (I) it can be seen that the instantaneous sound-pressure levels at microphone stations 2 (center of field) and 4 (300-meter distance) differ as much as 19 decibels. Graph (II) represents the instantaneous SPL values at the five microphone stations, of the same area 10 minutes after the formation of the SPL pattern of Graph (I). Graph (III) demonstrates the SPL differences between Graphs (I) and (II). It can be recognized that the SPL values at microphone station 4 changed by 20 decibels within a period of 10 minutes. Therefore, the spatial SPL fluctuations over a 300-meter distance, and the temporal fluctuations over a 10-minute period, can attain the same magnitude of ±20 decibels.

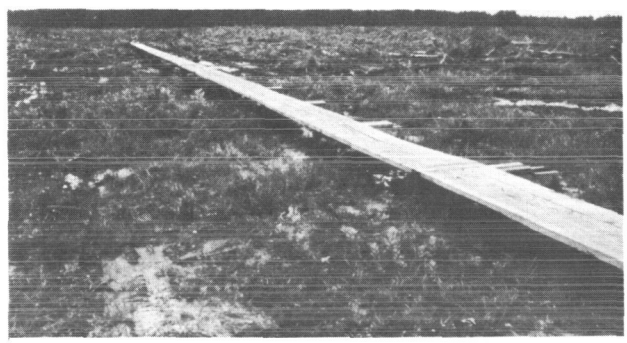

FIGURE 22. MICROPHONE CATWALK FOR SOUND-FLUCTUATION MEASURING FIELD, MTF

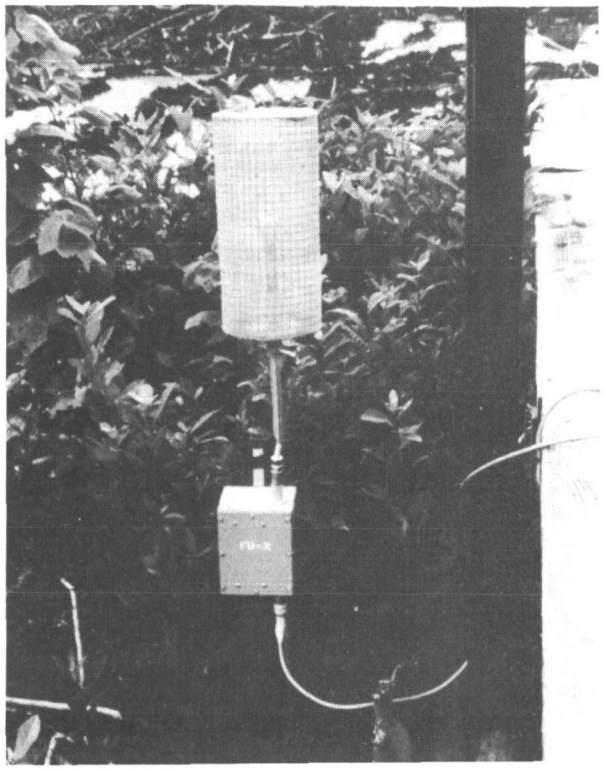

FIGURE 23. MICROPHONE SCREENING FOR SOUND-FLUCTUATION MEASURING FIELD, MTF

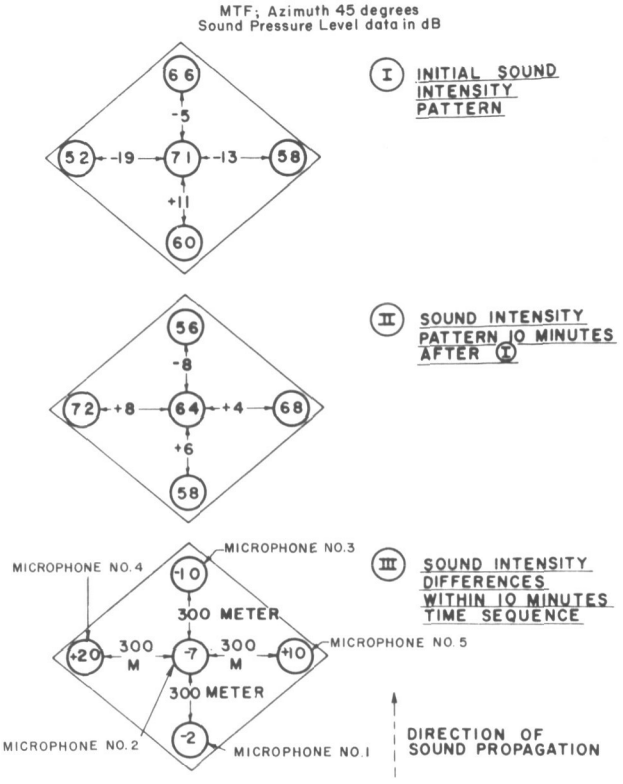

FIGURE 24. SOUND INTENSITY SPATIAL INHOMOGENEITIES AND TEMPORAL FLUCTUATIONS, MTF

IV. CONCLUSIONS

The extensive acoustic measuring program at MTF has generated, and still is generating for statistical completeness and reliability, a unique fund of acoustic far-field information. The novel approaches in measuring techniques and data analysis, which are being applied in this project, give promise of providing comprehensive and reliable contingency tables for the relationships between atmospheric parameters and far-field sound intensities. These tables are a basic prerequisite for high-confidence sound-propagation forecasting for static rocket-firing tests.

REFERENCES

1. Pridmore-Brown, D.; and Ingard, U.: Sound Propagation into the Shadow Zone in a Temperature-Stratified Atmosphere Above a Plane Boundary. NACA TN 3494, 1955.

2. Pridmore-Brown, D.; and Ingard, U.: Tentative Method for Calculation of the Sound Field About a Source Over Ground Considering Diffraction and Scattering into Shadow Zones. NACA TN 3779, 1956.

3. Essenwanger, O.: On a System of Profile Types of Sound Speed in the Lower Atmosphere. Army Missile Command, Redstone Arsenal, 1965 (to be published).

4. Essenwanger, O.: On the Frequency of Returning Acoustic Rays and Focusing for Huntsville and Mississippi Test Facility. U. S. Army Missile Command Report No. RR-TR-66-2, Redstone Arsenal, Ala., 1966.

5. Sieg, H.: Ueber die Schallausbreitung im Freien und ihre Abhaengigkeit von den Wetterbedingungen. Elektrische Nachrichten-Technik 17(1940) 193 (No. 9).

RESEARCH AND DEVELOPMENT IN INSTRUMENTATION FOR STATIC TESTING

By

Albert E. Schuler

SUMMARY

The varied MSFC research and development programs in instrumentation for static testing are summarized in this report. The work, done in-house and through contracts, is described under the categories of cryogenic fuel density measurements, mass flowmeters, liquid-level sensors, temperature-measuring instrumentation, damped accelerometers, digital transducers, and calibration systems.

Work on density measurements of cryogenic fuels, needed for better measuring accuracy, has resulted in the development of a very accurate point density sensor that uses a solid-state detector and a beta radiation source. Solutions to the special problem of measuring LH_2 density in suction lines are being evaluated. One densitometer under development uses X rays as a higher energy radiation source, which results in a faster response time.

MSFC initiated studies on mass flowmeters to meet the need for measurement of mass, rather than volume, of missile fuels. Several flowmeters, each with a different operating principle, are in various stages of development and test.

Investigations on liquid-level instrumentation is concerned with providing accurate and reliable discrete sensors for flow-rate determination. Two electronic level switches, one capacitive and the other conductive, have been developed successfully by MSFC. The most accurate and reliable all-purpose commercial unit tested by MSFC is an optical sensor.

Although the temperature of cryogenic fuels can be measured accurately, there is a problem of slow response because of test conditions. Sensor probes with fast response speed, based upon an MSFC design, have been developed and are being tested. In other in-house research on calorimeters, thermopiles were used successfully for radiation heat flux measurements.

An accelerometer operating by hydraulic damping, deformation of a composite mass, and signal generation by piezoelectric material, has been developed for use over higher frequency ranges without ringing. For testing and calibrating high-frequency-range accelerometers, a new calibration system was developed; this uses either a constant-displacement or a constant-acceleration mode of operation. MSFC also has developed a portable accelerometer calibrator.

A digital pressure transducer has been developed: it has an 11-bit binary output, a resolution of 1 count in 2047, and an accuracy better than 0.1 percent. A 36-channel data recording system is being developed, using 20 of the new pressure transducers, 16 different electrical signals, a multiplexer, and very accurate DC amplifiers.

The calibration of ultrahigh-vacuum gages can be done now through a multistage pressure reduction method, devised through an MSFC-sponsored contract. Other investigations on measurement of extreme values deal with very low water-vapor content of pressurizing gases (less than 1 part per million) and calibration of load cells for 5-million-pound (22-MN) forces.

Significant work has been done in automatic calibration systems. One system, for calibrating pressure gages, uses a pressure balance and has a calibration accuracy of 0.05 percent. Another automatic system, a thermocouple calibrator, can automatically measure and print the output of 12 thermocouples.

I. INTRODUCTION

The research and development activities of the Instrument Development Branch of Test Laboratory, Marshall Space Flight Center, consist of in-house and out-of-house basic and applied research. This review is a summary of major research activities and achievements, and covers density measurements of cryogenic fluids, mass flowmeters, liquid-level gages, special temperature-measuring instrumentation, damped accelerometers, digital transducers, calibration of vacuum gages down to 10^{-10} torr ($1.33 \times 10^{-8} N/m^2$), calibration of 5-million-pound (22.24-MN) load cells, and automatic calibration systems.

II. DENSITY MEASUREMENTS OF CRYOGENIC FUELS

During the first 25 years of work with liquid-propellant rockets, liquid oxygen (LOX) was measured quantitatively by weighing or by determining its volume with level gages. Volumetric and gravimetric values were converted through the use of density data in handbooks or international critical tables. The 0.5-percent disparity between calculation and measurement was attributed to measurement inaccuracy. In 1958, a test with repeated weighing at overflow demonstrated that LOX density changed with the time. A more elaborate measuring program established that the density of LOX in a missile tank differs from the density given in the handbooks. At the conditions for which the handbooks stated a density of 1.14 g/cm^3, accurate measurements of LOX showed 1.333 g/cm^3, a difference of 0.6 percent. There was an evident need for instruments to measure LOX density. Consequently, a research contract was awarded to Franklin Systems, Inc., with the result that prototype density measuring instruments were developed. These measured the average density of LOX in tanks of various diameters, using cobalt 60 as a radiation source at one side of the tank and a scintillation counter at the opposite side (Fig. 1). When tank diameters were too big, measurements were made across a secant instead of the diameter (part A, Fig. 1).

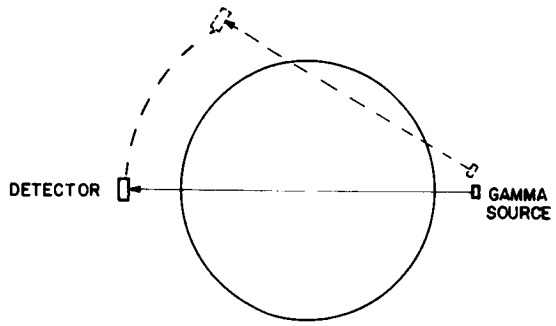

A. MEASUREMENT ACROSS DIAMETER AND SECANT

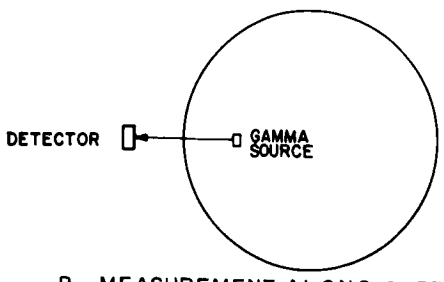

B. MEASUREMENT ALONG PART OF RADIUS

FIGURE 1. DENSITY MEASUREMENT OF CRYOGENIC FUEL IN A TANK

The scintillation counters, particularly the photomultiplier portion, were insufficiently stable. Therefore, a servo-type self-adjustment, with an alpha radiation source on the detector side, was added as a reference. Better repeatability could be obtained with this compensating feature, but for field use the equipment still was not reliable enough.

The contract was extended to learn whether other detectors would be better than scintillation counters, and the contract study showed that a xenon-filled ionization chamber was better. Under constant temperature, the repeatability of a densitometer with an ion chamber is 0.1 percent. The idea of compensating a scintillation counter with an alpha source, as mentioned, is now being used by several companies for other nuclear instrumentation.

An isotope radiation source submerged in LOX is represented by part B of Figure 1. With this arrangement it was possible to determine the average density of different layers of LOX next to the tank wall, in order to get information about the density profile across the tank. However, all the arrangements with average density measurements along a diameter, secant, or part of a radius were insufficient for determining density stratification. Therefore, a new research and development program to develop point-density sensors was started. These sensors use beta radiation from a strontium 90 radiation source, and a solid-state detector close to the source (Fig. 2). The entire unit is submerged in LOX at different locations in the tank so that the LOX density profile can be determined. The individual units are reliable for LOX measurements; a system using six detectors has been delivered to MSFC and is now being tested. The same method was used for point-density measurement in liquid hydrogen (LH_2), but more research had to be done, mainly in reference to resistance contacts and epoxy resins, so that the sensor could be made to withstand the low temperature. These problems have been solved, and LH_2 point-density measuring units in a 10-channel system will be available soon. For LOX and LH_2, the accuracy of these point-density sensors is about 0.1 percent for 10-second counting time, and about 0.2 percent for 1-second counting time.

When LH_2 was selected as the propellant for upper stages of Saturn vehicles, the deviations of LH_2 densities from handbook data were expected to be worse because the density of LH_2 changes 1.6 percent per degree Kelvin. However, it was found that the handbook density data for LH_2 agreed much better with the densities as measured for LOX. The explanation is that LH_2 is in vacuum-jacketed tanks, similar to the thermos flasks used in the laboratories where density data for handbooks are determined,

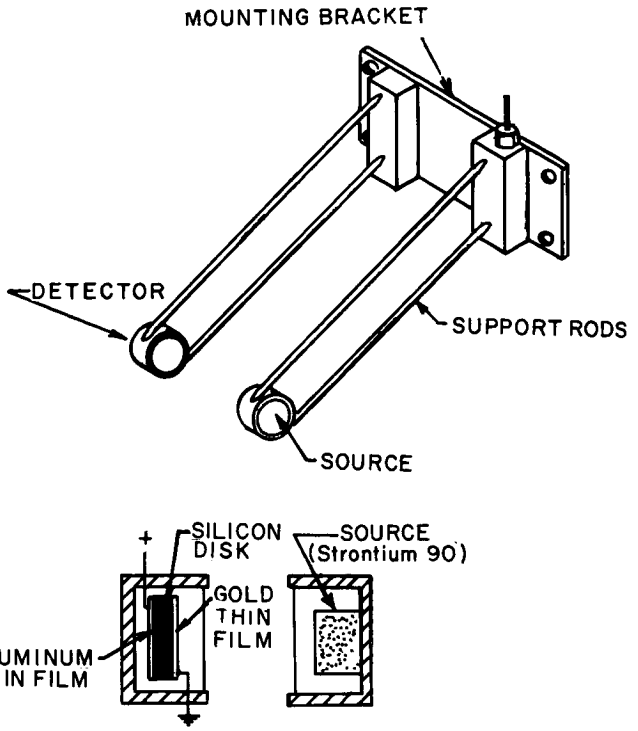

FIGURE 2. DENSITY MEASUREMENT OF CRYOGENIC FUEL AT A POINT WITHIN THE TANK

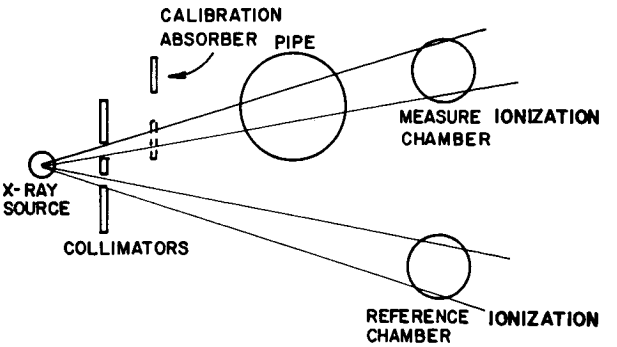

FIGURE 3. DENSITY MEASUREMENT OF LH_2 IN A PIPE, USING SPLIT X-RAY BEAM

while LOX in missiles is in uninsulated tanks and, therefore, because of the heat influx, the density deviates up to 0.6 percent.

These observations are true for tank containment. In regard to LH_2 suction lines there are other significant problems caused by two-phase conditions and density instabilities. Accurate measurements require densitometers with higher speeds of response than are needed for tanks. There is a current contract to develop a densitometer for LH_2 in the S-IVB suction line. In this development, X rays are used instead of isotopes to provide more radiation energy. Greater energy results in faster response. In addition, the radiation hazards are reduced, since X rays can be cut off. Figure 3 shows the arrangement schematically. The two-beam arrangement compensates for changes in the X-ray unit. An aluminum or a beryllium disk can be used as a calibration absorber by inserting it into the beam path.

The unit has been constructed for regular use and is in its final test phase. Indications are that 0.1-percent accuracy and a 0.5-second time constant have been achieved. Pending completion of testing, MSFC is using a less accurate instrument for making some measurements in the S-IVB suction line. This instrument uses available components: cesium 137 as a radiation source and an ionization chamber as a detector. The instrument has an acceptable repeatability for comparisons, but it cannot be used for absolute density measurements.

III. FLOWMETERS

The turbine-type, volumetric flowmeter has been used for flow measurements during the last two decades. These meters have been improved steadily and are now very accurate and reliable. However, the energy content of missile fuels is a function of the mass rather than of the volume.

Because of the uncertainty of density data as a function of pressure and temperature, and the increase in errors when three parameters must be measured to determine one value, the search for direct mass flowmeters was intensified.

A contract for the study of mass flowmeters for all propellants was awarded to Armour Research Institute (now IIT) by the Army Ballistic Missile Agency in 1958. On the basis of information provided by the study (which summarized the state of the art of flowmeters), a 1-inch (2.54-cm) GE angular momentum flowmeter was purchased for investigation by Armour. In addition, a contract was awarded to Potter Aeronautic Corp. for the production of a prototype gravimetric quantity meter for filling control. The Potter meter uses a standard volumetric turbine flowmeter and a float-operated densitometer which starts and stops the counting of pulses from the turbine flowmeter once every minute for a duration determined by the density. When this meter had been developed into an accurate and reliable instrument, MSFC had to abandon its interest in it for two reasons: Jupiter work had been transferred to the US Air Force, and a decision had been made to use level switches and differential pressure measurements for Saturn fuel filling control because of the desirability

of obtaining volumetric and gravimetric data. However, the Potter meter has now been found useful for filling control of Apollo storable propellants.

A more elaborate study, development, and evaluation contract for LH_2 mass flowmeters was initiated in 1961 with Wyle Laboratories. As required by the contract, a well designed calibration facility was created. Illustrated diagrammatically in Figure 4

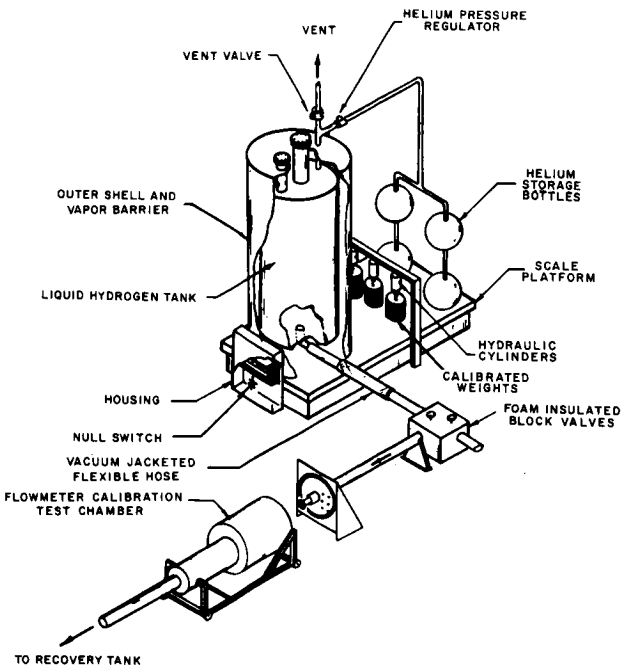

FIGURE 4. LH_2 FLOWMETER CALIBRATION STAND

is an LH_2 tank (with the usual valves for filling, drainage, pressurization, and venting) resting on a mechanical weighing scale. The tank is within a larger container and is insulated from it with glass wool (5 cm thick) and plastic foam (15 cm thick). Additional plastic foam insulation at the top and bottom covers the valves, fuel lines, etc. To eliminate the need for correction of the weight of pressurization gas (helium), there are four spherical helium storage tanks on the scale. Calibration masses in the form of drop weights are suspended on a gallows across the scale platform. The scale is used as a null detector rather than as an absolute-weight-measuring device. The tare is so adjusted that a capacitive null switch operates after constant flow is achieved. The null switch starts timers and counters or other flowmeter output recording systems after the calibration is started. Then the drop weights are lowered to the platform of the scale, and when a mass of LH_2 equal to the mass of the drop weights has been taken from the tank for flowmeter calibration, the null switch operates again and stops the timers and counters. In this way the LH_2 mass is directly compared with the mass of the drop weights. The vacuum-jacketed flexible hose provides fairly free movement of the scale, and the null switch always operates at the same platform position, which results in an accuracy of 0.1 percent. The flowmeters are inserted in a vacuum-jacketed calibration chamber big enough to accommodate any type flowmeter of the 3-in. (7.6-cm) class, which is the size of flowmeters investigated in this program. Two-phase flow is obtained by adding helium gas, and the mass measurement of the two-phase flow also is 0.1 percent accurate.

During this development program, the following five mass flowmeters were tested, evaluated, and modified.

a. A gyroscopic mass flowmeter (Decker Corp., Fig. 5) passes the liquid through a circular loop, thus simulating the rotating flywheel of a gyroscope. A motor-driven eccentric cam forces the loop to precess in an oscillating manner; the resulting rectangular torque causes a displacement of the loop, which is restrained by torsion members. The displacement of the loop is measured as a function of mass flow.

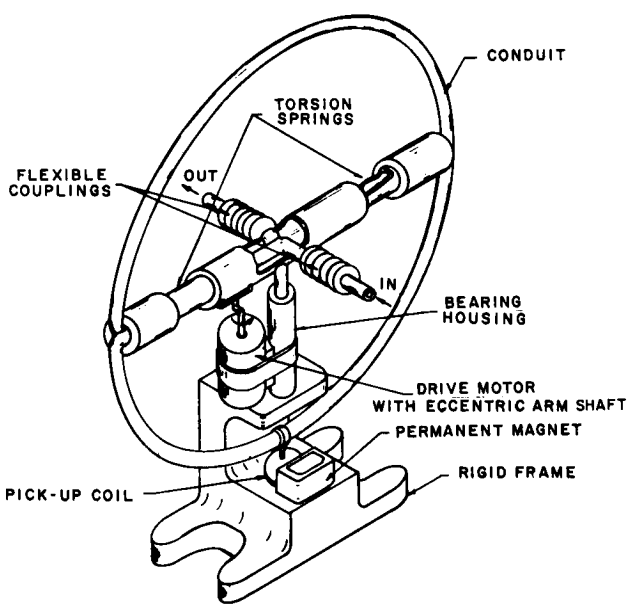

FIGURE 5. GYROSCOPIC MASS FLOWMETER (DECKER)

b. A twin-turbine mass flowmeter (Potter Aeronautics, Fig. 6) uses two turbines with different

blade angles that are coupled with a torsion spring and so rotates as a unit. The phase angle between the two turbines, or the time period between passing of fixed reference points on the two turbines, is measured as function of the mass flow. The velocity of the coupled turbine assembly is proportional to the volumetric flow.

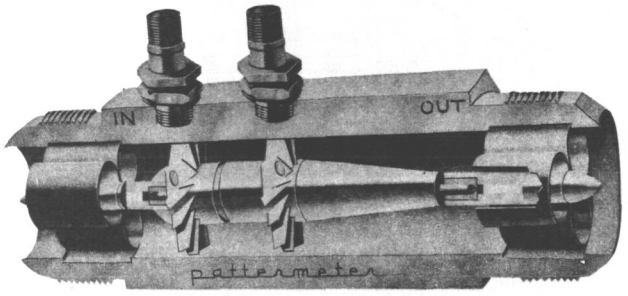

FIGURE 6. TWIN-TURBINE MASS FLOWMETER (POTTER)

c. The angular momentum mass flowmeter (General Electric Corp., Fig. 7) uses an impeller, driven at constant speed by a synchronous motor, to impart an angular velocity to the passing fluid. A turbine, immediately downstream, absorbs the angular momentum of the fluid, and its deflection against a spring is measured as a function of the mass flow.

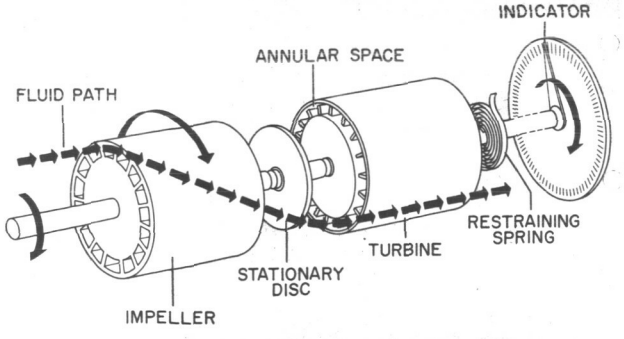

FIGURE 7. ANGULAR MOMENTUM MASS FLOWMETER (GE)

d. A constant-torque mass flowmeter (Waugh Engineering Co., Fig. 8) uses a turbine with zero blade angle, driven at constant torque by a synchronous motor with a magnetic hysteresis clutch. The speed of the turbine decreases inversely with increasing flow rate.

e. An inferential mass flowmeter (Quantum Dynamics, Fig. 9) measures flow volumetrically. It has a slave turbine to rotate the shaft for the sensing turbine to reduce inaccuracies from bearing drag, and it utilizes a high-frequency wave-absorption principle to detect the rotation of the turbine without magnetic loading. Fluid density is measured with a capacitive sensor, and the two signals for volumetric flow and density are combined into a signal for mass flow in a computer which also has outputs for analog density, analog velocity, digital mass flow, and digital volume flow.

The single-phase repeatability of the five flowmeters is shown in Table I. A repeatability of 0.1 percent was desired, but 0.5 percent was the best obtained. Although short of the desired accuracy, this achievement is useful in indicating the direction the work must take for attaining the 0.1-percent accuracy.

TABLE I. REPEATABILITY OF MASS FLOWMETERS DURING CALIBRATION WITH LIQUID HYDROGEN

Flowmeter	Repeatability (%)
Decker Corporation	
Vibrating gyroscopic mass flowmeter	±0.9
General Electric Company	
Angular momentum mass flowmeter	±0.5
(Using bypass principle)	±1.0
Potter Aeronautical Corporation	±0.5
Twin-turbine mass flowmeter	±0.12*
Waugh Engineering Company	
Constant-torque mass flowmeter	±0.5
Quantum Dynamics Corporation	±0.5
Inferential mass flowmeter	±0.1*

* Volumetric data

For volumetric measurement (Quantum and Potter meters), a repeatability of 0.1 percent was shown, which is the best accuracy obtainable as yet for LH_2 measurement. This accuracy and the versatility of the meters in being usable for gravimetric and volumetric measuring are distinct advantages. The additional turbine in both meters probably

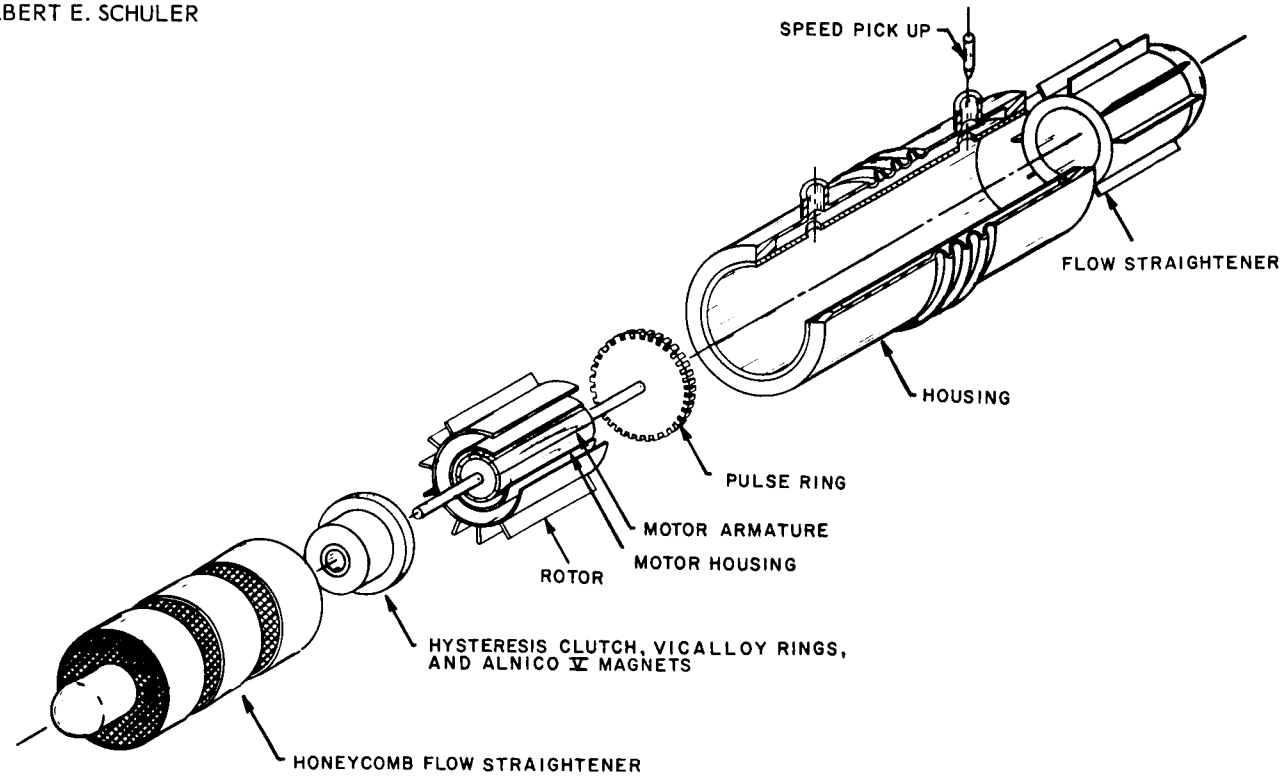

FIGURE 8. CONSTANT-TORQUE MASS FLOWMETER (WAUGH)

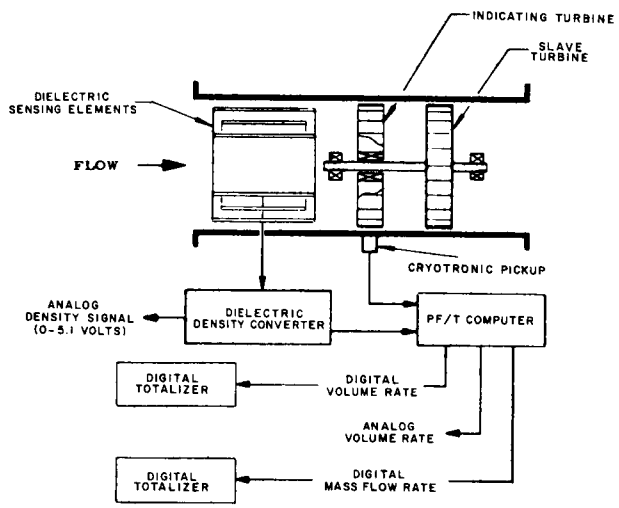

FIGURE 9. INFERENTIAL MASS FLOWMETER (QUANTUM DYNAMICS)

conditions the flow pattern so that detrimental line effects are reduced or eliminated. In the Quantum meter it serves as a slave turbine, rotating the shaft of the measuring turbine. The purpose of this arrangement is to reduce bearing drag. The Quantum densitometer system is good in principle, but it often fails to withstand the rough working conditions. When this deficiency is corrected by the manufacturer, the meter may be one of the best of the mass flowmeters.

The ideal flowmeter would have no moving parts and no obstructions in the line. Under contract with MSFC, Bendix Corp. is developing a capacitive flowmeter without moving parts (Fig. 10). The meter uses a wire mesh as a sensor for the ρv^2 term of the flowing liquid. The tendency of the mesh to move under the force of liquid flow changes a capacitance, causing electromagnets to initiate a servo-directed compensation. Honeycomb grids measure the liquid density through the capacity change, and a computer mixes these measurements to yield mass flow data. This capacitive meter is in the prototype stage, and is being tested and improved.

Neptune Meter Co. has developed a flowmeter which operates on a boundary-layer heat-conductivity principle and has no obstruction in the line. (This work has not been done under contract.) Metering based upon a heat-conductivity principle may be expected to have a relatively slow response. However, MSFC has purchased one of the Neptune meters and it will be tested by the Wyle calibration facility for speed of response and accuracy.

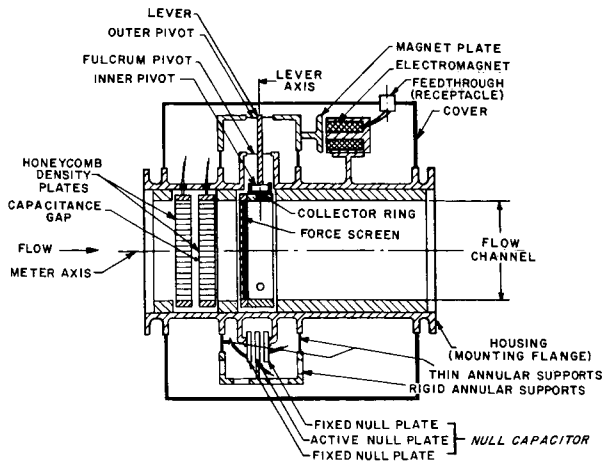

FIGURE 10. CAPACITIVE MASS FLOWMETER (BENDIX)

A considerable amount of research on the applicability of nuclear methods to mass flowmeter design has been done by government agencies and private industry. It was not evident until recently, however, that nuclear methods were suitable for MSFC applications. As a result of new advancements in nuclear technology, the idea of flowmeters based upon nuclear principles has appeared to warrant study by MSFC; therefore, it has initiated a feasibility study through a contract with Industrial Nucleonics Corp.

IV. LIQUID-LEVEL INSTRUMENTS

Most of MSFC research and development in the field of liquid-level measurements was done in-house, with some research funds being used to buy commercial products. The accuracy and reliability of continuous liquid-level gages were well advanced even during the early days of rocket development. It was obvious, however, that discrete liquid-level sensors would have to be used for flow rate determinations because the difference between two levels is required for flow rate, and less than 1-percent accuracy was obtainable with continuous-level gages. The special advantage of level switches is in their absolute accuracy, and the percentage accuracy of liquid-level measurements with discrete level sensors increases proportionally with the height of the tank. Better than 0.1-percent accuracy in flowmeter calibration can be obtained at calibration stands with tall tanks. At test stands flow rate determination is less accurate because of the turbulent surface of the liquid fuels.

Originally, float-operated level switches were used for LOX and alcohol measurements. By 1955, very accurate and reliable all-electronic level switches had been developed. Two types, capacitive and conductive, are illustrated diagrammatically in Figure 11.

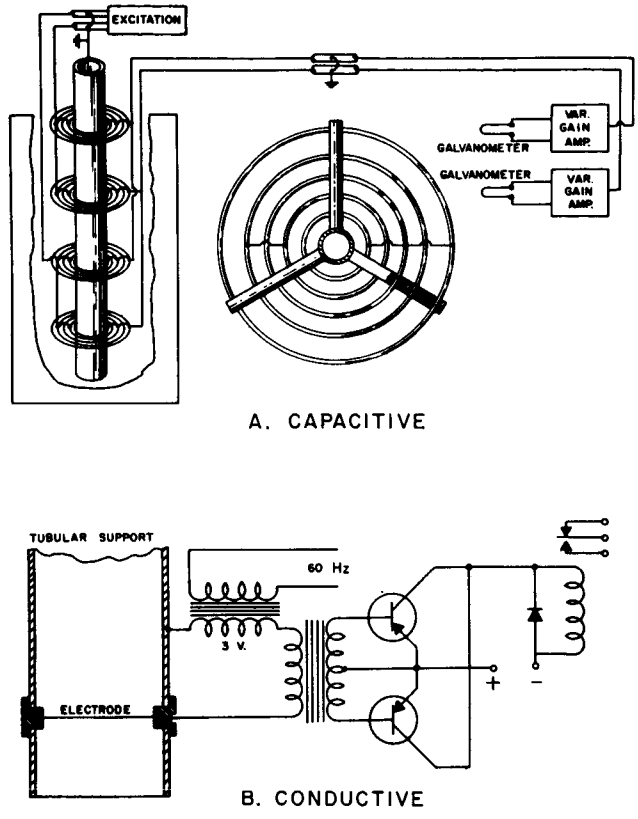

FIGURE 11. CAPACITIVE AND CONDUCTIVE DISCRETE LIQUID-LEVEL SENSORS

The capacitive switch (A, Fig. 11) uses rings as electrodes of a capacitor. Alternate rings are interconnected to serve as the two electrodes of a capacitor that varies its capacitance, depending upon whether there is liquid or gas between the rings.

The conductive switch (B, Fig. 11) uses a wire across a pipe. The wire is insulated from the pipe, and the resistance between wire and pipe decreases when the wire is submerged in conductive liquid. Water, or even missile fuel with much lower conductivity, operates the sensors.

Since private industry as well as aerospace agencies had been conducting research and development to produce better discrete liquid-level sensors, MSFC decided to replace its "homemade" probes with

commercial ones. Therefore, it bought ten each of five different types and tested them. A summary of the accuracy tests is given in Table II.

TABLE II. REPEATABILITY OF COMMERCIAL DISCRETE LIQUID-LEVEL SENSORS IN DIFFERENT LIQUIDS

Sensor Operating Principle	Repeatability millimeter (inch)			
	Water	RP-1 Fuel	LN_2	LH_2
Capacitive		±0.127 (±0.005)	±0.152 (±0.006)	±0.152 (±0.006)
Optical	±0.102 (±0.004)	±0.102 (±0.004)	±0.305 (±0.012)	±0.762 (±0.030)
Magnetostrictive	±0.305 (±0.012)	±0.305 (±0.012)	±0.254 (±0.010)	±0.305 (±0.012)
Piezoelectric	±0.330 (±0.013)	±0.102 (±0.004)	±0.102 (±0.004)	±0.254 (±0.010)
Thermal				±0.356 (±0.014)

Most of the switches were very accurate and reliable when tested in the laboratory, but they were much less so when used at the test stands. Therefore, the accuracy data shown in Table II do not reflect reliability in the field. The optical sensor (Fig. 12) appeared to be the most accurate and reliable sensor for all-purpose use. Many were used at various test facilities, but the "homemade" switches still seem to be the most reliable.

The results of work by MSFC and Trans-Sonics, Inc., have been combined to produce a continuous liquid-level gage, now used in the S-ICT missile at the MSFC test stand. Trans-Sonics research was in servo bridge-balancing; MSFC contributed its experience in dividing the level gage and using the sections in different parts of the bridge.

V. TEMPERATURE-MEASURING INSTRUMENTATION

In the past, MSFC did a considerable amount of research on temperature sensors as part of its thermal instrumentation program. Not much significant advance was made for thermocouples with various materials, or for oscillating crystal sensors. More success was achieved with platinum resistance thermometers, which were greatly improved through the work of private industry, done partly in close cooperation with MSFC.

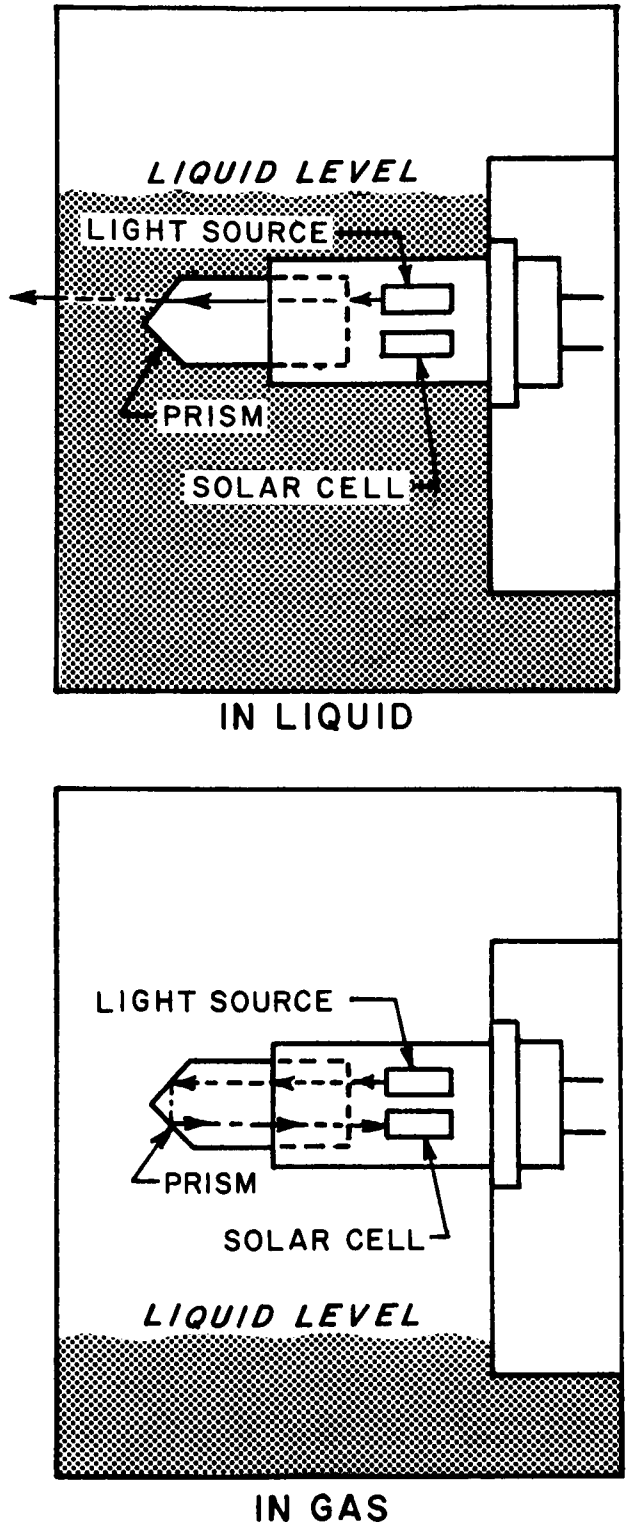

FIGURE 12. OPTICAL DISCRETE LIQUID-LEVEL SENSOR

At present, very accurate and reliable temperature measurements of cryogenic fuels can be made. However, the speed of response still is a problem. The temperature sensors are slow because the time constant is increased by the sturdy sensor-holding devices, which are necessary because of test-stand vibration. The following conditions illustrate the problem. The temperature of LOX in a Saturn I tank was -297.4° F (90.15°K), while the temperature of gaseous oxygen was approximately 400° F (478°K). When the LOX level dropped below the sensor, the sensor did not quickly indicate the high temperature of the gaseous oxygen but instead often indicated a lower temperature than the LOX, -300° F (89°K), because of LOX evaporation. The speed of response was improved with an MSFC-laboratory-devised thermocouple (Fig. 13). This has a 30-gage copper-constantan wire suspended in a slingshot-like bracket of minimum practical thickness. Its time constants are 0.6 second when submerged in LOX, 1.3 seconds when emerging with the bracket above the wire, and 2.6 seconds when emerging with the bracket below the wire.

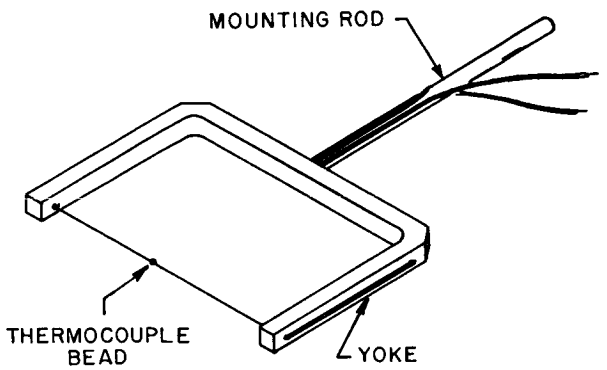

FIGURE 13. SLINGSHOT THERMOCOUPLE

In an attempt to obtain a better thermocouple than this slingshot type, MSFC had two companies make special resistance thermometers for faster speed of response. The sensors that were made had very thin wires and fragile holding arrangements. Since they were more fragile than the slingshot thermocouples and there was no improvement in the time constant, a research contract was awarded to another company for the development of sensors with the following specifications: a sensitivity of 0.01° F (0.0056°K); an accuracy of 0.05° F (0.0278°K) in the range of -425° to -410° F (19.3° to 27.6°K); and an accuracy of 0.5 percent at -425° F (19.3°K), with a response speed of 0.5 second. These sensors are being tested.

Considerable improvement in heat flux measurements was achieved by in-house research on calorimeters. The use of thermopiles for radiation heat flux measurements was one of the major achievements.

VI. DAMPED ACCELEROMETERS AND ACCELEROMETER CALIBRATION SYSTEMS

Accelerometers usable over higher frequency ranges without ringing were needed for more accurate vibration measurements. Gulton Industries studied this problem and developed a damped accelerometer (Fig. 14). The seismic mass of this instrument is

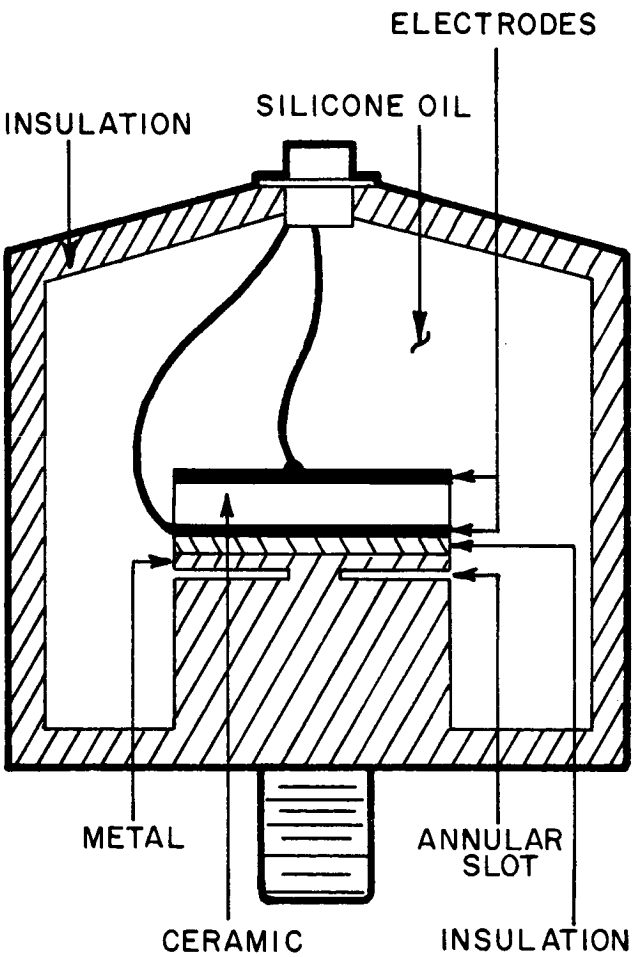

FIGURE 14. DAMPED ACCELEROMETER

a diaphragm-like structure composed of piezoelectric material and metal, supported at its center by a

column. Upward forces cause the composite mass to deform. As the edge of the material moves downward, the width of the annular slot decreases, forcing the silicone fluid to flow out. A downward force increases the width of the slot, and the fluid flows back into the slot. Thus, damping of the motion is achieved by the pumping of silicone in and out of the annular slot. Electric signals are generated by the bending of the piezoelectric element. The frequency response of these accelerometers is nearly flat up to 15 kHz (Fig. 15).

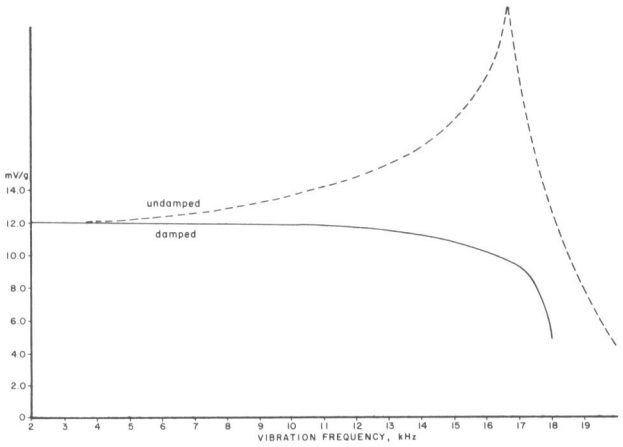

FIGURE 15. FREQUENCY CHARACTERISTICS OF DAMPED ACCELEROMETERS

A new calibration system was developed for absolute calibration and testing of accelerometers with high-frequency range. The calibration system, diagramed in Figure 16, uses either a constant-displacement or a constant-acceleration mode of operation. For constant displacement an interferometer measures fixed increments of displacement, and the shaker is regulated until a certain displacement is reached. When the output of the photomultiplier reaches null, the fringe disappearance indicates that the displacement of the shaker table is 4.11 microinches (0.104 μm) or a multiple of it. The 20-Hz oscillator modulates the intensity sensed by the photomultiplier, which results in higher sensitivity. The instrument accuracy is about 1 percent. The constant acceleration mode of operation uses the accelerometer in the table as a standard. This method is much less accurate, but it requires less time.

MSFC also uses a portable accelerometer calibrator, which it developed in-house (Fig. 17). The instrument uses a resonant frequency of a beam excited up to 20 gauss by an electromagnet and oscillating at a constant frequency of 120 Hz.

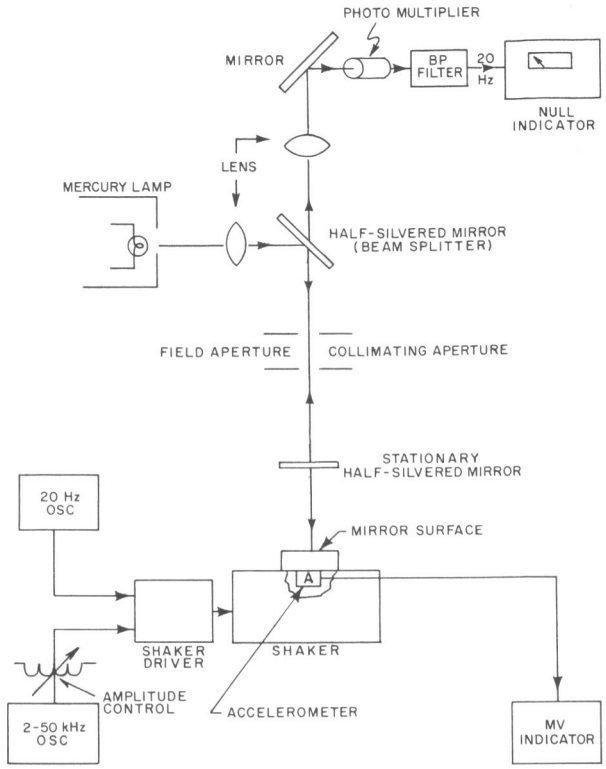

FIGURE 16. ACCELEROMETER CALIBRATION SYSTEM

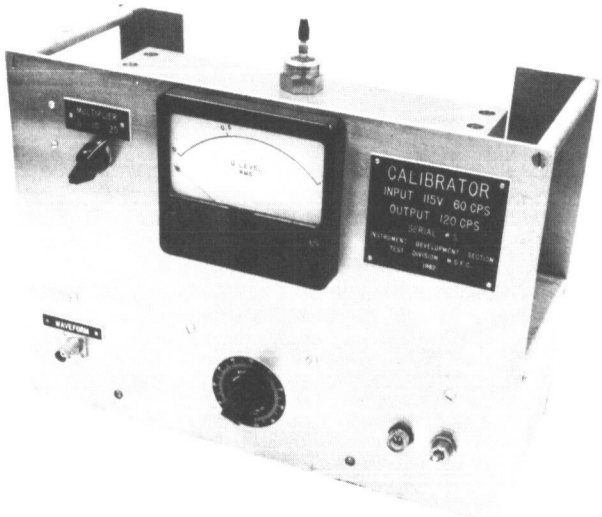

FIGURE 17. PORTABLE ACCELEROMETER CALIBRATOR

The application of laser techniques to accelerometer calibration is being studied by National Bureau of Standards, under contract.

VII. DIGITAL TRANSDUCERS

The "era" of digital transducers started in response to increasing accuracy requirements, the need for handling more channels with fewer cables, and many other reasons. In the field of digital measurement, MSFC and Giannini Controls Corp. developed a very accurate digital pressure transducer. In the measuring system, illustrated in Figure 18, the transducer uses a force balance and an up-down counter principle. The bellows convert the pressure into force, which is balanced by an electromagnetic torquer. A special two-bellows arrangement with slightly different effective areas of the bellows increases sensitivity and decreases the force; the result is a desirable reduction in the required torque. When there is an unbalance in the force from bellows and torquer, a differential transformer null detector gives signals to the counter, and a digital-to-analog converter conditions the signal of the counter to change the current for the electromagnetic torquer until it balances the force of the bellows. The counter also provides digital output in binary form (11 bits).

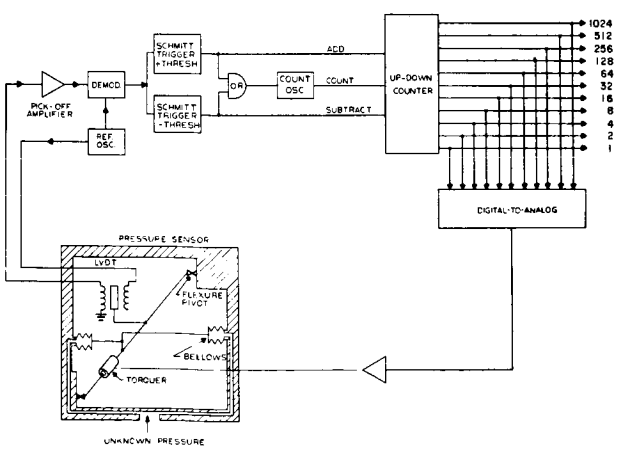

FIGURE 18. DIGITAL PRESSURE TRANSDUCER

The prototype digital pressure transducer which was delivered has a resolution of 1 count in 2047 and an accuracy of better than 0.1 percent. A great interest in this transducer was indicated by the inquiries from within the United States and from other countries.

Giannini Controls, under a development contract, is to provide a 36-channel digital transducer and data recording system. Four channels each will be used for pressures of 1, 10, 100, 500, and 1000 psi (0.69, 6.9, 69, 345, and 690 N/cm^2), respectively, and four channels each will be used for resistance thermometers, strain gages, thermocouples, and DC voltages. Electrical null balance and the same up-down counter principle (as in the other pressure transducer) are used for the electrical measurements. A digital multiplexer and magnetic tape recorder are included in this system. Most of the system components have been completed, with some features being improved; therefore, this research and development may be termed an important achievement in the field of digital transducers.

The pressure transducer discussed has a binary-coded digital output. MSFC also initiated the development of a miniature analog-to-digital converter to be used next to the transducer. In this system, developed by Trans-Sonics, Inc., the output of the transducer is fed to a paractor, which provides parametric amplification and comparison for digital conversion of very small signals. The paractor is part of the analog-to-digital conversion system and has to be in the immediate vicinity of the transducer so that electrical noise effects can be avoided. The rest of the system called logic can be several hundred feet away. For some applications, the paractor, which takes up 8 cm^3 (0.5 in.^{3}), will be constructed like an electrical connector so that it can be attached as an integral part of the transducer.

Packaged with the logic is a multiplexer which has been developed to scan the digital output of 120 channels and to send these signals through two pairs of shielded cables to the blockhouse. This will eliminate the noise effect on low-level signals, and it will make it possible to handle many more channels with fewer cables.

Since the research for a small analog-to-digital converter resulted in the development of the very promising paractor, the contract was extended for the development of a DC amplifier. Two prototype DC amplifiers have been delivered, for which Trans-Sonics, Inc., claims an accuracy of 0.01 percent under constant conditions, a zero drift of about 0.01 percent for a 10° F (5.56° K) temperature change, and a slope change of about 0.01 percent for a 3° F (1.67° K) temperature change. Tests and probable modifications or improvements are pending.

Twenty-five years ago, transducers were developed with slide wire, capacitive, magnetostrictive, differential transformer, or variable-reluctance pickups. Fifteen years ago, the strain-gage pickup started a new measuring technology, in which increasing numbers of strain-gage pickups were used for various measurements. Five years ago, the

idea of digital transducers gained momentum, and it can be expected that five years from now the direct digital transducer systems will have replaced many of the present strain-gage pickups and analog-to-digital conversion systems.

VIII. ULTRAHIGH-VACUUM CALIBRATION SYSTEM

In the calibration of vacuum gages below 10^{-5} torr (1 mN/m^2) the usual comparison with a standard cannot be used because none exists for this very low pressure. A research contract with National Research Corp. was initiated by MSFC to establish principles and develop equipment for creating the low pressures of accurately known values needed in calibrations of vacuum gages. The calibration system that was devised (Fig. 19) uses a series of three individually pumped pressure chambers, with the pressures decreasing in a ratio of 100 to 1 from chamber to chamber. The pressure of each chamber is kept constant by continuous pumping, and the pump and chamber interconnections have pressure attenuating orifices of known conductance. Thus, the pressure attenuation of each stage is mainly determined by the dimensions of these calibrated orifices. The small-conductance calibrated orifices between each pump and chamber also serve to minimize the effects of variations in pump speed.

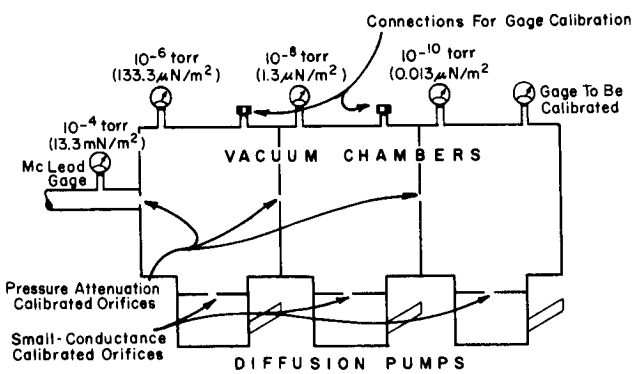

FIGURE 19. ULTRAHIGH-VACUUM CALIBRATION SYSTEM

The starting low pressure of the vacuum series is measured with a standard McLeod gage, which can measure down to 10^{-4} torr (1.3×10^{-2} N/m^2). The last of three pressure chambers will have 10^{-6} times the pressure measured by the McLeod gage; therefore the system can measure down to 10^{-10} torr (0.013 μN/m^2). This vacuum range is not dependent upon gas composition and temperature as long as there are no large temperature variations from point to point in the system. Errors in the orifice technique, due to leaks or to outgassing from the walls, are overcome by high mass flowrates and bakeout in the high-vacuum region. Thus, this multistage method depends mainly on the geometric dimensions of pressure attenuation orifices and the standard pressure reading, provided that a specified minimum pumping speed is maintained.

IX. INSTRUMENTATION FOR MEASUREMENT OF OTHER EXTREME VALUES

In addition to ultrahigh vacuum, instrumentation for measurement of extreme values includes the measurement of very low water-vapor content in pressurizing gases, and the development, testing, and calibration of load cells for very high forces.

Considerable in-house research has been conducted on dewpoint instruments. Consolidated Electrodynamics Corp. (not under contract) developed a "moisture monitor," which uses an electrolysis principle and Faraday's law to measure water vapor content of gases in amounts as low as one-half part per million.

Developmental work on high-capacity load cells has been going on for many years. Much of the work has been done by private industry with its own funds and through research contracts with government agencies. Suggestions and test data offered by MSFC added to the fund of knowledge and resulted in the production of load cells which are used for static test of S-ICT. To advance the state of the art, MSFC initiated a research contract with Fluidyne Engineering for the development of a 5-million-pound (22.24-MN) load cell only 4 in. (10.2 cm) high. Prototypes have been tested and improvements are being made.

MSFC prepared specifications for testing and calibrating high-capacity load cells. Using these specifications, Gilmore Industries designed and built a 5-million-pound (22.24-MN) load-cell calibrator, which is now in operation at MSFC. The equipment uses 225,000 kg (496,000 lb) of calibration masses or deadweights, with an accuracy of 0.003 percent. It uses hydraulic cylinders and load cells to calibrate up to 5-million pounds force (22.24 MN), with an accuracy of 0.02 percent. Any one of the calibration masses, or any combination of them, can be applied. This is an advantage over most of the other deadweight calibrators, which apply calibration masses only in the sequence in which they are stacked.

X. AUTOMATIC CALIBRATION SYSTEMS

Automatic calibration systems constituted another field in which MSFC did a considerable amount of research and development. Fifteen years ago the pressure balance was developed in-house for accurate reference pressure, and it was found most useful for calibration of pressure gages. Figure 20 shows an automatic pressure calibration system with a pressure balance as the heart of the system. A rotating piston converts the pressure into force, which presses down one arm of an equal-arm balance. This force is balanced by weights on the other arm of the balance. The pressure is regulated by adding or releasing air with solenoid valves. The accuracy of this calibrating system is 0.05 percent.

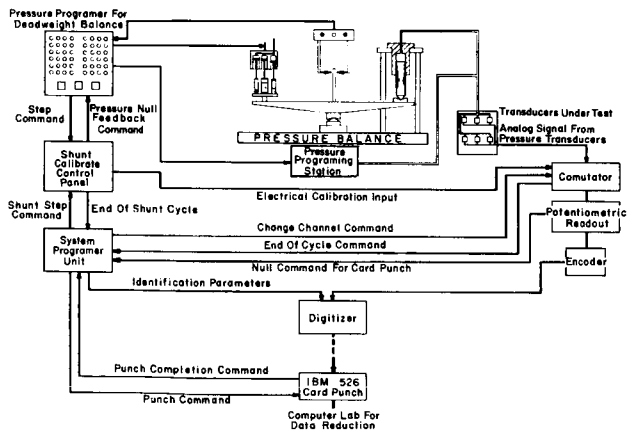

FIGURE 20. AUTOMATIC PRESSURE CALIBRATION SYSTEM

Under the impetus of expanding automation technology, MSFC initiated a research contract with Gilmore Industries for the automatic, laboratory-precision calibration of all pressure transducers on the Jupiter test stand, in which the pressure balance was used as a standard to obtain standard laboratory precision. Gilmore Industries proceeded to develop an automatic weight-handler for the pressure balance, and adapted a paper-tape programing device for automatic initiation and control of all the steps in pressure calibration. In this system, one group of transducers with the same pressure range are connected from the missile to the pressure balance by way of solenoid valves and manifolds. The appropriate weight increment for the pressure in the programed step calibration is applied, and the pressure balance is made to regulate the pressure. The transducer output then is recorded. Weights for the next pressure step are applied, and so on, until the calibration of the group of transducers is completed. The calibrated transducers are reconnected to the missile, and another group of transducers is connected to the pressure balance. The procedure is repeated until all the transducers are calibrated. A tape can be punched for any calibration program desired, so that calibration is fully automatic after a start button is pushed.

End-to-end calibration at the test stand is being replaced by shunt calibration. The resistance of shunt resistors is determined in the laboratory as a measure of pressure; then, instead of calibrating pressures directly at the test stand, an electrical calibration is made there with the shunt resistors.

As a result of this calibration work, the work load of the Instrument Laboratory has increased greatly. Consequently, automation in the laboratory and the use of computers for the tremendous data processing requirements have increased in importance. A computerized calibration system, developed to fulfill this need, is illustrated in Figure 20. The pressure transducers are in a heat chamber so that calibrations can be made at different temperatures. There may be up to 48 transducers in the chamber at one time. The pressure balance regulates the pressure, a digitizer conditions the signals of the pressure transducers, and an IBM card-puncher records the results on cards.

Other automatic calibration systems used by the laboratory are:

a. An automatic thermocouple calibrator which compares up to 12 thermocouples with an NBS-calibrated standard thermocouple in a temperature-controlled oven. The power supply to the oven is regulated by an electronic unit, and the outputs of the thermocouples are automatically printed after each step of temperature has been reached.

b. An automatic Mueller Bridge which balances automatically and prints the output of up to 12 resistance thermometers.

c. An automatic load cell calibration system which increases or decreases the force of a hydraulic jack until the output of a standard load cell is equal to an electric signal preset by a step switch. This system is for test stand application.

SOUND SUPPRESSION TECHNOLOGY RESEARCH AT MARSHALL SPACE FLIGHT CENTER

By

Fritz Kramer

SUMMARY

This report describes some of the development tests conducted at Marshall Space Flight Center on sound suppressor models. These devices are designed to reduce the sound radiated into the atmosphere from the exhaust jets of large rocket engines. From theoretical considerations, the overall sound reduction capability of the tested models was expected to amount to 40 decibels. However, residual sound, radiated from the rocket engine and its installation, limited the attainable overall suppression to 24 decibels. Suppression of very low sound frequencies remains a special area of endeavor in future investigations.

The models were designed to be self-contained. They proved to possess very good operational characteristics.

I. INTRODUCTION

The high-intensity sound generated by high-thrust rocket engines has been of great concern to Marshall Space Flight Center (MSFC) and particularly to Test Laboratory. Sound powers of tens of millions of acoustical watts from rocket engines installed in the booster stage of the Saturn V moon rocket had been predicted as early as 1960, when the booster stage was under development. Sound powers of smaller magnitude, generated during static testing of less powerful missiles, already had caused concern in the population of nearby residential areas. Focusing of sound rays under particular atmospheric conditions also was known to affect areas at great distances from the test site. Therefore, Test Laboratory was obligated to study means to alleviate or eliminate these acoustic effects. The program which was established for this purpose later developed into two main activities, sound prediction and sound suppression.

In sound prediction, existing meteorological conditions are evaluated and correlated with the sound power and the directional characteristics of the sound source. The magnitude of sound pressures expected in the area surrounding the test site is then determined through special computer programs. If meteorological conditions are unfavorable and too high a pressure level is predicted, the testing may have to be delayed or postponed. Sound prediction, therefore, is an operational activity, connected closely and directly with the test activity proper. It has to be performed for each test firing.

The purpose of sound suppression is to prevent the acoustic power from being generated, or from being radiated into the atmosphere. This requires a facility addition which may constitute a major investment. However, the sound suppressor, if designed as a self-contained unit, requires no operational procedures or personnel; it eliminates severe acoustic effects, and permits test firings at any time.

This report deals only with the sound suppression technology investigated at MSFC's Test Laboratory.

II. EARLY MODEL TESTS

The first tests conducted in 1960 and the following years may be considered today as exploratory from various points of view. Acoustic scaling laws were not well known, acoustic measuring and evaluation instrumentation was not well suited for field activities, and the mechanism underlying sound suppression was practically unknown. In addition, the sound sources, small liquid-propellant rocket engines, were inadequate acoustic models of the large powerplants. The power spectrum and kinetic energy of their exhaust jets did not properly simulate those of the large rocket engines. Also, there was no precedent for the design of rocket-engine sound suppressors. There was, therefore, little basis from which to start or extend. Most of the early models conceived and tested were either designed intuitively or along the lines of jet-engine devices. They employed baffles, perforated sheets, water sprays, and deflecting ducts to decelerate the rocket

exhaust gases and to spread them over a larger exit area, thus reducing the power of the generated sound.

Sound suppression obtained with some of these devices was encouraging: suppression of 19 decibels was obtained with a "diffuser cone," and 12 and 14 decibels with other devices. The sound source for these tests was a LOX-JP4 rocket engine with a thrust of 11.6 kN (2600 lb). When the system dimensions and other parameters of these devices were extrapolated to the size of the prototype for the Saturn V booster stage, however, serious technical shortcomings became apparent.

The difficulties with sound suppressors for rocket engines arise basically from the high temperature of the rocket exhaust and from the heat of recompression when the velocity of the jet is reduced. The exhaust gases have a temperature of about 1900°K (3000° F), and they leave the rocket exhaust nozzle with a velocity corresponding to a Mach number of 3.2 to 3.4. Although some exhaust gas at the periphery of the jet mixes immediately with air and reduces the temperature and velocity of this diffusion zone, the core of the jet remains unaffected for quite some distance (Fig. 1 and 2). Any obstacle placed into this supersonic stream causes formation of shock waves with an increase in temperature due to this recompression. The increase in temperature across a plane shock wave is given by the temperature ratio:

$$\frac{T_1}{T} = \frac{1}{M^2}\left[1 + \frac{2k}{k+1}(M^2 - 1)\right]\left[1 + \frac{k-1}{k+1}(M^2 - 1)\right], \quad (1)$$

in which T and T_1 are the temperatures in front of and behind the shock wave, respectively; M is the Mach number in front of the shock; and k is the ratio of specific heats of gas. Typical values of M and T_1 are given in Table I, for k = 1.20 and T = 1745°K (3000°R). It is evident that the structural material

TABLE I. GAS TEMPERATURE BEHIND SHOCK WAVE

Mach Number	T_1 °K	(T_1 °R)
2	2280	(4100)
2.5	2640	(4750)
3	3110	(5600)
3.5	3670	(6600)

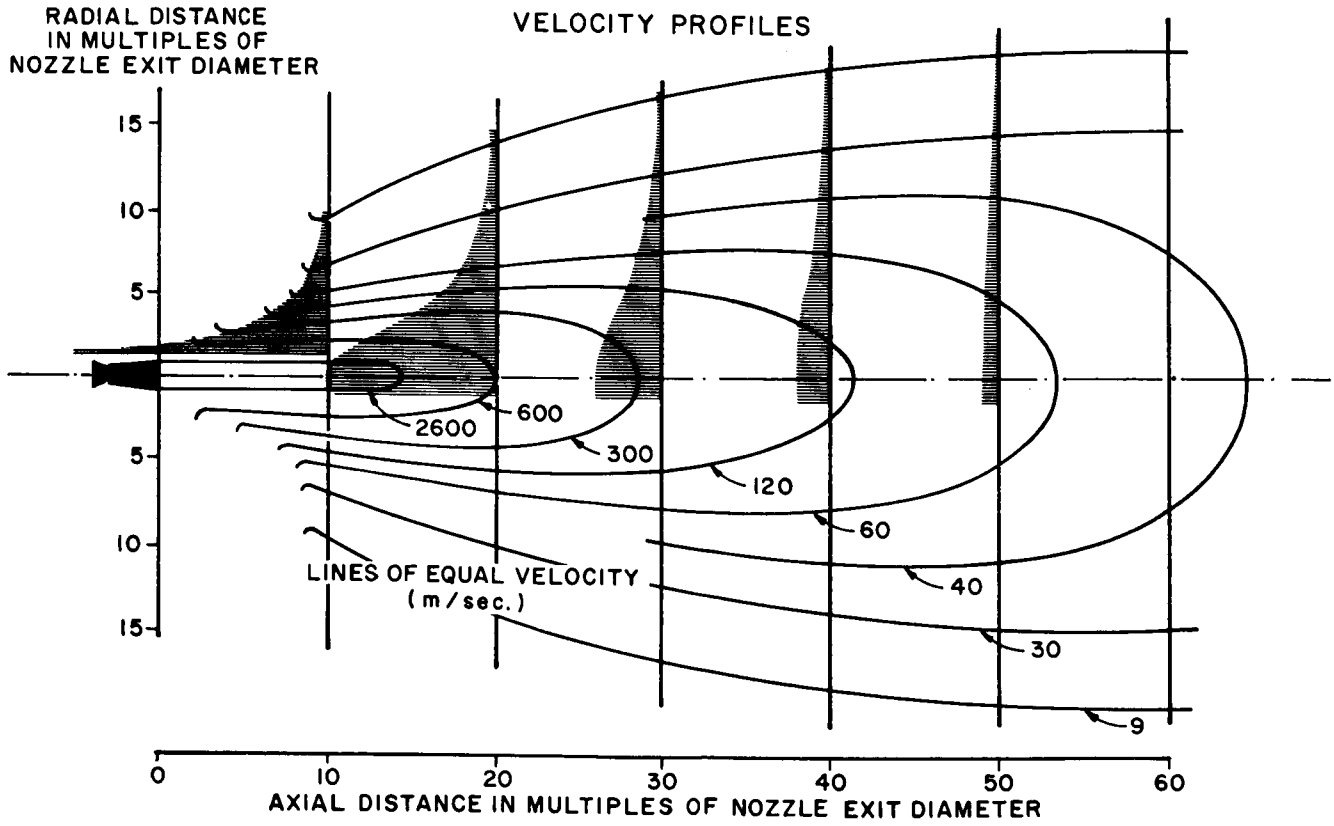

FIGURE 1. VELOCITY DISTRIBUTION IN ROCKET EXHAUST AT SEA LEVEL

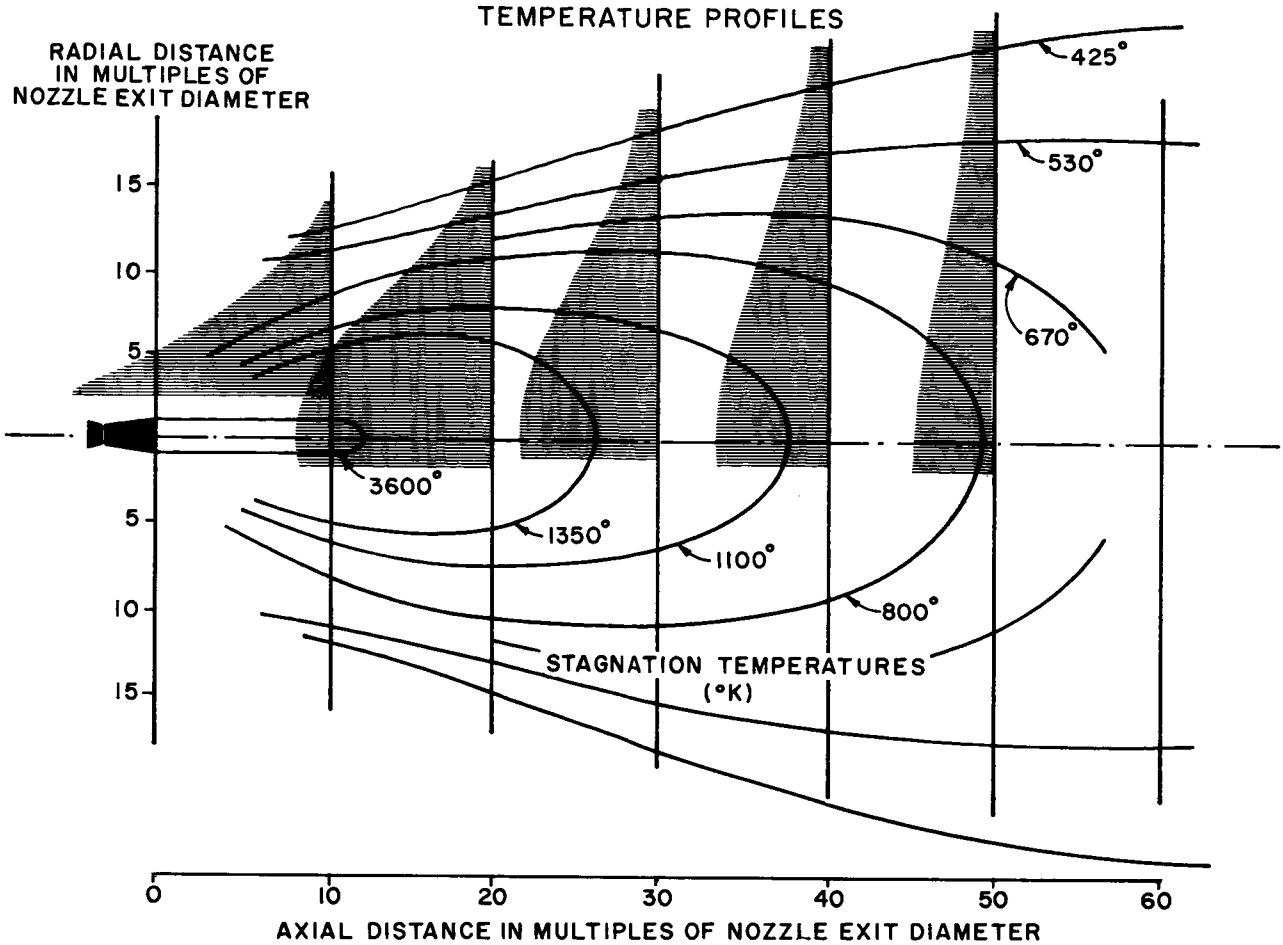

FIGURE 2. TEMPERATURE DISTRIBUTION IN ROCKET EXHAUST AT SEA LEVEL

of the sound suppressor, exposed to these temperatures, has to be cooled effectively to preserve its strength and structural integrity.

In the model tests, this cooling could be accomplished relatively easily by spraying water directly at these members. The amount of water needed ranged from n = 2.0 to n = 5.4, n being the weight ratio of cooling water flow rate to engine propellant flow rate. For a propellant flow rate of 7.5 kg/sec, the absolute flow rate of cooling water thus ranged from 0.015 to 0.04 m^3 (15 to 40 liters) per second. However, the propellant flow rate for the rocket engines of the Saturn V booster stage is 13 600 kg/sec (30 000 lb/sec). The water flow rate for cooling a sound suppressor based on these model types, therefore, would have to be from a minimum of 27 m^3/sec to a possible maximum of 73 m^3/sec. These flow rates would call for extremely large pumping stations with power requirements from 11.2 to 33.6 MW. The cost for such pumping stations with their associated equipment of valves, pipelines, and storage tanks would be prohibitive. A sound suppressor based on the design criteria developed in these early model tests was, therefore, not feasible.

In another approach, the rocket engine was fired into a sizable body of water. This method eliminated the cooling problem mentioned above, and accomplished an overall sound power reduction of 30 decibels; however, it required the largest structure of all models tested. (The water pool would have to be about 370 meters long and 170 meters wide for a Saturn V sound suppressor.) Also, explosions of propellants in the gaseous phase occurred from time to time, and the water mass was agitated so severely by the impinging jet that this method was not considered to be a practical solution to the sound suppressor design problem.

III. LATER TEST SERIES (1962 THROUGH SUMMER 1965)

By the summer of 1962, the continued studies on sound propagation and its effect on the surrounding areas had shown that the very low sound frequencies would require special attention because they are attenuated least by the atmosphere and can be felt strongly even as far as 15 kilometers from the test

site (Fig. 3). This fact created new requirements to be met by the sound suppressor: sound in the frequency range below 100 Hz was to be particularly well suppressed, and the threshold of annoyance of 110 decibels (ref 0.0002 microbar) was not to be reached in the populated areas surrounding a test site.

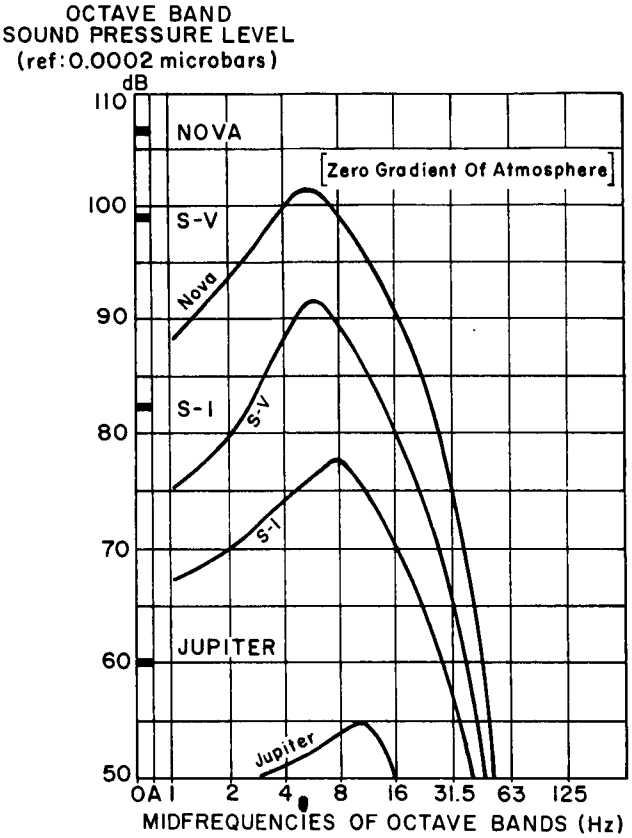

FIGURE 3. SOUND SPECTRA AT 15 KILOMETERS

The theory of Lighthill [1], that sound is generated aerodynamically, and that its power is proportional to the kinetic energy of the jet stream, contributed greatly to a basic understanding of the mechanism of sound suppression. The effectiveness of various designs now can be interpreted more easily in terms of gas exit velocity.

Figure 4 shows the relationship between sound power level of rockets and jet engines as a function of exhaust velocity. According to these test results, the sound power varies very closely with the sixth power of the exit velocity, if all other parameters remain constant. This relationship can be derived theoretically by expressing the kinetic energy $1/2mV^2$ in terms of the propellant flow rate and the exit area. The sound power (L_w) is obtained as

$$L_w = C_1 \frac{1}{g}\left(\frac{\dot{W}_p}{A_e}\right)^2 \cdot A_e \cdot v_e^6 . \qquad (2)$$

In this equation, $\dot{W}_p$ is the propellant weight flow rate, A_e is the exit cross-sectional area, and v_e is the gas exit velocity. This relationship leads to the conclusion that good sound suppression is basically identical with good velocity reduction before the exhaust gases are admitted to the open atmosphere.

In the models built in 1962, the large reduction of the gas velocity was obtained by adding a large amount of water to the exhaust gas within an ejector-diffusor arrangement, commonly known as a jet pump. The exhaust gas constitutes the primary fluid; the water is the secondary fluid, which is pumped in large quantities without any additional power requirements. Within the diffuser, the momentum exchange between the jet and the water reduces the gas velocity, according to the law of conservation of momentum, to a velocity which is given by the equation

$$v = v_e \frac{1}{1+n} . \qquad (3)$$

In the equation, v_e is the exit velocity of the rocket jet, and n is the mass ratio of water flow rate to gas flow rate. This simple equation is obtained by disregarding the entrance velocity of the water into the diffuser or by assuming it to be negligible.

The addition of mass to the jet is evidently very effective, yielding a ten-fold decrease in velocity for a mass ratio of nine. Figure 4 shows the effect of n on the exit velocity and on the corresponding sound power.

However, a sound power reduction as indicated in Figure 4 by the application of a certain n value is not possible. The relation in Figure 4 is true only if the velocity is the sole independent variable. This is true because the addition of water to the gas not only reduces the gas velocity from v_e to $v_e \cdot \frac{1}{1+n}$, but also increases the weight flow rate from $\dot{W}_p$ to $\dot{W}_p \cdot (1+n)$. The effect of mass addition on the sound power is obtained by introducing both these changes (or effects) into equation (2). This yields

$$L_w = C_2 \frac{1}{g}\left(\frac{\dot{W}_p}{A_e}\right)^2 \cdot A_e \cdot v_e^6 \left(\frac{1}{1+n}\right)^4 . \qquad (4)$$

While the unsuppressed sound power is directly proportional to the sixth power of the original exit

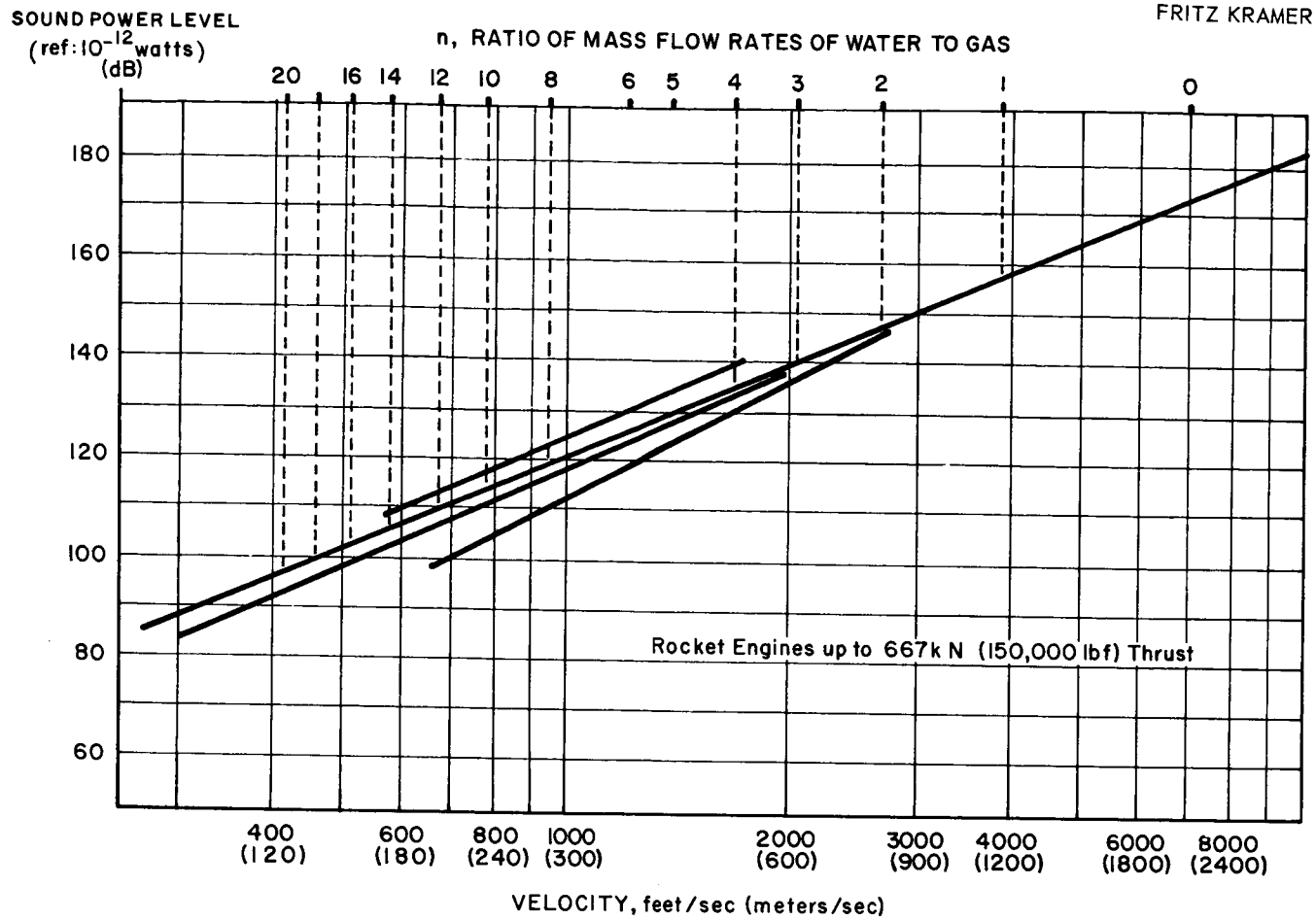

FIGURE 4. SOUND POWER LEVEL AS A FUNCTION OF EXHAUST VELOCITY

velocity v_e, the reduced power is inversely proportional to only the fourth power of the mass addition factor $(1 + n)$. Therefore, a sound power reduction of 40 decibels could be obtained theoretically for an n-value of 9 (or $1 + n = 10$) if all the water would take part in the momentum exchange, and if the gas emerging from the sound suppressor were the only remaining sound source. This, however, is not the case. Only a certain percentage (η) of the added water acts to reduce the gas velocity; therefore, the term $(1 + n)$ in equations (3) and (4) has to be replaced by the term $(1 + \eta \cdot n)$. Also, the rocket engine itself, the portion of its jet which is exposed to the atmosphere before entering the sound suppressor, and the structure of the sound suppressor, all emit some residual sound. The overall sound power of the installation, therefore, is the total emitted from all sources.

The residual sound power radiated from the powerplant, from its exposed jet, and from the sound suppressor structure may amount to only 1 percent of the initial acoustic power L_w, while the remaining 99 percent may be reduced by the sound suppressor by a factor of $(1/10)^4$ to a value of $0.99 \cdot 10^{-4}$ as obtained for $1/(1 + n)^4$ for $n = 9$. The total sound power still in existence amounts then to

$$\left(\frac{1}{100} + \frac{99}{100} \cdot 10^{-4}\right) L_w = 0.010099\ L_w \cong \frac{1}{10^2} \cdot L_w \quad (5)$$

With reference to the original sound power L_w, the new or suppressed sound power level is expressed as:

$$L_{w_{dB}} = 10 \cdot \log \frac{\frac{1}{10^2} L_w}{L_w} = 10 \cdot \log \frac{1}{10^2}$$
$$= -20\text{dB}. \quad (6)$$

This means that the new sound power level is 20 decibels lower than the original one.

This example shows that the residual sound power radiating primarily from the rocket engine(s) and the short length of the free jet(s) actually determine the overall suppression performance of the

sound suppressor. The power level of the residual power, which determines the maximum suppression obtainable, is given in Table II.

TABLE II. MAXIMUM SOUND SUPPRESSION OBTAINABLE AS A FUNCTION OF THE RESIDUAL SOUND POWER

Residual power ΔL_W (%)	Max. suppression ΔL_W* (dB)
1	-20
1/2	-23
1/4	-26
1/6	-28
1/8	-29
1/10	-30

*) ref 100% L_W

The overall sound suppression attained with the models (and later with the H-1 sound suppressor) was generally on the order of 21 to 24 decibels, regardless of the amount of additive water. Therefore, it can be concluded from Table II that the residual sound power in those models has been about 1 to 0.5 or 0.25 percent of the original sound power. Any future improvement in overall sound power reduction has to be accomplished through a reduction of this residual power by at least one order of magnitude. This probably will entail an enclosure around the rocket engine and its jet, which is objectionable from the test engineer's point of view. Unless some other means can be devised to contain the residual sound, it will be difficult to improve the overall sound suppression beyond the 24-decibel reduction obtained so far.

IV. INTERMEDIATE PROTOTYPE H-1

The model tests in 1962 initially employed a LOX-JP4 rocket engine with a thrust of 11 500 N (2600 lb), and later of 17 800 N (4000 lb). The Saturn V booster stage has a thrust of 33.4 MN (7.5 million lb). It was not considered advisable to apply the results from these model tests to the Saturn V sound suppressor, since no scaling law was known to be applicable to such an extreme difference in power. The scaling laws not only have to pertain to the acoustical domain, but to the hydraulic, gas dynamic, and structural aspects as well.

It was decided, therefore, to build an intermediate-size prototype, using a surplus H-1 rocket engine with a thrust of 735 kN (165 000 lb). This thrust level requires a sound suppressor of a size halfway between the small models and the Saturn V prototype. The overall suppression obtained with this sound suppressor was 21 decibels for a water flow rate of 8 to 10 times the gas flow rate. The sound power spectrum is shown in Figure 5. This spectrum is flat, with a maximum suppression of 30 decibels at the 125-Hz octave midfrequency. At the lower frequencies, suppression is only 9 decibels at the 4-Hz midfrequency, an indication that the low sound frequencies are more difficult to suppress than the frequencies in the audible range.

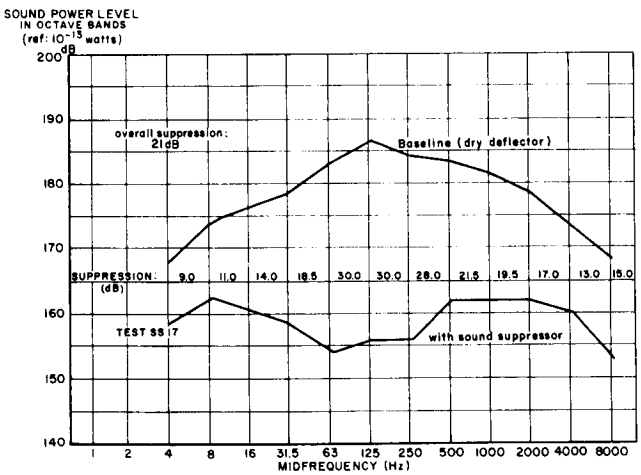

FIGURE 5. ACOUSTICAL PERFORMANCE OF SOUND-SUPPRESSION DEVICE

Except for the limited performance of the H-1 sound suppressor at the lower frequencies, the principle of mass addition in this intermediate prototype and in the small models has alleviated most or all of the previously existing problems. It has resolved the heating problem of the structure, it has solved the deceleration of the high-velocity, high-temperature jet within a very short distance and without the use of baffles or other obstacles, and it has completely eliminated the need for large pumping stations to provide the cooling water beyond that which is normally required for the operation of a test stand without a sound suppressor. In addition, the large flow rate of additive water for the Saturn V suppressor,

136 m^3/sec (for n = 10), is induced to flow almost immediately upon engine ignition without operational procedure or personnel. Full flow is established within 2 to 3 seconds, and the flow ceases within a like time interval upon engine cutoff. This concept of operational simplicity has always been a part of the development and test program, and remains the final goal for a feasible sound suppression system.

V. MODELS OF SATURN V DESIGN

The improvement of the H-1 sound suppressor in the low-frequency range was one objective in later tests. Other areas of interest were the decreasing efficiency of the jet pump with increasing model size, the water transport capability of the exhaust-steam mixture, thermodynamic properties of the gas-steam-air mixture, and the separation of the water component from the gas-steam mixture before the latter leaves the sound suppressor. Although these last areas are important for the proper operation and function of the sound suppressor, the acoustical performance remained the prime objective in all tests. The solution to these many problems was approached through tests with models of the Saturn V design.

A small model (1:20 scale), with five engines of 17.9 kN (4000 lb) thrust each, was used to study the acoustical and gas dynamics characteristics only. The small scale for this model was permissible, since gas flow scales properly (except for viscous effects) if the linear scale is selected as the square root of the mass flow, with the gas velocity being the same in the model and in the prototype. Since gas velocity is identical in model and prototype, the acoustical performance should be identical also. This is true because for dynamically similar systems the sound pressure spectra measured at similar positions are the same when measured in constant percentage frequency bands, and when frequency is scaled inversely proportional to the scale factor. The total acoustic power is, of course, proportional to the thrust.

The sound power spectrum obtained with this model is shown in Figure 6. It is noteworthy that the overall sound suppression is again 21 decibels, as observed in previous models, but that suppression at the lower frequencies is now 17 decibels at 2 and 4 Hz, and even 24 decibels at 8-Hz midfrequency of the octave band. Water flow rate corresponded to n = 8. According to the acoustic scaling laws, the 2, 4, and 8-Hz frequencies will shift to below 1 Hz in the prototype, and their power levels should increase by 26 decibels. It is believed that the reduction of the low frequency sound power in this model was obtained through the use of resonators. There remains some doubt, however, as to their effectiveness, since the performance in this low frequency area was not repeatable.

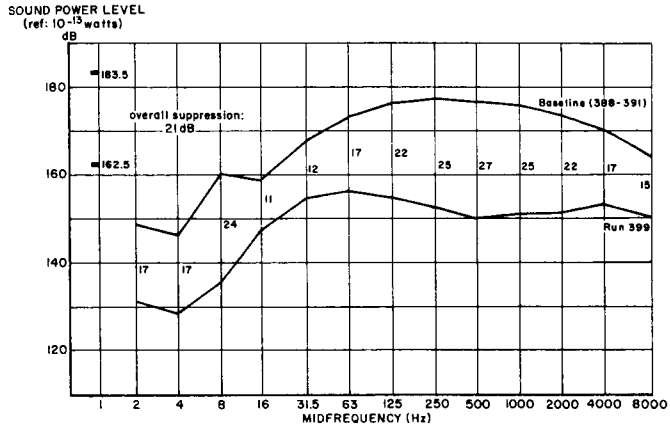

FIGURE 6. ACOUSTICAL PERFORMANCE OF A SOUND-SUPPRESSOR MODEL

Additional problems remaining in the operational area were studied with the H-1 sound suppressor, which was modified into a large model of the Saturn V suppressor design. The H-1 engine was replaced by a cluster of five rocket engines of 133 000 N (30 000 lb) thrust each, and the flat deflector used previously was replaced by a scale model of the deflector in the Saturn V test tower. The test objectives, mentioned above, scale according to Froude's model law. Additive water at mass ratio corresponding to n = 18 was necessary to meet all test objectives, such as the jet pump performance, water transport capability, and water separation. The theoretically possible sound power attenuation through resonators in the low-frequency range could not be verified by the acoustical measurements taken during these tests. It appears that this area deserves further study and research.

Figure 7 shows the sound power spectrum of the modified H-1 sound suppressor using the five-engine cluster (test SS 93) in comparison with the original model using the H-1 engine (test SS 17).

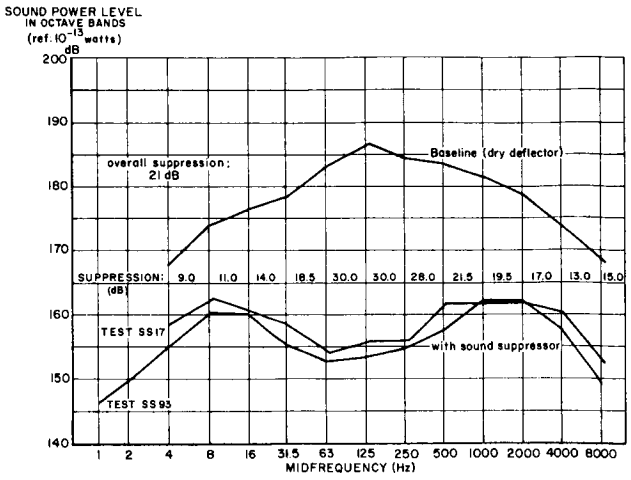

FIGURE 7. COMPARISON OF ACOUSTICAL PERFORMANCE OF TWO SOUND SUPPRESSORS

VI. CONCLUSIONS

The program was terminated in mid-1965, because at that time these basic objectives for a practical application had been accomplished:

1. The program had furnished a good basis for the design of a large sound suppressor for the Saturn V class booster stage.

2. It had met the requirement to sufficiently suppress the low-frequency sound so that certain criteria values of sound pressure level would not be exceeded.

Besides the above results for the practical application to the sound suppressor design, the following general and basic results have been obtained:

1. The basic mechanism in the reduction of the sound generated by rocket engines must be seen in the drastic reduction of the velocity of the exhaust jet before it can act on the still atmosphere and generate the sound through shear and turbulence.

2. The high temperature and velocity of the rocket exhaust defies the common approach to decelerate the gases through mechanical means, except in small units for which sufficient cooling water can be provided. For large rocket engines, the necessary flow rates of cooling water become excessive and prohibitively uneconomical.

3. The introduction of the jet pump, operated by the rocket jet as the driving fluid, solved both the problem of keeping the structure cool and of decelerating the exhaust jet effectively. It also allows for the design of a completely self-contained unit with no requirements for valves, auxiliary power, or operating personnel.

4. Attainable sound power level is equal to the sum of the residual sound power from various sources. These are: sound radiated from the rocket engine proper, sound generated by the part of the jet still exposed to the atmosphere before entering the sound suppressor, sound transmitted through the sound suppressor structure and its gas duct, and the sound generated by the escaping gas-steam mixture. The latter is considered immaterial compared with the other sound components.

5. Further reduction of the residual sound power is considered possible only through enclosing the free part of the rocket exhaust jet and the engine itself.

6. The suppression of low-frequency sound needs further study and experimentation. Present difficulty in obtaining greater suppression may be traced to the fact that the physical extension of structural members involved in the attenuation of the low-frequency sound is small compared with the wave length of the low-frequency sound waves. In addition, the high power of rocket noise may introduce nonlinear effects, not considered, for instance, in resonator theory and general attenuation mechanisms.

REFERENCE

1. Lighthill, M. J.: Jet Noise. AIAA Journal, vol 1, no. 7, 1963, pp. 1507-1516.

QUALITY ASSURANCE AND CHECKOUT RESEARCH AT MSFC

June 24, 1965

by

M. J. Berkebile
R. W. Neuschafer
R. L. Smith

TABLE OF CONTENTS

IMPROVEMENTS IN STAGE CHECKOUT

by R. L. Smith, Jr.

LIST OF ILLUSTRATIONS

CONTENTS (Continued)

LIST OF ILLUSTRATIONS (Concluded)

LIST OF TABLES

IMPROVEMENTS IN STRUCTURAL NONDESTRUCTIVE TESTING

by R. W. Neuschafer

LIST OF ILLUSTRATIONS

CONTENTS (Continued)

LIST OF ILLUSTRATIONS (Concluded)

LIST OF TABLES

IMPROVEMENTS IN ELECTRONIC COMPONENT TESTING

by M. J. Berkebile

CONTENTS (Continued)

LIST OF ILLUSTRATIONS

LIST OF TABLES

IMPROVEMENTS IN STAGE CHECKOUT

By

R. L. Smith, Jr.

SUMMARY

Improvements in the checkout of space vehicle stages are discussed in this report under four categories of work: a guideline document for analysis and checkout of space vehicle stages, improvements in automated checkout, checkout display requirements, and single parameter testing.

The guideline document, now used by NASA and supporting contractors, explains the rationale for all checkout requirements and provides general and specific checkout instructions.

Improvements in automated checkout have been obtained through the development of a digital event evaluator, a computer method for instrument calibration, and control methods for stage checkout. These improvements provide for simplified, more accurate data acquisition, for automatic readout, and for computer programing of the calibration of in-flight instrumentation. More work is needed on the refinement of computer-control operations that require manual intervention.

Work is continuing on checkout display requirements which deal with information presentations on real-time running status, troubleshooting, and assistance in test procedure generation. Some of the developments include the use of cathode-ray screens for displaying a matrix of variables, complex flow diagrams, and information stored in digital form.

In single parameter testing, a single signal (sine or complex wave, step function, exponential function, etc.) is the input to a device being tested, and the output signal is observed for both normal and deviate response. Current work is concerned with finding the appropriate combination of input and output signals for the precise computer identification of normal and faulty operation of various devices or systems.

I. INTRODUCTION

One of the major responsibilities of Quality and Reliability Assurance Laboratory is the checkout of vehicle stages after the completion of manufacturing assembly and static firing. Since many problems are encountered in this complex of operations, solutions have to be sought through studies and engineering developmental work. These are financed mainly through supporting research funds, although in some cases this support is not requested.

This report covers the following achievements in stage checkout improvement: a guidline document on stage analysis and checkout, automated checkout, checkout display requirements, and single parameter testing. The guideline document was written mainly in house, but some contract assistance was used (General Electric Corp., contract NASw-410). The other work, with the one exception, was supported entirely with research funds. The exception was the Digital Event Evaluator (for automated checkout). Its initial work used supporting research funds, but after its feasibility was established, it was completed under line-program funding.

II. GUIDELINE DOCUMENT FOR ANALYSIS AND CHECKOUT OF SPACE VEHICLE STAGES

Over the past ten years, MSFC has developed a pattern of operation in stage checkout which takes into account many variables, some of which are time available; safety considerations; engineering modifications in stage and checkout equipment, made during checkout; and extent of detail to which checkout is needed. This pattern has been re-examined a number of times with a view toward optimizing the process within these variables, and toward maintaining the general philosophy of conservative development, which has been a leading factor in the high degree of success for MSFC programs.

Stated generally, the objective of checkout is to establish that the vehicle stage complies with the following requirements: (1) it is built according to design documentation, (2) it functions according to design intent, (3) it will mate properly with the other vehicle stages, and (4) it will mate properly with the launch site ground equipment.

Satisfying the requirements of one checkout objective does not necessarily guarantee compliance by another. This has been demonstrated many times. An example is given by Jupiter AM 2 testing: when umbilicals were disconnected for simulation of lift-off during the simulated flight test, the missile became completely inoperative. It has been demonstrated a number of times, too, that when an item functions properly on the bench, this does not necessarily mean that it will function properly in the stage. It is safe to say that after testing in a complete checkout has been successfully completed, it is established only that the stage will perform properly at that point in time. Based on experience, stage performance may be predicted for future operations, provided that the tests are properly designed and the existing local limitations are recognized (e.g., a simulated flight test).

Problems with satisfying the general objectives of checkout were encountered as soon as MSFC began working with stage (and missile) contractors who were doing the building and checking out. The basic problem was that the contractors did not appear to have the same concern for care in all aspects as did MSFC. Therefore, MSFC requirements were set down not only to establish specific guidelines but to show the basic rationale for them.

Guidelines for the following areas of checkout were included in the document: (1) receiving inspection, (2) fabrication analysis, (3) analysis of components and minor subassemblies, (4) analysis of major subassemblies, (5) stage analysis, and (6) checkout of assembled stages. The document is intended to provide guidance that is sufficiently general to be applicable to any stage, yet sufficiently specific to ensure detailed coverage in technique and supporting rationale. For example, specific guidelines deal with planning, data coverage required, reporting, recordkeeping, and examples of operations on typical items of a stage.

III. IMPROVEMENTS IN AUTOMATED CHECKOUT

An evaluator of digital data, a computer method of instrument calibration, and advances in control methods for stage checkout constitute important achievements in the program to improve automated checkout. The results of these achievements have been or will be applied.

A. DIGITAL EVENT EVALUATOR

For many years Esterline-Angus (EA) drag pen recorders (Fig. 1) were used in checkout operations

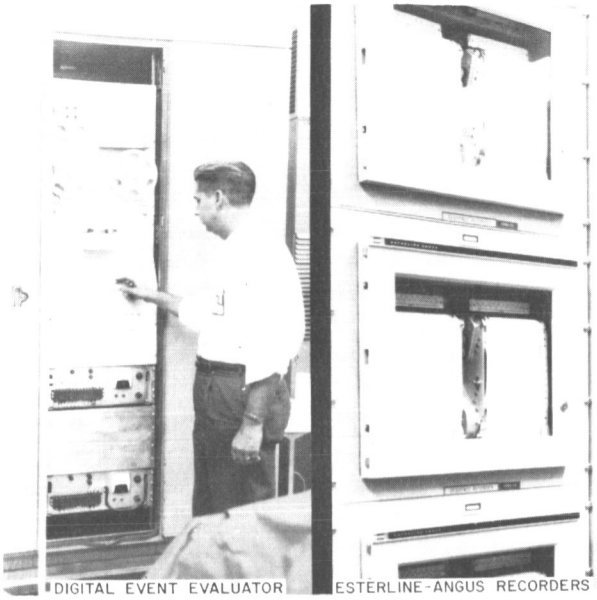

FIGURE 1. ESTERLINE-ANGUS DRAG PEN RECORDERS AND DIGITAL EVENT EVALUATOR

to provide a chronological record of occurrence of discrete events characterized by a step change in voltage between 0 and 28 volts. Each recorder chart contains 19 information channels and a time-pulse channel (Fig. 2). The record is qualitative except for time, which can be read to approximately 50 milliseconds.

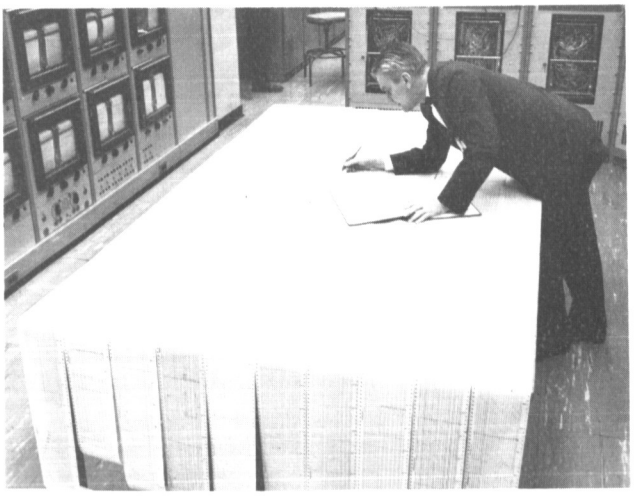

FIGURE 2. PRINTOUT OF TEST RESULTS, ESTERLINE-ANGUS RECORDER

The EA recorders were used because of the ease with which the number of information channels could

be increased (i.e., by adding recorders) and because of their capability of recording simultaneous occurrences. Evaluation of test results of major systems (e.g., overall tests) is based to a considerable extent on evaluation of discrete event records. During Jupiter work, use of 200 channels was fairly common; this meant that 10 to 12 recorder charts had to be aligned carefully and evaluated simultaneously. Such evaluation is tedious, time-consuming, and susceptible to human error. It was recognized even then that there was a need for an instrument to obtain these signal changes and to print out changes sequentially with information on the channel involved, the time of the change, and the direction of change. The major problem to be resolved in the development of the needed instrument was a capability for absorbing many simultaneous changes of state.

The Digital Event Evaluator (DEE) was developed to meet the need for such an instrument (Fig. 1). Its development was begun on supporting research funding, and the final development was completed on line-program funding. As shown in Figure 3, its

516	ON	23.128
516	OFF	23.148
516	ON	23.156
516	OFF	23.172
019	OFF	23.508
466	OFF	23.508
486	OFF	23.528
488	OFF	23.532
513	OFF	23.656
492	OFF	24.728
498	OFF	24.984
494	OFF	24.984
498	OFF	24.984
008	OFF	25.264
003	OFF	25.700
005	OFF	25.700
006	OFF	25.700
010	OFF	25.700
135	OFF	25.700
171	OFF	25.700
172	OFF	25.700
187	OFF	25.700
362	OFF	25.700
461	OFF	25.700
537	ON	25.700
CYCLE		25.704
012	OFF	25.708
016	OFF	25.708

FIGURE 3. PRINTOUT OF TEST RESULTS, DIGITAL EVENT EVALUATOR

output record is simplified and greatly reduced in size. As a consequence, the possibility of error in evaluation of the readout data is reduced. The time resolution of events is much more accurate, being approximately 4 milliseconds. Current test reports show an additional advantage: the DEE frequently picks up error information that could not be detected with the previous equipment. The DEE is now in use at all stage checkout areas and at the launch site (Kennedy Space Center).

B. COMPUTER METHOD FOR INSTRUMENT CALIBRATION

Inflight calibration of instruments, after the completion of manufacturing assembly, has posed several problems for a long time. In general, a given stage condition or function is measured by a transducer, the output of which is appropriately modified by a signal conditioner and passed along for telemetry transmission. A simple system for the instrument calibration of earlier space vehicles is illustrated diagrammatically in Figure 4. The

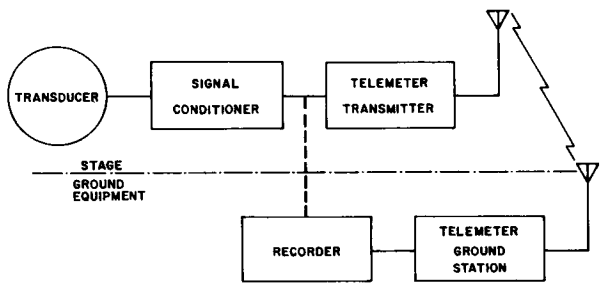

FIGURE 4. OBSOLETE METHOD FOR INSTRUMENTATION CALIBRATION

vertical dashed line represents a capability for hardwire connections to a recording facility so that one could determine whether a signal was within calibration tolerance before it reached the telemetry transmitter. The normal flow of a transducer/signal-conditioner system is from calibration to bench-level-quality verification, to installation into a stage, and to reverification and adjustment aboard the stage to ensure the maintenance of proper tolerance. This has always been a tedious and time-consuming task because of the large number of transducers involved.

With the advent of Saturn programs, basic improvements (Fig. 5) were made to ease some of the checkout problems associated with the system. A Digital Data Acquisition System (DDAS) was interposed between the signal conditioners and telemetry transmitters to provide a digital multiplexing function. A coaxial conductor link was made from the onboard DDAS to the ground checkout equipment, thereby providing greatly simplified access to instrument output signals. A Remote Automatic Calibration System (RACS) was added to facilitate setting the signal conditioners to known simulated inputs, thus providing an improved control

capability. As a result of these improvements, control of the RACS, readout from the DDAS, and evaluation of results could be accomplished by computer.

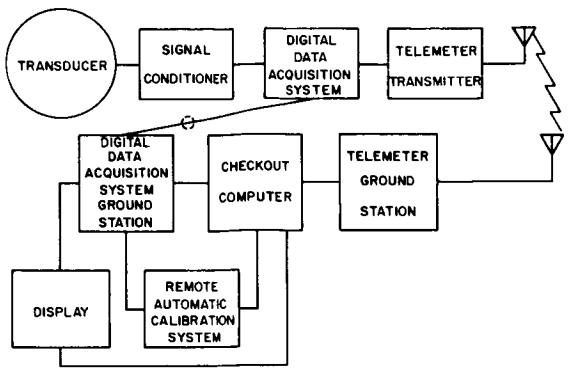

FIGURE 5. SATURN INSTRUMENTATION CALIBRATION SYSTEM

Even with these improvements, however, there remained the problem of having to adjust individually the gain settings of the signal conditioner amplifiers to correct for drift from their original settings. Consequently, an investigation of the entire complex system was initiated by MSFC in an attempt to better integrate the automatic stage checkout systems. The study was conducted by Nortronics Division of Northrop Corporation. Three possibilities for relief appeared worth investigating: modification of existing procedures by relaxing tolerances; an electromechanical servoloop; and completely automated, computer calculated and controlled calibration.

For reasons of feasibility and practicality, the completely automated, computer calculated and controlled calibration method was chosen for use. The method is illustrated in Figure 6, which is a representation of a calibration curve for a transducer and signal conditioner. The vertical axis is the value to be measured, and the horizontal axis is the telemeter output. The solid sloping line is the original calibration curve. A shift in the amplifier is represented by a dashed curve rotated about the origin. There are two calibration points built into the signal conditioner, one at a high point on the curve and one at a low point. Access to both points is controlled through the RACS, either manually or by computer. A given value of the sensed measurement on the shifted curve shows a different output from that of the original curve. Thus, the value read from telemetry would be incorrect if the curve shifted.

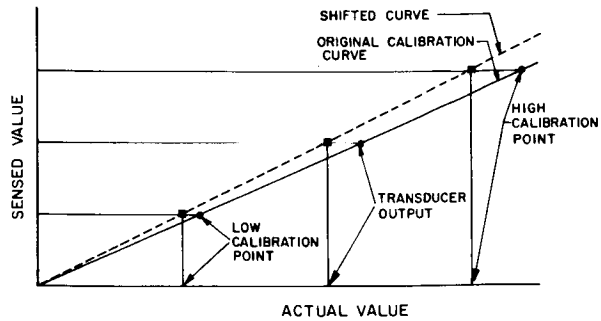

FIGURE 6. CALIBRATION CURVE FOR A TRANSDUCER AND SIGNAL CONDITIONER

Two facts were established to support further progress: transducers never drift or shift, and the amplifier's drift or shift is such that the output curve retains its original shape. Therefore, if the original bench calibration is established and the information fed to the computer, a program may be used to read out the existing calibration points, and the computer can calculate the amount of change for any given point on the curve. For simplification, the curve shown in Figure 6 is a straight line, although this is not essential to the process. This method offers the capability for using computer programing for calibration of flight instrumentation right from the beginning, once bench test data have been established. An upper limit for allowable drift can be established beyond which amplifiers are replaced. Other than this, no further need exists for the laborious manual methods previously used. Even further, it is entirely applicable to a situation in flight, orbit, or deep space in which knowledge by the astronaut of transducer calibration can be vital, and external adjustment difficult or impossible.

C. CONTROL METHODS FOR CHECKOUT

One of the more pressing needs for improvement in automated checkout is a means of allowing the test personnel adequate control of the process. This requirement is generally satisfied in a manual system through the use of manual switches and a predetermined test procedure.

Figure 7 shows the types of control which have been common in the past, in which each function is accomplished by a manual operation, the timing and necessity having been established by the procedure and the operator's assessment of information shown by the indicators.

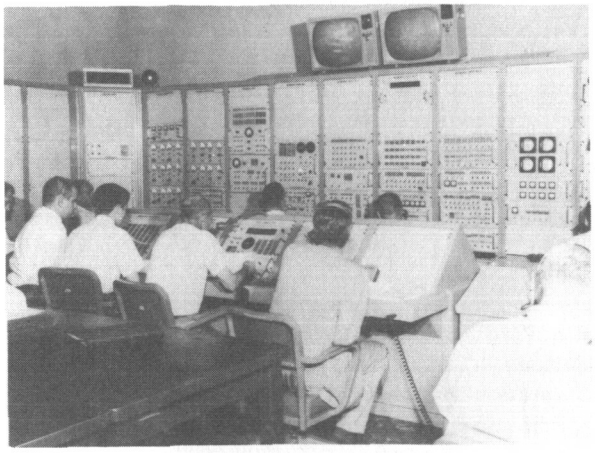

FIGURE 7. USE OF MANUAL CONTROL FOR CHECKOUT

```
READY
TEST
PROG?
77

START  77  0751  08-15-64

SEGMENT 000
SEGMENT 001
SEGMENT 203
SEGMENT 300
STEP    1
NO GO'S
D   25
STEP    3
NO GO'S
D  431
STEP    6
NO GO'S
D   90
D  144
STEP    8
NO GO'S
D  171
D  173 00102.
SEGMENT 000
```

FIGURE 8. COMPUTER PRINTOUT AFTER ENCOUNTERING TROUBLE

Computer-controlled tests generally proceed at a rate which makes it difficult for a person to keep up with the current step of the procedure. Nevertheless, manual intervention in the computer operation will be required at times, regardless of hard-wired safety controls and programed alternatives. Manual intervention is required when the computer has no alternative routines upon which to fall back, or when it has exhausted the routines which exist and then reports out the exception. (Figure 8 is an example of such a printout.) The person conducting the test assesses the symptom indications which are available, the location of the problem within the test procedure, and the major system which is in trouble. He then corrects or circumvents the difficulty and continues the test, or in some cases terminates the test in order to make necessary repairs.

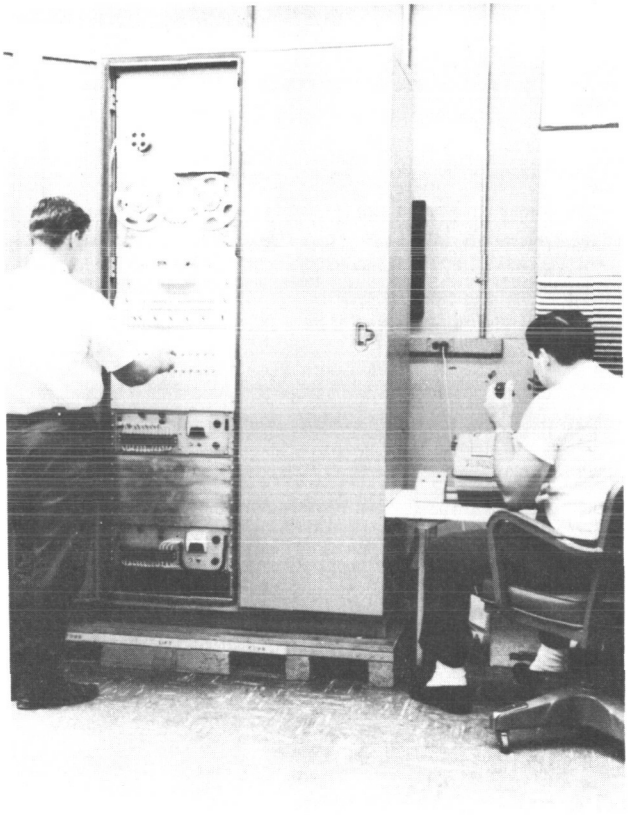

FIGURE 9. SWITCHING CONTROLS FOR MANUAL OPERATION, COMPUTER TROUBLESHOOTING

Figure 9 shows one arrangement of switching controls to allow selective manual operation for troubleshooting independent of the computer. At best, this provides a cumbersome approach to the problem. Manual capability to make some changes in computer memory to circumvent difficulty,

change values, and so on, also exist. However, this procedure depends upon an intimate knowledge of the computer and its programing, and can be dangerous because of the possibility of operator error or because of unforeseen effects on later portions of the program which are iteratively dependent on the modified section.

Solutions to problems of this type have been of a gross nature. For example, the well-known "panic button" can initiate a programed shutdown. Another possibility is illustrated in Figure 10, which shows a sight-operated switch whose function is based on light refraction from the operator's eye. The switch-

FIGURE 10. SIGHT SWITCH

ing operation is initiated when the operator turns his eyes to look at the switch. Sensitivity can be varied so that an involuntary glance will not operate the switch. The sight switch would be useful for setting a safe-condition system into operation (e.g., venting a tank to relieve excess pressure buildup), for bringing specific items up for display, etc. The sight switch is a single-switching operation and therefore is also a gross control. The switch was developed under contract by Spaco as part of the investigation by MSFC into the general problems of stage checkout control.

Refinements of the control problem will not come easily. They are dependent upon intimate knowledge of all systems involved in a given operation, and will vary from one system to another, so that general solutions will be infrequent. MSFC is continuing its investigation into specific areas of the Saturn V checkout systems to determine how refinements can be made in existing systems. As time and funds become available, it can be expected that more detailed solutions will be obtained.

IV. CHECKOUT DISPLAY REQUIREMENTS

A knowledge of existing conditions and symptoms is required for adequate checkout control. Three situations in automated checkout requiring information presentation are: real-time running status, symptom and system information for troubleshooting, and assistance in test procedure generation.

Figure 11 illustrates one means of providing information on real-time status. This photograph shows a bank of lights arranged to indicate existing status, as well as the progression of a sequence of events. This is useful during a rapidly sequenced operation such as engine ignition, but is generally not sufficient in itself.

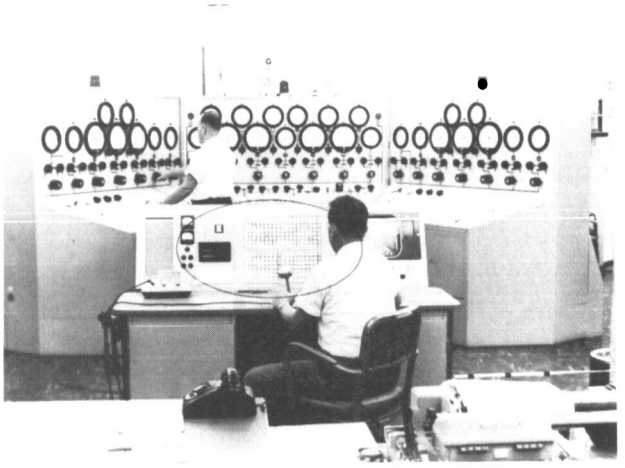

FIGURE 11. LIGHT INDICATORS FOR RAPID SEQUENCE TESTING

Figure 12 shows a panel with meters for information indication. These are useful in static condition, but generally are not useful during a computer-controlled test unless an observer for each meter or small group of meters is present to monitor the overall test status. The rapid progression of the test sequencing makes such use almost of no benefit to a test conductor.

The person conducting the test requires an overall awareness of test status and progress and a capability which will enable him to anticipate an action

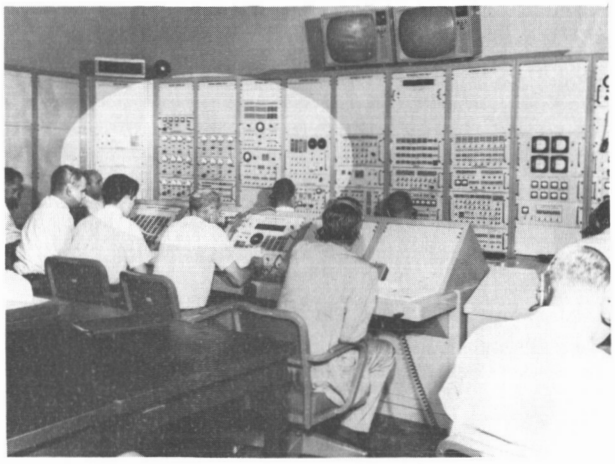

FIGURE 12. USE OF METERS FOR INFORMATION INDICATION

he must take. The combination of a computer and a cathode-ray-tube (CRT) display offers a good partial solution to the test conductor's problem. Many types of CRT displays are available. The problem of use in stage checkout is what to show on the display, and to what quantitative depth.

A simple analogy would be a situation in which one must know, from a remote location, the position at every instant of time of an individual walking from one corner of a room diagonally to the opposite corner. By placing sensors in a grid pattern one could place x and y digital indicators in the remote location and with a certain amount of estimating and a grid map, ascertain the position. A simpler solution would be to use a closed circuit television system with a screen in the remote location. The viewer could then have the necessary information instantly.

A matrix of variables with current quantitative status can be shown on a CRT screen. Table I shows a sample of what such a matrix could include. It is not intended to be typical, but to show a cross section of the type of information and how it is presented.

Studies as well as experience in checkout indicate that a person conducting a test requires qualitative real-time information analogous to the closed circuit television example while the computer is proceeding with a test. Therefore, a flow diagram, as indicated in Figure 13, would be very useful. In this case, the "flow" in the test can be indicated by a cursor, shading, or other means. Manual estimation is not required, and events requiring anticipatory action can be clearly indicated. When an involuntary computer "stop" occurs, the position of the stop is clearly shown, and it indicates a beginning point for remedial action.

TABLE I. SAMPLE MATRIX OF VARIABLES FOR CRT DISPLAY

	VOLTS	AMP.	N/m^2 (psig)	N/m^2 (psia)	ON/ OFF
BUS # 1	28.5	14			On
BUS # 2	29.2				Off
LOX TANK PRESSURE			310 k (45)		
FUEL TANK PRESSURE			172 k (25)		
TAIL SECTION PRESSURE				41 k (6)	
WATER PRESSURE			1 M (150)		

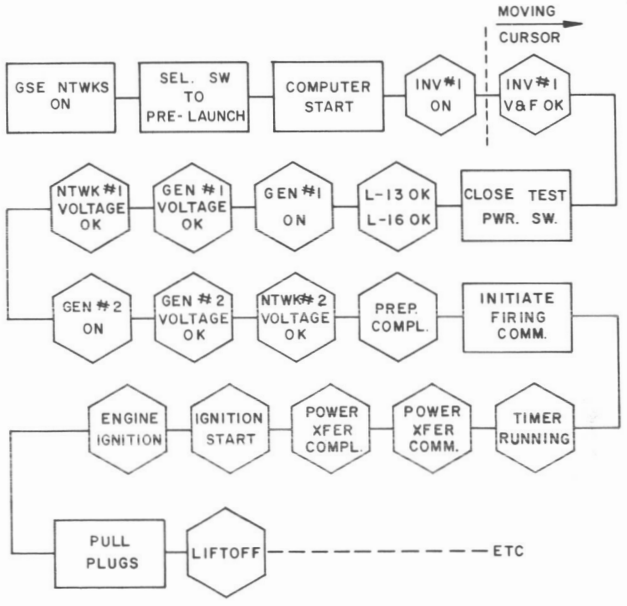

FIGURE 13. SAMPLE FLOW DIAGRAM FOR REAL-TIME PRESENTATION

When a stop has occurred, the conductor of the test must determine the nature of the problem, which frequently lies with a major subsystem of either the stage, the ground, or both. Because of the complexity of both stage and checkout equipment, the components involved may be located on several different pages of a large number of drawings. Tracing through all these to pinpoint the trouble can cause a number of problems, not the least of which is error in diagnosis. For several years, test engineers have sketched in extra information on drawings at various places to simplify

this tracing operation. Figure 14 shows a composite schematic of a fairly complex system which could be depicted in its entirely on as many as ten pages of stage and checkout system drawings. A number of details have been omitted to simplify the representation and bring together the essential elements to form a complete "picture" of the system. From this point it is comparatively easy to begin to troubleshoot the system by referring to the detailed documents as necessary.

information presentation, such as projection from microfilm, could be used to overcome the digital storage problem, although information would not be easily accessible. Magnetic tape offers a solution, although accessibility is a problem here also. A disk file may turn out to be the answer to the problem, since it can provide rapid access to its stored information. Also under investigation is the compatibility of these approaches with existing checkout systems.

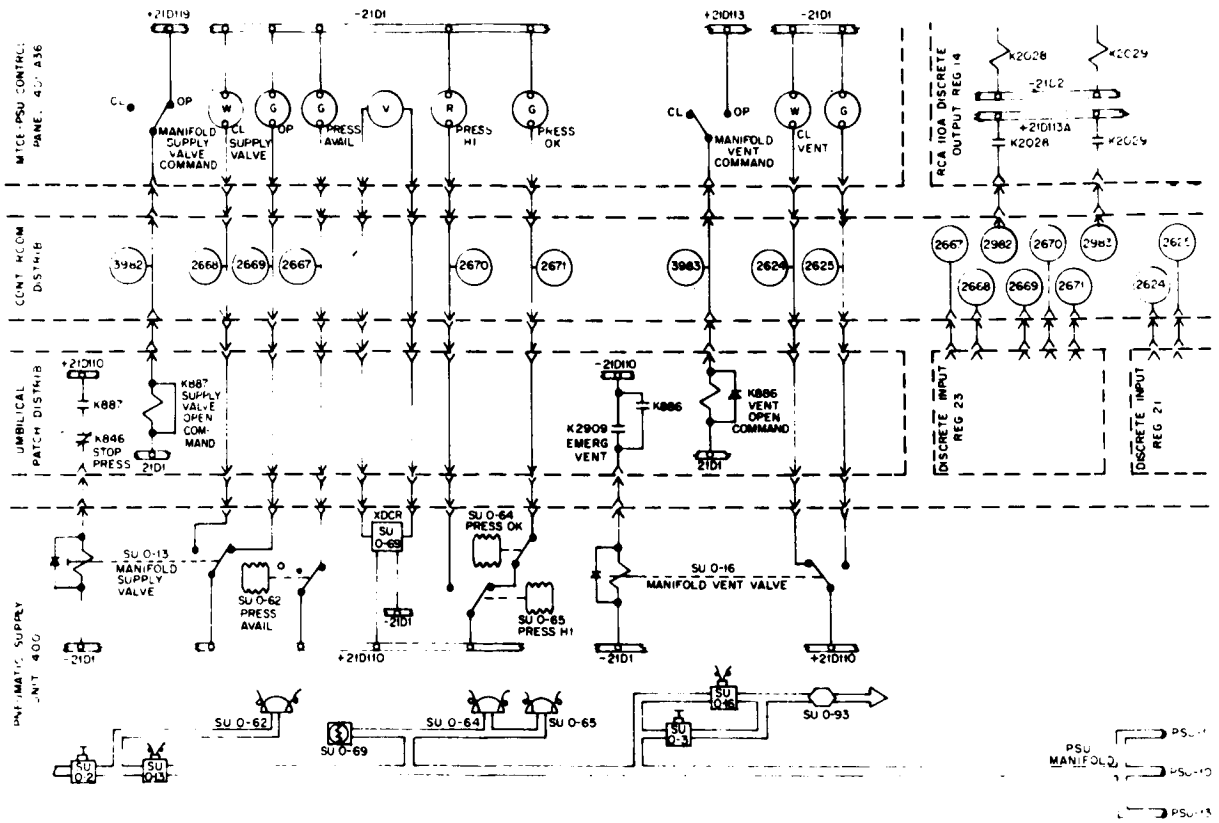

FIGURE 14. COMPOSITE SCHEMATIC OF AN INTRICATE SYSTEM

Studies have indicated that it is feasible to present this type of information on a CRT for troubleshooting. The launch site display system, for example, is capable of handling such a presentation in some respects. At present, MSFC is investigating the feasibility of digital storage in which all necessary composite schematics and a document "generation" breakdown (by divisions, subdivisions, etc.) could be displayed on a cathode-ray tube.

One disadvantage of digital storage is the large amount of memory required. Other approaches to

V. SINGLE PARAMETER TESTING

Single parameter testing deals with the introduction of a single input signal into a device, and the observation of all outputs for both normal response indications and deviations from normal. The feasibility of this technique has been established by two studies: one on the stable platform system (Emerson Electric, supervised by Astrionics Laboratory), and the other on the fundamentals of signals and network responses, (General Electric, Daytona, supervised by Quality and Reliability Assurance Laboratory).

A variety of input signals, such as a sine wave, a complex wave, a step-function input, or a growing exponential function, may be used. Considerations affecting the input signal are magnitude, time duration, necessity for repetition, and shock effect on the system under test. As a result of the input signal, various output signals from a given device are obtained. The best combination of these output signals, for a given input, must be chosen to provide a true "fingerprint" (i.e. precise identification) of the system being tested. The output signals should show a significant deviation in one or more parameters in the presence of an abnormality in order that fault indications may be observed. For maximum benefit, the output signal should be capable of computer analysis.

Achieving the proper balance for solutions of all the requirements indicated is the major problem involved. One study has indicated that a growing exponential function is the more desirable input up through third-order linear systems. A specific signal input and/or output "fingerprint" will exist for each item to be tested; like items should be capable of utilizing the same type input signal.

The advantage to single parameter testing is its simplicity in terms of testing. All that is necessary for its use is a capability to provide the input signal and to read and analyze the output. The outputs of most onboard devices are available, and computer analysis capability exists in the ground equipment. For each device to be tested in this manner, the only additions for existing onboard stage systems would be the signal source and input capability requirements. This could be approached in the same manner as the calibration provision in the signal conditioners for the instrumentation system. The approach thus becomes economical and practical, as well as technically feasible.

IMPROVEMENTS IN STRUCTURAL NONDESTRUCTIVE TESTING

By

R. W. Neuschaefer

SUMMARY

Advanced methods of nondestructive inspection of structural materials are described in this report.

A high-speed radiographic system has been designed for inspecting bulkhead welds of Saturn I-C propellant-fuel tanks. This system has saved half the time formerly used in radiographic inspection and has minimized work stoppage by reducing radiation hazards.

An ultrasonic inspection method, complementing the radiography method, has been developed for inspecting seam- and spot-weld joints in type 2219 aluminum. This is a quick inspection method and it provides a permanent, printed record. It also can identify spurious weld defects (enigmas) more rapidly than radiography can.

The feasibility of identifying various tempers of type 2219 aluminum has been investigated through application of a technique of eddy-current induction and measurement. The "O" condition was found to be easily identified, T62 temper the most difficult to identify, and T31, T37, T81, and T87 falling in between these extremes.

Formerly, hydrostatic testing of tapered-wall tanks was feasible because flight conditions could not be simulated with conventional test methods. To solve this difficulty, a zone-gradient pressurization system was conceived, and pressure seals and test fixtures designed, for testing a model-sized straight-wall tank under accurately simulated flight loading. The successful full-scale application of this system should significantly affect the future development of lightweight tapered-wall propellant tanks.

I. INTRODUCTION

In recent years the complexity of manufactured items has increased, while design margins have been reduced. As a consequence of these changing conditions, advancements in inspection techniques have been especially necessary.

The Analytical Operations Division of Quality and Reliability Assurance Laboratory has been specifically concerned with improving nondestructive techniques for inspecting structural materials. Some of its achievements in improved test or inspection methods are described in this report under investigations in a semiautomatic radiographic inspection system, ultrasonic techniques for inspecting spot and seam welds, eddy-current techniques for sorting tempers of type 2219 aluminum, and zone-gradient hydrostatic testing.

II. SEMIAUTOMATIC RADIOGRAPHIC INSPECTION SYSTEM

Industrial radiography has been in use since the start of the twentieth century for examining weldments, castings, and composite structures. The Saturn program, with welded tanks and very narrow design margins, has required a reevaluation of the radiographic methods previously employed. The first radiographic techniques used at MSFC possessed a radiation hazard and were slow; therefore, the primary consideration was given to the design and manufacture of a safe, high-speed radiographic system to assure the quality of S-IC bulkhead welds.

The system that was developed as a joint MSFC/Boeing Company effort (Fig. 1) uses two 31-meter

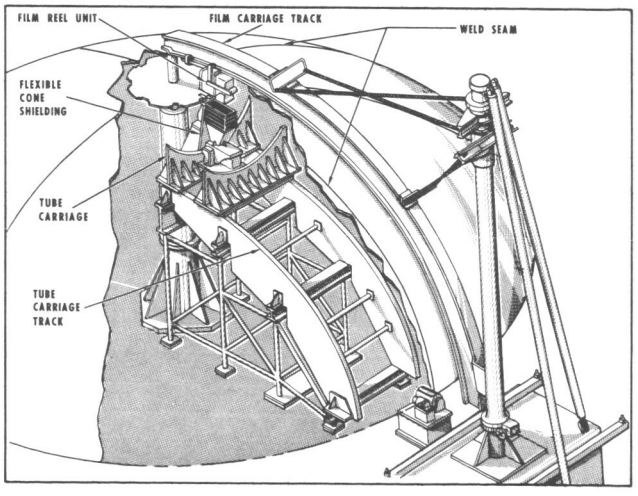

FIGURE 1. SEMIAUTOMATIC X-RAY SYSTEM

(100-ft) reels of film and a semiautomatic electrically controlled advancement of film, a film positioning unit, and an X-ray tube. The operation of this system is controlled from a single console.

There are five major groups of equipment in the new system:

1. The film-transfer unit, with reels driven by electric motor for rapid loading of X-ray film (Fig. 2)

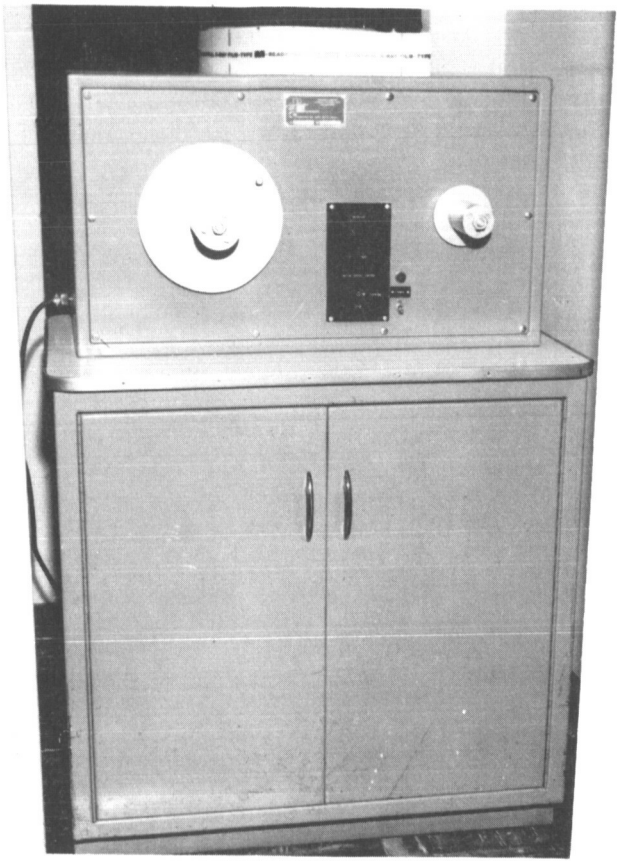

FIGURE 2. FILM-TRANSFER UNIT

2. Semiautomatic X-ray equipment consisting of several units which position the film and welds in correct alignment (Fig. 3)

3. The semiautomatic film-wrapper stripper which strips the lightproof paper wrapping from the films so that it may be automatically processed (Fig. 4)

4. The Pako semiautomatic processing equipment which develops, fixes, washes, and dries the film (Fig. 5)

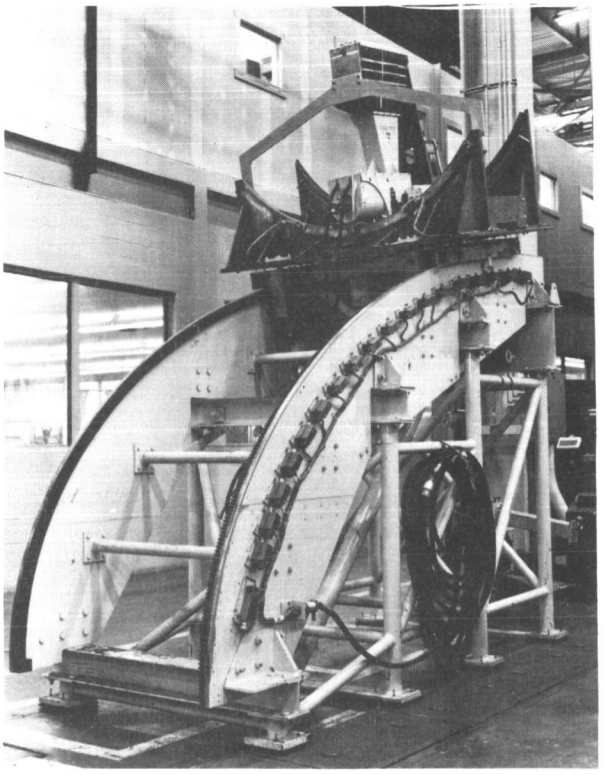

FIGURE 3. SEMIAUTOMATIC X-RAY EQUIPMENT

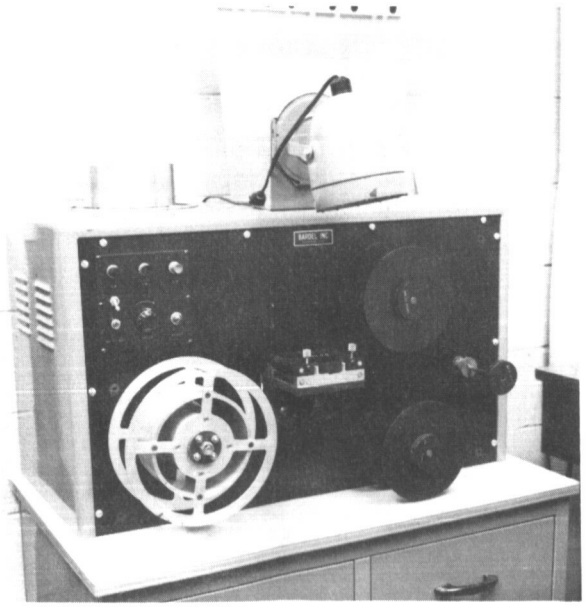

FIGURE 4. SEMIAUTOMATIC FILM-WRAPPER STRIPPER

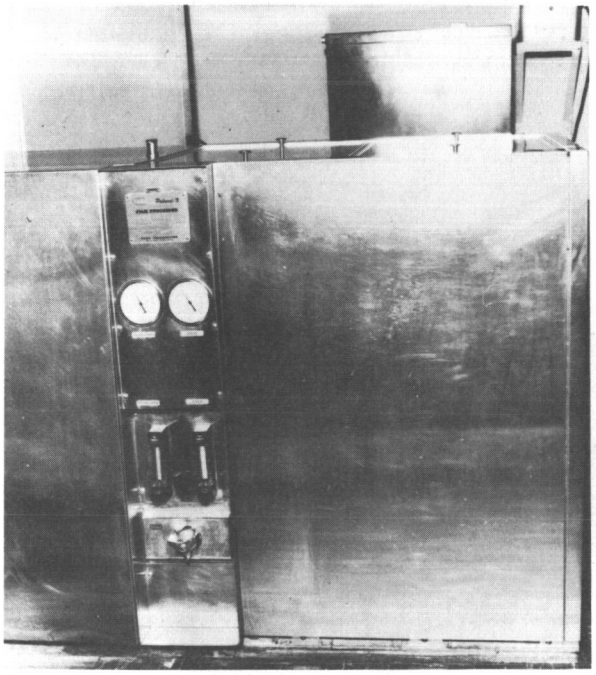

FIGURE 5. PAKO SEMIAUTOMATIC FILM PROCESSOR

5. A semiautomatic film-viewing console, which provides optimum film-viewing conditions and facilitates the handling of film on motor-driven reels (Fig. 6)

FIGURE 6. SEMIAUTOMATIC FILM-VIEWING CONSOLE

The new radiographic inspection methods have several advantages over the previously used ones. The total manhours required for exposing, processing, and reviewing film is approximately 50 percent less. The savings are not only in inspection time, but in the total time that the work area must be cleared. Because the radiation hazard has been reduced, personnel may work within 3 meters (10 ft) of the unit instead of the previous 15 meters (50 ft). Therefore, work stoppage has been reduced to a minimum. The transport fixture, moreover, is adaptable for ultrasonic testing.

III. ULTRASONIC INSPECTION OF SPOT AND SEAM WELDS

Although ultrasonic inspection equipment has been available since the 1940's, the specifications of the Saturn program have required the development of improved methods and equipment. Ultrasonic and radiographic inspection methods may be used to complement each other in many instances. Defects such as cracks, porosity, and inclusions in weldments may be detected by both radiographic and ultrasonic inspection methods. Ultrasonic inspection will locate and describe the serious defects (e.g., fine cracks and crack-like defects such as certain types of incomplete penetration and lack of fusion) with the highest degree of assurance, whereas radiography will more readily detect inclusions and small porosity.

The ultrasonic inspection techniques developed and applied by Quality and Reliability Assurance Laboratory are a new and important tool for the evaluation of spot and seam welds. The two ultrasonic methods employed consist of an angle beam-through transmission technique for spot welds, and a pulse-echo technique for seam welds. The angle beam-through transmission technique uses a transmitter and a receiver.

Research has been conducted principally in the field of wave propagation utilizing collimated probes, since commercially available ultrasonic equipment does not provide high resolution. A through-transmission ultrasonic system based on this research has been developed using small collimators capable of resolution surpassing that of commerically available probes. This development (Fig. 7), which is available for production use, has been engineered for scanning spot welds and for printing out the contour of the nugget at the interface.

For an ultrasonic evaluation of seam welds in plate material such as S-IC gores and skins, initial testing to determine technique has been per-

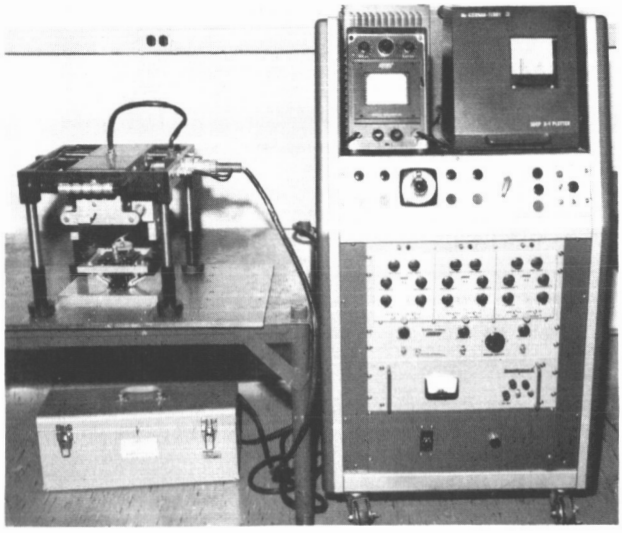

FIGURE 7. ULTRASONIC SPOT-WELD SCANNING SYSTEM

FIGURE 8. PORTABLE ULTRASONIC INSPECTION SYSTEM

formed utilizing an ultrasonic transceiver (the Krautkramer USK-4, Fig. 8). Pulse-echo techniques also have been used in this investigation. Internal porosity, cracks, incomplete penetration, and lack of fusion can be readily detected as a part of production inspection.

It was necessary to develop an automated scanning system in order to shorten the inspection time and provide a permanent inspection record. The result of this development was the simulated immersion-probe adapter for use on tooling developed for the semiautomatic radiographic system.

An ultrasonic automatic scanning and recording system (Fig. 9) was developed which produces one of the fastest "C" scans or facsimile recording of all equipment available.

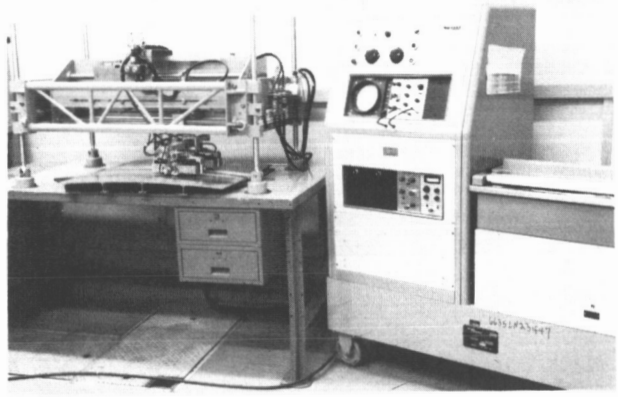

FIGURE 9. ULTRASONIC HIGH-SPEED SCANNING AND RECORDING SYSTEM

An example of the savings in money and time which can be attributed to ultrasonic testing occurred when several gore segment welds were rejected; radiography had disclosed what appeared to be a lack of sidewall fusion. A subsequent ultrasonic inspection revealed the indications to be radiograph enigmas (Fig. 10), believed to be caused by metal twinning. Although enigmas may be resolved by radiographing the material from several angles, ultrasonic inspection is more rapid; consequently, the technique currently is being employed to complement radiographic inspection.

IV. EDDY-CURRENT TECHNIQUES FOR SORTING TEMPERS OF TYPE 2219 ALUMINUM ALLOY

The temper of fabricated material for incorporation into space vehicles may not be known precisely, because incomplete or erroneous documentation accompanies the material received. The true condition of the material in the past could be ascertained only by destructive testing methods such as tensile strength and hardness testing. These tests were time consuming and difficult to perform because of the large size of some of the material. In addition, the destructive techniques are inherently undesirable.

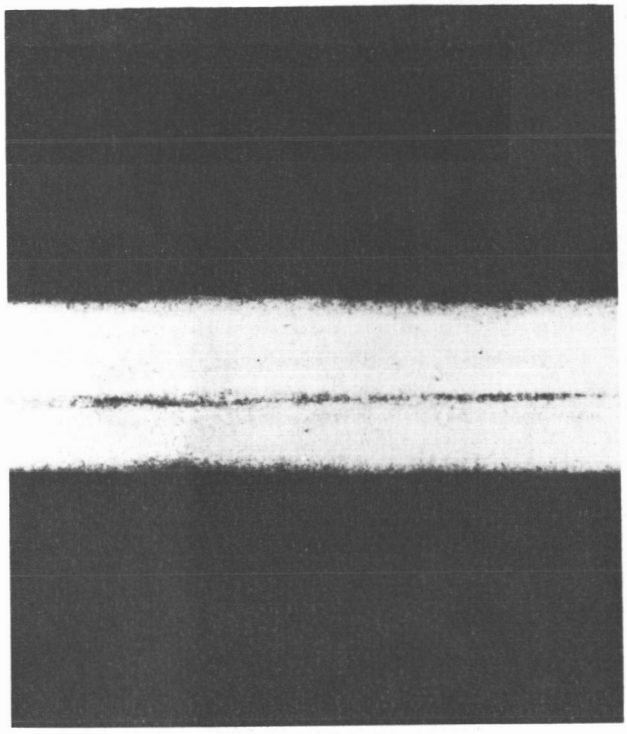

FIGURE 10. ENIGMA IN THE RADIOGRAPH OF A WELD

Because of the disadvantages stated, a research project was initiated to determine the feasibility of using commercially available eddy-current testing instruments to differentiate the various tempers of type 2219 aluminum alloy.

Eddy currents are induced into a metal specimen when it is placed in the field of a coil carrying alternating current. The impedance or opposition to the flow of induced eddy current is a function of the metal's electrical conductivity, which is influenced by the temper of the metal.

Test specimens were surface treated with coatings representative of those employed on space vehicle flight hardware for an evaluation of the influence of coatings on the instruments' temper-sorting capability. Figure 11 shows some representative surface specimens of two tempers which were subjected to eddy-current tests. Figure 12 shows the test setup using Magnaflux Corporation's eddy-current tester (FM-100), which is the most sensitive instrument evaluated to date.

Because there were a limited number of samples available, it was decided to conduct this initial statistical analysis to 95-percent confidence limits. A further study to refine the data will be conducted when more measurements are obtained.

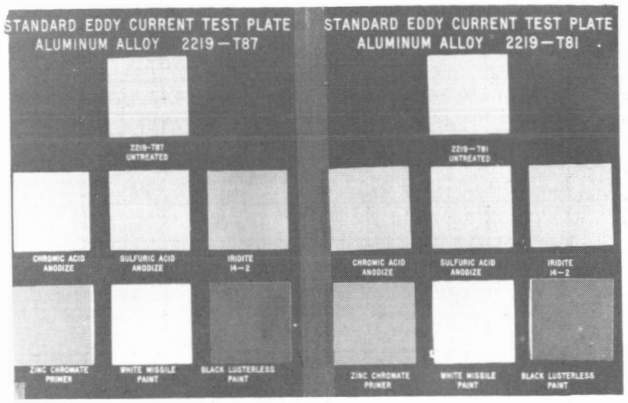

FIGURE 11. EDDY-CURRENT TEST PLATES

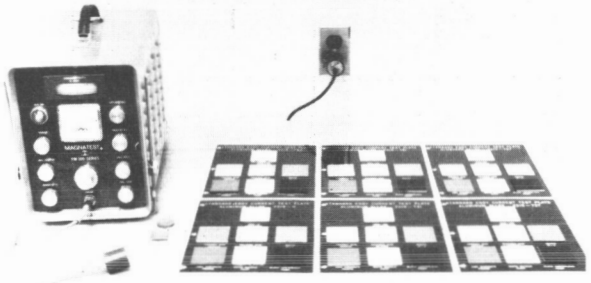

FIGURE 12. EDDY-CURRENT TEST SETUP

The raw data of this study were analyzed statistically for a determination of the following: (1) the significance of coating variations as compared to random variation together with operator effect and instrument error or drift (or both) and (2) the 95-percent confidence limits for the samples, and the number of samples for each temper.

An analysis of variance test was used to determine the significance of temper as compared to coating and residual. The F-ratio tests indicated that the effect of temper was of extremely high significance as compared to residual variation and coating. The temper data were analyzed to obtain values to be expected from all samples of each temper.

The feasibility of sorting tempers of 2219 aluminum alloy is summarized in Figure 13. Conductivity of the "O" condition or annealed material can be readily identified. The conductivity of tempers T31 and T37 overlap strongly. Temper T62 is partially overlapped by tempers T81 and T87 and is the most difficult to identify.

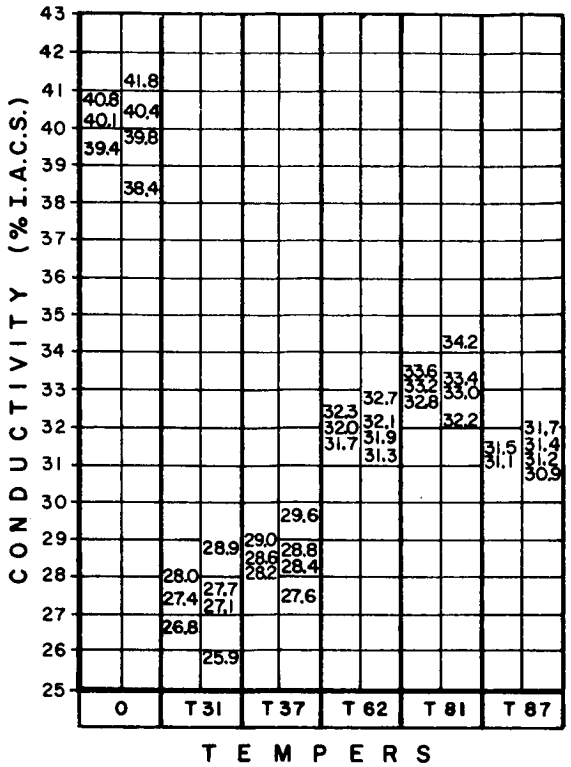

- VALUES IN LEFT SIDE OF EACH COLUMN ARE MEAN ($\bar{X}$) AND 95% LIMITS ($\bar{X} \pm 1.96s$) FOR TESTED SAMPLES.
- VALUES IN RIGHT SIDE OF EACH COLUMN ARE ESTIMATED RANGES OF MEANS (R) AND 95% LIMITS FOR ALL TEMPER SAMPLES OF SIMILAR COATING.

FIGURE 13. CONDUCTIVITY CHART FOR TYPE 2219 ALUMINUM ALLOY

V. ZONE-GRADIENT HYDROSTATIC TESTING

Hydrostatic testing is an important nondestructive testing method which is employed to verify structural integrity of S-IC tanks. At times this method may be destructive, but even in these cases worthwhile data are usually obtained from the test.

Hydrostatically proof testing propellant tanks to full operating pressure is customary in the space industry. The proof test is necessary because of the narrow margins imposed on vehicle design by weight considerations. As a result of these narrow margins, tanks have been designed with yield-to-design load ratios of 1.1 to 1.0, which means that any defect in raw or fabricated material can result in a catastrophe. Most defects will be revealed by in-process inspection; but only a full-load proof test can give the assurance required for a major vehicle, especially a manned vehicle.

Tapered-wall-thickness designs now used for large tanks cannot be tested by conventional means because conventional hydrostatic test conditions differ from those of flight. For example, water used in the test tank differs in density from flight propellant, and the test tank is not under the force of flight acceleration. (This is not a problem related to designs for constant wall thickness.)

The magnitude of the problem encountered in the hydrostatic test of large vehicle tanks can be readily seen by the analysis of the hypothetical tank shown in Figure 14. This tank is 19.5 meters (64 ft) long and

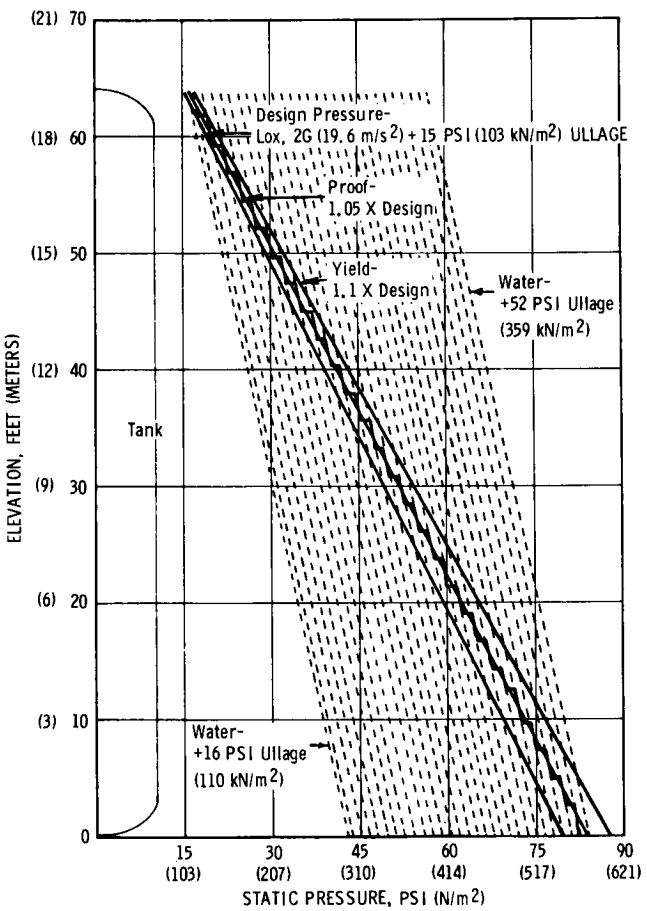

FIGURE 14. HYPOTHETICAL HYDROSTATIC TEST TANK

10 meters (33 ft) in diameter. It is subjected to an ullage pressure of 103 kN/m^2 (15 psig) and an acceleration force of 19.6 m/s^2 (2 g). The tank configuration and condition are similar to those of a Saturn

S-IC liquid-oxygen tank, under severe forces, except that the values have been rounded and all structural loads other than pressure have been ignored.

The maximum differential pressure of 441 kN/m^2 (64 psi) at the aft bulkhead is a function of liquid-oxygen density, head, acceleration, and ullage pressure. In comparison, the same tank filled with water for hydrostatic testing exhibits a maximum differential pressure of 191 kN/m^2 (27.7 psi), which is a function of water density, acceleration, and head. Under this condition, the aft bulkhead is pressurized only to 294 kN/m^2 (42.7 psig), which is 250 kN/m^2 (36.3 psig) under test pressure when the forward bulkhead is at full load. Conversely, the forward bulkhead is overloaded 250 kN/m^2 when the pressure at the aft bulkhead is at flight pressure.

The first condition is unacceptable because it does not provide the required assurance. The last condition, although a usable solution, is also undesirable because it imposes a design requirement for test that is heavier than needed for flight. In the example given, the test load would be 340 percent of the flight load, with a significant increase in tank weight.

The above conditions are delineated as height versus pressure plots in Figure 14. The dashed lines represent a family of pressure gradients obtained with water in a 9.8 m/s^2 (1 g) acceleration environment by varying ullage pressure in increments from 110 kN/m^2 to 393 kN/m^2 (16 psi to 57 psi). The three solid lines represent the design conditions, the required test condition, and the yield pressure. The extreme left and right gradients illustrate the conditions obtained by conventional methods when the test requirements of the upper and lower bulkheads are met.

Figure 15 illustrates a conception of the zone-gradient pressurization. This pressurization method consists of applying pneumatic pressure to the exterior of the tank to develop an acceptable approximation of the required gradient. This is accomplished with a dome-head section and a number of skirt sections enveloping the tank. The tank is segmented into a series of pressure zones isolated from each other through the use of inflatable seals.

Air pressure is applied directly to the external surface of the tank to provide infinite conformability, thus eliminating the local load discontinuities that would result from bladders. The inflatable seals (Fig. 16) are suited for zone isolation, they provide adequate clearance for fixture placement, and, when inflated, have sufficient conformability to adequately seal around welds and other minor irregularities.

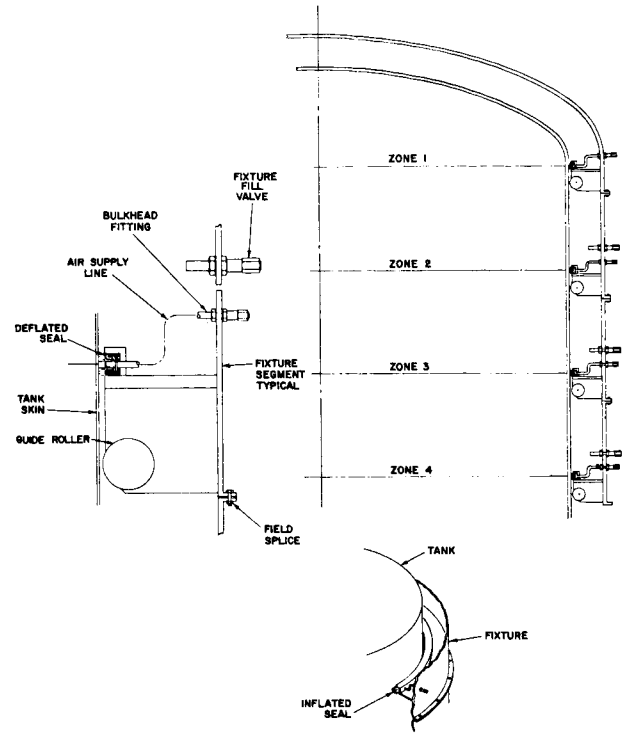

FIGURE 15. ZONE-GRADIENT PRESSURIZATION CONCEPT

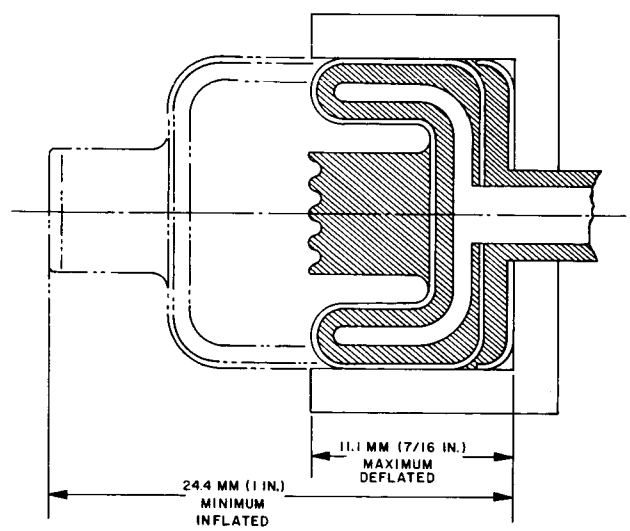

FIGURE 16. INFLATABLE SEAL

The pressure on the tank skin is the difference between internal and external pressure. Any desired gradient can be approximated by establishing the appropriate pressure in each external zone. The desired pressure gradient for testing the hypothetical

tank in Figure 14 and a close approximation of this gradient, which can be realized using the zone-gradient method, are shown as the proof pressure and the stepped pressure gradients in the figure. The pressure, although a function of height, never exceeds the yield strength nor goes below the design strength.

Problems were anticipated in the critical mechanical handling of the test fixture and in designing suitable seals. A model zone-gradient fixture was designed and built to prove the feasibility of the conception. The model fixture was assembled around a 1.8-m (70-in.) tank (Fig. 17), the inflatable seals were pressurized, and the zone pressure increased in accordance with the sequential pressurization schedule given in Table I. The pressure increments in all zones were typical of the stepped line shown in Figure 14. All pressures were maintained without difficulty and all seals were satisfactory.

The technical feasibility of the pressurization concept has been demonstrated; its economic feasibility now must be determined. This effort will require cost and design studies for a full-size zone-gradient system of a specific stage, cost- and weight-saving studies for the optimum tapered tanks on that stage, and a comparison of the two studies to determine gain in payload.

VI. CONCLUSIONS

No single nondestructive testing method will detect all defects in all materials. Radiography had been considered by some as a panacea for all inspection ills when it was first discovered, and ultrasonic techniques offered similar promise. However, each of these methods has been shown to have limitations.

Promising new technologies under development are infrared and microwave inspection methods, each system having certain inherent advantages and disadvantages.

The principal difficulty with inspecting today's advanced structures is that testing methods required to assure quality adequately require much time for their development. Consequently, quality assurance engineers are finding it necessary to improve and intensify quality-assurance support during advanced structures development.

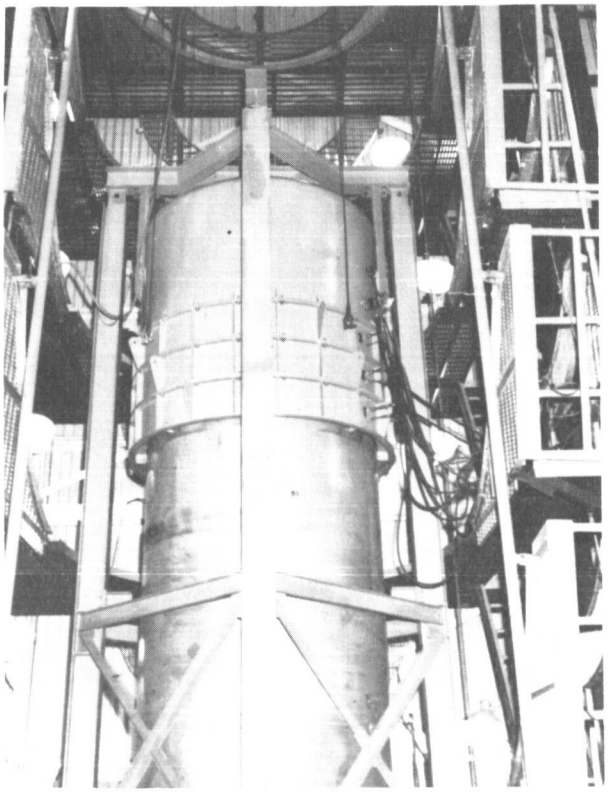

FIGURE 17. ZONE-GRADIENT FIXTURE ASSEMBLY

TABLE I. SEQUENTIAL PRESSURIZATION SCHEDULE

Event	Seal 1	Zone 1	Seal 2	Zone 2	Seal 3	Zone 3	Seal 4	Zone 4	Tank
Fill and pressurize tank									15
Install zone 1 fixture				no change					
Inflate seal 1	25								"
Pressurize zone 1	"	5							"
Raise tank pressure	"	"							20
Install zone 2 fixture				no change					
Inflate seal 2 increase seal 1	30	"	25						"
Pressurize zone 2	"	"	"	5					"
Increase zone 1	"	10	"	"					"
Increase tank pressure	"	"	"	"					25
Install zone 3 fixture				no change					
Inflate seal 3, increase seals 1 and 2	35	"	30	"	25				"
Pressurize zone 3	"	"	"	"	"	5			"
Increase zone 2	"	"	"	10	"	"			"
Increase zone 1	"	15	"	"	"	"			"
Increase tank pressure	"	"	"	"	"	"			30
Install zone 4 fixture				no change					
Inflate seal 4, increase seals 1, 2, and 3	40	"	35	"	30	"	25		"
Pressurize zone 4	"	"	"	"	"	"	"	5	"
Increase zone 3	"	"	"	"	"	10	"	"	"
Increase zone 2	"	"	"	15	"	"	"	"	"
Increase zone 1	"	20	"	"	"	"	"	"	"
Increase tank pressure	"	"	"	"	"	"	"	"	35

IMPROVEMENTS IN ELECTRONIC COMPONENT TESTING

By

M. J. Berkebile

SUMMARY

Improved and new methods of inspection screening of basic electronic parts and subassemblies are discussed in this report.

Investigations on monolithic integrated circuits have revealed major causes of failures. Quality and Reliability Assurance Laboratory has used this information in writing a procurement specification for an instrument to test AC and DC parameters of integrated circuits. When the equipment is in operation it will provide much needed standardization for reliable acceptance inspection of integrated circuits.

In the past, hermetically sealed relays which passed electrical inspection would fail later because of corrosion of relay contacts (atmospheric moisture had entered through undetected leaks in the seal). The difficulty of finding seal defects in acceptance testing has been simplified through the use of a nondestructive radioisotope tracer detection method. Current work is attempting to determine whether present leakage limits are adequate for extended space missions.

The reliability of soldered and welded electrical connections is not easily determined by visual inspection and often is judged by subjective criteria. Investigations were made, through contract support, to establish objective and reliable standards for verifying the reliability of such electrical connections. The solderability of component lead-connection material was determined as a basis for establishing solderability ratings. Analogous work was done for welded connections, and the results, combined with pull-test data, provided the basis for a weldability rating chart.

Electrical functional tests presently cannot indicate certain faults which will affect the operating life of a component. An infrared radiation test method of incipient failure detection is being investigated. With this method, infrared radiation patterns of normal and faulty components will be compared and, through projection, the operating life of the tested component will be calculated.

I. INTRODUCTION

The evaluation of new technology and its integration into NASA vehicle and space booster designs requires the simultaneous development of quality assurance requirements. In keeping pace with these new and amplified needs, Quality and Reliability Assurance Laboratory of MSFC has been undertaking projects that should most effectively provide a firm theoretical base for quality assurance requirements, produce new nondestructive test methods, and establish quality assurance requirements for advanced equipment, materials, methods, and processes.

A firm theoretical base for quality assurance requirements is more important in today's aerospace age than it ever was. This aspect of quality assurance was neglected in past years, with the result that the quality assurance function became very subjective. To remedy this deficiency, there has been an especially important need for research to determine correlations between primary functions and secondary phenomena. An example of such research under way at MSFC is the investigation on utilization of infrared emission to evaluate electronic equipment.

The cost, complexity, and frequent unavailability of space booster equipment generally precludes the use of destructive test methods. Consequently, the value of nondestructive test methods and equipment used to determine defective materials and components is incalculable. Work at MSFC on new nondestructive testing methods includes the use of radioactive tracers and infrared for testing the reliability of electronic components.

Integrating the requirements mentioned and then translating them to actual manufacturing conditions requires further research and development. This is known as manufacturing research. From this phase the quality assurance requirements are derived for implementation by production organizations. Examples of MSFC work leading to such require-

ments are the programs for defining weldability and solderability of materials and for determining critical parameters of process equipment such as welding machines.

II. QUALITY ASSURANCE REQUIREMENTS FOR INTEGRATED CIRCUITS

Since MSFC does not have specific quality assurance requirements for integrated circuits, requirements are being established by basing them upon manufacturing processes and the electrical parameters. This is being done by procuring integrated circuit devices from various manufacturers and subjecting these devices to extensive electrical tests in order to determine failure mechanisms and the most critical electrical parameters.

An idea as to the complexity of the integrated circuit is given by Table I, which lists the evolution of electronic packaging techniques beginning in the 1950's. The vacuum tube was followed by the module technique employing semiconductors with either a welded or a soldered module. To increase component density further, the thick-film and thin-film techniques coupled with multilayer interconnection boards are being utilized, and the integrated circuit packaging concept provides an even greater component density.

TABLE I. EVOLUTION OF ELECTRONIC CIRCUIT PACKAGING

Circuit; Year	Component Density, parts per cubic meter (parts per cubic foot)
Vacuum tube; 1950	35×10^3 (1×10^3)
Printed, transistor; 1955	35×10^4 (1×10^4)
Welded, transistor; 1957	35×10^5 (1×10^5)
Thin Film; 1959	35×10^7 (1×10^7)
Integrated; 1960	35×10^8 (1×10^8)

The thick-film technique (dating to World War II) allows a high degree of miniaturization at relatively low cost. In this technique, commonly known as screened circuitry, the electrical elements and conductors are formed by depositing electrically conductive pastes or inks onto a suitable substrate, producing a functional or partially functional circuit. The conductive pastes or inks are forced onto the substrate through a fine mesh screen which is imprinted with the desired circuit pattern. Only conductors and passive electrical elements can be produced by this process (capacitors and inductors to a very limited extent). Active elements are added to the circuit by soldering. The production and tooling costs for screened circuitry are much lower, and the process parameters less critical than they are for the thin-film and silicon monolithic techniques to be discussed. A comparison of these three techniques is given in Table II.

TABLE II. COMPARISON OF THREE MICROMINIATURIZED ELECTRONIC CIRCUITS

		Screen Printed	Thin Film	Silicon Monolithic
Cost	Facility	medium	low	high
	Large Lot	medium	high	low
	Small Lot (Custom)	low	medium	high
Reliability		unknown	unknown	unknown
Isolation		good	good	poor to fair
Design Flexibility		good	good	poor

A second major method of circuit miniaturization is the thin-film technique. Thin films (up to 10,000 Å thick) are deposited onto a substrate by any one of several methods, such as vapor deposition or sputtering. Although a great deal of research is being pursued for a method of depositing active components, at present the deposition of components, as with the thick-film technique, still is restricted to passive types. Thin films normally are deposited in a high vacuum (0.13 mN/m^2 or 10^{-6} torr), which is a disadvantageous feature of the process. Thin-film and thick-film techniques are applicable to both digital and analog circuitry. They are used primarily for linear circuits and high-speed digital applications.

Monolithic integrated circuits are more commonly used in digital applications than the deposited-film circuits mainly because of their lower cost in large quantities. The monolithic technique utilizes

a silicon substrate as the basic material, and develops a complete circuit within this substrate through successive masking, etching, and diffusion processes. Resistance, capacitance, isolation regions, and active devices thus are encompassed in the basic material. Thin films of aluminum are used to interconnect the element areas of the substrates and to form the bonding pads to which external leads are connected.

Semiconductor integrated circuitry is susceptible to several types of failures. These can be classified within two groups, quality and time dependent. The quality failures are caused by faulty workmanship. One of the most common faults, cracks and scratches in the circuitry, is caused by the improper use of the die-handling tools.

One of the time-dependent failures results from inadequate removal of etchant. When the etchant for the aluminum interconnecting paths is not removed completely, it continues to erode the aluminum, eventually opening the conducting path.

Another time-dependent failure results from the interaction of circuit metals. A vacuum-deposited thin film of aluminum forms the interconnections for the circuit components (semiconductors, resistors, etc.). Gold leads, attached to the aluminum surface, connect the integrated-circuit chip to other circuitry. Interaction between the aluminum and gold may result in corrosion, called Purple Plague, which alters or opens the circuit. A similar corrosion failure, called Black Plague, results from the interaction of aluminum, gold, and silicon at their interfaces.

A procurement specification has been written for an instrument that will test the various static or DC parameters and the dynamic or AC parameters of integrated circuits. This equipment is scheduled for delivery in October 1966. At present, there appears to be no other commercially available equipment that will handle the dynamic characteristics. The procurement of this equipment for use in MSFC acceptance testing will contribute greatly to the acceptance of reliable integrated circuits and assist in providing much needed standardization.

III. LEAK DETECTION TECHNIQUES FOR HERMETICALLY SEALED DEVICES

In the latter part of 1959 and the early 1960's, relays in electrical ground support equipment used at Kennedy Space Center (KSC) often failed early in operation, and supplying replacements became a major problem. The cause of failure was traced to inadequate protection of the electrical contacts. Acceptance functional testing of relays at MSFC indicated that the electrical parameters were acceptable. However, when the relays were in the humid environment at KSC, defective hermetic seals allowed moisture to enter the relay and deposit on the relay contacts. In time, the contact resistance increased, and eventually the relay ceased to function properly.

A nondestructive method for testing the hermetic seal of the relay was sought. After several methods were investigated, a radioisotope-tracer method was selected. It uses commercially supplied equipment called Radiflo (Fig. 1).

FIGURE 1. RADIFLO INSTALLATION

The Radiflo system operates in two phases. The first phase is the soak period in which the relays are pressurized in radioactive Krypton-85 within the activation chamber (Fig. 2). While in the activation tank, the parts are subjected to a pressure of approximately 300 kN/m^2 (3 atmospheres) for a designated period. At the end of the soak period, the parts are removed from the activation area and are allowed to degas for approximately one hour.

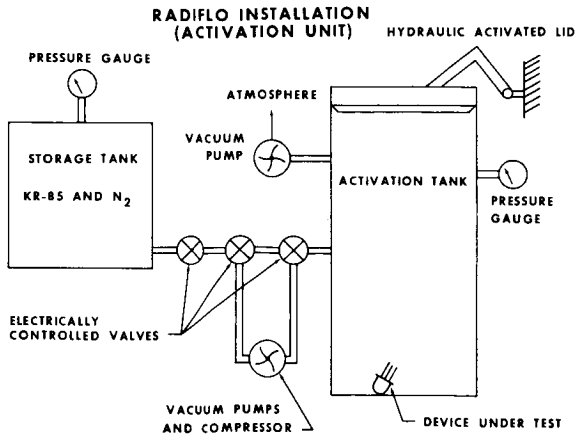

FIGURE 2. RADIFLO SYSTEM, SOAK PHASE

Counting is the second phase of the Radiflo operation. The parts are placed on a scintillation crystal electrically attached to a ratemeter (Fig. 3) which measures the counts per minute for the part under test. The basic leak rate formula, based on Poiseuille flow, is used to calculate the leak rate for the device. The MSFC acceptance criterion is 1 mN/m^2-cc per second (1 x 10^{-8} atm-cc per sec). All relays that leak in excess of this amount are rejected.

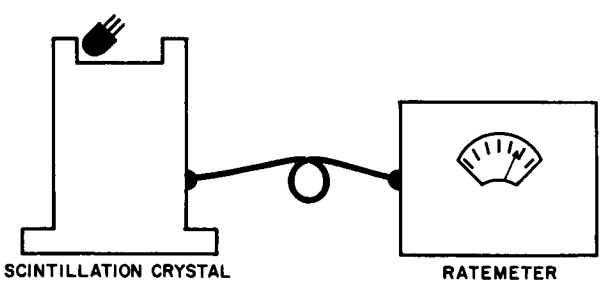

FIGURE 3. RADIFLO SYSTEM, COUNT PHASE

Experienced gained by using the Radiflo system for checking hermetic seals indicated that the results were frequently inconsistent with other hermetic-seal testing systems and Radiflo systems employed by industry. To obtain a better understanding of this inconsistency, MSFC awarded a contract to Mississippi State University in 1963 to investigate the irregularities in test data. As a result of this study, it was clearly shown that the basic concept using Poiseuille flow was not correct.

Molecular flow occurs at 1 mN/m^2-cc per second (10^{-8} atm-cc per sec) and is the leak-mode range which is of interest to MSFC. The difference between the Poiseuille flow and the molecular flow is due to the relationship between the size of the capillary diameter and the mean free path of the gas molecules involved. Poiseuille flow occurs when the diameter is considerably greater than the mean free path of the gas molecules. Molecular flow occurs when the diameter is considerably less than the mean free path of the gas molecules (Fig. 4).

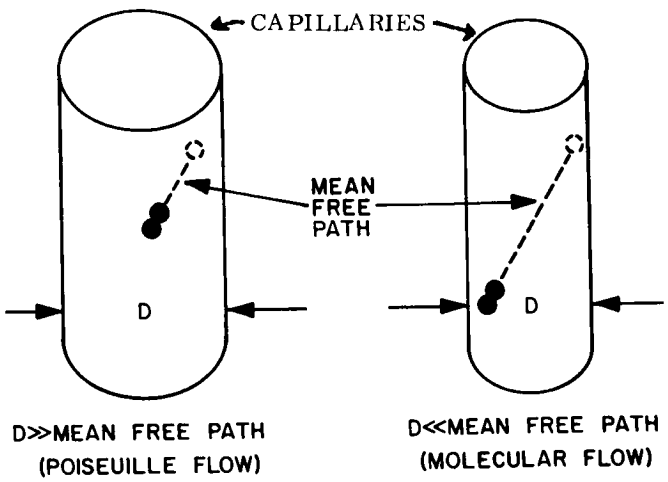

FIGURE 4. LEAK MODE

As shown in the following leak rate equations, the pressure terms (in the denominators) are squared only in the Poiseuille equation:

Poiseuille: Leak Rate = $R/ [KST(Pe^2 - Pi^2)]$

Molecular: Leak Rate = $R/ [KST(Pe - Pi)]$

An alternate method used by manufacturers of electronic parts to verify hermetic seals is the helium mass spectrometer technique. Figure 5 illustrates the mass spectrometer device which employs a bell jar, a vacuum pump, and an electronic velocity filter. The hermetically sealed electronic component, which previously had been filled by the manufacturer with 5- to 10-percent helium, is placed under the bell jar and a vacuum is produced. After sufficient vacuum has been obtained, an electronic velocity filter is operated. This device deflects the helium ions, by means of a magnetic field, into a predetermined slot. As the helium ions are deflected, they produce a current which is amplified and electrically measured.

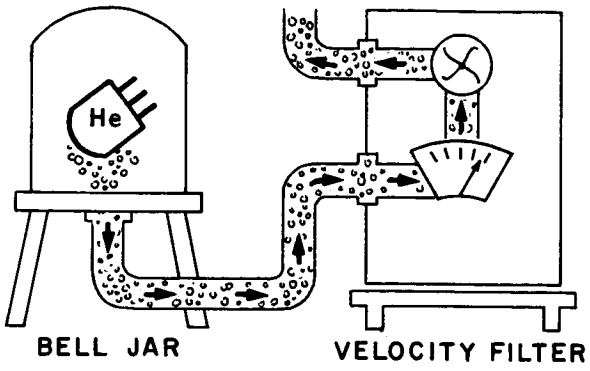

FIGURE 5. MASS SPECTROMETER HELIUM TRACER METHOD

Most vendors use the mass spectrometer for verifying hermetic seals, whereas MSFC uses the Radiflo system. The use of the two different systems results in conflicting and inconsistent test results. To resolve the problems of inconsistent test results, a mass spectrometer was obtained and used to test incoming parts. However, testing at this point did not reproduce the results obtained by the vendors employing the same technique. After an extensive study of this problem it was concluded that the use of the mass spectrometer could not effectively be employed in the MSFC acceptance testing. One reason is that the relays are filled with helium by the manufacturer, and there is no assurance that the helium is present within the part when it is checked at the receiving area. If the part leaked, tests using the mass spectrometer could not determine whether all the gas had leaked out before arrival or that none had leaked because of a good hermetic seal.

Most of the problems associated with Radiflo system have been solved and the system appears to be the optimum method for in-house verification of hermetic seals. There still are a few considerations which need attention; these are being investigated under a contract with Mississippi State University. The contract has two major objectives:

1) To find a correlation between the Radiflo and the mass spectrometer methods by envolving a factor that would correlate the two results and then specify a leak rate for the mass spectrometer method that would pass the Radiflo test.

2) To determine whether the present reject point of 1 mN/m^2-cc per second at a differential of 100 kN/m^2 (1 atmosphere) is adequate for extended space missions.

IV. SOLDERABILITY AND WELDABILITY VERIFICATION TECHNIQUES

One of the problems of electronic assembly inspection is the determination of whether a particular solder joint or weld module joint is a reliable connection.

This verification problem is exemplified by work such as soldering to a gold-plated printed circuit board. The gold combines with the solder and a gold/tin system results. The solder joint is discolored, and sometimes appears to be unsound due to porosity and discoloration. If the joint is welded instead of soldered, it is even more difficult to inspect visually. The answer to these problems would be to verify the solderability or weldability of electronic parts prior to the assembly operation at the receiving inspection level.

At times it appears that more concern is given to the electrical parameters of a device than to the compatibility of the lead material. Nevertheless, compatibility is essential: the lead material must be suitable to the soldering or welding operation required to connect the part to the next assembly, or an unacceptable assembly will result.

Contracts were awarded to the Martin-Marietta Corporation, Aerospace Division, and to the Lockheed Aircraft Corporation, Missile and Space Division, to establish standards of solderability and weldability of component lead materials and to provide an acceptable lead-material test for acceptance testing.

As a result of these contracts, a solderability test has been defined which closely simulates the production mode of flow soldering. The test, as shown in Figure 6, consists of several steps and the application of the solderability formula, $(KL_1 + L_2) / (D - d)$ = solderability rating. The first step is to bend the component lead around a 7.9 mm (5/16-inch) mandrel. The lead is then fluxed, dipped into molten solder, and finally submerged into a hot-oil bath. The lead is then removed, and after it has been cooled and cleaned, it is subjected to optical measurements and the dimensions, L_1, L_2, D and d, are obtained. In the formula shown, K is associated with L_1 as a weighing factor, L_1 is the inner length of the

solder area, L_2 is the outside length of the solder area, D is the diameter of the solder area, and d is the diameter of the lead.

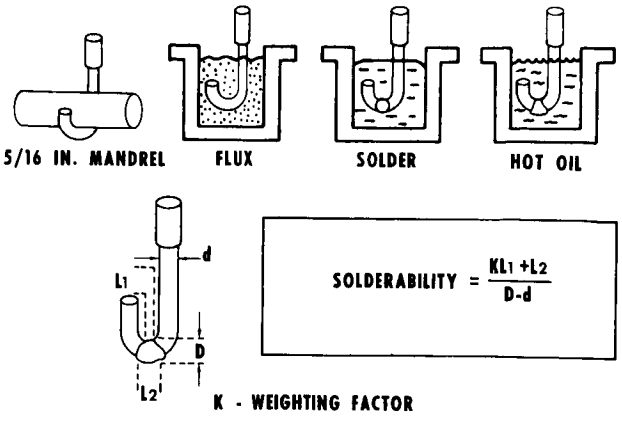

FIGURE 6. SOLDERABILITY TEST

The solderability-rating technique was employed for materials used in the fabrication of electronic assemblies to obtain the solderability test results shown in Figure 7.

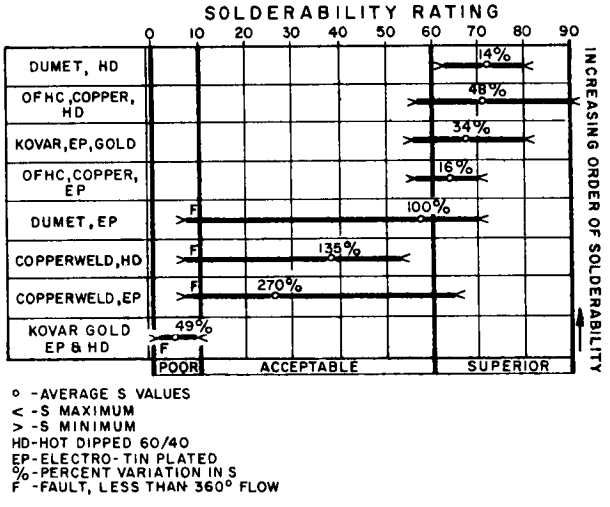

° -AVERAGE S VALUES
< -S MAXIMUM
> -S MINIMUM
HD-HOT DIPPED 60/40
EP-ELECTRO-TIN PLATED
%-PERCENT VARIATION IN S
F -FAULT, LESS THAN 360° FLOW

FIGURE 7. SOLDERABILITY TEST RESULTS

A similar analysis has been performed for welded modules. The welding test apparatus consists of a power supply with two electrodes. The component lead and interconnecting nickel ribbon are placed between the two electrodes and pressure is applied. The subsequent release of electrical energy welds the two materials.

To determine the quality of the weld produced, a pull test is employed which is essentially a tensile-shear force applied until the breaking strength of the weld is reached. By expanding this operation with variations of pressure and energy, a weld schedule is obtained. Figure 8 shows a weld-schedule chart with the weld pressure on the ordinate and the weld energy on the abscissa. When welds

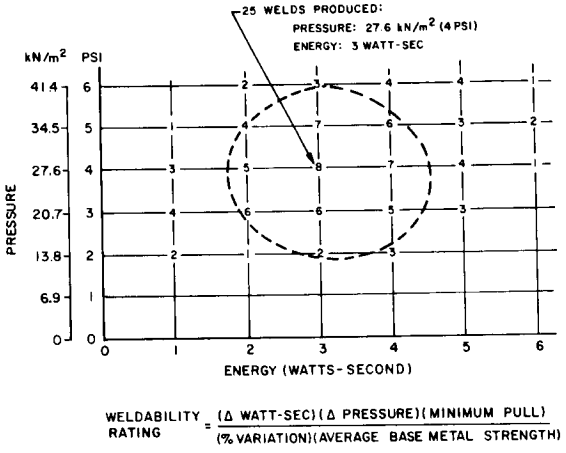

FIGURE 8. WELD SCHEDULE

are made with various pressures and energies, and this information is plotted on the chart, a weldability pattern is obtained. (The patterns will vary, depending upon the type and size of the material: some may be circular, others oblong.) The larger the area encompassed by this pattern, the better is the weldability of the material being tested. The optimum pressure/energy setting is determined from this weld schedule. In testing, 25 welds are produced from the optimum setting. The 25 welds are pull-tested and the results recorded. A weldability rating then is obtained from the weldability formula (Fig. 8) and the values obtained in the pull test.

This sequence has been used to obtain a weldability-rating chart, illustrated by Table III, which lists the basic parameters for weldability of the materials tested.

TABLE III. BASIC PARAMETERS FOR WELDABILITY RATING OF MATERIALS JOINED TO NICKEL "A" RIBBON

MATERIAL PLATING, SERIAL NO.	TYPE	Δ JOULES, (watt-sec)	Δ PRESSURE, Newtons (lbf)	VARIATION, Percent	MIN. PULL, Newtons (lbf)	AVG. TENSILE STRENGTH OF WEAKER MATERIAL	WELD-ABILITY RATING
BARE							
109	s.s. pins	5.25	62 (14)	15.6	72 (16.1)	20.54	3.7
114	Tantalum	3.29	53 (12)	14.1	68 (15.3)	20.54	2.2
107	Nickel "A"	4.17	45 (10)	17.8	67 (15.0)	19.8	1.8
108	Kulgrid 28	5.67	18 (4)	15.4	45 (10.1)	15.1	1.0
GOLD PLATED							
104	Dumet	3.83	27 (10)	11	73 (16.4)	20.54	2.8
112	Alloy 152	3.88	62 (14)	18.6	67 (15.1)	20.54	2.2
105	Kovar	2.86	53 (12)	17.9	69 (15.4)	20.54	1.4
111	Copperweld	4.00	45 (10)	20	28 (8.5)	13.1	1.3
113	Alloy 90	3.00	27 (6)	22.6	46 (10.4)	16.9	0.5
110	Alloy 180	2.33	18 (4)	116	15 (3.4)	18.9	0.014
TIN PLATED							
106	Cu OFHC	4.67	45 (10)	10.4	40 (9)	12.44	3.2
117	Nickel "A"	3.43	53 (12)	16.9	67 (15)	19.6	1.9
118	Dumet	4.00	53 (12)	23.5	67 (15.1)	20.54	1.5
119	Kovar	2.63	62 (14)	21.1	63 (14.2)	20.54	1.2

It is believed that with the development of these two major techniques, the determination of solderability or weldability will be simplified.

V. METALLIC COATING TECHNIQUES FOR MAINTAINING SOLDERABILITY

Recent laboratory tests and hardware evaluations have shown that present industrial techniques for silver-plating copper conductors are inadequate for preventing Red Plague. Copper is exposed to the atmosphere because of imperfections in the silver plating; in the presence of moisture and oxygen, a galvanic couple between the silver and copper is produced which eventually reduces the wire to powder.

Since this type of corrosion recently appeared on the guidance and control platform being produced by Bendix Corporation, an agreement was made to change from silver-plated wire to nickel-plated wire for work under this contract.

Various wire manufacturers are studying the silver-plating problems in an effort to improve the plating techniques. In addition, studies are under way to determine whether an underlay of nickel will prevent the Red Plague.

VI. INFRARED TESTING OF ELECTRONIC PARTS

Infrared testing of electronic parts will detect incipient failures that are not normally discovered by routine electrical functional testing. The objective of this new testing technique is to complement the electrical functional testing by scanning the electronic part during the functional test to determine the amount of infrared radiation emanating from the part under test.

In 1964, a procurement specification was written for obtaining an infrared test station to be installed by Boeing Company. The equipment (Figs. 9 and 10) was fabricated, and has been in operation

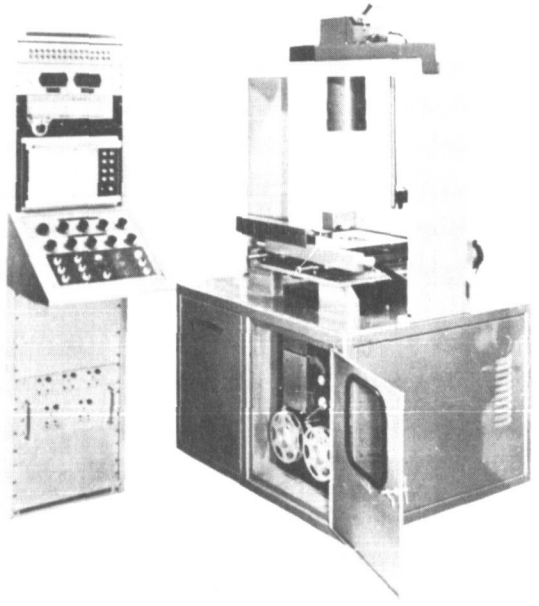

FIGURE 9. INFRARED TEST STATION

since September 1964. Current operations are aimed toward establishing a normal pattern for selected hardware configurations. Once a normal pattern is obtained for a device, subsequent testing can determine how far others deviate from the norm. With this information, the projected operating life of a particular device under test can be obtained.

One problem encountered is the variable emissivity of component surfaces, resulting from changes made by the vendor in the pigment or other characteristics of the paint or other protective coatings used on the devices. Because of the different surface-emissivity ratings, the infrared-radiation readout must be modified for each variable.

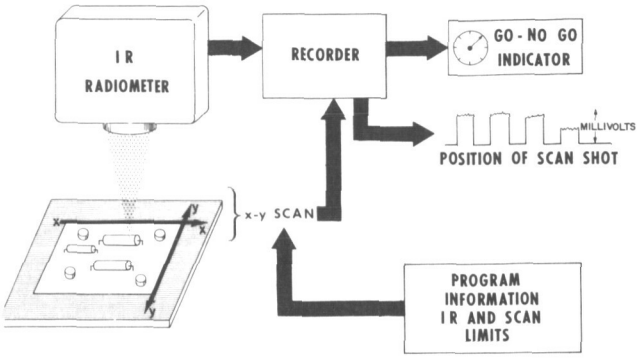

FIGURE 10. OPERATIONAL SEQUENCE OF INFRARED TEST STATION

The Martin Marietta Corporation, Aerospace Division, has a contract to develop a constant-emissivity coating that can be used on all components, thus making infrared measurements independent of the various coatings used on the devices. As shown in Figures 11 and 12, this test station provides a thermal profile of components placed on the X-Y table and in the operating mode.

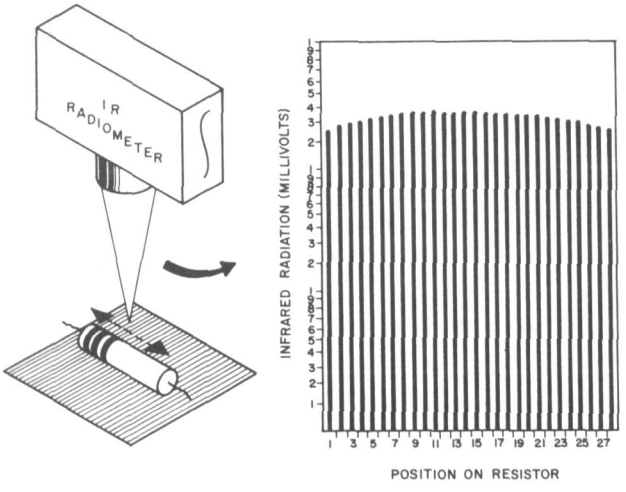

FIGURE 11. THERMAL PROFILE (END TO END) OF A CARBON COMPOSITION RESISTOR

It is too early to say that the infrared-radiation detection and recording system, currently under evaluation, will complement the present reliability

program. However, the test results are encouraging, and if the development of an emissivity coating to solve the surface variance problem is successful, then this system should provide a method of predicting the successful operating life of electronic parts and subassemblies.

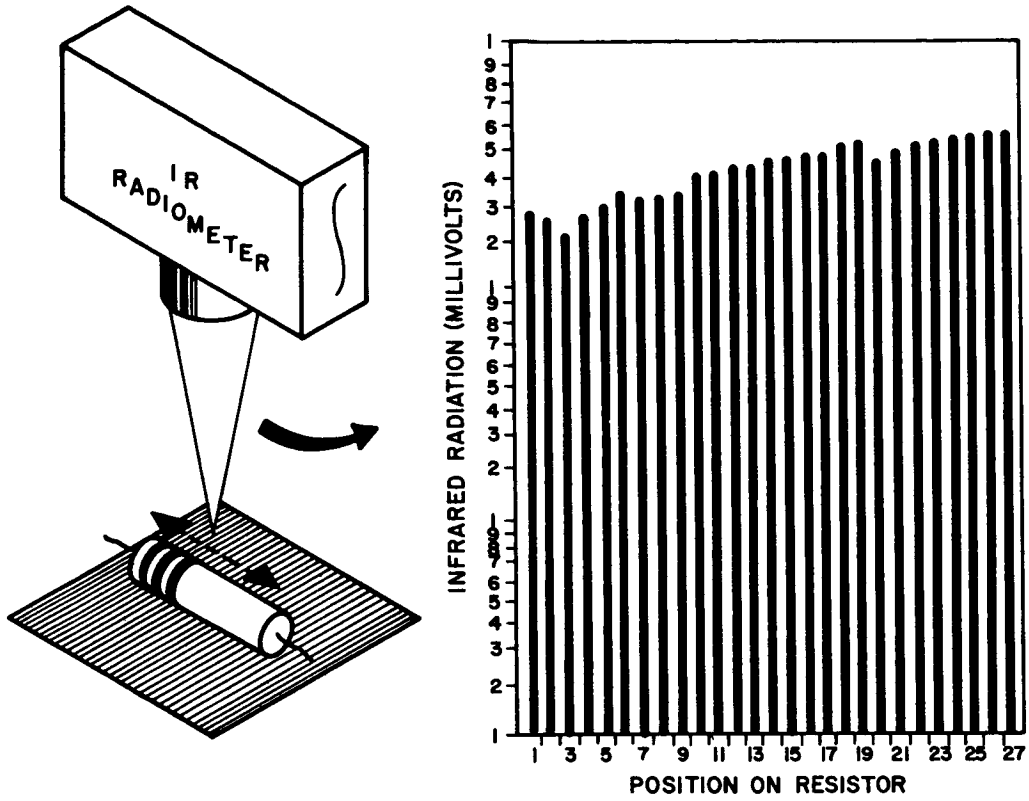

FIGURE 12. THERMAL PROFILE (END TO END) OF A WIRE-WOUND RESISTOR

TERRESTRIAL AND SPACE ENVIRONMENT RESEARCH AT MSFC

September 16, 1965

by

Charles C. Dalton
Dr. E. D. Geissler
James R. Scoggins
Orvel E. Smith
Robert E. Smith

TABLE OF CONTENTS

LIST OF ILLUSTRATIONS

UPPER ATMOSPHERIC PROPERTIES

by Robert E. Smith

LIST OF ILLUSTRATIONS

PROGRESS IN ATMOSPHERIC THERMODYNAMIC MODELS

by Orvel E. Smith

LIST OF ILLUSTRATIONS

METEOROID FLUX AND PUNCTURE MODELS FOR CISLUNAR SPACE

by Charles C. Dalton

LIST OF ILLUSTRATIONS

INTRODUCTION TO RESEARCH ACHIEVEMENTS REVIEW ON TERRESTRIAL AND SPACE ENVIRONMENT RESEARCH

By

Dr. E. D. Geissler*

The subject of this review is environmental research. Perhaps it would be more appropriate to refer to it as natural environment so that it will not be confused with induced environments. Another research review will cover aerodynamics and aerodynamic phenomena in connection with rocket flight and thus will be concerned with the flight induced environments.

Research activities on natural environmental conditions for all phases of space flight are carried out at MSFC by Aero-Astrodynamics Laboratory and Research Projects Laboratory. The major portion of the atmospheric research as related to the MSFC mission is accomplished by the Aerospace Environment Office under William Vaughan of the Aero-Astrodynamics Laboratory. Research is also conducted on the near-earth and space environment, including lunar, planetary, and solar characteristics with respect to radiation and magnetic fields, micrometeoroids, gravitational, and other astronomical constants, etc. Obviously, this is a very large task and a major portion of the relatively small manpower resources devoted to this area is directed toward maintaining a knowledgeable position on the space environment through contact with other NASA Centers, Government, and private organizations involved in related research programs. Research is required to organize various data into meaningful engineering inputs to our space-vehicle program. The responsibility of establishing formal MSFC project design criteria on natural terrestrial and space environment parameters is with Aero-Astrodynamics Laboratory. Major inputs come from Research Projects Laboratory as well as from other NASA, Government, and industry sources.

The results of environmental research will be restricted to discussions on atmospheric dynamics and thermodynamics and some properties of the upper atmosphere. The paper by Mr. James Scoggins will cover atmospheric dynamics pertaining to investitation of wind structures in which MSFC has been pioneering for several years. Mr. R. E. Smith's paper discusses research on model atmospheres including the upper atmosphere at satellite altitudes. Recent progress in atmospheric-thermodynamic models is presented in a paper by Mr. O. E. Smith. Material on photographic meteors, prepared by Mr. Charles Dalton, completes the environmental research results reported in this review.

An attempt has been made to strike a happy medium between the extremes of a mere enumeration of all activities and a detailed discussion of a narrow field. This is particularly difficult for the environmental activities in view of the extensive scope of the subject matter.

---

* Director, Aero-Astrodynamics Laboratory.

SOME RECENT ATMOSPHERIC DYNAMICS RESEARCH AT MSFC

By

James R. Scoggins

SUMMARY

Small-scale motions or turbulence, associated with vertical detailed wind profiles, are important in the design of large space vehicles. The development of a high-resolution wind measuring system which provides data that are more accurate by an order of magnitude than the rawinsonde system is described, and some typical high resolution wind velocity profile measurements are presented. The rawinsonde system provides wind data averaged over approximately 600 meters in the vertical direction with an rms error ranging between 2 and 15 meters per second depending upon conditions. In contrast, the recently developed high-resolution wind measuring system provides data averaged over approximately 50 meters in the vertical direction with an rms accuracy of approximately 0.5 meters per second. A comparison is made of drag curves for smooth spheres in a wind tunnel and for smooth and rough spheres rising in the atmosphere.

A statistical description of small-scale motions or turbulence is presented and some of the characteristics of turbulence are discussed. It is concluded that the spectrum of turbulence for space vehicles may be different from that for aircraft and from theory, and that, in general, the small-scale motions or turbulence is neither homogeneous, stationary, nor isotropic.

I. INTRODUCTION

Superimposed on the general circulation of the atmosphere are motions of various scales ranging in size from hundreds of miles in diameter down to the micro-scale where dissipation into heat takes place. These motions are influenced by the character of the underlying surface, stability of the atmosphere, gravity, rotation of the earth, and the distribution of mass which results in pressure gradient forces. In the free atmosphere where the wind flow has a small curvature, the larger scales of motions may be accurately represented mathematically.

Forces producing large-scale motions are primarily pressure gradient, Coriolis, gravity, and centrifugal. In principle, the smaller-scale motions are also governed by these forces; however, because of the sparsity of meteorological observing stations and unknown transfer processes, representation of these scales of motions analytically is impossible.

Small-scale motions are usually variable in time and space and, in general, are treated by empirical or statistical methods. In the design of aircraft and space vehicles, discrete gust shapes have been employed as well as statistical representations of turbulence. The discrete gust concept has the advantage of simplicity and relative ease in handling, while the statistical and empirical methods become more complicated, especially in application. The gust or turbulence representation employed in the design of vehicles and in the evaluation of the influence of small-scale motions or turbulence on vehicles is largely a matter of engineering judgment and is derived by conducting comparative analysis of the influence of various representations on the vehicle. Previously, small-scale motions, turbulence, or gusts have usually been represented by discrete gust shapes rather than by statistical representations. For space vehicles, the limitations of the wind profile measuring system did not permit the measurement of small-scale motions. Discussions on the use of wind data in space vehicle and aircraft design studies have been published [1-10]. A method has recently been developed by which these small-scale motions are measured. The following discussion will be concerned with the measurement and statistical descriptions of the small-scale motions or turbulence associated with vertical wind velocity profiles.

II. THE DEVELOPMENT OF A HIGH RESOLUTION WIND MEASURING SYSTEM

Until about five years ago, vertical wind profile measurements were made by the rawinsonde system. This system employs a reasonably large flexible balloon with an instrument package suspended 100 feet below the balloon. Deformation of the balloon and large inertia of the system prevent the

measurement of small-scale variations in the wind field. This balloon system is tracked by a radio direction finder which, because of its inaccuracies, introduces other uncertainties. Wind measurements provided by the rawinsonde system were averaged at altitude intervals of 600 meters altitude or more with an rms error of 2 to 15 meters per second depending upon conditions.

A description of the small-scale features of the vertical wind velocity profile is required in the development of large space vehicles. Since the rawinsonde system was not capable of providing the details required, MSFC undertook the development of a high-resolution wind measuring system about five years ago. Two contracts were let and both were unsuccessful. At about the same time, the Air Force Cambridge Research Laboratories proposed what appeared to be a feasible and simple method for measuring detailed vertical wind profiles [11]. This method consisted of tracking a smooth superpressure mylar sphere (called ROSE) with a ground-based radar. The sphere is shown in Figure 1. It was later learned that the data provided by this sensor were not accurate because of aerodynamically induced motions. The aerodynamic instability of this sphere was caused by vortex shedding which made the balloon to experience lateral motions even in a calm atmosphere. Figure 1 also shows a time lapse photograph of the ROSE balloon rising into the atmosphere. The images are at one-half second intervals and represent a one-quarter second exposure time. When this photograph was made, the atmosphere was practically calm.

Personnel of MSFC conceived and verified the idea that the aerodynamic instability of the sphere could be reduced by the use of roughness elements placed on the surface of the sphere [12 and 13]. Figure 2 shows the first experimental configuration of such a balloon. Balloons of this type have been given the name "Jimsphere." Figure 2 also shows an ascent of a Jimsphere similar to that shown in Figure 1 for the ROSE balloon. The aerodynamically induced oscillations have been reduced in amplitude.

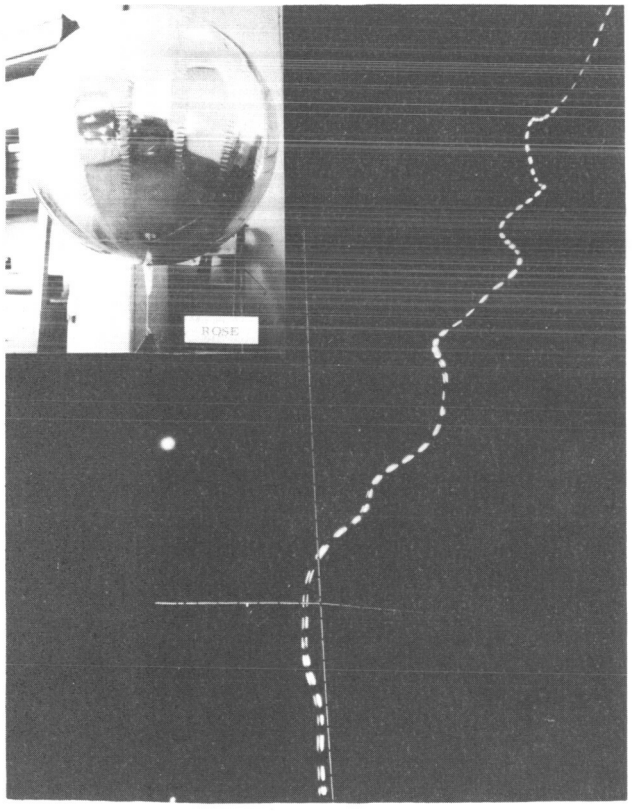

FIGURE 1. TIME LAPSE PHOTOGRAPH OF ROSE BALLOON RELEASED AT 11:25 P.M., AUGUST 2, 1963, DURING STABLE ATMOSPHERIC CONDITIONS AND LIGHT WINDS

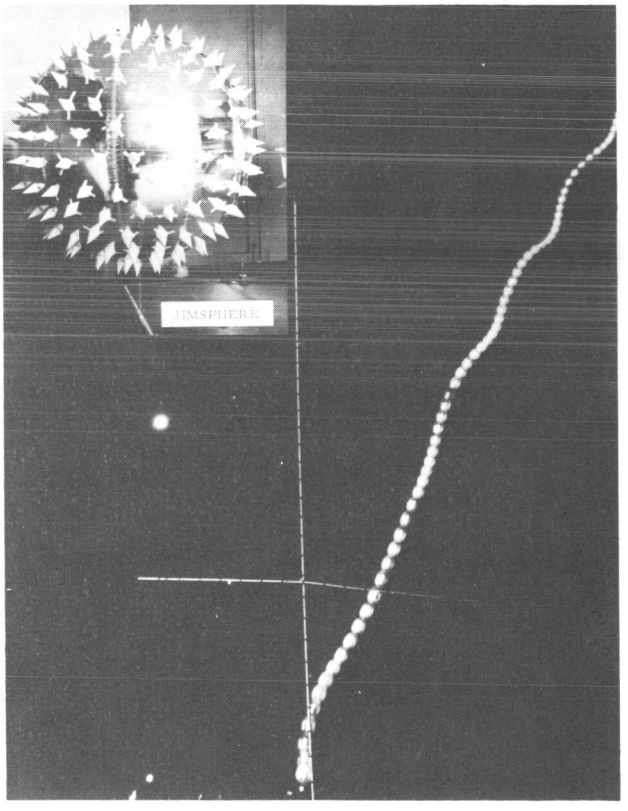

FIGURE 2. TIME LAPSE PHOTOGRAPH OF JIMSPHERE BALLOON RELEASED AT 11:54 P.M., AUGUST 2, 1963, DURING STABLE ATMOSPHERIC CONDITIONS AND LIGHT WINDS

Jimspheres similar to the one shown in Figure 2 were subsequently flown at the Kennedy Space Center and tracked by the FPS-16 radar. Some typical results of these experiments are shown in Figure 3. All the wind profile measurements shown in Figure 3 were made on the same day; therefore, the atmospheric conditions are similar for all measurements shown. The altitude in kilometers is presented on the ordinate, and the wind speed in meters per second is presented on a sliding scale on the abscissa. The same data reduction technique [14] was used for all flights. The influence of surface roughness elements is apparent. These profiles were measured in series, approximately one hour apart, with the exception of test 5414 which was measured approximately three hours after test 5411. Figure 3 shows that the horizontally induced motions are reduced considerably by the Jimsphere with 90 cups and reduced even further by a Jimsphere with 270 cups. The horizontally induced motions decrease as the surface roughness increases. The influence of an increase in the mass of the balloon on the observed small-scale motions was evaluated by inflating a ROSE balloon with a mixture of helium and air (test 5411) to provide the same buoyancy as the Jimsphere (test 5408). Figure 3 shows that the increased weight reduced the small-scale motion somewhat; however, the roughness elements provided a much larger reduction . The increased mass, which was approximately the same for the Jimsphere and ROSE, was about 1000 grams. The profile, as measured with the 1.22-meter diameter ROSE, is quite different from the profile measured with the 2.0-meter diameter ROSE. This is because the 1.22-meter balloon reaches the critical Reynolds number at approximately 5 kilometers altitude, and above this altitude operates at subcritical Reynolds numbers where the drag coefficient is large.

The next step in the development of the wind measuring system was to develop techniques for incorporating the surface roughness elements directly into the balloon. A contract was awarded to the G. T. Schjeldal Company for the development of the above techniques. A number of configurations were developed and flown at Kennedy Space Center and the optium configuration determined experimentally. Figure 4 shows the final Jimsphere configuration, which is a 2-meter diameter, superpressure, aluminized, 0.5-mil mylar sphere containing 398 conical roughness elements 3 inches high and 3 inches in diameter at the base. A mass of 100 grams is attached to the balloon at a

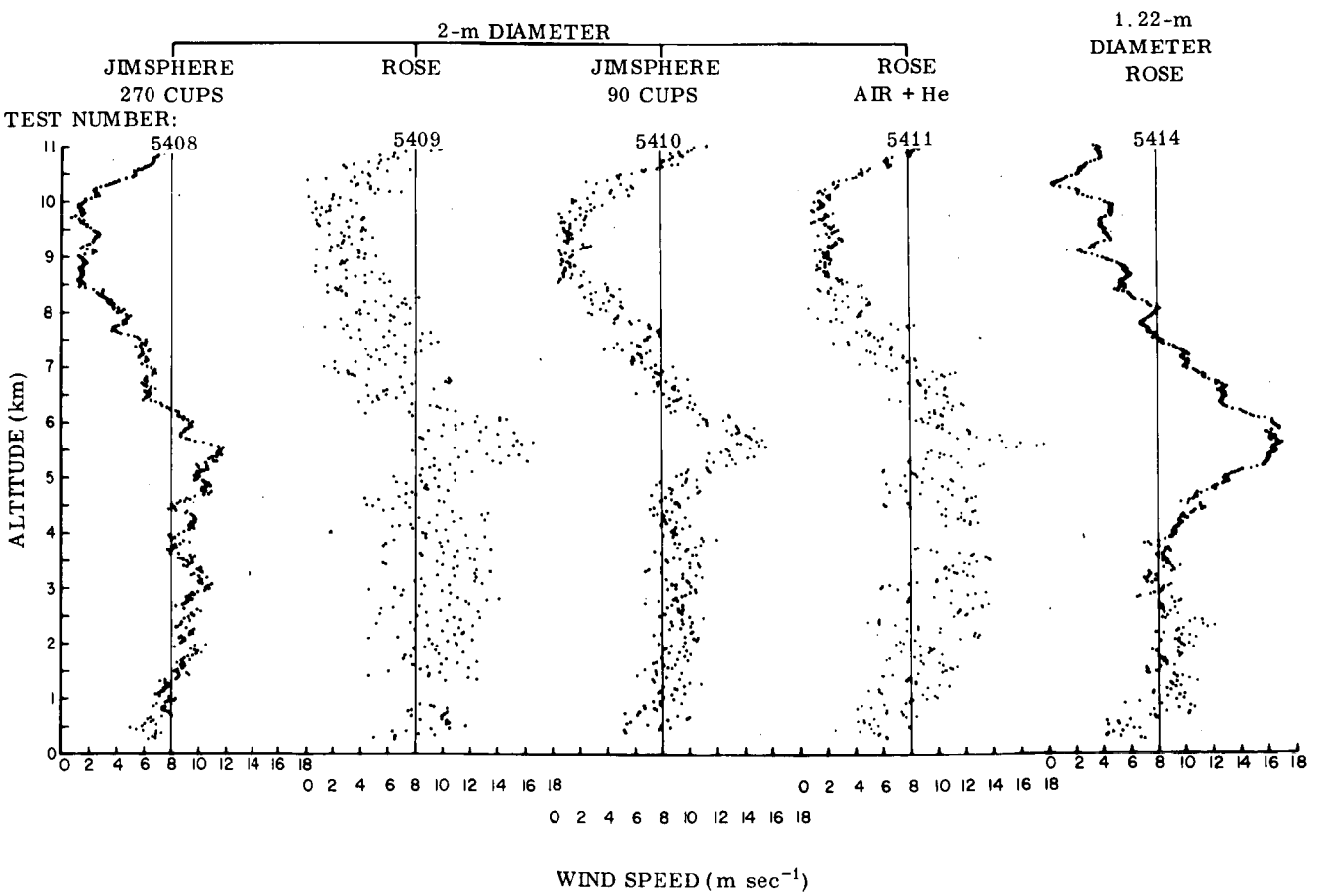

FIGURE 3. INDICATED SCALAR WIND SPEED PROFILES FOR DIFFERENT BALLOON CONFIGURATIONS

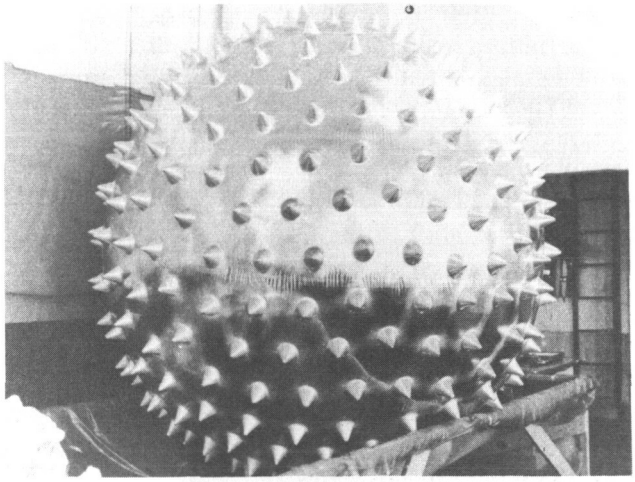

FIGURE 4. THE JIMSPHERE BALLOON WIND SENSOR

point to prevent rotation and thus provide better stabilization.

The detailed wind profile data provided by tracking this configuration with the FPS-16 radar appear to be adequate for the design of large space vehicles. The rms accuracy of the wind measurements provided by this system is approximately 0.5 meters per second over 50 meters in the vertical direction. This is an order of magnitude more accurate than provided by the rawinsonde system.

Drag curves for the Jimsphere, ROSE, and for smooth spheres in wind tunnels are shown in Figure 5. The solid curve was taken from Schlichting [15], while the other curves were computed from balloon ascents. The drag coefficient for the smooth sphere (ROSE) is generally higher than those obtained from smooth spheres in a wind tunnel. The drag curve for the Jimsphere shows that the drag coefficient is essentially independent of the Reynolds number. This is because the surface roughness elements induce flow separation near the equator of the balloon for the Reynolds numbers shown in Figure 5. Subsequent wind tunnel determination of the drag curve for the Jimsphere, using a scaled model, confirmed the drag curve presented in Figure 5. Since the value of the drag coefficient is rather large for all Reynolds numbers, the Jimsphere responds rapidly to winds at all altitudes.

Figure 6 shows a series of scalar (magnitude of vector wind) profiles which were measured using the Jimsphere. These profiles were measured in sequence at intervals of approximately 1.5 hours. Wind

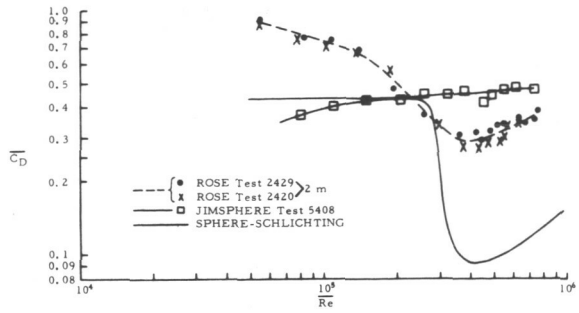

FIGURE 5. AVERAGE DRAG COEFFICIENT VS REYNOLDS NUMBER CURVES FOR ROSE AND JIMSPHERE BALLOONS AND FOR SMALL SPHERES IN WIND TUNNEL (WIND TUNNEL CURVE AFTER SCHLICHTING 1960)

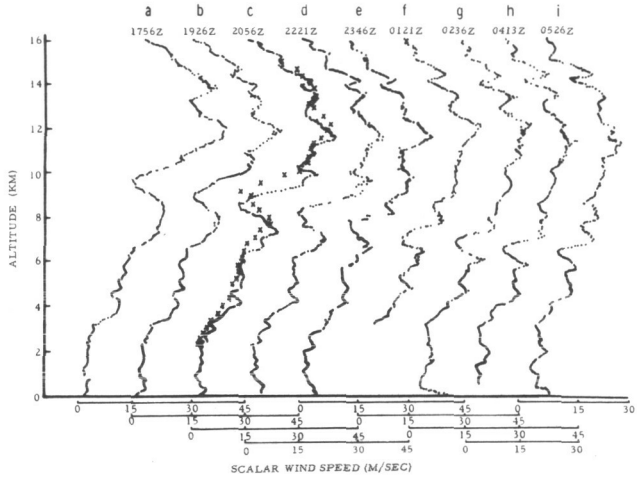

FIGURE 6. FPS-16 RADAR/JIMSPHERE PROFILES, WESTERN TEST RANGE

speed is given on the abscissa on a sliding scale, and altitude is given on the ordinate. The dots represent wind speeds as measured by the FPS-16 radar/Jimsphere system and averaged over approximately 50 meters in altitude. The rawinsonde profile measurement is superimposed on profile C in Figure 6. As pointed out earlier, the rawinsonde provides wind measurements averaged over approximately 600 meters in the vertical direction. Therefore, in the detailed profiles, relatively small-scale features which persist over long time periods can be observed. There are features which can be identified throughout the entire 12-hour period. Some of these detailed features are not discernible on the rawinsonde profile, yet they are very important in design considerations of large space vehicles.

III. STATISTICAL DESCRIPTIONS OF SMALL-SCALE MOTIONS OR TURBULENCE

Turbulence is difficult to define, but before an analytical representation is possible a definition must be clear. According to Lumley and Panofsky [16], turbulence has the following properties:

(a) Turbulence is observed to be rotational and dissipative; i.e., mechanical energy is transformed to internal energy.

(b) Turbulence is three-dimensional. The cascade of energy takes place by vortex stretching which requires the motion to be three-dimensional.

(c) Turbulence is nonlinear. The transfer of energy from one eddy size to another can take place only in a nonlinear way.

(d) Turbulence is stochastic. The velocity field cannot be predicted in detail.

(e) Turbulence is diffusive. A fluid particle in a turbulent fluid will wander about and move farther and farther from its initial location.

(f) Time and length scales of the turbulent motions that serve to transport properties are quite large, often of the same order as time and length scales characterizing the distribution of properties being transported.

(g) Turbulence is a continuum phenomenon.

As can be seen from the above properties, turbulence is not easily defined; it is even more difficult in practice than in principle.

In arriving at a meaningful definition of turbulence for space vehicles, the following must be considered:

(a) The seven properties of turbulence as given above.

(b) The characteristics of various scales of motions and their interdependence.

(c) Applicability of the definition of turbulence in space-vehicle design studies.

(d) Predictability of the small-scale motions for prelaunch monitorship.

In reference to the above conditions, turbulence is defined in this paper as the small-scale motions associated with FPS-16 radar/Jimsphere wind profiles that are not included in rawinsonde-measured wind profiles. Since most previous wind profile measurements were made using the rawinsonde system, this definition would permit the use of this data in defining steady-state velocity profiles and their associated statistical properties of turbulence. Turbulent motions are obtained from a detailed wind profile by defining a digital filter which will separate the small-scale motions from those which approximate the rawinsonde sounding.

Considering the vector-wind field as being composed of three components associated with an xyz orthogonal coordinate system, turbulence for aircraft and space vehicles in terms of one or more of these coordinate directions can be visualized. For an aircraft flying horizontally, the motions of primary concern are those normal to the flight direction or the vertical component of motion. On the other hand, for a space vehicle rising vertically, both horizontal components are of interest. Assuming the dissipation rate of eddies as normally observed in the atmosphere and applying dimensional analysis, an expression can be derived which shows that the spectrum of turbulence should be proportional to frequency to the -5/3 power [16]. This means that the shape of the spectra along the different directions should be the same but does not imply the same total energy. A spectrum of turbulence measured normal to the horizontal direction and commonly used in aircraft design studies is compared in Figure 7 with a typical spectrum measured normal to a space vehicle rising vertically through the atmosphere, and with a theoretical spectrum.

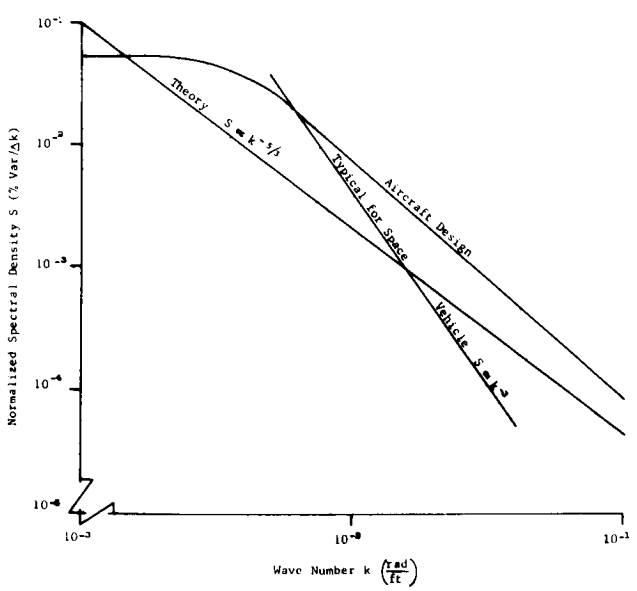

FIGURE 7. COMPARISON OF AIRCRAFT DESIGN, TYPICAL FOR SPACE VEHICLES, AND THEORETICAL TURBULENCE SPECTRUMS

The curves in Figure 7 show that the slope of the aircraft design spectrum agrees quite well with theory, but the typical spectrum for space vehicles does not. The slope of the spectrum for space vehicles varies with the meteorological conditions. The energy content associated with each spectrum is not given here since energy content is a function of the definition of turbulence and the meteorological conditions existing during the measurement.

The use of a spectrum of small-scale motions in computing vehicle responses requires the assumption that the means, variances, and other statistical parameters of the small-scale motions be invariant in flight time. The statistical properties of turbulence are measured in the space domain and applied in the time domain. These are not always reconcilable because of the highly organized features of some of the small-scale motions over limited altitude ranges and the changing speed of the vehicle with time.

The variances over intervals of 1 kilometer in altitude associated with the series of velocity profiles presented in Figure 6 and measured at approximately 1.5 hours apart are shown in Figure 8. From these variances, the degree of homogeneity, stationarity, and isotropy of the small-scale motions can be inferred. Therefore, the statistical properties of the small-scale motions are neither homogeneous, stationary, nor isotropic. This may cause problems in representing turbulence as a spectrum in vehicle response studies.

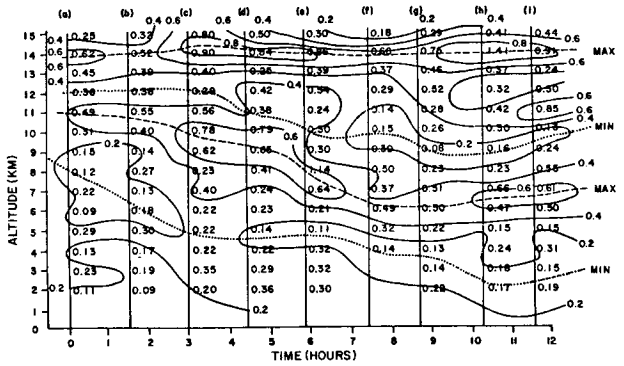

FIGURE 8. VARIANCES (m^2/sec^2) OF SMALL-SCALE MOTIONS COMPUTED OVER 1-km INTERVALS FOR WESTERN TEST RANGE

IV. FUTURE RESEARCH

There remains much to be done before a good definition and a good representation of turbulence for space vehicles is developed. Some of the work which is required and which is currently underway includes:

(a) Improvement in definition of atmospheric turbulence using improved wind measurements.

(b) Development of methods for applying atmospheric turbulence data to space vehicle response.

(c) Establishment of relationships between turbulence and such properties of atmospheric motions as wind shear, quasi-steady-state wind speed, divergence, and vorticity of the wind field, etc.

(d) Development of forecasting methods for prelaunch wind monitorship.

A concentrated program employing the best talent available is required to achieve these goals.

REFERENCES

1. Bowser, Leon J.: Power Spectral Density Techniques Applicable for Structural Design Criteria and Analysis State-of-the-Art Report. ASRMDS TM 62-4, Flight Dynamics Laboratory, Wright-Patterson Air Force Base Ohio, Feb. 1965.

2. Mazzola, L. L., et al.: Wind, Wind Shear, and Gust Design Criteria for Vertically Rising Vehicles as Recommended on the Basis of Wind Data from Eleven United States and Foreign Locations. Tech. Doc. Rept. ASD-TDR-62-909, Air Force Systems Command, Wright-Patterson Air Force Base, Ohio, Dec. 1962 (Secret Report).

3. Bieber, R. E.: Missile Structural Loads by Non-Stationary Statistical Methods. Lockheed Missile and Space Division TR LMSD 49703, 1959.

4. Geissler, E. D.: Problems in Attitude Stabilization of Large Guided Missiles. Aerospace Engineer, 19, Oct. 1960, pp. 24-29.

5. Hoelker, R. F.: Theory of Artificial Stabilization of Missiles and Space Vehicles with Exposition of Four Control Principles. NASA TN D-555, June 1961.

6. Tolefson, H. B.: Smoke-Trail Measurements of the Vertical Wind Profile and Some Applications. Proc. Natl. Symp. on Winds for Aerospace Vehicle Design, Air Force Surveys in Geophysics 1, no. 140, Mar. 1963, pp. 203-220.

7. Scoggins, J. R.; and Vaughan, W. W.: Problems of Atmospheric Wind Inputs for Missile and Space Vehicle Design. J. Spacecraft Rockets, vol. 1, no. 2, Mar.-Apr. 1964.

8. Press, Harry; Meadows, May T.; and Hadlock, Ivan: A Reevaluation of Data on Atmospheric Turbulence and Airplane Gust Loads for Application in Spectral Calculations. National Advisory Committee for Aeronautics, Langley Aeronautical Laboratory, Langley Field, Va., Report 1272, 1956.

9. Diederich, Franklin W.: The Response of an Airplane to Random Atmospheric Disturbances. Report 1345, National Advisory Committee for Aeronautics, Langley Field, Va., 1958.

10. Press, Harry; and Mazelsky, Bernard: A Study of the Application of Power-Spectral Methods of Generalized Harmonic Analysis to Gust Loads on Airplanes. Report 1172, National Advisory Committee for Aeronautics, Langley Aeronautical Laboratory, Langley Field, Va., 1954.

11. Leviton, R.: A Detailed Wind Profile Sounding Technique. Proc. Natl. Symp. on Winds for Aerospace Vehicle Design, 1, Air Force Surveys in Geophysics, No. 140, Air Force Cambridge Research Labs., 1962, pp. 187-196.

12. Scoggins, J. R.: Spherical Balloon Wind Sensor Behavior. J. Appl. Met., vol. 4, no. 1, Feb. 1965, pp. 139-145.

13. Scoggins, J. R.: Aerodynamics of Spherical Balloon Wind Sensors. J. Geophys. Res., vol. 69, no. 4, Feb. 15, 1964, pp. 591-598.

14. Scoggins, J. R.: An Evaluation of Detail Wind Data as Measured by the FPS-16 Radar/Spherical Balloon Technique. NASA TN D-1572, Washington, D. C., May 1963.

15. Schlichting, Hermann: Boundary Layer Theory. McGraw-Hill Book Co., Inc., New York, N.Y., 1960.

16. Lumley, John L.; and Panofsky, Hans A.: The Structure of Atmospheric Turbulence, John Wiley and Sons, New York, N. Y., 1964.

UPPER ATMOSPHERIC PROPERTIES

By

Robert E. Smith

SUMMARY

This study presents a comparison of the latest published standard atmospheres with explanations for the large variations in these standards above 100 kilometers. The effects of variations in solar activity on the different parameters of the upper atmosphere are also described. The study concludes with a brief review of planned research to acquire additional data for future model refinements.

I. INTRODUCTION

Prior to and immediately after the launching of the first satellites, there followed a succession of static models of the earth's atmosphere. These new models varied slightly from previously produced models in the lower atmosphere, but large differences were noted in the upper atmosphere. These large changes in the upper atmosphere were the result of measurements of atmospheric parameters by rocket-borne probes. Figure 1 depicts the vertical distribution of density in some recent static models and shows that it is primarily the uppermost regions of the atmosphere which have been altered by satellite data.

As additional data were accumulated from analyses of the orbital characteristics of the various satellites and from the direct measurements of rocket-borne probes, it was apparent that all the previous models together could not present an entire picture of the upper atmosphere. Although each of the previous models had adequately described the upper atmosphere at a specific time, it soon became apparent that an infinite number of these static models would be required to describe the upper atmosphere of the earth above 90 kilometers (km) because the atmosphere above this altitude is a very dynamic medium.

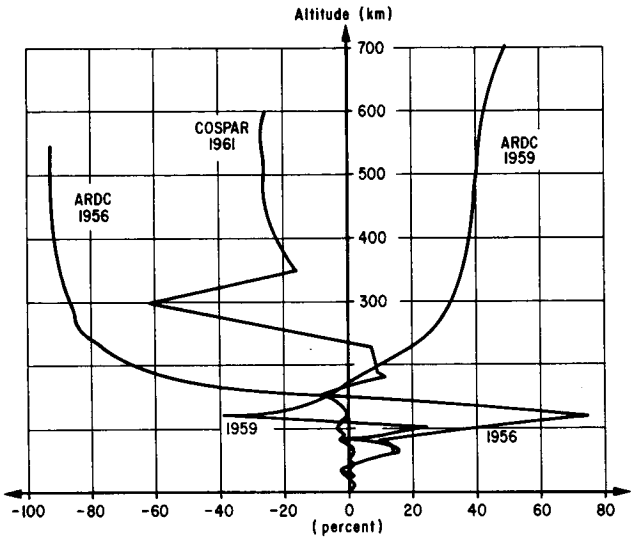

FIGURE 1. DENSITY OF ARDC MODEL ATMOSPHERE 1956, ARDC MODEL ATMOSPHERE 1959, AND COSPAR IRA 1961 COMPARED TO U. S. STANDARD 1962 AS A PERCENTAGE DEVIATION

II. DISCUSSION AND RESULTS

In this study, 90 km has been selected as the base of the upper atmosphere. From the surface to approximately 90 km, the composition of the atmosphere is generally accepted as being constant; thus, there is the same ratio of constituents at each level. For this reason, this portion of the atmosphere is called the homosphere. Above 90 km the composition changes with height because of selective absorption of solar energy. The absorption of solar energy is primarily in the ultraviolet portion of the spectrum as shown in Figure 2. The constituents are not mixed but are in diffusive equilibrium. This means that each constituent is distributed vertically according to weight. Therefore, the mean molecular weight of this medium decreases with increasing height. This

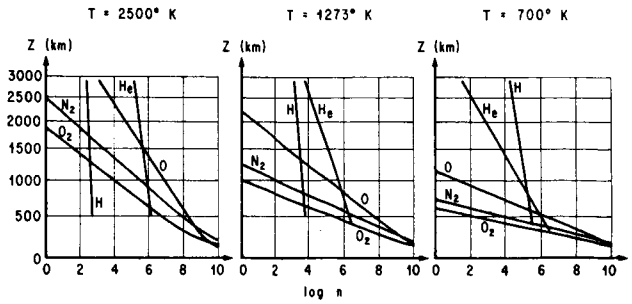

FIGURE 2. CONCENTRATION OF THE PRINCIPAL ATMOSPHERIC CONSTITUENTS AS A FUNCTION OF HEIGHT FOR THREE EXOSPHERIC TEMPERATURES

region is called the heteorosphere. Within the homosphere and the heterosphere there are many smaller-scale regions. Most of these smaller regions are caused by changes in the thermal structure. One of these regions is of particular concern to MSFC, and this region has been named the ignorosphere because very little is known about it. This region lies between 90 and 200 km above the surface of the earth, or just above the maximum height of most of the current meteorological sounding rockets and below the minimum height of most orbiting satellites. Therefore, data from this region are very sparse and only a few atmospheric parameters are known to any degree of accuracy. Figure 3 shows that the temperature in this region increases very rapidly with height. In this region, the mean molecular weight decreases very rapidly with height, and both the amount and type of constituents experience great variations.

The upper atmospheric parameters that are of primary importance to MSFC are the vertical distribution of density and the temporal and spatial variations of density. Figure 4 shows that the vertical distribution of density is a function of the amount of solar ultraviolet radiation reaching the earth. Therefore, the temporal and spatial variations of density are caused by the transient and the long-term variations in the solar radiation. Only one transient variation has been documented, the variation due to geomagnetic storms. These short-lived effects begin approximately 2 to 5 hours after the onset of the storm on the sun. These effects cannot be ignored because energetic particles ejected from the sun during these storms interact with the upper atmosphere and cause the density to increase by as much as a factor of ten.

Four separate long-term variations have been identified. Figure 5 shows that these are the diurnal, latitude, 27-day, and solar-cycle variations. Since the principal heat source in the upper atmosphere is the ultraviolet radiation from the sun, solar heating causes the atmosphere to expand upward toward the sun in its daily passage overhead. Although this upward expansion is a direct consequence of solar heating, it lags the subsolar point by about 2 hours at an altitude of 200 km. As a result of this daily upward expansion, the density in the ignorosphere has a minimum value at 1400 local sidereal time (LST) and a maximum value at 0400 LST between 120 and 180 km. Almost no diurnal variations occur between 90 to 120 km and between 180 to 185 km. At altitudes above 185 km the density has a maximum value at 1400 LST and a minimum value at 0400 LST. The magnitude of this diurnal variation is a function of altitude, latitude, and time with respect to the solar cycle. During periods of low solar activity, the ratio of the maximum value to the minimum value increases from 1 at 185 km

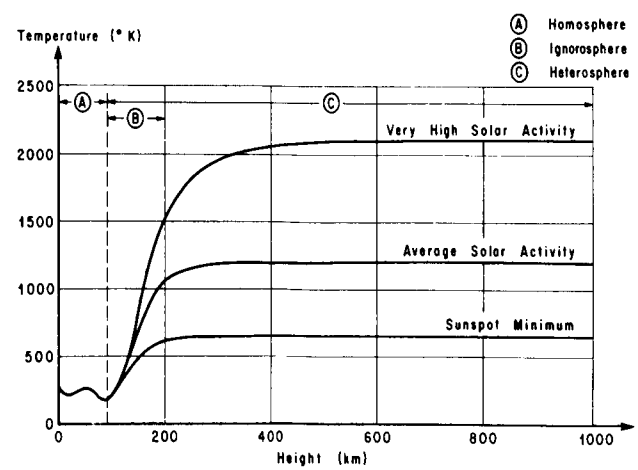

FIGURE 3. ATMOSPHERIC TEMPERATURE PROFILES

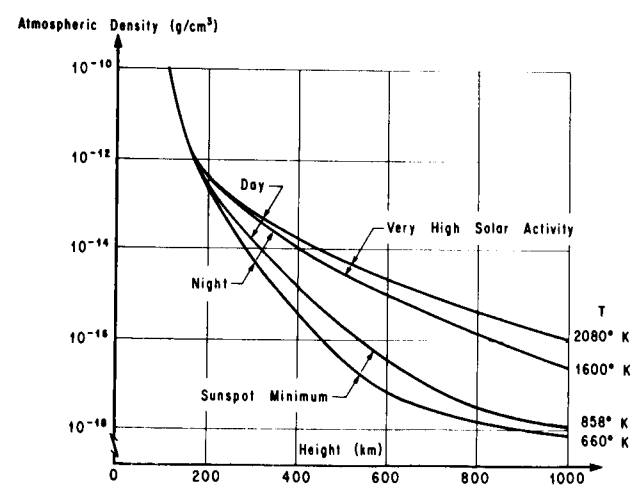

FIGURE 4. DENSITY PROFILES IN THE UPPER ATMOSPHERE

to 12 at 600 to 700 km. During periods of high solar activity, the ratio varies from 1 at 185 km to 25 at 600 to 700 km. At altitudes above 600 to 700 km, it is postulated that the magnitude of the diurnal variation decreases, but more experimental data are needed before exact values can be quoted.

INFLUENCE		100 - 200 km	200 - 1,000 km
Geomagnetic Storm		Unknown	Up to 10 × Increase
Diurnal	Min	1400 LST	0400 LST
	Max	0400 LST	1400 LST
	Max / Min	1 (185) (Min Solar Act)	12X (600 - 700 km)
	Max / Min	1 (185) (Max Solar Act)	25X (600 - 700 km)
27 day	Max / Min	Unknown	2 - 3X
Solar Cycle			
	Diurnal Min (Max) / Diurnal Min (Min)	Unknown	15 - 20X
	Diurnal Max (Max) / Diurnal Max (Min)	Unknown	30 - 35X
Latitude			
	Subsolar Point / Pole	Unknown	2X (200 km)
	Subsolar Point / Pole	Unknown	30X (800 km)

FIGURE 5. HETEROSPHERE DENSITY INFLUENCES

The 27-day variation is caused by the rotation of the sun causing active regions on the solar surface to reach positions from which ejected particles can influence the earth's atmosphere. The magnitude of these variations has not been completely documented, and as a result, exact figures cannot be quoted.

Solar-cycle variations are very large and are the result of variations in the total energy output of the sun. The daily minimum values at maximum solar activity are 15 to 20 times the minimum values at minimum solar activity, while the daily maximum values at maximum solar activity are 30 to 35 times the maximum values at minimum solar activity.

The latitude effect is the last variation that has been documented. Density decreases from the subsolar point to the antisolar point, except for the Northern Hemisphere in the fall when an unexplained increase occurs from the subsolar point to 30° to 40° north before the general decrease begins. The meridional gradient is much less in the summer in both hemispheres than in any other season. At the same altitude, the density over the Southern Hemisphere in its winter is less than the density over the Northern Hemisphere in its winter. Therefore, the minimum density in the upper atmosphere occurs over the South Pole. At 200 km the maximum variation between the subsolar point and the South Pole is approximately 50 percent and at 800 km the density at the subsolar point is up to 30 times as great as the density at the South Pole.

During the past year, a mathematical model of the upper atmosphere above 200 km has been developed which incorporates all these features. The variations that are well documented are included as explicit functions, while the variations that are less known or postulated are included as a composite variation which results in the prediction of an envelope of density for each altitude at any time, at any latitude, or at any portion of the solar cycle. As each of these variations becomes better defined, the mathematical model will be revised with the hope that the density envelope can be narrowed down to a single value.

Conditions between 100 and 200 km are radically different, and data from this region are still sparse. The Aero-Astrodynamics Laboratory has been deriving effective atmospheric density from the analysis of the orbital characteristics of the Saturn vehicles and payloads. The techniques developed have been applied to the analyses of the orbital decays of several other satellites with excellent results. These studies have added 8 to 10 more data points in this region. The Aero-Astrodynamics Laboratory is initiating a series of Nike-Tomahawk launches at Cape Kennedy. These rockets will carry payloads that will measure the density of the upper atmosphere between 100 and 350 km. Goddard Space Flight Center is also launching the same payloads from Wallops Island, Fort Churchill, and Point Barrow, Alaska. These programs combined will add 20 to 30 data points per year at each altitude. Therefore, it will be some time before this region of the upper atmosphere will be adequately defined.

BIBLIOGRAPHY

1. U. S. Standard Atmosphere, 1962, Washington, D. C., Dec. 1962.

2. Smith, Robert E.: An Automated Model for Predicting Aerospace Density Between 200 and 60 000 km Above the Surface of the Earth. NASA TM X-53062, June 1964.

3. Smith, Robert E. : An Automated Model for Predicting the Kinetic Temperature of the Aerospace Environment from 100 to 60 000 km Above the Surface of the Earth. NASA TM X-53104, Aug. 1964.

PROGRESS IN ATMOSPHERIC THERMODYNAMIC MODELS

By

Orvel E. Smith

SUMMARY

This study explains the need for a realistic atmospheric thermodynamic model for each space-vehicle launch site. Once such a model has been established, there is a need for uniform usage of the model by the several different organizational elements engaged in flight performance analysis and in establishing preflight trajectories. A brief evaluation of atmospheric models is presented in this study with particular attention given to the concept of a reference atmosphere.

I. INTRODUCTION

Atmospheric thermodynamic models are the average values of temperature, pressure, and density with respect to altitude. The normal procedure for constructing an atmospheric model is to define the mean values of temperature as linear segments versus altitude and to define the mean value of pressure at sea level. From these defined variables, pressure versus altitude is derived from the hydrostatic equation, and density versus altitude is derived from the equation of state. By using other thermodynamic equations, additional quantities can be derived and tabulated.

The development of atmospheric models has a long history, but in this study, only those models that have been developed in the past ten years will be examined. These models are as follows:

(a) National Advisory Committee for Aeronautics (NACA) Report 1235, 1955.

(b) Air Research and Development Command (ARDC) Model Atmosphere, 1956.

(c) United States Extension to the International Civic Aviation Organization (ICAO) Standard Atmosphere, 1958.

(d) Air Research and Development Command (ARDC) Model Atmosphere, 1959.

(e) United States Standard Atmosphere, 1962.

(f) Committee on Space Research (COSPAR) Reference Atmosphere, International Reference Atmosphere (CIRA), 1961.

(g) Patrick Reference Atmosphere, 1961.

(h) Patrick Reference Atmosphere, 1963 Revision.

(i) Inter-Range Instrumentation Group/Meteorological Working Group (IRIG/MWG) Range Reference Atmospheres

(1) Part I (1963-1965)

(2) Part II and Part III to be published, (1967).

(j) United States Supplemental Atmospheres to be published (1966).

II. DISCUSSION AND RESULTS

The defining properties of the first five models are identical from sea level to 11 kilometers. This is a result of the influence exerted by the aviation industries and of the international acceptance of these values as a standard. Another feature the first five models have in common is that they depict the idealized year-round mean conditions for the middle latitudes of the Northern Hemisphere.

The defining parameters of NACA Report 1235 (1955) were previously adopted by the ICAO on November 7, 1952. This model, which defined conditions from sea level to 65 800 feet, resolved slight differences in earlier atmospheric models that had been developed in the United States and Europe since the 1920's. As a result of the need for a standard reference by the aviation industries, the world had its first published Standard Atmosphere in 1955.

The development of rockets and ballistic missiles created a need for an atmospheric model with a higher altitude. The ARDC Model Atmosphere (1956) and the United States Extension to the ICAO

Standard Atmosphere (1958) were the first attempts made to satisfy this need. However, the space programs made these models obsolete shortly after they were developed.

The ARDC Model Atmosphere (1959) was the first space-promoted model atmosphere. However, a reevaluation of all previous models became apparent as data from meteorological rockets and satellites became available. In January 1960, a Working Group of the Committee on Extension to the Standard Atmosphere (COESA) set out to accomplish this task. The United States Standard Atmosphere (1962) was a result of the work done by this committee.

The Committee on Space Research (COSPAR) developed the International Reference Atmosphere, CIRA (1961). The COSPAR Reference Atmosphere was derived almost exclusively from density data that were obtained from satellite drag information. The values for temperature, pressure, and density differ from those of the United States Standard Atmosphere 1962.

Personnel at MSFC recognized that a standard atmosphere referenced to the middle latitudes did not meet the requirements for the design and operation of vehicles launched from Cape Kennedy. The concept of a "Range Reference Atmosphere" was developed and used in MSFC trajectory studies in 1960. The first publication in 1961 was known as The Patrick Reference Atmosphere (Annual). This model is based on atmospheric data for the first 30 km of altitude obtained from Patrick Air Force Base. The model is extrapolated to the 50-km level of the ARDC Model Atmosphere (1959) and is then extended to the 500-km level by using the ARDC Model Atmosphere (1959).

When the U. S. Standard Atmosphere (1962) was published, a revision of the old Patrick Reference was required. The revised Patrick Reference Atmosphere employed radiosonde and rocketsonde data to define atmospheric parameters below 90 km, and then employed the U. S. Standard Atmosphere (1962) to define the atmospheric parameters from 90 to 700 km. A computer subroutine known as PRA 63 is in the Computation Laboratory Library file for all MSFC organizations and all qualified requesters. This subroutine is specified for all theoretical trajectory and performance computations for MSFC vehicles launched from Cape Kennedy.

The IRIG Range Reference Atmospheres provide a preview of the specialized atmospheric models that are currently under development. These models are being developed for all of the major missile ranges. They are patterned after the Patrick Reference Atmosphere. The IRIG Range Reference Atmospheres are in three parts, as follows:

(a) Part I defines the atmospheric parameters to 30 km.

(b) Part II defines the atmospheric parameters from 30 to 90 km.

(c) Part III defines the variability of the atmospheric parameters.

The United States Supplemental Atmospheres will define the mean conditions for the following:

(a) Tropical (annual).

(b) Subtropical (summer and winter).

(c) Middle latitude (summer and winter).

(d) Subarctic (summer and winter).

(e) Arctic (summer, cold winter, and warm winter).

The linear segmented temperature profile of the U. S. Standard Atmosphere (1962) is contrasted (Fig. 1) with the continuous profiles of the Patrick Reference Atmosphere. The maximum temperature difference is 15°C at 15 km (tropopause). There is a crossover at 50 km (stratopause), and there is a coincidence of temperature at 90 km (mesopause).

Since density is one of the more important atmospheric variables affecting the vehicle performance, attention will be given to this parameter in Figure 2. Figure 2 shows that the Patrick Reference Atmosphere density is 3 percent lower than the U. S. Standard Atmosphere (1962) at sea level. The Patrick Reference Atmosphere density is 13 percent higher than the U. S. Standard Atmosphere (1962) at 15 km. This is the altitude region of maximum dynamic pressure on an aerospace vehicle which is the region of maximum winds. The density over Cape Kennedy is 8 percent higher than the U. S. Standard Atmosphere (1962) in the altitude region of 50 to 60 km. These deviations of density illustrate the value of having a well documented atmospheric model for each launch site.

Since the Patrick Reference Atmosphere is defined for mean annual conditions, a comparison with monthly mean conditions is made in Figure 3 to illustrate the range of variation. Because of a lack of data at higher altitudes, this comparison is feasible only for the first 30 km. During the winter months, the mean density at the surface is from 2 to 3 percent higher than the mean annual density; and the mean

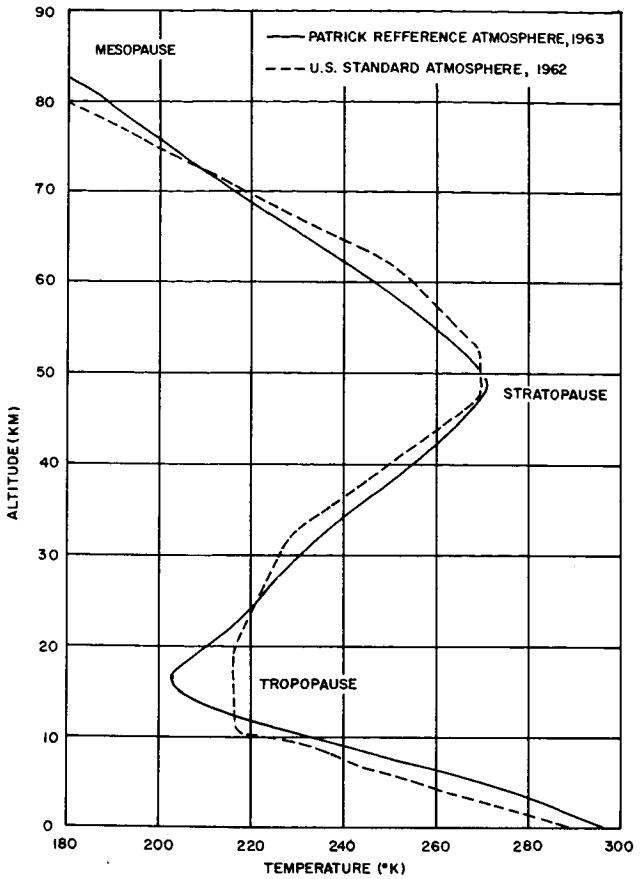

FIGURE 1. COMPARISON OF TEMPERATURE BETWEEN PATRICK REFERENCE ATMOSPHERE, 1963 AND U. S. STANDARD ATMOSPHERE, 1962

density at 15 km is 2 percent lower than the mean annual density. During July and August, the mean density at altitudes above 15 km is 3 percent higher than the mean annual density.

The atmospheric models discussed in this study have been derived to depict the mean value of several atmospheric parameters versus altitude. Considerable progress has been made in defining the mean state of the atmosphere by MSFC and the scientific community as a whole. A knowledge and a method of presenting the complete vertical structure of thermodynamic parameters are required in space vehicle

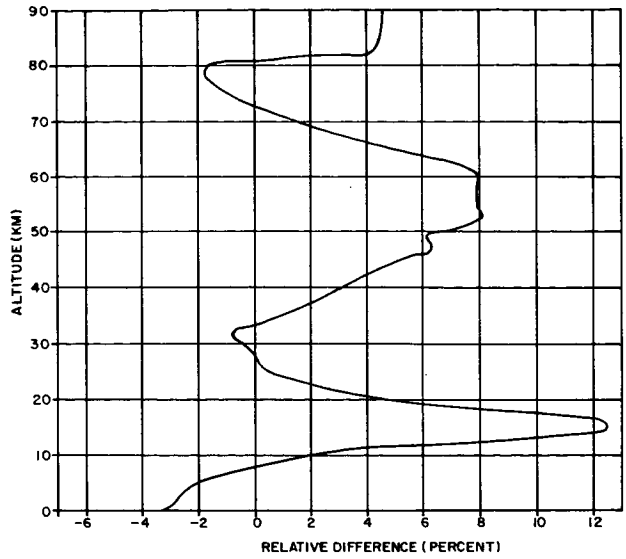

FIGURE 2. COMPARISON OF DENSITY BETWEEN PATRICK REFERENCE ATMOSPHERE, 1963 AND U. S. STANDARD ATMOSPHERE, 1962

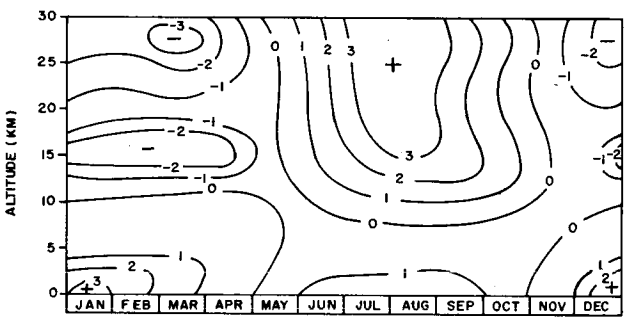

FIGURE 3. COMPARISON OF MONTHLY MEDIAN DENSITY OVER CAPE KENNEDY, FLORIDA (RELATIVE DEVIATION IN PERCENT)

design. A complete vertical structure of thermodynamic parameters is not defined by existing atmospheric models, and the range of variability is met only in part. Therefore, there are challenging engineering and research requirements to meet, even before the necessary atmospheric measurements are available.

BIBLIOGRAPHY

1. International Civil Aviation Organization, Montreal, Canada, and Langley Aeronautical Laboratory, Langley Field, Va. : Standard Atmosphere Tables and Data for Altitudes up to 65 800 ft. NACA Rept. 1235, 1955.

2. IRIG Document No. 104-63, Atlantic Missile Range Reference Atmosphere for Cape Kennedy, Florida (Part I). Secretariat, Range Commanders Council, White Sands Missile Range, N. M.

3. Kallmann, H. Bijl, et al.: COSPAR International Reference Atmosphere, 1961. CIRA 1961, North-Holland Publishing Co., Amsterdam, Interscience Publishers, Inc., New York, N. Y., 1961.

4. Minzner, R. A.; Champion, K. S. W.; and Pond, H. L. : The ARDC Model Atmosphere, 1959. Air Force Surveys in Geophysics No. 115, Geophysics Research Directorate, Air Force Cambridge Research Center, Aug. 1959.

5. Minzer, R. A.; and Ripley, W. S. : The ARDC Model Atmosphere, 1956. Air Force Surveys in Geophysics No. 86, Geophysics Research Directorate, Air Force Cambridge Research Center, Dec. 1956.

6. Smith, Orvel E.; and Weidner, Don K. : A Reference Atmosphere for Patrick AFB, Florida, Annual (1963 Revision). NASA TM X-53139, Sept. 23, 1964.

7. U. S. Standard Atmosphere, 1962. United States Government Printing Office, Washington 25, D. C., Dec. 1962.

METEOROID FLUX AND PUNCTURE MODELS FOR CISLUNAR SPACE

By

Charles C. Dalton

SUMMARY

Interrelated cubic polynomial models are constructed for log-puncture flux versus log-effective-target thickness and for log-mass-cumulative-incident flux versus particle mass which give the best agreement between meteoroid measurement satellite data and photographic meteor data without relaxing the assumption that p/d is independent of d for particles of different velocity, where p and d are puncturable thickness and particle diameter, respectively. An accurate account of the expected mean hazard for meteoroid puncture in earth orbit is needed for design and operation planning purposes for future programs. The model developed in this study should give a mean puncture flux accurate to within a factor of 2 probable error with a target equivalent thickness between 15 and 10^{-4} centimeters of aluminum. The corresponding model for mass-cumulative-incident flux is also developed.

DEFINITION OF SYMBOLS

Symbol	Definition
log	logarithm with base ten.
p	thickness of a just-puncturable sheet in centimeters.
d	projectile diameter in centimeters.
v	meteoroid air-entry velocity in kilometers per second.
v_m	meteoroid lunar-impact velocity in kilometers per second.
f(v)	probability density function for v.
m	mass of a meteoroid in grams.
$F_>$	flux of meteoroids of mass equal to or greater than m; mean number of hits per square meter per second per 2π steradians without earth shielding.
p_0	crater depth in centimeters for a semi-infinite target.
t	target subscript.
C	velocity of sound in kilometers per second in an unbounded solid.
E	$10^{-6} \times$ Young's modulus in kilograms per square centimeter.
ϵ	ductility, relative elongation in 2-inch gage length at fracture.
ν	Poisson's ratio.
$\bar{m}$	meteoroid mass in grams nominally sufficient to puncture.
ϕ	puncture flux; mean number per second per square meter of surface with 2π steradian exposure.
β_2 and β_3	respectively, the slope and intercept of the tangent to the curve for log $F_>$ versus log m.
β_5	logarithm of the puncture flux enhancement factor due to the statistical variation of the particle and impact parameters.
x_2, x	angle of impact of incident and of puncturing meteoroids, respectively, with respect to the surface normal in radians.
H_t	material hardness in Brinell units.
k_4	material parameter, (2/3) log $(\rho_t C_t)$ -1.162.
y	target parameter, $k_4 + \log p$.
$a_0, \ldots, a_3$	constants.
z	$\log \phi$, $a_0 + a_1 y + a_2 y^2 + a_3 y^3$.
R	radius of effectively shielding atmosphere, 6487 km.

H	$(\frac{1}{2})$ (perigee + apogee) -109 km, effective height above atmosphere.
ζ	$(\frac{1}{2})\{1 + \cos \sin^{-1}[R/(R+H)]\}$, relative exposability of randomly oriented surface [18].
At	second-square-meters (partially shielded).
Δp	centimeters thickness allowance for nonmetallic mass in capacitor structure.
M.L.	maximum likelihood value.
G	$10^{-6}\times$ torsion modulus in kilograms per square centimeter.
F_s and ϕ_s	mean incident and puncture flux, respectively, per second per square meter of a randomly oriented surface near the earth ($\zeta = \frac{1}{2}$).

I. INTRODUCTION

The author's paper [1], available April 1966, has been substituted here for the one which was presented by the author at the Research Achievements Review Meeting in September 1965. When sufficient puncture data for the Pegasus meteoroid measurement satellites were available in November 1965 [2], a major revision of the meteoroid hazard models was necessary. In January 1966, a paper by the author [3] showed that if linear relationships between the logarithms of puncture flux and target thickness for the Pegasus experiments and between the logarithms of mass-cumulative flux and particle mass for photographic meteors are to be extrapolated, then the target puncturable thickness for meteoroids of the same normal impact velocity would be proportional to the particle cross-sectional area. Recently, the NASA Meteoroid Technology Advisory Working Group objected unanimously in consideration of laboratory hypervelocity impact data for more massive dense particles at relatively lower velocity. The consensus which has been asserted by the working group is that meteoroid impact crater volume for a thick target should be nearly proportional to particle kinetic energy for impact at normal incidence.

II. DISCUSSION AND RESULTS

Previously, meteoroids with air-entry velocity only slightly in excess of escape velocity were expected to be much more abundant [4], especially for those of small mass, and that their flux in cislunar space might be strongly dependent on gravitational potential. However, a weighted analysis of photographic meteor data [5] shows no significant statistical relation between mass and velocity, and gives the velocity distribution shown in Figure 1. The weighted mean log velocity is log 27 kilometers per second; and only 25 percent of the total flux is caused by the gravity-effect factor. The remaining component, shown also in Figure 1, can be transformed into the distribution of lunar impact velocity

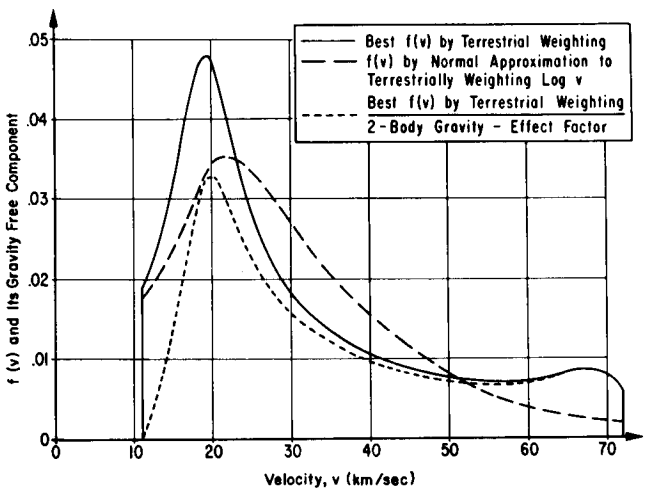

FIGURE 1. PROBABILITY DENSITY FUNCTION FOR METEOROID AIR-ENTRY VELOCITY

shown in Figure 2, with median coincidentally 27 kilometers per second. In the same analysis, the mean air-entry meteoroid flux was found to be

$$F = 10^{-14.49}\, m^{-1.34} \qquad (1)$$

when the particle material density is [6]

$$P = 0.44, \qquad (2)$$

and the least-countable mass m is in the interval $10^{-1.13} \leq m \leq 10^{-0.23}$. In establishing equation (1), the mass of the zero-visual-magnitude 30-kilometer-per-second meteor has been increased 0.2 order of

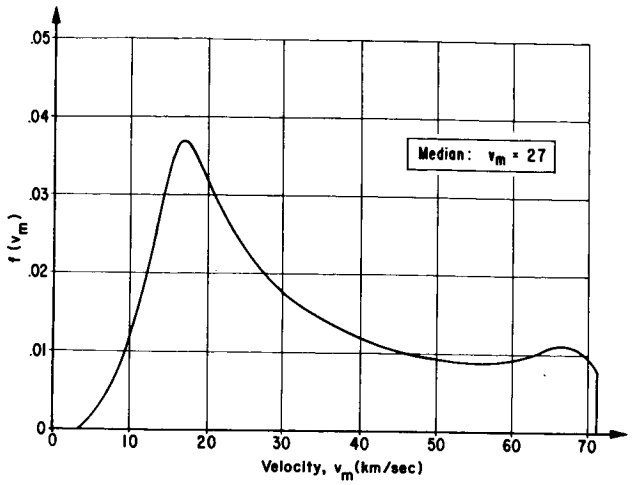

FIGURE 2. PROBABILITY DENSITY FUNCTION OF LUNAR-SURFACE IMPACT VELOCITY FOR PRIMARY METEOROIDS

magnitude over Whipple's [6] one gram estimate in consideration of the cube of the relative change in the 85 to 90 kilometer pressure for Reference 7 versus Reference 8 which Whipple used (basis: Reference 9). Correspondingly, the mean lunar-impact flux would be $10^{-14.61}\ m^{-1.34}$. When allowance is made for the mean solid angle of exposure for a surface in orbit, the mean flux will not differ appreciably from the fixed-level-surface values given above.

In a survey and multivariate analysis of available laboratory hypervelocity impact data, Reismann, Donahue, and Burkitt [10] found that in the highest of three velocity regimes the multiple-correlation coefficient is nearly maximized (to 0.989) by representing the relation between projectile and target parameters for impact at normal incidence as follows:

$$P_0/d = 2.5(v/C_t)^{0.50}(E/E_t)^{1.31}(\nu/\nu_t)^{8.0}(\epsilon/\epsilon_t)^{0.43}. \quad (3)$$

The relation between puncturable target thickness p and crater depth p_0 has been treated in considerable analytical depth by Andriankin and Stepanov [11]. Their results indicate that the ratio p/p_0 is a function of the projectile and target material parameters and of the impact velocity, varying between somewhat more than 1 to somewhat less than 2 for impact velocity above about 6 kilometers per second. Herrmann and Jones [12] illustrate experimental results (which they attribute to Kinard, et al., at NASA Langley) and an empirical formula indicating that, as target thickness is decreased toward the value p, the value of p/p_0 approaches

$$p/p_0 \rightarrow (1/1.3)^2 + 1 = 1.59. \quad (4)$$

If equations (3) and (4) are valid for meteoroid impact, then p/d is independent of d, and the slope of log ϕ versus log p should be three times the slope of log $F_>$ versus log m, where ϕ is the puncture flux corresponding to incident flux $F_>$. Therefore, if the slope of log $F_>$ versus log m for photographic meteors in the vicinity of 10^{-1} gram mass, expressed by the constant -1.34 in equation (1), were also applicable for the particles puncturing the meteoroid measurement satellites, then the slope of log ϕ versus log p should be -4.02 for the satellite puncture data. However, in a previous working paper [3], the value -1.966 for the slope of log ϕ versus log p was shown to fit the satellite data very well. At first the author [3] interpreted this discrepancy between the -4.02 and -1.966 results as indicating that p/d is not essentially independent of d for meteoroid impact circumstances; but, after extensive consultation and further analysis, the present interpretation is that the slope of log $F_>$ versus log m is not essentially independent of m.

Because puncture flux ϕ versus effective target thickness p is of more direct technological interest than incident flux $F_>$ versus particle mass m, even though the opposite might be true for scientific interests, a model should be developed first for ϕ versus p by using the satellite puncture data and computed values of ϕ and p corresponding to the photographic meteor data, equation (1). The relation between incident flux $F_>$ and puncture flux ϕ must be established through

$$F_> = 10^{\beta_3} m^{\beta_2} \quad (5)$$

and

$$\phi = 10^{\beta_3 + \beta_5} \bar{m}^{\beta_2}, \quad (6)$$

where β_2 and β_3 are respectively the slope and intercept of the tangent to the curve for log $F_>$ versus log m; $\bar{m}$ is the mass of the meteoroid which, with mean values of density ρ, velocity v, and angle of incidence x_2 with respect to the surface normal, is just sufficient to puncture the target of interest, and 10^{β_5} is the puncture flux enhancement factor [13] due to the statistical distribution of the parameters ρ, v, and x_2.

Recently equation (3) had been preferred [4, 3, 13, and 14] as a basis for the relative puncturability of targets of different materials. The preference of equation (3) was based both on the detailed involvement

of various material parameters and on the fact that the velocity exponent had the same value as had been preferred previously by the author [15 and 16] because it was intermediate between the values supported by different authors [12 and 17] at that time. The author [15 and 16] had preferred

$$p_0 = 10^{0.434} (\rho m/\rho_t H_t)^{1/3} (v \cos x_2)^{1/2} \quad (7)$$

where H is the material hardness in Brinell units. Then, by equations (1), (2), (4), and (7), a meteoroid with nominal mass $\bar{m} = 10^{-1}$ gram, nominal density $\rho = 0.44$, nominal velocity v = 27 kilometers per second, and nominal impact angle $x_2 = \pi/4$ radians impacting a sheet of 2024T-3 aluminum with density $\rho_t = 2.77$ and Brinell hardness $H_t = 120$ would just puncture the sheet of thickness $p = 10^{-0.017}$ or 0.96 centimeter. For the same conditions except with the intermediate value $\beta_2 = -1.23$, and equation (7), the author [13] found the puncture flux enhancement factor to be $10^{\beta_5} = 10^{0.70}$. Then, with equations (1), (5), and (6), the mean puncture flux for $\bar{m} = 10^{-1}$ would be $\phi = 10^{-14.45}$. A line between this point (log ϕ, log p) = (-14.45, -0.017) and the corresponding point for the thickest Pegasus target would have a slope of -4.02 = 3 (-1.34), which would support the extrapolation of equation (1) except that the puncture data for thinner targets (both on Pegasus and on Explorers XVI and XXIII) definitively establish a lower slope. To accept an abrupt change in slope from about -4 to about -2 does not seem reasonable in the immediate vicinity of the Pegasus data point. An assumption must be made that puncturable thickness p varies more steeply with velocity v than is indicated by equation (7). Therefore, the author prefers to abandon both of the formulations in equations (3) and (7) for meteoroid puncture.

The NASA-Ames penetration criterion by Summers [18] has been recommended recently for meteoroid puncture analysis by Dohnanyi [19]; i.e.,

$$p_0 = 3.56 \left\{ (m\rho/2\rho_t^2) \left[v(\cos s_2)/C_t \right]^2 \right\}^{1/3}. \quad (8)$$

Equations (4) and (8) indicate that p/d is independent of d. With $C_t = 6.25$ from Reference 10 for 2024T-3 aluminum, the nominal meteoroid, with $\bar{m} = 10^{-1}$, and with the values for the other parameters mentioned above, the puncturable thickness is $p = 10^{0.229}$ or 1.69 centimeters, which is 76 percent thicker than implied by equation (7).

Equations (4) and (8) lead to some revision in the puncture flux enhancement factor 10^{β_5} and in the probability density function of the angle of impact x of a puncturing meteoroid, as derived in Reference 13. To retain the same value 0.52 for the standard deviation of log puncturable mass instead of increasing to 0.57 would seem to be appropriate to account for the stronger dependence on velocity in equation (8). This accommodation is supported by a reduction in the standard deviation of the material density from 0.44 to 0.38. Then, by the derivation in Reference 13, differential puncture flux $d\phi$ must be multiplied by $e^{-\frac{1}{4}} (\cos x)^{-\frac{1}{2}}$. The results of this alteration are that

$$\beta_5 = 0.63 \quad (9)$$

$$f(x) = 1.77 (\cos x)^{1.54} \sin 2x. \quad (10)$$

Therefore, by equations (5), (6), (9), and (10), the puncture flux enhancement factor is 4.26 instead of 5.05; and the median impact angle x for the puncturing meteoroids is 34.7 instead of 33.5 degrees from the normal.

By equations (1), (5), (6), and (9), the mean puncture flux, which is implied by the puncture criteria expressed by equations (4) and (8) for $\bar{m} = 10^{-1}$ gram, is $\phi = 10^{-14.52}$, with $p = 10^{0.229}$ for 2024T-3 aluminum. Since equation (1) represents the photographic meteor data over the interval $10^{-1.13} \leq m \leq 10^{-0.23}$, the nominally puncturing mass is $m = 10^{-0.68}$ with $F_> = 10^{-13.579}$. The nominally puncturing mass corresponds to the point (log ϕ, log p) = (-12.949, 0.336) for 2024T-3 aluminum.

By introducing a material constant k_4 and a target parameter k_4 + log p and the values of the parameters already used with equations (4) and (8), the following can be written:

$$\bar{m} = 10^{3k_4 - 0.678} p^3 \quad (11)$$

$$k_4 = (2/3) \log (\rho_t C_t) - 1.162 \quad (12)$$

$$y = k_4 + \log p \quad (13)$$

$$= (1/3) \log \bar{m} + 0.266 \quad (14)$$

$$z = \log \phi \quad (15)$$

$$= a_0 + a_1 y + a_2 y^2 + a_3 y^3 \quad (16)$$

where $a_0, \ldots, a_3$ are constants to be determined below. Also,

$$\beta_2 = (1/3) (a_1 + 2a_2 y + 3a_3 y^2) \quad (17)$$

$$\beta_3 = z - 0.63 - \beta_2 \log \bar{m} \quad . \tag{18}$$

Therefore, with equations (5) and (14) through (18), the mass-cumulative flux $F_>$ is determined as a function of mass m.

The constant term in equation (12) for the material constant k_4 has been chosen so that the target parameter y in equations (13) and (14) vanishes for the photographic meteor value $\log \bar{m} = -0.68$ and $\log \phi = -12.949$. Therefore, in equation (16),

$$a_0 = -12.95, \tag{19}$$

and, by equations (1) and (11),

$$a_1 = -4.02 \; . \tag{20}$$

The values of the outer constants a_2 and a_3 in equations (16) and (18) must be determined by the satellite puncture data.

Puncture data for five meteoroid measurement satellites, compiled in Table I and adjusted to remove earth-shielding according to the mean solid angle of exposure, are plotted in Figure 3. The values of the physical constants for the materials are also given in Table I. The values used for p for the Pegasus sensors include a 10^{-3}-centimeter increment in consideration of the nonmetallic components of the capacitor puncture sensors [4].

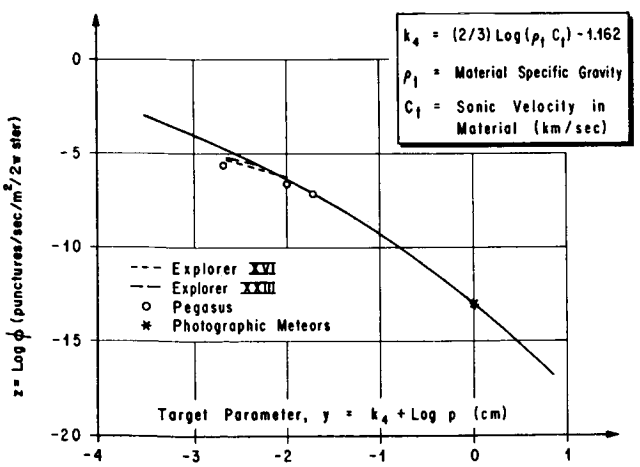

FIGURE 3. METEOROID PUNCTURE FLUX VS EFFECTIVE TARGET PARAMETER

The values of log ϕ, as shown in Table I and Figure 3, have been corrected for geometric shielding [20] by dividing the mean puncture flux by ζ. Poisson's ratio for the Explorer XVI transducer material was calculated from Baumeister [21] :

$$\nu = (E - 2G) / 2G. \tag{21}$$

Values for velocity of sound in the transducer materials were calculated with the extended-medium formula [10 and 22]

$$C = 9.90 \left\{ (E/\rho) \left[(1-\nu)/(1+\nu)\ (1-2\nu) \right] \right\}^{\frac{1}{2}} \tag{22}$$

instead of from the corresponding formula for thin plates [23].

The two conditions of the satellite puncture results from Table I and Figure 3 which are significant in determining constants a_2 and a_3 in equation (16) are (1) the values -1.717 and -7.171 for the abscissa y and the mean ordinate z, respectively, for the thickest Pegasus target, and (2) the values -2.383 and -1.58 for the abscissa y, and the Hastings [24] maximum slope dz/dy, respectively, for the Explorer XVI target of intermediate thickness. Therefore, by these two conditions and equations (16), (19), and (20),

$$a_2 = -0.424 \tag{23}$$

$$a_3 = -0.025 \; . \tag{24}$$

By equations (13), (15), (16), (19), (20), (23), and (24), the relation between puncture flux ϕ and target parameter (k_4 + log p) is

$$\log \phi = -12.95 - 4.02\ (k_4 + \log p) - 0.424\ (k_4 + \log p)^2 - 0.025\ (k_4 + \log p)^3 \tag{25}$$

where the material parameter k_4 is given by equation (12). The corresponding numerical results are superimposed on Figure 3 for comparison with the satellite puncture data. Although the Pegasus puncture flux has been adjusted upward to correct for the approximately 30 percent earth shielding, it has not been corrected upward to correct for any counting loss, which might be about 14 percent [25].

The values of mass-cumulative flux $F_>$ and mass m, corresponding to any point on the curve in Figure 3, can be computed most readily from

$$\log m = 3\ (k_4 + \log p) - 0.68 \tag{25a}$$

$$\log F_> = \log \phi - 0.63 \; . \tag{26}$$

For example, the thickest Pegasus target is being punctured by particles with about 1.5 micrograms mass. The results, which may be accurate to within a factor 2 probable error, are illustrated further in Figure 4 for the mass-cumulative flux $F_>$ (per effectively exposed hemisphere). For better comparison with other models, Figures 5 and 6 show the

TABLE I. DATA FOR TWELVE SATELLITE PUNCTURE TRANSDUCERS

ENTITIES	DATA AND SOURCES											
Satellite	Explorer XVI	Explorer XVI	Explorer XVI	Explorer XXIII	Explorer XXIII	Pegasus I	Pegasus II	Pegasus II	Pegasus II	Pegasus III	Pegasus III	Pegasus III
Launch Date	12-16-62	12-16-62	12-16-62	11-6-64	11-6-64	2-16-65	5-25-65	5-25-65	5-25-65	7-30-65	7-30-65	7-30-65
	[26]	[26]	[26]	[27]	[27]	[28]	[29]	[29]	[29]	[30]	[30]	[30]
Perigee (km)	750	750	750	463	463	497	506	506	506	529	529	529
	[26]	[26]	[26]	[27]	[27]	[28]	[29]	[29]	[29]	[30]	[30]	[30]
Apogee (km)	1180	1180	1180	980	980	745	748	748	748	532	532	532
H	856	856	856	612	612	512	518	518	518	422	422	422
	[24]	[24]	[24]	[27]	[27]	[2]	[2]	[2]	[2]	[2]	[2]	[2]
Punctures	44	11	0	24	25	125	121	18	58	71	14	41
	[24] Fin.	[24] Fin.	[24] Fin.	[27]	[27]	[2]	[2]	[2]	[2]	[2]	[2]	[2]
Tally Date	7-22-63	7-22-63	7-22-63	2-11-65	2-11-65	9-5-65	9-2-65	9-2-65	9-2-65	10-8-65	10-8-65	10-8-65
	[24]	[24]	[24]	[27]	[27]	[2]	[2]	[2]	[2]	[2]	[2]	[2]
Log At	7.060	6.738	6.512	6.731	7.065	7.953	7.737	8.014	9.101	7.587	7.938	8.951
ζ	0.734	0.734	0.734	0.703	0.703	0.688	0.689	0.689	0.689	0.672	0.672	0.672
	[24] M. L.	[24] M. L.	[24] M. L.									
Log ϕ	-5.266	-5.696	-6.275	-5.197	-5.514	-5.693	-5.492	-6.597	-7.176	-5.563	-6.619	-7.165
	[24]	[24]	[24]	[27]	[27]	[25]	[25]	[25]	[25]	[25]	[25]	[25]
$10^4(p-\Delta p)$	29.2	54.6	127	25.4	50.8	38±3	38±3	203±25	406±50	38±3	203±25	406±50
						[4]	[4]	[4]	[4]	[4]	[4]	[4]
$10^4(\Delta p)$	0	0	0	0	0	10	10	10	10	10	10	10
Log p	-2.535	-2.263	-1.896	-2.595	-2.294	-2.317	-2.317	-1.671	-1.381	-2.317	-1.671	-1.381
	[26]	[27]	[26]	[27]	[27]	[4] Al.	[4] Al.	[31] Al.	[31] Al.	[4] Al.	[31] Al.	[31] Al.
Material	Berylco 25	Berylco 25	Berylco 25	AISI 302	AISI 302	1100-H14	1100-H14	2024-T3	2024-T3	1100-H14	2024-T3	2024-T3
	[26]	[26]	[26]	[27]	[27]							
Condition	Annealed	Annealed	Annealed	½ hard	½ hard							
	[26]	[26]	[26]									
Rockwell No.	B 60	B 60	B 60									
	[32]	[32]	[32]	[31]	[31]	[10]	[10]	[10]	[10]	[10]	[10]	[10]
ρ_t	8.23	8.23	8.23	7.83	7.83	2.72	2.72	2.77	2.77	2.72	2.77	2.77
	[32]	[32]	[32]	[21]	[21]	[10]	[10]	[10]	[10]	[10]	[10]	[10]
E_t	1.195	1.195	1.195	1.941	1.941	0.703	0.703	0.745	0.745	0.703	0.745	0.745
	[32]	[32]	[32]	[21]	[21]							
G_t	0.457	0.457	0.457	0.745	0.745							
				[21]	[21]	[10]	[10]	[10]	[10]	[10]	[10]	[10]
ν_t	0.308	0.308	0.308	0.305	0.33	0.33	0.33	0.33	0.33	0.33	0.33	0.33
						[10]	[10]	[10]	[10]	[10]	[10]	[10]
C_t	4.44	4.44	4.44	5.73	5.73	6.12	6.12	6.25	6.25	6.12	6.25	6.25
	[33]	[33]	[33]	[31]	[31]	[10]	[10]	[10]	[10]	[10]	[10]	[10]
ϵ_t	0.46	0.46	0.46	0.15	0.15	0.20	0.20	0.18	0.18	0.20	0.18	0.18
k_4	-0.120	-0.120	-0.120	-0.061	-0.061	-0.348	-0.348	-0.336	-0.336	-0.348	-0.336	-0.336
k_4 + log p	-2.655	-2.383	-2.016	-2.656	-2.355	-2.665	-2.665	-2.007	-1.717	-2.665	-2.007	-1.717
Sensor Structure	Pressure Can	Pressure Can	Pressure Can	Pressure Can	Pressure Can	Capacitor Sand-wich	Capacitor Sand-wich	Capacitor Sand-wich	Capacitor Sand-wich	Capacitor Sand-wich	Capacitor Sand-wich	Capacitor Sand-wich

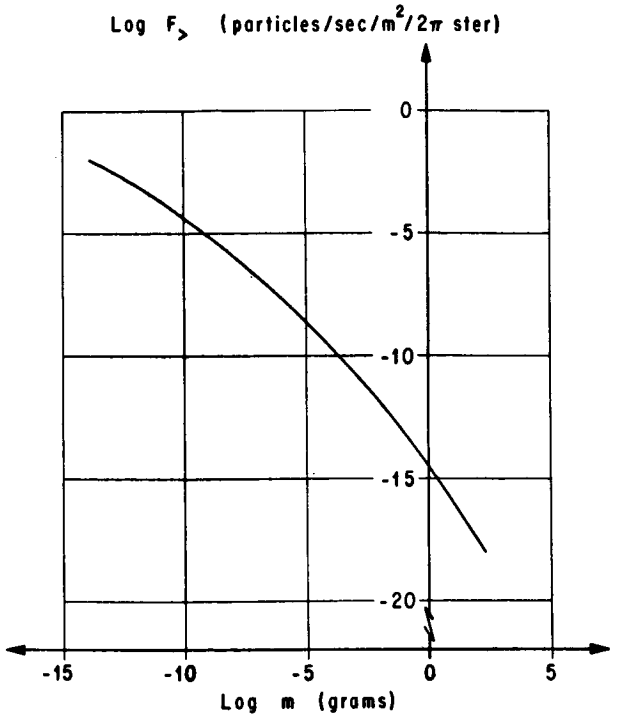

FIGURE 4. METEOROID MASS CUMULATIVE TERRESTRIAL MEAN INFLUX

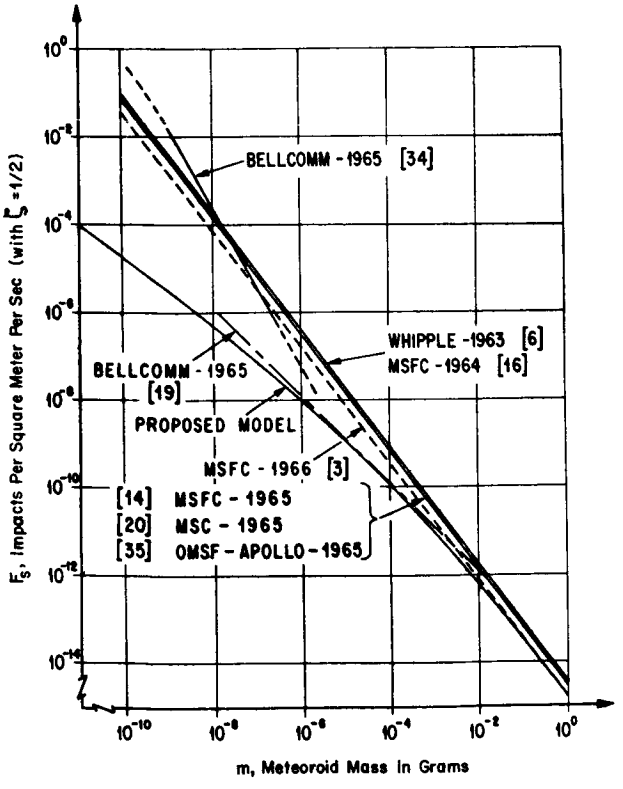

FIGURE 5. MEAN IMPACT FLUX OF METEOROIDS WITH MASS ≥ m FOR A RANDOMLY ORIENTED VEHICLE IN A NEAR EARTH ORBIT

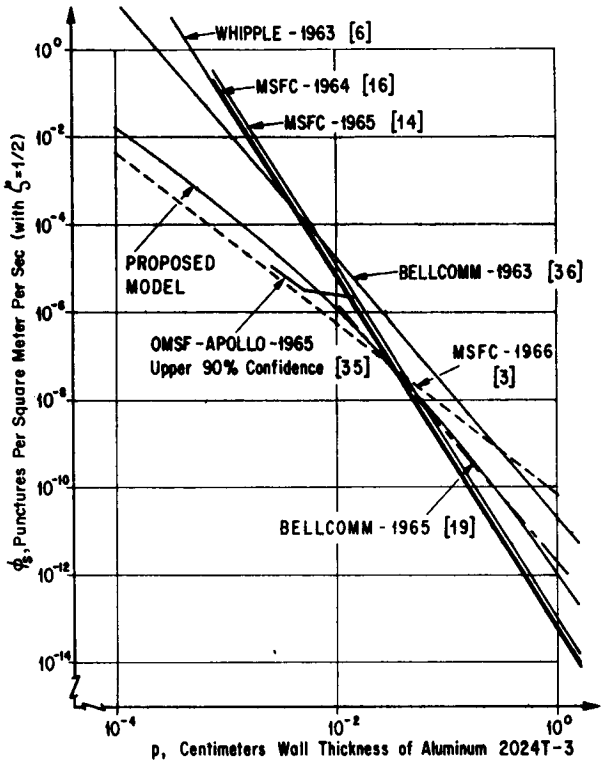

FIGURE 6. MEAN PUNCTURE FLUX FOR A RANDOMLY ORIENTED VEHICLE IN A NEAR EARTH ORBIT

mass-cumulative flux F_S and puncture flux ϕ_S for a randomly oriented vehicle at low orbital altitude from the earth.

III. EQUIVALENT PUNCTURABILITY

By equation (11), sheets of different materials must have the same meteoroid puncturability; then their target parameters must have the same value, meaning ($10^K 4p$) is invariant. For example, sheets of 2024-T3 aluminum must be 1.65 times as thick as for annealed Berylco 25 beryllium copper and 1.89 times as thick as for one-half hard AISI 302 stainless steel. However, the necessary weight of aluminum is still less in either case; and soft aluminum (1100-H14) is nearly as effective as 2024T-3.

REFERENCES

1. Dalton, C. C. : Revised Meteoroid Flux and Puncture Models. MSFC Working Paper No. R-AERO-Y-93-66, Apr. 1966.

2. Stuhlinger, E. : Meteoroid Measurements with Project Pegasus. Dec. 2, Reprint of Presentation at the Northeast Electronics Research and Engineering Meeting, Boston, Mass., Nov. 4, 1965.

3. Dalton, C. C. : Meteoroid Flux and Puncture Models. Working Paper # R-AERO-Y-77-66, MSFC, Jan. 26, 1966.

4. Dalton, C. C. : Cislunar Meteoroid Impact and Puncture Models With Predicted Pegasus Satellite Punctures. NASA TM X-53187, Jan. 13, 1965.

5. Dalton, C. C. : Statistical Analysis of Photographic Meteor Data, Part IV: Öpik's Luminous Efficiency and Supplemented Hawkins-Upton Weighting. NASA TM X- (to be published Sept. 1966.)

6. Whipple, F. L. : On Meteoroids and Penetration. J. Astron. Sci., vol x, no. 3, Fall 1963, pp. 92-94.

7. U.S. Standard Atmosphere, 1962. NASA, U.S. Air Force, U.S. Weather Bureau, Dec. 1962, Government Printing Office, Washington, D.C.

8. Mizner, R.A.; Champion, K.S.W.; and Pond, H.L.: The ARDC Model Atmosphere, 1959. Air Force Force Cambridge Research Center, TR 59-267, Air Force Surveys in Geophysics No. 115, Aug. 1959.

9. Öpik, E.J.: The Masses of Meteors. Memoires de la Societe Royale des Sciences de Liege, 4th Series, no. 15, 1955, pp. 125-146.

10. Reismann, H.; Donahue, J. D. ; and Burkitt, W. C. : Multivariable Analysis of the Mechanics of Penetration of High Speed Particles. Martin-Marietta Corp., Interim Technical Progress Report No. NASA CR-04-5, NASA Hq. Contract No. NAS7-219, June 10, 1964.

11. Andriankin, I. and Stepanov, Yu. S.: Impact Penetration Depth of Meteoric Particles. Artificial Earth Satellites, vol. 15, Jan. 1964, pp. 45-53.

12. Herrmann, W. and Jones, A. H. : Survey of Hypervelocity Impact Information. Aeroelastic and Structures Research Laboratory, Massachusetts Institute of Technology, Report No. 99-1, Sept. 1961.

13. Dalton, C. C. : Theoretical Relationships for Meteoroid Puncture Experiments. NASA TN D-3244, Feb. 1966.

14. Smith, R. E. : Space Environment Criteria Guidelines for Use in Space Vehicle Development (1965 Revision). NASA TM X-53273, May 27, 1965.

15. Dalton, C. C. : Estimation of Tolerance Limits for Meteoroid Hazard to Space Vehicles... . NASA TN D-1996, Feb. 1964.

16. Dalton, C. C. : A Meteoroid Flux and Puncture Model for Near-Earth and Cislunar Space. Aero-Astrodynamics Research and Development Research Review No. 1, NASA TM X-53189, Oct. 1, 1964, pp. 96-99.

17. Bjork, R. L. : Meteoroids versus Space Vehicles. ARS J. , vol. 31, no. 6, June 1961, pp. 803-807.

18. Summers, J. S. : Investigation of High Speed Impact : Regions of Impact and Impact at Oblique Angles. NASA TN D-94, Oct. 1959.

REFERENCES (Continued)

19. Dohnanyi, J. S. : The Meteoroid Environment of the Apollo Program. TR-65-211-5, Aug. 30, 1965, Task 11, Contract NASw-417, Bellcomm, Inc., Washington, D. C.

20. Burbank, P. B. ; Cour-Palais, B. G. ; and McAllum, W. E. : A Meteoroid Environment for Near-Earth Operations. NASA TN D-2747, Apr. 1965.

21. Baumeister, T., Ed. : Mechanical Engineers' Handbook. McGraw-Hill Book Co., Inc., New York, N. Y., 1958.

22. D'Ans, J. and Lax, E. : Taschenbuch für Chemiker Und Physiker. Springer-Verlag, Berlin, West Germany, 1943.

23. The International Dictionary of Applied Mathematics. D. Van Nostrand Co., Inc., New York, N. Y., 1960.

24. Hastings, E. C., Jr. : The Explorer XVI Micrometeoroid Satellite Supplement III. . . . NASA TM X-949, Mar. 1964.

25. Naumann, R. J. : Pegasus Satellite Measurements of Meteoroid Penetration (Feb. 16- July 20, 1965). NASA TM X-1192, Dec. 1965.

26. Hastings, E. C., Jr. : The Explorer XVI Micrometeroid Satellite Description and Preliminary Results. . . . NASA TM X-810, Feb. 1963.

27. O'Neal, R. L. : The Explorer XXIII Micrometeoroid Satellite Description and Preliminary Results for the Period November 6, 1964 through February 15, 1965. NASA TM X-1123, Aug. 1965.

28. Haussler, J. B. and Benson, R. H. : Saturn SA-9/Pegasus A Postflight Trajectory. NASA TM X-53251, Apr. 30, 1965.

29. Haussler, J. B. and Benson, R. H. : Saturn SA-8/Pegasus B Postflight Trajectory. NASA TM X-53309, Aug. 2, 1965.

30. Haussler, J. B. and Benson, R. H. : Saturn SA-10/Pegasus C Postflight Trajectory. NASA TM X-53340, Sept. 30, 1965.

31. Aerospace Structural Metals Handbook, Volume I, Ferrous Alloys. Project No. 7381, Task No. 738103, Contract No. AF33(615)-1184, Air Force Materials Laboratory, Research and Technology Division, Air Force Systems Command, Wright Patterson Air Force Base, Ohio, Second Revision: Mar. 1965.

32. Berylco 25s, Alloy Digest, Engineering Alloys Digest, Inc., Upper Montclair, N. J., Nov. 1952.

33. Wikle, K. G. and Alspach, L. D. : Beryllium-Copper Alloys. Mach. Des., July 16, 1964. pp. 154-171.

34. Dohnanyi, J. S. : The Micrometeoroid Environment of Project Apollo. Report No. TR-65-211-2, Task 11, Contract NASw-417, Bellcomm, Inc., Washington, D. C. , Feb. 25, 1965.

35. Natural Environment and Physical Standards for the Apollo Program. Report No. M-DE 8020.008 B, SE 015-001-1 NASA-OMSF, Washington, D. C., Apr. 1965.

36. Orrok, G. T. : The Meteoroid Environment of Project Apollo. Bellcomm, Inc., Washington, D. C. Jan. 31, 1963.

AERODYNAMICS RESEARCH AT MSFC

September 16, 1965

by

James O. Ballance
Werner Dahm
M. J. Fisher
Dr. E. D. Geissler
F. R. Krause
R. E. Larson
M. F. Platzer
Homer Wilson

TABLE OF CONTENTS

LIST OF ILLUSTRATIONS

UNSTEADY AERODYNAMICS

by M. F. Platzer

LIST OF ILLUSTRATIONS

CONTENTS (Continued) . . .

BASE- HEATING RESEARCH REVIEW

by Homer Wilson

LIST OF ILLUSTRATIONS

RAREFIED-GAS DYNAMICS

by James O. Ballance

LIST OF ILLUSTRATIONS

TURBULENT FLUCTUATION MEASUREMENTS WITH THE CROSSED-BEAM METHOD

by F. R. Krause, M. J. Fisher, and R. E. Larson

LIST OF ILLUSTRATIONS

INTRODUCTION TO RESEARCH ACHIEVEMENTS REVIEW ON AERODYNAMICS RESEARCH

By

Dr. E. D. Geissler*

The subjects in this aerodynamics review are varied and cover such topics as prediction methods of drag and lift characteristics, jet penetration in water, base-flow phonomena, optimum nose shape design and several topics related to aerodynamic measurements. The paper by Dr. F. Krause discusses a very promising new optical cross-correlation method. If the expected results of this method materialize, the state of the art of some aerodynamic measurement techniques will be advanced markedly.

Dr. Platzer's contribution concerns some major research activities in unsteady aerodynamics, a field which represents still several ticklish problems for the Saturn program (in particular, aerodynamic noise and ground wind oscillation). Mr. Homer Wilson reports on aerothermodynamic research studies, primarily base heating, which is not yet in a very satisfactory shape in spite of substantial experimental efforts. This is particularly true when it is necessary to predict new configurations.

A final paper by Mr. Jim Ballance gives a short discussion of studies on rarefied gas dynamics - a topic which, while not yet so prominent in producing engineering headaches for the designers of space vehicles, will undoubtedly be of growing concern with extended stay time in very high altitudes and which especially poses many unsolved questions concerning instrumentation.

The activities reported are all carried out with participation and supervision of personnel of the Aerodynamics Division, even though a major share is done by contractors in Government and industry. It is hoped that these presentations will succeed in impressing the reader with the scope and importance of aerodynamics research in space-vehicle design and will also illustrate the particular flavor of applied aerodynamic research which is in close connection with the development of space vehicles. Problems are stimulated by the need for practical answers and sometimes by results from flight tests rather than selected according to their academic appeal. The justification of aerodynamic research facilities at the vehicle development agency, besides the larger aerodynamic research center facilities, stems from similar reasons and appears amply demonstrated by efficiency in tackling immediate problems.

Aerodynamics of space vehicles are relatively unglamorous compared with, for example, development of power plants. With increasing size of vehicles, the immediate importance of aerodynamic forces versus inertial effects decreases. Whereas the performance of an airplane is the result of a direct balance between aerodynamic drag and lift characteristics versus available thrust, the performance for a big space vehicle is mainly defined by propulsive inertial balance. However, it must be kept in mind that the efficiency of the structural design causes increasing concern with increasing rocket size and this structural design is strongly influenced by aerodynamic loads (i.e., bending loads, necessary control forces, aerodynamic noise, base heating). The efficient design frequently favors shapes which are not conducive to undisturbed flow characteristics (protuberances and separation including geometry) and requires prediction of flow not encountered in airplane work.

* Director, Aero-Astrodynamics Laboratory.

GENERAL REVIEW OF AERODYNAMICS RESEARCH

By

Werner Dahm

I. INTRODUCTION

The scope of aerodynamics research at MSFC is determined by the fact that, in accordance with the Center's mission, it has to serve space vehicle development, and especially launch vehicle development. Under this guideline, this work includes: (a) development or improvement of analytical methods, and their adaptation to our needs; (b) experimental investigations; (c) development and improvement of experimental methods and facilities; (d) development of instrumentation and probing tools; and (e) general design studies.

As a further guideline, tasks which do not promise useful design applications within a period of about 5 years are considered beyond MSFC's scope. The majority of the tasks yield results which are applied within a much shorter period.

The following are some typical examples of our research work; some other areas will be covered in separate papers.

(a) Subsonic flow.

(b) Jet impact in water.

(c) Base-flow investigation.

(d) Effect of wall-to-total temperature ratio on hypersonic flow detachment.

(e) Variable porosity walls.

(f) Dynamic balance for Saturn forebody.

II. SUBSONIC FLOW

The aerodynamic characteristics of the Jupiter nose cone which are shown in Figure 1 are examples of the analytical work. This example is concerned with pressure and lift distribution on bodies of revolution in subsonic flow. The bodies which are dealt with always have a blunt base, a case which available theories could not properly handle. Therefore, a method was developed which consists of distributing singularities on the surface of the body, and using the special boundary condition that the rim-base pressure is equal to the base pressure, and that the local lift is zero. The base pressure cannot be given by inviscid theory, and must be known a priori; the zero-lift condition is an equivalent of the kutta-condition of wing theory, and reflects the fact that virtually no pressure difference can be maintained across the "dead air" of the wake.

Figure 1 compares analytical and experimental results on a blunt-nosed cone. A blunt-nosed cone was selected because a complete set of experimental data were available, and because the base effects are fairly pronounced. The zero-lift pressure distribution in the lower left corner coincides with the experimental results of Figure 1. This is also true for the lift distribution in the upper left corner of Figure 1. At this particular Mach number, lift and pressure over the rear 20 percent of the body are noticeably influenced by the base. As the Mach number decreases, the base influence extends further forward, and lift is lost on the rear of the body. The corresponding effects on the total lift and center of pressure can be seen on the 2 graphs on the right of Figure 1. Since the method correctly describes the flow field near the base including the effects of the base pressure, the effects of the rocket jets on the vehicle stability can be estimated once the base pressure with jets on is known.

Figure 2 shows another example of the application of this method in that it depicts the drag of cones with tip half angles from 15° to 90° as function of the base pressure. The experimental points were obtained from a water tunnel, where the base pressure is fixed by the cavitation conditions; therefore, the base pressure coefficient can be varied. Agreement between analyses and experimental results is very good. Closer inspection shows that the total drag varies less than the base drag, reflecting again the forward effect of the base pressure. Incidentally, the analysis yields a correct description of the major part of the cavitation bubble. This result is of interest to submarine applications; to us, it is only an interesting by-product.

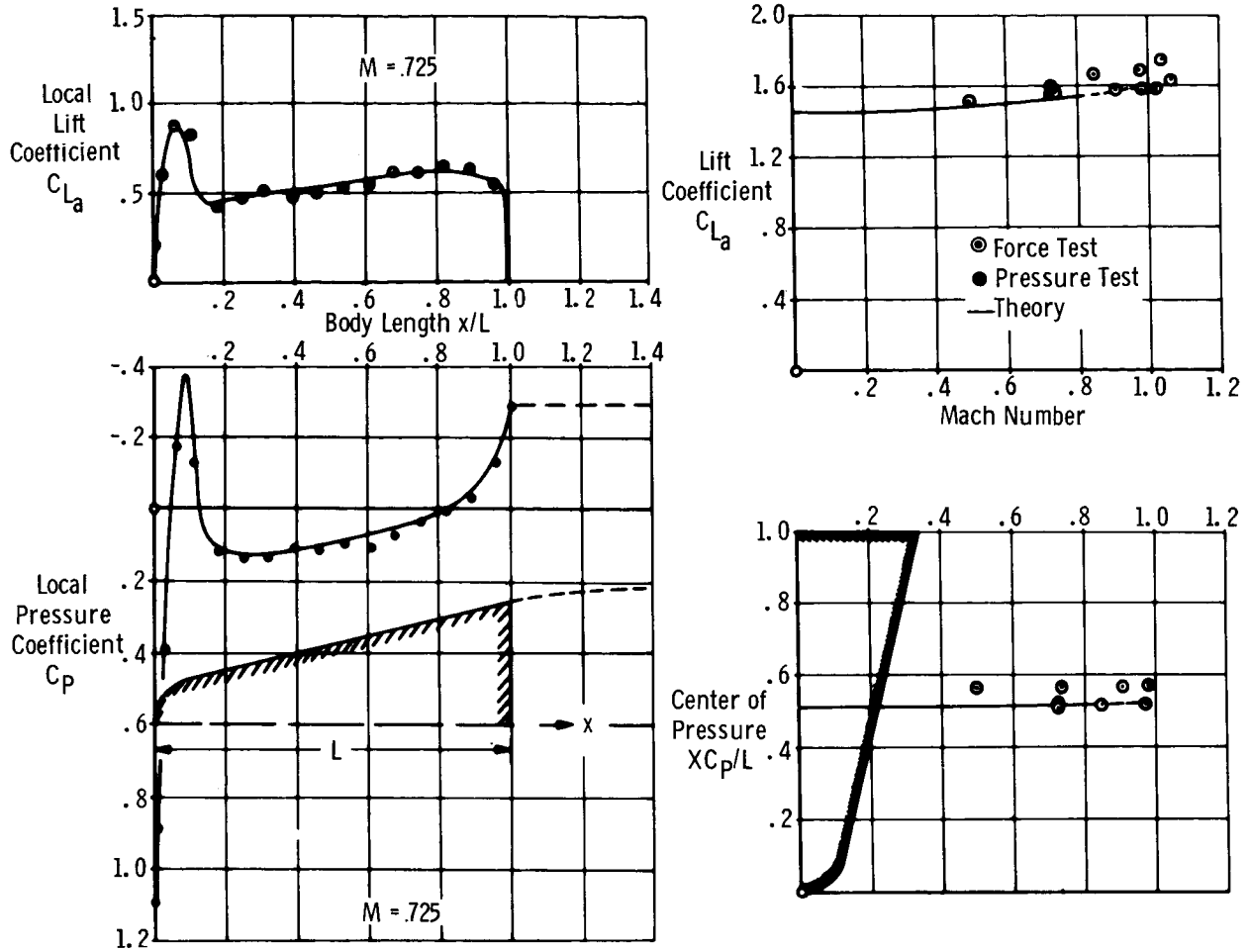

FIGURE 1. PRESSURE DISTRIBUTION ABOUT A JUPITER NOSE CONE

III. JET IMPACT IN WATER

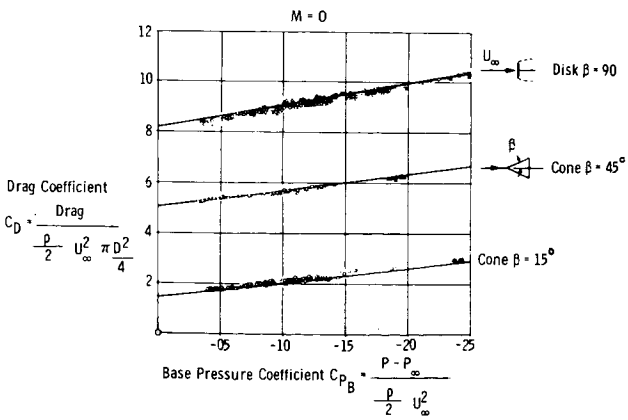

FIGURE 2. DRAG COEFFICIENT OF CONES OF DIFFERENT APEX AS A FUNCTION OF THE BASE PRESSURE COEFFICIENT

Jet penetration into water represents another example of our analytical work (Fig. 3). There are a number of reasons why launch facilities should be placed in the offshore waters such as launch-site real estate requirements. In this case the rocket jets would be discharged into the water, and it is necessary to know how deeply they penetrate. Scale-model simulation is practically impossible (it would require testing in a low-pressure chamber, or on a rocket sled under controlled, high acceleration). Therefore, the question has been attacked by composing a simple, approximate model of the process, and by checking the validity of this model with the results of small-scale jet tests. The model which was used was the well-known variation of the impact pressure of turbulent free jets with the distance downstream of the nozzle exit, and the fact that: (a) the penetration depth must correspond to the local impact

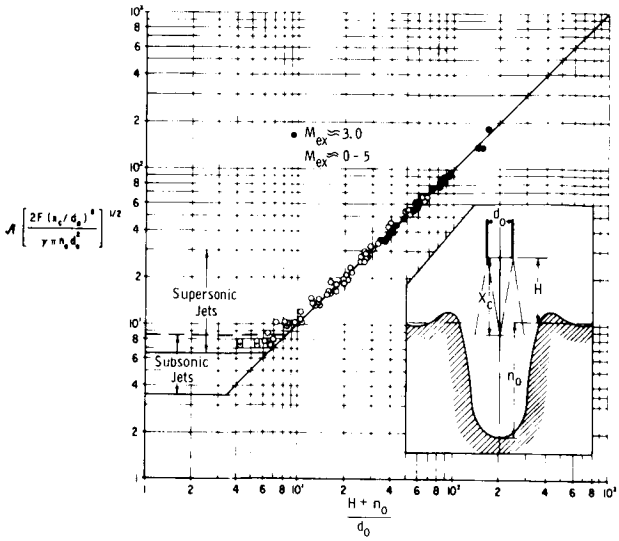

FIGURE 3. PENETRATION DEPTH OF SUB AND SUPERSONIC JETS IN WATER

pressure of the jet; and (b) the buoyancy of the cavity volume should equal the thrust of the engine. Figure 3 shows the correlation of a sizeable number of experiments with hot and cold subsonic and supersonic jets, using the resulting relations. The abscissa represents the distance of the apex of the cavity from the nozzle exit. The ordinate contains the thrust F, the specific weight of the liquid γ, the jet diameter d, the length of the inviscid jet core x_c, the penetration depth n_o, and a Mach number function. The horizontal lines correspond to cases where the inviscid core of the jet hits the bottom of the cavity. The inclined line corresponds to cases where $H + n_o > x_c$, i.e., where the "inviscid core" of the jet no longer reaches the bottom of the cavity. The correlation of the data in Figure 3 shows inherently that the presence of the water has essentially no effect on the impact pressure profile of the jet. The meaning of these data may be illustrated by an application to the F-1 engine.

F-1 engine:	H	n_o
	0	160' = 50 m
	100' = 30.4 m	93' = 28 m

For closely clustered jets, the penetration depth is somewhat larger than for single jets and can be estimated from a model test of the impact pressure profile in free air.

IV. BASE FLOW INVESTIGATION

The various base-heating problems encountered in high speed reentry as well as from our engine jets have, for a long time, aroused our curiosity about what really goes on in the so-called "dead-air zone" at the base. These processes have been studied on a two-dimensional, blunt based wing model at M = 3 with a turbulent boundary layer. Figure 4 shows a shadowgraph picture of the base area of this model. The white rectangle on the left is the rear end of the model, 15 inches (37.1 cm) high. The traces of the boundary layer, the Prandt-Meyer fan, the free shear layers, the tracking shocks, etc. can also be seen. Heat transfer and pressure distribution tests have been made on the base plate. The recirculation field, the free shear layers, and the base plate boundary layer have been probed with total pressure and temperature probes, wind vanes, an interferometer, and hot-wire anemometers. The lower part of Figure 4 shows the density and distribution at zero heat flux, taken from an interferometer test. The flow in the recirculation zone was found to be extremely turbulent, with $\sqrt{u'^2} = 0(\bar{u})$. The wind-vane tests of the mean velocity directions, shown by the arrows in the upper parts of Figure 4, deteriorated near the model centerline, indicating large outward flow angles rather than the required direction parallel to the centerline. The presumed cause is the high level of turbulence combined with strong shear flow effects. The main resistance to the heat transfer was found vested in a very thin base plate boundary layer, about 0.06 inches (0.152 cm) thick; the free shear layers played only a minor role. Outside of this base boundary layer, the total temperature is constant throughout the recirculation zone and the inner part of the shear layers. The base boundary layer is unlike any ordinary boundary layer. Its temperature profile seems to consist essentially of two straight lines, an outer one of small gradient dt/dx, and an inner one with steep gradient, which corresponds to the molecular heat transfer and reflects the existence of a laminar sublayer whose thickness is 0.005 inch (0.0127 cm). The cause of this peculiar profile is believed to be the extreme turbulence level of the recirculation zone. Figure 5 shows the effect of the base plate temperature on T_b, the total temperature in the recirculation zone. T_b is seen to be very little affected by the base plate temperature T_w. dT_b/dT_w indicates the distribution of the resistance to the heat flux between the free shear layers and the base boundary layer.

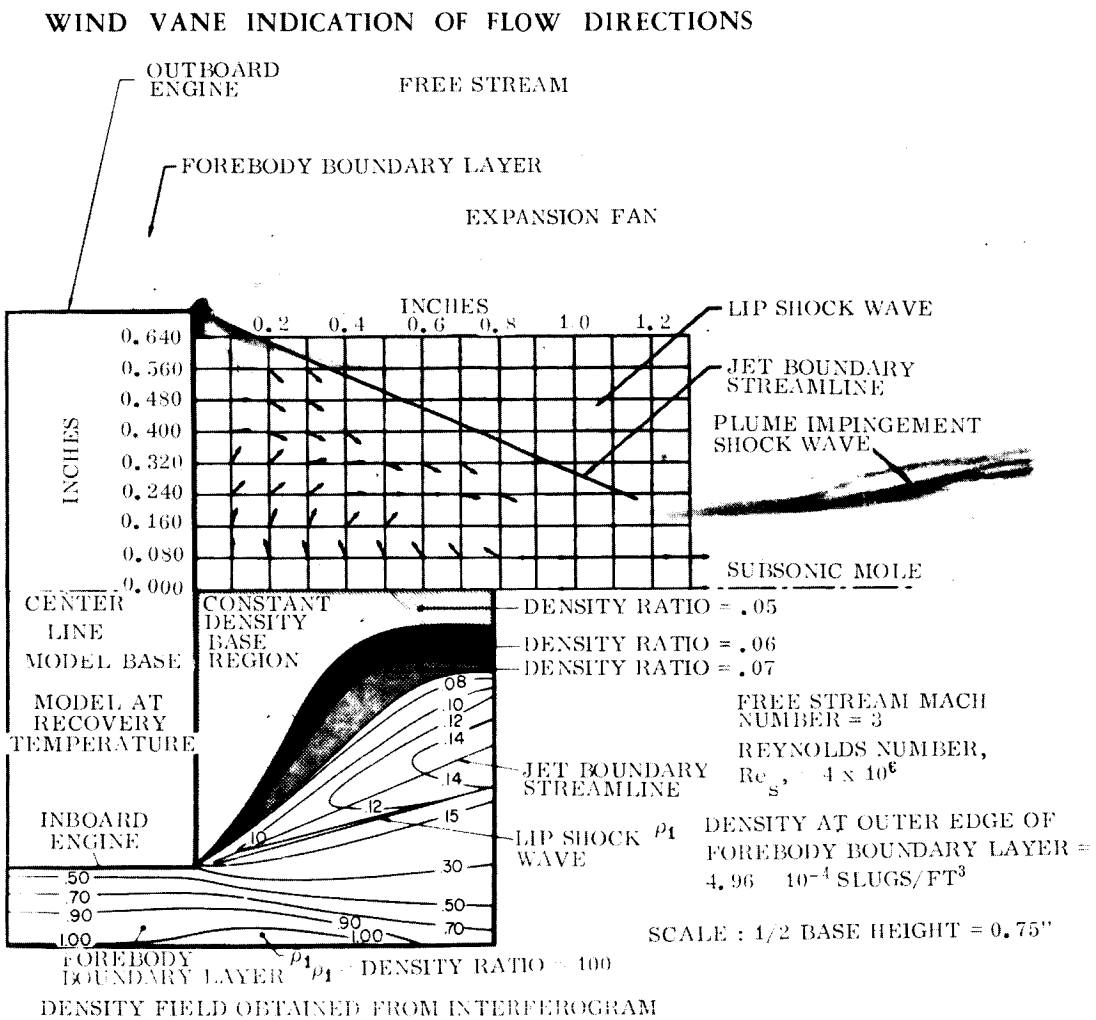

FIGURE 4. RECIRCULATION ZONE FLOW FIELD

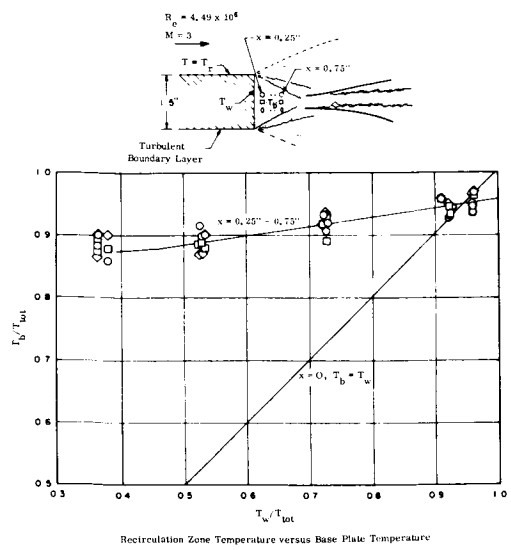

FIGURE 5. TWO-DIMENSIONAL BASE FLOW

V. EFFECT OF WALL-TO-TOTAL TEMPERATURE RATIO ON HYPERSONIC FLOW DETACHMENT

To assess factors that have to be observed for proper wind-tunnel simulation, the wall-to-total temperature ratio was varied in a wind-tunnel test of a Saturn forebody model at a Mach number of 6. Figure 6 shows schlieren pictures of the model at T_w/T_o = 0.88 and 0.22, demonstrating differences of flow detachment on the escape rocket-vehicle nose combination. Figure 7 shows the effect of T_w/T_o on the drag coefficient. At T_w/T_o near 1, the flow is fully detached and the drag is low. As the wall temperature decreases, the flow detachment recedes, increasing C_D, until the flow is fully attached and C_D has reached

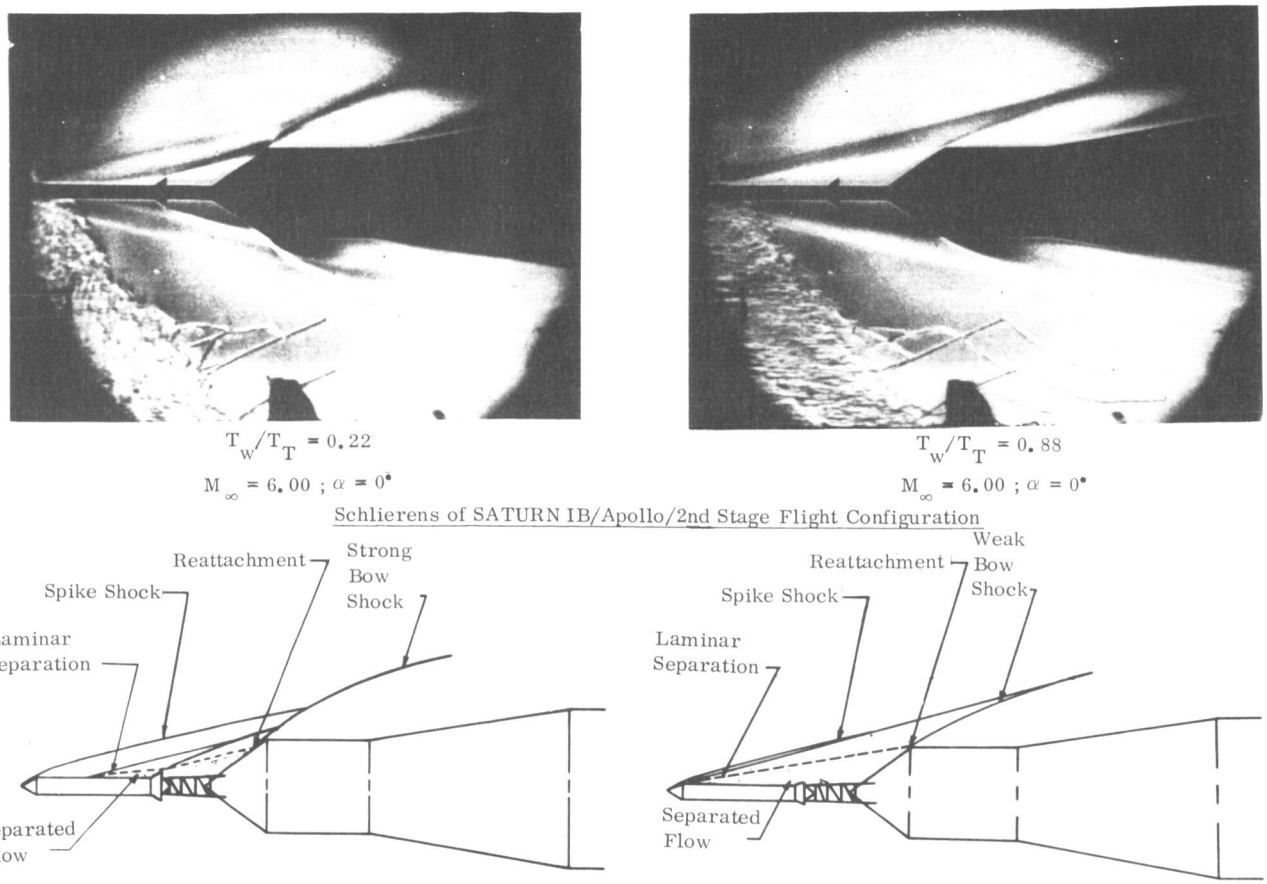

Effect of Temperature Ratio (Tw/T_T) on the Aerodynamic Flow Fields for Trajectory Reynolds Number Conditions

$Re_{Dia} = 0.22 \times 10^6$ (Trajectory) ~ D_{Ref} = 257"

FIGURE 6. SCHLIEREN PICTURES OF THE MODEL AT T_w/T_o = 0.88 AND 0.22

its maximum. A similar increase of C_D is obtained by a moderate increase of the Reynolds number. Therefore, it is believed that the observed reaction of the flow to T_w/T_o is caused by effects of the temperature ratio on boundary layer transition. The results indicate that under proper circumstances T_w/T_o must be observed as a similarity parameter.

VI. VARIABLE POROSITY WALLS

The MSFC 14 × 14-inch (35.56 × 35.56-cm) Trisonic Wind Tunnel uses a transonic test section with perforated walls. Use of perforated walls to reduce the wall interference is an accepted practice. Figure 8 shows a typical test section of this type. Normally, one fixed type of wall perforation is used throughout the transonic range, rather than perforations adapted individually to each Mach number. The price for this simplification is a reduced data accuracy. Our Facilities Branch has, therefore, developed walls of variable porosity (Fig. 9). They permit a change of the porosity by simply moving one of the two wall plates. The result is illustrated by the next two graphs. Figure 10 shows a cone-cylinder pressure distribution with fixed-porosity walls set for good average cancellation at $1.0 \leq M \leq 1.3$; Figure 11 shows the measured pressure distribution on the same body with our variable porosity walls set for optimum cancellation at this Mach number.

Outside agencies are becoming interested, i.e., LeRC, AEDC.

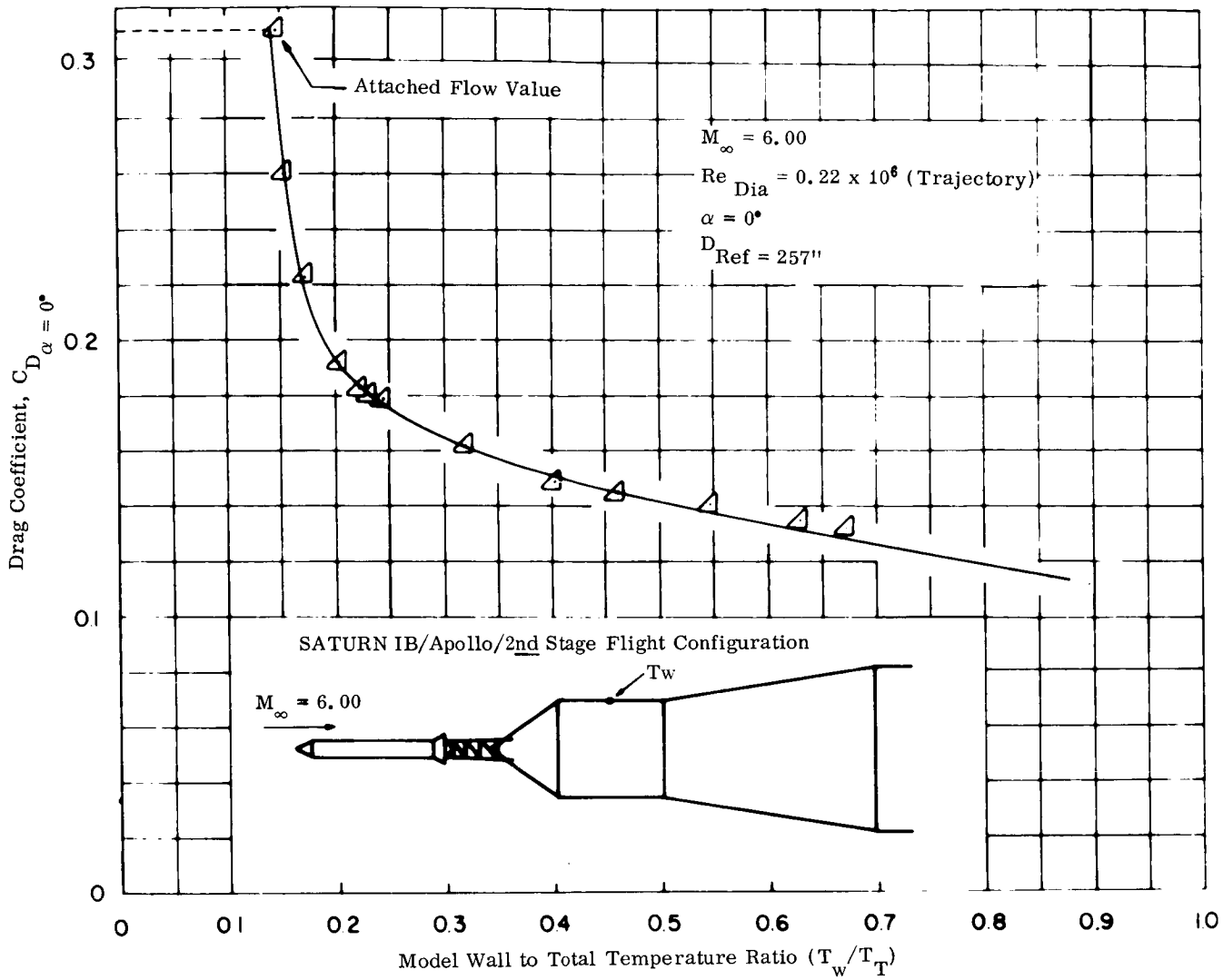

Variation of Drag Coefficient with Temperature Ratio (T_w/T_T) for Trajectory Reynolds Number Conditions

FIGURE 7. THE EFFECT OF T_w/T_o ON THE DRAG COEFFICIENT

VII. DYNAMIC BALANCE FOR SATURN FOREBODY

The aerodynamically unfavorable nose shape of the Saturn vehicles may give rise to dynamic bending instabilities. To perform wind-tunnel tests on these effects, a sting-mounted dynamic balance (Fig. 12) was designed. The balance forms an integral part of the model since its frame supports and stiffens the light external shell. This balance permits measurements at preselected frequencies ≤ 100 Hz, angles of attack, and amplitudes of ± 2½ degrees about the center of rotation. The frequencies are limited by stresses in the escape tower of the model. Preliminary tests in the transonic range proved that low internal damping was achieved. The aerodynamic damping is 70 to 85 percent of the total damping measured. The balance requires only simple electronic equipment, and permits high acceleration due to its ample torque and power.

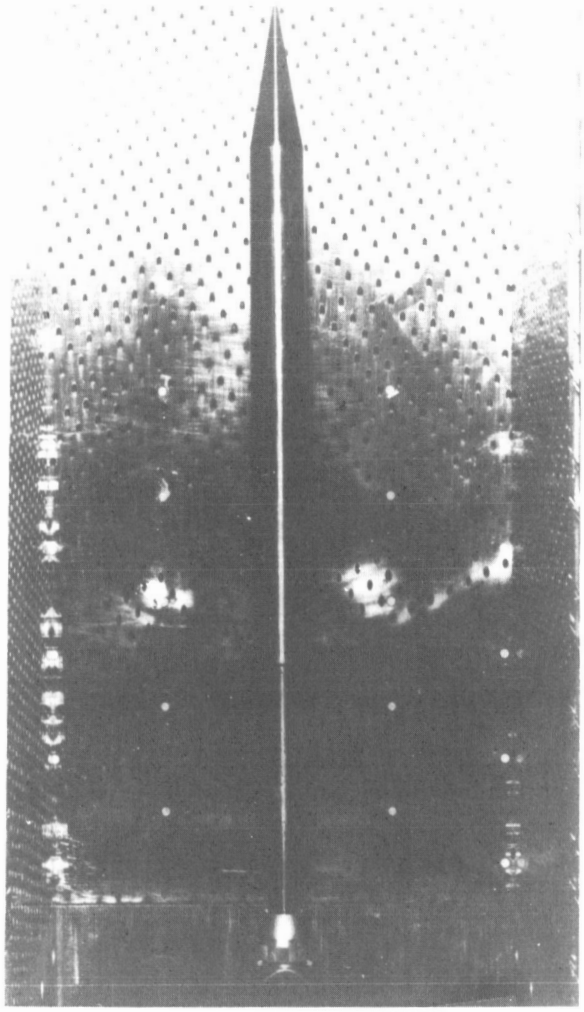

FIGURE 8. PHOTOGRAPH OF 20° CONE-CYLINDER IN TUNNEL

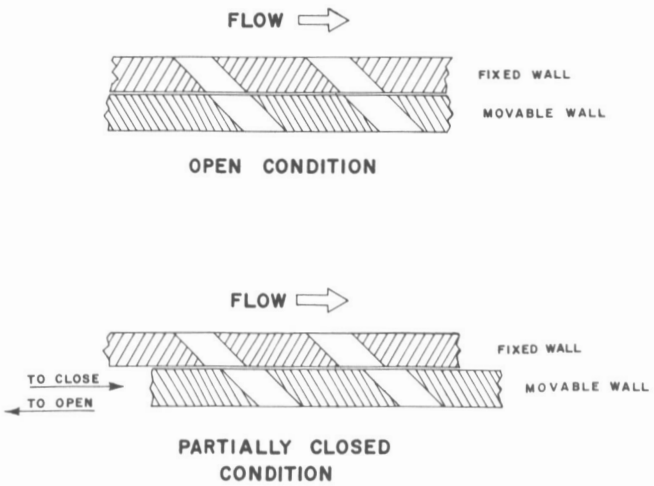

FIGURE 9. SKETCH OF VARIABLE POROSITY CONCEPT

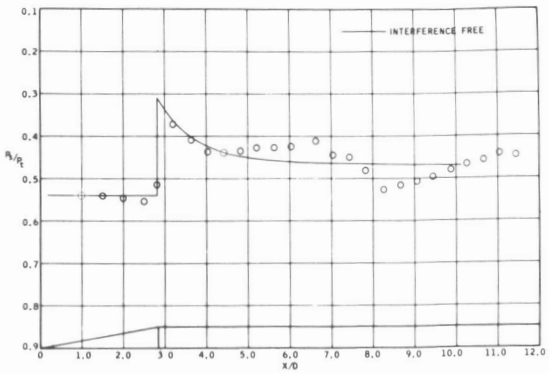

FIGURE 10. CONE-CYLINDER PRESSURE DISTRIBUTION AT M = 1.10 WITH A FIXED TUNNEL WALL POROSITY OF 7.5 PERCENT WITH 60° SLANTED HOLES

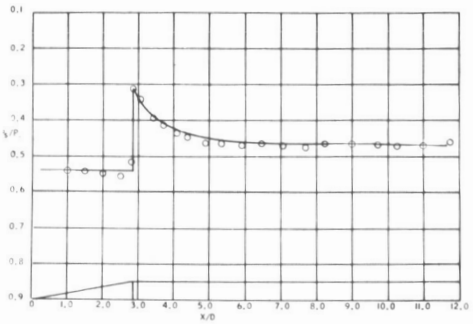

FIGURE 11. CONE-CYLINDER PRESSURE DISTRIBUTION AT M = 1.10 WITH VARIABLE POROSITY WALLS SET AT 1.6 PERCENT WITH 60° SLANTED HOLES

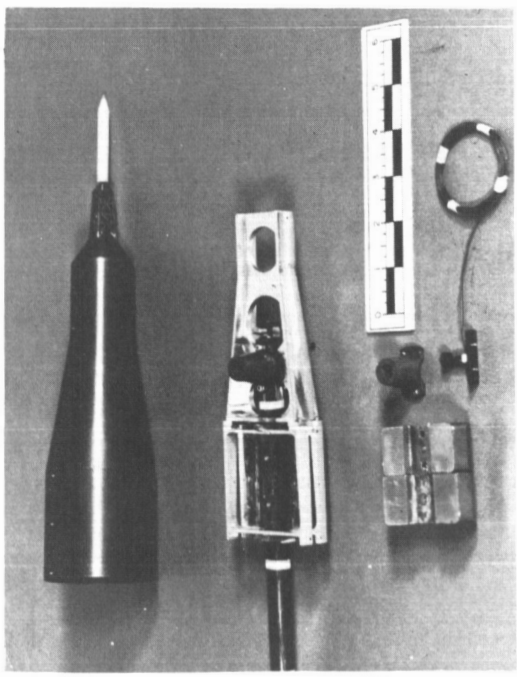

FIGURE 12. STING, MOUNTED DYNAMIC BALANCE

UNSTEADY AERODYNAMICS

By

M. F. Platzer

SUMMARY

This study briefly describes some of the problem areas in the Saturn launch vehicle development program that are related to unsteady phenomena. The two principal types of unsteady phenomena are self-excited phenomena and externally excited phenomena. Self-excited phenomena consist of panel flutter, body flutter, and fin flutter. Studies conducted in this area show that strong influences are exerted by the boundary layer. Concurrently, studies are being made to calculate the nonlinear and the linearized inviscid flow over pulsating and stationary wavy-walled surfaces.

The following three methods have been initiated for predicting aerodynamic damping: a linearized unsteady potential equation based upon a generalized Adams-Sears iteration process; a linearized method of characteristics solution for slowly oscillating pointed bodies of revolution that are of arbitrary profile and that are in supersonic flow; and a nonlinear method of characteristics solution.

Externally excited phenomena consist of buffeting loads, noise problems, and meteorological environment, such as wind gusts and atmospheric turbulence. Research to determine the power-spectral characteristics of various buffeting regions is in process. Theoretical studies are also being made on the relative contribution of regions of high-entropy production in the exhaust stream to the overall intensity, propagation, and directivity characteristics of the radiated acoustic energy.

I. INTRODUCTION

Unsteady aerodynamics are airflows that are time dependent and that may produce a dynamic response of the vehicle structure or control system. A characteristic feature of these response problems is that comparatively small aerodynamic forces may produce a very large or even catastrophic dynamic response. Aircraft wing flutter and the Tacoma Narrows Bridge failure are typical examples.

Unsteady phenomena can be divided into the general classes of self-excited and externally-excited phenomena. Self-excited phenomena shall consist of:

(a) Panel flutter.

(b) Body flutter.

(c) Fin flutter.

Externally excited phenomena shall consist of:

(a) Buffeting loads.

(b) Noise problems.

(c) Meteorological environment, such as wind gusts and atmospheric turbulence.

The primary objective of this study is to describe the efforts to provide an accurate description of unsteady aerodynamic forces to be used to furnish input information to the structures' and control systems' designer. No established procedures exist for determining an unsteady aerodynamic environment in connection with space vehicles or missiles. Therefore, this study is primarily of a research nature. However, these research results should be converted into useful design information as soon as possible.

II. PANEL FLUTTER

Panel flutter is the self-excited oscillation of a panel in a flow under the action of aerodynamic forces generated by the panel motion. The possibility of panel flutter was suspected in the early phases of the V-2 development. Since then, experiments have shown conclusively that flutter of surface skin panels can exist. Wind-tunnel tests showed that a traveling, wave-type, flutter condition caused panel failure within a period of a few seconds [1]. Recently, panel flutter occurred on the X-15 airplane as shown in Figures 1 and 2. In general, structural nonlinearities tend to limit the flutter amplitudes and, therefore, cause the modes of structural failure to be related to

fatigue rather than to the explosive fracture of the skin surface. However, it is quite dangerous to regard panel flutter only as a fatigue problem. Tests of the corrugation stiffened X-15 panels, e.g., revealed that flutter was very sudden and very severe. The panels failed unless flutter was stopped within a period of a few seconds.

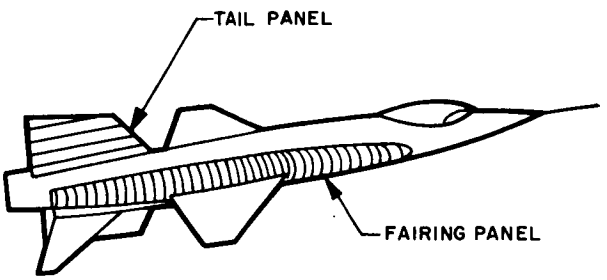

FIGURE 1. REGIONS OF X-15 RESEARCH AIRCRAFT AFFECTED BY PANEL FLUTTER

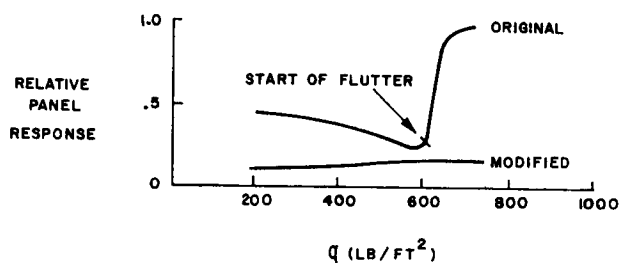

FIGURE 2. VARIATION OF PANEL-RESPONSE ENVELOPE WITH DYNAMIC PRESSURE OBTAINED FROM FLIGHT MEASUREMENTS ON AN X-15 SIDE-FAIRING PANEL

For this reason, it was considered necessary by the Aero-Astrodynamics and the Propulsion and Vehicle Engineering Laboratories to test the hat sections of the Saturn-IC stage. These tests, which were carried out by Boeing personnel in the Ames Research Center (ARC) 2- and 11-foot (0.61- and 3.35-m) tunnels, demonstrated the strong influence exerted by the boundary layer.

Theoretical flutter calculations are based upon inviscid linearized flow theory. Only recently has the need for taking into account the effect of the viscous boundary layer been recognized. For this reason, the Unsteady Aerodynamics Branch has initiated a cooperative research program with ARC and Georgia Institute of Technology to study the influence of the boundary layer on panel flutter. A decision was made to first explore the stationary flow over wavy-walled surfaces for varying boundary layer thicknesses. The first test in this program was scheduled for January 1966 at the ARC 2-foot (0.61-m) tunnel. The Mach number range to have been explored was $0.8 < M < 1.6$. Concurrently, theoretical inhouse studies are being carried out to calculate nonlinear and linearized inviscid flow over pulsating and stationary wavy-walled surfaces [2].

III. AERODYNAMIC-DAMPING STUDIES

As a result of the increased flexibility of the launch vehicles in the Saturn class, it has become necessary to investigate the aerodynamic damping characteristics of these vehicles during flight in the first three bending modes. Theoretical approaches to predict the aerodynamic damping are especially important because the simulation of elastic vehicle response in a wind-tunnel test is very complicated, and the results of this expensive test may be of limited value because of the wind-tunnel noise and the model-mount interference. Another factor in favor of the theoretical approach is that the elastic model usually necessitates a lead time of 1 year. Consequently, the test results become available when the vehicle design has been frozen.

For these reasons, the Unsteady Aerodynamics Branch tried to formulate theoretical approaches to predict the aerodynamic damping. These theoretical approaches had to be based upon inviscid attached flow concepts in order to make the problem mathematically tractable. So far, the following results have been obtained:

(a) A solution of the linearized unsteady potential equation has been worked out based upon a generalized Adams-Sears iteration process. This work is now complete [3] and Figure 3 shows one result that demonstrates the influence of body shape and Mach number upon the pitch damping coefficient.

(b) A linearized method of characteristics solution is presently being investigated for slowly oscillating pointed bodies of revolution that are of arbitrary meridian profile and are in supersonic flow. This method is an extension of the Oswatitsch-Erdmann characteristics method. Preliminary results for the steady case show a wide applicability [4].

(c) A nonlinear method of characteristics solution is being investigated by the Massachusetts Institute of Technology (MIT). This approach is based upon the superposition of small time-dependent angle of attack perturbations on a nonlinear axisymmetric flow field that is determined by the method of characteristics. Good results have been obtained for the oscillating cone [5].

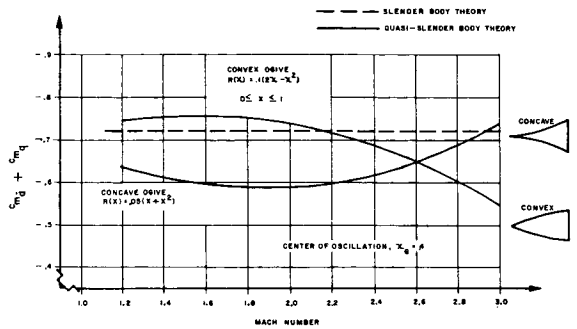

FIGURE 3. EFFECT OF MACH NUMBER ON FIXED AXIS DAMPING IN PITCH MOMENT COEFFICIENT FOR CONVEX AND CONCAVE PARABOLIC OGIVE OF THICKNESS RATIO 0.1

Calculation of damping characteristics, which are based upon attached flow concepts, are not sufficient for most of the current launch vehicle configurations. Blunt nose cones and steep interstage flares, which have become characteristic of space boosters, produce large regions of flow separation that dominate the aerodynamic loading over the vehicle in the transonic and the supersonic speed range, as shown in Figure 4. As a result, it has become necessary to take into account separated flow effects upon aerodynamic damping. The success of an analytical and experimental method of dynamic analysis of the Atlas-Able launch vehicles [6] suggested a possible adaptation to the Saturn launch vehicle configuration. This method is based upon the assumption that the total lift force on any part of the vehicle consists of the following components:

(a) Local lift, which is lift due to local motion at time t.

(b) Induced lift, which is lift induced by the wake created at the nose at time t-Δt.

This suggests that local lift is always in phase with the lateral vehicle motion and that induced lift is out of phase by the time lag Δt. These two assumptions make it possible to determine aerodynamic damping from static wind-tunnel tests thus eliminating expensive elastic model tests. This procedure is being applied to the various Saturn launch vehicle configurations.

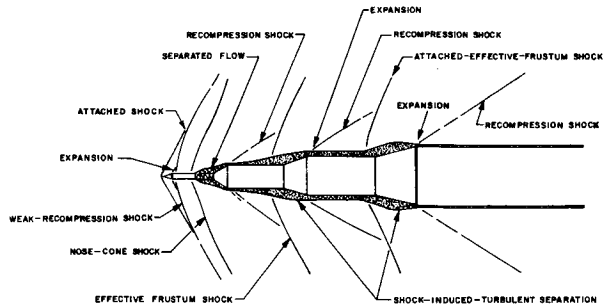

FIGURE 4. FLOW FIELD ABOUT TYPICAL SATURN SERIES VEHICLE

IV. BUFFETING

Buffeting is the pressure oscillation caused by separated flow. The launch vehicle interstage areas may cause intensive fluctuating pressures, and, consequently, severe structural loads as shown in Figure 5. In the separated flow region shown in Figure 5, a slowly circulating reverse flow exists, overlain by a free-shear flow. The highest fluctuating pressure levels are found to occur at the point of flow separation and reattachment. Current research is devoted to the determination of the power-spectral characteristics of these buffeting regions. The Unsteady Aerodynamics Branch has several research programs to analyze this problem. Perhaps the most significant program in this field is the protuberance wind-tunnel test which is being carried out in cooperation with ARC. This program is currently in the data reduction process and the results should be available in the near future.

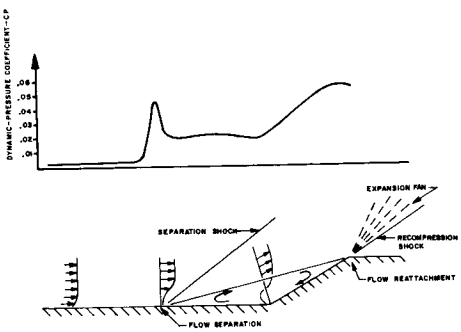

FIGURE 5. TYPICAL FLUCTUATING PRESSURE ENVIRONMENT FOR VEHICLE INTERSTAGE TYPE GEOMETRIES

V. ENGINE-GENERATED NOISE

Research in the field of engine-generated acoustics has been directed towards the determination of the predominant noise generation mechanisms in high-temperature, rocket exhaust flows. Present investigations include theoretical studies of the relative contribution of regions of high entropy production in the exhaust stream to the overall intensity, propagation, and directivity characteristics of the radiated energy. This work is being supplemented by experimental rocket exhaust studies using a substitute gas to simulate the predominant flow characteristics of the H-1 engine at a considerably lower temperature, thus allowing measurements to be made in the flow.

VI. GROUND-WINDS PROBLEM

A launch vehicle erected on the launch pad before liftoff is exposed to surface winds that may generate large dynamic loads under certain circumstances. Downstream from the body, a wake flow is created that is Reynolds number dependent and has characteristics which are difficult to describe mathematically. In certain cases, the well known Karman vortex street is obtained. At the higher Reynolds numbers, the vortex shedding is very dependent upon the type of flow in the vicinity of the body (laminar or turbulent boundary layer). Therefore, a distinction must be made between subcritical and supercritical flow regimes. Insufficient understanding of the mechanisms involved and lack of reliable calculation methods force most investigators to extract the aerodynamic forcing function from an analysis of the aeroelastic response of various launch vehicle configurations. The Unsteady Aerodynamics Branch has initiated an extensive wind-tunnel program on the different Saturn I, IB, and V configurations. Most of these tests are conducted at the Langley Research Center (LRC) and require aeroelastic models of about 5-percent scale. Unfortunately, for the Saturn V configuration, a full-scale Reynolds number cannot be simulated, thus introducing a further degree of uncertainty. Typical vehicle responses are shown in Figures 6 and 7. In both figures the vehicle base bending moment, because of steady drag, dynamic drag, and dynamic lift, is plotted versus the wind velocity. A typical noncritical response is shown in Figure 6, while a typical critical response due to dynamic lift at a specific wind velocity is shown in Figure 7.

The critical response is of primary concern to the vehicle designer since it may impose exceedingly high loads upon the vehicle. Unfortunately, the reason for the occurrence of such a critical response is little understood. The possibility for self-excited vibrations cannot be excluded at this time. Therefore, a cooperative research program between LRC, MSFC, and the Martin Company was formulated to investigate the aerodynamic forces on oscillating two-dimensional cylinders. These tests were conducted recently at LRC and the data are in the process

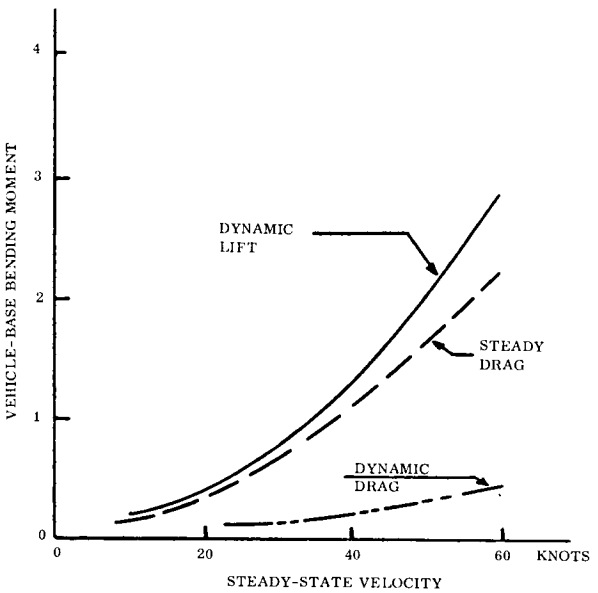

FIGURE 6. TYPICAL NON-CRITICAL RESPONSE

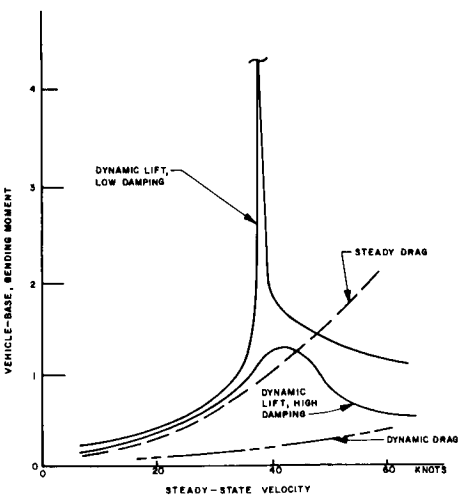

FIGURE 7. TYPICAL CRITICAL RESPONSE

of evaluation. This experimental program is being supplemented by an analytical studies program that should provide a better understanding of the basic flow-field characteristics.

VII. CONCLUSIONS

Unsteady aerodynamic effects present the launch vehicle designer with a series of important and challenging problems. Since these phenomena are little understood, a continuous and vigorous research effort is required.

REFERENCES

1. Hermann, R.: Private Communication. University of Alabama Research Institute, Nov. 1965.

2. Platzer, M.; Beranek, R.; and Saunders, L.: On Some Aerodynamic Aspects of the Panel Flutter Problem. 3rd Aero-Astrodynamics Research Review.

3. Platzer, M.; and Hoffman, G.: Quasi-Slender Body Theory for Slowly Oscillating Bodies of Revolution in Supersonic Flow. Proposed NASA TN (MSFC, Aero-Astrodynamics).

4. Sherer, A.: Analysis of the Linearized Supersonic Flow about Pointed Bodies of Revolution by the Method of Characteristics. LMSC/HREC TM 54/20-29, TM 54/20-46, TM 54/20-63.

5. Hsu, P. T.: Solution of the Supersonic Flow Field around an Oscillating Circular Cone. MIT Fluid Dynamics Research Lab. Report No. 64-5, Dec. 1964.

6. Woods, P.; and Ericsson, L.: Aeroelastic Considerations in a Slender, Blunt-Nose, Multi-stage Rocket. Aerospace Engineering, May 1962, pp. 42-51.

BASE-HEATING RESEARCH REVIEW

By

Homer Wilson

SUMMARY

The purpose of the studies described in this report is to gain more information related to the causes and control of heating problems. To help gain this information, an external flow facility was built to enable the Reynolds number to be varied by almost an order of magnitude; and at the same time, to provide a facility that would eliminate costly large-scale wind-tunnel tests. Data obtained from the external flow facility compared reasonably well with large-scale wind-tunnel tests. This facility allowed some limited Reynolds numbers on base heating to be determined. A similar but larger and more versatile facility has been proposed by MSFC.

This study also indicated that a flow field prevented the radiation of vehicles with clustered engine configurations from decreasing to near zero radiation as in single engine vehicles. The flow field results from an increasing altitude and decreasing ambient pressure causing the exhaust jets from the engines in a cluster configuration to expand and to impinge with the other jets in the cluster forming a shock wave. The shock waves force the exhaust gases back toward the base plate of the engine. The reverse exhaust gases will then flow radially outward between the nozzles into the atmosphere and may choke the engine at sufficiently high altitudes. This condition has caused severe heating on the Polaris and the center star areas of the Saturn vehicles.

For clustered LOX-H_2 upper-stage configurations, radiation may not be the predominant cause of heating, but it should be accurately computed since the stages fly a long period of time. In order to compute the radiation, the "band model" concept was used. To use this concept, it is necessary to know parameters such as spectral-line strength, spectral-line spacing and line half-width. Within the next year, all needed parameters are expected to be available.

Another problem studied was the dumping of combustibles along the vehicle or near the base area. If fuel-rich combustibles are entrained in the base region, large heating rates may occur. The results from the study show that upstream ejection of hydrogen can be accomplished without hazard of ignition or combustion by venting parallel to the surface through a perfectly expanded nozzle if it is displaced far enough from the vehicle to reduce hydrogen levels below flammability limits.

I. INTRODUCTION

The purpose of a research program in heating is to gain information which will improve the design of future space vehicles. The base heating problem on rocket vehicles is a combination of heating by convection and by radiation. For LOX-RP powered launch vehicles, radiation is high at sea level and decreases at higher altitudes (Fig. 1). The radiation at higher altitudes for single-engine vehicles like Jupiter decreases to near zero. Although the radiation

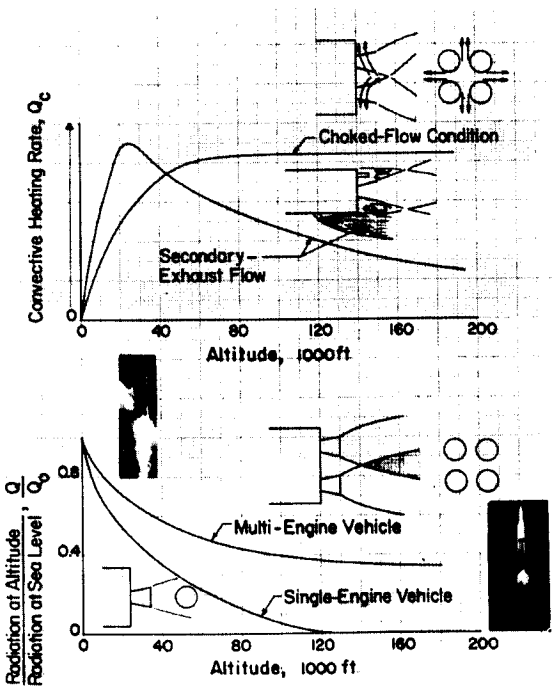

FIGURE 1. VARIATION OF RADIATIVE AND CONVECTIVE BASE HEATING WITH ALTITUDE FOR VARIOUS CONFIGURATIONS

of vehicles with clustered engine configurations is less at higher altitudes than at sea level, the impinging regions at higher altitudes apparently bring about a significant increase in the radioactive flux keeping the radiation of the vehicle from nearing zero. Upper stages powered by LOX-H_2 engines have little radiation, but the radiation should be accurately computed since the vehicles fly over a long period of time.

Convective heating for single-engine vehicles generally is small at all altitudes. For vehicles with clustered engine configurations, the impinging of the jets at high altitude sets up a recirculating flow field which causes large heating within the enclosed area.

Another problem to be reckoned with is the dumping of combustibles along the vehicle or near the base area. If fuel-rich combustibles are entrained in the base region, large heating rates may occur. These are usually a maximum in the transonic region and disappear above Mach 3 because of the absence of oxygen to support combustion.

II. SHORT-DURATION TECHNIQUE

Over the years, a wealth of flight and model data has been accumulated which was used as estimates of the thermal criteria for design purposes. Because these estimates have not been satisfactorily substantial, time has been spent on programs aimed at improving methods of generating design data and getting a better understanding of the problems. During early Saturn days, model data were obtained from scaled, long-duration model tests. This type of testing proved costly and complex, and generally provided data over a limited range of variables. About 4 years ago, the possibility of using other techniques for obtaining model data was explored and the short-duration technique was developed. This technique is illustrated in Figure 2.

By this technique, the propellants are stored in a pair of charge tubes and are contained by a pair of diaphragms or quick-acting valves at the end of each tube. When the diaphragms are ruptured, the gases flow into an injector, then into the combustion chamber where burning takes place. Ignition is usually by a spark plug. For high-altitude testing, the model is mounted in a vacuum tank. Testing time is determined by the time required for an expansion wave to traverse the charge tube (charge-tube length), the time required for the blast wave to travel to the tank walls and return, or the heating limitations of the model. Early results on a base plate indicate that thermal and pressure fields were established in $\frac{1}{4}$ to 1 millisecond and that several milliseconds of steady flow are available which is ample time to obtain the data.

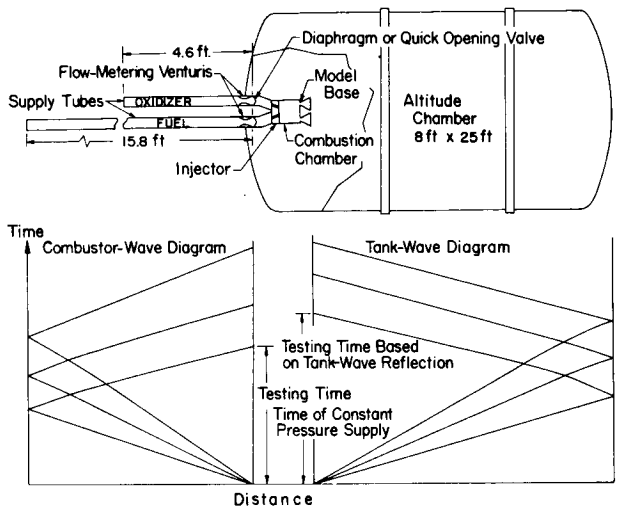

FIGURE 2. COMBUSTOR SCHEMATIC, SUPPLY TUBE-TANK WAVE DIAGRAM AND INSTALLATION

The short-duration technique has been used to obtain design data for S-IV, S-II, S-V, S-I, and Centaur stages. On a firing-to-firing basis, the short-duration technique is cheaper by an order of magnitude than the long-duration technique and provides data that compare reasonably well with long-duration model and high-altitude flight data. The big advantage of the short-duration technique is that many variables can be easily studied. The effects of engine deflection on base heating is shown in Figure 3a for a typical, five-engine configuration. The results show that on deflecting two outboard engines toward each other by 4 degrees the maximum heating rate increases by a factor of two. This is particularly important for design of the upper stages such as S-II.

Some effects of nozzle-wall temperature on base-heating rates are shown in Figure 3b. Increasing the nozzle-wall temperature from 80 to 1000° F (26.67 to 537.78° C) results in a significant increase in base-heating rate. This results from the fact that the low-energy exhaust gases that are reversed into the base have passed along the cooled nozzle-wall temperature.

The effect of a temperature step or discontinuity in the measurement of the film coefficient is shown in Figure 4a. Cooling the gage results in a large

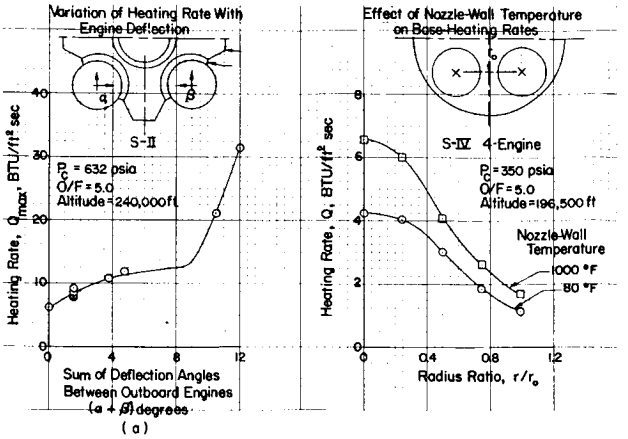

FIGURE 3. DATA OBTAINED USING SHORT DURATION TECHNIQUES OF VARIOUS ENGINE CONFIGURATIONS

increase in the film coefficient (almost a factor of two) as compared to a case where the gage temperature is equal to the plate temperature. This indicates that large errors may be present in our flight measurements where the copper-slug calorimeter temperature may be significantly different from that of the heat shield.

The effect of pressure of Reynolds number on base-film coefficient and recovery temperature is shown in Figure 4b. The initial portion of the curve shows that the film coefficient varies proportionally to the $\frac{1}{2}$ power of the pressure as would be expected for laminar flow, and the latter part of the curve shows that the film coefficient varies proportionally to the 4/5 power of the pressure as would be expected for turbulent flow. The base-recovery temperature varies proportionally to the 1/5 power of the pressure. The dependency of the recovery temperature on pressure or Reynolds number is brought about by the fact that the gases that get reversed into the base area are contained within the boundary layer of the nozzle, the state or energy level of which is primarily determined by the Reynolds number.

III. EXTERNAL-FLOW REYNOLDS NUMBER PROGRAM

In comparing model to flight data, where ambient flow effects are important, several discrepancies have occurred which seem to indicate that Reynolds number effects are present. Approximately 2 years ago, a program was initiated to build an external-flow facility which would enable the Reynolds number to be varied by almost an order of magnitude and at

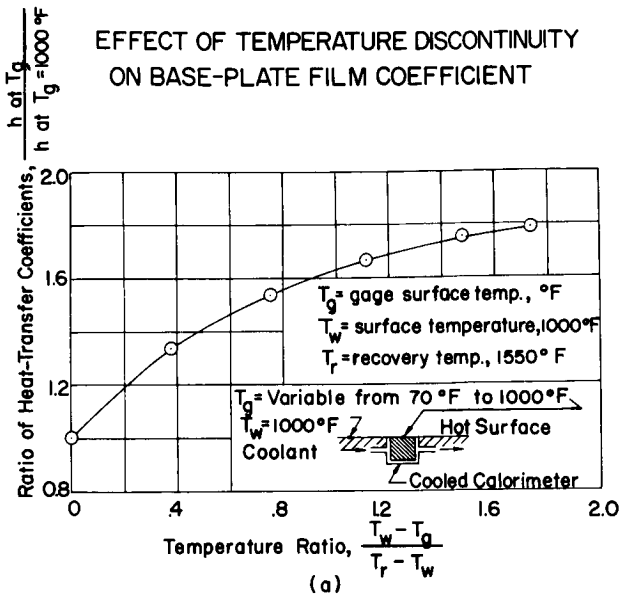

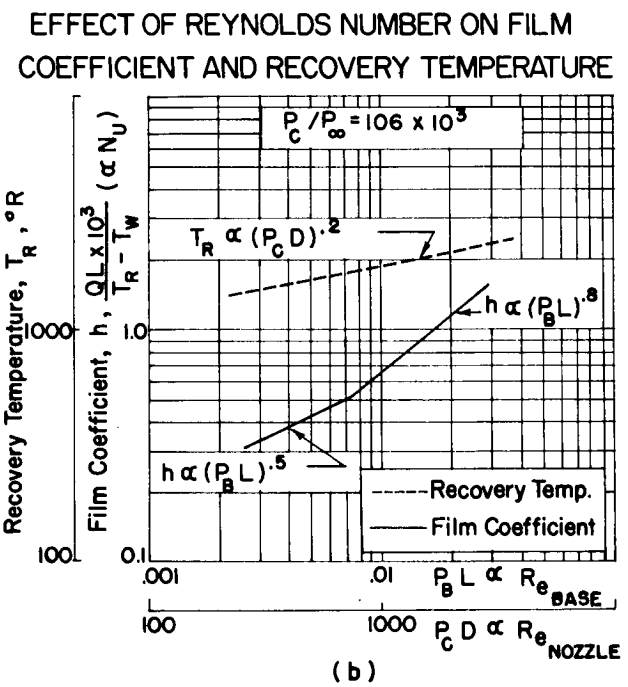

FIGURE 4. DATA OBTAINED WITH SHORT-DURATION TECHNIQUES

the same time provide a facility that would eliminate costly large-scale wind-tunnel tests. The facility has been developed and has been in operation for about 1 year (Fig. 5). It consists of a tube approximately 4 feet (1.22 m) in diameter and 30 feet (9.14 m) in length in which high pressure gas, 200 psi (1378951.44N/m^2) and lower is stored. A diaphragm retains the gas at the end of the tube. To the right of the diaphragm is the convergent-divergent nozzle which allows the Mach number to be varied. The flow is exhausted into a vacuum tank which is located on the far right of Figure 5.

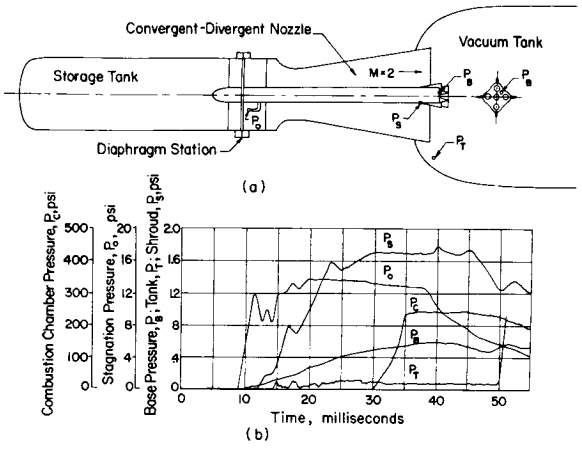

FIGURE 5. SCHEMATIC OF EXTERNAL FLOW FACILITY WITH SOME TYPICAL PRESSURE TRACES

To perform a test, the diaphragm is ruptured and a flow of a certain pressure level and Mach number in the nozzle is obtained for a few milliseconds. About the same time that steady flow is established in the nozzle, the model is fired and the test takes place. Hot and cold flow tests have been made in this facility. Figure 5 also shows typical traces from the early tests at a Mach number of 2.0. P_s is the shroud pressure just ahead of the base; P_o is the stagnation or tube pressure just downstream of the diaphragm; P_c is the combustion chamber pressure within the model; P_b is the typical base pressure trace; and P_t is the pressure within the vacuum tank. The large variation in P_t at approximately 50 milliseconds indicates the return of the blast wave and the end of the test.

The results show that for this length of storage tube approximately 20 milliseconds of constant-flow conditions are available for making tests. Because of the late firing of the combustor, only about 10 milliseconds were used. The storage tube and combustor supply tubes have been lengthened so that considerably longer testing time can be obtained.

Data obtained from the external-flow facility compared reasonably well with large-scale wind-tunnel tests. The external-flow facility has been built and put into operation for a cost of less than $75,000. By this facility, some limited Reynolds number effects on base heating were determined. This facility may reduce the number of, or even eliminate, costly wind-tunnel tests for Saturn base-heating studies. A similar but larger and more versatile facility has been proposed by MSFC and some feasibility tests for the facility have been made by MSFC.

IV. FLOW-FIELD VISUALIZATION

The flow field results from an increasing altitude and decreasing ambient pressure causing the exhaust jets from the rocket engines in a cluster configuration to expand and to impinge with the other jets in the cluster forming a shock wave. Figure 6a shows a sketch of the flow field. Because of the formation of the shock waves and the resulting pressure rise, a portion of the low-energy exhaust gases within the boundary layer of the nozzle wall and in the mixing layer around the periphery of the jets will not have sufficient energy to negotiate the pressure rise and will be forced back toward the base plate of the engine. The reverse exhaust gases will then flow radially outward between the nozzles into the atmosphere, or ambient flow, and may choke the engines at sufficiently high altitudes. This condition has caused severe heating on the Polaris and the center star areas of the Saturn vehicles.

Figure 6b is a schlieren photograph of the shock waves formed by the impinging jets. Some results from electron-beam density measurements on the short-duration S-IV four-engine model are shown in Figure 6c. The solid lines represent lines of constant density in the form of density ratio (ρ_b/ρ_c) where ρ_b is the ambient density in the reverse flow field and ρ_c is the density within the combustion chamber. The gas is hot nitrogen (2500° R) at a pressure of 200 psi (1378951.44N/m^2). The dashed lines represented the nozzle and the approximate plume impingement. The abscissa is the base radius and the ordinate is the number of inches downstream of the base plate. Starting at the centerline and proceeding toward the base plate, the density decreases which indicates an

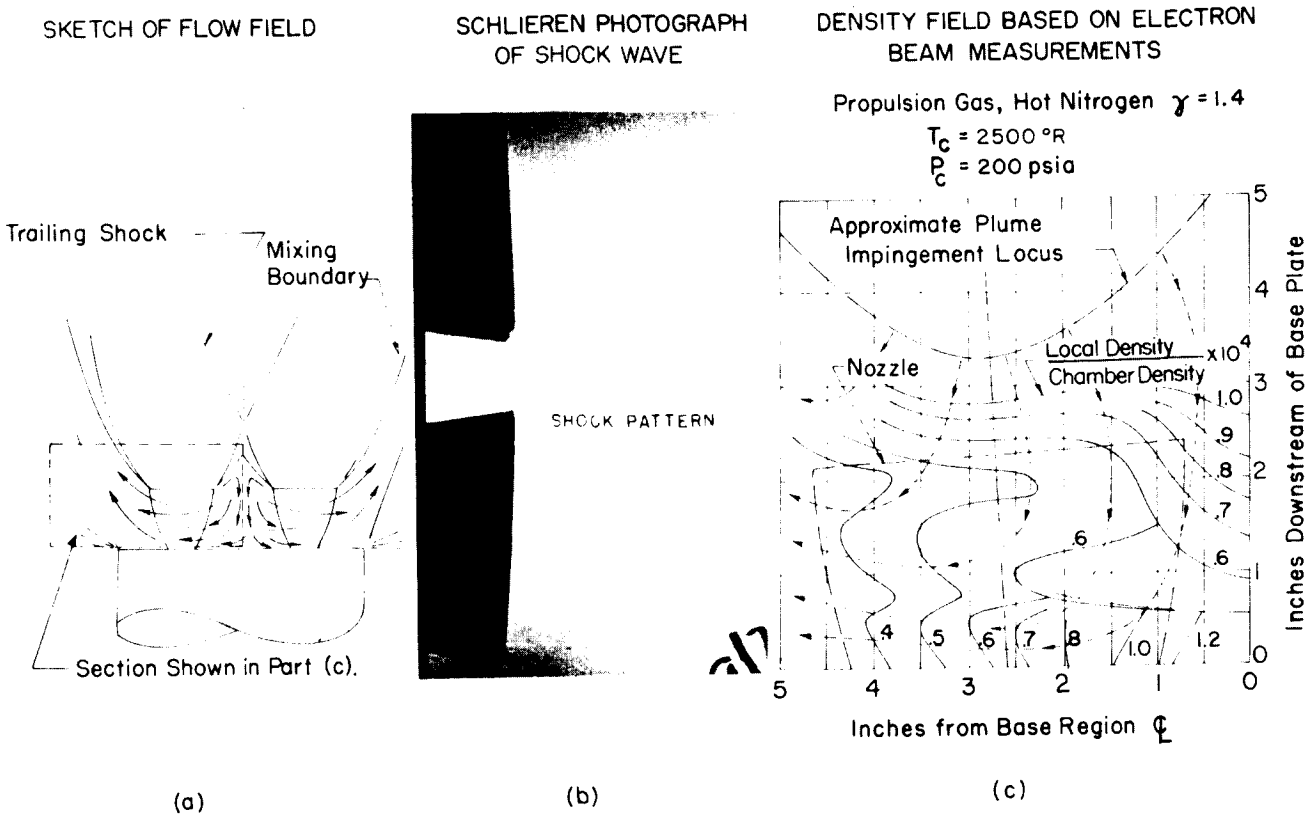

FIGURE 6. RESULTS FROM FLOW-FIELD, VISUALIZATION STUDY

accelerating flow field. A short distance above the base plate, a large increase in density occurs which indicates the presence of a shock wave. Moving farther from the base plate, the density decreases indicating an accelerating flow in that direction. This type of flow field has been studied and verified with conventional pressure instrumentation.

Only some of the initial results from the electron-beam tests are shown in Figure 6. Hardware has been assembled and an attempt at measuring temperature with the electron beam will be made in the near future.

An instrument for the measurement of local gas velocity using the optical Doppler technique is also under development. The Doppler frequency shift depends on the velocity of the moving particles and on the geometry of the scattering media. If the scattering geometry is fixed, measurement of the Doppler shift gives sufficient information to determine the velocity of the moving particles. This instrument has been built and velocity measurements have been made up to 150 feet per second (45.72 m/s). The instrument is presently being installed in a wind tunnel for measurements of Mach 3 to 5. This technique seems applicable also for gas-turbulence measurements, dynamic pressure transducer calibration, panel flutter studies, and many others.

V. RADIATION

As stated earlier, radiation is the main contribution to base heating for a properly designed LOX-RP first stage. For clustered LOX-H_2 upper-stage configurations, radiation may not be the predominant cause of heating, but it should be accurately computed since the stages fly a long period of time. In order to compute the radiation, the flow-field (velocity, pressure, temperature, composition, etc.) absorption data for radiating components and a radiant program for calculating the intensities must be known. Programs are in existence for calculation of the flow field from a single-engine configuration for frozen or equilibrium flow. Some rough estimates of the flow fields in the impinging regions are currently being used for design purposes. Recently, two programs have been started for computing the flow field for clustered configurations. One is a three-dimensional method of characteristics at Norair and the other is a finite difference scheme at General Dynamics/Convair.

Until some new programs were initiated, the techniques and data available to calculate the radiant heat from H_2O, CO_2, and CO used the total emissivity data of Hottel measurements during the late twenties and early thirties. These data could not be accurately extended to the range of low pressure high temperatures, and nonisothermal conditions existing in the fuels of current interest, RL-10, J-2, etc. It is possible to compute some of the data needed with existing high-speed computers, but this is difficult and would require an enormous amount of computing time. Therefore, the "band model" concept was used to describe the absorption coefficient for the radiating components. To use this concept, it is necessary to know such parameters as spectral-line strength, spectral-line spacing, and line half-width. Programs have been initiated and some results have been obtained for some of the band-model parameters needed. Within the next year, it is expected that all parameters needed will be measured so that radiation from present motors can be computable within the accuracy of existing flow fields.

Figure 7 presents some early results of the "band model" concept. The upper part of the curve compares experimental data with "band model" data for water vapor. The results indicate that the "band model" concept is relatively good. The graph in the lower left-hand corner compares the recent emission data of water vapor of GD/C (Ferriso and Ludwig) with Hottel's results. The results indicate that design data based on Hottel's results would underestimate heating rates. These results are supported by early experimental data. A comparison of the experimental absorption data for carbon with theory (Stull and Plass, modified for index of refraction) is shown in the lower right-hand graph. The results of the experimental absorption data are relatively good except at the lower wavelengths.

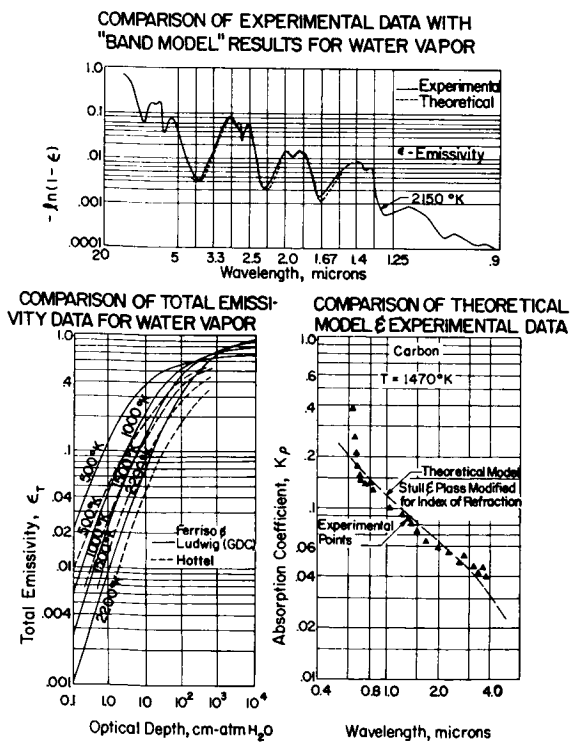

FIGURE 7. COMPARISON OF EXPERIMENTAL DATA WITH "BAND MODEL" RESULTS FOR WATER VAPOR

VI. INVESTIGATION OF COMBUSTION OF HYDROGEN IN A HYPERSONIC AIRSTREAM

Heat leaks to hydrogen-filled fuel tanks made it necessary in some cases to dump combustible hydrogen during flight. Since hydrogen will mix with the ambient air flow, the possibility of it combusting and releasing large amounts of heat in the vicinity of the vehicle has been investigated through a contract with General Applied Sciences Laboratories. Chemical kinetic studies were performed to determine where in the launch trajectory conditions would be favorable for combustion. Fluid mechanical mixing models were set up to investigate two dumping configurations: tangential slot injection, and injection by means of jets located parallel to, but removed from, the surface of the vehicle (Fig. 8). Also more sophisticated flow models employing finite-rate chemistry kinetics were developed.

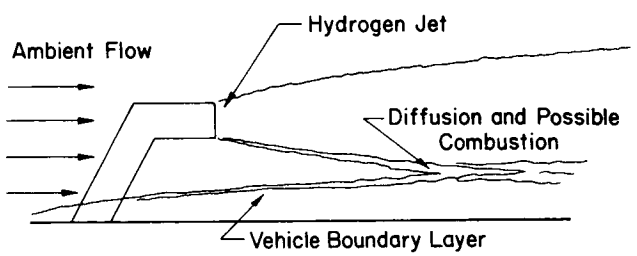

FIGURE 8. MIXING OF HYDROGEN JET WITH VEHICLE BOUNDARY LAYER

To help determine where in the launch trajectory conditions would be most favorable for combustion, two-phase flow phenomenon and the condensation and evaporation associated with the dumping of cryogenetic hydrogen were investigated. The analytical formulations from the above investigation were also supported by experimental investigations of both tangential slot and jet dumping configurations. The results from the above investigations have shown that the hydrogen and air will mix in lengths which are short compared to practical vehicle dimensions and will form mixtures whose composition will fall within

the combustion limits of the air-hydrogen system. If local hot spots are present in the flow field, such as high-static temperature occurring in the boundary layer or increased heating due to protuberances, combustion can be initiated. Combustion may not begin immediately, but may be suppressed because of the high heat capacity of the hydrogen.

The results of the investigation also show that upstream ejection of hydrogen can be accomplished without hazard of ignition or combustion by venting parallel to the surface through a perfectly expanded nozzle if it is displaced far enough from the vehicle to reduce hydrogen levels below flammability limits.

Some results of this program are being used in the Saturn Centaur studies.

RAREFIED GAS DYNAMICS

By

James O. Ballance

SUMMARY

This study develops two new techniques for the analysis of complicated impact pressure probes at various speed ratios and angles of attack. The first technique is based on the analogy of radiant-heat transfer to that of free molecular flow. The second technique uses the Monte Carlo method of selecting random numbers to follow the paths of individual molecules in a system.

The calculation of the drag coefficient of a concave hemispherical shell is extended from the limiting case where all incoming flow is perpendicular to the opening plane of the shell to the case where the incoming flow is at some angle α to the opening plane of the shell.

A modification of the Monte Carlo method is being used in the flow analysis of a cylindrical duct in the transition-flow regime. This method illustrates that a Knudsen number value based only on the diameter of the duct is not sufficient to define the limit for free molecular flow but that the length of the duct also has an important effect on the flow.

Thermal accommodation coefficients have been measured only for low-energy collisions and even then the results are questionable. A program is being conducted to measure the momentum and energy accommodation coefficients up to and exceeding the escape velocities on typical engineering surfaces. The experimental facility used to conduct these measurements is nearly completed, and it is hoped that useful data will be obtained by the end of the year.

I. INTRODUCTION

In the discussion of this topic, it is necessary to establish a reference. The best reference is the mean distance that a gas molecule travels between collisions with other gas molecules (mean free path). For standard conditions, the mean free path of an air molecule is approximately 6.6×10^{-8} meters. As the number of molecules per cubic meter (number density decreases, the mean free path increases. Figure 1 shows the mean free path for several different values of number density. To obtain a better understanding of the physical significance of these values of mean-free path, the altitudes for the various density levels as given by the United States Standard Atmosphere (1962) are also shown in Figure 1. When the number density is very low, the mean free path is so large that the collisions between gas molecules can be ignored for most studies involving conventional sized objects. This region is known as the free molecular flow regime. As the number density increases, the mean free path becomes very small, molecular collisions increase, and the flow approaches the continuum-flow regime. The parameter which describes these regions with reference to the object under study is the Knudsen number (Kn). The Knudsen number is the ratio of the mean free path to the characteristic dimension of the object. For example, the characteristic dimension of a cylinder is normally taken to be the diameter of the cylinder. Figure 2 shows the flow regimes as normally defined in terms of the Knudsen number.

(US Standard Atmosphere, 1962)

ALTITUDE (kilometer)	NUMBER DENSITY (molecule / m^3)	MEAN FREE PATH (meter)
0	2.55 x 10+25	6.6 x 10-8
50	2.14 x 10+22	7.9 x 10-5
100	1.04 x 10+19	1.6 x 10-1
150	4.10 x 10+16	4.0 x 10+1
200	7.82 x 10+15	2.2 x 10+2
250	2.49 x 10+15	6.8 x 10+2
300	9.50 x 10+14	1.8 x 10+3
350	4.15 x 10+14	4.1 x 10+3
400	1.96 x 10+14	8.6 x 10+3

FIGURE 1. MEAN FREE PATH OF AIR AT VARIOUS ALTITUDES

KN = KNUDSEN NUMBER

= λ/L WHERE λ = MEAN FREE PATH

L = CHARACTERISTIC DIMENSION

FREE MOLECULAR FLOW	KN > 10
TRANSITION FLOW	10 > KN > 0.1
SLIP FLOW	0.1 > KN

FIGURE 2. FLOW REGIMES FOR RAREFIED GAS-FLOW

This study is mainly concerned with the free molecular flow (Kn > 10) and the near free molecular flow (1 < Kn < 10) portion of the transition flow regime. This study is grouped into the following four basic types:

(a) Pressure probe characteristics for environmental measuring devices.

(b) Aerodynamic coefficients for orbiting vehicles in both transitional flow and free molecule flow regimes.

(c) Jet spending characteristics for propulsive jets, vent systems, etc., at orbital altitudes.

(d) Surface physics studies for high-velocity gas surface interaction.

II. PRESSURE PROBE CHARACTERISTICS

Measurements of density, composition, temperature, and other thermodynamic properties of the upper atmosphere are usually made on a gas that has been brought to rest in a density and composition-sensitive gage connected to the free stream by an orifice or an orifice-restricted tube. The flow parameters that relate the properties in the gage with the free stream are a function of the orifice size, tube length to diameter ratio, energy accommodation coefficients, relative velocities of the tube and free stream, thermal motion, angle of attack, etc. Calculated solutions for simple, impact pressure probes at various speed ratios and angles of attack have been made; but when more complicated geometries are considered, no convenient solutions exist. Two new methods are being used for this analysis which not only yield the desired parameters, but also give better insight into the problems.

The first method uses the analogy of radiant-heat transfer and free molecular flow. In free molecular flow, an assumption is made that molecules leave a surface element in a direction proportional to the cosine of the angle between the direction vector and the normal to the surface. Also, the molecules are assumed to travel in rectilinear paths between collisions with the surfaces. These assumptions are quite similar to those used in radiant heat transfer calculations. Figure 3 compares the molecular flow rate through a duct calculated by this method to the numerical solutions of Clausing [1].

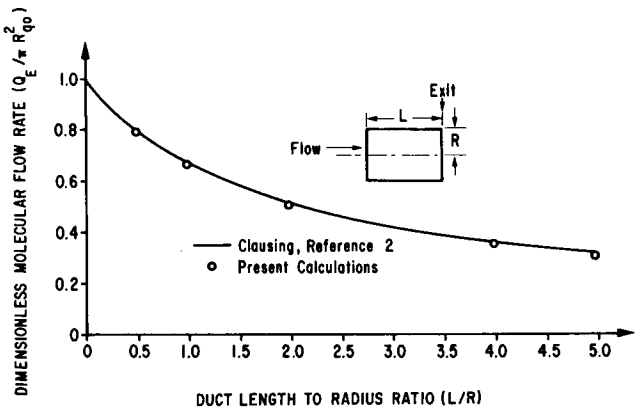

FIGURE 3. MOLECULAR FLOW RATE THROUGH DUCT AS A FUNCTION OF DUCT LENGTH TO RADIUS RATIO, L/R

A second method uses Monte Carlo techniques where random numbers are used to follow the path of individual molecules through the system. By following a large number of molecules (e.g., 10,000), the properties of the entire system can be determined. Figure 4 shows the transmission probabilities for tubes as a function of speed ratio. The speed ratio is the ratio of gage velocity to the random thermal speed of the gas molecules. The data in this study are for cases where there is relative motion between the tube and the gas, such as a density gage on a satellite. These data are believed to be the first ever published for orifice-restricted tubes. Figure 5 shows transmission probabilities as a function of the angle of attack. Here the speed ratio (S) is 2 and the length-to-radius ratio of the tube is 4. The lower curve is for the case where radius of the orifice (Ro) is the same as the diameter of the tube (i.e., there is no restriction). The upper curve shows the case where Ro is 0.707 of the radius of the tube (R). Also shown in Figure 5 are calculated values for the same case using the techniques developed in "Transmission Probability Determination with

Directed Mass Motion and with Mean Free Path Consideration" [2].

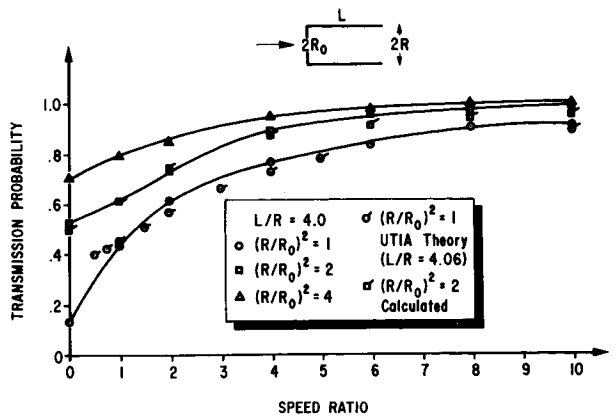

FIGURE 4. TRANSMISSION PROBABILITY FOR TUBES AT ZERO ANGLE OF ATTACK FOR VARIOUS SPEED RATIOS

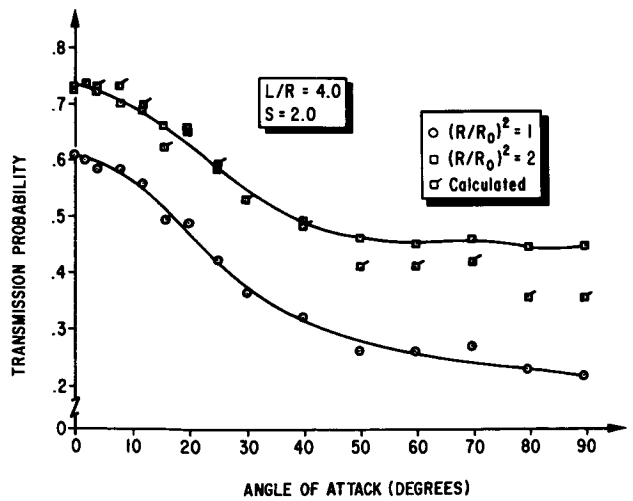

FIGURE 5. TRANSMISSION PROBABILITIES FOR ORIFICE RESTRICTED TUBE AT VARIOUS ANGLES OF ATTACK

III. AERODYNAMIC COEFFICIENTS

Aerodynamic coefficients, such as lift or drag, are easily calculated for free molecular flow on simple convex bodies; but when complex or concave bodies are considered, there are no satisfactory solutions. To illustrate the problem involved and to analyze an orbital system, a thorough study of an unusual configuration (the Pegasus satellite) is being made. From this study, more realistic drag coefficients will be generated.

The calculation of the drag coefficient of a concave hemispherical shell has been extended from the limiting case where all incoming flow is perpendicular to the opening plane of the shell to the case where the flow is at some angle α with respect to the plane of the shell [3]. Figure 6 presents the drag coefficient of a concave hemisphere for speed ratios of 4, 6, and 10 where the temperature ratio of the surface of the hemisphere (T_w) to that of the incident stream (T) is 0.4. Zero angle of attack is when the incoming flow is perpendicular to the plane of the opening of the hemisphere. By Monte Carlo methods this effort is being duplicated so that the assumption of hyperthermal flow may be investigated. Hyperthermal flow is that flow which exists when the ratio of the relative speed of an object to the random thermal motion may be ignored, e.g., S = 6. The flow may be considered to be a beam of molecules traveling in parallel paths at a constant velocity. Present theories extend this type of analysis to speed ratios as low as 6.

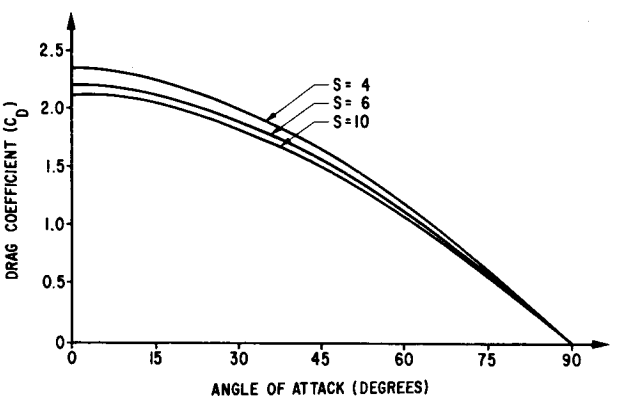

FIGURE 6. DRAG COEFFICIENT, $T_w/T = 0.4$

IV. JET-SPREADING CHARACTERISTICS

The problem of gas impingement of surfaces during low-mass flow or low-density venting has necessitated a closer look at the distribution of flow from tubes. While there is a great deal of information available for the situation where the gas (both in the tube and the free stream) is in the free molecule flow condition, little information is available for the case where the gas in the system

is in the transition flow regime. A modification of the Monte Carlo method is again being used for this study. Figure 7 presents typical data where this modified method was used to study the transition flow regime in a cylindrical duct. The probability

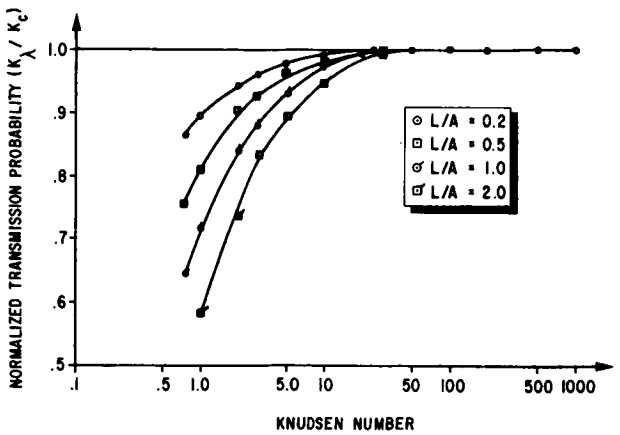

FIGURE 7. NORMALIZED TRANSMISSION PROBABILITIES AS A FUNCTION OF KNUDSEN NUMBERS FOR L/A VALUES OF 0.2, 0.5, 1.0 AND 2.0

(K_c) is the value deduced by Clausing [1] for the case of an infinitely long, mean free path. The transmission probability (K_λ) is obtained from the modified method for some mean free path λ. When the ratio K_λ/K_c is equal to 1, the system can be assumed to be in free molecular flow. The four curves shown in Figure 7 are for four different length-to-radius ratios (L/A). The curves illustrate that a Knudsen number value based only on the diameter of the duct is not sufficient to define the limit for free molecular flow but that the length of the duct also has an important effect on the flow.

V. SURFACE-PHYSICS STUDIES

While the gross effects of studies in rarefied flow are fairly well bounded, they are valid only when consideration is given to the interactions of the gas and the surfaces of the system under study. The microscopic actions in these flows are little known and understood. The parameters that specify these interactions are the reflection and accommodation coefficients. The reflection coefficients are:

$$\sigma = \frac{\tau_i - \tau_r}{\tau_i}$$

$$\sigma' = \frac{P_i - P_r}{P_i - P_s}$$

where

σ = reflection coefficient due to shear stress

σ' = reflection coefficient due to pressures

τ_i = shear stress due to incident mass

τ_r = shear stress due to reflected mass

P_i = pressure due to incoming free stream molecules

P_r = pressure due to reflected molecules

P_s = pressure due to reflected molecules at surface temperature

When $\sigma = \sigma' = 0$ specular reflections occur and when $\sigma = \sigma' = 1$ diffuse reflections occur. The thermal accommodation coefficient is:

$$\alpha = \frac{dE_i - dE_r}{dE_i - dE_s}$$

where

dE_i = energy due to incoming free stream molecules

dE_r = energy due to reflection molecules

dE_s = energy due to reflection molecules at surface temperature

When α is equal to zero, there is no exchange of energy and when α is equal to one, perfect accommodation takes place. A good method exists for measuring the momentum accommodation of gas molecules on surfaces under study. Thermal accommodation coefficients have been measured only for low-energy collisions and even then the results are questionable. A program is being conducted to measure the momentum and energy accommodation coefficients up to and exceeding the escape velocities on typical engineering surfaces. The experimental facility is nearly completed, and it is hoped that useful data will be obtained before the end of the year.

VI. EXPERIMENTAL FACILITIES

To verify the limits for the analytical solutions to the problems in this study, it is necessary to perform some experiments. These experiments may be performed in a low-density research chamber equivalent to that in use by the Aerodynamics Division. This facility is 3.5 ft. (1.07 m) diameter by 14 ft. (4.27 m) in length. A nozzle is being designed to produce a flow of Mach 4. However, it is doubtful that experimental facilities will ever be developed to explore adequately all the problems outlined in this study.

The Aerodynamics Division is conducting a modest program that promises to make a significant contribution in the field of rarefied gas dynamics.

REFERENCES

1. Clausing, P.: Uber die Stromung sehr verdunnter Gose durch Rohren von beliebiger. Ann Physik 12, 1932, p. 961.

2. Ballance, J. O.: Transmission Probability Determination with Directed Mass Motion and with Mean Free Path Consideration. Third International Vacuum Congress, Stuttgard, Germany, June 1965.

3. Wimberly, C. R.: Determination of Aerodynamic Force and Heat Transfer Properties for a Concave Hemispherical Surface in Free Molecular Flow. NASA TM X-53288, June 1965.

TURBULENT FLUCTUATION MEASUREMENTS WITH THE CROSSED-BEAM METHOD

By

F. R. Krause, M. J. Fisher,* and R. E. Larson**

SUMMARY

A new optical method has been developed for studying aspects of launch vehicle turbulence. The heart of the method is a new test arrangement for the remote sensing of local changes in radiative power. Early experimental results are given and show that most statistical turbulence parameters can be approximated which are commonly derived from "two point product mean values." The measurement of local thermodynamics' properties in turbulent flows becomes conceivable.

I. INTRODUCTION

The measurement of turbulent fluctuations in the environment of launch vehicles is necessary to provide the input for the statistical analysis of responses like rigid-body motions, elastic deformations, as well as heat transfer and acoustical loads. Solid probes introduce stabilizing walls and/or additional shock waves which interfere severely with the fluctuations of interest. A further instrumentation problem is to find probes with a sufficiently high resolution in space and time so the fluctuations are not integrated out. So far, all ground tests and flight instrumentation are restricted to pressure transducers, thin film gages, and accelerometers that are flush mounted in the vehicle surface. Fluctuation measurements in the flow have not proved to be feasible.

The required inputs or aerodynamic forcing functions are mathematically similar insofar as they should be expressed by an area integral over a space-time correlation function. The inherent numerical integration requires a large number of points and the experimental and numerical effort in providing these pointwise estimates is almost prohibitive, even if a large number of transducers are used in the vehicle walls. Therefore, this study proposes to use the integrating features of optical beams for a "one shot" estimate of area integrated correlation functions in the flow.

* IIT Research Institute

** Applied Science Division, Litton Industries

II. OPTICAL INTEGRATION OVER CROSS-CORRELATION AREAS

Statistical thermodynamics show that the light extinction coefficient μ is determined by the thermodynamic properties of the flow [1]. Therefore, its space-time correlation might be used to study the turbulent fluctuations of thermodynamic flow properties.

Consider the experimental arrangement in Figure 1. Two narrow beams of white light traverse a jet in the y and z directions. By an optical filter in front of the photo detectors, the received radiative power is limited to the wavelength interval $\Delta\lambda$ centered around the wavelength λ. The intensity fluctuations of the y and z beams are now correlated and normalized with the mean values. These operations lead to the measurable quantity

$$G(\xi,\tau)_x = \frac{\langle i_z(t)\, i_y(t+\tau)\rangle}{\langle I_y\rangle \cdot \langle I_z\rangle} \cdot \qquad (1)$$

Fisher and Krause [2] show analytically that the measurable quantity is related to the two-point product-mean value of the light extinction coefficient

$$R\mu(\xi,\tau)_x = \qquad (2)$$

$$\overline{\langle \mu'(s, y, z, t)\mu'(x+\xi, y+\eta, z+\zeta, t+\tau)\rangle}$$

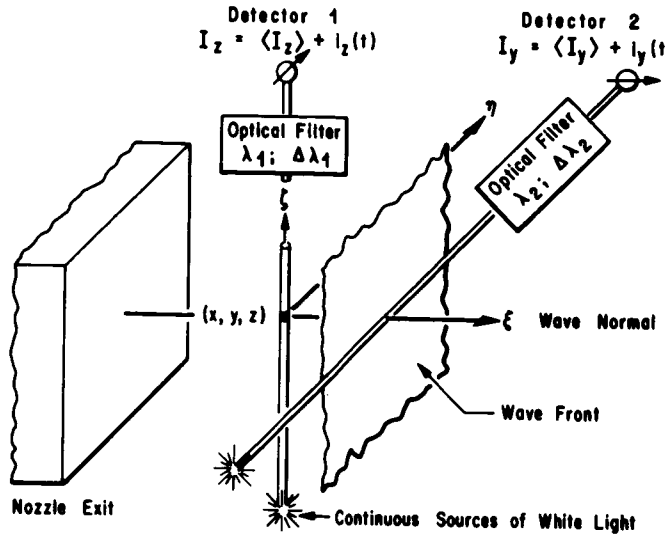

The crossed beam technique gives the integrated cross correlation function of light extinction coefficients.

$$\frac{\langle i_z(t)\, i_y(t+\tau)\rangle}{\langle I_z\rangle \quad \langle I_y\rangle} = G(\xi,\tau) = \iint_{-\infty}^{+\infty} R_\mu(\vec{\xi},\tau)\, d\eta\, d\zeta$$

$$R_\mu(\vec{\xi},\tau)_{\vec{x}} = \langle \mu'(\vec{x},t)\ \mu'(\vec{x}+\vec{\xi},t+\tau)\rangle$$

$$\mu(\vec{x},t,\lambda,\Delta\lambda) = \frac{\text{Filtered power loss along } \Delta Z}{\text{Filtered energy flux} \cdot \Delta Z \cdot \Delta X}$$

FIGURE 1. OPTICAL INTEGRATION OVER WAVE FRONTS IN TURBULENT FLOWS

by an area integration across the plane in which the beams have been aligned:

$$G(\xi,\tau)_x = \int_{-\infty}^{+\infty}\int_{\infty} R_\mu(\xi,\tau)_x\, d\eta\, d\zeta \ . \qquad (3)$$

The derivation of equation (3) shows that the wanted "one shot" estimate of area integrated correlation functions can be obtained, even in statistically inhomogeneous media, as long as there is one direction of homogeneity left. The wavelength λ and the spectroscopic resolution $\Delta\lambda$ may be adjusted to a specific thermodynamic property, such as density, species concentrations, and, hopefully, temperatures.

III. APPROXIMATION OF POINT MEASUREMENTS

The random nature of turbulent fluctuations assures that the integrand in equation (3) drops to zero over finite and mostly small distances. In this fashion, local information can be obtained that depends on the turbulence structure. To be more specific, assume that the dependence of R_μ on the beam separation ξ and the time separation τ might be approximated through a separation of variables. Within the validity of this assumption, all turbulence parameters can be obtained which are commonly derived from two point product mean values [3]. This is demonstrated in graphical rather than mathematical form.

The integral scale of turbulence follows from the space correlation as shown in Figure 2. It is equal to that separation distance which makes the cross-hatched areas equally big. The integral scale depends on the direction of the beam separation. The subscript x denotes a separation in the streamwise direction. If the beam separation is repeated along the remaining perpendicular y and z axis, the values L_y and L_z could be obtained. These values are used to calculate mean-square values from the measurements at zero-beam separation.

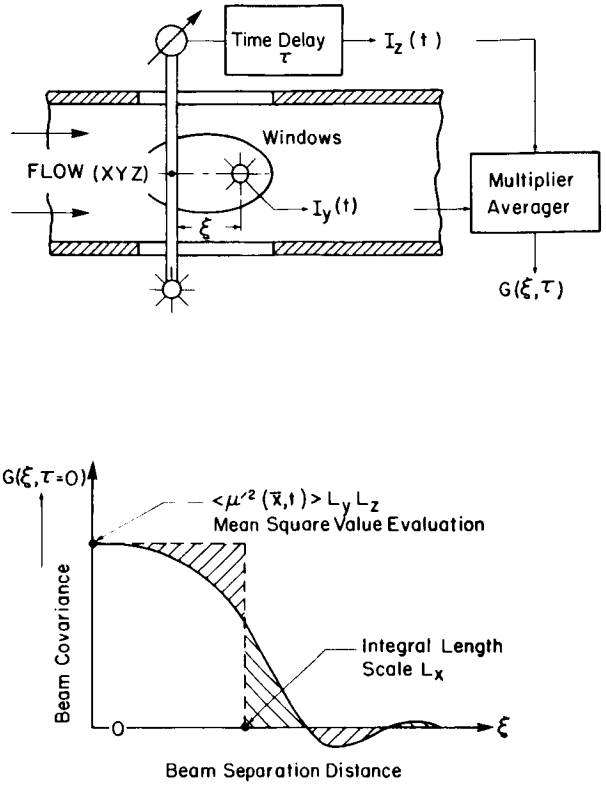

FIGURE 2. TURBULENCE SCALES AND INTENSITIES FROM CROSSED-BEAM COVARIANCE MEASUREMENTS

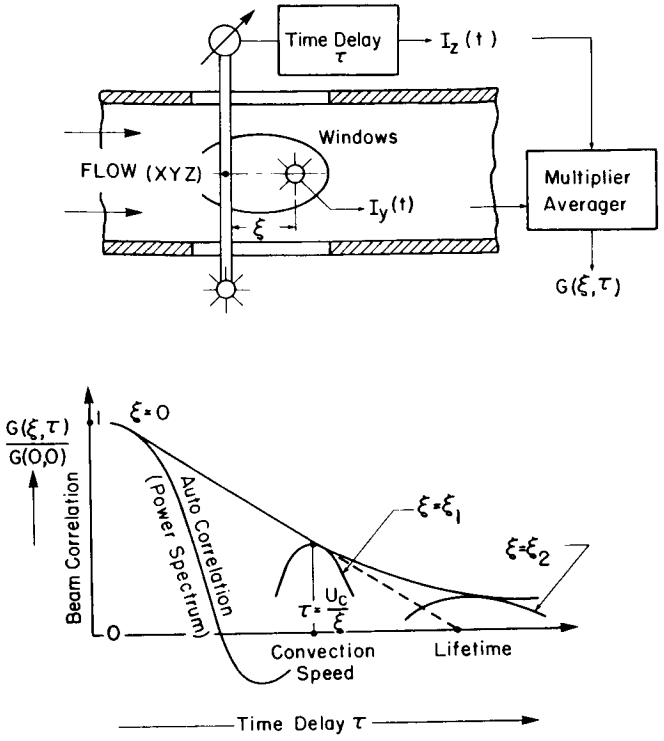

FIGURE 3. LOCAL POWER SPECTRA CONVECTION SPEEDS AND EDDY LIFETIMES FROM CROSSED-BEAM CORRELATION MEASUREMENTS

By the existing computer programs [4] for random vibration analysis, a time log can be introduced between the records of the two photo-detector outputs. Plotting the calculated G values against this time separation instead of space separation gives additional turbulence parameters as shown in Figure 3. For zero space separation, the measured temperature correlation function resembles the auto correlation and can be used to calculate the shape of the power spectrum. Plotting the temporal correlation function $G(\tau)_\xi$ for one constant space separation enables the bulk convection speed U_c to be read from the time lag corresponding to the first maximum correlation. Repeating this plot for several beam separations gives an envelope which indicates the eddy lift time.

The pointwise estimates are only approximately correct because of the assumed separation of variables. The case, which is not covered, occurs when the separation of variables is erroneous for turbulent fields with large scales. Large lateral scales now indicate that only relatively few wave-number components are involved in the turbulent exchange. Separation of variables assumes that the lateral wave number components do not interact. Thus, the case not covered would demand a strong interaction between a few lateral wave number components which are not communicated to other regions of the wave number space. Such a process will be broken up by the action of the nonlinear terms in the equations of motion. Therefore, the crossed-beam methods should give a good approximation of point measurements in almost all turbulent fields of practical interest.

IV. EXPERIMENTAL RESULTS

The most revealing and instructive test of the crossed-beam concept is to compare the optical approximation of point measurements with known hot-wire measurements. All measurements were taken in a subsonic (M=0.2) air jet exhausting through a 1-inch (2.5 cm) diameter nozzle into the atmosphere (Fig. 4). Light extinction was achieved by spraying a small amount of liquid nitrogen into the settling

chamber. This produces small water droplets in the exhaust flow which attenuate the crossed beams by scattering.

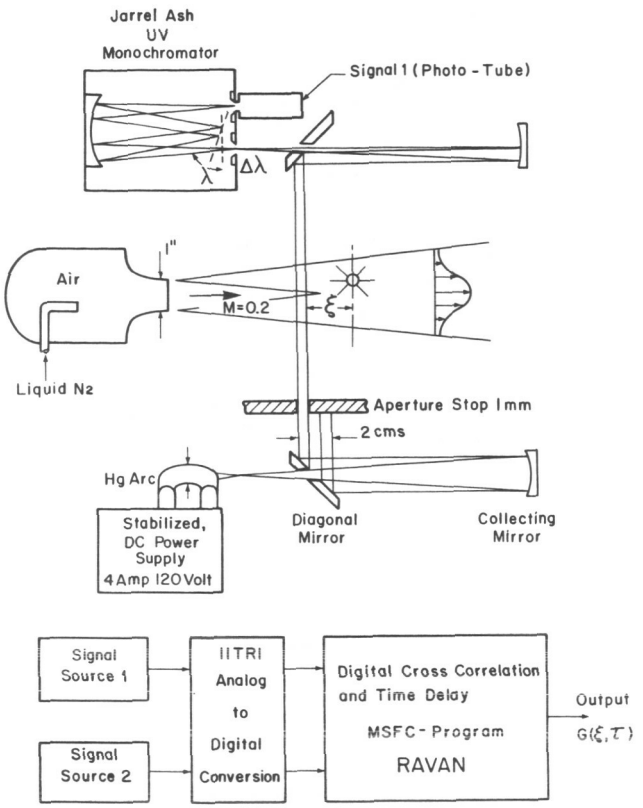

FIGURE 4. THE FIRST CROSSED-BEAM CORRELATOR

A diagram of the optical and electronic hardware is shown in Figure 4. A plane and a spherical mirror collects the light from a powerful mercury arc and transmits it as a parallel beam through the jet. A similar mirror combination projects the arc image on the entrance slit of a grating spectrograph. The aperture stop in front of the spectrograph is set at a beam diameter of 1 mm. The photo-multiplier then scans the first order spectrum of the grating. In this way, the wavelength interval $\Delta\lambda$ and the wavelength λ are adjusted by the width of the monochromator slit and the rotation of the grating respectively. By exchanging light sources, gratings, and photo detectors, the system is able to cover the spectrum from the vacuum ultraviolet (λ = 1200A) to the infrared ($\lambda = 25\mu$).

The above light source and detector arrangement is used to generate two beams, one in a horizontal direction and one in a vertical direction (Fig. 5).

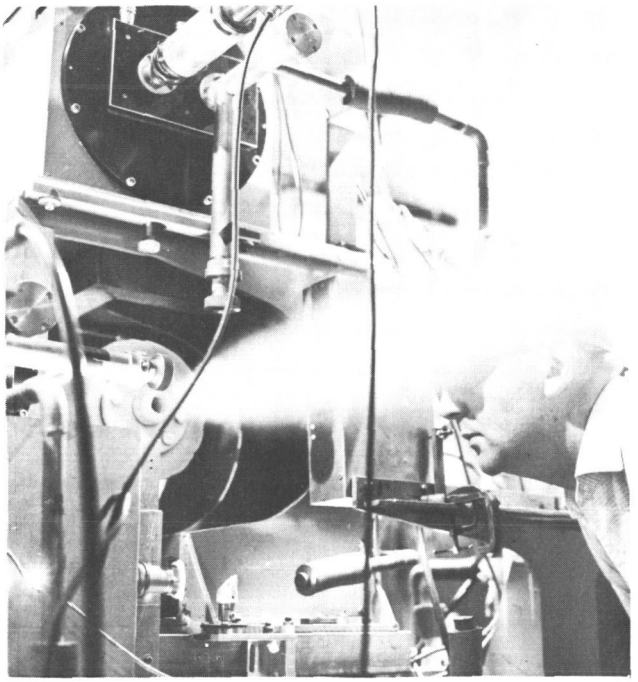

FIGURE 5. LIGHT SOURCE AND DETECTOR ARRANGEMENT

A lathe bed provides a mechanical support which allows the beams to be aligned parallel to the nozzle-exit plane. A beam separation in the streamwise direction gives longitudinal turbulence scales and convection speeds. Transport of the whole system allows us to repeat the measurements for all axial and radial traverses of the jet. However, beam orientation at an angle to the nozzle-exit plane is not possible and the associated lateral scales have not yet been measured.

The contribution of correlated, light-source fluctuation, created by power supply main ripple, was eliminated by electronic filters. Figure 6 shows measured, temporal cross correlation for various streamwise beam separations that were taken along the center of the shear layer 3 diameters downstream from the nozzle exit. Each curve is normalized by the maximum value of the correlation coefficient observed at that particular separation. This form of presentation was necessitated by a certain inconsistency of peak values which are not fully understood. However, the peaks of the various curves presented clearly indicate the presence of a convected, turbulent pattern. Plotting the known space separation against the time lags that are indicated by the maximum temporal correlation function results in a line. The slope of this line indicates the convection speed as discussed previously.

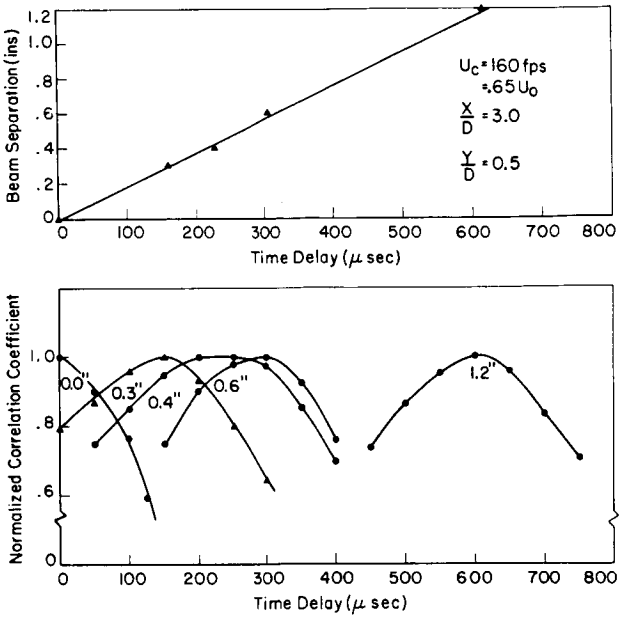

FIGURE 6. CONVECTION VELOCITY FROM CROSSED-BEAM CORRELATION

Figure 7 shows the temporal, cross-correlation results. The only difference from the previous results is that the beam interaction point has been moved radially outwards by 0.2 inch (0.51 cm). These figures yield two points on the convection speed profile which is established from the hot-wire measurements of Davis and Fisher [5] as shown in Figure 8. The difference between the crossed-beam measurements and the hot-wire measurements fall within the scatter of the hot-wire points. The spatial resolution of the crossed beam is good since the two measurements were only 0.2 inch (0.51 cm) apart.

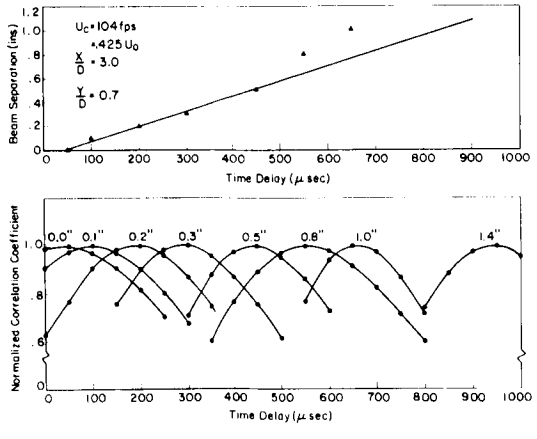

FIGURE 7. CONVECTION VELOCITY FROM CROSSED-BEAM CORRELATION

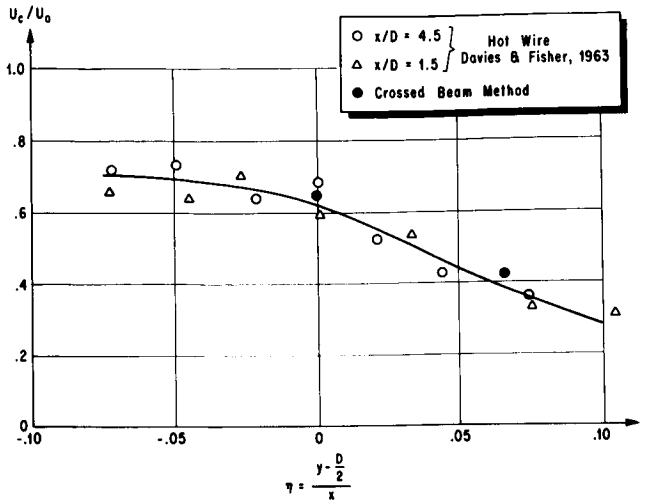

FIGURE 8. COMPARISON OF RADIAL DISTRIBUTION OF CONVECTION VELOCITY

The comparison between the optically determined space correlations and the hot-wire results of Laurence [6] and Bradshaw [7] are shown in Figure 9. The optical results fall in between the hot-wire

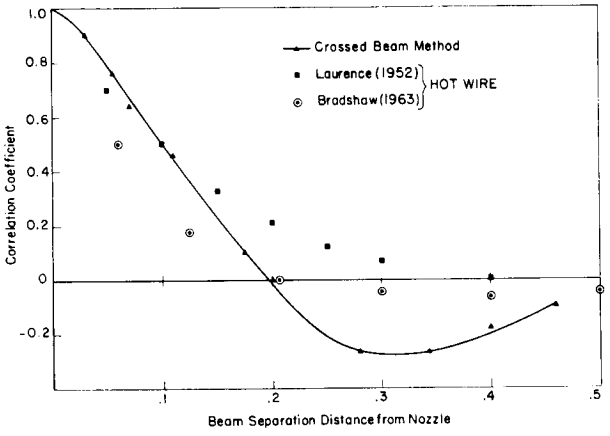

FIGURE 9. MEASUREMENT OF EDDY SCALES

results. Once again, this good comparison is very encouraging. At larger space separations, the crossed-beam method indicates considerable negative space correlation, whereas the hot-wire correlations have decayed to almost zero. Many of Laurence's auto-correlation measurements and Bradshaw's space correlations also show a negative loop, but its amplitude is generally less than that indicated by the crossed-beam method.

The discrepancies at the large space separations could be explained by errors in either the hot-wire or the crossed-beam method. The hot wire is subjected to all velocity components, and at large separations the transverse-velocity fluctuations could add so much noise that the correlation disappears. The crossed-beam method could provide erroneous results if the water droplets follow only the large-scale eddies. These eddies are limited to a range of small wave numbers which show a large correlation that disappears when all wave numbers are considered.

Figure 10 shows an initial measurement of the radial intensity profile of concentration fluctuations.

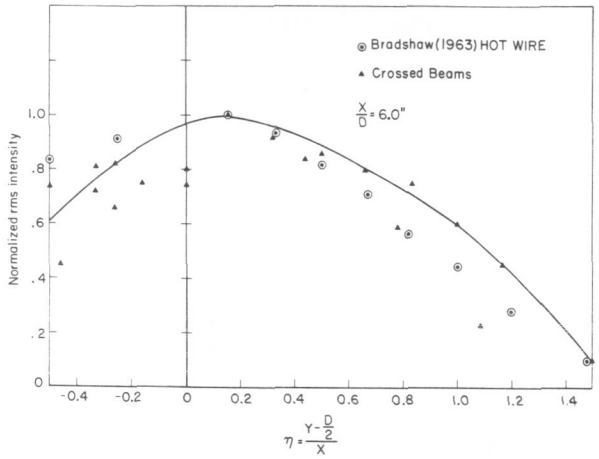

FIGURE 10. TURBULENT INTENSITY PROFILES

For this measurement, the beams were arranged to intersect in a plane 6 diameters downstream of the exit. The vertical beam was moved to various positions across the flow, thereby changing the radial location of the intersection point. For each radial separation, the rms amplitude was evaluated following the procedure that was already described in Figure 2. Since lateral scales cannot be measured with the present support, it was assumed to be equal to the longitudinal scale. In spite of this simplification, the agreement with the hot-wire results from Bradshaw are again very encouraging.

The crossed-beam results in Figure 10 are scattered. Any one determination shows a comparatively smooth variation of intensity and the peak value occurring close to the center of the shear layer as expected. However, the decrease on either side of the maximum varied in repeated runs. Since the runs were performed on days when the external relative humidity was very different, it is suspected that the water vapor content of the air delivered by the jet modified appreciably the degree of persistence of water droplets in the flow. Thus, it is tentatively concluded that the scattering of the results is a real effect associated with a lack of control in the introduction of the water droplet content rather than in the limitation of the crossed-beam method.

V. FUTURE APPLICATIONS

The first contribution to the Saturn program will be to measure turbulence shock-wave interaction in the plume impingement and recirculation areas of the S-IC and S-II rocket clusters. Model tests at MSFC's impulse base flow facility indicated extremely high fluctuations of wall pressures and heat-transfer rates as shown in Figure 11. These fluctuations create

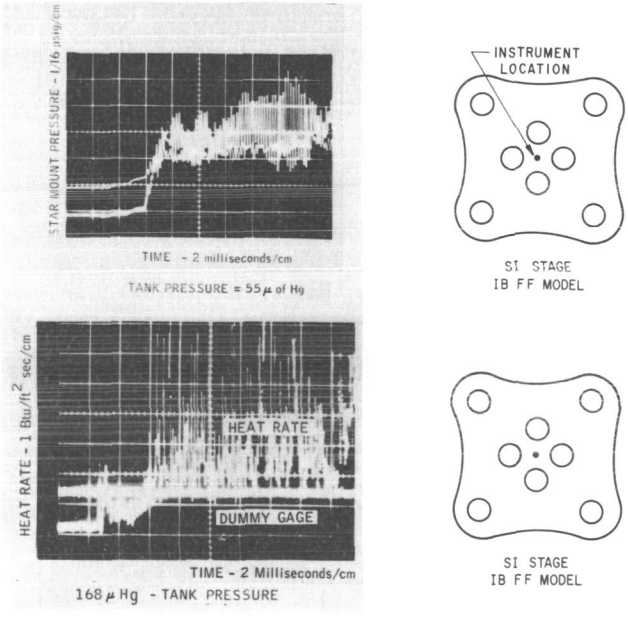

FIGURE 11. TURBULENT FLUCTUATIONS OF BASE PRESSURE AND HEAT TRANSFER RATES

problems when predicting heat-transfer rates. Turbulence levels of only 3 percent have sometimes increased the stagnation point heat transfer on cylinders up to 80 percent. Hot-wire measurements on the two-dimensional base-flow model already indicate turbulence levels in excess of 100 percent as shown in Figure 12. Therefore, the turbulence effects on heat transfer might play a dominant role. They could increase or decrease the heat transfer by either transporting the hot particles into the wall layers or

throwing them back from the wall. These effects cannot be included in the present model tests on analytical solutions. Therefore, the crossed-beam method is needed to study the turbulent heat and mass transport in base flows.

Other optical fluctuation measurements in clustered rocket exhausts are necessary to predict and/or prevent high acoustical loads on the upper stages. The presence of powerful Mach-wave and shock-wave sound radiation is shown on the shadowgraph in Figure 13. In the case of single jet, the sound radiations are not so dangerous, since they are directed away from the vehicle. However, on a rocket cluster, the sound radiation can pass through the subsonic hole between the plume impingement shocks and will then hit the vehicle directly. The presence of such a subsonic hole and the oscillation of the plume impingement shock are clearly indicated on the schlieren and interferograms of our two-dimensional base-flow model (Fig. 14). The associated aerodynamic feedback loops will produce a jet noise problem on the upper stages as soon as plume impingement and a choked-flow establish a finite base pressure. For the S-II stage, a conservative estimate of sound pressures is 153 dB.

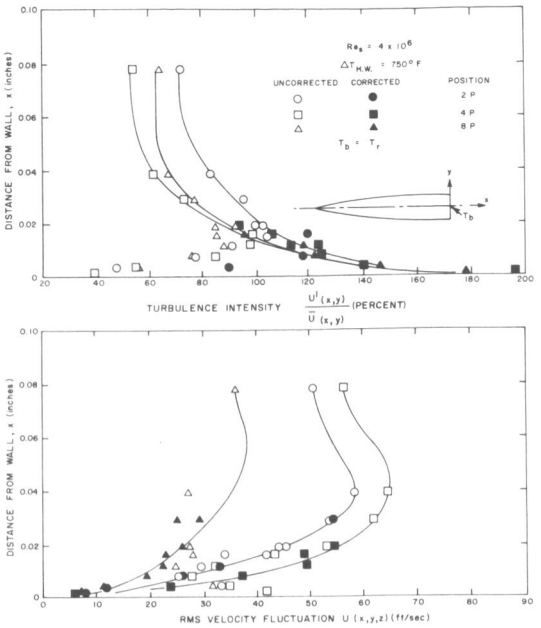

FIGURE 12. RMS VELOCITY PROFILES IN TWO-DIMENSIONAL BASE FLOW WITH AND WITHOUT WALL EFFECT

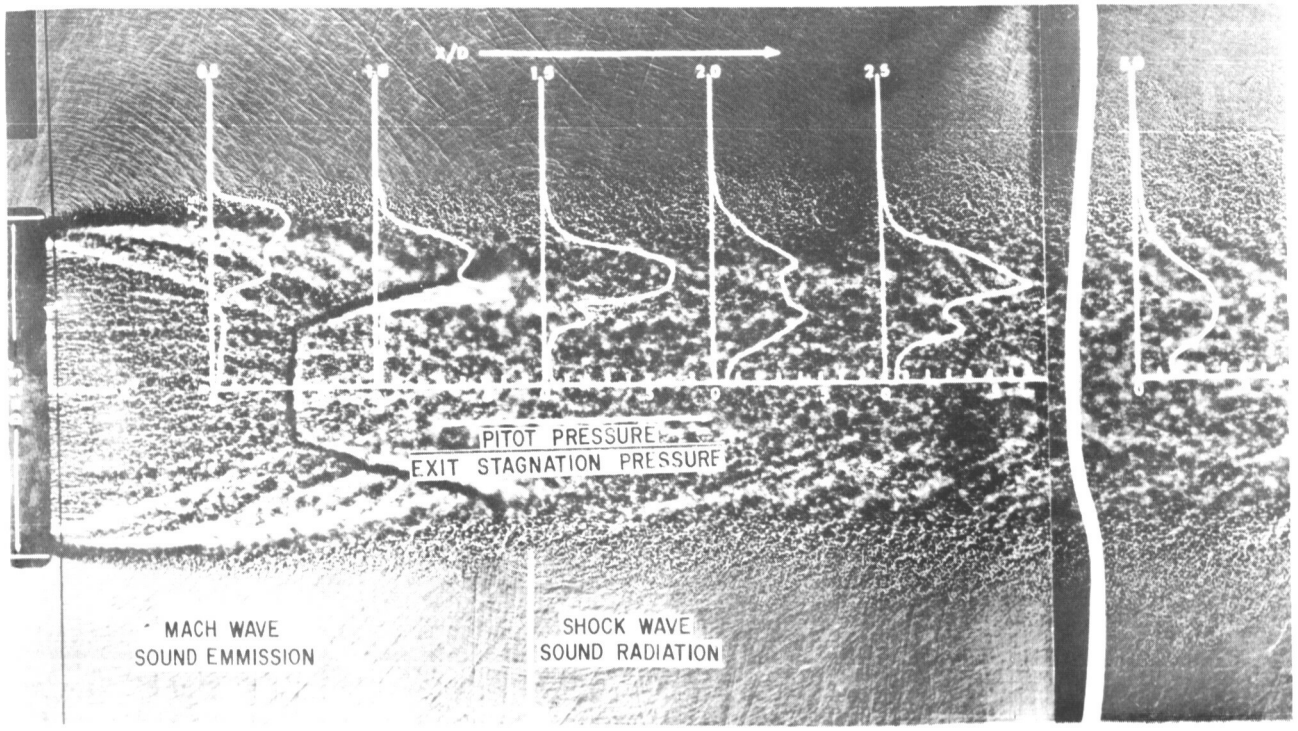

FIGURE 13. SUPERSONIC NOISE SOURCES IN A SINGLE F-1 ENGINE JET

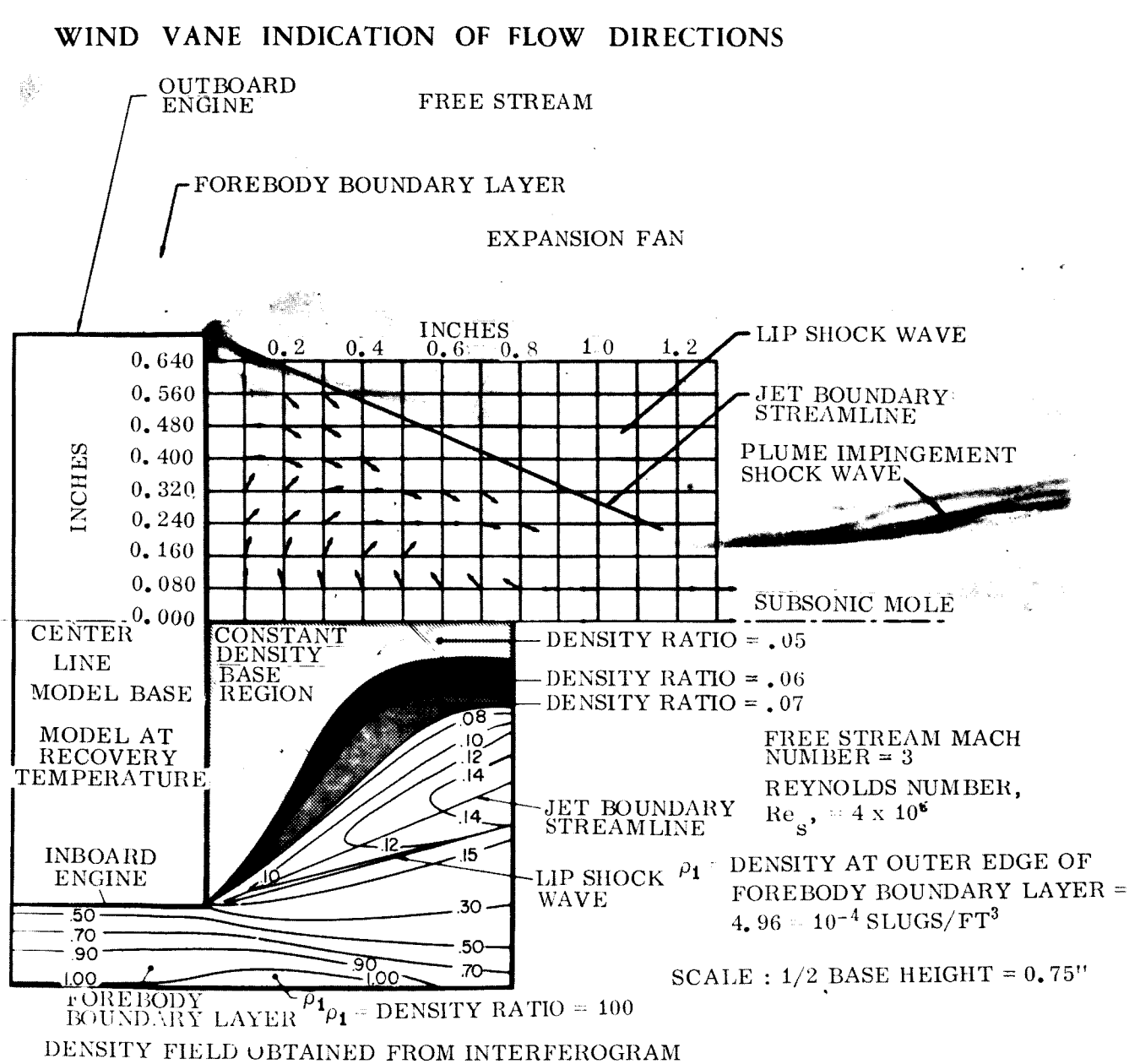

FIGURE 14. RECIRCULATION ZONE FLOW FIELD

The use of laser beams, if feasible, would allow crossed-beam measurements over vast areas. Speculations could also be made about water vapor, carbon dioxide, and ozone concentrations in the lower and upper atmosphere. A study of intense radiation belts is conceivable which use only detectors and no light sources.

If the crossed-beam method works on both particle scattering and gaseous absorption, it could be used on two-phase flows. Fuel mixing in combustion chambers, fuel droplets, and ion particles in liquid and solid rocket exhausts, gas bubbles, and condensation in tanks, etc., are some of the applications that might be of great interest to other laboratories.

The present development of technique is aimed at the oxygen absorption in the ultraviolet because of the importance of air flows. The insufficient storage capacity of the computer memory is the only limitation to getting accurate cross-correlation

estimates. However, a new computer program will eliminate this difficulty.

VI. CONCLUSIONS

Local fluctuation measurements through a space and time correlation of optical signals have been successful in a small subsonic jet where the light extinction was produced by scattering at water droplets. Comparison of the hot-wire data with the crossed-beam data lead to the following conclusions:

(a) Probe interference and cancellation problems were avoided.

(b) One shot estimates of area integrated correlation functions can be made.

(c) Approximations can be made on the local power spectra, convection speeds, turbulence scales, and eddy lifetimes.

(d) The crossed-beam method can work with existing random vibration computer programs. An extension that includes light extinction by gaseous absorption and/or emission would show the following potential:

(1) The adjustment to special theromodynamic properties, such as species concentrations by a proper selection of optical wave length and wavelength interval.

(2) Two phase-flow applications by independent measurement of droplet scattering and gaseous absorption.

(3) The measurement of combustion instability and plasma instability.

(4) The location and intensity of atmospheric concentration fluctuations and radiation belts.

REFERENCES

1. Chapman, S.; and Cowling, T. G.: The Mathematical Theories of Non-Uniform Gases. Second edition, Cambridge, 1960.

2. Fisher, M. J.; and Krause, F. R.: Local Measurements in Turbulent Flows Through Cross-Correlation of Optical Signals. Aero-Astrodynamics Research Review Number 2, NASA TM-X-53295, April 1965.

3. Hinze, J. O.: Turbulence. New York, N. Y., 1959.

4. NASA, MSFC, The Vibration Manual. (first edition) 1964.

5. Davis, P. O. A. L.; Fisher, M. J.; and Barrett, M. J.: The Characteristics of the Turbulence in the Mixing Region of a Round Jet. J. Fluid Mech., vol. 15, 1963, p. 337.

6. Lawrence, J. C.: Intensity, Scale and Spectra of Turbulence in the Mixing Region of a Free Subsonic Jet. NACA Rept. No. 1292, 1956.

7. Bradshow, P.; Ferriss, D. H.; and Johnson, R. F.: Turbulence in the Noise-Producing Region of a Circular Jet. Advisory Group for Aeronautical Research and Development, Report 450, Apr. 1963.

INSTRUMENTATION RESEARCH AT MSFC

September 30, 1965

by

Harlan Burke
Donald G. Davis
James C. Derington
Alexander Hafner, III
C. T. Paludan
Roy Williams

TABLE OF CONTENTS

Page

LIST OF ILLUSTRATIONS (Continued)

THERMALLY ISOLATED TEMPERATURE SENSOR FOR SPACE APPLICATION

by Harlan Burke

LIST OF TABLES

LIST OF ILLUSTRATIONS

LIST OF ILLUSTRATIONS (Continued)

UHF TELEMETRY DEVELOPMENT AT MSFC

by Donald G. Davis

LIST OF TABLES

LIST OF ILLUSTRATIONS

ADDRESSABLE TIME DIVISION DATA SYSTEM

by Roy Williams

LIST OF ILLUSTRATIONS

INTRODUCTION AND SUMMARY TO INSTRUMENTATION RESEARCH AT MSFC

By

C. T. Paludan

Presented at Research Achievements Review
September 30, 1965

The development of launch vehicles requires considerable flight instrumentation during research and development flight phases. In many cases, the needs of the vehicle designers can be met by conventional off-the-shelf instrumentation items previously used on earlier projects such as Jupiter or Air Force vehicles. However, a few requirements always exist that cannot be met with available hardware. Sometimes these requirements can be anticipated, and a research and development program can be initiated to meet the new requirement. Very often instrumentation must be defined far in advance of the delivery dates, not only because of the necessity for timely implementation into the documentation and procurement programs, but also because of restrictions and requirements from non-MSFC sources. An example of this is the UHF telemetry program, details of which will be given later.

As shown in the initial summary, MSFC is conducting instrumentation research in a number of areas. Table I summarizes some of the items being studied in other laboratories. These are generally for non-flight instrumentation. Many of the items shown have been presented at previous Research Achievements Reviews, or will be in the future. Table II summarizes some of the items being studied in Astrionics Laboratory strictly for flight instrumentation. Several specific tasks are discussed in detail. These are relatively typical of the type of effort that is required to fulfill the unusual requirements of instrumentation for launch vehicles and payloads. The goal of such tasks is finally to make available flyable hardware for implementation of existing or anticipated measuring requirements.

TABLE I
TYPICAL INSTRUMENTATION RESEARCH OTHER THAN BY ASTRIONICS

	I. Propulsion and Vehicle Engineering Laboratory
NAS 8-5491	Technique Development to Measure Vehicle Engine (Pulse Rocket) Performance
NAS 8-11311	Determination of Propellant Mass in a Large Storage Tank
NAS 8-5323	Theoretical Studies to Establish Design Parameters for Accurate Calorimeters
	II. Quality Assurance Laboratory
NAS 8-11705	Integration of Automatic Calibration System for Stage Instrumentation
NAS 8-11715	Development of Improved Sensing Methods and Devices for Stage Checkout
	III. Test Laboratory
In-House	Liquid Level and Quantity Instrumentation
NAS 8-11080	Point Density Sensor for Cryogenic Liquids

TABLE I (Cont'd)

NAS 8-11666	Development and Evaluation of High Capacity Load Cells
NAS 8-11072	High Thrust Measuring System
NAS 8-5186	Development of Damped Piezoelectric Accelerometers and Related Calibration Equipment
NAS 8-11534	Automatic Low Temperature Calibration System
NAS 8-11623	Prototype Cryogenic Temperature Measuring System
NAS 8-11629	Development of Low Range Absolute Pressure Calibration System
NAS 8-2673	Development of a Pressure Transducer Utilizing Friction Free Potentiometer
In-House	Cryogenic Environmental Effects on Transducers
NAS 8-5439	Development of Digital Reporting System
NAS 8-11076	Design and Development of an Improved Digital Measuring System
NAS 8-11088	Development of a Mass Computer
	IV. Aero-Astrodynamics Laboratory
NAS 8-11258	Local Optical Measurements of Turbulent Flow Properties on Ground Tests
-H- 71500	Research Study of Gas Density by Radiation Scattering
NAS 8-11220	Design and Development of a Breadboard Model of an Ultraviolet Air Density Gage
NAS 8-11046	Pressure Probe Characteristics in Transitional Knudsen Number Range
NAS 8-5350	Development of a Pressure and Force Transducer Calibration Procedure for the Hypersonic Shock Tunnel

TABLE I (Concluded)

	V. Manufacturing Engineering Laboratory
In-House	Development of Advanced Flight Strain Measuring Techniques
NAS 8-11115	Development of Instrumentation to Control Cleaning Procedures of Vehicle Components
In-House	Development of Continuously Monitoring X-Ray Examination of Weldments by Television Viewing
	VI. Research Projects Laboratory
-H- 71459	Thermal Radiation Measurement Techniques
-H- 71460	Thermal Testing Techniques
NAS 8-11202	Seismic Signals Resulting from Large Rocket Firings
In-House	Electric Field Meter Investigation
NAS 8-5336	Meteoroid Penetration Distributed Transducer

TABLE II
TYPICAL FLIGHT INSTRUMENTATION
RESEARCH BY ASTRIONICS LABORATORY

- Cryogenic Densitometer Using Nucleonic Technique
- Advanced Pressure Transducers
- RF Approach for Measuring Liquid Level
- Explosion and Explosion Hazard Detection and Evaluation
- Techniques for Measuring Ambient Air Density from Space Vehicles at Orbital Altitudes
- Inflight Hydrogen Detection by Mass Spectrometer
- Special Thermocouple Gages
- Fire Detection System for Cryogenic Fuel

TABLE II (Cont'd)

- Contoured Germanium Solid State Radiation Detector
- Advanced Heating Rate Transducers
- Thermally Isolated Sensor for Space Application
- Infrared Sensing System for Lunar Temperature Studies
- Cryogenic Temperature Sensor
- Special Calorimeter
- Quality Meter
- Strain Gage Accelerometer Using Piezoelectric Technique
- Vibration Spectrum Analyzer for Space Vehicles
- TV on Film Recorder for Flight Use
- Liquid/Vapor Sensor
- Transmitters
  - 220 MHz - 20W. T.W.T. (VHF)
  - 2200 MHz - 5W. S.S. (VHF)
  - 215 - 260 MHz 20W. S.S. (VHF)
- Airborne Tape Recorders
  - Analog
  - Digital
  - Combination Analog and Digital
- Time Division Multiplexers
  - Remote Programable Hi - Lo 810 Channel Multiplexer
- SS/FM Systems
  - Improved SS/FM Airborne Hardware
  - Improved SS/FM Demodulators (GSE)
- PCM Systems
  - Improved Analog to Digital Converter
  - Improved Remote Digital Submultiplexers
  - Airborne Computer Interface
- FM/FM Systems
  - Constant Bandwidth FM System
  - Improved IRIG FM/FM Hardware
- GSE for Automatic Telemetry Checkout
- Addressable Remote TM Multiplexers (Weight Reduction)
- Adaptive TM System (Bandwidth, Power and Weight Reduction)
- Advanced SS/FM Systems (Improved Accuracy, Phase Correlation and Response)
- Onboard Data Storage (For Use in Remote Orbital Operations)

TABLE II (Concluded)

INFLIGHT HYDROGEN DETECTION BY MASS SPECTROMETER

By

James C. Derington and Alexander Hafner, III

ABSTRACT

Methods of detection of hydrogen, hazardous mixtures, and explosions are discussed. The mass spectrometer developed for detection of hydrogen and explosive mixtures in flight is described in detail.

I. INTRODUCTION

The advent of liquid hydrogen-powered space vehicles increased the possibility of fires or explosions which could result in loss of a mission and loss of the crew. A need was therefore evident for inflight instrumentation that could lessen this danger. This paper summarizes Astrionics Laboratory's efforts in this area of instrumentation research and development and then concentrates on one particular phase as being typical, the inflight detection of hydrogen by mass spectrometer.

II. APPROACH AND APPLICATION

We have approached the problem from three aspects: (1) hydrogen detection; (2) hazard, or explosive mixture, detection; and (3) explosion detection. In a fully instrumented vehicle, several detectors could be located in the interstage areas or anywhere hydrogen could accumulate. The equipment could possibly be made a part of the emergency detection system, thereby providing a warning to the crew and ground monitors that a dangerous concentration of hydrogen was present, that an explosive mixture of hydrogen and oxygen was present, or that an explosion had occurred - in particular, the minor explosion which usually precedes a major hydrogen explosion. Appropriate action, such as abortion of the flight or possibly suppression of the explosion, could then be initiated. Another obvious use for such instrumentation would be to provide information, through telemetry, that would be a valuable analysis tool in case of hydrogen leakage or in case of a catastrophic failure.

III. DETECTION METHODS

When Astrionics Laboratory began investigating the problem, there were no detection instruments suitable for flight use and only a few non-flight instruments, none of which were completely satisfactory. A research and development program was therefore begun and various techniques were investigated. Some of the more promising are described below.

A. HYDROGEN DETECTION METHODS

The hydrogen detection methods currently under development or proposed for development are:

1. Kryptonate
2. Acoustic
3. Polarographic
4. Fuel cell
5. Mass spectrometer

The kryptonate method of hydrogen detection is currently under development by Astrionics Laboratory. The principle involved is the release of radioactive krypton 85 gas from a kryptonated base metal when exposed to hydrogen gas. The amount of radiation is a measure of the amount of hydrogen present. This technique offers promise of providing a good inflight hydrogen detector.

The acoustic method of hydrogen detection is currently under development by Propulsion and Vehicle Engineering Laboratory in cooperation with Astrionics. This technique uses the principle that the velocity of sound in a gas is a function of the molecular weight of the gas. A device using this principle can be designed to be specific for hydrogen and therefore has potential as an inflight hydrogen detector.

The polarographic technique uses a palladium membrane through which only hydrogen will diffuse. The hydrogen comes into contact with an electrolyte

between two electrodes, resulting in a change in the current produced, which is a measure of the amount of hydrogen present. This technique has several potential problems, such as poisoning of the membrane and freezing of the electrolyte, which must be solved before it can be used as an inflight detector.

The fuel cell method uses the normal fuel cell technique on a small scale to generate an electric current when both hydrogen and oxygen are present. If oxygen is contained in a small reservoir in the device, the device becomes a hydrogen detector, generating a current proportional to the amount of hydrogen present. This technique shows promise and will be developed in the near future, depending on the availability of funds.

B. HAZARD DETECTION METHODS

Hazard detection implies the detection of an explosive mixture of hydrogen and oxygen, rather than of hydrogen alone. Methods under investigation include the catalytic method, using a catalyst such as platinum to stimulate a reaction between any hydrogen and oxygen that are present. The resulting heat can be measured to provide an indication of the concentration of hydrogen and oxygen present and therefore of the explosive hazard. A mass spectrometer can be used for hazard detection by measuring the concentration of both hydrogen and oxygen.

C. EXPLOSION DETECTION METHODS

Explosion detection methods include a pressure rate-of-rise sensor, infrared rate-of-rise surveillance detectors, and ultraviolet detectors. Research and development work is underway on these detectors, and we hope to have flight hardware available in 1966.

IV. MASS SPECTROMETER

The mass spectrometer offered a solution to both hydrogen detection and hazard detection and appeared to be one of the most promising and most quickly attainable devices. Development was therefore begun on a spectrometer capable of performing this dual function as a flight instrument.

There are several types of mass spectrometers, including the magnetic deflection, time-of-flight, radio frequency, omegatron, and quadrupole mass spectrometers. Each has its advantages and disadvantages. Some have been used in satellite and other applications for qualitative and rough quantitative analysis, but none had all the desired features of high sensitivity, wide pressure range, good accuracy, and ruggedness for space vehicle environment. The quadrupole was chosen as the most promising for our application, and Consolidated Systems Corporation was selected to perform the research and development needed to produce a device to meet our requirements.

The quadrupole, like all mass spectrometers, has the general block diagram shown in Figure 1.

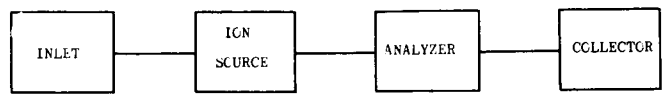

FIGURE 1. MASS SPECTROMETER GENERAL BLOCK DIAGRAM

The inner part of the spectrometer must operate at a pressure of 10^{-4} mm Hg or less, so the inlet can be a serious problem when the ambient pressure covers a wide range. In this application we will use a molecular leak to give flow rate in proportion to the partial pressures of the gases being analyzed. The molecular leak will take one of two forms which are being investigated. The first consists of a series of small holes, of the order of a few tenths of a micron, drilled in a thin gold foil by electron bombardment. The total flow rate will depend on how many such holes are formed. The second consists of a spherical valve seated in a circular knife-edge seat. The flow rate of this inlet aperture can be reduced by increasing the seating pressure. Tests indicate that this technique gives very good molecular flow without as great a clogging problem as has been experienced with the other construction.

The ion source is straightforward. A filament supplies ionizing electrons which are forced into a semicircular path by electrostatic focusing. The ions, formed by collision of the electrons with the gas molecules, are focused into the analyzer section by accelerating and focusing grids.

The analyzer section is the heart of the spectrometer. Here the ionized gases are separated according to mass. The different types of mass spectrometers differ mainly in the way the analyzer operates. The quadrupole analyzer, as shown on the simplified schematic view of Figure 2, consists of four rods, with opposing rods electrically connected and with a dc and an ac voltage applied to the rod pairs.

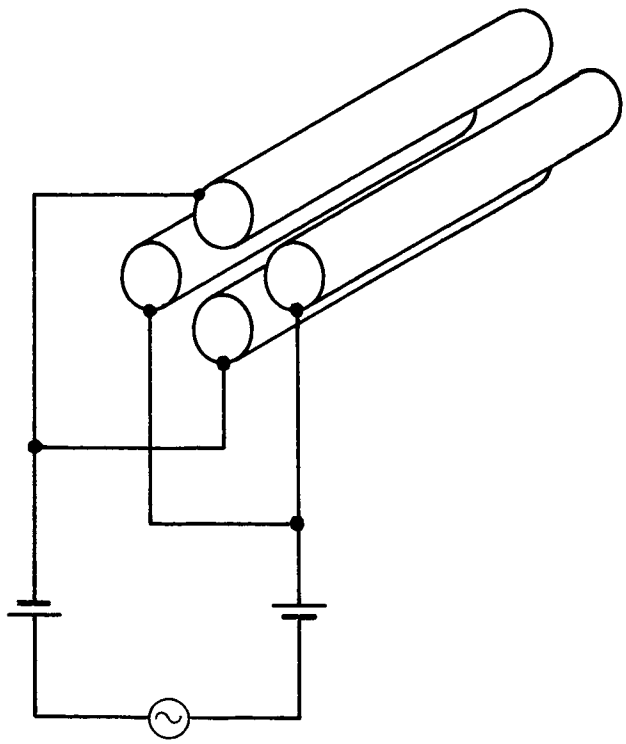

FIGURE 2. SIMPLIFIED SCHEMATIC OF QUADRUPOLE ANALYZER ROD ASSEMBLY

The ion source in front of the rod assembly projects a stream of ions from the sample gas longitudinally down the instrument between the rods. The combined dc and ac fields are such that only one mass will be resonant and will be focused toward the other end, the particular mass being selected by the voltage and frequency of the fields. All other masses collide with the rods and are collected by them. For this reason, the quadrupole is often referred to as a mass filter, analogous to an electrical bandpass filter, instead of a spectrometer, since it does not separate all ions present into a spectrum according to mass. In this case, two different excitation frequencies are selected and switched in so that both hydrogen and oxygen can be detected. The quadrupole can then serve as both a hydrogen detector and as an explosive mixture detector. A third oscillator frequency, tuned to resonate for iodine, is switched in periodically as a calibration reference. A small sealed quantity of iodine with a separate inlet system is supplied for this purpose.

The ions emerging from the other end of the analyzer strike the first dynode of an electron multiplier, which amplifies the resulting secondary emission electrons, thereby producing an output proportional to the amount of the particular gas present.

Figure 3, a complete block diagram of the quadrupole spectrometer, shows the four main parts plus all the auxiliary circuits such as the vacuum pumping system, reference gas supply, temperature controllers, control circuitry, etc.

The quadrupole spectrometer is comparatively simple and rugged mechanically and requires no magnet. Size, weight, and power are important, but satisfactory performance is the primary consideration. The spectrometer must be sensitive, since the lower explosive limit of hydrogen in air is about a four percent concentration. Response time must be short if it is to be useful as a warning device. Accuracy must be good enough that the measurement can be relied upon. Considering these factors, the specifications in Table I were derived.

TABLE I
SPECIFICATIONS FOR QUADRUPOLE MASS SPECTROMETER

1.	Ambient pressure:	760 to 10^{-4} mm Hg
2.	Temperature:	+75°C to -50°C
3.	Vibration:	35 G random
4.	Sensitivity:	7.6×10^{-3} mm Hg (partial pressure)
5.	Range:	7.6×10^{-3} to 200 mm Hg (partial pressure)
6.	Accuracy:	5% of reading
7.	Output:	0 to 5 V in three ranges
8.	Time Constant:	30 to 100 ms
9.	Power:	40 watts
10.	Operating Modes:	H_2 Only O_2 Only H_2 and O_2 alternately

The quadrupole rod assembly is shown in Figure 4; the ion source is at the left. Figure 5 shows the quadrupole analyzer mechanism packaged, with the inlet at the right, then the ion source, the analyzer section, the electron multiplier at the rear, and a small ion pump to maintain the internal vacuum during operation. The complete quadrupole mass spectrometer gas detector, with the case removed to show the electronic circuit cards, analyzer, reference source, pump, etc., is shown in Figure 6. Figure 7 shows the device in its case as it would appear for flight. The complete prototype package, including the electronic circuitry, is about 25 x 35 x 51 cm and about 23 kg in mass. Production versions could be considerably smaller, especially if only hydrogen detection was required. Delivery of the two prototype units is expected early in 1966. These could be flight tested on an early vehicle, although they are not presently scheduled to be flown. Production units could be available sometime next year.

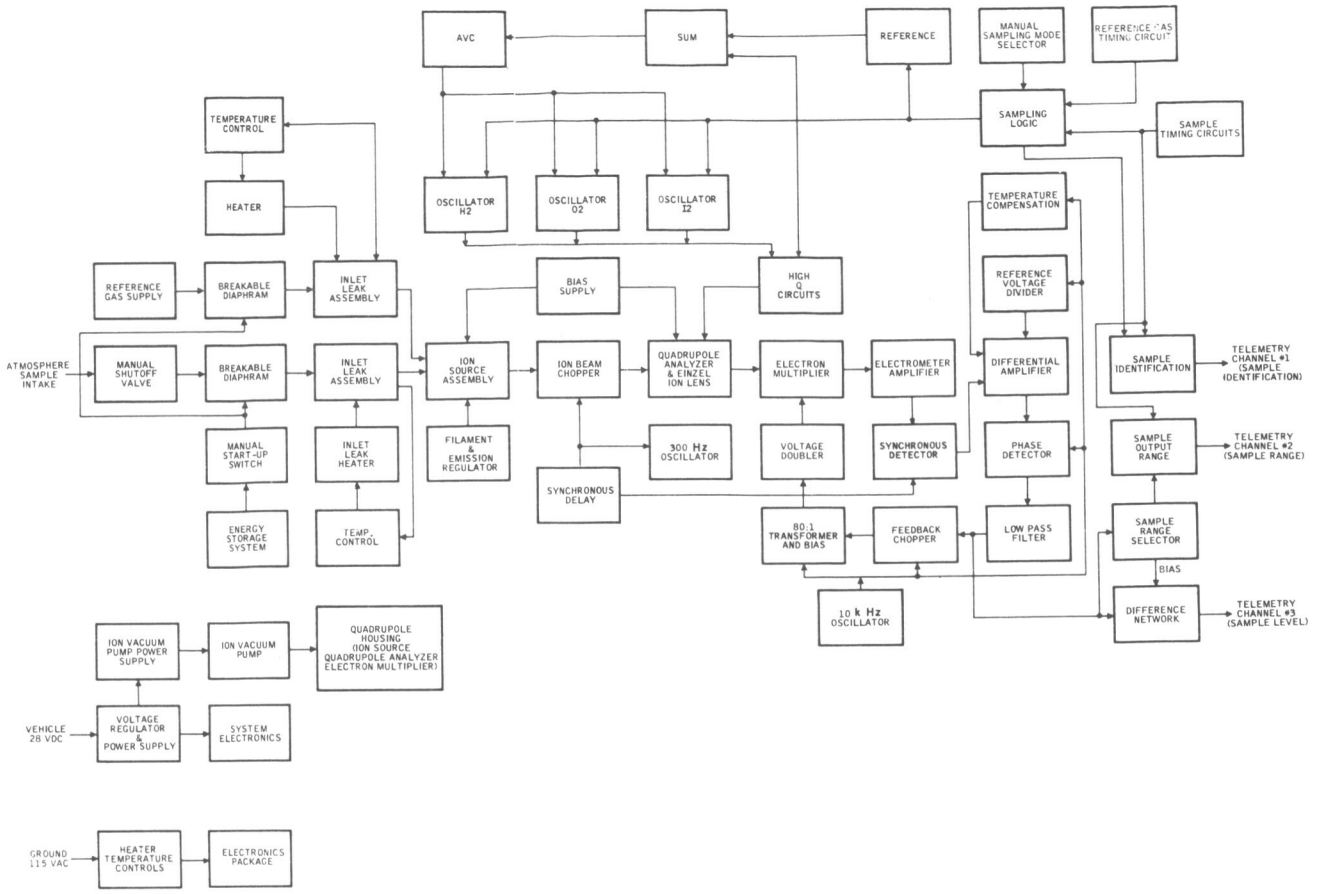

FIGURE 3. QUADRUPOLE MASS SPECTROMETER BLOCK DIAGRAM

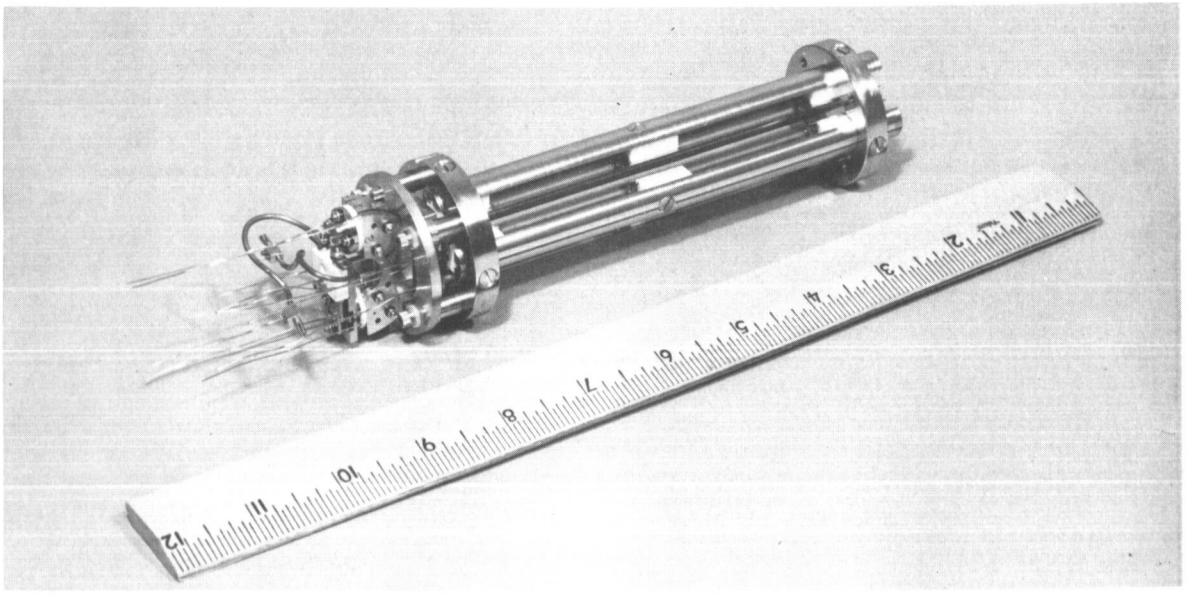

FIGURE 4. QUADRUPOLE ROD ASSEMBLY

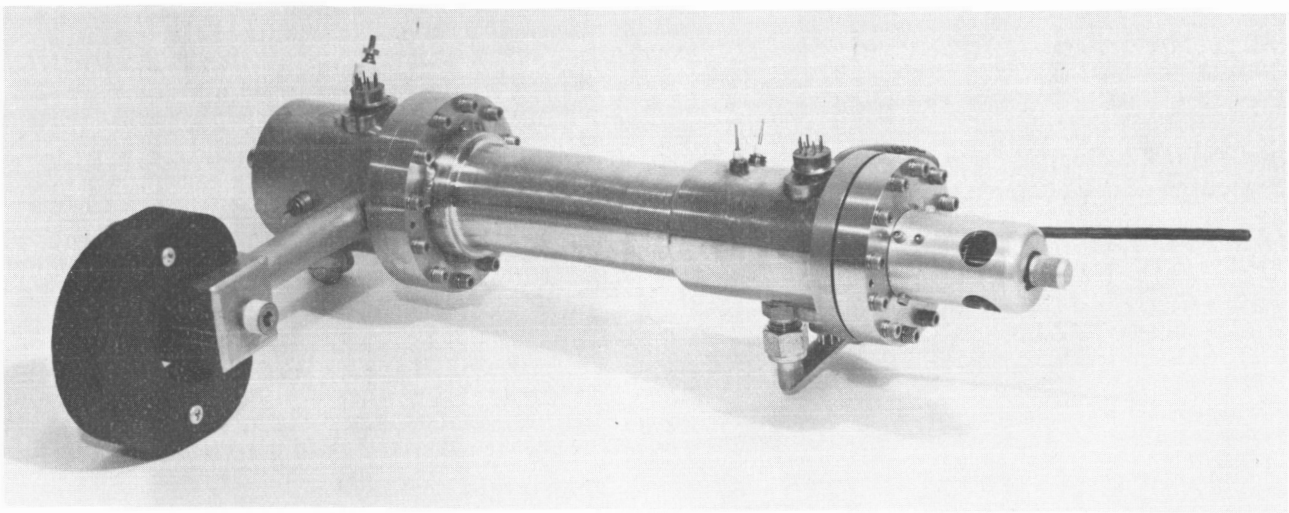

FIGURE 5. ASSEMBLED QUADRUPOLE ANALYZER MECHANISM

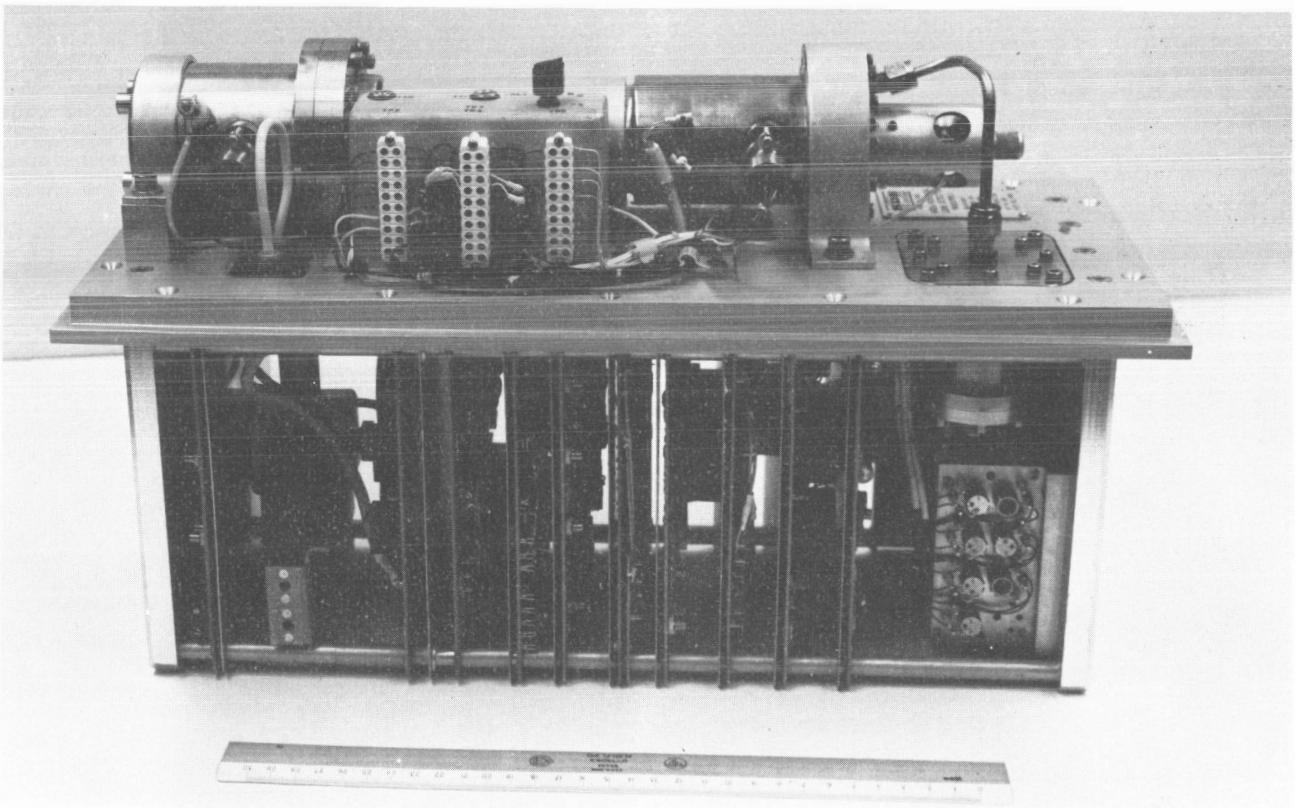

FIGURE 6. COMPLETE MASS SPECTROMETER, CASE REMOVED

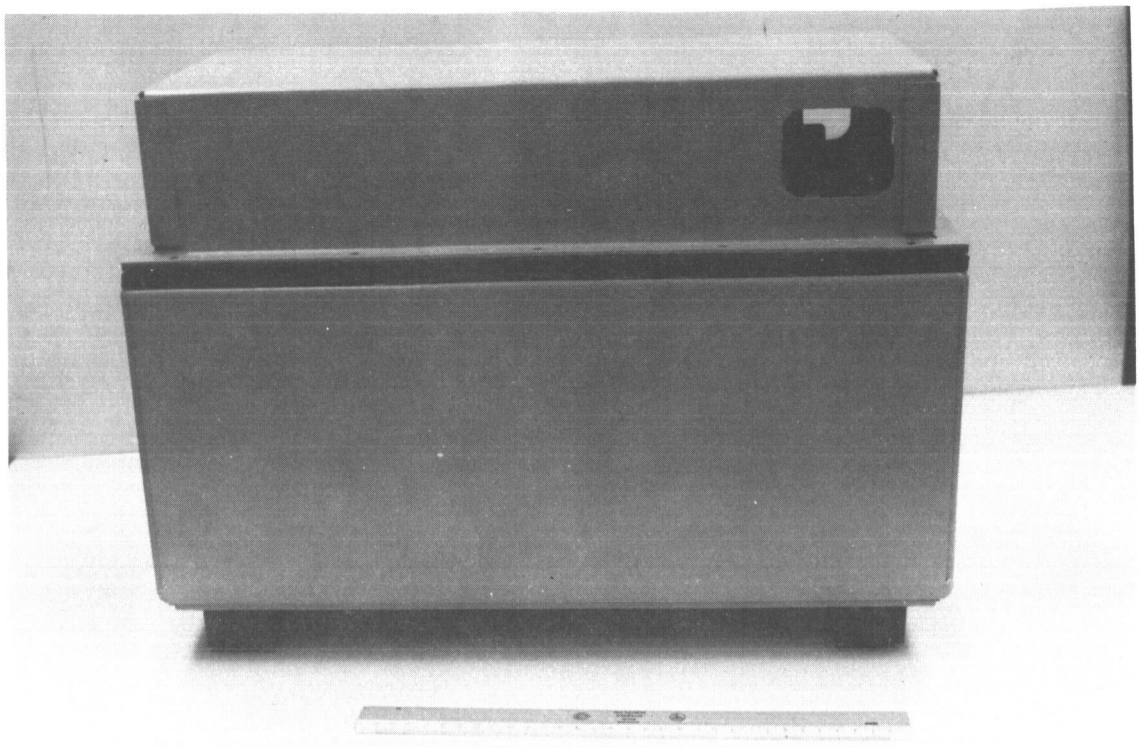

FIGURE 7. COMPLETE MASS SPECTROMETER WITH CASE

V. CONCLUSION

Considerable effort is being made to develop instrumentation suitable for inflight detection of hydrogen, explosive hazards, and explosions. The mass spectrometer is one example. The ultimate goal is to reduce the danger to the vehicles and to the crew.

N67-30585

THERMALLY ISOLATED TEMPERATURE SENSOR FOR SPACE APPLICATION

By

Harlan Burke

ABSTRACT

The requirements for inflight thermal sensors are discussed, as are the design guidelines for such instruments. The four-element thermal sensor experiment used on the Pegasus satellite is described and some of the flight measurements are presented.

GLOSSARY

C_1 = Conductance

R_1 = Radiance

C_T = Total thermal conductance

$C_2 = K_1A_1/l_2$

$C_3 = K_1A_1/l_3 + K_1A_1/\ l_1^2 + l_3^2$

$C_4 = K_1A_1/l_4$

K_1 = Conductivity of Ti (6AL-4V)

A_1 = Cross section of Ti support rods

$l_{1,2,3,4}$ = Lengths of Ti support rods

K_2 = Conductivity of constantan

A_2 = Cross section of electrical leads

l_5 = Length of electrical leads

A_3 = Surface area of sensing disc

E = Emissivity of gold coated underside

σ = Stefan-Boltzmann constant

P = Density of Al 6064

V = Volume of sensing disc

S = Specific heat of Al

I. INTRODUCTION

Inflight measurements originate when the need for confirmation of a vehicle system design or a control parameter is recognized. Many factors influence the selection of the measuring techniques and systems to be used in obtaining the desired data. Frequently a measuring problem arises that cannot be accomplished with either existing or modified components, and it becomes necessary to develop new methods and instruments. The thermally isolated sensor was selected to illustrate the development of an instrument to satisfy a unique measuring requirement.

The design of temperature control systems for space vehicles depends primarily on the application of the thermal radiation characteristics of the vehicle surfaces. It is essential that the thermal radiation properties of these surfaces remain stable when exposed to the space environment. The requirement that each space vehicle be successful in its mission has limited the use of new coatings whose properties are untested in space. As part of an investigation to study the long term stability of a number of new temperature-control coatings, an experiment was devised by Research Projects and Astrionics Laboratories to measure the radiation properties of surfaces in the space environment. This experiment has been included in the Explorer XI, Saturn SA-4, and the more recent Pegasus satellite flights.

Although the primary purpose of the investigation is to study the emissivity stability of surfaces, this discussion will describe the technique for measuring these characteristics during flight in space. Since each vehicle requires a different configuration, the Pegasus experiment package will be used as a typical example of the application of these techniques.

The method consists of measuring the temperature history of a number of thermally isolated test surfaces. Thermal isolation of the test surface from the satellite structure minimizes the extraneous heat losses of conduction and radiation from the sensor. A transient thermal analysis is used to determine the radiation characteristics of the surfaces from the temperature response curves.

Four different surfaces have been tested so far in this experiment. A fifth surface, which was designed to remain unchanged in space, was used as a reference. Comparisons of the temperatures of the test surfaces with that of the reference surface provide a basis for evaluating changes in the thermal characteristics of the test coatings. Additional coatings are scheduled for testing utilizing this technique on future space vehicles assigned to MSFC.

II. DESIGN GUIDELINES

The following design guidelines were set forth at the beginning of the program to assure overall accuracy and reliability in the technique for determining the radiation characteristics of the test surfaces:

1. Thermally isolated test surfaces to minimize corrections for heat exchanges caused by conduction and radiation.

2. Thermal mass of the test sensor to be such that the sensors would respond rapidly to temperature changes, yet have enough thermal lag to permit measurement of the rate of temperature decay as the sensor moves from the sunlight into the shadow.

3. Structural rigidity to withstand the space environment.

4. At least one stable reference surface so that any changes in the test surfaces caused by the space environment would be detected.

5. Telemetry and temperature measuring systems of sufficient sensitivity and accuracy.

III. RADIATION SENSOR DESIGN

In accordance with these requirements, the sensors were designed to minimize extraneous heat losses from the test surfaces. Careful attention was given to the selection of materials for the sensor assembly and to the preparation of the mounting configuration. Figure 1 is the completed sensor assembly in a cutaway view of the mounting cylinder.

This assembly differs from earlier models in that the aluminum sensor disc was supported by a single Kel-F support rod. When flight data indicated that the sensor temperature was approaching the point at which the Kel-F began to deteriorate, it became necessary to replace this material with one of higher temperature resistance.

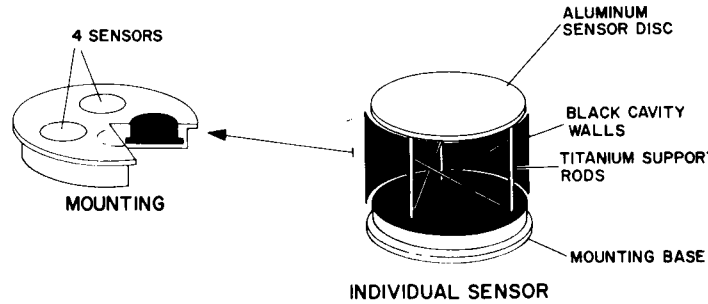

FIGURE 1. INSTALLATION DRAWING OF INDIVIDUAL SENSOR

In the present design, the sensor disc is supported by three 6AL4V titanium rods. The diameter of these rods was selected so that the conductive heat losses from the sensor disc through the rods did not exceed the heat losses through the Kel-F support rods of the previous sensors. The small size of these rods increased the flexibility of the unit, and cross braces were necessary to increase the mechanical strength to withstand the vibration of the vehicle.

The front surface of the sensor disc was coated with the material to be tested. An emissivity of $\cong 0.05$ was obtained for the back surface of the disc by vapor depositing gold on the surface after installation of the temperature sensor. Internal surfaces of the mounting base and the walls of the cylinder were black anodized to provide an emissivity of $\cong 0.70$. Thus, the low emittance surface of the sensor disc was installed in a cavity of comparatively high emittance characteristics.

The thermodynamic design properties of the sensor were determined by Research Projects Laboratory and are shown in Table I.

After finalization of the design, a contract was given for fabrication of the flight units. The contractor was unable to deliver acceptable units because of titanium-to-aluminum welding problems, poor emissivity of the gold coating on the back surface of the disc, and the close tolerances on the assembly necessary for mounting.

Astrionics Laboratory developed an electron beam welding technique to fuse the aluminum and titanium and a method of vapor depositing the gold over the back surface of the disc to provide the

desired emissivity. All of the flight units were fabricated and calibrated by this laboratory.

TABLE I
THERMODYNAMIC DESIGN PROPERTIES OF THE MMC THERMALLY ISOLATED SENSOR EXPERIMENT (R-RP-T-WP-6-64)

PROPERTY	EQUATION	VALUE
DIAGRAM	DISC o — C_1 — CASE, R_1	
CONDUCTANCE THROUGH THE SUPPORTS	$\frac{1}{C_T} = \frac{1}{C_2} + \frac{1}{C_3} + \frac{1}{C_4}$	$C_T = 2.5 \times 10^{-4}$ WATTS/°K
CONDUCTANCE OF THE ELECTRICAL LEADS	$C_5 = KA/\ell$	$C_5 = 0.05 \times 10^{-4}$ WATTS/°K
CONDUCTANCE FROM THE DISC TO THE CASE	$C_1 = C_T + C_5$	$C_1 = 2.6 \times 10^{-4}$ WATTS/°K
RADIANCE OF THE DISC TO THE CASE	$R_1 = AE\sigma$	$R_1 = 2.2 \times 10^{-4}$ WATTS/°K
HEAT CAPACITY OF THE UNCOATED DISC	$H_1 = PVS$	$H_1 = 1.03$ JOULES /°K

The radiation sensors were arranged in a cluster of four, as shown in Figure 2, for mounting on the Pegasus satellite. The overall weight of the sensor assembly was 563 grams.

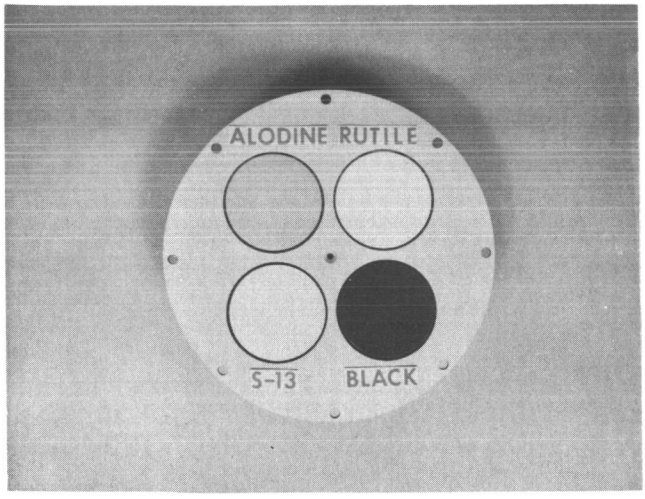

FIGURE 2. PEGASUS EXPERIMENT PACKAGE

Each sensor was coated with a different material by the Propulsion and Vehicle Engineering Laboratory. Table II is a list of the materials used in this experiment.

A 200 ohm nickel-element resistance thermometer encased in a thin sheet of bakelite was selected

TABLE II
COATINGS FOR MMC THERMALLY ISOLATED SENSOR EXPERIMENT

COATING	EMITTANCE	VEHICLE	PIGMENT	COMMENTS
BLACK PAINT	0.91	DOW CORNING SILICONE 808	CARBON BLACK ROYAL SPECTRUM MOCKS	DETERIORATES WHEN SUBJECTED TO A TEMPERATURE OF 370° C FOR TWO OR MORE HOURS. USED ON MMC STRUCTURE NEAR ELECTRONICS CANISTER. CONSIDERED AS A REFERENCE.
S-13 WHITE PAINT	0.89	POTASSIUM SILICATE	ZINC OXIDE	WILL BE THE EXTERNAL COATING ON THE S-IV, IU, AND APOLLO ADAPTER.
ALODINE	0.60 (VARIES FROM ONE PROCESSED GROUP TO ANOTHER)	CHEMICAL CONVERSION OF ALUMINUM-FORMS: ALUMINUM PHOSPHATE, CHROMIUM PHOSPHATE, WATER, FLOURIDES		USED ON THE MMC STRUCTURE AND DETECTOR PANELS.
RUTILE	0.78	SILICONE	TITANIUM DIOXIDE	CHOSEN FOR COMPARISON WITH TEST DATA FROM OTHER AGENCIES

as the temperature sensor because of its size, resistance to radiation, repeatability, resistance-versus-temperature curve over the desired range, and time response. Four of these resistance thermometers were used on the sensor discs. A fifth unit of higher resistance was mounted on the base plate to measure the temperature of the cavity walls. Since the base plate and the cavity housing were in good thermal contact, they were considered to be at the same temperature. This additional measurement permitted correction for heat exchanges between the test surfaces and the sensor mounting assembly. Figure 3 is a block diagram of the temperature measuring system for this vehicle.

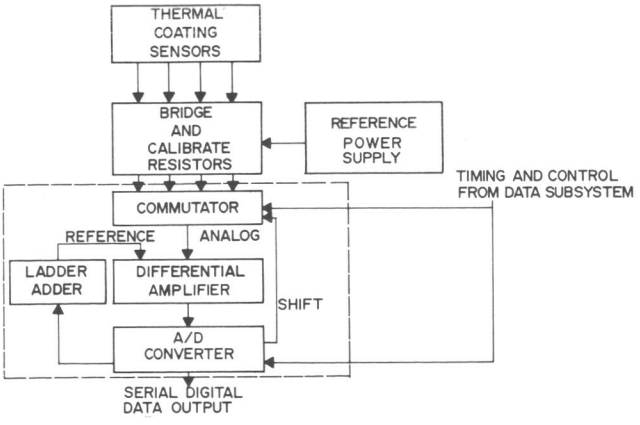

FIGURE 3. MMC TEMPERATURE SUBSYSTEM

The radiative constants were determined by total normal emittance measurements and were used to calculate a theoretical response curve for each sensor. The sensors were then placed in a test fixture

in a vacuum and alternately heated and cooled, as shown in Figure 4.

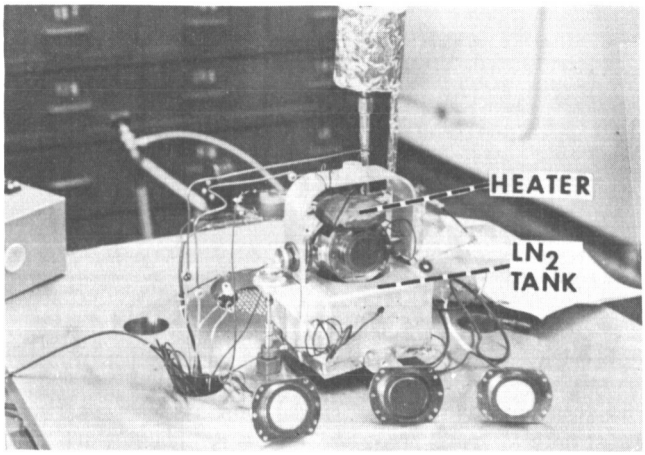

FIGURE 4. CALIBRATION FACILITY

The disc and case temperatures were monitored and compared with the calculated response curves. Figure 5 is typical of the data obtained from these tests.

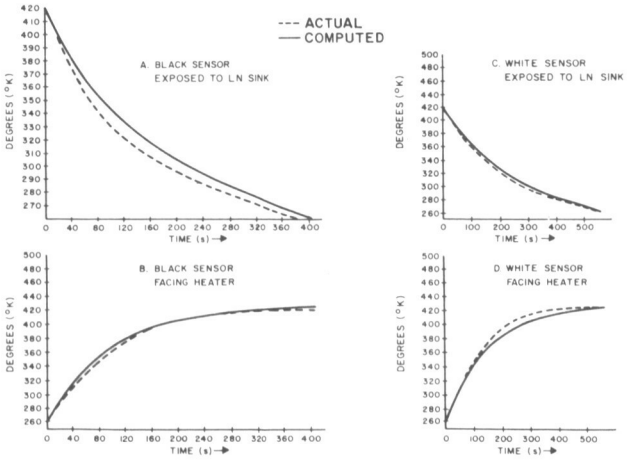

FIGURE 5. ISOLATED SENSOR: THEORETICAL AND MEASURED TEMPERATURE RESPONSE CURVES

IV. RESULTS OF FLIGHT MEASUREMENTS

The results of the flight measurements cannot be presented without considering the heating sources for the test surfaces in the space environment. In space, the surfaces receive heat primarily from direct solar radiation, reflected solar radiation from the earth, and direct radiation from the earth. In addition, a small amount of energy is transferred from the underside of the disc to the mounting cylinder. Energy from direct solar radiation is constant during the time that the sensor is in the sun. Heating from reflected sunlight varies with the sensor position and aspect. A computer program, written by Research Projects Laboratory, incorporates all the factors necessary in the data analysis of this experiment.

Reduction of the Pegasus A thermally isolated sensor data is continuing. The α_s/ϵ_T ratio of solar absorptance to infrared emittance as a function of sun time is shown in Figure 6. The data were taken from orbits in which the sensor was normal to the sun at points where the earth was not visible to the sensors. This condition permits the ratio of the solar absorptance to infrared emittance to be obtained from the steady state disc temperature, which is primarily a function of solar input. Details of data reduction can be obtained from R-RP-T of Research Projects Laboratory.

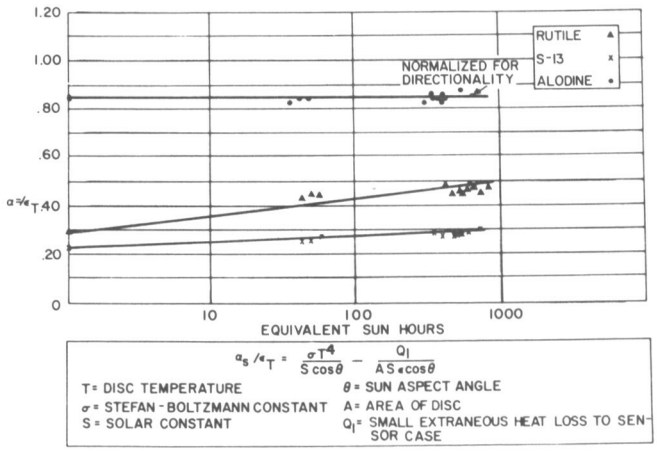

FIGURE 6. ABSORPTANCE-INFRARED EMITTANCE OF PEGASUS "A" REFERENCE SENSORS VS EQUIVALENT SUN TIME

V. CONCLUSION

The thermally isolated sensor is a useful tool for the materials research engineer in determining the properties of coatings and surfaces in the space environment. It also provides information in other areas of interest. For example, the Apollo Office observed an apparent change in the α/ϵ characteristics of the coating used on the service module adapter

on the SA-10 flight. This change was not observed in the protected thermal sensor package and was considered to be the result of some external condition. MSFC has been asked to place instrumentation upstream of the retrorocket exhaust to determine if this is the source of the problem. Thermally isolated sensors will be used in the testing program for the solution of this problem.

N67-30586

UHF TELEMETRY DEVELOPMENT AT MSFC

By

Donald G. Davis

ABSTRACT

The background of recent decisions relating to frequency bands used for telemetry and changes planned to be effective by 1970 are discussed. A telemetry program and details of UHF transmitter developments are presented.

I. INTRODUCTION

The radio frequency spectrum is considered a natural resource and, as such, its use is regulated by the Federal Government. The worldwide use of frequencies is covered by international treaties.

By means of the Communications Act of 1934, Congress designated that regulation of frequency utilization by government agencies be placed under the President and regulation of non-government radio and wire communications be placed under the Federal Communications Commission (Fig. 1).

The President has delegated the responsibility for regulation of government usage of radio frequencies to the Director of Telecommunications Management (DTM), who is an assistant director of the Office of Emergency Planning. The DTM is assisted in this by the Interdepartmental Radio Advisory Council (IRAC).

For many years the frequency band between 225 and 260 MHz has been designated by IRAC for interim use by the telemetering services. A target date of January 1, 1970, was established for completing the move of telemetering to two other frequency bands: 1435 to 1535 MHz and 2200 to 2300 MHz. Based on an agreement between NASA and DOD in 1963, MSFC has based its telemetry planning on almost exclusive use of the older 225 to 260 MHz band. However, in February 1965, DOD issued a firm directive to the three military services requiring that they completely vacate the 225 to 260 MHz band by January 1970. In March 1965, DOD requested that NASA also vacate this band so that it might be used for tactical and operational military communications. This matter is now under study by NASA and a decision is expected to be made within a few months (Table I).

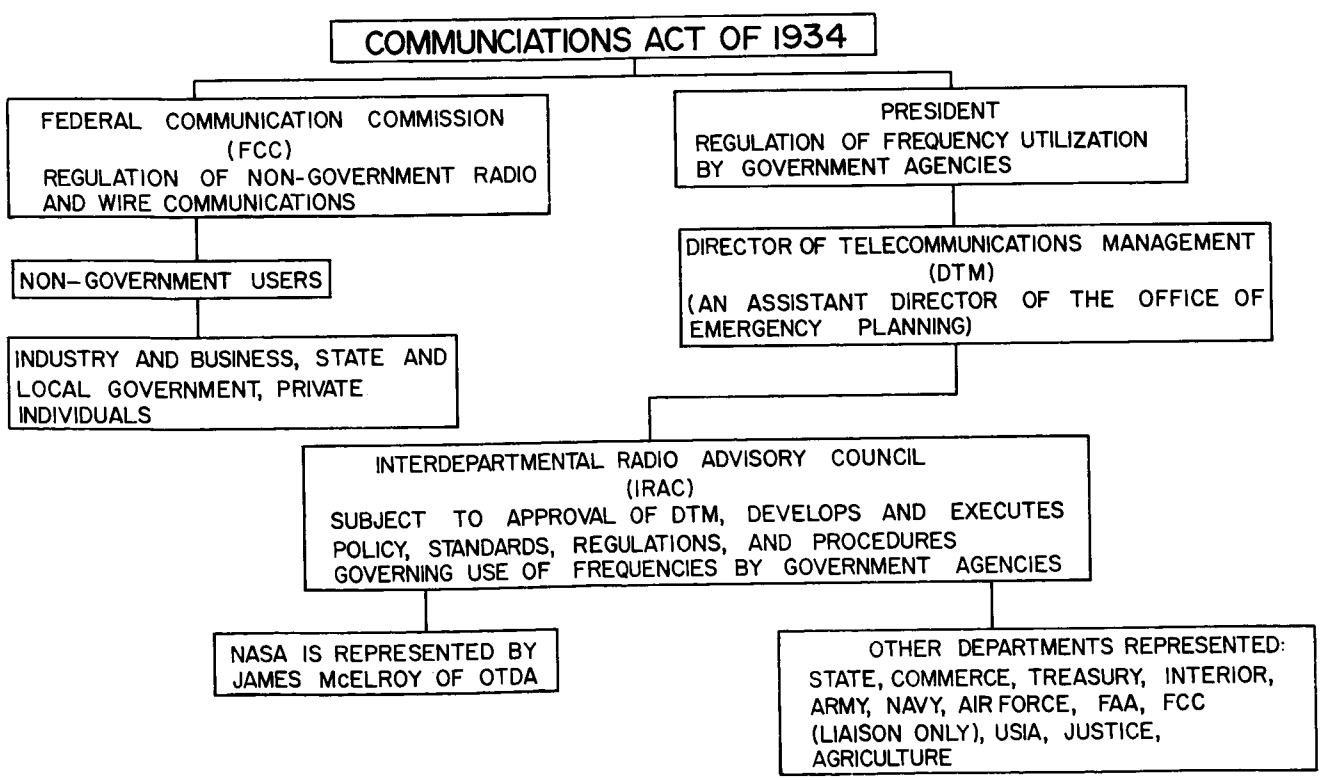

FIGURE 1. COMMUNICATIONS ACT OF 1934

TABLE I
TELEMETRY FREQUENCY ALLOCATION ACTIVITIES

1953-1956	- The 216 to 225 MHz frequency band was widely used for telemetering.
1956	- The military began use of the 216 to 225 MHz band for air defense radar. Telemetry users objected.
1958	- IRAC made available 44 channels in the 225 to 260 MHz band for interim telemetry use. A target date of January 1, 1970, was established for telemetering to vacate this band.
1958-1962	- Some telemetering development in the 2200 to 2300 MHz band by DOD agencies and NASA. Very little non-government sponsored industry effort.
1962	- DOD began to circulate reports encouraging industry to design 1400 MHz and 2200 MHz telemetry equipment.
1963	- A joint DOD/NASA memorandum to IRAC noted that "there is a need for continuation of telemetering operation in the 225 to 260 MHz band beyond 1970."
Feb. 1965	- MCEB issued a firm directive to the three military departments and notified IRAC that DOD telemetry operations would completely be removed from the 225 to 260 MHz band by 1970.
Mar. 1965	- Dr. Harold Brown, (then) Director of Defense R&D, wrote a letter to Dr. Seamens requesting that NASA vacate the 225 to 260 MHz band by 1970.
Apr. 1965	- NASA requested that IRAC delay its recommendation to the DTM pending completion of NASA study on future needs for telemetering in the 225 to 260 MHz.
June 1965	- VHF telemetry study group established with representatives from affected centers and NASA Headquarters.
Sept. 1, 1965	- Target date for completion of study.

In general, the 225 to 260 MHz band (generally referred to as the VHF telemetry band) is more desirable for telemetering space vehicles during launch and orbital operations than the higher frequency (or UHF) bands. This is due primarily to the relative difficulty of ground antenna acquisition of signals, the relative state of the art in development of equipment in the two bands, and the greater complexity of equipment for operation at the higher frequencies. After a space vehicle leaves earth orbit (for example, the translunar trajectory), the use of UHF frequencies becomes more advantageous because directional vehicle antennas are more easily implemented at the higher frequencies.

One of the major problem areas associated with telemetry operations at the UHF frequencies is the availability of RF transmitters which meet the necessary specifications. Since 1963 MSFC has carried on an active program in the design and development of UHF transmitters. Much of this work has been accomplished under the five contracts shown in Table II.

II. FIVE-WATT UHF TRANSMITTER DEVELOPMENT

In June 1963, a contract was awarded to Hallicrafters, Pacific Division, for a five-watt solid-state S-band transmitter. A block diagram of the proposed transmitter is shown in Figure 2.

TABLE II
MSFC UHF TRANSMITTER CONTRACTS

August 1, 1965

Contract Number	Date Awarded	Recipient	Objective	Status
NAS8-5497	June 1963	Hallicrafters, Inc. (Pacific Division)	Development of a 5-watt solid-state S-band transmitter	Contract cancelled in October 1964 for convenience of the government with no payment
NAS8-5494	June 1963	Radiation at Stanford (Later this group became Energy Systems, Inc.)	Development of a 20-watt hybrid S-band transmitter	Evaluation of first unit began in September 1965
NAS8-11771	June 1964	Energy Systems, Inc.	Development of a 5-watt solid-state transmitter	Transmitter components being assembled at contractor facilities
NAS8-11822	Jan. 1965	Electro-Mechanical Research, Inc.	Off-the-shelf purchase of 20-watt L-band transmitter	Delivery expected January 1966
NAS8-20505	June 1965	Energy Systems, Inc.	Development of 20-watt solid-state S-band transmitter	Various design approaches are being evaluated

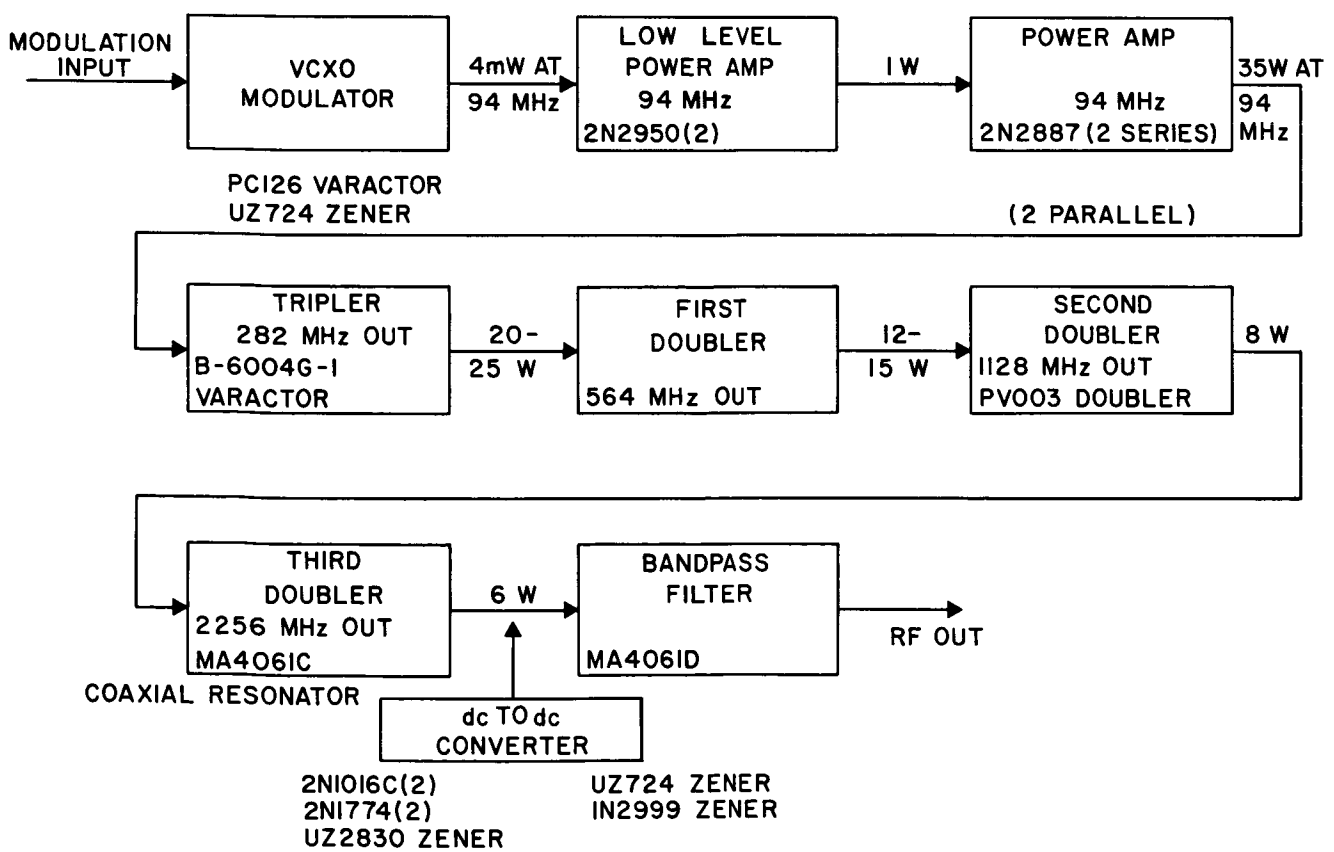

FIGURE 2. BLOCK DIAGRAM OF INITIAL 5-W TRANSMITTER DEVELOPMENT EFFORT

A voltage controlled crystal oscillator (VCXO) modulator was employed with output at 94 MHz. The 94-MHz signal was amplified to over 35 W in a power amplifier and then coupled to a multiplier chain of one varactor tripler and three varactor doublers. Power output at 2200 to 2300 MHz was to be 5 watts.

The required frequency was obtained by using an ideally cut quartz crystal with a temperature stability of about ±0.002 percent from -20° C to +90° C. By using negative-temperature-coefficient capacitors in series with the crystal, it was found possible to stabilize the drift to within ±0.001 percent of the frequency at 25° C while varying the temperature from -20° C to +85° C.

The low-level power amplifier stage produced 1 W output for 1 mW input for approximately a 30 db gain. Since the modulator output was about 4 mW, the low-level power amplifier supplied more than 1 W to the power amplifiers. The main power amplifier consisted of three parallel stages, each using four RF power transistors. With 1 W input, the measured output power was 35 W at 94 MHz.

The output of the power amplifier stage is applied to a tripler which uses a single ended varactor. The efficiency of the tripler was measured at about 60 percent, producing an output between 20 and 25 W at 282 MHz. Both the first and second doublers had an efficiency of about 60 percent, which resulted in an output of 9 to 10 W at 1128 MHz. The third doubler produces an output of approximately 6 watts at 2256 MHz.

In January 1964, a unit was demonstrated at MSFC. Tests run at that time demonstrated that the unit did not meet the specified requirements. In April 1964, Hallicrafters was visited by an MSFC technical representative who found that no progress had been made on correcting the problems that existed. In May 1964, the work was transferred to Hallicrafters in Chicago for completion.

In October 1964, nine months after scheduled delivery, the contract was cancelled for the convenience of the Government with no payment to the contractor.

III. TWENTY-WATT HYBRID TRANSMITTER

In June 1963, MSFC awarded contract NAS8-5494 to Energy Systems, Inc., (at that time it was called Radiation at Stanford) for the development of a 20-W S-band transmitter. A block diagram of the proposed transmitter is shown in Figure 3. Basically, it consists of circuitry generating the S-band frequency at a low power level to drive a traveling wave tube (TWT), which produces the required output power. A phase-locked loop, using a crystal oscillator as reference, is used to minimize the effects of incidental frequency modulation.

The circuitry is entirely solid state except for the final TWT. Excitation for the TWT is generated by a 190-MHz voltage-controlled oscillator followed by three stages of amplification, which provides an output of about 300 mW. This signal is applied to a varactor quadrupler and then to a varactor tripler. A bandpass filter is then used to eliminate undesired spurious outputs from the multipliers, resulting in about 25 mW at the input to the TWT.

A crystal oscillator operating at approximately 81 MHz is the basic frequency stabilizing element for the transmitter. This frequency is multiplied by a transistor tripler followed by a varactor times-9 multiplier and is then mixed in a hot carrier diode mixer with a sample taken from the TWT output via a directional coupler. This mixer provides a difference frequency of 89 MHz, which is amplified and fed to one side of an 89-MHz phase detector. An 89-MHz voltage-controlled oscillator, whose exact frequency is determined by the modulation input, is amplified and fed to the other side of the phase detector.

If these two frequencies are identical with a 90-degree phase difference between them, the output of the phase detector is zero. The output of this detector is fed through a loop stabilizing filter, and thence to the 190-MHz voltage controlled oscillator (VCO). If for any reason the 190 MHz VCO should drift toward a higher frequency, the phasor would start to advance relative to the phasor being generated by the VCO. This generates an error signal, which decreases the 190-MHz VCO frequency sufficiently that it stays locked to the 89-MHz VCO. However, if a modulation signal changes the frequency of the 89-MHz VCO in the upward direction, the phasor presented to the phase detector moves in such a direction as to cause the 190-MHz VCO to follow. From the diagram, observe that the 190-MHz VCO changes frequency only one-twelfth as much as the 89-MHz VCO because of the intervening multipliers and that frequency drift in the 89-MHz VCO is simply added to the output frequency of the transmitter rather than multiplied by 12.

One reason for choosing a phase-locked loop approach was as follows. There was some concern,

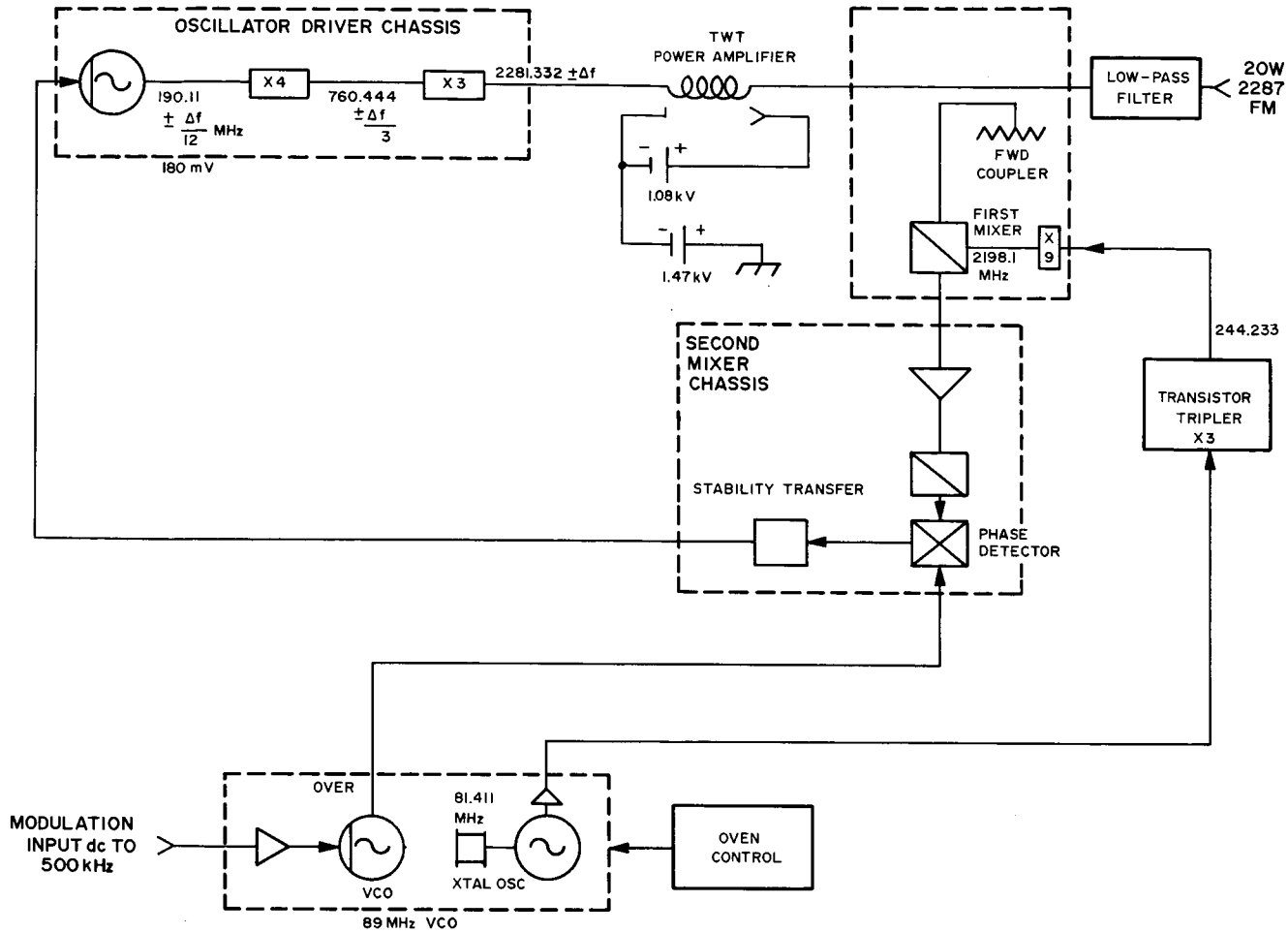

FIGURE 3. BLOCK DIAGRAM OF 20-W HYBRID TRANSMITTER

because of limited experience with TWT's under high vibration and low incidental FM requirements, that the vibration of the relatively long helix might cause a phase deviation which would have the appearance of incidental FM. The phase-locked loop connected in the feedback arrangement described tends to remove any phase modulation generated within the TWT. There were some data at the time the design approach was finalized indicating that the particular method of supporting the helix used by Hughes limited the peak phase deviation to only 2 or 3 degrees, with vibration levels exceeding those in the specification. However, it was deemed desirable to incorporate this scheme as a backup in case this turned out to be an optimistic estimate. However, the development contractor recently reported that there is very little difference in the incidental FM of the transmitter under vibration with the loop open or closed, indicating that the tube does not generate a significant amount of incidental FM when subjected to vibration.

The prototype 20-W transmitter was first tested at MSFC in December 1964. Several deficiencies in the design were discovered and the unit was returned to the contractor for additional development work. Subsequently, a unit which met most of the specifications was delivered in September 1965. At this time the contractor stated that he felt the existing design was not reproducible on a production basis. Redesign is now underway to alleviate this deficiency.

IV. FIVE-WATT SOLID-STATE S-BAND TRANSMITTER

In June 1963, MSFC awarded contract NAS8-11771 to Energy Systems, Inc., for the development of a 5-W S-band solid-state transmitter. The technical approach for this transmitter design is shown in

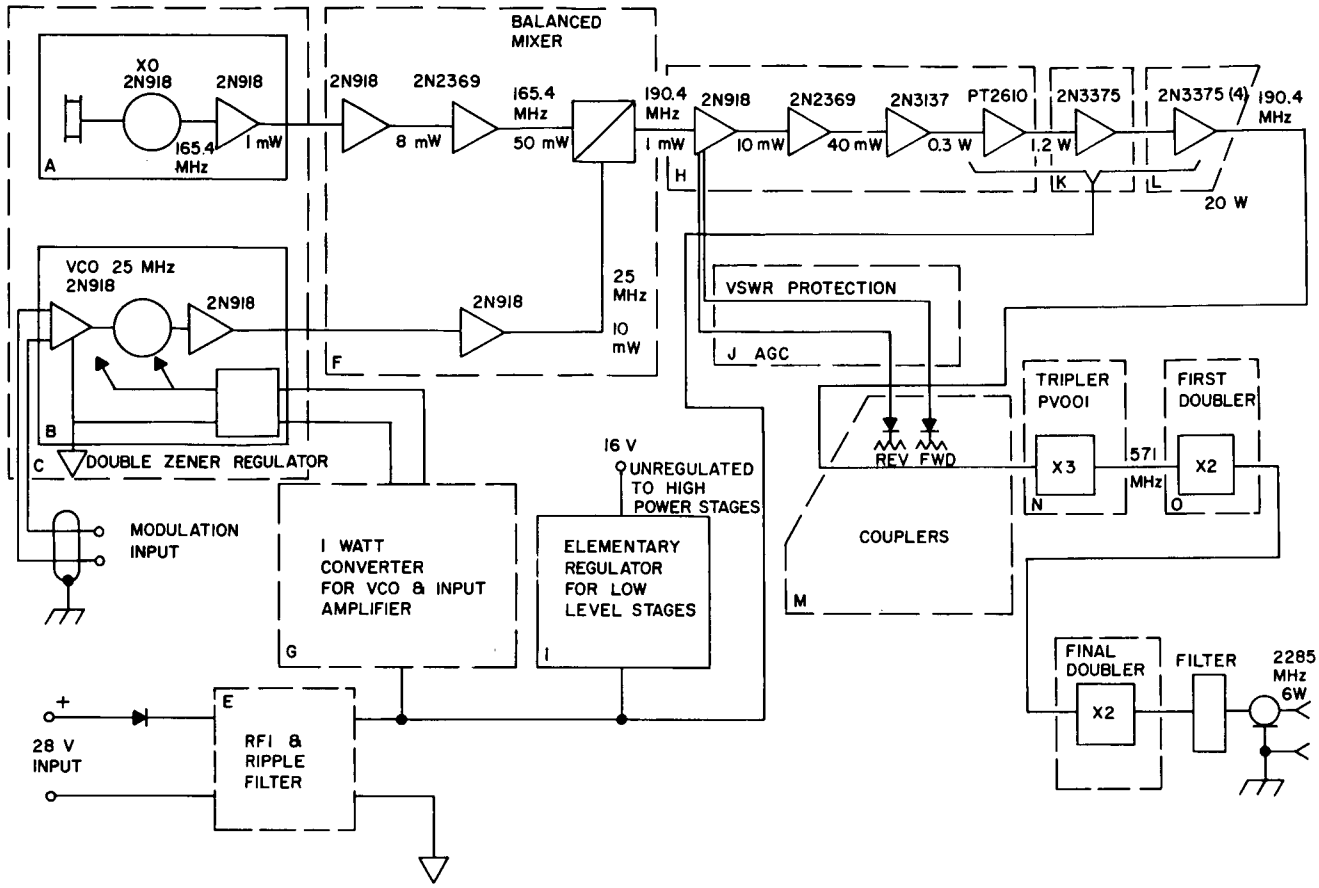

FIGURE 4. BLOCK DIAGRAM OF 5-W SOLID STATE S-BAND TRANSMITTER

Figure 4. A transistor that became available about the beginning of the development effort, the 2N3375 by RCA (development transistor RCA TA2307), enhanced the feasibility of the approach. It uses a type of construction called an "overlay" which employs an emitter electrode design whereby more periphery-to-emitter-area ratio has been achieved. This transistor is capable of operating directly from a 28-volt supply making it practical to operate high power VHF stages without voltage converters. The transistor is electrically insulated from the case and is connected through a high-thermal-conductivity ceramic insulator to its stud.

The fundamental frequency is generated by a stable crystal oscillator essentially identical with the one used in the 20-W TWT transmitter. The same package contains a one-stage amplifier to boost the power of the oscillator output to 1 mW. The milliwatt power level is increased by two amplifiers in series to obtain approximately 50 mW into the balanced mixer circuit. The other input to the mixer is generated by a voltage-controlled oscillator and its buffer amplifier. The VCO has a center frequency of 25 MHz and is approximately 10 times less stable in frequency than the crystal oscillator signal. However, since the VCO frequency is $7\frac{1}{2}$ times less than that of the crystal oscillator, the effect of VCO instability on the output frequency is correspondingly decreased. The VCO is driven from a stabilized dc amplifier which provides an input impedance of 10,000 ohms at the modulation input. The 25-MHz VCO is essentially the same design as the 89-MHz VCO used in the 20-W TWT transmitter. The stability is expected to be on the order of one part in 10^5 for the VCO and one part in 10^6 for the crystal oscillator. Therefore, the transmitter frequency stability should be approximately three parts in 10^6.

Based on the experience gained from the hybrid UHF transmitter, the balanced mixer uses hot carrier diodes. A balanced mixer was selected instead of a single-ended one to obtain the maximum possible elimination of the carrier frequency power with the intrinsic circuit characteristic without relying totally on filtering. The power is then introduced to a string

of five amplifier stages. These amplifiers, because of their staggered tuning, suppress unwanted frequency components of the mixer circuit and prevent these spurious signals from being applied to the varactor multipliers.

A parallel arrangement of transistors in the final power amplifier is used because it is simpler than a push-pull arrangement. This simplicity is realized only if separate emitter resistors are used, tending to make the stages self-adjusting so that their outputs will be more nearly identical. These four transistors are normally operated in a class C mode to obtain the best possible efficiency, and the collector current operating point is selected to obtain the closest possible approach to optimum large signal gain bandwidth.

The 20 W of VHF developed power is delivered through a pair of directional couplers to the varactor tripler, which operates at an efficiency of about 65 percent with an output power of about 13 W. Traps are placed at the input and output to prevent feedback of the second and third harmonics to the amplifier and the first and second harmonics to the quadrupler. The last two stages are doublers which provide an output of about 6 W at 2285 MHz.

The reverse power output from the directional coupler is used for voltage standing wave ratio (VSWR) protection and the forward power output is used for automatic gain control (AGC). The same control point is used for both VSWR and AGC controls and the signals are decoupled by diodes. High VSWR's at the quadrupler output of a multiplier chain of two stages are reflected to the final amplifier stage, but the transistors are protected by the VSWR detection circuit which reduces the power level of the final power amplifier proportional to the VSWR magnitude.

Breadboards of all sections of the 5-W UHF solid-state transmitter have been completed and tested both individually and as a system. All parameters that could be tested met the requirements with an output power greater than 6 W. The transmitter is now being packaged for final testing.

V. TWENTY-WATT SOLID-STATE TRANSMITTER DEVELOPMENT

In mid-1965 it seemed practical to undertake the development of a 20-W solid-state transmitter although it had not appeared feasible a year earlier. This decision was based on the rate at which the solid-state component companies had been completing designs for new S-band devices. The rate of progress in development of these devices makes it probable that changes in a design will be made before the production unit is released. Therefore, this task must follow the state of the art of solid-state components which are suitable for applications in S-band, high-power transmitters for airborne applications.

In June 1965, MSFC awarded contract NAS8-20505 to Energy Systems, Inc., for development of a 20-W solid-state UHF transmitter. The proposed approach to the design of this transmitter is shown in block diagram form in Figure 5. Note that the approach is similar to that followed in the 5-W S-band transmitter. The major challenge lies in the greatly increased RF power level. None of the low-level circuitry of the 5-W S-band transmitter, including the crystal oscillators, VCO, mixer, etc., requires significant changes to raise the power level by 400 percent. However, some minor differences exist because of the development of transistors which operate satisfactorily at higher frequencies and powers since the inception of the 5-W transmitter design.

The modulation input is applied through the VCO circuit to a balanced mixer where it is mixed with the reference signal from a crystal-controlled oscillator. The balanced mixer is essentially identical with the one used in the 5-W transmitter with a frequency scale-up. The mixer uses high performance silicon diodes, hot carrier diodes, and varactors. The bandpass filter is used to further enhance the spurious response of the circuit over what the intrinsic operation of the balanced mixer will provide.

The power is stepped up 10 db in each of the next two stages, increased to 1 W by the next stage, and finally to 5 W by the stage preceding the main amplifier.

There is now in development by RCA for NASA/GSFC a new transistor, the TA2675, which is expected to provide 20 watts of RF power at 430 MHz. The collector efficiency is expected to be about 50 percent and the gain about 6 dB at 430 MHz. The potential advantage in using this transistor is that the intermediate amplifier would require only one transistor and the final power amplifier would require only four paralleled transistors. These amplifiers must use two and eight 2N3733 transistors in parallel, respectively, if the TA2675 or an alternate does not become available.

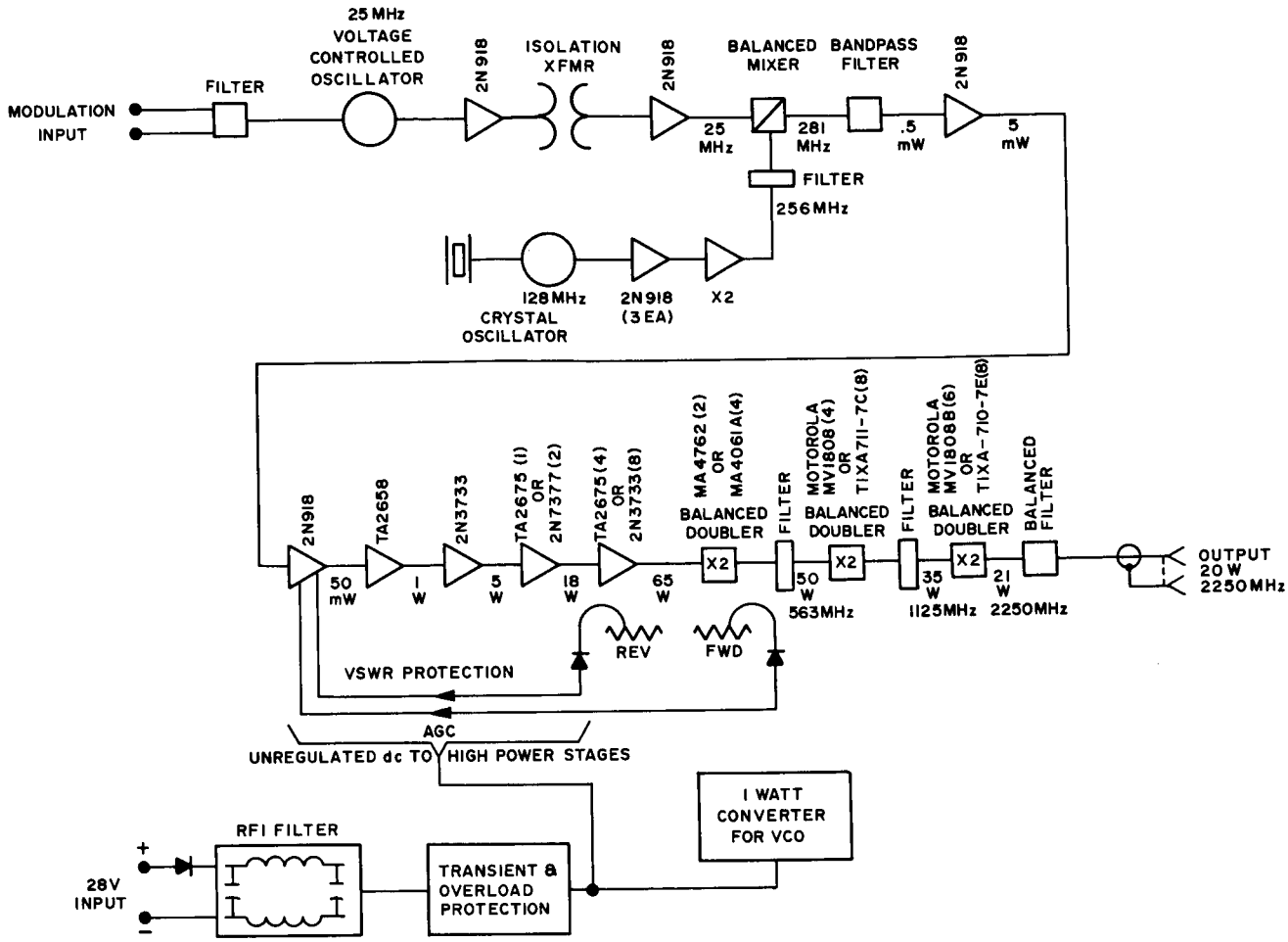

FIGURE 5. BLOCK DIAGRAM OF 20-W SOLID-STATE UHF TRANSMITTER

The present approach to paralleling the transistors is to lay them out in a symmetrical fashion in a circle around a center feed point to assure that the phase of the drive to each transistor is identical. Figure 6 is an example showing how the input circuitry to the paralleled transistors is expected to be arranged. (This shows the worst case of using eight transistors but the principle will remain the same if only four are used.) The 5-W source is delivered to two capacitors which provide a step up of impedance at point A. Transformers are symmetrically spaced in a radial pattern about the capacitor C_1 to resonate each of the input circuits. A step-down transformer, consisting of only one or two turns, is then used to link couple the input of each transistor. This provides the necessary physical spacing between the units so that they may be practically arranged on a common plate and also provides the lower impedance necessary to drive the large transistors.

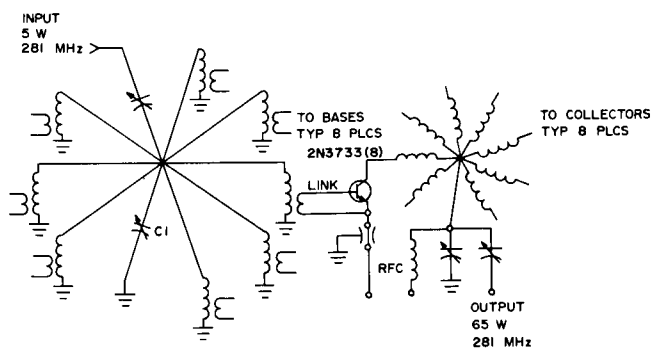

FIGURE 6. PARALLEL VHF POWER TRANSISTOR AMPLIFIER

The output of the main amplifiers is 65 W at 281 MHz. This output is applied to the multiplier change

consisting of three balanced doublers. The output of the first doubler is 50 W at 563 MHz; the second is 35 W at 1100 MHz; and the third is 20 W at 2200 MHz. The development of the 20-W solid-state UHF transmitter is in an early phase with major emphasis on determining the most appropriate solid-state devices to use.

VI. CONCLUSION

In February 1965, the Department of Defense directed the three services to completely remove telemetry operations from the 225 to 260 MHz band by 1970. Until recently NASA planning was based on the use of the 225 to 260 MHz band for an indefinite period beyond 1970. Shortly after the firm directive to the three services, DOD requested that NASA also vacate the VHF telemetry band so that these frequencies might be used for other high priority applications.

In June 1965, NASA convened an intercenter study group to investigate and define NASA requirements for telemetry frequencies beyond 1970 and to evaluate the impact of the move on program costs and schedules. The results of this study had not been released at the date of this report.

If NASA initiates the move in telemetry operations as requested by DOD, one of the major problem areas is likely to be availability of RF transmitters with the required performance and environmental capabilities. The purpose of the telemetry development program described in this report is to meet this requirement.

ADDRESSABLE TIME DIVISION DATA SYSTEM

By

Roy Williams

ABSTRACT

The advantages and design considerations of a central programer, a common address, and a data return bus are compared to the telemetry system of the Saturn IB.

I. INTRODUCTION

Present telemetry systems route individual transducer signals to a central telemetry package, adding the bulk and mass of numerous wires to the vehicle. The system described herein will eliminate most of this wiring by using a central programer, a common address, and a data return bus.

II. PRESENT DESIGN

With the increase in size and mission requirements of space launch vehicles has come an accompanying demand for measurements; this requires a significant increase in cables and connectors. The current study on an addressable time division data system seeks to eliminate most of these cables and connectors.

As an example of what may be done in this area, consider an application from the 200-series vehicles. The Saturn IB space launch vehicle shown in Figure 1 gives an overall view of the distance that some conductors are run. The telemetry package used as an example is in unit 13. Sixty percent of the transducers monitored are located in unit 9 next to the engines; 30 percent are located in unit 12.

Figure 2 shows that to reach from the instrument compartment in unit 13 to the measuring distributor in unit 9, 34 meters of conductors are required for each measurement; to unit 12, it takes 7.62 meters. The wire presently being used for these runs weighs 2.0 kilograms per 305 meters, which gives us approximately 0.22 kilogram of wire to unit 13 for each measurement and 0.05 kilogram to unit 12.

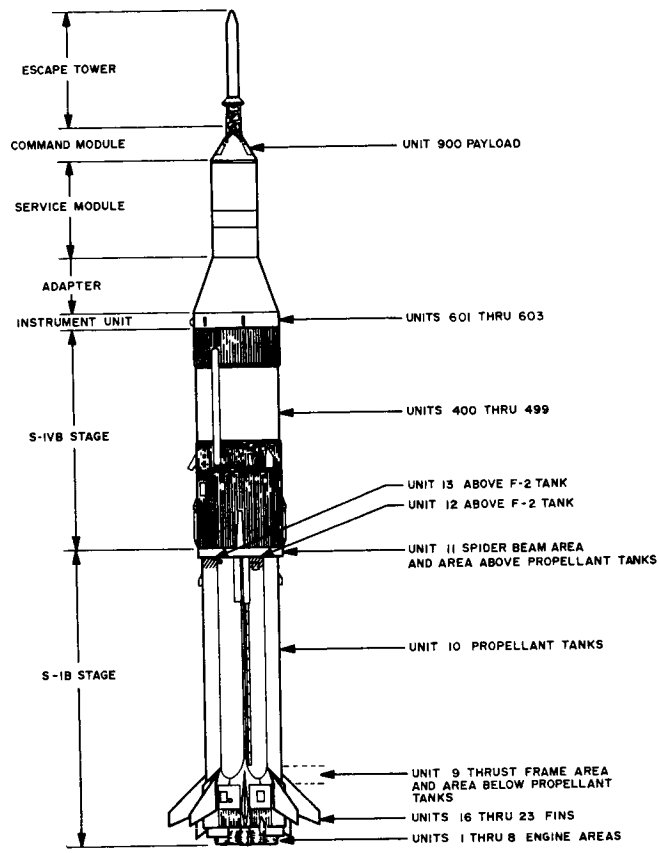

FIGURE 1. SATURN IB STAGE AND ELECTRICAL UNIT DESIGNATIONS

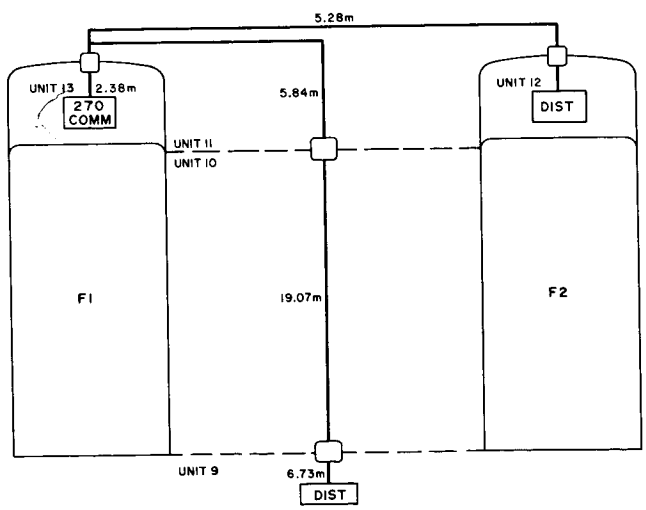

FIGURE 2. S-IB STAGE

III. PROPOSED DESIGN

If one wire could be used to carry the information and one wire to select or address the desired information, it would be possible to save approximately 41 kilograms minus the amount of weight added to the instrumentation. This is the type of system presently being evaluated.

Figure 3 shows the major elements of a system of this type. MSFC has a contract with Martin-Denver to furnish a study and prototype of the cables and measuring sources. The master programmer may be designed in house if the concept proves feasible.

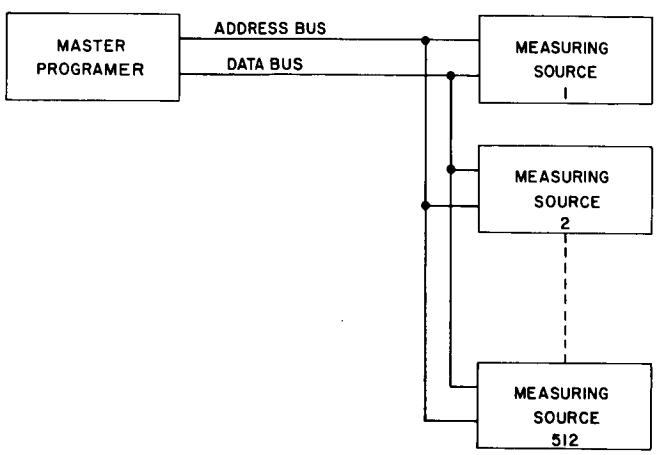

FIGURE 3. ADDRESSABLE TIME DIVISION DATA SYSTEM

The master programmer consists of an interrogator and an analog-to-digital converter. The data will be transmitted in analog form from the measuring source to the master programmer. There it will be converted to pulse code modulation. This signal then will be used to frequency modulate a transmitter. The measuring source consists of an address decoder and an address decoder and data switch. One measuring source might handle several transducers.

The interrogation signal consists of a serial digital waveform, containing the address of the measuring source to be interrogated, and timing or synchronization information. This signal uses one of the two system cables. The present plan is to use a return-to-zero signal with double amplitude pulses for synchronization as shown in Figure 4 for a 10-bit address.

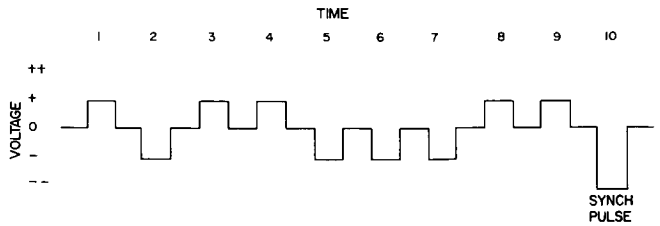

FIGURE 4. RETURN TO ZERO ADDRESS WAVEFORM

IV. ADVANTAGES OF PROPOSED DESIGN

The advantages of using a serial digital interrogation signal are that circuitry on both the transmitting and receiving ends is simple (no filters or oscillators are necessary) and integrated circuitry can be used to increase reliability and to reduce size, weight, and power consumption. To allow for expansion of the system, each address can be made one or two bits longer than the immediate requirements, thus adding two extra bits. For example, from 8 to 10 would expand the capability from approximately 500 to 1000 addresses. The address words will be easily changed, making it possible to interchange measuring sources and relocate them easily. The measurement source (Fig. 3) must be able to perform two functions; first, it must decode the address to the data system, and second, upon being addressed it must switch its data to the data bus.

The address decoder's function is to identify the address information from the address bus and convert it to a switching signal for interrogation of a specific data source. The decoder also must derive a clock or synchronization pulse from the address or contain a clock synchronizer to the address; in our case a synchronization pulse is transmitted with the address. It is important that decoder circuitry be highly reliable. A failure of a decoder can mean the loss of data from one or several sources; therefore, reliability will have to be a major consideration.

The measurement source switch can be one of two types, analog or discrete. The discrete data will be quite simple to handle; however, the analog, which can be low level or high level, will be much more difficult because of switching noise and switching voltage offsets. The data can be returned by three methods; pulse amplitude modulation, pulse position modulation, and pulse code modulation. It is planned that pulse amplitude modulation will be used. Pulse code modulation, from the standpoint of signal only,

is the most desirable; however, this would require an A/D converter for each measuring source. A/D converters are relatively large and expensive and would add a large amount of mass to the system. Because we operate in a closed system over a relatively short distance, pulse amplitude modulation can be used with little deterioration of the signal.

V. CONCLUSION

It can be seen that mass can be reduced by eliminating cables and reducing the size of the connectors. However, there are some problems in the area of reliability that must be overcome. As soon as it is possible to predict how much instrumentation is involved, an investigation of mass tradeoff will be initiated to determine the extent of the program.

POWER SYSTEMS RESEARCH AT MSFC

September 30, 1965

by

Dwight Baker
Richard J. Boehme
Edward E. Dungan
Charles Graff

TABLE OF CONTENTS

FUEL CELL SYSTEMS

by Richard J. Boehme

LIST OF TABLES

LIST OF ILLUSTRATIONS

CONTENTS (Continued). . .

TABLE OF CONTENTS

THE DEVELOPMENT OF AN IMPROVED ZINC/SILVER-OXIDE BATTERY

by Charles Graff

LIST OF ILLUSTRATIONS

CONTENTS (Continued). . .

THE ELECTRICAL POWER SYSTEM FOR THE PEGASUS SATELLITE

by Charles Graff

LIST OF ILLUSTRATIONS

TABLE OF CONTENTS

BRUSHLESS DC MOTORS

by Dwight Baker

LIST OF TABLES

LIST OF ILLUSTRATIONS

TABLE OF CONTENTS

SINGLE-ENDED SWITCHING TRANSFORMER REGULATOR

By Dwight Baker

CONTENTS (Continued). . .

LIST OF ILLUSTRATIONS

TABLE OF CONTENTS

ELECTRICAL POWER SYSTEMS STUDIES AT MSFC

by Edward E. Dungan

CONTENTS (Continued). . .

LIST OF TABLES

LIST OF ILLUSTRATIONS

FUEL CELL SYSTEMS

By

Richard J. Boehme

SUMMARY

The development of fuel cells at Marshall Space Flight Center is described. Program management and organization are summarized, basic hydrogen/oxygen fuel cell phenomena are reviewed, and developments centered around the asbestos matrix and static moisture removal are described. Practical systems and subsystems are discussed and performance figures are given.

I. INTRODUCTION

Investigation of fuel cell technology and its applicability to space vehicles dates back to 1958 at the Marshall Space Flight Center, which was then known as the Army Ballistic Missile Agency.

Surveys of power requirements for various mission concepts continued to indicate a growing need for fuel cell systems to furnish electrical energy. The range of power requirements for which fuel cells were anticipated is shown roughly in Figure 1. Tradeoff limits are only approximate, but the figure is still considered applicable today. These limits must be tempered with such factors as availability, complexity, reliability, and cost for any particular application.

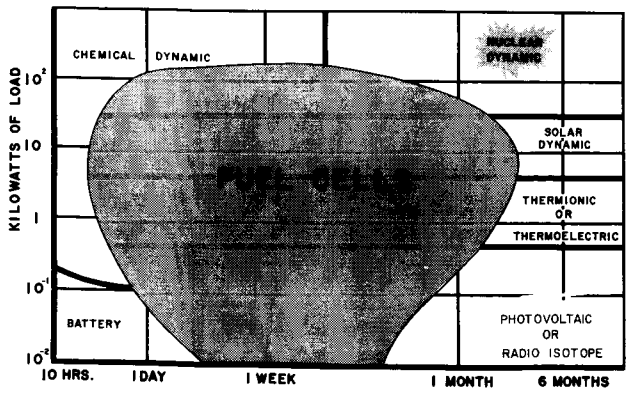

FIGURE 1. ANTICIPATED RANGE OF FUEL CELL POWER REQUIREMENTS

The present fuel cell program was initiated in November 1961 when proposals were solicited from 12 sources for research and development work.

The Allis-Chalmers system was selected as the one offering the most advantages for space vehicle application, at least for the next ten years, and a research and development contract was negotiated in May 1962. This work has been sponsored by the Office of Advanced Research and Technology.

II. PROGRAM SUMMARY

The fuel cell program established at the Marshall Space Flight Center is summarized as follows.

1. Major Effort. The major effort is represented by contract NAS8-2696, entitled "Fuel Cell Systems," with the Allis-Chalmers Manufacturing Company. The contract consists of three categories:

   a. Research and Technology Tasks

   b. Breadboard Systems and Laboratory Support

   c. Engineering Model Systems

2. Associated Contract. An associated contract (NAS8-5392) has been in effect since mid-1963 to supplement the program with theoretical studies, mathematical models, and computer analysis of systems and subsystems.

3. In-House Support. The in-house support for the program consists of five types of effort:

   a. Evaluation of Alternates. Components and subsystems.

   b. Preliminary Designs and Breadboards. Advanced electrical controls, converter, and instrumentation.

c. System Studies and Analyses. Electrical interface, thermal, and vibration.

d. System Testing and Evaluation. Performance, environmental, and interference.

e. Establishment of Guidelines. Preferred parts lists, fabrication techniques, and specifications.

III. MANAGEMENT

Program management has been quite successful. A small, informal working group of directly concerned personnel from the Office of Advanced Research and Technology, Office of Manned Space Flight, Manned Spacecraft Center, and Marshall Space Flight Center has been established for program planning and coordinated control. This group meets monthly to review the progress and to resolve outstanding problems.

Marshall Space Flight Center has the responsibility for contract administration; however, since August 1964, responsibility for technical supervision is shared by the Manned Spacecraft Center and the Marshall Space Flight Center.

IV. COMPARISON OF CELL TECHNOLOGY

Some of the objectives that have been achieved and the outstanding advantages of the system that has been developed are described in this paper. To establish these advantages, some of the basic fuel cell phenomena that characterize present hydrogen/oxygen fuel cell systems are reviewed.

Figure 2 depicts an early ion exchange membrane cell developed by the General Electric Company. This cell is basically an acid type. The porous electrodes consist of metallic screens embedded in platinum powder bonded to both sides of the exchange membrane. The 0.0254-cm (10-mil) thick polymer membrane represents an acid electrolyte between electrodes. Sulphonic acid was added later to increase the current capacity.

Gaseous hydrogen and oxygen admitted to the cell cavities are absorbed within the electrodes where, in the presence of the catalyst, a complex

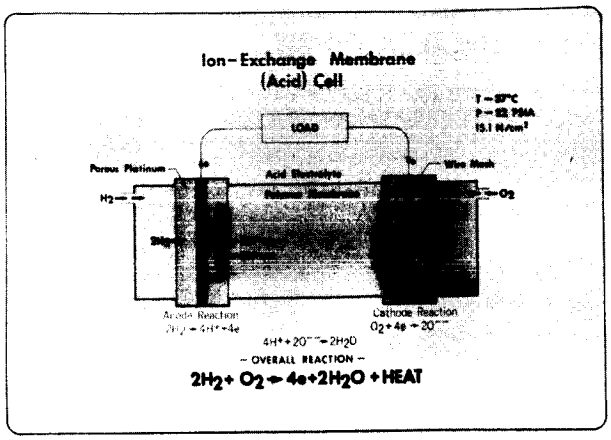

FIGURE 2. ION-EXCHANGE MEMBRANE (ACID) CELL

electrochemical reaction occurs that results in the simplified electrode reactions shown on the illustration. Electrical energy results from the electrons that are released by the ionization of hydrogen.

Transfer of the hydrogen ions through the membrane is accomplished by an electronic diffusion mechanism to a zone at the cathode, where they combine isothermally with the oxygen species to form water. Therefore water must be primarily removed from the oxygen side.

A temperature of 35°C and a pressure of about 15 N/cm^2 (22 psia) are normally used for this cell.

A basic alkaline cell used in the Allis-Chalmers system is shown in Figure 3. Note that the resultant reactions are similar, but the mechanisms are quite different. Major differences are:

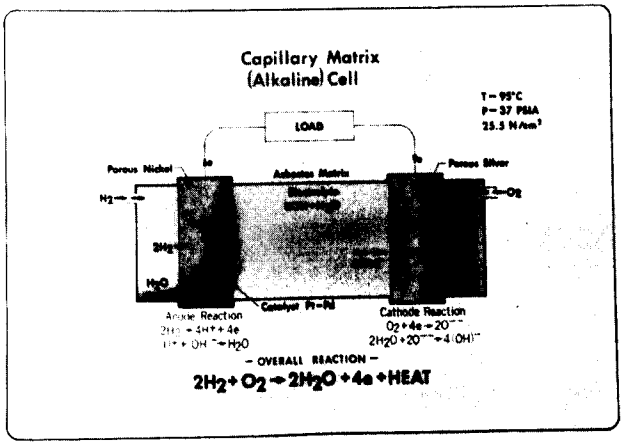

FIGURE 3. CAPILLARY MATRIX (ALKALINE) CELL

1. The electrolyte is a KOH solution held by the high capillary forces of a 0.0508 or 0.0762-cm (20 or 30-mil)-thick asbestos mat.

2. The porous anode consists of nickel sintered on a nickel screen and catalyzed with 4.6 mg/cm^2 each of platinum and palladium.

3. Allis-Chalmers now uses silver, without catalysts, for the cathode.

4. Electrical conduction within the cell is mainly attributed to hydroxyl (OH) ion transport.

5. Water is inherently formed at the hydrogen electrode and must be removed from that side.

6. Normal pressure and temperature for this cell are 25.5 N/cm^2 (37 psia) and 95°C, respectively.

The basic Bacon cell is used in the Pratt and Whitney Apollo fuel cell system. The basic reactions are no different from those described for the Allis-Chalmers cell. Notable differences not obvious from the basic diagrams of Figures 3 and 4 are:

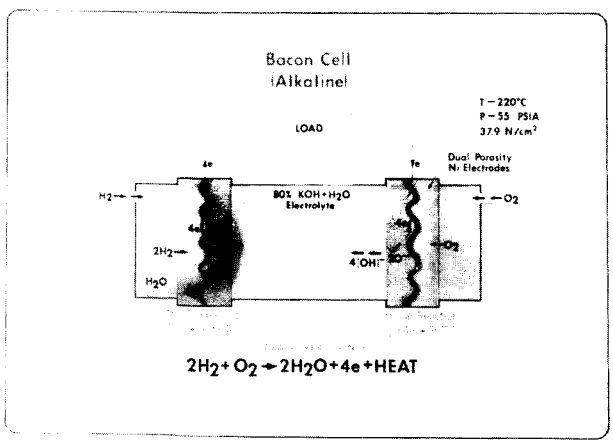

FIGURE 4. BACON CELL (ALKALINE)

1. Dual porosity sintered nickel electrodes are required without catalyst.

2. The KOH concentration of about 80 percent is a solid below 150°C. It must be retained between the porous electrodes.

3. Normal operating conditions are 37.9 N/cm^2 (55 psia) for pressure and about 220°C for temperature.

Inherent advantages that the Allis-Chalmers system has by virtue of its type and class of cells can be summarized as follows:

1. Alkaline cells inherently offer higher electrical performance, current density, and efficiency than do acid cells; they offer these advantages without the high probability of problems with materials. These advantages are even greater when ion exchange membranes are present, since ion exchange membranes incur higher impedance and are deteriorated by temperatures above 60°C, which limit the allowed chemical activity.

2. Presently, the ion exchange cells produce nonpotable water (pH = 2) and are severely limited in their shelf life and the number of starts.

3. Advantages of the Allis-Chalmers cell over the Bacon cell because of the lower temperature, pressure, and KOH concentration are:

   a. The more rapid degradation mechanisms are avoided, such as crystalline (or dendrite) growth, excessive cathode oxidation, plugging of manifold orifices, and problems with seal materials.

   b. Very long critical startup and shutdown and stresses created by phase change of electrolyte are avoided.

   c. Lower parasitic power is required for standby.

V. UNIQUE FEATURES AND OBJECTIVES

Ruggedness, simplicity, and stability — three of the primary objectives of the Marshall Space Flight Center program — have been met by developments centered around the asbestos matrix and the static moisture removal concept. Simultaneously, outstanding silver electrodes have been developed that have improved electrical performance and life.

Water management is of paramount importance to high performance and successful operation of fuel cells. Water is produced in the cells at a rate directly proportional to the load and must be removed or else the performance will decay as the cells become flooded. If too much moisture is removed, electrolyte drying can decrease performance and increase heating to the point of burnout.

Test results (Fig. 5) have shown that there is an optimum range of KOH concentration in the electro-

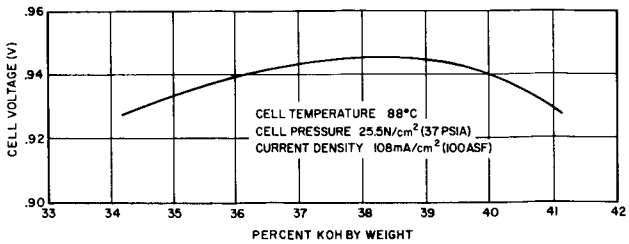

FIGURE 5. FUEL CELL TEST RESULTS

lyte for a given temperature and pressure. For the subject asbestos matrix cells, which operate at about 95°C and 25.5 N/cm^2 (37 psia), 27 percent KOH and 45 percent KOH have been established as the practical limits of electrolyte concentration for sustained operations. The electrolyte concentration, being dependent on the amount of water present, is controlled by the water removal subsystem based on the unique concept of static moisture removal.

Figure 6 shows a diagram of a cell cross section where asbestos is used as the electrolyte holder and as the water removal matrix. Moisture is re-

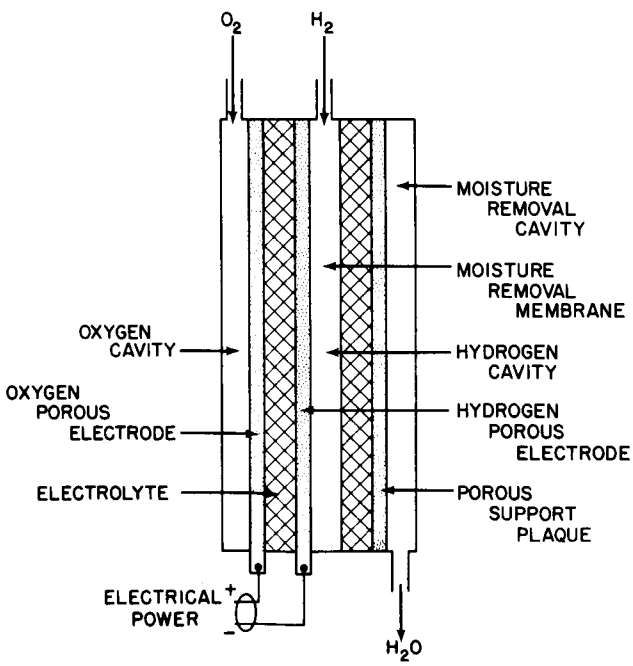

FIGURE 6. FUEL CELL CONSTRUCTION USING STATIC MOISTURE REMOVAL SYSTEM

moved statically and inherently at the proper rate by the moisture removal or transport matrix, which is saturated with a higher concentration KOH solution (say 45 percent) than the 37 percent present in the electrolyte holder. Because of the high capillary force of the asbestos on the KOH, the hydrogen is retained in the hydrogen cavity.

The vapor pressure at a given temperature exerted by each of the membranes will be inversely proportional to its KOH concentration. The vapor pressure of the KOH electrolyte as a function of concentration and temperature is given in Figure 7. The

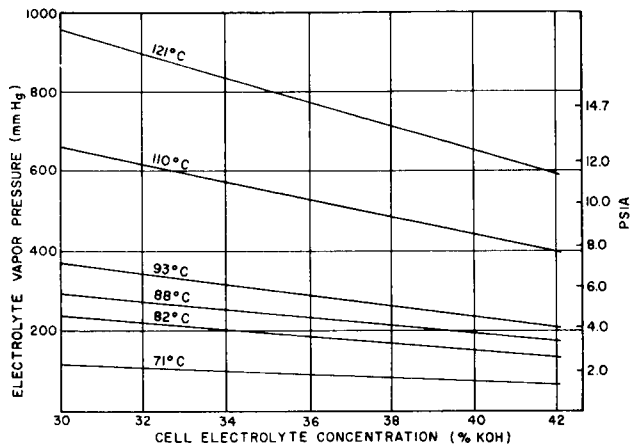

FIGURE 7. FUEL CELL ELECTROLYTE CONCENTRATION AS A FUNCTION OF VAPOR PRESSURE AND TEMPERATURE

water vapor molecules seek equilibrium with the reactant gas molecules, and the sum of the partial pressures of the gases equals the total cell pressure. Now, with the proper pressure setting in the water removal cavity added to the vapor pressure of the water removal matrix, equilibrium can be established for the desired electrolyte concentration.

When product water dilutes the electrolyte, its vapor pressure increases, thereby transferring moisture to the reactant gas. The water removal membrane, having a lower vapor pressure will absorb this moisture to establish partial pressure equilibrium. If the pressure of the water removal cavity is held constant, moisture will be delivered as vapor to the removal cavity by virtue of the increased vapor pressure of the removal matrix.

This concept can be compared to the Apollo fuel cell system which uses a recirculating hydrogen loop

where moisture is removed by circulating excess hydrogen through the cells. Water is then condensed and separated with a centrifugal separator.

VI. PRACTICAL SYSTEMS AND SUBSYSTEMS

The major module developed has been the "fuel cell module" (or stack) which is constructed from standardized cell components. The rugged construction of a single cell, having an electrode area of 372 cm^2 (0.4 ft^2), is illustrated in Figure 8. Plated magnesium plates give structural rigidity, provide the reactant and water removal cavities, serve as current

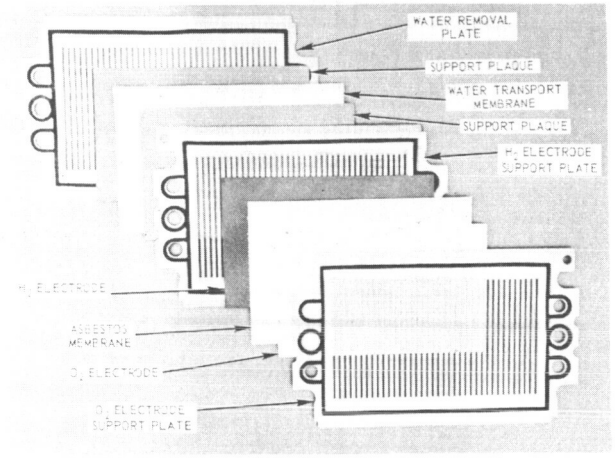

FIGURE 8. CELL CONSTRUCTION

collectors for external connections, and efficiently transfer heat out of the cell. The anode plates are electrodeless nickel plated and the cathode plates are plated with gold over nickel. Note the cell seals, which are rubber 0-ring gaskets, and the holes, which form an internal manifolding system when the cells are assembled into a stack. The support plaques are porous metal mats (similar to the electrodes) which evenly support the asbestos and keep it from being compressed into the cell cavities furnished by the manifold grooves in the plates.

The cells are assembled in parallel pairs and arranged so that one water removal cavity serves two cells, conserving weight and space. A closeup view of a typical assembly is shown in Figure 9. Here the intercell connection blocks, some instrumentation leads, and some of the rods which keep several tons of compression on the stack can be seen. The plate fins, which transfer cell heat to a circulating gas

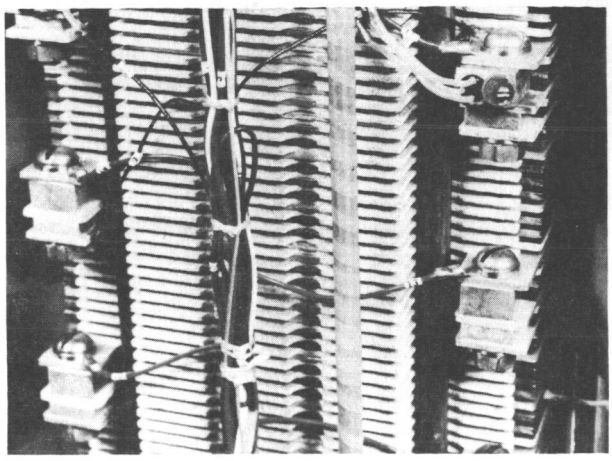

FIGURE 9. CLOSEUP VIEW OF TYPICAL ASSEMBLY

cooling system, are shown protruding beyond the fiberglass spacers to form slots for gas passages along the outer edges of the stack.

A breadboard assembly, without the outer canister, is shown in Figure 10 to demonstrate its rugged simplicity. The fiberglass ducts direct helium coolant gas from two blowers down over the cell fins. The return path is through the intercell slots to the canister and back through a heat exchanger on top of the stack. This is shown better in Figure 11, which diagrammatically depicts the secondary coolant system.

The modular design concept that has been followed throughout, together with the secondary coolant system, accomplishes the objective of versatility; with minimum design impact, this fuel cell system can be interfaced with just about any vehicle liquid cooling system. Neither the Apollo nor the Gemini system has such a feature. Each uses coolant tubes attached directly to each of the cells.

An overall system schematic is given in Figure 12; some of the subsystem features are as follows.

1. Inlet pressure regulators maintain balanced reactant pressures for optimum performance. Pressure differential is far less critical to this system than for the Apollo or Gemini systems because of the rugged cells and the high capillary force of asbestos.

2. The temperature-compensated vacuum-regulator control effects the proper water removal pressure and extends the allowable operating temperature range for startup purposes.

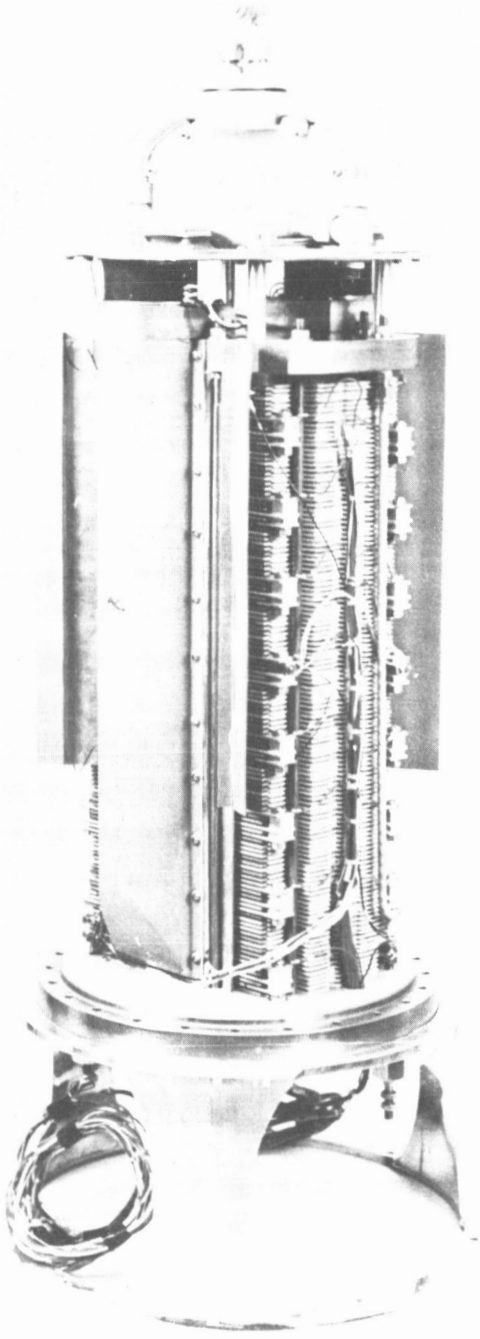

FIGURE 10. BREADBOARD ASSEMBLY WITHOUT OUTER CANISTER

3. The ampere-hour controller assures efficient minimum purging of inerts and impurities that build up in the reactant cavities. With a reactant purity of 99.9 percent, purging requires about 3 percent of the reactant consumed.

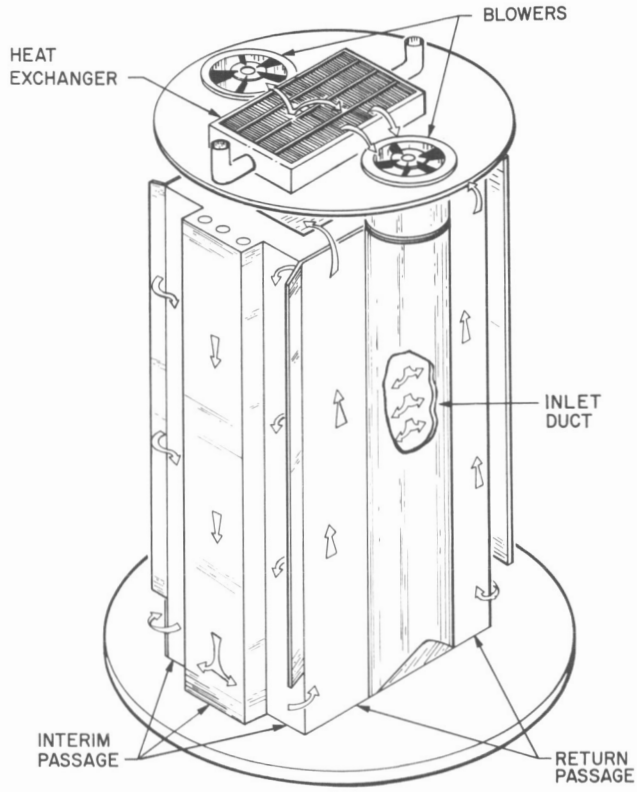

FIGURE 11. SKETCH OF BREADBOARD ASSEMBLY WITH OUTER CANISTER

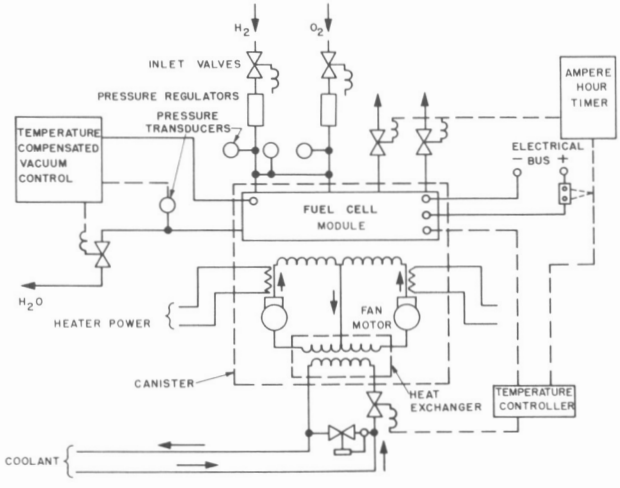

FIGURE 12. SYSTEM SCHEMATIC

4. The heater provides warmup in less than an hour for cold starts.

A complete engineering model system recently delivered to Marshall Space Flight Center for test and evaluation is illustrated by Figure 13.

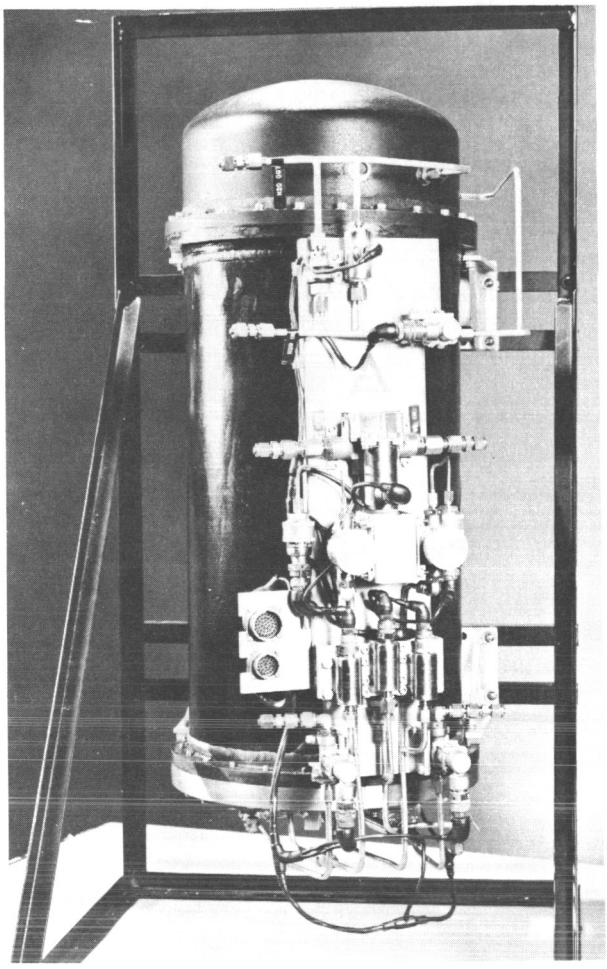

FIGURE 13. ENGINEERING MODEL SYSTEM

Figure 14 shows the special test equipment required to interface the system with the laboratory facilities.

The equipment shown is not a flight model, although the components are flight oriented. It has been heavily instrumented for test purposes; no particular attempts have been made to reduce weights or to environmentally qualify components. The control components (such as valves and transducers) shown in the foreground of Figure 13 have been mounted as removable modules on the front panel affixed to the canister housing. The entire reactant control assembly is also readily detached from the canister when particular installations require it. This feature provides accessibility to the assembly for maintenance or field repairs, which are both possible with this design.

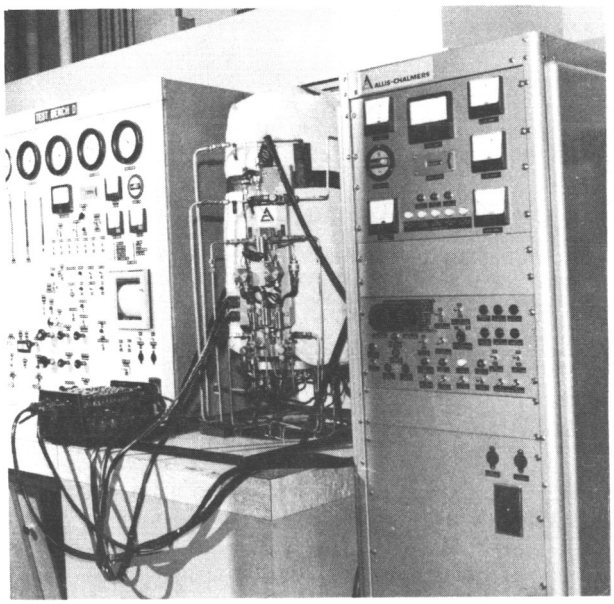

FIGURE 14. SPECIAL TEST EQUIPMENT

The rating of the delivered system is 2 kW at 29 volts, and it has an expected life well beyond the 720 hours initially designated as a design goal for this model. To achieve the 2 kW rating with the ± 2 volt regulation constraint for an output power range of 800 to 2000 watts, cells capable of sustaining current densities to 200 mA/cm^2 and having good regulation and long term stability had to be developed. This was accomplished with the incorporation of a high performance silver cathode designated as "Hysac Electrode." A typical volt-ampere characteristic for a cell with this electrode, as it would perform in a system, is shown in Figure 15; the trapezoid reflects the performance limits that an individual cell must maintain to fulfill the system requirements.

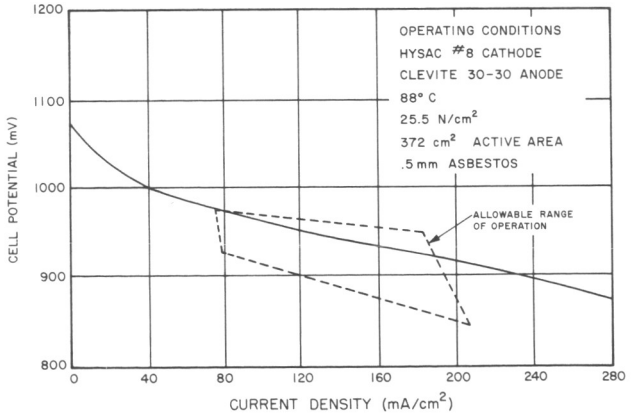

FIGURE 15. TYPICAL CELL VOLT-AMPERE CHARACTERISTIC

VII. SYSTEMS PERFORMANCE

Three extensively tested breadboard systems have shown good performance and progressive improvement and have pointed out problem areas. Breadboard systems were essentially the same as the later engineering models except that they used commercial auxiliary components and the fluid coolant subsystem was simulated with laboratory equipment. Also, the breadboards were rated for only 1800 watts. Only a brief account of these tests and the results are given here. These tests have been well documented in the quarterly reports distributed under contract NAS8-2696 (copies are available upon request).

The second breadboard system was tested at Manned Spacecraft Center using a composite load profile representing several NASA mission requirements. This profile appears in Figure 16, which shows several peaks to 1.8 kW. The system was subjected to several cycles of this profile during the first test phase, which demonstrated good performance with life to 500 hours.

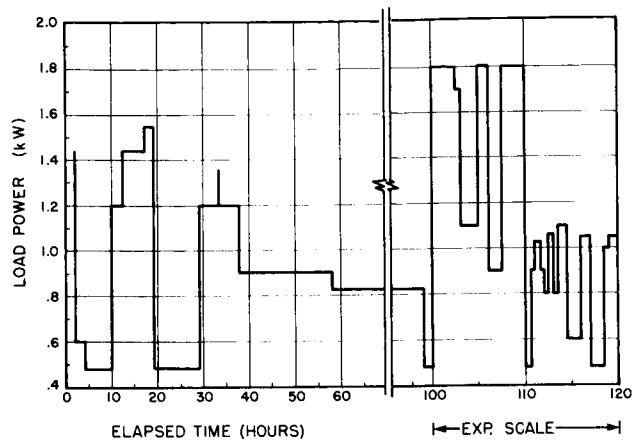

FIGURE 16. RESULTS OF BREADBOARD SYSTEM TEST

TABLE I. MISSION REQUIREMENTS VS BREADBOARD TEST RESULTS

	Mission Requirements			"35 Cell" Allis-Chalmers Breadboard Results		
Mission (1)		Power	Time (Hours)	Start	Hours 330	Hours 530
Gemini	total	610 to 1750 W (2) 23 to 30 V	340	2200 W @ 27 V	1800 W @ 26 V	1600 W @ 25 V
Apollo CSM	per mod	560 to 1420 W (3) 27 to 31 V	340	2200 W @ 27 V	1620 W @ 27 V	1400 W @ 27 V
LEM	per mod	130 to 1125 W 27 to 31 V	112	2200 W @ 27 V	1620 W @ 27 V	1400 W @ 27 V
Saturn	per mod	1750 W 26 to 31 V	6.5	2200 W @ 27 V	1800 W @ 26 V	

(1) Load profile for breadboard tests was a composite of requirements for all the missions listed.
(2) This peak will occur only during the two-day rendezvous missions.
(3) Emergency return one-module peak 2300 W @ 20 V (minimum).
Average power output: 3 modules 900 watts; 2 modules 1200 watts

Table I compares the output performance during the first test phase with the various mission requirements and demonstrates that the system was able to perform each of these missions. Total Gemini loads were used; whereas the Apollo, LEM, and Saturn requirements were prorated on a per module basis for these tests.

Following a long dormant period incurred by conversion of test facilities, various performance and life testing was resumed at the Manned Spacecraft Center. A useful life beyond 1000 hours was demonstrated, although the ± 2-volt regulation desired was not maintained. This unit did not have the "Hysac Electrode" or fully automatic electrical controls. The

output characteristics of the system for several times throughout the test life are given in Figure 17.

Similar performance and life characteristics of a subsequent model tested at Allis-Chalmers are shown in Figure 17 for comparison. The notable improvement in performance shown by the latter system reflects the incorporation of "Hysac Electrodes" and automatic electrical controls and the reduction of the thickness of the electrolyte matrices from 0.0762 to 0.0508 cm. (30 to 20 mils).

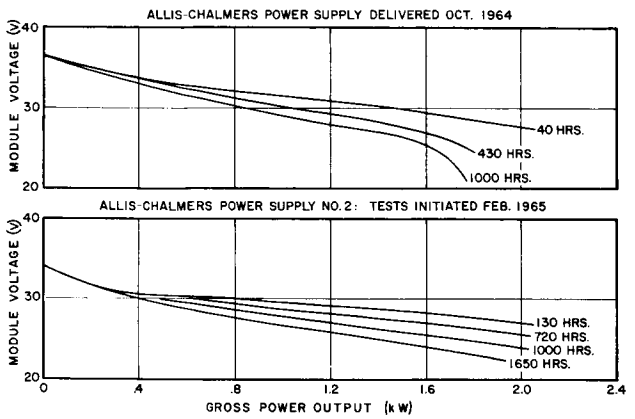

FIGURE 17. FUEL CELL OUTPUT CHARACTERISTICS

During the first 1500 hours, loads were varied between 500 and 2200 watts and held for long periods to give a total of 1,618 kWh delivered at an average load of 1.1 kW during these tests. The system maintained the ability to operate at the 2 kW level for long periods.

The thermal efficiency computed at the 400 hour mark was 65 percent for the latter system. Its specific fuel consumption to this point was 0.349 kg (0.77 lbm) per kWh. These tests demonstrated that this system, of the three compared, offers the highest energy density, the widest power range, and superior voltage regulation for longer operating times. It also was not critical to start up or shut down cycles.

VIII. FUTURE PLANS

As evidenced by the latest workscope and efforts planned for the near future by Manned Spacecraft Center, this system is considered one of the outstanding contenders, capable of improvement to meet the higher performance, reliability, and life requirements anticipated for the Apollo Applications Program.

THE DEVELOPMENT OF AN IMPROVED ZINC/SILVER-OXIDE BATTERY

By

Charles Graff

SUMMARY

Details of the investigations that led to the development of an improved primary zinc/silver-oxide battery are presented. Research was conducted in two areas, separator materials and variable factors. Results of the research are the development of a more effective separator system and an improved cell design.

I. INTRODUCTION

Requirements for flight batteries in the past have been for relatively high discharge rates for short periods. For these applications primary batteries with a specified wet stand of 72 hours have been used. These batteries have provided high power density and good voltage regulation.

For more recent flights, operating times have increased from minutes to hours and the vehicles have become more complex, requiring battery installation earlier in the countdown. In addition, operating procedures at Cape Kennedy require flight batteries for certain all-system testing. Recently, four sets of batteries have been required for each flight, increasing expense. Efforts have thus been directed toward development of a battery with a longer wet stand time and a limited recharge capability. If a battery can be developed that retains the desirable characteristics of the present primary battery, battery cost can be reduced significantly.

II. DEVELOPMENT PROGRAMS

In June 1963, a contract with the Eagle-Picher Company was initiated for investigations leading to the development of an improved primary zinc/silver-oxide battery. The primary objectives were:

1. Longer wet stand life
2. High energy-to-weight ratio
3. Low gassing
4. Good voltage regulation
5. Improved thermal characteristics.

Some of these requirements are not compatible and therefore require compromise.

With the limited funds available for this program, basic materials research could not be accomplished; therefore, an attempt was made to optimize the cell design for applications using currently obtainable components. The preliminary analysis resulted in a long list of variable factors, indicating that classical research methods would not give usable results with a reasonable amount of effort and cost. It was decided to split the project into two programs. One program would be for the investigation of separator materials and combinations of separator materials and would be pursued by classical research methods since they lend themselves to this approach. The other program would consider all other variable factors and was approached by a fractional factorial analysis, which is a statistically designed experiment.

III. SEPARATOR SYSTEM

Factors such as the battery voltage, voltage regulation, battery capacity, and wet stand time are functions of the separator characteristics.

Some of the desirable characteristics of a separator material are:

1. Low electrical resistance

2. High absorbency

3. Rapid wetting ability

4. Stability of all properties over a wide temperature range

5. Stability in concentrated potassium hydroxide

6. Resistance to oxidation

7. High oxygen permissibility (less important in the primary cells)

8. Ability to retard migration of silver and zinc ions

9. Good physical strength.

The first four of these are probably the more variable among commonly used materials and lend themselves to quantitative tests. In addition to laboratory tests of the listed characteristics, some cell cycle tests were devised for the most promising separators. These preliminary tests indicated that cellulosic membranes offered advantages in electrical resistance and absorbency while polyethylene was essentially inert to the caustic environment.

Although these tests provided useful information, the ultimate tests were in the construction and operation of test cells. Also, a number of variables in cell design require optimization of the separator system or combinations of separator materials. For this evaluation, combinations of separator materials were analyzed in test cells. Post-mortem examination of these cells showed an advantage of employing an "open" material next to the positive plate. This prevents damage to the membrane by crystalline formations. These formations otherwise tend to force the separator from the plate causing uneven discharge and tearing or puncturing of the membrane.

IV. INITIAL TESTS AND DESIGN GOALS

The fractional factorial analysis of the factors not investigated in the separator program was based on Addleman's Orthogonal Main-Effect Plan No. 11 from DDC Document Number AD272250.

There are eight factors, A through H; one with four levels, one with two levels, and six with three levels. Following instructions of the Addleman plan, a matrix was set up for analysis. This resulted in a requirement for 27 trials or cells. Details of this technique are well defined in Addleman's Orthogonal Main-Effect Plan. As a result of this study, 5 duplicate sets of 18 different cell designs were discharged at different stand times. The results of these tests indicated improved capacity retention for a higher concentration of potassium hydroxide and lower density electrode material with the use of a spongy formulation of the negative material. In addition, the use of silver grids and the low density electrode materials improved the voltage of the cell.

At the completion of the study phase, it was decided to state some specific design goals. The desire was to retain the electrical characteristics of the primary cell. Specific design goals are:

1. Stand time of 30 days

2. Stand temperature of 32° C

3. Cycle capability of 6 in 30 days

   (a) Five cycles at 25 percent depth

   (b) Final discharge of 100 percent capacity

4. Battery voltage during discharge of 1.4 ±0.1 volts per cell.

Data obtained during the first phase of the investigation indicated impressive stand characteristics for multiple wraps of membranes in conjunction with absorbent materials next to the positive and negative plates. Proper location of efficient, thin, separator materials permitted low cell impedance and the use of more active materials, thereby increasing capacity.

V. EXPERIMENT DESIGN

The first step in design of the experiment is to choose the significant variables as factors. Next, the number of levels of each of the quantitative and qualitative factors is chosen.

The chosen factors and their levels are:

A. Additives to electrolyte

A_0 None
A_1 1% Gel
A_2 MnO (at saturation)
A_3 LiOH (at saturation)

B. Electrolyte Concentration

B_0 35%
B_1 40%
B_2 45%

C. Positive material density

C_0 4.155 g/cc
C_1 4.520 g/cc
C_2 4.885 g/cc

D. Positive grid metal

D_0 4/0 Ni
D_1 4/0 Ag

E. Negative material density

E_0 2.440 g/cc
E_1 2.742 g/cc
E_2 3.050 g/cc

F. Additive content in negative plate

F_0 1%
F_1 2%
F_2 4%

G. Negative grid metal

G_0 Copper (4/0)
G_1 Silver flashed Cu (4/0)
G_2 Silver (4/0)

H. Negative formulation

H_0 Pasted
H_1 Sponge
H_2 Metallic

The porosity, or apparent density, was very important in the formulation of both the positive and negative plates. The limiting factors in securing low density electrodes are in the formulation techniques for producing electrodes.

VI. SUMMARY OF RESULTS

In several areas, compromise was required to obtain the optimum design. The changes in the overall design of the cell are summarized in the list below, which gives a comparison of the construction before and after development.

	PRESENT	IMPROVED
Positive Grid	Nickel	Silver
Silver Density	4.885-5.490 g/cc	4.270-4.575 g/cc
Negative Grid	Copper	Silver
Positive Absorbent	None	6.35×10^{-3} cm matted nylon
Membrane	#133 Visking	Two Thin Cellulose
Negative Absorbent	20.32×10^{-3} rayon	6.35×10^{-3} cm rayon

The most promising achievements are a more effective separator system, moderate recharge capabilities, and a smaller overall thickness. This allows the use of more active materials and actually increases the capacity of the cell. In addition, improved design and formulation of the plates increased the capacity.

A comparison of the discharge characteristics of the two cells is shown in Figure 1.

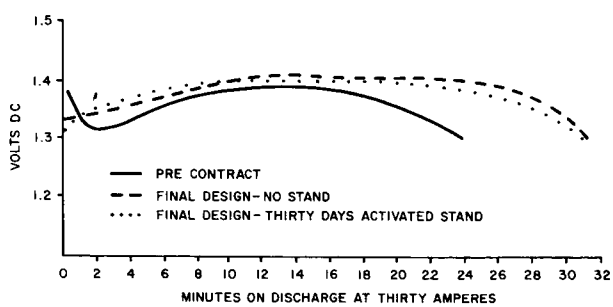

FIGURE 1. TYPICAL DISCHARGE CHARACTERISTICS, THIRTY AMPERES AT +23.9° C

Note that initial voltage in the cell after 30 days stand is a little higher than the cell with no stand time. This is probably the result of a higher charge state after the last partial discharge.

Future plans are to put some of the improved cells into a multi-cell battery to check the validity of the single cell test and also to build cells with larger electrode areas to see what type of scale-up problem might develop.

THE ELECTRICAL POWER SYSTEM FOR THE PEGASUS SATELLITE

By

Charles Graff

SUMMARY

The electrical power system developed for the Pegasus satellite by Fairchild Hiller with assistance provided by the Astrionics Laboratory of MSFC is described.

The power load for Pegasus is approximately 40 watts, with peaks occurring during interrogation intervals. Electrical power is provided by a photovoltaic, secondary battery power system. Solar energy conversion is accomplished with silicon solar cells. A battery with a nominal capacity of 6 ampere-hours provides power during the dark period, which varies between 35 and 15 minutes. Dual battery and recharge systems are provided.

Three Pegasus satellites are now in orbit with the power systems functioning properly.

I. INTRODUCTION

The Pegasus satellite was developed under contract by Fairchild Hiller. Astrionics Laboratory closely monitored and provided assistance in the development of the electrical power system.

The Pegasus satellite is an excellent example of the application of a photovoltaic, secondary battery power system. The load is approximately 40 watts with peaks occurring during interrogation intervals. The orbit is approximately 100 minutes with eclipse ratio variations from 35:65 to 15:85.

II. EQUIPMENT DESCRIPTION

A 23-cell nickel-cadmium battery with a nominal capacity of 6 ampere-hours was selected to provide power during the dark period. During the maximum eclipse time of 35 minutes, the load is supplied with 13 percent of the battery capacity.

The solar energy conversion for this satellite is accomplished with N-on-P silicon solar cells on four panels. The panels are deployed in orbit in the planes of a regular tetrahedron, giving maximum area utilization efficiency for solar cell panels on a randomly oriented satellite. The average power available during random orientation is 79 percent of the maximum from one panel.

The forward solar panel is 103.14 by 163.83 centimeters and contains 6160 solar cells in an arrangement of 55 parallel strings of 112 in series. Under test conditions at Table Mountain, California, the panel produced 115 watts at 42 volts. In orbit, the maximum power per panel is approximately 135 watts, and the average power from all four panels is approximately 110 watts. During the sunlit portion of the orbit, the solar cells power the 40-watt load directly while simultaneously charging the batteries. Approximately 48 watts are required for battery charging and about 20 watts are dissipated in the power-system electronics.

Figure 1 shows a block diagram of the entire Pegasus electrical power system. The four solar cell panels are connected through diodes to prevent back-loading through unilluminated panels.

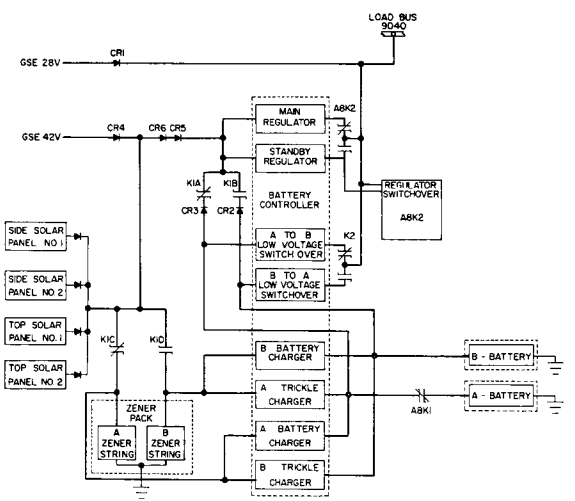

FIGURE 1. BLOCK DIAGRAM OF PEGASUS POWER SYSTEM

Ground support equipment inputs simulate both solar cell power at 42 volts and the battery power at 28 volts. The rest of the power system is fully redundant with dual batteries, chargers, and regulators and with automatic switchover capability if any unit malfunctions. The regulator switchover circuit monitors the load bus voltage and switches to the standby regulator if the voltage exceeds 35 volts or drops below 24 volts. The battery switchover circuits are activated through ground command. Once activated, the switchover is effected if the voltage drops below 24 volts. A ground-transmitted activation command prevents continuous switching back and forth if both batteries degrade to low voltage. Each battery has a main battery charger and a trickle charger; these are switched in pairs as the batteries are switched. Also, each pair of chargers has its own 42-volt zener diode voltage-limiting circuit which is also switched.

III. BATTERY RECHARGE

The battery recharge philosophy was derived from two major considerations. The first was to insure adequate recharge during the minimum orbital sunlight time of 65 minutes, and the second was to protect the battery from excessive gas buildup during the overcharge period.

To recharge the battery safely in the minimum 65-minute recharge time, it is necessary to charge at as high a current as allowable. Figure 2 shows the maximum allowable overcharge currents and voltages as functions of temperature which prevent the Pegasus battery from gassing excessively. It also shows that at high temperature the charge current may be large but the battery can be charged only to a relatively low terminal voltage.

In Figure 3, the family of battery charger characteristic curves shows that the voltage reaches its maximum safe limit before the charge current is reduced. The charger uses three types of feedback (current, voltage, and battery temperature) to accomplish this. Through this approach we obtain the maximum advantage of the battery's capability of using a higher recharge current at low temperatures. This technique provides maximum reliability and optimum economy of solar cell power.

The trickle chargers are constant-current devices with either a 100 mA or 500 mA capability. The normal mode is to maintain the standby battery on a 100 mA trickle charge. If the battery temperature should go high and increase the internal self-discharge current so that 100 mA will not maintain peak charge, the 500 mA rate may be switched in through ground command. The 500 mA rate will also be switched in after a battery switchover to revive the degraded battery.

The three Pegasus satellites are now in orbit and, to the best of our knowledge, the power systems are functioning properly.

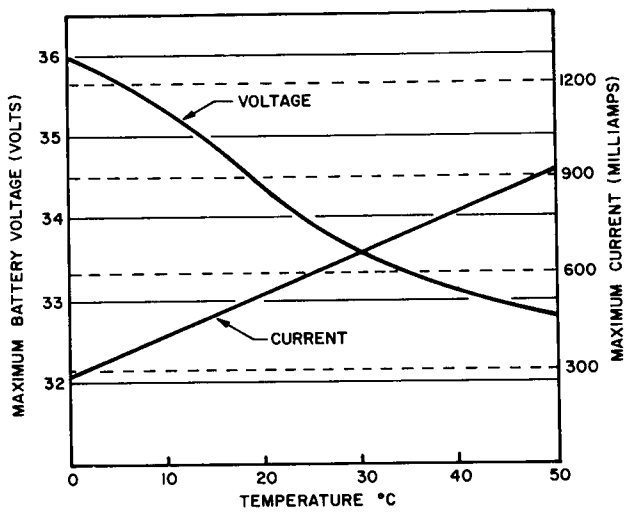

FIGURE 2. MAXIMUM OVERCHARGE AND CURRENT ALLOWABLE FOR PEGASUS BATTERY

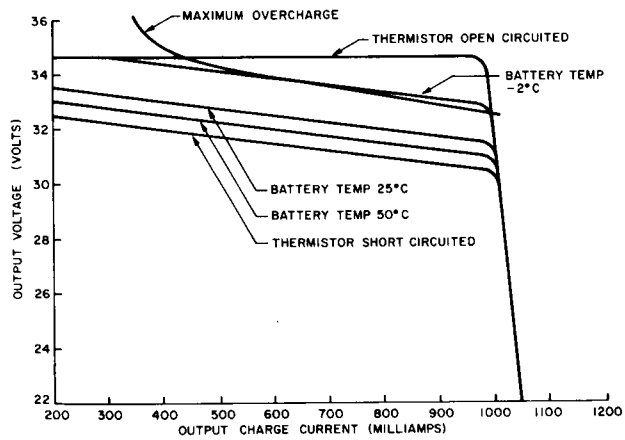

FIGURE 3. BATTERY CHARGER CHARACTERISTICS AND OVERCHARGE LIMITS

BRUSHLESS DC MOTORS

By

Dwight Baker

SUMMARY

Two brushless dc motor systems being used extensively in many space programs are described; the basic principles of operation of each are compared. In addition, the brushless dc motor and the conventional dc motor are compared, and the major advantages of each are discussed.

The present and proposed uses of brushless dc motors by MSFC are included to indicate the major advantages and future applications of these systems. Several future research and development tasks are proposed to indicate the additional efforts needed to meet the requirements for future programs.

I. INTRODUCTION

Many of the space programs require specialized motor-drive systems for liquid pumps, blowers, lunar vehicle drive systems, etc. To meet these requirements, development of improved drive systems capable of operating in the severe environments imposed by space missions will be necessary. Effort must be directed toward improved performance, high reliability, efficient operation over wide speed and load ranges, and improved maintenance-free operation for extended periods.

Because the primary electrical power sources of space vehicles are generally low voltage, dc types, motor system operation must be compatible with these limited capacity dc sources.

To provide for the existing and future requirements of these motor systems, MSFC has investigated and performed preliminary research and development on several of the brushless dc motor concepts. These efforts clearly indicate that brushless motors offer major advantages over conventional dc motors for many applications.

Most of the present brushless dc motor designs for space vehicles are limited to output power levels of a few hundred watts. This limitation is primarily caused by the lack of proper motor designs and of power transistors capable of switching the required current levels. Recent improvements in power semiconductor devices, electronic control techniques, and motor designs now make it possible to develop reliable motor systems rated at several kilowatts.

The term "brushless dc motor" does not necessarily indicate that the motor has the operating characteristics of conventional dc motors but only that the input to the system is a dc voltage and that the motor does not incorporate brushes for commutation.

II. COMPARISON OF BRUSHLESS DC MOTORS

Brushless dc motors may be divided into two major classifications, each subdivided according to the method used to control the motor. The motor types and control schemes which are now being used extensively are listed in Table I.

TABLE I. MOTOR TYPES AND CONTROL SCHEMES

A. Dc/ac-inverter-driven induction motor
1. Fixed frequency inverter
2. Variable frequency inverter
B. Rotor-position-sensing motor
1. Photoelectric sensor
2. Reluctance switch sensor
3. Hall generator sensor

The first type listed is an ac induction machine driven by an inverter that changes the dc input voltage to an ac square wave source by means of electronically controlled switching elements.

The second type employs basic dc machine principles of operation and incorporates electronic commutators in lieu of brushes and commutating bars.

The inverter induction-motor combination requires the inverter to convert the dc input voltage into an alternating source suitable for driving the motor. The inverter output voltage and frequency are controlled by the inverter; since semiconductor devices are normally used as output switches, the output waveform is a square or quasi-square wave. A significant improvement in system efficiency is realized by using this type of drive for the motor.

An elementary block diagram of a typical fixed frequency inverter induction-motor system is shown in Figure 1. The input voltage is connected to the

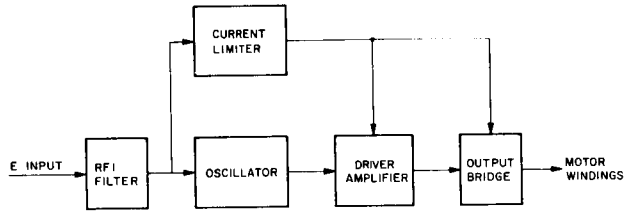

FIGURE 1. BLOCK DIAGRAM OF INVERTER INDUCTION MOTOR

oscillator, which controls the inverter operating frequency. The output signal from the oscillator is amplified by the driver amplifier and used to drive the output bridge stage. The induction motor windings are connected directly to the output bridge. The current limiter is required to limit the input current to an acceptable level during motor starting and stalled conditions.

Many variations in the design of the inverter induction-motor system are possible and depend on the application and method of implementation. By proper control of the motor voltage and frequency, efficient speed and torque control can be achieved over extremely wide operating ranges. In addition, the number of phases can be selected to provide optimum performance. Although more complex, multiple phase systems normally provide the advantages of higher starting torque, increased efficiency, lower harmonic content, and less electrical noise generated.

All motors of the rotor-position-sensing type are essentially the same although the method used to sense the rotor position may differ considerably. The maximum torque in the basic dc motor is produced when the armature and rotor fields are displaced by 90 electrical degrees. In this motor the position of the rotor is sensed and the sensing device produces an electrical signal that is used to maintain an approximate 90-degree relationship by activating the proper electronic commutating devices. Although a reluctance motor could be used for low power application, permanent magnets are generally used for the rotor because of the increased efficiency; therefore, the armature is the stator, i.e., opposite to that of a conventional dc motor.

A functional block diagram of a typical rotor-position-sensing motor appears in Figure 2. The

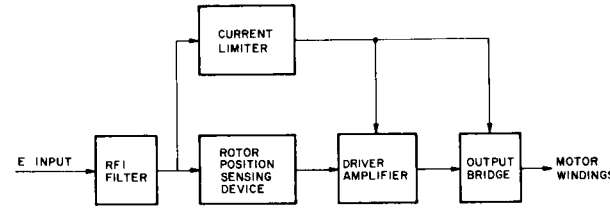

FIGURE 2. BLOCK DIAGRAM OF ROTOR POSITION SENSING MOTOR

only difference between this diagram and that of Figure 1 is that the oscillator section is replaced by the rotor-position-sensing device. Therefore, the output bridge frequency is controlled by the rotor speed in Figure 2, whereas the bridge frequency of Figure 1 is controlled completely by the oscillator stage.

The elementary circuit diagram shown in Figure 3 depicts a typical output bridge stage coupled to a three-phase motor. Note that the motor windings are connected directly to the bridge and require no transformer for coupling. This, however, normally requires a special motor winding because of the relatively low source voltage available. By eliminating the coupling transformer, an improvement in the size, weight, and efficiency of the system is normally realized.

The circuit of Figure 3 may be used for driving either the induction motor or the rotor-position-sensing motor. In the former case, the frequency is determined by the inverter design; for the latter case, the frequency is determined by the rotor through a feedback system that controls the commutators.

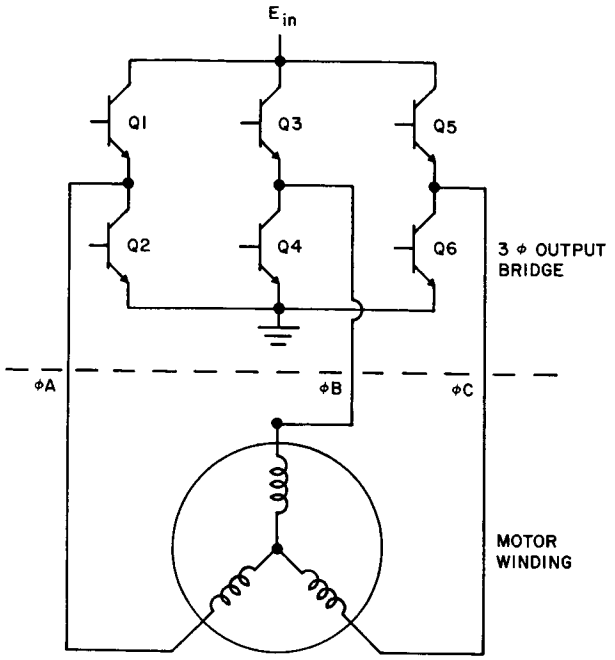

FIGURE 3. TYPICAL 3 ϕ OUTPUT BRIDGE AND MOTOR WINDING

A typical output bridge sequence and the resultant motor waveform for the circuit of Figure 3 are illustrated in Figure 4. This quasi-square wave has proven to be very satisfactory for driving properly designed motors.

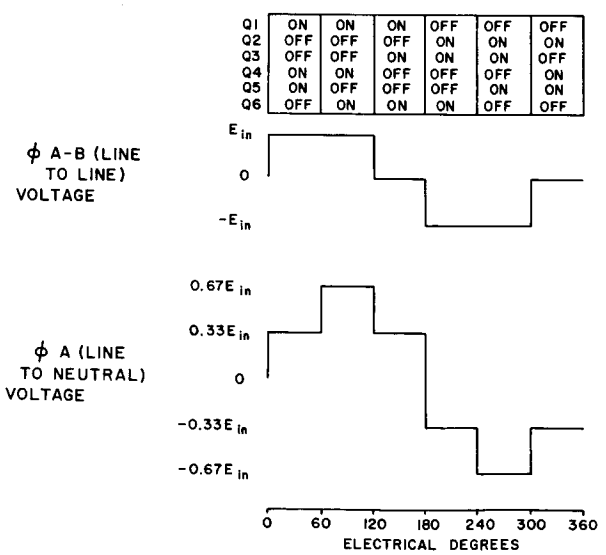

FIGURE 4. TYPICAL TRANSISTOR SEQUENCING AND MOTOR WINDING WAVEFORMS

III. COMPARISON OF BRUSHLESS AND CONVENTIONAL DC MOTORS

Although the brushless dc motor has only recently been used extensively in space vehicles, many significant improvements in performance over conventional dc motors have already been realized for many applications.

A. ADVANTAGES OF THE BRUSHLESS DC MOTOR

1. Operation in environments, such as vacuum, explosive, and high vibration, that forbid the use of conventional brushes.

2. Increased operating time without maintenance. No replacement of the electronic switching components should be necessary during the motor lifetime.

3. Efficient speed and torque control. Recently developed control techniques provide more efficient speed and torque control than obtained in the conventional dc motor for many applications.

4. Low control power. The brushless design requires extremely low control power for controlling the motor speed, torque, direction of rotation, etc.

5. Inverter or commutating devices may be located remote from the motor. In the event the motor environment is too severe, the electronic section may be located remote from the motor housing in a controlled environment.

6. Redundancy. Since the commutators are semiconductor devices, manual or automatic redundancy of the electronic section may be incorporated.

7. Reduced radio frequency interference. Arcing does not occur during electronic commutation.

B. DISADVANTAGES OF THE BRUSHLESS DC MOTOR

The major disadvantages of the brushless dc motors for most applications are:

1. Lower efficiency

2. Increased size and weight

3. Increased complexity.

Although these disadvantages normally apply to the motor design, use of the brushless motor design will often result in an improvement of system size, weight, efficiency, and complexity. As an example,

for conventional dc motor operation in a vacuum environment, it is often necessary to create an artificial environment suitable for brush operation. This usually results in a significant increase in system size, weight, and complexity.

IV. BRUSHLESS DC MOTORS FOR SATURN IB AND V VEHICLES

The following lists the present uses of brushless dc motors for the Saturn IB and V vehicles.

1. Environmental control system (ECS) coolant pump for the Instrument Unit. The ECS coolant pump motor is a rotor-position-sensing type which uses the photoelectric method of commutation control. This is a 3-phase, 400-watt motor operating from a 28-volt dc input power source.

2. LH_2 and LO_2 chilldown pumps for the S-IVB stage. This system uses the inverter/induction-motor system operating from a 56-volt dc source. This is a 3-phase motor rated at approximately 750 watts. The induction motor operates submerged in the LH_2 and LO_2.

3. LH_2 chilldown pumps for the S-II stage. This motor is essentially the same as item 2.

V. PROPOSED BRUSHLESS DC MOTOR APPLICATIONS

The following lists the proposed applications for the brushless dc motor.

1. Blowers for fuel cell cooling systems. This system will use the inverter/induction-motor combination. The motor will be a 2-phase unit rated at approximately 50 watts of output power and will operate from a 28-volt dc source.

2. Auxiliary hydraulic pump for the Saturn IB and V vehicles, S-IVB stage. The exact motor system has not been defined, but the motor will operate from a 56-volt dc source and will be required to deliver approximately 3.3 kilowatts.

3. Wheel drive for lunar vehicles. Although the exact motor requirements have not yet been determined, preliminary investigation indicates that the brushless dc motor (inverter/induction-motor combination with special controls) offers many desirable features for this application.

VI. FUTURE RESEARCH AND DEVELOPMENT REQUIREMENTS

Even though the brushless dc motor is already being used extensively in present space programs, many improvements for the system size, weight, efficiency, and reliability are urgently needed. The following are some of the development tasks that are essential to provide brushless designs capable of meeting the future missions.

1. High powered systems. Future programs will undoubtedly require higher powered systems than those presently available.

2. Redundant techniques. Future missions, such as lunar exploration, will place emphasis on reliability for extended operating times. This will certainly require the use of automatic and manual redundancy techniques.

3. Efficient current limiting techniques. Efficient methods of limiting the input current to safe levels during starting and stalled operation must be developed. Most present designs incorporate inefficient, brute-force current limiting schemes.

4. Variable frequency inverter/induction-motor systems. To provide excellent speed and torque control, variable frequency inverters and associated control circuitry must be developed.

5. System for wheel drive application. Future programs will require the development of electrical wheel drive systems capable of operating over wide speed and load ranges. In addition, efficient control techniques for controlling the speed, torque, direction of rotation, etc., of these wheels must be developed.

N67-30592

SINGLE-ENDED SWITCHING TRANSFORMER REGULATOR

By

Dwight Baker

SUMMARY

This paper describes the theory of operation of a single-ended switching transformer regulator capable of providing a highly regulated, electrically isolated output voltage. It also discusses the principal advantages of this technique over conventional methods. Electrical design calculations and procedures are included to assist the circuit designer in designing efficient, compact, and reliable dc-to-dc converters for specific applications.

A general circuit description and those equations considered pertinent in providing the necessary design information are included. Detailed mathematical analysis is not deemed necessary; therefore the design equations consider the components as idealized and neglect insignificant terms such as the resistance of the transformer winding, voltage drop across a saturated transistor, input source impedance, etc. Because component tolerances normally introduce the greater error in the final design, this consideration is valid.

LIST OF SYMBOLS

V_0	output voltage (volts)
V_1	primary winding N_1 voltage during time $T_2 - T_1$ (volts)
V_2	secondary winding N_2 voltage during time $T_2 - T_1$ (volts)
V'_2	voltage induced in winding N_2 during time T_1 (volts)
V_3	voltage induced in the sense winding (volts)
V_{CE}	transistor collector-to-emitter voltage during time $T_2 - T_1$ (volts)
V_{CR1}	forward voltage drop across diode CR1 (volts)
V_r	diode reverse voltage (volts)
V'_R	voltage ripple across capacitor C1 caused by capacitor impedance (volts peak to peak)
V''_R	voltage ripple across capacitor C1 caused by energy transfer (volts peak to peak)
i	current through N turns (amperes)
I_1	peak transistor collector current (amperes)
I_2	peak current in winding N_2 (amperes)
L_1	inductance of transformer winding N_1 (henries)
L_2	inductance of transformer winding N_2 (henries)
N	number of transformer turns
N_1	number of transformer primary turns
N_2	number of transformer secondary turns
N_3	number of turns in sense winding
W_1	energy stored in transformer at and of time T_1 (joules)
W_2	energy delivered by the transformer during time $T_2 - T_1$ (joules)

T_1	time required to store energy in transformer
$T_2 - T_1$	time required to deliver the stored energy (seconds)
T_3	period of one cycle (seconds)
P_I	input power (watts)
P_0	output power (watts)
Z_L	load impedance (ohms)
Z_c	capacitor impedance (ohms)
R_L	load resistance (ohms)
η	converter efficiency
ϕ	flux (webers)
k	constant of proportionality

I. INTRODUCTION

Some of the major problems of the conventional push-pull converter are discussed to show the merits of the single-ended switching transformer regulator.

Figure 1 is the basic circuit of the conventional push-pull converter; typical transistor voltage and current waveforms are included for reference during the following discussion.

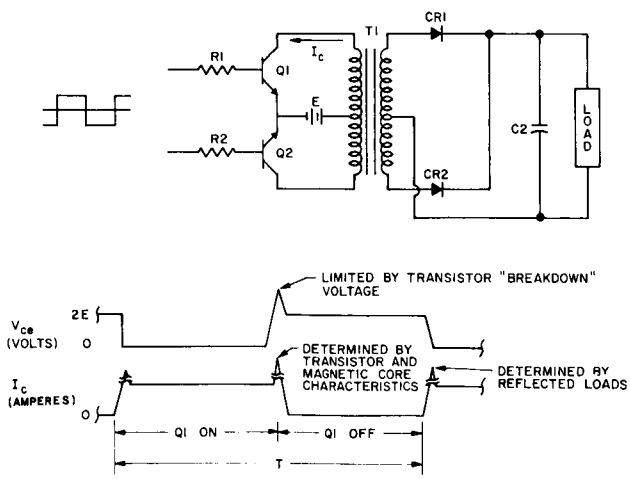

FIGURE 1. CONVENTIONAL METHOD OF DC-TO-DC CONVERSION

Unpredictable current and voltage transients occurring during the transistor switching time each half cycle contribute to inefficient operation and often lead to catastrophic failure.

The major causes of the conditions are:

1. Transistor "crossover" currents. Because of the switching characteristics of the transistor, both transistors conduct current simultaneously during the switching time and produce a current peak in these components each half cycle. The magnitude and duration are dependent on several factors such as the transistor storage time, rise and fall times, current gain, temperature, and loading effects. These factors vary with each component and it is extremely difficult, if not impossible, to eliminate this transient condition without affecting the performance or increasing the complexity of the design significantly.

2. Saturation of the magnetic core material. Symmetrical operation of the transformer requires that the product of the voltage applied to the transformer winding and the time this voltage is applied be identical each half cycle. Exact symmetry obviously cannot be achieved because of differences in the saturation voltages and switching characteristics of the transistors. Provided sufficient imbalance exists, the "square hysteresis loop" core material normally used in this type of design will saturate during each cycle of operation and produce a surge current in one of the transistors. Again, the amplitude and duration of the current transient will depend on factors such as the transistor, magnetic core, power source, and transistor drive characteristics.

3. Load reflection to primary winding. In the conventional transformer operation, the secondary loads will be continuously reflected to the primary and, in certain applications, will produce transient loading effects in the transistors. In addition, the diode capacitance in the rectifier bridge will reflect an extremely low impedance to the primary winding during the switching time each half cycle and cause current transients in the transistors.

4. Voltage transients. The leakage inductance of the transformer windings will normally produce a voltage transient across the transistor of sufficient magnitude to force the component into a secondary breakdown condition each cycle. This condition does not normally lead to a catastrophic failure, provided the transistor sustaining voltage is sufficiently high; it does result in additional power dissipation in the device.

5. Radio frequency interference (RFI) considerations. The design of the adequate RFI filters capable of suppressing the radiated and conducted interference levels is further complicated when several dc-to-dc converters of the same design are required, because the transient current conditions will vary with each component.

The foregoing discussion has described briefly several undesirable features of the push-pull principle of operation and leads to the conclusion that both current and voltage transients often affect the performance and reliability of the design.

II. THEORY OF OPERATION

Figure 2 is the basic single-ended switching transformer dc-to-dc converter developed by MSFC for transferring electrical energy from the input power source E_1 to the electrically isolated output load. In

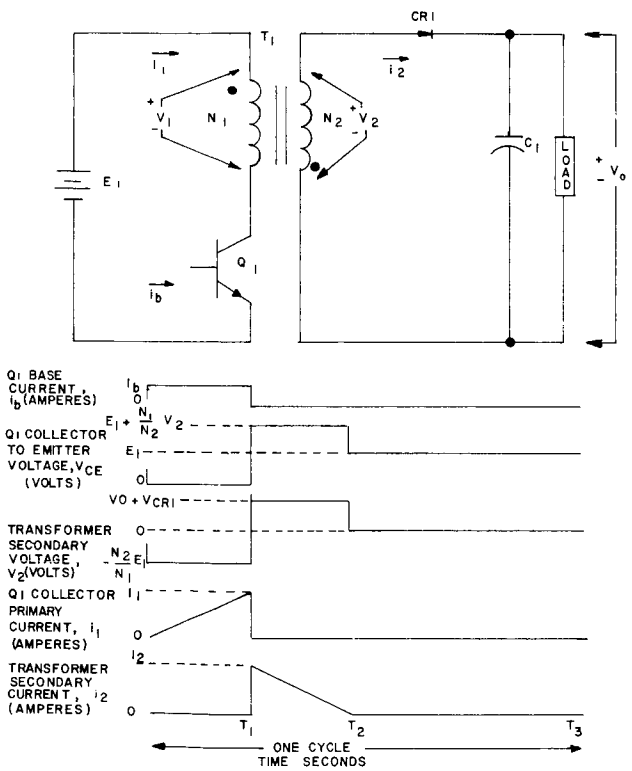

FIGURE 2. SINGLE-ENDED SWITCHING TRANSFORMER DC-TO-DC CONVERTER

addition to merely converting the input power to the desired output level, extremely accurate voltage regulation can be maintained by proper control of the switching frequency of transistor Q1. It should be emphasized that electrical power conversion, electrical output isolation, and voltage regulation can be accomplished in only one "stage" of operation requiring few components. Conventional methods normally require more than one stage and a significant increase in components to accomplish comparable results.

The transistor Q1 is driven into the saturated state for a specific period of time T_1; this connects the input power source directly across the transformer primary winding N_1. The voltage V'_2 induced into the secondary winding N_2 during time T_1 is expressed as

$$V'_2 = \frac{N_2}{N_1} E_1. \quad (1)$$

The secondary winding, phased as shown in Figure 2, results in diode CR1 blocking current flow in the transformer secondary winding during time T_1. Since no power is delivered by the transformer secondary winding during this time, the transformer may be regarded merely as an inductor consisting of N_1 turns and the magnetic core. All components except the inductor, transistor, and input power source may be disregarded, as shown in Figure 3.

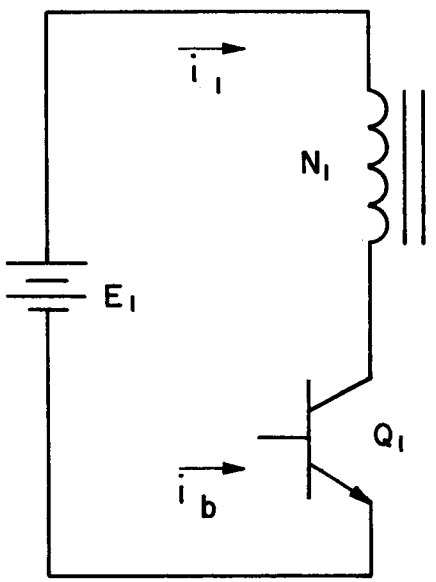

FIGURE 3. SIMPLIFIED CIRCUIT FOR TIME T_1 OPERATION

The equation for the primary current through the transistor may be calculated from the basic equation:

$$E_1 = L_1 \frac{di_1}{dt} \quad (2)$$

or

$$I_1 = E_1 \int_0^{T_1} \frac{1}{L_1} dt. \quad (3)$$

For the magnetic materials that exhibit a constant inductance with varying magnetomotive forces, equation (3) may be written as

$$I_1 = \frac{E_1 T_1}{L_1}. \quad (4)$$

Experimental results verify that the low permeability (60μ) Permalloy powdered magnetic cores presently being used in this design maintain a relatively constant inductance for magnetomotive forces up to about 40 A/cm (50 oersteds), which includes the normal operating range for present applications. From equation (4), the peak transistor current is proportional to the time the transistor remains in the saturated state. It is most important to note that the peak collector current in the transistor is completely independent of the output load (any value between a short and open circuit condition) and is determined solely by time T_1 for applications where E_1 is constant. By controlling this time to the desired fixed value, we can adjust the peak transistor current I_1 (Fig. 2) to correspond to the capabilities of the transistor with assurance that this value will not be exceeded during any phase of operation.

At time T_1, Q1 is switched to the OFF state causing a reversal of the flux change in the transformer. This action produces an induced voltage in each winding (N_1 and N_2) proportional to the number of turns and of opposite polarity to the polarity during time T_1.

The voltage induced into the winding N_2 will be clamped to the sum of the output voltage and the forward voltage drop across diode CR1.

$$V_2 = V_0 + V_{CR1}. \quad (5)$$

The voltage induced into the primary winding N_1 is given by

$$V_1 = \frac{N_1}{N_2} V_2 \quad (6)$$

or

$$V_1 = \frac{N_1}{N_2} (V_0 + V_{CR1}). \quad (7)$$

The transistor collector-to-emitter voltage during time $T_2 - T_1$ is the sum of the input voltage and the primary winding voltage:

$$V_{CE} = E_1 + V_1 \quad (8)$$

or

$$V_{CE} = E_1 + \frac{N_1}{N_2} (V_0 + V_{CR1}). \quad (9)$$

Since E_1, V_0, and V_{CR1} are relatively constant for a particular application, the voltage applied across the transistor collector-to-emitter terminals can be controlled by proper selection of the turns ratio $\frac{N_1}{N_2}$ to a level which will ensure freedom from secondary breakdown of the transistor. Equation (9) does not account for the low energy stored in the leakage inductance, which will produce a voltage transient across Q1, but this voltage can be controlled by incorporating a zener diode across the collector-to-emitter terminals of Q1 or by other transient suppression techniques. The value of the zener voltage must be between the value calculated in equation (9) and the secondary breakdown voltage of Q1.

During time $T_2 - T_1$, Q1 is in the nonconducting state and no electrical power is transferred by the primary winding N_1. The transformer can therefore be regarded merely as an inductor with N_2 turns. For circuit analysis during this time, all circuitry of Figure 2 may be disregarded with the exception of CR1, C1, the load, and the inductor as shown in Figure 4.

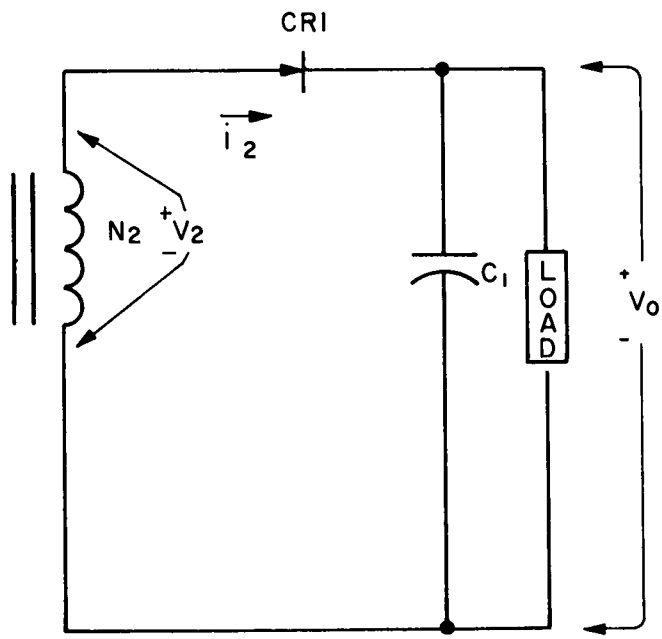

FIGURE 4. SIMPLIFIED CIRCUIT FOR TIME $T_2 - T_1$ OPERATION

At time T_1, the electrical energy stored in the transformer core material is given by the basic equation

$$W_1 = \frac{1}{2} L_1 I_1^2. \quad (10)$$

The energy delivered by the transformer during time $T_2 - T_1$ is given by

$$W_2 = \frac{1}{2} L_2 I_2^2 . \quad (11)$$

Since the energy stored during time T_1 must be equal to the energy delivered during time $T_2 - T_1$, equations (10) and (11) can be combined to calculate the peak current in winding N_2 at time T_1:

$$\frac{1}{2} L_1 I_1^2 = \frac{1}{2} L_2 I_2^2 \quad (12)$$

$$I_2 = \sqrt{\frac{L_1}{L_2}}\, I_1 . \quad (13)$$

The inductance of the transformer with N_2 turns may be calculated by considering that the magnetic flux is proportional to the magnetomotive forces. This is a valid assumption for the core material presently being used for this application, provided the transformer operating range is restricted as discussed previously.

Therefore,

$$\phi = kNi \quad (14)$$

or

$$i = \frac{\phi}{kN} . \quad (15)$$

Therefore,

$$\frac{di}{dt} = \frac{1}{kN} \frac{d\phi}{dt} . \quad (16)$$

By combining the basic equation

$$e = L \frac{di}{dt} \quad (17)$$

with equation (16), we obtain

$$e = \frac{L}{kN} \frac{d\phi}{dt} . \quad (18)$$

The general law for induced voltage is

$$e = N \frac{d\phi}{dt} . \quad (19)$$

Combining equations (18) and (19) yields

$$L = kN^2 . \quad (20)$$

Equation (20) verifies that the inductance of the transformer is proportional to the square of the turns.

Therefore,

$$\frac{L_1}{L_2} = \frac{N_1^2}{N_2^2} . \quad (21)$$

Combining equations (13) and (21) yields

$$I_2 = \frac{N_1}{N_2} I_1 . \quad (22)$$

Equation (22) shows that the peak current through winding N_2 is dependent only on the peak primary current I_1 and the transformer turns ratio N_1/N_2.

The time $(T_2 - T_1)$ required to discharge the transformer stored energy may be determined by considering the basic magnetic equation

$$V_2 = L_2 \frac{di_2}{dt} . \quad (23)$$

Since V_2 and L_2 are both essentially constant, the slope $\frac{di_2}{dt}$ may be considered constant.

Therefore, equation (23) may be written as

$$\frac{I_2}{T_2 - T_1} = \frac{V_2}{L_2} . \quad (24)$$

The time required to deliver the stored energy is given by rearranging equation (24) as follows:

$$T_2 - T_1 = \frac{I_2 L_2}{V_2} . \quad (25)$$

Therefore, the equation of the secondary winding current i_2 is

$$i_2 = I_2 - \frac{V_2}{L_2} (t - T_1) \quad (26)$$

where $T_1 \leq t \leq T_2$.

When equations (4) and (25) are combined, the ratio of the time $(T_2 - T_1)$ required to discharge the transformer to the time T_1 required to store the energy is given by

$$\frac{T_2 - T_1}{T_1} = \frac{I_2 L_2}{V_2} \frac{E_1}{L_1 I_1} . \quad (27)$$

By combining equations (21), (22), and (27), we obtain

$$\frac{T_2 - T_1}{T_1} = \frac{I_1 E_1}{I_2 V_2} \quad (28)$$

or

$$\frac{T_2 - T_1}{T_1} = \frac{N_2 E_1}{N_1 V_2} \quad . \tag{29}$$

The input power to the switching regulator is given by the basic equation,

$$P_I = \frac{1}{T_3} \int_0^{T_1} e_1(t) i_1(t) dt \, . \tag{30}$$

The input voltage $e_1(t)$ is a constant E_1 and $i_1(t) = \frac{I_1 t}{T_1}$.

Therefore, equation (30) may be written as

$$P_I = \frac{E_1 I_1}{T_1 T_3} \int_0^{T_1} t \, dt \tag{31}$$

$$P_I = \frac{E_1 I_1}{2} \frac{T_1}{T_3} \, . \tag{32}$$

From equation (32), the input power is directly proportional to the transistor duty cycle T_1/T_3.

In the normal operating condition, sufficient time is permitted for the transformer to deliver all stored energy prior to allowing the transistor to conduct. For this condition the maximum duty cycle can be determined as follows ($T_2 = T_3$):

$$\frac{T_1}{T_3} = \frac{T_1}{T_2} = \frac{T_1}{T_1 + (T_2 - T_1)} \, . \tag{33}$$

Combining equations (4) and (25) yields

$$\frac{T_1}{T_2} = \frac{\frac{I_1 L_1}{E_1}}{\frac{I_1 L_1}{E_1} + \frac{I_2 L_2}{V_2}} \tag{34}$$

or

$$\frac{T_1}{T_2} = \frac{1}{1 + \frac{I_2 L_2 E_1}{I_1 L_1 V_2}} \, . \tag{35}$$

Combining equations (21), (22), and (35) yields

$$\frac{T_1}{T_2} = \frac{1}{1 + \frac{N_2 E_1}{N_1 V_2}} \, . \tag{36}$$

Combining equations (6), (8), and (36) yields

$$\frac{T_1}{T_2} = \frac{V_{CE} - E_1}{V_{CE}} \, . \tag{37}$$

Therefore, the maximum input power to the switching regulator is given by combining equations (32) and (37) ($T_2 = T_3$ for maximum duty cycle).

$$P_I = \frac{E_1 I_1}{2} \frac{V_{CE} - E_1}{V_{CE}} \, . \tag{38}$$

The maximum output power can be determined as follows:

$$P_0 = \eta P_I = \eta \frac{E_1 I_1}{2} \frac{V_{CE} - E_1}{V_{CE}} \, . \tag{39}$$

Equation (39) will provide the designer with a quick means for calculating the maximum output power, provided the efficiency η can be adequately predicted. Although the efficiency is a function of several factors including the input voltage level, operating frequency, and circuit components, a satisfactory estimate can normally be made.

III. OUTPUT FILTER

The output ripple across the filter capacitor is produced by two factors: (1) the product of the peak current through the capacitor and the capacitor impedance, and (2) the energy that is transferred to the capacitor will naturally increase the output voltage and results in an output voltage variation. The ripple produced by the product of the peak capacitor current and the capacitor impedance is given by

$$V'_R = \left(I_2 - \frac{V_0}{Z_L}\right) Z_c \, . \tag{40}$$

The ripple resulting from the electrical energy transfer to the capacitor is given by equating the energy delivered to the capacitor to the energy delivered by the transformer minus the energy used in the load:

$$\frac{1}{2} C_1 (V''_R)^2 = \frac{1}{2} L_2 I_2^2 - \frac{V_0^2}{R_L} T_3 . \quad (41)$$

or

$$V''_R = \sqrt{\frac{L_2 I_2^2}{C_1} - \frac{2V_0^2 T_3}{C_1 R_L}} . \quad (42)$$

It should be emphasized that the output ripple is less than the sum of the values obtained from equations (40) and (42) since the peak variations of each occur at different times during the cycle. Equation (40) shows that the output ripple V'_R is directly proportional to the capacitor impedance and verifies why capacitors with low dissipation factors are desirable. Equation (42) verifies that large capacitance and small inductance values as well as high frequency operation are desirable in reducing the output ripple.

For most applications, capacitors are presently available which will maintain the output ripple below 0.1 volt peak to peak without additional filtering. As an example, electrolytic capacitors with a 1200 microfarad and 50-volt dc rating at 2 percent maximum dissipation factor are available in a package size of 12.3 cm^3.

Additional filtering may be included as required.

IV. OUTPUT OVERLOAD PROTECTION

Many applications require the voltage regulator to limit the input power to a specified value as well as not damage the regulator during output short circuit or overload conditions.

The single-ended regulator design can accomplish these requirements easily by not allowing Q1 (Fig. 2) to conduct until the transformer has been completely discharged (time $T_2 - T_1$). By the addition of a single winding on the transformer, a signal generated during the transformer discharge time can be used to prohibit the control section from driving transistor Q1 on until all of the transformer stored energy has been expended. The voltage induced into this sense winding is given by:

$$V_3 = \frac{N_3}{N_2} (V_0 + V_{CR1}). \quad (43)$$

From equation (43) the minimum sense voltage will occur during an output short circuit condition ($V_0 = 0$) and can be controlled to the desired value by proper selection of N_3. Note that this feature not only allows for protection during a short circuit condition but also during any overload condition.

From equation (32), the input power is proportional to the transistor duty cycle T_1/T_3. The duty cycle will decrease during an overload condition since the transformer discharge time (from equation (25)) is inversely proportional to the secondary voltage. Therefore, an output overload condition will actually result in a decrease in the input power.

Incorporating this minor addition to the circuit provides for a reliable overload protection as well as a reduction in the input power during an overload condition.

V. SINGLE-ENDED SWITCHING TRANSFORMER REGULATOR

The output voltage of the single-ended switching transformer dc-to-dc converter of Figure 2 can be precisely regulated by controlling the operating frequency and/or duty cycle of transistor Q1. Since many acceptable techniques exist for providing transistor Q1 with the desired signal, the control section will not be discussed in detail but will be mentioned briefly to stress some of the more important considerations in designing this section.

Figure 5 is a typical block diagram of the complete switching regulator that has been used exten-

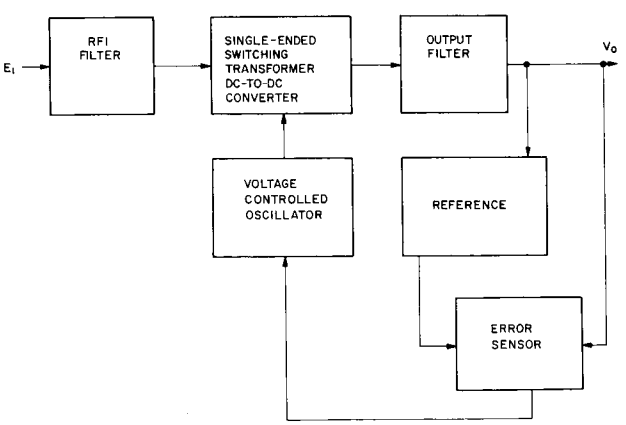

FIGURE 5. BLOCK DIAGRAM OF SINGLE-ENDED SWITCHING TRANSFORMER DC-TO-DC REGULATOR

sively in designing reliable, efficient, compact regulators for a variety of applications. The input voltage E_1 is connected to the input RFI filter. The output of the filter is connected to the input of the single-ended dc-to-dc converter (Fig. 2) which converts the input voltage to an electrically isolated output voltage. The output voltage is filtered and compared to the reference voltage. The difference is amplified and then provides a signal to the voltage controlled oscillator (VCO). The output of the VCO is a square wave and drives the single-ended dc-to-dc converter at the required frequency to maintain the desired output voltage. The output of the VCO is connected to the single-ended dc-to-dc converter through a pulse transformer to maintain the required electrical isolation between the input and output voltages.

For applications where the input voltage remains relatively constant, it is normally desirable to drive transistor Q1 (Fig. 2) into saturation for a fixed peak current each cycle. If the input voltage is variable, it is sometimes advantageous to drive Q1 on for a period of time T_1, which is inversely proportional to the input voltage E_1. This enables Q1 to operate at a fixed peak current each cycle regardless of the input voltage and provides the maximum power available from the regulator at the minimum input voltage.

VI. PRINCIPAL ADVANTAGES

The single-ended switching transformer regulator offers many distinct advantages as compared to conventional methods of regulation. Some of the principal features are discussed in the following paragraph.

One of the major current transient conditions in the push-pull method of conversion, as discussed previously, is caused by the inability to properly match the transistors' switching characteristics. The single-ended switching regulator, requiring only one transistor, eliminates this problem completely.

The single-ended technique eliminates the possibility of transformer saturation, a major cause of current transients in the push-pull version.

Unlike the push-pull converter, both primary and secondary voltage and current peak values can be precisely controlled to the desired levels by the proper selection of circuit parameters. This feature will allow the transistor to operate at a controlled stress level and will result in a significant improvement in reliability.

With only one power stage required (Fig. 2), a precisely regulated voltage, electrically isolated from the input power source, can be obtained. Conventional methods normally require two or more stages and significantly more components.

Since the voltage induced in the transformer windings is proportional to the number of turns in each winding, multiple output voltages are possible by proper selection of the transformer secondary windings.

This regulator is capable of a one cycle response time.

Overload protection can be incorporated by the addition of a transformer winding used to ensure the complete discharge of the transformer prior to turning on Q1 (Fig. 2). Note that the input power will be reduced during an output overload condition.

The maximum output power per regulator can be determined by equation (39). If additional power is required, direct paralleling of the outputs of two or more stages can be accomplished without affecting the regulator performance. These stages may use either a common or separate control section.

Another feature of the single-ended switching transformer regulator is that less-complicated RFI filters are required. This is possible because current waveforms are essentially constant from unit to unit.

Since transistor power losses during switching times (ON and OFF) are normally much less than the losses in the push-pull converter, the single-ended switching regulator can be operated at relatively high frequencies. A reduction in size and weight, plus an improvement in efficiency, will normally be realized by using this single-ended design.

VII. FUTURE EFFORTS

From equation (39), the maximum output power for a specific application (E_1 is constant) is dependent on the transistor switching capabilities (I_1 and V_{CE}) and the regulator efficiency (η). By selecting a family of transistors capable of delivering various output power levels, "standard" modules can be designed. Direct paralleling of these modules for increased output power could be accomplished as required. The only design necessary would consist of selecting the proper number of secondary turns N_2 where

$$N_2 = \frac{N_1 (V_0 + V_{CR1})}{V_{CE} - E_1} \qquad (44)$$

and one resistor value in the control section to obtain the desired output voltage.

To further reduce the regulator size and weight as well as to improve the reliability, recent efforts have been directed toward designing a standard integrated circuit control section that could be used for practically all applications. At present, it appears to be both possible and feasible to develop the complete control section in one package, with the exception of two "test select" resistors — one to adjust time T_1 (Fig. 2) and the other to adjust the output voltage to the desired level. This will result in a further size reduction as compared to the present design.

APPENDIX

DESIGN PROCEDURE

The following procedure is included to provide a systematic approach that may be used in designing the single-ended switching transformer regulator. No attempt is made to specify components or component stress levels to be used since reliability requirements vary with the application.

Sufficient time is allowed for the transformer to transfer all of the stored energy prior to switching on the transistor. This operating condition normally results in improved efficiency and less radio frequency interference with a sacrifice in the total output power capability of the regulator. In the event additional output power is required, direct paralleling of the output of two or more regulators is recommended.

In selecting the transistor in step 1, it should be noted that the maximum output power is limited by the peak collector current I_1 and the collector to emitter voltage V_{CE} (equation (39)).

The efficiency η in step 2 is dependent on several factors including the input voltage, switching frequency, transformer wire size, and components, and can be determined accurately only by thorough analysis. Provided state of the art components are used and the operating frequency is nominal for the components used, an efficiency of 0.9 should normally be attainable, provided the forward voltage drop across diode CR1 is much less than the output voltage V_0.

1. Select the transistor to be used and determine the collector to emitter voltage V_{CE} that the transistor is capable of reliably blocking and substitute into equation (45):

$$\frac{T_2}{T_1} = \frac{V_{CE}}{V_{CE} - E_1} \cdot \qquad (45)$$

Solve for the ratio $\frac{T_2}{T_1}$.

2. Determine the maximum output power (P_o) desired and substitute the value into equation (46).

$$I_1 = \frac{2P_o}{\eta E_1} \frac{T_2}{T_1} . \qquad (46)$$

Solve for I.

Provided the transistor selected in step 1 cannot reliably switch the peak collector current I_1 calculated in equation (46), it is necessary to select a transistor with increased I_1 and or V_{CE} capability and repeat steps 1 and 2.

3. Determine the transformer turns ratio N_1/N_2 from equation (47).

$$\frac{N_1}{N_2} = \frac{V_{CE} - E_1}{V_0 + V_{CR1}} \cdot \qquad (47)$$

4. Select the desired transistor on time T_1 and determine the transformer primary inductance from equation (48).

$$L_1 = \frac{E_1 T_1}{I_1} . \qquad (48)$$

5. From the transformer design manual, determine the transformer core type and size, and the number of secondary turns required (step 3 determines the ratio of primary and secondary turns N_1/N_2). Care should be taken to ensure that the inductance remains relatively constant over the operating range.

6. Select diode CR1 with the following characteristics:

(a) Minimum reverse breakdown voltage

$$V_r = \frac{N_2}{N_1} E_1 + V_0 . \qquad (49)$$

(b) Capability to switch the peak forward current I_2 where

$$I_2 = \frac{N_1}{N_2} I_1 . \quad (50)$$

(c) Capability to conduct a current which decreases linearly from I_2 (from step b) to 0 in time $T_2 - T_1$ where

$$T_2 - T_1 = \frac{N_2 E_1 T_1}{N_1 (V_0 + V_{CR1})} \quad (51)$$

at a diode duty cycle given by

$$\frac{T_2 - T_1}{T_2} = \frac{E_1 N_2}{E_1 N_2 + N_1 (V_0 + V_{CR1})} . \quad (52)$$

7. When a low output voltage ripple is required, a capacitor should be selected with as low a dissipation factor and as high a capacitance value as necessary.

The following equations are included as a guide in determining the capacitor type and capacitance value required.

The ripple caused by the capacitor impedance is given by

$$V'_R = (I_2 - \frac{V_0}{Z_L}) (Z_c). \quad (53)$$

The ripple produced by the transfer of the energy from the transformer to the capacitor is given by

$$V''_R = \sqrt{\frac{L_2 I_2^2}{C_1} - \frac{2V_0^2 T_3}{C_1 R_L}} . \quad (54)$$

Additional output filtering may be included when required.

ELECTRICAL POWER SYSTEMS STUDIES AT MSFC

By

Edward E. Dungan

SUMMARY

Electrical power systems applicable to earth orbital and to lunar surface missions are discussed. Saturn Instrument Unit lifetime extensions will require fuel cells and/or radioisotopes for primary power. Lunar surface vehicles such as the Mobile Laboratory (MOLAB) will use fuel cells that must be optimized for mass savings. Two computer programs are discussed and one is described.

I. INTRODUCTION

Electrical power systems studies in progress at MSFC include those applicable to both earth orbital and lunar surface missions. Current Saturn Instrument Units obtain primary power from onboard batteries that are capable of about six hours of continuous operation in the one to five kilowatt range. Missions requiring several days to a few weeks will depend upon fuel cells for primary electrical power. Extended missions, several weeks to one year, will necessarily be dependent upon radioisotopes for continuous primary electrical power since both battery and fuel cell masses would become prohibitive. Fuel cells and radioisotopes are both attractive for lunar surface missions. Solar devices are not being considered at this time since the long lunar night would require excessive storage batteries.

In advanced systems studies it is important that terminology be clearly defined to avoid confusion. The word "system" in this paper is defined to include one or more of the following: a primary power supply, a secondary power supply, an auxiliary power supply, a power distribution subsystem, and a heat dissipator such as a radiator. Radioisotopes, fuel cells, or batteries are used as primary power supplies depending upon the mission considered. Secondary power supplies, usually rechargeable batteries, also take care of short term peak loads. Auxiliary power supplies are used in low power applications for extended periods; for example, systems for nuclear auxiliary power (SNAP).

II. INSTRUMENT UNIT RADIOISOTOPE POWER SYSTEM

The Martin Company (Baltimore), under contract NAS8-20092, is investigating the application of radioisotopes to the Saturn Instrument Unit (IU). The title of the contract is "Establishing Design and Development Criteria for a Saturn Type Instrument Unit Electrical Power System (Radioisotopes)."

A. PURPOSE AND OBJECTIVES

The purpose of the Martin study is to set forth the basis for the integration of a radioisotope power supply into an Instrument Unit, not the design and technology or the development of a nuclear power module itself. The long range objectives for application purposes are to develop, test, and check out a power system and to build a system that will be compatible with launch vehicle missions. Constant power levels of 1 to 5 kWe will be required for mission durations from 1 to 24 months for the immediate earth orbital applications.

Assumptions and guidelines for the study include the following:

1. Assume that the power supply will be versatile enough that relatively minor modifications will be required to adapt it to various missions with power levels of 1 to 5 kWe and mission durations of 1 to 24 months.

2. The power supply will operate efficiently in any or all environments to be encountered such as launch; ascent; and orbital, escape, lunar, or deep space trajectories.

3. The power supply will be compatible with the electrical system and the configuration of Saturn type vehicles. Radiators will be designed for location within, on, or near the IU and for non-interference with operation of IU components (such as sensors or antennas).

4. Saturn IU electrical loads will be adhered to. Peak power demands may vary up to five kWe depending upon mission requirements.

5. The preliminary design of a radioisotope power supply should seriously consider the modular concept where, for example, generators of one kWe may be used in modules of one to five units. The complications of radiation shielding, including biological, should be anticipated in mass-tradeoff and design studies.

6. Availability of isotopes will be considered in detail and the selection of such isotopes will be made, with NASA's approval, by the contractor in the initial contract phase.

7. Associated nuclear radiation hazard problems of handling, launch, flight, and reentry will be studied and solutions satisfactory to all cognizant government agencies will be suggested during the early phases of the development program.

8. Reliability will be paramount and a testing program will be anticipated that will verify power supply reliability under all operating constraints. Minimum mass will be of major importance but will not be dominant over reliability.

B. STATUS AND SCHEDULE

The contract was initiated in July 1965. The first phase will be completed in March 1966. Four tasks are included in this phase: Task 1, Preliminary Evaluation; Tasks 2 and 3, Conceptual Design and Vehicle Integration; and Task 4, Data and Reports.

C. PROGRAM PLANS

Initial findings indicate the desirability of designing 500 W (net electrical) thermoelectric modules and limiting continuous IU power to 2 kWe. About 90 percent of the available lower Lunar Excursion Module (LEM) adapter surface is used for heat rejection radiators when low thermoelectric cold junction temperatures are desired. The module housing structure associated with Saturn integration will require additional design definition as system load specifications are established. The influence of the frontal generator fuel loading concept on the excess heat dump mechanism is to be studied.

The objectives of the next phase include the development and laboratory testing of a thermoelectric radioisotope power supply employing electrical heaters to simulate the isotope heat input. The simulator will meet all the design criteria and guidelines given above. The scope will include the design and development of the instrumentation required to monitor the simulator's performance. Operating manuals will include a description of the power supply, operating procedures, operational limits, and preliminary performance data. An experimental program plan will be developed for each laboratory test.

III. LUNAR SURFACE VEHICLE POWER SYSTEM

Electrical power system studies were completed during 1965 for lunar roving vehicle applications. Two vehicle design contracts that included fuel cells as the primary power supplies were completed by Boeing Company (NAS8-11411) and Bendix Systems Division (NAS8-11287). These studies were constrained for the Mobile Laboratory (MOLAB) mission manned operation of 14 days on the lunar surface in a shirtsleeve environment. Power profiles varied substantially throughout the mission because of electrical wheel drive loads over rough terrain. Reactant consumption rates were found to be sensitive to fuel cell design characteristics; thus, substantial mass penalties would be incurred if the system was not optimized. Computer programs were developed and used as a tool in power system preliminary design. Boeing's program is given here as an example of design application.

A. MOLAB FUEL CELL OPTIMIZATION PROGRAM

The selected mission required total power loads of five to six kWe. Power and energy logic is shown in Figure 1. These requirements were applied to a computer program that optimized payload mass.

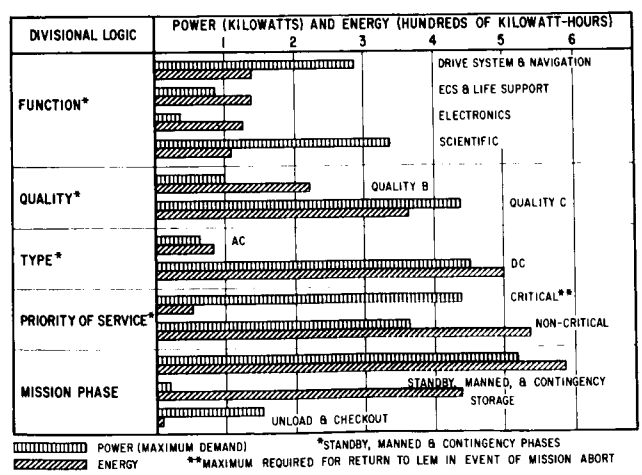

FIGURE 1. POWER AND ENERGY

Minimum mass constraints included the following:

1. Load profile

2. Radiator specific cooling capacity as a function of time

3. Maximum radiator area constraint

4. Voltage regulation constraint

5. Candidate fuel cell characteristics.

The results of the computer calculations included the following:

1. Relative mass comparison of fuel cell candidates

2. Startup time and parasitic energy requirements

3. Mass penalty as a function of specified voltage

4. Mass penalty as a function of varying power profiles.

A flow diagram that describes the program's capabilities is shown in Figure 2. The quality parameters are mission oriented and not part of an analytical optimization. The program served as a very useful tool in reducing mass requirements in Boeing's preliminary design studies.

B. IN-HOUSE COMPUTER PROGRAM

A joint study with in-house MSFC contractor personnel was made on an electrical power system for MOLAB (Appendix A). The primary purpose of the study was to develop parameters for an in-house computer program to be used in the analysis of the various mission constraints for lunar power applications. The power profile is shown in Appendix B. The computer program is described in Appendix C.

IV. CONCLUSIONS

Space power systems for extended missions usually represent a substantial percentage of the total payload mass. It becomes imperative that computer optimization techniques, such as those described in this paper, be applied in the program definition phase preceding design and development. Technology development may also benefit in considering the results of these applications. Mission requirement projections for future technology developments may not always predict optimum parameters, but basic classes of applications can be defined.

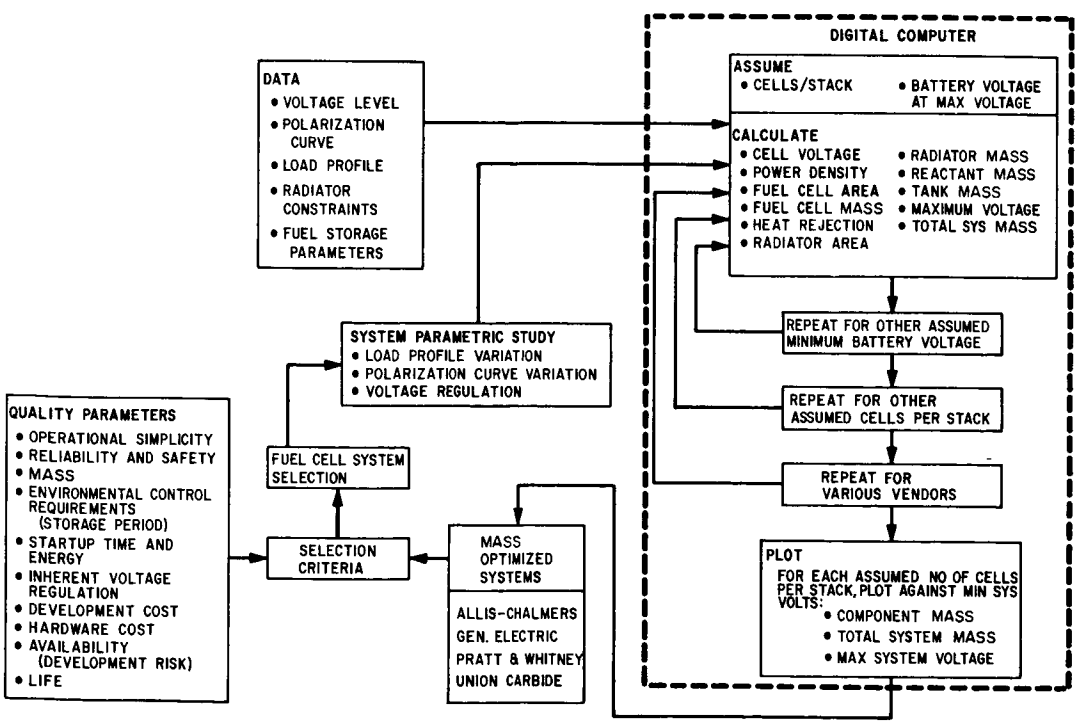

FIGURE 2. FUEL CELL SELECTION AND ANALYSIS

APPENDIX A

MOLAB STUDY ANALYSIS

A. SUMMARY

A study analysis was performed on the electric power system for the Lunar Mobile Laboratory (MOLAB) [1].

The primary chemical electric power system (CHEPS) consists of hydrogen/oxygen gas fuel cell modules, support reactant storage tankage, and a heat rejection mechanism in the form of a radiator. The secondary power system consists of a battery charged by an isotope power source. The functions of monitoring and control are provided by the power distribution system (PDS). The areas for investigation are as follows:

1. The interrelationships between arbitrary system parameters for a typical constant load profile and optimum system mass are determined for CHEPS.

2. The effects upon optimum CHEPS mass under load profile variations or arbitrary system parameters are examined.

3. A functional block diagram of the PDS is synthesized.

4. PDS equipment requirements are related to environment and internal functions.

5. Power areas within the PDS and interface are defined.

The study of item 1 showed that results obtained from "exact" and "linearized" closed voltage/current plots in the range of interest for hydrogen/oxygen fuel cells are invariable. Under the assumptions and conditions investigated, a broad minimum is found surrounding a specific system mass of 0.92 kg/kWh.

Findings relating to item 2 indicate a weak relationship between the number of fuel cells and the overall specific system mass for the profile investigated. Specific system mass varies from 0.77 kg/kWh for 7 fuel cell modules, each of 900 watt capacity, to 0.81 kg/kWh for 11 fuel cell modules, each of 900 watt capacity. Net difference in mass is 45.5 kg.

A block diagram of the PDS, as related to item 3, indicates the necessity of load separation into areas requiring good regulation and those where regulation is less important. Each area mentioned is serviced by a separate fuel cell bank. An additional fuel cell bank supplies loads which are intermittent but which require good regulation through power conditioning equipment. A diode switching arrangement, free of transient generation, is used to buffer fuel cell banks connected to intermittent loads.

Equipment requirements, as related to item 4, were examined relative to vibration, shock, acceleration, temperature, humidity, corrosive atmosphere, radiation, and combined effects. Certain environmental hazards such as electrical interference and dumped waste in vacuum are indicated. Equipment will be compatible with launch pad environment, Apollo launch, and six month lunar storage, as well as terrestrial transportation.

The major area of interest in item 5 was finding the proper mix of manual and automatic controls. Findings indicated a requirement for completely automatic control with a fail-safe stipulation. Failure of automatic control will cause a reversion to a manual override mode. A further stipulation requires that failure during the automatic mode will not damage interfacing equipment.

B. INTRODUCTION

The CHEPS for the MOLAB comprises a large fraction of total vehicle mass. It is significant that activity be directed analytically, for management of vehicular mass, in the area of CHEPS mass optimization. This report does not attempt to make specific recommendations for a particular design concept, nor does it attempt to compare or deduce basic fuel cell concepts. These aspects have been well covered in previous reports [2, 3]. This study seeks to further investigate selected topics of the analytical relationships existing between the electric power system and the established 14-day mission sequence [4]. Full utilization of computer programing techniques has been employed to accomplish these objectives.

The PDS performs the task of total power management and control in the electric power system;

although it is a minor fraction of system mass, its relationship to system performance and reliability is large. Selected functional aspects of the PDS are therefore a topic of this report.

C. OPERATIONAL-SEQUENCE-ORIENTED POWER PROFILE

1. General

Mass optimization of hydrogen/oxygen fuel cell electric power systems depends upon accurate assessments not only of total energy requirements, but also of power levels and durations. These considerations result directly from the variations in fuel cell efficiency with the level of power demand.

The establishment of a detailed operational sequence [4] permits development of an electric power demand profile, consequentially related to the operations described elsewhere in this report (Table A-I and Appendix B).

2. Guidelines and Assumptions

For the purpose of analysis of the specific mission power demand on the primary fuel cell electric power system and the related mass optimization, several guidelines and assumptions follow:

a. Integrated power demands related only to communication, navigation, telemetry, life support, locomotion, and astronaut entry and exit are presented.

b. Loads related to hole drilling, scientific measurements, etc., are not considered.

c. Loads related to launch operational checkout are exempt as it is assumed that cryogenic topping occurs after checkout but before launch.

d. Loads related to post LEM truck landing and roll-off phase and checkout are exempt; it is assumed that such operations are executed either under battery power or that potential fuel cell demands are negligible.

e. Power expenditures related to the dormant phase are derived from battery banks supported by nuclear electric power supplies.

f. No provision is made for contingencies not named above or related to the operational sequence.

3. Analysis

Each hour of the operational sequence [4] makes new demands on the electric power system. As each function is performed, an integrated running total is summated and is subtotalled for the particular day. Table A-I and Appendix B are a numerical and graphical accounting of these demands.

Because of the large variation from initial to final airlock pumping power, the demands are shown as simple spikes of momentary duration. Each spike denotes the entry or exit of the astronaut and consumes 0.1 kWh. During driving sequences, starting with the tenth day, power is increased because of requirements for driving illumination during the lunar darkness. It is assumed that cabin illumination is extinguished to conserve fuel during sleeping hours and during periods of absence from the vehicle.

The 14-day average power level is about 3.0 kWe. The daily average demand is 70.5 kWh per 24 hour day.

TABLE A-I
SUMMARY OF DAILY POWER REQUIREMENTS

Day	kWh
1	68
2	65
3	73
4	67
5	78
6	81
7	58
8	90
9	73
10	79
11	64
12	88
13	58
14	46
TOTAL	988

D. PRIMARY ELECTRIC POWER SYSTEM MASS OPTIMIZATION

1. General

For the purposes of analysis, the primary MOLAB power system is considered to consist of:

a. Hydrogen/oxygen fuel cell modules for generation of primary electric power.

b. Storage tankage for cryogenic storage of hydrogen and oxygen.

c. A heat rejection mechanism in the form of a space radiator.

The secondary power system, consisting of the battery banks, supplies the power required for start-up and is charged by a nuclear electric power source during all phases after launch. The heat generated by the nuclear power source is not a consideration, as it is assumed that such heat (about 1200 W) will be used for equipment temperature conditioning during the dormant phase and will contain its own radiator for excess heat dissipation.

2. Linearized Mass Optimization at Constant Load

A computer program that optimizes system mass under a constant load for arbitrary parameters is given in Appendix C. A linear approximation of the voltage/current curve was used. A sample run is included with numerical results. Optimization is accomplished for a mission duration of 336 hours. The current efficiency, first thought to be an arbitrary parameter, has proved to be a constant determined by atomic constants. The exact value is more nearly 0.0113 rather than the 0.015 kg per ampere hour that was used in the example. Results given in the main body of this report used the more accurate constant [5]. For the arbitrary parameter shown, optimum specific mass is shown to occur at a loading of 21 amperes and to have a value of 0.914 kg/kWh. The word "cell" as used in the appendix actually refers to a 900 W Allis-Chalmers fuel cell module. Voltage/current curves are taken from Reference 6. Specific mass varies in an extremely weak manner in the region of optimum loading.

3. Exact Mass Optimization at Constant Load

A computer program was again synthesized for optimization of system mass for constant load. The difference between this program and the one described in Section 2 is that a 100-point matrix of voltage and current points was taken from Reference 6. The results for specific system mass did not differ by more than one part in ten thousand from the findings of Section 2 in the vicinity of optimum loading. The results are invariable between linear and exact analysis.

4. Mass Optimization Related to Variable Load Profile

A third computer program was developed for mass optimization under variable load profile. A minimum for specific system mass was not found for these parameters.

5. Mass Optimization Related to Load Profile Variation

All values of load profile related to the referenced operational sequence and given in Appendix B were varied in 10 percent increments and run through the program developed in Section 4. The accurate value of 0.0113 kg per ampere hour was used for this analysis.

Table A-II is an accounting of various wattage levels by hours used as input data in the analysis and varies in 10 percent increments from nominal.

TABLE A-II
KILOWATT LEVELS FOR PROFILE VARIATIONS

Hours	-30%	-20%	-10%	Nom.	+10%	+20%	+30%
17.00	4.72	5.40	6.07	6.75	7.43	8.10	8.78
0.50	4.62	5.28	5.94	6.60	7.26	7.92	8.58
38.50	4.37	5.00	5.62	6.25	6.88	7.50	8.13
4.00	4.20	4.80	5.40	6.00	6.60	7.20	7.80
0.50	3.92	4.48	5.04	5.60	6.16	6.72	7.28
27.75	1.98	2.27	2.56	2.85	3.14	3.42	3.71
2.50	1.82	2.08	2.34	2.60	2.86	3.12	3.38
114.75	1.58	1.80	2.02	2.25	2.48	2.70	2.93
125.00	1.40	1.60	1.80	2.00	2.20	2.40	2.60

E. POWER DISTRIBUTION SYSTEM (PDS)

1. General

The MOLAB PDS interfaces with each subsystem requiring current within the MOLAB vehicle as well as all of the generators of electric power and storage battery banks. The primary function of the PDS is to monitor, control, and regulate all expenditures of electrical power. Placed in this position, between source and load, the PDS must budget individual subsystem power requirements and arbitrate individual demands as related to proper total system function. This area is most critical when related to total system performance and reliability.

2. Command Functions

A generalized functional block diagram is shown in Figure A-1. Note that the philosophy de-

veloped above is applicable to the relationship of PDS between source and load. Remote command and remote display are defined as signal functions received or transmitted by command receivers or transmitters which may be aboard MOLAB. Actual

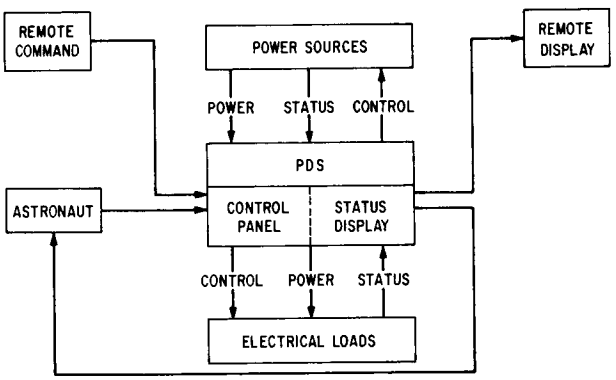

FIGURE A-1. POWER DISTRIBUTION SYSTEM FUNCTIONAL INTERFACE BLOCK DIAGRAM

origin and destination of such control functions may be at the blockhouse, Deep Space Instrumentation Facility, or LEM as related to prelaunch or postlaunch checkout. Possible requirements related to signal coding, source identification, or anti-jamming are not considered part of the PDS function and are beyond the scope of this report. Power-demand control for command receivers is not a PDS function during the dormant phase. All MOLAB operational responses are available upon receipt of applicable remote commands.

Local command functions received by the PDS originate in the sources of power, electrical equipment loads, and the astronauts. These command functions elicit automatic responses, depending upon their mutual relationship, or normalcy, and may be manually inhibited or actuated by the astronaut.

3. General Requirements and Problem Areas

The level of astronaut activity, established in the previously referenced 14-day operational sequence, firmly precludes from consideration any but the highest level of automaticity in the PDS. Out-of-tolerance function is proclaimed by both visible and audible signal, as such a condition may arise while the astronauts sleep.

Failure of any single element of the PDS will not lead to degradation of performance or loss of function. A malfunction detection system will be incorporated to perform self-check operations upon the decision logic section. Full use will be made of widely available, compact, highly reliable integrated circuits and multiple redundancy voting logic in both these areas.

Load division will be such that intermittent loads such as air conditioning, locomotion, air lock pumping, etc., which may not require good regulation, are bus separated from loads such as navigation, communication, etc., where better regulation may be required. Load separation, along with the accepted requirements for fuel cells, of voltage variation limited to 28 ± 2 V for a three-to-one change in load should preclude all necessity of prime power regulating devices of questionable reliability and performance. However, if instrument circuits are voltage sensitive, line isolation and regulation should be provided locally within the equipment involved.

A buffering arrangement can be used as a means of isolating intermittent load transients (Fig. A-2). Power diodes of large junction areas are connected between fuel cell modules. Application of intermittent loads back-biases the diode and affords a smooth load transition such that the more constant load bus

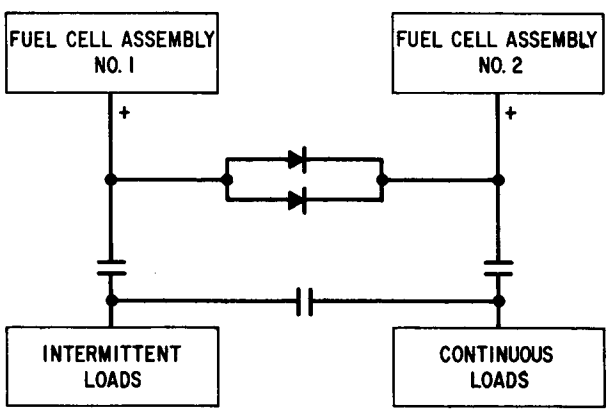

FIGURE A-2. KILOWATT LEVELS FOR PROFILE VARIATIONS

undergoes a slight decrease in voltage, whereas the voltage on the intermittent bus drops and is isolated. Since power diodes are small, compact, and may be structure mounted and paralleled, with potential drops not exceeding 1 volt and 100 amperes or more, no heat dissipation or regulation problem is encountered.

Incorporation of automatic control, if improperly attempted, can result in a degradation of reliability in the event of a failure. The same is true for a malfunction detection system. Failure of an auto-

matic control or malfunction detection system will cause the system to revert to the manual override mode. Such failure, furthermore, must not damage interfacing equipment.

4. Environmental Considerations

All externally located connective wiring, clamps, etc., must withstand the combined effects of vacuum, ultraviolet radiation, and lunar temperature extremes. Further requirements are to withstand the shock and vibration associated with Apollo launch, LEM truck landing, and terrestrial transportation. All major components will be sealed and shielded from RFI and be immune to the effects of humidity or dumped wastes in vacuum.

F. RESULTS

Several tentative results can be drawn from the analysis of previous sections.

1. A variable load profile rather than a constant load profile is necessary for accurate optimization of system mass.

2. Small variations in variable load profile produce small variations in specific system mass.

3. The power distribution system, although it represents only a small fraction of power system mass, will play a large role in system performance and reliability.

4. The power distribution system should be fully automated and fail safe, returning to the manual override mode under failure.

5. Load division should be maintained between intermittent and continuous loads.

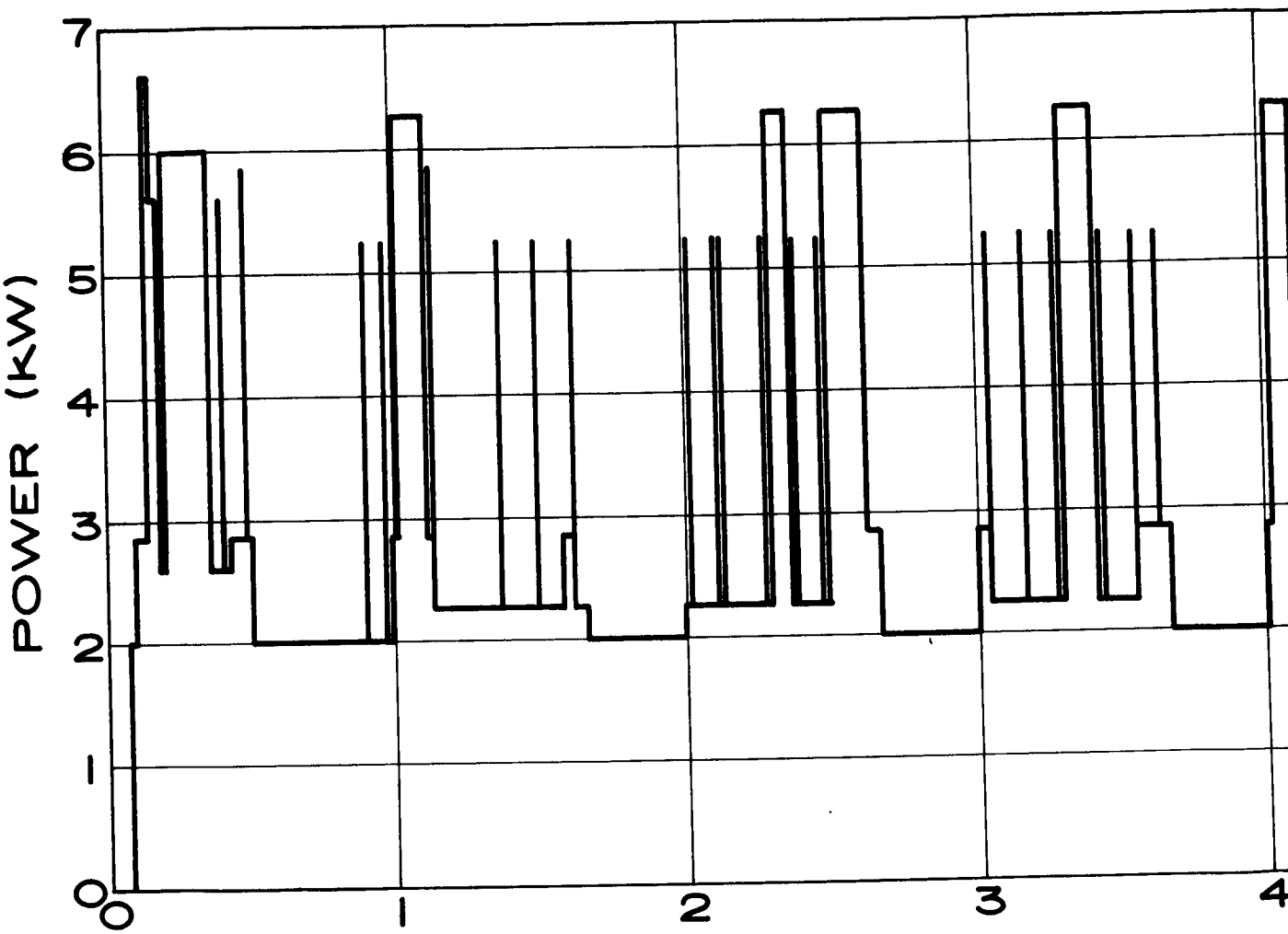
POWER (KW)
0
1
2
3
4
5
6
7
0
1
2
3
4

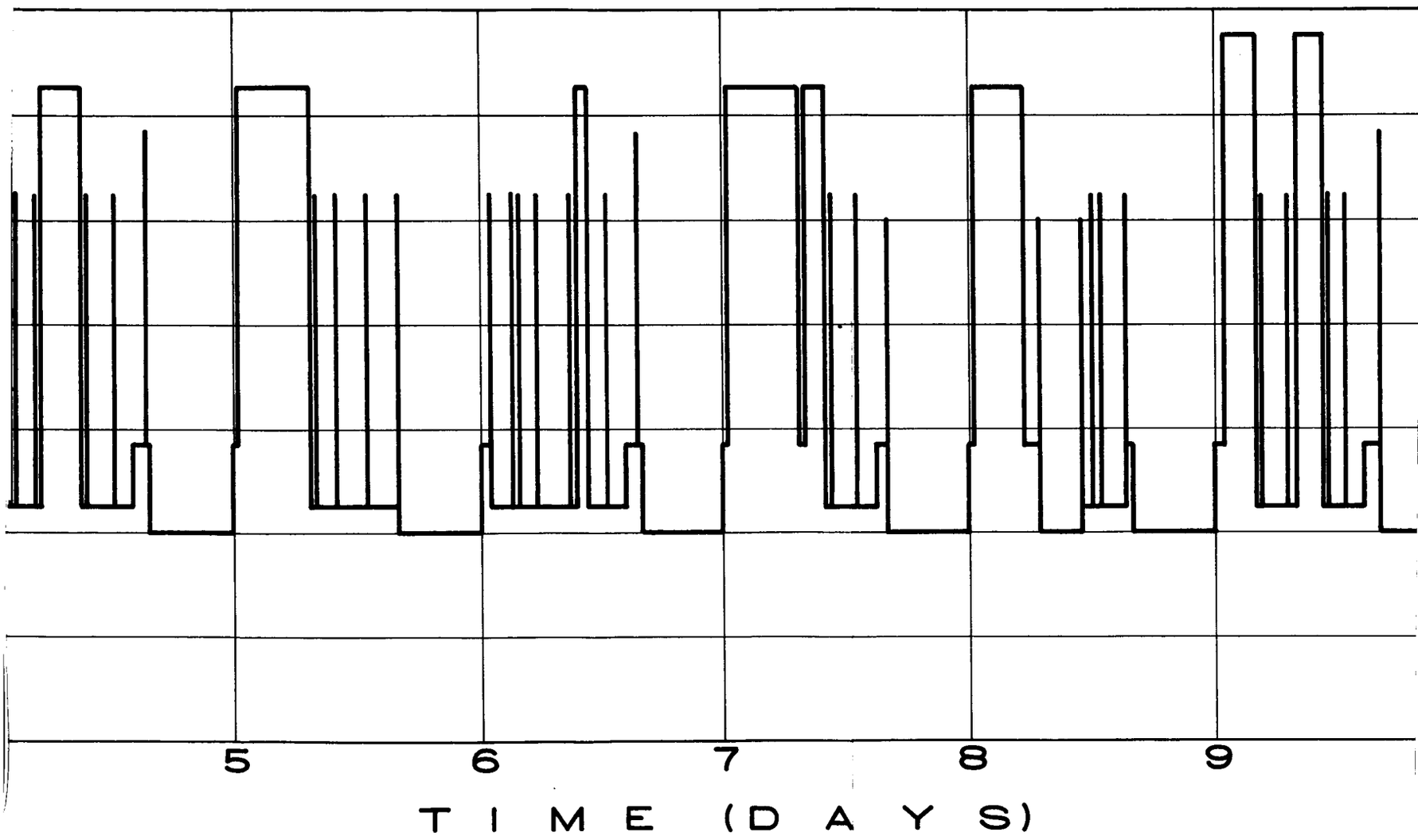
5
6
7
8
9
TIME (DAYS)

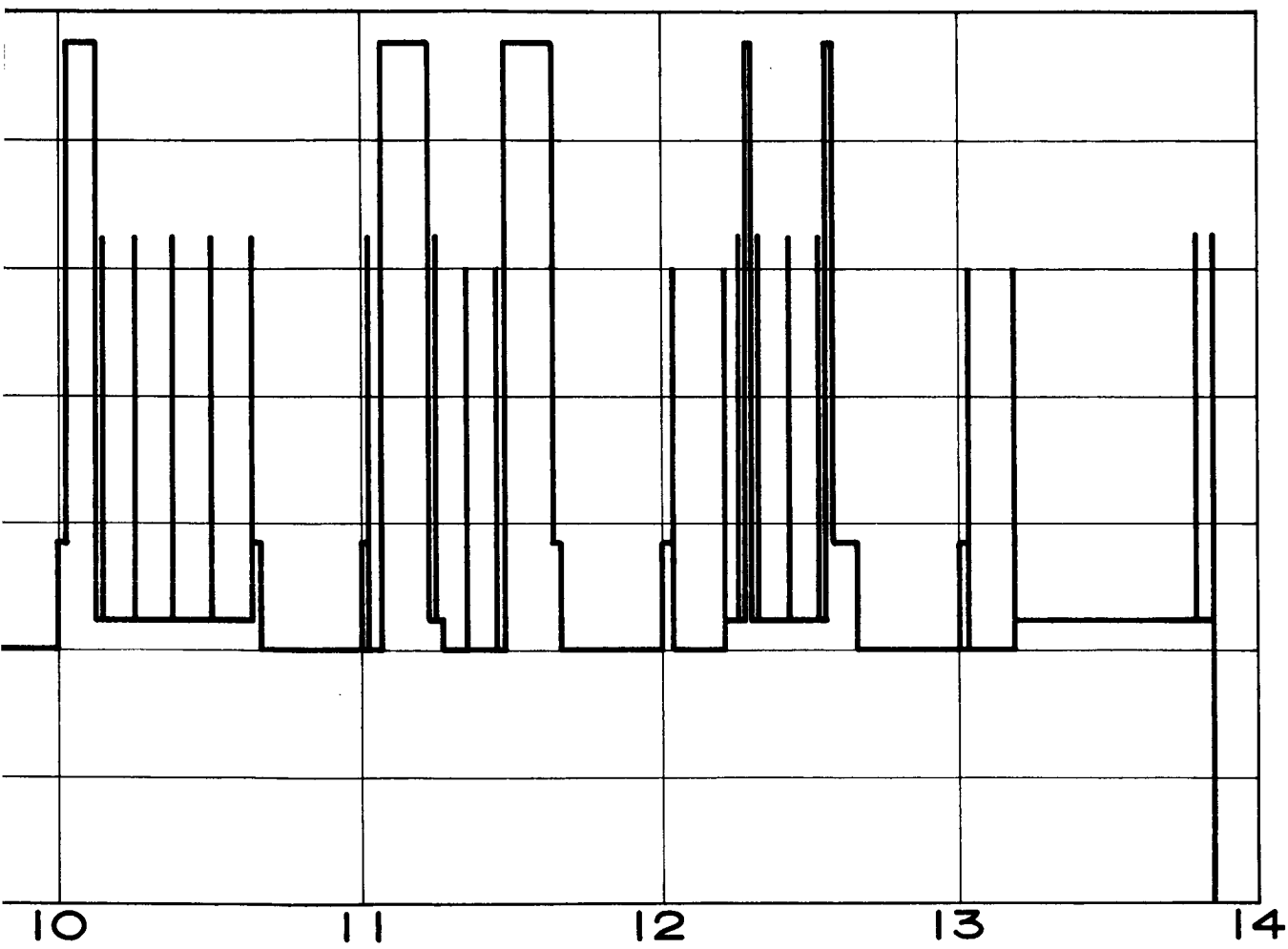
10
11
12
13
14

APPENDIX C

COMPUTER PROGRAMS FOR FUEL CELL MASS OPTIMIZATION

A. STATEMENT OF PROBLEMS

The efficiency of a fuel cell is highest at light loads and the specific fuel consumption is lowest. To operate a fuel cell at light loads requires an oversize, and hence heavier, fuel cell. For a given mission profile and duration there is a design that has a minimum overall mass including fuel cells, fuel, tankage, and heat radiator. Two types of optimization would be useful for system design: first, an optimization of system mass at constant load for missions of arbitrary duration; second, a program that could optimize the design for a specific load profile.

B. SUMMARY OF WORK DONE

Three computer programs were written, debugged, and run successfully. These are:

1. Constant load mass optimization for arbitrary fuel cell parameters as follows: ratio of tank mass to fuel mass, mass of fuel cell, radiator mass in kilograms per watt, fuel mass in kilograms per ampere hour, fuel cell open circuit voltage, fuel cell internal resistance, fuel cell maximum efficiency, and total operating time at constant load. The values of open circuit voltage and internal resistance were chosen to closely follow the nonlinear EI curve of the fuel cell in the region of interest.

2. As above but with an exact rather than a linearized E I characteristic for the fuel cell. The optimums obtained with both programs were identical, justifying the simplicity of the linearized analysis. The cell EI curve was put in as a matrix of one hundred numbers (voltages) at one-ampere increments of fuel cell current taken from curves supplied by the manufacturer.

3. A load profile analysis and mass optimization were written and run to accept up to 20 successive steps of arbitrary duration in the load profile and pertinent fuel cell data. This gives as an output, the voltage regulation, fuel, and other masses and net kilograms per kWh for the mission as a function of the number of fuel cells used.

C. CONSTANT LOAD MASS OPTIMIZATION PROGRAM

Assumptions:

1. Tank mass is a constant factor, A, times total fuel mass.

2. Fuel consumption is a constant factor, D, times total ampere hours.

3. Radiator mass is a constant factor, C, times radiated thermal power in watts.

4. The fuel cell mass is a constant, B, in kilograms.

5. The fuel cell efficiency at light load is U.

6. All power not delivered to the load is delivered to the radiator.

Procedure:

The fuel cell is run in 1-ampere increments up to the maximum number of amperes allowed for a prescribed mission duration of T hours. The total fuel consumption, electrical output, heat output, and radiator, tankage, and fuel mass are computed. The net-mass-to-kWh ratio is computed for each operating level and printed in the results. Visual inspection of the computed answers quickly shows the optimum operating point from the standpoint of minimum net kilograms to kWh as well as the range of loads over which the mass does not deviate from the minimum by a prescribed tolerance.

Mathematical Analysis:

1. Amperes, X, is an independent variable.

2. XT is total ampere hours where T is operating time.

3. DXT is total fuel mass.

4. ADXT is total tank mass.

5. E is the open circuit fuel cell voltage, R is the resistance; hence E-XR is the output voltage.

6. (E - XR) times X is P, the output power, in watts.

7. 0.001 PT is the output kWh.

8. $\frac{EX}{U}$ is the theoretical input power.

9. $\frac{EX}{U}$ - P is thermal power to radiator.

10. C ($\frac{EX}{U}$ - P) is the radiator mass.

11. B + (1 + A) DXT + C ($\frac{EX}{U}$ - P) is net system mass.

12. Mass-to-kWh ratios are obtained by dividing line 11 by line 7.

D. EXACT CONSTANT LOAD MASS OPTIMIZATION PROGRAM

This program is identical with the previous program except that the voltages at one ampere increments are E(1) for zero amperes on open circuit voltage; E(2) is the output voltage at 1 ampere, etc., up to E(100), the output voltage at 99 amperes.

Mathematical Analysis:

The only differences from program I are the respective steps:

6. XE (K - 1), where X is K, the output power.

7. TXE (K - 1) (0.001) is the output kWh.

8. $\frac{E(1)\ X}{U}$ is the input power.

9. $\frac{E(1)\ X}{U}$ - XE (K - 1) is the power to the radiator.

10. Radiator mass is C times Step 9.

11. B + (1 + A) DXT + C $\frac{E(1)\ X}{U}$ - XE (K - 1) is net system mass.

E. EXACT LOAD PROFILE MASS ANALYSIS PROGRAM

In addition to mass, this program computes voltage regulation for each step of the profile and interpolates on the input EI matrix to determine the exact voltage and current for a specified profile power. Complete parameters are generated for system designs employing any desired total number of fuel cells, including fractional, and for fuel cells of any characteristics as in the programs described in C and D.

Input Data:

In addition to input data on the fuel cell, the following is set into the data cards: the minimum and the maximum number of fuel cells that are to be used; the number of intermediate designs that are to be analyzed; and the fuel cell load profile in successive Ti, Pi (where Pi is the power level of a particular step in the load profile and Ti is its duration). All steps of constant power level may be grouped together if desired to minimize input data.

Procedure:

1. As a first step the total kWh is computed by integrating the power profile. During this integration, the maximum power level is noted.

2. Next, a system having the minimum number of cells is analyzed. For this system the maximum watts per cell and the current per cell are computed from the input power, the thermal power, and the radiator mass. The radiator is sized to the maximum watts computed in step one by multiplying the waste-power-per-cell times the number of cells.

3. Each step of the profile is next considered. From the power level per cell, the corresponding voltage and current are obtained by quadratic interpolation.

4. From the current per cell times the number of cells, the total ampere hours and fuel for the particular cell are integrated.

5. After integration of the last step, total fuel consumption and tank mass are obtained.

6. The steps from 2 to 5 are then repeated for another assumed number of fuel cells.

Mathematical Analysis:

Little novelty in mathematical analysis arises except in the greater logical complexity and from the fact that voltage and current must be interpolated between the matrix values to obtain prescribed output power. Because power is not linear in voltage and current, the interpolation involves the solution of a quadratic equation. The interpolation is otherwise linear.

REFERENCES

1. Delong, C. O.: ALSS MOLAB Studies, Section 10, Task Report on Power System Studies. TMX-53032. 10, Marshall Space Flight Center, October 27, 1964.

2. Dungan, E. E.; and Delong, C. O.: Apollo Logistic Support Systems MOLAB Studies, Fuel Cell Power Systems for MOLAB. IN-R-ASTR-64-13, Marshall Space Flight Center, March 16, 1964.

3. Merrifield, D. V.: MOLAB Power System Considerations. Future Studies Branch, John F. Kennedy Space Center, May 25, 1964.

4. King, R. L.; and Meyers, O. R.: Apollo Logistic Support Systems MOLAB Studies, Task Report on Mission Operational Aspects Study. TMX-53032. 2, Marshall Space Flight Center, March 1964.

5. Platner, J. L.; and Hess, P. D.: Static Moisture Removal Concept for Hydrogen-Oxygen Fuel Capillary Fuel Cell. Allis-Chalmers Research Division, September 1963.

6. Hydrogen-Oxygen Fuel Cell Systems for Space Applications. Space and Defense Sciences Department, Allis-Chalmers Research Division, August 1963.

ASTRODYNAMICS-OPTIMIZATION THEORY AND GUIDANCE THEORY RESEARCH AT MSFC

October 28, 1965

by

Clyde D. Baker
C. C. Dearman
Dr. E. D. Geissler
Arthur J. Schwaniger

TABLE OF CONTENTS

INTRODUCTION TO RESEARCH ACHIEVEMENTS REVIEW ON ASTRODYNAMICS OPTIMIZATION THEORY AND GUIDANCE THEORY

by Dr. E. D. Geissler

SATURN GUIDANCE CONCEPTS

by Clyde D. Baker

LIST OF ILLUSTRATIONS

LIST OF ILLUSTRATIONS (Concluded)

RESEARCH ACHIEVEMENTS IN OPTIMIZATION TECHNIQUES

by C. C. Dearman

LIST OF ILLUSTRATIONS

ASTRODYNAMICS RESEARCH AT MSFC

by Arthur J. Schwaniger

CONTENTS (Continued)...

LIST OF ILLUSTRATIONS

LIST OF ILLUSTRATIONS (Concluded)

INTRODUCTION TO RESEARCH ACHIEVEMENTS REVIEW ON ASTRODYNAMICS OPTIMIZATION THEORY AND GUIDANCE THEORY

by

Dr. E. D. Geissler*

The three subjects discussed in this review, guidance theory, optimization theory, and astrodynamics, are very closely related. They deal with trajectory shaping and are of central importance in the activities of the Aero-Astrodynamics Laboratory. Since they are strongly concerned with mathematical concepts and methods, these subjects are not easy to present in a satisfactory fashion to an audience which is a fairly mixed composition with respect to background and interests. Let it be clearly understood that these papers are directed to the nonspecialist; complete papers of particular use to specialists are available or are in preparation.

We have selected somewhat different approaches in the three papers towards the subject matter, ranging from a fairly thorough description of one particular guidance concept in the first, to a more general discussion of the status of mathematical tools in optimization theory in the second, and finally to a description of some examples of classes of trajectories in astrodynamics with primary appeal to geometrical visualization. Thus, we have not attempted to survey actually systematically all activities related to the subject matter.

The conceptual development of guidance schemes at MSFC is the primary responsibility of the Aero-Astrodynamics Laboratory, whereas our Astrionics Laboratory is the primary agent for the implementation and mechanization of such schemes, i.e., the transformation of equations into a physical set of operable, functional equipment. This obviously requires very close cooperation between the two laboratories to have the full benefit of feedback of practical viewpoints and experience into the theoretical framework. This cooperation has been effective over many years in an exemplary fashion and was one important factor for the very successful accomplishment of our guidance systems in actual flights.

A fairly major change in our guidance philosophy took place at our agency a few years ago at the inception of the Saturn space vehicle program. The switchover from ballistic rockets with more limited range and more uniformly defined trajectories to space vehicles, which call for more variety of trajectory shaping, and the availability of a new computer technology, which permits rather large scale digital computations aboard a flying vehicle, induced us to deviate from the old Δ - minimum scheme that was used successfully on various vehicles like Redstone, Jupiter, Pershing, etc., and that was tailored to use analog equipment with prime emphasis on simplicity and accuracy. The new concept, which we call adaptive guidance, aims at generality in view of the many different mission geometries of multistage space vehicles, flexibility in view of frequent changes in physical characteristics of vehicles prior to flight as well as in flight, and performance optimization in the presence of major physical disturbances (e.g., engine-out cases), plus of course, accuracy of achievement of final end conditions. Various mathematical approaches are feasible toward accomplishment of these goals, and several have been explored in some detail at MSFC. Two of them, the polynomial adaptive guidance and the iterative guidance scheme, have been carried through the successful application in fullscale Saturn I earth orbital flights.

The selection of the iterative guidance scheme for the follow-on Saturn IB and Saturn V flight programs has been made based on decisive advantages in terms of flexibility with regard to changing physical characteristics, i.e., switchover to alternate mission for engine-out cases and easy adaption to a wide variety of complex three-dimensional mission profiles with a minimum of previous ground computation. A good description of both adaptive guidance systems has been given by Dr. W. Haeussermann at the August AIAA Meeting at San Francisco. Our first paper by Mr. Clyde Baker, Chief of the Astrodynamics & Guidance Theory Division, complements Dr. Haeussermann's paper by sketching the various mathematical options towards our adaptive guidance scheme and describing in somewhat more detail the particular mathematical features of the iterative guidance scheme. For more details, I refer you to the third issue of the semiannual Aero-Astrodynamics Research Report. Mr. Baker does not go into a comparison of this scheme with other similar schemes developed independently and approximately concurrently at MIT, STL, and Aerospace Corporation. Suffice it to say that we have studied these other

* Director, Aero-Astrodynamics Laboratory.

methods and have found, in spite of many similarities, some specific advantages of our iterative guidance scheme.

There is a very complex pattern of interactions between the theoretical scheme with

a. The particular mission requirements in terms of mission profile geometry and operational constraints and alternate mission requirements for engine out, etc.

b. Hardware considerations such as trade-offs between computer memory and complexity of equations and frequency of onboard computations.

c. Practical computational requirements such as need of preflight computations in view of parametric changes.

All of this demonstrates the extreme importance of a close marriage between the guidance theory development and the system development.

In view of this, a continuation of support by OART, NASA Headquarters for advanced guidance studies at MSFC, appears to us very desirable and important. We hope that this review may be of some help to underscore the value of these efforts.

With respect to the second paper by Mr. Dearman, on optimization theory, I would like to make the following observations: The application of optimization theory to trajectory shaping only is discussed in this paper, and this subject is obviously closely related to guidance theory. Most of the concepts and methods are equally applicable to other problems, in particular to control problems. Several studies related to this field are carried on by and under sponsorship of the Aero-Astrodynamics Laboratory.

An attempt has been made to describe the subject without use of equations. At the same time we did not mean to oversimplify the matter for the sake of popularization. Since optimization theory is concerned with subtle points, we cannot expect a very easy paper; however, I believe Mr. Dearman succeeded in producing a very lucid presentation on his subject. The impression may be gained from his paper that in view of the shortcomings of the present state of optimization theory, no answers can be found to many practical trajectory problems. In many cases engineering intuition and/or extensive numerical work (parametrical treatment) can substitute for more rigorous mathematical methods and produce practically acceptable optimum or near optimum solutions. The motivation for improving theory in such cases is more for reduction of computational effort and more direct assurance of optimality of a solution.

The final paper on astrodynamics by Mr. Schwaniger is probably the most acceptable one to those not familiar with the subject matter since it describes largely geometric properties of classes of trajectories. Lack of time did not permit much discussion of computational tools. While the general trend in engineering is towards more abstraction and complexity due to improvements in theory, availability of powerful computers, and increasing complexity of problems and capability for thorough optimization, there is still a need and a place for simplification especially for surveys as aids in mission synthesis. This is not only to make economical use of computers, but also to gain insight into characteristic features of solutions which may otherwise escape the attention or grasp of the investigator. There has been a creative interplay throughout the history of physical science between the intuitive approach proceeding from specific cases to generalization (inductive) and the abstract approach which typically deduces individual cases from general theory (deductive); we believe there will be a continued need for this dual approach.

The term astrodynamics has been historically used by astronomers for dynamic analysis of the motion of heavenly bodies; the prime change has been the recent emphasis of powered trajectories, i.e., bodies under the influence of forces other than gravity.

SATURN GUIDANCE CONCEPTS

by

Clyde D. Baker*

SUMMARY

The basic problem in space guidance is to develop some relatively simple way to compute the direction of thrust at points along a trajectory which will permit meeting the desired terminal conditions of the trajectory. The development of such a guidance law or guidance scheme usually involves some method to approximate the calculus of variations solution which maximizes payload.

Four such approximations are discussed in this paper. Three are polynomial type approximations to a closed loop steering function. The fourth method, which is actually used for Saturn guidance, is a closed form solution of the calculus of variations problem using a simplified earth model.

GLOSSARY

Adaptive guidance mode - This means that, at each point in the flight, the choice of steering angle made at that point is always the one which tends to maximize the payload delivered to the required end condition of the trajectory problem.

Iterative guidance mode -
Series reversion method -
Guidance function expansion method -
Least square curve fitting -

} Four methods of obtaining adaptive guidance.

Δ minimum guidance - A guidance mode continuously to correct the steering angle to force the vehicle to stay on a predetermined trajectory.

F/m - Thrust to mass ratio

Isp - Specific Impulse - The ratio of thrust measured in kg to kg of propellant consumed per second.

Mixture ratio shifts - Change in propellant management during flight affecting both thrust level and mass flow of propellant.

Open loop steering - Synonymous with steering without feedback

Time-to-go - That time remaining before thrust cut-off in a flight.

$\tilde{\chi}$ - Principal part of angle χ such that $\tilde{\chi}$ plus an additional small angle is equal to the actual steering angle χ.

SECTION I. INTRODUCTION

This discussion deals with the research work that has been carried out for the development of guidance concepts for the Saturn vehicles. This work was motivated by the development of new mathematical techniques for maximization of payloads through optimization methods and by the development of digital computers to replace analog computers as onboard hardware. It was also obvious that space trajectories would require greater flexibility to cope with sudden changes such as engine out conditions and that more flexibility must be permitted in the selection of flight profiles.

We are primarily concerned with the iterative guidance law developed for Saturn vehicles to meet these new requirements of space-age guidance. However, we will briefly discuss some of the other techniques which were studied in parallel during the development of the iterative guidance mode.

A typical space guidance problem is that of placing a space vehicle into a specified circular orbit about the earth. This particular problem will be emphasized as a typical problem. The iterative guidance law will achieve a wide variety of other guidance tasks such as injecting a spacecraft into a specified lunar orbit or soft land a vehicle at a preselected point on the surface of the moon. The discussion will be limited to the problem of injection

* Chief, Astrodynamics and Guidance Theory Division, Aero-Astrodynamics Laboratory.

into a circular orbit about the earth, because the basic principles involved are the same for all specific applications.

This problem is illustrated in Figure 1.

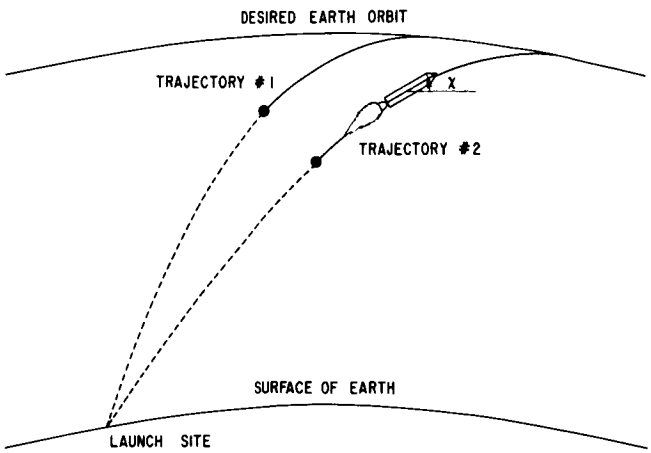

FIGURE 1. CIRCULAR EARTH ORBIT

Trajectory #1 is a nominal trajectory, and trajectory #2 is one in which some perturbation has occurred during the flight. The guidance problem in both cases is to choose the angle χ between the longitudinal axis of the vehicle and some reference direction so that the vehicle enters the desired orbit. Normally, it is additionally required that the vehicle be placed into the orbit with maximum payload or, what is equivalent, minimum burning time. Obviously, the steering angles in trajectories #1 and #2 will be different because of the different forces acting on the vehicle during the flight caused by the perturbation assumed in trajectory #2.

Guidance is active only after the vehicles are out of the atmosphere when the aerodynamic forces are zero. The flight during the first stage, shown by the dotted lines, is controlled by the autopilot, and the main concern during this portion of the flight is to keep the aerodynamic forces from destroying the vehicle. This discussion is concerned with the second stage only when guidance is active. This portion of the trajectory is shown by the solid line.

SECTION II. THE GUIDANCE PROBLEM

The development of a guidance concept for the problem just illustrated is somewhat unusual as an engineering problem. A typical difficulty in engineering is to find more accurate mathematical solutions for a given problem. Somewhat the reverse is true in the development of a guidance concept.

For example, by means of the calculus of variations, a precise mathematical tool exists for the calculation of the steering angles which will guide the vehicle into the desired orbit. However, there are two principal difficulties with the calculus of variations solution.

First of all, the numerical calculations required to establish the steering angles are far too complex to be carried out aboard the vehicle. The solutions of the calculus of variations equations require a computer the size of the IBM 7094, which obviously cannot be flown with the vehicle.

In the second place, the solution of the calculus of variations equations does not provide the steering law in feedback form. This last comment deserves some clarification.

The form of the solution of the calculus of variations to the problem stated is to provide the steering angles χ as a function of time. Furthermore, to obtain this solution, all physical and environmental conditions which will occur during the flight must be known before the launch takes place.

If the vehicle weight during the actual flight is different from that assumed for the determination of the steering angle, the steering will be incorrect. The same is true if the engine Isp is not nominal or winds during the first stage are different from those assumed for the guidance calculations. In fact, the steering law will be incorrect if any of the information assumed for the calculations is different from that actually encountered during the flight.

What is needed is a closed loop feedback steering law. This means that the steering angles should not be functions of time alone as the calculus of variations solution provides. The steering law should be provided as a function of position, velocity, and acceleration, i.e., onboard measurable quantities. Then if the vehicle experiences different forces during flight from those which were predicted, there is a basis to take these variations into account and to correct the steering angles accordingly.

SECTION III. FOUR GUIDANCE CONCEPTS

Four different concepts will be discussed for reducing the amount of onboard computations and obtaining a closed loop steering law. These concepts

have been studied both in-house and by MSFC contractors. All four have in common an approximation to the calculus of variations solution. These four concepts, (1) series reversion method, (2) guidance function expansion, (3) least square curve fitting, and (4) iterative guidance mode, are shown schematically in Figure 2 and all are referred to as being adaptive. This simply means that at each point in the flight, the choice of the steering angle made at that point is always the one that tends to maximize the payload delivered to the required end conditions of the trajectory problem.

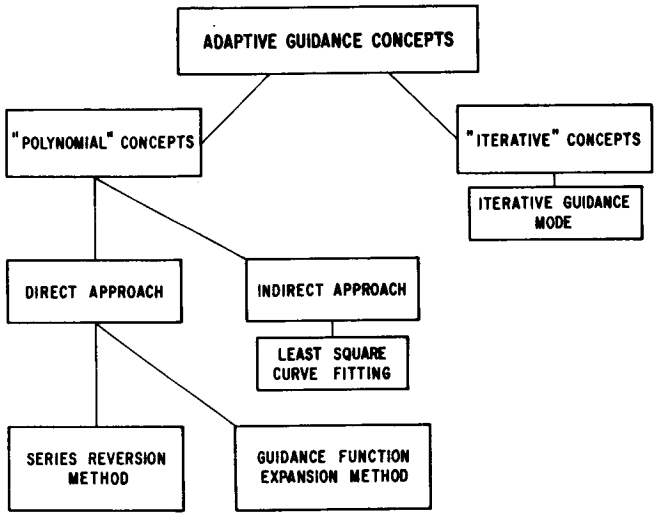

FIGURE 2. GUIDANCE CONCEPTS

Three of these concepts result in polynomial type expansions of the steering angle as functions of the current position, velocity, and acceleration of the vehicle. The fourth concept (iterative), which is actually the one used on Saturn vehicles, is an approximate explicit solution to the trajectory optimization problem.

A. CALCULUS OF VARIATIONS SOLUTION

Because all four of these concepts have their bases in the calculus of variations solution, this solution will be briefly outlined to provide a background for the modifications which have resulted in the four concepts which are of primary interest here.

To simplify the discussion of the mathematical equations, a somewhat simplified version of the original problem of injecting into a circular earth orbit will be desired. Consider then on Figure 3 the problem of the flight of a space vehicle on a flat, nonrotating earth where the gravitational vector is constant and always parallel to the y-axis. The object of the guidance system is to deliver the vehicle from the

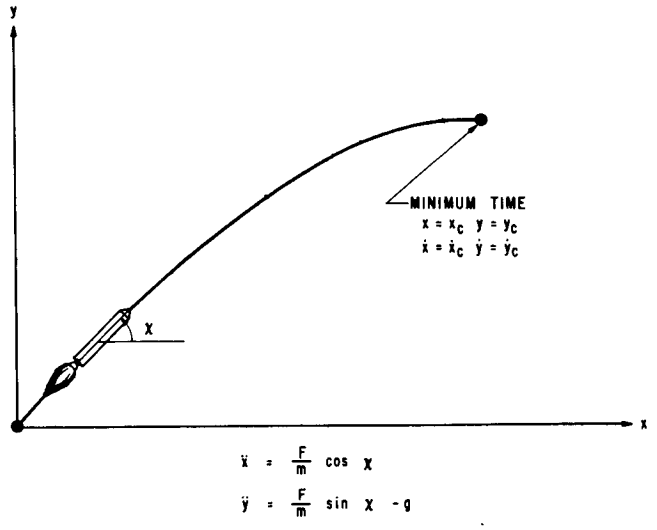

FIGURE 3. A SIMPLIFIED TRAJECTORY

launch site shown at the origin of the x, y coordinate system to a fixed position in space with a fixed velocity. This is to be accomplished in the shortest possible time with a fixed thrust magnitude and fixed burning rate of the propellant. The angle χ as shown on the slide is the only choice to be made.

The equations of motion of this simplified trajectory are shown below the trajectory. Applying the calculus of variations to this problem, the solution for χ is given in Figure 4.

$$\tan \chi(t) = \frac{P_3}{P_1} = \frac{a+bt}{1+ct}$$

$$a, b, c \quad \text{are constants}$$

FIGURE 4. CALCULUS OF VARIATIONS SOLUTION FOR χ

Mathematically, the equation for $\tan \chi$ contains four unknown quantities, a, b, c, and t_c evaluated at engine cutoff time. There are four terminal conditions to be fulfilled, two position coordinates, and two velocity coordinates. By integrating the equation in $\ddot{x}$ and $\ddot{y}$, it is then possible to obtain four equations in the four unknowns. These equations, of course, can be solved by some means to obtain values of a, b, c, and t_c. After some manipulations these values can be used to obtain the trajectory illustrated in Figure 3.

Here again, for emphasis, observe that the angle χ depends only upon time during the flight since the constants a, b, and c must be calculated before the equations of motion may be integrated. Thus the angle χ would remain the same function of time regardless of how thrust or mass flow (propellant) changed during flight. This is one undesirable aspect of the calculus of variations solution. The other undesirable feature is that a high speed computer is required to obtain the values of a, b, and c in a reasonable length of time.

Thus the calculus of variations type solution provides an open loof type of guidance. The steering angle is obtained as a function of time which remains the same regardless of what disturbances occur during the flight. For disturbed flights, then, the COV solution trajectory will not provide the desired accuracy of the terminal trajectory conditions. The discussion will be directed toward describing four techniques for converting the COV solution into a true feedback system which will provide the desired accuracy when disturbances are present. The first one to be described is the series reversion method.

B. THE SERIES REVERSION METHOD

The basic idea of the series reversion method is to obtain the values of a, b, c, and t_c in terms of the instantaneous vehicle coordinates of position, velocity, and acceleration. This is illustrated on Figure 5.

$$a = f_1(x, \dot{x}, y, \dot{y}, F/m)$$

$$b = f_2(x, \dot{x}, y, \dot{y}, F/m)$$

$$c = f_3(x, \dot{x}, y, \dot{y}, F/m)$$

$$t_c = f_4(x, \dot{x}, y, \dot{y}, F/m)$$

FIGURE 5. SERIES REVERSION SOLUTION

All the mathematical details of this method are of little interest here. Briefly stated, however, the process involves expressing the cutoff position, velocity, and time in a set of Taylor's Series involving the current position, velocity, and acceleration with the values of a, b, c, and t_c. By a simultaneous reversion of this set of Taylor's Series which involves a very considerable amount of work, it is possible to obtain the equations shown on Figure 5. Explicit forms of these equations are shown on Figure 6.

$$a = a_0 + a_1x + a_2y + a_3\dot{x} + a_4\dot{y} + a_5x^2 + a_6y^2 + a_7\dot{x}^2 + a_8\dot{y}^2 + \cdots$$

$$b = b_0 + b_1x + b_2y + b_3\dot{x} + b_4\dot{y} + b_5x^2 + \cdots +$$

$$c = c_0 + c_1x + c_2y + \cdots +$$

$$t_c = t_0 + t_1x + t_2y + \cdots +$$

FIGURE 6. SERIES REVERSION

These equations may then be evaluated to obtain the constants a, b, c, and t_c, and the angle χ is then easily obtained from these constants.

The advantage of such a representation of the angle χ is that as the actual trajectory deviates from the expected trajectory, the values of a, b, c, and t_c change accordingly to guide the vehicle back to the desired end points and do this in the minimum amount of time. The disadvantages of such a scheme are several.

First, there is a tremendous amount of work involved in the in the calculation of the equations shown on Figure 5. In the second place, these equations must be reevaluated for each new set of terminal conditions since the actual cutoff values of position and velocity are contained as parameters in the system of equations.

Finally, the number of terms required in the Taylor's Series expansion described previously is likely to be so high that the computer storage problem becomes prohibitive.

C. THE GUIDANCE FUNCTION EXPANSION METHOD

The guidance function expansion method is in many respects similar to the series reversion technique and has essentially the same advantages and disadvantages. A brief description of this method is given leaving out most of the mathematical detail.

The basic concept again is to devise some means to calculate the values of a, b, c, and t_c as functions of the vehicle current position, velocity, and acceleration. Figure 7 shows the form of the solution of the guidance function expansion method.

$$a = a^* + \frac{\partial a}{\partial x}\Big|_{t=t^*}^{(x-x^*)} + \frac{\partial a}{\partial \dot{x}}\Big|_{t=t^*}^{(\dot{x}-\dot{x}^*)} + \frac{\partial a}{\partial y}\Big|_{t=t^*}^{(y-y^*)} + \frac{\partial a}{\partial \dot{y}}\Big|_{t=t^*}^{(\dot{y}-\dot{y}^*)} + \frac{\partial a}{\partial t}\Big|_{t=t^*}^{(t-t^*)}$$

$$b = b^* + \frac{\partial b}{\partial x}\Big|_{t=t^*}^{(x-x^*)} + \cdots +$$

$$c = c^* + \frac{\partial c}{\partial x}\Big|_{t=t^*}^{(x-x^*)} + \cdots +$$

$$t_c = t^* + \frac{\partial t_c}{\partial x}\Big|_{t=t^*}^{(t-t_x)} + \cdots +$$

FIGURE 7. GUIDANCE FUNCTION EXPANSION SOLUTION

Observe that this method also involves an expansion of the values of a, b, c, and t_c into a Taylor's Series. However, in this case, the expansion is carried out about some preselected point on a nominal optimal trajectory. This point is identified by the coordinates x^*, $\dot{x}^*$, y^*, $\dot{y}^*$, and t^*. There are several variations of the guidance function expansion method which selected several points about which to carry out the series expansion, or in one case, the reference point is allowed to move continuously along the curve.

Much work has been devoted to the study of the first two methods just described, but neither has ever been carried out to the point of obtaining an actual steering equation. The number of terms required in the Taylor's Series is likely to be so large as to be prohibitive.

D. THE LEAST SQUARE CURVE FIT

The least square curve fitting technique is probably the simplest of the four methods conceptually and will now be explained. The equation which is desired as an end product of the curve fitting technique is shown on Figure 8. Here, the idea is to express the steering angle χ directly in terms of the position, velocity, and acceleration, together with products of these coordinates.

$$\begin{aligned} x = {} & a_0 + a_1\dot{x} + a_2\dot{y} + a_3 x + a_4 y + a_5(F/m) + a_6\dot{x}^2 + \\ & a_7\dot{y}^2 + a_8 x^2 + a_9 y^2 + a_{10}(F/m)^2 + a_{11}\dot{x}\dot{y} + a_{12}\dot{x}x + a_{13}\dot{x}y + \\ & a_{14}\dot{x}(F/m) + a_{15}\dot{y}x + a_{16}\dot{y}y + \cdots + \end{aligned}$$

FIGURE 8. THE LEAST SQUARE CURVE FITTING

The coefficients of this polynomial, a_i, ($i = 1, 2, 3 \ldots 16, \ldots$) are obtained by precalculating optimal trajectories with various types of disturbances deliberately introduced into the trajectories. Then from a sampling of the steering angles associated with the values of the coordinates on each of these trajectories, a least square curve fit is made which minimizes the sum of the squares of the errors in the angle χ at each of the points selected in the curve fit.

This method appears to be more of an art than a science for several reasons. A number of choices must be made somewhat arbitrarily. These include the number of terms to include in the equation, the actual terms which will appear in the equation, the number of trajectories which should be precalculated to include in the least square curve fitting process, and finally some choice must be made of the points to be utilized from a given trajectory. There has not been a clear answer, and there is still none as to how these choices should be made. Some people have been successful in making these selections so that adequate steering functions have been computed by this process. The flights of SA-6 and SA-7 were guided by steering functions generated in this manner, and the accuracy obtained was certainly satisfactory.

Perhaps the biggest fallacy in the technique, however, lies in the tacit assumption that the polynomial which produces the least sum of squares of errors in expressing the angle χ as a function of the coordinates also provides the best steering law. Since this is not true, an additional constraint was placed on the curve fitting, that the partial derivatives of the angle χ with respect to the coordinates in the curve fit would match the partial derivatives of the angle χ with respect to the coordinates obtained directly from the calculus of variations.

This constraint vastly improved the steering law when guidance was applied to a single stage only.

However, the additional complexities imposed upon the curve fitting by multiple stages and the introduction of the step mixture ratio shift, together with the requirements of continuously variable launch azimuths, caused the decision to drop the polynomial curve fits in favor of the iterative guidance mode which will now be discussed.

E. THE ITERATIVE GUIDANCE MODE

Because the iterative guidance mode has been successfully flown on SA-8, 9, and 10 and shows promise of providing the accuracy, performance optimization, and flexibility for future Saturn vehicles, it will be discussed in considerably more detail than

the previous three. The basic problem remains to devise some means to express the constants a, b, c, and t_c as functions of the current coordinates of the vehicle. In the three previously described techniques, these constants were obtained by series representations. The methods differed principally in the way in which the coefficients of the series were derived. The iterative guidance techniques solve for these values of a, b, c, and t_c in a basically different way.

To illustrate the iterative guidance concept, consider once again the problem of placing a vehicle in a desired circular orbit around the earth. The concern will be only that the circular orbit is obtained, and no conditions will be placed upon the exact point at which the vehicle enters the circular orbit. Removal of the constraint on the point at which injection occurs makes possible some simplification of the guidance law to obtain this orbit. In this case the guidance law can be written as shown in Figure 9.

$$\tan \chi = a + bt$$

$$\chi \approx A + Bt$$

FIGURE 9. ITERATIVE GUIDANCE LAW FOR CIRCULAR ORBIT

This law is only an approximation even for the flat earth model, but it is an excellent approximation. A further simplification is made that the angle χ itself may be expressed as a linear function of time where this linear function is different from the linear law obtained for tan χ.

This expression for $\chi = (A + Bt)$ may now be substituted into the equation of motion as shown on Figure 10. These equations appear somewhat complicated, but there are only two essential simple facts that should be noted about these equations. First of all, they contain only three unknowns. These are A, B, and t_c. All other information is either known or measured during flight. The second significant thing to note is that there are only three conditions to be satisfied at injection. These are $\dot{x}_c$, $\dot{y}_c$, and y_c. The fourth coordinate x_c has been eliminated by eliminating the constraint on the range at which injection takes place.

This means that if some relatively simple way can be found to solve these three equations in three unknowns, the guidance problem will be solved. The

$$\ddot{x} = \frac{F}{m} \cos (A + Bt)$$

$$\ddot{y} = \frac{F}{m} \sin (A + Bt) - g$$

$$\dot{x}_c = \int_0^{t_c} \frac{F}{m} \cos (A + Bt)\,dt + \dot{x}_0$$

$$\dot{y}_c = \int_0^{t_c} \frac{F}{m} \sin (A + Bt)\,dt - gt_c + \dot{y}_0$$

$$x_c = \int_0^{t_c}\int_0^{t} \cos (A + Bt)\,dt^2 + \dot{x}_0 t_c + x_0$$

$$y_c = \int_0^{t_c}\int_0^{t} \sin (A + Bt)\,dt^2 - \frac{gt_c^2}{2} + \dot{y}_0 t_c + y_0$$

FIGURE 10. EQUATIONS OF MOTION AND THEIR INTEGRALS

remainder of the discussion will be concerned with the problem of solving these equations with an indication of what impact on accuracy and performance results from the necessary simplification made to solve the equations.

In order to solve the equations, one additional bit of information from the calculus of variations is useful. This fact is that if the only conditions to be fulfilled at cutoff time are velocity conditions, that is, only $\dot{x}_c$ and $\dot{y}_c$ are prescribed at cutoff time, then the calculus of variations states that the steering angle under these conditions is a constant.

This fact has two important consequences. As a first step in the solution of the three simultaneous equations, it is possible to satisfy the velocity conditions with a constant steering angle which makes the integration of the equations of motion trivial. Thus the solution for required velocity has temporarily been separated from the problem of calculating the required altitude, and the equations of motion have been greatly simplified.

The equations of motion for a fixed steering angle together with their first integrals are shown on Figure 11. The last two equations can be solved for χ as shown on Figure 12. It should be noted that at this point in the solution, the value of t_c is not known in the equations for tan χ.

The next step in the solution is to satisfy the additional condition that y_c equals the required value. The value of $\tilde{\chi}$ is the principal part of the original angle $\chi = A + Bt$. Let this be rewritten as shown in Figure 13.

$$\ddot{x} = \frac{F}{m}\cos\tilde{\chi} \qquad m = m_0 - \dot{m}t$$

$$\ddot{y} = \frac{F}{m}\sin\tilde{\chi} - g$$

$$\dot{x}_c = -\frac{F}{\dot{m}}\ln(m_0 - \dot{m}t_c)\cos\tilde{\chi} + \dot{x}_0$$

$$\dot{y}_c = -\frac{F}{\dot{m}}\ln(m_0 - \dot{m}t_c)\sin\tilde{\chi} - g t_c + \dot{y}_0$$

FIGURE 11. CONSTANT STEERING ANGLE EQUATIONS

$$\tan\tilde{\chi} = \frac{\dot{y}_c + g t_c - \dot{y}_0}{\dot{x}_c - \dot{x}_0}$$

FIGURE 12. CONSTANT STEERING ANGLE χ

$$\chi = \tilde{\chi} - K_1 + K_2 t$$

FIGURE 13. SEPARATED FORM OF χ

This expression is substituted into the equations of motion to obtain the equations as shown on Figure 14.

$$\ddot{x} = \frac{F}{m}\cos(\tilde{\chi} - K_1 + K_2 t)$$

$$\ddot{y} = \frac{F}{m}\sin(\tilde{\chi} - K_1 + K_2 t)$$

FIGURE 14. EQUATIONS OF MOTION

By making the assumption that $-K_1 + K_2 t$ is a small angle so that the sine of the angle is equal to the angle and that the cosine of this angle is equal to one, these equations may be integrated in closed form. These closed form solutions are indicated on Figure 15. These equations satisfy all of the terminal conditions.

$$\dot{x}_c = f_1(K_1, K_2, t_c, \dot{x}, \dot{y}, x, y, F/m)$$

$$\dot{y}_c = f_2(K_1, K_2, t_c, \dot{x}, \dot{y}, x, y, F/m)$$

$$x_c = f_3(K_1, K_2, t_c, \dot{x}, \dot{y}, x, y, F/m)$$

$$y_c = f_4(K_1, K_2, t_c, \dot{x}, \dot{y}, x, y, F/m)$$

FIGURE 15. CLOSED FORM SOLUTIONS FOR $\dot{x}_c$, $\dot{y}_c$, x_c, y_c

These equations appear to be essentially the same as similar equations which have appeared in the description of some of the previous guidance concepts. They are in principle very different because algebraic representations can be obtained for each of them. This means that they do not have to be re-solved when the terminal conditions are changed. In the previous guidance concepts these representations were given in numerical form only.

The significance of the equations of Figure 15 is that their solutions can be programmed on a relatively small computer and that the values of K_1, K_2, t_c, and χ can be solved as functions of the current vehicle coordinates. Figure 16 shows the explicit form of the equations on Figure 15.

$$\tau = V_e/\frac{F}{m} \qquad A_1 = V_e \ln\left[1-(T/\tau)\right]$$

$$A_2 = A_1\tau - V_e T$$

$$A_3 = -A_2 + TA_1$$

$$A_4 = A_3\tau - \left[(V_e T^2)/2\right]$$

$$\phi_T = (A_3 + V_0 T)/\eta_T$$

$$\xi_0 = X_0\cos(\phi_0 + \phi_T) - y_0\sin(\phi_0 + \phi_T) \text{ and similarly for velocity}$$

$$\eta_0 = X_0\sin(\phi_0 + \phi_T) + y_0\cos(\phi_0 + \phi_T)$$

$$g^* = \tfrac{1}{2}(g_0 + g_T) \qquad \phi^* = \tfrac{1}{2}\phi_T$$

$$\begin{cases} \Delta V_0^2 = (\dot{\xi}_T - \dot{\xi}_0 - g^* T\sin\phi^*)^2 + (\dot{\eta}_T - \dot{\eta}_0 + g^* T\cos\phi^*)^2 \text{ Solve for T} \\ \Delta V_0 = -V_e \ln\left[1-(T/\tau)\right] \end{cases}$$

$$\bar{\chi}_\xi = \tan^{-1}\left[(\dot{\eta}_T - \dot{\eta}_0 + g^* T\cos\phi^*)/(\dot{\xi}_T - \dot{\xi}_0 - g^* T\sin\phi^*)\right]$$

$$P = A_3\cos\bar{\chi}_\xi \qquad Q = A_4\cos\bar{\chi}_\xi$$

$$R = \eta_T - \eta_0 - \dot{\eta}_0 T + \tfrac{1}{2} g^* T^2\cos\phi^* - A_3\sin\bar{\chi}_\xi$$

$$K_1 = (A_2 R)/(A_1 Q - A_2 P) \qquad K_2 = (A_1 R)/(A_1 Q - A_2 P)$$

$$\chi_\xi = \bar{\chi}_\xi - (K_1 - K_2 t) \qquad \chi = \chi_\xi - \phi_0 - \phi_T$$

Check velocity or T for cutoff. Stop computation of K_1 and K_2 when T becomes small. (T as shown in these equations = t_c, time of cutoff, used in text.)

FIGURE 16. ITERATIVE GUIDANCE EQUATIONS

1. Accuracy Considerations. Some explanation must now be given of the accuracy to be expected of the iterative guidance concept. Many approximations have been made to arrive at the closed form solutions of the equations presented. First of all, the earth model chosen was a flat, nonrotating earth. After that several small angle approximations were made to simplify the integration of the equations of motion. With the aid of Figure 17, some of the effects of these simplifications will be interpreted.

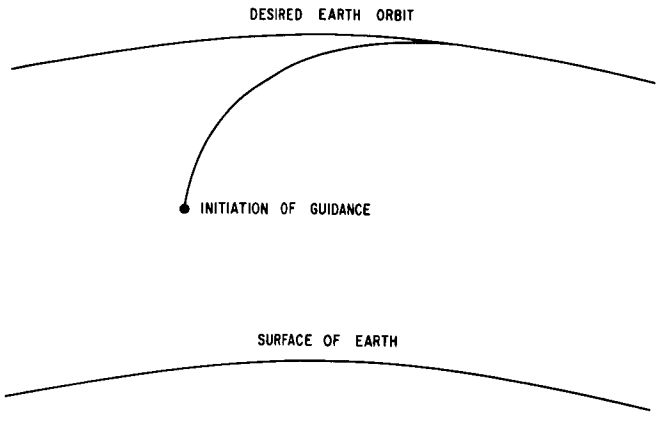

FIGURE 17. ITERATIVE GUIDANCE MODE COMPUTATIONS

At the initiation of guidance as shown in the figure, an initial value of the steering angle χ is computed. This angle is not precisely correct because of the many simplifications. But this angle is used to guide the vehicle for some brief interval of time, say one or two seconds. Then a recomputation of the angle χ is made based upon the coordinates at the later time. This process is repeated at short time intervals throughout the remainder of the flight. As time progresses, the assumptions become more accurate until at the instant of cutoff they are exact. Thus, the scheme is a self-correcting process for the errors committed by the simplifications and it is also self-correcting for any perturbations which may occur during the flight. This is true because the problem is resolved at each computation step without regard to what has happened in the past. Final accuracy of the terminal conditions is assured by this self-correcting feature.

2. Optimality. While the very nature of the process insures the desired accuracy of the system, maximizing the payload by this technique is not guaranteed. For example, it is necessary to correct for the assumption of constant magnitude and constant direction of the gravity vector.

This compensation is made by introducing into the equations of motion a weighted average of the gravity magnitude and direction between the current point on the flight and the final point. It is also necessary to rotate the coordinate system so that one axis coincides with the local vertical at the cutoff point. This is done to avoid introducing difficulties into the equations of motion by awkward end conditions if the coordinate system is not rotated.

Some additional accuracy problems arise when this concept is extended to cover multiple guided stages and the programmed mixture ratio shifts. These problems are more in the nature of minor annoyances because solutions have always been found so that the payload loss of the IGM as compared to the strict calculus of variations solution is negligible.

3. Stability and Error Analysis. The partial derivatives of attitude with respect to the state variables are the most significant criteria for stability and accuracy. The F/M derivative is small during the entire flight, eliminating this usually rather noisy measurement as trouble source. However, as the trajectory optimization is based on a predicted relation of the future thrust profile for a stage to the instantaneously measured value, any major thrust change will cause a performance loss.

The other derivatives start at low values and increase approximately inversely proportional to the time-to-go (for velocity errors) or its square (for displacement). The tightening of the guidance loop toward the end of flight is very desirable as it keeps residual errors small. However, it creates a potential stability problem. This problem was eliminated without causing a significant error by stopping computation of the steering equations at a given time-to-go (e.g., T = 20 seconds) and flying open loop. A better method is to freeze the time-to-go at a minimum value and continue guidance.

The low guidance gains at early flight make the system very tolerant to major disturbances, noise, and time lags during this phase.

Guidance scheme errors for realistic variations of initial conditions (Fig. 18) are very small. The effects of performance variations, changes in air density, and winds are equally insignificant.

A time lag of five seconds from measurement to steering command causes no error and no loss of weight in orbit. A 40-sec lag caused 3-km altitude error and 11 percent payload loss.

Periodic thrust fluctuations with a maximum amplitude of 65 percent of nominal and periods of 5 to 100 seconds create no serious stability problem.

INITIAL STAGE VARIABLE				PAYLOAD LOSS	INJECTION ERRORS		
Δx_1	$\Delta \dot{x}_1$	Δy_1	$\Delta \dot{y}_1$		Altitude	Velocity	Path Angle
km	m/s	km	m/s	percent	m	m/s	degrees
2.7	0	0	0	.11	.1	0	.001
0	143	0	0	.32	.13	-.04	0
0	- 57	0	0	.07	.1	.01	.001
0	0	1.0	0	.11	.1	0	.001
0	0	0	78	.14	.1	-.01	0
0	0	0	-80	.11	.1	0	.001

FIGURE 18. ITERATIVE GUIDANCE MODE ACCURACY & PERFORMANCE

4. Present and Future Guidance Research. The iterative guidance mode as just described provides accuracy, optimality, and flexibility for the examples shown on Figure 19.

1. Single Stage to Orbit
2. Multiple Stages to Orbit
3. Earth - Moon Guidance
4. Earth - Mars Guidance
5. Plane Change Capability
6. Three Dimensional Guidance
7. Flexibility for Alternate Guidance & Abort

FIGURE 19. ITERATIVE GUIDANCE ACHIEVEMENTS

Actual calculations have demonstrated its capability for placing a space vehicle into earth orbit by a single guided stage to orbit; it is also successful with two stages to orbit including a step mixture ratio shift which essentially becomes three guided stages to orbit.

The iterative guidance mode has been used successfully also to guide trajectories out of earth orbit to the moon and also to guide to the planets. This is an impressive list of accomplishments for a guidance concept, and others could be related concerning flexibility to change to alternate mission after launch and to handle abort situations which may occur during flight.

However, the intent at this point is to describe the guidance situation for which the iterative guidance mode has not been demonstrated adequately and to indicate what efforts are being made to provide satisfactory guidance for these cases.

As a general comment, it may be pointed out that iterative guidance mode does not perform satisfactorily at present when any one of the following three conditions shown in Figure 20 is encountered.

1. Low Thrust to Weight Ratio
2. Large Central Angle
3. Rendezvous

FIGURE 20. NECESSITIES OF NEW OR IMPROVED METHODS

a. The first limitation occurs when thrust to weight ratio is less than a few tenths of one g. Under these conditions the approximations which are made in the derivation of IGM become so inaccurate at this thrust level that satisfactory performance is not attained. Thus new concepts are being sought for low thrust interplanetary flights where the thrust levels are of the order of a small fraction of one g.

b. The second limitation of the IGM occurs when the central arc, i.e., the angle at the center of the earth between the point of beginning of guidance and termination of guidance, exceeds approximately thirty degrees. Starting from earth orbit with low thrust trajectories, it is sometimes necessary to spiral around the earth several times before the velocity of the space vehicle reaches essentially escape velocity. IGM so far has not proved adequate for these cases.

c. A third category which must be studied carefully is a trajectory where all coordinates are specified at the terminal end of guidance as in rendezvous. IGM has not yet been shown adequate for such cases. It may be possible to modify the iterative scheme to handle all three of these problem areas. Until such modifications are made, efforts will be directed toward studying other concepts together with attempts to modify the iterative concept.

BIBLIOGRAPHY

1. Hoelker, R. F.: The Evolution of Guidance Theory and Trajectory Analysis into a Single Scientific Discipline. Presented at the Meeting of the Institute of Navigation, Williamsburg, Va., June 1961.

2. Miner, W. E.; Schmieder, D. H.; and Braud, N. J.: The Path-Adaptive Mode for Guiding Space Flight Vehicles. ARS Guidance, Control and Navigation Conference, Stanford, California, August 1961. Revised Mar. 1962, Reprint from Progress in Astronautics and Rocketry, 1962, Academic Press, New York, New York.

3. Baker, C. D.: A Minimum Fuel Reserve Guidance System. NASA Internal Note 3-64, Jan. 14, 1964.

4. Smith, I. E.; Hart, J. J.; and Chandler, D. C.: Procedure for Implementing A Simplified Path Adaptive Scheme. NASA Internal Note 25-62, July 31, 1962.

5. Horn, H. J.; Martin, D. T.; and Chandler, D. C.: An Iterative Guidance Scheme and its Application to Lunar Landing. MSFC Report MTP-AERO-63-11 (Limited Distribution) February 6, 1963.

6. Horn, H. J.: Application of an Iterative Guidance Mode To A Lunar Landing. Paper No. 1504 (63) presented at IIIrd European Space Flight Symposium and 15th Annual Meeting of the DGRR in Stuttgart, Germany, May 22-24, 1963. Reprinted in: Raumfahrtforschung, Heft 2, Apr.-June 1964, pp. 49-54.

7. Smith, I. E.; and Deaton, Jr., E. T.: An Iterative Guidance Scheme for Ascent to Orbit (Suborbital Start of the Third Stage.) MSFC Report MTP-AERO-63-44, May 29, 1963.

8. Fried, B. D.: On the Powered Flight Trajectory of an Earth Satellite. Jet Propulsion, vol. 27, June 1957, pp. 641-643.

9. Lawden, D. F.: Optimal Rocket Trajectories. Jet Propulsion, vol. 27, Dec. 1957, p. 1263.

10. Fried, Burton D.: Trajectory Optimization for Powered Flight in Two or Three Dimensions. Space Technology, ed. by H. Seifert, 1959, pp. 4-9.

11. Perkins, F. M.: Flight Mechanics of Ascending Satellite Vehicles. Jet Propulsion, vol. 26, May 1956, pp. 352-358.

12. MacPherson, D.: An Explicit Method of Guiding a Vehicle From an Arbitrary Initial Position and Velocity to a Prescribed Orbit. Aerospace Corp. Rep. TDR-594 (1565-01) TN-1, Feb. 13, 1961.

13. Cherry, G. W.: Orbit Insertion Guidance Technique. Space Guidance Analysis Memo 30, MIT, Instrumentation Laboratory, Nov. 29, 1962.

14. Cherry, G. W.: A Unified Explicit Technique for Performing Orbital Insertion, Soft Landing, and Rendezvous with a Throttleable Rocket-Propelled Space Vehicle. AIAA Guidance and Control Conference, Aug. 12-14, 1963.

15. Perkins, F. M.: Optimum Guided Ascent. Aerospace Corp. Rep. SSD-TDR-64-120, June 1964.

RESEARCH ACHIEVEMENTS IN OPTIMIZATION TECHNIQUES

by

C. C. Dearman*

SUMMARY

This paper is a survey of the work that has been done at MSFC in attempting to compute optimal, i.e., minimum-fuel, multistage trajectories for space missions. In the early studies, attempts at trajectory optimization were confined to single-stage trajectories. The calculus of variations was the optimization technique principally employed in these studies as well as in the more complex problems which followed. With the discovery of the work by C. H. Denbow, who theoretically, at least, solved a large class of variational problems, work was begun on computing fuel-minimizing, Apollo type, multistage trajectories. While Denbow's extension of the classical theory of the calculus of variations provided for the optimization of multistage trajectories, it demanded that all state variables be continuous. Therefore, it was not satisfactory for solving realistic multistage trajectories in which some state variables, for example, the mass, are discontinuous functions of time at those points of vehicle stage separation where the large mass of the burned-out stages are detached from the vehicle. Therefore, it was necessary to extend Denbow's work to include discontinuous variables. This was done, but only necessary conditions for an optimum were found. At present, there have been discovered no sufficient conditions for the case involving discontinuous state variables as have been found for the Denbow problem with continuous state variables, and unless sufficient conditions are satisfied by the trajectory it cannot be said to be fuel minimizing. This, briefly, is the state of the theory at present.

In attempting to calculate fuel-minimizing multistage trajectories on a digital computer, several difficulties have arisen which have prevented computation of the trajectories. These difficulties seem to stem from the introduction of the additional differential equations and new variables, called Lagrange multipliers, required by the theory. The problem is being investigated both in-house and by outside contractors.

Conducted simultaneously with the studies in multistage trajectory optimization were the studies in low-thrust trajectories, optimal orbital transfers, and optimal reentry trajectories. In the first two of these studies, the calculus of variations techniques proved to be unsuccessful, and other optimizing methods were employed. All of these studies, however, are in the exploratory stage, and much work remains to be done.

RESEARCH ACHIEVEMENTS IN OPTIMIZATION TECHNIQUES

The research in optimization techniques and its applications to problems of space flight at Marshall Space Flight Center has been largely geared to attempts to determine optimal guidance schemes and optimal control laws for space vehicles. The problems in optimization relative to the development of optimal control laws were discussed at the Research Achievements Review Series No. 3 which was held last April. Research in optimization techniques as it relates to space vehicle guidance is the subject of this review. This relation to guidance has two important aspects that motivate the research. These are (1) the development of optimal guidance schemes, and (2) the testing of nonoptimal guidance by providing optimal trajectories as standards for comparison. Both aspects demand the existence of a capability for generating optimal, that is, minimum-fuel trajectories, in both perturbed and unperturbed cases.

In the first aspect, the development of optimal guidance functions, it appears necessary that a suitable sampling of perturbed optimal trajectories meeting all constraints and boundary conditions and satisfying the equations of motion be generated as a preliminary but essential step. The development of the guidance equations from the sampling of perturbed optimal trajectories and, indeed, the selection of the sampling itself, are very difficult problems and do not properly belong in a discussion on optimization techniques even though they are significant motivating factors in the discovery and use of these techniques. In the second aspect, the testing of nonoptimal guidance procedures, the amount of fuel required for nonoptimal guidance in a perturbed trajectory can be compared with the strictly minimum-fuel trajectory subjected to the same perturbations, thereby possibly forming the basis for a judgement

* Scientific Assistant, Aero-Astrodynamics Laboratory.

as to the adequacy of the nonoptimal guidance procedure.

The research in optimization of trajectories may be categorized as shown in Figure 1.

1. Multistage (Apollo - type) Trajectories
2. Low Thrust Trajectories
3. Impulsive Orbital Transfer
4. Reentry Trajectories
5. Supporting Research Activities

FIGURE 1. RESEARCH IN TRAJECTORY OPTIMIZATION

Mathematically, low-thrust trajectory optimization, impulsive orbital transfer, and reentry trajectory optimization are special cases of the problem in the first category, and the solution of this problem, at least theoretically, implies the solution of the others. However, research in these categories was carried on simultaneously with research in problems in the first category because the considerable difficulties encountered with problems in the first category did not portend an early solution. Also, it was thought that study of the less general problems might shed some light on the multistage problem.

The fifth category, supporting research activities, has been confined largely to studies in celestial mechanics and its application to the motion of spacecraft in cislunar and solar space and to methods of obtaining approximate solutions of the two-point boundary value problem of which the optimal trajectory problem is but a special case.

Figure 2 shows the principal contractors who have worked in the areas of trajectory optimization that we have just discussed.

It is clear from the foregoing that the research in optimization has been motivated almost entirely by the necessity for solving intensely practical problems of immediate and lasting interest in the space program.

When work was first begun several years ago by what is now called the Astrodynamics and Guidance

AREA OF RESEARCH	CONTRACTORS
1. Calculus of Variations	Vanderbilt U., Southern Illinois U., Republic Aviation, Grumman Aircraft, Hayes International, General Electric, Auburn U., Analytical Mechanics Assoc., United Aircraft, Martin-Marietta, Lockheed Aircraft
2. Low Thrust Trajectories	Aeronutronics (Ford), Grumman Aircraft
3. Impulsive Orbital Transfer	North American Aviation, United Aircraft
4. Reentry Trajectories	Auburn U., Raytheon
5. Supporting Research a. Celestial Mechanics b. Multivariant Approx. c. Two-Point Boundary Value Problem	U. of Kentucky, U. of North Carolina, Northeast Louisiana S. C., Georgia Institute of Tech., Chrysler Corporation Missile Division, U. of Wisconsin

FIGURE 2. CONTRACTOR PARTICIPATION IN TRAJECTORY OPTIMIZATION RESEARCH

Theory Division of the Aero-Astrodynamics Laboratory on the problem of generating optimal guidance functions for missions involving multistage trajectories, a survey was made of existing optimization techniques in an attempt to discover the technique that would be most practicable for the solution of trajectory optimization problems. The survey led to the selection of the calculus of variations as the most likely candidate for solving the problems. Other techniques are known under such names as the Pontryagin maximum principle, the method of steepest descent, and dynamic programming. The calculus of variations, however, had enjoyed a long and fruitful history of development, and because of this it was the most mature and most highly refined of all known methods.

In this country, the work of G. A. Bliss and his students in the calculus of variations at the University of Chicago Department of Mathematics was available in the form of published books and scores of research papers. Also, in the long history of the development of calculus of variations, many practical applications of the theory had appeared in numerous publications; these were considerably in excess of the number of applications of the other optimizing techniques. Thus, it was that major emphasis, both in-house and among outside contractors employed for the purpose of assisting in the solution of the problem, was given to exploiting the capabilities of the calculus of variations. However, "a foot was kept in the door of the other techniques," so to speak, by assigning some studies in them to contractors and to maintaining a relatively small in-house effort in these techniques as well. Because the principal effort was in exploiting the techniques of calculus of variations, it is this technique that will be emphasized in this review.

Let us consider the general problem of directing a space vehicle from a prescribed initial state to a prescribed terminal state. Let us further suppose that some steering law is available. The state of a space vehicle is considered to be known at any given time t when certain defining parameters are known. For the purposes of discussion here the state of the vehicle will be considered to be known if its position coordinates, velocity components, thrust, mass, and burning rate are known at the given time. Thus, in what is usually called the "state space," nine coordinates are required to define the state of the vehicle at any time. It is to be emphasized at this point that this particular choice of stage coordinates is not necessarily the best choice. It is entirely possible that another choice would make the problem more tractable and the computational aspects much easier to perform. The determination of the best choice of state variables is under continual study.

As a consequence of the number of variables chosen to define the instantaneous state of the vehicle, the equations of motion, considered as a system of first-order differential equations, are nine in number. These equations must be solved simultaneously in order to obtain a solution curve or trajectory in state space. Perhaps it should be mentioned that the solution is obtained by numerical means by a digital computer and not by analytical methods. The attainment of the solution by analytical methods would be, of course, the more desirable, but no one as yet has been able to do this except for simplified cases.

Any solution curve or trajectory must pass through the initial point in state space and must satisfy terminal conditions and numerous constraints as well. Figure 3 illustrates a solution of the equations of motion.

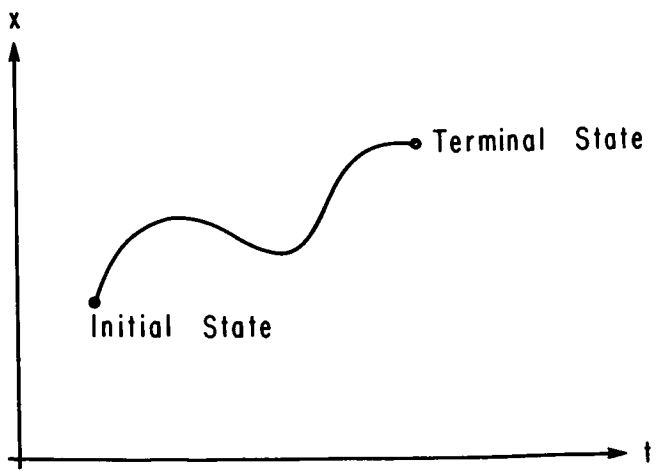

FIGURE 3. A SOLUTION CURVE IN STATE SPACE

Now, if it is required that the solution curve be the optimal or minimum-fuel trajectory, then some optimizing technique must be employed to insure this requirement. As will be discussed in more detail in the sequel, the requirement of optimality introduces additional differential equations and new variables called Lagrange multipliers which must be solved for simultaneously with the nine equations of motion, and "there's the rub," as we shall see.

It was clear from the beginning of the studies in trajectory optimization that the problem of optimization of an arbitrarily general multistage trajectory that began from launch on earth and ended upon return to earth would be far too complex a problem to attack initially. It was decided to concentrate on the problem of optimizing only that part of a multistage trajectory whose initial point is just outside the earth's atmosphere and whose terminus is a prescribed lunar orbit as shown in Figure 4. This trajectory represents a part of an Apollo type trajectory.

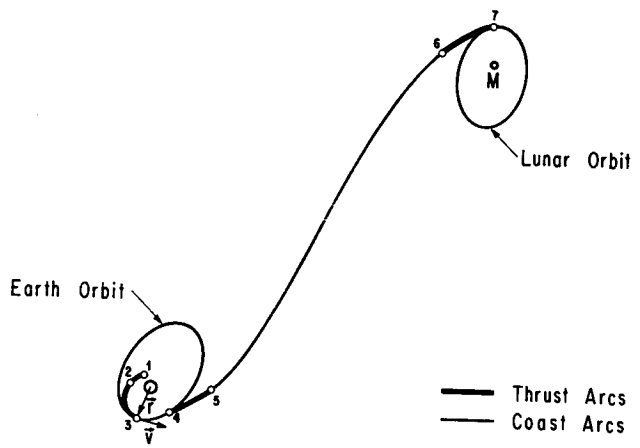

FIGURE 4. A MULTISTAGE TRAJECTORY

No effort was made in the early studies to compute a calculus of variations (COV) trajectory for the atmospheric portion of the flight. Even when this computation is done now, certain simplifications, such as exponential atmosphere, are usually made which probably cannot be tolerated in realistic simulations. Even when the simplifications are not made, as in the deck recently compiled by R. E. Burns of the Aero-Astrodynamics Laboratory, only necessary conditions are satisfied; this means that the resulting COV trajectory is not guaranteed to be fuel minimizing.

In retrospect it appears that the problem of optimizing that portion of the Apollo type trajectory

illustrated in Figure 4 is itself too complicated a problem for a beginning effort. Some less ambitious program may be decided upon to provide a simpler problem. Dr. Jan Andrus of General Electric Company and Dr. M. G. Boyce of Vanderbilt University, who have been working for us for several months on this trajectory optimization problem, are rather of the opinion that simpler problems should now be attacked in an effort to learn how to overcome some of the difficulties that have been encountered in our attempts to solve the more complex multistage trajectory problem.

Let us now describe the multistage trajectory to which we have applied the techniques of the COV. Assume that point 1 in Figure 4 represents the termination of an S-1C stage above the earth's surface and that at this point all state variables are known. The point is also presumed to be outside the earth's atmosphere so that the entire space vehicle is there subject only to thrust and gravitational forces. At point 2 assume that the S-II stage is detached and that the S-IVB stage engines are ignited. These separating and igniting actions in the beginning studies were assumed to occur simultaneously. Of considerable significance in the evolution of the optimization problem is that at point 2 the mathematical model of the motion of the vehicle was based on the assumption that there existed discontinuities in the state variables of thrust, burning rate, and mass because of the separation sequence that occurred at that point. It is the assumption of discontinuities in these three state variables that has been the source of many problems, some of which have not yet been solved.

At point 3 the vehicle enters an essentially elliptical orbit of a specified shape and size. This requires that the distance of the point from the earth's center, the velocity of the vehicle at the point, and the angle between the radius vector and velocity vector be specified. The location of point 3 on the ellipse, the orientation of the plane of the ellipse relative to the coordinate system used and the orientation of the ellipse within the plane are not specified. In all studies thus far undertaken, point 3 has been chosen as the perigee of the ellipse thereby fixing the angle between the radius vector r and velocity vector v at 90°. The remaining unspecified factors, the orientation of the plane of the ellipse and the orientation of the ellipse within the plane, are to be determined by the optimization procedure. Because a coast arc is entered at point 3, the thrust and burning rate are reduced to zero. If, as it has been assumed, this is done instantaneously, discontinuities appear again in these two variables.

The optimization process is used to determine point 4 and the time t_4 of the space vehicle's arrival there when thrust is again initiated. The time of flight from point 4 to point 7, where the vehicle enters the lunar orbit, is specified. This is done by initiating thrust at point 4 such that the time lapse between points 4 and 7 is equal to the specified time. This condition of specified flight duration is imposed to prevent the lunar transfer trajectory from extending over an excessively long time. It may be possible for a space vehicle in a minimum-fuel trajectory without a time constraint to coast for years before entering the desired lunar orbit.

At point 5, the burned out S-IVB stage of the vehicle is separated and the thrusting and burning rate both die out to zero. The vehicle is now on a free flight lunar transfer trajectory. At point 6, a retrothrust maneuver is initiated so that the vehicle may be placed into the prescribed lunar orbit. At point 7, the specified lunar orbit is entered.

It will be noted in the physical description of the problem just given that the trajectory consists of several parts or stages and that at time points defining the terminus of some of the stages, and simultaneously the origin of the stages following, it is assumed that there exist discontinuities in some of the state variables. The existence of the several stages and the assumption of discontinuities in some of the state variables provided considerable obstacles in the use of the classical theory of the calculus of variations in optimizing multistage trajectories. For in the classical theory, it is demanded that there exist only one stage, i.e., that the function to be minimized depend on the coordinates of the endpoints of the trajectory and not on the coordinates of any intermediate points. The classical theory further requires that the state variables be continuous functions of time and have continuous derivatives at least up to a specified order. Thus, the beginning efforts in applying the calculus of variations to trajectory optimization were necessarily confined to attempts to optimize a single stage, because it was only for this that the necessary mathematical tools were known at that time to be available.

The optimization of the one-stage trajectory is an example of the classical problem of Mayer in the calculus of variations and was first recognized as such by P. Cicala and A. Miele in 1956. It is enlightening to observe that the problem of Mayer is a special case of the more general problem of Bolza. Because the Bolza problem may be transformed into the Mayer problem and vice versa, one hears the trajectory optimization problem frequently referred

to as a Bolza problem, as a Mayer problem, or as a Bolza-Mayer problem. But regardless of whether the problem is formulated as a problem of Bolza or as a problem of Mayer it presents similar difficulties when attempts are made to solve it. At best we can, at the present time, do no better than to find a numerical solution on the digital computer. An analytical solution will probably always elude us.

However, the basic theory of the classical Bolza (or Mayer) problem may be considered to be almost complete. By almost complete, we mean that a set of necessary conditions for an optimum has been found that, when suitably modified, forms a set of conditions sufficient to guarantee an optimum at least when compared with a certain class of solutions. The necessary conditions are the multiplier rule-a corollary of which is the famous Euler-Lagrange differential equations, the condition of Weierstrass, the condition of Clebsch, and the Jacobi or so-called fourth necessary condition.

It is important to observe that these four necessary conditions for the problem of Bolza are only loosely analogous to the conditions bearing the same names for the simpler problems in two-dimensional state space. Any attempt, therefore, to illustrate these conditions for the problem of Bolza by use of geometric diagrams in the plane would lead to confusion and erroneous impressions.

It may be deduced from the basic theory of the calculus of variations that every minimum-fuel, flyable trajectory must satisfy these conditions. However, it must be noted, since these conditions are only necessary, that there may exist nonminimizing trajectories that also satisfy them. Therefore, a COV trajectory which satisfies only some or all of the necessary conditions is not necessarily a minimum-fuel trajectory. About the most that can be said for such a trajectory is that it is a promising candidate for a minimum-fuel trajectory. For this discussion, the important fact is that slight modification of the last three of these conditions transform the necessary conditions into a set of sufficient conditions.

It is rather common practice to designate the four necessary conditions for the problem of Bolza by the Roman numerals I, II, III, IV as shown in Figure 5. If a trajectory is an optimum trajectory, it must satisfy these conditions. The modifications of the conditions that transform them into a set of sufficient conditions are designated by the symbols I, II', III', IV'. Any trajectory that satisfies all of these conditions is an optimum trajectory.

1.	The Multiplier Rule (Corollary - Euler - Lagrange Differential Equations)	I
2.	The Condition of Weierstrass	II
3.	The Condition of Clebsch	III
4.	The Jacobi or Fourth Necessary Condition	IV

All Optimal Trajectories Must Satisfy All the Necessary Conditions.

FIGURE 5. NECESSARY CONDITIONS IN THE CALCULUS OF VARIATIONS

Now, it is possible to calculate a COV trajectory on a digital computer by invoking only some of the necessary conditions. All necessary conditions are not required for the computation. However, to guarantee that the computed trajectory is indeed an optimum trajectory, it must satisfy all four sufficient conditions. Even if the sufficient conditions are satisfied, however, there is no assurance that the trajectory satisfying them is unique. There may be other trajectories which use no more fuel and satisfy the same conditions. If a set of conditions could be found which were at once both necessary and sufficient, then the trajectory satisfying them would be optimum at least among all trajectories of its class and lying in some neighborhood of it. For the trajectory problem, which, as we have mentioned before, is an example of the problem of Bolza, there have been discovered no conditions that are both necessary and sufficient.

In the evolution of attempts to find an optimum trajectory, it was considered expedient to employ the easier to invoke necessary conditions for COV trajectory calculation rather than to use the more severe and more numerous sufficiency conditions. The experience and knowledge gained thereby could later be used to apply the sufficiency conditions if that should appear to be desirable. However, up to this time no serious attempt has been made to invoke sufficient conditions even for the single stage case. Instead, concentration of the multistage problem has been made in the hope that a least a set of necessary conditions could be determined from which a solution curve could be found that would satisfy them. There was always the strong conviction that physical considerations would be sufficient to guarantee that this solution curve was indeed a minimum-fuel trajectory, at least among all trajectories that satisfied the physical conditions of the problem if not among

all mathematically possible trajectories. When it appeared that the single stage problem was essentially solved, it was decided to attack the multistage problem with the assumption of continuity of state variables even though discontinuities, as mentioned before, in some of them had been assumed to exist in what was then believed to be the more realistic mathematical model. Several of the contractors who had been working on other aspects of trajectory optimization were asked to begin investigating the multistage trajectory problem. When the problem was discussed with Dr. Boyce of Vanderbilt University, one of the contractors, several months after the work with some other contractors had been initiated, he pointed out that, effectively, the multistage problem with continuous state variables had been investigated and solved by C. H. Denbow and that his results had been published in his doctoral dissertation at the University of Chicago in 1937. Not only had Denbow found necessary conditions for a minimum in the general problem of Bolza for the multistage case with state variables continuous, but he had found a set of sufficiency conditions as well.

Immediately work was begun on extending the work of Denbow to include the case with discontinuities in the state variables. This investigation was advanced considerably by the work of Dr. R. W. Hunt, a consultant for the division and professor of mathematics at Southern Illinois University. Hunt applied Denbow's methods to a Mayer formulation of the multistage problem and permitted discontinuities in the state variables and constraints at the staging points. However, Hunt's extension required that the times of staging be fixed, but not necessarily known. Hunt obtained three necessary conditions which the minimum-fuel trajectory must satisfy, but no set of sufficient conditions. The necessary conditions for the case he treated are analogues to the multiplier rule, the Weierstrass condition, and the Clebsch condition, respectively.

M. G. Boyce and J. L. Linnstaedter of Vanderbilt University Department of Mathematics further extended the work of Denbow and Hunt to include control variables, finite equation conditions, and inequality constraints. Boyce and Linnstaedter also obtained necessary conditions for their more general problem, but no sufficient conditions.

This is the state of the theory at present. Although much has been done toward the solution of finding the minimum-fuel trajectory for multistage type missions, much remains to be done. For example, for the classical problem of Bolza, many necessary conditions have been found, but for its generalizations by Hunt or Boyce and Linnstaedter, only three necessary conditions have been obtained. Since these three conditions have not resolved some serious difficulties in attempts to compute by digital simulation a trajectory satisfying them, it appears that further efforts should be made to obtain other necessary conditions analogous to those already obtained for the classical problem of Bolza, which, when used instead of or possibly in conjunction with the necessary conditions already known, will resolve some of the difficulties presently encountered. In addition, it is of paramount importance that serious efforts be started on the development of a set of sufficient conditions because the satisfaction by the solution curve of necessary conditions does not guarantee that it is an optimum solution. If a solution curve satisfies sufficiency conditions, however, it is indeed an optimum, at least when compared to other trajectories in a certain neighborhood that are flyable and satisfy the imposed constraints and boundary conditions.

Although these suggestions for the direction which further research should take have assumed the existence of discontinuities in the state variables, mass, thrust, and burning rate, the continuous variable approach to obtaining a minimum-fuel trajectory still has some attractive qualities. Because the thrust and burning rate are not physically discontinuous functions of time, it might be more realistic to obtain a continuous approximation of their rapid decreases and increases at the staging points where engine cutoff and reignition occur. The only physical discontinuity, that of mass, could be approximated by a very rapidly decreasing function. Then all state variables could be considered as continuous throughout the trajectory and the work of Denbow, modified for the trajectory problem, could be used. As mentioned previously, in Denbow's work, necessary conditions as well as sufficient conditions have been found. The trajectory obtained by satisfying the sufficient conditions would be at least one minimum-fuel trajectory for the imposed conditions. Guidance functions could then be derived around this trajectory as the nominal.

Thus, by way of summary, it may be said that if a sufficiently accurate mathematical model of the physical system is obtained by considering all state variables as continuous functions of time, although some of them may be very steeply increasing or decreasing at certain staging points, or physically discontinuous at these points, then the basic mathematical theory sufficient to guarantee a minimum-fuel multistage trajectory is available for use. If it is not adequate to consider all state variables as continuous functions of time, but to take as discontinuous at certain staging points the steeply rising

or falling variables such as thrust and burning rate and to treat the physical discontinuous mass as mathematically discontinuous, then only necessary conditions are available for use. In this case, finding sufficient conditions may be a matter of much importance. Some in-house work is being done on this problem now.

So far, we have not discussed several difficulties which have been encountered in attempting to compute minimum-fuel trajectories on a digital computer. Basically, the difficulties arise because of the introduction of additional differential equations which result from applying the methods of the calculus of variations. Among these new differential equations, as we have mentioned, are some which introduce new variables which we call Lagrange multipliers. These new variables result, of course, from invoking the multiplier rule. If you recall, we stated that the state variables at point 1 (Fig. 4) on the trajectory, the initial point, were known. With the introduction of the Lagrange multipliers, however, we add new variables whose values at point 1 are not known. They must be determined if we are to direct the vehicle in an optimum manner to point 2. In fact, not only must these multipliers be known at point 1, but they must be determined at every integration time step along the trajectory when thrust is being applied. This statement, of course, implies that the multipliers are intimately related to the vehicle's pitch and yaw angles, as indeed they are. In fact, the relations of the multipliers to the pitch and yaw angles are through simple trigonometric expressions.

In early attempts to calculate multistage trajectories, only two stages were used. In one effort the boost stage was the first stage; from boost burnout to a specified earth orbit was the second stage. No attempt was made in the early efforts to apply the calculus of variations to the boost stage. Instead, a zero-lift trajectory was calculated from the initiation of tilt, ten seconds from liftoff, until booster burnout. From that point a COV second stage trajectory to the specified orbit was calculated. Of course, a different tilt program for the booster might result in a trajectory which, overall, uses less fuel than the trajectory originally calculated. To try to find a better overall trajectory, a family of boost trajectories was generated by using different kicks at tilt initiation. From the burnout point for each of the boost trajectories, a COV second stage trajectory to the specified earth orbit was calculated. Then, by interpolation, the kick which would initiate the tilt program of the booster that would result in the best overall trajectory was determined. The result was not a proven minimum fuel trajectory, but at least it was better than any member of the trajectory family.

Simultaneously with the study just described, attempts were made to compute two-stage COV trajectories with both stages lying outside the earth's atmosphere. Continuity of all state variables was assumed, and no attempt initially was made to satisfy any necessary conditions except the Euler-Lagrange differential equations. While the state variables were taken to be continuous throughout both stages, it was not known whether the Lagrange multipliers were also continuous especially at the staging points. It was intuitively felt that the multipliers were continuous throughout both stages, and COV trajectories were calculated with this assumption. The question of multiplier continuity was answered for continuous state variables by M. G. Boyce of Vanderbilt University.

In late 1962, Boyce applied some necessary conditions to a simplified multistage problem. He assumed that all state variables were continuous and avoided the vexing problem of discontinuity in the mass at staging points by assuming that the mass was a known function of time; as such it was not a state variable. He further assumed that a fuel minimizing trajectory existed and that it was the unique solution to the equations of motion. With these assumptions, of course, Boyce could then declare that the trajectory which he obtained from invoking only necessary conditions must be a fuel minimizing trajectory. Boyce's principal contribution, however, was his proof that the Lagrange multipliers were continuous not only throughout each stage but at the staging points as well. Because his proof is valid for any finite number of stages, it represents a significant contribution.

In the complex trajectory illustrated in Figure 4, the determination of precise values of the initial Lagrange multipliers made heavy demands on the analyst's experience, ingenuity, and ability to communicate successfully with whatever gods have control of such matters. But so much spadework has been done in the past that now, with the experience gained, it is not too time consuming to calculate at least reasonable first approximations of them. An iterative procedure called the "differential correction scheme," formulated as a part of the contract requirements by G. N. Nomicos of Republic Aviation, is then employed to find more nearly precise values of the Lagrange multipliers at point 1. Having found the Lagrange multipliers and having been given the state variables which define point 1, the computation can be begun which, hopefully, will result in an optimum trajectory with the correct retrothrust maneuver at point 6.

Unfortunately, difficulties, the nature of which are not fully understood, have arisen which thus far have prevented the successful computation of the trajectory from point 1 all the way to point 7. The difficulties, whatever they may be, prevent the retrothrust maneuver at point 6. Thus far, no trajectory, proven to be a minimum-fuel multistage trajectory from point 1 to point 7, has been computed. Investigations and studies are being made from both in-house and by private contractors to locate the difficulties.

The trouble seems to lie in the convergence properties of the iterative scheme for finding the initial values of the Lagrange multipliers to high precision. The scheme simply will not converge to any value unless the first approximations of the multipliers in some instances, but not all, are very, very close to their exact values. In other cases, the scheme converges to a value which is not acceptable because its subsequent use does not permit attainment of the objective or desired terminal state for the stage. That is to say, the terminal state is extremely sensitive to changes in the initial values of the Lagrange multipliers. If these multipliers at point 1 are not known with great precision, the desired terminal state cannot be attained.

A hopeful remedy seems to lie in the use of another iterative process, the so-called Newton-Raphson method. It appears at present that this scheme will converge for rougher first approximations than the differential correction scheme that is now in use. But whether it will converge to sufficiently accurate values of the initial values of the multipliers is as yet not known.

The remarks just made might imply that the situation relating to multistage trajectory computation is in a sad plight, indeed. Be assured that this is not the case at all. We can calculate quite satisfactory multistage trajectories for any desired missions. While these trajectories may not be strictly minimum-fuel trajectories, they nevertheless require the expenditure of less fuel than is available for use. The purpose of optimization is to find that trajectory, if it exists, which will use the least possible amount of fuel to accomplish the mission. The savings in fuel over nonoptimum trajectories could possibly be converted into payload. We must be prepared, however, for the possibility that the savings will be negligible. But we will never know whether they are or not until successful optimization of the trajectories has been achieved.

Conducted simultaneously with the studies in multistage trajectory optimization are studies in the optimization of low-thrust trajectories. The goal of the low-thrust trajectory optimization project is the development of techniques and computer programs for determination of minimum-time or minimum-fuel trajectories for both geocentric orbital transfer and interplanetary rendezvous and flyby operations. Successful low-thrust trajectory optimization techniques would be essential in the generation of optimal guidance schemes. The problem of optimizing low-thrust trajectories was attacked by classical variational methods but with little success. The principal difficulties are again those of the two-point boundary value problem arising out of attempts to find numerical solutions of the Euler-Lagrange equations. The use of the method of gradients, a technique employing successive approximations, one of the so-called direct methods of the calculus of variations, has been explored by several contractors, especially by H. K. Hinz and his associates at Grumman Aircraft. This is an attempt to circumvent some of the difficulties of the two-point boundary value problem. Of course these difficulties are also inherent in optimizing multistage trajectories but they are somewhat heightened in the case of low-thrust trajectories which may spiral about the earth many hundreds of times before departing into the transfer trajectory. The length of time involved is so great that large accumulations of round-off and truncation errors are made. A second difficulty associated with the use of the successive approximations techniques, which seemingly must be employed, is the need to store control variables as functions of time. If the functions are rapidly changing the amount of computer storage required may become prohibitive. A third difficulty, already encountered in the discussion of multistage trajectories, is the extreme sensitivity of terminal conditions to changes in initial values of the Lagrange multipliers. In an attempt to surmount this last difficulty in a relatively simple problem, H. K. Hinz and his associates at Grumman Aircraft considered the specific problem of determining the optimum thrust steering program that would minimize the time to transfer between coplanar circular orbits in a central force field. Both orbits encircle a single body. Since they considered the thrust magnitude as fixed, minimum transfer time was equivalent to minimum fuel consumption. The use of the generalized Newton-Raphson method of successive approximations permitted the computation of optimum thrust steering programs for progressively increasing values of final time for trajectories up to the final time for 21 revolutions about the earth. But for transfers involving 21.5 revolutions or more, the method did not converge to an accuracy of four significant figures of the Lagrange multipliers. Higher precision integration schemes seem to offer the best hope of obtaining convergence to more significant figures.

The third area of research in trajectory optimization is in impulsive orbital transfers. The orbital transfer in the multistage trajectory we have been discussing is nonimpulsive. The aim of this research is to attempt to gain knowledge in this simplified transfer problem that would help in the understanding of nonimpulsive transfers.

The impulsive thrust orbital transfer is, of course, an idealization. In the two-impulse case, for example, there is one instantaneous thrust to get from the initial orbit onto the transfer trajectory and a second instantaneous thrust to get into the terminal orbit as illustrated in Figure 6.

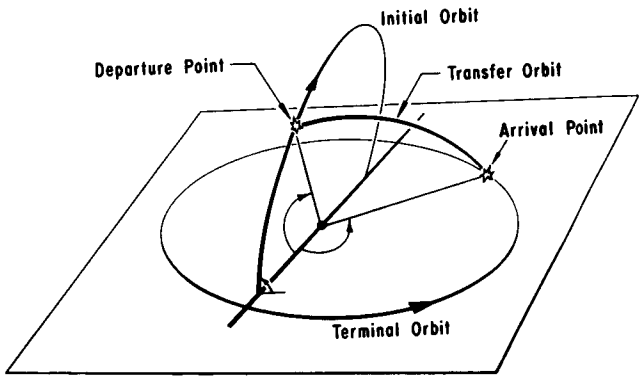

FIGURE 6. TWO-IMPULSE ORBITAL TRANSFER

Investigations have been made using one, two, and three impulse transfers. Because mathematical formulation of the problem leads to expressions which, except for special cases, are analytically intractable, the studies were made largely by numerical methods.

Dr. D. F. Bender and his associates at North American Aviation, Inc., are responsible for the majority of the numerical work that has been done by contractors in impulsive orbital transfers. They have done some important analytical work as well. F. W. Gobetz of United Aircraft has contributed to the problem of optimum low-thrust orbital transfers.

However, all of these studies in orbital transfer, whether impulsive or low-thrust, were made with mathematical models that represented considerable simplifications of the physical model that actually exists. Their usefulness is therefore limited to design studies and for suggesting modes of attack on the more realistic problems. The present stage of this research is still somewhat exploratory; it has not progressed to the point where valid conclusions may be made that would be helpful in multistage trajectory optimization.

The fourth area of trajectory optimization which has been studied is the atmospheric reentry trajectory wherein the reentry vehicle is subject only to gravitational and aerodynamic forces.

Because no thrusting, except for control jets, is employed, attention was directed toward minimization of the accumulated gravitational forces on the vehicle's occupants. In mathematical form, this means the minimization of the integral of the square of the total aerodynamic acceleration. The optimization analysis which results from this formulation of the problem may be treated as a problem of Lagrange in the classical calculus of variations with fixed end-points or as a Pontryagin fixed end-point problem. The fixed end-points are, of course, the initial point of the reentry trajectory on the edge of the earth's atmosphere and the known and fixed terminal point on the earth's surface. It is assumed that the reentry vehicle's control system is capable of directing the vehicle to the desired landing point. Studies in this area thus far by out-of-house contractors have been done mainly by W. A. Shaw and his associates at Auburn University and by Blanton and Muzyka of Raytheon Corporation. They have treated the problem both as a Lagrange problem and, therefore, used the methods of the classical calculus of variations and as a Pontryagin fixed end-point problem and used Pontryagin's maximum principle as the optimization technique. Results from each of the methods are identical, but both approaches were taken to determine whether one offered any computational advantage over the other. The answer appears to be in the negative.

In these beginning studies the most vexing problem in trajectory optimization, that of determining the initial values of the Lagrange multipliers, was sidestepped by assuming that the multipliers were known. The Euler-Lagrange equations were formulated and solved simultaneously with the equations of motion, and a trajectory was obtained which satisfied them and certain specified constraints. Such a trajectory, of course, may not be the optimal trajectory since it satisfies only one necessary condition. Studies could be continued to determine whether the trajectory which satisfies this one necessary condition also satisfies sufficiency conditions, several sets of which are available for the single-stage two fixed point problem.

In summary, then, if the study of the problem of multistage trajectory optimization is to be

continued, it is essential that a primary effort be directed toward determining a means for finding the initial values of the Lagrange multipliers to much greater precision than seems to be possible using presently available methods. If this problem can be successfully resolved, certainly a multistage trajectory can be found that satisfied some necessary conditions. If, additionally, we are eventually able to show that this trajectory also satisfies a set of sufficient conditions, we can with certainty say that a minimum-fuel trajectory has been found.

It appears that the best way to accomplish these aims for the realistic multistage problem is through attacking much simpler trajectory optimization problems. Having solved these, the realistic problem can be approached, it is to be hoped, by adding additional constraints one at a time.

BIBLIOGRAPHY

Optimization of Multistage Trajectories

1. Boyce, M. G.: An Application of Calculus of Variations to the Optimization of Multistage Trajectories. Progress Report No. 1 On Studies in the Fields of Space Flight and Guidance Theory. MSFC Report MTP-61-91, Dec. 18, 1961, pp. 9-29.

2. Boyce, M. G.; and Linnstaedter, J. L.: Necessary Conditions for a Multistage Bolza-Mayer Problem Involving Control Variables and Having Inequality and Finite Equation Constraints. Progress Report No. 7 On Studies in the Fields of Space Flight and Guidance Theory. NASA TM X-53292, July 12, 1965, pp. 8-31.

3. Chapman, R. M.; Lynn, D. W.; and Henderson, J. R.: Launch Trajectories with Inequality Constraints. Progress Report No. 6 On Studies in the Fields of Space Flight and Guidance Theory. NASA TM X-53150, Oct. 16, 1964, pp. 121-141.

4. Denbow, C. H.: A Generalized Form of the Problem of Bolza. Contributions to the Calculus of Variations 1933-1937. University of Chicago Press, 1937, pp. 453-484.

5. Hermes, H.: Investigation of Sufficiency Conditions and the Hamilton-Jacobi Approach to Optimal Control Problems. Progress Report No. 6 On Studies in the Fields of Space Flight and Guidance Theory. NASA TM X-53150, Oct. 16, 1964, pp. 49-121.

6. Moyer, H. G.: Optimal Multistage Rocket Flight and Other Discontinuous Variational Problems. Progress Report No. 4 On Studies in the Fields of Space Flight and Guidance Theory. MSFC Report MTP-AERO-63-65, Sept. 19, 1963, pp. 25-59.

Low-Thrust Trajectory Optimization

1. Ainsworth, O. R.: Minimum-Fuel Propelled Flight Differential Equation in Terms of Position, Velocity, Angle of Attack and Its Higher Derivatives. Progress Report No. 1 On Studies in the Fields of Space Flight and Guidance Theory. MSFC Report MTP-AERO-61-91, Dec. 18, 1961, pp. 91-103.

3. Hinz, H. K.; and Moyer, H. G.: Three-Dimensional Low-Thrust Trajectory Optimization. Progress Report No. 2 On Studies in the Fields of Space Flight and Guidance Theory. MSFC Report MTP-AERO-62-52, June 26, 1962, pp. 5-44.

3. Hinz, H. K.: Optimal Low-Thrust Near-Circular Orbital Transfer. Progress Report No. 2 On Studies in the Fields of Space Flight and Guidance Theory. MSFC Report MTP-AERO-62-52, June 26, 1962, pp. 52-75.

4. Hinz, H. K.: Optimum Earth-to-Mars Trajectories for Low-Thrust Vehicles. Progress Report No. 4 On Studies in the Fields of Space Flight and Guidance Theory. MSFC Report MTP-AERO-63-65, Sept. 19, 1963, pp. 7-25.

5. Hinz, H. K.; McGill, R.; and Taylor, G.: Some Numerical Results of Geocentric Low-Thrust Trajectory Optimization. Progress Report No. 7 On Studies in the Fields of Space Flight and Guidance Theory. NASA TM X-53292, July 12, 1965, pp. 347-372.

6. Kelley, H. J.; Hinz, H. K.; Pinkham, G.; and Moyer, H. G.: Low-Thrust Trajectory Optimization. Progress Report No. 1 On Studies in the Fields of Space Flight and Guidance Theory. MSFC Report MTP-AERO-61-91, Dec. 18, 1961, pp. 7-91.

BIBLIOGRAPHY (Continued)

7. Kenneth, P.; and Taylor, G. E.: Computation of Optimal Interplanetary Low-Thrust Trajectories with Bounded Thrust Magnitude by Means of a Generalized Newton-Raphson Method. Progress Report No. 7 On Studies in the Fields of Space Flight and Guidance Theory. NASA TM X-53292, July 12, 1965, pp. 373-392.

8. Passmore, H.: Orbital Element Equations for Optimum Low-Thrust Trajectories. Progress Report No. 3 On Studies in the Fields of Space Flight and Guidance Theory. MSFC Report MTP-AERO-63-12, Feb. 6, 1963, pp. 63-97.

9. Passmore, H.: A First-Order Delaunay Solution for Minimum-Fuel, Low-Thrust Trajectories. Progress Report No. 7 On Studies in the Fields of Space Flight and Guidance Theory. NASA TM X-53292, July 12, 1965, pp. 297-345.

10. Pinkham, G.: A Reference Solution for Low-Thrust Trajectories. Progress Report No. 2 On Studies in the Fields of Space Flight and Guidance Theory. MSFC Report MTP-AERO-62-52, June 26, 1962, pp. 44-52.

11. Pinkham, G.: An Application of a Successive Approximation Scheme to Optimizing Very Low-Thrust Trajectories. Progress Report No. 3 On Studies in the Fields of Space Flight and Guidance Theory. MSFC Report MTP-AERO-63-12, Feb. 6, 1963, pp. 57-63.

Optimal Orbital Transfer

1. Bender, D. F.: A Comparison of One-and Two-Impulse Transfers for Nearly Tangent Coplanar Elliptical Orbits. Progress Report No. 5 On Studies in the Fields of Space Flight and Guidance Theory. NASA TM X-53024, Mar. 17, 1964, pp. 155-173.

2. Bender, D. F.; and McCue, G. A.: Optimal One-Impulse Transfer between Coplanar Elliptical Orbits. Progress Report No. 7 On Studies in the Fields of Space Flight and Guidance Theory. NASA TM X-53292, July 12, 1965, pp. 123-153.

3. Gobetz, F. W.: Optimal Variable-Thrust Rendezvous of a Power-Limited Rocket between Neighboring Low-Eccentricity Orbits. Progress Report No. 6 On Studies in the Fields of Space Flight and Guidance Theory. NASA TM X-53150, Oct. 16, 1964, pp. 141-179 and NASA TM X-53292, July 12, 1965, pp. 155-222.

4. Jurovics, S. A.: Orbital Transfer by Optimum Thrust Direction and Duration. Progress Report No. 6 On Studies in the Fields of Space Flight and Guidance Theory. NASA TM X-53150, Oct. 16, 1964, pp. 141-179.

5. Lee, G.: An Analysis of Two-Impulse Orbital Transfer. Progress Report No. 4 On Studies in the Fields of Space Flight and Guidance Theory. MSFC Report MTP-AERO-63-65, Sept. 19, 1963, pp. 167-213.

6. Lee, G.: On a Restricted Comparison of Two-Impulse and One-Impulse Orbital Transfer. Progress Report No. 5 On Studies in the Fields of Space Flight and Guidance Theory. NASA TM X-53024, Mar. 17, 1964, pp. 155-173.

7. McCue, G. A.: Optimal Two-Impulse Orbital Transfer and Rendezvous between Inclined Elliptical Orbits. Progress Report No. 4 on Studies in the Fields of Space Flight and Guidance Theory. MSFC Report MTP-AERO-63-65, Sept. 19, 1963, pp. 135-167.

8. McCue, G. A.; and Bender, D. F.: Numerical Investigation of Minimum Impulse Orbital Transfer. Progress Report No. 7 On Studies in the Fields of Space Flight and Guidance Theory. NASA TM X-53292, July 12, 1965, pp. 89-121.

BIBLIOGRAPHY (Continued)

Reentry Trajectories

1. Harmon, G.; and Shaw, W. A.: An Investigation of Minimum Drag Re-entry Paths. Progress Report No. 5 On Studies in the Fields of Space Flight and Guidance Theory. NASA TM X-53024, Mar. 17, 1964, pp. 37-83.

2. Muzyka, A.; and Blanton, H. E.: Optimum Earth Re-entry Corridors. Raytheon Company Technical Summary Report FR-65-127, Mar. 30, 1965.

3. Raney, D.; and Shaw, W. A.: Preliminary Investigations on Six Dimensional Optimum Re-entry Trajectories. Progress Report No. 4 On Studies in the Fields of Space Flight and Guidance Theory. MSFC Report MTP-AERO-63-65, Sept. 19, 1963, pp. 83-121.

4. Reece, J. W.; and Harmon, G.: A Maximum Principle Re-entry Study. Progress Report No. 7 On Studies in the Fields of Space Flight and Guidance Theory. NASA TM X-53292, July 12, 1965, pp. 33-63.

Supporting Research Activities

1. Cavoti, C.: Rocket Booster Vertical Climb Optimality. Progress Report No. 3 On Studies in the Fields of Space Flight and Guidance Theory. MSFC Report MTP-AERO-63-12, Feb. 6, 1963, pp. 97-138.

2. Cavoti, C.: Optimum Retrothrust in a Gravitational Field. Progress Report No. 5 On Studies in the Fields of Space Flight and Guidance Theory. NASA TM X-53024, Mar. 17, 1964, pp. 117-145.

3. Kelley, H. J.: Singular Extremals in Lawden's Problem of Optimal Rocket Flight. Progress Report No. 4 On Studies in the Fields of Space Flight and Guidance Theory. MSFC Report MTP-AERO-63-65, Sept. 19, 1963, pp. 309-323.

4. Kelley, H. J.: A Transformation Approach to Singular Subarcs in Optimal Trajectory and Control Problems. Progress Report No. 4 On Studies in the Fields of Space Flight and Guidance Theory. MSFC Report MTP-AERO-63-65, Sept. 19, 1963, pp. 323-333.

5. Kelley, H. J.: An Optimal Guidance Approximation Theory. Progress Report No. 5 On Studies in the Fields of Space Flight and Guidance Theory. NASA TM X-53024, Mar. 17, 1964, pp. 83-97.

6. McGill, R.; and Kenneth, P.: Solution of Variational Problems by Means of a Generalized Newton-Raphson Operator. Progress Report No. 5 On Studies in the Fields of Space Flight and Guidance Theory. NASA TM X-53024, Mar. 17, 1964, pp. 9-37.

7. Nafoosi, A. A.; and Passmore, H.: On an Application of the Hamilton-Jacobi Theory to High-Thrust Rocket Flight. Progress Report No. 7 On Studies in the Fields of Space Flight and Guidance Theory. NASA TM X-53292, July 12, 1965, pp. 267-296.

8. Nomicos, G. N.: Differential Correction Scheme for the Calculus of Variations. Progress Report No. 4 On Studies in the Fields of Space Flight and Guidance Theory. MSFC Report MTP-AERO-63-65, Sept. 19, 1963, pp. 59-83.

9. Payne, M.: Dirac's Generalized Hamiltonian Dynamics and the Pontryagin Principle. Progress Report No. 6 On Studies in the Fields of Space Flight and Guidance Theory. NASA TM X-53150, Oct. 16, 1964, pp. 7-49.

BIBLIOGRAPHY (Concluded)

10. Pines, S.: Constants of the Motion for Optimum Thrust Trajectories in a Central Force Field. Progress Report No. 5 On Studies in the Fields of Space Flight and Guidance Theory. NASA TM X-53024, Mar. 17, 1964, pp. 97-117.

11. Richman, J.: Two-Point Boundary Value Problem of the Calculus of Variations for Optimum Orbits. Progress Report No. 3 On Studies in the Fields of Space Flight and Guidance Theory. MSFC Report MTP-AERO-63-12, Feb. 6, 1963, pp. 29-57.

12. Richman, J.: Approximate Initial Values of Lagrange Multipliers for the Two-Point Boundary Value Problem. Progress Report No. 6 On Studies in the Fields of Space Flight and Guidance Theory. NASA TM X-53150, Oct. 16, 1964.

General

1. Bliss, G. A.: Lectures on the Calculus of Variations. The University of Chicago Press, 1946.

2. Cicala, P.: An Engineering Approach to the Calculus of Variations, Revised Second Impression. Libreria Editrice Universitaria Levrotto and Bella, Torino, 1964.

3. Gelfand, I. M.; and Fomin, S. V. (R. A. Silverman trans. and ed.): Calculus of Variations Revised English Edition. Prentice-Hall, Inc., 1963.

4. Lawden, D. F.: Optimal Trajectories for Space Navigation. Butterworths, London, 1963.

ASTRODYNAMICS RESEARCH AT MSFC

by

Arthur J. Schwaniger*

SUMMARY

The term astrodynamics and the nature of that field are very briefly discussed. Then a brief coverage of some of the research projects in astrodynamics is given. These include earth-moon trajectories, interplanetary trajectories, and the various models used for trajectory studies. In the area of earth-moon transits, Apollo type transits and periodic orbits studied for possible Pegasus orbits are discussed in some detail. In the area of interplanetary flight, reference is made only to the specific publications available and the types of problems being studied. The trajectory models used are primarily the restricted three-body model and for interplanetary studies a matched-conic model. The use of precision models using complete ephemeris data and the current approach to such a model are mentioned. Finally, some of the future areas of effort are given.

GLOSSARY

Perisel - On a trajectory, the point of closest approach to the center of the moon.

Barycenter - The center of mass of two bodies in a trajectory model.

MEP - Moon-earth orbit plane.

Perigee Belt - The locus of perigee points of a class of earth-moon transits.

Perisel Belt - The locus of perisel points of a class of earth-moon transits.

Vertex - The point representing the region at which a family of transits converges.

Class of Transits - All transits having a common perigee radius, perisel radius, and transit time between these points.

Family of Transits - Transits, all of one class, which have perigee on a straight line segment of the perigee belt or perisel on a straight line segment of the perisel belt.

Periodic Orbit - A trajectory which periodically repeats itself.

Transition Orbit - A trajectory which includes both near elliptical motion around earth and near elliptical motion around the moon with one or more transitions between the two.

Cislunar - On this side of the moon or between earth and moon, or sometimes more generally in the vicinity of earth and moon.

Flyby Transit - A trajectory which passes near one of the celestial bodies, but does not stop or remain any appreciable time near the body.

Swing-By Transit - A trajectory which passes near a celestial body and utilizes the bending by its gravitational attraction to be directed to another celestial body.

Central Force Field - Usually a gravitational field at all points of which the force is directed toward one central point.

Libration Point - A point at which a body tends to remain stationary due to cancelling effects of gravitational and centrifugal forces at that point.

Launch Azimuth - the direction measured in a horizontal plane at launch of the projection of the intended flight path on that plane. The reference is usually the north direction.

---

* Chief, Astrodynamics Branch, Aero-Astrodynamics Laboratory

Conic Flight - Flight in a central force field; it is shaped like a plane section of a cone. The focus of the conic is located at the center of force.

Central Angle - The angle measured at the center of earth between any two position vectors of a space vehicle's flight path.

Inertial Space - The space associated with an interial, or in other words stationary, reference frame.

Rotating Frame - A reference frame or coordinate system which rotates.

Restricted Model or Restricted Three-Body Model - A model of a gravitational system of two massive bodies which revolve in circles about their common center of mass and a third body of negligible mass which moves in that gravitational system.

Three-Body Problem - The problem of motion of three massive bodies under mutual gravitational attraction.

SECTION I. INTRODUCTION

Astrodynamics is the treatment of problems in celestial mechanics as they apply to contemporary space flight. Classical celestial mechanics has dealt with the description of orbits in various gravitational models primarily in terms of application to the natural bodies in the solar system or simply for academic reasons. It has relied on the resources of higher mathematics in describing motion in the system and has had only observation of natural bodies by which to test its results. Astrodynamics deals with the determination of flight paths for propelled and unpropelled spacecraft and with the matching of flight paths to booster flight characteristics.

In addition to the standard methods of celestial mechanics, astrodynamics uses high speed computers to evaluate numerically many of the previously unsolved equations of celestial mechanics. Astrodynamics studies also seek simplified concepts for a better understanding of space problems and their rapid solution.

In any exploration effort the choice of a path that satisfies as many of the exploratory missions requirements as possible is one of the most basic problems. The work of astrodynamics in providing a thorough description of the paths available to the experimenter, therefore, is of primary importance to the mission.

The following is a brief review of some research efforts that have been made and are being made in astrodynamics at the Marshall Space Flight Center.

Even with the availability of our huge, very high speed computers the problem of representing all possible trajectories by computing large quantities of exact trajectories, which incorporate a precise representation of the gravitational fields of the solar system, is virtually impossible. Trajectories that are very nearly correct can be, and are, calculated for specific applications to well defined missions; however, the computer time required for these calculations is prohibitively large and the character of the trajectory so complicated by the complexity of the real solar system that it is not feasible to exclusively utilize these calculations in providing the general description of trajectories that is necessary for the planning of a mission. The aim of the Astrodynamicist, therefore, is to provide approximate descriptions of trajectory behaviors that are adequate for general mission planning, and to gain accurate descriptions of trajectory behavior by refinement of the approximate descriptions to continually bring them into closer agreement with the precise results of complicated approaches. Thus extensive use is made of approximate models.

SECTION II. RESTRICTED THREE-BODY MODEL STUDIES

A. APOLLO TYPE TRANSITS

Much of our effort in the study of trajectories in earth-moon space has utilized the restricted three-body model. This model is pictured in the first figure.

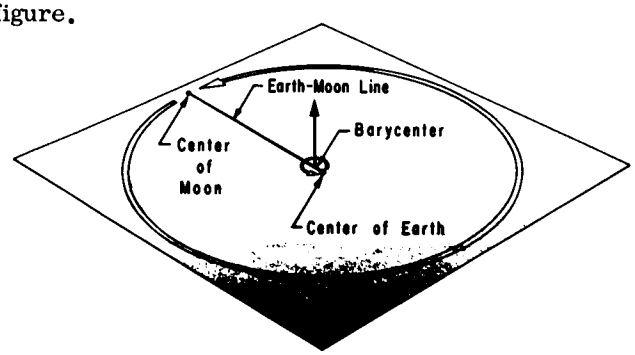

FIGURE 1. RESTRICTED THREE-BODY MODEL

The earth and moon are assumed to revolve in a plane, which we will designate the earth-moon plane for a plane of reference, and they move in circles about their center of mass, the barycenter. The

plane of motion, referred to as the MEP or moon-earth plane, and the line connecting the centers of earth and moon are usually used as references. The use of the earth-moon line implies a rotating coordinate system. The results of our studies of trajectories applicable to Apollo type missions have been published in a series of reports entitled, "Lunar Flight Study Series" and have in a sense been summarized in another larger report, "A Comprehensive Astrodynamic Exposition and Classification of Earth-Moon Transits." A very brief review of the main points of the report can be given as follows. A class of earth-moon transits is defined by three parameters: The radial distance of close approach to the center of earth (radius of perigee), the radial distance of close approach to the center of the moon (radius of perisel), and the time of transit between these points. Under this classification all transits within a given class (specified radius of perigee, radius of perisel, and time of transit) have a near circular band of perigee positions from which departure is made. This is illustrated for several classes in Figure 2. The radii of perigee and perisel are constant over the classes shown, with only transit time variable.

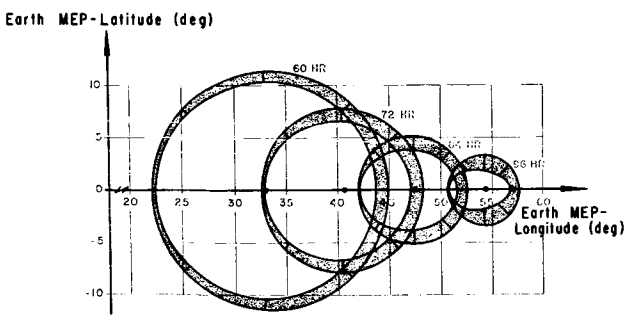

FIGURE 2. LOCI OF ALL POSSIBLE PERIGEES FOR CLASSES C(T_i, 6,555 KM, 1,923 KM), T_i = 60, 72, 84 and 96 HR

At the moon the locations of perisel points of a class also form an annular belt, (all points in this belt have the same radial distance from the center of the moon) as shown in Figure 3. It is also found that all transits of a class depart from a point in the departure belt in a predetermined radial direction. (To visualize the transit it is noted that the trajectory of a given class of transits is horizontal at the perigee belt and the direction of the trajectory is generally away from the center of the perigee belt.) The arrival at the moon is in a direction generally toward the center of the perisel arrival belt. Subclasses or families of trajectories are identified by

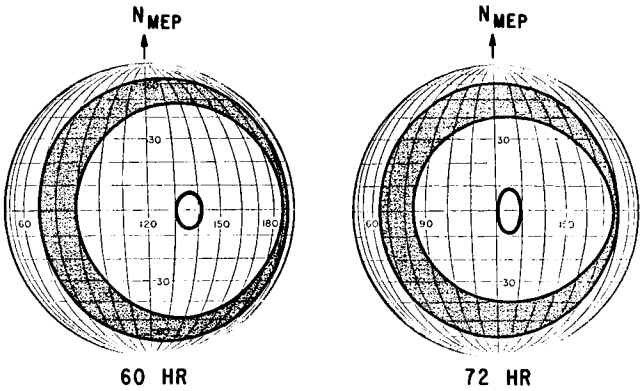

FIGURE 3. SURVEY OF ARRIVAL AREAS AT MOON FOR TRANSIT CLASSES C(60 HR, 6,555 KM, 1,923 KM) AND C(72 HR, 6,555 KM, 1,923 KM)

considering those transits whose perigees lie within the belt width on a line from the central point in the belt. Such a subclass or family is shown in Figure 4.

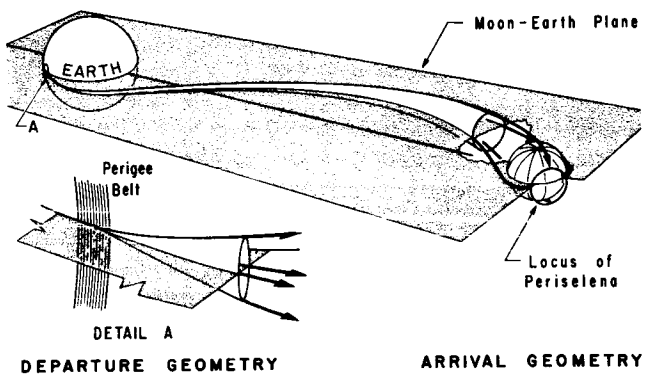

FIGURE 4. FAMILY OF TRANSITS ENVELOPING MOON

The fixed parameters of the family are the classifying parameters, flight time, radius of perigee, radius of perisel, and the horizontal path angles associated with perigee and perisel. Depending on the placement of perigee as stated above and the remaining parameters (velocity magnitude and azimuthal direction) at perigee a family of trajectories can envelope the moon from all directions. The trajectories pass horizontally through the perisel belt toward the center of the belt. The region of convergence of all trajectories of a family near the center of the perisel belt is called the vertex and this region is small enough to be considered a point. The perisel points of the family lie on a near circular locus within the perisel belt for the family class.

Each class of transits is in fact composed of such families, the perigee belt being composed of the perigee line segments and the perisel belt the locus of all perisel circles. The vertices of the families within a class also form an annular locus within the perisel belt. If the true orientation of the earth's and moon's equators is superimposed on the MEP system, geographical coordinates can then be used in the design of a lunar mission. An example is shown graphically in Figure 5.

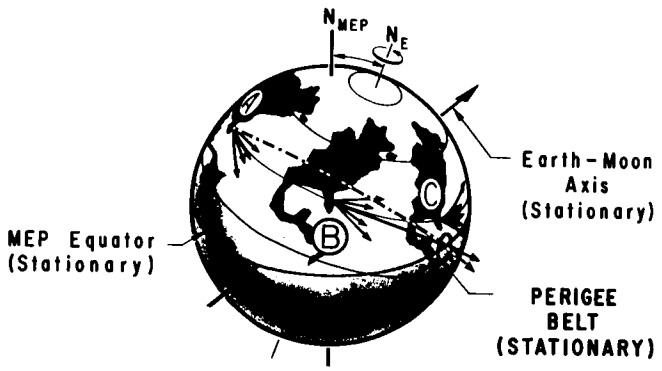

FIGURE 5. DEVELOPMENT OF LAUNCH WINDOW BY RELATING TRUE EARTH AXIS AND EQUATOR TO MEP-REFERENCE SYSTEM

Positions A, B, and C represent three successive times in the day at which launch is considered. The belt of perigee points that will produce a flight of desired time and close approach distance to the moon is indicated. The arrows indicate the spread of launch azimuths that are acceptable from range safety considerations. One must then determine when, if at all, the launch position on the earth is such that the azimuthal aiming direction, and the powered flight central angle will place perigee on the perigee belt with proper direction away from the center of the belt. One can see that several possibilities for the flight may be available in this case, particularly if a parking orbit is used to extend the arc of flight (central angle) from liftoff to the perigee of the transit.

To place perigee of the trajectory on the indicated perigee belt with direction away from the center of the belt, the flight must pass over the center of the belt. The earliest launch time at which this can be done while staying within range safety restriction of launch azimuth is represented by point A. From this launch time the azimuth of launch is at the northern range safety limit, and the central angle of flight to the perigee location is so large that a coast phase in a parking orbit will be required to place perigee at the specified point. The flight originating at the time represented by point B has a much smaller central angle so that little or no coast in parking orbit is required. The latest time at which launch is possible will occur when the central angle from the launch point to the perigee belt becomes smaller than the central angle of flight with no parking orbit, or when the most southerly azimuth acceptable for range safety is reached. On Figure 5 the most southerly azimuth angle shown at location C does not provide a trajectory that will pass through the perigee belt and therefore a launch is not possible.

B. IMAGE TRANSITS IN THE RESTRICTED MODEL

Another feature of the material is that it can be readily interpreted for moon-to-earth flights. This is possible because of image or reflection principles inherent in the restricted three-body model. Detailed explanation of these principles and their application would be too lengthy for this presentation. However, a brief explanation of the basic principle is in order here because it will be referred to again in connection with other projects.

This principle can be intuitively understood as illustrated in Figure 6.

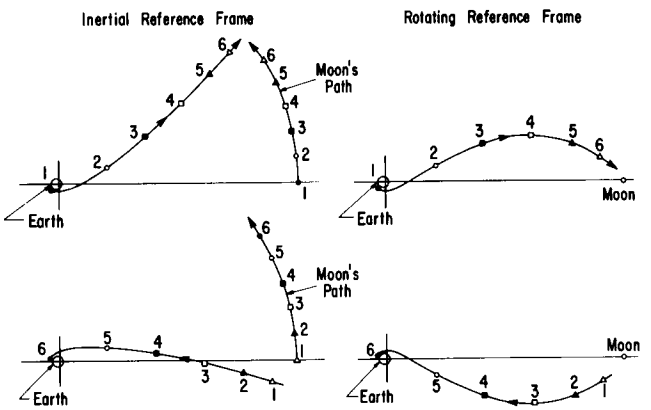

FIGURE 6. IMAGE OR REFLECTION TRAJECTORIES IN THE RESTRICTED THREE-BODY MODEL

Consider the motion of a vehicle toward the moon in inertial space as illustrated on the upper left. At the start, the spacecraft is at point 1 on its path and the moon at point 1 on its orbit. The moon moves counterclockwise as viewed from the north with successive locations of the bodies occurring as indicated by the numbers. This motion appears in the rotating frame as illustrated at upper right. If such motion, indicated in the inertial frame, can occur, then the same paths of the two bodies can also occur with the reverse motion, with the moon's motion clockwise and the

vehicle moving toward earth. This is equivalent to viewing the motion from the southerly direction. If this reverse motion is viewed, however, from what would now be the north direction so that the moon's motion again appears counterclockwise, the path appears as indicated at lower left. This path is clearly an image of the first but the motion is from moon to earth rather than from earth to moon.

In the rotating frame illustrated at the lower right, the image path is a reflection on the earth-moon line of the original path and the direction is reversed. Although this explanation has been limited to two dimensions, it can be extended to three dimensions with the result that all data concerning earth to moon transits can be transformed to represent moon-to-earth transits.

Since Apollo type missions were being considered, the flight times concerned with in the survey are not very large. During such time intervals the moon moves only about one seventh of a revolution or less around the barycenter, and the circular arc representing the moon's motion in the model is a sufficiently accurate approximation of any segment of the true more elliptical orbit. The action of the sun's gravity over this time period is also negligible for the approximation desired. One should not infer, however, that the restricted problem finds no other application. Another of the projects being pursued at this center is the study of periodic orbits in the restricted three-body problem. Poincare's justification for the study of periodic orbits in the restricted three-body model was that such orbits represent one of the very few openings to the solution of the restricted problem. This fact still provides one point of justification for their study. Dr. Arenstorff of the Computation Laboratory has given an analytic proof for the existence of the periodic orbits even when they encompass both earth and moon and their motion is highly different from circular.

C. PERIODIC ORBITS

A systematic generation of periodic orbits on the computer has been initiated in an attempt to uncover a pattern or patterns by which the nature and classification of the orbits will be more fully understood. To generate periodic orbits we again use the reflection on the earth-moon line. Because of this reflection, a trajectory that crosses the earth-moon line perpendicular to it will continue with the path after the crossing being a reflection of the path before the crossing. It follows that if a trajectory has two perpendicular crossings of the earth-moon line it closes on itself and is periodic in the rotating system.

To determine a periodic orbit the calculation is started on the earth-moon line with direction perpendicular to it. Figure 7 shows the trajectory geometry that develops for a typical case.

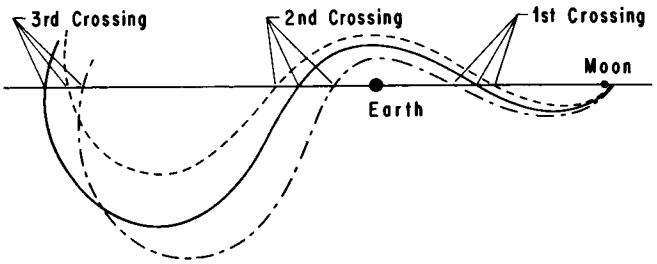

FIGURE 7. DEVELOPMENT OF PERPENDICULAR CROSSING OF EARTH-MOON LINE

The magnitude of the velocity vector is then adjusted until trajectories are generated whose velocity component along the earth-moon line changes direction at at given crossing. In Figure 7 the third crossing is chosen. Zero velocity component along the line, at the time of crossing, indicates perpendicular crossing. The periodic orbit is then determined by isolating, within the capability of the computing scheme being used, the trajectory with zero velocity along the earth-moon line at the time of crossing. The task of classifying all orbits is considerably complicated by the fact that the orbits can have many different basic shapes and further that some of these are extremely complicated shapes. Some examples of the less complicated orbit shapes are shown in Figures 8 and 9.

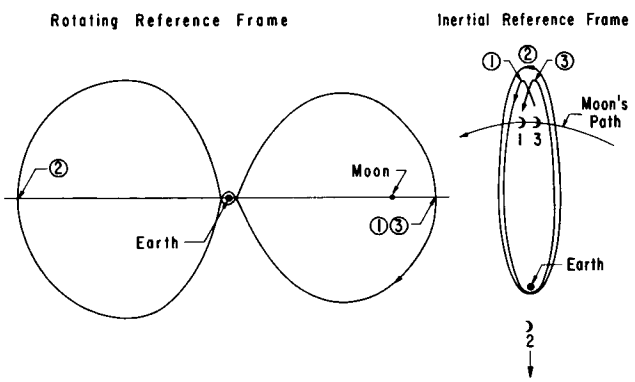

FIGURE 8. A PERIODIC ORBIT IN THE RESTRICTED THREE-BODY MODEL

In these the orbit is shown in both rotating and inertial coordinates. In the rotating frame the orbit is seen looping from the vicinity of earth through space with one loop passing around the moon. In the inertial system the orbit is nearly elliptical with the

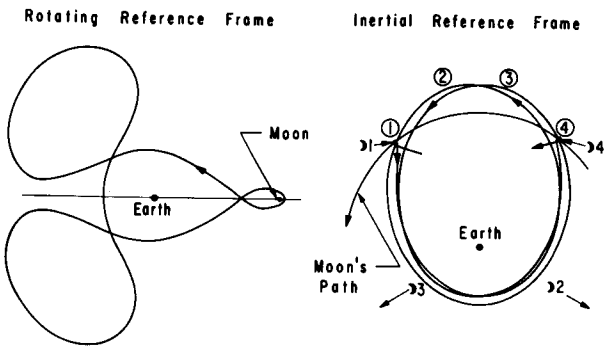

FIGURE 9. A PERIODIC ORBIT IN THE RESTRICTED THREE-BODY MODEL

ellipse being highly distorted by lunar gravity at times when the position of the moon is near that of the small body on the orbit. Some examples of the more exotic shapes are given in Figures 10 and 11.

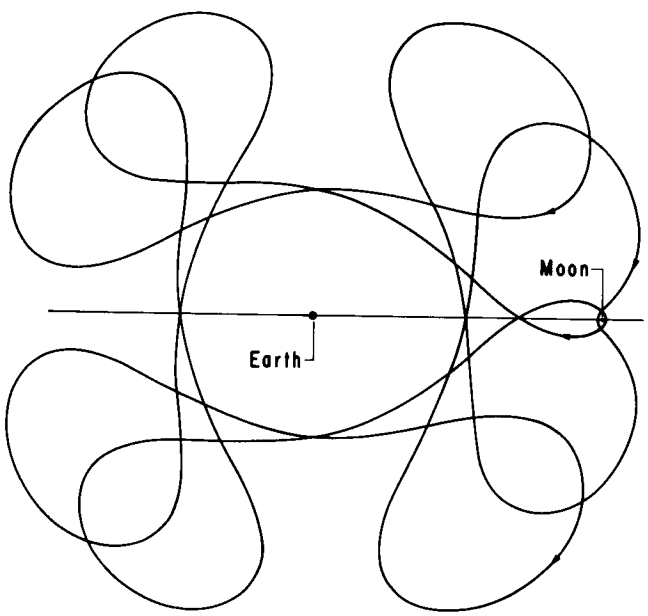

FIGURE 10. A PERIODIC ORBIT IN THE RESTRICTED THREE-BODY MODEL

Another kind of orbit that occurs in the restricted model is shown in Figure 12. This kind of orbit, called a transition orbit, was discovered by M. C. Davidson of Computation Laboratory. This orbit is, for several revolutions, nearly an ellipse about the earth. On one revolution, however, the orbit passes near the libration point between earth and moon. This

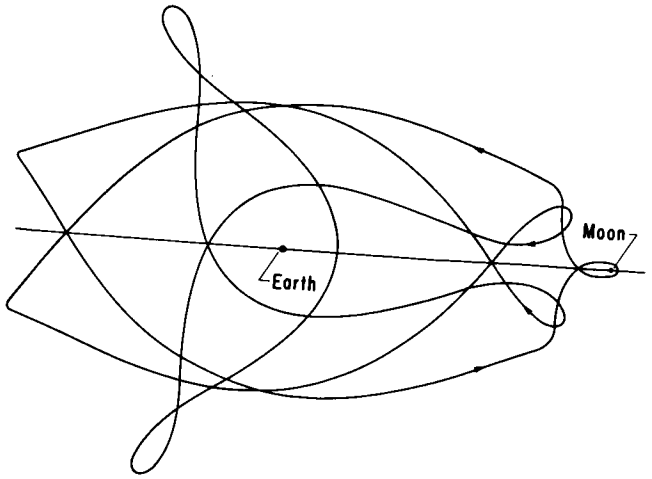

FIGURE 11. A PERIODIC ORBIT IN THE RESTRICTED THREE-BODY MODEL

is a point at which the centrifugal force on a body moving with the rotating earth-moon system, combined with the force of the moon's gravity, is just balanced by the force of earth's gravity. As it passes this point, the orbit is distorted and eventually is temporarily captured by the moon. Its motion now becomes essentially elliptic around the moon until, after several revolutions there, it comes back to near the libration point and is temporarily recaptured by earth.

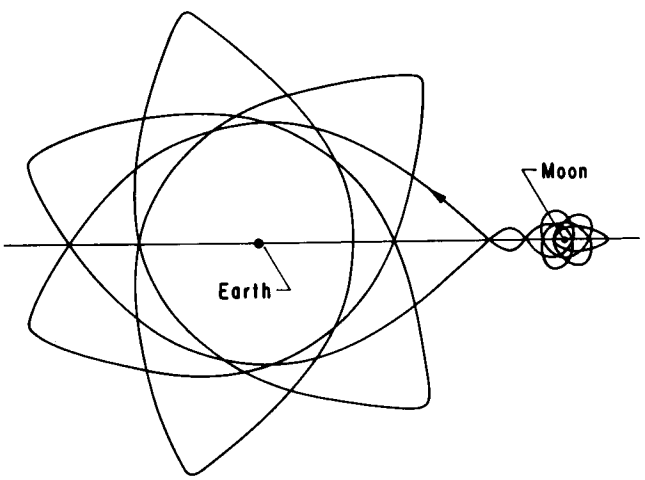

FIGURE 12. A TRANSITION ORBIT IN COORDINATE SYSTEM ROTATING WITH EARTH-MOON SYSTEM

SECTION III. PERIODIC AND NEAR PERIODIC ORBIT APPLICATIONS

In general the periodic orbits of the restricted model will not reappear as periodic orbits if the

moon's path is deviated from circular to one more representative of its real path or if the gravitational attraction of the sun is introduced in the model. Some of them, however, may appear that are near periodic for at least a limited time. The possibility of application of the near periodic orbits to many space exploration missions gives another justification for the study of periodic orbits in the restricted model. Such orbits that pass at least a few times near both earth and moon have obvious value for photographic missions and missions to measure and evaluate the nature of the cislunar space. If any of these orbits can be maintained over long periods with reasonably small orbit correction, they may even be utilized for ferry vehicles that shuttle between points close to earth and close to the moon during each orbit period and can be used by men during the major portion of the trip from earth to moon and back.

When an actual mission application is to be considered, for which a long period orbit is required or for which the orbit must meet certain specifications over long periods of time, the effects of the sun's gravity and the elliptical shape of the moon's orbit must be considered. Such a mission was recently investigated. It was proposed that a Pegasus type payload be placed in an orbit that would provide for determination of the density of micrometeoroids in cislunar space. No midcourse guidance or propulsion after insertion was to be provided. With this restriction it soon becomes apparent that the orbit cannot approach very near to the moon and continue on a repeating path, due to the varying distance and velocity of moon relative to earth. Therefore it was decided to study only periodic or near periodic orbits, which essentially avoid encounter with the moon. Two efforts were made to find orbits to satisfy this and similar proposals. The first effort, done in-house, was an investigation of the periodic orbit that passes near the earth twice each month making two loops in space with one of these loops encompassing the moon as seen in the rotating frame. This is the orbit that was shown in Figure 8. We note that although the orbit does encompass the moon its closest approach distance to the moon is almost one fourth the earth-moon distance. The second effort, which was done by Lockheed, was a study of orbits that were near periodic and that reached to various distances from earth while avoiding the moon as much as possible and not looping around the moon. In both these cases the problem, then, is to determine what orbits are available that will approximately repeat themselves in cislunar space over a specified mission duration and what opportunities are available to launch the spacecraft into these orbits. Although the proposed orbit layouts avoid encounter of the moon and spacecraft, these very high apogee orbits are nevertheless highly perturbed by both the moon and sun. These perturbations can easily cause the perigee of the orbit to decrease so far that the spacecraft will collide with the earth early in its lifetime, even on its first return to earth. On the other hand, if the proper orientation of the orbit is chosen relative to the moon's and sun's positions the perturbations will increase the perigee radius. It was found that to gain an understanding of the perturbations due to sun and moon and their positioning relative to the spacecraft, the effects of each body had to be studied separately.

The orbits investigated in the Lockheed effort were classified by the ratio of the number of revolutions of the moon to the number of revolutions of the spacecraft. Four of these are represented in Figure 13. Several intermediate ratios not shown here were also included. The one-eighth ratio orbit was the smallest considered and the one-half ratio the largest.

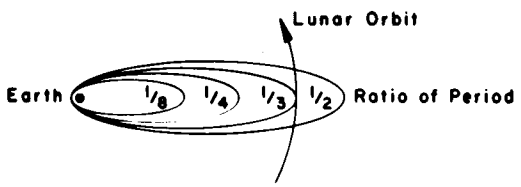

RATIO T_M/T	APOGEE (km)	PERIGEE VELOCITY $V - V_E$ (m/sec)
1/8	185,000	-194
1/4	297,000	-123
1/3	362,000	-98
1/2	476,000	-66

FIGURE 13. ORBIT TYPES INVESTIGATED

In both efforts the displacement of perigee due to the sun alone was found to be essentially a function of only the ratio, and the orientation of the major axis of the orbit relative to the direction of the sun. The effect of orientation is shown in Figure 14. The orbit maintains a nearly space-fixed orientation. The displacement increases from the time the orbit major axis is aligned in the direction of the earth-sun line until the major axis is perpendicular to the earth-sun line. This time interval is one-fourth of a year. Then perigee displacement decreases until the major axis is again aligned in the earth-sun direction. This implies then, that if a flight is initiated with the major axis in a similar direction as the earth-sun line the sun's gravitational perturbation will increase the length of the major orbital axis and therefore moves the perigee between its initial height and

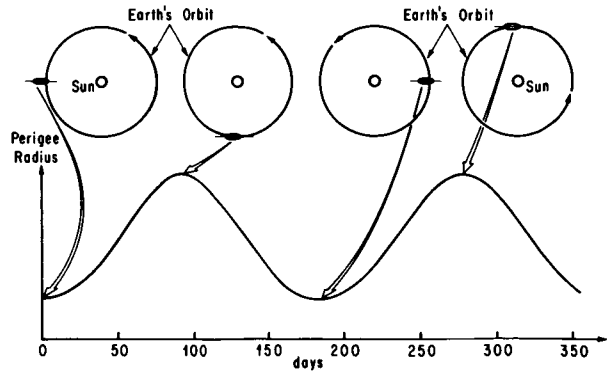

FIGURE 14. NATURE OF SUN'S PERTURBATION OF PERIGEE RADIUS AS A FUNCTION OF SPACECRAFT ORBIT ORIENTATION

a definite greater height. On the other hand, if the original alignment is perpendicular to the earth-sun line, the sun's effect produces perigees always lower than or equal to the initial perigee height. The effect of ratio of the orbit is shown in Figure 15, where it is seen that only the magnitude of the displacement is decreased as ratio decreases. The position of the spacecraft in its orbit at any time does not greatly affect the perturbation history since the direction of the sun changes only very little during any one revolution of the spacecraft in the orbit.

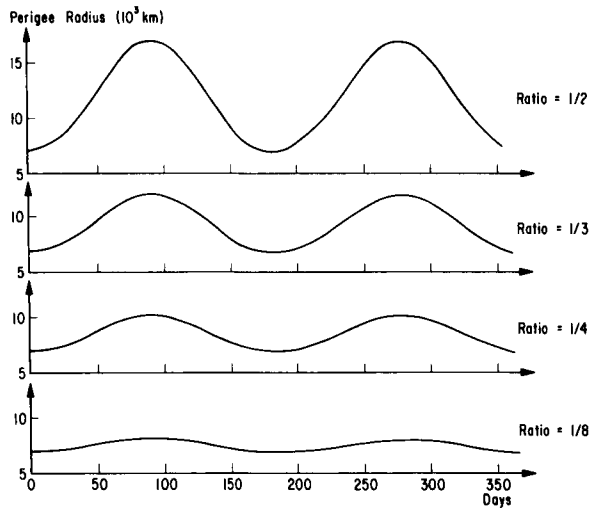

FIGURE 15. EFFECT OF ORBIT RATIO ON SUN'S PERTURBATION OF PERIGEE

In determining the effects of the moon on the spacecraft orbit, both the position of the spacecraft at any time relative to the position of the moon and the alignment of the spacecraft orbit relative to the major axis of the moon's orbit must be considered. As an example of this, we refer to the Lockheed effort. By the definition of the study, the spacecraft position is chosen so as to maintain large distances between moon and spacecraft. This is done by keeping the major axis of the orbit as far as possible from the earth-moon line at the times when the spacecraft is at apogee. Figure 16 illustrates this for two of the ratios by indicating the positions of the moon at the times of apogee of the spacecraft's orbit.

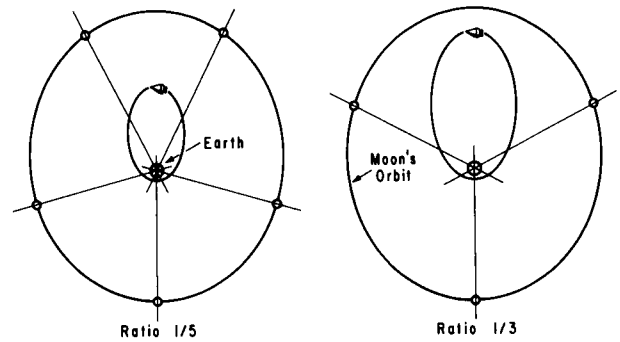

FIGURE 16. ORIENTATION OF ORBIT TO MAINTAIN DISTANCE FROM MOON (Positions of Moon Indicated at Times of Spacecraft Apogee)

The effect of the ellipticity of the moon's orbit appears as a function of the angle between the major axes of the moon's orbit and the spacecraft orbit as illustrated in Figure 17.

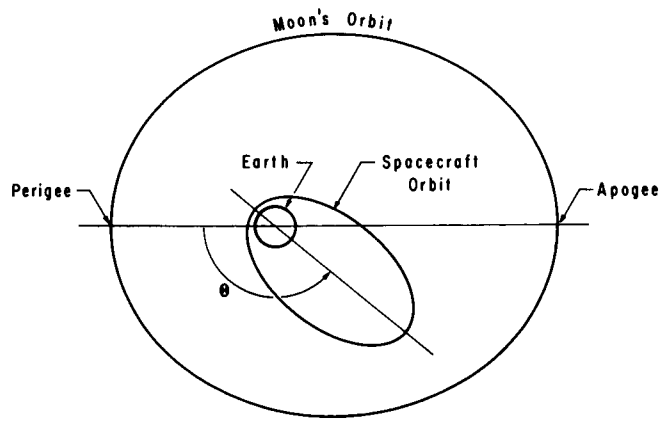

FIGURE 17. PRIMARY PARAMETER AFFECTING PERTURBATION OF SPACECRAFT ORBIT DUE TO ELLIPTICITY OF MOON'S ORBIT

The change of perigee radius as a function of the angle, θ, is illustrated in Figure 18, for the ratio

one-half orbit which avoids the moon.

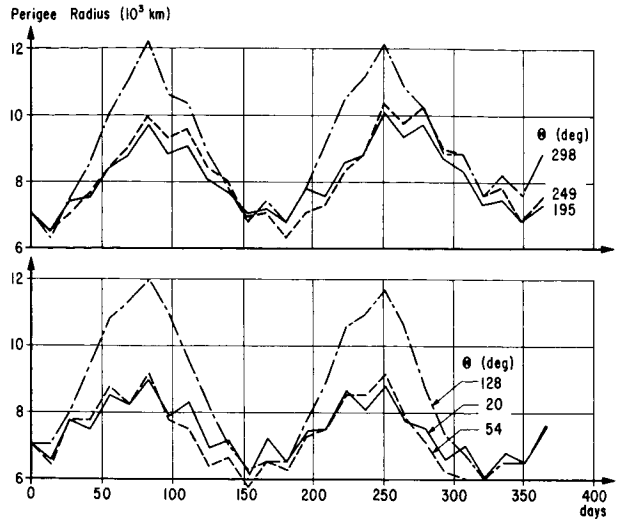

FIGURE 18. EFFECT OF RELATIVE ORIENTATION OF MAJOR AXES OF MOON'S ORBIT AND SPACECRAFT ORBIT

It is observed that for this case the lunar perturbation of perigee is generally always upward. The magnitude of the perturbation, however, is dependent on the angle, θ, with maximum upward displacement of perigee occurring for θ in the neighborhood of 120 degrees or 300 degrees.

Once the separate perturbations of the sun and the moon are known, the combined effect of the two on the spacecraft can be very well approximated by a simple addition of the two separate perturbation curves.

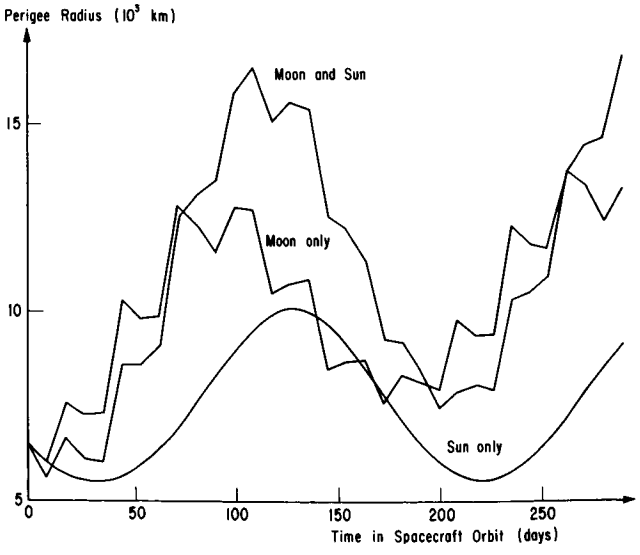

FIGURE 19. COMPARISON OF PERTURBATIONS BY SUN AND MOON SEPARATELY WITH PERTURBATION BY SUN AND MOON TOGETHER

The lower curve in Figure 19 is perigee history with only the sun acting on the orbit. The next higher curve is perigee history with only the moon acting. The third curve is the perigee history due to the actual effect of both bodies acting together. It is easily seen that this curve will be very well approximated by addition of the other two.

The launch windows for a mission using orbits of the type discussed here, then, must be chosen at times such that the orientation of the moon's orbit, the spacecraft orbit, and the position of the sun will produce upward or zero displacement of the perigee over the time interval desired.

SECTION IV. INTERPLANETARY TRANSITS

The major effort in astrodynamics research here, as in the national space program, is in the areas of lunar and cislunar orbits and the discussion has therefore been devoted primarily to these efforts. Nevertheless, a great deal of effort has been already made and is being continued into the areas of interplanetary trajectory study, and this deserves mention here. A "Study of Manned Interplanetary Flyby Missions to Mars and Venus" was recently completed by Advanced Projects Study Branch. The report contains an "in-depth" mission analysis study of manned interplanetary flyby missions to Mars or Venus during the 1970s using Apollo technology and hardware wherever possible. Because the planetary orbits are inclined to the earth's orbit, even though only by a few degrees, the trajectory geometry changes appreciably over long time periods. The time interval that must be studied to cover a representative number of all possible Earth-Mars transits is about 15 years. The opportunities to fly reasonably short flight time, low energy transits will occur each 2.2 years. For Earth-to-Venus transits the interval to be studied is about 8 years, and the applicable transit opportunities are available each 1.6 years. Work is being continued to expand the above study to complete these cycles.

Another project now in progress is the study of so-called swing-by trajectories for Earth-to-Mars flyby transits by way of Venus. This type of transit goes first to the vicinity of Venus, where that planet's gravitational attraction is used to turn the trajectory to Mars. It offers as the main advantage a much lower reentry velocity on the return trip to Earth than that occurring on a direct flight to Mars.

These and almost all studies of interplanetary flight use a "matched-conic" model to approximate the trajectory. This model assumes that flight between

two planets can be represented by a combination of three segments of conic flight or flight in a central force field. This model is illustrated in two dimensions in Figure 20.

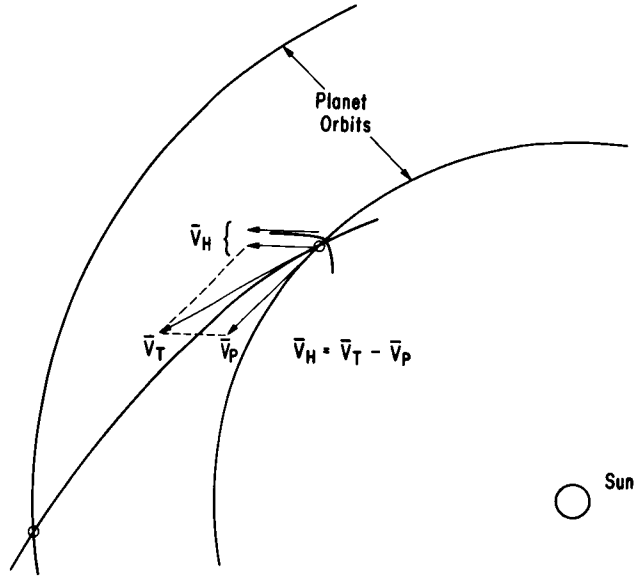

FIGURE 20. DETERMINATION OF HYPERBOLIC EXCESS VELOCITY VECTOR, $\bar{V}_H$

The trajectory in the region sufficiently distant from the planet so that the planet's gravitational attractions are negligible is taken to be an ellipse connecting the centers of the two planets and having the sun at one focus. The trajectory near the planet then is taken to be a hyperbola with the planet at one focus. It is then assumed that, at a distance so far from the planet that its gravitational attraction is negligible, the velocity vector ($\bar{V}_H$ on Figure 20) on this hyperbola is equal to the difference between the velocity vector relative to the sun ($\bar{V}_T$ on Figure 20) of the ellipse at its encounter with the planet and the velocity vector relative to the sun ($\bar{V}_P$ on Figure 20) of the planet at that time. This vector difference, therefore, is called the hyperbolic excess velocity vector and is used to define a hyperbola that represents the orbit near the planet.

The assumptions made in the construction of this model may seem rather gross; however, transits calculated in this manner are actually remarkably good approximations to the correct solution. On the other hand, when detailed study of a specific transit or family of transits is needed, for example, to determine guidance accuracy requirements to accomplish a mission, the exact equations of motion incorporating precise representation of the significant solar bodies, must be solved. The same is true when final analysis of earth-moon flights is necessary.

SECTION V. PRECISION TRAJECTORY PROGRAM

Neither the representation of the solar system or the solution of the equations of motion of a small body can be obtained except by numerical methods. The problem of assuring accuracy of these numerical solutions is another area of effort here. Dr. Hans Sperling of Aero-Astrodynamics Laboratory is now developing a computer program with which we hope to be able to compute realistic trajectories with the precision of the computation assured for 12 to 16 digits even over long transit times. To do this the method presently being considered incorporates integration of the differential equations of motion for all of the bodies to be included in the model as well as those for the spacecraft. The initial conditions for the integration of the equations are obtained from the best known ephemerides of the solar system. Integration of the motion of the model eliminates the problems of uncertain error magnitude introduced when ephemeris data are incorporated into a program by numerical interpolations from tabulated data. The entire system of equations is solved by a numerical integration technique using successive power series expansions.

At present these techniques have been employed in a computer program which includes four finite bodies and one massless body in the model. Three of the finite bodies are treated as point masses or homogeneous spheres. One oblateness term is incorporated in the gravitational function for the fourth body. This program is operational and can be used for some applications; however, many additional features such as triaxial shape of the moon, more oblateness terms for earth, and radiation pressure from the sun must be added to achieve the accuracy necessary for many projects. Work is continuing in this direction.

Only the highlights of the projects discussed were given here. Most of the details are available in the publications mentioned and in other published material from the various organizations involved.

SECTION VI. FUTURE EFFORTS

Future problems of astrodynamics include the natural continuation of the projects discussed plus several new areas. Perhaps the most urgent future problems are those concerning Voyager flights. Considerable detailed analysis of trajectory characteristics will be required in the layout of the actual flight to be chosen. Launch and injection windows will be determined, equations of cutoff conditions for the booster flight will be required, and methods of midcourse

correction maneuvers will be formulated.

In addition the search for more comprehensive description and classification of all orbits in the restricted three-body model will be continued. Investigation of the possibility of utilizing three-body trajectory behavior in interplanetary flight, in particular, simulating a transition orbit in the Mars-sun system or Jupiter-Sun system and thereby forming a round trip trajectory that includes several orbits of the target planet, has been initiated. Methods of evaluating the three-body trajectory behavior under the influence of perturbations of the solar system are also being continued. The mastery of problems such as these will be necessary before large-scale exploration of the solar system is possible.

BIBLIOGRAPHY

1. Herring, G. P.: A Comprehensive Astrodynamic Exposition and Classification of Earth-Moon Transits. NASA TM X-53151, Oct. 21, 1964.

2. Arenstorf, R. F.: Periodic Solutions of the Restricted Three-Body Problem Representing Analytic Continuation of Keplerian Motion. NASA TN D-1859, May 1963, and Am. J. Math., vol. 85, 1963,pp. 27-35.

3. Miele, A.: Theorem of Image Trajectories in the Earth-Moon Space. Boeing Sci. Res. Lab., Flight Sci. Lab., Rep. no. 21, D1-82-0039, Jan. 1960.

4. Causey, W. E.: Characteristic Features of Some Periodic Orbits in the Restricted Three-Body Problem. NASA TM X-53108, Aug. 17, 1964.

5. Modification of a Pegasus Spacecraft to Perform a Cislunar Mission. NASA TM X-53279, June 14, 1965.

6. Herring, G. P.: The Reduced Three-Body Problem: A Generalization of the Classical Restricted Three-Body Problem. NASA TM X-53088, July 16, 1964.

7. Wood, R.; and others: Study of Manned Interplanetary Fly-By Missions to Mars and Venus. NASA TM X-53055.

8. Bullock, Lamar E.: Conic Solutions to the Interplanetary Transfer Problem with Constant or Minimum Injection Energy. NASA TM X-53319, Aug. 16, 1965.

ADVANCED TRACKING SYSTEMS RESEARCH AT MSFC

January 27, 1966

by

Robert M. L. Baker, Jr.
Robert H. Benson
Howard Dielmann
John W. Harden, Jr.
Robert J. Hill
Grady H. Saunders

TABLE OF CONTENTS

ADVANCED SPACEBORNE DETECTION, TRACKING, AND NAVIGATION SYSTEM STUDIES

by John W. Harden, Jr.

LIST OF TABLES

LIST OF ILLUSTRATIONS

CONTENTS (Continued). . .

AROD TRACKING AND NAVIGATION SYSTEM

by Grady H. Saunders

LIST OF TABLES

LIST OF ILLUSTRATIONS

CONTENTS (Continued). . .

TRACKING, COMMUNICATIONS, AND ORBIT DETERMINATION FOR LUNAR SPACE VEHICLES

by Robert M. L. Baker, Jr., Robert J. Hill, Howard Dielmann, and Robert H. Benson

CONTENTS (Continued). . .

LIST OF TABLES

LIST OF ILLUSTRATIONS

ADVANCED SPACEBORNE DETECTION, TRACKING, AND NAVIGATION SYSTEM STUDIES

By

John W. Harden, Jr.

SUMMARY

Various combinations of navigation observables were investigated for their effect on the different phases of typical manned lunar missions and an earth space station rendezvous. The primary emphasis is on determination of accuracy required of onboard navigation sensors, such as devices for measuring range, angle, and range rate to distant bodies and beacons.

I. INTRODUCTION

The research discussed covers part of a continuing effort in the astrionics area. The overall effort is aimed at examining future NASA space missions to determine the requirements that will be imposed on hardware for these missions. The primary emphasis in this work was on the determination of accuracy requirements for onboard navigation sensors, including tracking devices. The missions assumed were a manned lunar mission similar to Apollo and an earth space station rendezvous. The following study plan was employed:

1. Problem Definition
   a. Fixed inputs
   b. Problem requirements
2. Analytical Solution
   a. Analytical operation on problem requirements
   b. Optimum solution to problems
   c. System description
3. Mechanization
4. Verification

The purpose of the first of the four steps is to pinpoint areas requiring research and technology development. Rather than assuming certain types of equipment operating in a proposed configuration, we took a general approach to determining system requirements. This approach defines the basic problems with respect to the goals to be realized, the constraints imposed by physical law and natural phenomena, and the possible mechanical solutions to the problem.

The second step, the analytical solution, generates an ideal nominal solution and provides parametric variations about nominal values. Only when the mechanization phase is reached do we study specific devices.

The mechanization studies result in a prototype design and verification studies are then performed as a test.

This method of organizing the work reveals the basic system problems requiring solution independent of mechanization and the need to develop new subsystems and devices that will significantly improve system performance.

The work was broken into the natural divisions afforded by the mission phases: midcourse, lunar parking and descent orbits, lunar landing, lunar ascent, and earth space station rendezvous. Each phase was treated independently of the others, except that requirements of each were set by working backward from a known end point. For example, the requirements of the first three phases were based on a required landing point accuracy.

II. MIDCOURSE PHASE

Figure 1 shows the model used for the midcourse phase of the work, based on a fixed time of arrival

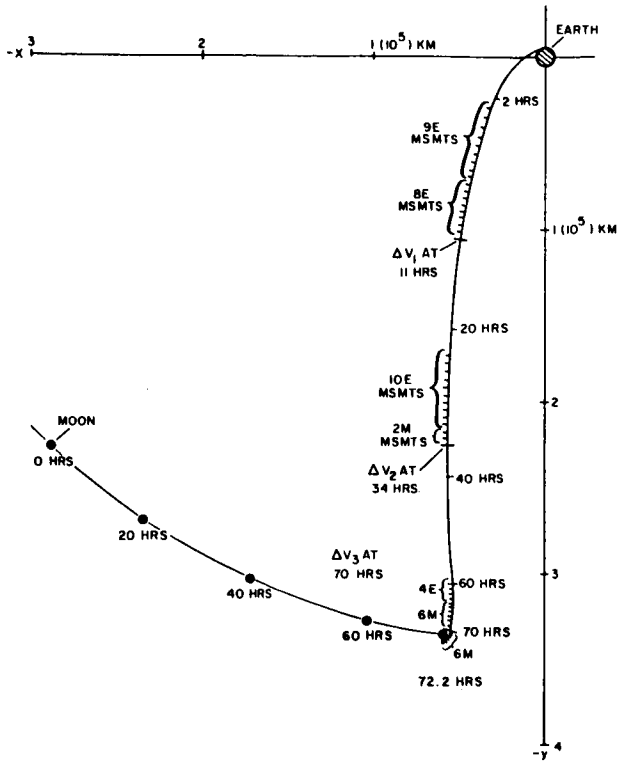

FIGURE 1. STANDARD MIDCOURSE GUIDANCE SCHEDULE USED IN STUDY

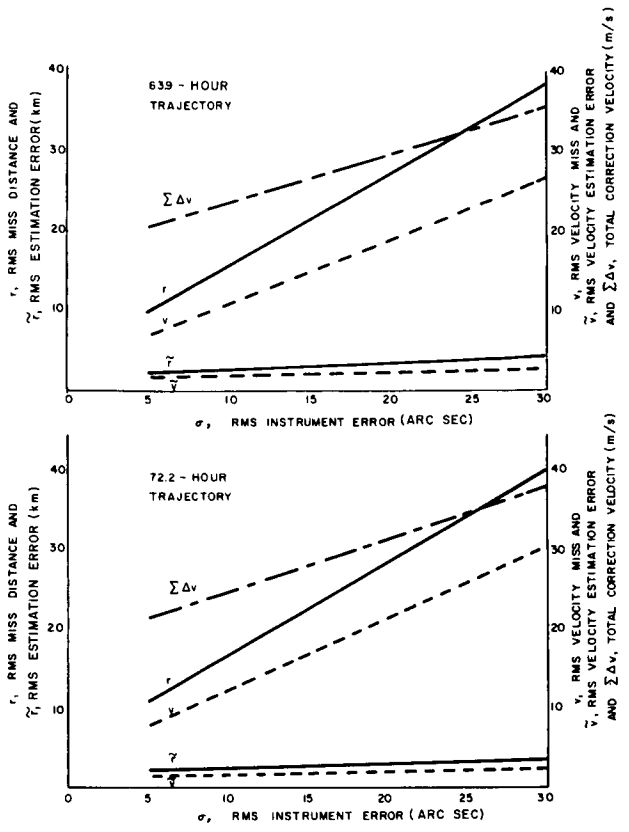

FIGURE 2. EFFECT OF SENSOR ACCURACY ON GUIDANCE SYSTEM PERFORMANCE (PERISELENUM RESULTS)

(FTOA) guidance scheme. The first tradeoff investigated showed that injection errors do not affect deviations or estimations of the end point, but the impulse required for the midcourse corrections increases in direct proportion to the injection errors.

The effects of navigation data accuracy on the desired final state at periselenum are shown in Figure 2. Angle measurements were the basic data considered. Relatively poor navigation data can be used without degrading the knowledge of state if a correspondingly large impulse is available. Timing errors of 0.1 and 1.0 seconds in taking the measurements were negligible. A similarly shaped curve results when the tradeoffs for errors in execution of the midcourse correction are considered. We can replace the horizontal scale with the correction error and draw a similar conclusion; namely, that accurate execution of the impulses is not required, but the impulse required increases with inaccuracy.

Landmark and horizon uncertainties affect terminal conditions (Table I). As shown, the actual deviations and impulse do not increase significantly, but the knowledge of state is degraded.

TABLE I. EFFECT OF LANDMARK AND HORIZON UNCERTAINTIES ON TERMINAL CONDITIONS

	r(km)	V(m/s)	$\tilde{r}$(km)	$\tilde{V}$(m/s)	$\Sigma\Delta V$(m/s)
Standard Errors	16.8	12.1	2.38	1.50	24.4
Doubled Errors	18.7	13.0	3.68	2.23	24.7

One of the most promising areas of improvement lies in ranging. A rather startling improvement in the end point deviations can be achieved by the addition of an onboard range measurement (Fig. 3). Five measurements taken over a 20-minute period before the third midcourse correction will give this improvement. The range is 16,000 km, and for optics, this means a disc measurement to 10 arc seconds.

Figure 4 shows the requirements that result if we range with pulsed microwave techniques. Power is shown as a function of range, with antenna diameter as a parameter. The use of earth-based tracking versus the various onboard techniques discussed does

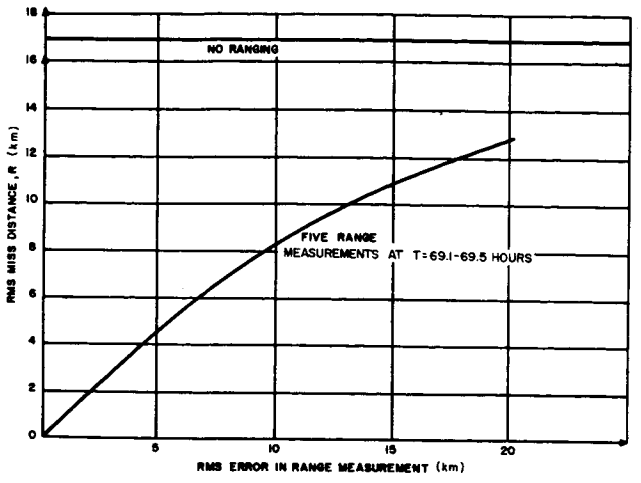

FIGURE 3. REDUCTION OF PERISELENUM MISS DISTANCE BY ADDITION OF FIVE RANGE MEASUREMENTS TO THE STANDARD SCHEDULE

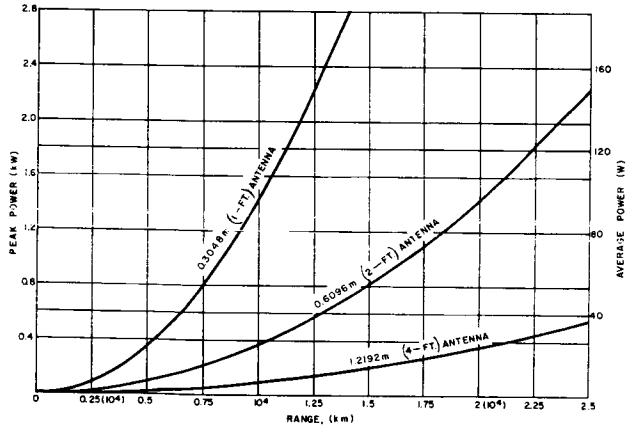

FIGURE 4. POWER AND DISH SIZE REQUIREMENT FOR RANGING OFF LUNAR SURFACE

result in more accurate state determination, but the overall system performance does not improve, since the final state accuracy is dictated by the velocity correction accuracy.

Some conclusions on midcourse are:

1. For observables, angles to the moon and earth, near in plane, give satisfactory results. No out-of-plane data are necessary.

2. In guidance, variable time of arrival (VTA) will give better performance than FTOA. The trajectory parameters such as mission time, plane orientation, and periselenum altitude do not significantly affect guidance system performance.

3. In data management, a system capable of solving for systematic as well as random errors proved beneficial since the contribution to error was of the same magnitude for both.

III. ORBITAL PHASE

Considered first in the orbital phase were the data processing procedures, observables, and allowable errors. Figure 5 demonstrates the most significant result in the data management area; i.e., the sensitivity coefficient used in the navigation computation procedure must be taken from the estimated orbit rather than from a nominal orbit, or the estimated position error grows monotonically.

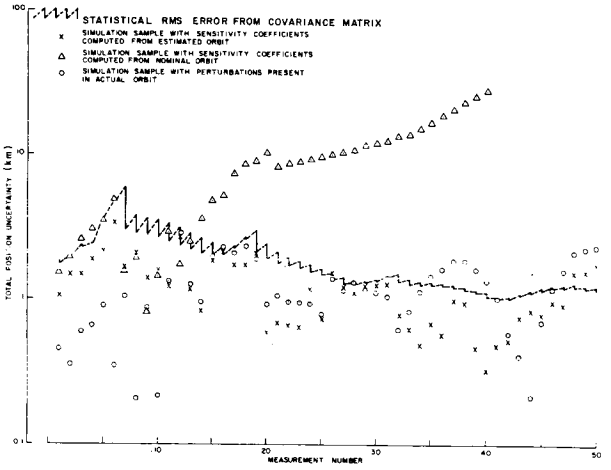

FIGURE 5. TOTAL POSITION UNCERTAINTY VERSUS TIME (CASES 1, 2, AND 3)

The navigation technique used was based on three stars and local vertical. Using two stars in or near the orbital plane and one near the pole of the orbit, with about 1 1/4-milliradian (3.5-arc minute) accuracy on the angular measurements and a two-minute measurement interval, will result in a satisfactory final state deviation at the end of the descent arc (Fig. 6). An interesting result demonstrated is the near linear relationship between miss distance and instrument error times the square root of the measurement interval.

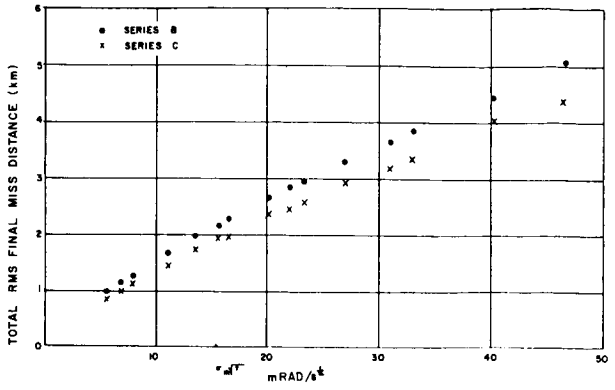

FIGURE 6. FINAL MISS DISTANCE AS A FUNCTION OF INSTRUMENT ERROR AND MEASUREMENT FREQUENCY

The major conclusions on the orbit and descent area are:

1. For observables, star-vertical measurements result in low requirements for data, power consumption, field of view, and ease of implementation. Altitude measurements give no appreciable improvement.

2. Final navigation errors are relatively insensitive to initial errors.

3. In data processing, the estimated orbit rather than a nominal must be used as a basis for all computation, and the approximation of a patched conic is suitable for representing the orbit. Biases and constants can be solved for with a noticeable increase in performance.

4. Timing uncertainties of up to a tenth second have little effect on accuracy.

5. FTOA guidance does not perform well from a fuel standpoint. VTA is noticeably better.

IV. LANDING PHASE

The landing phase begins at periselenum of the descent arc. The geometry of the situation is shown in Figure 7. Two types of navigation were assumed because of the possible observables of line of sight (LOS) range and angle to a beacon, and their rates; LOS range, and angle to a point on the lunar surface, and their rates; altitude and altitude rate; vehicle acceleration; and the direction of the local vertical.

The first type of guidance was beacon tracker, which used range, range rate, angle, and angle rate. The second was Doppler, which used altitude, angle of the LOS to the landing point, and two components of range rate to the surface in known directions.

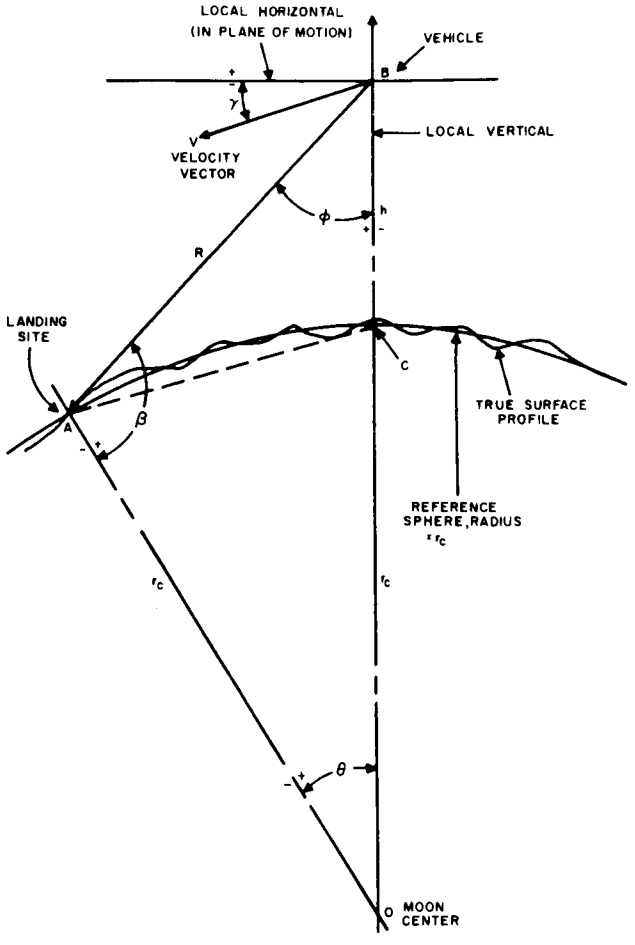

FIGURE 7. LUNAR LANDING GEOMETRY

We assumed a certain set of possible errors in each of these quantities and a possible range over which these were varied. Each error model included random and bias components and a proportional term. These errors were used in the two navigation schemes described. Terminal vertical position, horizontal position, and horizontal velocity were relatively insensitive to sensor performance. The terminal vertical velocity errors were significant, however. The greatest random error contribution to this was in the range and LOS angle measurements. The greatest bias error contributors were in range and range rate. For guidance, a gravity turn trajectory has certain advantages when begun at low altitudes. This advantage decreases and finally becomes negative as altitude increases.

In summary, range and angle measurements and range rate from the spacecraft to a beacon or the surface are the measurements in which improvement will give the greatest benefit.

V. LUNAR ASCENT

The lunar ascent phase (Fig. 8) was treated in two ways to establish the sensor specifications based on assumed launch position errors and a given error allotment in state at thrust termination. Three ascents were considered: minimum time, minimum energy, and parking orbit. The first two we call direct and the latter parking.

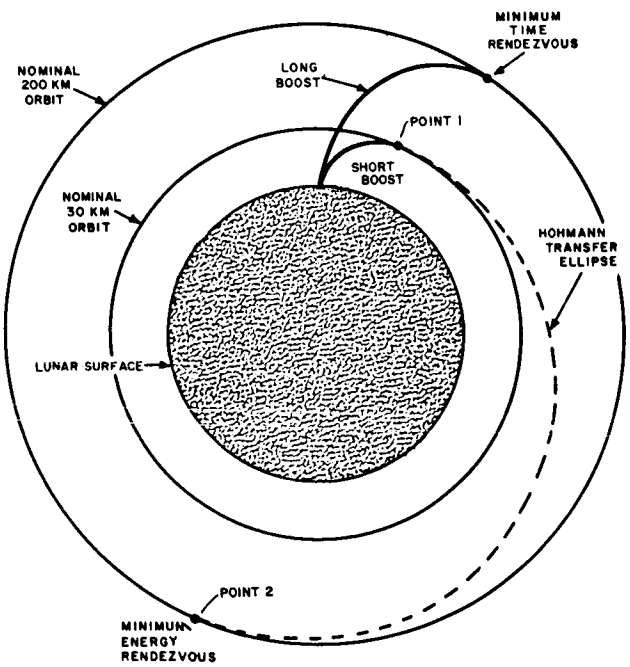

FIGURE 8. DIRECT ASCENT TO RENDEZVOUS

The sources that will contribute to ascent trajectory errors (Fig. 9) are selenophysical uncertainties and guidance error. Guidance error includes errors of sensors such as the platform, gyros, and accelerometers, as well as computation and thrust termination errors. The selenophysical uncertainties include all errors in the launch site position caused by oblateness, rotation effects, and gravity anomalies. The transfer errors are those that occur at terminal rendezvous because of the inaccurate injection.

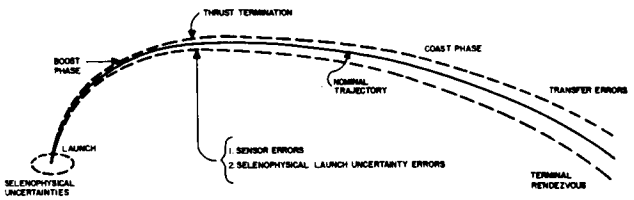

FIGURE 9. ASCENT TRAJECTORY

The criterion chosen for the error allocation was that the fuel requirements caused by injection errors should not be more than 20 percent over the nominal Hohmann case. This results in a requirement at injection of 1.4 km in position and 1.5 m/s in velocity (3σ).

Table II shows the amount of deviation that can be allowed in the guidance system. The resulting sensor requirements for meeting this allocation showed that the parking ascent places more severe requirements on the sensors primarily because of time. However, these requirements can be met with existing techniques and equipment.

TABLE II. 3-σ ERRORS AT THRUST TERMINATION (30 KM)

Errors	Position (km)	Velocity (m/s)
Guidance System	0.131	1.264
Selenophysical	1.380	0.598
Guidance Plus Selenophysical	1.383	1.398
Total Allowable	1.400	1.500

VI. LUNAR ORBIT RENDEZVOUS

The sensor accuracy requirements for the lunar orbit rendezvous are determined for observing target motion in terms of range, range rate, and angular rate of the line of sight.

The guidance used in the terminal rendezvous is shown in Figure 10. In essence, the line of sight between the chaser and target vehicles is controlled

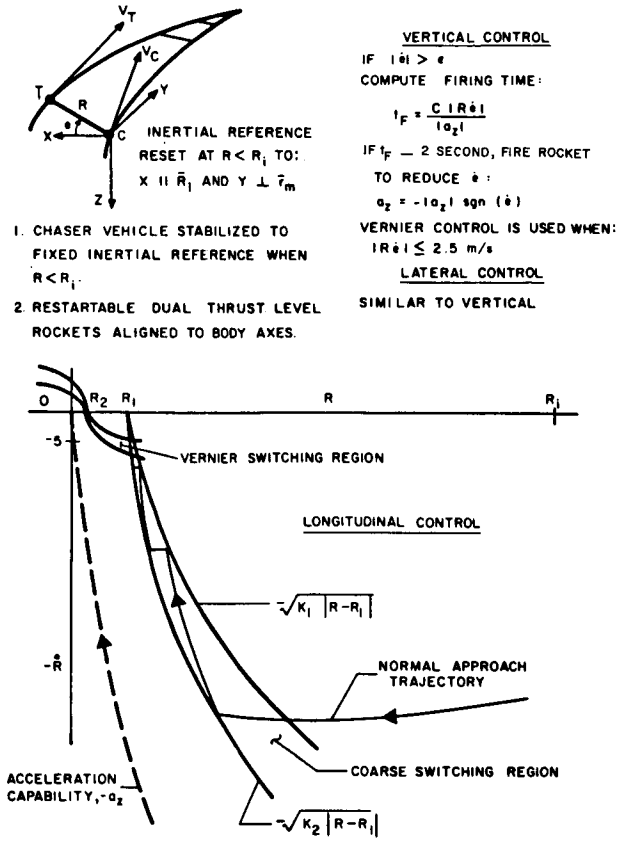

FIGURE 10. RENDEZVOUS GUIDANCE (LUNAR ORBITAL RENDEZVOUS)

to a low rate and range rate is controlled within a band as a function of range. The band of range rate versus range is determined from the dispersions that occur after the transfer from the lower orbit.

Table III gives the injection sensor requirements for successful accomplishment of lunar orbit rendezvous as determined during the launch phase study. Table IV shows the corresponding sensor requirements for accomplishing the rendezvous. The requirements outlined in Tables II and III are within reach of current technology.

VII. EARTH BASED RENDEZVOUS

The earth based rendezvous phase was treated much the same as the lunar case. Six combinations of observables were investigated: range and range rate; angle and angular rate; range and angle; range rate and angle; range, range rate, and angle; and range, angle, and angular rate. The best combination of three observables turned out to be range, range rate, and angle. The best combination of two was range and range rate.

TABLE III. INJECTION SENSOR REQUIREMENT

Quantity Measured	Dynamic Range		Max Allowable rms (1σ) Sensor Error
	Max	Min	
Altitude	+40 km	0	0.93 km
Incremental Velocity	+50 m/s	0	0.17 m/s
Pitch Angle	+90 deg	-90 deg	1.7 deg
Yaw Angle	+180 deg	-180 deg	7.4 deg
Range	+500 km	0	0.86% of R
Inclination Angle	+5 deg	-5 deg	0.27 deg

TABLE IV. RENDEZVOUS SENSOR REQUIREMENTS

Quantity Measured	Dynamic Range		Max Allowable rms (1σ) Sensor Error
	Max	Min	
Range	30 km	0	1.1% of R or 11 m
Range Rate	+10 m/s (opening)	-50 m/s (closing)	0.55 m/s
LOS Angular Rates	2 m rad/s	-2 m rad/s	0.55 m rad/s
Vehicle Attitude (Pitch, Roll, and Yaw)	+180 deg (yaw) +90 deg (pitch & roll)	-180 deg (yaw) -90 deg (pitch & roll)	0.2 deg firing period (to reduce cross-coupling) 5 deg during tracking (vehicle may change attitude to accommodate LOS angle limits)

The results of the earth phase rendezvous were similar to the lunar rendezvous and showed that present capability is sufficient to perform the task. Improvement in basic sensors would significantly decrease fuel requirements. The major saving would come through decreasing random and bias errors in range, range rate, and angle.

VIII. CONCLUSIONS

Work similar to this has been done on an unmanned lunar landing and is continuing in the area of interplanetary flight. For the interplanetary work, a manned Mars mission similar to this is assumed, except that the landing phase is excluded.

These efforts lead to research in those areas where current technology is not sufficient to handle the job. Among the areas of research discussed here, probably the most critical is range measurement from a spacecraft to a planetary body over long ranges. Second, improvement in range, angle, and range rate from a spacecraft to a beacon on the surface of the moon will give improvement in landing accuracy. Third, a fairly sophisticated onboard data management system is required.

N67-30598

AROD TRACKING AND NAVIGATION SYSTEM

By

Grady H. Saunders

SUMMARY

An advanced range and orbit determination (AROD) system is an advanced vehicle-based radio navigation and tracking system providing accurate position and velocity data onboard the vehicle in near real time and capable of operating with simple unattended ground stations. The system concept, design, and principles of operation of the tracking equipment are described. A description is given of the method of computing vehicle position and velocity from the measured data. Finally, the expected system performance and the sources of error in the system are given.

The AROD system is being developed by the George C. Marshall Space Flight Center. The development program is conducted under the sponsorship and direction of the Office of Tracking and Data Acquisition, National Aeronautics and Space Administration, Washington, D. C.

I. INTRODUCTION

Development of an advanced range and orbit determination (AROD) system and research and development on electronically steered antenna arrays that have application to AROD are discussed. AROD is a radio navigation and communication system that determines position and velocity of launch and space vehicles from data supplied by a vehicle-based tracking system using transponders on the ground, in satellites, or in other locations controlled by signals from the vehicle-borne system. The program is experimental with no specific mission requirements. It has been funded on the basis of possible uses in manned space flight and other future missions.

The objectives of the program are (1) to implement a system concept that will give the maximum utilization and effectiveness in the integration of tracking and communications, (2) to exploit the full potential of a radio system as an integral part of the navigation and guidance schemes for space and orbital missions, and (3) to reduce the cost and complexity of ground facilities. The objectives are most nearly approached by the use of the vehicle-based system with equipment designed to meet general requirements and options in equipment to satisfy the more specialized mission requirements.

AROD has the basic capability and flexibility required for use in all phases of a variety of missions. It can be used with inertial and other systems for active guidance and navigation for manned or unmanned vehicles, and it can be used for evaluating vehicle performance. With tracking data, time reference, and system control in the vehicle, transponders may be located in remote unattended locations without restraints as to location geometry or interstation communications. With freedom to operate with transponder stations of various capabilities, the system can be operated in any one of several modes without basic change to the system. To take advantage of that flexibility and to provide for the optimum integration into space and launch vehicle systems, the vehicle-borne system is planned as a basic system with optional features to fulfill particular needs. Compatibility with other radio systems and use of the equipment for other communication purposes was an important consideration.

Position and velocity output of AROD is in near real time. The lag in time between an event and the readout or display of the data is less than 0.5 second, and it can be reduced to less than 0.1 second if the need for the smaller time lag should exist. Events are identified in relation to time within 10 microseconds. Position and velocity can be computed in the vehicle by an AROD data processor or by a shared multipurpose data processor. In addition, or as an alternative to processing the tracking data in the vehicle, it can be transmitted over the AROD control or tracking link to the ground for processing. Position and velocity can be expressed in any coordinate system by use of the appropriate transformations in the computation program.

The concept of AROD as an integrated vehicle radio navigation and communication system is illustrated in Figure 1. The major elements are the radio tracking system, the system control, and the data processor. Options in equipment provide for adaptability to specific missions and for sharing the use of equipment such as the computer, communication channels, data displays, etc., with other vehicle-borne systems.

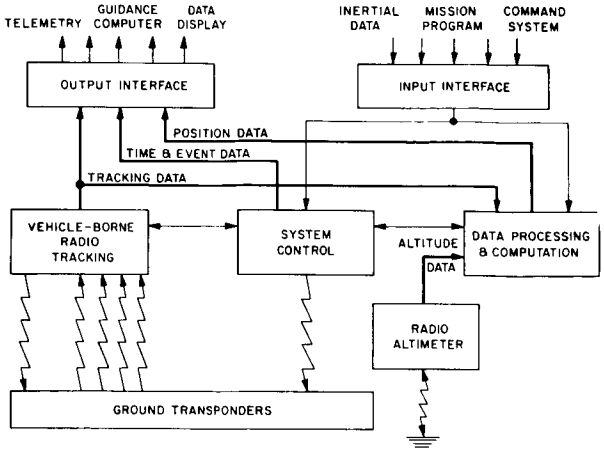

FIGURE 1. INTEGRATED VEHICLE RADIO NAVIGATION AND COMMUNICATION SYSTEM

The radio tracking section of AROD is the essential element common to all options unmodified, except for provisions for different modes of operation. The altimeter function represents optional separate equipment at this time; however, as indicated by the present state of development, the altimeter function can be incorporated into the basic tracking system by relatively minor design changes. The incorporation is expected to be accomplished with the first design revision.

The vehicle-borne tracking system can communicate simultaneously with four transponder stations (Fig. 1). Simultaneous tracking data from four stations enable the system to determine the position of a transponder on the ground or in another vehicle or spacecraft under certain conditions. This capability is expected to be used for locating remote transponder sites and for refining the determination of the position of all transponder sites. The redundant tracking data available permit the refinement and checking in near real time of the vehicle position. In addition to the tracking function, all radio links, both vehicle-to-ground and ground-to-vehicle, lend themselves to other communication uses such as voice, telemetry, or command. This use can be accomplished by modulating such signals on the carriers without disturbing the tracking operation.

The control section of the vehicle-borne system controls the functioning of the vehicle-borne tracking system, the data processor, and other AROD vehicle-borne system functions. It also controls the operation of the ground transponders. The vehicle, mission, and degree of integration of vehicle systems determine the number of control functions; therefore, options are required in the system control. A VHF station control link from the vehicle to the ground provides a communication channel for control of the transponders. Transponders are placed into operation as required and as scheduled by the vehicle-borne system control. The VHF link is needed only when rapid acquisition of transponders is required; otherwise, control can be exercised through the S-band tracking channel.

The data processor processes the radio tracking and altimeter data and computes vehicle position and velocity. Provision is made for supplementary use of position, velocity, and acceleration data that may be available from inertial or other vehicle-borne systems external to AROD. The use of the AROD computer is optional. Some mission requirements can be satisfied by transmitting the tracking data and other data to the ground for processing; in other cases, a vehicle-borne computer external to AROD can be used, leaving only signal processing and programing to be performed within the system.

Equipment for a feasibility demonstration model of the AROD tracking system is currently under development. The demonstration model, consisting of a vehicle-borne tracking system and three ground transponders, was delivered in November 1966. It will be subjected to laboratory tests, including investigations of the characteristics of the system under simulated spaceflight conditions. The test operation will be concluded with an operational demonstration using aircraft. An inflight experiment is planned to determine the operational characteristics of the system under spaceflight conditions and to demonstrate the capability and suitability of the system for a variety of missions and uses. When the test program on the demonstration model nears completion, construction of flight qualified equipment for the inflight experiment could begin (probably in April 1967). The latest developments in theory and techniques have been used in the feasibility model. Significant advances in microminiaturization made in recent years have been used in the vehicle-borne system. Although maximum use of such techniques

could not be made because of the necessity of retaining design flexibility and accessibility, a high degree of microminiaturization and use of integrated circuitry were necessary to attain a feasible system. Another step in the miniaturization of the vehicle-borne system will be taken in the construction of flight approved equipment. Greater reliability and reduction in overall costs are definitely shown as a result of microminiaturization and the use of integrated circuitry in developing the demonstration model.

The functions of the AROD data processor have been duplicated on general purpose computers and data processing equipment, and the design problems have been analyzed. Results show that no development program for the data processor is needed. When a flight prototype is required, it will be designed and packaged in conformance with the design and packaging developed for system control. The functions of system control are drastically reduced when the data processor is incorporated as an option, since many of the functions performed by system control in the basic system can be performed by the required operations of the data processor.

The present AROD system concept is a result of progressive development in the study of tracking and navigational problems originally encountered in the Jupiter and Saturn programs. In the earlier phases of system definition, emphasis was placed primarily on satisfying requirements for evaluating launch vehicle system performance and for vernier guidance of space and orbital injections. Later work has been concerned with other potential applications compatible with the utility and growth potential of a system based on the AROD concept.

An independent feasibility study of the tracking system was initiated in July 1962. This was followed by a design study, now completed. The present development of a feasibility demonstration model of the vehicle system and three transponders was completed in October 1966, and the following test operation will be completed in April 1967. One experimental antenna system for the transponder will be available for the test operation. Prototype transponder antennas may or may not be available for the inflight experiment. In case the prototype antennas are not available, one transponder station will be equipped with the experimental antenna system and other stations will be equipped with test antennas.

Other work on the AROD program now in progress or planned includes investigating the feasibility of using ocean-borne and satellite-borne transponders to determine the suitability for power sources for remote unattended stations, and optimum methods of data processing. Implementation of the inflight experiment and applications of AROD techniques to a wide range of navigation and tracking problems are being studied.

II. DESCRIPTION OF TRACKING SYSTEM

The tracking system was designed to meet maximum requirements for range and range-rate data such as that for injection, orbital transfer, and possible emergency situations in both manned and unmanned orbital and space missions. In many instances, accurate position and velocity data are essential at times when tracking conditions and tracking geometry are unfavorable; therefore, somewhat less than ideal tracking conditions were assumed.

In some cases, the high data rate available to meet the maximum requirements is not essential. For example, when the vehicle is in free fall or in powered flight where the forces acting on the vehicle are assumed sufficiently well known, position and velocity can be established and predicted for a given time from much less data than that required to give an independent determination from real time tracking data only. Some missions can possibly be satisfied with range and range-rate data from one or two stations, perhaps at infrequent intervals. In that case, suitable options in vehicle-borne equipment would yield some savings in weight and power consumption.

The range measured to a transponder is the two-way transmission path from the vehicle to the transponder and return. The distance to the transponder from the vehicle is determined as one-half the double path distance after corrections have been made for movement of the vehicle during the transit time of the signal. Range rate is determined from the Doppler shift of the carrier for the two-way transmission path, the range rate of the vehicle being determined as one-half of the corrected double path range rate. Corrections to range and range rate for movement of the vehicle during the transit time and other corrections, such as those needed to account for the difference in the earth's velocity between transponder sites, are performed in data processing.

Figure 2, a block diagram of the tracking system, illustrates the relations between elements of the vehicle-borne system and elements of the transponder.

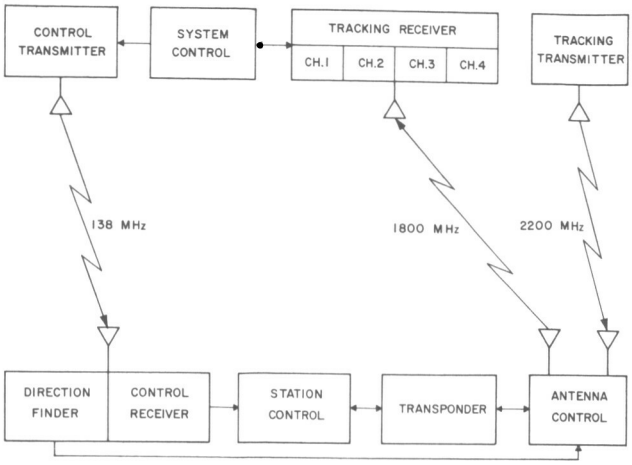

FIGURE 2. BLOCK DIAGRAM OF THE TRACKING SYSTEM

As shown in the diagram of the vehicle-borne system in Figure 3, all frequencies and time signals used in the vehicle system are derived from a single source.

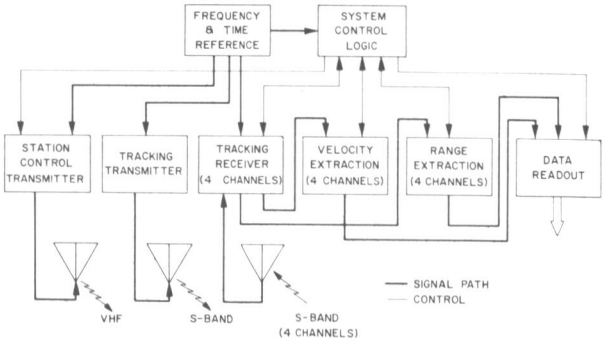

FIGURE 3. BLOCK DIAGRAM OF THE VEHICLE-BORNE SYSTEM

Drive signals for the tracking transmitter and the timing unit, heterodyne frequencies for the receiver channels, Doppler reference frequencies, etc., are coherently synthesized from a single frequency provided by the crystal-controlled master oscillator. Operations throughout the system are synchronized with this source.

The tracking transmitter and a four-channel tracking receiver are duplexed into a single antenna which radiates the tracking signal to all transponder stations within range of the vehicle. Transmission from the vehicle is in the frequency range of 2200 to 2300 MHz with an approximate bandwidth of 16 MHz. Each transponder station can operate on any one of four frequencies in the range of 1700 to 1800 MHz. The frequency on which a transponder transmits is controlled by the vehicle-borne system and is determined by the availability of receiver channels. Thus the vehicle-borne system can perform tracking operations with four transponders simultaneously. Figure 4 shows a vehicle-borne system mounted on a laboratory test fixture.

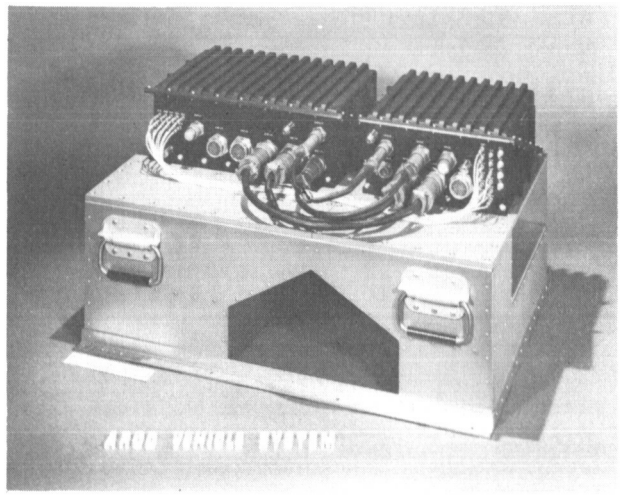

FIGURE 4. PHOTOGRAPH OF THE VEHICLE-BORNE SYSTEM MOUNTED ON A LABORATORY TEST FIXTURE

The transmitter is biphase modulated by a PRN-coded tracking signal composed of a low speed and a high speed code, which is designed to reduce the frequency and time search required for acquisition and to give reasonable protection against incidental interference. The usual acquirable codes were ruled out because of the high Doppler rates and the undesirable spectral properties which increase intermodulation problems. The high speed code rate is 6.4 MHz, which is the basic clock frequency in the vehicle-borne transmitter, and the low code rate is 1/511 that of the high speed code. The autocorrelation function of the signal with both codes applied is shown

in Figure 5. The power spectral density of the signal, which is approximately the sum of the separate spectral densities of the two codes, is shown in Figure 6. The effective bandwidth of the high speed code is essentially 6.4 MHz and that of the low speed code is 12.5 kHz.

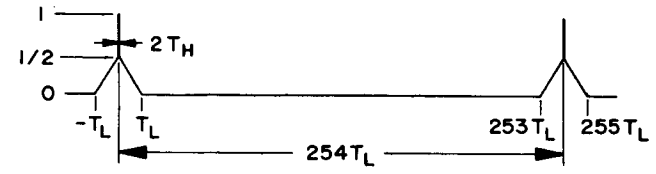

FIGURE 5. AUTOCORRELATION FUNCTION OF THE COMBINED HIGH AND LOW SPEED CODES

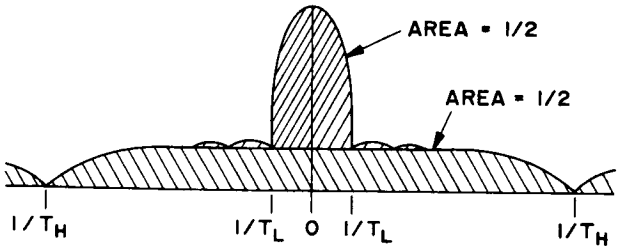

FIGURE 6. POWER SPECTRAL DENSITY OF THE SIGNAL WITH THE HIGH AND LOW SPEED CODES APPLIED

Both codes are transmitted from the vehicle-borne transmitter at all times, but only the low code is retransmitted from the transponder during the signal acquisition period to reduce acquisition time in the vehicle. The correlation function for the low-code-only signal is shown in Figure 7. After the transponder signal is acquired by one of the channels of the vehicle-borne receiver, the high speed code is applied to the transponder modulation and the return transmission becomes the same as the downlink. Because aid in acquiring the signal from the vehicle is provided in the transponder by the control link, removal

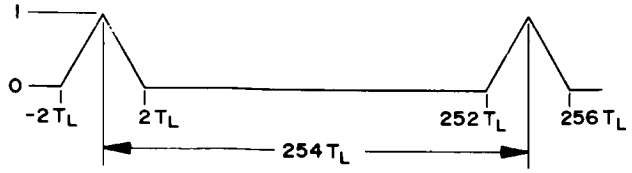

FIGURE 7. AUTOCORRELATION FUNCTION FOR THE LOW SPEED CODE ONLY

of the high speed code from the vehicle transmission is not necessary during the acquisition period. The low speed code could be removed from both links after the signal is acquired, thereby increasing the efficiency, but leaving it on facilitates reacquisition in case of a momentary dropout of the signal.

The use of the same code on all four channels assures that the signals between transponders will be uncorrelated because of differences in range and Doppler shift. Additional reduction in cross correlation and cross modulation is obtained by separating the channels in frequency by twice the expected maximum Doppler frequency shift. Thus rejection of a signal from a second channel has the advantage of the effective noise bandwidth of the high code. During acquisition, the problem is more complex and to some extent depends upon the rejection afforded by differences in Doppler, narrow bandwidths in the receivers, and offset carrier frequencies.

The station control section of the vehicle-borne system controls the operation of the transponder stations through the station control transmitter, which operates in the frequency range of 135 to 140-MHz. Initially, all of the transponder equipment is off, except for the part of the station control receiver necessary to permit activation of the transponder from the vehicle. The station identifications and the criteria for terminating operations with each transponder station are stored in the station control section on the vehicle. The stored station identifications and the termination criteria can be changed while the vehicle is on the launch pad either by hardwire link or through a communication channel on the tracking link. The station program can be changed after launch by command transmitted over the tracking link or by a communication channel external to AROD.

The stations are programed in the order in which they are to be used. Alternate stations are programed if the importance of the data from a given prime station warrants the inclusion of an alternate station in the program. Operation with a transponder station is terminated when the vehicle reaches a predetermined range from the station, or if the data are processed on the vehicle, when a predetermined elevation angle or degree of geometrical dilution is reached.

The data readout section presents range and range-rate data from the four receiver channels simultaneously at intervals of 0.25 seconds. The time of measurement and the identifications for the transponder stations are also presented along with each set of range and range-rate data. Characteristics of the data output are given in Table I. Interface buffers are used between the readout and external

nonsynchronized telemeter or data processors when they are required. Timing signals accessible externally are nonambiguous over a five minute period.

TABLE I. CHARACTERISTICS OF DATA OUTPUT

Item	Number	Readings/s	Bits/Reading	Bits/s
Range	4	16	24	384
Range Rate	4	16	21	336
Time	1	4	25	100
Station Identification	4	16	4	64

The transponder system includes unattended transponder stations and other compatible facilities as required to meet particular mission requirements. Minimal equipment costs and flexibility of installation of unattended transponders make the placement of transponder stations to meet the requirements of a single mission feasible and practical. Transponder stations can be distributed as dictated by mission requirements and by geographic and topographic constraints. A particular pattern of geometry of station locations is not required. Likewise, the choice of sites is not limited by the availability of ground communications and data reference links, nor by many of the construction and facility problems associated with the usual ground-based system.

Unattended stations are placed in operation by control signals transmitted from the vehicle over a VHF communication link. Only that part of the VHF receiver needed to receive the initial turn-on signal is active while the station is in the off condition. The transponder VHF antenna is incorporated into a direction finder which determines the direction from which the vehicle signal arrives and thus gives the direction for pointing the S-band tracking antenna. Other means of initially turning the transponders and pointing the antennas may be used. A ground communication channel may be used if available, or a special HF or LF link may be used in cases where it may be advantageous, or transponders may be turned on by signals from satellites. Ideally, complete control of the transponder would be exercised by use of the same RF link as that used for tracking, and it is feasible for short ranges for which nondirective S-band antennas could be used. For longer ranges, a spatial search with a directive transponder antenna could be made to acquire the signal from the vehicle, but the periodic search necessary to acquire the initial turn-on signal is incompatible with fast acquisition of low altitude, high velocity vehicles.

The unattended transponder station is shown in Figure 8. The major elements of the tracking section are an electronically steered antenna array, a coherent receiver, a frequency translator, and a transmitter. A correlating signal generated in the transponder provides for coherent detection of the vehicle tracking

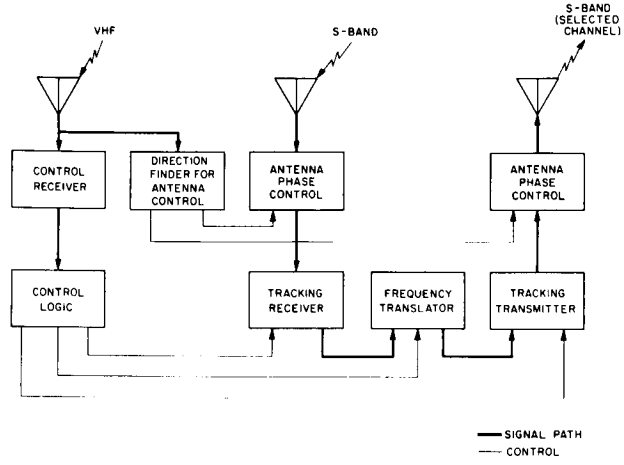

FIGURE 8. BLOCK DIAGRAM OF THE UNATTENDED TRANSPONDER

signal and furnishes a coherent carrier at one of four return frequencies with modulation synchronized with the received range modulation. Acquisition of the tracking signal from the vehicle is aided by using the Doppler shift that appears on the VHF control link to compensate for the Doppler shift on the incoming tracking signal. A signal transmitted over the control link aids in synchronizing the transponder correlating signal with the received range modulation. The initial transmission from the transponder is modulated by the low speed code only and is compensated for Doppler shift by means of the Doppler shift estimate, thus aiding the vehicle-borne receiver in acquiring the returned signal. The high speed code is added after the vehicle-borne receiver has acquired the initial signal from the transponder.

The control section of the transponder consists of the direction finding antenna, a control receiver, and a control unit containing the logic and circuitry needed to decode communications from the vehicle system and exercise control of the transponder as ordered from the vehicle system. The relatively large antenna aperture with low directivity resulting from the

use of VHF for the control link allows it to be used in a direction finder to point the tracking antenna in the approximate direction of the vehicle, thus permitting moderate directivity in the tracking antenna without requiring spatial search to acquire the tracking signal. The tracking antenna is steered by phase switching controlled by digital information from the direction finder.

Verification of certain actions and events in the transponder, such as receiver locked, transmitter Doppler shift compensated, etc., is transmitted to the vehicle over the tracking link.

An unattended transponder station installation is shown in Figure 9. The VHF control and direction

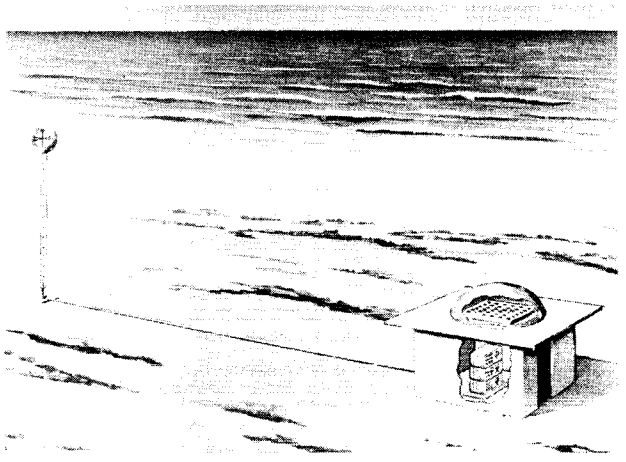

FIGURE 9. PICTORIAL REPRESENTATION OF AN UNATTENDED TRANSPONDER

finding antenna is on the mast at the left; the prefabricated hut on the right, which can be bolted together on the site, contains the transponder. The tracking antennas are enclosed in a weatherproof bubble on the metal roof that serves as a ground plane for the antennas. The physical arrangement of the station depends somewhat upon the type of power source used. With a solar cell power source the solar cells would be mounted on a surface similar to the roof of the transponder enclosure and enclosed in a bubble. The structure could be supported by the walls of an enclosure or by posts. The storage batteries associated with the solar cell power source could either be placed in the enclosure with the transponder or in an enclosure under the solar cells. The preferred placement of the solar cell structure would be to the right of the transponder and in line with the transponder and the VHF antenna at approximately the same height as the tracking antennas.

The weight and size of any section of the transponder station is limited to that which can be carried and installed by two men. The station plan minimizes the need for site preparation such as grading and clearing of vegetation. At sites where it might be needed, the soil would be treated to retard the growth of vegetation. Transponders can be placed on satellites, space vehicles, etc.; thus the physical construction of the transponder corresponds to that of the vehicle system rather than that of the unattended ground station. Weight and power for a satellite transponder, as compared with a ground station transponder, would be drastically reduced.

III. DESCRIPTION OF OPERATION

Operation is started at launch or at some predetermined time or event established by mission requirements. When the vehicle-borne system begins operation, all transponder stations within range of the vehicle are placed on standby by a signal transmitted over the VHF control link. The stations on standby are completely activated except for the transmission of a return signal to the vehicle. Each activated station acquires the vehicle tracking signal by determining the direction of arrival of the control signal, pointing the tracking antenna, and performing the signal lock operation in the receiver. Excitation for the transmitter is generated, but no signal is radiated until an order to "on," directed to a specific station, is received.

Stations are ordered "on" as scheduled in the station program stored in system control. The "on" order includes instructions as to which of the four channel frequencies is to be used. The initial transmission from the transponder is compensated for Doppler shift, based on the estimation made in the transponder system, so that it arrives at the vehicle at approximately the rest frequency of the selected receiving channel. Thus the vehicle-borne system is aided in acquiring the returned signal without extensive frequency search.

When the returned signal is acquired, a "track" order is issued to the transponder station. The Doppler shift compensation in the transponder is then removed and the returned frequency is swept at a regulated rate to a frequency coherent with the frequency of the signal received by the transponder. When the coherent condition is achieved, the high speed code is applied verifying the returned signal coherency to the vehicle-borne receiver. Tracking

begins after the high speed code is applied by the transponder and correlated by the vehicle-borne receiver. If the signal is lost by the vehicle-borne system during the frequency sweep, the transponder is ordered back to "on" and the acquisition cycle is started again. When the vehicle reaches the range limit stored in the system control for a particular station, tracking with that station is terminated and the station is ordered back to "standby." The next scheduled station is ordered to "on" and its acquisition is started. The terminated station is timed to go "off" in a short time after returning to "standby."

After a number of trials at acquiring stations, if a particular station does not respond, the alternate for the nonresponsive station is acquired. If no alternate exists, the program is advanced to the next station in the sequence. In those instances when the vehicle may be out of range of any station for a time, a sequential search is made for the unused stations of the program, four at a time, until a station is acquired. The program is then continued in the normal manner from that point.

IV. DETERMINATION OF POSITION AND VELOCITY

An independent real time determination of position requires tracking data from a minimum of three stations or two stations and an altimeter. The ability to determine position and velocity during critical phases of a mission is assured by the use of four receiving channels on the vehicle that enables the vehicle-borne system to obtain range and Doppler shift data with respect to three stations while a fourth station is being acquired. With a full complement of transponder stations within range of the vehicle, data from four stations will be available except for short periods when tracking with one station has been terminated and a replacement is being acquired. This transfer of tracking from one station to another requires not more than 2.5 seconds when the station being acquired is near maximum range. Stations at closer range or higher antenna gain will be acquired more rapidly than unattended stations.

This abundance of tracking data will not be available at all times, either because it is not necessary or because suitably locating the stations may be impossible physically or prohibitive in cost. Under conditions where tracking data are received intermittently from one to four stations, and insufficient real time data are available to determine a position, an obvious recourse is to extrapolate the vehicle position based on previous tracking data and the best available information on the dynamics of the vehicle. The extrapolation can be verified by tracking data from one source or more rapidly from two sources.

In some cases there may be advantages in locating transponder stations so close together that they constitute a range and angle measuring system (interferometer). As with any angle measuring system, the angle resolution depends upon the distance between stations, the accuracy with which station locations are known in relation to each other, the accuracy with which the transponder delays are known, and the phase or range resolution of the system. Correct time correlation between stations is inherently assured by the common time based for all channels on the vehicle.

Various conditions of operation and choice of options in the vehicle-borne system do not require changes in design or differences in operational methods in the vehicle-borne tracking system. The sectionalized construction allows the option of excluding sections of equipment and in some cases permits a choice of functional parameters such as power level of the tracking transmitter. As an example, if Doppler velocity information is not required, the equipment can be placed in a smaller package with the complete range-rate readout section excluded. If only one tracking channel is needed, three tracking channels, three range readout subsections, and three range-rate readout subsections can be omitted in addition to sections in the system control associated with the three excluded channels. The tracking system is designed to gather tracking data in an optimum manner, and its function is defined once the choice of options in equipment is made. The adaptation to specific point-to-point difference in the operating conditions, such as variations in the number of stations available, the amount and type of data available, etc., is a function of the data processing.

The tracking geometry associated with the determination of position from range data is shown in Figure 10. The quantities measured and made available for processing at a given time are the double path distances S_1, S_2, S_3, and S_4 to each of the four transponders A_1, B_2, C_3, and D_4, respectively. The corresponding station coordinates are X_1 Y_1 Z_1, X_2 Y_2 Z_2, and X_4 Y_4 Z_4. Altitude data can be substituted for one of the range measurements when needed. The measured distances are in electrical phase units related to the clock frequency of the system, and velocity is in phase counts per 0.25 second. The station coordinates are stored in the data processor in corresponding units of electrical phase. Vehicle position and velocity are computed with the data in the phase units. After the

computations, corrections, iterations, and smoothing are completed, conversion is made to metric units.

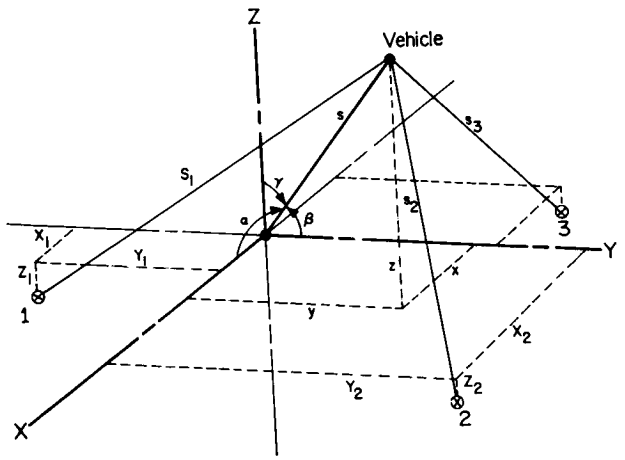

FIGURE 10. TRACKING GEOMETRY FOR DETERMINING POSITION

To establish a uniform method of computing for all tracking conditions, a three station solution is used exclusively. The refinement of position determination that accrues from the use of more than three stations is obtained by forming multiple sets of three stations. Any combination of three stations for which the range data from the stations can be correlated in time can form a set. With the stations A, B, C, D, the following sets can be formed:

$$\text{ABC, BCD, CDA, DAB} \qquad (1)$$

Consecutively formed sets that contain stations in common also contribute to the smoothing. For example, the next formation of station sets would occur when operation with station A is terminated and station E is acquired. One of the original sets is retained with three new sets formed that have common stations with three sets of the original group. These are BCD, CDE, DEB, and EBC.

The equations for a three station solution for position are

$$\begin{aligned} S_1^2 &= (x - X_1)^2 + (y - Y_1)^2 + (z - Z_1)^2 \\ S_2^2 &= (x - X_2)^2 + (y - Y_2)^2 + (z - Z_2)^2 \\ S_3^2 &= (x - X_3)^2 + (y - Y_3)^2 + (z - Z_3)^2 \\ S^2 &= x^2 + y^2 + z^2 \end{aligned} \qquad (2)$$

where S_1, S_2, and S_3 are the ranges from stations A, B, and C, respectively.

S is the range from coordinate center to the vehicle, and x, y, z are the vehicle position coordinates.

The solutions are of the form

$$S^2 = \frac{-2\vec{P}\cdot\vec{Q} - 1}{2P^2} \pm \sqrt{(2\vec{P}\cdot\vec{Q} - 1)^2 - \frac{Q^2}{P^2}}$$

$$x = P_x S^2 + Q_x \qquad y = P_y S^2 + Q_y \qquad (3)$$

$$z = P_z S^2 Q_z$$

where P_x, P_y, and P_z are constants for a station set and Q_x, Q_y, and Q_z are factors containing constants and the measured quantities and

$$\begin{aligned} P^2 &= P_x^2 + P_y^2 + P_z^2 \\ Q^2 &= Q_x^2 + Q_y^2 + Q_z^2 \\ \vec{P}\cdot\vec{Q} &= P_x Q_x + P_y Q_y + P_z Q_z \ . \end{aligned} \qquad (4)$$

The P constants are computed and stored for use in the four sets formed by the four stations selected for operation. When a change of station occurs, one set of P constants is retained and three new sets are computed and stored for the new station sets.

Before being used in computing the position, range measurements are corrected for movement of the vehicle during the signal transit time. Where the average velocity of the vehicle during the transit interval is v, and the signal velocity is c, the corrected range is

$$S = S_m\left(1 - \frac{v}{c}\right) \qquad (5)$$

where S_m is the measured range for the double path. The range is referred to the time of initial transmission from the vehicle to obtain a constant period between measurements. For long ranges, corrections to range must be made for movement of the earth during the signal transit period.

Vehicle velocity is determined in a manner similar to that used to determine position. The Doppler shifts in respect to the transponders are the measured quantities, and the velocity coordinate components and velocity in respect to the coordinate center are computed. To determine velocity in

respect to a transponder, the frequency difference between the tracking carrier of the returned signal from the transponder and a reference frequency in the vehicle-borne system is measured and summed over the interval $\tau = t_2 - t_1 = 0.25$ seconds. The summed frequency difference divided by the summing interval gives the average phase rate for the interval τ. For all cases considered, a negligible error is created by using the average velocity over the period as the instantaneous velocity at time $t_1 = \tau/2$. However, although the summing interval for the return transmission starts at t_1 and ends at t_2, the summing interval for the forward transmission starts at $(t_1 - \Delta t)$ and ends at $(t_2 - \Delta t)$ where Δt is the transit time for the double path. The time at the center of the measuring interval for the Doppler shift of the forward transmission is then $t_1 - \Delta t + \tau/2$. The total Doppler shift summed is

$$\Sigma\phi = 2\pi \int_{t_1}^{t_2} F\left[1 - \left(\frac{v_1 + v_2}{c}\right) + \frac{v_1 v_2}{c}\right] \quad (6)$$

where F is the frequency of the returned signal; v_1 is the velocity of the vehicle in respect to the transponder during the summing interval of the forward transmission; and v_2 is the average velocity of the vehicle during the summing interval of the return. For long transit times and severe vehicle flight dynamics (e.g. lunar distances and lunar landing), the velocity difference, $v_2 - v_1$ must be taken into account. The coordinate system for earth-based transponders is oriented so that correcting for the velocity of the earth at each transponder site can be done by adding or subtracting from two components of the computed vehicle velocity. The time assigned to the corrections involves approximations that are well within a range that produces negligible error. The equations for velocity are derived from the range equations (2). The derivatives are

$$\begin{aligned} S_1\dot{S}_1 &= (x - X_1)\dot{x} + (y - Y_1)\dot{y} + (z - Z_1)\dot{z} \\ S_2\dot{S}_2 &= (x - X_2)\dot{x} + (y - Y_2)\dot{y} + (z - Z_2)\dot{z} \quad (7) \\ S_3\dot{S}_3 &= (x - X_3)\dot{x} + (y - Y_3)\dot{y} + (z - Z_3)\dot{z} \ . \end{aligned}$$

The solutions for $\dot{x}$, $\dot{y}$, and $\dot{z}$ are of the form

$$\dot{x} = \frac{\begin{vmatrix} S_1\dot{S}_1 & (y - Y_1) & (z - Z_1) \\ S_2\dot{S}_2 & (y - Y_2) & (z - Z_2) \\ S_3\dot{S}_3 & (y - Y_3) & (z - Z_3) \end{vmatrix}}{\begin{vmatrix} (x - X_1) & (y - Y_1) & (z - Z_1) \\ (x - X_2) & (y - Y_2) & (z - Z_2) \\ (x - X_3) & (y - Y_3) & (z - Z_3) \end{vmatrix}} \quad (8)$$

The importance of accurate position data in obtaining accurate velocity data is shown by these relationships. This fact is not always recognized.

Where position and velocity are computed from more than one station set, with data referred to the same time, a certain amount of error checking and smoothing can be done and is necessary in the functioning of the system. This is performed before transformation of the computed quantities from the coordinate system in which the measurements were made. Any further treatment of the data depends upon the use to be made of it.

V. ERRORS AND GEOMETRICAL DILUTION

Equipment and thermal noise errors and the uncertainty in propagation and in the location of transponders are classified as measuring errors to distinguish them from geometrically amplified errors (geometrically diluted accuracy). Equipment errors analyzed in the AROD system description and the error budget given in system characteristics are the best present estimates of the equipment and thermal noise errors. Propagation errors, considered in some detail in the AROD design feasibility report, can be reduced by the application of standard corrections; however, the magnitude of the residual errors is not well established. The AROD inflight experiment is expected to give information on the errors and methods for correction.

Errors in the survey of the transponder locations are not expected to contribute significantly to the overall error budget. In addition to the capability of the system to locate and refine the knowledge of the location of transponder sites, recent analysis of the use of tracking systems on satellites to define the position of ground stations shows that, in any case, errors from this source can be made negligible.

The accuracy probability of any given position determination is a function of the probable range measurement accuracies as geometrically diluted. Geometrical dilution is a function of the measuring geometry and it is common to all spatial measuring devices.

An illustration of the geometrical dilution in a multistation ranging system is given in Figure 11. The distance measured to a vehicle from a single station A, within the accuracy of $S_1 \pm \Delta S_1$, defines the position of the vehicle to be within a spherical shell

TABLE II. RADIO TRACKING SYSTEM DESIGN CHARACTERISTICS

	VHF Control Link	S-Band Tracking Link	
		Air-to-Ground	Ground-to-Air
Transmitter power (W)	6	10	20
Allocated bandwidth (MHz)	±.075	16	20
Maximum velocity (m/s)	±12,000	±12,000	±12,000
Minimum velocity (m/s)	0	0	0
Range ambiguity (km)	--	--	2,000
Range accuracy (m)	--	--	±.604
Range resolution (m)	--	--	.183
Velocity accuracy (m/s)	--	--	±.0148
Velocity resolution (m/s)	--	--	.026
Essential data rate (bits/s)	50	50	50

of thickness $2\Delta S_1$. The station is at the center of the sphere and the median radius of the sphere is S_1. Similarly, measurements from stations B and C also form spherical shells as shown. The uncertainty in position of the vehicle must then be within the volume formed by the intersections of the spherical shells. This volume is described as the possible error volume for the position determination. Obviously, the size and shape of the error volume is a function of the positions of the transponders in relation to the vehicle and of the positions of the transponders in relation to each other as well as the errors in measurements.

TABLE III. SUMMARY OF INSTRUMENTATION ERRORS

Error Source	Range (m)		Velocity (m/s)	
	Peak	rms	Peak	rms
Vehicle Equipment				
a. random noise errors	0.47	0.175	0.0137	0.0056
b. processing equip. errors	0.78	0.32	--	--
c. data extraction errors	0.62	0.316	0.0325	0.0124
Transponder Station Equip.				
a. random noise error	0.47	0.175	0.0137	0.0056
b. processing equip. error	0.78	0.32	--	--
Total	3.12	0.604	0.0699	0.0148

The probable error of a tracking system as used in a particular geometry is usually expressed as the probable error volume with the major and minor axes of the volume specified. In the case where tracking data are processed on the vehicle, use of the predetermined error volumes to establish the data quality from point to point on the vehicle flight path would require the storage or transmission of large

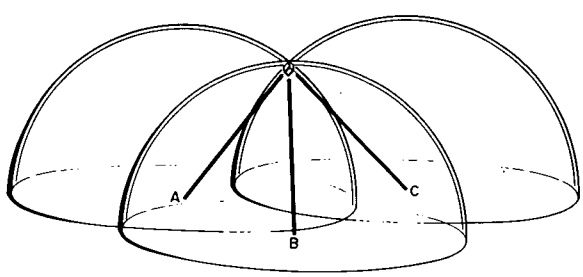

FIGURE 11. GEOMETRICAL DILUTION

amounts of information. The magnitude and direction of the maximum probable error can be computed on

the vehicle, but the simplest method to establish the overall data quality including the effect of geometrical dilution is to substitute the determined position quantities into the range equations (2). Thus some specific errors can be detected and the overall quality factor can be determined. The substitution method is favored also because the processing procedure is identical with that used when complete tracking data are not available. Details of both methods will be described in a NASA report to be published later.

Present work in the study and simulation of data processing methods and techniques is to be continued. The results will be used to define the design of an optimum vehicle-borne data processor and the optimum interface techniques to be used with multipurpose vehicle-borne computers. The results should be useful in other areas of data processing and communication systems.

VI. ANTENNA DEVELOPMENT

The design of the vehicle-borne antennas is directly involved with the vehicle design and the mission of the vehicle; therefore, no specific designs for these antennas have been made. Design requirements have been minimized by the rather severe restriction placed on the system by assuming 0 db gain for the vehicle-borne tracking antenna and for the VHF control antenna. Furthermore, these antennas can be linearly polarized since the ground based antennas are designed to receive signals of any polarization and to radiate a circularly polarized signal.

A block diagram of the antenna system of the unattended ground transponder is shown in Figure 12. The control receiver, the tracking receiver, and the tracking transmitter are obviously not a part of the antenna system, but are included in the diagram to show the functions of the antennas. The 12 dB gain of the tracking antenna of the unattended transponder station is sufficient only to hold the vehicle radiated power requirement down to 10 watts for the intended ranges and data rates. Because of the antenna directivity resulting from the required gain, the tracking antenna must be directed or steered by the use of information from the VHF direction finder or some other source to establish initial communications with the vehicle. After the antenna radiation pattern is positioned and the receiver acquires the signal from the vehicle, the

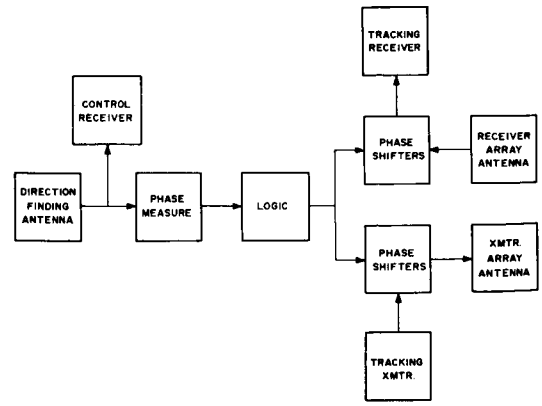

FIGURE 12. DIRECTION FINDER ELEMENTS AND ARRANGEMENT

antenna steering may be continued by direction-finder data, or it may be steered by commands from the vehicle.

The direction finder antenna system determines the direction from which the vehicle signal arrives at the transponder site by measuring the phase relation between elements of the antenna array in much the same manner as a standard manually operated direction finder. In this case, however, the knowledge about the direction in three dimensions is obtained from a signal that may have any polarization. Phase differences that are functions of the direction angles are measured electronically, converted to digital information, and applied to a logic system that electronically steers the tracking antennas by adjusting the phase relation between the antenna elements (Fig. 12).

The direction from which the signal arrives must be determined about an azimuth of 360 degrees and an elevation angle of 90 degrees with an accuracy of approximately ± 5 degrees in the horizontal plane and in any vertical plane up to an elevation of 45 degrees above the horizon. Because the design range is shorter for the higher elevation angles, the directivity of the tracking antennas is reduced by "spoiling" to allow a larger uncertainty in the direction angle. Design of the direction finding array is thereby simplified and construction and installation problems are reduced by allowing the use of a planar rather than a volume array.

The range and utility of the unattended station could be increased by increasing the gain of the tracking antenna, but a significant increase in gain would necessitate a search by the tracking antenna over the solid angle error of the direction-finder system. After tracking communications are established, the tracking antenna could be steered on the

tracking signal. Developments in solid state devices since the beginning of the AROD program make these improvements in the unattended station system feasible where they were not before. Studies in signal processing and in signal processing antennas indicate that, in addition to increasing the gain and reducing the noise level in the tracking array, the tracking signal can be acquired rapidly without aid from the VHF system. These studies are expected to continue and the improvements will be incorporated into the system whenever feasible. Results of the studies in signal processing and signal processing antennas have applications in many areas other than AROD.

The direction finding antenna ideally should be omnidirectional and able to respond to signals of any polarization. A four element array at an optimum position above a ground plane approaches the desired characteristics. The array consists of four elements as shown in Figure 13; each element

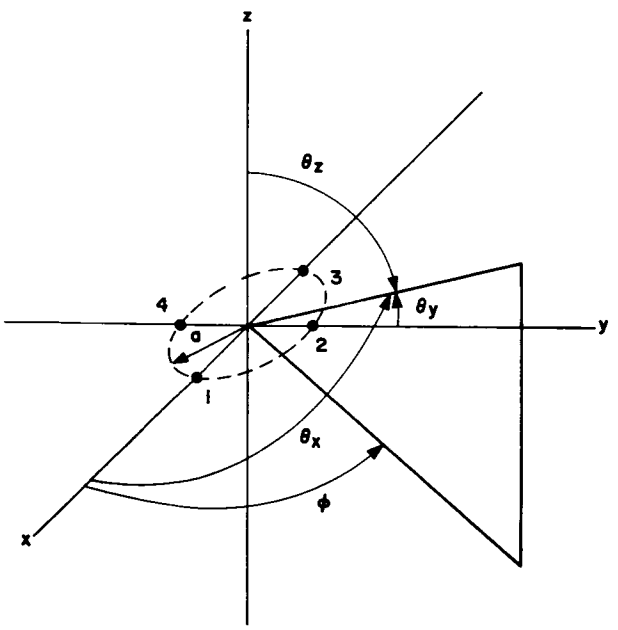

FIGURE 13. GEOMETRY OF DIRECTION FINDING ARRAY WITH POINT SOURCES

is composed of a vertically polarized and a horizontally polarized dipole antenna. The array may be considered as being two separate arrays, one consisting of the horizontal dipoles and the other consisting of the vertical dipoles. A matrix system of phase lines allows signals to be extracted from the array. These signals are proportional to the direction cosines of the arriving signal. The action of the direction finding array may be determined by considering a four element array of point sources (Fig. 13). This array is described in terms of the terminal voltages of each antenna by

$$
\begin{aligned}
V_1 &= f_1(\theta, \phi)e^{jka\cos\theta}{}_x = I_1Z_{11} + I_2Z_{12} + I_3Z_{13} + I_4Z_{12} \\
V_2 &= f_2(\theta, \phi)e^{jka\cos\theta}{}_y = I_1Z_{12} + I_2Z_{11} + I_3Z_{12} + I_4Z_{13} \\
V_3 &= f_3(\theta, \phi)e^{-jka\cos\theta}{}_x = I_1Z_{13} + I_2Z_{12} + I_3Z_{11} + I_4Z_{12} \\
V_4 &= f_4(\theta, \phi)e^{-jka\cos\theta}{}_y = I_1Z_{12} + I_2Z_{13} + I_3Z_{12} + I_4Z_{11}\,.
\end{aligned}
\tag{9}
$$

In these equations Z_{11} is the sum of the self-impedance of each element and the input impedance to the line, Z_{12} is the mutual impedance between one element and the nearest adjacent element, and Z_{13} is the mutual impedance between one element and the element diametrically opposite. The individual elements of the array must be in the same environment for equations (9) to be be valid. The conditions satisfying the requirement are

$$
\begin{aligned}
f_2(\theta, \phi) &= f_1(\theta, \phi + \tfrac{\pi}{2}) \\
f_3(\theta, \phi) &= f_1(\theta, \phi + \pi) \\
f_3(\theta, \phi) &= f_1(\theta, \phi + \tfrac{3\pi}{2})\,.
\end{aligned}
\tag{10}
$$

The equivalents from equations (10) are substituted into equations (9) with C = 12.8 as determined from the properties of the tracking array, with

$$
\begin{aligned}
-Cl &= ka\cos\theta_x \\
-Cm &= ka\cos\theta_y,
\end{aligned}
$$

and then "l" and "m" appear in equations (9) as phase angles, with the scale factor C on the antenna terminal voltages. The quantities to be measured include the mutual impedance; but if the elements are identical, the equations may be uncoupled. The scheme for accomplishing this depends on forming the sequence voltages $V_R^{(0)}$, $V_R^{(1)}$, $V_R^{(2)}$, and $V_R^{(3)}$, where the superscripts indicate the sequence numbers. The derivation of the sequences and their combination to produce an output proportional to the direction cosines is described in "Final Report, Automatically Scanned Antenna Systems," Contract NAS8-11251, 20 Jan. 1966, by Auburn University.

Measured phase data are converted to digital format and used to operate the logic system that selects the proper phase relations in the tracking antennas to give a radiation phase front normal to the direction of the arriving signal as determined by the direction-finder array.

A digital switching system shown in Figure 14 processes the information from the direction finder for application to the drivers of the phase switches of the tracking antenna. The digitized values of "l" and "m' are produced in sequence at the output of the analog-to-digital converter with possible output values of ABCD and EFGH for "l" and "m," respectively. With the inputs ABCDEFGH to the combinational switching network, the outputs y_1 through y_{140} are produced to control the phasing of the tracking array. With each clock pulse, the z hold network is advanced to a value of z corresponding to the value of y. This value of z is held until it is updated by a new value of y.

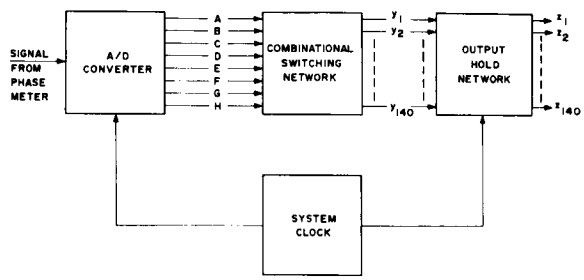

FIGURE 14. BLOCK DIAGRAM OF DIGITAL SWITCHING SYSTEM

The experimental antenna uses techniques developed in a research program in electronically scanned arrays at S-band frequencies separate from the AROD program. The tracking antennas being constructed for the AROD feasibility model are experimental units designed to satisfy the minimum requirements for the AROD unattended transponder.

The transmitting and receiving antennas are of identical construction except for the frequency of operation. An elliptically polarized pattern is produced which can be scanned over a full hemisphere. Each antenna is a planar square array consisting of 36 cavity-backed crossed slots as shown in Figure 15. An experimental array is shown in Figure 16.

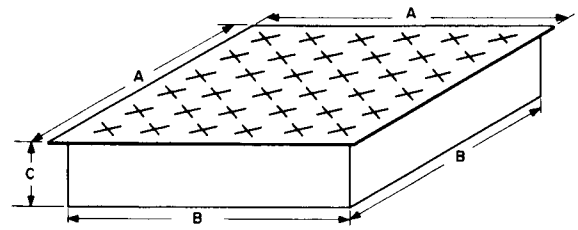

DIMENSIONS

RECEIVING (2.214 GHz)		TRANSMITTING (1.800 GHz)	
A	38.8 cm	A	46.5 cm
B	36.3 cm	B	43.9 cm
C	9.0 cm	C	10.1 cm

FIGURE 15. TRACKING ARRAY

Each element is circularly polarized and the complete array is circularly polarized in a direction normal to the plane of the array. The polarization of the array becomes increasingly elliptical as the pattern is directed away from the normal until a direction parallel to the plane of the array is reached where the field is plane polarized normal to the plane of the array. Figure 17 shows the cross slot antenna and illustrates the method of feeding energy into the cavities to produce the circular polarization. The measured polarization pattern at the 36 slot array is shown in Figure 18. Figures 19 and 20 are examples of the measured and calculated patterns of the array as a function of the steering. As to be expected in phase steering a low gain planar array over a large angle, the minor lobes become quite large when the pattern is directed away from the optimum gain directions. The measuring geometry is defined in Figure 21.

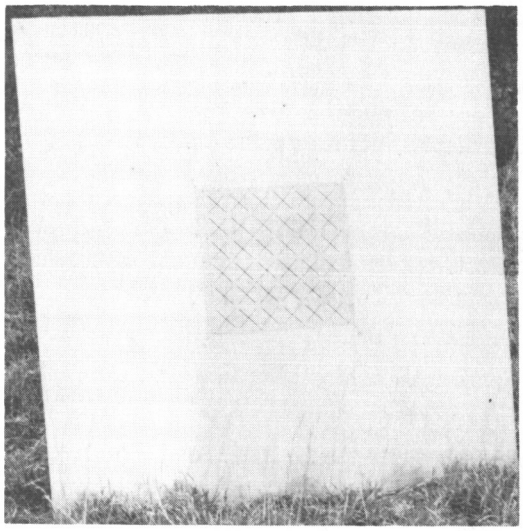

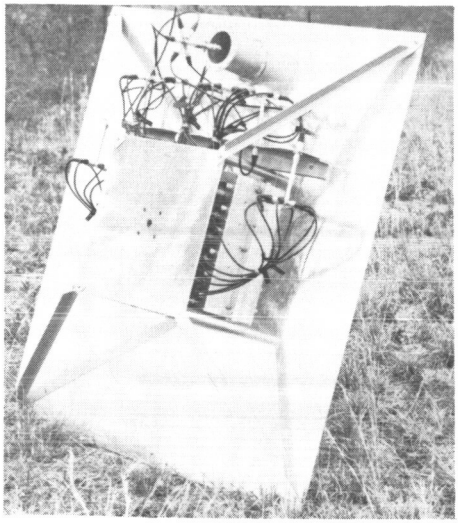

FIGURE 16. EXPERIMENTAL MODEL OF TRACKING ARRAY

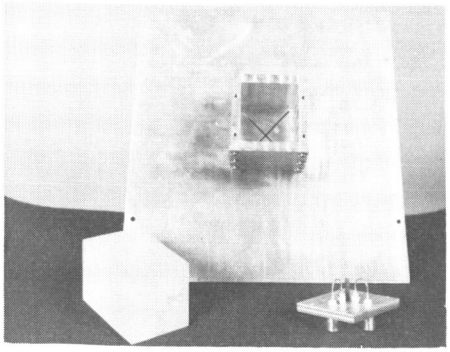

FIGURE 17. CAVITY-BACKED SLOT AND FEED

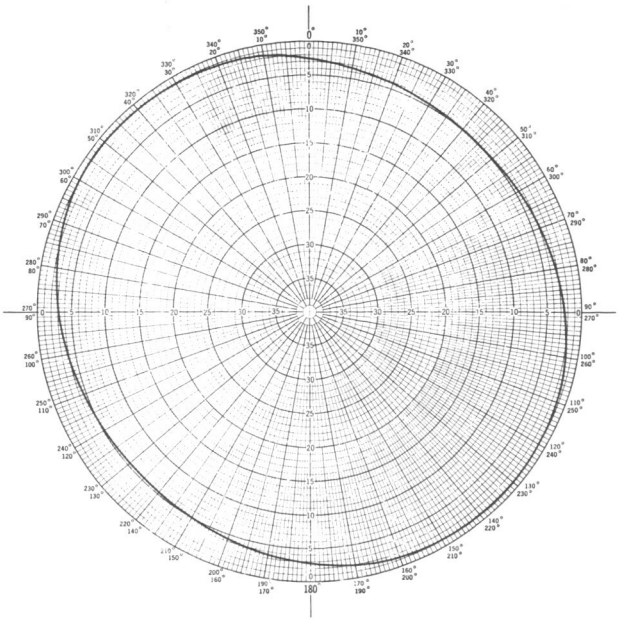

FIGURE 18. POLARIZATION PATTERN OF TRACKING ARRAY FOR THE l = 0, m = 0 BEAM POINTING

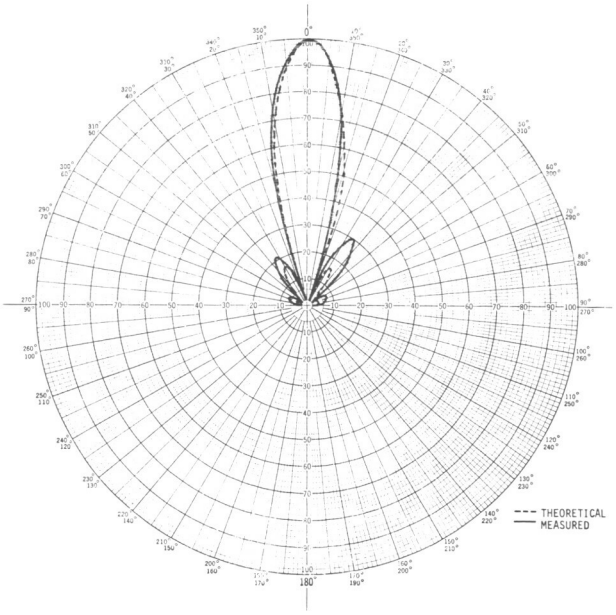

FIGURE 19. TRACKING ARRAY PATTERN IN X - Z PLANE FOR l = 0, m = 0 BEAM POINTING

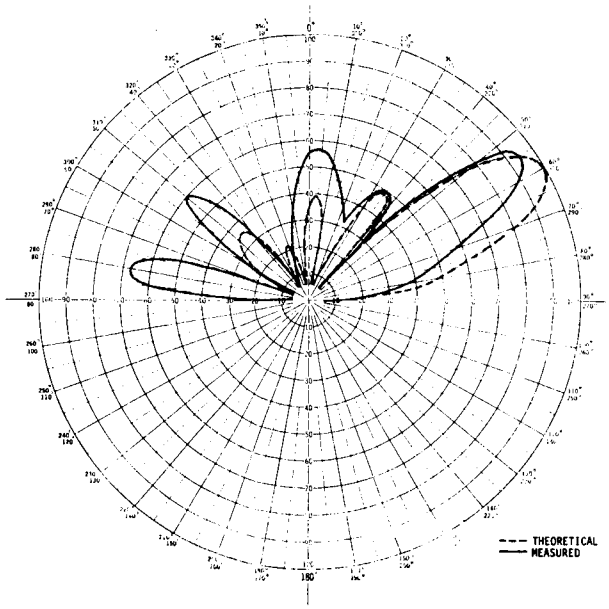

FIGURE 20. TRACKING ARRAY PATTERN IN X - Z PLANE FOR l = 0, m = -7 BEAM POINTING

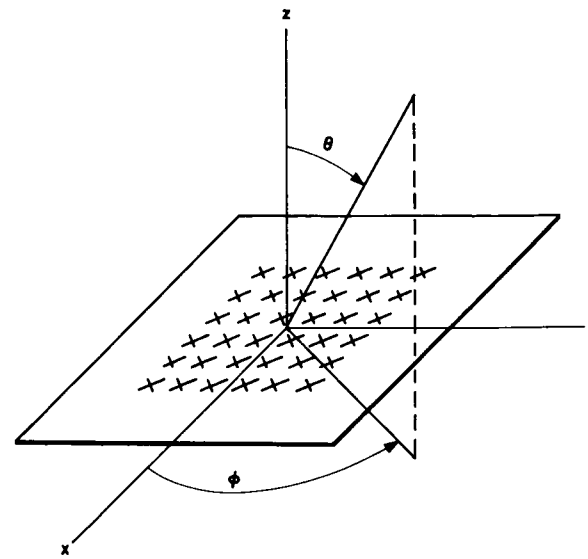

FIGURE 21. MEASURING GEOMETRY OF TRACKING ARRAY

TRACKING, COMMUNICATIONS, AND ORBIT DETERMINATION FOR LUNAR SPACE VEHICLES

By

Robert M. L. Baker, Jr.*, Robert J. Hill, Howard Dielmann*, and Robert H. Benson

SUMMARY

This paper presents methods of predicting tracking and communication data for space vehicles in the earth-moon space. Also presented is the application of the prediction and the utilization of tracking data to problems of orbit determination. To make such predictions and determinations, a method of trajectory simulation that applies at the present time to the earth-moon space has been developed, but the methods are general enough to apply to interplanetary tracking prediction and orbit determination.

LIST OF SYMBOLS

Superscripts

$\dot{}$	"dot derivative" denotes a derivative with respect to time, excluding perturbations.
$'$	"prime derivative" denotes a derivative with respect to $\widehat{X}$.
$\grave{}$	"grave derivative" denotes a derivative with respect to time that involves only perturbations.
$\widehat{\ }$	denotes a universal variable.
*	denotes universal variable quantities defined by Pitkin.

Subscripts

e	Encke reference orbit.
o	initial or epoch value.
r	value of quantity at rectification.
T	topos or observing station coordinate.

Subscripts (Cont'd)

$\odot$	Sun
$\mathfrak{D}$	Moon
$\otimes$	Earth

Special Symbols

$\lvert\ \rvert$	absolute value (magnitude).
$x \rightarrow y, z$	two other equations can be obtained by replacing x by y and then by z.
$\triangleq$	equal to by definition.

English Symbols

a	the semimajor axis of an elliptical orbit or the semitransverse axis of a hyperbolic orbit.
$c =$	$1 - \frac{r}{a}$ or the speed of light in a vacuum.
$\widehat{C} =$	$a\left(1 - \cos\left(\frac{\widehat{X}}{\sqrt{a}}\right)\right)$.
$D =$	$r\,\dot{r}/\sqrt{\mu}$
e	the eccentricity of a conic.
f	general symbolism for a function such as $\widehat{M} - r_0\widehat{X} - D_0\widehat{C} - c_0\widehat{U}$ or $3 - \frac{3 \cdot 5}{2}q + \frac{3 \cdot 5 \cdot 7}{3!}q^2 + \ldots$ or for one of the two coefficients comprising the f and g series.
$\vec{f}$	the flux vector of incident radiation.

* Dr. Baker and Mr. Dielmann are with Computer Sciences Corporation, El Segundo, California.

English Symbols (Cont'd)

g	the symbol for the other of the two coefficients comprising the f and g series.
h	the altitude or angular distance of a spacecraft above the horizon.
M	the mean anomaly.
n	the mean motion.
P	the period of a satellite orbit.
p	the parameter or semilatus rectum = $a(1 - e^2)$.
q	the perifocal distance = $a(1 - e)$ or the quantity $[(r/r_e)^2 - 1]/2$.
r	the magnitude of the radius vector, $\vec{r}$, from the principal focus (e.g., geocenter) to the space vehicle.
$\hat{S}$ =	$\hat{X} - \frac{1}{a}\hat{U}$.
$\dot{s}$	the tangential velocity (= $\lvert \dot{\vec{r}} \rvert$).
t	the time as measured in conventional units such as hours, minutes, or seconds.
$\hat{U}$ =	$a^{3/2}\left(\frac{\hat{X}}{\sqrt{a}} - \sin\left(\frac{\hat{X}}{\sqrt{a}}\right)\right)$.
$\hat{X}$	the universal variable argument.
x, y, z	are coordinates measured along three orthogonal axes (e.g., the geocentric equatorial system of date).

Greek Symbols

α	right ascension.
δ	declination.
ξ, η, ζ	the departures from a reference orbit in Encke's method.
θ	the sidereal time.
μ	the sum of the mass of the primary and the spacecraft in units of primary masses (e.g., earth masses). Thus $\mu \cong 1$ for most cases of interest.

Greek Symbols (Cont'd)

$\vec{\rho}$	a vector from an observatory (topos) to a spacecraft.
τ	a characteristic unit of time = $k(t - t_0)$ where k stands for the geocentric, selenocentric, heliocentric, etc. gravitational constant (about 13.6 minutes for the geocentric case).
λ	the longitude.
Φ	the gravitational potential.
φ	the latitude.
Ω	the longitude of the ascending node.
ω	the argument of perifocus, i.e., the angle between the line of nodes and the perifocus direction.

I. INTRODUCTION

Concern for tracking and communications data arises primarily from two sources. These are in-flight, real-time analysis and post flight, detailed analysis.

In real-time analysis, it is necessary to know how systems such as the propulsion and guidance system are currently functioning. For flights involving man, there are systems related to crew safety, such as the life support system, which require that inflight knowledge be telemetered to mission control. If the vehicle is in orbit for a number of revolutions, it may become necessary to update the guidance system from tracking data. During orbital flight, future state is predicted to alert tracking stations of the position and the time at which acquisition might be expected. Also, in the case of noncatastrophic failures, it might be desirable to attempt an alternate mission. This type of decision will be based on tracking and telemetry data, and the command for such an attempt will be given by the mission control center through the communications network.

In post-flight analysis, detailed evaluation requires using all available data, smoothing randomness and correcting biases for many weeks after the flight has terminated. It is the purpose of this detailed analysis to evaluate the vehicle systems such as the guidance system, the propulsion system, and the structural elements for any deviations from nominal performance so that the systems may be

improved. The tracking and communications system is evaluated during this post-flight period. Errors in station location may be detected as well as certain malfunctions in the telemetry system.

Certain perturbations, due to non two-body gravitational fields and radiation forces, are subjected to scrutiny during the period of flight evaluation. Thus our knowledge about the size, shape, and gravitational constant for the moon may be increased as more data become available.

Detailed orbit determination is an important part of post-flight trajectory analysis. The term "orbit determination" is the definition of the orbit the vehicle traversed as described from tracking and telemetry data. The goal is to determine the exact orbit which the space vehicle has traveled.

There are many factors of uncertainty which diminish exactness of orbit determination, among which are errors in tracking data such as timing errors, bias errors, random errors in measurements and errors in station location. Other uncertainties also affect the accuracy of detailed orbit determination, for example, uncertainties in the gravitational forces, relativistic Doppler shift, speed of light, planetary, solar, and lunar ephemerides, and errors inherent in orbit determination methods themselves. Through the application of research efforts some of these errors and uncertainties may be reduced for future orbit evaluation.

There are certain fundamental aspects of astronautics that are enhanced by the judicious analysis of tracking and telemetry data. The quantity and quality of tracking and communications data must be studied in advance to determine if the requirements of evaluation are satisfied. To perform such a study, two primary questions must be answered: (1) How can the tracking coverage be accurately defined by simulation, and (2) Is the expected tracking and communications coverage adequate?

The first question is rather elementary, but the implementation of it is another matter. Tracking coverage must be defined by means of an accurate trajectory simulation model and with an accurate tracking model. The answer to the second question differs from mission to mission, and the question needs to be answered with respect to many criteria such as flight evaluation requirements, guidance system updating and data transmission.

With respect to data transmission for early Apollo flights, the tracking and communications coverage is adequate. For later flights such as AAP missions where multiple experiments in communications and remote sensing will be performed, there may be extensive quantities of data, and the problem may become more critical.

The current research program is primarily concerned with the first question--the development of an accurate trajectory simulation model and an accurate tracking model flexible enough to handle many diverse studies of tracking in the earth-moon space. The backbone of the trajectory and tracking simulation model is an Encke prediction routine. Over one hundred years ago the German astronomer, J. F. Encke, proposed a method of handling special perturbations that has proved well suited to slightly perturbed orbits such as ballistic lunar trajectories. Encke's method differs from ordinary integration techniques in that the differential accelerations are integrated rather than the total accelerations. The differential accelerations are formulated as the difference between a true orbit and a reference conic. A reference conic is determined at the initial point of the integration. If there were no disturbing forces such as more than one attracting body, gravitational harmonics and solar radiation forces, then the vehicle would follow this reference conic. However, these forces perturb the vehicle, and it actually progresses along another path called the true orbit. Figure 1 shows the relationship between the reference orbit and the actual path or true orbit of the vehicle. Note that at the point of tangency or "osculation" both the true and the reference orbit exhibit the same position and velocity*

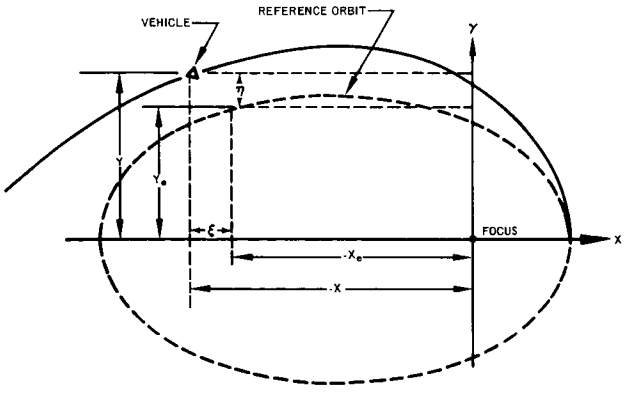

FIGURE 1. DEVIATION FROM REFERENCE ORBIT

* The term "osculating orbit" implies both a tangency and the same velocity, while the term "intermediary orbit" only implies tangency.

II. DEVELOPMENT OF THE ENCKE EQUATIONS

Let x, y, z denote the actual position of the object; x_e, y_e, z_e the position of a hypothetical object (moving without perturbations) at the same time on the reference orbit; and ξ, η, ζ, the difference between the true rectangular coordinates and those of the reference orbit, i.e.,

$$\xi \triangleq x - x_e \quad x \to y, z; \quad \xi \to \eta, \zeta. \tag{1}$$

At osculation ξ, η, and $\zeta = 0$. Figure 1 shows the relationship between the reference orbit and the actual path of the vehicle.

The differential accelerations between the actual and the reference orbit positions of the rocket are

$$\frac{d^2\xi}{d\tau^2} = \mu\left[-\frac{x}{r^3} + \frac{x_e}{r_e^3}\right] + \hat{x} = (\ddot{x} - \ddot{x}_e) + \hat{x};$$

$$\xi = \iint \frac{d^2\xi}{d\tau^2}\, d\tau^2 \quad x \to y, z; \ \xi \to \eta, \zeta. \tag{2}$$

The first parenthesis on the right-hand side is the difference between the two-body accelerations on the reference orbit and on the actual path, and $\hat{x}$ represents the total perturbing component. Time need not always be utilized as an independent variable in equation (2) of Encke's method. If E (or F for hyperbolic orbits) is used as an independent variable, we are able to circumvent the solution of the transcendental Kepler's equation at each point of the reference orbit when the computation of x_e, y_e, z_e and r_e is required.*

One of the purposes of Encke's method is to reduce the number of significant figures carried in the calculations. Taking the difference of the nearly equal two-body accelerations, $\ddot{x} - \ddot{x}_e$, $x \to y, z$, would only increase the number required and is therefore undesirable. From another point of view, the "noise" introduced in the numerical subtraction of $\ddot{x}_e$ from $\ddot{x}$ could initially be as large as the perturbative term $\hat{x}$ and thereby reduce the accuracy of the entire procedure. We take the differences of the nearly equal accelerations, e.g., $\ddot{x} - \ddot{x}_e$, by the following alternative procedure:

$$\ddot{x} - \ddot{x}_e = \frac{\mu x_e}{r_e^3} - \frac{\mu x}{r^3}$$

$$= \frac{\mu}{r_e^3}\left\{\left[1 - \left(\frac{r_e}{r}\right)^3\right] x - \xi\right\} \triangleq \frac{\mu}{r_e^3}\left\{\left[1 - (1+2q)^{-3/2}\right] x - \xi\right\}$$

$$x \to y, z; \quad \xi \to \eta, \zeta. \tag{3}$$

That is, we set

$$q \triangleq \frac{(r/r_e)^2 - 1}{2},$$

where the new paramter q is developed from

$$r^2 = (x_e + \xi)^2 + (y_e + \eta)^2 + (z_e + \zeta)^2 \tag{4}$$

$$= r_e^2 + 2[\xi(x_e + \tfrac{1}{2}\xi) + \eta(y_e + \tfrac{1}{2}\eta) + \zeta(z_e + \tfrac{1}{2}\zeta)].$$

$$\left(\frac{r}{r_e}\right)^2 = 1 + 2[\xi(x_e + \tfrac{1}{2}\xi)/r_e^2 + \eta(y_e + \tfrac{1}{2}\eta)/r_e^2$$

$$+ \zeta(z_e + \tfrac{1}{2}\xi)/r_e^2] \triangleq 1 + 2q.$$

Finally,

$$1 - \left(\frac{r_e}{r}\right)^3 = 1 - (1+2q)^{-3/2}$$

$$= 3q - \frac{3\cdot 5}{2!} q^2 + \frac{3\cdot 5\cdot 7}{3!} q^3 - \cdots \triangleq fq \tag{5}$$

so that $\ddot{x} - \ddot{x}_e = (\mu/r_e^3)(fqx - \xi)$ and the individual $\ddot{x}$ and $\ddot{x}_e$ need never be explicitly computed ($x \to y, z$) (see Fig. 2 where fq (the "q series") is numerically obtained by solution of equation (5) or from tables given in Planetary Coordinates (1960)).

In contrast to Cowell's method, only the differential accelerations due to perturbations are integrated to obtain the actual position of the vehicle. Taking advantage of this fact, we find that longer intervals can be chosen in the step-by-step integration process. A careful choice of the reference orbit is necessary in order to make the method most effective.

If at some date after the epoch the true orbit begins to differ appreciably from the reference orbit,

* However, in return for this simplification, the differential equation of motion (2) becomes rather complicated.

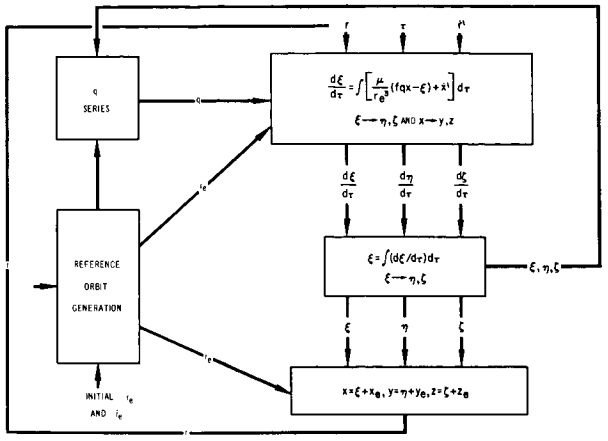

FIGURE 2. REFERENCE ORBIT

a new "osculating" reference orbit must be chosen as a new starting point at the later date. This process is called "rectification" (again initially $x = x_e$, $\xi = 0$, etc.) (see Fig. 3). The decision to rectify is usually made whenever the integrated portion of the solution (x, y, z) is a fixed ratio of the exact two-body term (x_e, y_e, z_e). However, we could use

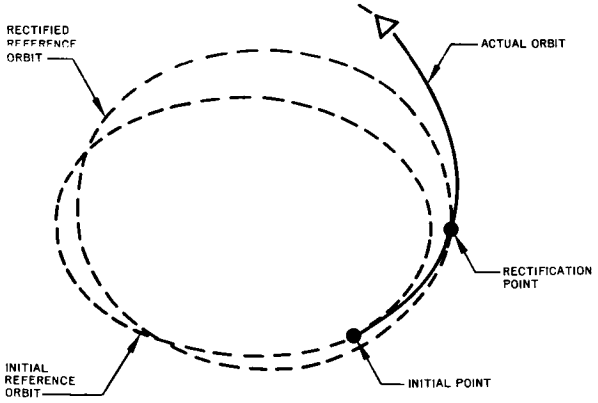

FIGURE 3. RECTIFICATION

a more sophisticated round-off error control for the purpose of defining the appropriate time for rectification. In this same connection, if the orbit is periodically rectified, there is an added advantage to Encke's method: a part of the perturbative terms $\ddot{\hat{x}}$, $\ddot{\hat{y}}$, and $\ddot{\hat{z}}$ in equation (2) can be computed in advance quite accurately on the basis of the space vehicle's coordinates on the reference orbit. Thus, knowing in advance the position of the moon or planets, perturbative acceleration equations (to be discussed presently) can be precomputed for a large number of steps in advance of the actual integration. Such a procedure is not particularly recommended for drag perturbations because the small difference between the true and the reference orbit may lead to large differences in atmospheric density and hence in the perturbations.

The use of Encke's method in connection with the differential correction gives rise to a slight problem at the time of rectification. The partial derivatives in the S matrix (elements of the form $\partial x/\partial x_0$, etc.) apply to a correction of the initial state (subscript 0), which after rectification strictly means the state at the time of rectification (subscript r). Thus, after rectification we must "up date" the S matrix by multiplying it by the old S matrix, so that a typical term (after the first rectification) is

$$\left(\frac{\partial x}{\partial x_r}\right)\left(\frac{\partial x_r}{\partial x_0}\right) .$$

This is simply an application of the chain rule, so that if there were three rectifications, we would have

$$\left(\frac{\partial x}{\partial x_0}\right) = \left(\frac{\partial x}{\partial x_{r3}}\right)\cdot\left(\frac{\partial x_{r3}}{\partial x_{r2}}\right)\cdot\left(\frac{\partial x_{r2}}{\partial x_{r1}}\right)\cdot\left(\frac{\partial x_{r1}}{\partial x_0}\right), \text{etc.}$$

While on the topic of partial derivatives, it might be well to mention a peculiarity of analytical partials when they are based upon the two-body, Encke reference orbit elements. Often the departures of the true orbit from the reference orbit, although not sufficiently large to require a rectification, do result in a crossing back and forth of the reference and the true orbit in the case of satellites. There is also an inevitable lead or lag of the true and reference orbit position. Thus the analytical partial derivatives follow a periodic fluctuation (from some hypothetically exact partials) and this periodicity slowly moves out of phase, especially if rectification is not required for several revolutions.

The Encke philosophy can also be applied to the computation of a number of orbits (termed "variant orbits") that lie very close to some standard, i.e., orbits that differ slightly in initial conditions. In this case the reference orbit would be the standard orbit about which can be computed an envelope of variant orbits. Such a procedure is particularly useful in sensitivity or guidance error computations.

What values we adopt are significant for the starting constants, ξ_0, $\dot{\xi}_0$, and so forth. In normal perturbation integrations by Encke's method (not

variant orbits), it is customary to start with an osculating orbit at t_0. For this orbit the following equations hold:

$$x_0 = x_{eo}, \qquad \dot{x}_0 = \dot{x}_{eo}, \text{ etc.} \tag{6}$$

Accordingly,

$$\xi_0 = 0, \qquad \dot{\xi}_0 = 0, \text{ etc.} \tag{7}$$

Thus, at the end of the integration we generally have

$$x = x_e + \xi, \qquad \dot{x} = \dot{x}_e + \dot{\xi}, \text{ etc.} \tag{8}$$

The convenience of the osculating orbit for a normal perturbation integration lies simple in the fact that the $\ddot{x} - \ddot{x}_e$ term of equation (2) is zero, and further that fq, q, ξ, etc., start out with zero values. However, these advantages of the osculating orbit do not preclude our using other than zero values for one or more of the six initial integration constants, ξ_0, η_0, ζ_0, $\dot{\xi}_0$, $\dot{\eta}_0$, $\dot{\zeta}_0$.

The unified and universal variables can also be effectively used in Encke's method for the generation of the reference orbit. Their advantage over specialized formulas arises especially in the case of nearly parabolic elliptical orbits that are perturbed by the moon into nearly parabolic, hyperbolic orbits. In this transitional regime the computation of the reference orbit becomes most difficult, and as pointed out by Herrick, considerable accuracy is lost in Encke's method. Such a degradation of accuracy is also encountered near the apogee of such earth-moon reference orbits when they are nearly rectilinear (as is almost always the case), and a method similar to the unified variables has been utilized by C. Herrick of Convair in this problem.

In what follows we present the procedural equations for generation of the reference orbit by means of universal variables. (For simplicity of notation the subscript e has been omitted from the reference orbit coordinates.)

$$r_0^2 = \vec{r}_0 \cdot \vec{r}_0 \tag{9}$$

$$\frac{\dot{s}_0^2}{\mu} = \frac{\vec{r}_0 \cdot \dot{\vec{r}}_0}{\mu} = \frac{\vec{r}_0}{\sqrt{\mu}} \cdot \frac{\dot{\vec{r}}_0}{\sqrt{\mu}} \tag{10}$$

$$D_0 = \frac{r_0 \dot{r}_0}{\sqrt{\mu}} = \frac{\vec{r}_0 \cdot \dot{\vec{r}}_0}{\sqrt{\mu}} = \vec{r}_0 \cdot \frac{\dot{\vec{r}}_0}{\sqrt{\mu}} \tag{11}$$

$$\frac{1}{a} = \frac{2}{r_0} = \frac{\dot{s}_0^2}{\mu}. \tag{12}$$

Note that

$$c_0 = 1 - \frac{r_0}{a}, \quad e^2 = 1 - \frac{p}{a}, \quad e = 1 - \frac{q}{a}, \tag{13}$$

$$\widehat{M} = \widehat{n}(t - t_0) = \tau\sqrt{\mu}, \quad \widehat{n} = k'\sqrt{\mu}; \tag{14}$$

and

$$\widehat{M} = r_0\widehat{X} + D_0\widehat{C} + c_0\widehat{U}. \tag{15}$$

At every time point t equation (15) is to be solved for $\widehat{X}$. It can be solved iteratively for $\widehat{X}$ with the aid of the formulae for $\widehat{C}$ and $\widehat{U}$. A starting value for $\widehat{X}$ (for 1/a positive) is $\widehat{M}/a$.

As pointed out by E. Pitkin (1964), in order to maintain the full accuracy obtainable and minimize roundoff error, it is desirable to "nest" the series in the following fashion for computational purposes:

$$\widehat{C} = \frac{\widehat{X}^2}{2} - \frac{1}{a}\frac{\widehat{X}^4}{24}\left[1 + \frac{\widehat{X}^2}{a\,5\cdot 6}\left(1 + \frac{\widehat{X}^2}{a\,7\cdot 8}\,(1 - \ldots)\right)\right]$$

$$\widehat{U} = \frac{\widehat{X}^3}{6} - \frac{1}{a}\frac{\widehat{X}^5}{120}\left[1 + \frac{\widehat{X}^2}{a\,6\cdot 7}\left(1 + \frac{\widehat{X}^2}{a\,8\cdot 9}\,(1 - \ldots)\right)\right]. \tag{16}$$

If such nesting is not accomplished, the factorials in the denominators of the unnested terms will lead to machine overflow. The order of computation must be from inside the parentheses outward. In terms of elliptic forms,

$$\widehat{C} = a\left(1 - \cos\frac{\widehat{X}}{\sqrt{a}}\right)$$

$$\widehat{U} = a^{3/2}\left(\frac{\widehat{X}}{\sqrt{a}} - \sin\frac{\widehat{X}}{\sqrt{a}}\right). \tag{17}$$

A starting value for $\widehat{X}$ when 1/a is negative is obtained by solving the cubic equation formed when only one term of $\widehat{C}$ and $\widehat{U}$ are used in equation (15). As noted by Pitkin (1964), such an approximation does not always work. As also found by Pitkin (1964), the solution of equation (15) is not entirely straightforward. Following the Newton approximation procedure where

$$f(\widehat{X}) = \widehat{M} - r_0\widehat{X} - D_0\widehat{C} - c_0\widehat{U} \tag{18}$$

(and the right-hand term when set equal to zero is the universal variable form of Kepler's equation), we find the derivative analytically by

$$f'(\hat{X}) = -r_0 - D_0 \hat{S} - c_0 \hat{C} = -r. \qquad (19)$$

The next improved value of $\hat{X}$ is then used to compute new values of $\hat{C}$, $\hat{U}$, and $\hat{S}$, and a new iteration for $\hat{X}$ initiated; i.e., if $\hat{X}_{(1)}$ is the first approximation for $\hat{X}$, e.g., equal to $\hat{M}/a$ for elliptical orbits (a is positive), or the solution to the cubic

$$\hat{M} = r_0 \hat{X}_{(1)} + D_0 \frac{\hat{X}_{(1)}}{2} + c_0 \frac{\hat{X}^3_{(1)}}{6}$$

for hyperbolic orbits * (a is negative), then the improvement (correction) to $\hat{X}$ is

$$\delta \hat{X}_{(1)} = \frac{f(\hat{X}_{(1)})}{-f'(X_{(1)})} = \frac{f(\hat{X}_{(1)})}{r} .$$

The second approximation is then

$$\hat{X}_{(2)} = \hat{X}_{(1)} + \delta \hat{X}_{(1)} .$$

The iteration is continued to the ith iteration at which point it is terminated when

$$(\delta \hat{X}_{(1)})^2 = \frac{r_i \epsilon}{|D_i| + |c_i \delta X_{(i)}|} ,$$

where ϵ can be taken as 10^{-8}, $c_i = 1 - r_i/a$, and $D_i = \vec{r}_i \cdot \dot{\vec{r}}_i/\sqrt{\mu}$. This termination criterion results from Ostrowski's theorem is discussed on p. 68 of Pitkin (1964).

Let us now quote from Pitkin's findings (1964) (Note $\hat{C}^* \triangleq a\hat{C} - a\hat{X}^2/2$ and $\hat{U}^* \triangleq a\hat{U} - a\hat{X}^3/6$): "It is at this point that much trouble has been encountered in attempts to use universal variables. There is a great temptation to use a first order correction technique, particularly in differential correction work, because of the particularly simple forms for the derivatives of the universal variables:

i) $\hat{U}^{*\prime} = \hat{C}^*$ ii) $\hat{C}^{*\prime} = \hat{U}$

iii) $\hat{U}' = \hat{C}$ iv) $\hat{C}' = \hat{S}$

v) $\hat{S}' = 1 + \alpha C$.

The corrections would then seem to be

$$\delta \hat{U}^* = \hat{C}^* \delta \hat{X}; \qquad \delta \hat{C}^* = \hat{U} \delta \hat{X}; \text{ etc.} \qquad (20)$$

This approach has been found inadequate in this work because Kepler's equation can be satisfied within a given tolerance with erroneous values of $\hat{C}$ and $\hat{U}$. The subsequent representation of $\vec{r}$ and $\dot{\vec{r}}$ from the elements $\vec{r}_0$ and $\dot{\vec{r}}_0$ will then be in error since $\hat{C}$, $\hat{U}$ and $\hat{S}$ appear in the representation coefficients (f and g series). To correct this difficulty, higher order terms must be introduced in the correction formulae. Taking the Taylor series expansion for $\hat{U}^*$, for instance,

$$\hat{U}^{*(2)} - \hat{U}^{*(1)} = \delta \hat{U}^* = \hat{U}^{*\prime} \delta \hat{X} + \hat{U}^{*\prime\prime} \frac{\delta \hat{X}^2}{2} + \ldots , \qquad (21)$$

substituting for the derivatives and nesting for computational accuracy gives to fifth order

$$\delta \hat{U}^* + \delta \hat{X} \left[\hat{C}^* + \frac{\delta \hat{X}}{3} \hat{C} + \frac{\delta \hat{X}}{4} \left(\hat{S} + \frac{\delta \hat{X}}{5} (1 + \alpha \hat{C}) \right) \right] \qquad (22)$$

and likewise

$$\hat{C}^* = \delta \hat{X} \left\{ \hat{U} + \frac{\delta \hat{X}}{2} \left[C + \frac{\delta \hat{X}}{3} \left(S + \frac{\delta \hat{X}}{4} (1 + \alpha \hat{C} + \frac{\delta \hat{X}}{5} \hat{S}) \right) \right] \right\} . \qquad (23)$$

It has been found that five or more terms of the Taylor expansions are needed to obtain agreement with results obtained either by classical formulas or by recomputation of the universal variables from their (defining) series forms." Pitkin has chosen to recompute the variables $\hat{U}$, $\hat{C}$, and $\hat{S}$ from their defining series.

Continuing our example of developing the Encke reference orbit using universal variables, we introduce the f and g notation

$$f = 1 - \frac{\hat{C}}{r_0} \qquad (24)$$

* In elliptical orbits the value of $|\hat{M}/a^{3/2}|$ should always be reduced to modulo 2π before beginning the iteration for $\hat{X}$. This keeps the number of terms required of the universal series to a minimum. If $\hat{M}/a^{3/2} \geq 2\pi$ one makes the change

$$\hat{M}_{new} = \hat{M}_{old} - 2\pi a^{3/2} .$$

Double precision arithmetic is usually useful for this shift.

$$g = \frac{\widehat{M} - \widehat{U}}{\sqrt{\mu}} = \tau - \frac{\widehat{U}}{\sqrt{\mu}} \tag{25}$$

$$\widehat{S} = \widehat{X} - \frac{1}{a}\widehat{U} = \frac{d\widehat{C}}{d\widehat{X}} \tag{26}$$

$$g = \frac{r_0\widehat{S} + D_0\widehat{C}}{\sqrt{\mu}} \tag{27}$$

and

$$\vec{r} = f\vec{r}_0 + g\dot{\vec{r}}_0 \ . \tag{28}$$

If velocity is also desired, then we calculate, using equation (26),

$$r = r_0 + D_0\widehat{S} + c_0\widehat{C} \tag{29}$$

$$\dot{f} = -\frac{\sqrt{\mu}}{r\,r_0}\widehat{S} \tag{30}$$

$$\dot{g} = 1 - \frac{\widehat{C}}{r} \tag{31}$$

$$\dot{\vec{r}} = \dot{f}\vec{r}_0 + \dot{g}\dot{\vec{r}}_0 \ . \tag{32}$$

The aim of the foregoing formulation has been to put the semimajor axis, a, into the denominator, so that terms involving it will become zero for parabolic orbits, and to keep the eccentricity, e, in the numerator so that terms involving it will become zero for circular orbits; in other words we wish to avoid terms which tend to large values. (Note that $e^2 = c_0^2 + 1/a(D_0^2)$.)

At every t we can produce a new set of $\vec{r}$ and $\dot{\vec{r}}$, so that if necessary, it is a simple matter to shift the epoch from t_0 to t. Thus, by replacing the designations t, $\vec{r}$, $\dot{\vec{r}}$, by t_0, $\vec{r}_0$, $\dot{\vec{r}}_0$, we can improve the convergence of the series for the next step or steps.

If it is desired to let $t = t_0$ increase beyond one-half period, we can subtract the period P from $t - t_0$, automatically shifting the epoch, without changing the values of the parameters $\vec{r}_0$ and $\dot{\vec{r}}_0$. More exactly, in the universal formulation, the epoch is shifted by subtracting $2\pi\sqrt{a}$ from $\widehat{X}$ when $\widehat{X} > \pi\sqrt{a}$. As noted by Pitkin, if one shifts $\widehat{U}$ and $\widehat{X}$ each period, then there is no need to worry about series convergence.

III. ADVANCED EQUATIONS

Aside from precise prediction, the most important application of the Encke procedure is to form a part of a differential correction orbit determination program. We essentially proceed by employing the Encke predictor to "represent" or compute observations of a spacecraft as if it were on our first approximation or preliminary orbit. Residuals are then formed by subtracting the computed data (e.g., $\dot{\rho}_c$ based upon the preliminary orbit) from the observed data (e.g., $\dot{\rho}_0$). The purpose of the differential correction process is to define the orbital parameters (and/or other characteristics of the system) such that these residuals are minimized. Such a minimization is usually taken in the least squares sense; i.e., the parameters are adjusted until the sum of the squares of the residuals is a minimum. Thus we assume that the residuals, $\Delta\dot{\rho}_i$, are related to improvements of the parameters, e.g., Δa, Δe, ... or, in general, Δp_1, Δp_2, ... Δp_j, ..., Δp_n (in which even the observation station's coordinates or relevant astrodynamic constants could be considered as parameters). The most general relationship between these quantities is a Taylor series in n variables,

$$\dot{\rho}_{io}(p_{o1}, p_{o2}, \cdots, p_{oj}, \cdots, p_{on}, t_i) = \dot{\rho}_{ic}(p_{c1}, p_{c2}, \cdots, p_{cj}, \cdots, p_{cn}, t_i) + \frac{\partial\dot{\rho}(p_{c1}, p_{c2}, \cdots, p_{cj}, \cdots, p_{cn}, t_i)}{\partial p_{c1}}(p_{o1} - p_{c1}) + \cdots, \tag{33}$$

where $\Delta\dot{\rho}_i \triangleq \dot{\rho}_{io} - \dot{\rho}_{ic}$ stands for any i th "observed-minus-computed" residual and $\Delta p_j \triangleq p_{oj} - p_{cj}$ is an improvement to any j th parameter (p_{oj} being an "objective" value of the j th parameter and p_{cj} being the "conjectured" value; p_{oj} is a constant).

Thus for n observations of range-rate:

$$\Delta\dot{\rho}_1 = \left(\frac{\partial\dot{\rho}_1}{\partial p_1}\right)\Delta p_1 + \left(\frac{\partial\dot{\rho}_1}{\partial p_2}\right)\Delta p_2 + \cdots + \left(\frac{\partial\dot{\rho}_1}{\partial p_j}\right)\Delta p_j + \cdots + \left(\frac{\partial\dot{\rho}_1}{\partial p_n}\right)\Delta p_n$$

$$\Delta\dot{\rho}_2 = \left(\frac{\partial\dot{\rho}_2}{\partial p_1}\right)\Delta p_1 + \left(\frac{\partial\dot{\rho}_2}{\partial p_2}\right)\Delta p_2 + \cdots + \left(\frac{\partial\dot{\rho}_2}{\partial p_n}\right)\Delta p_n$$

$$\vdots$$

$$\Delta\dot{\rho}_i = \left(\frac{\partial\dot{\rho}_i}{\partial p_1}\right)\Delta p_1 + \left(\frac{\partial\dot{\rho}_i}{\partial p_2}\right)\Delta p_2 + \cdots + \left(\frac{\partial\dot{\rho}_i}{\partial p_j}\right)\Delta p_j + \cdots + \left(\frac{\partial\dot{\rho}_i}{\partial p_n}\right)\Delta p_n$$

$$\vdots$$

$$\Delta\dot{\rho}_N = \left(\frac{\partial\dot{\rho}_N}{\partial p_1}\right)\Delta p_1 + \left(\frac{\partial\dot{\rho}_N}{\partial p_2}\right)\Delta p_2 + \cdots + \left(\frac{\partial\dot{\rho}_N}{\partial p_j}\right)\Delta p_j + \cdots + \left(\frac{\partial\dot{\rho}_N}{\partial p_n}\right)\Delta p_n . \qquad (34)$$

The difficulty in differential correction is usually not scarcity of data, but rather the difficulty in solving equations (34) for the correction to the elements (Δp_j's) that yield the minimum sum of the squares of the residuals. Although this problem is manifested by so-called "ill-conditioning" of the matrix identified with the least squares solution for equations (34), the basic problem is more physical than mathematical. Often we find that the observed data are simply not of a character that allows for the "measurement" of a given parameter of a system. Thus, no matter what the quantity or quality of these data, the system still remains defective. The lack of coupling between the observational data and the elements being sought is often indicated by the smaller size of the off-diagonal terms in the $(A^T A)^{-1}$ matrix which we shall develop presently. For example, Speer at Marshall Space Flight Center has found that the angles and magnitude of the burnout velocity vector ($\dot{s}, \theta, A$) can be corrected accurately by down-range tracking data, but not the position of burnout (r, α, δ). Forcing the differential correction to define position as well as velocity simply leads to a singularity in the matrix inversion process.

Equation (34) can be inverted and solved for the values of $\Delta p_1, \ldots \Delta p_j, \ldots \Delta p_n$, to be added to the original values of the parameters (or station coordinates or astrodynamic constants) $p_1, \ldots p_n$, thereby yielding an improved set (provided the number of residuals, N, equals or exceeds the number of parameters, n, and there are no singularities in the inversion). When N exceeds n, the most probable values of the Δp_j are usually found by least squares from which the standard deviation of the elements can be obtained as a by-product of the inversion.

The recomputed parameters $p_{j\,new} = p_{j\,old} + \Delta p_j$ can then be substituted back into equation (34) and if N = n the residuals would now be all identically zero. Unfortunately, even in this case the n parameters would still not exactly fit the N observations since there exists truncation error in the establishment of equation (34). Thus more nonlinear terms might still be included in the series equation (33). The influence of this truncation error is often forgotten and could, if the Δp_j's were fairly large, assume an importance exceeding that of the observational errors themselves. Of course, if the improved parameters are used to recompute improved partials in equation (34) when the inversion is repeated, then the Δp_j's should become smaller and the inversion would exhibit much less truncation error if the nonlinear, truncated terms are not too large initially. (Although the parameters p_j will surely change with time due to perturbations, they pertain here only to the orbit at some fixed time of "osculation." We are therefore establishing improvements to the time-constant osculating orbital elements. "Osculating" here implies a particular two-body orbit that would have been traversed by the space vehicle if all the perturbative forces had been instantaneously removed from this time forward. Since this fictitious orbit is tangent or "kisses" the actual true orbit, it is termed osculating orbit and is defined by osculating orbital elements.)

It is difficult to avoid the inversion process in establishing general analytical expressions for corrections to the elements even in the "filter" theory approach. If we wish to avoid inversion, the redetermination of the orbit may be used, perhaps based on a minimum number of normal points (e.g., three sets of α and δ), but the disadvantages of redetermination remain. In short, it is preferable to treat the problem as dynamic and continuing rather than as a static redetermination process.

It seems wise to digress briefly at this point upon the subject of weighted least squares, since the procedure has rather universal application to many problems in astrodynamics (e.g., plate constants, smoothing, evaluation of astrodynamic constants

from observation data, etc.). Taking equation (34) as our example, we would like to select the values of a typical parameter improvement Δp_j, such that the sum of the squares of the weighted residuals, a typical member of which is

$$w_i^2 \left[\Delta\dot{\rho}_i - \sum_{j=1}^{n} \left(\frac{\partial \dot{\rho}_i}{\partial p_j} \right) \Delta p_j \text{ (selected)} \right]^2 \triangleq w_i^2 \delta_i^2 , \tag{35}$$

is a minimum; i.e., such that $\sum_{i=1}^{n} w_i^2 \delta_i^2$ is a minimum, or for the typical improvement in p_j,

$$\partial \left(\sum_{i=1}^{N} w_i^2 \delta_i^2 \right) \Big/ \partial \Delta p_j = 0.$$

Following this logic, we conclude that

$$\sum_{i=1}^{N} w_i^2 \delta_i \left(\partial \delta_i / \partial \Delta p_j \right) = 0 ,$$

or from equation (35),

$$\sum_{i=1}^{N} w_i^2 \left\{ \Delta\dot{\rho}_i - \frac{\partial \dot{\rho}_i}{\partial p_1} \Delta p_1 - \frac{\partial \dot{\rho}_i}{\partial p_2} \Delta p_2 - \right.$$

$$\left. \cdots - \frac{\partial \dot{\rho}_i}{\partial p_j} \Delta p_j - \cdots - \frac{\partial \dot{\rho}_i}{\partial p_n} \Delta p_n \right\} \left\{ \frac{\partial \dot{\rho}_i}{\partial p_1} + 0 \right\} = 0,$$

$$\sum_{i=1}^{N} w_i^2 \left\{ \Delta\dot{\rho}_i - \frac{\partial \dot{\rho}_i}{\partial p_1} \Delta p_1 - \frac{\partial \dot{\rho}_i}{\partial p_2} \Delta p_2 - \right.$$

$$\left. \cdots - \frac{\partial \dot{\rho}_i}{\partial p_j} \Delta p_j - \cdots - \frac{\partial \dot{\rho}_i}{\partial p_n} \Delta p_n \right\} \left\{ \frac{\partial \dot{\rho}_i}{\partial p_j} \right\} = 0,$$

$$\sum_{i=1}^{N} w_i^2 \left\{ \Delta\dot{\rho}_i - \frac{\partial \dot{\rho}_i}{\partial p_1} \Delta p_1 - \frac{\partial \dot{\rho}_i}{\partial p_2} \Delta p_2 - \right.$$

$$\left. \cdots - \frac{\partial \dot{\rho}_i}{\partial p_j} \Delta p_j - \cdots - \frac{\partial \dot{\rho}_i}{\partial p_n} \Delta p_n \right\} \left\{ \frac{\partial \dot{\rho}_i}{\partial p_n} \right\} = 0. \tag{36}$$

Equation (36) is obtained by observing that since $\Delta\dot{\rho}_i$ is a typical observed-minus-computed residual, and since the observed portion remains a constant (as does the "objective" portion of Δp_j),

$$\frac{\partial \Delta\dot{\rho}_i}{\partial \Delta p_j} = \frac{-\partial \dot{\rho}_{ci}}{-\partial p_{cj}} = \frac{\partial \dot{\rho}_i}{\partial p_j} .$$

Furthermore, $\partial\dot{\rho}_i/\partial p_j$ and Δp_j selected do not participate in a change with any p_j. Expanding the typical member of equation (36) we find:

$$\sum_{i=1}^{N} w_i^2 \left(\frac{\partial \dot{\rho}_i}{\partial p_1} \frac{\partial \dot{\rho}_i}{\partial p_j} \right) \Delta p_1 + \sum_{i=1}^{N} w_i^2 \left(\frac{\partial \dot{\rho}_i}{\partial p_2} \frac{\partial \dot{\rho}_i}{\partial p_j} \right) \Delta p_2 +$$

$$\cdots + \sum_{i=1}^{N} w_i^2 \left(\frac{\partial \dot{\rho}_i}{\partial p_n} \frac{\partial \dot{\rho}_i}{\partial p_j} \right) \Delta p_n$$

$$= \sum_{i=1}^{N} w_i^2 \left(\frac{\partial \dot{\rho}_i}{\partial p_j} \right) \Delta\dot{\rho}_i , \quad j = 1, 2, \ldots, n \tag{37}$$

which is the typical jth member of a system of n equations in n unknowns (the Δp_j's). These are the so-called "normal equations" and here reduced the problem of N equations in n unknowns (where $N >> n$) to the soluble set of n equations in the n unknown Δp_j's.

In matrix notation equations (34) (with all weights taken as unity) become

$$\underbrace{\begin{bmatrix} (\partial\dot{\rho}_1/\partial p_1) & \cdots & (\partial\dot{\rho}_1/\partial p_j) & \cdots & (\partial\dot{\rho}_1/\partial p_n) \\ \vdots & & \vdots & & \vdots \\ (\partial\dot{\rho}_i/\partial p_1) & \cdots & (\partial\dot{\rho}_i/\partial p_j) & \cdots & (\partial\dot{\rho}_i/\partial p_n) \\ \vdots & & \vdots & & \vdots \\ (\partial\dot{\rho}_N/\partial p_1) & \cdots & (\partial\dot{\rho}_N/\partial p_j) & \cdots & (\partial\dot{\rho}_N/\partial p_n) \end{bmatrix}}_{A} \underbrace{\begin{bmatrix} \Delta p_1 \\ \vdots \\ \Delta p_j \\ \vdots \\ \Delta p_n \end{bmatrix}}_{\Delta\vec{x}}$$

$$= \underbrace{\begin{bmatrix} \Delta\dot{\rho}_1 \\ \vdots \\ \Delta\dot{\rho}_i \\ \vdots \\ \Delta\dot{\rho}_N \end{bmatrix}}_{\Delta\vec{z}} \tag{38}$$

or symbolically $A\,\Delta\vec{x} = \Delta\vec{z}$ (where $\Delta\vec{x}$ and $\Delta\vec{z}$ can be looked upon as n and N dimensional vectors, respectively). We have not replaced the specific range-rate observations $\dot{\rho}_i$ by a general observation vector $\vec{z}$. Again it is emphasized that $\dot{\rho}$ is only a typical datum. In general, $\vec{z}$ might have the form

$$\Delta\vec{z} = \begin{bmatrix} \Delta\dot{\rho}_1 \\ \Delta\rho_1 \\ \vdots \\ \Delta\dot{\rho}_i \\ \Delta\rho_i \\ \vdots \\ \Delta\dot{\rho}_N \\ \Delta\rho_N \end{bmatrix} \quad \text{or} \quad \Delta\vec{z} = \begin{bmatrix} \Delta\alpha_1 \\ \Delta\delta_1 \\ \vdots \\ \Delta\alpha_i \\ \Delta\delta_i \\ \vdots \\ \Delta\alpha_N \\ \Delta\delta_N \end{bmatrix}$$

In these cases $\Delta\vec{z}$ is a column matrix composed of 2N data taken during N observations. Such a data set is perfectly usable if the partial derivatives that compose A are suitably chosen; e.g., we would form $\partial\dot{\rho}_i/\partial p_j$, $\partial\rho_i/\partial p_j$, $\partial\alpha_i/\partial p_j$, $\partial\delta_i/\partial p_j$, etc. Even more inhomogeneous mixing of data is also acceptable, and the $\Delta\vec{z}$ may be composed of residuals in data obtained from various different sensors at different times; e.g.,

$$\Delta\vec{z} = \begin{bmatrix} \Delta\rho_1 \\ \Delta h_1 \\ \Delta A_1 \\ \Delta\rho_2 \\ \Delta\alpha_{T2} \\ \Delta\delta_{T2} \\ \Delta\rho_3 \\ \Delta\rho_4 \\ \Delta\rho_5 \end{bmatrix} \quad \text{etc.},$$

which would imply that data are being collected from a sensor giving range-rate and horizon-system angles ($\dot{\rho}$, h, A), a sensor giving range and direction in an equatorial system (ρ, α_T, δ_T), and a sensor giving a series of ranges (ρ's). In each case the partial derivatives should be suitably modified. If N = n we have a square matrix that can be uniquely inverted; i.e., symbolically the inversion is A^{-1} where we define

$$A^{-1}A = \begin{bmatrix} 1 & 0 & \cdots & 0 \\ 0 & 1 & \cdots & 0 \\ 0 & 0 & \cdots & 0 \\ 0 & 0 & \cdots & 0 \\ . & . & & . \\ . & . & & . \\ . & . & & . \\ 0 & 0 & \cdots & 1 \end{bmatrix} . \qquad (39)$$

In this case we have the same number of equations (n) as we have unknowns (N = n); i.e., we have just as many parameters and observations. This inversion process (denoted as "A inverse" or simple as A^{-1}) is simply a formal procedure or symbolism for systematically applying Cramer's rule in which, given $\vec{z}$ in terms of a linear equation in $\vec{x}$ (i.e., $A\Delta\vec{x}$), we solve for $\Delta\vec{x}$ in terms of $\Delta\vec{z}$. A shorthand symbolism for the inversion is $\Delta\vec{x} = A^{-1}\Delta\vec{z}$, again just a symbolism for Cramer's rule.

The proof of the least squares symbolism in matrix notation is (where N > n) rather ad hoc. We attempt to achieve a square matrix by multiplying both sides of equation (38) by the transpose of the matrix A, termed A^T. A transpose of a matrix is simply generated by substituting rows for columns, e.g., in this case

$$A^TA = \begin{bmatrix} (\partial\dot{\rho}_1/\partial p_1) & \cdots & (\partial\dot{\rho}_i/\partial p_1) & \cdots & (\partial\dot{\rho}_N/\partial p_1) \\ \vdots & & \vdots & & \vdots \\ (\partial\dot{\rho}_1/\partial p_j) & \cdots & (\partial\dot{\rho}_i/\partial p_j) & \cdots & (\partial\dot{\rho}_N/\partial p_j) \\ \vdots & & \vdots & & \vdots \\ (\dot{\rho}_1/\partial p_n) & \cdots & (\partial\dot{\rho}_i/\partial p_n) & \cdots & (\partial\dot{\rho}_N/\partial p_n) \end{bmatrix} \begin{bmatrix} (\partial\dot{\rho}_1/\partial p_1) & \cdots & (\partial\dot{\rho}_1/\partial p_j) & \cdots & (\partial\dot{\rho}_1/\partial p_n) \\ \vdots & & \vdots & & \vdots \\ (\partial\dot{\rho}_i/\partial p_1) & \cdots & (\partial\dot{\rho}_i/\partial p_j) & \cdots & (\partial\dot{\rho}_i/\partial p_n) \\ \vdots & & \vdots & & \vdots \\ (\partial\dot{\rho}_N/\partial p_1) & \cdots & (\partial\dot{\rho}_N/\partial p_j) & \cdots & (\partial\dot{\rho}_N/\partial p_n) \end{bmatrix} . \qquad (40)$$

An explicit evaluation of this matrix product is

$$A^T A = \begin{bmatrix} \sum_{i=1}^{N} (\partial\dot{\rho}_i/\partial p_1)^2 & \cdots & \sum_{i=1}^{N} (\partial\dot{\rho}_i/\partial p_1)(\partial\dot{\rho}_i/\partial p_j) & \cdots & \sum_{i=1}^{N} (\partial\dot{\rho}_i/\partial p_1)(\partial\dot{\rho}_i/\partial p_n) \\ \vdots & & \vdots & & \vdots \\ \sum_{i=1}^{N} (\partial\dot{\rho}_i/\partial p_1)(\partial\dot{\rho}_i/\partial p_j) & \cdots & \sum_{i=1}^{N} (\partial\dot{\rho}_i/\partial p_j)^2 & \cdots & \sum_{i=1}^{N} (\partial\dot{\rho}_i/\partial p_j)(\partial\dot{\rho}_i/\partial p_n) \\ \vdots & & \vdots & & \vdots \\ \sum_{i=1}^{N} (\partial\dot{\rho}_i/\partial p_1)(\partial\dot{\rho}_i/\partial p_n) & \cdots & \sum_{i=1}^{N} (\partial\dot{\rho}_i/\partial p_j)(\partial\dot{\rho}_i/\partial p_n) & \cdots & \sum_{i=1}^{N} (\partial\dot{\rho}_i/\partial p_n)^2 \end{bmatrix} \tag{41}$$

with $a_{kj} = \sum_{i=1}^{N} (\partial\dot{\rho}_i/\partial p_k)(\partial\dot{\rho}_i/\partial p_j)$ being the typical matrix element. $A^T A$ is now a square (n x n) matrix.
To recover the least squares normal equations, we form $A^T \Delta\vec{z}$; i.e.,

$$\begin{bmatrix} (\partial\dot{\rho}_1/\partial p_1) & \cdots & (\partial\dot{\rho}_i/\partial p_1) & \cdots & (\partial\dot{\rho}_N/\partial p_1) \\ \vdots & & \vdots & & \vdots \\ (\partial\dot{\rho}_1/\partial p_j) & \cdots & (\partial\dot{\rho}_i/\partial p_j) & \cdots & (\partial\dot{\rho}_N/\partial p_j) \\ \vdots & & \vdots & & \vdots \\ (\partial\dot{\rho}_1/\partial p_n) & \cdots & (\partial\dot{\rho}_i/\partial p_n) & \cdots & (\partial\dot{\rho}_N/\partial p_n) \end{bmatrix} \begin{bmatrix} \Delta\dot{\rho}_1 \\ \vdots \\ \Delta\dot{\rho}_i \\ \vdots \\ \Delta\dot{\rho}_N \end{bmatrix} = \begin{bmatrix} \sum_{i=1}^{N} \Delta\dot{\rho}_i \, \partial\rho_i/\partial p_1 \\ \vdots \\ \sum_{i=1}^{N} \Delta\dot{\rho}_i \, \partial\rho_i/\partial p_j \\ \vdots \\ \sum_{i=1}^{N} \Delta\dot{\rho}_i \, \partial\rho_i/\partial p_n \end{bmatrix} \tag{42}$$

Hence the least squares form is obtained from

$$\Delta\vec{x} = (A^T A)^{-1} A^T \Delta\vec{z}; \tag{43}$$

that is

$$\begin{bmatrix} \Delta p_1 \\ \vdots \\ \Delta p_i \\ \vdots \\ \Delta p_n \end{bmatrix} = [\text{equation (41)}]^{-1} [\text{equation (42)}].$$

Thus we solve for the improvements to the parameters. If the weights are included in this symbolism, then

$$\Delta\vec{x} = (A^T \vec{W} A)^{-1} A^T \vec{W} \Delta\vec{z}, \tag{44}$$

where

$$\vec{W} \triangleq \begin{bmatrix} w_1^2 & & & & \\ & w_2^2 & & & \\ & & \ddots & & \\ & & & w_i^2 & \\ & & & & \ddots \\ & & & & & w_N^2 \end{bmatrix}$$

IV. ENGINEERING APPLICATIONS OF THE RESEARCH

The ultimate goal of the research efforts described in the previous sections is to develop automated procedures to predict tracking and communications and procedures for orbit determination. This section presents explanations of the automated

procedure and engineering applications. The evolvement of methods which predict tracking coverage to methods of orbit determination is only natural since the inputs to orbit determination methods are tracking and communications data.

The basic Encke computer program, which is the backbone of tracking prediction and orbit determination, was mentioned in the introduction, and the refinements which are incorporated were explained in the text. For a more detailed explanation of the implementation of the Encke equations, a cursory flow diagram of the computation procedure is presented in Figure 4.

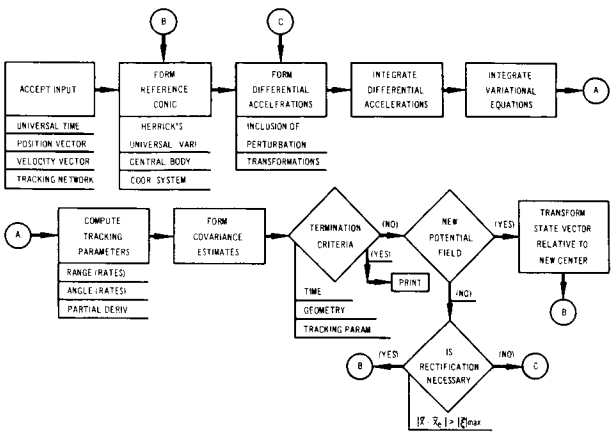

FIGURE 4. FLOW OF THE ENCKE - TRACKING PROGRAM

The program accepts inputs of universal time, position vector, velocity vector, and the tracking network. The tracking network may include the standard Deep Space Instrumentation Network, Manned Space Flight Network, and any other sites that should be desired by the investigator including lunar based sites for parametric studies. Since the program includes an aspherical moon (with provision for triaxiality), the lunar stations may be considered in their true selenographic position.

The flow diagram of the program indicates the order of the computations which are performed. The first four blocks are in line with the normal Encke procedure. It is at this point (starting with the integration of the variational equations) that the program takes on the special purpose features related to orbit determination and tracking prediction. The variational equations, when integrated, give the necessary partial derivatives of the initial conditions (based on the desired epoch) which are of prime importance for orbit determination. After the variational equations are integrated, tracking parameters are computed.

In this section of the program, the values which are of interest to the aerospace engineer investigating the tracking and communications coverage of a space mission are computed. Certain values are measured by each type of tracking system; for example, the Unified S-Band system measures two angles (x-angle and y-angle) that are angular rotations about two mutually perpendicular earth-fixed coordinates, and range and range rate, while other systems measure parameters such as range sum, range difference, azimuth, and elevation. The measured parameters of each tracking site are computed based on the relative position and velocity of the space vehicle and the tracking station. These computations include the refinement of atmospheric refraction. In addition to measured parameters, other parameters are computed such as elevation angle, acquisition time, and maximum elevation angle.

The desired result of tracking a space vehicle is to determine the exact path of its trajectory. Since radar measurements are noisy, the geometrical solutions for position and velocity are noisy. This noise is random and has associated with it a statistical distribution; thus the solution for position and velocity contains, implicitly, an associated statistical distribution. Any complete study of tracking coverage should include the error bounds of determining the position and velocity of the spacecraft. Each of the tracking systems has associated with it a certain statistical distribution of its measured parameters. These statistical distributions can be independent or correlated; for this reason the partial derivatives of the geometric solution of position and velocity (with respect to measured parameters) are computed so that covariance matrices of the vehicle state can be formulated. From these covariance matrices and their associated eigen vectors, either "error ellipsoids" can be determined or the statistical distribution of the state may be specified by Monte Carlo methods.

From this point on in the flow diagram of Figure 4, the Encke procedure is again compatible with other trajectory computation procedures.

The process of flight evaluation and particularly orbit determination, which is carried on during and for several weeks after the mission of the spacecraft has terminated, uses the basic ingredients of the

Encke prediction program. The basic orbit determination procedure is outlined in block form in Figure 5. The term "orbit determination" is meant to imply the building or generation of the orbit which the space vehicle has traversed by use of tracking and telemetry data.

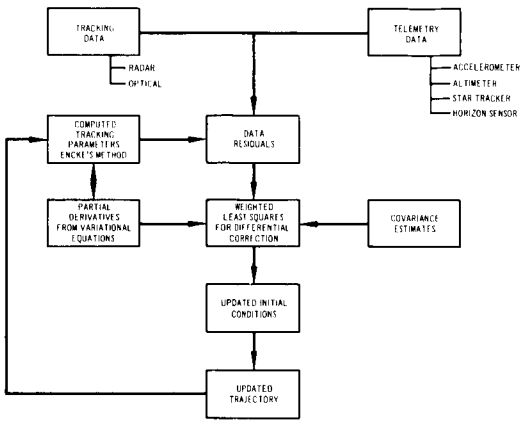

FIGURE 5. ORBIT DETERMINATION

The program is constructed to accept tracking and telemetry data. These data are noisy, not only in the classical statistical sense, but also in the stochastic sense. If an orbit were constructed using only the tracker inputs, it would show discontinuities both in position and velocity. Such discontinuities simply do not exist in the trajectories of orbiting bodies. To overcome tracking system discontinuities, tracking parameters are computed by the use of the Encke prediction program and data residuals are formed. These data residuals are then processed by a weighted least squares method (the weighting being a function of the partial derivatives from the variational equations and the covariance estimates). From the weighted least squares processer comes a set of updated initial conditions which are integrated forward to form an updated trajectory which in turn gives new partial derivatives, new data residuals and new initial conditions after weighted least squares processing. This process is continued or reiterated until a suitable orbit is determined.

One of the primary considerations of an accurate orbit determination program should be its ability to solve for a large number of unknown variables or error sources. These unknown variables are over and above the position and velocity vectors previously discussed. Of primary consideration should be error sources of the following nature: station coordinate errors, tracking observation bias, tracking observation timing errors, aerodynamic drag, earth's gravitation constant, velocity of light, etc. These error sources can contaminate the solutions of position and velocity to such an extent that very erroneous results could be obtained.

During the post-flight orbit determinations of the Saturn I vehicles SA-6 and SA-7, it was observed that a possible station location error existed for the Carnarvon, Australia, tracking site. An attempt was made to isolate this probable error source. Solutions were made for the position and velocity vectors and the effects of drag over nine separate orbital arcs using tracking data from all available sources. When all solutions converged to stable values, after several iterations, solutions were then made only for the latitude and longitude of the Carnarvon tracking site. The differential corrections obtained from these solutions are given in the table below:

TABLE I. ORBITAL ARCS USED IN CARNARVON COORDINATE SOLUTIONS

Orbital Arc	Vehicle	Date of Orbital Arc	Differential Correction Carnarvon Latitude (deg)	Differential Correction Carnarvon Longitude (deg)
Arc # 1	SA-6	5-28-64	0.0033	0.0037
Arc # 2	SA-6	5-29-64	0.0002	0.0029
Arc # 3	SA-6	5-29-64	0.0032	0.0061
Arc # 4	SA-6	5-30-64	0.0044	0.0043
Arc # 5	SA-7	9-18-64	0.0051	0.0024
Arc # 6	SA-7	9-19-64	0.0013	-0.0041
Arc # 7	SA-7	9-20-64	0.0000	0.0041
Arc # 8	SA-7	9-21-64	-0.0006	0.0021
Arc # 9	SA-7	9-21-64	0.0029	0.0011
Mean			0.0022	0.0025

An error ellipsoid of these differential corrections is shown in Figure 6. This error ellipsoid describes the ninety-five percent probability boundaries on the differential corrections. All corrections plotted in this figure were reasonable in magnitude (with respect to the estimated possible station location errors for Carnarvon) and lie primarily in one quadrant. The mean value of the differential corrections for latitude (0.0022 deg) and for longitude (0.0025 deg) is also shown on the error ellipsoid. This mean

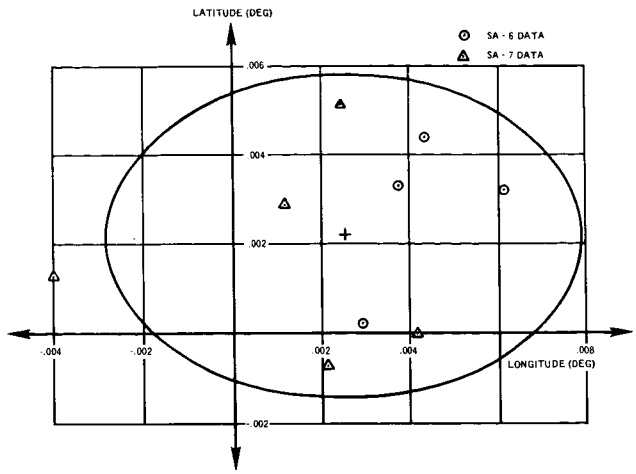

FIGURE 6. CARNARVON STATION COORDINATE ERROR ELLIPSE

error value represents approximately 250 meters and 280 meters in latitude and longitude, respectively. Applying these mean differential corrections to the Carnarvon station coordinates reduced the Carnarvon range residuals approximately thirty percent. The small sample size and the relatively small corrections obtained do not justify changing the Carnarvon station coordinates. They do, however, point out a need for future investigation.

Determining station locations to a very high degree of accuracy will be much more feasible for translunar flight when multistation tracking over long time periods will be possible. These long periods of tracking information, relatively free of the earth's atmospheric effects (one of the major error sources in the mathematical formulation of an ephemeris generation program), should provide sufficiently accurate tracking data for determination of any of the previous error sources mentioned, particularly station coordinate errors, station observation bias and station observation timing errors.

This example of station location error has been presented to clarify what is meant by "error sources" of the following nature: similar types of statistical solutions of bias, timing gravitational constant, etc. The techniques described previously are applied to these additional types of errors.

V. CONCLUSIONS

This paper described the research and engineering applications in tracking and communications in the earth-moon space. The goal of the research has been to develop automated procedures of tracking prediction and orbit determination which are useful to the engineer working in these areas.

The computer program which uses the Encke method is at the present time a four-body model (earth, moon, sun and spaceship). The methods described previously can, with slight modification, be used for interplanetary prediction and orbit determination. With the inclusion of ephemerides data of Mars, Venus and other planets of interest, the model discussed could be used for interplanetary prediction.

To be included in the near future are such refinements as relative correction to the Doppler shift, onboard data editing techniques and a study of the feasibility of using regularized variables. There is also a need to include perturbations which the vehicle gives to its own path, such as venting forces. The nature of such forces will be known from telemetry data which are included in orbit determination. There is, however, a problem in predicting this type of force since it appears to be random per se. Therefore, the incorporation of such data into any prediction procedure is a problem of serious concern.

Full utilization of the tools developed will come through practice and modification. As new sensing devices are developed for ground based and onboard tracking, the procedure must be modified to keep up with current technology. As new instruments are developed and tested the techniques described herein will be versatile enough that sophisticated studies of tracking and communication may be performed.

COMMUNICATIONS SYSTEMS RESEARCH AT MSFC

January 27, 1966

by

John G. Gregory
Carl T. Huggins
Paul M. Swindall

TABLE OF CONTENTS

HYDROGEN MASER RESEARCH ACHIEVEMENTS AT MSFC

by John G. Gregory

LIST OF TABLES

LIST OF ILLUSTRATIONS

CONTENTS (Continued). . .

DEVELOPMENT OF A SOLID-STATE IMAGE CONVERTER

by Carl T. Huggins

LIST OF ILLUSTRATIONS

PROPAGATION STUDIES

by Paul M. Swindall

CONTENTS (Continued). . .

LIST OF ILLUSTRATIONS

HYDROGEN MASER RESEARCH ACHIEVEMENTS AT MSFC

By

John G. Gregory

SUMMARY

The basic principles and the construction of a hydrogen maser and its potential as a highly stable frequency reference for precision tracking systems are discussed. Improvements in stability and size are presented and future improvements are proposed. Results of measurements of relative frequency stability of two masers and the comparison of a hydrogen maser and a cesium beam are discussed. Also presented is the status of the hydrogen maser program and possible areas of application.

LIST OF SYMBOLS

X - dimensionless measure of the external magnetic field, $X = \frac{\mu_e B_E}{\Delta W}$

I - quantum number related to the nuclear angular momentum

F - quantum number related to the total angular momentum of the entire atom

m_F - magnetic quantum number

μ_e - electronic dipole moment

B_E - external magnetic field

W - energy of the atom

I. INTRODUCTION

Tracking, communication, and guidance requirements for the launch, earth orbital, and deep space phases of a mission often demand highly stable frequency sources possessing a high order of short and long term frequency stability as well as a high degree of intrinsic reproducibility. Many tracking systems, such as MSFC's ODOP and command and communications system, use the doppler frequency for range measurements. Range rate measurements require a high order of short term stability; in range measurements the emphasis is placed upon long term stability.

More stringent requirements are placed upon long term stability when position data are required in addition to range and range rate data. Employing a three-station geometry and integrating the Doppler frequency gives position as well as range data. The three station configuration requires that the Doppler data obtained be referenced to a common, highly stable frequency source. This can be accomplished by transmitting a frequency reference from one station to the other two stations. Transmitting a stable frequency reference is undesirable because such transmission:

1. Is susceptible to variations caused by weather and atmospheric conditions.

2. Is a potential source of electromagnetic interference, particularly near the launch area.

3. Places limitations on the station geometry.

A solution to these problems would be to provide each station with its own frequency reference, whose instability would be a negligible factor in the determination of range, range rate, and position. In 1961, MSFC began a search for such a frequency source and found that the hydrogen maser, invented by Dr. Norman Ramsey of Harvard University, had excellent possibilities for providing long and short term stability. A contract was awarded to the Quantum Electronics Division of Varian Associates*, which had been working in the frequency control field with both hydrogen and cesium, to develop a hydrogen maser frequency source. The hydrogen maser

* Contract NAS 8-2604, principal experimenters are Dr. Robert Vessot and Dr. Jacques Vanier.

was chosen because it has the following desirable characteristics:

1. It has a narrow line width, resulting from atoms having a long interaction time in a very unperturbed condition.

2. Doppler shifts of the first order are very small because the average velocity of the atoms in the bulb is nearly zero.

3. Being a maser oscillator, the device has inherently low noise and avoids the disadvantages of electronic servos used to seek the center of the line.

II. BASIC THEORY

A hydrogen maser oscillator is a device which relies on three processes for successful operation:

1. Dissociation of molecular hydrogen into atomic hydrogen.

2. Selection of atoms of the proper energy state.

3. Storage of these atoms for a relatively long period of time.

A functional schematic diagram of the atomic hydrogen maser is given in Figure 1. Molecular hydrogen is dissociated by an electrical discharge and the atoms are formed into a beam. This beam contains atoms at various energy levels. Figure 2 shows the Zeeman splitting of the hyperfine energy levels of the ground electronic states of hydrogen. It is important to note that energy levels for which $m_F = 0$ leave the zero magnetic field axis with zero slope. Transitions between these levels afford the best opportunity for making highly stable frequency sources because the transition frequencies are least dependent upon fields arising from the environment.

The beam, containing hydrogen atoms in the various states, is passed through a state-selecting magnet where, by virtue of the differences in the effective atomic dipole moments, the upper pair of hyperfine levels are focused into a converging beam while the lower pair of hyperfine levels are deflected out of the beam (Fig. 2).

The beam containing the higher pair of hyperfine Zeeman states is passed into a specially coated quartz storage bulb located inside an RF cavity. The atoms make random collisions with the walls of the coated bulb and are reflected. During this process,

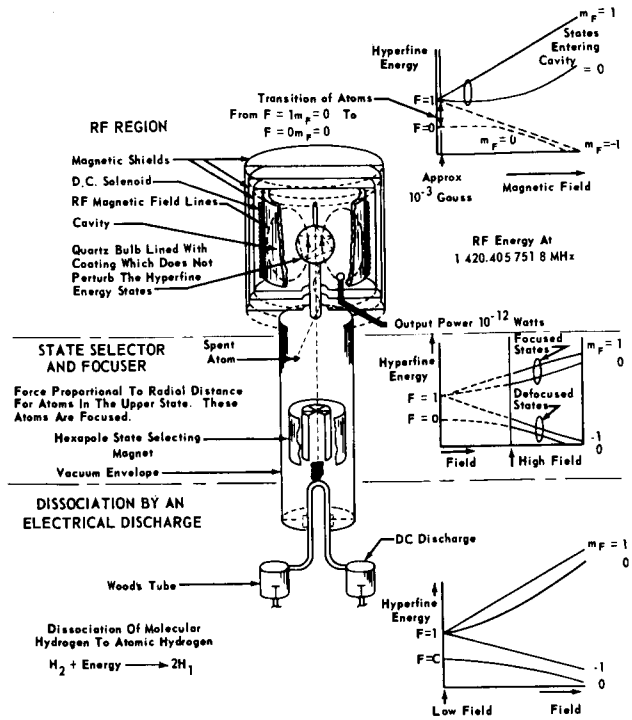

FIGURE 1. SCHEMATIC DIAGRAM OF THE HYDROGEN MASER

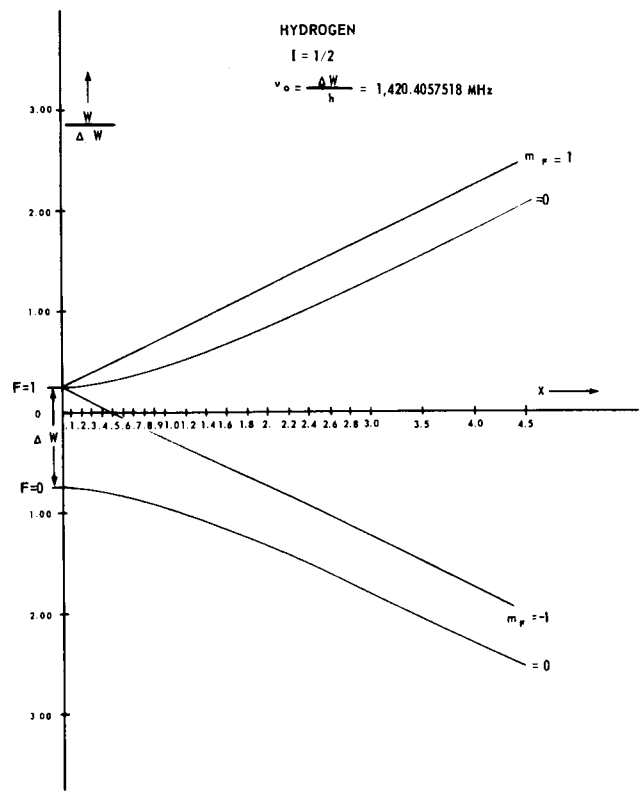

FIGURE 2. ZEEMAN ENERGY DIAGRAM FOR ATOMIC HYDROGEN

the atoms interact with the microwave field within the RF cavity which is tuned to the frequency of the hyperfine frequency of the F = 1, $m_F = 0 \rightarrow$ F = 0, $m_F = 0$ transition. The interaction between the atoms and the microwave field continues until the atoms give up their energy usefully to the microwave field. Interaction periods in the order of one second have been achieved. The long interaction time permits coherent stimulation of the hydrogen atoms and sustained maser oscillation. This is detected by means of a small coupling loop. The power level available is approximately 10^{-12} watts.

The quartz storage bulb and the RF cavity are surrounded by three sets of magnetic shields and a set of coils, as shown in the upper part of Figure 1. The magnetic shields are used to reduce the ambient field. The coils are used to produce a small, uniform magnetic field whose component is along the beam axis for the purpose of separating the Zeeman levels to be sure only the F = 1, $m_F = 0$ states in the selected atoms contribute to the maser action. It is important to point out also that, except for atomic hydrogen, the space within the maser is evacuated and that provisions are made for removing the expended hydrogen.

III. DESCRIPTION OF A HYDROGEN MASER

Figure 3 is a schematic diagram of a hydrogen maser similar to the two which were built for MSFC. The base of the maser, which is about the size of a desk, houses the hydrogen supply, discharge assembly, vacuum system, and thermal and magnetic field controls. The upper portion is cylindrical, 82 cm long and 48 cm in diameter, containing the storage bulb, microwave cavity, magnetic field coils, thermal coils, and magnetic shields. Figure 4 shows an enlarged view of the upper portion of the maser. Figure 5 is a photograph of one of MSFC's masers undergoing tests.

Commercial grade hydrogen, stored in a small tank, is passed through a controlled leak into a palladium purifier and then to the discharge chamber (Figs. 3 and 4). The discharge chamber, approximately 2.5 cm in diameter and 2.5 cm long, is located between two RF coils resonated at 112 MHz (Fig. 6). A solid-state crystal-controlled oscillator generates 10 watts of power and produces a discharge in the gas which dissociates molecular

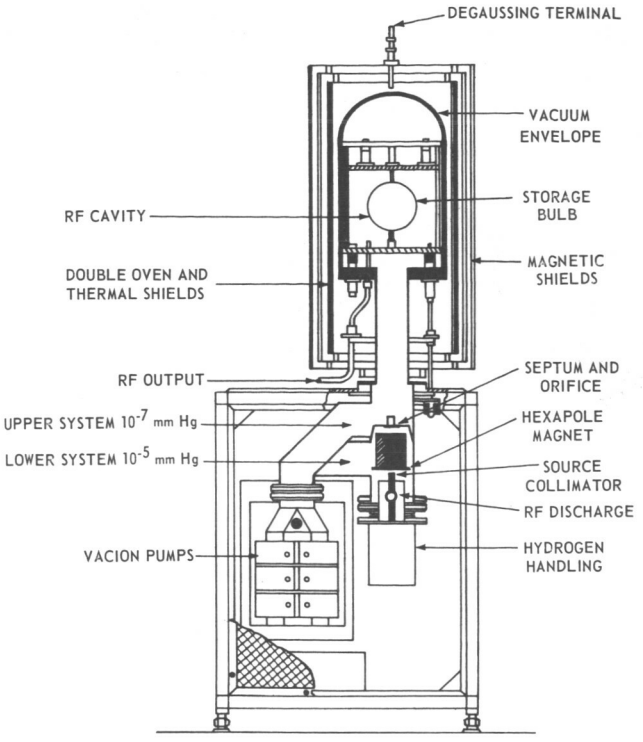

FIGURE 3. HYDROGEN MASER CUTAWAY

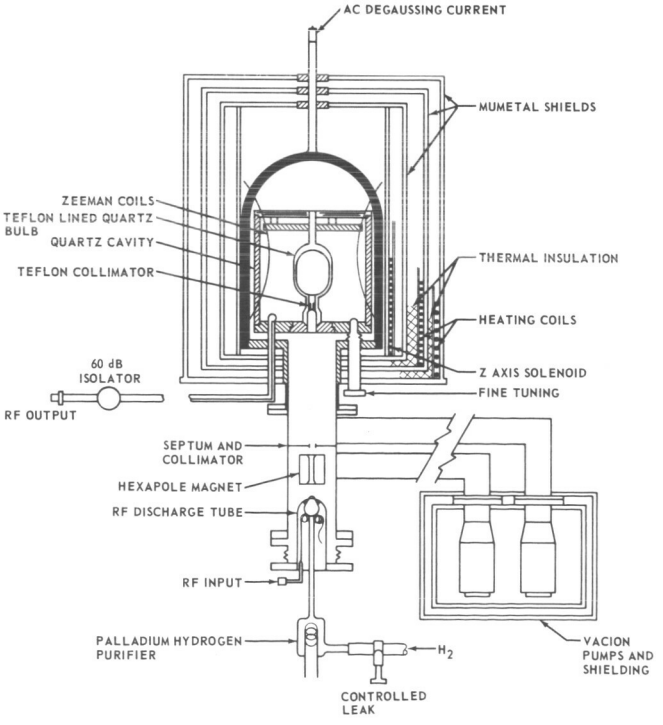

FIGURE 4. HYDROGEN MASER TOP ASSEMBLY

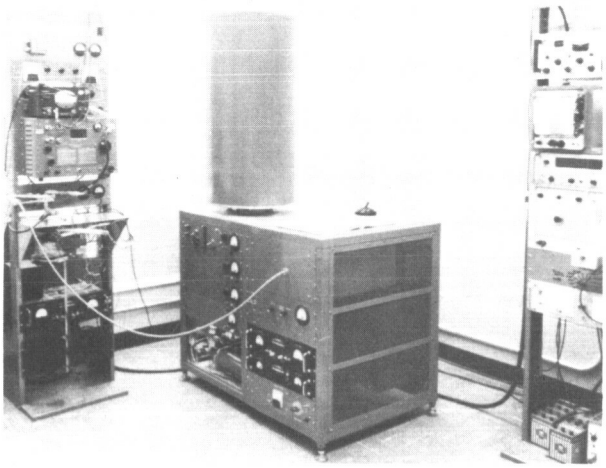

FIGURE 5. HYDROGEN MASER AT MSFC

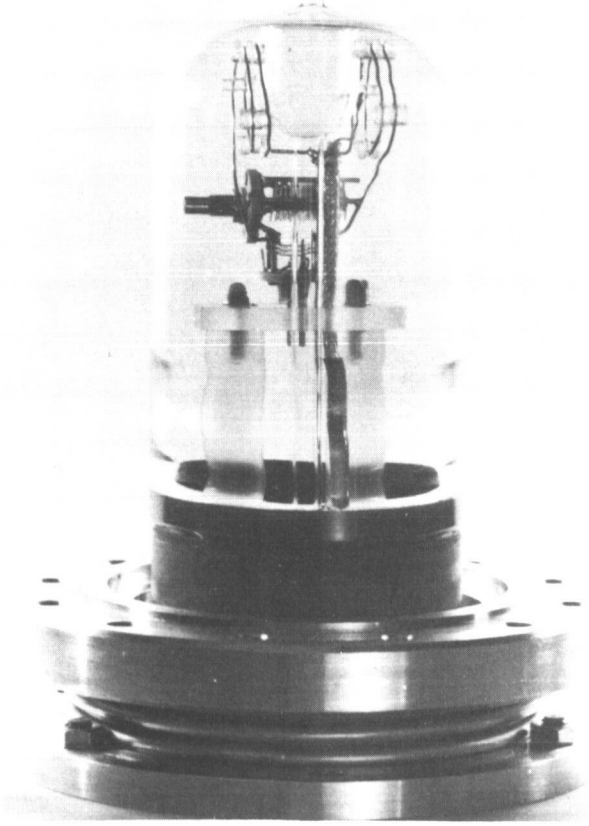

FIGURE 6. RF DISCHARGE SOURCE ASSEMBLY

hydrogen into atomic hydrogen. The pressure in the discharge can be set from 0.2 to 0.02 mm Hg. A beam of atoms is formed by allowing the atoms to escape through a multitube collimator having about 400 tubes, each tube averaging 0.038 mm in diameter with walls 0.005 mm thick. The collimator (Fig. 7) is approximately 1.4 mm in diameter and 1.4 mm long and is located at the output of the source. The collimator allows a total flux into the lower vacuum system of about 10^{16} atoms/s, so that a pressure of 10^{-5} mm Hg can be maintained by a VacIon pump with the maser in operation. The beam containing hydrogen atoms in selected states proceeds through a collimator to the upper vacuum chamber evacuated by another VacIon pump. The upper vacuum chamber, maintained at a pressure of 10^{-7} mm Hg, encloses the storage bulb and RF cavity. This prevents atmospheric disturbances from detuning the cavity. Also, differentially pumping the source and storage bulb chamber prevents excessive beam scattering.

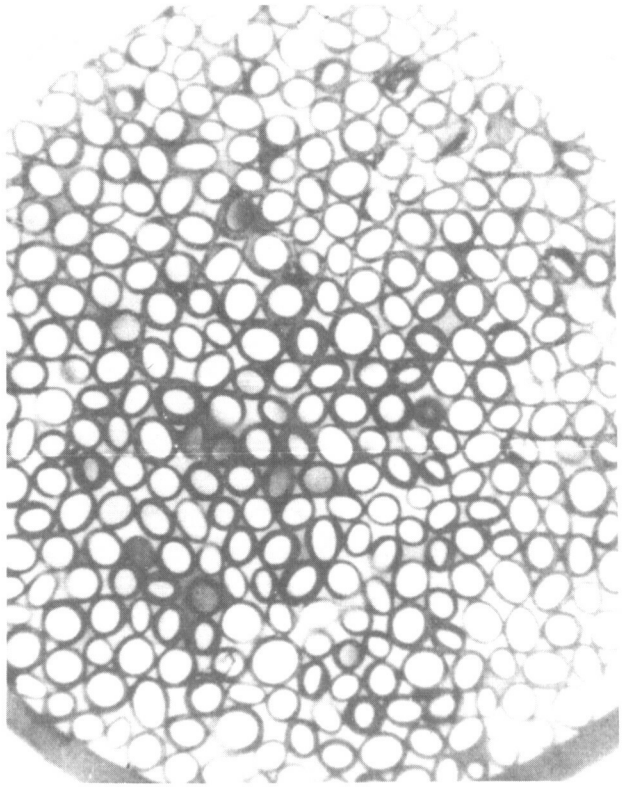

FIGURE 7. COLLIMATOR CROSS SECTION

The RF cavity (Fig. 8) is made of a fused quartz cylinder silvered on the inside and isolated from the bell jar with thin-walled quartz tubes. Having the cavity under vacuum in a bell jar provides a good thermal environment. The bell jar (Fig. 8) enclosing the cavity is made of copper and is welded to a copper base plate that contains the weld joints to the tuner and output coupling. Surrounding the bell jar assembly is a triple set of mumetal shields and a double oven built as one assembly. The inner oven is controlled

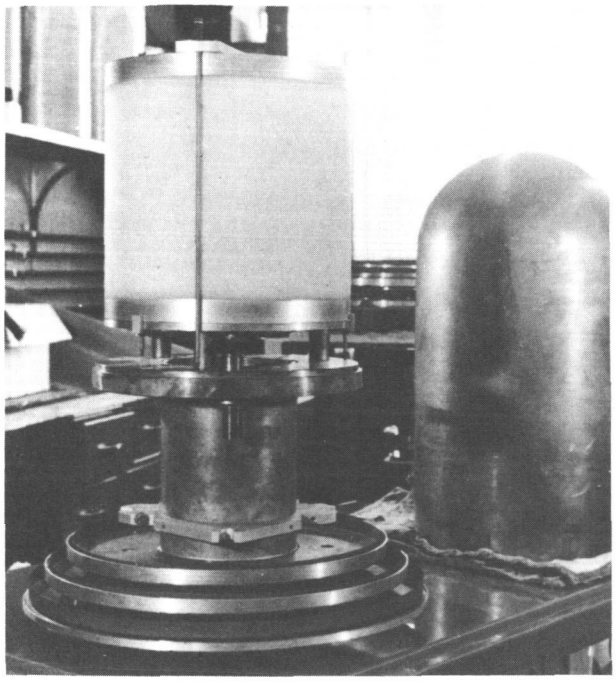

FIGURE 8. RF CAVITY ASSEMBLY

to 1/100 °C at a temperature of 40° C. The outer oven is set at 39° C. Cavity temperature is monitored by a platinum thermal bridge on the bell jar and controlled by an electronic servo system. The cavity mode is the cylindrical TE_{011} mode, which has only azimuthal wall currents; therefore, good contact between the cylinder and end plates is not required. The unloaded cavity resonates with a length and diameter equal to 27.6 cm. The theoretical Q is 87 000 for silver plated walls; however, in practice, a Q of 60 000 is obtainable. The quartz storage bulb does not appreciably affect the Q, but will decrease the resonant length of the cavity. To compensate for the peculiarities of the storage bulb, the position of one end plate is adjustable.

The quartz storage bulb is oval with a nominal diameter of 15 cm and is coated with teflon. Control of the lifetime of atoms in the bulb is obtained by the size of the bulb and by the size and flow factor of the collimator. Very simple collimators are made of solid teflon or by coating a pyrex plug and are seated like a stopper in the mouth of the bulb.

As a result of the quadratic field dependence of the desired transition, it is desirable to reduce the ambient field at the storage bulb to a very low value. The most satisfactory way to accomplish this is to use magnetic shields. Three concentric cylindrical mumetal shields reroute externally applied field lines away from the interior, and the inner shield forms a cylindrical equipotential surface for the fields generated by the interior solenoid. The solenoid is used to counteract the earth's magnetic field and to introduce a small uniform component along the beam axis for separating the Zeeman levels.

IV. FREQUENCY MEASUREMENTS

An extensive frequency stability measurement program was undertaken to determine the performance of the two masers developed for MSFC. The program consisted of measuring:

1. The relative long and short term stability of MSFC's two hydrogen masers.

2. The precision to which a given pair of masers can be reset with respect to frequency.

3. The ratio of cesium to hydrogen frequencies of hyperfine separation.

A very simple method for making frequency comparison measurements to determine the relative frequency stability between two masers is presented in Figure 9. The output from each maser is fed through an isolator providing 60 dB of isolation. The

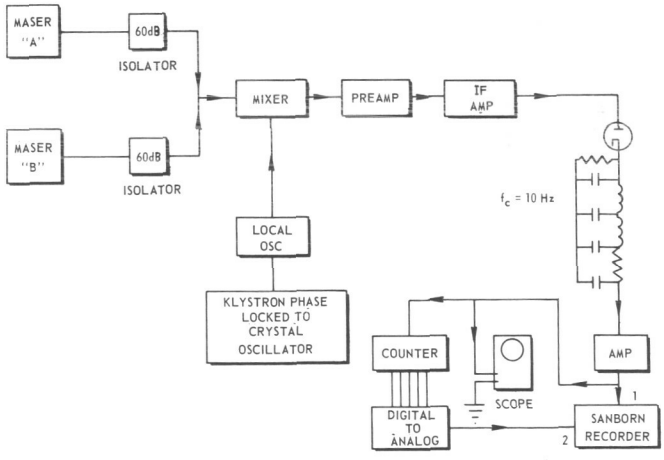

FIGURE 9. FREQUENCY COMPARISON RECEIVER

signals are then both connected to the input of a receiver consisting of an IF amplifier terminated in a diode. The output of the diode is filtered and fed to a strip chart recorder. The filtered signal also operates a counter that measures the beat period or the period for 10 beats. The counter is connected to a digital-to-analog converter whose output is also

recorded on the strip chart. Figure 10 is a sample of some of the initial measurements made on MSFC's two masers.

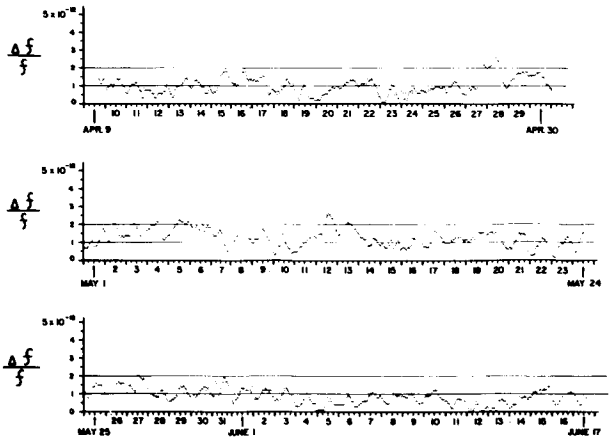

FIGURE 10. FREQUENCY DIFFERENCE BETWEEN TWO HYDROGEN MASERS

V. ACCOMPLISHMENTS

The maser program sponsored by MSFC has led to the design of the H-10 maser which represents the first step in reducing the size of the hydrogen maser. Figure 11 is a schematic diagram of the H-10, and Figure 12 is a photograph of a pair of H-10's in their final stages of completion. The H-10 maser is 56 cm square at the base, 200 cm high, and weighs about 360 kg. Improvements have been made in the vacuum system, thermal control system, and electronic packaging.

The following table lists the characteristics of the hydrogen maser achieved under MSFC's program with Varian Associates.

TABLE I. HYDROGEN MASER STABILITY

(rms deviation from the mean)

One second	5×10^{-13}
One minute	6×10^{-14}
One hour	3×10^{-14}
One day	2×10^{-14}
One month	3×10^{-13}
Resetability	$\pm 5 \times 10^{-13}$

Nominal Resonance Frequency 1420.405751 MHz

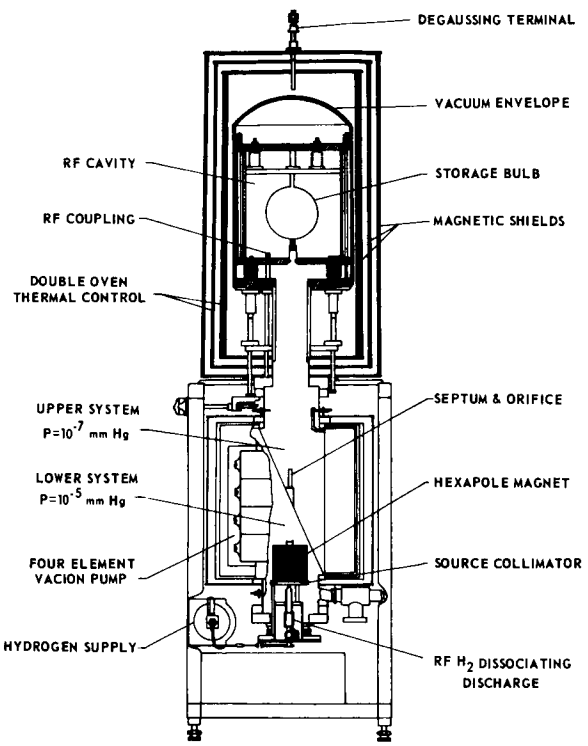

FIGURE 11. H-10 ATOMIC HYDROGEN FREQUENCY STANDARD

A program is underway to reduce the size of the present H-10 to approximately half. Investigations are being carried out with a spherical quartz dielectric cavity (Fig. 13). This cavity is considerably smaller than the cylindrical cavity now used and would allow a substantial reduction in the size of the magnetic and thermal shields. The quartz spherical cavity would be quite rugged and could be the first step in the design of a hydrogen maser for space application.

VI. APPLICATION

Hydrogen masers are presently being evaluated or are on order by various NASA centers, JPL, Harvard University, and the National Bureau of Standards (Boulder, Colorado). The hydrogen maser, because of its excellent long and short term frequency stability, is useful for laboratory time-frequency measurements, for spectroscopy, and as a frequency reference for precision tracking systems. These applications deal only with the ground based hydrogen maser. In space it may be applied in the area of geodetic research, navigation, time distribution, and important physical experiments such as the relativistic gravitational red shift.

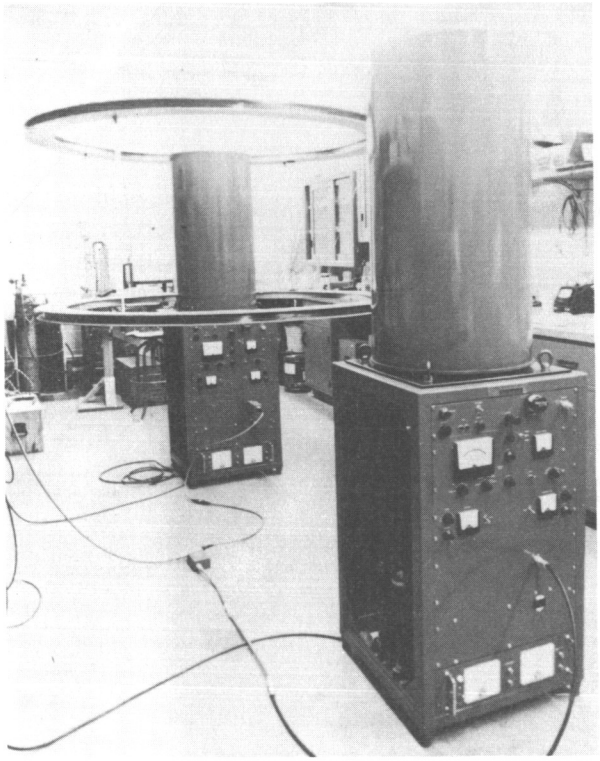

FIGURE 12. H-10 MASER ASSEMBLY COMPLETION

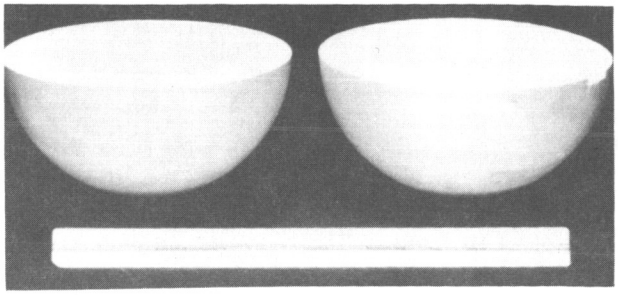

FIGURE 13. SPHERICAL QUARTZ CAVITY

BIBLIOGRAPHY

1. Vessot, R. F. C.; and Peters, H. E.: The Design and Performance of an Atomic Hydrogen Maser. IRE Trans. Instr., vol. I-II, Dec. 1962, pp. 183-187.

2. Vessot, R. F. C.; Peters, H. E.; and Mueller, L: A Comparison of Performance Characteristics of Hydrogen, Thallium and Ammonia Masers. 1965 Proc. 19 Annual Frequency Control Symposium.

3. Vessot, R. F. C.: Frequency Stability Measurements Between Several Atomic Hydrogen Masers. Quantum Electronics III. P. Grivet and M. Bloembergen, Eds., Columbia UP (New York), 1964.

4. Vessot, R. F. C.; and Peters, H. E.: Frequency Beat Experiments with Hydrogen Masers. 1963 Proc. 17 Annual Frequency Control Symposium.

5. McCoubrey, A. O.: Frequency Control by Microwave Atomic Resonance. The Microwave Journal, Nov. 1961.

6. McCoubrey, A. O.: A Survey of Atomic Frequency Standards. Proc. IEEE, special issue on Frequency Stability, pp. 116-135.

7. Ramsey, N.: Molecular Beams. Oxford Press (New York), 1956.

8. Kleppner, D., et al.: Hydrogen Maser Principles and Techniques. Phys. Rev., vol. 138, m. A972, 1965.

9. Singer, S. F.: Application of an Artificial Satellite to the Measurement of the General Relativistic Red Shift. Phys. Rev., vol. 104, No. 1, Oct. 1956.

N67-30601

DEVELOPMENT OF A SOLID - STATE IMAGE CONVERTER

By

Carl T. Huggins

SUMMARY

A solid-state image converter equivalent to the vidicon and capable of imaging radiation from the near infrared to 11 000 Å is discussed. The image converter and its associated circuit comprise a very small solid-state television camera designed for space use. A monolithic mosaic of phototransistor elements is complemented by densely packed integrated electronic circuits containing commutating switches, logic and switch-pulse generating circuits, and a video preamplifier (emitter follower amplifier).

I. INTRODUCTION

In 1960 and 1961, when the testing of tubes for television cameras for space use was begun, it was found that the operating environment was the most serious problem associated with the television system. Tests in 1960 through 1963 indicated that obtaining pictorial information by the use of conventional television imaging tubes was not the best electronic means. Conceivably a system operating on the basis of solid-state technology could ultimately provide the device for obtaining this pictorial information without having most of the objectional features of present standard and experimental cameras.

A system was envisioned in which the present imaging device, a conventional tube, would be replaced by a solid-state image converter operating on the basis of photoelectric effects and associated with circuitry using the most minute solid-state devices available. A program was outlined for development beginning in 1962 to produce as the ultimate goal a solid-state television camera compatible with standard television resolution and data rates.

Such a camera could then be improved to be compatible with our current closed-circuit systems for higher-resolution pictorial information transmission. This need not necessarily be for use with spaceborne cameras but could be used for other purposes such as data storage or conversion, or commercial use in sports, news, and educational broadcasting.

Ultimately, it is felt that this type of camera would be the one best suited for the extended space environment encountered on interplanetary missions. Because of the small size of this device, a number of them would occupy the same volume in a spacecraft as one standard flight television camera and consume equal or less power. Therefore, this device is directly related to the future planning of orbital, lunar, and planetary missions that may require the use of pictorial information. Since this camera, as will be explained later, uses digital logic in extracting information, it is applicable to any rate of readout. Its output could be transmitted over extremely narrow band or wide band RF links or over narrow band closed circuits such as telephone lines; but the circuit alterations necessary for this bandwidth change are extremely minor.

II. COMPLETE SYSTEM

The complete system in a 15.2 x 10.2 x 8.9 cm case is shown in Figure 1. The components of the camera are the mosiac sensor, the video preamplifier, the logic circuitry, and the commutating switches. Figure 2 shows the mosaic and supporting electronics. The silicon mosaic wafer is 1.3 cm square and utilizes a standard 16 mm lens system.

The readout circuitry packaged in the welded modules contains the required commutating switches, the logic and switch pulse generating circuits, and the video preamplifier (emitter follower amplifier) between the mosaic and the switches. These circuits permit high packing density since they are all molecular. Also included in the package are horizontal and vertical sweep generators and a video mixer amplifier. The power consumption is less than 4 watts.

A. MOSAIC SENSOR

The mosaic sensor is the solid-state equivalent of the vidicon and can image radiation in the visible

and near infrared regions to 12 000 A. It is read out through a combination of metallized interconnections, bonded leads, and a printed circuit board instead of the beam-scan techniques employed by vidicon and image orthicon tubes.

Selection of material for the sensor was based on considerations of both reliable fabrication techniques and material spectral response. Silicon was selected to satisfy both conditions. To minimize cross talk, that is, to maximize isolation between the individual elements while maintaining high resolution, imaging is accomplished by conversion of light to current in discrete sensor regions, all of which are contained in a single monolith. The mosaic concept was introduced to achieve this large number of discrete isolated elements interconnected in a configuration in which each photo element could be sequentially interrogated as an isolated device without necessitating an unwieldy number of individual leads. The concept of XY interconnections was introduced to provide a structure both manageable in its number of leads and compatible with conventional viewing systems that accept XY data.

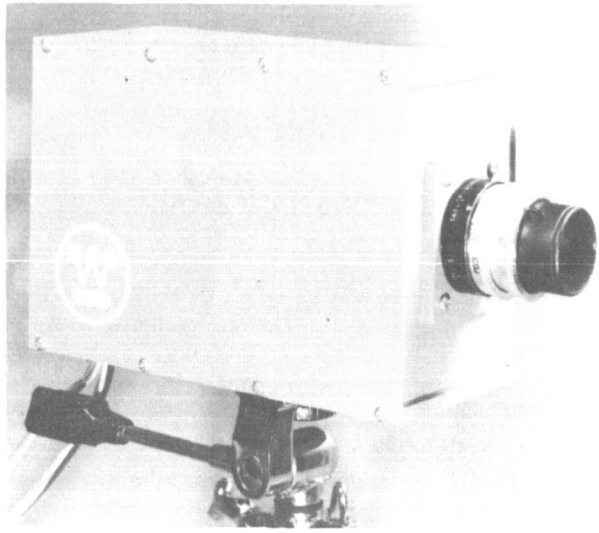

FIGURE 1. COMPLETE SOLID-STATE TELEVISION CAMERA

The mosaic sensor is a matrix of 50 x 50 NPN phototransistors on .254 mm centers, giving a total of 2500 phototransistors on a single monolith. Figure 3 shows a block diagram of the image converter.

The phototransistor elements have a square geometry with discrete emitter and base regions,

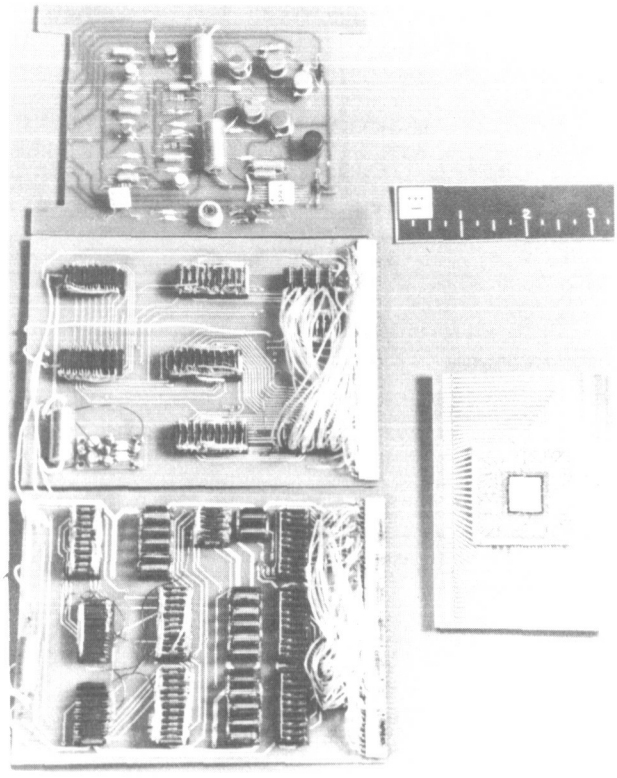

FIGURE 2. MOSAIC AND SUPPORTING ELECTRONICS

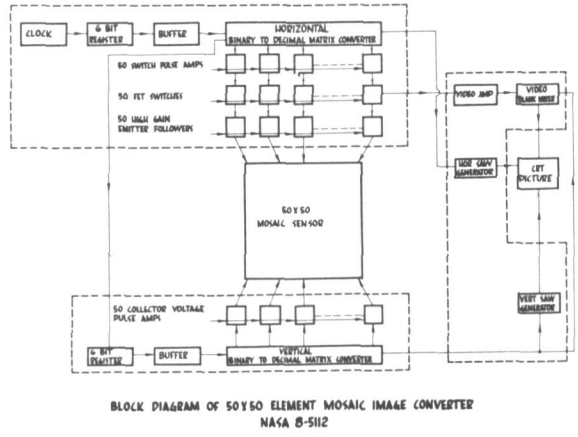

BLOCK DIAGRAM OF 50Y50 ELEMENT MOSAIC IMAGE CONVERTER
NASA S-5112

FIGURE 3. BLOCK DIAGRAM OF THE IMAGE CONVERTER

but with collector regions common to a column of 50 elements (Fig. 4). No electrical access is provided to the individual phototransistor base regions. The emitters are interconnected with evaporated aluminum strips in 50 isolated columns.

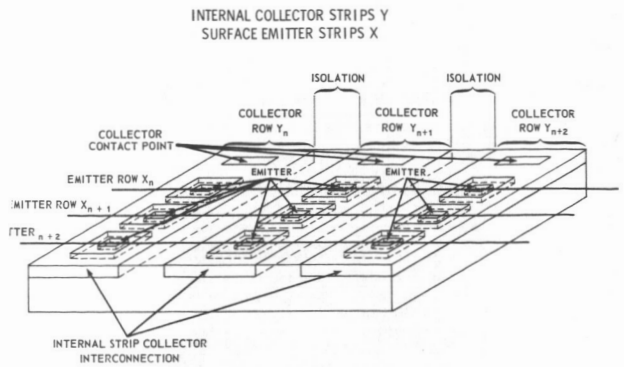

FIGURE 4. SECTION OF MOSAIC WITH XY INTERCONNECTIONS

Unique access to any individual element of the XY mosaic is available through one of the X and one of the Y external leads. Only the single element that lies at the intersection of these XY interconnections is interrogated.

Since a phototransistor structure was selected for the discrete photon detectors of which the mosaic is composed, the diffusion junction depths must be optimized with respect to photon absorption, surface recombination must be minimized, bulk minority carrier lifetime must be maximized, and the width of the depletion layer at the base collector junction must be large. Extreme processing control is not necessary to obtain useful single phototransistor elements; however, it is absolutely essential to fabricate a uniform mosaic of as many as 2500 elements.

This structure of light-sensitive elements with XY diffused and deposited interconnections is shown in Figure 5; the inset is an 8 x magnification.

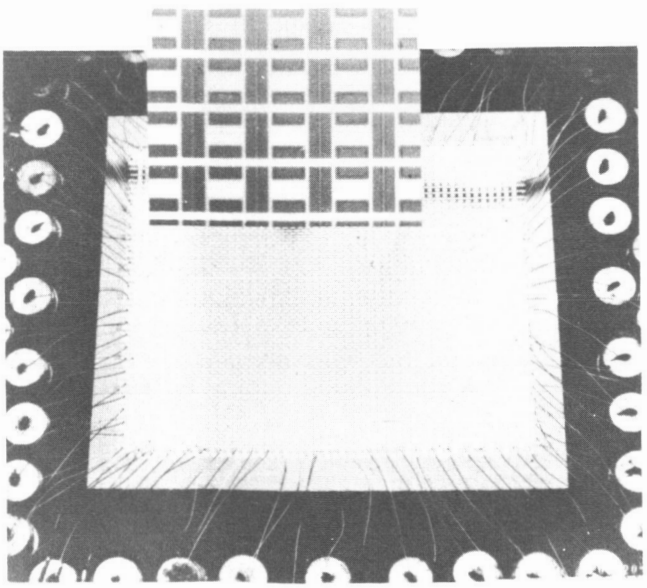

FIGURE 5. A 2500-ELEMENT MOSAIC

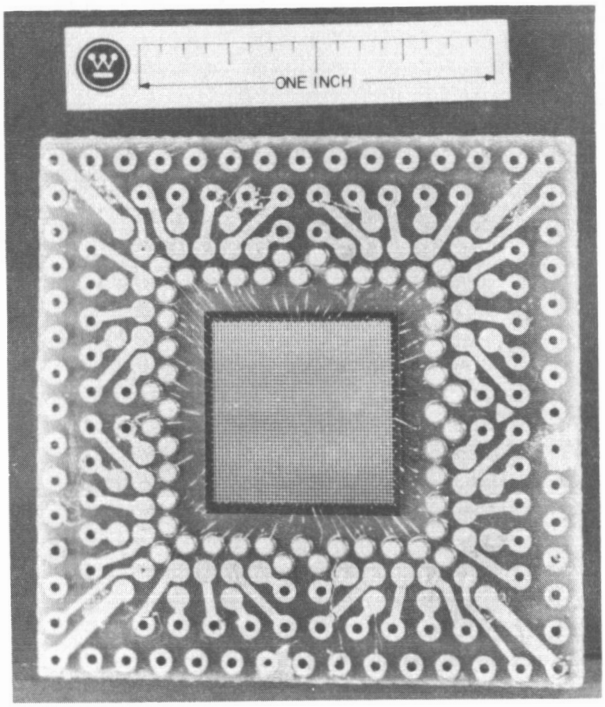

FIGURE 6. MOSAIC MOUNTED FOR TESTING

Figure 6 shows the mosaic mounted for testing.

B. VIDEO PREAMPLIFIER

Like a vidicon camera tube, a phototransistor element is a current generator and therefore requires a current amplifier, the gain required being substantial and depending on the level of light falling on the mosaic. To prevent noise from being generated by unwanted transients in the switch circuits, it is necessary to put the amplifier before the readout switch. The amplifiers in use now have a current gain of 300 at one microampere and an input impedance of 300 000 ohms. This allows operation in the linear area of the amplifier curve and produces sensitivity near that of the vidicon.

The video preamplifier (emitter follower amplifier) is necessary in the readout commutating circuitry for a number of reasons. The most important is that the impedance can be made much smaller so that switching speeds required to read out mosaics of much larger than 50 x 50 elements can be readily obtained.

C. LOGIC CIRCUITRY

Since clock frequencies approaching 1 MHz will ultimately be needed, flipflop binary logic was chosen because of its compatibility with integrated

molecular circuitry. From experience gained with diode matrix ring counting, it was decided to use standard NPN flipflop binary logic. Reliable operation of the flipflop was assured because of the sequential nature of the set/reset operation in the register of flipflops which divide the clock frequency and because of the nominal fan-out requirements. The logic provides the timing for pulsing the emitter readout switches, for application of voltage pulses to the collector rows of phototransistors, and for synchronizing the horizontal and vertical saw generators for the monitor.

The sampling switches multiplex 2500 mosaic analog signals onto one output resistance. Since there are 50 discrete elements on a line, the dwell time per element is about 6.6 μs and the clock frequency is 150 kHz. For the line switching, the dwell time is 50 elements times 6.6 μs, or 330 μs. The clock frequency for this sweep is synchronized with the element sweep, which is 3 kHz.

Readout is accomplished by applying a voltage to a 50-element collector strip and sequentially commutating the rows of emitter elements. In this way it is possible to read sequentially one element at a time while cutoff is maintained for all other elements.

The required timing for the series of 50 pulses to drive the 50-element commutator for both X readout and Y readout of the mosaic sensor is obtained from the 6-bit flipflop register. Since only 50 of the available 64 sequential outputs of the register are used, a carryover function or reset logic provision is necessary at the termination of readout of each line and row of mosaic sensor elements. This eliminates readout dead time. A diode matrix converter is used for translating each number to decimal notation. Amplifiers are needed at the output of the converter to provide correct amplitude and phase to drive each of the field-effect transistor switches. The Y readout logic is similar to the X readout logic, but it operates at a clock rate of only 3 kHz.

D. COMMUTATING SWITCHES

The sampling switches are now field-effect junction transistors so used as to provide excellent isolation between gate and source drained circuits, low noise level, and no offset voltage requirements. In addition, they require only one polarity-switching pulse. The signal handling capability of the switches ranges from 1 millivolt to 1 volt. These sampling switches multiplex 2500 mosaic analog signals onto one output resistance.

III. FUTURE PLANS

Present progress indicates that a more economical, compact, and reliable camera requiring less power can be made. As for its performance, we believe that the completion of the program will bring about better geometrical fidelity, greater dynamic range, less image smearing, and new types of signal processing with digital scanning. Of great importance to the lunar and planetary landing program is the fact that this is the only camera we know of that can be made completely sterile. The present contract period of performance is scheduled to produce a mosaic containing 100 x 128 elements. This will prove the feasibility of producing a mosaic containing 200 x 256 elements which is approximately equal to the resolution of the commercial home television receiver.

A second area of investigation is in coupling by means other than by wire. In this particular case, the one best adapted is the electro-optical coupling. As the number of elements increases, a method must be produced that will reduce the number of connections between the mosaic and the readout equipment. A 50 x 50 mosaic requires 100 connecting leads (Fig. 6), while a 200 x 256 mosaic will require 456 leads. Quantity production with this number of leads is considered highly impractical even if done by hand.

The program has, therefore, expanded into three areas instead of one: (1) processing improvements of the monolithic structure, (2) electro-optical coupling (this area must keep pace with the first or we are faced with an impractical interconnection problem), and (3) electronic peripheral timing and readout equipment, which requires a rate of time of operation increase that keeps pace with the element number increase in the monolith.

IV. CONCLUSIONS

The experimental results and the development of techniques to achieve them have proven that it is both feasible and practical to produce a solid-state camera equal in performance to an industrial camera. Its small power consumption, size, and weight plus its long life make it suitable for many uses in commerce, medicine, industry, and space. The work on this project was done by the Electronic Research Laboratory under the technical supervision of the author for NASA.

PROPAGATION STUDIES

By

Paul M. Swindall

SUMMARY

A method for increasing the accuracy of telemetry signal strength predictions is discussed. The systems considered are novel in that they have dc-to-20kHz signal strength recording responses. They make simultaneous phase coherent recordings of right circular, left circular, vertical, and horizontal polarizations. Research will continue in an effort to resolve propagation anomalies in preparation for manned vehicles.

I. INTRODUCTION

Accurate inflight signal strength measurements are necessary to verify the design and performance of RF and antenna systems. Such measurements may also be used to analyze the effect of rocket exhaust flames on the phase and amplitude of signals. Other propagation anomalies may be revealed by accurate signal strength information.

Because multipath propagation occurs normally at low altitudes when the signal level is high and appears as a low frequency periodic function, it will not be considered in this report.

II. TELEMETRY MEASUREMENTS

A. ANTENNA RADIATION

Antenna radiation patterns are a major factor in the transmission of data from the vehicle to ground stations. The patterns are developed and determined by scale modeling techniques, which must necessarily involve a number of assumptions, approximations, and simplifications. A reliable means for evaluating the accuracy of the antenna pattern scaling technique was needed.

B. RECORDING STATIONS

Field strength measurements on RF systems are made by the Atlantic Missile Range, but these measurements are secondary to data recording and are typically ± 5 to 6 dB in error and occasionally an order of magnitude in error. This is to be expected, since normally the automatic gain control (AGC) voltage of standard data receivers is used for signal strength recordings. This AGC voltage is logarithmic; and though it gives a wide dynamic range, it compresses the information, especially at high signal levels.

Other factors that limit the usefulness of the standard range recordings are:

(1) Early in the flights, the vehicle is close to the receiving stations and the receivers are near saturation.

(2) Frequency response is limited to a few cycles, or at best to a few hundred.

(3) Generally only one or two polarizations are recorded; four or more are needed for complete analysis.

Funds were requested for five specially instrumented stations. The amount approved permitted crude but accurate instrumentation of two vans.

A simple straightforward approach was used (Fig. 1); the best readily available commercial equipment was assembled inhouse with a minimum of modification. A manually tracked antenna, the most critical part of the system, was developed inhouse because of limited time and funds.

C. DESIGN REQUIREMENTS

To define the system performance completely requires all senses of polarization simultaneously; i.e., left circular, right circular, vertical, and

horizontal. In addition to steady state or low frequency response average signal information, instantaneous information was desirable to determine the noise characteristics imposed on the signal. The data on the signal are neglected and used only for identification. Some of the design goals were to have a recording of all polarizations, linear signal strength, wide frequency response, mobility, and the best obtainable accuracy. Higher frequencies are also needed for particular aspects of studies for which the data are now being used. The vans might possibly be converted to S-band for use with the UHF telemetry and the command and communication system on the Saturn V program.

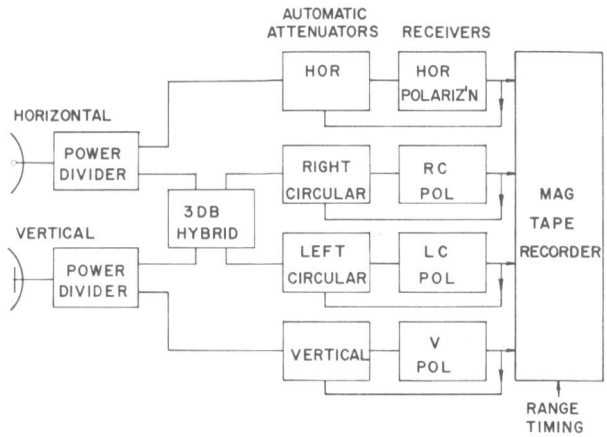

FIGURE 1. SIMPLIFIED BLOCK DIAGRAM OF RECEIVING STATION

These vans, specifically instrumented for signal strength measurement for complete analysis, are the only ones known to be in existence using the technique described here. They have been used to track vehicles other than Saturn, such as Atlas-Centaur, Polaris, and Titan, though the difficulty involved in automatic data handling has only recently been solved with a new computer program developed by the MSFC Computation Laboratory. Some minor improvements are being added to the stations for easier data handling and better compatibility. When these are completed, this computer program, as well as the reduced data, will be made available to interested people studying flame effects and other propagation effects.

III. PARABOLIC DISH ANTENNA

Figure 2 shows an antenna with a 3.05 m diameter parabolic reflector and a novel feed arrangement. The feed arrangement improves the side lobe structure, thus reducing the multipath data deterioration caused by ground reflection of the side lobes.

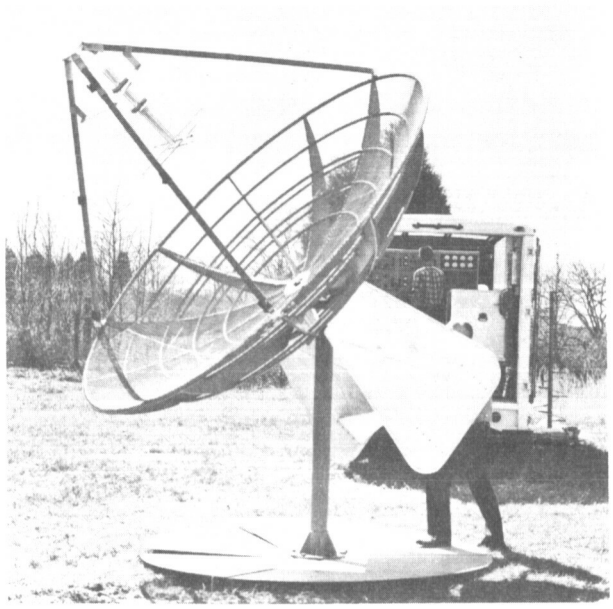

FIGURE 2. OVERALL VIEW OF PARABOLIC DISH, TURNSTILE ANTENNA

The turnstile element (Fig. 3) and the half wavelength reflector comprise a feed which has reduced side radiation. The phase center of the feed is apparently shifted nearer the ground plane and a considerable percentage of the power reradiated by the resonant reflector. This secondary radiation from the 1/2-wavelength reflector edges is cancelled at 90 deg because it has 180 deg phase difference perpendicular to the antenna lobe. This phenomenon reduced the first side lobe of the prototype 1/4-scale design from minus 10 or 12 dB to minus 15 or 16 dB. The feed was shifted off center, which reduced the radiation toward the ground 1 or 2 dB more. In the final full scale model, with careful focusing, the first side lobe was down 16 or 17 dB; all other side and back radiation was reduced 20 dB or more. The main lobe is a more accurate approximation of an ideal wedge shape than is normally accomplished.

The dual element or parasitic technique for impedance matching also served as a broadbanding device, increasing the useful turnstile bandwidth by a factor of three or more. The calculations in Figure 4 show the relations of mutual impedance of the parasitic element to the input impedance of one driven element of the reflector.

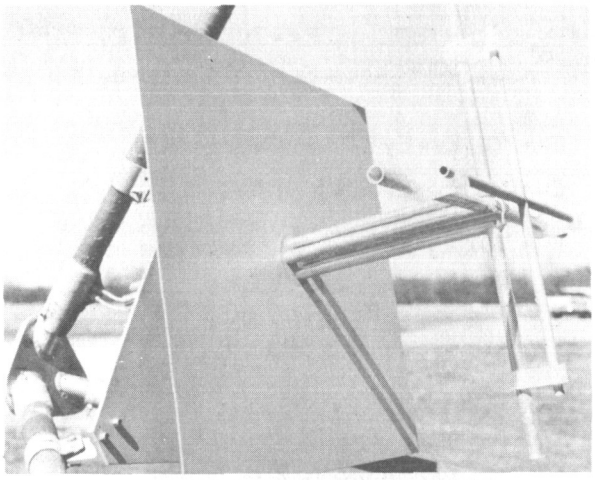

FIGURE 3. TURNSTILE ANTENNA IN PARABOLIC DISH

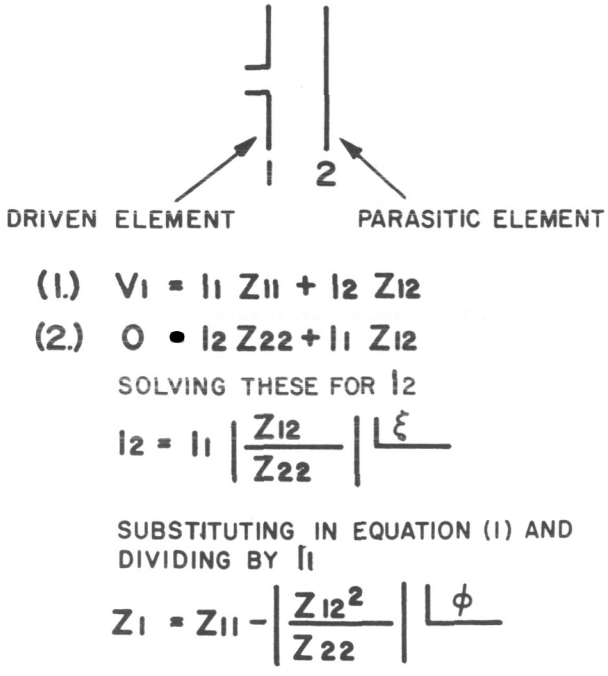

FIGURE 4. IMPEDANCE COMPENSATION

The signal from the antenna is fed into a 3-dB hybrid coupler where the circular components are derived (Fig. 5). Then, it feeds through the AGC step attenuators controlled by an output from the receivers. These attenuators either increase or decrease the sensitivity of the receivers in 10 dB increments, depending on the signal strength. The increments of 10 dB were chosen so that spurious or

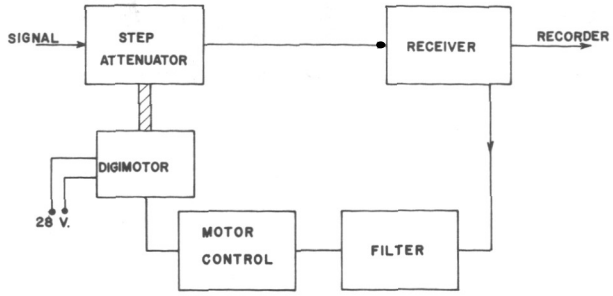

FIGURE 5. EXTERNAL AUTOMATIC GAIN CONTROL LOOP

transient fluctuations in the signal would cause minimum loss in data and yet keep the receivers in their most linear range. Though loss of data occurs during switching (approximately 6 ms), this method eliminates errors normally associated with conventional receiver AGC and transient response.

Figure 6 shows the van and antenna as they were shipped to the Cape; Figure 7 shows the controls in the van. Each van was made portable and mobile

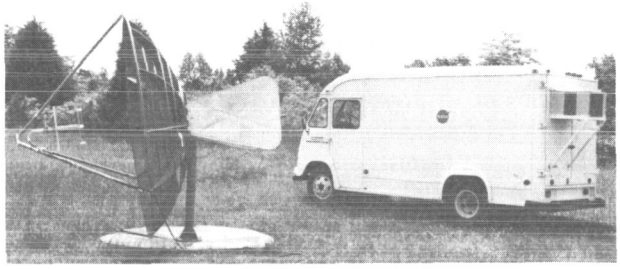

FIGURE 6. TRACKING VAN AND ANTENNA

with self-contained power generators and WWV receivers to monitor time signals from the National Bureau of Standards. They could be operated without external power or range timing if necessary, though power and timing have been available at all sites.

IV. DATA

A. DATA REDUCTION

A major problem was that no technique was available for automatically reducing the data and

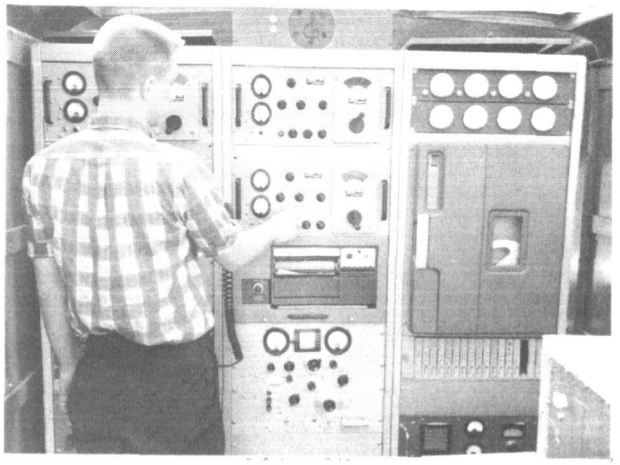

FIGURE 7. CONTROLS IN PROPAGATION STUDIES VAN

only typical small samples of a few seconds interval could be reduced manually. The early part of the project yielded only manually extracted average data except for particular times when exact retro-rocket firing time, ullage firing time, or stage separation could be identified by the effect of the functions on the signal.

B. COMPUTER PRINTOUT

The tapes were then used in establishing a computer technique automatically to reduce the flame data. The digital technique yields data at 10 rms intervals with a 1 kHz response. The equations involved in the solution of the angle of the polarization ellipse (r) are shown in Figure 8.

The computer printout (1) gives a sample of the data corrected for calibration for each sense of polarization, (2) contains the calculated angle of the polarization ellipse (Fig. 9, equation 1), (3) contains calculations of the validity of the data (Fig. 9, equations 2 and 4), and (4) gives a go/no-go indication in one column to show if the data are good or bad. In other words, with the four simultaneously received phase-related signals, one receiver channel can be checked against the others. As indicated, equation 4 must always equal 1; any deviation from 1 indicates errors in one or more of the polarizations. In the case of an excessive constant deviation from 1, the final data accuracy can be improved by inserting a constant correction in one or more polarization calibrations. The limit for ± 1 dB error is 0.6 to 1.3. Figure 10 shows a sample computer

$$E_x \angle 0^\circ \\ E_y \angle \phi^\circ \Big\} \text{HYBRID COUPLER} \begin{cases} E_R = .707\left[E_x \angle 0^\circ + E_y \angle \phi + 90^\circ\right] \\ E_L = .707\left[E_x \angle \phi^\circ + E_y \angle \phi^\circ\right] \end{cases}$$

$$E_R = .707\left[E_x + E_y(\cos\phi + j \sin\phi + 90^\circ)\right]$$

$$E_R = .707\left[E_x + E_y \sin\phi + j\, E_y \cos\phi\right]$$

$$E_L = .707\left[E_y \cos\phi + j\, E_x + E_y \sin\phi\right]$$

1. $2E_R^2 = E_x^2 + E_y^2 - 2E_xE_y \sin\phi$
2. $2E_L^2 = E_x^2 + E_y^2 + 2E_xE_y \sin\phi$

BY COMBINING 1. AND 2. $\sin\phi = \dfrac{E_L^2 - E_R^2}{2E_xE_y}$

$$r = 1/2 \text{ ARCTAN } \frac{2E_xE_y\cos\phi}{E_x^2 - E_y^2}$$

$$\cos\phi = \frac{\sqrt{(2E_xE_y)^2 - (E_L^2 - E_R^2)}}{2E_xE_y}$$

$$r = 1/2 \text{ ARC COS } \frac{E_x^2 - E_y^2}{2E_L E_R}$$

FIGURE 8. MATHEMATICAL ASPECTS OF ACQUIRING ALL POLARIZATIONS

1. $r = 1/2 \cos^{-1} \dfrac{E_x^2 - E_y^2}{E_L E_R}$

2. $\dfrac{1}{\text{AXIAL RATIO}} = \dfrac{E_R^2 - E_L^2}{E_R^2 + E_L^2} \quad -1 \leq \dfrac{1}{AR} \leq +1$

3. $PF = \dfrac{E_R^2}{E_R^2 + E_L^2}$ PERCENTAGE OF POWER IN RIGHT CIRCULAR COMPONENT

4. $A = \dfrac{E_x^2 + E_y^2}{E_L^2 + E_R^2}$ SHOULD ALWAYS EQUAL ONE

FIGURE 9. CHECK EQUATIONS

printout of the tabulated data, and Figure 11 shows a sample of an analog recording displaying the step functions in the data generated by the external 10 dB AGC attenuators.

C. ACCURACY

In the design of the receiving system, all errors were kept to a minimum practicable. A conservative receiving system relative accuracy of ± 1 dB included calibration error and circularity error in the receiving antenna. Absolute error is more dependent upon absolute calibration of the calibration generator, absolute gain of the antenna, and other absolute measurements. A conservative estimate of the accuracy of the overall receiving station is approximately ± 2 dB.

SPØNSØR BILLY R. PAGE R-CØMP-RRM ØRIGINATØR W. H. SWØRTWØØD R-CØMP-GE

PØLARIZATIØN PRØBLEM

TIME	EH	RH	EV	RV	EL	RL	ER	RR	EQ. 1 1/AR	EQ. 2 PR	EQ. 3 L	EQ. 4	ERRØR	CØUNTS HIGH
92.402	0.000630	4	0.000336	4	0.000316	3	0.000686	3	0.370	0.825	0.429	0.893	0	0
92.412	0.000660	4	0.000333	4	0.000301	3	0.000692	3	0.393	0.840	0.340	0.960	0	0
92.422	0.000677	4	0.000345	4	0.000328	3	0.000736	3	0.383	0.834	0.396	0.889	0	0
92.432	0.000643	4	0.000339	4	0.000292	3	0.000719	3	0.413	0.859	0.390	0.876	0	0
92.442	0.000664	4	0.000345	4	0.000306	3	0.000711	3	0.398	0.844	0.369	0.934	0	0
92.452	0.000647	4	0.000342	4	0.000316	3	0.000707	3	0.382	0.833	0.415	0.893	0	0
92.462	0.000643	4	0.000328	4	0.000297	3	0.000651	3	0.374	0.828	0.328	1.018	0	0
92.472	0.000656	4	0.000333	4	0.000328	3	0.000692	3	0.386	0.816	0.397	0.923	0	0
92.482	0.000664	4	0.000325	4	0.000301	3	0.000702	3	0.399	0.844	0.327	0.937	0	0
92.492	0.000639	4	0.000339	4	0.000306	3	0.000656	3	0.363	0.821	0.377	0.998	0	0
92.502	0.000609	4	0.000328	4	0.000301	3	0.000686	3	0.390	0.838	0.440	0.851	0	0
92.512	0.000647	4	0.000342	4	0.000301	3	0.000697	3	0.396	0.842	0.385	0.930	0	0
92.522	0.000686	4	0.000333	4	0.000316	3	0.000715	3	0.387	0.837	0.327	0.950	0	0
92.532	0.000664	4	0.000328	4	0.000301	3	0.000681	3	0.387	0.836	0.311	0.988	0	0
92.542	0.000656	4	0.000336	4	0.000306	3	0.000697	3	0.389	0.838	0.367	0.937	0	0
92.552	0.000639	4	0.000333	4	0.000306	3	0.000661	3	0.367	0.823	0.374	0.978	0	0
92.562	0.000668	4	0.000322	4	0.000292	3	0.000666	3	0.391	0.839	0.243	1.041	0	0
92.572	0.000647	4	0.000333	4	0.000311	3	0.000635	3	0.342	0.806	0.339	1.059	0	0
92.582	0.000651	4	0.000322	4	0.000292	3	0.000692	3	0.407	0.849	0.326	0.937	0	0
92.592	0.000625	4	0.000336	4	0.000297	3	0.000681	3	0.393	0.841	0.407	0.912	0	0
92.602	0.000630	4	0.000328	4	0.000297	3	0.000661	3	0.380	0.832	0.370	0.961	0	0
92.612	0.000647	4	0.000333	4	0.000287	3	0.000681	3	0.407	0.849	0.332	0.970	0	0
92.622	0.000647	4	0.000336	4	0.000306	3	0.000719	3	0.403	0.847	0.402	0.870	0	0
92.632	0.000664	4	0.000333	4	0.000271	3	0.000635	3	0.401	0.846	0.146	1.158	0	0
92.642	0.000630	4	0.000330	4	0.000292	3	0.000671	3	0.394	0.841	0.373	0.945	0	0
92.652	0.000643	4	0.000322	4	0.000297	3	0.000702	3	0.406	0.849	0.366	0.890	0	0
92.662	0.000664	4	0.000316	4	0.000287	3	0.000661	3	0.395	0.841	0.225	1.043	0	0
92.672	0.000620	4	0.000322	4	0.000297	3	0.000676	3	0.390	0.839	0.399	0.894	0	0
92.682	0.000639	4	0.000330	4	0.000287	3	0.000651	3	0.388	0.837	0.322	1.023	0	0
92.692	0.000651	4	0.000328	4	0.000292	3	0.000692	3	0.407	0.849	0.333	0.944	0	0
92.702	0.000634	4	0.000314	4	0.000292	3	0.000630	3	0.367	0.823	0.299	1.039	0	0
92.712	0.000643	4	0.000330	4	0.000297	3	0.000651	3	0.374	0.828	0.332	1.022	0	0
92.721	0.000639	4	0.000330	4	0.000306	3	0.000635	3	0.349	0.811	0.348	1.040	0	0
92.731	0.000639	4	0.000328	4	0.000287	3	0.000618	3	0.366	0.823	0.279	1.111	0	0
92.741	0.000647	4	0.000336	4	0.000287	3	0.000651	3	0.388	0.837	0.305	1.052	0	0
92.751	0.000620	4	0.000333	4	0.000287	3	0.000686	3	0.401	0.851	0.403	0.894	0	0
92.761	0.000647	4	0.000316	4	0.000292	3	0.000651	3	0.381	0.833	0.287	1.020	0	0
92.771	0.000625	4	0.000325	4	0.000301	3	0.000686	3	0.390	0.838	0.406	0.882	0	0
92.781	0.000639	4	0.000328	4	0.000297	3	0.000686	3	0.397	0.843	0.370	0.921	0	0
92.791	0.000651	4	0.000322	4	0.000297	3	0.000711	3	0.411	0.852	0.353	0.889	0	0
92.801	0.000660	4	0.000314	4	0.000282	3	0.000692	3	0.401	0.857	0.263	0.957	0	0
92.811	0.000647	4	0.000322	4	0.000292	3	0.000640	3	0.374	0.828	0.283	1.055	0	0
92.821	0.000656	4	0.000316	4	0.000292	3	0.000661	3	0.387	0.837	0.272	1.015	0	0
92.831	0.000643	4	0.000316	4	0.000292	3	0.000686	3	0.404	0.847	0.336	0.922	0	0
92.841	0.000647	4	0.000333	4	0.000306	3	0.000676	3	0.377	0.830	0.367	0.962	0	0
92.851	0.000651	4	0.000316	4	0.000297	3	0.000635	3	0.363	0.821	0.267	1.067	0	0
92.861	0.000656	4	0.000316	4	0.000297	3	0.000686	3	0.397	0.843	0.313	0.947	0	0
92.871	0.000639	4	0.000325	4	0.000301	3	0.000666	3	0.377	0.830	0.359	0.960	0	0

FIGURE 10. SAMPLE COMPUTER PRINTOUT

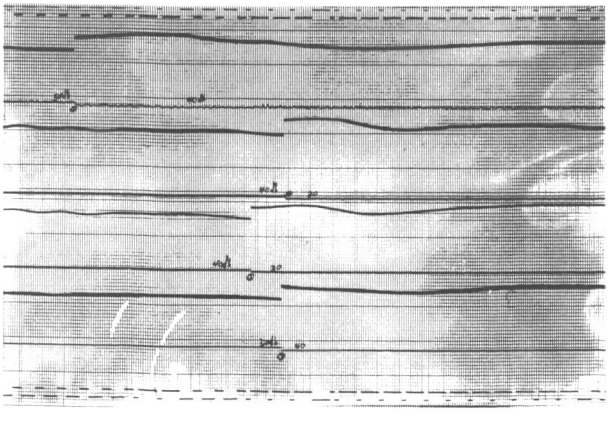

FIGURE 11. SAMPLE ANALOG RECORDING

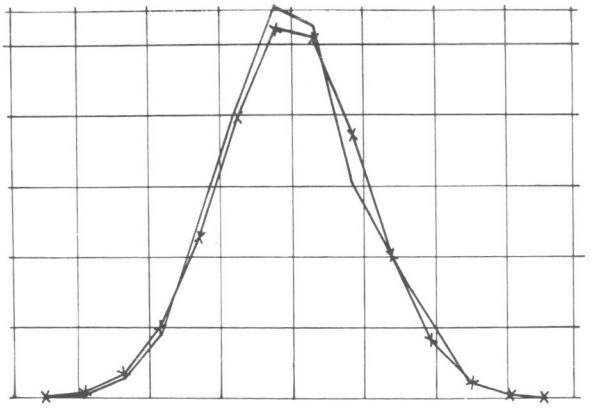

FIGURE 12. GAUSSIAN DENSITY COMPARED WITH MEASURED DENSITY

D. SA-10 NOISE SPECTRUM

Figure 12 shows the noise power spectrum plotted from data received on Saturn I, vehicle SA-10, during retrorocket firing. This curve shows that the noise spectrum is generally normal or Gaussian. The only deviation, which appeared at particular times during preliminary analysis, is a resonance effect from the reinforcement and cancellation (acoustical interference pattern) caused by

the clustering of engines. This resonance tends to peak the flame modulation, and therefore the signal, at certain frequencies.

Observations indicate a possible acoustic resonance modulation effect on the flame that appears as a shaping or peaking of the noise distribution curve at the acoustic resonance. This has not been completely substantiated but an effect has been observed that can be explained by this phenomenon. This effect approximates the resonant frequency of the engine or rocket nozzle in question.

E. FLAME ATTENUATION CONTOURS

Figure 13 shows a typical plot of predicted flame attenuation contours at Cape Kennedy for different vehicle altitudes. These are projected from a ray drawn from a vehicle antenna tangent to the inviscid boundary of the plume. Because they are mobile, the receiving stations can be placed at optimum locations to obtain data for comparison of actual and predicted flame attenuation. Figure 14 shows this comparison on SA-10, identifying the first and maximum flame effects and recovery. The smooth lines are predicted data and the plotted points are actual measurements; it can be seen that some error in the predictions is present. These and future measurements will be used to improve the accuracy of later predictions.

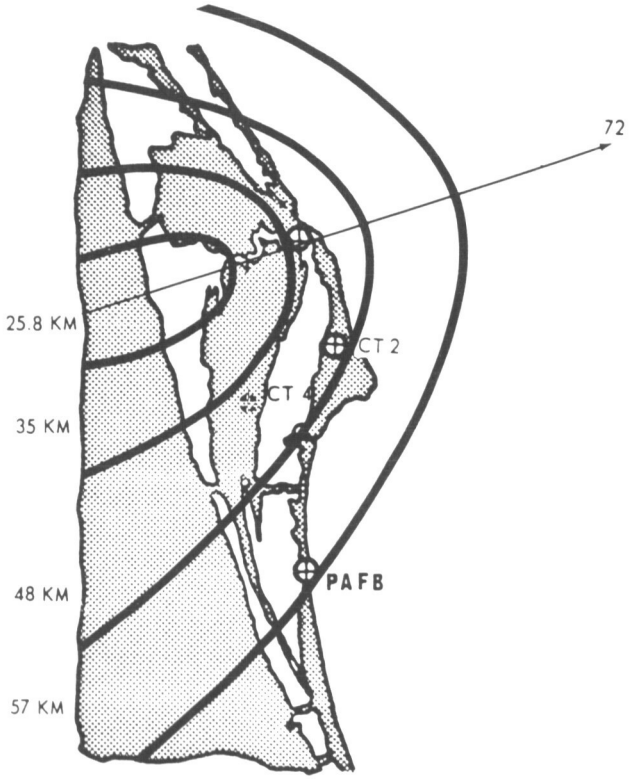

FIGURE 13. PREDICTED FLAME ATTENUATION CONTOURS FROM S-IC MAINSTAGE ENGINES

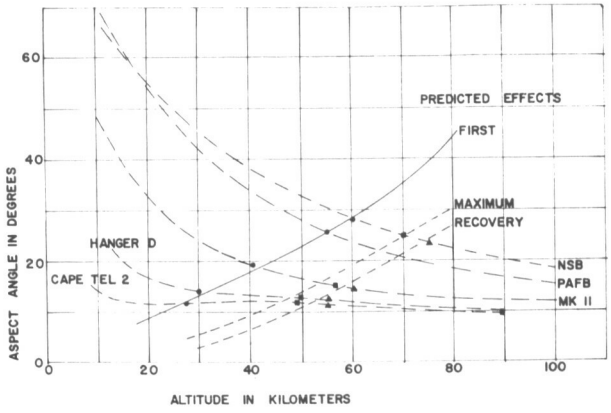

FIGURE 14. ACTUAL AND PREDICTED FLAME ATTENUATION

V. CONCLUSIONS

This research effort should continue, possibly with more emphasis on retaining or improving tracking, recording, and calibration accuracy. The information gathered will continue to be useful until the critical propagation anomalies are completely resolved in preparation for manned vehicles.

Another particularly important function of these receiving stations will be recording signal strength in the planned orbital antenna pattern experiment, in which the vehicle will be rolled to perform a more complete analysis of full scale antenna patterns.

STRUCTURES RESEARCH AT MSFC

January 6, 1966

by

J. F. Blumrich
H. R. Coldwater
C. E. Gassaway

TABLE OF CONTENTS

LIST OF TABLES

LIST OF ILLUSTRATIONS

CONTENTS (Continued)...

STRENGTH ANALYSIS RESEARCH

by H. R. Coldwater

CONTENTS (Continued) . . .

LIST OF TABLES

LIST OF ILLUSTRATIONS

VIBRATION AND ACOUSTICS STRUCTURAL RESEARCH

by C. E. Gassaway

CONTENTS (Concluded). . .

LIST OF ILLUSTRATIONS

N67-30603

STRUCTURAL RESEARCH FOR ADVANCED DESIGNS

By

J. F. Blumrich

SUMMARY

Various research activities in support of advanced structural design are discussed. Design problems concerning short and long-term storage of cryogenic liquids are examined. Other design investigations concerning environmental protection are described, including micrometeoroid, heat, and sterilization studies. Applications of new materials are noted, and configuration studies are presented, including new tank shapes, and shock absorbers and pads for unmanned landing vehicles.

In the program discussed, design data have been published in handbook form for several environmental protection problems. Hardware has been manufactured for testing of new tank configurations, beams of various new materials, and novel landing gear elements.

I. INTRODUCTION

The range of investigations into Saturn requirements and the solution of problems as they arose has greatly increased knowledge in the structural field as well as in technology. Knowing this present status and considering it in the light of potential future vehicles and activities permits us to define the main categories of structural technology in which our knowledge is insufficient.

In broad terms an examination of space programs, structural elements and structural technology are shown in Figure 1. The center box lists typical future vehicles and activities. Each of these items will need several or all of the structural elements listed in the left box. The right box lists categories of structural technology in which knowledge is lacking. The dependence is obvious; any lack in structural technology

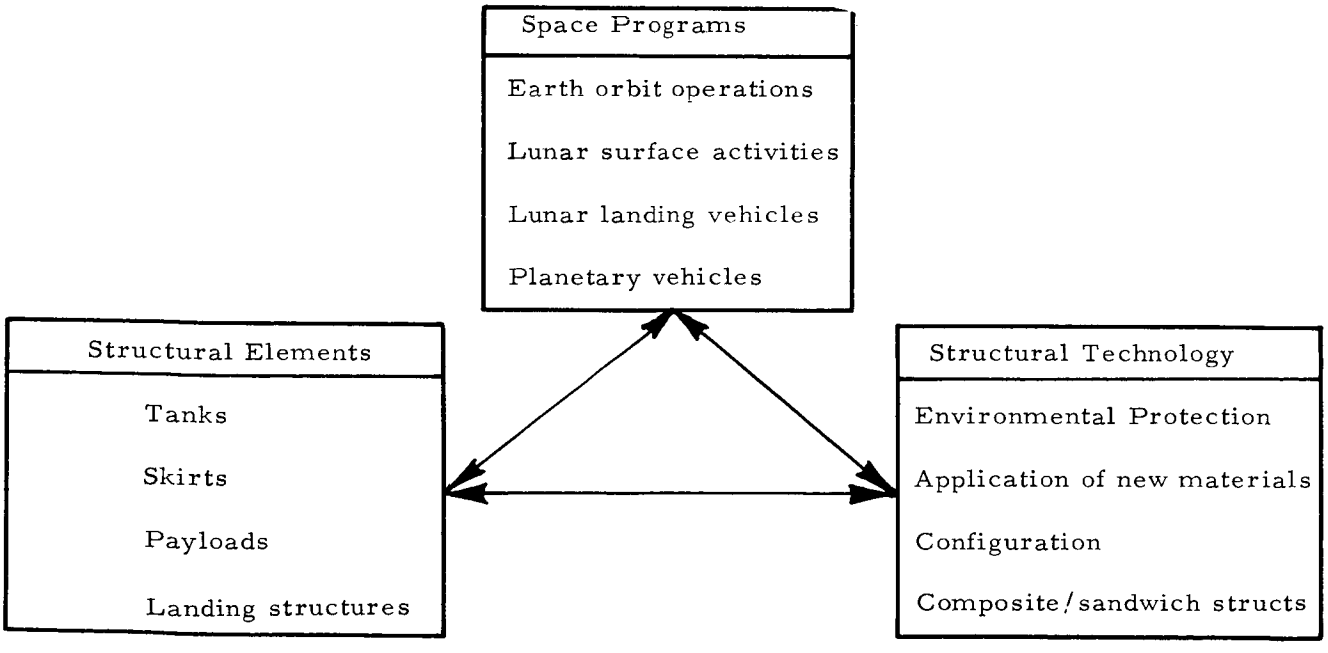

FIGURE 1. INTERRELATION OF SPACE PROGRAMS AND STRUCTURES

affects the flight hardware and through it the program. Figure 1 therefore shows that structural technology has a direct influence on space programs. Table I demonstrates in greater detail the criticality of the elements of structural technology to various vehicles and operations. The majority of these elements are essential to all programs cited. Table I also suggests that tasks independent of specific missions, programs, and vehicles are the most logical approach to the problem of furthering structural technology.

The work described in the following paragraphs is done in close cooperation with all pertinent groups within MSFC and through contracts with Industry. Companies involved and respective areas of structural research are listed in Table II.

II. ENVIRONMENTAL PROTECTION

A. CRYOGENIC STORAGE

The problem of cryogenic storage in general, and LH_2 insulation in particular, is at the top of our priority list. Study of design problems in this area began about 1962. We distinguish between two main groups, short-term storage up to two weeks, and long-term storage up to one year.

1. Short-Term Storage. Most of the emphasis has been placed on short-term storage. In-house, MSFC is surveying all facets of the task for a direct attack on the problem using the existing Linde and National Research Corporation (NRC) multilayer insulation. Out-of-house, MSFC is guiding its contractors in taking the broader view of not limiting action to existing insulations only, but in conceiving new insulations as well. Figure 2 shows a tank of 2.67 m diameter being wrapped with Linde insulation.

The Linde insulation requires evacuation; the NRC type requires purging. Both insulations must therefore have an outer barrier. Flexible jackets were used for that purpose, and developed their own specific problems. The jacket wrinkled; it interfered with the insulation; the seal of its seams was often imperfect; and it often did not deflect sufficiently at penetrations. In turn, the penetrating items, such as tank supports and suction lines, dictated a series of component tests to solve local problems. Figure 3 shows one example of an insulated penetration.

Purged insulations have their own problems. First, air must be replaced by a purge gas. Then, immediately after launch, the purge gas must be removed. For best results, the rate of gas removal should correspond with the rate of drop in ambient temperature. Removal of purge gas at that rate has not yet been achieved. Typical features of a purged insulation are shown in Figure 4.

TABLE I. APPLICABILITY OF STRUCTURAL TECHNOLOGIES TO VARIOUS PROGRAMS

	Expendable Launch Vehicle	Reusable Launch Vehicle	Earth Orbit Operations	Lunar Operations	Planetary Operations
Cryogenic Insulation and Propellant Transfer	X	X	X	X	X
Meteorite Protection			X	X	X
Docking and Landing Gear		X	X	X	X
Airlocks		X	X	X	X
Expandable Structures			X	X	X
Payload Shrouds	X	X	X	X	X
New Tank Development	X	X	X	X	X
Unpressurized Structures	X	X	X	X	X
Reusable Heat Protection		X			X

TABLE II. ORGANIZATIONS PARTICIPATING IN MSFC STRUCTURAL ENGINEERING RESEARCH

Cryogenic Storage	- Goodyear Aerospace Corporation, Akron, Ohio Linde Division/Union Carbide Corporation, Tonawanda, New York Martin Company, Baltimore, Maryland National Research Corporation, Boston, Massachusetts Naval Ordnance Test Station, Chinalake, California North American Aviation/S&ID, Downey, California Wyle Laboratories, Huntsville, Alabama
Micrometeoroid Protection	- Arnold Engineering Development Center, Tullahoma, Tennessee
Heat Protection	- Aeronca Manufacturing Corporation, Middletown, Ohio
Sterilization	- Avco Corporation, Wilmington, Massachusetts General Electric Company, Philadelphia, Pennsylvania
Material Application	- Fairchild Hiller Farmingdale/Republic Aviation Division, Long Island, New York Lockheed, Huntsville Research & Engineering Center, Huntsville, Alabama
Shock Absorber	- The Bendix Corporation, South Bend, Indiana
Nose Cones	- Lockheed, Huntsville Research & Engineering Center, Huntsville, Alabama
Sandwich	- General Dynamics, Fort Worth, Texas Goodyear Aerospace Corporation, Akron, Ohio North American Aviation, Los Angeles Division

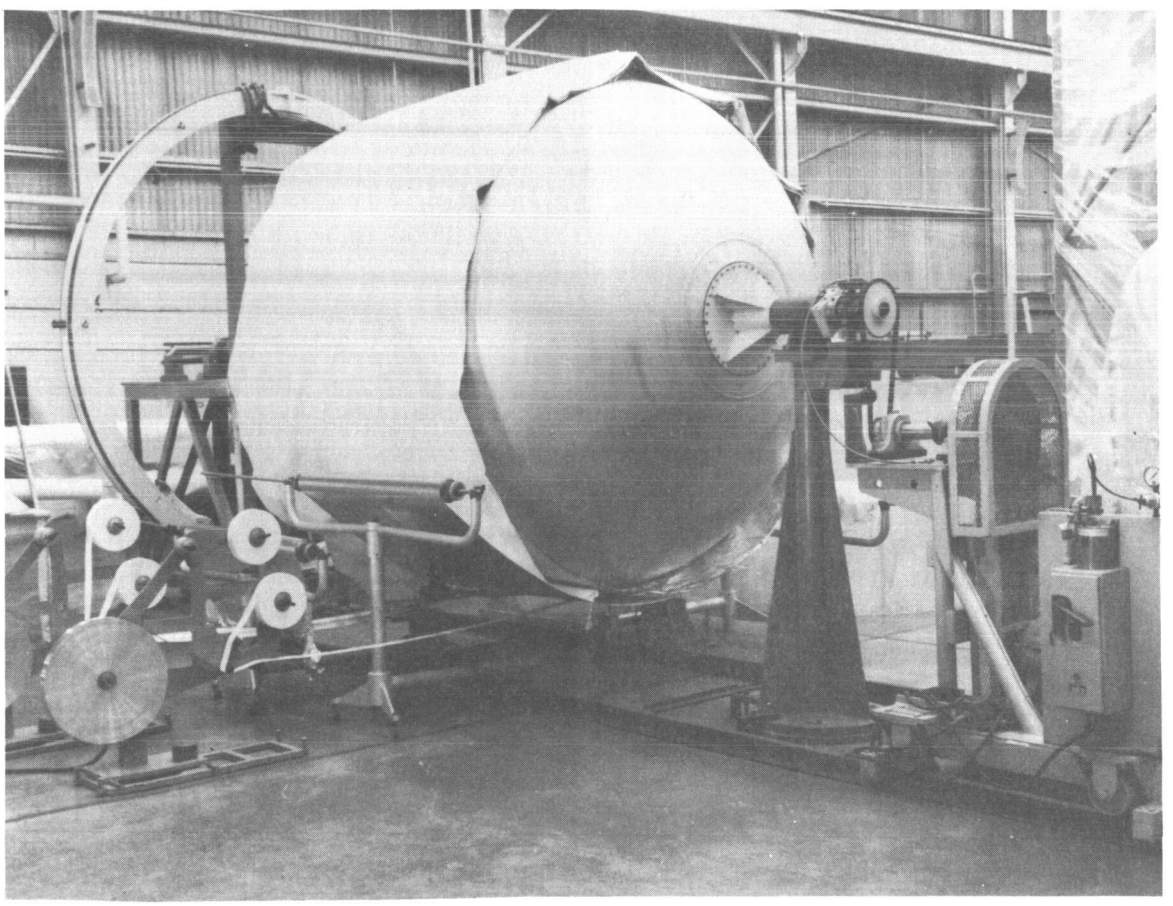

FIGURE 2. 2.67 M DIAMETER CRYOGENIC TEST TANK WRAPPING WITH HIGH PERFORMANCE INSULATION

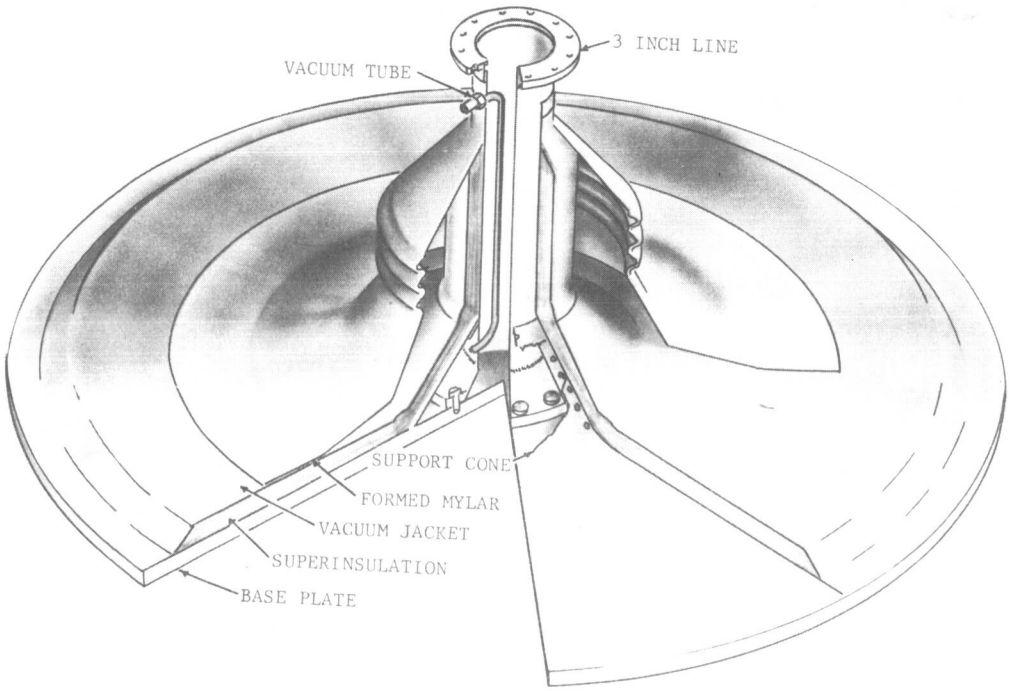

FIGURE 3. EXAMPLE OF INSULATED PENETRATION

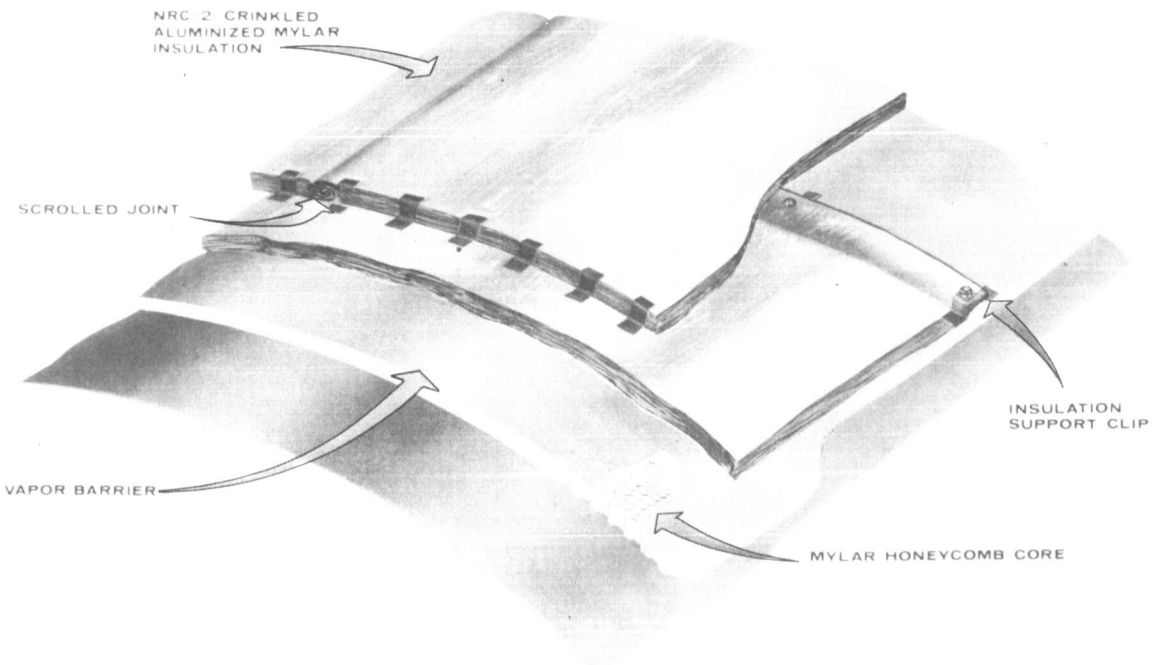

FIGURE 4. PURGED INSULATION WITH SUB-LAYER

Stainless steel suction lines are necessary to reduce heat input. To avoid leakage at flanged connections, a bimetallic joint of stainless steel and aluminum was developed and tested successfully.

There has been significant progress. We are now setting up a test with a fully insulated 105-inch tank. The remaining test program for this tank includes a rocket sled test to combine acceleration and vibration at cryogenic temperatures, and a full thermal test to check the proper function of the insulation.

2. Long-Term Storage. In late 1965, work was started on the long-term storage problems. The tanks involved are large in diameter; it is therefore apparent that an insulation is needed which can be exposed to aerodynamic loads and heating. Until such insulation is developed, a protective shroud must cover the insulation.

The main problems, however, are the tank supports and the attachment of the insulation. For long-term storage, the heat input through the support is a dominating factor that makes the development of retractable supports necessary, i.e., supports that are not touching the tank during periods of low acceleration. Unless reliquefaction of boil-off LH_2 becomes feasible, it is expected that the insulation blanket will be up to 7 to 10 cm thick. Attachment, purging, and venting of such a system are very difficult.

B. HEAT PROTECTION

To this point, all discussion was based on a low-temperature environment. Another environment comes from the heat to which heat shields above the engines and near the skins of reentry vehicles are exposed. These heat problems have been solved, within certain limits, by others working in this area. Current study of structures in high-temperature environments at MSFC is oriented toward reusability, the goal being structures that will withstand 50 duty cycles. In the heat shield work, S-IC criteria are the foundation. For reentry vehicles we assumed a wing panel of a reusable stage with a maximum temperature of 1275° C. The results are very encouraging; one heat shield panel failed after 7 hours exposure to the dynamic environment (which is far beyond the requirement), and a second panel failed under combined heat and pressure loads during the 27th cycle. The wing panels are ready for testing. Development of the heat shield is continuing.

C. MICROMETEOROID PROTECTION

A space environmental hazard to consider is that of micrometeoroids. MSFC is sponsoring the production of a design criteria handbook for micrometeoroid protection. The information is being obtained from widely scattered technical literature and includes shielding concepts, structural suggestions, and design information. It should be useful for both hardware and conceptual design work.

The situation in micrometeoroid protection is quite similar to that in cryogenic insulation in 1962; concepts are available but no practical solutions exist. Therefore, a thorough design and manufacturing exercise is needed to solve the obvious problems and those which are certainly hidden.

D. STERILIZATION

About 1963, the criteria were established requiring planetary-landing vehicles to be sterilized by heat at 135° C for periods up to 70 hours. At that time, from a structural point of view, the most outstanding of a series of questions were the following:

1. What deformations will occur?

2. What is the significance of joining methods and joint designs?

3. What temperature distribution occurs during heating and cooling?

4. What procedures are necessary during fabrication and assembly to assure compatibility with the sterilization requirement?

As a result of MSFC-contracted studies, a design handbook supplying this knowledge is available. Study contracts are generating information about associated manufacturing problems and capsule investigations. These studies will be important in their own fields; they will also be used to update the sterilization design handbook.

E. HOT JET IMPINGEMENT

The last item for discussion of the environmental influences is the heat input a vehicle may be exposed to immediately after landing on the moon. This problem became evident during the 1962 work on the design of the lunar logistics vehicle.

A survey was made to learn what work had been or is being done on this problem. Only the shape of craters formed in sand exposed to rocket engine plumes had been studied. Therefore, limited tests were done at MSFC with hot jets in an atmospheric environment. Under that condition, the results were not expected to be conclusive, but to indicate whether

there was a problem at all. We found that fine grained and light materials were blown away, leaving a cool crater. We found also that a surface of gravel was eroded far less and that the temperature of the remaining material was raised significantly. For example, after an exposure of about 60 seconds, the temperature of the gravel surface was 1300° C; three hours later, the temperature had only dropped to 530° C. The consequences of a locally hot lunar surface after touchdown are serious. MSFC is therefore continuing to study this problem.

III. MATERIALS APPLICATIONS

Activities in this area are aimed at establishing design requirements for new materials, as well as for new processes for established materials. Very close cooperation is therefore required between design and fabrication personnel. The shops have to learn what can or must be done with a certain material; and designers must learn to meet and make use of certain material characteristics. To illustrate the situation by an example, aluminum technology and design principles cannot be used to produce a fiberglass structure.

An entirely new manufacturing process was introduced recently: diffusion bonding. Much is still to be learned: by the fabricator to expand the technique, by designers to know how and where to use it.

The application of beryllium in sheet metal structures is still hampered by its brittleness, which determines fabrication methods and design by influencing such basic items as bending of sheet metal, straightness of edges, bonding, and use of fasteners.

Fiberglass requires an entirely different treatment because of its unique advantage that the fibers can be placed where they are needed.

To compare several new materials in their application to a basic structural element, a box-beam program was initiated. An aluminum box beam (203 × 254 × 2438 mm) was designed as a reference structure. Beams of beryllium, beryllium-aluminum, titanium, magnesium-lithium and fiberglass were designed and are now being built. The beryllium box beam is the largest sheet metal beryllium beam ever fabricated.

IV. CONFIGURATIONS

A. TANK SHAPES

New tank shapes are studied to establish configurations shorter or less expensive than present structures. In other words, the goal of these activities is increased economy. Two examples may quickly explain this. Shorter tanks mean shorter vehicles, smaller bending moments, higher vehicle frequencies -- advantages which go far beyond the tank itself. An entirely different situation can exist in the payload area, as for instance in the unmanned lunar logistics vehicle studied here a few years ago. The mass of the landing gear was directly dependent on the height of the center of gravity above the ground. Shorter tanks meant a reduction of that height; the consequent mass saving in the landing gear was directly available for increase of the payload mass.

The following promising configurations have been considered:

1. Multicell Tank
2. Semitoroidal Tank
3. Flat Bulkhead Tank

Figure 5 shows a length comparison of multicell and semitoroidal tanks for a hypothetical vehicle. Figure 6 illustrates the application of a semitoroidal design to the S-II stage. The reduction in length is not significant. The mass reduction of slightly less than 10 percent in this particular case indicates a potential for at least some mass savings in other cases. Most important, however, is the reduction of production costs and other problems which is achieved by eliminating the common bulkhead.

In Figure 7 a length comparison of the S-IC stage with a flat-bulkhead stage is given.

In connection with these illustrations it should be pointed out that such comparisons with existing stages are necessary to determine if a new concept is really better. Only if that process reveals its advantages can it be used with confidence for future applications. These comparisons should, therefore, not be construed as attempts to replace such existing structures.

Figure 8 shows the 200-inch multicell tank, which is the first of our series of 200-inch test tanks. On the right side is the support ring that will be used for all 200-inch test tanks.

Besides their other advantages, all three designs, multicell, semitoroidal, and flat bulkhead, also offer great flexibility as far as number and arrangement of engines are concerned.

Repeatedly metioned by other sources, but never tested in a size approaching hardware dimensions, was the torus tank. Such a tank was therefore also included in the MSFC series of 200-inch diameter test tanks.

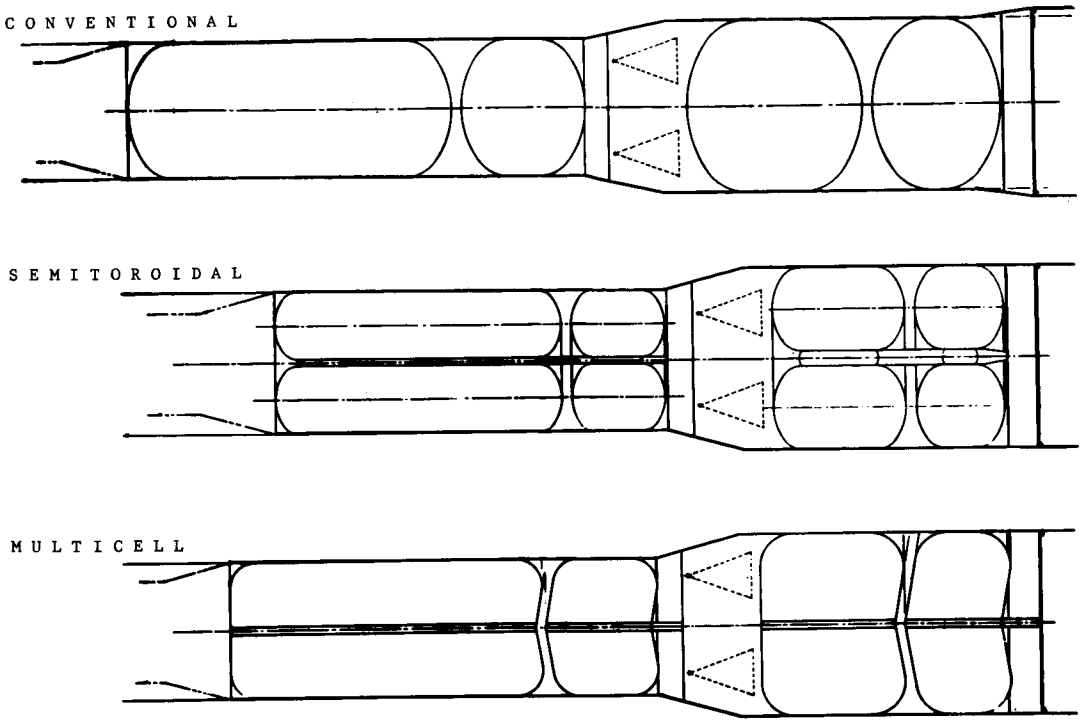

FIGURE 5. LENGTH COMPARISON FOR HYPOTHETICAL VEHICLE, CONVENTIONAL, SEMITOROIDAL, AND MULTICELL DESIGNS

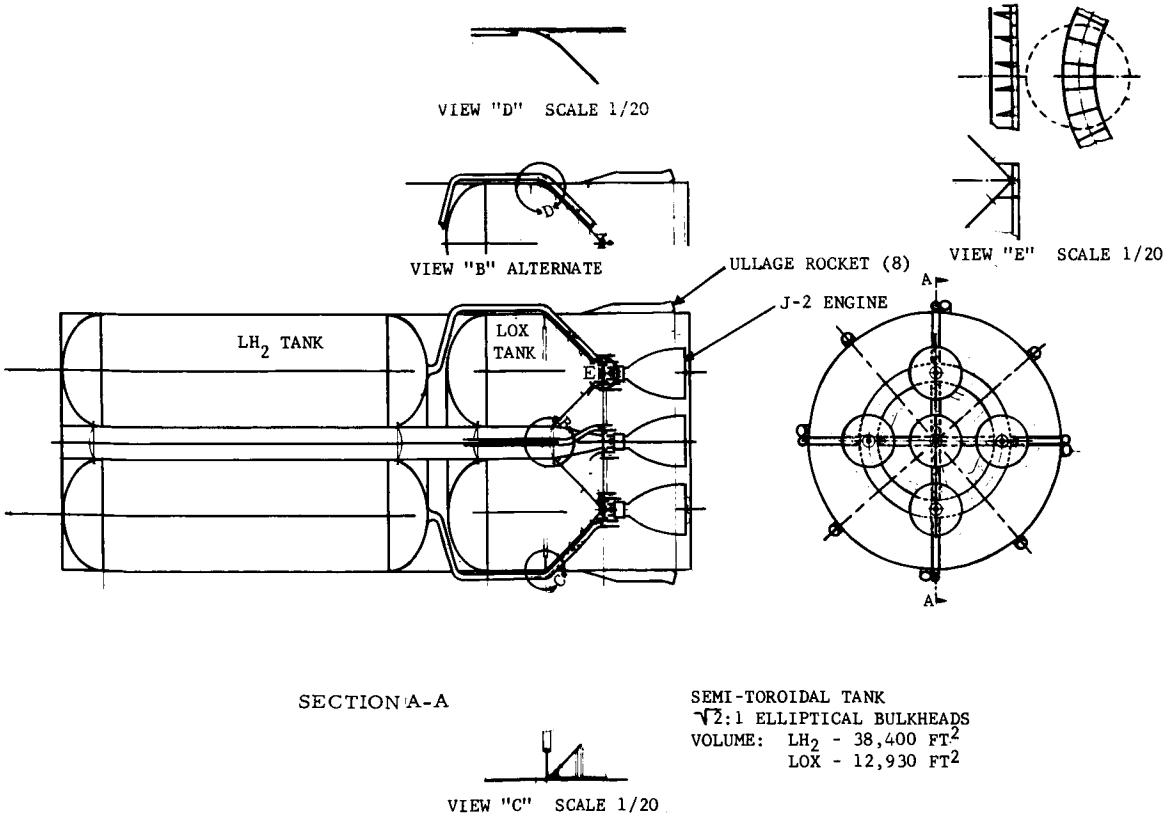

FIGURE 6. S-II STAGE IN SEMITOROIDAL DESIGN

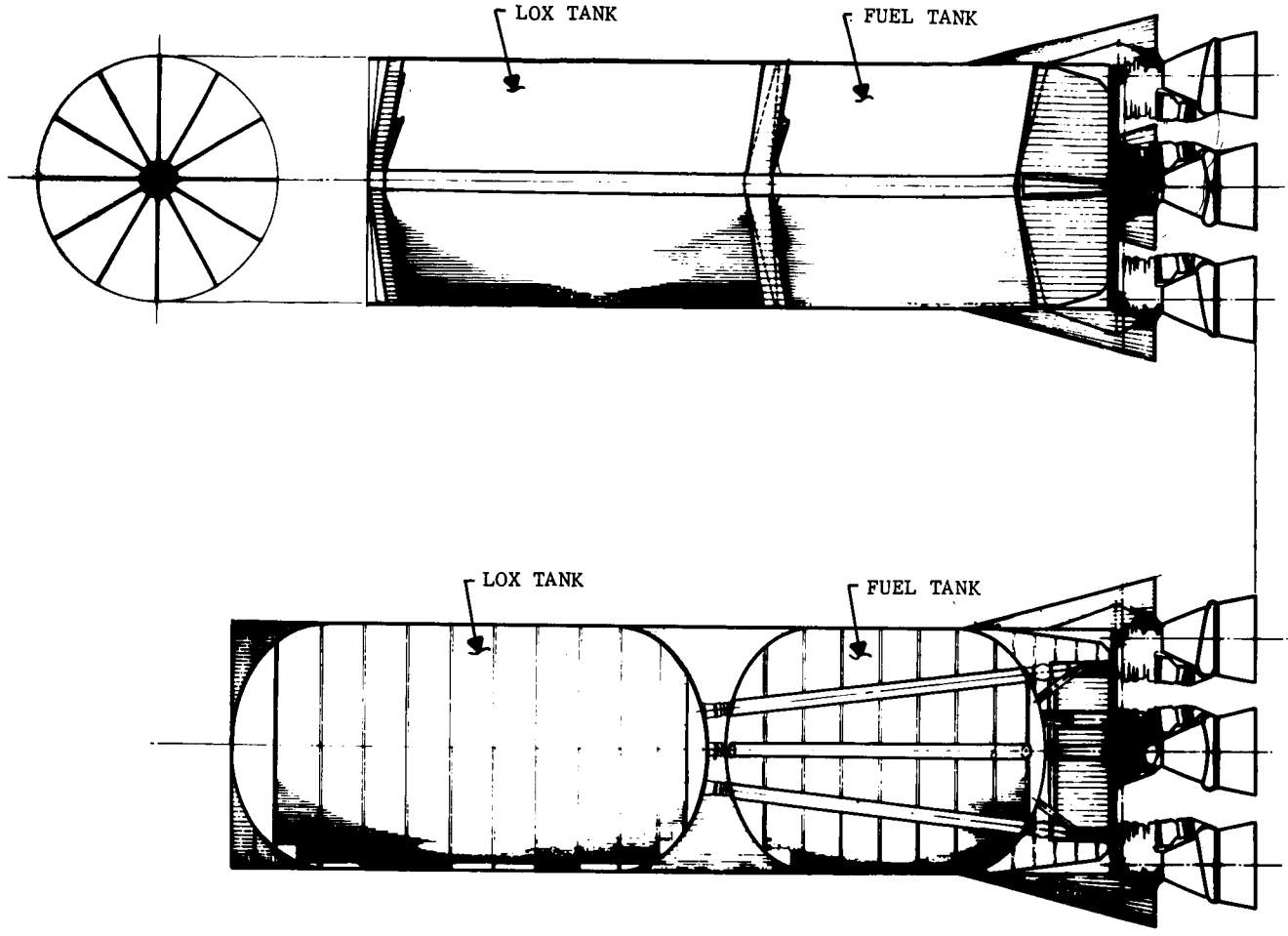

FIGURE 7. S-IC STAGE LENGTH COMPARISON, CONVENTIONAL AND FLAT BULKHEAD DESIGNS

B. LANDING GEAR STRUCTURES

MSFC became involved in these problems while studying unmanned lunar landing stages. The assumptions for landing under emergency conditions were necessarily more severe than those used in the Apollo manned lunar landing program, and required entirely new design approaches. The shock absorber and the landing pad described in the following are some of the results of this study.

1. Shock Absorbers. Figure 9 shows the heavy-duty shock absorber that would be required. Essentially, it consists of two heavy telescoping tubular structures. Inside the outer tube is a crushable honeycomb cylinder which is the actual shock absorbing element. Dynamic tests are being prepared that will not only answer design and functional questions but will also render information important for the analysis of landing dynamics. Two additional shock absorbers of different design are ready for testing and will provide design and functional confirmation for differing concepts.

2. Landing Pads. Another important part of such landing gears is the landing pad. Figure 10 shows a large pad developed here. Tests have confirmed its ability to absorb energy in the radial direction. Figure 11 is the load-deflection diagram of one of the dynamic tests. Note the very low rebound. Figure 12 shows a pad after a maximum-load impact test.

For this pad design, it had to be proved that the pad does not dig into the ground when moving along the surface. Drag tests conducted on an 20.3 cm diameter model with various loads, velocities, and soils, confirmed that the pad will always assume a positive angle of attack. Figure 13 and 14 give a good illustration of the severe conditions under which the correctness of pad design was proven.

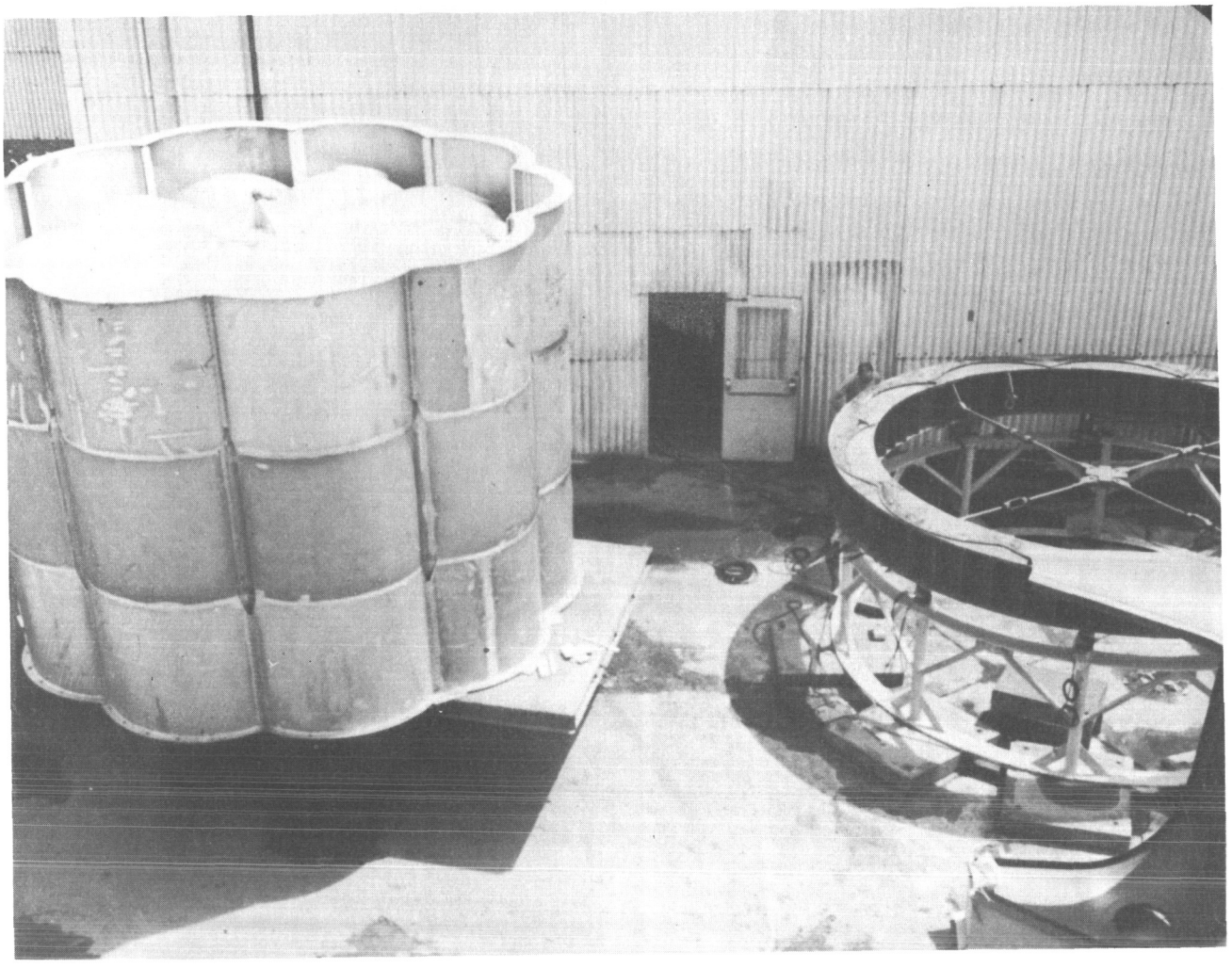

FIGURE 8. 200-INCH-DIAMETER MULTICELL TEST TANK

C. NOSE CONES

In cooperation with the Aero-Astrodynamics Laboratory, configurations and designs of nose cones were studied. The results will soon be available and will permit quick determination of optimum shape and structure of nose cones for given requirements such as volume, minimum weight, or cost.

1. Sandwich Development. The main emphasis in this field is still on honeycomb. However, some other promising sandwich forms are emerging. To its own disadvantage, honeycomb was over-advertised by sources that forgot such practical things as edge members and load introduction. These practical necessities are now coming into proper perspective. Design and feasibility of heavy gage honeycombs are being investigated under two MSFC contracts. A third contract provides for study of the characteristics and potential of sandwiches other than honeycomb. Analytical results of that contract have been reduced to a very convenient form of which an example is shown in Figure 15.

V. CONCLUSIONS

To achieve the national goals of the space program, the highest priority for manpower, facilities, and funds at MSFC has been assigned to the Saturn Space Vehicles. The cryogenic insulation program for short-term storage has resulted in successful design and assembly procedures. We are ready to put full emphasis on long-term storage. Specific data and information were developed for the design of nose cones, of micrometeoroid protection, and for structures that have to be sterilized. Test beams of

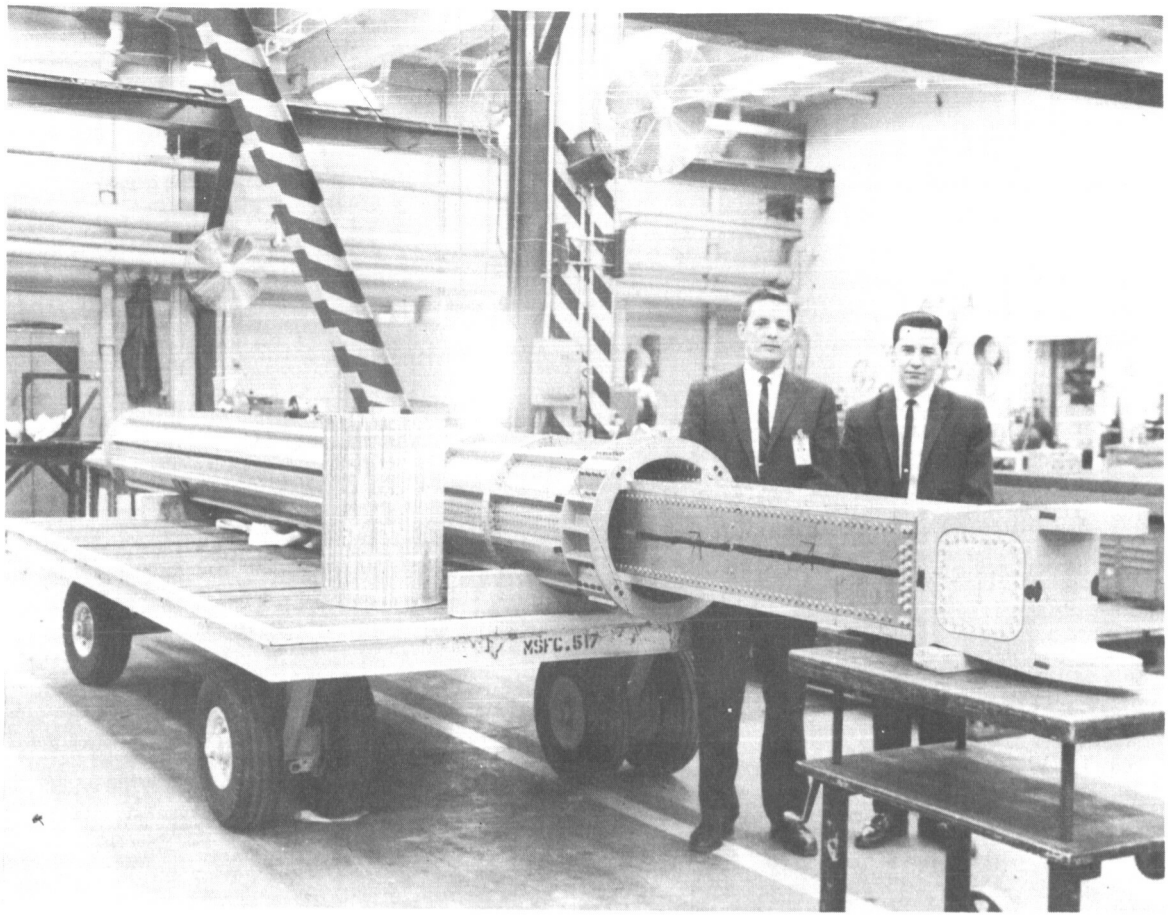

FIGURE 9. HEAVY DUTY SHOCK ABSORBER

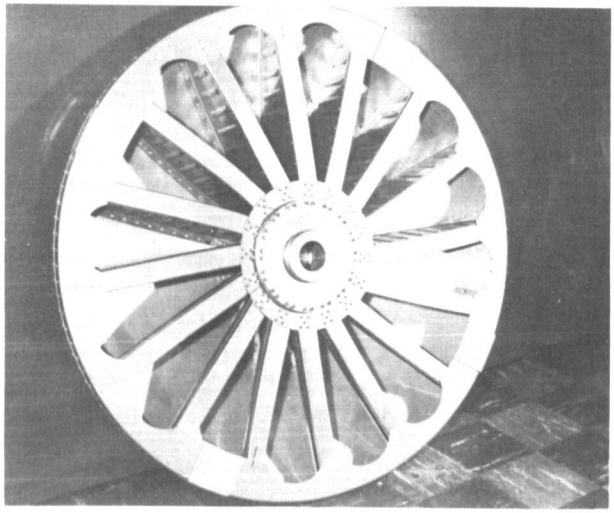

FIGURE 10. 52-INCH DIAMETER LANDING PAD

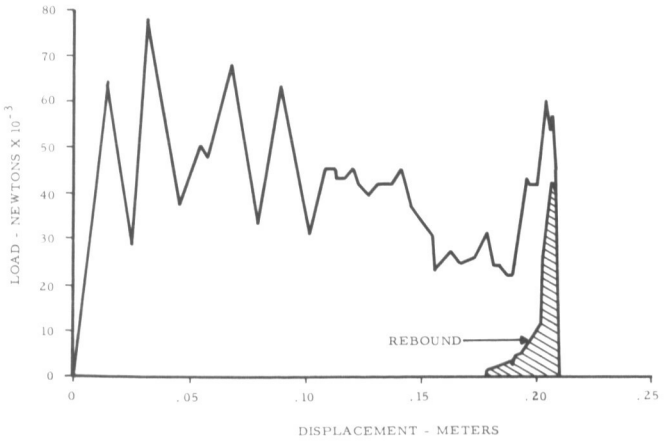

FIGURE 11. LOAD-DISPLACEMENT CURVE LANDING PAD IMPACT TEST

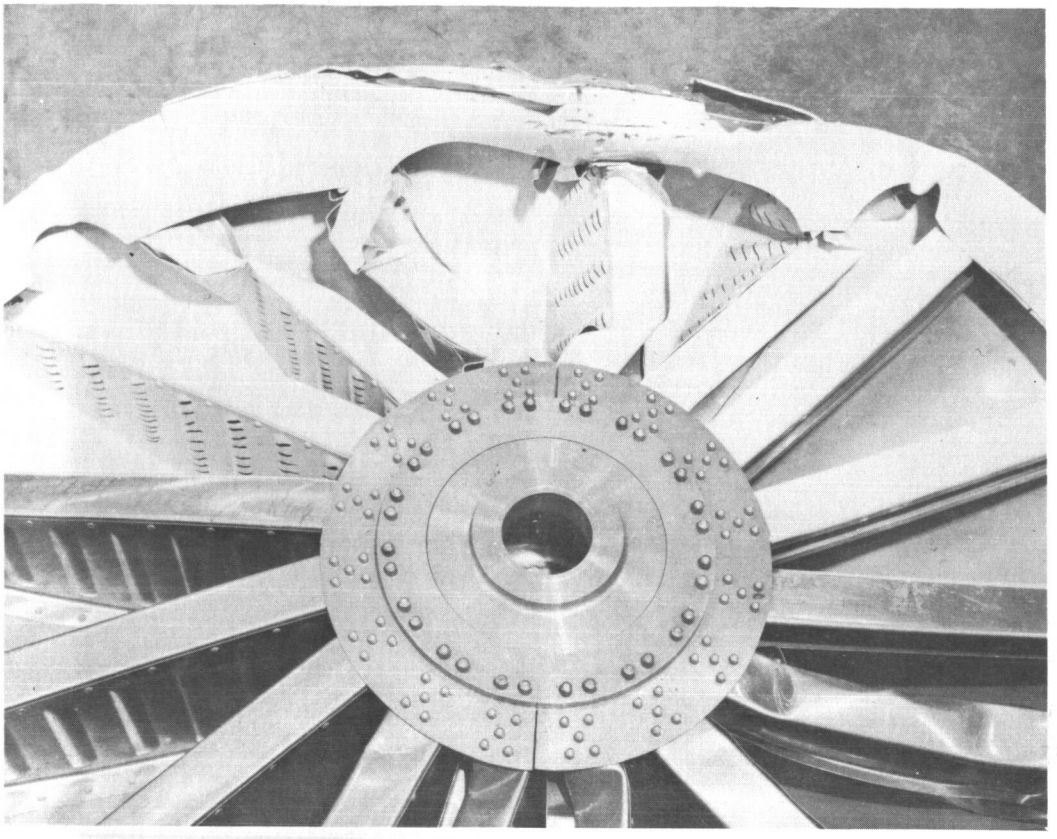

FIGURE 12. LANDING PAD AFTER DYNAMIC IMPACT TEST

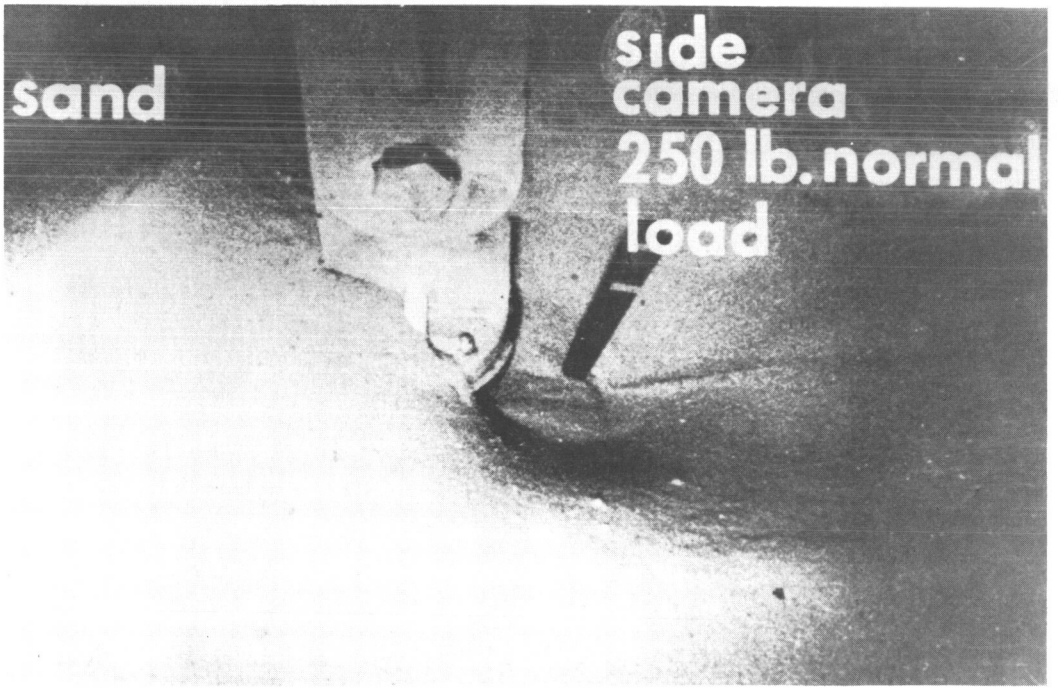

FIGURE 13. 8-INCH DIAMETER LANDING PAD DRAG TEST ON SAND

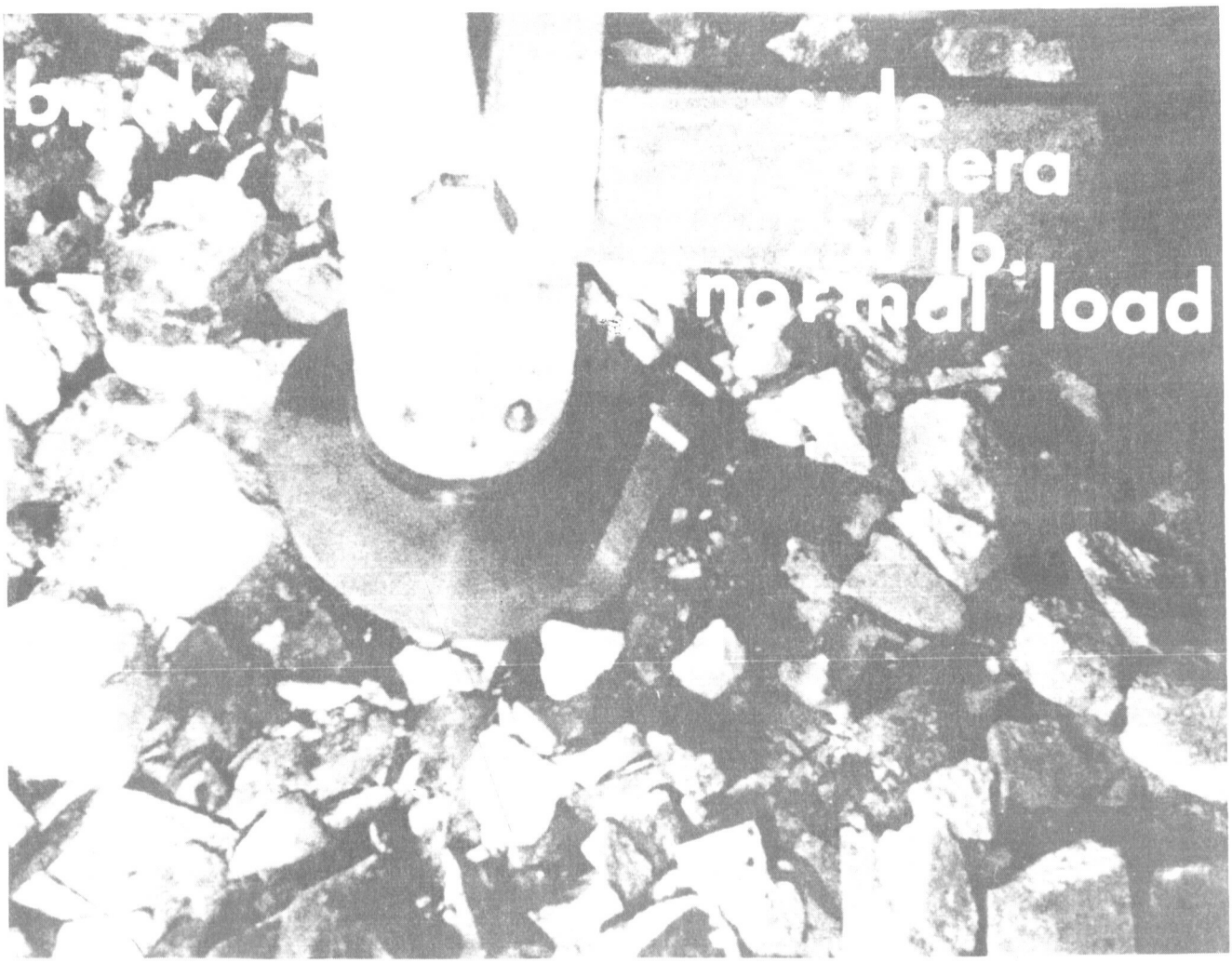

FIGURE 14. 8-INCH DIAMETER LANDING PAD DRAG TEST ON BRICK

various new materials have been designed and built. New tank configurations were studied, and some of them have been developed enough that test tanks can be built. Landing structures for unmanned vehicles have been investigated and unique design solutions have been developed into test hardware. Heavy gage honeycomb structures were developed and the potential of sandwiches other than honeycomb was investigated.

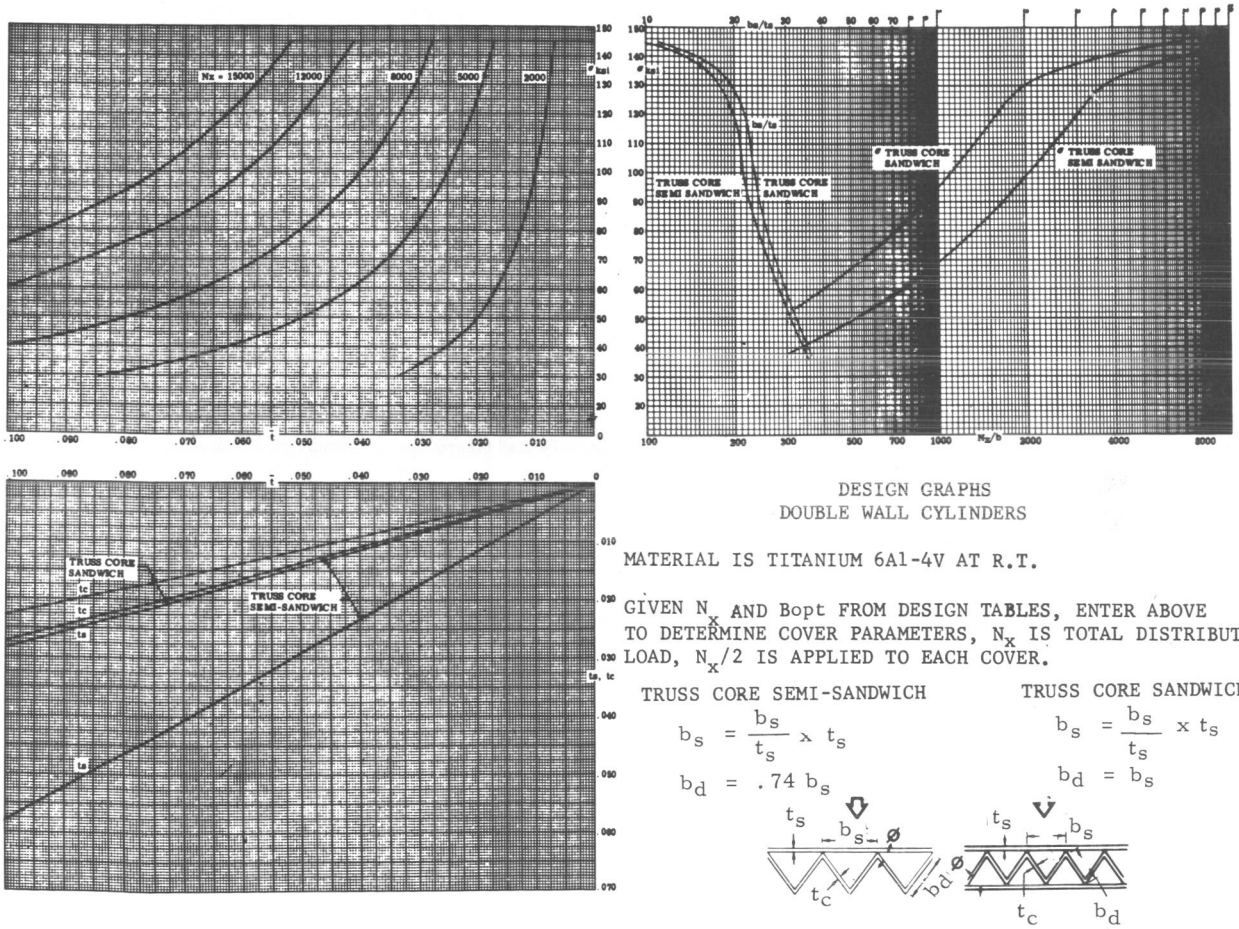

DESIGN GRAPHS
DOUBLE WALL CYLINDERS

MATERIAL IS TITANIUM 6Al-4V AT R.T.

GIVEN N_x AND Bopt FROM DESIGN TABLES, ENTER ABOVE TO DETERMINE COVER PARAMETERS, N_x IS TOTAL DISTRIBUTED LOAD, $N_x/2$ IS APPLIED TO EACH COVER.

TRUSS CORE SEMI-SANDWICH

$$b_s = \frac{b_s}{t_s} \times t_s$$

$$b_d = .74\, b_s$$

TRUSS CORE SANDWICH

$$b_s = \frac{b_s}{t_s} \times t_s$$

$$b_d = b_s$$

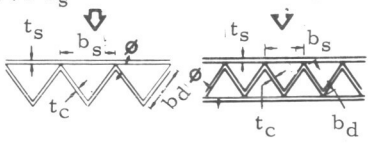

FIGURE 15. DESIGN GRAPH FOR DOUBLE-WALL CYLINDER

N67-30604

STRENGTH ANALYSIS RESEARCH

by

H. R. Coldwater

SUMMARY

This paper discusses recent research efforts in the areas of Advanced Vehicle Technology and Juncture Stress Fields Peculiar to Multicellular Pressure Vessels.

The Advanced Vehicle Technology Program is working to develop a large panel/cylinder stability criteria in preparation for designing future space vehicles, whose size will make the costs and facilities for structural qualification testing prohibitive. The program, though restricted, has yielded some accuracy in correlating $\frac{1}{4}$- and full-scale panels and cylinders.

The function of the Juncture Stress Fields Program is to devise adequate analytical methods for deriving optimum use of multicellular structures.

I. INTRODUCTION

Historically the buckling problem has been of primary concern in the design, development, and analysis of all shell structures, both pressurized and non-pressurized. Almost all the research work being conducted under the cognizance of the Strength Analysis Branch, Structures Division, Propulsion and Vehicle Engineering Laboratory, MSFC, is directed toward better understanding of the buckling phenomena and increasing the ability to predict accurately the various buckling loads for shell structures.

The functions of the Strength Analysis Branch are:

1. To establish strength requirements and specifications for conceptual design, preliminary design, and detail design.

2. To perform analyses for analytical verification of structural integrity of launch and space vehicles.

3. To establish test requirements and plans to flight-qualify launch and space vehicle structural components.

4. To develop new methods and theories in the field of strength analysis through supporting research programs and in-house studies.

The area of concern for this report is research in strength analysis methods. Table I presents the various efforts sponsored by OART and OMSF under the technical supervision of the Strength Analysis Branch. I will discuss in detail the first two items: (1) Advanced Vehicle Technology; and (2) Juncture Stress Fields Peculiar to Multicellular Pressure Vessels.

II. ADVANCED VEHICLE TECHNOLOGY PROGRAM CONTRACT NAS8-9500

The Advanced Vehicle Technology Program, NASA Contract NAS8-9500, consists of such items as cryogenic testing, materials development, structural development, and technology application to RIFT. For this discussion only structural development will be covered.

A. PURPOSE

The major purpose of this program was to develop large panel/cylinder stability criteria, including analysis, by modifying and testing stiffened tank wall panels. Future launch and space vehicles will in all probability be larger than existing vehicles; therefore, it will become prohibitive from an economic standpoint to test structures of the size contemplated (i.e., 70 feet in diameter, as proposed in the post-Saturn studies). We will not be economically able to afford test structures and facilities to do full-scale structural qualification testing. This program is a logical step to prepare for this eventuality and to develop the capability and confidence necessary for scale-model testing of full-scale hardware.

B. SCOPE OF WORK

The program was divided into three phases. Phase I covers full-scale panel testing to define the effects of end-restraint, curvature, and stiffener eccentricity on the buckling capability of the structure; also, the buckling pattern must be established to insure that the panels are large enough to allow development of some buckle pattern that will be experienced in a full cylinder of the same configuration. Phase II

TABLE I. STRUCTURAL TECHNOLOGY

1. ADVANCED VEHICLE TECHNOLOGY PROGRAM	OART 706-77-00	NAS8-9500	LOCKHEED MISSILES & SPACE CO. SUNNYVALE, CALIFORNIA
2. STUDY OF JUNCTURE STRESS FIELDS PECULIAR TO MULTICELLULAR PROPELLANT CONTAINERS	OMSF 103-11-01	NAS8-11079 6-29-63 to 3-29-64 NAS8-11480 11-23-64 to 12-23-65	LOCKHEED MISSILES & SPACE CO. PALO ALTO, CALIFORNIA
3. A THEORETICAL AND EXPERIMENTAL INVESTIGATION OF SHEAR LAG IN STIFFENED SHELLS AND THE STRESS ANALYSIS OF CONE FRUSTRUMS AND SEGMENTS	OMSF 124-11-06	NAS8-20164 NAS8-11155 NAS8-5158 (10-15-62)	UNIVERSITY OF ALABAMA UNIVERSITY, ALABAMA
4. STUDY OF STABILITY OF UNPRESSURIZED SHELL STRUCTURES UNDER STATIC LOADINGS	OMSF 124-11-06	NAS8-11181 5-20-65 to 2-20-66	GENERAL DYNAMICS CORPORATION GD/CONVAIR SAN DIEGO, CALIFORNIA
5. ELASTIC BEHAVIOR OF SANDWICH SHELLS	OMSF 124-11-06	NAS8-5255 3-20-63	BOARD OF CONTROL UNIVERSITY OF FLORIDA GAINESVILLE, FLORIDA
6. RESEARCH INVESTIGATION OF BULKHEAD CYLINDRICAL JUNCTIONS EXPOSED TO COMBINED LOADS, CRYOGENIC TEMPERATURES AND PRESSURES	OMSF 103-11-00	NAS8-5199 12-28-62 Mod. 12-28-63	BOARD OF CONTROL UNIVERSITY OF FLORIDA GAINESVILLE, FLORIDA
7. EXPLORATORY STUDIES AND ANALYSIS OF THE PROBLEMS OF BUCKLING OF CYLINDRICAL SHELLS WITH INCLINED STIFFENERS	OMSF 124-11-06	NAS8-5324 6-14-63	BOARD OF CONTROL UNIVERSITY OF FLORIDA GAINESVILLE, FLORIDA

investigates the 1/4-scale panel buckling characteristics to provide data for correlation with full-scale panels. The data are used also to refine and verify developed analytical methods for predicting buckling loads of stiffened shells. Phase III investigates 1/4-scale cylinders that are fabricated from panels tested under Phase II, with the data from these tests being correlated with the full-scale and 1/4-scale panel test data.

C. PHASE I

1. Testing. The Phase I [1] testing was performed on a single panel, but consisted of several configurations. The original panel (Fig. 1a) was straightened and tested as a flat panel (Fig. 1b) for stiffener eccentricity effects. The loaded ends had a configuration as shown in Figure 1c. The next test (Fig. 1e) required cutting 12 inches off each of the loaded ends of the panel to determine end-fixity factor effects. The loaded ends had a configuration as shown in Figure 1d. The flat panel was then cut in half to form two panels of equal size. These panels were formed so that one panel had the stiffeners on the outside of the skin (Fig. 1f) and the other (Fig. 1g) stiffeners on the inside of the skin. The panel configuration is shown in Figure 1h.

Figure 2 represents a panel (Fig. 1f) in the test configuration. The data for this particular test are shown in Table II, which presents the test data acquired during Phase I and is the basis for the developed conclusions.

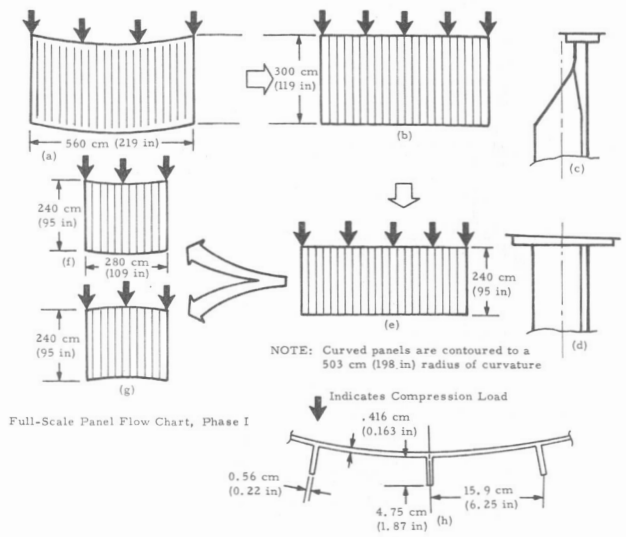

FIGURE 1. PHASE I TEST PANEL CONFIGURATIONS

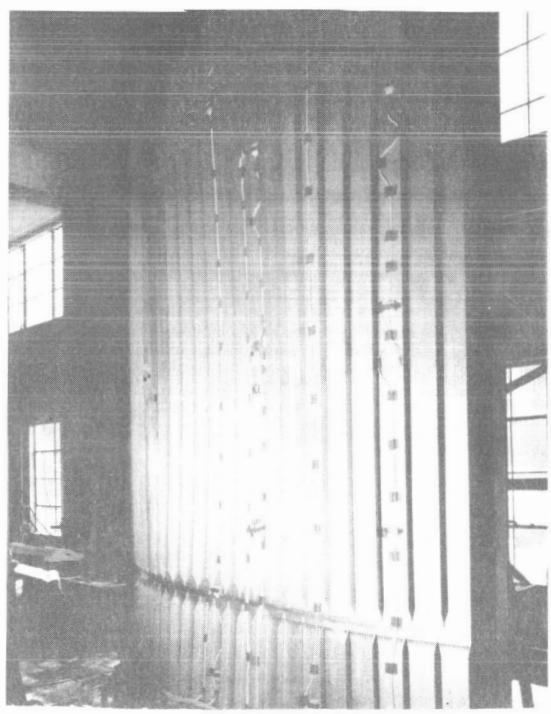

FIGURE 2. TEST OF EXTERNALLY STIFFENED FULL-SCALE PANEL (240 cm x 280 cm)

2. Evaluation and Conclusions. Evaluation and comparison of the test data shown in Table II proved that buckling loads can be predicted within engineering tolerances. Other conclusions established from the test data are:

a. The combination of panel curvature and stiffener eccentricity (stiffener outside) produced the most significant increase in the buckling load.

b. The second most significant variable increasing the buckling load was the combination of end-moment and fixity factor. Eccentricity of the stiffener (end-moment) at the loaded ends was more significant than the end-fixity. The end-moment effect is significant although lower in magnitude than indicated by theory. The eccentric loading of the externally stiffened panels adds to the stability, while eccentric loading of the internally stiffened panels lowers the stability.

c. Height change effects are greater for curved panels than for flat panels, indicating that changes in height may alter the effect of other variables such as end-moments.

Although these are conclusions that are not new in the business, they indicate that the performance of the test panels and data are in the proper sense.

D. PHASE II AND III

1. Test Objectives. The primary objectives of the Phase II and Phase III [2] portions of this program were to:

a. Evaluate the 1/4-scale and full-scale panel test results for possible scale effects (scale factor).

b. Confirm the panel-cylinder relationship by the Experimental Analysis Method. This is the evaluation of the stability behavior of cylinders through the testing of cylindrical segments (panels).

c. Evaluation of the theoretical analysis methods by comparison of experimental data with theory predictions.

In order to achieve these goals, the following secondary objectives were established:

a. Develop test techniques which would provide reliable data from test models for correlation with full-scale specimen tests.

TABLE II. COMPARISON OF EXPERIMENTAL AND THEORETICAL RESULTS

Test Configuration	Panel Size (cm)	Test Load (N)	(N_{cr}) Test av. (N/cm)	Max. Test (μ cm/cm)	(N_{cr}) Max. Test (N/cm)	N_{cr} Theory (N/cm)	N_{cr} Theory (N/cm)	Fixity Factor
2b	300 x 560 (119 x 219)	378,000 (85,000)	675 (388)	159	679 (390)	735[a] (420)	NA	1.0
2e	300 x 560 (95 x 219)	1,112,000 (250,000)	1975 (1140)	615	2330 (1500)	2330[a] (1500)	NA	2.5
2f	240 x 280 (95 x 109)	1,827,000 (411,000)	6530 (3750)	1,575	6776 (3870)	7180[c] (4100)	6250[b] (3570)	2.5
2g	240 x 280 (95 x 109)	1,000,000 (225,000)	3570 (2050)	1,000	4275 (2440)	3940[c] (2250)	3990[b] (2280)	2.5

(a) Wide-column load for end-fixity factors indicated.

(b) Critical line load from new classical theory for other than simple supports.

(c) Critical line load from classical theory considering restraint of Poisson's ration expansion adjusted for end fixity of 2.5 by increasing the wide-column load.

(d) Numbers in parentheses represent pounds and pounds/inch, respectively.

b. Demonstrate the feasibility of "retest" techniques in stability testing. This is control of elastic buckling to prevent permanent damage to test specimens and allow subsequent reuse in cylinder tests.

c. Obtain test data suitable for evaluating shell analysis methods particularly with respect to:

(1) The effect of stiffener eccentricity.

(2) The effects of various boundary conditions, including end-moments.

(3) Sensitivity to initial imperfections.

2. Test Specimens. The 1/4-scale panels were manufactured, fabricated and tested according to the plan as shown in Figure 3. The panels after testing were fabricated into cylinders and then tested as shown in Figure 4. Twenty-nine panels and six cylinders were tested during this program. It must be noted that the completion of this program depended on the successful application of the retest-technique. In general all program objectives were achieved.

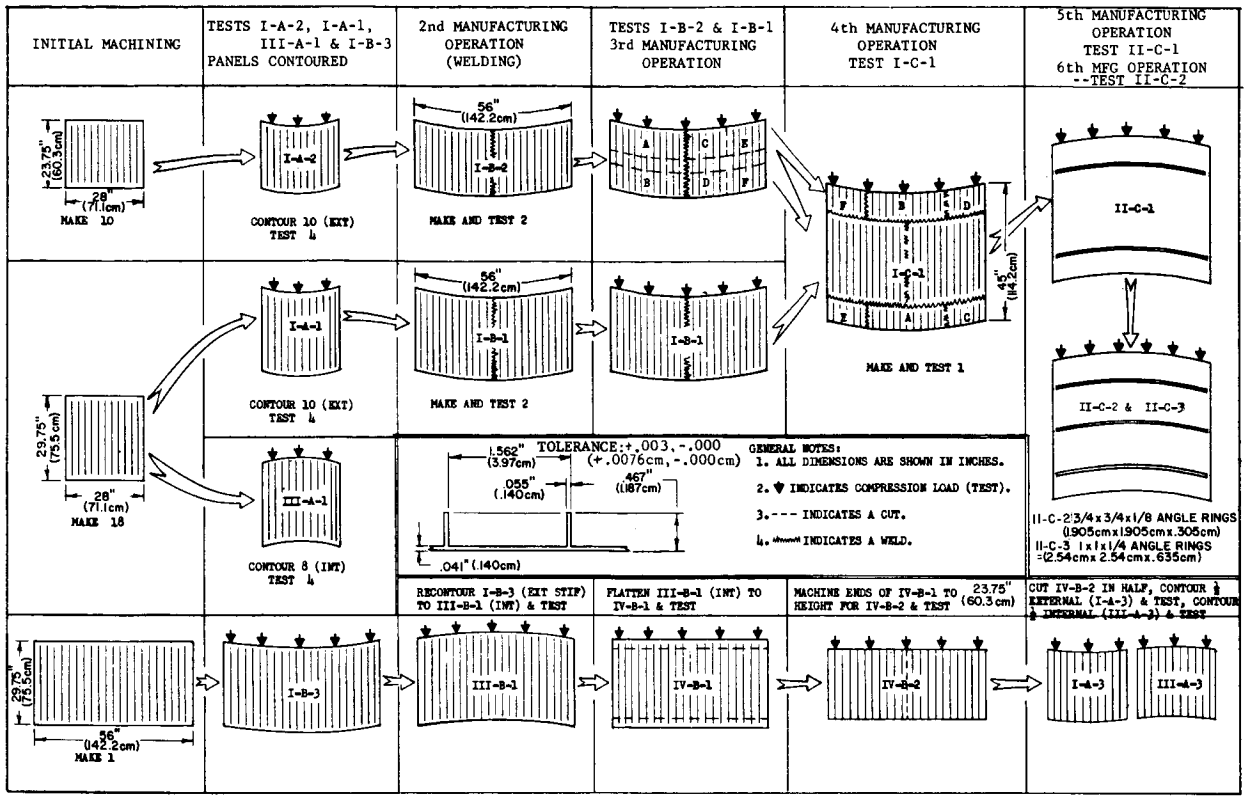

FIGURE 3. 1/4-SCALE MODEL PANELS

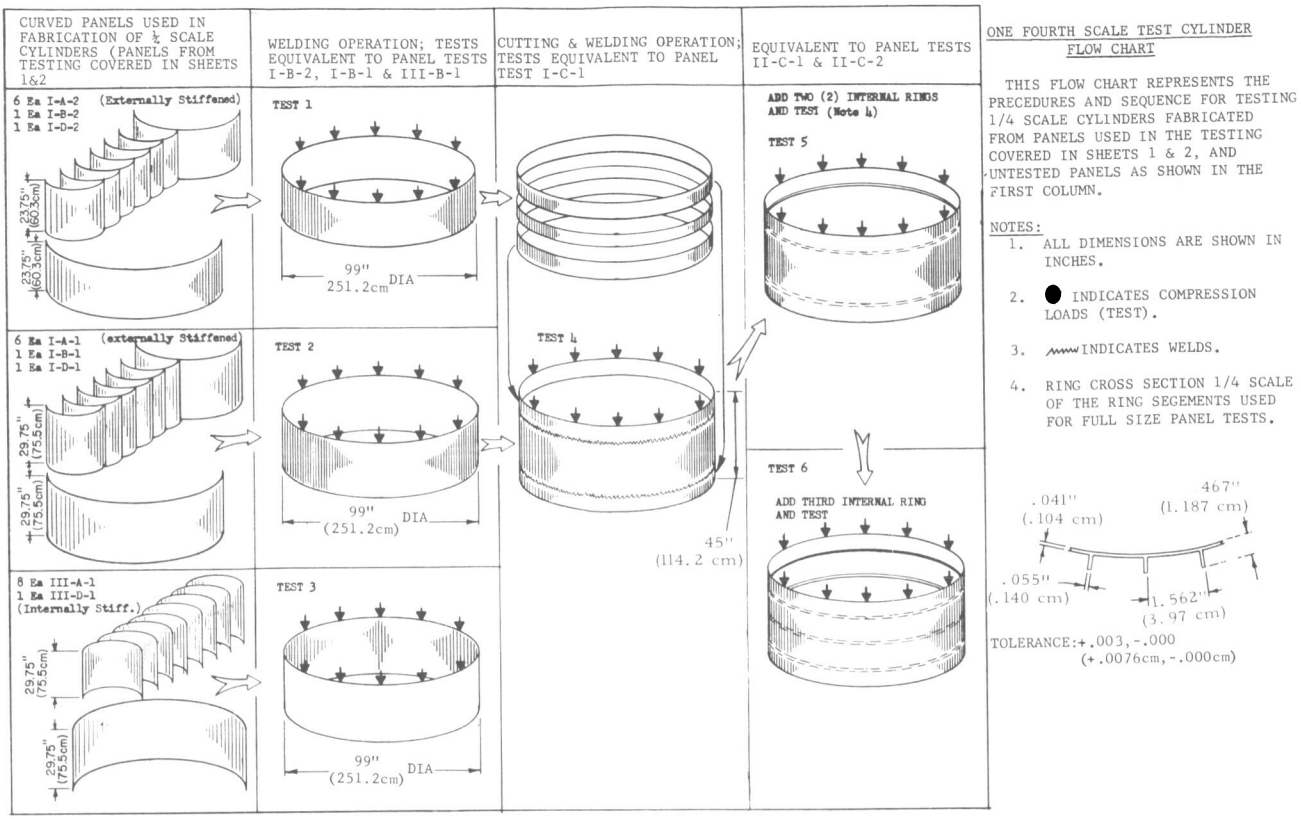

FIGURE 4. 1/4-SCALE MODEL CYLINDERS

One-fourth scale test panels in the test configuration are shown in Figures 5a and 5b. The panel in Figure 5a is an externally stiffened panel; whereas, the panel in Figure 5b is an internally stiffened panel.

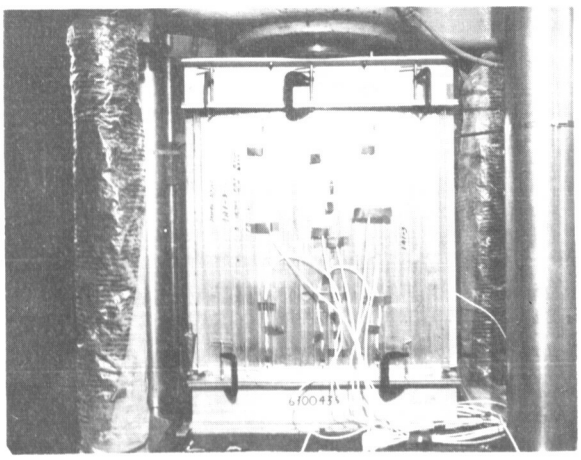

FIGURE 5a. EXTERNALLY STIFFENED 1/4-SCALE PANEL

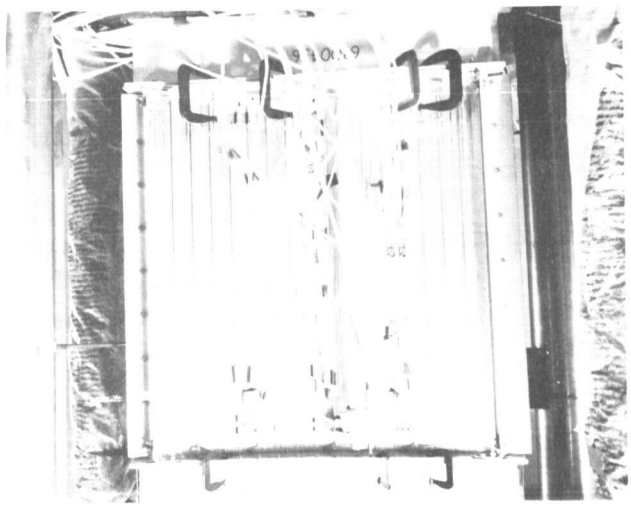

FIGURE 5b. INTERNALLY STIFFENED 1/4-SCALE PANEL

Figure 6 is a 1/4-scale cylinder that has been fabricated from various test panels as indicated (Fig. 4).

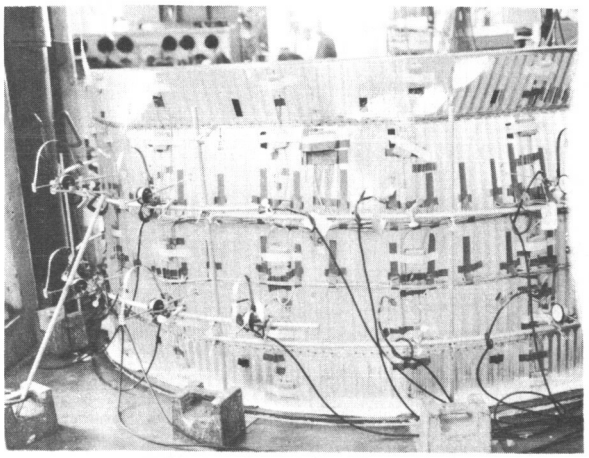

FIGURE 6. 1/4-SCALE CYLINDER TEST

3. Evaluation and Conclusions. The results of Phase II and Phase III as presented in [2] provided data to establish the following conclusions:

a. No special scale effect exists between the full-scale and 1/4-scale specimens. A direct ratio exists.

b. Results confirm that stability of integral bar-stiffened cylinders can be evaluated through testing of cylindrical segments (panels).

c. Results indicate that theory will be applicable to all orthotropic configurations when used with the Lockheed Theoretical Analysis Method, "Buckling of Orthotropic Cylinders under Axial Compression."

d. Successful testing of twenty-six 1/4-scale panels and five 1/4-scale cylinders without permanent damage demonstrates the ability to use controlled elastic buckling techniques and to permit the reuse of panels for the development of scale cylinder test specimens.

e. Fabrication and loading tolerances must be scaled and very closely controlled to be representative of the full-scale specimens.

(1) Stiffener straightness is extremely critical for externally stiffened cylinders and panels.

(2) End parallelism is critical as mismatch between the bearing surface of the test fixture and loaded ends of specimen caused a definite load distribution problem. Use of teflon pads or combined teflon and soft aluminum pads at the loaded ends produced excellent distribution and results.

f. Manufacturing and test tolerances appear to have reached a practical limit in the 1/4-scale models for a 33-foot diameter shell. Full-scale panels were manufactured using ±0.010-inch tolerance, whereas, the 1/4-scale panels were manufactured using a ±0.003, -0.000 tolerance.

E. SUMMARY AND RECOMMENDATIONS

Methods of analysis utilizing the results of the test program have been developed for confirming the accuracy and validity of correlating 1/4-scale and full-scale panels and cylinders. Structural configurations evaluated have been restricted to integral bar-stiffened aluminum specimens; however, to take full advantage of the work already accomplished and to establish valid methods and data for further and future application, it is necessary to expand the theories to investigate a wider range of efficient structural configurations for stiffened shells. It is also necessary to obtain sufficient experimental data through additional test programs to cover influential parameters for these wider ranges of configurations. All of these data will aid in upgrading the methods of analysis to insure more reliable and more optimum structural designs.

III. JUNCTURE STRESS FIELDS PROGRAM

A. GENERAL DISCUSSION

The second item for discussion is the investigation of juncture stress fields peculiar to multicellular propellant containers, NASA Contracts NAS8-11079 and NAS8-11480. The design approach to large launch and space vehicles that incorporates multicellular, nonpressure-stabilized, propellant containers, introduces unique juncture stress field analysis problems. This program has been developed to provide the necessary analytical methods to realize optimum use of multicell type structures.

The configuration of multicellular tanks as shown in Figure 7 is typical of configurations investigated in this program.

The bulkheads, or cell enclosures, of these radially arranged containers are composed of partial truncated cones and a spherical transition section to the partial cylinder section that forms the outer wall. The internal radial webs separating the cells function as anti-slosh baffling in addition to handling shear loads through a tension field pattern development. The perforated, partially stiffened webs extend radially

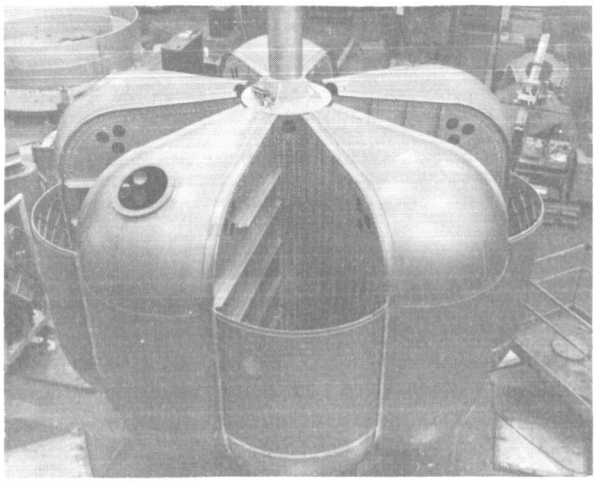

FIGURE 7. 10 CELL-MULTICELL TANK IN FABRICATION

from a center tubular section to the juncture of two outer wall sections and longitudinally between adjacent cell end closure junctures.

The attachment of each radial web to upper and/or lower adjacent bulkheads and each web to the outer peripheral partial cylinder junctures is accomplished by an extruded Y-section welded to the outer curved sections and mechanically joined to the web.

The attachment of upper skirt partial cylinder sections to the multicellular structure is accomplished, peripherally, by a partial Y-ring section at the spherical transition section-container outer wall juncture and, longitudinally, at the intersection of the partial Y-ring sections with the intercellular juncture extrusion.

In order to achieve the necessary vehicle reliability and optimum strength/weight design of multicell configurations, it was absolutely essential to clarify fully and reduce to theory all the discontinuity effects peculiar to these junctures. No previous theoretical investigation of these problems of multicell propellant container junctures had produced any theory or methods of analysis of technical significance.

B. OBJECTIVES

The investigations performed under this contract [3,4] were to:

1. Develop a theory and analytical approach for predicting membrane and discontinuity stress fields, deflections, and buckling loads of both isotropic and orthotropic shells. The developed approach is to be based on elastic theory of stresses for thin shells, and to include thermal and various other load environments.

2. Develop digital computer programs for rapid solution of the equations developed in the theory for predicting stresses and deformations, using both isotropic and orthotropic shell segments.

3. Develop design curves, encompassing practical ranges of specified design parameters.

C. METHOD OF ANALYSIS

Figure 8 illustrates the general appearance of multicell configurations investigated, together with the range of parameters covered in the development of design curves and criteria.

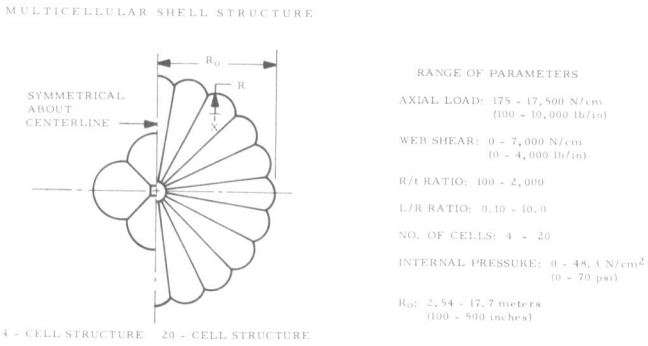

FIGURE 8. MULTICELLULAR SHELL STRUCTURE

The method decided upon for the solution of the complete shell structure is similar to the "slope-deflection" procedure used in the analysis of indeterminate space structures. The structure is first analyzed in terms of the behavior of the simple elements (cone, sphere, cylinder, and plate) as represented by stiffness matrices which relate the boundary forces on the element to boundary displacements. From this information and necessary conditions of equilibrium and displacement compatibility between elements, a set of equations can be formed and solved to yield solutions for the actual element displacement boundary values corresponding to the continuous structure. Once the displacement boundary values for the elements are known, the stresses throughout the various elements can be determined from the stiffness functions.

The major difficulty in this method is the determination of the stiffness matrices for the individual

shell elements. This difficulty was overcome through the finite difference reduction of the shell equations. The success of the method is dependent on the ability to solve large sets of algebraic equations accurately and in reasonable computer time.

A very comprehensive computer program was developed and has the capability of solving up to 4300 algebraic equations simultaneously. A numerical technique called matrix factorization was found to be most suitable to provide sufficient accuracy for the determination of boundary-layer behavior of fixed-edge shells.

After establishment of the necessary coordinate systems and directions for stress and moment resultants (Fig. 9) sample problems were run to prove the method and to verify the computer program capability.

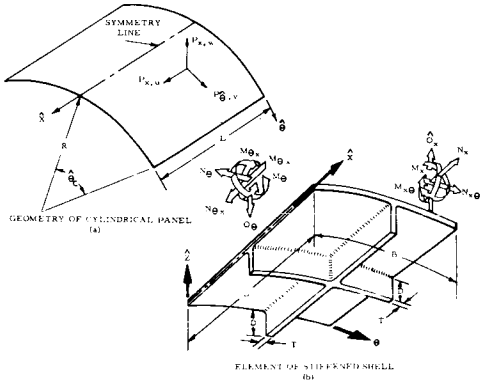

FIGURE 9. TYPICAL SHELL ELEMENT GEOMETRY AND COORDINATE SYSTEM

The geometry and coordinate system (Fig. 9a) is representing the surface or body forces; the u, v, and w, representing the deflections in the directions as shown; and the M, N, and Q (Fig. 9b) representing the moment and stress resultants.

Figure 10 is a plot of the "w," or radial deflection caused by normal pressure and is a typical example of data presentation. For this case there are two axes of symmetry (horizontal and vertical through the midpoint of the panel). The computer program will print out similar data for spherical and conical segments.

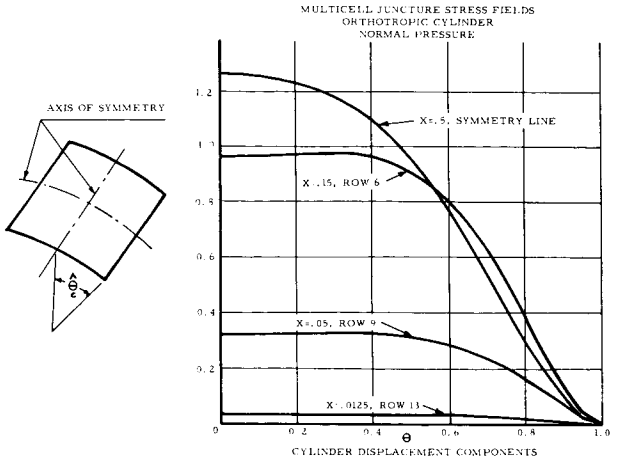

FIGURE 10. RADIAL DISPLACEMENT DUE TO NORMAL PRESSURE (FIXED EDGES)

D. RESULTS AND CONCLUSIONS

Results of the program indicate that:

1. A general theory has been developed which will predict membrane, discontinuity, and buckling stress fields for multiple-connected shell structures; however, the discontinuities at the juncture of the various shell elements were found to be minor contributors to the overall stress picture of any particular juncture. Sample problems have been run and checked to prove the correctness of the method.

2. The numerical methods used for solving large systems of linear algebraic equations involved in the analysis of juncture stress fields and buckling loads are feasible and provide the most efficient means of attacking problems of this nature. The finite difference technique for solving the equations proved to be most effective, as closed form techniques generally are not applicable to structures with multiple shell elements.

3. The feasibility of adapting these methods of analysis to digital computer solutions was proved, and as a spin-off, the capability of solving very large systems of linear algebraic equations simultaneously was developed and proved to work.

4. Design curves were developed to aid in the design and analysis of multicell type structures, covering the normal design parameters and relationships. All the work performed during this study has been documented and reported [3, 4].

E. SUMMARY AND RECOMMENDATIONS

Presently, a structural testing program is being conducted in-house on a 200-inch-diameter, 10-cell multicell tank. Figure 7 is a picture of this structure in manufacture. To date, one pressure test has been conducted on the tank and cursory data checks indicate good correlation between the developed theory and test. In the future slosh tests, combination axial load and pressure tests, cryogenic tests and flow tests will be performed on this structure and data will be correlated with theory.

There are still areas of concern remaining in the strength analysis of multicell structures. There is a definite need for better methods of predicting shear and tension field stresses in the web plates (cell walls). There is a definite need for determining the non-elastic characteristics of multicell structures, that is, to investigate plastic effects on capability. These are some of the problem areas still associated with multicell structures; these require resolution to make this program a complete and meaningful method for analysis and design.

REFERENCES

1. Lunsford, L. R.: Structural Panel Stability Development Program, Phase I. Lockheed Missiles and Space Company Report A746888, April 30, 1965.

2. Lunsford, L. R.: Structural Panel Stability Development Program, Phases II and III. Lockheed Missiles and Space Company Report A770422, October 30, 1965.

3. Tsui, E. Y. W.; Brogan, F. A.; Mossard, J. M.; Stern, P.; and Stuhlman, C. E.: Investigation of Juncture Stress Fields in Multicellular Shell Structure. NASA CR-61050, February 1964.

4. Lockheed Missiles and Space Company Report M-77-65, Volumes I through IX. Juncture Stress Fields in Multicellular Shell Structures:

   Volume I: M-77-65-5, Brogan, F. A.: Numerical Methods of Solving Large Matrices, August 1965.

   Volume II: M-77-65-1, Tsui, E. Y. W.; Brogan, F. A.; and Stern, P.: Stresses and Deformations of Fixed-Edge Segmental Cylindrical Shells, June 1965.

   Volume III: M-77-65-2, Tsui, E. Y. W.; Massard, J. M.; and Stern, P.: Stresses and Deformations of Fixed-Edge Segmental Conical Shells, June 1965.

   Volume IV: M-77-65-4, Tsui, E. Y. W.; Chen, C. T.; and Stern, P.: Stresses and Deformations of Fixed-Edge Segmental Spherical Shells, July 1965.

   Volume V: M-77-65-6, Stern, P.; and Chen, C. T.: Influence Coefficients of Segmental Shells, August 1965.

   Volume VI: M-77-65-7, Chen, C. T.; and Stern, P.: Analysis of Multicellular Propellant Pressure Vessels by the Stiffness Method, November 1965.

   Volume VII: M-77-65-3, Pittner, E. V.; Almroth, B. O.; and Sobel, L. H.: Buckling Analysis of Segmental Orthotropic Cylinders under Uniform Stress Distribution, July 1965.

   Volume VIII: M-77-65-8, Almroth, B. O.; Brogan, F. A.; and Pittner, E. V.: Buckling Analysis of Segmental Orthotropic Cylinders under Non-Uniform Stress Distribution, December 1965.

   Volume IX: M-77-65-9, Tsui, E. Y. W.: Summary of Results and Recommendations, December 1965.

VIBRATION AND ACOUSTICS STRUCTURAL RESEARCH

by

C. E. Gassaway

SUMMARY

This paper describes four areas of current research on the effects of vibration and acoustics on vehicle structure.

The volume of test flight data restricts its use by flight evaluation engineers. More efficiency has been obtained by programing computers to select only the pertinent information and compare it with specifications.

Methods for determining operational loads are inadequate for dynamics analysis engineers. Research indicates that measuring structural impedance may be an accurate technique for this function. The impedance method may also be applicable in dynamic testing and investigations will determine its possible use as an improved testing technique. This could supplement subscale testing which is not yet reliable.

The factors of structural response to environment are also noted with a description of research efforts in this field.

I. INTRODUCTION

Some of the problem areas in which the Vibration and Acoustics Branch is currently performing research are:

1. Optimum utilization of test data
2. Dynamic load design criteria
3. Estimating the environment
4. Dynamic testing

Briefly, an introductory remark will be made about each, followed by a somewhat more detailed review.

Item No. 1: A large amount of vibration and acoustics data has been obtained from space vehicles. Both Air Force and NASA are flying many R&D vehicles to obtain this data. None of this vibration data has been put together so that an engineer could utilize it to the extent and in the manner he would like. In addition, with the increase in vehicle size (and the accompanying increase in numbers of measurements), the increased launch density in the future, and the decreased manpower available to do the job, it becomes an increasingly difficult task to perform flight evaluation. Research work has been done to cope with these problems.

Item No. 2: After definition of the environmental data, it is first necessary to perform analysis to determine dynamic loads existing in the structure (This requires a thorough knowledge of the structural dynamic characteristics), and secondly to convey the results of the dynamic analysis to the structural designer to incorporate in his design during the formative stages. Under this item will be discussed some of the research efforts that are currently underway to support the dynamicist with the new techniques of both analysis and conversion for the design engineer.

Item No. 3: The term "environment" includes the vibro-acoustic as well as the transportation and shock environment. The principal problem here is to establish the response of a structure to engine-generated acoustics, aerodynamics, structure-borne vibrations, and transportation shock, when the structure is not yet defined, as in the case of future vehicles.

Item No. 4: As vehicles get larger and larger, it becomes increasingly difficult to obtain test specimens because of cost, and if obtained, it becomes impractical, or at least extremely difficult to perform testing because of the state of the art of test equipment. Some of the subsystems on today's vehicles are larger than the complete vehicles in the past. It is evident that model testing will become an increasing requirement in the future. There are many unknowns associated with dynamic model testing. It is readily apparent that geometric scaling is not necessarily dynamic scaling. Some of the aspects of the research for such testing will be discussed here.

With this brief introduction, we shall examine each item in more detail.

C. E. GASSAWAY

II. OPTIMUM UTILIZATION OF TEST DATA

As stated in the introduction, data are utilized for two distinct purposes. One is to perform flight evaluation, i.e., to determine whether a flight is normal; and the other is to provide the engineer with a better handle on utilization of the structural performance in the gross sense.

It became evident that we were receiving more vibration and acoustic data than could be handled on a piecemeal basis. The development of digital data reduction techniques also provided more detailed knowledge of the data from each measurement. The obvious solution was to operate on the data statistically in some manner to achieve the desired end results.

Since we were dynamicists and not statisticians, and since there were indications that this type of statistical effort was unique, several research contracts were let, to determine the best technique to pursue. Among these were one to Research Triangle [1] and one to Measurement Analysis Corporation [2]. The results have been a program that can perform both tasks. First, this program establishes a statistical population for a particular measurement from static firing vibration data as shown in Figure 1. It then

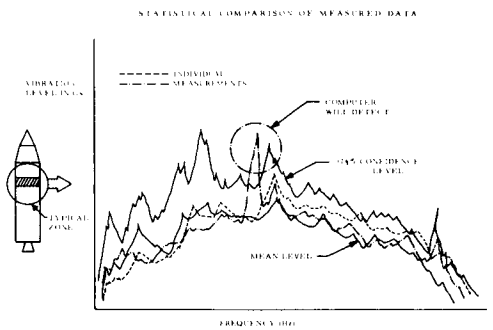

FIGURE 1. STATISTICAL COMPARISON OF MEASURED DATA

compares individual measurements against the statistical population of those measurements. The computer will ignore all data except that which falls outside the 97 1/2 percent C. L. estimate. In this manner, the flight evaluation engineer has only to examine the computer printout to determine which measurements are not normal and require individual evaluation effort.

The second task the program achieves is that of summing all measurements within a specification zone or subzone, comparing the new data to the population, adding the data to the old zone description to update the zone statistics, and comparing the results to the qualification specifications. This provides the specification engineers with a running tab on how good the spec is and what type of revision is justified. Results to date have been encouraging: the technique is proven; however, additional research work is required to modify the techniques to provide still more efficient methods of accomplishing the same results.

III. DYNAMIC LOAD DESIGN CRITERIA

A. LOADS DETERMINATION

Perhaps the title is misleading in that the word "criteria" does not completely encompass the first item here, i.e., loads determination.

Recent developments in the instrumentation and data acquisition field have provided a new tool for the analytical engineer in the impedance measuring system.

Some may not be familiar with the term "structural impedance" or "mechanical impedance." Webster gives the definition of impedance as "the resistance of a film to the passage of a substance." Mechanical or structural impedance can be described as the resistance of a structure to the passage of energy, or specifically, the ability of a structure to impede the conversion of input energy to response motion. This characteristic is dictated by the mass, stiffness, and damping properties of the structure and is a frequency dependent phenomenon, as shown in Figure 2. Each line on this graph represents idealized conditions:

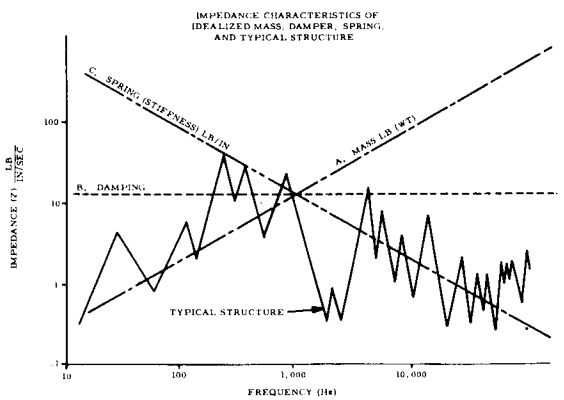

FIGURE 2. IMPEDANCE CHARACTERISTICS OF IDEALIZED MASS; DAMPER, SPRING AND TYPICAL STRUCTURE

a. - Constant mass line which increases in impedance with increasing frequency.

b. - Viscous dashpot or damper (which is frequency independent).

c. - Idealized constant spring line (stiffness) which decreased in impedance with increasing frequency.

All structures are complex combinations of those idealized curves leading to the typical point impedance graph shown. The valleys or dips in this curve indicate resonant frequencies where the structure is "soft" or has low resistance to the passage of energy. Peaks represent hardness or high resistance. Some peaks are 2 to 3 orders of magnitude higher than the valleys. It is these wide variations of impedance values, and the fact that we are dealing with a wide range of frequencies and amplitudes in the forcing functions, that make it necessary to consider the effects of impedance on shock and vibration reliability. The preceding discussion has dealt with point impedance (or local impedance), which can be defined as the resistance of a point to the passage of energy with the input at that same point. "Transfer impedance" can be defined as the resistance of a given point to the passage of energy with the input at another (or remote) location. In a structure that complies with ideal boundary conditions and mode shapes, the transfer impedance is reversible. In a general sense, the impedance serves as a measure of the spread of vibration from one location to another. The phase relationship of the force and the response motion must be retained.

The measurement of each of these terms simultaneously, retaining the phase relationship, is accomplished using an impedance head between the shaker, and the specimen of interest is shown in Figure 3. The impedance head is nothing more than a transducer to measure the force throughout and the velocity response. (Sleeve transmits force through crystal; reference mass transmits force, e.g., velocity through crystal). Note that the impedance head may be relatively small, on the order of one inch in diameter and one inch in length, for use with very small force generators. Among other uses, the impedance measuring system apparently will be suitable for measurement of loads under the random use environment.

Historically, methods for determining operational loads utilize strain gages and the accompanying calibration procedures and inherent limitations, or the use of accelerometers and a knowledge of the mass distribution of the system of interest.

Either of these techniques is suitable when applied within the limits consistent with good results.

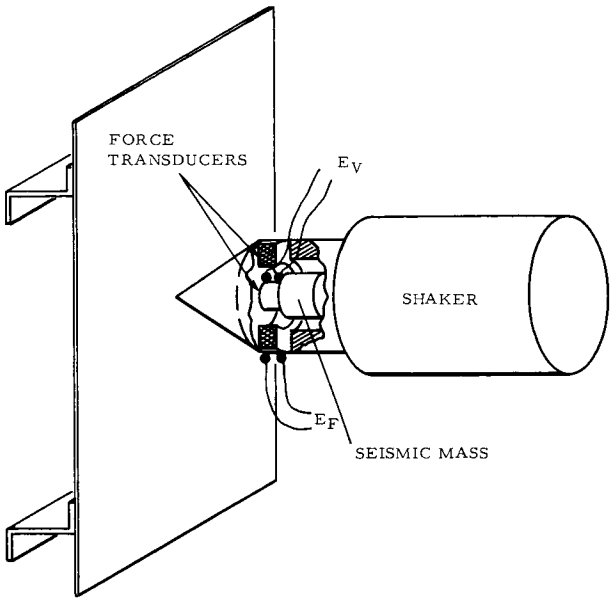

FIGURE 3. TYPICAL IMPEDANCE MEASURING SET-UP

Unfortunately these limits have never completely encompassed the needs of the dynamics analysis engineer. The impedance technique is currently being researched to extend the loads measuring capability. Impedance has been used in many instances to evaluate complex system dynamic behavior, seldom used to establish environmental loads, and never, to our knowledge, to define loads under random load conditions. The purpose of this research work is to develop and utilize such a technique.

The concept is fairly simple and straightforward. The impedance is measured at the points where force data are required, and the velocity of these points is measured during exposure to the environment. The forces existing at these particular points may then be calculated by the equation

$$Fw(e) = Zw\ Vw(e)$$

where $Z_w = \frac{Fw}{Vw}$

and $Fw(e)$ = Environmental force spectrum

Zw = Measured impedance spectrum

$Vw(e)$ = Environmental motion spectrum

Fw = Force spectrum of Z test

Vw = Motion spectrum of Z test

In other words, (measured impedance) (measured motion in operation) = Forces present. Tests conducted on the S-IC fuel suction lines and F-1 turbopump tests were the first to verify this concept of loads measurement. The impedance characteristics of each system were obtained independently by The Boeing Company, through the use of small shakers and impedance heads. The specimens were then mated and installed in actual service at MSFC and the motion characteristics obtained. From the impedance and velocity relationship (which includes phase) the force spectra at the mating planes were obtained.

It is extremely important that additional research be expended in the area of impedance research since we have only scratched the surface of applicability. Earlier work in impedance would have given a better Saturn vehicle, since critical areas could have been detected early, allowing more thorough coverage of instrumentations during static firings. Research is needed to determine accuracy and limitations and to widen the scope of vision to impedance techniques.

B. CONVERSION TO "STATIC LOAD EQUIVALENTS"

Once the dynamic loads are measured, the dynamicist must express these loads in the same terms in which the material properties are expressed, i.e., static load values. This has long been a major problem to those in the dynamics field. If these dynamic loads could be converted to 'equivalent static loads' the communication barrier between the designer and the dynamicist would be penetrated.

If we express this relationship as: Static equivalent load = (optimum design factor, K) (dynamic load), the problem would be to solve for K. This solution for K for the random case will not be the same as K for the sine case, and further, one might suspect that these values of K will vary for different materials.

Research efforts are currently underway by Douglas Aircraft Company [3], Santa Monica, California, to establish this relationship. Some of the achievements to date have been with 4130 steel and 2024T4 aluminum. Tests were conducted over a range of K values which had been selected for a 10-minute fatigue lifetime under random environments. Figure 4 shows the results of the research for 2024T4 aluminum. On the left is the optimum design random factor, on the right is the sine factor plotted against required life cycles. Note that there is not much spread between the least squares fit and the 95 percent C.L. curve. This indicates a degree of predictability. From this plot, one can select an optimum design factor K for this material for any given lifetime and natural frequency.

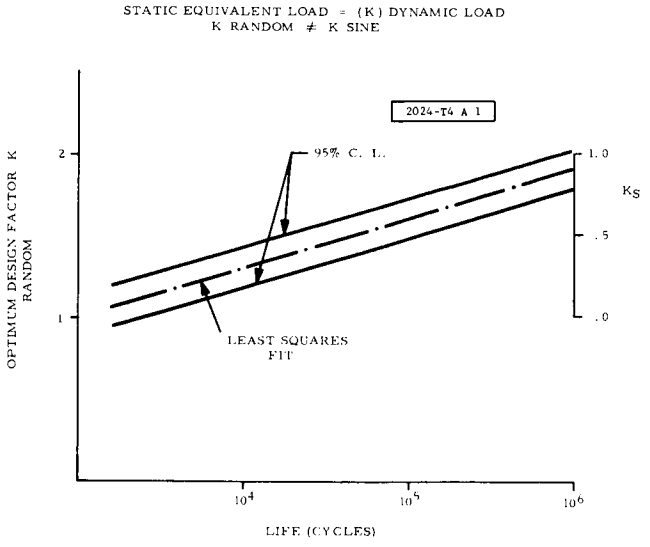

FIGURE 4. STATIC EQUIVALENT LOAD CONCEPT

This research work encompasses only 4130 steel (140 - 160 ksi) and 2024T4 aluminum. Similar research is required to provide the optimum design factors on all other materials currently in use, as well as the more sophisticated materials such as composite structures, as mentioned before, as potential candidates for future vehicle application.

C. THE EFFECTS OF DESIGN PARAMETERS ON SHELL STIFFNESS

Under certain circumstances, the dynamics engineer is placed in the position of not having a specimen for test purposes and he must analytically determine the dynamic effects of altering the design of a vehicle. In the case of the shell type structure, additional components may be mounted on the shell wall or rearranged, or the designer may change any of the design parameters which he normally controls, such as internal pressurization, skin thickness, or ring and longitudinal stiffener sizes or spacing. There has been no established method to determine changes in the dynamic shell stiffness due to changes in these design parameters.

There have been some techniques used, but they were not applicable over the range of configurations that can be foreseen for future vehicles.

A great deal of research effort has been exerted by Republic [4] to determine shell stiffness variation with changes in design parameters. The results show

some departure from previously accepted theory. The structure will respond with certain predictable results, some of which are shown in Figure 5, in simplified

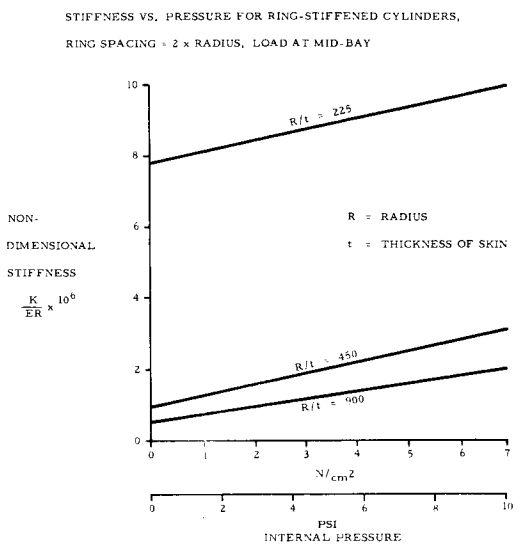

FIGURE 5. EFFECTS OF INTERNAL PRESSURE ON LOCAL STIFFNESS

form. This plot shows variation in local stiffness as a function of internal pressure for various vehicle radius/skin thickness ratios (R/T). The family of curves in Figure 6 shows the effects of added weight on frequencies and mode shapes for various internal pressures. (Note R/T = 450, which is approaching

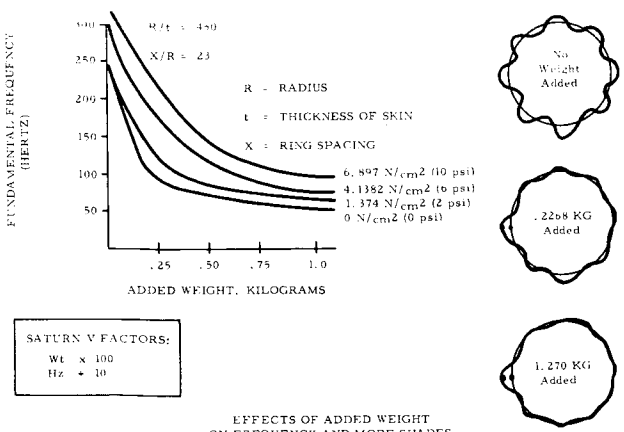

FIGURE 6. EFFECTS OF ADDED WEIGHT ON FREQUENCY AND MODE SHAPES

the practical limits of today's technology.) Particular note should be paid to the mode shapes. While this figure is not sufficiently accurate to indicate the results precisely, the decrease in response around the shell is evident when the local mass is increased. Also, note the difference of these mode shapes from that expected when a static load is applied. These are scale results and for a vehicle of Saturn V class, multiply weights shown by 100 and divide frequencies shown by 10.

The results of this research are now available for use as far as they go. As a matter of fact the research was exerted primarily in the R/T ratio of 450 so the results would be immediately applicable to the Saturn V vehicle, and they have been used recently for some existing hardware.

Additional efforts are required to determine response characteristic changes with additional mass configurations. This particular research that has been performed has indicated that positive results are attainable and has indicated the most straightforward techniques of the test procedure.

IV. ESTABLISHING THE ENVIRONMENT

A. INDUCED ENVIRONMENTS

In establishing the environment, i.e., the vibration response of a particular point of the structure, it is required that one know something about the forcing function (whether it be engine-generated acoustics, aerodynamic boundary layer pressure fluctuation, mechanical vibration, etc.) and the transfer function, which is a unique function of the structural characteristic. At present we do not understand well enough the complexities of each of these factors. A complete knowledge of the forcing function would require knowledge of the temporal and spatial characteristics in conjunction with the mode shapes of the structural response. In addition, one needs a knowledge of the structural frequency selectivity characteristics (specifically the frequency response function) which, when coupled with the forcing function, can provide a solution to the vibro-acoustic response.

To investigate the forcing function, one research effort is currently underway at IIT Research Institute [5]. In an effort to simplify the test setup and eliminate some of the complex variables such as compressibility, a study was chosen upon liquid flow in thin walled pipes. In this manner the boundary layer was easier to control and the experimental apparatus was relatively inexpensive.

The emphasis here was to measure very precisely the characteristics of the forcing function (the boundary layer eddies) and to calculate the pipe response in terms of frequency response functions. The resulting calculations can then be compared to experimental data and the accuracy verified.

Another research effort by Wyle Laboratory [6], Huntsville, was similar to the first, except in this case a very complicated structure was selected and experiments conducted to determine very precisely the frequency response function and calculations made of the forcing function. The results were then to be compared to test results.

The results of these two programs will be given in forthcoming reports. Complete analyses of these programs will take several months of evaluation. There have been two spin-offs which are notable.

A very special small transducer was developed by IIT Research Institute and was successfully utilized to determine the spatial correlation of small scale turbulence. These transducers were small enough to mount at 30/1000 inches on centers.

A computer program was developed by Wyle to provide on line, real time determination of frequency response functions. This implies the accurate reproduction of two signals with phase retention through the signal conditioners and the computer.

B. TRANSPORTATION VIBRATION AND SHOCK ENVIRONMENTS

Another of the very real problems facing the designer is that of finding a reliable definition of the transportation vibration and shock environments in the four major modes of transportation, i.e., air, water, rail, and highway. A reliable definition from a unified standpoint has not been available. A member of our organization was Marshall's representative on the Environmental Criteria Subcommittee of the NASA Steering Committee for Uniform Design Criteria. An investigation in support of this subcommittee's activities revealed the lack of a unified definition. A contract was let to General American Transportation [7] to research all available literature and organize applicable data into one source for transporation from start of fabrication to launch site. This effort resulted in a criteria document (for components) which the design engineer or packaging engineer can utilize as a reference source for transportation vibration and shock environments. This criteria has been submitted to the Steering Committee. It has been well received by packaging and design engineers that have been exposed to it.

V. DYNAMIC TESTING

The problems of dynamic testing are increasing at an alarming rate. The state of the art in testing large specimens is being taxed already and the availability of specimens is even more of a problem. The dynamic test vehicle has long been used as a low-frequency test article. The need for transfer function data across the stage interfaces and the need to understand the complex interplay of forcing functions prompted us to attempt to obtain high frequency testing on the DTV. Furthermore, it was apparent that this vehicle would probably be the last of the complete full scale vehicles dedicated to dynamic testing, and since there existed an accurate 1/10 scale model which is currently under test at Langley, an unparalleled opportunity presented itself to obtain model - full scale correlation. Once this correlation was achieved, then models could be utilized with a greater degree of confidence for future work on such items as shrouds, skins, and other parts, as well as entire vehicles. Of course the testing of segments of a vehicle brings about other problems such as mismatch of boundary conditions and the like.

Through using the newly developed impedance techniques, it is anticipated that many of these problems could be overcome. It has been planned to do model - full scale correlation using the impedance techniques.

While the DTV program as such has not officially been approved, it is rapidly becoming evident that there will be no impedance program incorporated because of lack of funds and schedule problems. Therefore, we have requested that upon completion of the DTV program, the entire vehicle be restacked and turned over to us for a period of not less than four months to obtain sufficient data for our purposes. In addition, since the 1/10 scale model, presently at Langley, is scheduled for use for approximately an additional two years, it is extremely important that another 1/10 scale model be obtained to provide the correlation so sorely needed.

Figure 7 shows our mechanical impedance research schedule for the next two years. The model - full scale correlation will be accomplished using hardware as it becomes available, dovetailed with the static load tests and the high force vibration tests.

In this pursuit of the impedance concept, an impedance instrumentation trailer is under development, scheduled for delivery in the very near future. This trailer was designed for multi-channel data acquisition measuring force and velocity with phase retention, and

computing the impedance. Once this equipment is submitted to use, it is anticipated that impedance testing will rapidly become an accepted technique and indeed will play a dominant role in dynamics testing in the future.

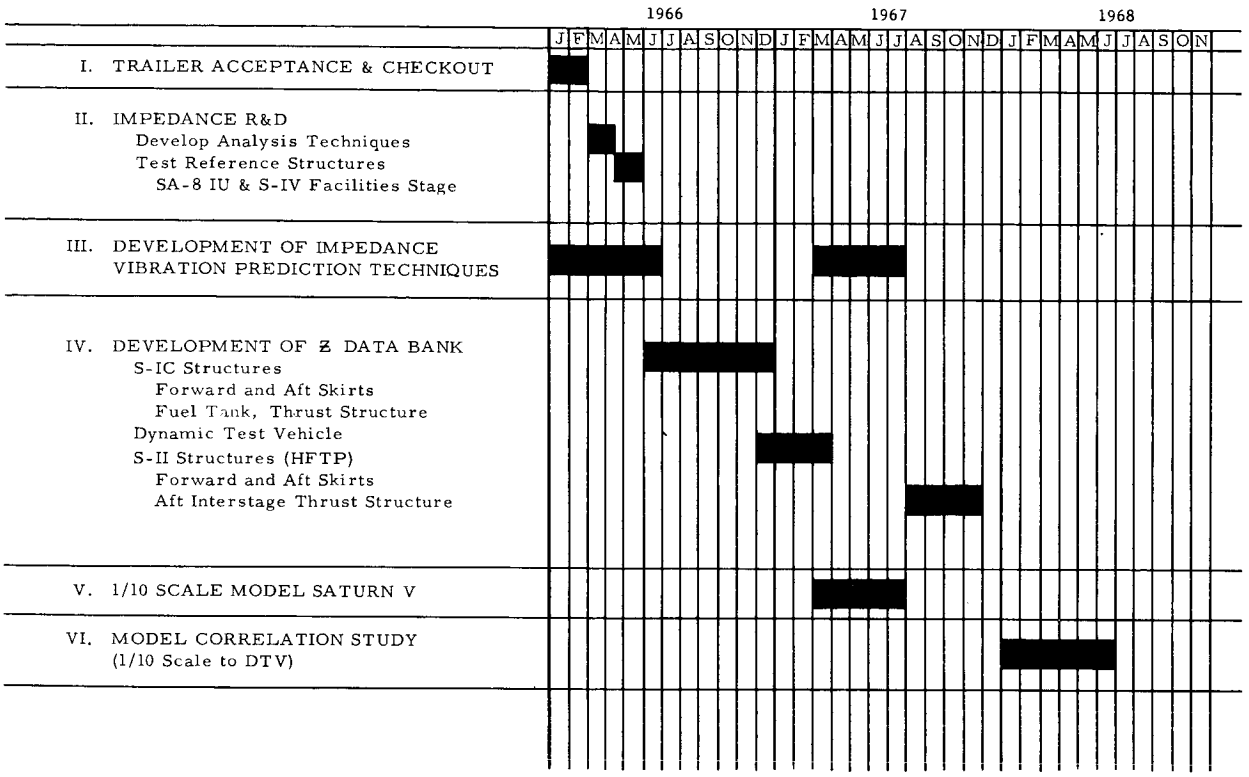

FIGURE 7. IMPEDANCE PROGRAM SCHEDULE

VI. CONCLUSIONS

Successful programs have been accomplished in vibration and acoustics research activities. Computer programs have been developed to efficiently process the large amount of data obtained from test programs. Design information has been obtained for definition of static equivalent loads that simulate dynamic environments. Better understanding of the effects of added weights on the frequencies and mode shape of shell structures under internal pressure has been accomplished. Transportation vibration and shock environmental data has been published and the relationship between forcing functions and frequency response functions has been empirically investigated. All of these areas need considerable additional investigation. A promising tool that is being used at MSFC to pursue research is the mechanical impedance technique, which will be used for both full and sub-scale testing and subsequent analytical evaluations.

REFERENCES

1. Research Triangle, Contract No. NAS8-11316, Advanced Studies of Stationary Processes.

2. Measurement Analysis Corporation, Contract No. NAS8-11154, Development of a Method for the Statistical Comparison of Environmental Data.

3. Douglas Aircraft Company, Contract No. NAS8-11617, Development of Optimum Design Procedures for Handling Space Vehicle Vibration Environments.

4. Republic Aviation Company, Contract No. NAS8-11514, Experimental Determination of System Parameters for Thin-Walled Cylinders.

5. Illinois Institute of Technology Research Institute, Contract No. NAS8-11248, Study of Vibrations Induced in Thin-Walled Pipes by Fluid Flow.

6. Wyle Laboratories, Contract No. NAS8-11262, Research Acoustic Impedance Testing on Saturn Instrument Unit.

7. General American Transportation, Contract No. NAS8-11451, Transportation Design Criteria.

MATHEMATICS AND COMPUTATION RESEARCH AT MSFC

January 6, 1966

by

Richard F. Arenstorf
C. L. Bradshaw
Erwin Fehlberg

RESEARCH IN COMPUTATIONAL MATHEMATICS AND LANGUAGES

by C. L. Bradshaw

NEW ONE-STEP INTEGRATION METHODS OF HIGH ACCURACY

by Erwin Fehlberg

RECENT DEVELOPMENTS IN ANALYTICAL CELESTIAL MECHANICS

by Richard F. Arenstorf

RESEARCH IN COMPUTATIONAL MATHEMATICS AND LANGUAGES

By

C. L. Bradshaw*

SUMMARY

The problems associated with effectively relating machine languages and problem oriented language for efficient use of computers is discussed. The need for improvements in the man-machine relationship and economic improvements of trade-offs that can be achieved between presently developed machine languages to broaden the participation and usefulness of the computer in space programs is emphasized.

The impact of standardization on computer utilization, the consequent reduction in redundant effort and relief from the continual need for the reformulation of the problem is shown as an important objective of the Computation Laboratory and some achievements in this area are discussed.

I. INTRODUCTION

Computers have become an essential tool in the research and development programs of our nation. They have also become a very expensive and sensitive item in our nation's budget. Research into computational mathematics and languages can lead to a more effective use of this most important tool. This research effort can attack the overall problems on five main fronts:

1. Improving the mathematics involved in obtaining a computer solution to an engineering or scientific problem,

2. Improving the computer programming languages used in problem solution,

3. Obtaining a more effective use of computing hardware and software as relates to specific classes of problems,

4. Development of more efficient computer hardware, and

5. Improving the man-machine relationship as relates to automatic computing devices.

MSFC has done or sponsored considerable research in areas which have direct application to the areas mentioned above. This survey will show the MSFC efforts in these areas. This presentation will be followed by two papers which will be more explicit in two of these areas.

II. COMPUTATIONAL LANGUAGES

As mentioned earlier, computers are now being used to solve many diverse problems in the fields of engineering, science, and business. The fast computing speed and large internal memory of general purpose computers are valuable assets to those who prepare the problem solution. However, the language of computers is a sequence of numbers which usually is reduced by the machine to a sequence of ones and zeros, and this machine language is generally foreign to the problem solution prepared by an expert in a specialized area. Thus, there is a gap between the language of a problem and the language of a machine for solving it. The seriousness of this gap is intensified by the fact that there are almost as many machine languages as there are kinds of computers. Therefore, work performed in machine language at one site is often of little value elsewhere if the machines are different.

To reduce this gap, many programs have been prepared so that on the one hand they can be understood by computers and on the other hand they will accept as input a higher level language which is closer to the problem and is called the source language. The techniques to implement programs which accept source languages fall into two overlapping categories. The simplest is to have the computer interpret statements of the source language and process the intent when it is recognized. The more popular technique is to translate the source program into an object program which is either in machine language or closer

* Deputy Director, Computation Laboratory

to machine language. In the latter technique, the source program may have several equivalent representations since the object language from one translation may be the source language for another.

Pragmatically, a language is defined in terms of what a processor (whether it be called compiler, translator, or assembler) will recognize correctly for the user. In other words, a computer language is directly or indirectly the language for input to a computer. Consequently, standardization with a group of users is necessary to determine what is mutually agreed to as being the language.

When the users of a language are allowed to participate in the formulating process, a more mature version of the language can be produced more quickly. The definition of ATOLL II (Automatic Test Oriented Launch Language), which we will now describe, illustrates how the changing needs of the user can be incorporated into the language design during definition to avoid producing numerous languages. In such an environment, the trade-offs between features desired and the implementation cost can be evaluated realistically.

ATOLL II is a problem-oriented language for real-time launch vehicle testing. The language is structured like FORTRAN (Formula Translation) and includes, in addition, real-time test-oriented statements, a more elaborate data description capability, a limited ability to manipulate symbolic or other non-numeric values, and an ability to include inline symbolic coding.

The language provides the capability to manipulate both the ground support equipment and the launch vehicle. It provides for real-time delays, for control based on maintaining a sequence of events where event execution is time related with respect to previous functions.

The language is open ended in that the user may define what appears to the user to be additional source statement types. Thus, the compiler can be adapted to the problem area as new specifications are prepared in the language.

The language is block structured to permit dynamic allocation of variable and temporary storage. This feature, in combination with a provision to automatically segment a test into independent programs, assures that the object space required for test programs can be kept very small.

The language has been designed to satisfy many of the requirements and desires of management, the launch system engineer, and the computer programmer. According to dynamic definition techniques which have been developed, this language has evolved rapidly over the past year. ATOLL II is fully documented and available for study.

We now would like to mention the problem of language translation. Since much programming effort has already been expended in languages which are now obsolete, or for which processors are not readily available, there is interest in the capability to translate a program into another language which is available. Also, it is desirable to minimize the number of different languages a user must learn.

Many super-processors have been proposed which are "machine independent." The purpose of such a processor is to allow preparation of compilers for classes of languages rather than for only a specific one. Until recently, insufficient information was available to determine what classes are sufficiently defined for implementing in such general terms. However, some efforts have been quite successful in the areas of assemblers and context-free languages. How to proceed with context-sensitive languages is not yet clear, although preliminary efforts in this direction are being made.

Some of the most dramatic developments in software have been seen in operating systems, or so-called control programs. Control programs are being given the tasks of handling computer interrupts, doing bookkeeping on jobs, servicing remote terminals on a priority basis, scheduling memory and computer time, editing and merging of programs, and total data management. As techniques of mechanizing such tasks are developed, the user is freed from meticulous operations and his turn-around time is shortened so that his time can be used more productively.

One problem area which has experienced many attempts but little success is that of preparing language processors. Early attempts such as Jovial and Neliac have proved to be educational but economically unfavorable. Recent developments in assembly level languages have improved expressibility, stratified the control of symbol expressions, incorporated list structures, and refined recursive macro capability with conditional parameter substitution. Yet, more work is needed to fill the gap between the kinds of languages which are easily implemented and the kinds of statements which users in specialized areas find most appropriate for the problem at hand.

An example of a specialized area which has justified the development of a new language is trajectory programming, which is discussed in the next section.

III. THE MSFC TRAJECTORY LANGUAGE

In the past, MSFC scientific programmers have worked individually with the engineer in the development of programs which were designed, programmed, checked out, and documented specifically for that engineer's need. This relationship of programmer to engineer has proved effective because of the nature of past problems and the limited language and systems capabilities. Specifically, in the past, many programs were large and involved with long production lifetimes. More recently, however, desired programs cover a wider range of applications with more limited use. This fact makes it imperative that our scientific programmers produce and maintain many more programs. Also, software advances have been made which open the door to a more general and sophisticated approach to the trajectory applications area. There seems to be no choice but to re-evaluate our overall procedures and optimize where possible. As the result of careful investigation, it has been determined that the function of setting up and maintaining trajectory programs can and must be optimized to a maximum reasonable level. At this point, the maximum level of optimization or automation cannot be ascertained; however, some optimization can be realized. This is possible when one realizes that the entire area of trajectory computation, when taken as a whole, is a set of associated problems with many elements in common.

The form that a problem may acquire in the process of being prepared for computation will vary widely within the range of imagination, experience, and other resources possessed by individuals who perform this task. For this reason, it is frequently difficult and time consuming for one person to use or become familiar with a program that was written by someone else. It is also a time consuming task for a programmer to modify his own program. Detailed documentation relieves this problem to some extent, but the more documentation there is to be studied, the more complicated the task becomes. It is necessary, or at least desirable, to restrict the general overall structure of programs to conform as nearly as possible to a general well defined standard model. As a result of the language and systems improvements and increased workloads, it was imperative that research be done to establish a faster, less expensive, and more useful service by developing a trajectory oriented programming system.

With the increasing demands for faster results from man and the computer, it has become obvious that these demands cannot be met with present resources. With the cost of manhours increasing and the cost of computing machine time decreasing, more burden must be placed on the computer by the use of more problem oriented systems. The trajectory programmer must be enabled to do a better job in a shorter time and at less cost to meet these demands.

We answer the question, "How can a trajectory oriented programming system help eliminate some of the effort required by the man in the man-to-machine cycle?" as follows:

1. Construct the programs in modular form. Programs could consist of elements called modules and can be thought of as building blocks for many programs. This will eliminate repetitive efforts since modules may be interchanged to create completely different programs without major reprogramming effort.

2. Standardize nomenclature. To implement the modular concept, standardization is necessary. It enables the programmer and the user to communicate in well defined terms, eliminating confusion in definition of coordinate systems, mathematical models and units. Documentation of work done will be more effective and meaningful. Programs written by other programmers will be easier to interpret and understand.

3. Standardize organization of programs. The user and programmer can communicate at a common level. The programmer would be free to do more useful and creative work in other areas. New users and new programmers can become familiar with programs and trajectory concepts earlier. Interchanging of programs will be easier. Programs will be easier to modify and maintain simply by changing and modifying only the necessary modules. Programs will be easier to evaluate since the programming effort will be isolated from system functions. Organization of the problem will be simplified since much of the logic will be handled by the system preprocessor.

We next look at the impact on utilization.

A problem oriented language and system will enable the programmer to drastically cut the time required in setting up and maintaining a trajectory related program. This savings results from the programmer being able to use precoded subroutines and sub-programs as the need arises. These precoded elements will be fully documented and completely checked out beforehand, thus freeing the programmer from these routine tasks.

A library will be established for the programmer and the user. Therefore, the engineer will be relieved

of the never ending problem of reformulation and rechecking of requests and proposals. As routines are developed and pooled by users, much redundant effort will be eliminated.

Better documentation of work will be provided by a standardization of program logic.

We now look at the difficulties in developing a trajectory system of this type. To be widely useful and accepted, a trajectory system must satisfy the requirements of all the users. Each user usually has a special interest which emphasizes certain areas more than others; for instance, the engineer whose primary concern is trajectory optimization puts a different emphasis on the guidance package than will the engineer whose primary concern is simulating the on-board guidance computer. In actual practice, it is difficult to satisfy the needs of the many users with one trajectory system. Even though difficult, sufficient research has been done to demonstrate the feasibility of further research of such effort.

We must recognize the research that must be carried on in the development of a problem oriented system.

1. Problem areas must be analyzed to determine the feasibility of developing and implementing a trajectory language, in our case, to see if the trajectory area is sufficiently large to justify such an effort. We have determined that it is large enough.

2. Work done by other laboratories and installations must be investigated to determine if they are doing work in this area. If so, we must establish why the effort, amount of effort, state of development, and evaluation of their effort relative to our needs.

3. Our own needs, present and future, must be investigated considering customer contacts, past requirements, survey of existing programs, what future needs are expected to be.

4. Methods must be developed for providing the following:

a. Program logic - to allow the programmer to direct the flow of the program in extremely involved logical paths.

b. Events - all complex trajectory programs involve some type of events or interrupts; much planning and analysis are required prior to writing a program. Examples of events are engine cutoffs, weight drops, high-q and tilt arrests.

c. Integration - much research needs to be done in this area to allow the user to select integration schemes to give the desired accuracy for his problems.

d. Input and Output - the present laborious effort of writing long lists and involved format statements must be simplified.

Our future plans are as follows:

1. Develop and implement an upward compatible trajectory oriented programming system. It must also be emphasized that all future programs written in the MSFC trajectory system will be FORTRAN IV compatible with other installations.

2. Prepare abstracts for all modules both mathematical and program.

3. Prepare a users manual for the system including complete description of statements and their source output.

4. Provide training for the users.

5. Study feasibility of adapting preprocessor to another machine. The Vectran Engineering Simulation System (VESS) preprocessor has already been translated to ALGOL and will process FORTRAN IV statements on the Burroughs B-5500 computer.

The trajectory oriented programming system planned by MSFC, Marshall Vectran Engineering Simulation System (MARVESS), contains the only preprocessor which actually provides a system function that will recognize a set of statements and create a trajectory program. No other system which we have studied can provide these necessary features.

IV. AMTRAN

I would like to mention at this time one other research effort which is underway at our Center and has as its goal the improvement of the man-machine relationship. This effort, which has been given the name Automatic Mathematical Translator (AMTRAN), is directed by Dr. Robert Seitz of the Research Projects Laboratory. AMTRAN is designed to be an automatic programming, on-line, multi-terminal computer system which should afford marked improvements in programming, debugging and turn-around times when it is fully developed. The system permits

a scientist or engineer to enter mathematical equations in their natural mathematical format as they appear in a textbook and, barring complications, to obtain an immediate graphical display of the solution on an output display device. The system is intended to be used for straightforward problem solution by the engineer or scientist with little computer experience while at the same time providing the flexibility required by the experienced programmer to solve non-routine problems. A "sampler" version of the system is now available using a modified IBM 1620 computer.

V. RANDOM PROCESS THEORY

The purpose of research in this area is to examine the existing Computation Laboratory techniques used to reduce and analyze random process data toward the objective of devising new or improved applications of statistics and random process theory. The specific goals of this research are to reduce the data editing and computer usage time, to increase the "accuracy" of the statistical estimates of the processed data, and to recommend future applications of existing data reduction equipment. These improvements are to be a result of the investigation of the techniques used by the Computation Laboratory and the appropriate application of:

1. Digital filtering techniques
2. Correlation function analysis
3. Spectral smoothing techniques
4. Special functions or processing
5. Spectrum analysis of nonstationary functions.

Research contracts were undertaken to study numerical smoothing and differentiation methods. With these studies, digital filtering techniques were developed and investigated. The main effort was devoted to linear digital (numerical) filters for performing smoothing, differentiation, and integration of discrete data and to do error analysis for these filters.

The mathematical foundations were rigorously justified by beginning with classical Fourier theory and following through with the development of generalized functions which led to specific functions used for filtering. This work is well documented in NASA Contractor Report CR-136. These desired digital filtering techniques were derived and are now being successfully applied to test data.

The Computation Laboratory also initiated a research study with the Cornell Aeronautical Laboratory to do research in areas which would satisfy the Laboratory requirements of:

1. Studying and applying the available random data processing techniques to the existing MSFC problems, and

2. Developing new and improved techniques of data processing.

The following discussion indicates that the above requirements are being satisfied.*

A. DIGITAL FILTERING

Selection of an appropriate sampling interval which produces negligible frequency folding is paramount to accurate digital data processing. The vast amount of literature available which describes digital simulation of transfer functions from the time response point of view can be used to produce prewhitening filters having specific frequency characteristics.

Taking the Tustin Transform of an analog notch filter will produce a digital filter which can be used for pre-whitening, with the possibility of total rejection of one frequency. These notch filters contain relatively few weights.

In situations where the power spectral density function of only a band of frequencies is of interest, digital heterodyning may provide a computational time savings in data processing.

B. CORRELATION FUNCTIONS

After reading the analysis of different methods of estimating correlation functions, one should conclude that modifications should be made to any existing computational technique that does not consider both the accuracy of estimates and the computer time required. Many types of correlation function estimators are given (autocorrelation being a special case of cross-correlation). Extensive study of the "half-polarity" correlator is presented. Computer programs are outlined, which will calculate, in minimum time, the "half-polarity" and "full-precision" correlation functions. It is also suggested that correlation computational techniques given in the reference are applicable.

* Research Studies of Random Process Theory and Physical Application, NASA CR-61081.

C. OPTIMAL SMOOTHING OF POWER SPECTRAL DENSITIES (PSD)

The appropriate application of proper techniques will produce spectral estimates with greater accuracy and also eliminate the need for pre-whitening of the signal prior to processing.

In June, 1965, a 12-month extension to the project was initiated. The objectives are to extend and expand the techniques under the initial effort. Primary investigations will be the application of the non-stationary correlation function theory and digital correlation function computation techniques. The following list summarizes the technical effort and indicates the order of priority:

1. Non-stationary data processing

2. Stationary data processing

3. Block diagrams covering application of data processing techniques developed.

The following are the major accomplishments to date:

1. The discrete data non-stationary correlation function theory has been developed.

2. A solution for the form of the optimum filters to be used in the discrete data correlation function detector has been obtained.

VI. DISCRETE OPTIMIZATION TECHNIQUES

This laboratory has a contract with the University of Tennessee to do research in Discrete Optimization Techniques. The principal investigator is Dr. Gordon Sherman of the University's Computing Center and Mathematics Department.

The problem is to maximize (minimize) a function defined on a given finite set. Typical examples are: the shortest tour problem, the job shop scheduling problem, and the transportation problem. Satisfactory solutions are available for some problems of this class, while complete enumeration of all alternatives, if it were possible to do so, is the only known way of producing solutions for other cases.

Dr. Sherman has taken a stochastic approach to the problem with the basic idea of combining intelligent search with random search. He has produced a family of algorithms that are quite efficient in the shortest tour type problem. These problems were used as test cases since the most research had already been done on them. Detailed explanation of the method, algorithms, and results may be found in an article called "Discrete Optimizing" by Reiter and Sherman in the September 1965 issue of the Journal of Industrial and Applied Mathematics.

VII. ANALOG COMPUTATION AND SIMULATION

The traditional tool for simulation of dynamic systems has been the analog computer. The similarity between the real system and the program on the analog computer, and the possibility of identifying a block of the real system as a group of computer components, gives the simulation technique the advantage of a model-like representation. This allows for an easy introduction of modifications and immediate observation of the effects of these changes. There are certain shortcomings in the use of analog computers. These are in the lack of random access memory, limited arithmetic precision, awkwardness in performing complex arithmetic, and others. These shortcomings led to a combination of the analog with the general purpose digital computers, thus preserving the advantages of the analog while overcoming most of the shortcomings. This type of system is called a hybrid system.

Hybrid computation, however, introduces problems itself. Even though at many different places detailed investigations have been conducted, it was felt necessary to secure the support of an academic institution for basic studies in the area of error analysis of hybrid computation.

Since this is a difficult and complex field, these studies are expected to become a long range effort. Some investigations have already been conducted by the Georgia Institute of Technology. The time limit for this review allows us to report only on the problem area, the approach, and the more important results. Dr. Finn (of Georgia Tech) has investigated the errors introduced by sampling, by hold operation (zero and first order) for periodic, pulse shaped, and stationary band limited random functions of time. The sampling rate must be at least high enough to avoid fold over. When the highest frequency present in the continuous signal is f maximum, then the sampling frequency must be more than 2 f maximum to avoid fold over. This is well known and follows directly from a frequency presentation of the sampled signal.

When we concentrate on wide sense stationary random processes as time functions, we can make statistical predictions about the expected error and, what is more meaningful, the expected error square since the probability of positive and negative errors is equal. We can determine sampling rates, limiting the probability of our error to exceed a preset limit. The theory allows us to determine upper and lower bounds for the ratio mean square error for a band limited random process as a function of the sampling rate (zero hold). These investigations are intended to be extended to higher order hold sampling techniques where similarly interesting results can be expected.

For sampling periodic functions, upper bounds for the ratio mean square error can also be given under the assumption that the initial phase is uniformly distributed over all possible values in a random fashion.

Dr. Finn has concentrated on investigating the error introduced by replacing the continuous function of time X(t) with a sampled representation using zero order and first order hold. Dr. Hammond, also of Georgia Tech, has worked on a system of n first order differential equations. With little loss in generality, he starts with a class in which the first derivative is represented explicitly as a function of position and time. The hybrid computer uses its analog part for integration and its digital part for function generation. This allows one to derive for the error a system of linear differential equations. For short intervals the coefficients in these equations can be considered as constant and the forcing function can be approximated by a staircase function. This not only allows one to use Laplace techniques for their analytical solution, but also provides a computer program of moderate complexity which can be incorporated with the hybrid program. A test program is presently set up in the Simulation Branch of the Computation Laboratory to study the usefulness of this approach.

VIII. NUMERICAL INTEGRATION

Because of the tremendous cost of modern computing equipment and the considerable amount of time used to perform certain types of studies, for example, orbit calculations, very substantial savings in computer time and dollars can be realized by even modest improvements in numerical integration techniques. The Computation Laboratory, in a continual search for better integration methods, has a dynamic program in mathematical and numerical analysis. This program is carried out by in-house staff members, specialists on a consulting basis, and through contracts with universities and some industrial firms.

The numerical integration of differential equations demands quite a large amount of computing time. Therefore, a great deal of attention has been given to devising more efficient methods of integration. The laboratory has a research contract with Vanderbilt University, Nashville, Tennessee, for the investigation of improved techniques for numerical integration of differential equations. The principal investigator on the contract has been Professor E. B. Shanks of the University's Mathematics Department. Professor Shanks has devoted his efforts primarily to a study of Runge-Kutta type processes. At the time the contract began, there existed the well-known Runge-Kutta formulas of fourth order requiring four evaluations of the function; the Kutta-Nystrom formulas of fifth order requiring six evaluations; and the less well-known Huta formulas of sixth order requiring eight evaluations.

A paramount problem in trying to increase the order of the formulas in the Runge-Kutta sense is that the number of conditions to be satisfied increase exponentially (essentially) and by the fact that the degree of the resulting algebraic conditions increases by two at each stage; for example, a seventh-order formula with nine evaluations involves 58 algebraic conditions with about half of them of twelfth degree. In such a complex system the notation becomes cumbersome and a problem in itself. However, the problem became tractable through use of the tensor calculus notation.

Dr. Shanks has been able to develop formulas of the sixth order with seven evaluations; seventh order with nine evaluations; eighth order with twelve evaluations; and ninth order with seventeen evaluations.

By adopting a new view point in which not all of the algebraic conditions were exactly satisfied, Dr. Shanks has been able to develop formulas of fifth order accuracy with five evaluations; sixth order with six evaluations; seventh order with seven evaluations; and eighth order with ten evaluations. All experience to date indicates that these formulas are more efficient than any of this type known previously. Additional details may be found in NASA Technical Note D-2920 and "Solution of Differential Equations by Evaluation of Functions," Mathematics of Computation, January 1966.

NEW ONE-STEP INTEGRATION METHODS OF HIGH ACCURACY

By

Erwin Fehlberg*

SUMMARY

New numerical methods for the solution of periodic trajectories for the restricted three-body problem are presented and factors affecting both the accuracy of results and the reduction of electronic computer time through the use of the new methods are discussed. Extension of the Runge-Kutta method to higher order of accuracy and the establishment of a pure series expansion method with transformation of the original differential equations to a second-degree algebraic system and application of recurrence formulas has provided a method to more effectively use computer capability and point the way for use of the new methods in many space problems.

I. INTRODUCTION

The development of the electronic computer has created a need, and that need is becoming increasingly urgent, for more accurate, more powerful numerical methods of computation. The computer is, of course, nothing more than a piece of hardware, however complex. It obeys whatever numerical methods are programmed into it. Most numerical methods were developed long ago when the only tools available to mathematicians were pencil and paper, and perhaps a few tables of pre-calculated values (sines, cosines, logarithms, etc.). The advent of the simple desk calculator helped. But even with the desk calculator, computational procedures had to be kept simple. Complicated operations, no matter how refined or necessary for the solution of certain complex problems, were impractical or impossible.

The rapid development of the modern electronic computer caught most mathematicians unprepared to use other than their old methods on the new hardware. Even now, the numerical methods used at many computer facilities are still the old desk calculator methods. For example, the standard method of Runge and Kutta, still widely used for the numerical integration of differential equations, was developed around 1900. The method was quite suitable for use with hand-operated desk calculators.

But many of the scientific and engineering problems at Marshall Space Flight Center have become so involved that use of the standard, turn-of-the-century methods is completely out of the question. Not only are these methods often extremely slow, consuming excessive amounts of expensive computer running time; they are inaccurate, producing unreliable results. Thus there is a pressing need at the Marshall Space Flight Center for new, more advanced computational methods designed especially for use with the modern electronic computer.

The Computation Laboratory has been actively seeking modern numerical methods suitable, in particular, for the solution of problems in astronautics and celestial mechanics. In recent years, several new approaches to the solution of ordinary differential equations have been developed in which such problems are expressed. One new approach is based on a power series expansion combined with a sophisticated, high-order Runge-Kutta procedure. Unlike the old methods still in widespread use, these new methods can conveniently be extended to any high-order accuracy desired.

These powerful, high-order methods drastically reduce the errors involved in the numerical integration of differential equations. Such errors originate both in the physical limitations of the computer, i.e., round-off errors, and in the limitations of the numerical method programmed into the computer, i.e., truncation errors. Moreover, in problems like the three-body problem, the new methods proceed in large integration steps without impairing accuracy. Thus they are also much faster than conventional methods, which must proceed in extremely small steps to preserve some accuracy.

The Marshall Space Flight Center is conducting extensive theoretical and numerical studies of periodic orbits of vehicles in the earth-moon system.

* Technical Staff, Computation Laboratory

Data precisely defining a large number of such periodic orbits have been obtained using the new methods. Considering the effect of the truncation error, and to give some idea of the accuracy and speed possible with these methods, a sample periodic orbit in the restricted three-body problem was computed and found to retain its periodicity to within 0.01 millimeter (the distance from the earth to the moon is 384,000 kilometers). The computation took only about 5 percent as long as with the conventional Runge-Kutta-Nyström method.

These new methods can, of course, be used to solve many other problems in addition to problems in celestial mechanics. They are fully reported in the literature.

II. AVAILABLE INTEGRATION METHODS

A. MULTISTEP METHODS

Methods for the numerical integration of differential equations are, broadly speaking, either multistep or one-step. Multistep methods were developed as early as the nineteenth century, mainly for problems in astronomy. As their name indicates, these methods use the information from several backward computation steps in calculating the solution for the current step. Multistep methods (e.g., the methods of Adams, Cowell, Gauss, etc.) are very efficient for problems that can be integrated in steps of constant size. Since many such problems are encountered in astronomy, it is not at all surprising that a number of multistep methods have been developed by astronomers. Multistep methods also have the very great advantage that they generally require only one or two evaluations of the differential equations per step, and they can be extended to any order of accuracy simply by adding higher-order difference terms to the formulas. Hence, unlike the Runge-Kutta method, which is the classical one-step method, they are quite fast on an electronic computer; they are economical, and they can be made very accurate.

But multistep methods do have a number of major disadvantages. They are not self-starting, but require a special starting procedure. A history of known values is needed before computation can begin. Thus a number of backward values must be created by means, for example, of an iterative procedure. And if the integration step size has to be changed during the computation, if, for instance, the step size must be reduced to preserve accuracy, additional time-consuming iterations are needed to build a new difference scheme—time-consuming because the iterated values for the changed step size must be of high accuracy. For these reasons, among others, multistep methods are largely restricted to problems that can be integrated entirely in steps of the same size. This is, of course, the case in the determination of astronomical orbits, where the distances between the attracting bodies are changing, but not radically.

This is not at all the case in, say, the interesting orbits of the restricted three-body problem. Figure 1 shows a typical periodic orbit of the restricted three-body problem. The earth and the moon are the two attracting masses. These and the space vehicle are shown in the rotating coordinate system, in which the x-axis always extends from the earth to the moon. Every fifth integration step is indicated, except in the vicinity of the earth, where the steps were too numerous to show. Obviously, the integration steps in the vicinity of both the earth and the moon are much smaller than those where the vehicle is far from either attracting body.

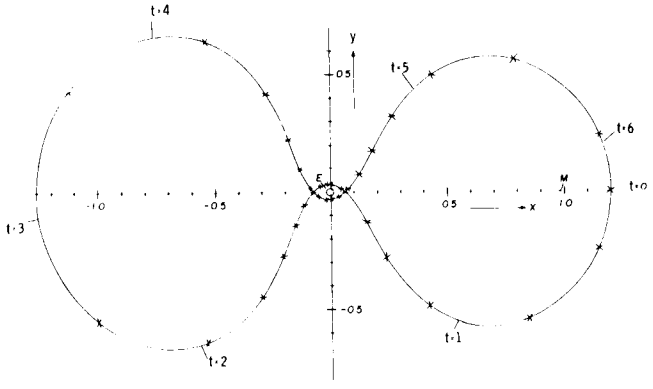

FIGURE 1. PERIODIC ORBIT OF THE RESTRICTED THREE-BODY PROBLEM

This kind of flexibility—to be able to increase the step size as much as possible or to be able to decrease it as much as necessary—is essential for efficient integration of such problems as the restricted three-body problem. It speeds the integration during the large part of the orbit where the space vehicle is near one or the other of the attracting masses.

This need for flexibility in the size of the integration step is caused by two kinds of error that accumulate during a computation. Too large a step size results in an unacceptably large truncation error because truncation error is proportional to a certain power of the step size. Too small a step size not only slows the computation, thus wasting

expensive machine time, even more seriously, it results in an unacceptably large round-off error because round-off error is a direct function of the number of steps that must be taken to compute the entire problem.

For use with computers, the ability to selectively vary or to automatically control the integration step size is fundamental to the efficient, fast-and-accurate integration of problems like the restricted three-body problem. This cannot be done with multistep methods except at considerable expense in increased complexity and increased computer running time.

B. ONE-STEP METHODS

One-step methods lend themselves more readily to step-size variation. In fact, the step size can be changed at any time and can immediately be accommodated to local conditions at any point in an integration. One-step methods are also self-starting. But they, too, have a number of disadvantages. The classical Runge-Kutta method is of only fourth-order accuracy. Several extensions have been made in the last decade, notably by Shanks [1, 2], but Shanks' method, the most accurate Runge-Kutta procedure developed to date, is still of relatively low-order accuracy (up to eighth-order). Runge-Kutta methods also tend to be slow because of their great complexity. The differential equation must be evaluated many times for each integration step. Shanks' eighth-order method, for example, requires 12 evaluations per step. If, in addition, the differential equations are complicated, if they contain transcendental functions (sine, cosine, exponential functions, etc.), the method becomes excessively slow and the cost in computer running time will certainly be high.

Another weakness of Runge-Kutta methods is that they, too, like the multi-step methods, lack an economical procedure for automatically adjusting the step size to the local conditions of the problem. As with all one-step methods, the step size can be changed at any time, but no economical control procedure seems to exist to do it automatically. In fact, using Runge-Kutta methods, one never knows whether the proper step size (for a combination of maximum accuracy and speed) is being used. There is no easy way to determine this. Apart from somewhat doubtful rule-of-thumb control procedures, there exists only Richardson's well-known method of the deferred approach to the limit. A step is computed, recomputed with half the step size (or double the step size), and then, by an extrapolation procedure, the results of the two computations are compared. This, however, doubles the computational effort or, more exactly, doubles computer running time merely for the benefit of step-size control.

This, briefly, was the state-of-the-art in methods for integrating differential equations when the Computation Laboratory began research in the field. The available methods were rather inaccurate and slow, and costly in machine time even for the solution of a relatively simple problem like the restricted three-body problem. For more complex problems in orbital mechanics, like the n-body problem, they could well turn out to be prohibitively slow and, worse, intolerably inaccurate. An original, starting 16-digit accuracy could easily dwindle to two or one or no accurate digits at the end of a long, complex computation. Also, it seemed absurd to pay heavily for auxiliary features like step-size control.

III. POWER SERIES EXPANSION METHOD

As a first quick improvement, the range of problems normally solved by pure power series expansions was expanded [3]. The use of pure power series expansions to solve differential equations is not exactly new, of course.* But unless the differential equation under consideration was extremely simple, pure power series expansion methods had generally been discarded as leading to cumbersome and lengthy computations for the derivatives they require. And, in fact, the method suggested requires a repeated total differentiation of the differential equation(s) with respect to the independent variable to obtain the necessary coefficients of the power series expansion.

Only a few years ago, the repeated total differentiation of a differential equation was not considered feasible, since, with increasing order, the derivatives become rather unwieldy expressions. But with fast electronic computers such a procedure is generally quite feasible. It is well-known that in the last few years considerable progress has been made in the automatic differentiation of formulas by computers.

Moreover, as an even more effective approach, apart from a straight-forward differentiation of the differential equation(s), a great number of these can be differentiated in a rather simple way by first transforming them, through introduction of auxiliary functions, into algebraic differential equations of the

* All commonly used integration procedures are, in fact, based in part on a power series expansion. The coefficients of Runge-Kutta formulas or the coefficients of multistep methods are obtained by expanding in power series (Taylor series, etc.) and then finding systems of equations of condition for these coefficients.

second degree. For special differential equations the procedure has been outlined in earlier papers by Steffensen [4], Rabe [5], and the author [3]. The procedure is based on the fact that the high-order derivatives of a second-degree system of differential equations can be conveniently obtained on a computer by recurrence formulas.

This can best be illustrated by the transformation procedure in a simple example. Consider the differential equation

$$\frac{dx}{dt} = e^{-x} . \tag{1}$$

Introduce the auxiliary function

$$e^{-x} = u \tag{2}$$

and obtain from equations (1) and (2) a system of second-degree algebraic differential eaquations

$$\frac{dx}{dt} = u, \quad \frac{du}{dt} = -u^2 . \tag{3}$$

Substituting the power series expansions

$$x = \sum_{\nu=0}' X_\nu \cdot (t - t_0)^\nu, \quad u = \sum_{\nu=0} U_\nu \cdot (t - t_0)^\nu \tag{4}$$

into equation (3) and comparing coefficients for the terms with $(t - t_0)^n$ results in the following recurrence formulas for the coefficients in equation (4):

$$\left.\begin{aligned} (n+1)\, X_{n+1} &= U_n \\ (n+1)\, U_{n+1} &= -\sum_{\nu=0}^{n}{}' U_\nu \cdot U_{n-\nu} \end{aligned}\right\} \quad (n=1,2,3,\dots) \tag{5}$$

Since the first coefficient X_0 is known from the initial value $x(t_0)$ for the step and the first coefficient U_0 can be obtained from equation (2), all following coefficients X_ν, U_ν ($\nu = 1, 2, 3, \dots$) can easily be computed from the recurrence formulas of equation (5), a very convenient procedure for electronic computers.

It is quite obvious, too, that the power series expansion method allows for an extremely simple automatic step-size control. Assuming truncation of the expansion in equation (4) for x after the term $X_n(t-t_0)^n$, the leading term of the truncation error of x can easily be found by extending the computation to the next coefficient X_{n+1}. If the truncation error turns out to be too large or too small, the step size at Δt can be adjusted immediately in such a way that $|X_{n+1}\,(\Delta t)^{n+1}|$ remains within prescribed limits. (For safety it might sometimes be advisable to consider more than just one term of the truncation error.) Unlike Runge-Kutta or multistep methods, no repetition of any computation is necessary if the step size fails to meet the requirements for the magnitude of the truncation error. The Computation Laboratory knows of no other method that offers such easy step-size control.

In this simple example, there is no real need to introduce auxiliary functions, since a repeated differentiation of the differential equation (1) can be performed without difficulty. A more representative example follows to illustrate how convenient the method can be.

IV. POWER SERIES EXPANSION METHOD APPLIED TO THE RESTRICTED THREE-BODY PROBLEM

Clearly, the following equations, for the restricted three-body problem in the rotating coordinate system, are not nearly so simple as equation (1):

$$\left.\begin{aligned} \frac{d^2x}{dt^2} &= x + 2\frac{dy}{dt} - (1-\mu)\frac{x+\mu}{[(x+\mu)^2 + y^2]^{3/2}} \\ &\quad - \mu\frac{x-(1-\mu)}{[(x-1+\mu)^2 + y^2]^{3/2}} \\ \frac{d^2y}{dt^2} &= y - 2\frac{dx}{dt} - (1-\mu)\frac{y}{[(x+\mu)^2 + y^2]^{3/2}} \\ &\quad - \mu\frac{y}{[(x-1+\mu)^2 + y^2]^{3/2}} \end{aligned}\right\} \tag{6}$$

where μ = the relative mass of the moon in the earth-moon system.

There exists a first integral of these equations of motion, the so-called Jacobi integral

$$J = \frac{1}{2}\left[\left(\frac{dx}{dt}\right)^2 + \left(\frac{dy}{dt}\right)^2 - x^2 - y^2\right] - \frac{1-\mu}{[(x-1+\mu)^2+y^2]^{1/2}}$$

$$- \frac{\mu}{[(x-1+\mu)^2 + y^2]^{1/2}} = \text{Const.} \tag{7}$$

Auxiliary functions are again introduced

$$\left.\begin{aligned} r^2 &= (x+\mu)^2 + y^2, \quad s^2 = (x-1+\mu)^2 + y^2 \\ u &= \frac{(1-\mu)}{r^3}, \qquad v = \frac{\mu}{s^3} \end{aligned}\right\} \tag{8}$$

Introducing equation (8) into equation (6) transforms the original system into the following second-degree algebraic system, which can be integrated directly by power series expansions:

$$\left.\begin{aligned} \frac{d^2x}{dt^2} &= x + 2\frac{dy}{dt} - u(x+\mu) - v(x-1+\mu), \\ \frac{d^2y}{dt^2} &= y - 2\frac{dx}{dt} - uy - vy \\ r\frac{du}{dt} + 3u\frac{dr}{dt} &= 0, \quad s\frac{dv}{dt} + 3v\frac{ds}{dt} = 0, \\ r^2 &= (x+\mu)^2 + y^2, \quad s^2 = (x-1+\mu)^2 + y^2 \end{aligned}\right\} \qquad (9)$$

Again, of course, new differential equations for the auxiliary functions have been added, but the new system is completely algebraic, containing only products of two functions throughout.

Let the power series expansions be

$$\left.\begin{aligned} x &= \sum_{\nu=0} X_\nu (t-t_o)^\nu, \quad y = \sum_{\nu=0} Y_\nu (t-t_o)^\nu \\ u &= \sum_{\nu=0} U_\nu (t-t_o)^\nu, \quad v = \sum_{\nu=0} V_\nu (t-t_o)^\nu \\ r &= \sum_{\nu=0} R_\nu (t-t_o)^\nu, \quad s = \sum_{\nu=0} S_\nu (t-t_o)^\nu \end{aligned}\right\} \qquad (10)$$

The first coefficients X_o, X_1 and Y_o, Y_1, are known at the beginning of the integration step. The forst coefficients R_o, S_o, U_o, and V_o are then determined from equation (8).

Inserting power series expansions from equation (10) into the original system of equation (9), the following recurrence formulas for the succeeding coefficients are obtained:

$$\left.\begin{aligned} 2R_oR_n &= \sum_{\nu=0}^{n} X_\nu X_{n-\nu} + 2\mu X_n + \sum_{\nu=0}^{n} Y_\nu Y_{n-\nu} - \sum_{\nu=1}^{n-1} R_\nu R_{n-\nu} \\ 2S_oS_n &= \sum_{\nu=0}^{n} X_\nu X_{n-\nu} - 2(1-\mu)X_n + \sum_{\nu=0}^{n} Y_\nu Y_{n-\nu} - \sum_{\nu=1}^{n-1} S_\nu S_{n-\nu} \\ nR_oU_n &= -3\sum_{\nu=1}^{n} \nu R_\nu U_{n-\nu} - \sum_{\nu=1}^{n-1} \nu U_\nu R_{n-\nu} \\ nS_oV_n &= -3\sum_{\nu=1}^{n} \nu S_\nu V_{n-\nu} - \sum_{\nu=1}^{n-1} \nu V_\nu S_{n-\nu} \\ (n+1)nX_{n+1} &= X_{n-1} + 2nY_n - \mu U_{n-1} + (1-\mu)V_{n-1} - \sum_{\nu=0}^{n-1} (U_\nu + V_\nu)X_{n-1-\nu} \\ (n+1)nY_{n+1} &= Y_{n-1} - 2nX_n - \sum_{\nu=0}^{n-1} (U_\nu + V_\nu)Y_{n-1-\nu} \end{aligned}\right\} \quad (n = 1,2,3,\ldots) \qquad (11)$$

Thus all the Taylor coefficients of X and Y can be obtained. These expressions can be extended to as many terms as desired. There is no restriction whatsoever on the order of the formulas. This is in distinct contrast to Runge-Kutta formulas, in which each advance of only one order in accuracy has taken many years to establish and, as mentioned earlier, the highest known order is only the eighth. There is no such problem with recurrence formulas. It is such recurrence formulas, evaluated automatically on the computer and extended to any order desired, that form the basis of both the pure power series expansion method and, as will be shown in the next section, the improved Runge-Kutta method developed by the Computation Laboratory. By a suitable transformation the original differential equation(s) is reduced to a second-degree algebraic system and then the recurrence formulas are applied whose coefficients are determined automatically on the computer.

The Computation Laboratory has solved many problems—restricted three-body, motion of an electron in the field of a magnetic dipole, and others—by a pure power series expansion method. However, while the method proved superior to other existing methods, there still seemed to be some room for improvement. For example, the number of terms in all the sums in equation (11) increases with increasing n. Hence computer running time gets longer for higher-order coefficients.

It is well known, too, that power series expansions have certain limitations with respect to the truncation error. When one truncates the expansion, there is no way of covering the remainder of the error, which is roughly equal to the leading term. This is unavoidable in a power series expansion, although it is even more of a problem in multistep methods. This need not be such a problem with Runge-Kutta methods, and it is for this reason that the Computation Laboratory has developed the Runge-Kutta transformation method, which combines the high-order accuracy of power series expansions with a good coverage of the truncation error. In fact, since, to a certain extent at least, the leading term of the truncation error can be covered, the Runge-Kutta transformation method radically reduces the truncation error.

Thus a combination of the two methods should not only be more accurate than the pure power series method, it should also provide an advantage in speed because larger step sizes can be used. The combined method is described in the next section.

V. RUNGE-KUTTA TRANSFORMATION METHOD

A. FORMULAS OF ANY DESIRED HIGH ORDER

Consider only second-order differential equations since it is these that are most frequently encountered in physics and mechanics. (The method works for first-order systems as well [6].) For brevity, formulas for only a single equation will be written, although the method holds in exactly the same way for systems. Letting x be the original dependent variable, then:

$$\left.\begin{aligned} \ddot{x} &= f(t, x, \dot{x}) \\ x(t_0) &= x_0,\ \dot{x}(t_0) = \dot{x}_0 \end{aligned}\right\} \qquad (12)$$

Next a transformed variable x_T is introduced, which equals the original variable minus the first m+2 terms of the power series expansion for x

$$x_T = x - \sum_{\nu=1}^{m+2} X_\nu (t - t_0)^\nu \qquad (13)$$

$$\dot{x}_T = \dot{x} - \sum_{\nu=1}^{m+2} \nu X_\nu (t - t_0)^{\nu-1} \qquad (14)$$

Performing this subtraction results in a function with zero derivatives for $t=t_0$ up to the m+2nd order. The following differential equation is obtained for the transformed function x_T:

$$\left.\begin{aligned} \ddot{x}_T &= f_T = f - \sum_{\nu=2}^{m+2} \nu(\nu-1) X_\nu (t - t_0)^{\nu-2} \\ x_T(t_0) &= x(t_0) = x_0,\ \dot{x}_T(t_0) = 0 \end{aligned}\right\} \qquad (15)$$

That the first m+2 derivatives equal zero considerably faciliates establishment of Runge-Kutta equations of condition. Furthermore, accuracy can be of any high order desired simply by subtracting enough terms from the original function. In other words, a very simple function is always created that has zero derivatives up to the m+2nd order. Runge-Kutta formulas of any high order desired can then be obtained for this transformed function merely by choosing m sufficiently large. For example, the Runge-Kutta formulas for the transformed differential equation (15) just given would read

$$\left.\begin{aligned} k_1 &= f_T(t_0 + \alpha_1 h,\ x_0,\ 0)\ h \\ k_2 &= f_T(t_0 + \alpha_2 h,\ x_0 + \beta_0 k_1 h,\ 0 + \beta_1 k_1) h \\ k_3 &= f_T(t_0 + \alpha_3 h,\ x_0 + \gamma_0 k_1 h + \delta_0 k_2 h,\ 0 + \gamma_1 k_1 \\ &\quad + \delta_1 k_2) h \\ k_4 &= f_T(t_0 + \alpha_4 h,\ x_0 + \epsilon_0 k_1 h + \zeta_0 k_2 h + \eta_0 k_3 h,\ 0 + \epsilon_1 k_1 \\ &\quad + \zeta_1 k_2 + \eta_1 k_3) h \end{aligned}\right\} \qquad (16)$$

and

$$\left.\begin{aligned} x_T &= x_0 + (C_1 k_1 + C_2 k_2 + C_3 k_3)\ h + 0(h^{m+5}) \\ \dot{x}_T &= 0 + C_1' k_1 + C_2' k_2 + C_3' k_3 + 0(h^{m+5}) \\ \hat{x}_T &= x_0 + (\hat{C}_1 k_1 + \hat{C}_2 k_2 + \hat{C}_3 k_3 + \hat{C}_4 k_4) h + 0(h^{m+6}) \end{aligned}\right\} \qquad (17)$$

Three substitutions yield an accuracy in x, $\dot{x}$ to the h^{m+4th} term, where m is the number of differentiations performed in equation (13) before x can be replaced by x_T. The fourth substitution in equation (16) yields the truncation error term required for automatic step-size control.

Thus an additional advantage of this approach, which also distinguishes it from any other Runge-Kutta formulas, is the very simple, economical (in computer running time) procedure for control of the truncation error. Only the first three evaluations are needed for the actual computation; the fourth evaluation gives an improved value for $\hat{x}$ which is accurate to one further power of h. By subtracting these terms, the leading term of the truncation error is represented with sufficient accuracy

$$T_x \approx x_T - \hat{x}_T = [(C_1 - \hat{C}_1) k_1 + (C_2 - \hat{C}_2) k_2 + (C_3 - \hat{C}_3) k_3 - \hat{C}_4 k_4] h\ . \qquad (18)$$

Full details on these new high-order Runge-Kutta formulas are given in reference 6.

B. FORMULAS WITH AN ARBITRARILY SMALL TRUNCATION ERROR

It may be noted, without going into detail, that in more recent work the Computation Laboratory has established Runge-Kutta formulas in which a parameter σ and the absolute value of all members of the

leading term of the truncation error, for x_T as well as for $\dot{x}_T$, can be made as small as desired, but not zero since some coefficients would then become infinite. Full details on these high-order formulas with an arbitrarily small truncation error are given in reference 7.

These new formulas required again a suitable transformation of the original differential equations. This transformation is based on a power series expansion. Any desired degree of accuracy can be obtained by doing only three or four evaluations of the differential equations. This is not possible with other Runge-Kutta type formulas now found in the literature. There is a small penalty to be paid in computer time since the recurrence formulas must be evaluated. The additional computation is not great and, because the method is of high order, the integration can proceed in larger steps without impairing accuracy. The computer running time is much faster than for other known integration methods. This is shown in Section VII.

VI. SOME OTHER MODERN RUNGE-KUTTA FORMULAS

Briefly, for comparison, consider two other modern Runge-Kutta methods: the Shanks explicit method and the Butcher implicit method. To simplify comparison, both methods are presented in eighth-order form. As mentioned earlier, Shanks' formulas are available only to the eighth order. Butcher's implicit formulas are available to any order.

First, consider Shanks' explicit formulas [1,2] for $\dot{x} = f(x)$

$$
\left.
\begin{aligned}
k_1 &= f(x_0)\,h \\
k_2 &= f(x_0 + \alpha_{21}k_1)\,h \\
k_3 &= f(x_0 + \alpha_{31}k_1 + \alpha_{32}k_2)\,h \\
k_4 &= f(x_0 + \alpha_{41}k_1 + \alpha_{42}k_2 + \alpha_{43}k_3)\,h \\
&\cdot \\
&\cdot \\
&\cdot \\
k_{12} &= f(x_0 + \alpha_{12,1}k_1 + \ldots + \alpha_{12,11}k_{11})\,h \\
\hline
x &= x_0 + \sum_{\nu=1}^{12} C_\nu k_\nu + 0(h^9)
\end{aligned}
\right\} \qquad (19)
$$

Each integration step here requires 12 substitutions, k_1 through k_{12}, which are multiplied by certain weight factors and summed to obtain the new value for x. But because these formulas include no procedure for controlling the truncation error, each integration step really requires 23 substitutions if Richardson's extrapolation procedure is used for step-size control, i.e., 2·12 substitutions with one substitution omitted since the first substitution occurs twice in the computation.

In 1964, Butcher [8, 9] published two noteworthy papers on implicit Runge-Kutta methods. Following are his eighth-order formulas for $\dot{x} = f(x)$:

$$
\left.
\begin{aligned}
k_1 &= f(x_0)\,h \\
\hline
k_2 &= f(x_0 + \beta_{21}k_1 + \beta_{22}k_2 + \beta_{23}k_3 + \beta_{24}k_4)\,h \\
k_3 &= f(x_0 + \beta_{31}k_1 + \beta_{32}k_2 + \beta_{33}k_3 + \beta_{34}k_4)\,h \\
k_4 &= f(x_0 + \beta_{41}k_1 + \beta_{42}k_2 + \beta_{43}k_3 + \beta_{44}k_4)\,h \\
\hline
k_5 &= f(x_0 + \beta_{51}k_1 + \beta_{52}k_2 + \beta_{53}k_3 + \beta_{54}k_4)\,h \\
\hline
x &= x_0 + \sum_{\nu=1}^{5} C^1_\nu k_\nu + 0(h^9)
\end{aligned}
\right\} \qquad (20)
$$

Unlike explicit formulas, where the increments for x: k_1, k_2, k_3, etc., are successively computed, each value depending only a previous values, implicit formulas require an iterative computation. Any increment k_ν depends not only on the preceding increments k_1, k_2, ... $k_{\nu-1}$ but also on k_ν itself and on the succeeding increments $k_{\nu+1}$, $k_{\nu+2}$, ... Naturally, this iterative computation is more involved than the straightforward procedure for explicit Runge-Kutta formulas. But implicit formulas do require considerably fewer substitutions than explicit formulas. Formulas (20) require only five substitutions, only three of which are iterative, per step versus 12 for the comparable Shanks' formulas. However, the iteration tends to be slow. This is demonstrated in Table I.

TABLE I

COMPARISON OF TWELFTH-ORDER METHODS, RESTRICTED THREE-BODY PROBLEM. (1)

Method	Final x	Final $\dot{y}$	Number of Steps	Computer Running Time (min)
RKB (2)	1.20000 00000 00013	-1.04935 75098 30328	216	0.88
PSE (3)	1.19999 99999 99981	-1.04935 75098 30303	493	0.21
RKT 1 (4)	1.20000 00000 00001	-1.04935 75098 30321	389	0.15
RKT 2 (5)	1.20000 00000 00013	-1.04935 75098 30332	290	0.13

(1) Corresponding results for Shanks' eighth-order formulas are: 1.20000 00000 00002; - 1.04935 75098 30310; 814 steps; and 0.46 minute. Note that eighth-order formulas are, of course, not competitive in speed or accuracy with twelfth-order formulas. This is far more obvious in more complex differential equations, as can already be seen in the more complex, but still relatively simple, case of the restricted four-body problem.

(2) RKB = Runge-Kutta-Butcher method [8, 9]
(3) PSE = Power series expansion method [3]
(4) RKT 1 = Runge-Kutta-transformation method [6]
(5) RKT 2 = Runge-Kutta-transformation method [7]

VII. CONCLUSIONS

As an example of the computing speeds possible with the modern methods described, the periodic orbit shown in Figure 1 was computed. The orbit has the following initial values:

$$x_0 = 1.2,\ y_0 = 0,\ \dot{x}_0 = 0,\ \dot{y}_0 = -1.04935\ 75098\ 30320 \qquad (\mu = 1/82.45) \qquad (21)$$

To preserve sufficient accuracy for a true comparison of the methods, the initial value $\dot{y}_0$ was computed in 20-digit arithmetic. The computations were executed on an IBM 7094, Model II computer (16 digits). Table I shows the results for one complete orbit.

For all methods compared in Table I, we lose about two digits on a 16-digit computer. The Butcher method, which uses the fewest integration steps, is extremely accurate but it is also extremely slow. In all cases, however, the deviations are negligible, being of the order of 0.01 millimeter for this particular orbit. But the method is nearly seven times as fast as the Butcher method, i.e., it would cost about seven time as much in computer rentals to use the Butcher method. Thus, even in a relatively simple problem like this example, it pays to use the most efficient integration method available.

A group, headed by Mr. Mert C. Davidson, is being set up in the Computation Laboratory to explore, in detail, applications of these methods to practical problems that will exploit their full possibilities. For example, a program has already been written to solve the complete n-body problem (including oblateness terms), as a whole, with no reliance on data from relatively inaccurate external sources like ephemeris tables, etc. The computation of this problem has been rapid and highly successful. But many new worthwhile applications still need to be developed and exploited.

Finally, it should be noted that the subject matter of this paper is given much more thorough coverage in the paper New One-Step Integration Methods of High-Order Accuracy Applied to Some Problems in Celestial Mechanics, which will be published shortly by NASA.

REFERENCES

1. Shanks, E. B.: Formulas for Obtaining Solutions of Differential Equations by Evaluations of Functions. (Unpublished, may be obtained from Vanderbilt University, Department of Mathematics, Nashville, Tenn.)

2. Shanks, E. B.: Solutions of Differential Equations by Evaluations of Functions. Math. Comp. Vol. 20, 1966, pp. 21-38.

3. Fehlberg, E.: Zur numerischen Integration von Differentialgleichungen durch Potenzreihen-Ansätze, dargestellt an Hand physikalischer Beispiele, Z. angew. Math. Mech., Vol. 44, 1964, pp. 83-88. (Available in English as NASA TN D-2356, Oct. 1964.)

4. Steffensen, J. F.: On the Restricted Problem of Three Bodies. Mat.-Fys. Medd. Dan. Vid. Selsk., Vol. 30, No. 18, 1956.

5. Rabe, E.: Determination and Survey of Periodic Trojan Orbits in the Restricted Problem of Three Bodies. Astron. J., Vol. 66, 1961, pp. 500-513.

6. Fehlberg, E.: New High-Order Runge-Kutta Formulas with Step Size Control for Systems of First- and Second-Order Differential Equations. Z. angew. Math. Mech., Vol. 44, Sonderheft, T17-29, 1964.

7. Fehlberg, E.: New High-Order Runge-Kutta Formulas with an Arbitrarily Small Truncation Error. Z. angew. Math. Mech., Vol. 46, 1966.

8. Butcher, J. C.: Implicit Runge-Kutta Processes. Math. Comp., Vol. 18, 1964, pp. 50-64.

9. Butcher, J. C.: Integration Processes Based on Radau Quadrature Formulas. Mach. Comp., Vol. 18, 1964, pp. 233-244.

RECENT DEVELOPMENTS IN ANALYTICAL CELESTIAL MECHANICS

Richard F. Arenstorf*

SUMMARY

For the restricted problem of three bodies the derivation of periodic solutions different from the classically known ones is discussed and the ideas used for their existence proofs are briefly outlined and related to classical methods. In particular, the derivation of closed perturbed precessing elliptic orbits of arbitrary eccentricity and small major axis about the smaller one of the two attracting bodies with arbitrary mass ratio is indicated. Two numerical examples of recently discovered closed trajectories are included.

I. INTRODUCTION

Among the problems of celestial mechanics, which are important for space flight applications, the restricted three-body problem plays a central role. This problem is concerned with the description of the possible trajectories of a particle (manned or unmanned satellite, meteorite, planetoid) of negligible mass under the gravitational attraction from two heavy celestial bodies, which are assumed revolving according to Kepler's laws on circles about each other. Limiting our attention to the two-dimensional case the equations of motion of the particle can be written in the form

$$\ddot{x} + 2i\dot{x} - x = -\nu(x+\mu)\,|x+\mu|^{-3} - \mu(x-\nu)\,|x-\nu|^{-3} \quad ,$$

$$(\dot{} = d/dt \ , \ i^2 = -1) \qquad (1)$$

where $x = x_1 + ix_2$ is the complex position vector of the particle, referred to a rectangular coordinate system, which rotates with unit angular velocity about the center of mass of the two heavy bodies with masses μ and $\nu = 1_{-\mu}$ as origin.

The attempt, among others, to exhibit periodic solutions of equation (1) has received great emphasis and led to some success through the work of Hill, Poincaré, Birkhoff and others, and is still being pursued vigorously. It will be our sole concern in this presentation. The study of periodic solutions of equation (1) is of interest for several reasons. First, since the restricted three-body problem presents a non-integrable dynamical system, every contribution toward an understanding and a description of its general solution afforded by particular solutions is highly welcome. Second, recent advances by Kolmogorov, Moser and Arnold in the areas of stability and almost periodic motions have led to an understanding of the behavior of dynamical systems in the vicinity of its periodic motions. And third, some periodic solutions of equation (1) are of great practical interest in dynamical astronomy or in space flight mechanics.

Our present knowledge of periodic solutions of equation (1) is still modest. Without discussing the classically known solutions, which are either near the libration points, or are close to circular solutions (for small $\mu > 0$, or, for arbitrary μ, when near one of the masses or far away from both masses), or which are inside a closed zero-velocity oval about the heavier mass closing only after many revolutions, etc., we will give a description of some recently discovered periodic solutions and of the ideas used for their existence proofs. These new solutions are characterized by their relationship to Keplerian elliptic motions of positive and possibly large eccentricities, presenting relative to equation (1), a situation which classical researchers attempted in vain to illuminate although they had essentially created the methods with which to attack such problems.

II. PROBLEM

Let us describe our problem. Equation (1) approximates the equation of motion for the Kepler problem (two-body problem with one mass transformed to rest)

$$\ddot{z} = -mz\,|z|^{-3} \ , \quad m > 0 \qquad (2)$$

in an inertial coordinate system after a rotation $z = e^{it}x$; for example, if $\mu > 0$ is very small, $m = \nu$

* Staff Scientist, Computation Lab., MSFC.

and the particle does not approach the smaller body too close (planetary case), or when the particle moves in the vicinity of the smaller one of the attracting bodies (satellite case), etc. Now equation (2) has elliptic solutions, say with major half axis $a > 0$ and eccentricity ϵ, $0 < \epsilon < 1$. Such a solution is closed in the rotating x_1, x_2 coordinate system, if its period $T_0 = 2\pi a^{3/2}$ is a rational multiple of the period 2π of e^{it}, i.e., if $a = (m/k)^{2/3}$ with integers m, $k \neq 0$. Under this assumption the resulting rotating elliptic orbit to be described by $x = x^*(t)$ is closed after $k - m$ revolutions about the origin, having the period $T^* = 2\pi m$. The problem is to find periodic solutions $x = x(t)$ of equation (1) which are near $x^*(t)$.

This problem can, in the simpler planetary case, be solved with the classical methods devised by Poincaré. The only additional idea needed consists of the application of an appropriate periodicity condition instead of the classical condition of return of the motion to its initial state after time $T > 0$. This classical condition leads to a singular case, even after reduction with the help of the Jacobian integral of equation (1), when applied to the generation of periodic solutions of equation (1) from the above $x^*(t)$. The difficulty can be overcome by using the condition

$$x(t) = \text{real}, \ \dot{x}(t) = \text{pure imaginary at } t = 0 \text{ and } t = \tfrac{1}{2}T > 0 \qquad (3)$$

for a solution $x = x(t)$ of equation (1). Equation (3) implies that the curve $x = x(t)$ $(0 \leq t \leq T)$ becomes symmetric about the real axis of the x-plane and closed. Thus, $x(t)$ becomes periodic with period T. To satisfy equation (3), the solutions x of equation (1) represent analytic functions not only of t, but also of the parameter μ in equation (1) and of the initial position and velocity coordinates

$$x_j(0) = \xi_j, \ \dot{x}_j(0) = \eta_j, \ (j = 1,2). \qquad (4)$$

Then equation (3) can be rewritten as

$$x_2(\tfrac{1}{2}T, \xi_1, \xi_2, \eta_1, \eta_2, \mu) = \dot{x}_1(\tfrac{1}{2}T, \xi_1, \xi_2, \eta_1, \eta_2, \mu) = 0, \quad \xi_2 = \eta_1 = 0 \qquad (5)$$

giving two scalar real equations for the unknowns T, ξ_1, η_2. When $\mu = 0$, these equations have a known solution (say T^*, ξ_1^*, η_2^*) belonging to the generating solution $x^*(t)$ of equation (1) with $\mu = 0$ after proper choice of its initial values. Since the respective Jacobian determinant with respect to T and η_2 does not vanish (to establish this fact constitutes the decisive part of the existence proof), the implicit function theorem leads to the existence of solutions for T, ξ_1, η_2 of equation (5) near T^*, ξ_1^*, η_2^* for sufficiently small $\mu > 0$ and thus to periodic solutions of equation (1) near $x^*(t)$ [1].

By proper choice of m, k, and ϵ above the precessing elliptic orbit $x^*(t)$, $(0 \leq t \leq T^*)$ can be made to pass the attractive bodies at prescribed small distances and this property will still hold for the resulting periodic trajectories $x(t)$, $(0 \leq t \leq T)$ of equation (1) with $\mu > 0$, since μ is small. Such trajectories are of great astronautical interest for space flight in the Earth-Moon system.

III. SATELLITE CASE

We now come to the more difficult satellite case of our problem. This time we need new ideas to show that periodic solutions $x(t)$ of equation (1) near $x^*(t)$ exist (since $\nu > 0$ is small, for instance) and the periodic motion is to take place in the near vicinity of the body of mass ν (called planet), where the disturbance exerted by the other more massive body, being nearly at rest in the inertial coordinate system, causes large deviations from Keplerian motion for the third body near the revolving planet. If $x^*(t)$ is simplified to a circular solution by putting $\epsilon = 0$ and dispensing with the condition that $T_0/2\pi$ be rational, our problem has been solved already in different ways by Hill, Brown, Moulton, Wintner and Siegel. But these results, which are based on power series expansions of the coordinates x_1, x_2 in powers of the small period, give no indication of the existence of periodic solutions near $x^*(t)$ with $\epsilon > 0$ and small $a = (m/k)^{2/3}$. The first result in the direction of the present problem, although only in the planetary case, was obtained by Birkhoff using the Poincaré - Birkhoff fixed point theorem for annulus mappings, and more recently by Moser, who used the Birkhoff - Siegel fixed point theorem for local area-preserving mappings to get a more accurate description of the location of the obtained solutions of equation (1). A similar result in the satellite case, giving for each sufficiently small value of the Jacobian integral the

existence of countably many periodic solutions which close only after many revolutions about the planet, was recently established by Conley using the Poincare-Birkhoff fixed point theorem and a new construction of the classically known nearly circular solutions mentioned above. These periodic solutions of equation (1) still lack a more accurate geometrical description. Adequate references to the literature are contained in references 1 and 2.

We shall now give a brief description of the ideas and techniques which lead to the existence of countably many families of 1-parametric solutions $x(t)$ near $x^*(t)$ in the satellite case of equation (1), belonging to sufficiently small values of $m/k = a^{3/2}$ and having the family parameter ϵ which ranges over suitable closed intervals contained on $0 < \epsilon < 1$. These solutions exist for all $0 < \nu < 1$.

We transform equation (1) by a translation $w = x + \mu$ into

$$\ddot{w} + 2i\dot{w} - w + \nu w|w|^{-3}$$

$$= -\mu(1 + (w-1)|w-1|^{-3}) = P_0(w). \qquad (6)$$

Here the right hand term $P_0(w)$ is the disturbing function, which vanishes at $w = 0$, i.e., at the location of the small planet of mass ν. At $w = 0$, the left side is singular, however. Replacing $P_0(w)$ by 0 in equation (6) leads, after the rotation $z = e^{it}w$, to equation (2) with $m = \nu$. Thus equation (6) is close to the integrable Kepler problem for small $|w|$ even though $\mu = 1 - \nu$ is not small. Again, use of the periodicity conditions of equation (3), with x replaced by w, is decisive and assures a non-vanishing Jacobian relative to the unperturbed elliptic motion $x^*(t)$. Rewriting equation (3) in the form of equation (5), however, is of no use since now μ is not considered as a small available parameter, but is fixed and nearly 1. Despite this we shall solve equation (3) with equation (4) for T and η_2, as in the case of equation (5), with the help of an implicit function theorem by application of the following idea.

We replace in the right side of equation (6) the given function $P_0(w)$ by an arbitrary function $P(w)$ from a suitable set F of functions, which contains $P_0(w)$ especially. The resulting solutions $w(t)$ (or $x(t) = w(t) - \mu$ just as well) then depend upon their initial values and upon $P(w)$. Therefore equation (3) can be rewritten in the form of equation (5), but with μ replaced by P if P is the name of the chosen function $P(w)$ from F. Now P can be considered as a generalized parameter varying over F, instead of the real parameter μ. When $P = 0$ (the zero element in F), equation (5) again has a known solution (say T^*, ξ^*_1, η^*_2) determined by $x^*(t)$. Thus, using an appropriate implicit function theorem we arrive at the existence of solutions T, ξ_1, η_2 of equation (5) near T^*, ξ^*_1, η^*_2 for sufficiently small P of F (say for $\|P\| \leq r^*$) after having introduced a suitable norm $\|..\|$ on F. But then it is decisive that the given P_0 in equation (6) satisfies $\|P_0\| \leq r^*$ to obtain periodic solutions of equation (6). Since P_0 is not available to choice, a lower estimate is needed for r^* and not merely the existence of an $r^* > 0$ with the above property.

The derivation of this estimate requires not only a precise application of an implicit function theorem, but also sufficiently accurate knowledge of the general solution of equation (6) for initial values near ξ^*_j, η^*_j, $(j = 1, 2)$ and a time range at least as large as the anticipated period T near T^*, so that sharp estimates of the perturbation of $w(t)$ from Keplerian motion $w^*(t)$ can be obtained. For this purpose the solutions of equation (6) have to be constructed by a suitable method of perturbation theory. Because of the singularity of equation (6) at $w = 0$ the motion of the satellite is considered in an annulus about the planet which contains the precessing Keplerian elliptic orbit $w^*(t)$. The value of $\|P_0\|$ depends on the size of this annulus and thus on m, k, ϵ, and μ. The main difficulty arises from the fact that $\|P_0\|$ becomes small along $w^*(t)$ only, when $a = (m/k)^{2/3}$ becomes small, leading to an increase of the required range (from 0 to at least $2\pi k$) of the independent variable, for which the eccentric or the true anomaly can be taken. But thereby the above r^* decreases with decreasing m/k, almost defeating our goal $\|P_0\| \leq r^*$. This difficulty does not appear in the classical case of circular $w^*(t)$, or $\epsilon = 0$, mentioned earlier.

IV. CONCLUSION

Summarizing, we can say that generalization of Poincaré's small parameter method to the non-parametric case by considering the disturbing function itself as a generalized small parameter belonging to a normed function space leads to applicability of classical methods again, and, together with suitable periodicity conditions, for example equation (3), and with sufficiently accurate convergent methods of perturbation theory, to an existence proof for periodic solutions $x(t)$ of equation (1) near $x^*(t)$ in the elliptic satellite case with arbitrary μ in $0 < \mu < 1$ [2].

Finally, by numerical extension of the latter families of periodic orbits to greater distances from the small planet, interesting new trajectories of the restricted three body problem have been found which do not belong to the satellite case or to the planetary case. Some of these pass repeatedly near both attractive bodies [3]; others have been found by my collaborator, M. C. Davidson [4]. Among the latter ones are trajectories which demonstrate the phenomenon of temporary capture with satellite motion about each one of the attractive bodies and periodically alternating transitions from the vicinity of one body to the vicinity of the other. Two examples (Figs. 1 and 2) will be included here. They are drawn in the rotating x_1, x_2 coordinate system under the assumption that the attractive bodies represent earth E and moon M with $\mu = 0.0123 \approx 1/82$. They constitute numerical solutions of equation (1).

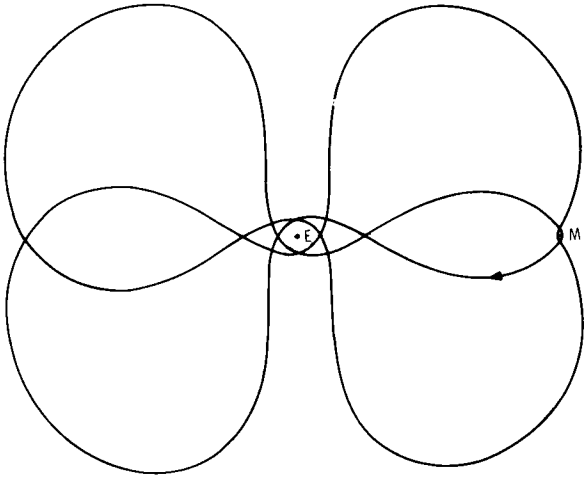

FIGURE 1

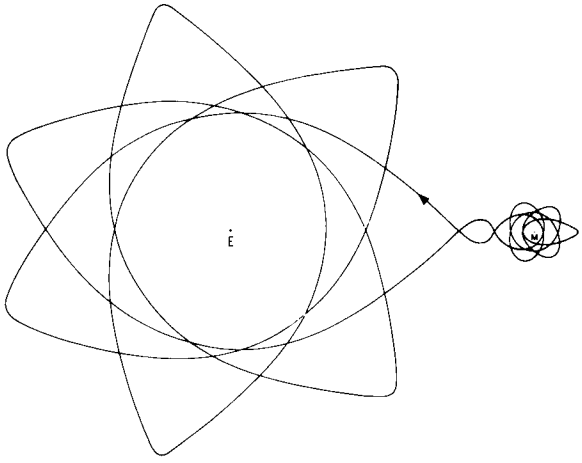

FIGURE 2

REFERENCES

1. Arenstorf, R. F.: Periodic Solutions of the Restricted Three Body Problem Representing Analytic Continuations of Keplerian Elliptic Motions. Amer. J. of Math., Vol. 85, 1963, p. 27-35.

2. Arenstorf, R. F.: A New Method of Perturbation Theory and its Application to the Satellite Problem of Celestial Mechanics. to appear in Crelle's Journ. f.d. Reine u. Angew. Math., (1966).

3. Arenstorf, R. F.: Periodic Trajectories Passing Near Both Masses of the Restricted Problem of Three Bodies. Proceedings XIV International Astronautical Congress, Vol. IV, 1963, p. 85-97.

4. Davidson, M. C.: Numerical Examples of Transition Orbits in the Restricted Three Body Problem. Astronautica Acta, Vol. X, 1964, p. 308-313.

ADVANCED PROPULSION RESEARCH AT MSFC

February 24, 1966

by

W. Y. Jordan, Jr.
Joseph C. King

TABLE OF CONTENTS

ELECTRIC PROPULSION APPLICATION STUDIES AT MSFC

by Joseph C. King

LIST OF TABLES

LIST OF ILLUSTRATIONS

LIST OF ILLUSTRATIONS (Concluded)

NUCLEAR VEHICLE SYSTEM STUDIES AND SUPPORTING RESEARCH AND TECHNOLOGY

LIST OF TABLES

LIST OF ILLUSTRATIONS

N67-30609

ELECTRIC PROPULSION APPLICATION STUDIES AT MSFC

By

Joseph C. King

SUMMARY

Recent work performed or sponsored by MSFC in the area of electric propulsion applications is summarized. The work reported is mainly in the mission study category, although a technology-type study of electric power conditioning systems is included. Two particular applications are treated, the lunar supply and manned Mars missions. Results are presented in the areas of trajectory analysis, vehicle design, and mission planning. The discussions given here are necessarily brief; a list of references for detailed information is provided.

I. INTRODUCTION

MSFC has been involved for several years in various studies of electric propulsion applications (Table I).

TABLE I. ELECTRIC PROPULSION APPLICATION STUDIES

STUDY TOPIC	PERFORMED BY
Low-Thrust Trajectories in Earth-Moon Space	Research Projects Laboratory (MSFC)
Electric Vehicles for Lunar Supply	General Electric Co.*
Electric Power Conditioning	Electro-Optical Systems, Inc.*
Manned Mars Mission Using Electric Propulsion	United Aircraft Corp.**
Electric Manned Mars Vehicles	General Electric Co.**
Electric Manned Mars Vehicle	Research Projects Laboratory, and Advanced Systems Office (MSFC)

* Supervised by Research Projects Laboratory
** Supervised by Advanced Systems Office

All but one of the investigations fall into the mission and trajectory study category. The first two pertain to lunar applications, and the last three concern various aspects of manned Mars missions. Only the power conditioning study is focused on a particular area of subsystem technology.

In the discussion to follow, only brief descriptive information on highlights of the various studies will be included. More detailed or comprehensive information can be obtained from the references cited. The discussions will be grouped according to the similarities noted in the preceding paragraph.

II. LUNAR MISSION APPLICATIONS

The lunar cargo mission for electrically propelled vehicles has interested various investigators since 1959. The present series of studies at MSFC began about four years ago with a small inhouse effort. As is often the case in preliminary mission studies, the first problem encountered was a need for approximate trajectory information which could be employed conveniently. The apparent lack of such information led to a study of methods for approximating low-thrust lunar trajectories, which in turn led to a new technique for synthesizing such approximations.

The new synthesizing technique employs a basic "building block" of the type shown in Figure 1. This is a typical low-thrust spiral, the type of trajectory an electric vehicle follows in escaping from a massive body such as the earth. Only the last few turns of the spiral are shown because of the large number and close spacing of the preceding ones. The illustration also shows a thrust cutoff point and the coasting ellipse the vehicle subsequently follows to its farthest excursion (apoapsis).

In the present scheme, each one-way trajectory is approximated by two such spiral-coast building blocks, one centered about the earth and the other about the moon. They are chosen and oriented so that their

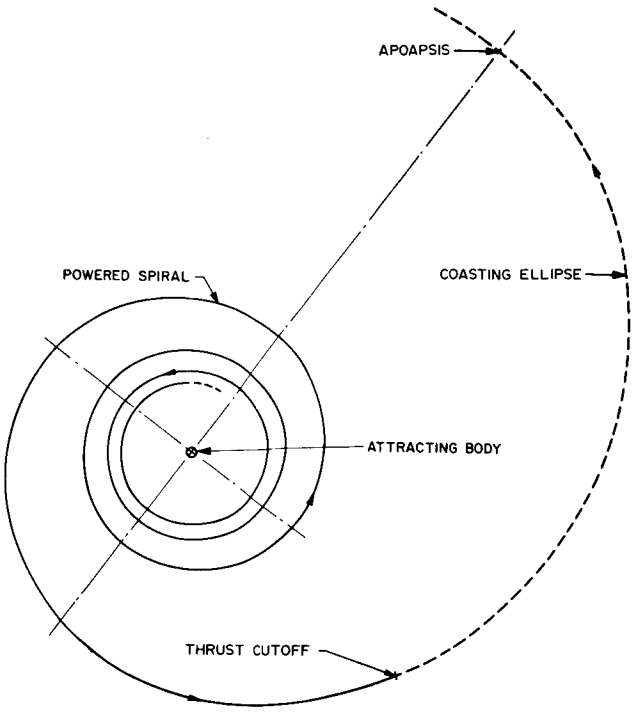

FIGURE 1. LOW-THRUST SPIRAL WITH CUTOFF AND COAST

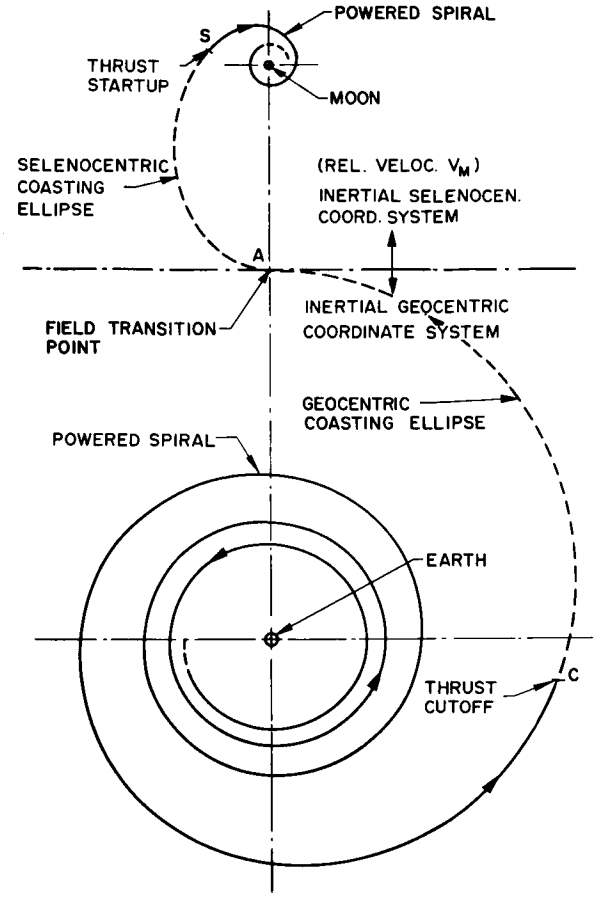

FIGURE 2. COMPOSITE TRAJECTORY FORMED BY COLLINEAR MATCHING

apoapsides coincide at a point on the earth-moon line (Fig. 2).* In the overall trajectory approximation, the vehicle starts in a low orbit about the earth, spirals out to the cutoff point, and coasts to the transition point (apoapsis) under the earth's gravitational influence. At this point, the vehicle is assumed to begin coasting under the influence of the moon only. It follows the selenocentric ellipse to the thrust startup point and then spirals down under retrothrust to a low orbit about the moon. This basic process is reversible, so that moon-to-earth trajectories can be synthesized in a similar manner. The general method is termed "collinear matching" because of the characteristic alignment of the earth, the transition point, and the moon. Further information on the collinear matching method and its applicability is given by King [1].

In addition to this inhouse trajectory work an overall study of the lunar supply mission was begun in 1964 through a contract with General Electric Company. This study investigated all the important factors - technological, operational, and economic - to be considered in determining the feasibility of applying electric propulsion to the lunar supply mission. The complete mission profile involved in this application is shown schematically in Figure 3. This illustration shows a low-thrust trajectory similar in form to the one in Figure 2, and it also shows the high-thrust propulsion phases required for transportation between the surfaces of the earth and moon and the respective low satellite orbits.

One type of vehicle that resulted from GE's design studies is shown in Figure 4. In this vehicle the nuclear reactor is placed forward at the apex of the conical section and the Rankine-cycle power conversion equipment is contained inside the cone. The surface of the cone serves as the primary radiator. The cylindrical section contains the chemically propelled lunar landing stage, as well as the electric thrusters and propellant supply.

The primary advantage of electric propulsion in the lunar mission application is the greatly increased

* Two different reference frames are used in this figure to simplify the trajectory shape.

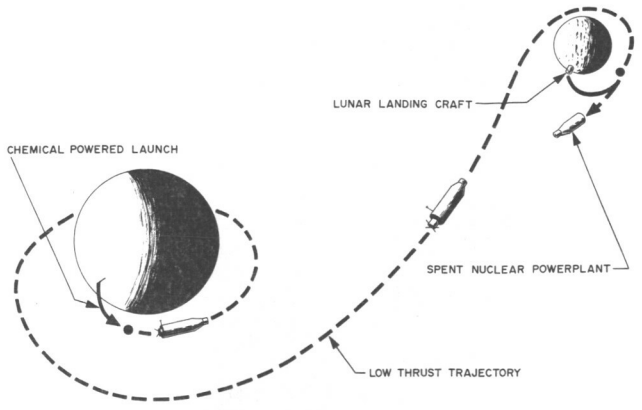

FIGURE 3. ELECTRIC PROPULSION FOR LUNAR CARGO APPLICATIONS

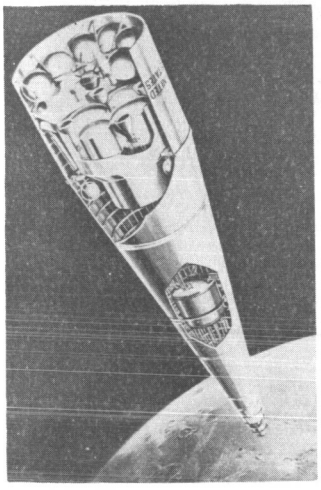

FIGURE 4. LUNAR CARGO VEHICLES

payload mass that can be delivered to the lunar surface for a given launch mass. This advantage is shown in Figure 5 in terms of the mass of the orbit transfer stage for various types of transfer propulsion. A chemically propelled transfer stage is represented by the point on the right side of the graph, which indicates a payload of 11 510 kg. The nuclear rocket, in comparison, permits a lighter transfer stage and delivers a payload of about 18 120 kg. The nuclear-electric stage, however, is capable of delivering much larger payloads, the actual value of which varies with the trip time involved. For the particular design shown in Figure 4, the payload is about 27 200 kg (corresponding to a trip time of about 140 days).

The electric lunar vehicle can also be designed to deliver its own electric powerplant to the lunar surface. For this mode of operation, the separate lunar landing stage is eliminated and the landing propulsion system is integrated into the electric

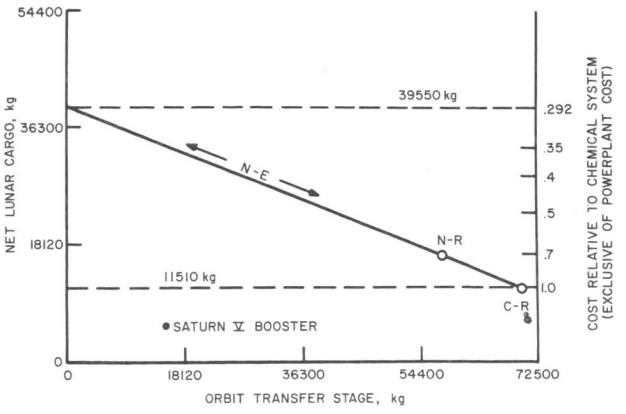

FIGURE 5. LUNAR CARGO VERSUS TRANSFER STAGE MASS

powerplant structure. Such an arrangement can provide an electric power source of a megawatt or more to support extensive facilities on the lunar surface. One possible design of the powerplant assembly is shown in Figure 6.

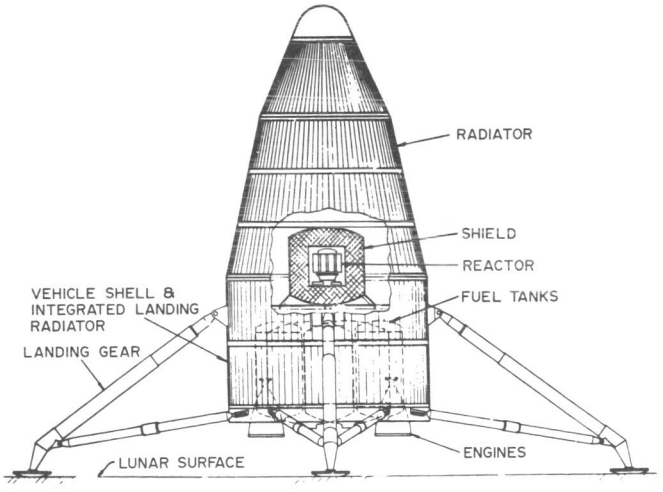

FIGURE 6. POWERPLANT ASSEMBLY ON LUNAR SURFACE

Still another attractive mode of operation applies the electrically propelled vehicle in combination with the Saturn-Apollo (chemical) system. The electric system is used basically to deliver an oversized landing vehicle to the lunar orbit, which permits a substantial overall gain in payload fraction for the mission while retaining the short trip times of the chemical mission for the manned transfers. This

mode of operation, along with the other electric vehicle applications, is described in detail by Larson [2].

III. POWER CONDITIONING

An important element of any electric propulsion system is the power conditioning equipment. This subsystem is needed to transform the raw output of the power supply into the various special forms required by the thruster system. The equipment required for this function, along with the necessary controls, switchgear, and transmission lines, comprises a substantial portion of the mass and complexity of the overall propulsion system. In addition, the power conditioning equipment interacts with other major elements of the propulsion system (e.g., powerplant and thrusters) and should be expected to influence their design. Until recently, the broad subject of power conditioning (PC) for the large propulsion systems of the future had not received a detailed and systematic study, although current applications (small scale) and various special areas had been treated. In order to provide some insight into the probable characteristics of large future systems, a general study was initiated in 1964 through a contract (NAS8-11257) with Electro-Optical Systems, Inc. (EOS).

The nature of this study is such that the results include large amounts of complex engineering data, so it is not feasible to present more than a brief summary of several major conclusions (detailed information is given by Osugi [3]). In general, power conditioning requirements depend heavily on two outside factors: the type of conversion system in the power source, and the type of thruster being employed. In regard to the latter, EOS specified several basic "models" that appeared to represent the likely range of input characteristics fairly satisfactorily. The anticipated conversion systems, on the other hand, were identified as either the turbo-alternator or thermionic types, although promising trends in solar array R&D were noted. Based on these assumptions, the following conclusions were reached in several important areas:

1. Specific Masses. Near the one megawatt level, the PC subsystem is expected to have a mass of 1.3 to 3.5 kg/kW, depending on converter and thruster characteristics. The combination of thermionic conversion with electromagnetic thrusters appears most favorable with respect to PC weight.

2. Efficiency. Expected efficiencies (PC subsystem) are in the range of 85 to 97 percent. The above conversion/thruster combination also promises the highest efficiency of the several combinations studied.

3. Specific Impulse Variability. It appears that specific impulse variations (to improve vehicle performance) of ± 50 percent can be provided without undue penalties in system characteristics.

4. Key Limitations. Progress in the development of PC subsystems is currently limited primarily by the lack of reliable, high-power circuit components. The needed components probably will not be developed except in response to demand derived from space propulsion requirements.

IV. MANNED MARS MISSIONS

The remaining major area of effort in electric propulsion at MSFC is in the mission study category, specifically, the manned Mars mission. This particular mission has probably received a greater concentration of effort over the years than any other mission. Narrowing the field to recent studies based on electric propulsion, there have been several separate efforts at MSFC, both inhouse and contracted. In the former category, one conceptual study was reported in 1962 by Stuhlinger and King [4]. Shortly thereafter, a comprehensive study of electric propulsion prospects was begun under a contract with Rand Corporation, and the manned Mars mission figured prominently in a study by Pinkel [5].

More recently, two additional study contracts have been let, one with General Electric Company and one with United Aircraft Corporation. United Aircraft is giving major emphasis to the rapid computation of optimum trajectories. This aspect of low-thrust interplanetary mission studies presents considerable mathematical and computational difficulty, and these problems were particularly troublesome in the new studies because of the large number of trajectories needed to explore the full range of trip possibilities.

United Aircraft has made substantial progress in alleviating the computing problems, and some of their results are shown in Figures 7 and 8. The new calculations are based on a procedure called the Newton-Raphson algorithm, which permits the calculation of optimum trajectories in much less computing time

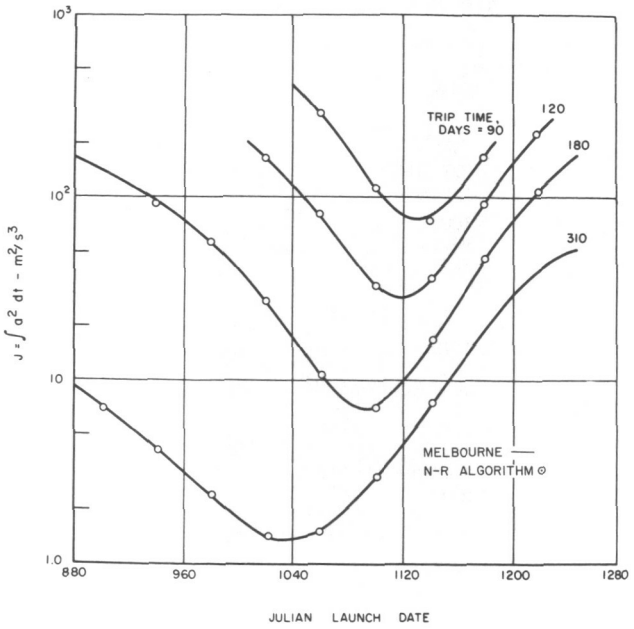

FIGURE 7. GENERALIZED NEWTON-RAPHSON ALGORITHM

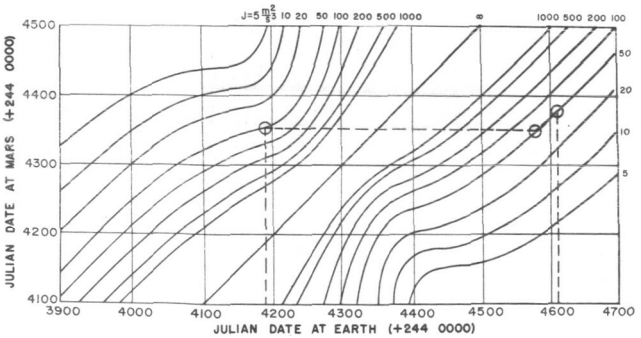

FIGURE 8. MINIMUM J FOR EARTH-MARS ROUND TRIPS

than previous methods. The accuracy of the new technique is quite adequate, as Figure 7 indicates. This figure shows propulsion requirements (J) for Earth-Mars trips for various launch dates and trip times, and it is clear that the new data (the individual points indicated) correspond closely to those obtained by previous methods (the curves shown). Figure 8 shows a type of trajectory chart often used in mission planning. Such charts are useful in selecting pairs of trajectories (inbound and outbound paths) that minimize overall propulsion requirements for round trips and yet satisfy timing constraints on the mission. It is clear that many separate trajectories must be computed to plot the contours shown on this chart. Further details on United Aircraft's trajectory work, and other phases of their study, are given by Ragsac [6].

Concurrent with the United Aircraft work, General Electric has been studying vehicle configurations and other aspects of electrically propelled manned Mars vehicles. Figure 9 shows one vehicle concept that has resulted. In this configuration, the two lower arms are independent nuclear-electric powerplants with reactors at each tip and main radiators along the cylindrical portions. The crew

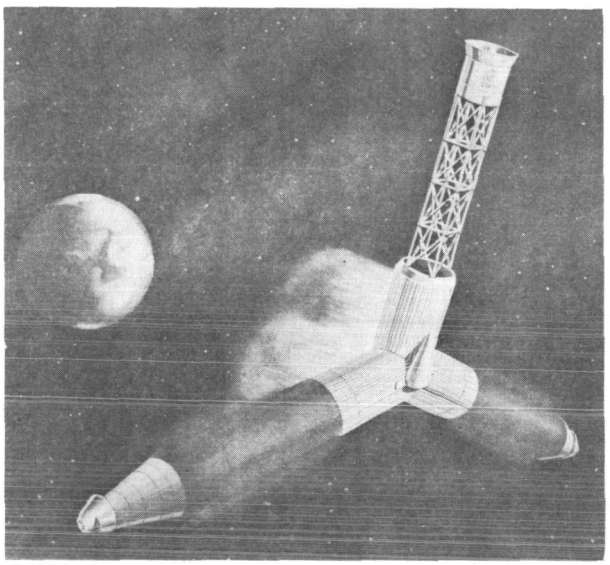

FIGURE 9. APPLICATION OF NUCLEAR ELECTRIC PROPULSION TO MANNED MARS MISSIONS

capsule is at the top, having been deployed after launch on its extendable boom. The vehicle is assembled in a low earth orbit, after which it is propelled to escape by a nuclear rocket stage (not shown in Figure 9). For structural reasons, the two powerplant arms are folded into a compact parallel configuration during the earth escape propulsion phase. For interplanetary flight, the vehicle is deployed as shown, and it rotates in the plane of the arms in order to simulate gravity in the crew capsule. The electric thrusters are placed around the junction of the arms (the location of the center of gravity and axis of rotation) to avoid undesired torques on the vehicle. Further detail is given by Coates and Brown [7].

General Electric has also studied several designs of manned Mars vehicles based on the use of solar cells instead of nuclear powerplants for propulsion power. One such concept is shown in Figure 10. In the lower drawing, the vehicle is shown as it is assembled for the earth escape propulsion phase (nuclear stage attached, prior to deployment of solar arrays and mission modules). The upper right-hand drawing shows the solar-electric vehicle fully deployed for the interplanetary flight phases. This design satisfies three operational requirements: the solar arrays remain normal to the sun's rays, artificial gravity is provided (the mission modules revolve independently), and the thrust direction can be varied in the ecliptic plane as needed (the thruster array, shown at the center of the main column, can be directed). The attractive feature of the solar-powered vehicle is that it offers a means of bypassing the technological problems of developing a large nuclear powerplant that is light-weight and long-lived. The required solar arrays are quite large and costly, however.

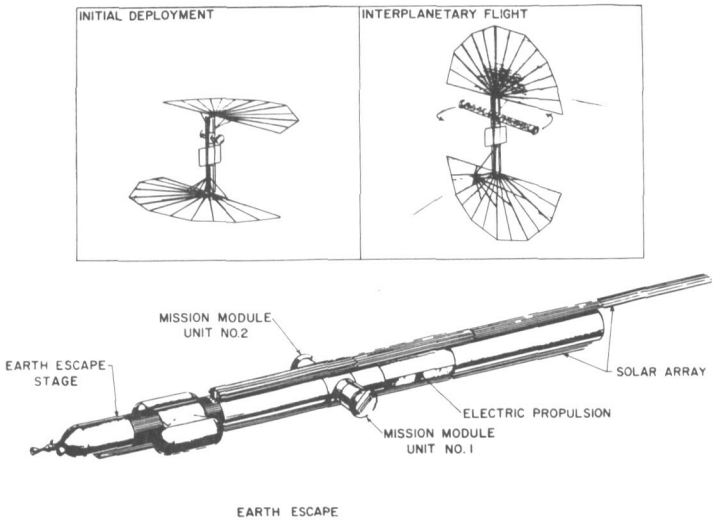

FIGURE 10. NONROTATING VEHICLE CONCEPT

Looking somewhat farther into the future, one can envision manned Mars vehicles of improved performance, based perhaps on power reactors with in-pile thermionic conversion of heat to electricity, heat pipes for the transfer of waste heat, and advanced electromagnetic thrusters. One design of such a vehicle, shown in Figure 11, was reported recently [8]. This vehicle also is propelled to earth escape by a nuclear stage (not shown in the illustration). The reactor and thrusters are shown at the top center

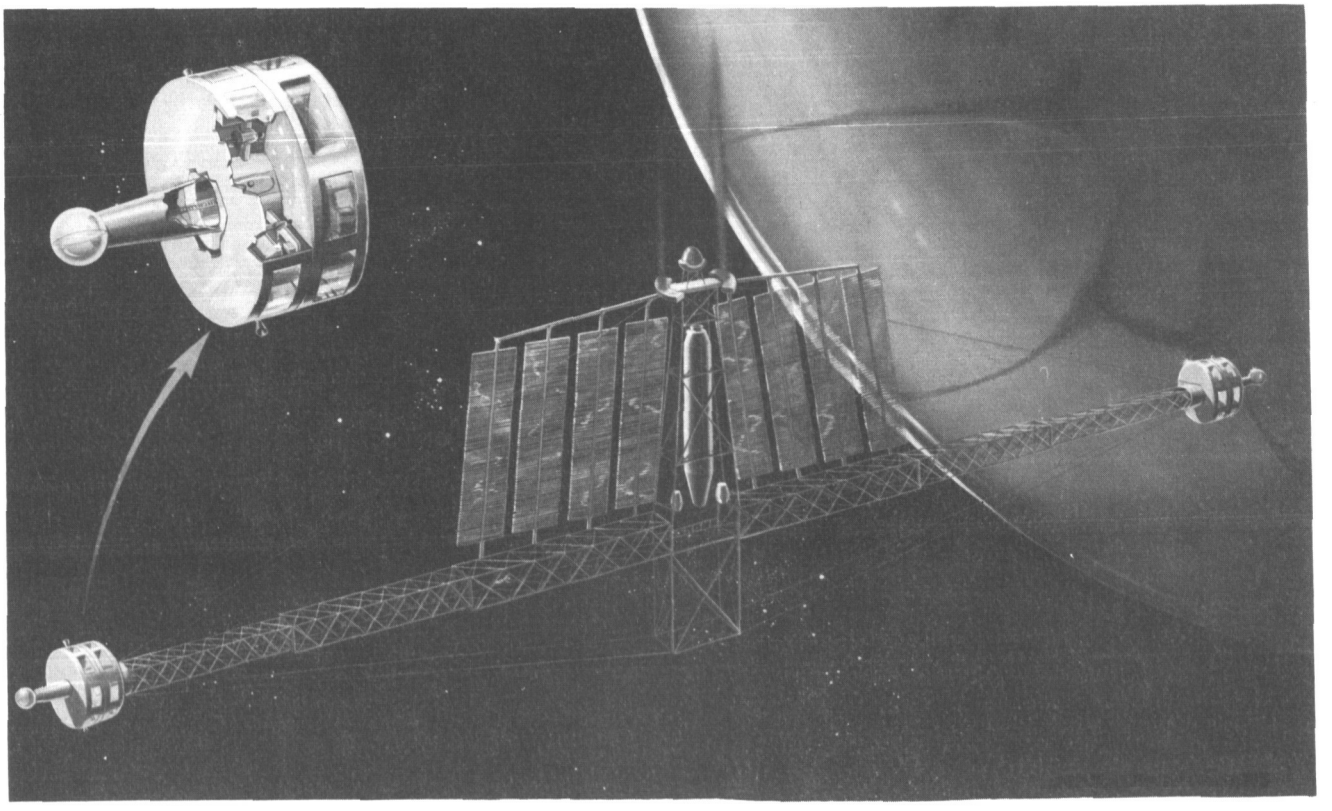

FIGURE 11. ELECTRICALLY PROPELLED MANNED MARS VEHICLE

location on the vehicle, on the axis of symmetry about which the vehicle rotates. This rotation provides artificial gravity in the two identical crew cabins located at the ends of the extended arms. The large, flat panels are radiator sections, and the Mars excursion module is in the center of the radiator array, placed on the axis of rotation to permit launching while the main vehicle is rotating. Some of the characteristics of the vehicle are given in Table II.

TABLE II. ELECTRIC VEHICLE CHARACTERISTICS

Performance:	Electric power	20 MW
	Specific power (of propulsion system)	0.16 kW/kg
	Power conversion efficiency (electric power to thrust)	85 percent
	Initial thrust acceleration	1.12×10^{-3} m/s^2
Mass:	Propulsion System	123 000 kg
	Propellant	153 000 kg
	Payload (crew facilities, Mars excursion module, etc.)	112 000 kg
		388 000 kg

The components for the electric vehicle are delivered to an assembly orbit by three uprated Saturn V's. Two additional Saturn V's are required to deliver the nuclear escape stage components.

In studying the overall mission with which this vehicle is associated, a nominal departure time of May 1986 was selected. This particular "window" is especially desirable because it combines a very favorable configuration of the planets with a predicted minimum of the solar cycle. Of the key developments which would be required in the meantime, the electric power system promises to be the major technological hurdle.

V. CONCLUSION

Studies of electric propulsion systems for human missions have shown that the greatest advantage of electric propulsion over all-chemical or all-nuclear propulsion is the greatly increased payload mass that can be delivered to the lunar surface for a given launch mass. Another advantage is that electric propulsion systems can deliver their electric power plants to the lunar surface for further operations there.

Studies of power conditioning systems for electric propulsion systems showed that the power conditioning system is expected to have a mass between 1.3 and 3.5 kg/kW, that the combination of thermionic conversion with electromagnetic thrusters appears most favorable with respect to mass, that expected efficiencies are in the range of 85 to 97 percent, that specific impulse variations of ± 50 percent can be provided, and that progress in the development of power conditioning subsystems is limited by the lack of reliable, high-power circuit components.

Missions studies of electrically-propelled manned flights to Mars have resulted in considerable progress in trajectory computation procedures and in conceptual designs of a number of different Mars vehicles using various kinds of power plants. The development of the electric power system appears to be the major technological hurdle to be overcome before manned missions to Mars become a reality.

REFERENCES

1. King, Joseph C.: A Natural First Approximation to Low-Thrust Trajectories between Satellite Orbits of the Earth and Moon. AIAA Journal, vol. 3, no. 8, August 1965.

2. Larson, John W., et al.: Electrically Propelled Cargo Vehicle for Sustained Lunar Supply Operations. GE (MSD), Final Report on Contract NAS8-11207, June 28, 1965.

3. Osugi, Fred S.: Analysis of Electrical Propulsion Electrical Power Conditioning Component Technology. Electro-Optical Systems, Inc., Tech. Sum. Report on Contract NAS8-11257, July 8, 1965.

REFERENCES (Concluded)

4. Stuhlinger, E., and King, J. C.: Concept for a Manned Mars Expedition with Electrically Propelled Vehicles, Electric Propulsion Development. AIAA Progress Series, vol. 9, Academic Press, 1963.

5. Pinkel, B., et al.: Electric Propulsion in Space: Mission Comparisons, Development Cost, Reliability, and Their Implications for Planning. Rand Corp. Final Report on Contract NAS8-11081, NASA RM 4056, August 1964.

6. Ragsac, R. V.: Study of Low Acceleration Space Transportation Systems. United Aircraft Corp. Report D-910262-3, Contract NAS8-11309, July 1965.

7. Coates, G. L., and Brown, H.: Study of Low Acceleration Space Transportation Systems. GE Ph. 1 Study Report on Contract NAS8-11423, June 30, 1965.

8. Stuhlinger, E.; King, J. C.; Shelton, R. D.; and Woodcock, G. R.: Study of a Nerva Electric Manned Mars Vehicle. AIAA/AAS Stepping Stones to Mars Meeting, Baltimore, Maryland, March 28-30, 1966.

NUCLEAR VEHICLE SYSTEM STUDIES AND SUPPORTING RESEARCH AND TECHNOLOGY

By

W. Y. Jordan, Jr.

SUMMARY

The research achievements and related activities at MSFC in the field of nuclear rocket vehicle system studies are summarized. Recent mission-oriented systems and applications studies have indicated that the best compromise size for a solid core nuclear rocket engine is in the 890 000- to 1 112 000-N thrust class. Vehicle design and performance studies, conducted concurrently with the engine sizing investigations, indicate that the greatest flexibility in space missions and overall performance potential could be gained by a modular vehicle design concept. This concept is based on a propulsion module containing a single NERVA engine (1 112 000-N thrust class) and a 10.06-m diameter stage of variable propellant capacity. This stage would have optional provisions for clustering the individual modules, and design features allowing adaptation of the propulsion modules to the environmental conditions over a broad spectrum of space missions and applications. The engine, vehicle and mission studies have defined a flight system concept toward which the advanced research and technology activities are oriented. The supporting research achievements reported include nuclear radiation transport and shielding analysis; nuclear flight safety and systems analyses; research and development of materials suitable for a radiation, cryogenic, and vacuum environment; and research on nuclear instrumentation, semiconductors, and other critical components and devices.

I. INTRODUCTION

The feasibility and performance potential of nuclear rocket propulsion has now been thoroughly demonstrated by the extensive series of successful reactor tests during the past two years and by very recent breadboard engine system tests involving the successful operation of all major components of a nuclear rocket engine. The creation of the technological base upon which a full scale nuclear engine development program could be initiated is nearing attainment. Therefore, it is becoming increasingly necessary to orient the continuing technological research efforts toward the ultimate requirements and objectives for space flight. In accomplishing this, the fine line of distinction between technology-oriented and development-oriented activities becomes less important and the usefulness of the end product is assured.

It is within this general background that the Marshall Space Flight Center's recent nuclear vehicle system studies and supporting research and technology objectives have been drawn. These specific objectives are:

1. Mission and application studies to determine the logical role of nuclear systems in the national space program,

2. System studies and vehicle design to define the most appropriate candidate flight system(s) and to carry the candidate system(s) into detail definition, and

3. Advanced research activities in specific problem areas to create the technological base and facilities upon which a sound flight development program can be initiated.

The first two areas have within the past two years centered around a concentrated study program within MSFC at the Lockheed Missiles and Space Company, the Thompson-Ramo-Wooldridge (TRW) Space Systems Group under the sponsorship of NASA and under the guidance of MSFC, the Space Nuclear Propulsion Office, and the Office of Advanced Research and Technology (OART). Throughout the period of study, close cooperation, guidance, and support were also contributed by the Space Nuclear Propulsion Office (SNPO)-Cleveland, Lewis Research Center and the Los Alamos Scientific

Laboratory. Valuable guidance, monitoring and support came from the Office of Manned Space Flight (OMSF) and additional data and technical support came from the Aerojet-General Corporation's Rocket Engine Operations - Nuclear (REON) and Westinghouse Astronuclear Laboratory.

The third category of activity covering a broad spectrum of nuclear vehicle research and technology under the sponsorship of OART was performed within the MSFC laboratories and under contract with industrial contractors or universities and research institutes. These contracted activities are listed in Appendix A. A thorough discussion of these activities was presented in NASA TMX-53301, dated July 1, 1965, "Radiation Physics Research at MSFC," by Dr. R. D. Shelton, Research Projects Laboratory.

II. MISSION AND APPLICATION STUDIES

The high cost of rocket development underscores the desirability of a propulsion and vehicle concept that offers multimission space capability with maximum flight-hardware commonality. The broader the spectrum of potential missions a given system can satisfy, the lower will be the cost and development investment in each particular mission. Because of the inherent characteristics of the nuclear rocket engine, e. g., high specific impulse and high specific mass, relative to chemical rockets, the most suitable space applications are the relatively high energy missions (high velocity and large payloads). A summary of the missions deemed most suitable to the nuclear rocket, which have historically received the greatest attention, is listed in Table I. In studying these potential applications the two prime objectives were to: (1) determine if a compromise engine size could be found that could satisfy all requirements with a high level of performance, and (2) establish a vehicle concept for utilizing the engine that could offer the desired multimission capability with common hardware.

A mission matrix was investigated that included lunar missions, planetary flyby missions, and planetary stopover missions involving several thousand combinations of mission mode cases, propulsion and vehicle systems. The nominal mission criteria established for the investigations are shown in Table II. The scaling laws used to relate the mass of the propellant tanks to the total usable propellant mass and trip time are given below for various propellants and mission phases. Also included are the primary assumptions used in formulating these equations.

TABLE I. POTENTIAL APPLICATIONS FOR NUCLEAR ROCKET PROPULSION

· Lunar Logistics	Saturn V
· Planetary and Solar Probes	3rd Stage
· Manned Planetary Flyby	1 or 2 Earth Orbital Rendezvous
· Heavy Cislunar Logistics	Saturn V Earth Launch Vehicle
· Manned Mars Exploration	Multiple EOR
Earth Departure (Clustered)	Saturn V or Post Saturn ELV
Mars Braking	
Mars Departure	
· Reusable Interorbital Systems	Orbital Operations Saturn V or Post Saturn

PRIMARY ASSUMPTIONS

1. Except for the depart-Earth phase, the equations for cryogenic propellant tanks do not contain the mass provisions required for tank insulation. The insulation mass for the Mars braking and return stages is calculated separately by a computer subroutine which is based upon the mission dependent parameters.

2. All equations include the mass provisions required for micrometeoroid protection.

3. The equations for the depart-Earth phase contain tank insulation and micrometeoroid mass provisions sufficient for 90 days.

4. The equations for all chemical propellant tanks (non-nuclear) include the required engine mass. The engine, structure and accessories have been sized to maintain a constant thrust-to-initial-stage-mass ratio of approximately 0.7.

The following nomenclature is used in the scaling law equations:

$W_{p\,max}$	The maximum usable propellant capacity for a single tank module
W_j	Final tank or stage jettison mass; total empty stage mass including propellant residuals (kg)
W_p	Usable propellant mass (kg)
T	Total time exposed to micrometeoroids (days)

TABLE II. NOMINAL MISSION CRITERIA

GENERAL

Specific Impulse
- Nuclear - 800 s
- Cryogenic Chemical (LO_2/LH_2) - 440 s
- Storable Chemical - 330 s

Attitude Control
- 1 percent each leg

Micrometeoroid Protection

Optimum Cryogenic Insulation/Boiloff

MARS STOPOVER MISSION CRITERIA

Earth Recovered Payload	4536 kg
Mission Module (8 Man)	31 100 kg plus solar flare shield
Mars Lander (MEM)	36 300 kg
Mass Recovered from MEM	680 kg
Life Support Expendables	22.7 kg/day
Stopover Time	20 days
Midcourse Correction	100 m/s each leg storable propellant

FLYBY MISSION CRITERIA

Earth Landed Payload	3860 kg
Mission Module (3 Man)	29 500 kg including solar flare shield
Planet Probe	4536 kg
Life Support Expendables	18.15 kg/day
Planet Passage Altitude	Mars - 1000 km ($R_d = 1.3$) Venus - 1000 km ($R_d = 1.16$)
Midcourse Correction	200 m/s outbound leg 300 m/s inbound leg Storable propellant

LUNAR TRANSFER MISSION CRITERIA

Payload in 185.2 km Lunar Orbit	45 360 to 181 500 kg
Midcourse Correction	30 m/s storable propellant
Transfer Time	70 hr

Depart-Earth Stage - LH_2 - 10.06-m dia.

$$W_{p\,max} = 155\,300 \text{ kg}$$

$$W_j = 0.1644\, W_p + 2910$$

Depart-Earth Stage - LO_2/LH_2 - 10.06-m dia. (common bulkhead)

$$W_{p\,max} = 699\,000 \text{ kg}$$

$$W_j = 0.0485\, W_p + 8410$$

Arrive-Planet and Depart-Planet Stage - LH_2 - 10.06-m dia.

$$W_{p\,max} = 155\,300 \text{ kg}$$

$$W_j = 0.12\, W_p + 0.01492\, T^{1/3} (0.02577\, W_p + 223)^{4/3} + 3800$$

Arrive-Planet and Depart-Planet Stage - LO_2/LH_2 - 6.605-m dia. (common bulkhead)

$$W_{p\,max} = 317\,500 \text{ kg}$$

$$W_j = 0.0469\, W_p + 0.01492\, T^{1/3} (0.01021\, W_p - 47.1)^{4/3} + 5400$$

Depart-Planet Stage - $N_2O_4/A\text{-}50$ - 6.605-m dia. (separate tandem tanks)

$$W_{p\,max} = 362\,500 \text{ kg}$$

$$W_j = 0.0284\, W_p + 0.01492\, T^{1/3} (0.0027\, W_p + 624)^{4/3} + 5740$$

Arrive-Earth Retro Stage - LO_2/LH_2 - 6.605-m dia. (internal tanks)

$$W_{p\,max} = 68\,000 \text{ kg}$$

$$W_j = 0.0855\, W_p + 0.01492\, T^{1/3} (0.0186\, W_p + 440)^{4/3} + 1300$$

Arrive-Earth Retro Stage - $N_2O_4/A\text{-}50$ - 6.605-m dia. (internal tanks)

$$W_{p\,max} = 68\,000 \text{ kg}$$

$$W_j = 0.0427\, W_p + 0.01492\, T^{1/3} (0.00595\, W_p + 229)^{1/3} + 1410$$

Outbound Leg Midcourse Correction and Planet Capture Orbit Circularizing Stage - N_2O_4/A-50 - 6.605-m dia. (internal tanks)

$W_{p\,max}$ - 45 360 kg

$$W_j = 0.1154\,W_p + 0.0259\,T^{1/3}(0.00656\,W_p + 221)^{4/3} + 539$$

Inbound Leg Midcourse Correction Stage - N_2O_4/A-50 - 6.605 m dia. (internal tanks)

$W_{p\,max}$ - 11 320 kg

$$W_j = 0.0665\,W_p + 425$$

To evaluate the mission matrix with the extremely large number of trajectory, mission mode, propulsion, and design parameters involved, several machine computer programs had to be developed by TRW. The development of these programs represented a major research task within itself, and their successful development and utilization constitute a substantial achievement in the necessary technology to perform mission and systems analyses.

Figures 1 and 2 give a typical example of the results obtained for a Mars stopover mission. They show how initial mass in Earth orbit and firing time vary as a function of the number of engines (propulsion modules) in the depart-Earth stage. In the case shown in Figure 2, three 667 000-N thrust engines for Earth departure are optimum in terms of minimum mass. The same unit thrust level is used in all stages, i.e., Earth orbit injection, Mars arrival and Mars departure. The upper stages utilize single engines only. The maximum burning time associated with the minimum mass here is approximately 1800 seconds. Where only one burning time curve is shown for several depart-Earth clusters, the maximum burning time occurs in either the arrive- or depart-Mars stages, and does not depend on the number of engines used for Earth departure. The mission could be made with two 890 000-N thrust engines for Earth departure with a small mass penalty and approximately the same burning time requirement.

Optimum engine thrust increases as the energy requirements increase in the more difficult years. In consideration of other major parameters, such as engine operating time, the required number of modules in the cluster, and the performance margin in the event of increased payload requirements or decreased engine performance, the tentative thrust-

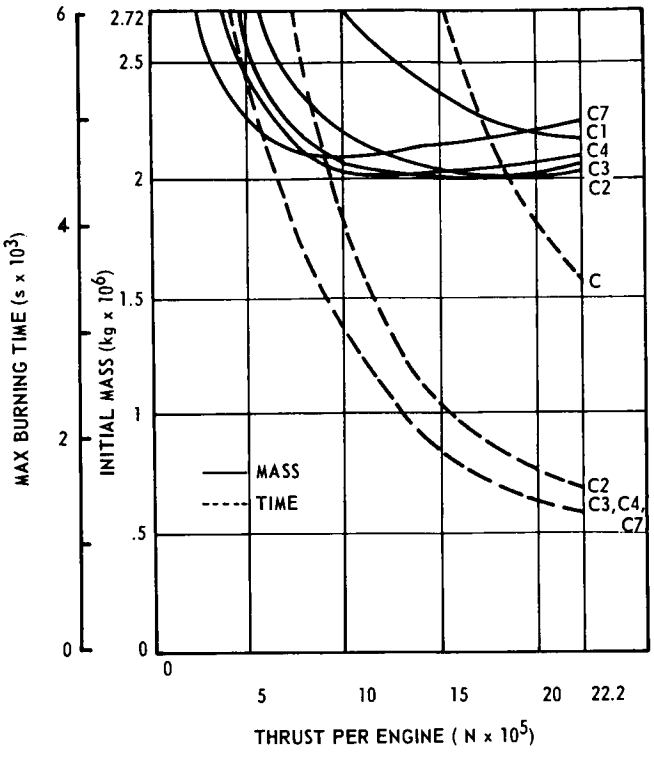

FIGURE 1. TYPICAL MISSION EVALUATION RESULT 1978 MANNED MARS STOPOVER MISSION

level goal for a NERVA propulsion system will be between 890 000 and 1 112 000 newtons. It should be emphasized that the thrust level evaluations were based on the same size engine in each stage of the Mars mission vehicle, so that the choice of engine size includes upper-stage requirements. The use of a nuclear engine of 222 000 to 333 000-N thrust in the terminal stages offered small, if any, performance gain in the easy years and resulted in a loss of performance and the necessity of clustering of upper stages in the more difficult years.

Figure 3 shows the effect of nuclear-engine thrust level on the performance of a nuclear third

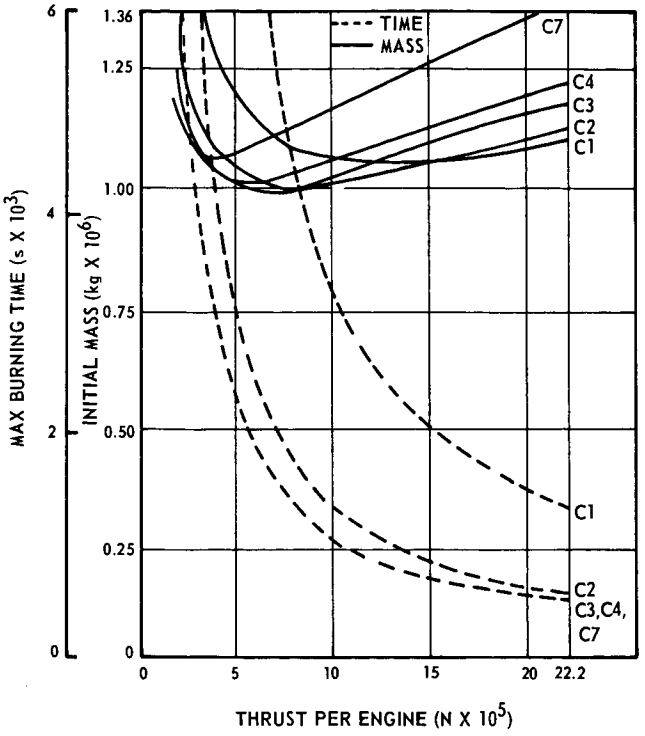

DEPART EARTH NUCLEAR
ARRIVE MARS NUCLEAR

DEPART MARS NUCLEAR
ARRIVE EARTH AERO PLUS STORAGE
RETRO TO 15 km/s

NUCLEAR SPECIFIC IMPULSE - 800 s

C.....C7 REPRESENT THE NUMBER OF MODULES IN THE DEPART EARTH STAGE. EACH MODULE CONTAINS ONE ENGINE.

FIGURE 2. TYPICAL MISSION EVALUATION RESULT 1982 MANNED MARS STOPOVER MISSION

stage on Saturn V in suborbit-start mode. Engine-system masses for the NERVA were determined at a point design of 1 023 000- N thrust and held fixed over the range of thrust from 667 000 to 1 112 000 newtons. The results show that the high thrust engine yields performance equal to or higher than that of the low thrust engine for all three vehicle cases. Although the difference in payload is not sufficient to justify a large engine for this application alone, it is interesting to note that the same engine size that represents the best compromise for planetary applications would be useful as a Saturn V third stage and would be a logical step in the development evolution toward the ultimate applications of the propulsion module.

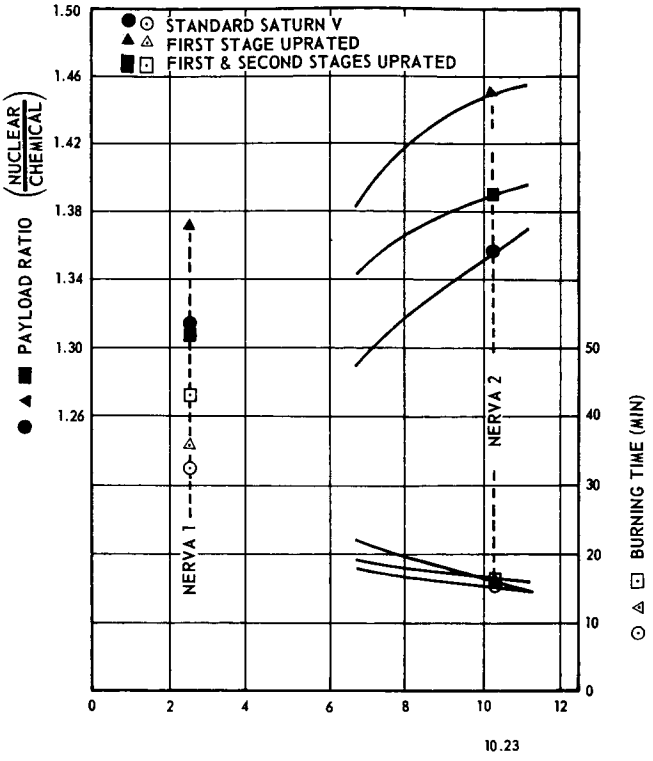

FIGURE 3. SATURN/NUCLEAR UPRATING POTENTIAL

Vehicle design and performance studies, conducted concurrently with the engine sizing investigations, resulted in a modular stage building block approach toward the long term evolution of operational systems. A propulsion module concept, as illustrated in Figure 4, offers a multimission capability and

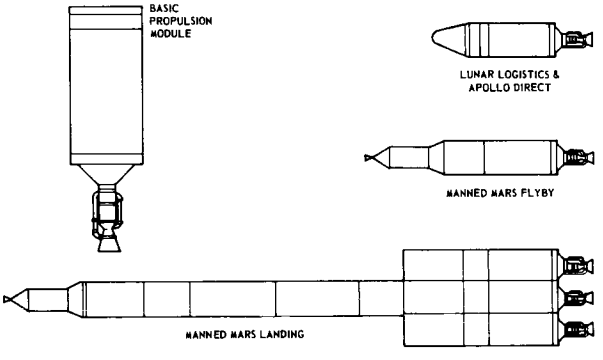

FIGURE 4. MODULAR VEHICLE APPLICATIONS

maximum operational flexibility across the spectrum of potential applications with a maximum of hardware commonality. This concept, used throughout the

engine sizing and payload performance studies and parametric design sensitivity studies, will be discussed further in Section III. The result of some of the orbital launch mass comparisons for the various mission modes and propulsion stages is summarized in Figure 5. The launch mass for nuclear systems is substantially lower than that for the chemical systems, nuclear systems varying from about 20 to 35 percent of the chemical system values for the all-propulsive mode.

Results of additional performance investigations of nuclear and chemical systems are shown in Figures 6 and 7 for Mars and Venus manned flyby missions and unmanned solar system probe missions.

III. SYSTEM STUDIES AND VEHICLE DESIGN

One of the major objectives of the recent studies has been to develop parametric design sensitivity data on both propulsion and vehicle systems to serve as a guide and index of figure of merit in designing for maximum performance. Some typical data of this type are shown in Table III and Figures 8 and 9; a comprehensive parametric data book containing a host of such sensitivity data has been compiled by TRW.

In order to gain the flexibility and multimission space capability offered by the modular vehicle system concept, it appears that (1) the basic propulsion module must have a variable tank capacity (2) that variable propellant modules must be used or (3) that some combination of the two must be adopted. An example of the various configurations which arise as a possibility is shown in Figure 10. Although the design investigations are still in process, an attempt is being made to select a concept and configuration that yields the highest degree of commonality in the basic hardware. A propellant capacity of 1 023 000-N thrust has been tentatively selected as the most appropriate midrange design point. The propulsion module, as shown in Figures 11 and 12, requires provisions for rendezvous and clustering of modules and thermal and meteoroid protection of the hydrogen propellant for deep space applications. An advanced structural and thermal design will be required to meet the requirements of long-term storage while achieving a reasonable overall stage mass fraction. One promising concept is a double-wall construction. The inner shell, which forms the propellant tank, consists of a cylindrical section with a $\sqrt{2}/1$ elliptical forward bulkhead and a 45-deg-half-angle ellipti-conical aft bulkhead. The propellant tank is supported at the aft end of the cylinder by a conic frustrum which transfers longitudinal loads into an outer, load-bearing shell. The outer shell

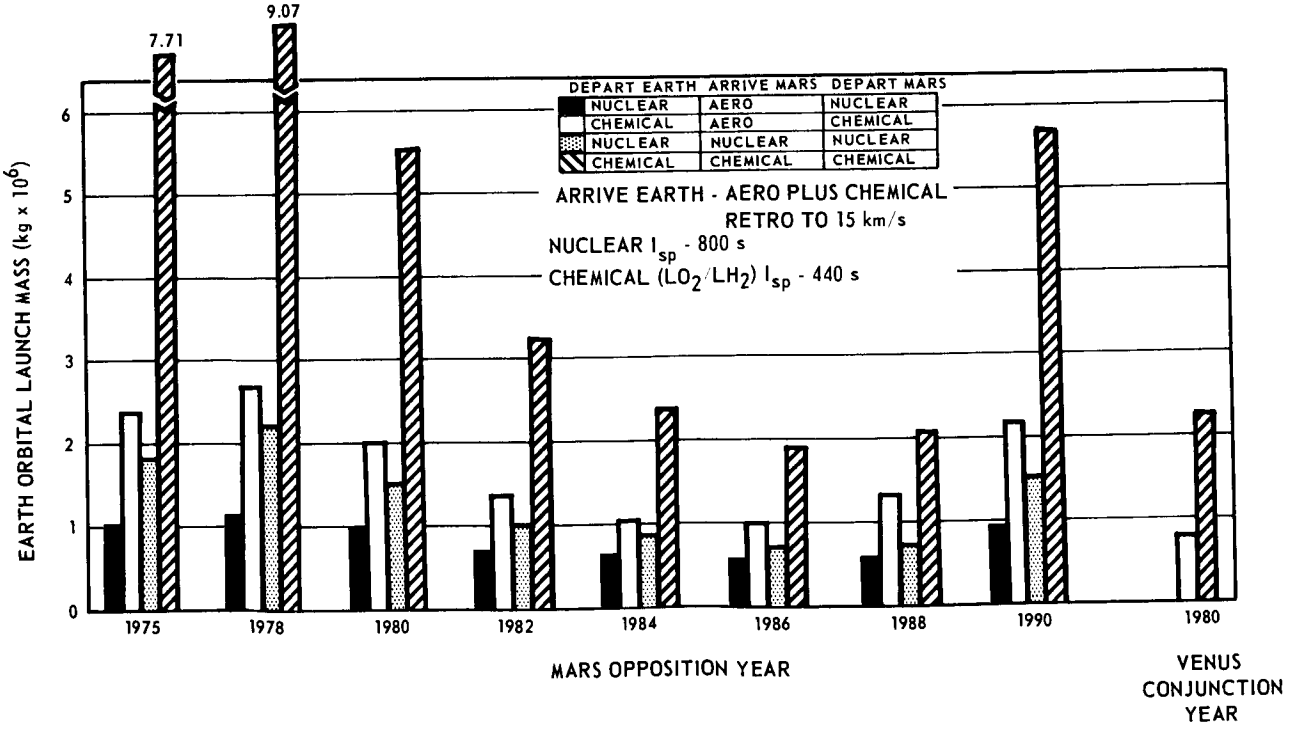

FIGURE 5. ORBITAL LAUNCH MASS COMPARISONS

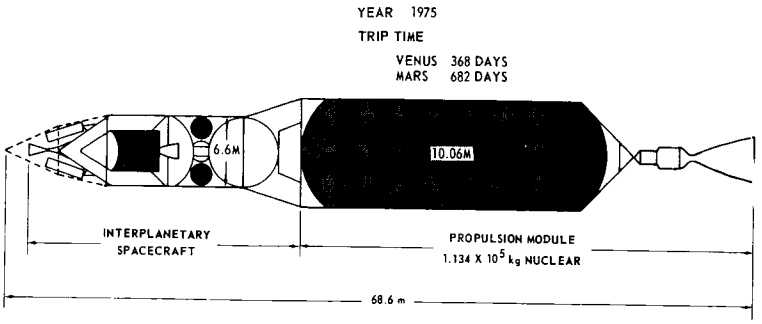

	MARS		VENUS	
	NUCLEAR	CHEMICAL	NUCLEAR	CHEMICAL
ORBIT LAUNCH MASS (kg)	284,000	497,000	187,800	287,000
INJECTED PAYLOAD (kg)	88,200	88,200	67,000	67,000
INJECTION PROPELLANT (kg)	140,500	354,000	73,800	173,000

FIGURE 6. NUCLEAR ORBIT LAUNCH CONFIGURATION FOR FLYBY MISSIONS

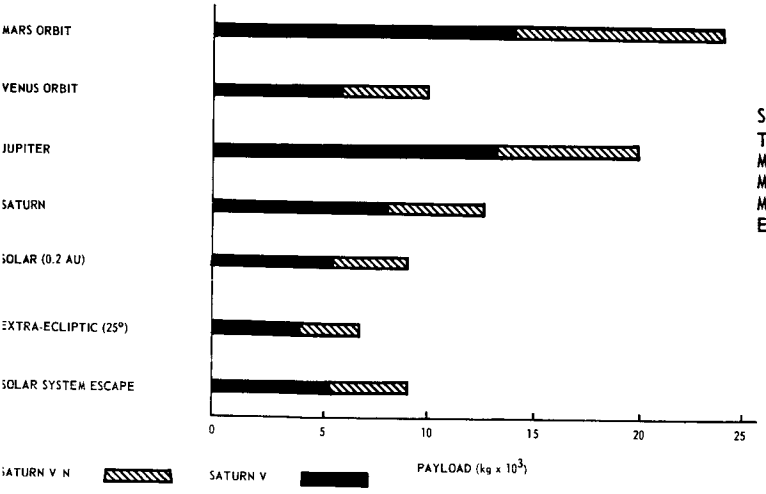

FIGURE 7. INTERPLANETARY MISSION SUMMARY

TABLE III. TYPICAL VEHICLE SENSITIVITY TO PROPULSION PARAMETERS 1982 MARS STOPOVER

Engine Performance Parameter	Vehicle Sensitivity
Specific Impulse	$-2270 \frac{\text{kg Vehicle Gross Mass}}{\text{Sec Specific Impulse}}$
Engine or Structure Mass	$+17 \frac{\text{kg Vehicle Gross Mass}}{\text{kg Engine Mass}}$
Engine Thrust	-0.0306 to $-0.306 \frac{\text{kg Vehicle Gross Mass}}{\text{Newtons Engine Thrust}}$
Reactor Exit Gas Temperature	$-327 \frac{\text{kg Vehicle Gross Mass}}{\text{Degree of Temperature (°K)}}$
Nozzle Expansion Ratio	$-680 \frac{\text{kg Vehicle Gross Mass}}{\text{Unit Increase Area Ratio}}$

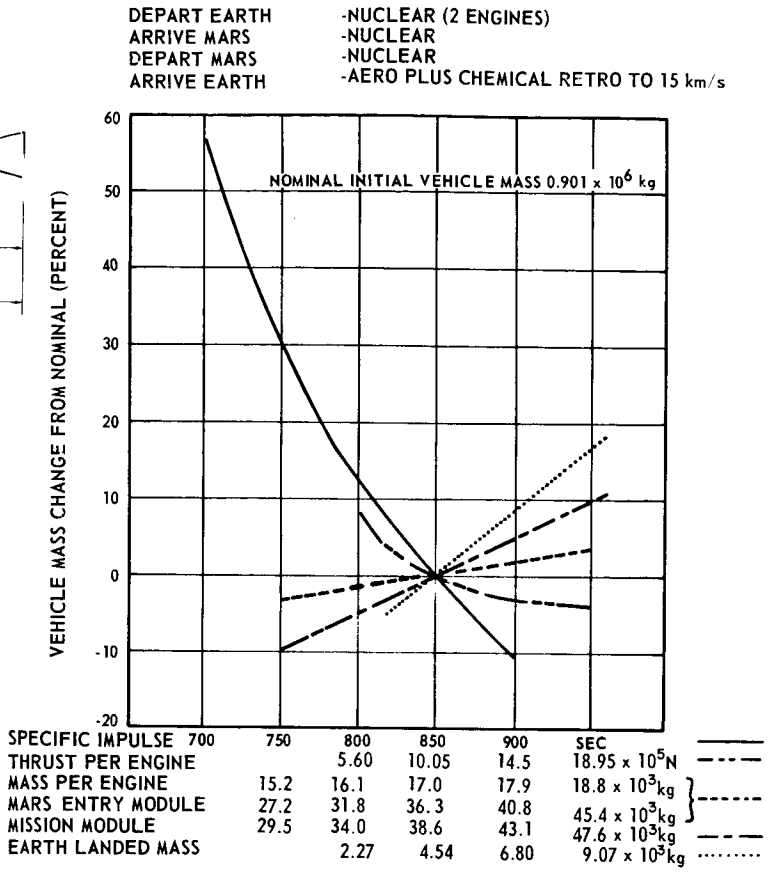

FIGURE 8. VEHICLE MASS SENSITIVITY MARS STOPOVER MISSION 1982

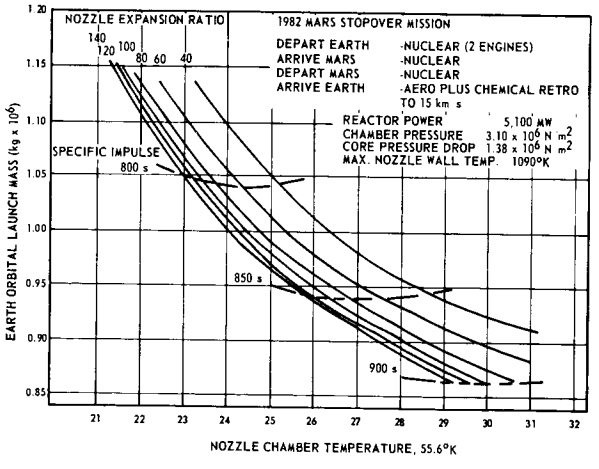

FIGURE 9. EFFECT OF NOZZLE EXPANSION RATIO AND NOZZLE CHAMBER TEMPERATURE

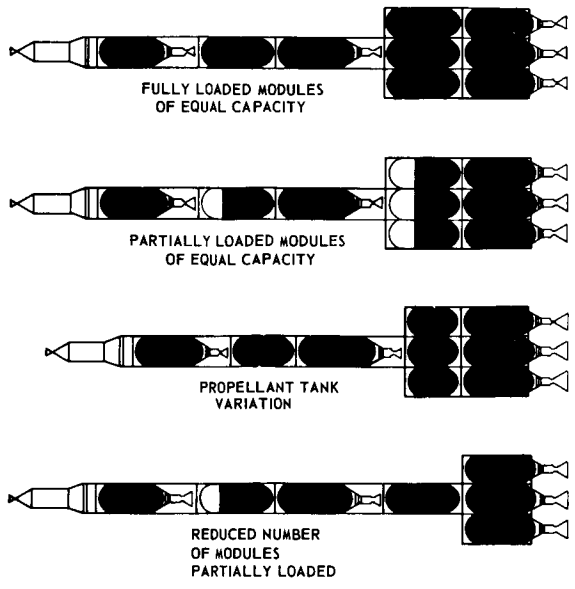

FIGURE 10. CONFIGURATION VARIATIONS VERSUS MISSION REQUIREMENTS

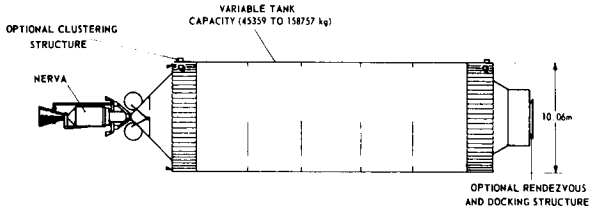

FIGURE 11. PROPULSION MODULE CONCEPT

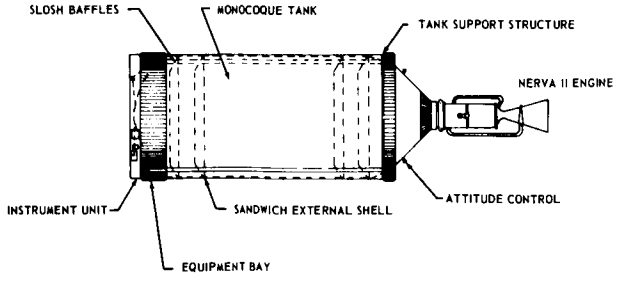

FIGURE 12. MODULE INBOARD PROFILE

is a sandwich cylinder which resists vehicle axial loads, shears and bending moments. Lateral loads on the internal tank are transmitted through radial members connecting the inner and outer shells. The nuclear-engine thrust loads are transmitted to the outer cylindrical shell through the aft conical thrust structure. Loads from upper and lower stages are transferred through the nuclear stage by corrugated interstage skirts.

Propellant thermal protection is provided by foam insulation bonded to the outside of the inner tank to prevent condensation while on the launch pad, and superinsulation between the foam and the outer wall for long-term propellant storage. The outer shell has sandwich construction for strength and meteoroid protection. Attachments for clustering modules would be located on the structure fore and aft. While this presently appears to be a promising cryo-structural concept, much additional design study and supporting technology will be required to evaluate its integrity and desirability.

The problem of propellant heating in the nuclear stage is unique since in addition to the normal solar, convective and conductive loads which are transmitted into the propellant in chemical stages, the nuclear stage experiences an additional intense heat input from nuclear radiation. This problem is illustrated by the graph shown in Figure 13. The propellant temperature rise results in a vapor pressure rise during engine operation; an additional tank

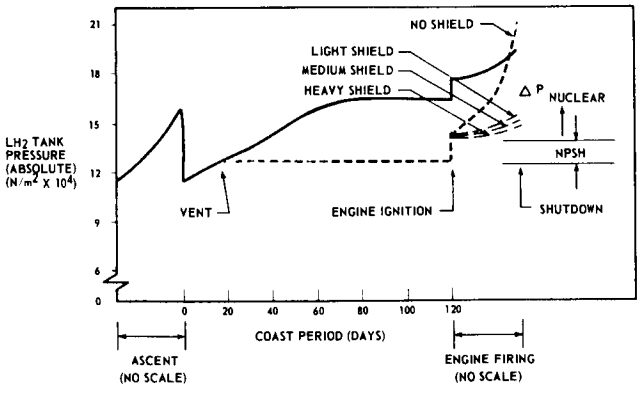

FIGURE 13. LH_2 TANK PRESSURE HISTORY

pressure increment equal to the turbopump net positive suction head (NPSH) requirements must be provided to prevent cavitation of the pump, unless a zero NPSH turbopump can be developed. A tradeoff, therefore, arises between engine shielding and the extent of propellant heating allowable. In order to solve this problem and establish the best overall system design, additional supporting research and technology is required in the areas of nuclear energy transport, shielding and propellant thermo/fluid-dynamic behavior under the heating conditions. Some of the nuclear research work underway and its results are covered in Section IV.

IV. SUPPORTING RESEARCH AND TECHNOLOGY

The activities in this area currently underway either at MSFC or under MSFC contracts include the following:

1. Nuclear engineering research under the Research Projects Laboratory covering radiation environmental mapping, dose rate calculations, energy transport, shielding analysis, and development of analytical and computational techniques;

2. Nuclear stage materials technology under the Materials Division of Propulsion and Vehicle Engineering Laboratory covering the combined effects of reactor radiation, temperature and vacuum on engineering materials;

3. Research and development under the Astrionics Laboratory of nuclear instrumentation, such as gamma and neutron spectrometers and semiconductor materials for radiation environment;

4. Nuclear flight safety systems research under the Advanced Studies Office of Propulsion and Vehicle Engineering Laboratory to assess the nature and magnitude of nuclear flight hazards, the identification and evaluation of potential countermeasures and safety systems, and the definition and design of selected systems.

A summary of the contracted activities covering these areas of research is given in Appendix A along with those covering mission studies and vehicle design.

V. NUCLEAR FACILITIES INVESTIGATION AND DESIGN

The Test Laboratory and the Facilities and Design Office maintain a continuous program of study, research, engineering, and design of facilities required to support advanced nuclear vehicle cold flow and hot test experimental technology programs. Current MSFC support, under the direction and coordination of the Test Laboratory, is being provided to the Space Nuclear Propulsion Office in the preliminary engineering evaluation of integrated engine/vehicle test-stand concepts for the Nuclear Rocket Development Station.

VI. CONCLUSIONS

As a result of the recent MSFC inhouse and contracted program of research under the sponsorship of the Space Nuclear Propulsion Office, OART, and OMSF, a modular nuclear vehicle concept has been developed that offers a multimission space capability, based upon the large NERVA engine, with a maximum of overall commonality of hardware for applications across the spectrum of potential missions. The modular approach appears to be the key to a sound development program and orderly evolution from initial ground testing to first flight, Saturn V applications, and ultimately to manned planetary exploration. Much additional research and design effort is required in advance of any possible development program. In addition the recent study program has established the framework of supporting vehicle research and technology requirements necessary from initial ground testing to ultimate use. The supporting research and technology activities have provided some of the basic tools for analysis, design, and further research and have advanced the level of knowledge in most of the critical areas at least to the extent of defining the nature and magnitude of the problems. Much additional research work is necessary in the areas of long term propellant storage; advanced structures with meteoroid protection; instrumentation, materials, and components suitable for use in the radiation environment; and nuclear/thermo/fluid-dynamic engineering in the areas of radiation transport, shielding, and resulting propellant and feed system behavior, structural and component heating, radiation effects, and materials activation. These areas of research must be pursued in conjunction with the modular system definition and design work in order to maintain a sound, well-integrated program of research and design.

APPENDIX A

Listing of recent MSFC nuclear vehicle studies and supporting research and technology contracts.

A. Advanced Systems Office, Planetary and Nuclear Systems Group.

Thompson Ramo Wooldridge/Space Systems Contract NAS8-5371: Mission-Oriented Study of Advanced Nuclear System Design Parameters --

Mission matrix performance evaluation, nuclear engine sizing, configuration analyses, sensitivity of engine/vehicle performance and design parameters.

B. Advanced Systems Office, Planetary and Nuclear Systems Group.

Lockheed Missiles and Space Company Contract NAS8-20007: Modular Nuclear Vehicles, Technology Problems and Safety Systems --

Investigation and design of modular nuclear vehicle concepts, evaluation of configurations and reference vehicle design, engine/stage integration, delineation of technology problems, facility requirements research, nuclear safety systems research, investigation and design.

C. Astrionics Laboratory.

Lockheed Georgia Company, Contract NAS8-5332: Irradiation of Electronic Parts and Breadboard Type Equipment --

a. Study and testing efforts for preselection of components where manufacturing process associated with transistors causes change in gain at 10^2 - 10^3 R.

b. Test of capacitors in nuclear environment.

c. Test thermistors and transistors in nuclear environment.

d. Test breadboard static inverter in nuclear environment.

D. Astrionics Laboratory, Instrumentation Division.

Illinois Institute of Technology, Contract NAS8-11885: Development of Fast Neutron Spectrometer --

A prototype or breadboard system will be tested in reactor flux to determine efficiency of system over broad energy range and sensitivity of system to gamma radiation.

E. Astrionics Laboratory, Applied Research Branch.

Bendix Corporation, Contract NAS8-20135: Study to Investigate the Effects of Ionizing Radiation on Transistor Surfaces --

a. Selection of transistors for operation in ionizing radiation environment.

b. Investigate methods to be used in incoming quality control.

c. Better under-surface behavior.

d. Determine radiation threshold damage levels for selected devices presently aboard Saturn vehicle.

F. Astrionics Laboratory, Applied Research Branch.

Westinghouse Corporation, Contract NAS8-11861: Design, Development and Fabrication of Prototype Silicon Carbide Amplifiers --

a. Six units to be built by Westinghouse.

b. Units to be tested in temperature environment (573° K to 673° K) and radiation environment (10^{14} - 10^{15} NVT) by MSFC.

G. Propulsion and Vehicle Engineering Laboratory, Materials Division.

Illinois Institute of Technology, Contract NAS8-11160:

A comprehensive computer program has been developed and experimentally validated to predict the induced neutron activation under a wide variety of irradiation conditions for all stable isotopes of all elements and combinations of elements.

H. Propulsion and Vehicle Engineering Laboratory, Materials Division.

Hughes Aircraft Company, Contract NAS8-20210:

The combined effects of particulate and electromagnetic radiation, including ultraviolet, are being determined in situ in vacuum for certain dielectric materials and thermal control coatings.

I. Propulsion and Vehicle Engineering Laboratory, Materials Division.

General Dynamics/Fort Worth, Contract NAS8-2450:

The combined effects of reactor radiation, temperature (310.8° K to 20° K), and test medium (air, vacuum, LN_2 and LH_2) have been determined in situ for a wide variety of engineering materials typically used on space vehicles.

J. Research Projects Laboratory, Nuclear and Plasma Physics Branch.

Lockheed-Georgia Company, Contract NAS8-9500: Evaluation of Methods For Computing Nuclear Rocket Radiation Fields --

Critical evaluations were made for a series of computer programs suitable for theoretical predictions of radiation fields in nuclear rocket systems. Ten computer programs covering point-kernel, discrete ordinates and Monte Carlo methods were examined as a part of this study.

K. Research Projects Laboratory, Nuclear and Plasma Physics Branch.

Lockheed-Georgia Company, Contract NAS8-5180: Computer Programs for Shielding Problems in Manned Space Vehicles--

This study extended and refined certain space radiation shielding codes. Approximations in the proton penetration code were improved. Three new shielding codes were written during this effort.

L. Research Projects Laboratory, Nuclear and Plasma Physics Branch.

General Dynamics/Fort Worth, Contract NAS8-5182:

A Monte Carlo procedure for the IBM-7094 has been developed to perform calculations of the radiation heating in propellant tanks and the radiation environment about a nuclear rocket stage. The procedure is made up of seven codes.

APPENDIX B

TECHNICAL REPORTS, NOTES, PAPERS AND MEMORANDA

PUBLISHED BY

ADVANCED SYSTEMS OFFICE

PLANETARY AND NUCLEAR SYSTEMS GROUP*

1. Harris, R. J.; and Saxton, D. R.: Lunar Mission Velocity Requirements for Nuclear Vehicles. NASA TM X-51409, 2 April 1962, UNCLASSIFIED, (also M-P&VE-FN-62-DRS-7).

2. Harris, R. J.: Trajectory Simulation Applicable to Stability and Control Studies of Large Multi-engine Vehicles. NASA TN D-1838, 2 January 1963, UNCLASSIFIED, (also MTP-P&VE-F-63-1).

3. Fellenz, D. W.; and Harris, R. J.: Influence of Weight Parameters on the Propulsion Requirements of Orbit-Launched Vehicles. NASA TN D-1525, May 1963, UNCLASSIFIED, (also MTP-P&VE-F-62-2).

4. Harris, R. J.; and Saxton, D. R.: Departure Weight and Propulsion Requirements for Manned Mars Landing Missions Employing Nuclear Propulsion. NASA TM X-50123, 23 May 1963, UNCLASSIFIED, (also M-P&VE-FN-63-DRS-7).

5. Harris, R. J.; and Austin, R. E.: Orbit-Launched Nuclear Vehicle Design and Performance Evaluation Procedure for Escape and Planetary Missions. NASA TN D-1570, June 1963, UNCLASSIFIED, (also MTP-P&VE-F-62-11).

6. Austin, R. E.; and Kearns, G. B.: Lunar Mission Performance Evaluation Procedure for Orbit-Launched Nuclear Vehicles. NASA TN D-2157, April 1964, UNCLASSIFIED, (also MTP-P&VE-A-63-20).

7. Staff of Advanced Studies Office: Modified Launch Vehicle (MLV) Saturn V Improvement Study Composite Summary Report. NASA TM X-53252, 2 July 1965, UNCLASSIFIED.

8. Jordan, W. Y.: Project Rover, Status of the Nuclear Rocket Flight Test Program. M-S&M-F-1-60, 13 October 1960, CONFIDENTIAL.

9. Jordan, W. Y.; and Saxton, D. R.: Summary of Some Nuclear Rocket Propulsion Systems. M-S&M-FE, 4 November 1960, SECRET.

10. Heyer, J. W.: Investigation of Thrust Structure Heating from NERVA Class Nuclear Rockets. M-S&M-FE, 12 April 1961, CONFIDENTIAL.

11. Saxton, D. R.; and Harris, R. J.: Lunar Landing and Return Payloads for Nuclear C-3 Boosted Vehicles. S&M-FE-61-DRS-1, 4 August 1961, C/RD.

12. Saxton, D. R.; and Harris, R. J.: Lunar Landing and Return Payloads for Nuclear C-4 Boosted Vehicles. S&M-FE-61-DRS-3, 10 August 1961, C/RD.

13. Saxton, D. R.: Preliminary Definition of the C-5/NERVA Nuclear Launch Vehicle Configuration. M-P&VE-FE-61-DRS-12, 16 November 1961, CONFIDENTIAL.

14. Jordan, W. Y.; Saxton, D. R.; and Johns, S. A.: Technical Guidelines and Saturn C-5 Preliminary Vehicle Data for the Saturn D Studies. M-P&VE-FE-62-WYJ-1, 3 January 1962, CONFIDENTIAL.

* Nuclear Systems Group was transferred from P&VE Laboratory to Advanced Systems Office, October 1965.

15. Saxton, D. R.: Nuclear Stage Abort Trajectory Data for Several Saturn/Nuclear Vehicles. M-P&VE-FE-62-DRS-2, 22 January 1962, C/RD.

16. Wilke, R. C.: Correction of NERVA Reactor Weights. M-P&VE-FN-62-RCW-3, 31 January 1962, C/RD.

17. Harris, R. J.; and Saxton, D. R.: Lunar Mission Velocity Requirements for Nuclear Vehicles. M-P&VE-FN-62-DRS-7, 2 April 1962, UNCLASSIFIED, (also NASA TMX-51409).

18. Saxton, D. R.: Preliminary Definition of the Nova/Nuclear Vehicle Configuration. M-P&VE-FN-62-DRS-8, 21 April 1962, C/RD.

19. Jordan, W. Y.: Comments on Proposed Redesign of NERVA Engine Nozzle. M-P&VE-FN-62-WYJ-11, 4 May 1962, UNCLASSIFIED.

20. Heyer, J. W.: The B-4/NERVA Engine Designs. M-P&VE-FN-62-JWH-13, 17 May 1962, C/RD.

21. Saxton, D. R.: Preliminary Definition of the Nova/NERVA Lunar Cargo Carrier. M-P&VE-FN-DRS-14, 21 May 1962, C/RD.

22. Whiton, J. C.: Parametric Shielding Requirements for Background Protons and Electrons in the Orbital Altitude Range of 100 - 1100 km. M-P&VE-FN-62-JCW-15, 23 May 1962, UNCLASSIFIED.

23. Heyer, J. W.: Equation of State for Gaseous Para-hydrogen M-P&VE-FN-62-JWH-20, 17 September 1962, UNCLASSIFIED.

24. Whiton, J. C.: Shielding Requirements, Clustering. M-P&VE-FN-62-JCW-24, 8 October 1962, UNCLASSIFIED.

25. Rosinski, K. D.: Some Aspects of Post Shut-Down Radiation. M-P&VE-FN-62-JCW-25, 22 October 1962, UNCLASSIFIED.

26. Manning, H. S.: A Bibliography on Nuclear Rocket Applications. M-P&VE-FN-62-HSM-28, 6 November 1962, UNCLASSIFIED.

27. Saxton, D. R.; Harris, R. J.; and Manning, H. S.: Preliminary Calculations for a 470-day Mars Landing and Return Mission. M-P&VE-FN-62-DRS-29, 14 November 1962, C/RD.

28. Heyer, J. W.; and Harris, R. J.: Preliminary Investigation of the Performance Advantage of a Low-Power Density Nuclear Engine Design. M-P&VE-FN-62-JWH-30, 30 November 1962, C/RD.

29. Heyer, J. W.: Program for the Calculation of Pulsed Aftercoolant Transients. M-P&VE-FN-62-JWH-31, 12 December 1962, UNCLASSIFIED.

30. Saxton, D. R.: Trajectory Simulation of Thrust Decay and Aftercooling Transients. M-P&VE-FN-62-DRS-32, 31 December 1962, C/RD.

31. Heyer, J. W.: A CHAC-2 Investigation of the NERVA NRXB. M-P&VE-FN-63-JWH-1, 23 January 1963, C/RD.

32. Harris, R. J.: Definition and Presentation of Minimum Stage Mass Fractions for High-Energy Missions. M-P&VE-FN-63-RJH-2, 26 February 1963, UNCLASSIFIED.

33. Whiton, J. C.: Radiation Environment Associated with Operational Nuclear Systems during Rendezvous. M-P&VE-FN-63-JCW-3, 19 March 1963, UNCLASSIFIED.

34. Heyer, J. W.: Parametric Study of a 3000-MW Nuclear Rocket Engine: The Effect of Power Density on Reactor Weight and Gas Exit Temperature. M-P&VE-FN-63-JWH-4, 29 March 1963, C/RD.

35. Nixon, R. F.: A Nuclear Rocket Engine with a 55-Inch Diameter Core. M-P&VE-FN-63-RFN-6, 27 May 1963, C/RD.

36. Harris, R. J.; and Saxton, D. R.: Departure Weight and Propulsion Requirements for Manned Mars Landing Missions Employing Nuclear Propulsion. M-P&VE-FN-63-DRS-7, 23 May 1963, UNCLASSIFIED, (also NASA TM X-50123).

37. Rosinski, K. D.: Comparison of Fission Product Decay Data. M-P&VE-FN-63-KDR-8, 4 June 1963, UNCLASSIFIED.

38. Mead, C. W.: Faster Startup of NERVA Engine. M-P&VE-FN-63-CWM-10, 20 September 1963, UNCLASSIFIED.

39. Austin, R. E.: Nuclear Engine Performance Charts (Orbital Start). M-P&VE-FN-63-REA-12, 30 July 1963, C/RD.

40. Whiton, J. C.: Preliminary Performance Study, Nuclear Pulse Propelled Vehicle. Memo P-105-6, 6 August 1963, SECRET.

41. Mead, C. W.: Nuclear Engine Aftercooling. M-P&VE-FN-63-CWM-15, 30 August 1963, UNCLASSIFIED.

42. Manning, H. S.: S-N Stage Thrust Vector Control System. M-P&VE-FN-63-HSM-17, 25 September 1963, UNCLASSIFIED.

43. Cramer, S. N.: Summary of Recent Work with Reactor Neutronic Program ZIP. M-P&VE-FN-63-SNC-19, 27 September 1963, C/RD.

44. Saxton, D. R.: Growth Potential of the Saturn V Vehicle with Nuclear Third Stages. R-P&VE-ANS-63-DRS-22, 11 October 1963, C/RD.

45. Saxton, D. R.: Vehicle Data for Clustering Study Configuration. R-P&VE-ANS-63-DRS-24, 25 October 1963, UNCLASSIFIED.

46. Harris, R. J.: Preliminary Nuclear Pulse Vehicle Performance Support Data. R-P&VE-AN-63-RJH-25, 28 October 1963, C/RD.

47. Manning, H. S.: Technical Guidelines for the Operational Safety Analysis for Advanced Nuclear Missions Study. R-P&VE-ANS-63-HSM-26, 29 November 1963, UNCLASSIFIED.

48. Priest, C. C.; and Nixon , R. F.: A Review of Systems for Nuclear Auxiliary Power. R-P&VE-AN-63-CCP-27, 20 November 1963, C/RD.

49. Mercier, D. R.: Nozzle Performance. R-P&VE-AN-64-7, 9 January 1964, UNCLASSIFIED.

50. Nixon, R. F.; and Priest, C. C.: Comments on Selection of the Power System for the In-House Mars Fly-by Study. R-P&VE-AN-64-8, 9 January 1964, UNCLASSIFIED.

51. Heyer, J. W.: Suggested Performance Characteristics for Phoebus Class Nuclear Engines. R-P&VE-AN-64-15, 22 April 1964, C/RD.

52. Austin, R. E.: Preliminary Performance Estimates for 10-Meter Nuclear Pulse Vehicle. R-P&VE-AN-64-18, 24 February 1964, S/RD.

53. Patton, E. H.: Nuclear Calculations with Program ZIP. R-P&VE-AN-64-22, 3 April 1964, C/RD.

54. Priest, C. C.: Vehicle Power Supply for the In-House Mars Fly-by Study. R-P&VE-AN-64-23, 14 February 1964, UNCLASSIFIED.

55. Harris, R. J.: Mars Fly-by Capability of 5000 MW Nuclear Engine. R-P&VE-AN-64-31, 12 February 1964, C/RD.

56. Priest, C. C.: Facilities Review of Potential Contractors of Chemical Electric Power System for the Mobile Laboratory (MOLAB). R-P&VE-AN-64-37, 24 February 1964, UNCLASSIFIED.

57. Mead, C. W.: Effect of Core Pressure Drop on Weight and Performance of a Nuclear Engine with a 55-inch Diameter Core. R-P&VE-AN-64-43, 6 March 1964, C/RD.

58. Mercier, D. R.: Nozzle Weight Calculation. R-P&VE-AN-64-48, 13 March 1964, UNCLASSIFIED.

59. Priest, C. C.: The Application of the SNAP Reactor Systems to Manned Lunar Operations. R-P&VE-AN-64-50, 16 March 1964, C/RD.

60. Patton, E. H.: A Parametric Study of Simple Graphite Reactors Using Three-group, Multi-region Theory. R-P&VE-AN-64-51, 19 March 1964, UNCLASSIFIED.

61. Stephens, W. T.: Representative Manned Capsule Design Data for Specified Missions. R-P&VE-AN-64-55, 17 March 1964, CONFIDENTIAL.

62. Mercier, D. R.: Pressure Vessel Weight Calculation. R-P&VE-AN-64-59, 23 March 1964, UNCLASSIFIED.

63. Mead, C. W.: Effect of Various Design Parameters on Nuclear Engine Weight. R-P&VE-AN-64-67, 6 April 1964, UNCLASSIFIED.

64. Priest C. C.: Comparison of In-House Developed Core Heat Transfer Program with LASL, WANL and Rocketdyne Programs. R-P&VE-AN-64-68, 10 April 1964, CONFIDENTIAL.

65. Harris, R. J.: Nuclear Safety Study Mission Models II and III - Manned Mars Fly-by and Mars Landing. R-P&VE-ANA-64-69, 9 April 1964, CONFIDENTIAL/RD.

66. Saxton, D. R.: Nuclear Safety Study Mission Model I, 70-hr. Lunar Transfer Injection via One EOR of MLV Saturn V-1. R-P&VE-AN-64-70, 8 April 1964, UNCLASSIFIED.

67. Austin, R. E.: Propulsive Braking Trajectory Program. R-P&VE-AN-64-79, 15 April 1964, UNCLASSIFIED.

68. Saxton, D. R.: Lunar Mission Potential of the NERVA Engine with Uprated Saturn Vehicles. R-P&VE-AN-64-83, 21 April 1964, UNCLASSIFIED.

69. Propulsion and Power Section: Inhouse Procedure for Evaluating Thrust, Impulse and Engine Weight for the Hot-Bleed Cycle Nuclear Rocket Engine. R-P&VE-AN-64-88, 29 April 1964, C/RD.

70. Mead, C. W.: Nuclear Engine Weight and Performance Parametric Study. R-P&VE-AN-64-98, 21 May 1964, CONFIDENTIAL.

71. Priest, C. C.: The Application of SNAP-8 To A Manned Space Station, Phase II of NASA Contract NAS3-4160. R-P&VE-AN-64-101, 28 May 1964, UNCLASSIFIED.

72. Priest, C. C.: Core Heat Transfer Data for Nuclear Engine Weight and Performance Parametric Study. R-P&VE-AN-64-107, 8 June 1964, C/RD.

73. Whiton, J. C.: Nuclear Pulse Vehicle Performance Estimates for Use in Study of Reconnaisance Landing Mission to Mars, Venus Swing-by Mode. R-P&VE-AN-64-108, 9 June 1964, SECRET.

74. Nunnery, J. N.: Computer Programs. R-P&VE-AN-64-109, 12 June 1964, UNCLASSIFIED.

75. Harris, R. J.: Sizing of Nuclear Orbit Launch Vehicles for Manned Mars and Venus Missions. R-P&VE-AN-64-112, 16 June 1964. (Incorporated into FPO Internal Note 1-64 by H. O. Ruppe).

76. Hood, D. S.: Removal Cross Section Computer Program. R-P&VE-AN-64-123, 26 June 1964, UNCLASSIFIED.

77. Nunnery, J. N.: Lockheed Module DI Design. R-P&VE-AN-64-137, 5 August 1964, UNCLASSIFIED.

78. Saxton, D. R.: Lunar Logistics Mission Potential of Nuclear Stages with Uprated Saturn Vehicles. R-P&VE-AN-64-139, 10 August 1964, C/RD.

79. Saxton, D. R.: Review of Structural Weight Equations to be Employed by S. T. L. under Contract NAS8-5371 (P-107). R-P&VE-AN-64-141, 15 July 1964, UNCLASSIFIED.

80. Whitehead, M.: Ring Frame Analysis. R-P&VE-AN-64-148, 21 October 1964, UNCLASSIFIED.

81. Stephens, W. T.: Weight and Volume Requirements for Manned Spacecraft - A Literature Survey. R-P&VE-AN-64-151, September 1964, CONFIDENTIAL.

82. Harris, R. J.; and Saxton, D. R.: Mass Fraction Data for 'Mission Oriented Study of Advanced Nuclear Systems' STL, NAS8-5371. R-P&VE-AN-64-158, 21 September 1964, UNCLASSIFIED.

83. Saxton, D. R.: MLV-Saturn V-1N Vehicle Control Study Input Data. R-P&VE-AN-64-161, 28 September 1964, UNCLASSIFIED.

84. Rosinski, K. D.: The Study of a Topping Cycle Configuration for the Solid Core Nuclear Rocket Engine. R-P&VE-AN-64-164, 2 October 1964, CONFIDENTIAL.

85. Mercier, D. R.: Program for the Calculation of Flow Parameters of a Perfect Gas Expanding Isentropically through a Nozzle. R-P&VE-AN-64-165, 5 October 1964, UNCLASSIFIED.

86. Rosinski, K. D.: Space Vehicle Activation. R-P&VE-AN-64-170, 9 October 1964, UNCLASSIFIED.

87. Hood, D. S.: Total Mission Proton and Cosmic Radiation Dose for Manned Mars Landing Missions. R-P&VE-AN-64-175, 19 October 1964, UNCLASSIFIED.

88. Mercier, D. R.; and Nixon, R. F.: NERVA I and II Nuclear Engine Summary Data. R-P&VE-AN-64-181, 28 October 1964, C/RD.

89. Byrd, A. W.: Gas Core Reactor Concepts. R-P&VE-AN-64-183, 29 October 1964, C/RD.

90. Nixon, R. F.: Environmental Radiation in Near Earth Orbit. R-P&VE-AN-64-196, 17 December 1964, UNCLASSIFIED.

91. Nixon, R. F.: Comparison LMSC and MSFC Nuclear Engine Aftercooling Estimates. R-P&VE-AN-65-3, 13 January 1965, UNCLASSIFIED.

92. Saxton, D. R.: Study of Modular Nuclear Vehicles, Technology Probems, and Safety Systems, LMSC, Contract NAS8-20007 (FPO P-107B). R-P&VE-AN-65-8, 28 January 1965, UNCLASSIFIED.

93. Austin, R. E.: Nuclear Pulse Vehicle Performance for Manned Mars Mission. R-P&VE-AN-65-10, 25 February 1965, S/RD.

94. Mead, C. W.: Nuclear Vehicle Design and Performance Parameter Sensitivity Study. R-P&VE-AN-65-11, 21 January 1965, UNCLASSIFIED.

95. Saxton, D. R.; and Whitehead, M.: Propulsion Module Sizing for MLV-Saturn V-3. R-P&VE-AN-65-16, 10 February 1965, UNCLASSIFIED.

96. Harris, R. J.: Study of Modular Nuclear Vehicles, Technology Problems, and Safety Systems, LMSC, P-107B. R-P&VE-AN-65-19, 10 February 1965, UNCLASSIFIED.

97. Nixon, R. F.: NERVA II Reference Engine for the Modular Vehicle Design Study, NAS8-20007. R-P&VE-AN-65-21, 16 February 1965, C/RD.

98. Harris, R. J.: Comparison of Mars Stopover Mission Requirements for Several Mission Mode/Propulsion System Combinations. R-P&VE-AN-65-24, 23 February 1965, UNCLASSIFIED.

99. Priest, C. C.: Startup Procedure for the NERVA I Nuclear Engine. R-P&VE-AN-65-27, 25 February 1965, C/RD.

100. Byrd, A. W.: Glow Plug Gaseous Core Nuclear Rocket Engine Weight and Performance. R-P&VE-AN-65-28, 26 February 1965, UNCLASSIFIED.

101. Mead, C. W.: Attitude Control Force Required for Nose Steering of an Interplanetary Vehicle Employing A Rigid Non-Gimbaled Engine Mounting System. R-P&VE-AN-65-31, 3 March 1965, UNCLASSIFIED.

102. Saxton, D. R.: NERVA II Reactor Flight and Static Test Vibrational Environment Analysis Input Data. R-P&VE-AN-65-32, 8 March 1965, UNCLASSIFIED.

103. Whitehead, M.: Ground Wind Load Analysis for Launch Analyses. R-P&VE-AN-65-35, March 1965, UNCLASSIFIED.

104. Whitehead, M.: Ground Wind Load Analysis Program, ANS 16-0-0. R-P&VE-AN-65-35, 10 March 1965, UNCLASSIFIED.

105. Patton, E. H.: Shielding of Radioisotope SNAP Units. R-P&VE-AN-65-37, 8 March 1965, UNCLASSIFIED.

106. Nunnery, J. N.: Lunar Unmanned Mission Performance Program, ANS 14-0-0. R-P&VE-AN-65-44, 15 March 1965, UNCLASSIFIED.

107. Nunnery, J. N.: Calculation of Thickness and Weight of Meteoroid Protection Program, ANS 9-0-3. R-P&VE-AN-65-45, 16 March 1965, UNCLASSIFIED.

108. Nunnery, J. N.: Calculation of Basic Weight, Ellipsoidal Bulkhead Program, ANS 11-1-1. R-P&VE-AN-65-46, 16 March 1965, UNCLASSIFIED.

109. Nunnery, J. N.: Orthotropic Cylindrical Tank Optimization Program, Unflanged Stiffeners, ANS 10-1-3. R-P&VE-AN-65-47, 16 March 1965, UNCLASSIFIED.

110. Stephens, W. T.: Determination of Earth Reentry Weight Requirements for Return from a Mars Mission. R-P&VE-AN-65-49, 18 March 1965, UNCLASSIFIED.

111. Hooper, B. J.: Double Pass Tie Rod. R-P&VE-AN-65-52, 26 March 1965, C/RD.

112. Whitehead, M.: Ground Wind Load Analysis Program, ANS 16-0-1. R-P&VE-AN-65-54, 16 March 1965, UNCLASSIFIED.

113. Mercier, D. R.: Optimum Nuclear Engine Nozzle Area Ratio for Earth Escape Missions. R-P&VE-AN-65-63, 20 April 1965, UNCLASSIFIED.

114. Nixon, R. F.: Nuclear Vehicle Thrust Vector Control Requirements and Interrelations between Engine and Stage Control Systems. R-P&VE-AN-65-64, 23 April 1965, UNCLASSIFIED.

115. Saxton, D. R.: Nuclear Systems Group Contribution to the Summary volume of Saturn V Improvement Studies. R-P&VE-AN-65-65, 26 April 1965, UNCLASSIFIED.

116. Byrd, A. W.: Nuclear Engine Afterheat Removal, Comparison of Analysis and Test Results. R-P&VE-AN-65-67, 30 April 1965, UNCLASSIFIED.

117. Mercier, D. R.: Computer Program to Calculate Centers of Gravity and Moments of Inertia for Nuclear Vehicles. R-P&VE-AN-65-68, 7 May 1965, UNCLASSIFIED.

118. Priest, C. C.: Propellant Tank Insulation for Storage in Earth Orbit. R-P&VE-AN-65-73, 12 May 1965, UNCLASSIFIED.

119. Kearns, G. B., Jr.: Propellant Requirements for One-Rendezvous Lunar Logistics Missions Employing the Reference Propulsion Module. R-P&VE-AN-65-77, 28 May 1965, UNCLASSIFIED.

120. Saxton, D. R.: Selection of Reference Module Propellant Capacity. R-P&VE-AN-65-79, 12 May 1965, UNCLASSIFIED.

121. Nixon, R. F.: Thrust Vector Control. R-P&VE-AN-65-80, 26 May 1965, UNCLASSIFIED.

122. Byrd, A. W.: Fast Metallic Nuclear Rocket Engines. R-P&VE-AN-65-88, 28 May 1965, S/RD.

123. Kearns, G. B., Jr.: Curve Fit for Parametric Orbit-to Injection Characteristic Velocity Data. R-P&VE-AN-65-90, 13 August 1965, UNCLASSIFIED.

124. Nixon, R. F.: Thrust Vector Control Requirements of Nuclear Vehicles. R-P&VE-AN-65-92, 9 June 1965, UNCLASSIFIED.

125. Mercier, D. R.: Nuclear Rocket Engine Optimization Program, NOP. R-P&VE-AN-65-93, 11 June 1965, UNCLASSIFIED.

126. Saxton, D. R.: Minutes of the Second Bimonthly Progress Review, Contract NAS8-20007 (Modular Nuclear Vehicle). R-P&VE-AN-65-99, 15 June 1965, UNCLASSIFIED.

127. Priest, C. C.: Space Power Systems Data Book. R-P&VE-AN-65-100, 22 June 1965, C/RD.

128. Byrd, A. W.: Thermionic Space Power Reactor Systems. R-P&VE-AN-65-102, 23 June 1965, C/RD.

129. Mead, C. W.: Modular Nuclear Vehicle Sizing Program for Manned Interplanetary Fly-by or Stopover Mission. R-P&VE-AN-65-109, 13 July 1965, UNCLASSIFIED.

130. Funderburg, R. L.: Lunar Unmanned Mission Performance Program, ANS 14-0-1. R-P&VE-AN-65-111, 15 July 1965.

131. Saxton, D. R.: NERVA 2 Acceleration Profiles. R-P&VE-AN-65-113, 19 July 1965, UNCLASSIFIED.

132. Nunnery, J. N.: Current Status of Master Design Program (Single Wall Tank Version). R-P&VE-AN-65-115, 20 July 1965, UNCLASSIFIED.

133. Nunnery, J. N.: Sandwich Cylinder Program, BECO Interim Report. R-P&VE-AN-65-118, 29 July 1965, UNCLASSIFIED.

134. Nixon, R. F.: Vehicle Design Anomalies Requiring Thrust Vector Trim of a Nuclear Engine. R-P&VE-AN-65-120, 29 July 1965, UNCLASSIFIED.

135. Nixon, R. F.: Nuclear Technology Vehicle Cold Flow Test Development Plan. R-P&VE-AN-65-126, 10 August 1965, UNCLASSIFIED.

136. Mercier, D. R.: Propellant Tank Insulation for Earth to Mars Interplanetary Mission. R-P&VE-AN-65-128, 11 August 1965, UNCLASSIFIED.

137. Saxton, D. R.: Interstage Weight Data for AGC. R-P&VE-AN-65-137, 25 August 1965, UNCLASSIFIED.

138. Manning, H. S.: Lateral Surface Area of a Right Oblate Hemiroidal Segment. R-P&VE-AN-65-138, 25 August 1965, UNCLASSIFIED.

139. Manning, H. S.: Volume of Right Oblate Hemiroidal Zones. R-P&VE-AN-65-145, 31 August 1965, UNCLASSIFIED.

140. Nunnery, J. N.: Sandwich Cylinder Design. R-P&VE-AN-65-149, 13 July 1965, UNCLASSIFIED.

141. Nunnery, J. N.: Aft Bulkhead Geometry. R-P&VE-AN-65-150, 10 August 1965, UNCLASSIFIED.

142. Allen, J. G.: Subsystem Weight Equation. R-P&VE-AN-65-151, 23 August 1965, UNCLASSIFIED.

143. Hooper, B. J.: Use of the Propellant in a Nuclear Vehicle as a Heat Sink during Earth Orbital Storage/and Conversion of the Propellant of a Nuclear Vehicle from Para to Ortho Hydrogen. R-P&VE-AN-65-152, 1 September 1965, UNCLASSIFIED.

144. Saxton, D. R.: Saturn V Performance Capability. R-P&VE-AN-65-155, 7 September 1965, UNCLASSIFIED.

145. Manning, H. S.: The Inclination of a Plane Containing Two Arbitrary Radius Vectors. R-P&VE-AN-65-156, 7 September 1965, UNCLASSIFIED.

146. Austin, R. E.: Effect of Coast Period on the Payload Capability of the Saturn V/Nuclear Vehicle. R-P&VE-AN-65-157, 8 September 1965, CONFIDENTIAL.

147. Woods, A. D.: Volume and Surface Area of Propellant Tanks. R-P&VE-AN-65-158, 10 September 1965, UNCLASSIFIED.

148. Funderburg, R. L.: COTAWOMP (Calculation of Thickness and Weight of Meteoroid Protection) Program ANS-9-1-0. R-P&VE-AN-65-161, 4 September 1965, UNCLASSIFIED.

149. Mercier, D. R.: Comparison of Propellants for Use in A Nuclear Rocket Engine on A Mars Mission. R-P&VE-AN-65-163, 20 September 1965, UNCLASSIFIED.

150. Nixon, R. F.: Data for Analyzing Nuclear/S-II Stage Separation. R-P&VE-AN-65-164, 20 September 1965, UNCLASSIFIED.

151. Saxton, D. R.: Minutes of the Fourth Bimonthly Progress Review, Contract NAS8-20007 (Modular Nuclear Vehicle). R-P&VE-AN-65-166, 20 September 1965, UNCLASSIFIED.

152. Nixon, R. F.: Evaluation of STL Aftercooling Data from SWOP. R-P&VE-AN-65-167, 29 September 1965, UNCLASSIFIED.

153. Woods, A. D.: War Eagle Program, ANS 1-1-0. R-P&VE-AN-65-168, 30 September 1965, UNCLASSIFIED.

154. Byrd, A. W.: Use of a Specifically Designed Heat Pipe As A Thermionic Emitter to Provide a Source of Electrical Energy. R-P&VE-AN-65-172, 30 September 1965, UNCLASSIFIED.

155. Saxton, D. R.; Manning, H. S.; Funderburg, R. L.; and Nunnery, J. N.: Geometry, Surface Area, Volume, Centroid, and Inertia of Nuclear Propulsion Module Propellant Tank Components. R-P&VE-AN-65-174, 29 September 1965, UNCLASSIFIED.

156. Jordan, W. Y.: Preliminary Program Definition of Nuclear Ground Test Module. R-AS-VP-3-66, 4 January 1966, UNCLASSIFIED.

157. Saxton, D. R.: Nuclear Propulsion Module Data for Saturn V Improvement Studies. R-AS-VP-11-66, 20 January 1966, UNCLASSIFIED.

158. Saxton, D. R.: Ground Wind Resistance of G. T. M. R-AS-VP-21-66, 10 February 1966, UNCLASSIFIED.

159. Woods, A. D.: Computer Program Writeup COTAWOMP. R-AS-VP-33-66, 24 February 1966, UNCLASSIFIED.

160. Woods, A. D.: Computer Program Writeup Payload Adjustment Program. R-AS-VP-41-66, 8 March 1966, UNCLASSIFIED.

161. Woods, A. D.: Computer Program Writeup Propellant Tank Sizing Program. R-AS-VP-44-66, 10 March 1966, UNCLASSIFIED.

162. Jordan, W. Y.: Theoretical Performance and Thermodynamic Working Charts for the Nuclear Hydrogen Rocket. ABMA DSP-TN-6-58, 22 July 1958, S/RD.

163. Jordan, W. Y.: Some Considerations of Nuclear Rocket Propulsion for the Second Stage of Saturn. ABMA DSP-TN-3-59, 10 February 1959, SECRET.

164. Callaway, R. C.; Galzerano, A. W.; Thomas, P. G.; Whitehurst, D. C.; Jordan, W. Y.; and Saxton, D. R.: Preliminary Performance Data of Saturn Space Vehicles. ABMA DSP-TN-8-59, 1 May 1959, SECRET.

165. Jordan, W. Y.: Weight and Cost Data Comparison of Chemical and Nuclear Powered Vehicles for the Lunar Soft Landing Mission. ABMA DSP - Internal Note 8, 13 May 1959, SECRET.

166. Jordan, W. Y.: Saturn-Nuclear Rocket Flight Test Vehicle. ABMA DSP-TN-17-59, 19 October 1959, S/RD.

167. Saxton, D. R.: A Summary of Plasma Propulsion Systems. ABMA DSP-TN-1-60, 2 February 1960, UNCLASSIFIED.

168. Haarmann, W. E.; and Saxton, D. R.: Comparison of Nuclear Rocket, Ion and Plasmajet Propulsion for a Mars Mission. ABMA DSP-TN-3-60, 19 May 1960, CONFIDENTIAL.

169. Whitehurst, D. C.: Optimization of Saturn D-2. ABMA DSP Internal Note 4, 3 June 1960, CONFIDENTIAL.

170. Jordan, W. Y.; and Saxton, D. R.: Project Rover, A Summary of Thrust Vector Control Systems for Nuclear Rocket Upper Stages. ABMA DSP Internal Note 6, 30 June 1960, SECRET.

171. Jordan, W. Y.; and Saxton, D. R.: Some Considerations of Nuclear Rocket Flight Testing. MTP-M-S&M-F-61-3, 0 March 1961, C/RD.

172. Heyer, J. W.: Nuclear Rocket Aftercooling Requirements. MTP-M-S&M-F-61-10, 18 March 1961, CONFIDENTIAL.

173. Nuclear Systems and Applications Section: Nuclear/Saturn (C-4) Lunar Vehicle Study. MTP-M-S&M-F-61-17, 8 September 1961, C/RD.

174. Sanford, E. M.: Summary of the ORION Nuclear Pulse Propelled Vehicle Studies. IN-M-P&VE-F-61-3, 9 November 1961, S/RD.

175. Prescott, A. D.: After-Shutdown Radiation Field of a 1000 MW Reactor in Space. MTP-P&VE-F-61-14, 1 December 1961, C/RD.

176. Fellenz, D. W.; and Harris, R. J.: Influence of Weight Parameters on the Propulsion Requirements of Orbit-Launched Vehicles. MTP-P&VE-F-62-2, 29 May 1962, UNCLASSIFIED, (also NASA TND-1525).

177. Nuclear Systems and Applications Section: System Study of the Nuclear/Saturn (C-5) Lunar Vehicle. MTP-P&VE-F-62-5, 11 September 1962, C/RD.

178. Harris, R. J.; and Austin, R. E.: Orbit-Launched Nuclear Vehicle Design and Performance Evaluation Procedure for Escape and Planetary Missions. MTP-P&VE-F-62-11, 8 November 1962, UNCLASSIFIED, (also NASA TN D-1570).

179. Nixon, R. F.: Nuclear Rocket Engine Performance, Isentropic Expansion of Frozen Hydrogen in the Nozzle. MTP-P&VE-F-63-4, 9 January 1963, UNCLASSIFIED.

180. Cramer, S. N.: Two-Group, Two-Region Reactor Calculations. IN-P&VE-F-63-7, 22 August 1963, C/RD.

181. Harris, R. J.; and Jones, R. M.: An Investigation of an Earth Orbit Launch Window for a Manned Mars Mission with Constant Mars Arrival Date. IN-P&VE-F-63-8, 29 August 1963, UNCLASSIFIED.

182. Dyess, O. M.: Meteoroid Protection for Space Vehicles, A Literature Survey. IN-P&VE-A-63-9, 8 October 1963, UNCLASSIFIED.

183. Austin, R. E.; and Kearns, G. B.: Lunar Mission Performance Evaluation Procedure for Orbit-launched Nuclear Vehicles. MTP-P&VE-A-63-29, 8 October 1963, UNCLASSIFIED, (also NASA TN D-2157).

184. Mead, C. W.: Nuclear Engine Afterheat Removal. IN-P&VE-A-64-1, 7 January 1964, UNCLASSIFIED.

185. Saxton, D. R.; Whiton, J. C.; Spier, R. C.; Dicus, D L.; and Crosswell, A. R.: Indirect Crew Dose from Reactor Operation at Sea Level. IN-P&VE-A-64-6, 30 April 1964, UNCLASSIFIED.

186. Priest, C. C.: Thermal Analysis of Nuclear Engine Core. IN-P&VE-A-64-14, 20 July 1964, C/RD.

187. Mercier, D. R.: Compressible Flow Parameters for Dissociating Hydrogen. IN-P&VE-A-64-15, 5 August 1964, UNCLASSIFIED.

188. Jordan, W. Y.: Project Rover, Nuclear Rockets for the National Space Program. Presented to the Ninth Meeting of the Rover Coordinating Group. 8 June 1960, SECRET.

189. Jordan, W. Y.; Saxton, D. R.; and Thomas, P. G.: Nuclear Rocket Stages Increase Saturn's Payload Capability. IAS Paper No. 61-64, Published in Aerospace Engineering, Vol. 20, No. 5, May 1961, UNCLASSIFIED.

190. Jordan, W. Y.; Heyer, J. W.; Saxton, D. R.; Whiton, J. C.; and Wilke, R. C.: Mating Nuclear Propulsion with Saturn for the Lunar Mission. M-P&VE-FN-62-WYJ-6, 22 March 1962, C/RD, Presented at Cleveland, Ohio, 8 March 1962 IAS Meeting.

191. Jordan, W. Y.: The Use of Nuclear Rockets: Lunar Landing and Beyond. M-P&VE-FN-62-WYJ-26, 12 October 1962, UNCLASSIFIED, AGARD Lecture, Brussels, Belgium.

192. Harris, R. J.; and Saxton, D. R.: Departure Weight and Propulsion Requirements for Manned Mars Landing Missions Employing Nuclear Propulsion. NASA TM X-50123, 23 May 1963, UNCLASSIFIED, Presented at Mars Mission Technology Conference, Lewis Research Center, (also M-P&VE-FN-63-DRS-7).

193. Manning, H. S.: Active Impact Control. M-P&VE-FN-63-HSM-5, 30 April 1963, UNCLASSIFIED, Presented to the Rover Flight Safety Panel Meeting, Cape Canaveral, Florida, 1 May 1963.

194. Manning, H. S.: Safety Systems Design Integration: An Introductory Survey. Presented at the 2nd RIFT W V DIW G meeting. M-P&VE-FN-63-HSM-13, 23 August 1963, C/RD.

195. Jordan, W. Y.; and Nixon, R. F.: Nuclear Rocket Propulsion. R-P&VE-AN-64-65, 1 April 1964, UNCLASSIFIED, (Contribution to Mark's Handbook).

196. Jordan, W. Y.: Nuclear Vehicle Systems Briefing. R-P&VE-AN-64-193, 13 November 1964, UNCLASSIFIED, Presented to Rover Committee.

197. Jordan, W. Y.: Nuclear Vehicle Systems Data. R-P&VE-AN-65-20, 16 February 1965, UNCLASSIFIED, Presented at LASL Rover Meeting.

198. Jordan, W. Y., Jr.; Harris, R. J.; and Saxton, D. R.: The Modular Appraoch Toward the Evolution of Nuclear Rocket Systems. R-P&VE-AN-65-58, 9 April 1965, UNCLASSIFIED. Published in Astronautics & Aeronautics, June 1965.

199. Saxton, D. R.: Saturn V Nuclear Uprating Studies. R-P&VE-AN-65-61, 13 April 1965, UNCLASSIFIED.

APPENDIX C

MAJOR REPORTS GENERATED BY CONTRACTORS

IN THE PERFORMANCE OF FUNDED STUDIES

SUPERVISED BY THE ADVANCED SYSTEMS OFFICE

PLANETARY & NUCLEAR SYSTEMS GROUP*

1. Reactor In-Flight Test (RIFT) Final System Study. GD/A report AE61-0140; NAS5-749, 6 March 1961, S/RD.

2. Reactor In-Flight Test Program, Final Report. LMSD-895075; NAS5-643, 15 March 1961, C/RD.

3. Final Report, Reactor In-Flight Test System. Martin Report NASA-CR-61-2; NAS5-648, March 1961, S/RD.

4. NERVA Engine-Vehicle Interactions. DAC Report SM-38499, March 1961, Confidential.

5. Saturn D Preliminary Design Study Final Report. GD/A report AE61-1017; NAS8-1600, 1 November 1961, S/RD.

6. Nuclear Test Stage (Rift Program) Final Preliminary Design Report. GD/A report AE61-1151; NAS8-526, 15 December 1961, S/RD.

7. Saturn D (Nuclear Rocket Upper Stage) Design Studies, Final Report. LMSC-704191; NAS8-1601, 15 December 1961, C/RD.

8. Reactor In-Flight Test Vehicle Systems Study, Final Report. LMSC-704192; NAS8-524, 26 December 1961, S/RD.

9. RIFT Final Technical Summary Report. Martin Report NASA-CR-61-3; NAS8-525, December 1961, S/RD.

10. RIFT, Reactor In Fight Test, Final Study Report Phase II. DAC Report SM-39164, NAS8-527, December 1961, S/RD.

11. C-5 Nuclear System Performance and Sizing Analysis. LMSC-B061068; NAS8-5600, 29 August 1962, C/RD.

12. Saturn D (Nuclear Rocket Upper Stage) Mission Studies, Final Report. LMSC-B007036; NAS8-1601, 31 August 1962, C/RD.

13. Saturn D Mission Study Final Report. AE62-0667; NAS8-1600, 31 August 1962, S/RD.

14. Nuclear Vehicle Flight Safety Study - Summary Report for Phases I and II. LMSC/B061396 (NSP 63-19); NAS8-5203, 31 July 1963, C/RD.

15. Nuclear Flight Executive Program - Phase III Report. LMSC/A304973; NAS8-5203, 31 January 1964, Unclassified.

---

* Nuclear Systems Group was transferred from P&VE Lab to Advanced Systems Office, October 1965.

16. Nuclear Pulse Space Vehicle Study GA-5009; NAS8-11053, January 1964, Secret.

17. Reusable Nuclear Ferry Vehicle Preliminary Design Study. LMSC-B007429; NAS8-5020, 28 February 1964, Unclassified except Volume III.

18. Performance Evaluation of Uprated Saturn V Launch Vehicles Using Nuclear Third Stages. LMSC/A664282; NAS8-9500 (Task 5.2), 10 June 1964, Confidential.

19. Module Designs for Assembly into Nuclear Orbital Vehicle. LMSC/A650541; NAS8-9500 (Task 5.2), 11 June 1964, Unclassified.

20. Nuclear Safety Study - Mission Model Analyses Final Report. LMSC-B108421; NAS8-9500 (Task 5.4), 31 July 1964, Confidential.

21. Preliminary Guidelines for the preparation of Nuclear Vehicle Flight Safety Performance Specifications. LMSC/A664243; NAS8-9500 (Task 5.4), July 1965, Unclassified.

22. Nuclear Flight Executive Program, Phase IV Report, Nuclear Vehicle Flight Safety Study. LMSC-A664268; NAS8-5203, 31 August 1964, Unclassified.

23. Addendum to Nuclear Flight Executive Program, Phase IV Report, Nuclear Vehicle Flight Safety Study. LMSC-B108679; NAS8-5203, 31 August 1964, Confidential.

24. Parametric Study of Ranking-Cycle Space Nuclear Power Systems. BECO Technical Note R-113; NAS8-5289, August 1964, Unclassified.

25. Parametric Performance Study of Nuclear Propelled Space Vehicles. BECO Technical Note R-114; NAS8-5289, September 1964, Unclassified.

26. Nuclear Heating Effects in Propellant in Clustered Pairs of Nuclear Stages. LMSC/A703725; NAS8-9500 (Task 5.2), November 1964, Unclassified.

27. Operational Safety Analysis for Advanced Nuclear Missions. GD/FW, FZK-220; NAS8-11131, 31 December 1964, C/RD.

28. Nuclear Vehicle Flight Safety Systems Performance Studies. LMSC/A651156; NAS8-9500 (Task 5.4), 11 January 1965, Confidential.

29. Mission Oriented Advanced Nuclear System Parameters Study, Final Report. STL reports 8423-6005-RU000 thru 8423-6013-RU000; NAS8-5371, February 1965, some volumes C/RD.

30. Feasibility of Saturn V Class Earth Launch Vehicles for Orbital Assembly of Mars Mission Vehicles, Interim Report. SIB-TR-5; BECO TD A2-ANX-001; NAS8-20073, 30 June 1965, Unclassified.

31. Nuclear Static Test Stage, Systems Definition and Component Analysis, Interim Report. BECO TD A2-ANX-002; NAS8-20073, 30 June 1965, Unclassified.

32. NERVA 2 Class Nuclear Stage (Module) Development Using Saturn V/S-IC Hardware and Facilities. Boeing report D5-13149, 13 August 1965, Unclassified.

33. S-II Stage Hardware for Nuclear Ground Tests. NAA report AS-65-21, September 1965, Confidential.

34. Cold Flow Test Program for the Nuclear Propulsion Module. Rocketdyne report BC1 66-4, September 1965, Confidential.

35. Nuclear Static Test Stage, Systems Definition and Component Analysis, Final Report. BECO TD A2-ANX-002; NAS8-20073, 30 September 1965, Unclassified.

36. Nuclear Propulsion Module Master Design Program. BECO TD A2-ANX-004; NAS8-20073, 15 October 1965, Unclassified.

37. Modular Nuclear Vehicle Performance Characteristics, Final Report. LMSC/A775190; NAS8-20007, October 1965, Unclassified.

38. Feasibility of Saturn V Class Earth Launch Vehicles for Orbital Assembly of Mars Mission Vehicles, Final Report. SED-TR-2; BECO TD A2-ANX-001; NAS8-20073, 29 October 1965, Unclassified.

39. Test Requirements - Nuclear Stage (Preliminary). LMSC-A765547; NAS8-20007, 1 November 1965, Unclassified.

40. Analog Simulation of a Nuclear Cold-Flow Test Stage. BECO TD A2-AVX-012; NAS8-20073, 30 December 1965, Unclassified.

41. Nuclear Propulsion Module Radiation Environment. BECO TD A2-AVX-014; NAS8-20073, 31 December 1965, Unclassified.

APPENDIX D

TECHNICAL REPORTS GENERATED UNDER CONTRACT OR INHOUSE BY THE ASTRIONICS LABORATORY

1. Lockheed Georgia Company: Polymeric Materials Data, Report No. 17, Georgia Nuclear Laboratories, NAS8-5332, May 1965.
2. Lockheed Georgia Company: Components Irradiation Test 14, Georgia Nuclear Laboratories, NAS8-5332, May 1965.
3. Lockheed Georgia Company: Components Irradiation Test 13, Georgia Nuclear Laboratories, NAS8-5332, April 1965.
4. Lockheed Georgia Company: Components Irradiation Test 12, Georgia Nuclear Laboratories, NAS8-5332, March 1965.
5. Lockheed Georgia Company: Components Irradiation Test 11, Georgia Nuclear Laboratories, NAS8-5332, January 1965.
6. Lockheed Georgia Company: Components Irradiation Test 10, Georgia Nuclear Laboratories, NAS8-5332, February 1965.
7. Lockheed Georgia Company: Components Irradiation Test 9, Georgia Nuclear Laboratories, NAS8-5332, January 1965.
8. Lockheed Georgia Company: Components Irradiation Test 7, Georgia Nuclear Laboratories, NAS8-5332, September 1964.
9. Lockheed Georgia Company: Irradiation of Transformer Feedback Amplifiers and Polarized Capacitors, Report No. 20, Georgia Nuclear Laboratories, NAS8-5332, December 1964.
10. Lockheed Georgia Company: Components Irradiation Test 8, Georgia Nuclear Laboratories, NAS8-5332, October 1964.
11. Coleman, D.: Gamma/Annealing/Gamma-Neutron Test for General 2N657A, Transitron 2N657A, and Bendix 2N1711 Transistors, R-ASTR-RT Report, September 1965.
12. Coleman, D.: Gamma/Annealing/Gamma-Neutron Test for General Electric 2N657A and Westinghouse 2N1016D Transistors, R-ASTR-RT Report, October 1965.
13. Burke, H.; Ponder, T.; Clayton, W.; and Crouch, C.: Nuclear Radiation Effects Test of Typical MSFC/Astrionics Measurement Components, IN-R-ASTR-65-1 Internal Note, January 1965.
14. Kennedy, B. W.: Affects of Gamma Radiation on Selected Potting Compounds and Insulating Materials, MTP-ASTR-P-63-16, November 1963.
15. Westrom, J. W.; and Atorthy, D. C.: Design Guidelines for Circuitry in a Nuclear Reactor-Propelled Spacecraft, Lockheed - Huntsville Research and Engineering Center, October 1965.
16. The Bendix Corporation, The ST-124 Inertial Space Platform, Final Report, Phase I, Radiation Study, Eclipse-Pioneer Div., July 1963.

APPENDIX E

TECHNICAL REPORTS GENERATED UNDER CONTRACT

OR INHOUSE BY THE PROPULSION & VEHICLE

ENGINEERING LABORATORY, MATERIALS DIVISION

1. Lucas, W. R.: Effects of Vacuum and Nuclear Radiation on Engineering Materials. The Am. Soc. for Test. and Mat. Sp. Tech. Pub. No. 363, 1964.

2. McKannan, E. C.; and Gause, R. L.: Effects of Nuclear Radiation and Cryogenic Temperatures on Engineering Materials. NASA TMX-53152, 22 October 1964.

3. Gause, R. L.; and McKannan, E. C.: Effects of Nuclear Radiation, Cryogenic Temperature, and Vacuum on the Electrical Properties of Dielectric Materials. NASA TMX 53230, 30 March 1965.

4. McKannan, E. C.; and Gause, R. L.: Effects of Nuclear Radiation and Cryogenic Temperature on Nonmetallic Engineering Materials. Spacecraft and Rockets, vol. 2, no. 4, July-August 1965.

5. General Dynamics, Ft. Worth: First Annual Report, Volume I: Radiation-Vacuum Tests. FZK-161-1; Contract NAS8-2450, 5 January 1963.

6. General Dynamics, Ft. Worth: First Annual Report, Volume II: Radiation-Cryotemperature Tests. FZK-161-2; Contract NAS8-2450, 5 January 1963.

7. General Dynamics, Ft. Worth: Second Annual Report, Volume I: Radiation-Vacuum and Radiation-Vacuum-Cryotemperature Tests. FZK-188-1; Contract NAS8-2450, 1 May 1964.

8. General Dynamics, Ft. Worth: Second Annual Report, Volume II: Radiation-Cryotemperature Tests. FZK-188-2; Contract NAS8-2450, 1 May 1964.

APPENDIX F

TECHNICAL REPORTS GENERATED UNDER CONTRACT

OR INHOUSE BY THE RESEARCH PROJECTS LABORATORY

1. Burrell, M. O.: Space Radiation Doses During Planetary Missions. NASA TMX-53190, Jan 20, 1965.

2. Burrell, M. O.: The Calculation of Proton Penetration and Dose Rates. NASA TMX-53063, Aug 17, 1964.

3. Schofield; Smith; and Hill: Shielding Problems in Manned Space Vehicles. Lockheed-Georgia Co. ER-5997; NASA Contract NAS8-879, Dec 1962.

4. Hill, C. W., et al: Computer Programs for Shielding Problems in Manned Space Vehicles. Lockheed-Georgia Co. ER-6643; NASA Contract NAS-5180, Jan 1964.

5. Hill, C. W., et al: Data Compilation and Evaluation of Space Shielding Problems. Lockheed-Georgia Co. ER-7777, vols. I and II; NASA Contract NAS8-11164, Aug 1965.

6. Burrell, M. O.: The Calculation of Proton Penetration and Dose Rates. NASA TM-X-53063, Aug 17, 1964.

7. Second Symposium on Protection Against Radiation in Space. NASA SP-71, 1964.

8. Data Compilation and Evaluation of Space Shielding Problems. ER 7777, volume I; NASA Contract 8-11164, 1965.

9. Data Compilation and Evaluation of Space Shielding Problems. ER 7777, volume II; NASA Contract 8-11164, 1965.

10. Webber, W. R.: An Evaluation of the Radiation Hazard Due to Solar-Particle Events. Boeing Company, Report No. D2-90469, Dec 1963.

11. Burrell, M. O.; and Wright, J. J.: Orbital Calculations and Trapped Radiation Mapping. NASA TMX-53406, Mar 8, 1966.

12. A Study of Radiation Effects On Composite Structures. Lockheed-Georgia Comapny, NASA Contract NAS8-20206, May 25, 1966.

13. Evaluation of Methods For Computing Nuclear Rocket Radiation Fields. Lockheed-Georgia Co. ER 8236; NASA Contract NAS8-9500, Jan 1966.

14. Collins, D. G.; and DeVries, T. W.: Monte Carlo Calculations of Energy Depositions and Radiation Transport. General Dynamics/Fort Worth, vol. II; NASA Contract NAS8-5182, Dec 21, 1963.

LUNAR AND METEOROID PHYSICS RESEARCH AT MSFC

February 25, 1966

by

Gerhard B. Heller
James B. Dozier, Jr.

TABLE OF CONTENTS

LUNAR PHYSICS AT MSFC

by Gerhard B. Heller

LIST OF TABLES

LIST OF ILLUSTRATIONS

CONTENTS (Continued). . .

LIST OF ILLUSTRATIONS (Continued)

METEOROID AND HYPERVELOCITY IMPACT PHYSICS RESEARCH AT MSFC

by James B. Dozier

LIST OF TABLES

CONTENTS (Concluded). . .

LIST OF ILLUSTRATIONS

LUNAR PHYSICS AT MSFC

By

Gerhard B. Heller

SUMMARY

The papers summarized in this report were given at the Research Achievements Review of Lunar Physics on February 25, 1966. Lunar mission studies have been carried out at Marshall Space Flight Center (MSFC) since 1959 under an Office of Space Sciences Administration (OSSA) assignment. The Office of Manned Space Flight (OMSF) assigned lunar exploration studies to MSFC under AES (Apollo Extension Systems) which then became AAP (Apollo Applications Program). In this Achievements Review the status of lunar surface mission studies was presented by H. Gierow. This served as a general background to the discussions of research achievements. Research on mechanical properties of simulated lunar materials was presented by S. Fields and H. Weathers. Potential lunar materials have been investigated in vacuum chambers at pressures to 10^{-10} newtons per square meter. A thermal model of the lunar surface layers was analyzed by B. P. Jones and J. Harrison. Computer programs were developed that allowed a correlation of heat waves traveling into the moon and of infrared radiation (IR) cooling and heating curves with microwave and IR measurements. So far, none of the thermal models was found to be compatible with all the various measurements.

Research on the bidirectional emittance of electromagnetic radiation, especially IR, was pursued by C. D. Cochran and J. Harrison of Research Projects Laboratory (RPL). Angular dependence of IR radiation differs with lunar longitude and latitude. Another aspect of IR investigations was the far IR analysis of minerals which showed considerable band structure in the far IR.

A computer study of the solar albedo radiation from the moon as it affected a lunar surface craft was discussed by B. P. Jones. It was based on Hapke's treatment of the photometric function.

Lunar surface models, design criteria and the rocket exhaust impingement on simulated lunar surfaces were discussed. Geophysical models have been derived by the U. S. Geological Survey (USGS) and by RPL inhouse and under contract. Geological interpretations and mission planning were based on these models.

INTRODUCTION

Lunar physics has been a subject of research and mission studies since 1959. A study of a soft lunar landing and scientific exploration was conducted by Marshall Space Flight Center (MSFC) for the lunar and planetary organization in the Office of Space Sciences Administration (OSSA). Results were published in 1960 [1]. In 1962, MSFC received an assignment from the Office of Manned Space Flight (OMSF) to study missions for scientific exploration on the moon, and assignments from OMSF and the Office of Advanced Research and Technology (OART) for lunar research. A symposium series, entitled "Physics of the Moon," was held at MSFC in the fall of 1963, and was published as NASA Technical Note D-2944 [2].

This report describes lunar research conducted at MSFC and by MSFC's contractors. Mission and project studies indicate the extent of the research activity. An important activity at MSFC is the contact with other NASA centers, government agencies and the scientific community. A close relationship exists with the U. S. Geological Survey (USGS) in Washington and its branch of Astrogeology in Flagstaff and Menlo Park. Lunar geophysics and geology play prominent roles in scientific mission studies and in lunar research.

Research at the Aero-Astrodynamics Laboratory of MSFC is concentrated on aerodynamic studies of rocket jets impinging on the lunar surface and the establishment of environmental engineering criteria for such interactions of lunar surface craft. Aero-Astrodynamics Laboratory is also doing some studies of the lunar environment.

The Research Projects Laboratory is concerned with the study of the lunar environment, lunar scientific missions, scientific experiments, instrumentation and geophysical models of the moon. Research is done at the Research Projects Laboratory in some selected areas of lunar surface environment, lunar geophysics, thermal aspects of lunar materials and lunar resources.

Present knowledge of the moon's surface is obtained from visual observations, including earth-based and televised spacecraft photographs, and from sensors using electromagnetic radiation.

Figure 1 shows the full moon with landing or impact sites of successful lunar probes. Ranger VII impacted in a previously nameless mare which has been named Mare Cognitum, and Ranger VIII impacted in Mare Tranquilitatis. Ranger IX impacted in the crater Alphonsus. The most recent landing site of the Russian LUNA landing vehicle is in the eastern part of Oceanus Procellarum.

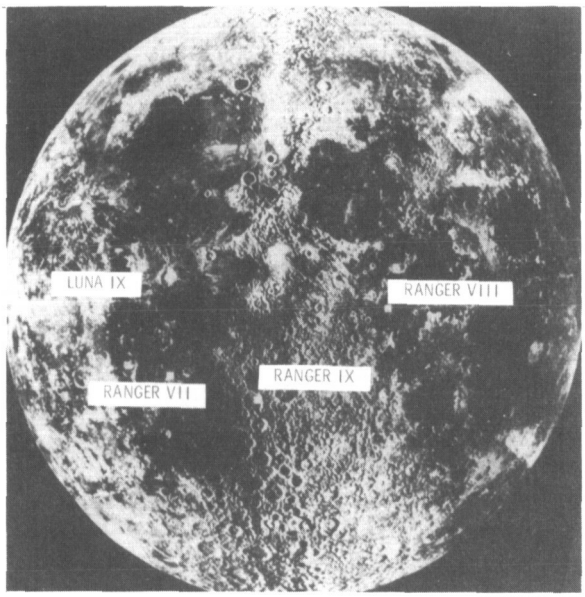

FIGURE 1. FULL MOON WITH SITES OF RANGER AND LUNA IMPACTS

LUNAR SCIENTIFIC MISSION STUDIES

The mission planning efforts for early post-Apollo can be divided into two activities, the first of which concerns the evaluation and selection of potential experiments of scientific or technical merit that are suitable for lunar surface explorations. When candidate experiments are established, various techniques and instruments for obtaining the scientific data must be evaluated. The second activity of lunar surface mission planning may be referred to as operations analysis. That is, after selecting typical experiments and instruments, an investigation is required to determine the best way to accomplish missions on the lunar surface.

Some suggested measurements and equipment categories that evolved from the first activity are as follows: (1) surface geology, (2) subsurface geology, (3) LEM/shelter laboratory geology, (4) surface geophysics, (5) subsurface geophysics, (6) geochemistry, (7) emplaced scientific stations, and (8) astronomical measurements. During the lunar surface explorations, one of the main interests will be the acquisition of information analysis and definitions concerning the geological aspects of lunar surface and subsurface features. Collection of samples will be made for return to earth; the exact location of such samples and any interesting features will be noted [3-11].

The LEM/shelter measurements will be conducted in or near the LEM/shelter. Samples will be selected and analyzed prior to their return to earth. Because of the limited return capability, only the most meaningful samples should be selected, and as much information as possible obtained from the eliminated samples.

The surface geophysics measurement category will include such instruments as the magnetometer and gravimeter and will be used to conduct magnetic and gravity surveys during the lunar mission. Active and passive seismic investigations are also being considered. Another experiment will be the measurement of the mechanical properties of the lunar surface materials, with emphasis upon determining the properties of unconsolidated materials (those that will not be returned to earth for evaluation).

The subsurface geophysics category will require instruments mounted on a subsurface probe to include a thermal diffusivity experiment, a gamma-gamma density experiment, a thermal probe, and a magnetic susceptibility experiment as well as others.

In the geochemistry category, interest will be in natural, active nuclear, and gaseous measurements. The five nuclear measurements being considered are natural gamma for formation identification, spectral gamma radioactive isotope identification, gamma-gamma to establish material density, neutron-gamma for element determination and neutron-neutron measurements to look for hydrogenous material. The gas analysis experiments will be required to perform rapid localized analysis for gaseous emission from the moon's interior, as well as routine residual atmospheric analysis.

The astronomical measurements will consist of two types: optical and radio astronomy.

A typical concept of the lunar drill is portrayed in Figure 2. This particular drill will be capable of drilling to depths in excess of 30.5 meters, and will

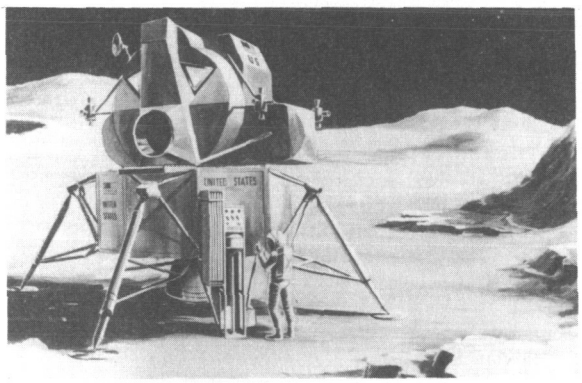

FIGURE 2. MOON DRILL, TYPE 2

provide a borehole of about 5 centimeters in diameter with a 2.5-centimeter core, portions of which will be taken back to earth for analysis. This particular concept uses pure rotary motion for drilling. A drill head unit is connected to the upper surface power system by a rigid drill stem. The core and chips are removed by the wire-line technique which enables removal without withdrawing the drill casing. The approach used is quite conventional and used in drilling operations on the earth. However, the approach to cooling and chip flushing makes the system unique. With a closed two-phase cooling system, tests have shown that this unit will be able to drill without a flushing medium and still remain within the equipment's thermal tolerances. Investigations are also being carried out for a different drill concept which requires both rotary motion and percussive action.

The Emplaced Scientific Station (ESS) is essentially a group of instruments which will be checked out, calibrated and left on the lunar surface for a period of time (up to two years) after departure of the astronauts, to record scientific data expected to show temporal variations. This particular concept is quite similar to the one being considered for use in the Apollo Lunar Surface Experiment Package (ALSEP) program. The main difference in the two is that in the Apollo Applications Program (AAP) there will be more mass available for scientific experiments, and therefore different concepts are employed. This concept uses a central ESS and a series of remote stations referred to as satellites. Figure 3, a typical central station, will have such instruments as a magnetometer, gravimeter, seismometer, mass spectrometer, electric field meter, meteorite panels, and other atmospheric measuring equipment. The typical remote stations would employ a short-period vertical seismometer, a magnetometer, a thermal sensing probe, and an electrical field meter. An ALSEP appears to be an appropriate selection for a satellite station.

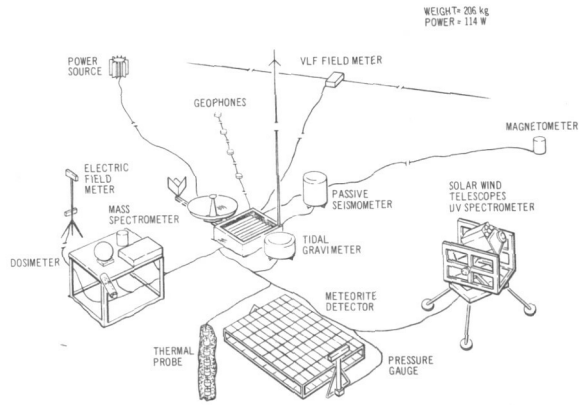

FIGURE 3. CENTRAL STATION GROUP I AND RTG

A typical lunar site at which a specific mission has been studied is shown in Figure 4. The

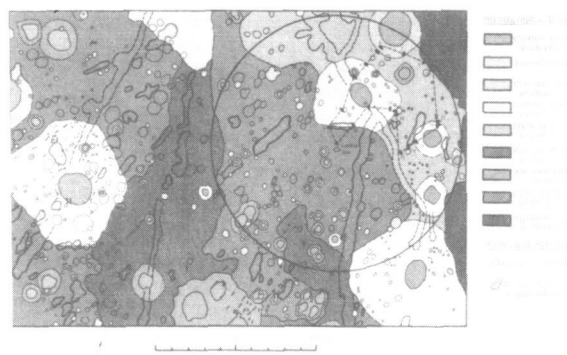

FIGURE 4. PHOTOGEOLOGIC MAP OF THE FLOOR OF THE CRATER ALPHONSUS

particular site lies in the Alphonsus Crater region, and the geological interpretation shown was made by the U. S. Geological Survey from the Ranger IX photographs. This mission analysis was made with the assumption that a small lunar-roving vehicle would be available. The circle in the figure represents the radial distance capability for the mission, which in this case was 8 kilometers. The lines on the right side of the figure are contours which reveal the topography of the area. The geological interpretation of the surface is listed to the right side of the figure. Four types of craters are shown: impact craters, volcanic craters, funnel-type craters and a collapse feature. In addition to crater interpretations, surface material variations are shown. The upper right-hand portion of the figure is representative of the Alphonsus wall material. The large central region is crater floor material which possesses an unusual albedo characteristic, that is, it has the lowest albedo of any material on the lunar surface. The superimposed dotted lines are representative of typical traverses during the mission. The lower left area represents a region which is referred to as a cratered floor material. Due to the resolution, this particular picture does not reveal this unusual concentration of small craters.

The Number 1 traverse will essentially be a run in which samples are collected and the operation of the vehicle is checked out. The second traverse shown is planned for the immediate vicinity of the LEM/shelter, and would be used to emplace the central ESS satellites. Sorties 3 and 4 are typical of those required to emplace the satellites. Two sorties or two earth days are required to emplace each satellite station. One day is used to transport the drill to the station site, to drill and to log a 3.05-meter hole. The second day is required to transport and emplace the satellite station. Other sorties will be required to conduct an active seismic experiment and geological/geophysical reconnoiters to interesting points.

The primary objective for any lunar surface mission on early post-Apollo will be to obtain information about the lunar surface and its environment. Therefore, most of the missions being studied are geophysical/geological reconnaissance missions and are quite typical of the mineral and oil operations conducted here on earth.

STUDY OF MECHANICAL PROPERTIES OF SIMULATED LUNAR MATERIAL

Interpretations of the measurements from earth-bound observations and Ranger photographs have been made with respect to the texture and composition of the lunar surface material. Various investigators have stated that the moon does not seem to have any appreciable dust layer, but appears to be covered with underdense or vesicular material, the density of which increases with depth.

The present research task concerns the study of the forces between particles under ultrahigh vacuum. Knowledge of the mechanical properties of lunar materials is important in interpreting measurements for emplacement of scientific instruments on the moon, and for studies of lunar resources. Earlier research was conducted at a number of places including MSFC. The vacuum applied was limited to the range of 10^{-6} to 10^{-4} newtons per square meter. It was found that this vacuum range was not sufficient to assure outgassing of the particles. The surface adsorption of gases or impurities was of decisive importance in studies of particle adhesion [12]. The vacuum chamber now used for the work at MSFC is an oil-free system with an ultimate range of 10^{-10} newtons per square meter (approximately 10^{-12} torr).

Microphotographs of four types of materials now being investigated are shown in Figure 5. The glass spheres (lower right) are used for comparison and analysis of geometric effects. Pumice and basalt are particles that most likely resemble materials existing on the moon.

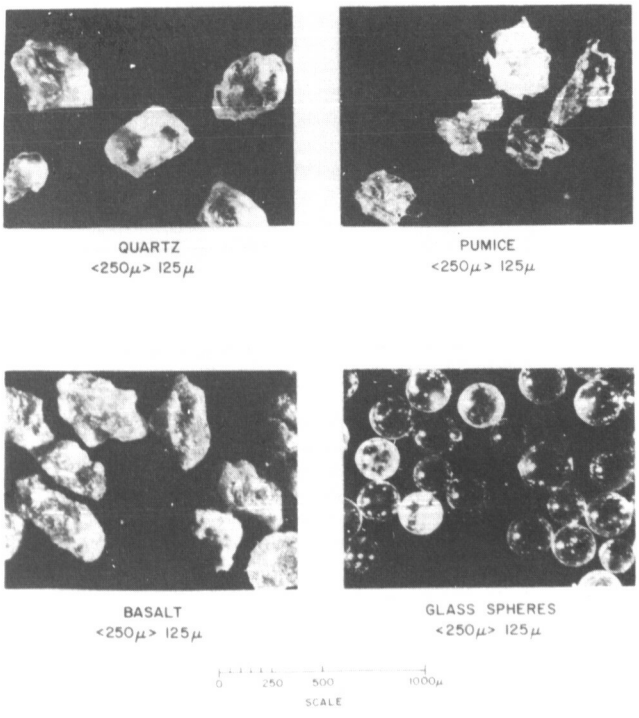

FIGURE 5. MICROPHOTOGRAPHS OF LUNAR TYPE MATERIALS

Dynamic penetration experiments are conducted in both atmospheric and vacuum environments. Metal probes are allowed to free-fall into a prearranged mass of granular material. The depth of penetration of the probe is dependent upon the following parameters: (1) environment pressure and residual gas composition, (2) size of particles, (3) shape of particles, and (4) bulk density.

The mass of the probe and its free-fall distance are held constant. With particles in the range of 62 to 125 micrometers size, the probe's penetration depth into the granular material begins to increase upon attaining a moderate vacuum of 10^{-5} newtons per square meter (10^{-7} torr).

Adhesion characteristics of granular material in a vacuum environment are investigated at 10^{-10} newtons per square meter. A stainless steel drum, 0.25 meter long and 0.15 meter wide, is rotated inside the vacuum chamber. The drum contains the powder to be investigated and is rotated at 1 rpm by using a magnetic rotary seal. The material is lifted up the side of the drum by slats protruding from the inner wall and is then allowed to fall freely to the bottom. This process allows an effective outgassing and removal of adsorbed gases.

Some results of this investigation are shown in Table I. After fifteen minutes of tumbling at 2.3×10^{-9} newtons per square meter (1.7×10^{-11} torr), 100 percent of the basalt powder adhered to the metallic surface and the grains stuck together. For comparison, only 20 percent of the glass spheres adhered to the drum.

MATHEMATICAL MODELS FOR THE THERMAL HEAT WAVES OF THE MOON

Infrared sensors, thermal radiation in the microwave region and radar reflections allow one to look below the lunar surface and form conclusions concerning the properties of lunar soils. Techniques using radiation in various wavelengths of the electromagnetic spectrum have also been proposed for the scientific exploration of the moon. A literature survey on lunar thermophysics was conducted by the Redstone Scientific Information Center [13,14]. The earlier report covers literature up to 1963. The second report [14] covering the period 1963 to 1965 is almost as large as the first report as a result of the scientific community's interest in this subject. An inhouse study has been made of the heat waves traveling into the interior of the moon because of the thermal cycle of lunation* [15].

THERMAL MODEL

Descriptive differential equations for conductive and radiative heat transfer were written and solved numerically on a 7094 computer. In the model used it was assumed that the moon is a semi-infinite solid with solar insolation and Stefan-Boltzmann radiation at the surface. The equations were written for a unit area of surface at the lunar equator.

*Jones, Billy P.: Diurnal Lunar Temperatures (to be presented at the AIAA Thermophysics Specialist Conference, April 17-19, 1967).

TABLE I

EXPERIMENTS WITH SIMULATED LUNAR MATERIALS AT HARD VACUUM

Sample	Size (Micron)	Weight (gm)	Pressure (N/m^2)	Time for 100% Sticking	Remarks
Basalt	10 to 20	180	2.3×10^{-9}	15 min	Adhesion began immediately and at end of time period 100% of the material adhered.
Basalt	20 to 37	180	2.9×10^{-10}	15 min	100% adhesion.
Basalt	37 to 62	180	ATM	---	No adhesion after 12 hours rotation.
			1.3×10^{-7}	30 min	100% adhesion.
Basalt	37 to 62	300	1.7×10^{-9}	---	Less than 5% adhesion after 24 hours. Outgassing limited.
Glass Spheres	20 to 37	180	1.3×10^{-9}	---	Rotated 24 hours. Approximately 20% of material adhered.
Crushed Glass	20 to 37	180	2.7×10^{-10}	---	After 30 min. approximately 98% adhered. Continued for 24 hrs with no further adhesion.

The moon was partitioned into n isothermal layers with respect to depth, and the corresponding n differential equations were solved simultaneously. Temperature was the dependent variable, and time and distance from the moon's surface were the independent variables. The thermal properties appeared as parameters in the equations. By varying these parameters, the calculated temperatures were brought into the best possible agreement with experimental temperatures. The parameter values that provided the best fit were assumed to be representative of the material properties of the moon. The experimental temperatures for the surface were taken from IR data by Sinton; Saari, and Shorthill; and Murray and Wildey. The temperatures beneath the surface were obtained from microwave measurements made by Gibson, Zelinskaya, Troitskii and Fedoseev, Troitskii and Zelinskaya, and others.

RESULTS AND CONCLUSIONS

The calculated curves (solid lines) represent the equatorial temperature for various depths throughout a lunation. Of the cases studied, the (IR) data for the best agreement with surface temperature were obtained when $\alpha_s/\epsilon_t = 1$, with $\alpha_s = 0.87$, and $\epsilon_t = 0.87$. Other pertinent data are given in Table II. Many case studies have been made for a homogeneous model with these results:

(1) a homogeneous model can duplicate the IR data alone.

(2) a homogeneous model can duplicate the microwave data alone, but the thermal properties are not the same for the one that describes the IR data.

(3) the same homogeneous model does not seem to collate both IR data and microwave data.

Two multilayer models were studied. In one, the values for the conductivity k and for the volumetric heat capacity ρc were varied with depth according to a third degree polynomial, and in the other model with depth according to a first degree polynomial. The case where the third degree polynomial was used is shown in Figure 6.

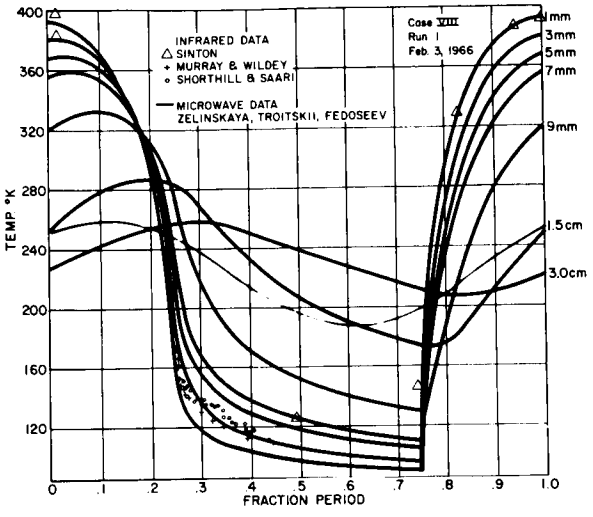

FIGURE 6. THERMAL MODEL OF THE MOON COMPARED TO IR AND THERMAL MICROWAVES

The surface values for k and ρc are assumed to be the same as that for powdered olivine (70 micrometers particle size), and at 2.20 meters depth to be the same as that for basalt. After studying the continuous models, it appears that:

(1) Both microwave and IR data do not seem to collate with either model.

TABLE II

PROPERTY DATA ASSUMED FOR CALCULATIONS

CGS UNITS

Model	(cm) Depth	$\frac{\text{joules}}{\text{sec cm °K}}$ k	$\frac{\text{gm}}{\text{cm}^3}$ ρ	$\frac{\text{joules}}{\text{gm °K}}$ c	$\alpha(=\epsilon)$	
Multilayer (Properties vary linearly with depth)	0 220	1.26×10^{-5} 2.52×10^{-3}	2.0 3.3	0.84 0.84	0.87	Case VII, Run 6
Multilayer (Properties vary according to 3rd degree polynomial)	0 220	1.26×10^{-5} 2.49×10^{-2}	2.0 3.3	0.84 0.84	0.87	Case VIII, Run 1

(2) Although the agreement of the microwave and IR data is fair when compared with the continuous model shown in Figure 6, the match with a calculated curve is good only near the surface.

It should be noted that the heat wave traveling into the surface has a decreasing amplitude and an increasing phase shift with depth. Research in this area is continuing. Mathematical models are expected to allow the analysis of remote sensing by earth-based or lunar-flight instruments.

BIDIRECTIONAL PROPERTIES OF LUNAR IR RADIATION

Earlier studies of the lunar IR emittance, based on measurements by Sinton, revealed a variation with viewing angle (Fig. 7) in the emittance at the subsolar point. The emittance changes from a maximum for zero degrees viewing angle as measured from the vehicle, to 0.60 of this maximum at 90 degrees viewing angle. If the angular distribution of the emittance with an azimuthal angle deviating from the equatorial plane is assumed to be uniform, and if a maximum value of the emittance of 0.98 is assumed, the total hemispherical emittance for the subsolar point at zero degrees is determined as 0.89 [5].

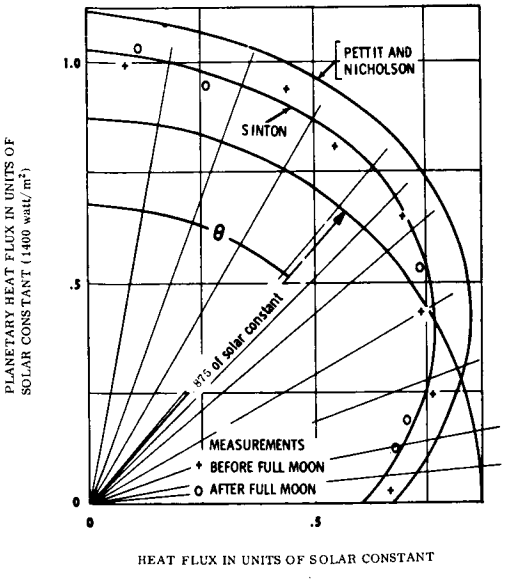

FIGURE 7. POLAR DIAGRAM OF IR FLUX DENSITY AT SUBSOLAR POINT

Research has been carried out inhouse at RPL and Brown Engineering Company to determine the angular properties of the lunar IR radiation for various phases and bidirectional viewing angles (lunar coordinates) [16]. Measurements made by Shorthill and Saari of Boeing during a lunar eclipse were evaluated.

If measured from the subsolar point prior to the eclipse, thermal anomalies can be seen against a background of gradual temperature variations with lunar coordinates.

Figure 8 represents a log-log plot of a temperature traverse vs. the cosine of the angle measured from the subsolar point at a phase angle of 90 degrees. An attempt was made to establish the characteristics of the lunar surface disregarding the anomalies and choosing points of equal albedo (Fig. 9) for a lunar phase of -2.27 degrees. The temperature dependence follows a $\cos^{1/4}\theta$ law from $0.20 < \cos\theta < 1$. When $\cos\theta < 0.20$, the temperature follows a $\cos^{1/6}\theta$ law. An analysis of the subsolar point as a function of $\cos\theta$ showed a $\cos^{1/6}\theta$ relationship identical to that of Sinton. The angular dependence with respect to lunar latitude shows a similar break as in Figure 8.

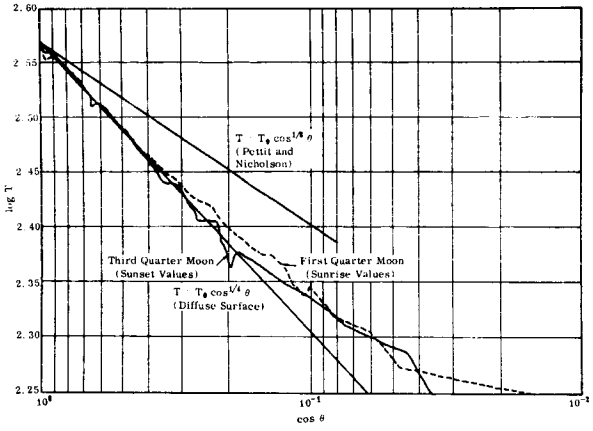

FIGURE 8. VARIATION OF BRIGHTNESS TEMPERATURE T WITH θ, ANGULAR DISTANCE FROM SUBSOLAR POINT FOR LUNAR PHASES ± 90°

The total hemispherical emittance cannot be determined from the evaluation made thus far because only relative values are shown. It can be assumed that the maximum emittance value at the subsolar point as viewed at a phase angle of 45 or 90 degrees is not the same as that for the Sinton case described earlier. Brightness temperatures and not absolute temperatures are traced in Figures 8 and 9. It is intended that research in this area be continued.

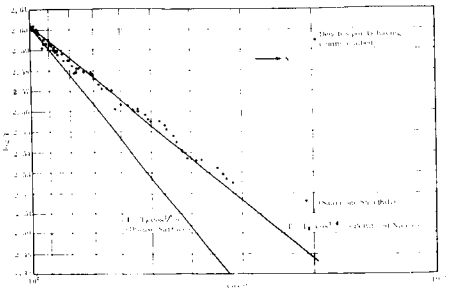

FIGURE 9. VARIATION OF BRIGHTNESS TEMPERATURE T WITH θ, ANGULAR DISTANCE FROM THE SUBSOLAR POINT FOR LUNAR PHASE -2° 16' 6.7"

RPL has an IR radiometer which was built under contract with Southern Research Institute [17]. Although it is a laboratory instrument, RPL plans to use it with the astronomical telescope of the Rocket City Astronomical Association on Monte Sano Mountain, Huntsville, Alabama to make lunar IR measurements. A study of the IR transmissivity of the local area has revealed that good measuring conditions exist quite frequently. With the use of IR narrow band filters, variations in atmospheric transmittance can be greatly reduced.

ADAPTATION OF THE PHOTOMETRIC FUNCTION OF THE MOON FOR VEHICLE ENERGY EXCHANGE*

The photometric function of the moon has been investigated and an adaptation of the theoretical treatment has been made for the thermal heat transfer to lunar surface vehicles. A simplified version of the photometric function can be expressed as a product of three terms:

$$I(i, \epsilon, \alpha) = \left[E_0 \left(\frac{\cos i}{\cos i + \cos \epsilon}\right) a d\omega\right]\left[\frac{2}{3\pi}\left(\frac{\sin \alpha + (\pi - \alpha)\cos \alpha}{\pi}\right) b\right]\left[B(\alpha, g)\right]$$

where

$$B(\alpha, g) = \begin{cases} 2 - \frac{\tan \alpha}{2g}\left(1 - e^{-g/\tan \alpha}\right)\left(3 - e^{-g/\tan \alpha}\right) & \text{for } \alpha \neq \frac{\pi}{2} \\ 1 & \text{for } \alpha = \frac{\pi}{2} \end{cases} \qquad (1)$$

$$g = \frac{2y}{\tau}$$

The symbols in equation (1) are as follows:

$I(i, \epsilon, \alpha)$ = total energy per unit area per unit time reaching the detector (on earth)

E_0 = radiant energy per unit area per unit time, normal to the incidence direction

i = angle between the direction of incident solar energy and the normal to the apparent surface

ϵ = angle between a reflected ray reaching the detector and the normal to the apparent surface

α = angle between the direction of incident solar energy and the direction of observation

a = light sensitive area of the detector

$d\omega$ = solid angle of the acceptance cone of the detector

b = total reflectivity of a particle or lump of material; (1 - b) is the fraction of incident energy which is absorbed

$g = \frac{2y}{\tau}$, where

- y = the effective radius of the retrodirective tube
- τ = mean free path of an incident ray through the semiopen surface. Assumed to be equal to $1/n\,\sigma$, where
  - n = number of reflecting objects per unit volume, and
  - σ = average cross-sectional area of an object, particle or lump of material.

In this equation derived by Hapke, the first bracket is the Lommel-Seeliger reflection law (causes the function to go to zero as i goes to $\pi/2$);

*Jones, Billy P.: Hapke's Lunar Photometric Function Adapted to Vehicle Energy Exchange (Internal Report, R-RP-INT-64-13, Research Projects Laboratory, April 1, 1964; to be published later as a NASA TM X.)

the factor in the second bracket is the Schoenberg scattering law for a single, opaque, Lambert sphere; the factor in the third bracket is a retrodirective reflection derived from geometrical considerations of a delicate, highly porous structure. The terms are illustrated on Figure 10. Modification of Hapke's

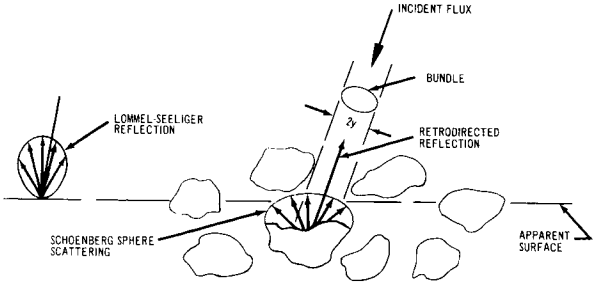

FIGURE 10. SCHEMATIC OF BASIC TERMS OF LUNAR PHOTOMETRIC FUNCTION

function for use in energy balance calculations for vehicles on the lunar surface requires the following interpretations and substitutions:

detector = dA_2 on the vehicle surface

a = $dA_2 \cos \theta_2$, since the detector area is always perpendicular to the observed central line of reflection, whereas dA_2 on the vehicle is not; the $\cos \theta_2$ accounts for projection of dA_2 in direction of observed reflection

$d\omega = \frac{dA_1 \cos \epsilon}{S^2} = \frac{dA_1 \cos \theta_1}{S^2}$, since $\epsilon = \theta_1$, by definition

Therefore,

$ad\omega = \frac{\cos \theta_1 \cos \theta_2 \, dA_1 dA_2}{S^2}$, a familiar expression in radiative exchange

α = angle between incident solar flux and the line-of-sight from dA_2 to dA_1. For a particular vehicle geometry this angle can be expressed in terms of the other three, i.e., $\alpha = \alpha(i, \theta_1, \theta_2)$

With these interpretations and substitutions, the expression for the energy flux received by dA_2 from dA_1 becomes:

$$I[i, \theta_1, \theta_2, \alpha(i, \theta_1, \theta_2)] = \left[E_\odot \left(\frac{\cos i}{\cos i + \cos \theta_1}\right)\left(\frac{\cos \theta_1 \cos \theta_2}{S^2}\right) dA_1 dA_2\right] \left[\frac{2}{3\pi} b\left(\frac{\sin \alpha + (\pi - \alpha)\cos \alpha}{\pi}\right)\right]\left[B(\alpha, g)\right]$$

which can be expressed as

$$I(i, \theta_1, \theta_2, \alpha) = \left[E_\odot \left(\frac{\cos \theta_2}{\sec \theta_1 + \sec i}\right) \frac{dA_1 dA_2}{S^2}\right]\left[\frac{2}{3\pi} b\left(\frac{\sin \alpha + (\pi - \alpha)\cos \alpha}{\pi}\right)\right]\left[B(\alpha, g)\right],$$

where

$$B(\alpha, g) = \begin{cases} 2 - \frac{\tan \alpha}{2g}\left(1 - e^{-g/\tan \alpha}\right)\left(3 - e^{-g/\tan \alpha}\right) & \text{for } \alpha \le \frac{\pi}{2} \\ 1 & \text{for } \alpha \ge \frac{\pi}{2} \end{cases} \qquad (2)$$

and

$$g = \frac{2\gamma}{\pi}, \quad (0 \le g \le 1).$$

In order to calculate the total energy transferred from an area of the moon, A_1, to a vehicle, an integration is required over the respective areas, A_1 and A_2 (a double integration). It is also necessary to substitute an explicit expression for $\alpha = \alpha(i, \theta_1, \theta_2)$ for the particular vehicle geometry prior to the integration. The term in the energy balance for A_2 would be $\alpha_S I$, where α_S is the absorptivity of surface A_2 with respect to the solar spectrum.

A more detailed study will be published later in a NASA TMX. Inhouse measurements on the albedo of simulated lunar materials are being conducted at RPL.

LUNAR SURFACE MODEL AND DESIGN CRITERIA

An analysis of the Ranger photographs has been made at MSFC relative to present knowledge of the moon and the planning of lunar surface missions. Figure 11 shows a photo from Ranger IX. The frame size covers an approximate area of 40 by 40 kilometers. This picture was chosen because it shows a variety of interesting lunar features, such as an impact crater, secondary craters, a halo crater, collapse features, and a rille. The evaluation of the Ranger pictures by the chief investigators (Drs. Shoemaker and Kuiper and their co-workers) has helped to improve the planning of scientific lunar missions.

Studies of geophysical models of the moon have been conducted by Research Projects Laboratory and Brown Engineering Company [18-21]. The geological age has been determined from the fact that rocks and dust thrown from craters, or flows

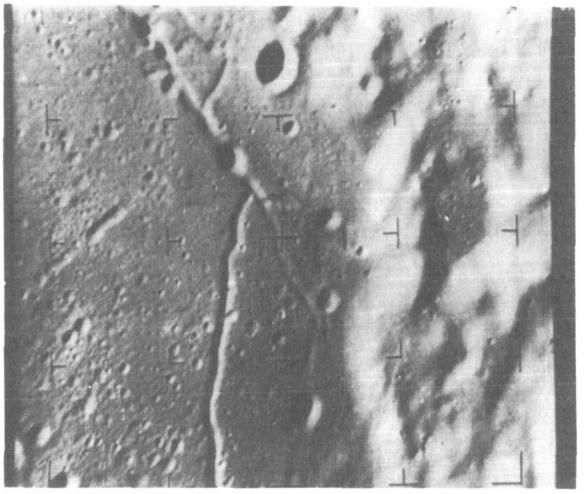

FIGURE 11. PHOTOGRAPH OF CRATER ALPHONSUS FROM RANGER IX

filling in the mare basins, cover the layers of the moon. A study of a geophysical model of the moon is presently under way by J. Bensko of Research Projects Laboratory and Hayes International Corporation under contract to MSFC [22]. One interpretation of the lunar surface and subsurface geology in the Appennine Mountain region (Fig. 12)

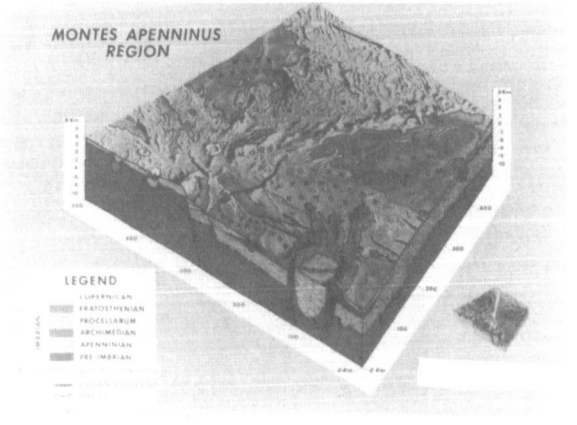

FIGURE 12. SURFACE GEOLOGY OF THE MOON

is based upon work by the U. S. Geological Survey. The oldest lunar formation in the figure is called Pre-Imbrian. The mountain material is called Appenninean and is younger than the Pre-Imbrian upon which it rests. Other formation materials, shown in sequence of age, are named according to the crater Archimedes, the Oceanus Procellarum and the craters Eratosthenes and Copernicus [23].

Another aspect of lunar surface analysis is presented by the work of the Aero-Astrodynamics Laboratory, especially that of W. Vaughn in lunar terrain analysis. These studies formulate the lunar environmental design criteria for landing gear and for surface mobility studies [24-27]. Topographic maps developed from the Ranger VII pictures indicate that the lunar Mare Nubium photographed by Ranger VII has a 7. 9-percent slope in the 10 to 20-degree range for a linear traverse. This is near the 5 percent postulated by a model published earlier by Mason, McCombs and Cramblit [28].

Topographic maps produced by the USGS Branch of Astrogeology, using Ranger VIII pictures, are being used in the analysis. Figure 13 shows a photograph taken from a lunar surface model which was prepared from these maps by the USGS for MSFC. The elevation angle of the illuminating light is 23 degrees above the horizontal.

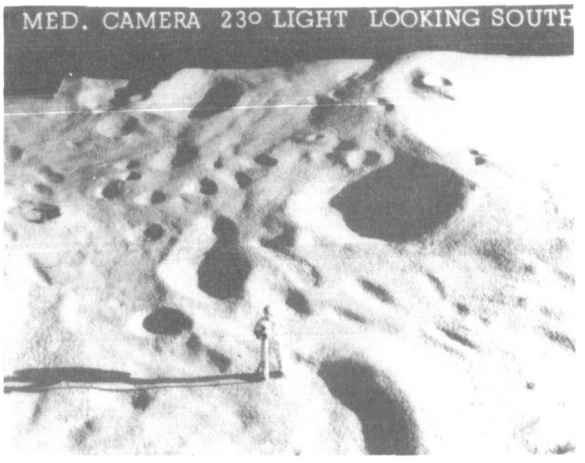

FIGURE 13. PHOTOGRAPHIC STUDY OF LUNAR LIGHTING CONDITIONS

ROCKET EXHAUST IMPINGEMENT ON SIMULATED LUNAR SURFACE SHAPES

The Propulsion and Vehicle Engineering Laboratory has conducted tests on two problems,

the solutions of which are required for design studies of lunar vehicles. One series of tests was to determine the effects of a rocket exhaust jet on various types of expected lunar surface materials. In another series, the friction of landing gears was determined by drag tests. The two series of tests were concluded during 1965, and the results were reported in an earlier achievements report of this series [29].

Presently, tests are in progress in the Aero-Astrodynamics Laboratory to study the aerodynamic problem connected with jet impingement. Pressure levels in the combustion chamber are 200 to 500 newtons per square meter, exhausting into a vacuum chamber to provide overall pressure ratios of 3 to 8×10^7. The objectives of the program are:

(1) To estimate the forces and heat transfer rates caused by plume impingement,

(2) To estimate erosion rates, cavity shapes, and rock or sand dispersion,

(3) To determine heat transfer rates caused by the rocket exhaust.

The program is so new that no results can be reported at this time, but will likely be published at a later date.

ANALYSIS OF SIMULATED LUNAR MATERIALS IN THE FAR INFRARED

Measurements of IR spectra have been conducted by several investigators concerned with lunar geology and earth remote sensing. The problem of light scattering becomes appreciable if the diagnostic wavelength equals the scattering diameter of the particles. It appears desirable to extend investigations into the far IR to a wave number of 50 per centimeter. The spectrum of albite shown in Figure 14 has a range of wave numbers from 675 to 50 per centimeter, measured by A. D. Little, Inc. under contract to MSFC [30]. Several other minerals have been investigated, such as serpentine, hornblende, troilite, chrondrite, and its components forsterite and fayalite.

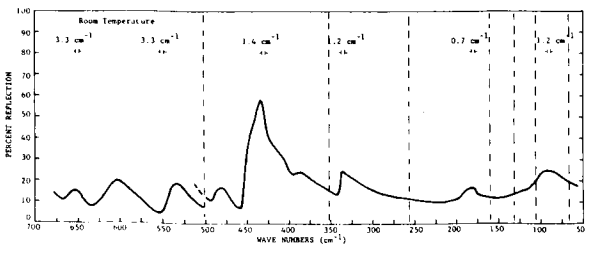

FIGURE 14. FAR INFRARED REFLECTION OF ALBITE

Another aspect of the underdense material expected to be found on the surface of the moon is the determination of its diffusivity and thermal conductivity. Experiments have been conducted at Research Projects Laboratory and at A. D. Little, Inc. to determine these thermal properties [31]. The thermal conductivity of pumice powder as a function of the gas pressure and particle size is shown in Figure 15. In a vacuum the thermal

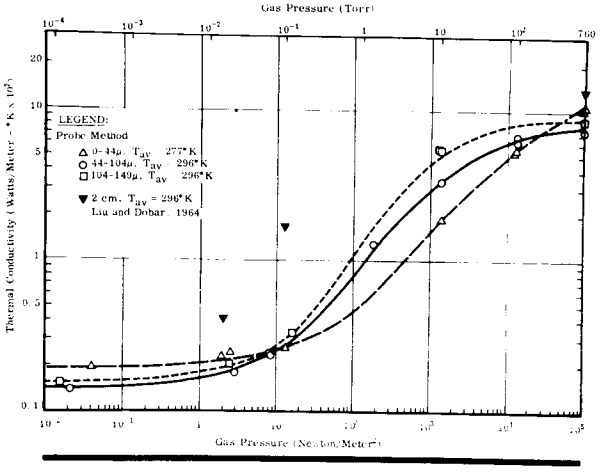

FIGURE 15. THERMAL CONDUCTIVITY OF POWDERED PUMICE - EFFECT OF PARTICLE SIZE

conductivity of pumice powder is two orders of magnitude less than the conductivity in air. The particle size has a smaller influence on the thermal conductivity than the vacuum. It is interesting to note that the smallest particles have the highest value of the conductivity k at ambient pressure, and the lowest k at pressures from 3×10^4 to 1.1×10 newtons per square meter. Below 10 newtons per square meter the k value is again the highest of the three samples shown. Another result of this research concerns the influence of the bulk density on heat transfer. If the density is reduced, the heat transfer decreases. The heat transferred goes through a minimum and rises again at very low bulk densities. At low bulk densities the radiative heat transfer mode becomes the predominant one.

CONCLUSION

The study of lunar scientific missions and research work on lunar physics have been conducted at MSFC since 1959. Studies of lunar missions were carried out under assignments from OSSA and OMSF. Lunar inhouse research is sponsored by OART. Results presented were based on both inhouse research by various Research and Development Operations Laboratories and by MSFC contractors.

The research achievements presented constitute a high level of lunar-oriented scientific capability. The coverage is not all-inclusive, but the specific examples presented are an indication of the knowledge and research capabilities at Marshall (see Appendix A).

The scientific areas and studies specifically covered in this report are lunar scientific exploration, mechanical properties of simulated lunar materials, a thermal model of the lunar surface, a computer program to determine the effects of lunar photometric function on the radiation equilibrium of lunar surface craft, lunar IR measurements and their angular dependence, the far IR investigations of minerals, aerodynamics of rocket impingement, and rock and slope distribution on the lunar surface.

REFERENCES

1. Bucher, G. C., ed.: A Lunar Exploration Program Based Upon Saturn-Boosted Systems, Report DV-TR-2-60, Army Ballistic Missile Agency, Huntsville, Alabama, February 1960.

2. Bucher, G. C.; and Stern, H. E., eds.: Physics of the Moon, NASA TN D-2944, November 1965.

3. Stanley, J. T.; and Lucas, W. C.: Northrop Report NAS CR 61103, January 1965.

4. Zaitzeff, E. M.; and Tiffany, O. L.: Scientific Mission Support Study. Bendix Report BSR-1207, November 1965.

5. Zaitzeff, E. M.; and Tiffany, O. L., eds: Scientific Mission Support Study. The Bendix Corp., Contract NAS8-20199, May 5, 1965.

6. Weber, A. W., et al.: NASA TM X-53287, June 28, 1965.

7. NASA 1965 Summer Conference on Lunar Exploration and Science held at Falmouth, Mass. NASA SP-88, 1965.

8. Model of Lunar Surface (Model of a Ranger VII Landing Site). (USGS Flagstaff, January 4, 1965.)

9. McDuffie, J. M.: Objectives of Investigations Conducted upon Lunar Surface as an Approach to Ranking Experiments for AES Mission. Technical Memo R-5-65-5, Brown Engineering, May 27, 1965.

10. Rogers, J. R.: A Geological Analysis of Five Proposed Apollo Extension System Missions. Tech Memo R-7-65-2, Brown Engineering, July 1965.

11. McDuffie, J. M.: Approach to the Problem of Optimum Experimentation for AES Lunar Surface Missions. Tech Memo R-7-1-65, Brown Engineering, July 1, 1965.

12. Weathers, H. M.; and Fields, S. A.: Dynamic Penetration Program for Simulated Lunar Soils. R-RR-T-WP-19-65, December 1965.

13. McNutt, W. P., et al.: Lunar Thermophysics. RSIC-419 Report sponsored by USAOMC and NASA-MSFC, June 1965.

14. McNutt, W. P., et al.: Lunar Thermophysics. RSIC-462, Supplement to RSIC-419, September 1965.

15. Schocken, K.: Thermal Environment of the Terrestrial Planets, Supplement 5. NASA TM X-53241, April 28, 1965.

16. Montgomery, C. G.; and Six, F.: Empirical Determination of an Expression for Predicting the Lunar Thermal Emission at Various Angles of Observation. Interim Progress Report RPL-13870-1, Contract No. NAS8-20166, prepared by Brown Engineering, January 8, 1966.

17. Bird, Jr., A. N.; and Cisco, D. L.: Development and Construction of an Infrared Radiometer. Final Report under Contract NAS8-11762, Southern Research Institute (7402-1633-X), July 30, 1965.

18. McDuffie, J. M.; Rogers, J. R.; Robinson, J. E.; and Heaps, S. N.: A Lunar Surface Mission Based on a Minimum Performance Traverse Vehicle. Brown Engineering Tech Note R-175, January 1966.

19. Rogers, J. R.: An Analysis of Proposed Lunar Sites for Post-Apollo Missions. Tech Note R-158, Brown Engineering, October 1965.

REFERENCES (Concluded)

20. McDuffie, J. M.: A Numerical Approach to the Selection of Experiments to Meet Objectives of Lunar Investigations. Brown Engineering, Tech Note R-162, October 1965.

21. Robertson, J. R.; Scalf, J. E.; and White, J. E.: Lunar Surface Exploration. Brown Engineering, Tech Note R-160, November 1965.

22. Sanders, R.: Lunar Terrain Analysis. Contract NAS8-20173, Hayes International Corp., June 26 to December 25, 1965.

23. Rogers, J. R.: An Illustration of the Geology of the Moon, Montes Appennius Region. Brown Engineering, Tech Memo AA-1-65-6, January 1965.

24. Howard, W. W.; and Buller, R. L.: Space Environment Criteria: Space Environment Bibliography. NASA CR-61036 under Contract NAS8-11285, Aerojet General, Azusa, California, February 3, 1965.

25. Rogers, J. R.; and Vaughn, O. H.: Lunar Environments: An Interpretation of the Surface of the Moon and its Atmosphere. NASA TM X-53124, September 1964.

26. Heaps, S. N.; and Scoggins, W. H.: Lunar Terrain Analysis. Hayes Aircraft Report Tech Report H-MOL-20-R, April 30, 1965.

27. Smith, R. E.: Space Environmental Criteria Guidelines for Use in Space Vehicle Development. NASA TM X-53273, May 1965.

28. Mason, R. L.; McCombs, W. M.; and Cramblit, D. C.: Engineering Lunar Model Surface (ELMS). KSC TR83-D, X64-16787, April 14, 1964.

29. Blumrich, J.: Structures Research at Marshall Space Flight Center. NASA TM X-53424, October 1966.

30. Aronson, J. R.; Emslie, A. G.; Allen, R. V.; and McLinden, H. G.: Far Infrared Spectra of Silicate Minerals for Use in Remote Sensing of Lunar and Planetary Surfaces. A. D. Little, Inc., Final Report under contract NAS8-20122, April 15, 1966.

31. Wechsler, A. E.; and Glaser, P. E.: Thermal Properties of Postulated Lunar Surface Materials. Report under contract AF 19-(628)-421: NAS8-1567, (Proceedings of the Lunar Surface Materials Conference, Boston, Mass.) Academic Press, May 1963.

APPENDIX A

LUNAR PHYSICS RESEARCH REPORTS GENERATED INHOUSE BY
THE RESEARCH PROJECTS LABORATORY

1. Cochran, C. D.; and Fountain, J. A.: Infrared Lunar Temperature Measurements. R-RP-T Working Paper, January 15, 1963.

2. Cochran, C. D.; and Fountain, J. A.: Polarization of the Moon. R-RP-T Working Paper, January 15, 1963.

3. Cochran, C. D.: Infrared Methods of Measuring the Moon's Temperature. Physics of the Moon, NASA TN D-2944, November 1965.

4. Cochran, C. D.: RPL Radiometer. R-RP-T Working Paper, April 6, 1966.

5. Cochran, C. D.: Considerations for the Purpose and Scope of Infrared Experiment to be Performed on the Moon from Lunar Orbit. R-RP-T Working Paper, June 20, 1966.

6. Cochran, C. D.; and Fountain, J. A.: Infrared Spectroscopy, Radiometry and Thermal Imagery of Mars and Venus. R-RP-T Working Paper, July 6, 1966.

7. Cochran, C. D.; and Fountain, J. A.: Thermal Conductivity Measurements. Progress Report presented at Second Annual Southeastern Seminar on Thermal Sciences, July 25, 1966.

8. Cochran, C. D.; and Fountain, J. A.: Thermal Infrared Studies. R-RP-T Working Paper, July 25, 1966.

9. Cochran, C. D.: RCAA Telescope Improvements for Useful Infrared Astronomy. R-RP-T Working Paper, September 2, 1966.

10. Fields, S. A.; and Weathers, H. M.: Status of OART Funded Projects in Lunar Physics. presented to members of the OART Research Program, R-RP-T-WP-6-65, Marsh 23, 1965.

11. Fields, S. A.; and Weathers, H. M.: Abstracts of Papers on Dynamic Penetration Experiments. R-RP-T-WP-11-65, July 1965.

12. Fields, S. A.: The Behavior of Simulated Lunar Materials in an Ultrahigh Vacuum Environment. presented at the 43rd Annual Meeting of the Alabama Academy of Science, April 1-2, 1966.

13. Fields, S. A.; and Weathers, H. M.: Dynamic Penetration Experiments Utilizing Quartz Material. R-RP-T-WP-5-66, May 1966.

14. Harrison, J. K.: A Means of Measuring the Thermal Emission of the Moon Using a Lunar Orbiting Satellite. Masters Degree Thesis, U. of Ala., August 1964.

15. Harrison, J. K.: Computer Program--Cryogenic Storage on the Moon (Subroutines A and C). NASA TM X-53270, June 6, 1965.

16. Harrison, J. K.: Brightness Temperatures on the Moon as a Function of Angle of Observation. M-RP-INT-66-4, August 10, 1966.

17. Heller, G. B.: The Thermal Model of the Moon. Physics of the Moon, NASA TN D-2944, November 1965.

18. Jones, B. P.: Hapke's Lunar Photometric Function Adapted to Vehicle Energy Exchange. R-RP-INT-64-13, April 1964.

19. Jones, B. P.: Thermal Properties of the Moon as a Conductor of Heat (A Survey). Physics of the Moon, NASA TN D-2944, November 1965.

20. Jones, B. P.; Gates, D.W.; Harrison, J.K.; and Watkins, J.R.: Lunar Thermal Environment. NASA TM X-53499, August 26, 1966.

21. Russell, L.W.: Lunar Radiometric Experiment. R-RP-T-WP-3-66, March 1966.

22. Schocken, K.: The Thermal Balance on the Moon. M-RP-INT-62-9, August 1962.

23. Schocken, K.: The Thermal Environment of the Terrestrial Planets. MTP-RP-62-7, September 15, 1962.

24. Schocken, K.: The Thermal Environment of the Terrestrial Planets (1st Supplement). MTP-RP-63-5, April 24, 1963.

25. Schocken, K.: The Thermal Environment of the Terrestrial Planets (2nd Supplement). MTP-RP-63-6, August 16, 1963.

26. Schocken, K.: The Lunar Surface. R-RP-INT-63-17, November 25, 1963.

27. Schocken, K.: The Thermal History of the Moon. R-RP-INT-64-2, January 13, 1964.

28. Schocken, K.: Heat Transfer by Infrared Radiation in Powders. R-RP-INT-64-7, February 12, 1964.

29. Schocken, K.: The Thermal Environment of the Terrestrial Planets (3rd Supplement). TM X-53016, March 2, 1964.

30. Schocken, K.: The Thermal Environment of the Terrestrial Planets (4th Supplement). TM X-53138, September 30, 1964.

31. Schocken, K.: The Composition of the Moon. R-RP-INT-65-9, August 25, 1965.

32. Schocken, K.: The Thermal and Electrical Conductivity of Powders. R-RP-INT-65-15, November 1965.

33. Weathers, H.M.; Bensko, J.; Cortez, J.L.; and Fields, S.A.: Lunar Surface Conditions. Lunar Logistic System, Vol. III, MTP-M-63-1, March 15, 1963.

34. Zwiener, J.M.: Thermal Control Analysis of Objects on the Lunar Surface. Physics of the Moon, NASA TN D-2944, November 1965.

METEOROID AND HYPERVELOCITY IMPACT PHYSICS RESEARCH AT MSFC

By

James B. Dozier

SUMMARY

A research and development program in meteoroid technology is described in this review. The purpose of this program is to provide input data to spacecraft design criteria and to the calculation of mission probabilities for both manned and unmanned missions. The direct measurement of penetration frequencies of structural material is used to directly generate engineering design data as well as to infer other properties of meteoroids.

A meteoroid simulation and impact phenomena study program deals with the development of techniques for accelerating threshold particles to near-meteoroid velocities, the experimental simulation of cratering, shock, and ionization phenomena and development of theoretical methods which accurately predict experimentally observed phenomena. The meteoroid environment studies program involves the Pegasus flight measurements and a laboratory program to assess Pegasus and other flight and ground-based measurements and to develop, test, and calibrate sensors for the measurement of various meteoroid parameters.

Inhouse research and development, which provide essential support for the whole program, include the reduction, evaluation, and analysis of flight data, the construction of mathematical meteoroid models from the data, failure and rupture criteria measurements, detector calibration, development of hydro codes, and study of ionization and flash phenomena.

INTRODUCTION

"Shooting Stars," the bright luminous trails produced by frictional heating of meteoroids, have attracted the attention of observers for centuries. Astronomers developed optical, and later radar techniques for determining mass distributions and orbital parameters of meteoroids, and many meteoroids that partially survived the passage through the atmosphere were collected and analyzed for composition and physical properties. In the late 1950's, the academic interest in the cosmological implication of the origin of meteoroids was supplemented by an immediate practical need for a sufficiently detailed knowledge of the meteoroid environment in the solar system to provide criteria for spacecraft design.

The Marshall Space Flight Center has been pursuing a broad meteoroid physics program directed toward a full understanding of the meteoroid environment in space and the effect of this environment on spacecraft components. Such information furnishes an input to spacecraft design criteria and provides the means to calculate mission probabilities for both manned and unmanned missions. The program may be divided into (1) meteoroid simulation and impact phenomena studies and (2) meteoroid environment studies. The goal of the simulations and impact phenomena work is to acquire a complete understanding of the physics of impact in order to predict the results of the impact of any projectile (meteoroid) on any target (spacecraft) and to relate impact phenomena to projectile properties. The goal of the meteoroid environment studies is an understanding of the meteoroid environment in the solar system. This would ultimately require a knowledge of the mass distribution, the velocity distribution, and the physical properties of meteoroids (see Appendices A and B).

A complete knowledge of the meteoroid environment and of the physics of impact will result in the ability to provide engineering design criteria for any mission and for any required mission success probability. It is also possible within the framework of the program to secure direct meteoroid penetration frequency measurements in several thicknesses of specific materials as is done in the case of the Pegasus satellites, and to thereby provide engineering design criteria directly.

IMPACT PHENOMENA AND METEOROID SIMULATION

The work carried on under the general heading of Impact Phenomena may be divided into three general areas: acceleration techniques, experimental techniques, and theoretical studies (Figs. 1 and 2). Each of these areas involve a number of subjects as shown in Figure 3.

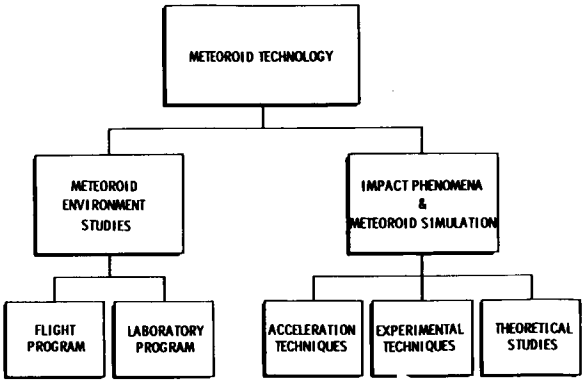

FIGURE 1. METEOROID PHYS.. PROGRAM

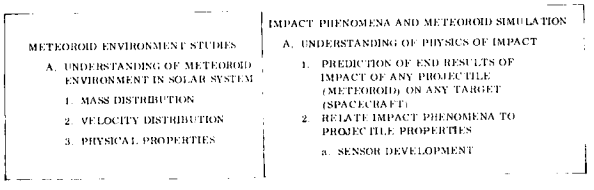

FIGURE 2. PROGRAM GOALS

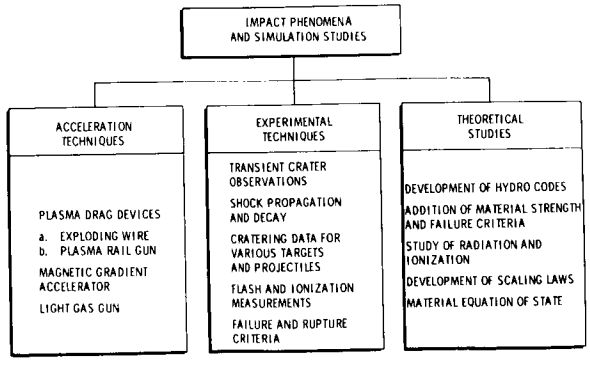

FIGURE 3. STUDIES TO PROVIDE ENGINEERING DESIGN CRITERIA

ACCELERATION TECHNIQUE

The velocity range of interest for meteoroids is from 10 kilometers per second to 70 kilometers per second. The electrostatic accelerators have the capability of exceeding the lower limit of meteoroid velocities, but a few microns is the maximum particle size for which these accelerators are useful. Principal emphasis in this laboratory has been in the development of accelerators capable of accelerating particles in the 100-micron to 1000-micron size. Particles of this size are capable of penetrating spacecraft walls and are numerous enough to present a problem to spacecraft design. Plasma drag devices and magnetic gradient accelerators may be capable of accelerating 100- to 1000-micron particles to velocities of 25 kilometers per second. Of considerable interest in providing experimental data for study of impact phenomena are larger particles at higher velocities. The light gas gun has been used extensively for accelerating larger particles, and although many techniques have been attempted to augment its velocity capability, it has still not achieved velocities much above the minimum meteor threshold.

Plasma Drag Devices. In this area, the goal is to develop a practical method for accelerating particles in the 100-micron to 1000-micron size to velocities near 20 kilometers per second. An early effort provided support to North American Aviation in setting up a facility and developing an exploding wire accelerator. This gun operates from a plasma generated by electrically heating a lithium wire to drag accelerate glass beads ranging to 90 microns in size. Velocities of 12 to 16 kilometers per second are routinely achieved with this device and a maximum velocity of near 20 kilometers per second has been achieved for 50-micron spheres. Increasing the velocity of the plasma by increasing the heat energy imparted to it restricts the type of projectile that can be accelerated, and a somewhat different technique is being developed to overcome this disadvantage of the exploding wire. A contract with MB Associates to develop a plasma rail gun is under way. This device magnetically accelerates a metallic plasma that is formed by a capacitor discharge through a metal film used to short-circuit a pair of conducting rails. The plasma is subsequently contained and accelerated by self-generated magnetic fields. Velocities of 10 kilometers per second have been obtained with particles of 400-micron size. An optimization program is now under way to improve these figures.

Magnetic Gradient Accelerator. A program is being carried out with Aerojet General Nucleonics to develop a magnetic gradient accelerator. Very large, nonuniform magnetic fields are developed by explosively compressing ordinary magnetic fields. A conducting cylinder containing an axial magnetic field is surrounded by a high explosive. The explosive is then detonated in such a way as to rapidly

collapse the cylinder and compress the magnetic field. A slotted, tapered flux concentrator on the axis of the cylinder forms a large axial gradient in the field. The large magnetic gradients thus produced can theoretically be used to accelerate diamagnetic particles. Magnetic flux densities exceeding 10 megagauss have been achieved and material has been accelerated. However, in light of the fantastic (multimegabar) pressures, it is extremely doubtful that anything other than a fast jet can emerge from the device. This, together with the cost and extreme destructive nature of the experiment, presently makes such a device appear unattractive as a useful accelerator.

Light Gas Gun. Much of the work involving meteoroid simulation can be done only with larger mass projectiles than can be accelerated with plasma drag techniques. The light gas gun is the most useful accelerator in the larger mass range. Uniform velocities are more readily attainable, particle integrity is more readily maintained, and diagnostics are more easily achieved. The principal drawback of the light gas gun is its limited velocity range. At present, velocities of 7.5 kilometers per second can be achieved routinely. The maximum velocities have been approximately 9 kilometers per second. In an effort to increase this velocity, Denver Research Institute has undertaken a velocity augmentation effort. A number of shots achieving velocities greater than 9 kilometers per second have been recorded. The maximum velocity so far obtained has been slightly in excess of 10 kilometers per second. This program is continuing in an effort to define the parameters affecting velocity so that higher velocities may be routinely achieved.

THEORETICAL AND EXPERIMENTAL TECHNIQUES

The approach taken to assure understanding of the impact problem is to combine experimental programs with our theoretical calculations so that the various necessary assumptions can be tested. In addition, empirical results have been invaluable in formulating engineering design criteria and for indicating areas of interesting theoretical study. It is necessary to pursue both experiment and theory because the highly complex, short-time scale interactions involved in a hypervelocity impact are generally far too complicated to be completely described theoretically. Spacecraft bombarded with impacting meteoroids that may be quite porous and fragile and which may have velocities several times faster than can be obtained experimentally requires that a plausible albeit simplified model be constructed to theoretically predict the salient features of the impact phenomena. The ability to interpret such phenomena will present a better understanding of meteoroid experiments and aid in designing future experiments that will give more information on the actual nature of the meteoroids as well as help in designing and evaluating various structures for their protective ability.

The theoretical problem is immensely complicated. Fortunately, substantial previous work has been done by the AEC in the area of solid state physics at extreme pressures. The equation-of-state data generated for many solids are fundamental to the impact problem. Energies of several hundred megajoules per kilogram are available at meteoroid velocities, which is several orders of magnitude higher than conventional explosive yields. On an atomic scale, several electron volts per atom are available which correspond to kinetic temperatures of hundreds of thousands of degrees. Pressures of tens of megabars are generated which are orders of magnitude higher than any material strength and greater than pressures at the interior of the earth. Under such extreme conditions, materials such as Fe or Al are compressed to twice their normal densities and are constrained solely by their inertia and in this sense behave as fluids. Thus, it is natural to treat such a problem by integrating the equations of fluid flow with appropriate boundary conditions. A technique for handling such a problem describes the material by a series of mass points that are moved through a Eulerian grid by satisfying conservation of energy and momentum. In this way, mass, energy, and momentum are transported. The general features of this technique are indicated in Table I and Figures 4 and 5. Such calculations have

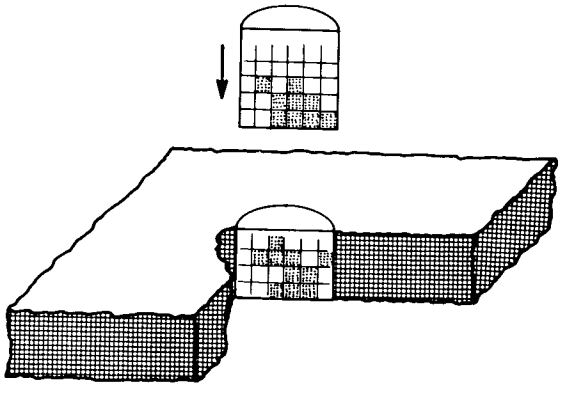

FIGURE 4. PARTICLE-IN-CELL (PIC) CODE TECHNIQUE

TABLE I. PARTICLE-IN-CELL CODE CALCULATIONS

INITIAL REQUIREMENTS

1. Set up grid cells
2. Represent undisturbed material by assigning an arbitrary number of mass points per cell
3. Assign impact velocity to mass points representing projectile

STEP I

1. Calculate cell pressures
2. From pressure gradients, calculate average cell accelerations
3. Calculate change of internal energy for cells from pressure and velocity changes
4. Use the rates determined in 2 above to predict new velocities at time Δt later
5. Use changes calculated in 3 above to determine new internal energies

STEP II

1. Using appropriate averaging techniques, determine an average velocity and an average internal energy for each mass point in each cell
2. Move each mass point by an amount Δt times the average velocity

STEP III

1. Count new number of mass points in each cell to determine new density
2. Sum momenta and internal energy to get new velocity and internal energy of each cell
3. Use equation of state to obtain new pressure for each cell
4. Repeat entire process by beginning Step I again

been carried out and yielded information concerning shock propagation and decay which were subsequently measured in the laboratory under a contracted program. The agreement was encouraging. Other transient phenomena such as crater growth, emission of photons, electrons, and ions, and rear-surface deformation and rupture are presently being studied to provide additional features that may be checked experimentally. New codes are being developed that describe the strength effects of the material after pressures have subsided to the point that strength becomes important. Such codes should be able to predict the final crater dimensions which present hydrodynamic codes cannot do.

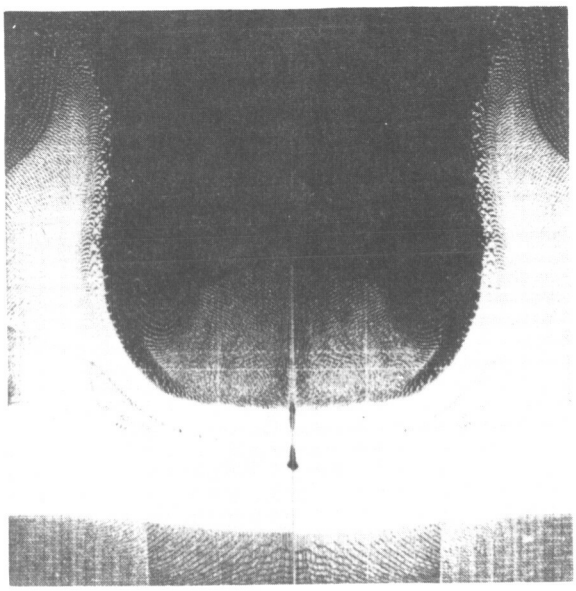

FIGURE 5. THE PARTICLE-IN-CELL METHOD

METEOROID ENVIRONMENT STUDIES

A definitive knowledge of the meteoroid environment in space can be gained only from in situ measurements of the environmental parameters. A detailed picture should include knowledge of the meteoroid mass distribution, the velocity distribution, and the physical characteristics. A flight measurement program must be supplemented by a ground-based measurements program and a laboratory program to obtain maximum information. An active program of flight measurements supported by a broad laboratory program is being conducted at the present time (Fig. 6).

PEGASUS

The Pegasus Meteoroid Satellite program was conceived and executed entirely at MSFC. A series of three satellites built under contract by the Fairchild-Hiller Corporation were launched on Saturn flights SA-8, SA-10, and SA-9 on February 16, May 25, and July 30, 1965, respectively. These satellites have been successfully returning data since that time. Figure 7 is an artist's conception of the Pegasus satellite in orbit. The extended wings are covered by capacitor detectors which produce an electrical signal when penetrated by a meteoroid. These signals are stored and later telemetered back together with additional information to aid in data

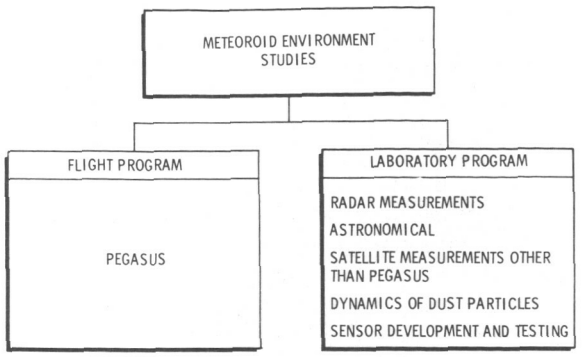

FIGURE 6. PROGRAMS TO DEFINE THE METEOROID ENVIRONMENT

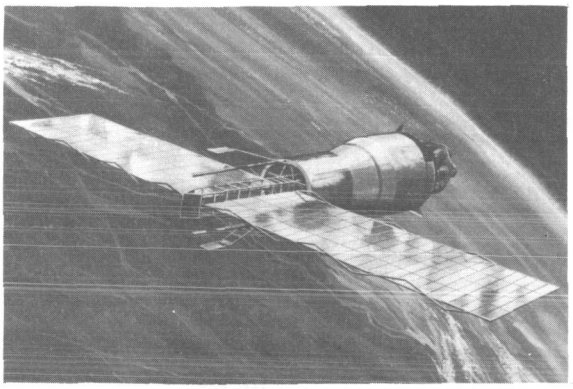

FIGURE 7. PEGASUS SATELLITE

analysis. The primary mission of the Pegasus Project is to measure the frequency of meteoroid penetrations through aluminum sheets of various thicknesses. At the present time, some data have been returned. The penetrating flux figures for the 0.4-, 0.2-, and 0.038-mm thickness target sheets that serve as the exposed faces of the detectors are tabulated in Table II. These data are plotted together with data from other satellites and from ground-based observations (Fig. 8). Other curves plotted in Figure 8 indicate earlier estimates of the meteoroid environment as derived from optical and radar measurements. The Pegasus satellites represent a highly successful program that promises to provide data of sufficient validity to revise our present picture of the meteoroid environment.

TABLE II. PEGASUS PENETRATION DATA

Thickness mm	Valid Penetrations	Area Time m^2 day	Flux No./m^2 day
0.4	180	44687	0.00402
0.2	45	2848	0.0158
0.038	344	2013	0.171

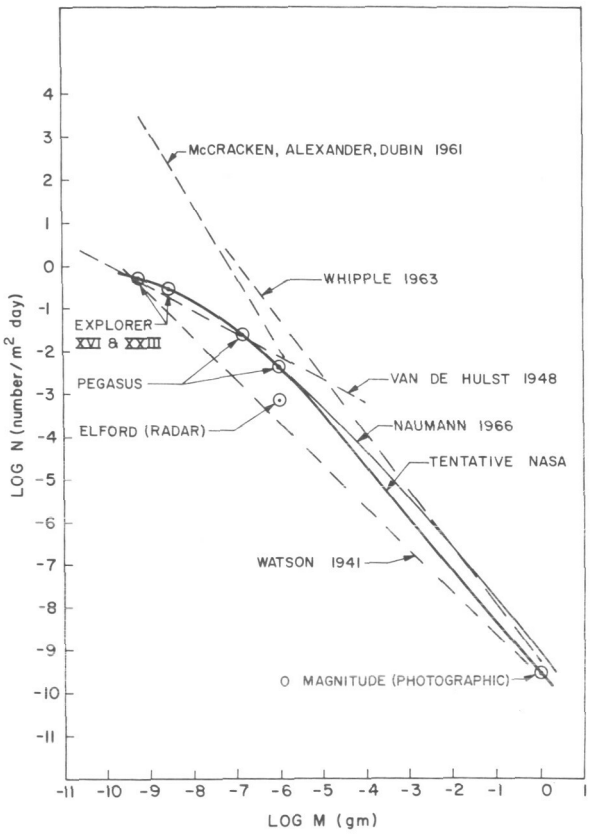

FIGURE 8. EXPERIMENTAL AND THEORETICAL METEOROID MASS FLUX

LABORATORY PROGRAM

A broad laboratory program provides support for the flight program. Data from other flight programs and from ground-based measurements are used to aid in analysis of Pegasus data. These data include those derived from radar measurements, astronomical measurements, and other satellites

such as Explorers XVI and XXIII. A sensor development and testing program is used to aid in calibration of detectors and in the development of new detectors. Theoretical studies of the dynamics of dust particles aid materially in understanding the derived data.

A contract with the National Research Council of Canada provides for reduction of available data from radar measurements. These data provide much useful information concerning temporal variations in meteoroid fluxes and can be used in assessing Pegasus data. They also provide data in a different size range than the Pegasus data and can thus be used to aid in completing the picture of the meteoroid environment.

Contracts with North American Aviation and Hayes International provide the means to determine the mass of a threshold penetrating particle for the Pegasus detectors. This represents information necessary to a comparison of Pegasus data with those derived by means of other detection techniques.

APPENDIX A

SELECTED PAPERS ON METEOROID PHYSICS PUBLISHED BY MSFC

1. D'Aiutolo, C. T.; Kinard, W. H.; and Naumann, R. J.: Recent NASA Meteoroid Penetration Results from Satellites. Presented to International Symposium on Orbits and Dust, Smithsonian Astrophysical Observatory, August 1965. To be published in Smithsonian Contributions to Astrophysics.

2. Dalton, C. C.: Statistical Analysis of Photographic Meteor Data -- Part I -- Opik's Luminous Efficiency and Supplemented Whipple Weighting. NASA TM X-53325, September 1965.

3. Naumann, R. J.: A Physical Basis for Scaling Hypervelocity Impacts. Proceedings of the Seventh Hypervelocity Impact Symposium, February 1965.

4. Naumann, R. J.: Pegasus Satellite Measurements of Meteoroid Penetration (Feb 16 - July 20, 1965). NASA TM X-1192, December 1965.

5. Stuhlinger, E.: Meteoroid Measurements with Project Pegasus. Presented to the Northeast Electronics Research and Engineering Meeting, Boston, Mass., November 1965.

APPENDIX B

CONTRACTOR REPORTS GENERATED UNDER MSFC SPONSORSHIP

1. Bjork, R. L.: Impact of a Porous Aluminum Projectile. Proceedings of the Seventh Hypervelocity Symposium, February 1965.

2. Chapman, R. L.: Meteoroid Impact Simulation by Magnetic Gradient Particle Acceleration Technique. Aerojet General Nucleonics AN-1490.

3. Charest, J.A.: Measurements of Shock Wave Pressures Generated by Hypervelocity Impact in Aluminum. General Motors TR-64-58, November 1964.

4. Cox, J. B.: Development of Particle-in-Cell Code. Brown Engineering Company, RPL-14000-1, January 1966.

5. Gould, M. J.: Meteoroid Penetration Distributed Transducer. Northrop Space Laboratories NSL 65-138-1, September 1965.

6. Meyers, C. L.; and Charest, J.A.: Research on the Properties of Optimum Meteoroid Shields. General Motors TR 64-48, September 1964.

7. Payne, J. J.: Impacts of Spherical Projectiles of Aluminum, Stainless Steel, Titanium, Magnesium, and Lead into Semi-infinite Targets of Aluminum and Stainless Steel. AEDC-TR-65-34.

8. Pjerrou, G. M.; and Farnham, J. F.: Development of a Micrometeoroid Accelerator. MB Associates MB-R-66137, February 1966.

APPROVAL

RESEARCH ACHIEVEMENTS REVIEWS
Volume I, Series 1 through 22

The information in these reports has been reviewed for security classification. Review of any information concerning Department of Defense or Atomic Energy Commission programs has been made by the MSFC Security Classification Officer. These reports, in their entirety, have been determined to be unclassified.

William G. Johnson
Director, Experiments Office